

Proceedings of the

68th DAE SOLID STATE PHYSICS SYMPOSIUM

December 18-22, 2024

Organized by
Bhabha Atomic Research Centre
Trombay, Mumbai, India

Editors
Jitendra Bahadur
Himal Bhatt
Ajay Singh
L.M. Pant

Sponsored by
Board of Research in Nuclear Sciences
Department of Atomic Energy
Government of India

ISBN: 978-81-967453-0-1



Proceedings of the 68th DAE Solid State Physics Symposium

December 18-22, 2024

Organized by
Bhabha Atomic Research Centre
Mumbai, India

Sponsored by
Board of Research in Nuclear Sciences
Department of Atomic Energy
Government of India

Editors

Jitendra Bahadur
Himal Bhatt
Ajay Singh
L. M. Pant

Title:

Proceedings of the 68th DAE Solid State Physics Symposium

Editors:
Jitendra Bahadur
Himal Bhatt
Ajay Singh
L.M. Pant

Copyright © Publisher

All rights reserved. No part of this book may be reproduced or transmitted in any form or by any means, electronic or mechanical, including photocopying, recording, or any information storage and retrieval system without permission, in writing, from the publisher.

Published by:
Scientific Information Resource Division
Bhabha Atomic Research Centre,
Trombay, Mumbai,
Maharashtra, 400 085 India
Email: headsird@barc.gov.in

Printed by:
Bhabha Atomic Research Centre,
Trombay, Mumbai,
Maharashtra, 400 085 India

Edition:
First Print: 2025

ISBN: 978-81-967453-0-1

Preface: 68th DAE Solid State Physics Symposium

The DAE Solid State Physics Symposium (DAE-SSPS) is one of the premier annual scientific gatherings in India, bringing together researchers working across diverse areas of condensed matter physics. Organized each year at different locations across the country, the symposium provides an important platform for scientists, faculty members, and research students to exchange ideas, present recent advances, and foster collaborations in various domains of condensed matter research. The 68th edition of the symposium, DAE Solid State Physics Symposium 2024 (DAE-SSPS 2024), was held at the DAE Convention Centre, Anushaktinagar, Mumbai, during December 18–22, 2024. The symposium was organized by the Bhabha Atomic Research Centre (BARC), Mumbai, under the auspices of the Board of Research in Nuclear Sciences (BRNS), Department of Atomic Energy, Government of India.

DAE-SSPS continues to be among the largest scientific events in the country dedicated to condensed matter physics. The 2024 symposium witnessed the participation of 680 registered delegates, including around 400 research students and 13 distinguished scientists from abroad. The scientific program comprised 7 plenary lectures, 40 invited talks, 28 oral presentations, 18 Ph.D. thesis presentations, and 15 Young Achiever Award presentations, in addition to 640 poster presentations. The scientific deliberations covered a wide spectrum of topics in condensed matter physics, including phase transitions and dynamics; soft matter including polymer and biological systems; nanomaterials; experimental techniques and devices; single crystals, glasses and amorphous systems; surfaces, interfaces and thin films; computational methods and electronic structure; dielectric, ferroelectric and piezoelectric materials; transport properties and semiconductor physics; magnetism and superconductivity; energy materials; and one-, two- and quantum materials. The symposium was inaugurated on 18 December 2024 by Suresh Gosavi, Vice-Chancellor of Savitribai Phule Pune University, Pune. L. M. Pant, Convener of DAE-SSPS 2024, welcomed the participants, while S. M. Yusuf, Director of the Physics Group at BARC, delivered the introductory address. An evening lecture on the topic “Intersection of Physics and Artificial Intelligence” was delivered on the opening day by Santanu Chaudhury of Indian Institute of Technology Delhi. The symposium concluded on 22 December 2024, with a comprehensive summary presented by S. M. Sharma, former Director of the Physics Group at BARC. In his concluding remarks, he highlighted the remarkable evolution of the symposium into an internationally recognized forum that continues to showcase significant scientific discoveries, emerging research trends, and notable achievements across the field of condensed matter physics.

We gratefully acknowledge the valuable guidance and support of the members of the advisory and organizing committees of DAE-SSPS 2024. We also extend our sincere appreciation to the members of the local organizing committee for their tireless efforts in ensuring the smooth conduct of the symposium. Our thanks are also due to the manuscript reviewers, members of the Young Achiever Award and Ph.D. thesis evaluation committees, and the poster reviewers for their careful evaluation and selection of the contributions.

We are pleased to present the Proceedings of DAE-SSPS 2024, which document a representative selection of the scientific contributions presented during the symposium and reflect the vibrant research activities in condensed matter physics.

Jitendra Bahadur, Himal Bhatt, Ajay Singh and L. M. Pant
Bhabha Atomic Research Centre, Mumbai, India

(Editors)

Table of content

Title	Authors	Page
Preface: 68th DAE Solid State Physics Symposium		
The Emergence of Density Wave and Supersolid Phases in Driven Optical Lattice	Sheshgiri S. Shettigar , Ramesh V. Pai	13
Topological Phases of Non-Linear 1D Kitaev Chain using Quench Dynamics	Rakesh Kumar Malakar, Rittwik Chatterjee, Asim Kumar Ghosh	16
Effect of TeO2/SeO2/Al2O3 on Thermal and Structural Aspects of LGS Glass-ceramics	Suresh Suragani, Hanumantha Rao Kotcharla, Venkata Sambasiva Rao Miriyala, Tirupataiah Chereddy	19
Orbital Magnetic Field Driven Phases in the Spin - 1/2 Falicov - Kimball Model on A Triangular Lattice	Swati Pandey, Umesh K. Yadav, Pradip K. Priya	22
Phase transition in Zr and Nb substituted Zr under pressure: Ab-initio study	B. D. Sahoo, K. D. Joshi	25
Topological Phase Transition in two-leg SSH ladder with Further Neighbor Hopping	Rittwik Chatterjee, Rakesh Kumar Malakar, Asim Kumar Ghosh	29
Interacting Gr$\ddot{u}$neisen parameters in the spin 1/2 XX chain extended with three spin interactions	Vrushali Kapase, Pradeep Thakur, P. Durganandini	32
Dynamic Structure Factor of Warm Dense Homogeneous1 Electron Gas	Priya Arora, R. K. Moudgil	35
Weak Field Induced Spin-Correlation In BaCo2(As1-xPxO4)2	Jai Dev, Shamma Jain, Surajit Sardar, Surinder Pal Singh, Pallavi Kushwaha	38
Nonequilibrium Work Fluctuations in Force-induced Melting of a Short B-DNA	S. Siva Nasarayya Chari, Prabal K. Maiti	41
Active Rod Inside a Rigid Ring Exhibits Non-Monotonic Tracer Dynamics	Vrinda Garg, Radha Raman, Baburao Simma, Surya K. Ghosh	44
Small Angle Neutron Scattering Study of Hydrophobic Silica Aerogels	A. A. Talkatkar, R. Raut Dessai, D. Sen	48
In-situ Fabrication Of ZnO@PVA Nanocomposite Film: A Flexible Free-standing Film With Antimicrobial Activity	Saiyad Akhirul Ali, Sarathi Kundu, Himadri Nath, Aditya Narayan Konwar, Debajit Thakur	51
Cholesterol-induced Modification in Lysozyme-DMPA Mixed Langmuir Monolayer	Himadri Nath, Sarathi Kundu,Saiyad Akhirul Ali	54
Statistical Properties of Passive, Self-Propel and Janus Particle in Ordered Crowding	Baburao Simma, Vrinda Garg, Surya K. Ghosh	57
Percolation/Relaxation Behaviour Of Cold Pressed PVDF/CoFe2O4 Polymer Nanocomposites	Harsha Chouhan, Maheswar Panda	60
Micro-scale Dynamics in Disordered Polymers and Gels Influences Macroscale Response	Debjani Bagchi, Shipra Bhatt, Tithi Joshi	64
Miscibility, Compatibility and Intermolecular Interaction Analysis of Oxypropylene Blends with Isobutene and Acrylonitrile	Mandakini Bara, Padmaja Patnai, Dipan Kumar Das, Santanu Kumar Nayak	67
Electronic and Optical characterization of polypyrrole thin films: A UV -Visible Absorption Study	Lincy K Alex, Lakshmi Vijayan	70
Recycling of medical face mask waste to an engineering materials: A study on the nonwoven polypropylene nitrile rubber blend	Satyabrata Sahoo, Smita Mohanty, Sanjay K. Nayak	73
Development of Sustainable Absorbent Wheat Gluten-Based 1 Composition: Evaluation of Properties	Roshni Pattanayak, Swayam Pragyan Behera, Sukanya Pradhan, Smita Mohanty	76
Optimal Transport conditions of a Run and Tumble Particle in a Ratchet potential	Arjun S R, Ronald Benjamin	80
Synthesis and Characterization of Anatase Phase Nanocrystalline-TiO2 by Hydrothermal Method	Nidhi Garg, Lori Rastogi, Arup Dasgupta	83
Augmented field emission properties from MoO3 rods derived via chemical route	Anima Mahajan, Menaka Jha, Santanu Ghosh	86

Structural, Magnetic, and Raman Analysis of Strontium-Doped Nickel-Zinc Nano Ferrite	Hanamanta Badiger, B.G. Hegde	89
Chemical Synthesis, Characterization And Magnetic Behavior Of NiLaxFe2-xO4 (0 \leq x \leq 0.3) Nanomaterials	Rajshekhar Balagi, R. N. Panda	92
Optical Characterization of Hydrothermally Synthesized Quantum Dots: Insights and Analysis	Avinash Kumar, Ishant Kumar, Sandeep Kumar, and Arvind K Gathania	95
Graphene Nanoplatelets Reinforced Polyvinylidene Fluoride-Hexa-Fluoro Propylene 1 Nanocomposite for Potential Electromagnetic Interference Shielding Applications	Gayathri Thanasekaran, M. Vijayajayanthi	98
Influence of Electrolyte in enhancing the electrochemical performance of polyaniline-based electrodes for supercapacitor	Amisha, Aman Deep Acharya Yugesh Singh Thakur	101
Impact of Site-selective Carbon Doping in Tuning the Spectral Features of Triangular-shaped Boron Nitride Quantum Dots	Aathira Haridas, Tushima Basak, Tista Basak	104
Synergistic Electrochemical Performance of MoSSe@CoMoO4 Composite as Advanced Supercapacitor Electrodes	Poonam Lakhiwal, Santosh Kumar Mahapatra	107
Room Temperature Synthesis of Ag@Au Core- Shell Nanostructures by Controlled Transmetallation Reaction	Krishnaprabha M, Manjunatha Pattabi	110
Synergistic Effect of Silver Nanoparticles on Magnetic Hyperthermia of Fe3O4 Nanoparticles	Ishu Attry, Pooja Jarora and Bhupendra Chudasama	113
Magnetic Properties Of CoCrxFe2-xO4 Nanomaterials Synthesized By Sol-Gel Autocombustion Route Using Double Fuel (Citric Acid And Glycine) Approach	Anagha B. Patil[1] and Rabi N. Panda	116
Influence of Annealing Temperature on Structural, Morphological and Optical Properties of Î²â^'Ga2O3	Abhishek Sharma, Kartikay, Tulsi, Saumya Chauhan, Shreya Thakur, Aman Bhalaria, and Vir Singh Rangra	120
Site-Selective Photoluminescence and Multi-Color Emission via Vis/NIR Dual Mode Excitation of Rare-Earth Doped Inorganic Nanophosphors	Ib Singh Deo, Mohini Gupta, and G. Vijaya Prakash	123
AuNPs@Ag Nanodendrites for Volatile Organic Compound Detection based on Surface Enhanced Raman Scattering	V.S. Vendamani, S. Venugopal Rao	126
TiO2 Nanotubes and rGO Nanocomposite Integrated Electrochemical Sensor for Cd2+ Ion Detection	Dasari Swarna, Sushma Tripathi, Anjana Biswas and Prathibha C.	129
Tuning of Structural and Magnetic Properties of MnFe2O4 Nanoparticles Through Cerium Ion Substitution	Bhaskar Pandey, R. C. Srivastava H. K. Verma and C. S. Joshi	133
An Electrospinning Approach Towards the Production of Bio Degradable Mulch Films	Sayana K V, Vishwanath T	136
Temperature Dependent Tunable Optical Property Analysis of In2Se3 Thin Films	Mukesh Mishra and AgniKumar G Vedeshwar	139
Cross-sectional Transmission Electron Microscopy Study of As-grown CuO nanowire Sample Synthesized by Thermal Oxidation Method	Pabitra Sahu, Himanshu Srivastava, Mahendra Babu, Pragya Tiwari and A.K. Srivastava	142
Investigation of the effect of gamma irradiation on the structural and magnetic properties of Ni-Co ferrite/graphene oxide nanocomposite	H. K. Verma, R. C. Srivastava, C. S. Joshi and G. C. Joshi	145
Antibacterial and Photocatalytic activities of g-C3N4/STO for biomedical and Water treatment application	Tusharkanta Nayak, Debashish Nayak, Deviprasad Sahoo, T M Naren Vidaarth, Smita Mohanty, and Akshaya K Palai	149
Reduced Graphene Oxide Using Graphene by Modified Hummer Process	Nileema Patil, J. R. Mahajan	152
Increased Defect Sites and Enhanced Fluoride Adsorption by Nanocomposite of Silver Oxide and Hydrogen Tri Titanate Nanotubes	Prathibha C., Anjana Biswas, Dasari Swarna, Sushma Tripathi	155

Exploring the Electronic and Optical Properties of Armchair SiC (8,8) SWNTs Using First-Principles Calculations	Nibedita Nayak, Santanu Kumar Nayak, Dipan Kumar Das and Padmaja Patnaik	158
Degradation studies of Dichlorvos Pesticides using Copper Nanoparticles	Chetan Pant, Divyanshu Pant, Deepak Chauhan and Puja Goel	161
Phonon Confinement and Size Effect in the Raman Modes of K0.5Na0.5NbO3 Lead-free Ceramics	Manish Saha, Saket Asthana and Manish K. Niranjan	164
Mixed State of rGO/GO for Efficient Removal of Cadmium Ion from Water	Sushma Tripathi, Dasari Swarna, Anjana Biswas and Prathibha C.	167
Synthesis of polymer functionalized manganese iron oxide nanoparticles by using thermal decomposition method in magnetically activated hyperthermia therapy	Satish S. Phalake, Vishwajeet M. Khot	170
Hydrothermally Synthesized Titanium Dioxide Nanorods Assembled in Rice Ball Morphology for Application in Ultraviolet Light Detection.	Vishakha Zimba, Brahmamaya Sahu, N. Meghana, Jhasaketan Nayak	173
Enhanced Room Temperature Ammonia Gas Sensing in La Doped ZnO Nanorods	Manami Midday, Abhinav Mahapatra, Priyanshi Tiwari, R.S. Ajimsha, Pankaj Misra	177
Exploring Gold Nanoparticle Morphologies for Enhanced Surface-Enhanced Raman Scattering (SERS) Applications	Sneha Senapati, Arvind Kaushik and J.P. Singh	182
Solution-Processed CdTe Nanoparticle Memory Device	Himanshu Marothya, Atul Sachan, Vishwas Acharya and Sandip Mondal	187
Zinc Ferrite/Polyaniline Nanocomposites for High-Capacity Energy Storage	B. M. Bangalkar, R N. Kambale, Y. S. Waghode, S Habibuddin, V. A. Bambole	190
Green Route Synthesis of CuO Nanoparticles utilizing Trema Micrantha Leaf Extracts.	Vrushali Raut, Jui Tambe and Trupti Chavan	193
Study of Structural, Morphological and Optical Properties of CuS Nanomaterials	Priya Chandra, K. S. Ojha	197
Thorough Structural Analysis of MACE-grown SiNWs and Its Future Prospectives	Anand Kumar, Avadhesh Kumar Sharma, Kapil Saxena	201
Mechanical property evaluation of Alloy 690 at different strain rates and temperatures	Sagar Chandra, Sudhanshu Sharma, Ather Syed, N Naveen Kumar, Mahendra K Samal, Vivek M Chavan	204
Study of effect of loading rate on plastic deformation behaviour and fracture toughness of SA516Gr70 steel	Sudhanshu Sharma, Ather Syed, Mahendra K Samal, Vivek M Chavan	207
On the Optical Response of a MgZnO/ZnO HEMT	Saheb Chakraborty, Radha Raman Pal and Sutanu Dutta	210
On the Thermal Sensitivity of a GaN MODFET for High Field application	Prabir Kumar Shit, Radha Raman Pal, and Sutanu Dutta	213
A Method of aligning CNTs in nanocomposite polymer films	Bhakti Hirani and P.S. Goyal	216
Fabrication and Application of P(VDF-TrFE) Copolymer Films for X-ray Detection in Synchrotron Radiation Sources.	S.R. Kane, S. Satapathy, Ajit Kumar Singh, P.K.Jha, P.K.Mehta	219
Development of Nanocomposite Films having Low Dielectric Constant for Microelectronics Applications	Deepali Shrivastava, P S Goyal, S K Deshpande	222
First Results of Single Grating Based Multi-contrast X-ray Imaging Technique at Imaging Beamline of Indus-2	Balwant Singh, Ashish K. Agrawal, Yogesh S. Kashyap, Payal Singhai and Mayank Shukla	225
Vertically Aligned Hexagonal MoSe2 Nanoflakes for Supercapacitor Applications	Akshay Tomar, Prachi Gurawal, and Ramesh Chandra	228
Mathematical Modeling of Vertical Focusing Monochromator	Venkateswara Rao G, A.D.Patil and Sameer Bhatt	231
Visible-light Effect on CV-Characteristics in Transparent MOS Device	Moumita Indra and Sandip Mondal	234

Comparative Study of BF3 Based Neutron Detectors with Cylindrical and Cuboid Geometry Using COMSOL and FLUKA Software	Arkaprabha Bhowmik, Shraddha S Desai, Shylaja Devan, Mala N. Rao	237
Design of Enclosure Chamber of Large 2D PSD for SANS Diffractometer at Dhruva Reactor	Shraddha S Desai, Saurabh Gupta, V K Shrivastava, Mala N Rao, V K Aswal	240
Conceptual design of an innovative shock absorber for possible application in Dhruva reactor	J. V. Mane, S. Sharma, J. S. Misal, K. K. Verma, S. Chandra, V. M Chavan	243
Sealed D-T Neutron Generator for Borehole Logging and Bulk Material Characterization	Prashant Singh, Mayank Shukla, Tushar Roy, M.R. More, Shefali Shukla, Ravi Baribaddala and Yogesh Kashyap	246
Temperature dependent electrical transport properties of W/WS2 junction	Prachi Gurawal, Somdatta Singh, Akshay Tomar, Vivek K. Malik, and Ramesh Chandra	249
Efficient Transmission Gate with Charge Plasma Doping: A Simulation Study	Gagan, Himanshu Marothya Devender Kumar Soni and Vishwas Acharya	253
micro-Kelvin Laboratory at BARC for Physics Research at Ultra Low Temperature	Neetesh Cheeta, Anil Kumar, D Sarkar, K Dutta, S K Gamre, K M Rajbhoj, I B Thapa, R Pradeep, H H Patil, D Karmakar, Jagannath, L M Pant	256
Analysing the changes observed in Neutron diffraction peaks of Cs6H(HSO4)3(H2PO4)4 crystal as it undergoes Deterioration	Rajul Ranjan Choudhury and R. Chitra	260
Investigating the Role of Strontium on the Bioactivity of Silicate Glass and the Effect of Doping Fe	S. Rane and R. Raut Dessai	264
Growth of single crystal diamond substrates via welding assisted microwave plasma enhanced chemical vapour deposition	Khyati Upadhyay, Abhay Dasadia, Jordan Moshcovitis and Vanaraj Solanki	267
Single Crystal Growth of Sn doped Ca2RuO4 using Optical Floating Zone Technique	N. Budania, B. C. Sahoo, A. Jain, S. M. Yusuf	270
Soft x-ray energy calibration in bl-03, Indus-2 with an in-house grown potassium acid phthalate crystal	Shruti Gupta, Rajkumar Gupta, Praveen K.Yadav Amit Saxena, Rajeev Bhatt, Indranil Bhaumik, and Mohammed H. Modi	274
Evaluation of Light Induced Metastable Defects in Se90Ag6Sb4 Amorphous Chalcogenide Thin Films by Space Charge Examination	Anjani Kumar, S. Shukla, Prince K. Singh and Rajeev Gupta	278
Silicon Surface Energy Modification Using UV, IR Laser and RF Plasma Exposure	Bijay Verma, Praveen K. Yadav, Manoj Kumar Singh, Mohammed H.Modi and A.K. Choubay	281
Modifications Of The Structural, Electronic Structure and Magnetic Properties of PrVO3 Thin Films By 100 MeV Au Ion Irradiation	Shivank Kalia, Pankaj Bhardwaj, Varun Ranade, Keun Hwa Chae, Rajesh Kumar and Ravi Kumar	285
Fabrication of Al2O3 Nanopore By Anodization Technique for SERS Application	Najmeh H. Dehkordi and Rajeshkumar S. Hyam	289
Towards Sustainable Construction Materials: CO2 Sequestered M-Sand-Cement Blocks	Md Zamil Hasan Shovon, Vasanthmani I., Arunachaleshwar V, Malavika Sunil and B. M. Jaffar Ali	291
Trap Dynamics in ALPO Capacitive Devices	Atul Sachan, Sandip Mondal	294
Effect of Stacking of Layers and Variation of Ag Layer Thickness in (Cu, Al)-SnO2/Ag Layer on Optical and Electrical Properties	Anju Dutt, Harpreet Singh, Sangeeta, Anand Kumar	298
Structural and Optical Properties of Reactively Sputtered Nanostructured NiO Thin Films for NO2 Gas Detection	Debarati Bhattacharya, Amrita Das, Sipra Choudhury, Swapan Jana,	301

	Kailasa Ganapathi, Vijay Karki, S.K. Ghosh and Surendra Singh	
Interfacial Free Energy of Solid on Solid fcc Cu/fcc Pb Interface: A Molecular Dynamics Study	Ankosh D. Deshmukh, Abhik Choudhury, Saswata Bhattacharyya, Gandham Phanikumar, M. P. Gururajan and Vaishali Shah	304
Ultra-Broadband Resistive Microwave Meta Absorber for Stealth Technology	Priyanka, Himanshu B. Baskey, Prashant S. Alegaonkar	307
Effect of Post Deposition Annealing Temperature and Duration on Structure of DC Sputtered Sn Films	Damu V. Rupnar, D. Goyal, M. Kaur, P. Sarawade, Niranjan S. Ramgir	311
Structural and Optical Properties of NiO Thin Films Deposited Using Ni Pellet by PLD Technique with Varying Laser Energy	Kartikey Bhardwaj, Vipul Rastogi and Anirban Mitra	314
Low interface trap states in Solution Processed Silicon-Graphene oxide stacked MOS Device	Vishwas Acharya, Atul Sachan, Sandip Mondal	317
Theoretical Insights Towards Interfacial Engineering And Device Optimization Of CH3NH3SnI3 Perovskite Solar Cells By SCAPS-1D	Arushi Sharma, Himanshu, Ekta Yadav, Kamlesh and M.S. Dhaka	321
Synthesis of Tungsten Carbide Thin Film by Ion Beam Sputtering	Rajnish Dhawan, Abhay Bhisikar, Maheswar Nayak	324
Fabrication and Characterization of Thin Film Coating on Large Area for Development of X-ray Mirrors	Faiyaz Mollick, Jitendra Kumar, Maheswar Nayak, P.K. Gauttam, V. K. Raghuwanshi, S. R. Kane, Pooja Gupta and Nageswara Rao Pothana	327
WS2-Ag Nanocomposite-based SERS Substrates with an Ultralow Detection Limit for Pesticide Thiram	Arvind Kaushik, Sneha Senapati, J.P. Singh	330
Surface studies of Non-evaporable Getter thin film	Nidhi Gupta, Kaushik Dutta, Jagannath	334
Molecular Engineering and Investigation of Novel Donor Molecule Based on [D-Ï€-D] Type Architecture	Ankit Kargeti, Shamoon Ahmad Siddiqui, Tabish Rasheed	336
Ab initio Study of Intermediate Band Solar Cell Material: V Substituted MgSnP2	G. Kruthika, and P. Ravindran	339
Molecular dynamic study of dental material TEGDMA with 1% gold nanoparticles.	B N Amruth, H Somashekarappa, M Maurya, M B Nandaprakash and R Somashekar	342
Electronic Structure and Thermoelectric Properties of Single-layer 1D and 2D MoS_2	Poulami Biswas and Molly De Raychaudhury	346
Thermodynamic Properties of Small Aluminum Clusters	Amit Kumar, Balasaheb J. Nagare, Raman Sharma, and Dilip. G. Kanhere	349
Structural and Optoelectronic Properties of Monolayer ScBiS3 under Pressure: A First Principle Approach	Riddhi Desai, Yashasvi Naik, H. P. Patel and P. B. Thakor	352
Tuning MXene Monolayer via -OH Functionalization: DFT Insights into Structural and Optoelectronic Properties	Nidhi Modi, Yashasvi Naik, S. J. Khengar, D. B. Shah, and P. B. Thakor	355
A DFT study of electronic, optical and mechanical properties of LiBaBr3 perovskite for opto-electronic applications	Anuradha, Sunil Kumawat and Gunjan Arora	358
A DFT Study on Optoelectronic Properties of GaAlS2 Homo-bilayer	Disha Mehta, Yashasvi Naik, Nidhi Modi, P. R. Parmar, and P. B. Thakor	361
MgClBr vdW homobilayer as a promising UV-light detector	Yashasvi Naik, Disha Mehta, H. R. Mahida, Riddhi Desai, and P. B. Thakor	364
Quantum Computation of Small Atomic Clusters Using Subspace-Search Variational Quantum Eigensolver	Kaushik Das, Narender Paul and Ashok Kumar	367

CdS-Janus van der Waals Heterostructure for Green Hydrogen Fuel Production	G. Tejaswini, Anjana E Sudheer, M. Vallinayagam, M. Posselt, S. Mani Prakash and D. Murali	370
Study of mechanical properties of nanowires(Ni,Cu,Ag) using classical molecular dynamics simulation	Mohd Hassanain, Narender Paul and Ashok Kumar	373
Structural, Electronic and Thermal Stability of Janus Silicene monolayers: First-Principles Study	Kamal Dev, Manish Patial, Ishan Kaundal, Kritika Thakur, Arun Kumar	376
Experimental and DFT studies on Cubic Structured Ô‘-FeSi Semiconductor	Hanna Shirin P H, Hashir P, P P Pradyumnan	379
Investigation of native defects on the PbIBr Janus monolayer: A DFT study	Aditya Shankar, Anjana E Sudheer, G. Tejaswini, D. Murali, M. Posselt	382
A Review of Theoretical Approach to Study the Anomalous Behaviour of Strongly Correlated Heavy Fermion System	Namita Shadangi, Prayasha Satpathy	385
Investigating the mechanism of magnetic moment suppression in Quaternary Heusler alloy CoCrVAl	Ataur Rahman and Jagdish Kumar	389
Enhancement of Relaxor Properties in NKBT via BMN Additive	Ranjan Kumar Sahu, Saket Asthana	392
Insight into the electrical properties of Ni doped SrBi2Nb2O9 Aurivillius ceramics prepared through microwave sintering method	Anurag Pritam	395
Wind Energy Harvester Based on Electrospun CNT/DNA Doped Poly(vinylidene fluoride co hexafluoropropylene) Composite Nanofibers	Priti Sundar Barman, Prakriti Adhikary	398
Comparative Simulation of Piezoelectric Output at Different Inclinations in ZnO, BaTiO3, and PZT-4 Nanorods for the Development of Tactile Sensors	Laishram Anamika Devi, Aparna Singh, and Pramod Kumar	401
New Oxygen Deficient Double Perovskite Ceramic Compound: YSrCuFeO5	Rashmi Rekha Sahoo, R.N.P. Choudhary	404
Investigation of structural and dielectric studies of Ho substituted Nd2CoMnO6 Double Perovskite compounds	Nibedita Nayak and S. Ravi	407
Tailoring the Electrical Properties of [0.98KNLNS-0.02BNZSH] Lead-Free Ceramics through Variation in Sintering Temperature.	Aditi, Amit Kumar, V.Kumar	410
Ce and Bi Doped BCZT Based Lead-Free Ceramic: A Material with High Dielectric Constant	Bhawna, Sapna Kumari, V. Kumar	413
Synthesis and Characterization of Eco-friendly NiFe2O4 Octahedrons Spinel Ferrite for Multi-Faceted Applications	Dharti J. Tank, Ved B. Bharadva, Chetna C. Chauhan and Abhishek A. Gor	416
Fabrication and Characterization of Barium Hexaferrite Film Based Device for Neuromorphic Applications	Ved B. Bharadva and Dharti J. Tank, Abhishek A. Gor	420
Near Room Temperature Dielectric Relaxation in Lead Free 0.67BiFeO3-0.33BaTiO3 (BF-33BT) Piezoceramic	Samanway Mohanta, Koushik Dey, A. Tripathy, Ashutosh Anand, D. Kumar, V. G. Sathe, D. K. Shukla	423
Multiferroicity and Magneto-capacitance in BaTi1-xFexO3-Î´(x= 0, 0.02, 0.1, 0.15 and 0.2)	Arunangsu Banerjee and Subhajit Sarkar	426
Variation In Dielectric Properties Of Sm^{+2} Doped Lead Titanate Prepared By High Energy Ball Milling	Sona Kumari, R.K.Chaudhary and S.K.Sinha	430
Investigation of Charge Transport Properties of RGO-CuSe-Based Schottky Diode by Tuning Graphene Content	Mainak Das, Dhananjoy Das, Supravat Ghosh and Partha Pratim Ray	433
Electron-Phonon Interaction Effects on Electronic Transport in â€œBiteâ€• Defective Graphene Nanoribbons	Sandeep Kumar	436
Novel TCAD Approach Precisely Simulating Charge Collection Efficiency of 4H-SiC Alpha-particle Detectors	Vivek Jaiswal and P. Vigneshwara Raja	439
Thermal Annealing Induced Enhancement of Electrical Performance in PDMS Assisted Exfoliated multilayer MoS2 based Field Effect Transistor	Samiksha, Ramesh Singh Bisht and Pramod Kumar	442

Co-existence of ferro-antiferromagnetism and transport properties in full Heusler alloy Fe2MnAl	Aparna Ashok and Neeru Bhagat	445
Vertical Schottky Barrier Diodes fabricated from ZnGa2O4 epilayer grown by MOCVD	Siddharth Rana, Fu-Gow Tarntair, Ray Hua Horng and J.P. Singh	448
Invar Behavior In Nearly Stoichiometric TiFe2	Myren Azavedo, and K. R. Priolkar	451
Exploring 3d transition metal substituted MnCo0.7Fe0.3Ge	S. Shanmukharao Samatham, Sateesh Pinninti, Akhilesh Kumar Patel, Gowrinaidu Babbadi, Ch. Komala Lakshmi, Ramachandra R. K, M. Chandra Sekhar, Nataraju Gandla, Sankararao Yadam, K. G. Suresh	454
First-principles study of the electronic structure and magnetism in highly frustrated two-dimensional magnet CsTbSe2	Kuldeep Kargeti, Shovan Gayen, and S. K. Panda	457
Role of Magnetic field on Electronic Specific Heat of Anderson Lattice Model: An Application to Colossal Magnetoresistive Manganites (Re1-x A x MnO3)	Sunil Panwar	460
Structural and Magnetic Properties of the Cluster-Glass Phase of Pseudo-1-D Spin-Chain Compound Ca3Co2O6	Amit Maurya, D pal	463
Edge States for a Ribbon Oriented in the Diagonal Direction in 2D Antiferromagnetically Ordered Semimetals	Garima Goyal and Dheeraj Kumar Singh	466
Structure, Morphology and Magnetic Properties of TmCrO3	Vishesh Sharma, Sumit Pokhriyal, Darren M. Stohr, Awanish Kumar Sharma, N. P. Lalla, and Shivani Sharma	469
Large Magneto-caloric Effect near Room Temperature in Ni37Co13Mn34Ti16 alloy	Sandhya Negi, Anil Chouhan, Abhijit Chowdhury, Rashmi Singh and Vishnu Kumar Sharma	472
Beyond ferromagnetic resonance: Effect of inertia tensor on dynamic susceptibility.	Subhadip Ghosh and Ritwik Mondal	475
Characterization of CeO2 Nanoparticles with Er3+ Doping: 1 Insights from X-ray Diffraction to Magnetic Behavior	R. Niruban Bharathi and G. Rekha	478
Exploration of Structural and Magnetic Properties of Nd-doped LaCrO3	Kousik Sutradhar and D. Pal	481
Structural and Magnetic Properties of Sm2FeCrO6	Meenakshi, Ramovatar, Surendra Kumar	484
Inhomogeneous Melting of Vortex Lattice in Superconducting thin Films of MoGe	Rishabh Duhan, Subhamita Sengupta and Pratap Raychaudhuri	487
Low Frequency Electrodynamics of A Pinned Vortex Liquid	Subhamita Sengupta, Sitakanta Behera, Rishabh Duhan and Pratap Raychaudhuri	490
Synthesis and Structural Study of Pre-lithiated Silicon Anode in Different Atmospheric Conditions	Ashish Kumar Mishra, Monika, Anjali and Balbir Singh Patial	493
Exploring ZnFe2O4 Hollow Microspheres as Supercapacitor Electrode Material	Moisilee Dutta, Priyanka Saha, Rituparna Mondal and Sanjay Kumar	496
Effects of different mass loading of La2NiCrO6 on the electrodes in supercapacitor performance	I. Ajin and A. Chandra Bose	499
Impact of Electrolytic Cations in the Pseudocapacitive Performance of SrFeO3-Î´	T. Lavaneethan, I. Ajin, and A. Chandra Bose	502
Rod-shaped nanostructured Mn-doped CuO Electrocatalyst for oxygen evolution reaction	Afreen A. Chaudhary, Dushyant C. Kothari and Pradip B. Sarawade	505
Effect of Addition of Pb3O4 on the Energy Release of Al/CuO Nanothermite	Rahul, K. K. Sharma and Vimal Sharma	508
Examining potential of Mn0.7Zn0.3Fe2O4 Solid Microspheres as Supercapacitor Electrode Material: Study on its Electrochemical Performance	S. Gazi, P. Saha, K. Sarkar, R.Mondal, S. Kumar	511

Relaxor SBT/PVDF-HFP Ferroelectric Flexible Films for Energy Storage and Harvesting Application	Lalit Kumar Jena, Saket Asthana	514
Study of Nickel Cobalt Oxide as an Electrocatalyst for Oxygen Evolution Reaction in a Wide Range of Alkaline pH	Manjiree Thakur, Dushyant C. Kothari, Pradip Sarawade	518
Li7La3Zr2O12: A Solid - State Electrolyte For Thin Film Batteries	Anjali, Weon Cheol Lim, Aditya Sharma, Moditma, Sangsul Lee, Hyun Joon Shin, Keun Hwa Chae and Jitendra Pal Singh	521
SrMnO3 Perovskite Nanoparticle Embedded in NiCo2O4 Nanoflower as Electrocatalyst for Oxygen Evolution	Poonam Mor, Krishna Kanta Halder, Sourabh Barua	524
Two-Dimensional Be2P4/BP Heterostructure as an Anode Material for Sodium-Ion Batteries	Nidhi Verma and Ashok Kumar	527
Electrochemical Synthesis Of Nickel Hydroxide, Cobalt Hydroxide And Their Layered Double Hydroxide For Supercapacitor Application	Neha M. Phadte, RajeshKumar Shankar Hyam	530
Exploring Supercapacitive property of MoS2/g-C3N4 composites on Screen-printed Carbon Electrode	Ragini Chaturvedi, Amit Garg	533
Modulating Perovskite Stability Through Incorporation of 2D Spacer Cations for Solar Cell Application	Km Sakshi, Abhimanyu Singh Rana and Soumyendu Roy	536
Bifunctional NiSe2 Nanoclusters for Supercapacitor and Photocatalytic Dye Degradation Applications	Ravi Pratap Singh, Prashant S. Alegaonkar, Kamlesh Yadav	539
Co-precipitation Synthesis of Cobalt Ferrite (CoFe2O4) Nanoparticles and Their Supercapacitor Applications	Daud Ahmad Ansari, Mehraj Ud Din Rather, Sharika Afreen and Shahid Husain	542
Functionalisation of Selenium monolayer with Platinum dichalcogenide for the green Hydrogen production	Anjana E Sudheer, Golla Tejaswini, D Murali, and Matthias Posselt	545
Enhanced Photo catalytic Performance of MoS2/bg-C3N4 Hetero-structures for Hydrogen Evolution Reaction: A First-Principles Study	Chet Ram, Vaishali Thakur, Bharti Thakur, Pitamber Kumar, Abhishek Chandel, Anjna Devi, Yogyata Pathania, Surjeet Kumar, Pushpender Singh, Arun Kumar	548
A First-Principles Study of Structural and Electronic Properties of 2-Idoethylammonium Lead Iodide Perovskite	Ritika Negi, Anjali, Nitika Ranpatia, Diya Sharma, Monika Chandel, Yogyata Pathania, Anjna Devi, Surjeet Kumar, Arun Kumar	551
Impact of Heat Treatment on Phase formation and the Transport Properties of AgSbTe2 Thermoelectric Materials	S Asha Bhandarkar, Poojitha G, Ashok Rao and Anand Pal	554
Study on Electrochemical Performance of Glass-Ceramics Based Composite Solid Electrolyte for Lithium Battery	Anurup Das and Madhumita Goswami	557
Synthesis and characterization of MnO2 for high performance supercapacitor electrode application	Shameela P, Fuad Hamdi K, Maneesh Chandran and P. Muhammed Shafi	560
CdSe Quantum Dot Synthesis and Application in Quantum Dot Dye Sensitized Solar Cell	Yugandhara S. Waghode, Bhagyashri Bangalkar, Syed Habibuddin Syed Abed Ali, R N Kamble, R R Kalesh, Vaishali A Bambole	563
Synthesis of MoS2 Thin Films from Bulk-like to Monolayer and Their Valence Band Offset with SiO2 Interfaces	U. K. Goutam, Jagannath, Jyoti Prakash, D. Bhattacharya and L. M. Pant	567
Photocatalytic Degradation of Methyl Orange Using Borophene/TiO2 Quantum Dots Nanocomposite Under UV Light Irradiation	Akanksha Pandey, Tanuja Mohanty	570
Exploration of Hydrogen Decorated Two-dimensional Graphullerene: a First Principle Investigation	Satish Kumar, Monika Gupta, Sanjeev Thakur, Reena Kumari, Anjna Devi, Sheetal Dhiman, Monika Chandel, Arun Kumar	573
Investigation of structural, morphology, thermal, and magnetic properties of Ni0.90Cu0.10Te2 single crystal	Rajkumar Sokkalingam and Arumugam Sonachalam	576

First-Principles Study of Optoelectronic and Photocatalytic Properties of Two-Dimensional AlAs/SbI3 van der Waals Heterostructure	Ramandeep Singh, Poonam Chauhan, and Ashok Kumar	579
Tunable Electronic Properties of Dirac Cone Square Tellurene(Ïf-Te2)	Ritika Rani, Ankush Bharti, Narender Paul and Raman Sharma	582
Two-dimensional van der Waals Electrical Contact of Janus MoSSe with Dirac Semi-Metal FeB2 Monolayer	Ankush Bharti, Ritika Rani, Jaspreet Singh, Ashok Kumar, Rakesh Rathore and Raman Sharma	585
Electron and Phonon Hydrodynamics in Graphene	Subhalaxmi Nayak, Cho Win Aung, Thandar Zaw Win, Ashutosh Dwibedi, Sabyasachi Ghosh, Sesha Vempati	588
Electronic, Mechanical and Electron Transport Properties of 2D Penta-Si3P2S Monolayer	Sangeeta Meena, Ramandeep Singh, Nidhi Verma and Ashok Kumar	592
Effect of Residual Oxygen in Atmospheric Pressure Chemical Vapor Deposition growth of monolayer MoS2	Shubham Mingwal, Himanshu Srivastava, Rahul Aggarwal, A.K. Srivastava and Pragya Tiwari	595
MoS2 Nanostructures for Selective Detection of 2,5-Dimethylfuran: A Potential Breath Test Marker for Lung Cancer	Saransh Chanouria, Nikhil Kumar, Deeksha Kumari, Ritika, Radhika Sharma, Samiksha Chauhan, Sheetal Dhiman, Yogyata Pathania, Arun Kumar	598
XPS and Structural Characterization of Layered MoS2 Formed by Thermal Evaporation	Megha Mishra and Teny Theresa John	602
Effect of Solvents in Optical Tuning of WS2 Quantum Dots	Naresh Mandhan, Vidyotma Yadav, Tanuja Mohanty	606
Engineering Zinc Oxide Electron Transport Layers for MAPbI3 Perovskite Solar Cells	Anand Pandey	610
Carbon nanotube based composite thin film coatings for stray light control space applications	Sonia Saini, Kuntala Bhattacharjee and Girish M. Gouda	613
The Future of Wearable Sensors: Ultrasensitive PDMSPEDOT: PSS-AgF Nano-composites for Stretch and Motion Sensing	Debashish Nayak, Tusharkanta Nayak, Deviprasad Sahoo and Smita Mohanty, Ram Bilash Choudhary	618
Energy Harvesting by Cellulose-PEDOT: PSS Aerogel-Based Triboelectric Nanogenerator	Deviprasad Sahoo, Debashish Nayak, Sashwata Sahoo, Tusharkant Nayak, and Smita Mohanty	621

The Emergence of Density Wave and Supersolid Phases in Driven Optical Lattice

Sheshgiri S. Shettigar [a)] and Ramesh V. Pai

School of Physical and Applied Sciences, Goa University, Taleigao Plateau, Goa 403 206, India

[a)]sheshgiri.shettigar@gmail.com

Abstract. In a periodically shaken lattice, bosons are transferred from the ground state to the excited band when the shaking frequency is increased. Motivated by the idea that the excited atom may be treated as a Rydberg atom, we study the two-band extended Bose Hubbard model by considering the nearest-neighbor interactions for the excited band boson using the CMFT+DMRG method. In our calculations, we obtain the superfluid order parameter and the boson density for the lower band and the excited band and identify the underlying Mott insulator (MI), π- superfluid ($\pi - SF$), the Density Wave (DW), and the Supersolid (SS) phases. The DW phase and the SS phase are due to the nearest neighbor interaction and the intra-band interactions. Density of bosons play very important role in the determination of the DW and the SS phases.

INTRODUCTION

Novel approaches to the study of quantum many-body physics and the simulation of quantum phase transitions have been made possible by ultracold atoms trapped in optical lattices [1-2]. In this context, the most researched phase transition, from the theory and the experiment point of view, is the superfluid (SF) to Mott Insulator (MI) transition [3–5]. Manipulating bosons in the optical lattice leads to novel phases. Driven optical lattice research has recently gained popularity because of the hybridization of the lowest Bloch bands results from the lattice's resonant shaking. In a driven lattice, recent experiments demonstrate continuous to discontinuous transition between Mott insulator and superfluid phases [6-7]. The bosons move from the lowest to the excited band with increased shaking frequency. Motivated by these results, we treat the excited atoms in the shaken lattice as Rydberg atoms capable of experiencing extended interactions. We study this system using the two-band extended Bose Hubbard model with nearest-neighbour interaction for the excited band bosons by applying the density matrix renormalization group with the mean-field (CMFT+DMRG) method [8].

MODEL AND METHOD

Our model is given by:

$$\hat{\mathcal{H}} = -t_a \sum_{\langle i,j \rangle} \left(\hat{a}_i^\dagger \hat{a}_j + \hat{a}_j^\dagger \hat{a}_i \right) + t_b \sum_{\langle i,j \rangle} \left(\hat{b}_i^\dagger \hat{b}_j + \hat{b}_j^\dagger \hat{b}_i \right) + \frac{U_a}{2} \sum_i \hat{n}_i^a \left(\hat{n}_i^a - 1 \right) + \frac{U_b}{2} \sum_i \hat{n}_i^b \left(\hat{n}_i^b - 1 \right) + \frac{\Omega}{2} \sum_i \left(\hat{a}_i^\dagger \hat{b}_i + \hat{b}_i^\dagger \hat{a}_i \right) + V \sum_i \hat{n}_i^a \hat{n}_i^b - \mu \sum_i \left(\hat{n}_i^a + \hat{n}_i^b \right) + \Delta \sum_i \hat{n}_i^b + V_b \sum_i \hat{n}_i^b \hat{n}_{i+1}^b \quad (1)$$

The boson creation (annihilation) operators for the ground state and the excited state band are, respectively, given by a_i^+ (a_i) and b_i^+ (b_i) for lattice site i. The first (second) term represents the hopping of bosons between the nearest neighbor sites with hopping amplitude $t_a > 0 (t_b > 0)$. The number operators are given by $n_i^a = a_i^+ a_i$ for the ground state band and, $n_i^b = b_i^+ b_i$ for the excited state band. The third and the fourth terms in the equation represent the on-site intra-band interactions with strength U_a and U_b. The fifth term in expression (1) gives the intra-band coupling with an interaction strength Ω, while the sixth term gives the intra-band interaction with strength V. The next term with chemical potential μ controls the number of bosons in the system. The penultimate term gives the effective detuning between the two bands with strength Δ and the final term with strength V_b represents the nearest-neighbor interaction for the bosons in the excited state band. In the CMFT+DMRG method, we divide the whole lattice into clusters of *L* sites [8]. We decouple one such cluster from the neighboring sites by applying the mean-field approximation: $a_i = \psi_i^a + \delta a_i$, $b_i = \psi_i^b + \delta b_i$ and $n_i^b = \rho_i^b + \delta n_i^b$ to the model given by (1). Here, $\psi_i^{a(b)} = \langle a_i (b_i) \rangle$ is the superfluid order parameter for the ground-state

(excited-state) band and $\rho_i^b = \langle n_i^b \rangle$ is the density order parameters for the excited state band. We solve the model using the CMFT+DMRG methods [8] iteratively, keeping 50 eigenstates in the left and right reduced density matrix. Throughout our calculations, we have retained only those states, in the reduced density matrix, whose weight exceeds 10^{-8}. We calculated the superfluid order parameter ψ_i^a and ψ_i^b and, the density order parameter ρ_i^b in a self-consistent manner. Commencing with a lattice of size L = 3, we build the lattice by performing the iterations mentioned above to achieve a final system size of L = 501.

RESULTS AND DISCUSSIONS

In our calculations, we have set the scale for parameters with $t_a = 1$ and in this unit, we set $t_b = 10.75$, $U_a = 24.0$, $U_b = 14.41$, $V = 19.67$, $V_b = 1.5 \times t_b = 16.13, \Omega = k\, f^2 A$ and $\Delta = \Delta_E - hf$ with $k = 462.96 Hz^{-1}m^{-1}$, $h = 1$, and $\Delta_E = 19.7kHz$. These parameters are chosen motivated by the recent experiment [6,7]. Here, f and A are the shaking frequency and the shaking amplitude respectively. We have kept the shaking amplitude fixed at $A = 1nm$ throughout our calculations and, varied the shaking frequency from 15kHz to 19.7kHz. Using the ground state wave function from our CMFT+DMRG method, we calculate the superfluid order parameter $\psi_i^a = \langle a_i \rangle$ and $\psi_i^b = \langle b_i \rangle$ and, the density order parameters $\rho_i^a = \langle n_i^a \rangle$ and $\rho_i^b = \langle n_i^b \rangle$. The nearest-neighbor interaction V_b in the model (1) supports two additional phases, the density wave (DW) and the Supersolid (SS) phases apart from the usual MI and the $\pi - SF$ phases [6,7]. We study the effects of the nearest-neighbor interaction V_b, for two values of chemical potential $\mu = 7.0$ and $\mu = 12.5$ to demonstrate then DW and the SS phases. We plot, in Fig. 1, $\psi_i^{a(b)}$ and $\rho_i^{a(b)}$ for $220 < i < 280$ (i.e., center part of the lattice with L=501) to demonstrate the convergence of $\psi_i^{a(b)}$ and $\rho_i^{a(b)}$, which show a staggered behavior reflecting DW phase (left panel) and supersolid phase (right panel). To identify phases, we define average densities $\bar{\rho}_a = \frac{1}{2}\left(\rho_i^a + \rho_{(i\pm i)}^a\right)$, $\bar{\rho}_b = \frac{1}{2}\left(\rho_i^b + \rho_{(i\pm 1)}^b\right)$, respectively, for the lower and the upper (excited) band. It may be noted that, from Fig. 1, $\bar{\rho}_{a(b)}$ is independent of the lattice position. The average density of the lattice is given by $\bar{\rho} = \bar{\rho}_a + \bar{\rho}_b$. Similarly, $\bar{\psi}_a = \frac{1}{2}\left(|\psi_i^a| + |\psi_{(i\pm1)}^a|\right)$ and $\bar{\psi}_b = \frac{1}{2}\left(|\psi_i^b| + |\psi_{(i\pm1)}^b|\right)$ as the average superfluid order parameter for the lower and the excited band, respectively. We also define, $\Delta^a = |\rho_i^a - \rho_{(i\pm1)}^a|$, $\Delta^b = |\rho_i^b - \rho_{(i\pm1)}^b|$, $\delta\psi^a = \left||\psi_i^a| - |\psi_{(i\pm1)}^a|\right|$ and $\delta\psi^b = \left||\psi_i^b| - |\psi_{(i\pm1)}^b|\right|$ to measure the difference in density and superfluid order parameters between two adjacent sites. The DW and SS phases have finite values of Δ^a and Δ^b.

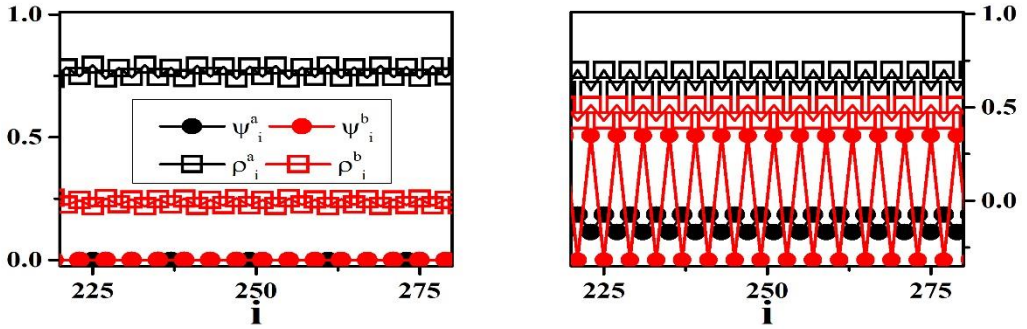
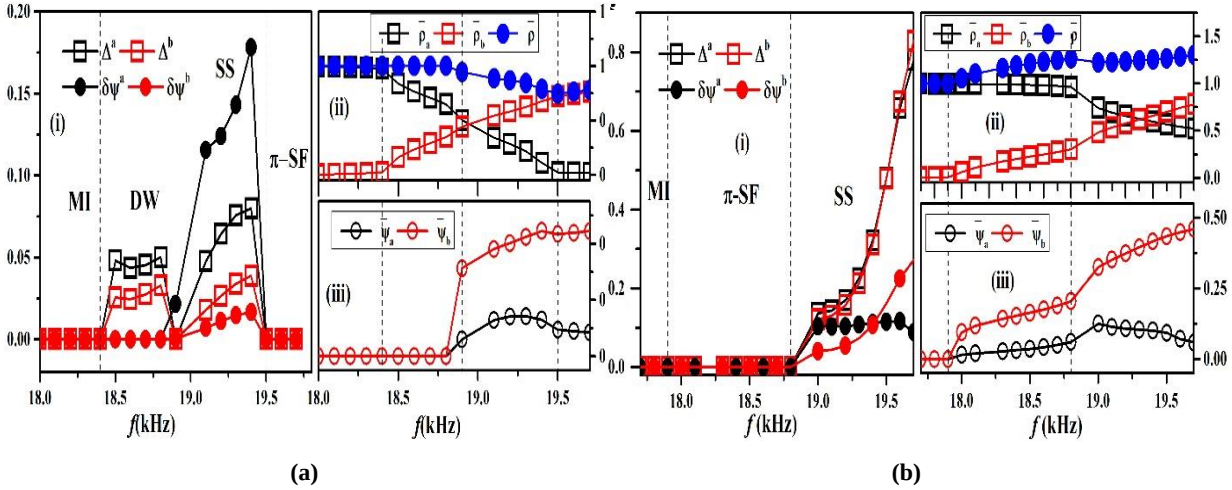


Figure 1. Plot of $\psi_i^{a(b)}$ and $\rho_i^{a(b)}$ as a function of lattice position i for (a) the density wave phase for $\mu = 7.0$ and $f = 18.6\ kHz$, and (b) the supersolid phase for $\mu = 12.5$ and $f = 19.0\ kHz$.

The DW (MI) phase has $\psi_i^{a(b)} = 0$, $\bar{\psi}_{a(b)} = 0$, $\Delta^{a(b)} \neq 0\ (= 0)$ and $\bar{\rho} = 1$. The SS ($\pi - SF$) phase, however, has $\Delta^{a(b)} \neq 0\ (= 0), \delta\psi^{a(b)} \neq 0 (= 0)$. We plot the phase diagram for $\mu = 7.0$ and 12.5, respectively, in Fig. 2(a)(i) and Fig. 2(b)(ii). The phase diagram is obtained from the plots of $\bar{\rho}_{a(b)}$, $\bar{\psi}_{a(b)}$ and $\bar{\rho}$ (as in Figs. 2(a,b) (ii), (iii)) as a function of the shaking frequency f. As seen in Fig. 2 (a) (ii), for low frequencies, the system is in the MI phase (with $\bar{\rho}_a = 1,\ \bar{\rho}_b = 0$). Increasing f causes bosons from the ground-state band to excite to the upper band. Here, the average density $\bar{\rho} = 1$, however, $\bar{\rho}_a \neq \bar{\rho}_b \neq 1$. The lower and upper band act together as a single insulating unit. The upper band experiences the nearest neighbor interaction yielding oscillation in density. The inter-band interaction V translates this effect to the lower band leading the system to the Density Wave phase. Upon increasing f even further, more bosons from the lower band are transferred to the upper band, the total density $\bar{\rho}$ drops below unity and $\Delta^{a(b)} \neq 0, \delta\psi^{a(b)} \neq 0$, leading to the supersolid phase. For very large values of f the system goes into the $\pi - SF$ phase (see Fig 2 (a) (ii)). For chemical potential, $\mu = 12.5$, as we see in Fig.

2 (b) (i), the system goes through a phase transition from the MI to the $\pi - SF$ and then to the SS phase. Similar to the former case, the system is present in the MI phase for smaller values of f, but when the frequency is increased (Fig. 2 (b) (ii)), the lower band bosons continue to be in the MI phase (with $\bar{\rho}_a = 1$). However, any added bosons when frequency is increased occupy the upper band yielding the $\pi - SF$ phase. The effects of V_b and V are negligible at this point and only begin to gain prominence for larger values of f. On increasing f further (Fig 2 (b) (iii)), Ω becomes large and lower band bosons move to upper band causing the system to enter into the SS phase with intermediate values of $\bar{\rho}_a$ and $\bar{\rho}_b$.

In conclusion, we have studied the two-band extended Bose Hubbard model with nearest-neighbor interaction V_b, for the excited-band bosons. The system exhibits the DW and SS phases in addition to the MI and $\pi - SF$ phases. The combined effect of V_b and V, for intermediate densities of the lower and upper bosons causes the system to be in the DW phase whenever $\bar{\rho} = 1$ and in the SS phase whenever $\bar{\rho} \neq 1$.



(a) **(b)**

Figure 2. (i) Graph of $\Delta^{a(b)}$ and $\delta\psi^{a(b)}$, **(ii)** Graph of $\bar{\rho}$ and $\bar{\rho}_{a(b)}$ and **(iii)** Graph of $\bar{\psi}_{a(b)}$ as a function of shaking frequency f for **(a)** $\mu = 7.0$ and **(b)** $\mu = 12.5$.

REFERENCES

1. I. Bloch, J. Dalibard, and W. Zwerger, Rev. Mod. Phys. 80, 885 (2008).
2. M. Greiner, O. Mandel, T. Esslinger, T. W. Hansch and I. Bloch, Nature **415**, 39 (2002).
3. C. Gross, and I. Bloch, I. Science **357**, 995 (2017).
4. M. Lewenstein, A. Sanpera, and V. Ahunger, *Ultracold Atoms in Optical Lattices: Simulating quantum many-body systems* (Oxford University Press, Oxford, 2013) and references therein.
5. A. Eckardt, Rev. Mod. Phys. **89**, 011004 (2017).
6. B. Song, S. Dutta, S. Bhave, Jr-Chiun Yu, E. Carter, N. Cooper, and U. Schneider, Nature Phys, **18**, 259 (2022).
7. S. Shettigar, B. Alavani, and R. V. Pai, AIP Conference Proceedings, 2995(1):020005, 01 (2024).
8. P. P Gaude, A. Das, and R. V. Pai, J. Phys. A: Math. Theor. **55**, 265004 (2022).

Topological Phases of Non-Linear 1D Kitaev Chain using Quench Dynamics

Rakesh Kumar Malakar[1,*], Rittwik Chatterjee[2] and Asim Kumar Ghosh[3]

[1,2,3]*Department of Physics, Jadavpur University, 188 Raja Subodh Chandra Mallick Road, Kolkata 700032, India*

[*] Corresponding author: rkmalakar75@gmail.com

Abstract. The p-wave Kitaev chain in one-dimension hosts unpaired Majorana fermions in the topological phase. We employ quench dynamics to detect the topological phase using non-linearity induced time dependent differential equations of Majorana state wavefunctions, governed by the Hamiltonian involving Majorana pairing. Two different phase diagrams corresponding to the trivial and topological phase have been obtained using the time evolution of the Majorana states in the weak non-linear region.

Keywords: Topological phase, Kitaev chain, Majorana fermions, quench dynamics, edge states, winding number.

INTRODUCTION: THE MODEL AND THE HAMILTONIAN

The Kitaev model (1) is a prototype of one-dimensional (1D) superconductor that hosts zero energy Majorana modes in the topological phase. The Tight Binding Hamiltonian has the following form,

$$H = -\mu \sum_j C_j^+ C_j - t \sum_j (C_{j+1}^+ C_j + C_j^+ C_{j+1}) + \sum_j \left(\Delta\, C_j C_{j+1} + \Delta^* C_{j+1}^+ C_j^+\right) \qquad (1)$$

where, μ is the onsite energy, t is the nearest neighbor (NN) hopping amplitude and $\Delta = |\Delta| e^{i\theta}$ is the complex superconducting term. C_j is the annihilation operator corresponding to the j^{th} fermionic site.In the momentum space, the system exhibits two phases distinguished by the topological invariant called the winding number (ν). One is the trivial phase with $\nu = 0$ when $\mu > |2t|$ and the other is the topological phase with $\nu = 1$ when $\mu < |2t|$. So, $\mu = |2t|$ is the topological transition point. The paper aims at detecting these phases using quench dynamics.

Hamiltonian in terms of Majorana fermions

Defining, $\gamma_j^a = e^{\frac{i\theta}{2}} C_j + e^{-\frac{i\theta}{2}} C_j^+$ and $\gamma_j^b = i(e^{-\frac{i\theta}{2}} C_j^+ - e^{\frac{i\theta}{2}} C_j)$, where, γ_j^a and γ_j^b are the Majorana operators corresponding to the j^{th} fermionic site. Using these set of relations, the Hamiltonian in equation (1) can be written as,

$$H = \frac{i\mu}{2} \sum_{j=1}^{N} \gamma_j^b \gamma_j^a + \frac{i}{2}(|\Delta| + t) \sum_{j=1}^{N-1} \gamma_j^b \gamma_{j+1}^a + \frac{i}{2}(|\Delta| - t) \sum_{j=1}^{N-1} \gamma_j^a \gamma_{j+1}^b \qquad (2)$$

Here, we can think of two cases:

1. When $t = |\Delta| = 0$ but $\mu \neq 0$, the intra-cell Majorana pairing takes place. Each Majorana pairs up, leaving no Majorana unpaired. This corresponds to the trivial phase.
2. When $t = |\Delta| \neq 0$ but $\mu = 0$, the inter-cell Majorana pairing occurs in such a way that two Majorana fermions, one at each end, are left unpaired. This corresponds to the topological phase.

The following table shows the topological properties, highlighting the correspondence between the winding number and the presence of unpaired Majorana fermions.

Condition	Winding number	Unpaired Majorana
$\mu > \|2t\|$	0 (trivial)	absent
$\mu < \|2t\|$	1 (topological)	present

The detection of these unpaired Majorana fermions, hence, the topological phase, can be done using quench dynamics which we will discuss in the next section.

DETECTION OF THE TOPOLOGICAL PHASES USING QUENCH DYNAMICS

In general, a discrete non-linear time-dependent Schrödinger equation for an arbitrary lattice site, say, $'j'$, of a 1D model is written as,

$$i\frac{d\psi_j}{dt} + \sum_{m=1}^{N} M_{jm}\psi_m + \zeta\left|\psi_j\right|^2\psi_j = 0 \qquad (3)$$

The third term is the non-linear term controlled by the parameter ζ. M_{jm} is the hopping matrix involving pairing of the j^{th} site with the other sites (m).

For the linear system, with $\zeta = 0$, we diagonalize the hopping matrix as, $M\,\overline{\psi_p} = E_p\,\overline{\psi_p}$ $(1 \le p \le N)$, E_p and $\overline{\psi_p}$, being the eigenvalues and eigenvectors of the hopping matrix M and obtain N decoupled equations, $i\frac{d\overline{\psi_p}}{dt} + E_p\overline{\psi_p} = 0$, whose solutions have a form, $\overline{\psi_p}(t) = e^{-iE_pt}\overline{\psi_p}(0)$.

At $t = 0$, the initial state is expanded as, $\psi_j(0) = \sum_p C_p\,\overline{\psi_p}\,(0)$.

The topological phases are characterized by the zero energy edge states $\overline{\psi_e}$. The localization of the edge states leads to the approximation of the corner lattice state, $\psi_1(0) \approx c\overline{\psi_e}(0)$, say, for the corner site, $j = 1$. After time evolution, $\psi_1(t) = ce^{-iE_et}\overline{\psi_e}(0)$, where, E_e is the eigenvalue of the edge state and $E_e = 0$. Therefore, $\psi_1(t) = c\overline{\psi_e}(0)$.This means that even after the evolution with time, the wavefunctions corresponding to the corner sites remain saturated and do not decay with time. This feature is only seen in the topological phase of the system.

This concept has been used to distinguish the topological phases in a non-linear Su-Schrieffer-Heeger model (2), (3), (4), (5).

The Kitaev model hosts Majorana edge states in the topological phase. In order to study the time evolution of the Majorana states of the Kitaev chain, here, we have introduced below, the time dependent coupled non-linear differential equations, following equation (3). Thinking Kitaev model as a chain of Majorana fermions, M_{jm} involves the pairing of any j^{th} site Majorana fermion of one type, say a(or b) with an m^{th} site Majorana fermion of the other type, say b(or a), in accordance with equation (2). The resulting equations corresponding to the wavefunctions (ψ_j^a and ψ_j^b) of two types of Majorana fermions γ_j^a and γ_j^b are as following,

$$i\frac{d\psi_j^a}{dt} = \frac{(|\Delta|+t)}{2}\left(\psi_{j+1}^b - \psi_j^a\right) + \frac{(|\Delta|-t)}{2}\left(\psi_{j-1}^b - \psi_j^a\right) + \mu\left(\psi_j^b - \psi_j^a\right) - \zeta\left|\psi_j^a\right|^2\psi_j^a \qquad (4)$$

$$i\frac{d\psi_j^b}{dt} = \frac{(|\Delta|-t)}{2}\left(\psi_{j+1}^a - \psi_j^b\right) + \frac{(|\Delta|+t)}{2}\left(\psi_{j-1}^a - \psi_j^b\right) + \mu\left(\psi_j^a - \psi_j^b\right) - \zeta\left|\psi_j^b\right|^2\psi_j^b \qquad (5)$$

We consider a Kitaev chain of 20 Majorana fermions belonging to 10 fermionic sites. This results in 10 pairs of coupled differential equations of Majorana states, ψ_j^a and ψ_j^b with $j = 1,2,3\ldots,10$. Here, the idea is to apply impulse to the corner states of the chain when $t = 0$ and observe the time evolution of these 20 Majorana states, by numerically solving the differential equations. With an initial condition that $|\psi_1^a(0)| = |\psi_{10}^b(0)| = 1$

and $\psi_1^b(0) = \psi_{10}^a(0) = \psi_j^s(0) = 0$ with $j = 2,3,4 \ldots, 9$, (s =a or b), we explore the phase diagrams using contour plots depicting the time evolution of the Majorana states in the weak non-linear region ($\zeta = 0.5$).

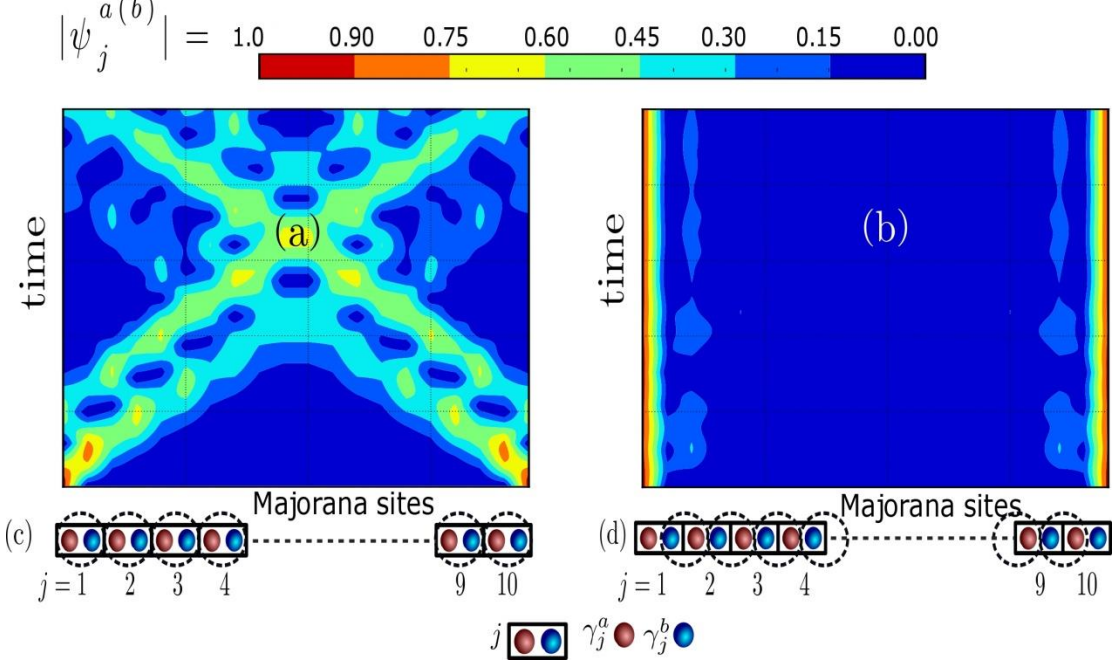


FIGURE 1. Phase diagrams showing the time evolution of the Majorana states with $\zeta = 0.5$ for (a) trivial phase with $|\Delta| = t = 0.5$ and $\mu = 1.5$ (b) topological phase with $|\Delta| = t = 1.5$ and $\mu = 0.5$. The horizontal and the vertical axes represent the Majorana site and the time respectively. The color bar shows the magnitude of the Majorana state wavefunctions. The quench Dynamics is done for 10 fermionic sites or equivalently 20 Majorana fermionic sites. The Majorana pairing corresponding to the (c) trivial phase and (d) topological phase are shown below their respective phase diagrams.

Result and Conclusion

It is seen that in the topological region (with $|\Delta| = t = 1.5$ and $\mu = 0.5$), the wavefunctions of the corner sites $|\psi_1^a|$ and $|\psi_{10}^b|$ remain saturated. The reddish stains at the two ends in the contour plot in Fig.1(b) are because of the saturation of the corner states. Such a picture is not found in the trivial region (with $|\Delta| = t = 0.5$ and $\mu = 1.5$) where, no state is saturated as shown in Fig.1(a). The Majorana pairing corresponding to the two phases are shown in Fig.1(c) and 1(d)**.** It is noted that the unpaired Majorana fermionic states stay undecayed with time, characterizing the topological phase. Such a feature is not seen in the strong non-linear region.

Therefore, the topological phases of 1D Kitaev model have been distinguished using quench dynamics.

ACKNOWLEDGMENTS

The work is done with support of DST/INSPIRE Fellowship/2019/IF190085 and UGC Fellowship – 211610042893.

REFERENCES

1. A Yu. Kitaev, Phys.-Usp. Vol. 44, pp. 131-136 (2001).
2. M. Ezawa, Phys. Rev. B Vol. 104, pp. 235420 (2021).
3. M. Ezawa, Phys. Rev. B Vol. 105, pp. 165418 (2022).
4. M. Ezawa, Phys. Rev. Research Vol. 4, pp. 013195 (2022).
5. R K. Malakar and A K.Ghosh, J. Phys. Condens. Matter, Vol. 35, pp. 335401 (2023).

Effect of $TeO_2/SeO_2/Al_2O_3$ on Thermal and Structural Aspects of LGS Glass-ceramics

Suresh Suragani[1], Hanumantha Rao Kotcharla[1], Venkata Sambasiva Rao Miriyala[2], Tirupataiah Chereddy[1, *]

[1]*Department of Physics, School of Applied Science and Humanities, Vignan Foundation for Science, Technology, and Research, Guntur, Andhra Pradesh 522213, India.*
[2]*Department of Physics, Bapatla Engineering College, Bapatla -522101, A.P., India.*

[*] Corresponding author: chereddyt@gmail.com

Abstract. $25Li_2O$-$10GeO_2$-$60SiO_2$-5R (R= TeO_2, SeO_2, Al_2O_3) were synthesized by melt-quenching. X-ray diffraction (XRD) analysis confirmed the ceramic nature of the samples. Energy-dispersive X-ray spectroscopy (EDS) was utilised to ascertain the chemical composition of the samples. According to the Matusita model corresponding to Differential Thermal Analysis (DTA), the activation energy of crystallization (E_c) was found to be 285.49 kJ/mol at a heating rate of 10°C/min. The Avrami index (n) is 2 for the 5 mol% Al_2O_3 doped sample, indicating a slight predominance of bulk over surface crystallization. The sample was doped with 5 mol% of Al_2O_3 and had superior thermal stability.

Keywords: Melt quenching, Glass ceramics, Thermal stability**,** Crystallization kinetics**,** Activation energy of crystallization

INTRODUCTION

The technological applicability of germanosilicate glass ceramics includes solid electrolyte applications and semiconductors [1]. TeO_2 glass ceramics are known for their optical transparency, corrosion resistance, and chemical durability [2]. SeO_2 demonstrates significant semiconductor properties with potential applications in photonics and electronics [3]. Incorporating Al_2O_3 into LGS glass ceramics increases their chemical durability and thermal resistance. This study aims at a non-isothermal examination of the crystallization kinetics of LGS glass ceramics [4].

EXPERIMENTAL PROCEDURE

Samples were prepared using the melt quenching technique and high-purity reagents, including Li_2CO_3, GeO_2, SiO_2, TeO_2, SeO_2, and Al_2O_3. Procedures and characterization techniques are outlined in prior studies [5, 6].

RESULTS AND DISCUSSION

XRD and EDS

XRD patterns of the LGS-Se sample in Fig. 1 show peaks attributed to main crystalline phases, such as $Li_2(Si_2O_5)$ and $Li_2Ge_2O_5$. These peaks were identified with ICSD data. EDS spectrum of synthesized samples, presented in Fig. 2, reveals the occurrence of significant elements like Ge, Si, Te, Se, Al, and O, with minimal Se content and no detection of lithium since lithium is a light element.

Thermal Studies

DTA curves in Fig. 2 show both exothermic and endothermic peaks. LGS-Al sample has a temperature difference (ΔT) of 149 °C and a higher crystallization temperature (T_x) due to its cohesive energy. T_x is calculated using Lasocka's equation [7]: $T_x = A_x + B_x \ln(\alpha)$, where A_x represents the crystallization temperature and B_x indicates the change in glass transition temperature. $\ln(\alpha)$ vs. T_x plots for all samples show a strong linear relationship (Fig. 1(c)), with the corresponding A_x and B_x values listed in Table 2. The JMA model describes the transformed precursor as $\chi = 1 - \exp(-Kt^n)$, where n is the crystal growth exponent and K, the reaction rate, is given by $K = K_0 \exp(-E_c/RT)$ [8, 9]. Here, K_0 denotes the frequency factor. In the non-isothermal method, the correlation between crystallization fraction (χ) and E_c, as per Matusita et al. [9], is: $ln[-ln(1-\chi)] = -n\, ln\alpha - 1.052mE_c/RT$ + constant, where m and n depend on the crystal growth mechanism and dimensionality, also in the formula, where $\chi = A_T/A$, A is the total area of the exothermic peak from the onset temperature of crystallization (T_x) to completion. A_T is

the area of the peak between T_x and T, which varies with temperature. Also, if the number of nuclei rises during the heating in the DTA run, n will be m+1 [10].

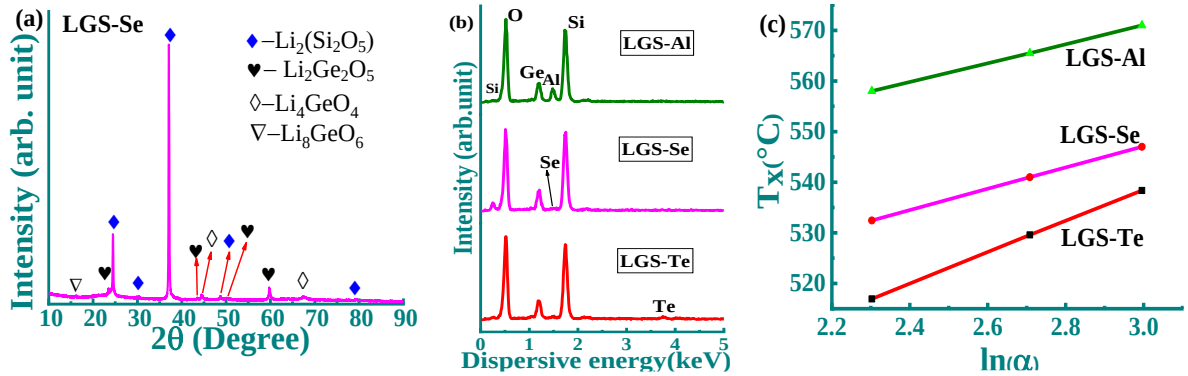


FIGURE 1. (a) XRD spectra of LGS-Se sample. (b) EDS spectra of the LGS-Te/Se/Al samples. (c)*Tx* vs *ln*(α) plot.

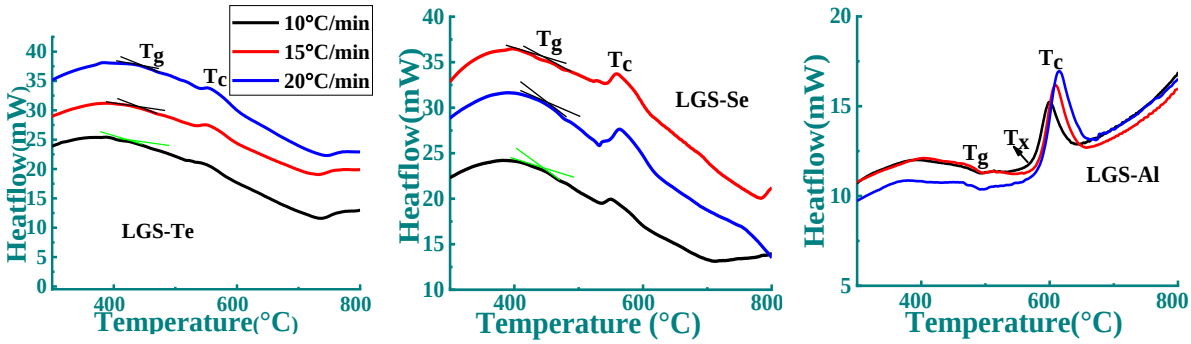


FIGURE 2. DTA curves of LGS-R (Te, Se, Al) samples at 10/15/20 °C/min.

TABLE 1. DTA data of LGS-Te/Se/Al samples (°C/min).

Sample	T_g (°C)			T_x (°C)			T_c (°C)			ΔT (°C)		
	10	15	20	10	15	20	10	15	20	10	15	20
LGS-Te	427	440	448	517	529	538	551	556	562	124	116	114
LGS-Se	447	449	452	533	541	547	553	562	563	106	113	111
LGS-Al	450	466	472	558	565	571	599	609	612	149	143	140

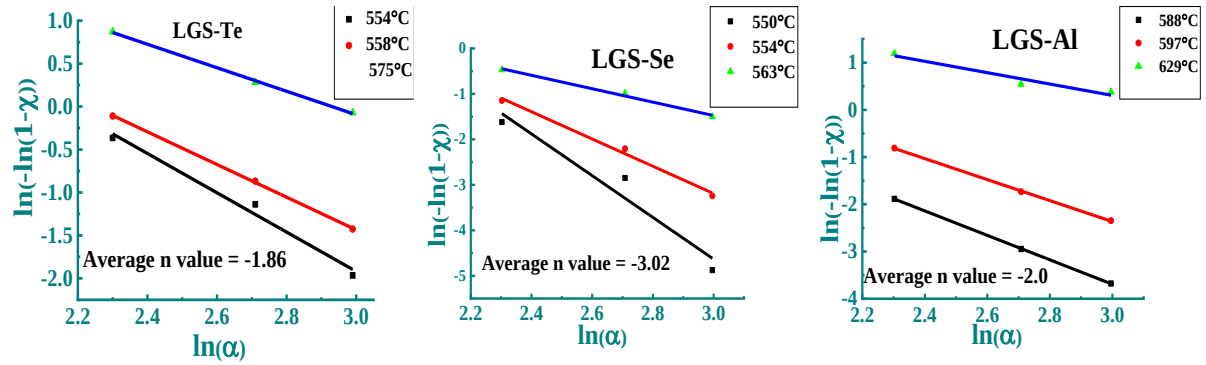


FIGURE 3. *ln*[-*ln*(1-χ)] versus *ln*(α) plot to evaluate n for LGS-R (Te, Se, Al) samples.

The slope of the ln [− ln (1 − χ)] versus ln α curve provides the value of n shown in Fig. 3, and values of n and m are listed in Table 2. The kinetic exponent "n" was determined based on the crystallization mechanism proposed by Mahadevan et al. [9]. The values of "n" and "m" for LGS-Te and LGS-Al indicate the volume nucleation and one-dimensional growth, but for LGS-Se, it is two-dimensional growth. In Fig. 4, the plots of ln[-ln(1-χ)] against 1000/T at various heating rates for the samples exhibit almost uniform slopes in most of the temperature range and deviate at high temperatures or in regions with substantial crystallized fractions. However, this is possibly

due to the saturation of nucleation sites in the final crystallization stage or the limitation of crystal growth by particle size. Furthermore, the E_c values obtained from the slopes of the curves between ln[-ln(1-χ)] and 1000/T at various heating rates for all glass ceramic samples are presented in Table 2. These observations suggest that the activation energy decreases as the heating rate increases for LGS-Te and Al samples. The average E_c of the LGS-Al sample exhibits the maximum value compared to the LGS-Te sample, which can be attributed to the increase in the formation of BOs.

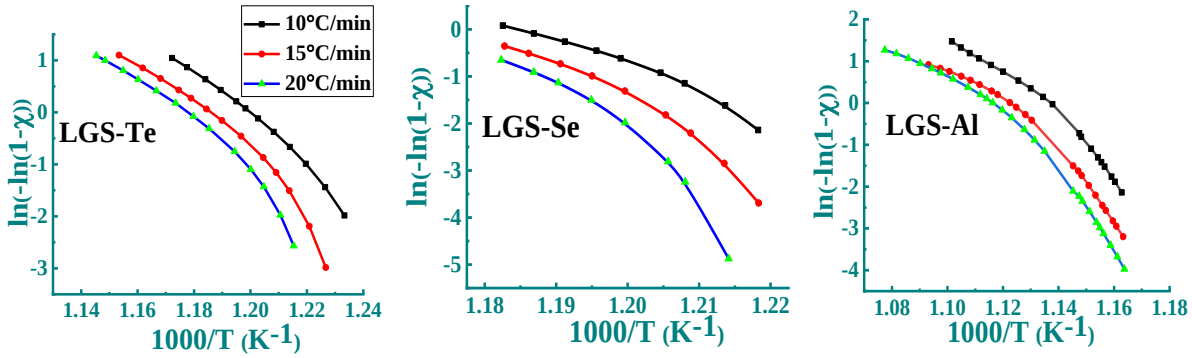


FIGURE 4. *ln*[-*ln*(1-χ)] versus *ln*(α) plot to evaluate n for LGS-R (Te, Se, Al) samples.

TABLE 2. Crystallization kinetic parameters of all samples (°C/min).

Sample	A_x (°C)	B_x (min)	n	m	E_c (kJ/mol)		
					10	15	20
LGS-Te	446	30.93	1.86	1	279.7	247.87	238.23
LGS-Se	484	21.01	3.02	2	298.03	415.70	603.78
LGS-Al	515	18.74	2.00	1	285.49	258.49	263.31

CONCLUSION

Samples mentioned above were made using melt quenching with subsequent heat treatment. XRD patterns exhibited distinct peaks, indicating a ceramic nature. DTA studies revealed thermal stability and crystallization kinetics. The 5 mol% Al_2O_3-doped sample had a higher activation energy of crystallization and improved thermal stability due to the increased number of bridging oxygen units. This sample is a thermally stable candidate and may be suitable for use in thermal sealants.

ACKNOWLEDGMENTS

The authors are grateful to the management and CoExAMMPC of Vignan Foundation for Science, Technology, and Research, Guntur-522213, for their valuable support in characterizing the samples.

REFERENCES

1. Yulong He, Gaoling Zhao, Huijun Qin, Jianxun Wang, Gaorong Han, Opt. Commun. Vol. 315, pp. 59-62 (2014).
2. M. A. Merzliakov, V. Kouhar, G. E. Malashkevich, E. V. Pestryakov, Opt. Mater. Vol. 75, pp. 142-149 (2018).
3. C. V. K. Reddy, R.B. Rao, K.C. Mouli, D. V. R. K. Reddy, K. V. B. Rao, Ionics Vol. 18, pp. 65–73 (2012).
4. Sudha Mahadevan, A. Giridhar, A.K. Singh, J. Non-Cryst. Solids Vol. 88, pp. 11-34 (1986).
5. S. Suragani, K. H. Rao, L. N. Patro, Ch. Tirupataiah, Ceram. Int. Vol. 51, pp. 13597–13614 (2025).
6. S. Suragani, K. H. Rao, L. N. Patro, Ch. Tirupataiah, J. Alloys Compd. Vol. 1022, 179799 (2025).
7. M. Lasocka, Matter. Sci. Eng. Vol. 23, pp. 173-177 (1973).
8. M. Avarami, J. Chem. Phys. Vol. 7, pp. 212-225 (1940).
9. K. Matusita, T. Konatsu, R. Yorota, J. Mater. Sci. Vol. 19, pp. 291-296 (1984).
10. A. Das, M. Goswami, C. Nayak, A. Ananthanarayanan, Mater. Chem. Phys. Vol. 295, 127086 (2023).

Orbital Magnetic Field Driven Phases in the Spin-1/2 Falicov-Kimball Model on A Triangular Lattice

Swati Pandey [a)], Umesh K. Yadav and Pradip K. Priya

Department of Physics, Ewing Christian College, Prayagraj – 211003, India

[a)]Corresponding author: pandey14swati@gmail.com

Abstract. To study the impact of external magnetic field on spin -1/2 Falicov - Kimball model on a triangular lattice, numerical methods and Monte Carlo simulation techniques are employed. It is found that a metal to insulator transition accompanied by segregated phase to regular/mixed phase takes place with change in the magnetic field at low values of onsite Coulomb correlation. Transition from metallic phase to insulating is not observed by variation of magnetic field at high Coulomb correlation. These findings can be used to create high energy storage devices as well as electric and magnetic sensors.

Key words. Strongly correlated electron systems, Triangular lattice, Phase transition, Magnetic field, Metal-Insulator transition

INTRODUCTION

In Condensed Matter Physics, alteration from insulating to metallic phase is crucial [1]. Systems such as GdI_2 [2] and its doped variants, $NaTiO_2$ [3] and VO_2 [4,5] etc. exhibiting novel phases e.g. charge, orbital, magnetic order and metal-insulator transitions are layered, strongly correlated electron system. These systems can be explained by the Falicov-Kimball model (FKM) [1]. The FKM, which has two types of states: itinerant state and localized state was originally introduced to describe the transition from insulator to metal in rare-earth and in compounds like transition metal [1,2]. With the inclusion of external magnetic field this problem will be even more intricating. In such systems it will be interesting to study the tandem effect of electron correlation in the presence of uniform external magnetic field.

In this study, we have considered the spin-dependent FKM on two-dimensional triangular lattice in the presence of uniform external magnetic field including the electron correlation between the itinerant electrons (d-electrons) and localized electrons (f-electrons). In this study, we have explored the effects of uniform external magnetic field on the ground state properties of the spin-dependent FKM. Further, effect of external magnetic field on insulator to metal transition is also explored.

METHODOLOGY

The FKM Hamiltonion on a triangular lattice with different spin-dependent interaction terms in the presence of finite uniform external magnetic field is expressed as,

$$H = -\sum_{<ij>,\sigma}[t_{ij}\exp\left\{\frac{ie}{\hbar}\int_{\overrightarrow{R_j}}^{\overrightarrow{R_i}}A(\vec{r}).d\vec{r}\right\} + \mu\delta_{ij}]d_{i,\sigma}^{\dagger}d_{j,\sigma} + U\sum_{i,\sigma}(f_{i,-\sigma}^{\dagger}\,f_{i,-\sigma} + f_{i,\sigma}^{\dagger}f_{i,\sigma})\,d_{i,\sigma}^{\dagger}\,d_{i,\sigma} + U_f\sum_{i,\sigma}f_{i,-\sigma}^{\dagger}\,f_{i,-\sigma}f_{i,\sigma}^{\dagger}f_{i,\sigma} + E_f\sum_{i,\sigma}f_{i,\sigma}^{\dagger}\,f_{i,\sigma} \quad (1)$$

Where, $< ij >$ indicates the lattice's nearest neighbor (NN) sites. The $f_{i,\sigma}^{\dagger}$ & $f_{i,\sigma}$ ($d_{i,\sigma}^{\dagger}$ & $d_{i,\sigma}$) are respectively, the creation and destruction operators for f- (d-) electrons with spin $\sigma = (\uparrow,\downarrow)$ at a site i. The hopping amplitude t_{ij} = t for nearest neighbor hopping and otherwise it is zero. Initial term denotes the moving energy of spin-1/2, d-electrons in the presence of uniform external magnetic field caused by vector potential **A(r)** and hopping is chosen position dependent (Peierls substitution) on the underlying triangular lattice and μ is the chemical potential. The next term is spin-independent onsite Coulomb potential among f- and d-electrons of strength U. The next term is the onsite interaction between f-electrons of up and down spins having strength U_f and last term denotes the f- electron's spin-independent dispersion less energy. The scale of energy is chosen with $t = 1$. Using numerical-diagonalization on a finite underlying triangular lattice with periodic boundary conditions, the eigenvalue spectrum of the FKM Hamiltonian is calculated. The classical Monte-Carlo simulation procedure is used to determine the average values of the physical quantities by annealing the f-electron's configurations. Methodology in detail can be found here [6, 7].

RESULTS AND DISCUSSION

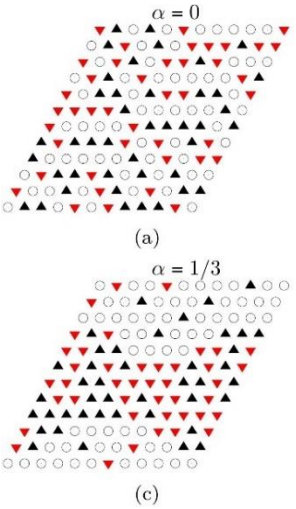


FIGURE 1. Configurations of ground state f-electrons for U=1 and (a) α=0 (b) α=1/4 (c) α=1/3 (d) α=5/12, where filled black up and red down triangles denote sites occupied by f-electrons of up and down spins respectively and open black circle corresponds to

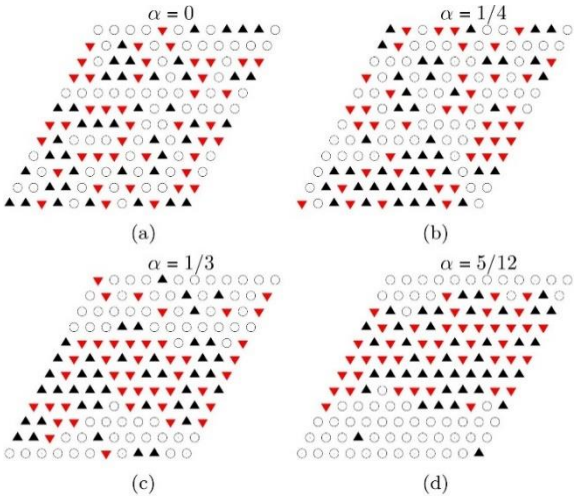


FIGURE 2. Configurations of ground state f-electrons for U=5 and (a) α=0 (b) α=1/4 (c) α=1/3(d) α=5/12. Here it indicates that ground state configurations changes with change in the magnetic flux.

The effects of uniform external magnetic field on the ground state configurations of f-electrons are explored. We have restricted our study for one fourth filling case i.e. $N_f + N_d = N$ where $N_f = N_{f\uparrow} + N_{f\downarrow}$, $N_d = N_{d\uparrow} + N_{d\downarrow}$ here ↑ and ↓ symbols indicate the spin-up and spin-down, N, N_f and N_d are the total number of sites, number of f-electrons and d-electrons respectively. In this study we have chosen N = LxL (L=12). In this present work, we have obtained ground state (minimum internal energy) configurations of f-electrons, energy gap (Δ) and density of states (DOS) for particular values of $N_f = 84$ and $N_d = 60$ at U/t = 1 and 5 for various chosen numerical values of magnetic flux (α) per plaquette.

In Fig. 1 the ground state patterns of localized f-electrons for U/t = 1 is displayed at various values of flux (α). For this chosen value of N_f nearly regular phase (a) at α = 0, segregated and nearly regular phase (mixed phase) at α = 1/4 & 1/3 (b & c) and segregated phase (d) is seen for α = 1/2. As magnetic field increases phase segregation is seen in the system. Segregation in patterns of f-electrons with uniform external magnetic field with finite U is seen in many experimental studies for different systems [8]. In Fig. 2 ground state patterns of localized f-electrons are shown at U/t = 5 for different values of α. It is found that the nearly regular, mixed and segregated phases are also seen similar to U/t = 1. Unlike the case of U/t = 1, here phase segregation is not complete.

We have estimated the energy gap with α (on the Fermi energy (E_F)) for U/t = 1 & 5 and depicted in Fig. 3. It clearly shows the transition from insulator to metal in the system at U/t = 1 for α = 5/12 as the energy gap goes to zero and stays finite at other chosen values of α. This result can be explained from on the patterns shown in Fig.1. At α = 5/12 a phase segregation of localized electrons is seen. Therefore, d-electrons find enough space to move from one part of lattice to other and hence it shows metallic nature. While in case of nearly regular and mixed phases movement of d-electrons is blocked by the presence of f-electrons and hence those phases are insulating in nature. Unlike to the case of U/t = 1, here at U/t = 5 we have found that the energy gap never closes to zero at all chosen values of α. Thus, there is no transition from metallic to insulating state observed for U = 5. These results are very similar to already reported results for the FKM with uniform external magnetic field where Zeeman splitting term was also included. [6]

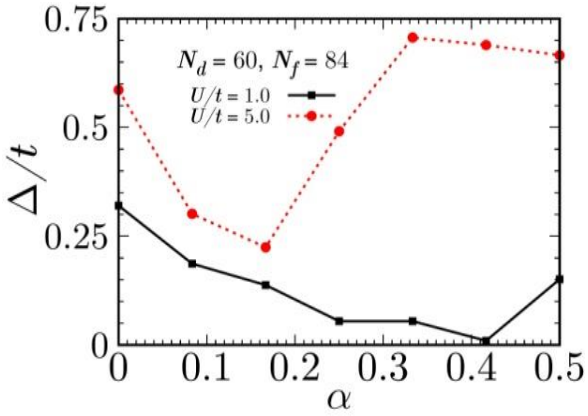


FIGURE 3. Magnetic flux (α) dependence of energy gap at U/t = 1 & 5.

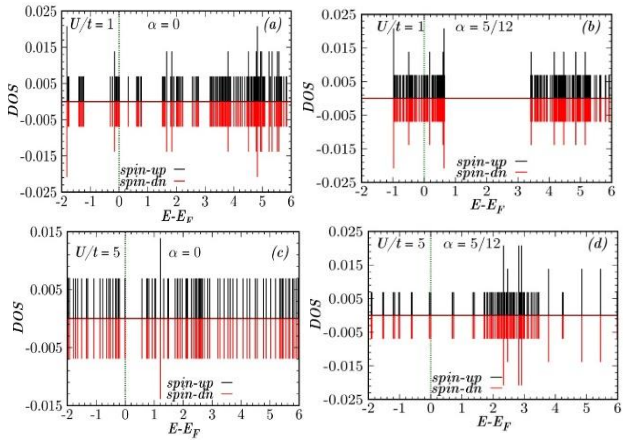


FIGURE 4. DOS of up and down sspin d-electrons at various chosen values of U/t and α. The dotted lines show the position of Fermi level (E_F).

In Fig.4 density of states (DOS) for up and down spin d-electrons are depicted. In Fig.4 (a) DOS is shown for U/t = 1 and α = 0. A finite gap is noted for both spin channels around E_F. This clearly shows the insulating state. In (b) DOS is plotted at U/t = 1 and α = 5/12 showing the vanishing gap around E_F. That shows the metallic state. In Fig 4 (c & d) DOS is given at U/t = 5. It shows that the energy gap remains finite for all values of α and system shows insulating character.

In conclusion, we have studied the influence of uniform external magnetic field on a triangular lattice by studying the Falicov-Kimball model. We have found that the magnetic field strongly affect the ground state patterns of localized electrons. An insulator to metal transition is found for small value of U/t at certain value of magnetic field and this transition is accompanied by the segregated phase to regular or mixed phase. No insulator to metal transition in the ground state is seen at large values of U/t. Further, the results are of experimental importance, as they can facilitate the development of electric and magnetic sensors as well devices with high energy storing capacity.

ACKNOWLEDGMENTS

All the authors equally contributed in the manuscript and acknowledge the CSTUP, India for the financial support via research grant No. CST/D-1525 (Project Id:3304).

REFERENCES

1. L. M. Falicov and J. C. Kimball, Phys. Rev. Lett., Vol. 22, pp. 997(1969)
2. A. Taraphder, L. Craco, M. Laad and A. Yaresko, Phys. Rev. Lett., Vol. 101, pp. 136410-1 – 136410-4 (2008)
3. D.I. Khomskii, T. Mizokawa, Phys. Rev. Lett., Vol. 94, pp. 156402-1 – 156402-4 (2005)
4. Y. H. Matsuda, D. Nakamura, A. Ikeda, S. Takeyama,Y. Suga, H. Nakahara, and Y. Muraoka, Nature Communications, Vol. 11, pp. 3591 (2020)
5. Y. H. Matsuda, Y. Muraoka, D. Nakamura, A. Ikeda, Y. Ishii, X.-G. Zhou, H. Sawabe, and S. Takeyama, Journal of the Physical Society of Japan, Vol. 91, pp. 101008 (2022)
6. U.K. Yadav, Eur. Phys. J. B, Vol. 93(12), pp. 221 (2020)
7. S. Pandey, U. K. Yadav and P. K. Priya, Eur. Phys. J. B, Vol. 97, pp. 169 (2024)
8. U.K. Yadav, T. Maitra, I. Singh, A. Taraphder, J. Phys. Condens. Matter, Vol. 22, pp. 295602 (2010)

Phase transition in Zr and Nb substituted Zr under pressure: *Ab-initio* study

B. D. Sahoo [1,a)], K. D. Joshi[1,2]

[1]*Applied Physics Division, Bhabha Atomic Research Centre, Mumbai, India 400085*
[2] *Homi Bhabha National Institute, Mumbai, India, 400094*
[a)] *Corresponding author:* bdsahoo@barc.gov.in

Abstract. Understanding the effect of Nb addition on the structural, mechanical and thermodynamic properties of Zr claddings is critical for nuclear reactor service safety. In the present work, we have investigated the phase diagram of Zr up to 40 GPa as well as Nb as substituted Zr using the first-principle electronic band structure method. In pure Zr, our calculation predicts alpha (α) to omega (ω) and omega (ω) to beta (β) transitions at pressures of 0.5 GPa and 27.5 GPa respectively. With inclusion of temperature (at 300 K) α to ω the transition pressure occurs at 1.2 GPa, which agrees with experimental value of ~2 GPa. In case of Zr-2.77%Nb our calculation predicts ω phase to be a stable at 0 K but at higher temperature of 600 K, α phase became stable over ω phase, similarly omega to beta transformation takes place at pressure 22.5 GPa. Our lattice dynamical calculations produce experimental phonon dispersion curve for α phase in Pure Zr, β-Nb and also predicts the dynamical stabilization of Zr-2.77%Nb at ambient condition which support our static lattice calculations.

INTRODUCTION

Due to their great biocompatibility, zirconium alloys in particular have been utilised as cladding materials for nuclear fuel. [1]. Pure Zr undergoes an alpha (α) to beta (β) transition around 1135 K when heated. The inclusion of beta stabilizing metals, such as Nb, lowers the temperature, while Sn, known as α stabilizer, increases the transition temperature. From the high temperature β phase, after cooling the reverse β to α transformation happens [2]. On the high-pressure side, the α to ω phase transition in pure Zr has been observed to occur between 2 and 6.5 GPa under hydrostatic conditions [3]. The initial experimental evidence of the ω to β transformation in Zr was reported by Xia et al. [4] to occur at a transition pressure of around 30 GPa. The α to ω and ω to β transition pressures have been found to depend on composition, pressure transmitting medium and, on the temperature [5-7]. It has recently been demonstrated that by combining the high-pressure torsion method (HPT) with compression and shear, certain high-pressure phases of Group IV pure transition metals can be stabilised at room temperature and atmospheric pressure. Pure ω and β Zr [8] and pure ω Ti have been stabilised under ambient circumstances using this process. It has been discovered that the volume percentage of high-pressure phases that stabilise under ambient conditions is directly related to the applied compression stress for a fixed value of the shear strain (γ) [9].

Experimental research on Zr-Nb alloys revealed that at low temperatures (T < 890 K), α-Zr with a hexagonal close-packed (HCP) structure dominates, while β-Nb grains with body-centered cubic (BCC) structures are incorporated into the matrix during Nb precipitation. Doping Nb lowers matrix α-Zr grain diameters and boosts β-Nb precipitate levels [10]. The limited mobility of Nb in α-Zr results in interstitial and substitutional Nb atoms in the supersaturated HCP structure. We know that fuel cladding materials serve in aqueous conditions with high temperatures and high neutron flux, and are prone to corrosion as well as displacement damage from neutron impact. As a result, a full study of the characteristics of Zr-based alloys is required and critical for service safety, namely corrosion resistance. Several experimental studies looked at the mechanical properties of Nb-containing alloys in the presence of defects. Long et al. [11] discovered that irradiated samples have a higher yield limit than non-irradiated samples when comparing fast neutron irradiated and non-irradiated Zr-2.5Nb pressure tubes. Up to this time, it is unclear whether and how Nb addition improves the other properties of Zr-based alloys from a physical standpoint, despite the fact that the concept of doping Nb has gained momentum in the field of engineering [12].

In this paper, we have utilized density functional theory (DFT) technique to investigate the influence of Nb addition in Zr on the structural and phase transition properties at high pressure. The effect of Nb doping on phonon dispersion spectrum of the system have been also evaluated.

THEORETICAL METHOD

The Vienna Ab initio Simulation Package (VASP) was used to carry out the density functional theory (DFT)-based first-principles computation [13]. The plane waves basis set has been set with a cut-off energy of 600 eV for both the Zr and Nb, respectively, and the projector augmented wave (PAW) pseudo potential with Generalised

Gradient Approximation (GGA) on the exchange-correlation part has been selected. The Monkhorst-Pack k-grid spacing mesh of 2πx 0.03 $Å^{-1}$ has been selected to ensure that the total energy calculations are converted to better than 1 meV/atom. 3 × 3 × 2 supercell for α phase, 2 × 2 × 3 supercell for ω phase and 3 × 3 × 2 for β phase containing total 36 Zr atoms have been used to obtain the crystal structure. We have substituted one Zr atom with Nb atom, So that, the concentration of doping Nb studied here is about 2.77% (Zr35Nb), closely with the situation of Nb solid solubility in the Zr matrix. During iteration process, the hexagonal symmetry has been preserved. Valence electrons adopted for Zr and Nb are $4s^2 4p^6 5s^2 4d^2$ and $4p^6 5s^1 4d^4$ respectively. Lattice dynamical simulations were performed using the Phonopy methodology, which is based on the small displacement method and uses a supercell approach.

RESULTS AND DISCUSSIONS

Before analysing the Nb defect in Zr matrix, we have first optimized the supercells of perfect hcp α-Zr (2 atom) and simple hexagonal ω-Zr (3 atom) and bcc β-Nb (2 atom). Lattice parameters of Pure Zr are 3.235 Å and 5.185 Å along *a* axis and *c* axis, respectively, which is in better agreement with the experiments (3.233 Å and 5.149 Å [14,15]). The calculated lattice parameter of Nb is 3.321 Å which is comparable to the experimental data of 3.303 Å [16]). The comparison of difference enthalpy of the α, ω and β phases at 0 K suggests that in pure Zr at zero pressure the α phase is stable which is in contrast with earlier theoretical calculation [17] but in line with the experimental and some other theoretical calculations [4,5,18]. Upon compression the α phase will transform to ω phase at ~ 0.5 GPa at 0 K and thermal correction at 300 K using quasi harmonic approximation (QHA) shifts α to ω phase transition to 1.2 GPa which agrees with experimental data of 2-7 GPa. At still higher pressures the ω phase in pure-Zr will transform to β phase at pressures 27.5 GPa in agreement with previous theoretical and experimental results [4,5,17]. For Zr-2.77%Nb, our calculation predicts omega phase is stable at 0 K, but with inclusion of thermal correction using QHA predicts α phase is stable around ~ 600 K, at higher pressure of 22.5 GPa, ω to β phase transformation takes place as shown in Fig-1. From the above analysis we conclude that with addition of Nb, the transition pressure of ω to β reduced from 27.5 GPa to 22.5 GPa. The zero-pressure volume per atom (V_0), bulk modulus (B_0) and its pressure derivative (B_0') determined for α, ω and β phases from theory are compared with the experimental values in Table 1 for both Zr and Zr-2.77%Nb. Our lattice dynamical calculations (phonon dispersion) also produce the dynamical stability of α-Zr, β-Nb and α-Zr-2.77%Nb phases, as all have positive phonon frequencies along high symmetry directions of Brillouin zone as shown in Fig-2 which supports our static lattice calculations.

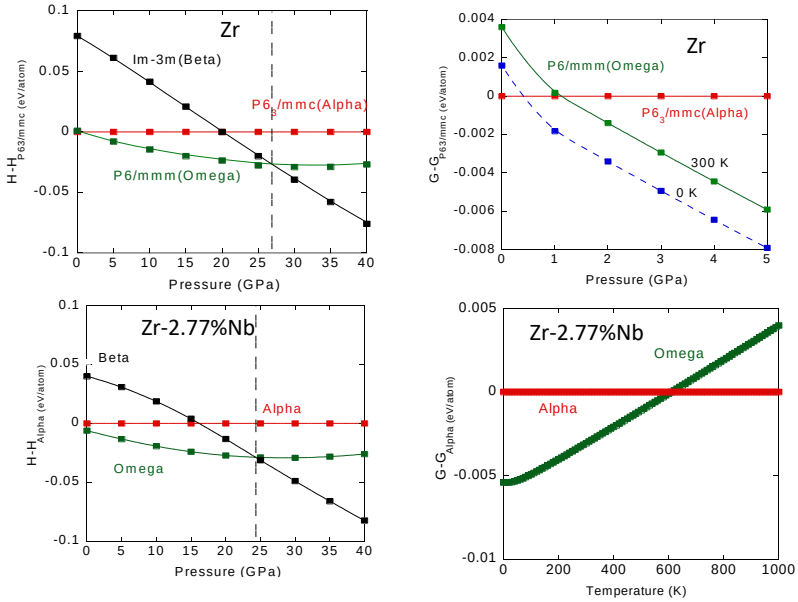


FIGURE 1. The enthalpy difference and Gibbs free-energy difference of Zr and Zr-2.77%Nb.

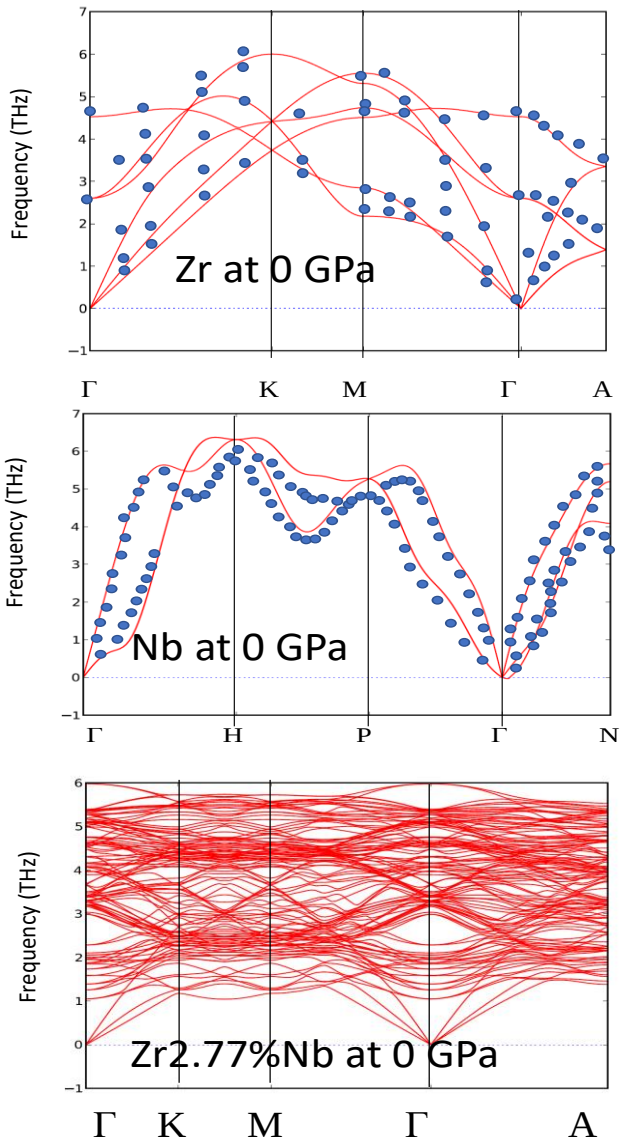


FIGURE 2. The phonon dispersion curves of Zr (α), Nb(β) and Zr-2.77%Nb (α) at 0 GPa.

TABLE 1. Theoretical and experimental lattice constants, Bulk modulus B_0 and its derivative B_0' for the Zr, Nb Zr-2.77%Nb.

Compound	a(Å)	b(Å)	c(Å)	V_0(Å^3)	B_0	B_0'
Zr (α)	3.235, 3.233[15]	3.235,3.233[15]	5.185,5.149[15]	23.508, 23.280[15]	94.64, 94.0[15]	3.18,3.10[15]
Zr(ω)	5.055	5.055	3.151	23.253, 22.980[15]	94.69,109.0[15]	3.52, 2.05[15]
Zr (β)	3.579	3.579	3.579	22.94, 23.28[15]	80.67,88.38[15]	3.82
Nb	3.314, 3.303[16]	3.314,3.303[16]	3.314,3.303[16]	18.204,18.017[16]	164.34,168.00[16]	3.73, 3.43[16]
Zr2.77%Nb(α)	3.226	3.226	5.180	23.382	96.03	3.11
Zr2.77%Nb(ω)	5.048	5.048	3.141	23.115	95.84	3.63
Zr2.77%Nb(β)	3.580	3.580	3.580	22.943	103.31	2.52

To summarize, detailed first principles electronic band structure calculations combined with QHA approximation have been performed in Zr and Zr-2.77%Nb system as a function of hydrostatic compression. For pure Zr, our calculation produces α to ω transition occurs at 1.2 GPa at 300 K compared to experimental data of 2-7 GPa. At higher compression ω to β phase transition occurs around ~ 27.5 GPa. For Zr-2.77%Nb system our calculation predicts ω phase is stable at 0 K, but at temperature above 600 K produces α phase to be stable over ω phase and ω to β phase transition occur at 22.5 GPa. The ground state properties compare well with the existing

experimental data [15-16]. The structural stability of the predicted phases is further substantiated by analyzing the dynamic stability in the respective pressure regime of stability. The validation of the high pressure in Zr-2.77%Nb predicted alloy awaits more experimental works in future.

REFERENCES

1. S. Banerjee, P. Mukhopadhyay, Phase Transformations: Examples from Titanium and Zirconium Alloys Pergamon Materials Series, 1st edition, Elsevier, Amsterdam, 2007.
2. I. Manna, P.P. Chattopadhyay, F. Banhart, H.J. Fecht, Appl. Phys. Lett. 81, 4136 (2002).
3. S K Sikka, Y K Vohra and R Chidambaram Prog. Mater. Sci., 27, 245 (1982)
4. H. Xia, S. J. Duclos, A. L. Ruoff, and Y. K. Vohra, Phys. Rev. Lett. 64, 204 (1990).
5. H. Xia, A. L. Ruoff, and Y. K. Vohra, Phys. Rev. B 44, 10374 (1991).
6. R.G. Hennig, D.R. Trinkle, J. Bouchet, S.G. Srinivasan, R.C. Albers, J.W. Wilkins, Nat. Mater. 4, 129 (2005).
7. D. Errandonea, Y. Meng, M. Somayazulu, D. Häusermann, Phys. B: Condens Matter 2355, 116 (2005)
8. M.T. Pérez-Prado, A.P. Zhilyaev, Phys. Rev. Lett. 102, 175504 (2009).
9. K. Edalati, E. Matsubara, Z. Horita, Met. Mater. Trans. A 40, 2079 (2009).
10. H.L. Yang, Y. Matsukawa, S. Kano, J. Nucl. Mater. 481, 117–124 (2016) .
11. F. Long, L. Balogh, D.W. Brown, Acta Mater. 102, 352–363 (2016).
12. D.O. Northwood, Des. 6 (2), 58–70 (1985).
13. G. Kresse and J. Furthmuller, Comput. Mater. Sci. **6**, 15 (1996).
14. J. Goldak, L.T. Lloyd, C.S. Barrett, Phys. Rev. B 144 (2) 478–484 (1966).
15. Y. Zhao Y, J Zhang, C Pantea, J Qian, and L Daemen, P Rigg, R S Hixson, and G T Gray III, Y Yang and L Wang, Y Wang and T Uchida, Phys. Rev B 71, 184119 (2005)
16. R. Roberge, J. Less Common Met. 40 (1), 161–164 (1975).
17. R. Ahuja, J.M. Wills, B. Johansson and O. Eriksson, Phys. Rev.B 48, 16269 (1993).
18. J S Gyanchandani, S C Gupta S C, S K Sikka and R Chidambaram, High Press. Res. 4 472 (1990).

Topological Phase Transition in two-leg SSH ladder with Further Neighbor Hopping

Rittwik Chatterjee[1,*], Rakesh Kumar Malakar[1] and Asim Kumar Ghosh[1]

[1]*Department Of Physics, Jadavpur University,188, Raja Subodh Chandra Mallick Road, Kolkata,700032*
**Corresponding author: rittwikchatterjee@gmail.com*

Abstract. This study explores the phase transition in a two-leg-coupled Su-Schrieffer-Heeger (SSH) chain incorporating extended next-nearest-neighbor (NNN) terms. We have already seen the effects of intra-cellular and inter-cellular hopping terms, denoted as v and w, respectively, alongside the coupling terms t_1 *and* t_2 that link the two one-dimensional SSH chains. We will investigate the influence of additional NNN terms t_3 *and* t_4 within each leg of the chain. Previous research has shown that without these extended terms, the winding numbers (W) of the system ranges from -1 to 1. Our analysis reveals that by varying the coupling parameters, the winding numbers (W) can shift from -2 to +2, uncovering new topological phases. Furthermore, introducing extended NNN terms causes the winding numbers (W) to extend to ranges from -3 to +3, and with further extensions, this range broadens to -4 to +4. These findings highlight the significant impact of extended NNN interactions on the topological properties of the two-leg-coupled SSH chains.

Keywords: topological phases, SSH model, winding number, two-leg ladder, further-neighbor hopping, phase transition

SECTION I: INTRODUCTION TO THE MODEL

The Su-Schrieffer-Heeger (SSH) model, a cornerstone in the study of topological phases, reveals intriguing properties in one-dimensional systems with alternating hopping parameters. In this study, we extend the model to a two-leg coupled SSH chain, incorporating next-nearest-neighbour (NNN) interactions (1). The intra-cellular parameters v and w, along with the inter-cellular parameters $t_1$and t_2, yield winding numbers ranging from -1 to 1 (2). The paper is organized as follows: Section II describes the methodology for calculating winding numbers to construct phase diagrams. Section III presents the results, highlighting the impact of extended NNN terms on topological phases. Finally, Section IV discusses the implications of these findings and suggests directions for future research. By extending the NNN term across additional unit cells, we observe how the winding number range evolves and uncover new topological phases.

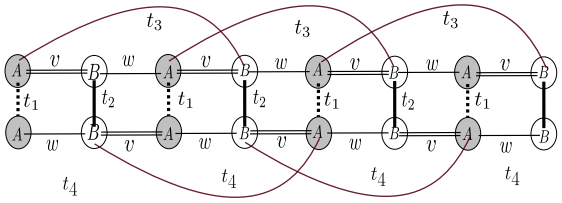


Figure 1: Schematic Diagram of the two-leg-coupled SSH model. The model includes intra-cellular hopping terms v and w, inter-cellular coupling terms $t_1 and\ t_2$, and next-nearest-neighbor (NNN) terms t_3 *and* t_4.

SECTION II: THEORETICAL MODEL AND WINDING NUMBERS

Here, the field operator $\alpha_{j,n}$ $(\alpha_{j,n}^{+})$ annihilates (creates) a particle at sublattice α (which can be a or b) of the n-th leg and j-th unit cell. The intra-leg hopping strengths are denoted by v and w, while the inter-leg hopping strengths are denoted by t_1 and t_2. This form of the Hamiltonian describes two-leg-coupled SSH chains with staggered inter-leg hoppings and opposite dimerizations.The Hamiltonian can be formulated as the following two-leg-coupled SSH model:

$$H^{n}{}_{SSH} = \sum_{j=1}^{N}\left(va^{+}{}_{j,0}b_{j,0} + wa^{+}{}_{j,1}b_{j,1} + t_1\, a^{+}{}_{j,0}a_j + t_2 b^{+}{}_{j,0}b_{j,1}\right) + \sum_{j=1}^{N-1}\left(wa^{+}_{j+1,0}b_{j,0} + va^{+}_{j+1,1}b_{j,1}\right) + \sum_{j=1}^{N-2}\left(t_3\, a^{+}_{j,0}b_{j+n,0} + t_4 b^{+}_{j,1}a_{j+n+1,1}\right) + H.c.$$

The Bloch space Hamiltonian is $\psi_k^{\dagger} H(k)\psi_k$, where $\psi_k = \left(a_{k,0}, b_{k,0}, a_{k,1}, b_{k,1}\right)^T$ and

$$H^n(k) = \begin{bmatrix} 0 & 0 & t_1 & w + ve^{-ik} + t_4 e^{(n+1)ik} \\ 0 & 0 & v + we^{ik} + t_3 e^{-nik} & t2 \\ t_1 & v + we^{-ik} + t_3 e^{nik} & 0 & 0 \\ w + ve^{ik} + t_4 e^{-(n+1)ik} & t_2 & 0 & 0 \end{bmatrix}$$

$$= \begin{bmatrix} 0 & h^{\dagger} \\ h & 0 \end{bmatrix}$$

$$where,\ h = \begin{bmatrix} t_1 & v + we^{-ik} + t_3 e^{nik} \\ w + ve^{ik} + t_4 e^{-(n+1)ik} & t_2 \end{bmatrix}$$

Here, n can be 1, 2, or 3, corresponding to the 1st, 2nd, or 3rd next-nearest-neighbor (NNN) models, respectively. Now to determine the winding number, the topological invariant we will calculate here, $W = \int \frac{dk}{2\pi i} Tr[h^{-1} d_k h]$, With this, we can demonstrate the necessary phase diagrams in the parameter space.

SECTION III: TOPOLOGICAL PHASE TRANSITION

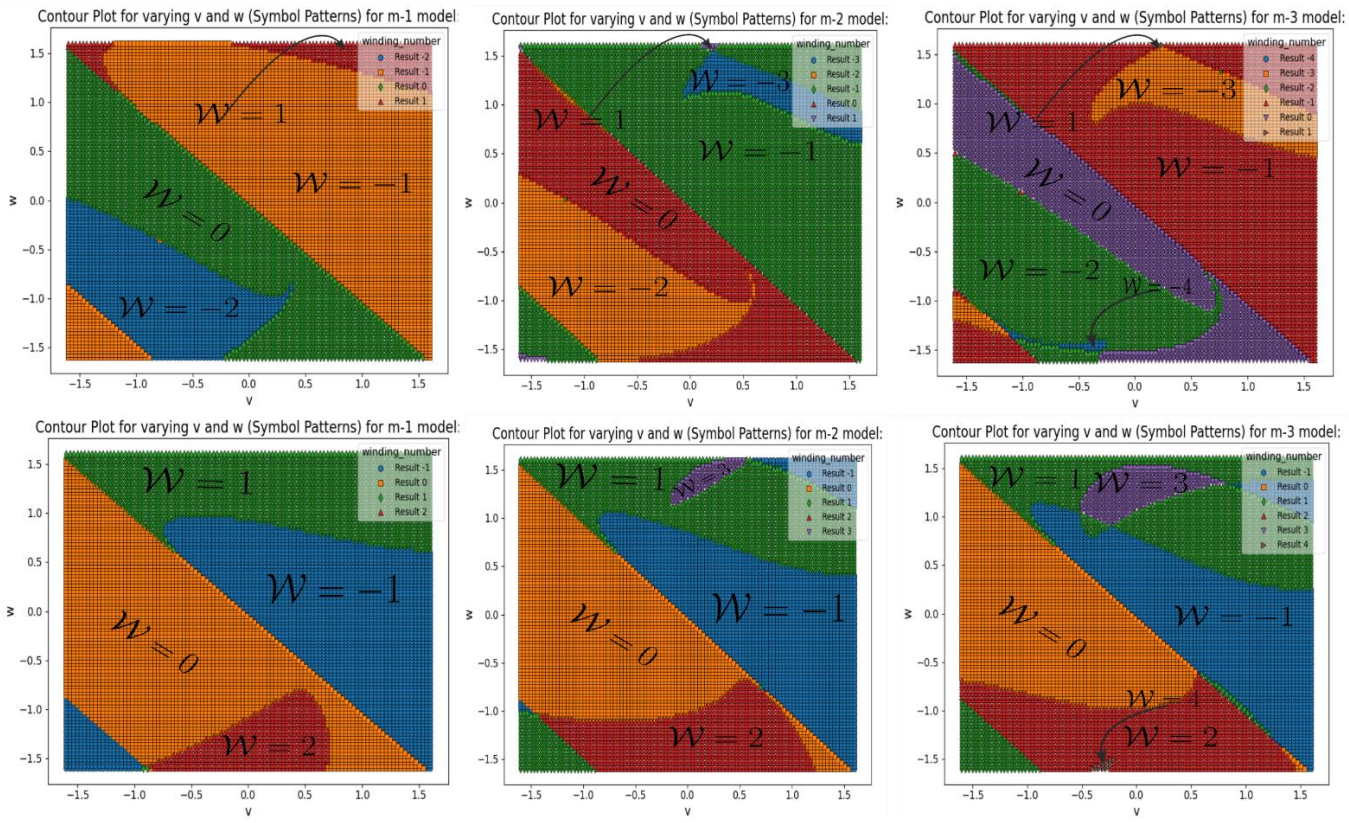


Figure 2: Phase diagrams on w-v plane for the two-leg SSH ladder model with varying next-nearest-neighbor (NNN) extensions. The first row shows phase diagrams for the parameter set $t_1 = 1.4, t_2 = 1, t_4 = 1, and\ t_3 = 1.5,$ corresponding to the 1st, 2nd, and 3rd NNN extensions. The second row shows phase diagrams for the parameter set $t_1 = 1.4, t_2 = 1, t_4 = 1.5, and\ t_3 = 1$, also corresponding to the 1st, 2nd, and 3rd NNN extensions. In each diagram, the hopping terms v and w are varied from 0 to 2 and -2 to 2, respectively, illustrating the topological phases in parameter space.

For simplicity, the models with 1st, 2nd, and 3rd next-nearest-neighbor (NNN) extensions are referred to as the m_1, m_2, and m_3 models, respectively. For the parameter set: $\mathrm{t}_1 = 1.4, \mathrm{t}_2 = 1, \mathrm{t}_3 = 1.5, \mathrm{and}\ \mathrm{t}_4 = 1$, the winding number varies from -1 to 2 for the m_1 model, from -1 to 3 for the m_2 model, and from -1 to 4 for the m_3 model. For the parameter set: $\mathrm{t}_1 = 1.4, \mathrm{t}_2 = 1, \mathrm{t}_3 = 1, \mathrm{and}\ \mathrm{t}_4 = 1.5$, the winding number varies from 1 to -2 for

the m_1 model, from 1 to -3 for the m_2 model, and from 1 to -4 for the m_3 model. We have considered three models, denoted as m-n, where n varies from 1 to 3. For the case where $t_3 > t_4$, we observed that the winding numbers (W) vary from -1 to (n+1), and the case where $t_3 < t_4$, we observed that the winding numbers (ν) vary from –(n+1) to 1. This indicates the emergence of new topological phases as the NNN terms are varied, providing a deeper understanding of the SSH model's behavior under extended interactions.

SECTION IV: DISCUSSION

We introduced extension terms in a two-leg SSH ladder model, and by extending these terms to the next-nearest neighbors, we observed additional topological phases, resulting in new winding numbers.

Model:	Winding Numbers:
1st NNN two-leg SSH ladder	-2,-1,0,1,2
2nd NNN two-leg SSH ladder	-3,-2,-1,0,1,2,3
3rd NNN two-leg SSH ladder	-4,-3,-2,-1,0,1,2,3,4

ACKNOWLEDGMENTS

I sincerely thank the University Grants Commission (UGC) for awarding us the Junior Research Fellowship (JRF) 211610042893-ACTIVE, as well as the DST/INSPIRE Fellowship/2019/IF190085.

REFERENCES

1. Engineering topological phases of any winding and Chern numbers in extended Su–Schrieffer–Heeger models., Rakesh Kumar Malakar and Asim Kumar Ghosh. s.l. : J. Phys.: Condens. Matter, 2023.

2. Topological phases and type-II edge state in two-leg-coupled Su–Schrieffer–Heeger chains. Tianqi Luo , Xin Guan , Jingtao Fan , Gang Chen and Suo-Tang Jia. 2022, IOP Publishing Ltd, p. 9.

Interacting Grüneisen parameters in the spin 1/2 XX chain extended with three spin interactions

Vrushali Kapase[1], Pradeep Thakur[2] and P. Durganandini[3, *]

[1, 3]*Department of Physics, Savitribai Phule Pune University, Pune 411007, Maharashtra, India*
[2]*School of Physical Sciences, National Institute of Science Education and Research, Jatni 752050, Odisha, India*
[2]*Homi Bhabha National Institute, Training School Complex, Anushaktinagar, Mumbai 400094, Maharashtra, India*
*Corresponding author: pdn@physics.unipune.ac.in

Abstract. We study the interaction dependent caloric effects in the exactly solvable spin-1/2 XX chain model in the presence of three-spin interactions of the XZX+YZY and XZY-YZX types. We introduce and compute novel 'interacting' Grüneisen ratios and study their dependence on the three spin interaction strengths. We show that interacting Grüneisen ratios not only capture the phase diagram but can also be used to characterize the nature of quantum phase transitions.

Keywords: Quantum phase transitions, three spin interactions, caloric effects, interacting Grüneisen ratios

INTRODUCTION

Quantum phase transitions (QPTs) in low dimensional spin systems are being intensely investigated in recent years due to their relevance both as tractable paradigmatic models of strongly interacting many-body systems and experimental realization in many quasi-one dimensional compounds[1, 2]. An important way to experimentally identify and characterize QPTs is via Grüneisen parameters which quantify the enhanced caloric effects at very low temperatures near a quantum critical point(QCP), usually tuned by some external parameters like pressure, magnetic field, etc [3, 4, 5]. In recent years, caloric effects due to interaction parameters driving the QPTs have also begun to be explored [6]. In this work, we study the spin- 1/2 XX spin chain model extended with three-spin interactions of the XZX+YZY and XZY-YZX types [7]. The model exhibits a rich ground-state phase diagram with multiple gapless spin-liquid phases and QPTs between them [8, 9]. When both kinds of three spin interactions are present, the model shows novel orbital antiferroelectricity and higher dimensional magnetoelectric order in a certain parameter regime [10]. The magnetic Grüneisen ratio quantifying the magnetocaloric effect tuned by the magnetic field has also been studied [11]. In this work, we study the caloric effects of the three spin interaction strengths by introducing novel interacting Grüneisen ratios. We show that the interacting Grüneisen ratios not only capture the phase diagram but can also be used to characterize the nature of QPTs between the different gapless spin-liquid phases. We mention here that the caloric studies are also of practical importance in refrigeration technology as it is possible to realize such spin chain systems with tunable interaction strengths on various platforms [4, 5].

MODEL

The Hamiltonian H for the XX spin- 1/2 chain extended with three spin interactions, in the presence of external magnetic field h_z in z-direction and electric field E along y direction can be written as [9]:

$$H = \sum_n J(S_n^x S_{n+1}^x + S_n^y S_{n+1}^y) + (A-2BE)(S_n^x S_{n+1}^z S_{n+2}^x + S_n^y S_{n+1}^z S_{n+2}^y) + (B+2AE)(S_n^x S_{n+1}^z S_{n+2}^y - S_n^y S_{n+1}^z S_{n+2}^x) + E(S_n^x S_{n+1}^y - S_n^y S_{n+1}^x) - h_z S_n^z \quad (1)$$

where S_n^a, a= x, y and z denote spin operator at the nth site of the spin chain, J (> 0) is the strength of the nearest neighbor XX interaction, A and B denote the strengths of the three spin interactions of the XZX + YZY and XZY-YZX types respectively [3]. The above Hamiltonian can be diagonalized by a Jordan-Wigner fermion transformation of the spin operators and subsequent Fourier transform (the lattice constant is set to1):

$$H = \frac{1}{2\pi}\int_{-\pi}^{\pi} dk \varepsilon_k c_k^+ c_k + \frac{Nh_z}{2} \qquad \text{where,} \quad \varepsilon_k = -h_z + J\cos(k) - E\sin(k) - \frac{(A-2EB)}{2}\cos(2k) + \frac{(B+2AE)}{2}\sin(2k) \quad (2)$$

The partition function $Z_N = Tre^{-\beta H}$ can be then easily obtained from which various thermodynamical quantities like the free energy, entropy, magnetization, etc. can be computed exactly. In earlier work [10], we showed (for the case with no external fields), the existence of a critical curve C (B_c , A_c) (see Fig.1(A) and Fig. 2(A)) in the three spin interaction parameter space separating two gapless spin liquid phases, the so called SL_1 and SL_2 phases. It was also observed that the critical points, A_c=0, B_c =±1, are qualitatively different from that of the other QCPs along the curve and correspond to different universality classes. In the following, we discuss the nature of the caloric effects due to the three spin interactions by defining novel interacting Grüneisen ratios in an effort to identify and characterize the nature of the different QCPs along the critical curve. Interacting Grüneisen ratios Γ_A and Γ_B are defined (in analogy with magnetocaloric effect) and given as (s is entropy per spin; Boltzmann constant k_B=1):

$$\Gamma_A = -\frac{1}{T}\frac{(\partial s/\partial A)_T}{(\partial s/\partial T)_A} = \frac{1}{T}\left(\frac{\partial T}{\partial A}\right)_s = \frac{\int_{-\pi}^{\pi} d k \varepsilon_k n_k (1-n_k)(E\sin(2k) - \frac{1}{2}\cos(2k))}{\int_{-\pi}^{\pi} d k \varepsilon_k^2 n_k (1-n_k)} \quad \text{where,} \quad n_k = \frac{1}{1+e^{\varepsilon_k/T}}$$

$$\Gamma_B = -\frac{1}{T}\frac{(\partial s/\partial B)_T}{(\partial s/\partial T)_B} = \frac{1}{T}\left(\frac{\partial T}{\partial B}\right)_s = \frac{\int_{-\pi}^{\pi} d k \varepsilon_k n_k (1-n_k)(E\cos(2k) + \frac{1}{2}\sin(2k))}{\int_{-\pi}^{\pi} d k \varepsilon_k^2 n_k (1-n_k)} \quad (3)$$

RESULTS

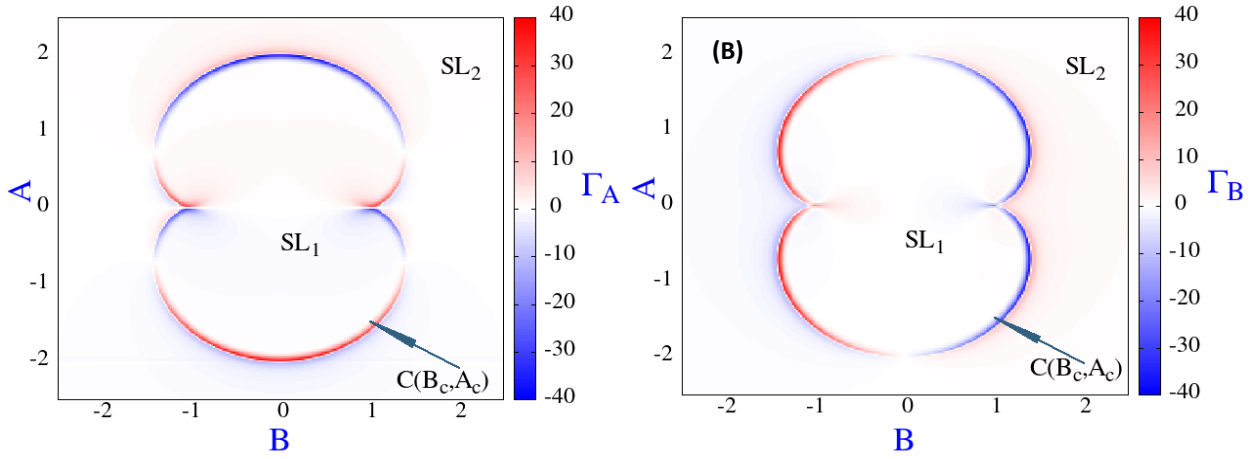


FIGURE 1 The A-B dependence of (A) Γ_A and (B) Γ_B at T=0.006, E=0, h_z = 0

From Figs.1(A) and (B) showing the A−B dependence of the interacting Grüneisen parameters Γ_A and Γ_B at T=0.006, we observe that both Γ_A and Γ_B capture the ground state phase diagram identifying the critical curve C(Bc, Ac) separating the SL1 and SL2 phases as the curve across which the ratios change sign very sharply. Interestingly it can be seen that $\Gamma_A(\Gamma_B)$ also change sign along the critical curve C(Bc, Ac) at points where the derivative ∂C/∂A (∂C/∂B) vanish identically. It can be seen from the figure that in general, $\Gamma_A(\Gamma_B)$ is an even (odd) function of B but an odd (even) function of A. $\Gamma_A(\Gamma_B)$ vanishes identically when A = 0 (B=0). The number of QCPs changes from two (located at A ~ ±2) at B=0 to three (at A ~ ±1.5, 0) at B=±1 and then to four (at A ~ ±1.16, ±0.25) at B=1.32. This can be seen more clearly from the 1-d plots in Fig.2 showing the A (B) dependence of $\Gamma_A(\Gamma_B)$ for some representative fixed values of B(A) respectively.

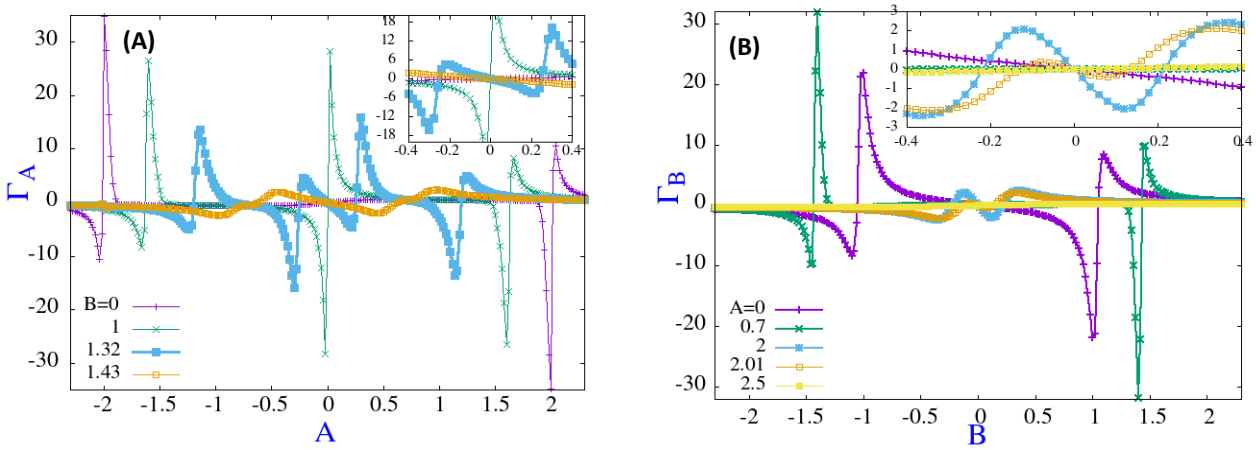


FIGURE 2 (A) The A dependent of Γ_A for B fixed and (B) B dependent of Γ_B for A fixed at T=0.006, E=0, h_z = 0.

From Fig.2 (A) (and inset) we observe that the nature of the QCPs at A_c=0, B_c =1 is different from the other QCPs. From Fig.2 (B) (and inset), we see that the QCPs at A_c~0.7, $B_c \sim \pm 1.43$ and $A_c \sim 2$, B_c =0 correspond to special cases with a different nature of QCPs. We can further quantify this from the derivatives of Γ_A and Γ_B with respect to A and B [11]. We mention here that the temperature dependence of the Grüneisen ratios is $\sim 1/T$ along the critical curve and hence does not provide a way to differentiate between the different kinds of QCPs. However, the interaction strength dependence of interacting Grüneisen ratios does point to a way to identify the different classes of QCPs.

CONCLUSIONS

We have introduced and defined interacting Grüneisen ratios of Γ_A and Γ_B in the XX spin chain extended with three spin interactions. We show that these can be used to identify and characterize the phase diagram. The nature of qualitatively different QCPs can also be obtained from the interaction strength dependence of interacting Grüneisen ratios. Work is in progress to study these effects in more detail [11].

ACKNOWLEDGMENTS

V.K. thanks UGC, India for financial support though the CSIR-UGC Fellowship. P.D. acknowledges SERB, India for financial support through the CRG/2019/003757 and MTR/2019/001411 grants.

REFERENCES

1. S. Sachdev, Quantum phase transition, 2nd ed., Cambridge University Press, Cambridge, 1999.
2. Q. Faure, et al., Nature Physics, Vol. 14, pp. 716 (2018).
3. L. J. Zhu, M. Garst, A. Rosch, and Q. M. Si, Phys. Rev. Lett., Vol. 91, pp. 066404 (2003).
4. P Gegenwart, Rep. Prog. Phys., Vol. 79, pp. 114502 (2016).
5. B. Wolf et al, Proc. Natl. Acad. Sci. USA Vol. 108, pp. 6862 (2011).
6. Y. Yu, S. Zhang,and X. Guan, Phys. Rev. Res., Vol. 2, pp. 043066 (2020)
7. M. Suzuki, Phys. Lett. A, Vol. 34, pp. 338 (1971).
8. I. Titvinidze and G. I. Japaridze, Eur. Phys. J. B, Vol. 32, pp. 383 (2003).
9. M. Topilko, T. Krokhmalskii, O. Derzhko, and V. Ohanyan, Eur. Phys. J. B, Vol. 85, pp. 278 (2012).
10. P. Thakur and P. Durganandini, Eur. Phys. J. B, Vol. 96, pp. 51 (2023).
11. V. Kapase, P. Thakur and P.Durganandini (in preparation).

Dynamic Structure Factor of Warm Dense Homogeneous Electron Gas

Priya Arora[1] and R. K. Moudgil[1,*]

[1]Department of Physics, Kurukshetra University, Kurukshetra – 136 119, Haryana (India)

[*]Corresponding author: rkmoudgil@kuk.ac.in

Abstract. Warm dense matter (WDM) is an exotic state of matter marked by extreme density, temperature, and pressure. It naturally occurs in astrophysical environments, such as the interiors of brown dwarfs and other stellar objects. Interestingly, it can also be produced in laboratories using various techniques. The dynamic response property, such as the dynamic structure factor $S(q,\omega)$, is crucial for understanding the WDM critically, as it can be directly probed in x-ray Thomson experiments. Theoretically, this property is determined by the electron density's response to an external space-time dependent perturbation. In this paper, we report on the $S(q,\omega)$ of a warm dense three-dimensional homogeneous electron gas (3DHEG), which was determined using the finite-temperature version of the dynamical self-consistent mean-field theory developed by Singwi *et al*. Our results are compared directly with the recent ab-initio results of Dornheim et al., obtained using the path integral Monte Carlo (PIMC) simulations. Our study reveals that the static and dynamic local-field correction theories exhibit a reasonably good agreement with the PIMC simulations as compared to the random phase approximation. Our results underscore the significant impact of exchange-correlation effects on $S(q,\omega)$, as characterized by a red shift in the plasmon frequency with increasing coupling and its broadening at large wave vectors.

Keywords: homogeneous electron gas, dynamic structure factor, warm dense matter, dynamic density response function, dynamic local field correction factor

INTRODUCTION

The warm dense matter (WDM) regime is a key area of research in condensed matter physics and is of fundamental importance, both because it occurs naturally, and can also be produced and probed in the laboratory. However, its theoretical description is quite challenging due to complicated interplay of many effects, including quantum degeneracy, thermal effects, and many-body correlations. In principle, quantum Monte Carlo (QMC) simulations can account for all these effects simultaneously, but they are hindered by the Fermionic sign problem. Despite of a significant progress in understanding the static properties [1], the theory of dynamic density response ($\chi(q,\omega)$) of the warm dense electron system, which is of paramount importance in applications of the WDM, is still lacking. In this framework, $\chi(q,\omega)$ plays a crucial role, since its imaginary part determines the dynamic structure factor $S(q,\omega)$, which can be directly accessed through X-ray Thomson scattering measurements [2]. It is only recently that the QMC methods [3-5] have been extended to explore the dynamic properties of the warm dense 3DHEG, and first ab initio results for $S(q,\omega)$ were reported by Dornheim et al. [3]. Motivated by this, in this study we have employed the quantum STLS (qSTLS) approach [6] to deal with many-body correlation effects on $S(q,\omega)$ of the warm dense 3DHEG.

THEORETICAL FORMALISM

The warm dense unpolarized 3DHEG can be viewed as a system of $N = N^{\uparrow} + N^{\downarrow}$ electrons immersed in a rigid charge neutralizing background. To completely describe its thermodynamic state, two basic parameters need to be specified (i) the electron density parameter (or Coulomb coupling parameter) $r_s = a_0^{-1}(3/4\pi n)^{1/3}$, where a_0 is the Bohr atomic radius and n is electron density and (ii) the degeneracy parameter $\tau = k_B T/\varepsilon_F$, with $\varepsilon_F = \hbar^2 k_F^2/2m$ being the Fermi energy. To determine the dynamic structure factor, we study the response of 3DHEG to an external space-time dependent electric potential $V^{ext}(r,t)$. Here, the wave vector and frequency dependent response function $\chi(q,\omega,T)$ plays a pivotal role, which in the linear response regime is given by

$$\chi(q,\omega,T) = \frac{\chi_0(q,\omega,T)}{1 - V(q)[1 - G(q,\omega,T)]\chi_0(q,\omega,T)},$$

with $V(q) = 4\pi e^2/q^2$, and $\chi_0(q,\omega,T)$ representing the density response of electron system having no interactions, which is readily known [7]. The dynamic local-field correction (LFC) factor $G(q,\omega,T)$ contains all exchange-correlation effects beyond the mean-field approximation, i.e., by setting $G(q,\omega,T) = 0$ random phase approximation (RPA) can be recovered. The generalization of the dynamical STLS approach to finite temperature gives $G(q,\omega,T)$ as

$$G(q,\omega,T) = -\frac{1}{n}\int \frac{d\boldsymbol{q}'}{(2\pi)^3}\frac{\chi_0(\boldsymbol{q},\boldsymbol{q}',\omega,T)}{\chi_0(q,\omega,T)}\frac{V(q')}{V(q)}[S(|\boldsymbol{q}-\boldsymbol{q}'|;T)-1].$$

Further, the dynamic structure factor $S(q,\omega,T)$ can be obtained from $\chi(q,\omega,T)$ using the fluctuation-dissipation theorem as

$$S(q,\omega,T) = -\frac{\mathrm{Im}\chi(q,\omega,T)}{\pi n(1-e^{-\beta\omega})};\ \beta = \frac{1}{k_B T}.$$

Evidently, the numerical computation of $S(q,\omega,T)$ is centered around the LFC factor $G(q,\omega,T)$.

RESULTS AND DISCUSSION

The numerical results for the $S(q,\omega,T)$ are depicted in Fig. 1 at the Fermi temperature for r_s=10 and q/q_F=1.88. Due to the intermediate wave vector chosen here, a broad peak is observed in $S(q,\omega,T)$. Evidently, there is a better agreement between the PIMC data and our qSTLS results in terms of both the peak position and width across the entire frequency range as compared to the RPA. Additionally, static LFC-based calculations also closely approximate the PIMC data, showing only a slight deviation from the qSTLS curve. This consistency is expected, as dynamic correlations play a significant role primarily at low temperatures. In contrast, the RPA, which entirely neglects correlation effects, reproduces the broad peak only qualitatively.

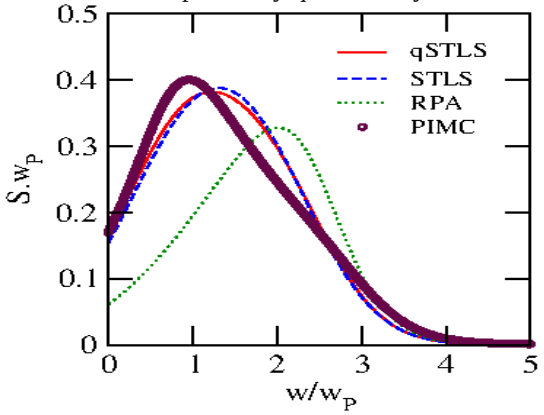


Figure 1. Dynamic structure factor $S(q,\omega,T)$ for r_s=10, q/q_F=1.88 at Fermi temperature. The Symbols represent the PIMC simulation data [3], while the solid and dashed lines have been obtained within the finite-temperature qSTLS and STLS schemes. Dotted line correspond to RPA results. Here, $\omega_p = 4\pi ne^2/m$, is the usual plasmon frequency.

Furthermore, in Fig. 2, our results for $S(q,\omega,T)$ alongside PIMC simulations at τ=1, illustrating its variation with (a) r_s and (b) wavevector q are presented. It can be inferred that as density is decreased, a red shift in the peak position of $S(q,\omega,T)$ is observed for a fixed q. Notably, incorporating LFC within the mean-field approximation via STLS and qSTLS schemes generally yields a good agreement with the PIMC results. At r_s=2, the STLS curve is practically indistinguishable from the PIMC data. However, at r_s=4 and 6, distinctions emerge particularly at intermediate frequencies, yet the red shift is well-reproduced. At r_s=10, the highest coupling strength examined in this study, clear differences in the curves highlight strong exchange-correlation effects in $S(q,\omega,T)$ of the warm dense 3DHEG. As expected with increased density, broader spectra are observed at the same value of q/q_F. The right panel of Fig. 2 presents results at r_s=10 for different q values ($0.63q_F$, $1.88q_F$, $2.94q_F$). For the smallest wave number, $0.63q_F$, a relatively sharp peak slightly above the plasmon frequency ω_p is observed in $S(q,\omega,T)$, indicating the presence of a well-defined collective electron density excitation (i.e., the plasmon excitation) in the 3DHEG. Remarkably, our results accurately reproduce this peak at this small value of q. With increasing wave number, the plasmon peak shows a noticeable dispersion, with the peak however broadening, indicating a damping of the plasma excitation. Our results closely match the PIMC data, showing only slight differences in peak position. Finally, at nearly three times the Fermi wave number, all three spectra exhibit similar widths.

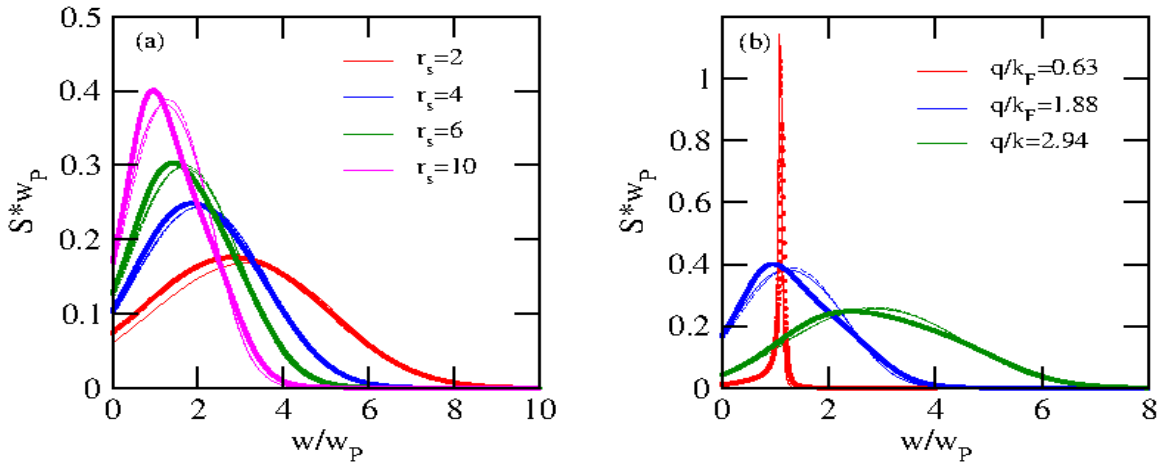


FIGURE 2. Dynamic structure factor $S(q,\omega,T)$ for (a) q/q_F=1.88 at indicated r_s (b) r_s=10 at indicated q, at Fermi temperature. The Symbols represent the PIMC simulation data [3], while the solid and dashed lines have been obtained within the finite-temperature qSTLS and STLS schemes.

SUMMARY AND CONCLUSIONS

In this paper, we have presented a theoretical study of the dynamic structure factor of the warm dense 3DHEG, incorporating exchange-correlation effects beyond the RPA using the static and dynamic LFC factors. Our results are compared with the PIMC simulations by Dornheim *et al*. over a wide coupling regime at Fermi temperature. We demonstrate a significant improvement over the RPA and successfully reproduce the PIMC $S(q,\omega)$ from the electron liquid (r_s=10) to the WDM) regime (r_s=2). Our study highlights the crucial role of correlation effects in understanding the dynamical behavior of the warm dense 3DHEG.

ACKNOWLEDGMENTS

One of the authors (Priya Arora) is grateful to DST, New Delhi for providing financial assistance in the form of WOS-A.

REFERENCES

1. T. Dornheim *et al.*, Phys. Plasmas **30**, 032705 (2023).
2. S. H. Glenzer and R. Redmer, Rev. Mod. Phys. **81**,1625 (2009).
3. T. Dornheim, S. Groth, J. Vorberger, and M. Bonitz, Phys. Rev. Lett. **121**, 255001 (2018).
4. T. Dornheim, *et al*., Phys. Rev. Lett. **125**, 235001 (2020).
5. A.V. Filinov *et al.*, Phys. Rev. B **107**, 195103 (2023).
6. T. Hasegawa and M. Shimizu, Phys. Soc. of Japan **55**, 2278 (1986).
7. G. F. Giuliani and G. Vignale, Quantum theory of the electron liquid (Cambridge University Press, Cambridge, UK, 2005).

Weak Field Induced Spin-Correlation In $BaCo_2(As_{1-x}P_xO_4)_2$

Jai Dev[1,2], Shamma Jain[1,2], Surajit Sardar[1,2], Surinder Pal Singh[1,2], Pallavi Kushwaha[1,2,*]

[1]*CSIR-National Physical Laboratory, Dr. K.S. Krishnan Marg, New Delhi 110012, India*
[2]*Academy of Scientific & Innovative Research (AcSIR), Ghaziabad-201002, India*

[*]*Corresponding author: pallavi.kushwaha@nplindia.org*

Abstract. Materials with a honeycomb lattice are of significant scientific interest, particularly as potential Kitaev Quantum Spin Liquid (KQSL) materials. This interest stems from their ability to host high spin states and effective angular momentum, properties crucial for realizing exotic quantum phenomena. $BaCo_2(As_{1-x}P_xO_4)_2$ is one such compound, characterized by its rhombohedral crystal structure (space group R-3) where the Co^{2+} ions are arranged in a honeycomb lattice. Our current research focuses on the influence of minor phosphorus substitution for arsenic (As) in polycrystalline $BaCo_2(As_{1-x}P_xO_4)_2$ on its magnetic behavior. We investigated this using magnetization measurements. Remarkably, introducing just 1% phosphorus caused a noticeable change in the material's magnetic ordering. The antiferromagnetic ordering temperature (T_N) decreased from approximately 5.4 K to 4.5 K. Furthermore, the doped sample exhibited an intermediate magnetic state between 16 K and 20 K, appearing as a hump in the magnetization curve. This state is highly sensitive to the sample's measurement history and vanishes at very low magnetic fields. Complementary frequency-dependent AC magnetization measurements further support our findings. These measurements revealed a shift in the transition temperature, indicating the presence of spin correlations that persist well above the antiferromagnetic ordering temperature in this system.

Keywords: Magnetic frustration, Quantum spin Liquid, Kitaev Model, Heisenberg interaction, AC susceptibility

INTRODUCTION

Low energy states in condensed matter are heavily influenced by interactions and fluctuations. At low temperatures, materials generally become ordered due to reduced thermal fluctuations. However, some geometrically frustrated magnets remain disordered, resulting in a spin liquid (SL) state where the ground state is dynamic[i,ii]. A related state, the quantum spin liquid (QSL), arises from quantum fluctuations, showing strong spin-correlations without long-range order, even at 0 K. This extensive entanglement leads to residual spin entropy, making QSLs significant for quantum physics and computing[iii,iv]. KQSL stem from strong anisotropy and bond-dependent interactions on a honeycomb lattice, as described by the Kitaev model. This model predicts quantum and topological spin-liquids and Majorana quasiparticles. Achieving a KQSL state requires dominant Kitaev interactions, typically found in materials with strong spin-orbit coupling[v,vi]. Most research has focused on 4d and 5d transition-metal honeycomb lattices like α-$RuCl_3$ and $NaIrO_3$. Although these materials exhibit strong Kitaev interactions, they also show conventional magnetic order at finite temperatures due to non-Kitaev interactions. Suppressing these interactions with magnetic fields can reveal KQSL states[vii,viii]. Here, phosphorus has been used to disturb the magnetic ordering and push the magnetic transition to much lower temperatures. This study demonstrates that phosphorus introduces a clear signature of spin correlation starting at a higher temperature with an additional magnetic state.

EXPERIMENTAL DETAILS

The polycrystalline $BaCo_2(AsO_4)_2$ and 1% phosphorus doped $BaCo_2(AsO_4)_2$ samples were synthesized following the same method used in earlier studies. Powder X-ray diffraction patterns were obtained using a Rigaku system with CuK_α radiation, and Rietveld refinement was conducted with FullProf software. DC and AC magnetization measurements were performed using a Quantum Design MPMS-XL7 with a SQUID option.

RESULTS AND DISCUSSION

X-ray diffraction patterns and Rietveld refinement reveal that both parent and 1% phosphorus-doped compounds were synthesized in a rhombohedral R-3 space group with lattice parameters a = 4.99 Å, c = 23.49 Å and a = 5.00

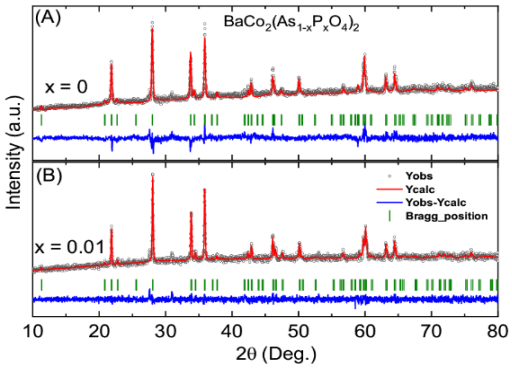


FIGURE 1. *(A-B): Rietveld refinement of room-temperature powder x-ray data of $BaCo_2(As_{1-x}P_xO_4)_2$ for x = 0 and 0.01 samples.*

Å, c = 23.40 Å, respectively (**FIGURE 1(A-B)**). A close observation shows that samples shown a unknown minor impurity peak at near 31˚. Temperature-dependent magnetization at various magnetic fields were conducted in Zero Field Cooled Warming (ZFCW) and Field Cooled Cooling (FCC) protocols, shows an antiferromagnetic (AFM I) phase transition near 5K (T_{N1}) for both the parent and 1% phosphorus-doped compounds (**FIGURE 2 (A-B)**). Interestingly, a second transition near 18K (T_{N2}) at 100 Oe is observed only in the 1% phosphorus-doped compound, which disappears at 0.1T. Furthermore, the divergence between the ZFCW and FCC magnetization curves indicates the emergence of a magnetically disordered state—possibly a spin-glass or spin-liquid phase—in both synthesized samples. This divergence becomes more pronounced with increasing external magnetic field, implying a kinetic arrest of the AFM phase at low temperatures. Interestingly, the splitting observed in the 1% phosphorus-doped sample is marginally greater than that in the undoped compound. At elevated fields, spin alignment tends toward an AFM II configuration, suggesting a competition between AFM I and AFM II interactions. This interplay likely stabilizes a spin-glass-like ground state. This hypothesis aligns with recent neutron scattering studies on $BaCo_2(PO_4)_2$, which reported the coexistence of two distinct short-range magnetic orders below the magnetic ordering temperature, even though conventional spin-glass behavior was not directly observed[13]. The presence of both AFM I and AFM II magnetic states is further confirmed by the isothermal magnetization measurements performed at 1.8 K **(FIGURE 2(C))**. To gain deeper insight into the spin-glass characteristics, we carried out dynamic AC susceptibility measurements **(FIGURE 3)**. In spin-glass systems, magnetic moments are subject to random, competing short-range interactions, leading to irreversible and metastable magnetic states. The AC susceptibility was measured over a frequency range of 1 Hz to 1.2 kHz. Notably, the real part of the AC susceptibility exhibits a clear frequency dependence below the second Neel temperature (T_{N2}), which is considered strong evidence of spin-glass behavior arising from short-range magnetic correlations. Based on these observations, we propose that in the 1% phosphorus-doped sample, the external magnetic field suppresses the AFM II component, potentially

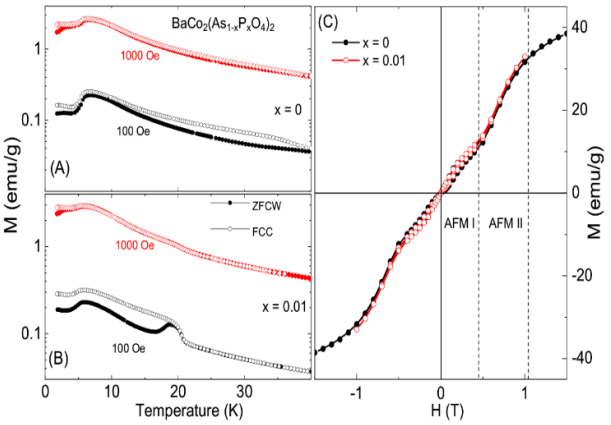


FIGURE 2. *(A-B) Temperature depended magnetization at 100 Oe and 1000 Oe magnetic field of $BaCo_2(As_{1-x}P_xO_4)_2$ (Top) x = 0 (bottom) for x= 0.01 samples. Solid and open symbol corresponding to ZFCW and FCC protocol. (C) Isothermal magnetization at 1.8 K for x = 0 and 0.01 samples.*

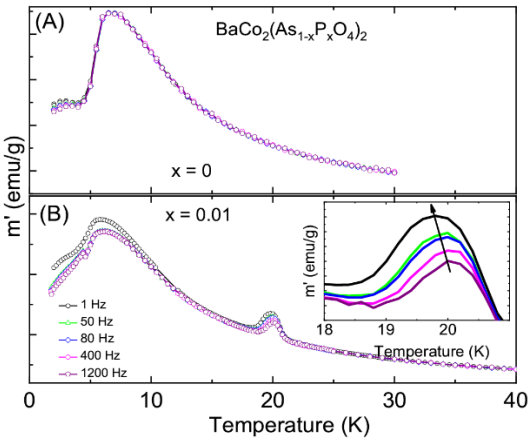


FIGURE 3. *(A-B): AC susceptibility as a function of temperature measured at labeled frequencies of $BaCo_2(As_{1-x}P_xO_4)_2$ for x = 0 and 0.01 samples. Insect to (B): Enlarge version of AC susceptibility as a function of temperature.*

stabilizing a quantum state reminiscent of that predicted by the Kitaev model. This hypothesis is consistent with previous findings in α-$RuCl_3$, where an external field suppresses the Heisenberg-type AFM order, giving rise to a quantum spin-liquid-like state[ix,x].

CONCLUSION

We successfully synthesized polycrystalline samples of both the pure compound, $BaCo_2(AsO_4)_2$, and its 1% phosphorus-doped counterpart. Both materials possess the characteristic honeycomb lattice structure. Our magnetization studies revealed intriguing magnetic behavior in the doped sample. In addition to the established low-temperature antiferromagnetic (AFM) transition at $T_{N1} \sim 4.5$ K, an intermediate magnetic state emerged at $T_{N2} \sim 18$ K. We attribute this additional AFM transition to the coexistence and competition of two distinct AFM phases (AFM I and AFM II). This competition likely leads to a disordered state, potentially a spin-glass. Further evidence for this spin-glass behavior comes from AC susceptibility measurements. These measurements showed frequency-dependent transitions below T_{N2} in the 1% phosphorus-doped compound, a strong indicator of spin-glass characteristics. Significantly, we observed that applying stronger magnetic fields suppressed the AFM transition at T_{N2}. This suggests that by weakening the Heisenberg antiferromagnetic interaction, we might be driving the system towards a quantum phase that aligns with predictions of the Kitaev model.

ACKNOWLEDGMENTS

The authors would like to express their gratitude to the Director of the National Physical Laboratory (NPL) and Dr. M. Majumdar for their valuable insights and fruitful discussions. We also extend our thanks to CSIR, India, for the research fellowship, and to AcSIR-NPL for facilitating Ph.D. registration.

REFERENCES

1. K. Binder, A. P. Young, Spin glasses: Experimental facts, theoretical concepts and open questions, Rev. Mod. Phys. Vol. 58, pp. 801–976 (1986).
2. L. Balents, Spin liquids in frustrated magnets, Nature Vol. 464, pp. 199–208 (2010).
3. T. Mizoguchi, L. D. C. Jaubert, M. Udagawa, Clustering of Topological Charges in a Kagome Classical Spin Liquid, Phys. Rev. Lett. Vol. 119, pp. 077207 (2017).
4. L. Savary, L. Balents, Quantum spin liquids: a review, Repo. on Prog. in Phys. Vol. 80, pp. 016502 (2017).
5. C. Castelnovo, R. Moessner, S. L. Sondhi, Spin Ice, Fractionalization, and Topological Order. Annu. Rev. Condens. Matter Phys. Vol. 3, pp. 35–55 (2012).
6. J. Chaloupka, G. Jackeli, G. Khaliullin, Kitaev-Heisenberg model on a honeycomb lattice: Possible exotic phases in iridium oxides A2IrO3. Phys. Rev. Lett. Vol. 105, pp. 027204 (2010).
7. K. Ran, J. Wang, W. Wang, Z.-Y. Dong, X. Ren, S. Bao, S. Li, Z. Ma, Y. Gan, Y. Zhang, J. T. Park, G. Deng, S. Danilkin, S.-L. Yu, J.-X. Li, J. Wen, Spin-wave excitations evidencing the Kitaev interaction in single crystalline α-RuCl3, Phys. Rev. Lett. Vol. 118, pp. 107203 (2017).
8. K. Kitagawa, K. Kitagawa, T, Takayama, Y. Matsumoto, A. Kato, R. Takano, Y. Kishimoto, S. Bette, R. Dinnebier, G. Jackeli, H. Takagi, A spin–orbital-entangled quantum liquid on a honeycomb lattice, Nature Vol. 554, pp. 341–345 (2018).
9. A. Banerjee, P. L.-Kelley, J. Knolle, C. Balz, A. A. Aczel, B. Winn, Y. Liu, D. Pajerowski, J. Yan, C. A. Bridges, A. T. Savici, B. C. Chakoumakos, M. D. Lumsden, D. A. Tennant, R. Moessner, D. G. Mandrus, S. E. Nagler, Excitations in the field-induced quantum spin liquid state of α-RuCl3. NPJ Quant. Mater. Vol. 3, pp 8 (2018).
10. R. Zhong, M. Chung, T. Kong, L. T. Nguyen, S. Lei, R. J. Cava, Field-induced spin-liquid-like state in a magnetic honeycomb lattice, Phys. Rev. B Vol. 98, pp. 220407 (2018).

Nonequilibrium Work Fluctuations in Force-induced Melting of a Short B-DNA

S. Siva Nasarayya Chari[1,*] and Prabal K. Maiti[2]

[1]*Department of Physics, Faculty of Science, University of Allahabad, Prayagraj – 211002, Uttar Pradesh, India.*
[2]*Centre for Condensed Matter Theory, Department of Physics, Indian Institute of Science, C V Raman Ave, Bengaluru – 560012, Karnataka, India.*

[*]Corresponding author: snchari@allduniv.ac.in

Abstract. A system of a solvated canonical B-DNA of 12-base pairs with the specified sequence is initially equilibrated in a state of zero external force f acting on it. After equilibration, a switching experiment is performed over the system by pulling one end of the DNA while restraining its other end. The finite time pulling process is performed at a constant rate of the applied force, until a maximum value of $400\ pN$. The associated nonequilibrium work done (W) during this process is determined by numerically integrating the force-extension curve, as a function of the applied force. An ensemble of the work values, $p(W)$ is obtained by repeating the pulling experiments a large number of times. The free energy difference (ΔF) between the equilibrium and force-induced melted states of the DNA is determined by employing the Jarzynski equality. The value of ΔF is found to be in close agreement with the conventional equilibrium methods.

Keywords: Work fluctuations, DNA pulling, Switching experiment, Free energy calculations, Jarzynski equality.

INTRODUCTION

Understanding the processes of DNA denaturation, replication of DNA, and their associated free energy differences is important to gain insight into fundamental mechanisms that happen at the level of nucleosomes. Free energy calculations of the molecules like DNA, and RNA under various physiological conditions are highly useful in drug manufacturing. A short double-stranded DNA (dsDNA) can be made to undergo denaturation either by heating or by applying an external force. The latter method is referred to as the force-induced melting [1] of dsDNA. This is a finite-time process in which DNA is switched from an initial equilibrium state A to a final nonequilibrium, unzipped state B. If the pulling process is not so far from equilibrium, then one can invoke the Jarzynski equality(JE) [2] or the Crooks Fluctuation Theorem(CFT) [3] to estimate the equilibrium free energy difference ΔF, between the two states of the DNA. Here, we consider a 12-base pair canonical B-DNA and determine its equilibrium free energy difference along the pathway of force-induced melting, by employing the JE. Methods of the Simulation and the results are discussed in the following section.

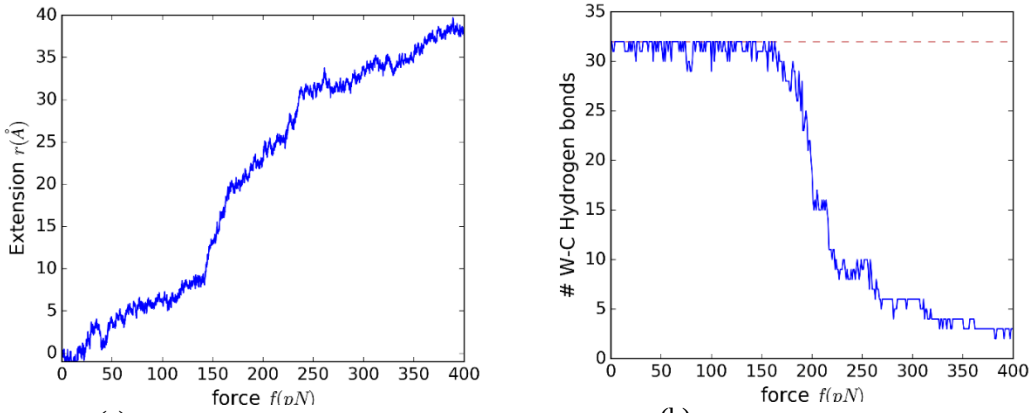
NUMERICAL EXPERIMENT

The structure of a 12-base pair double-stranded B-DNA with the sequence *CGCGAATTCGCG* is created with the LEaP module of the AMBER 10 software [4]. The *parambsc0* force field parameters are used to describe the molecular interactions associated with the DNA. Na^+ counter-ions (22 in number) are added with Joung-Cheatham parameters [4] to neutralize the charge on DNA. It is then solvated with the TIP3P [5] water molecules. It is made sure that the DNA is surrounded by about 10Å of solvent shell even in the fully stretched configuration. The system is then equilibrated at the temperature of 300 K with a standard equilibration protocol [1] and then an ensemble of equilibrium configurations of the system is collected to perform the switching experiment. A time-dependent pulling force,

$$f(t) = f_0 + (f_1 - f_0)\frac{t}{\tau} = f_0 + t(\delta f_\tau) \tag{1}$$

is applied to one end of the DNA, on the $O3'$ and $O5'$ atoms in particular, while keeping the other end of the DNA fixed by applying a strong positional restraint. In eq. (1), the parameters $f_0 = 0$, $f_1 = 400\ pN$, and the rate of pulling, $\delta f_\tau = 10^{-4} pN/fs$ which is about two orders of magnitude faster than the laboratory experiment. The resulting extension of the DNA with the applied pulling force is depicted in Fig. 1(a). From the figure, we observe a structural transition in DNA around $150\ pN$ [8]. The number of Watson-Crick Hydrogen bonds (H-bonds) [10]

that are intact between the base pairs of the DNA during the pulling process is shown in Fig. 1(b). The figure indicates that the maximum number of H-bonds was intact until about $150\ pN$. That means the original B-DNA has now transited to an S-DNA [6]. Further increasing $f(t)$ destroys the H-bonds, as evident from Fig. 1(b).



(a) (b)

FIGURE 1. (a). Extension of the DNA molecule in Å observed with the applied pulling force in pico Newtons. (b). The number of Watson-Crick Hydrogen bonds that are intact in DNA as a function of the pulling force. The dashed line indicates the maximum possible number of 32 H-bonds.

The associated work done during this process is obtained as,

$$W = \int_0^{400\,pN} x(f)df\,, \tag{2}$$

where $x(f)$ corresponds to the extension at force f. The above integral is numerically estimated using a trapezoidal rule. This constitutes one switching experiment. A hundred such pulling experiments were carried out, with each one starting from an initial equilibrium state A, of $f = 0$, and ending with the state B, of $f = 400\ pN$, may not be in equilibrium, yielding an ensemble of work values. Figure 2(a) shows the fluctuating work values with each performed experiment, at the chosen rate of pulling and the corresponding normalized work distribution $p(W)$ is presented in Fig. 2(b). From Fig. 2(b) we note that $\langle W\rangle > \Delta F$, implying a positive dissipation, $W_d = (\langle W\rangle - \Delta F) > 0$, satisfying the Callen-Welton theorem [7], and consistent with the Second law of Thermodynamics. However a small fraction of the work values in the left tail of $p(W)$, where $W < \Delta F$, would violate the Second law [8].

The equilibrium free energy difference ΔF between the states, *A* and *B* of the system could be estimated from the nonequilibrium work distribution $p(W)$ by employing the Jarzynski equality,

$$\begin{aligned} &\left\langle e^{-\beta W}\right\rangle = e^{-\beta\Delta F}\,, \\ &\Rightarrow \Delta F = -\frac{1}{\beta}\ln\left\langle e^{-\beta W}\right\rangle, \end{aligned} \tag{3}$$

where $1/\beta = k_B T$, and the averaging $\langle \ldots \rangle$ is done over the ensemble of pulling trajectories. From eq. (3), we obtained $\Delta F = 91.2$ kcal/mol, which is in close agreement with the equilibrium simulations performed [9] on the same system using the conventional Umbrella Sampling(US) method. However, the control parameter in methods like US is the molecule's end-to-end length ξ, unlike in a pulling process where force f is controlled. Therefore, the trajectory of microstates the system goes through during the process, hence the unzipping pathways could be different for both methods. Despite this, the ΔF value agrees closely for both of them.

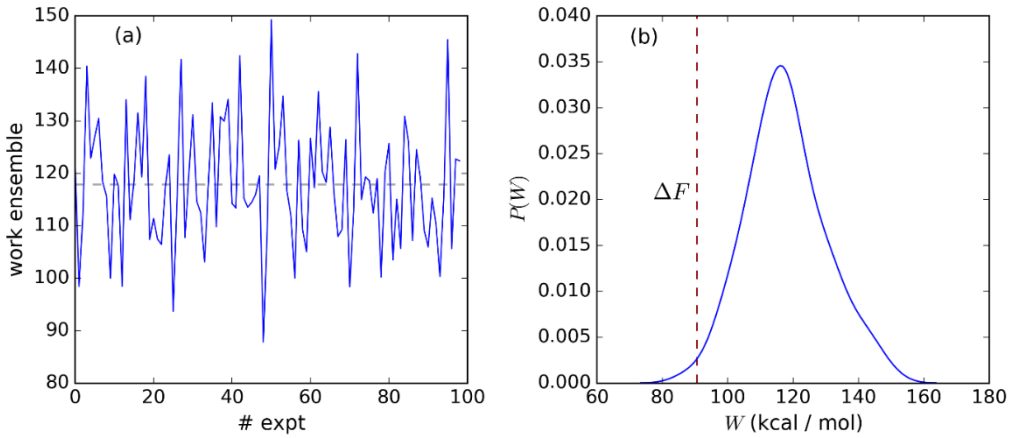


FIGURE 2. (a). Work values (in units of kcal/mol) with the corresponding experiment number; the dashed line represents the average work $\langle W \rangle$. (b). Normalized work distribution $p(W)$, the dashed line corresponds to the equilibrium ΔF $(= 91.2$ kcal/mol) obtained from the Jarzynski equality.

To summarize, a finite time switching process is performed on a canonical B-DNA with 12 base pairs. The equilibrium free energy difference between the natural zipped and the unzipped states of the DNA is determined using the Jarzynski equality, which is found to be in close agreement with the conventional Umbrella sampling method despite the possible differences in the sampled trajectory of microstates, and the pathway of unzipping. Therefore, Jarzynski equality is a viable nonequilibrium method for this system for free energy calculations. However, the work fluctuations become observable only for small systems. The average work $\langle W \rangle \to \Delta F$, and $p(W) \to \delta(W - \Delta F)$ as one tends to the thermodynamic limit.

ACKNOWLEDGMENTS

SSNC thanks the Computational facility provided by the Department of Physics, Indian Institute of Science. The computational facility at the Solid State and Structural Chemistry Unit(SSCU), Indian Institute of Science, Bengaluru is highly acknowledged.

REFERENCES

1. M. Santosh and P. K. Maiti, J. Phys. Condens. Matter vol. 21, pp. 034113 (2008).
2. C. Jarzynski, Phys. Rev. Lett. vol. 78, pp. 2690–2693 (1997).
3. G. E. Crooks, J. Stat. Phys. vol. 90, pp. 1481–1487 (1998).
4. D.A. Case, T.A. Darden, T.E. Cheatham, III, C.L. Simmerling, J. Wang, R.E. Duke, R. Luo, M. Crowley, R.C. Walker, W. Zhang, K.M. Merz, B. Wang, S. Hayik, A. Roitberg, G. Seabra, I. Kolossváry, K.F. Wong, F. Paesani, J. Vanicek, X. Wu, S.R. Brozell, T. Steinbrecher, H. Gohlke, L. Yang, C. Tan, J. Mongan, V. Hornak, G. Cui, D.H. Mathews, M.G. Seetin, C. Sagui, V. Babin, and P.A. Kollman, AMBER 10 (University of California, San Francisco, 2008).
5. W. L. Jorgensen, J. Chandrasekhar, J. D. Madura, R. W. Impey, and M. L. Klein, J. Chem. Phys. vol. 79, pp. 926–935 (1983).
6. J. F. Léger, G. Romano, A. Sarkar, J. Robert, L. Bourdieu, D. Chatenay, and J. F. Marko, Phys. Rev. Lett. vol. 83, pp. 1066–1069 (1999).
7. H. B. Callen and T. A. Welton, Phys. Rev. vol. 83, pp. 34–40 (1951).
8. S. S. N. Chari, K. P. N. Murthy, and R. Inguva, Phys. Rev. E vol 85, pp. 041117 (2012).
9. S. S. N. Chari, and P. K. Maiti, (unpublished).
10. A base pair C-G will possess 3 H-bonds, and A-T will have 2 H-bonds. An H-bond is considered intact if the two atoms are within a distance of 3.2Å and the angle between the base pairs is above a threshold angle of 130°. It is considered to be broken otherwise.

Active Rod Inside a Rigid Ring Exhibits Non-Monotonic Tracer Dynamics

Vrinda Garg[1], Radha Raman[1], Baburao Simma[1], and Surya K. Ghosh[1, *]
[1] *Department of Physics, National Institute of Technology, Warangal, Telangana, 506004, India*

[*]Corresponding author: skghosh@nitw.ac.in

Abstract. Self-propelled objects refer to biological entities that consume energy from the environment or utilize their internal chemical energy to generate directed motion. We study the behavior of self-propelled rods in two dimensions, confined in a rigid ring using Langevin dynamics simulations. To investigate the dynamics of the rods, we measure the number of unique visits made by the rod in the circular confinement with varying Peclet number (Pe). For the passive rod with a lower value of Pe, we observe that the rod explores central as well as the peripheral regions. As we increase the active force of the rod, at intermediate Pe, the rod exhibits only the peripheral motion along the confinement. Counterintuitively, if we further increase the Pe, the rod again starts to perform both the bulk and peripheral motion, a similar trend of motion as for the lower Pe. To elucidate the dynamics, we compute the Mean Squared Displacement (MSD) of the rod. Contrary to common belief, though the MSDs are monotonically increasing with Pe, the nature of the trajectory is switching between the localized peripheral and diffusive bulk motion, which we finally quantify by measuring the unique block visit.

Keywords: Langevin Dynamics, active rod, random walk, anomalous diffusion, active force, soft matter, biophysics, visit matrix.

INTRODUCTION

Confinement and walls in soft matter and biological physics are ubiquitous. The confined geometries have a strong impact on the dynamics of passive and self-propelled particles. For cellular functioning and development, the efficient delivery of cellular components, molecular cargo, and proteins to their targeted site, i.e., intracellular transport within a cell is of utmost importance [1]. The cell interior is a crowded and heterogeneous environment. Modeling intracellular transport in a complex environment is a major challenge. For intracellular transport, two basic mechanisms exist: passive diffusion in the cytosol and directive transport along polymerized cytoskeletal filaments, such as microtubules and actin filaments [1, 2]. Passive diffusion can be considered as the Brownian motion while the directive motion is direction-specific, enabling the biomolecules to travel long distances. Applications include receptor trafficking, virus trafficking, nuclear transport, self-organization of subcellular structure, and molecular motor for the motor-driven intracellular transport inside the cell [2, 3].

We study the dynamics of the passive and self-propelled rod moving inside the rigid ring. We compute MSD of the center of mass of the rod. The dynamics of rod are found to be dependent on the strength of the active force. We find that the passive rod is diffusing slowly and once the activity starts acting, we observe a bulk and peripheral motion of the rod inside the ring. To quantify this combined bulk and peripheral trajectory, we investigate the number of blocks visited by the rod inside the ring mimicking the transport of vesicles in the layered structure of the eukaryotic cell. This study will help in precisely locating the position of the block that has been visited.

MODEL AND METHODOLOGY

We have developed a model of passive and active rod comprised of five beads that moves as a single entity, each bead with same diameter σ, mass m. Each bead in the rod is connected via harmonic potential,

$$V_{harmonic}(l) = k_h (l-l_0)^2$$

where spring constant is given by k_h and set to be 100 in LJ units. l_0 is the equilibrium distance between the two

beads, each of size σ connected by the bond length of σ in LJ units. The circular confinement is modeled as a rigid ring of the diameter 32σ with the periphery having circular beads each of diameter σ. The confining square box

can be represented as R_{Box} (x, y), where x ∈ [–21 21], y ∈ [–21, 21] with periodic boundary conditions in all directions.

The interaction between the beads of rigid rod, ring, and between the rod and the ring are set as excluded volume interactions [4]. It is modeled using truncated Lennard-Jones (LJ) potential, which is commonly known as Weeks-Chandler-Andersen (WCA) potential as

$$U_{LJ}(r_{ij}) = \begin{cases} 4\epsilon[(\frac{\sigma_{ij}}{r_{ij}})^{12} - \left(\frac{\sigma_{ij}}{r_{ij}}\right)^{6}] + \varepsilon, & for\ r_{ij} \leq 2^{\frac{1}{6}}\sigma_{ij} \\ 0, & otherwise \end{cases}$$

Here, the distance between i and j particle is given as $r_{ij} = |r_i - r_j|$, the effective diameter of the interacting pairs is $\sigma_{ij} = (\sigma_i + \sigma_j)/2$ and interaction strength of the potential is given by ε. LJ parameters defining the fundamental units of mass, distance, and energy are represented by m, σ, and ε corresponds to time scale as $t = \sqrt[2]{m\sigma^2/\varepsilon}$ and force scale as f = ε/σ in ps and pN respectively.

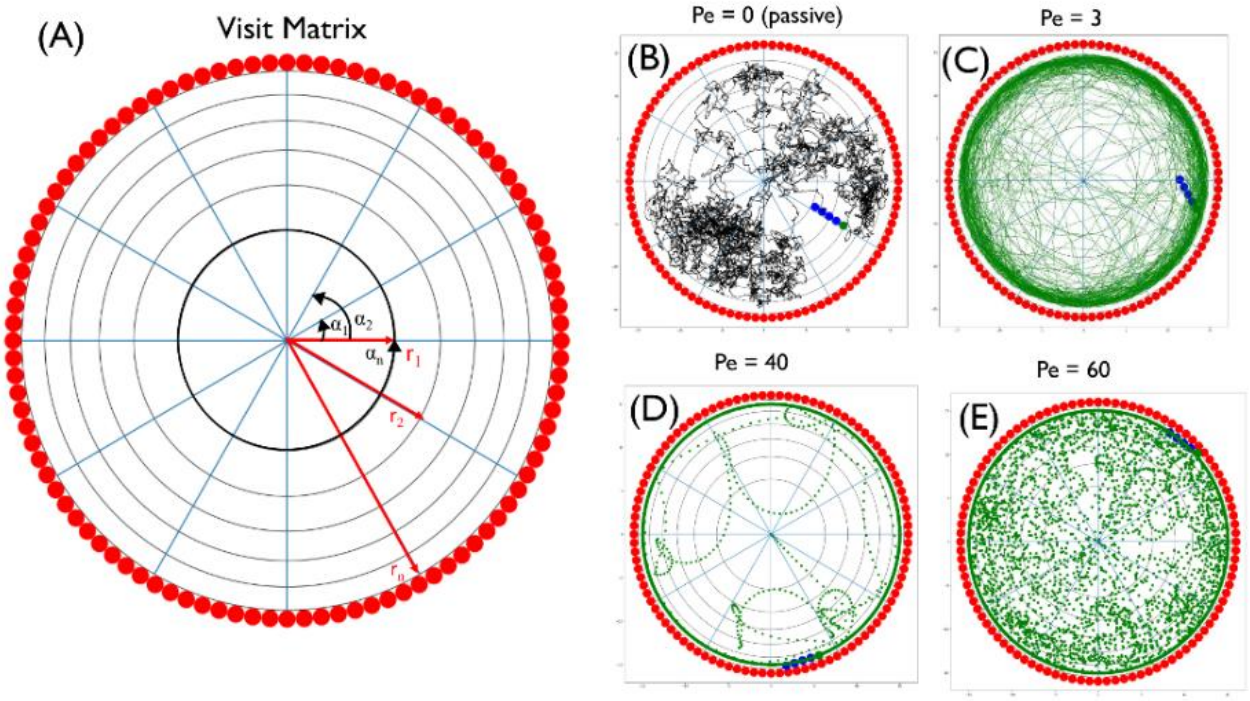


FIGURE 1. Schematic representation of (a) Visit Matrix, and (b) the trajectory of rod inside ring showcasing the number of blocks being visited (green). Pe = 0, passive rod exhibiting random Brownian diffusive motion and covering all the area under the ring. (c) Pe = 3, lower active force, initially the rod is moving in the bulk but later on, exhibits peripheral motion. (d) Pe=40, for intermediate activity, initially rod bounces from the periphery and then exhibits peripheral motion. (e) Pe = 60, for higher activity it shows the similar behavior as that of the lower active force (Pe).

We performed coarse-grained simulation using LAMMPS simulation package [5]. In our simulation, each bead dynamics is directed by the Langevin equation and can be given as

$$m\frac{d^2r(t)}{dt^2} = -\xi v(t) + F^R(t) - \nabla\left(U_{LJ} + U_{harmonic}\right) + F_a,$$

where position is given by r, velocity of each bead is v, mass is given by m, gravity by g, and the friction coefficient is given by ξ, and F^R represents thermal fluctuation which is the random forces satisfying the fluctuation-dissipation theorem,

$$\langle F_i^R(t)\rangle = 0, \qquad \langle F_i^R(t) \cdot F_j^R(t')\rangle = 2dk_BT\,\xi\,\delta_{ij}\delta(t-t'),$$

such that each bead diffusivity is related to the friction coefficient by $D = k_B T/\xi$, where the dimension of the system is d, (d = 2, for our system), the Boltzmann constant is k_B, and the temperature is given by T. In our

simulation, the dimensionless parameters being used are T = 1.0 and friction ξ = 0.7 in LJ units. Activity is achieved by applying a propulsive or active force along the axis of the rod and acting on each monomer of the rod. The strength of the active force is expressed in terms of a dimensionless quantity Peclet number Pe, which can be defined as $\frac{F_a \sigma}{k_B T}$. Thus, Pe=0 recovers the passive rod [6]. All the simulations are carried out using a Langevin thermostat, to start with, a truly random orientation of the rod placed at the center of the ring. We averaged our data over 100 independent realizations to get satisfactory statistics. All the simulations have been carried out for 5×10^8 steps and the simulation integration with a time step of $\Delta t = 0.0005$.

We have developed a visit matrix to examine the dynamics of the rod inside the ring and to find how many times a rod has visited a particular area. Divide the region inside the ring into blocks of equal area. Suppose we choose m number of radii r_i defined as $r_1, r_2, \ldots\ldots, r_m$ where $1 \leq i \leq m$ and n number of angles $\boldsymbol{\alpha}_j$ defined as $\boldsymbol{\alpha}_1, \boldsymbol{\alpha}_2, \ldots\ldots, \boldsymbol{\alpha}_n$ where $1 \leq j \leq n$ from the center of the rigid ring each consisting of a block such that $\boldsymbol{\alpha}_j - \boldsymbol{\alpha}_{j-1}$ remains constant. Rod is introduced in the ring and the time evolution of the rod inside ring is represented by the Visit Matrix concept (see Fig. 1(a)).

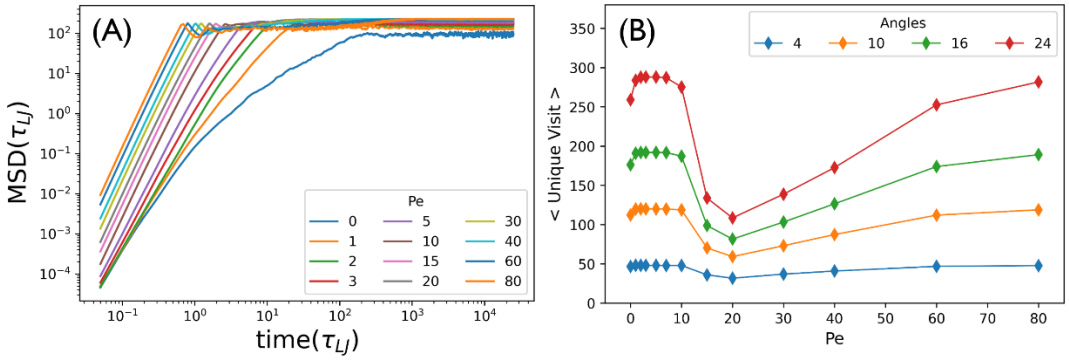


FIGURE 2. (a) MSD as a function of time with the varying activity as Peclet number Pe. (b) Average unique visit performed by the rod inside the confinement as a function of Pe with the varying angles in between the blocks to define the visit matrix.

RESULTS

To understand the dynamics of rod, we first compute the MSD of the center of mass of the rod. We notice that for Peclet number Pe = 0 (Passive rod) (Fig. 1 (b)) the rod exhibits random Brownian motion. At small and intermediate timescales, the rod diffuses both in the bulk and at periphery (see Fig. 2(a)). At large timescales, rod shows peripheral movement which attributes to saturation in its MSD. As activity (Pe > 0) starts to act in, initially for lower Pe rod starts to diffuse in the bulk and then spent most of its time close to the boundary leading to saturation in its MSD (Fig. 1(c)). As the active force increases (Fig. 1(d)) (at intermediate Pe), there are times when the rod moves near the periphery and persistently pushes the periphery before rotating and exhibiting localized peripheral motion along the boundary which can be attributed to a dip in the MSD values leading to non-monotonicity in the curve. Subsequently, rod follows the boundary at large timescales. This results in the plateau and saturation in MSD. In stark contrast to this as active force further increases (Fig. 1(e)) (higher Pe), rod shows both bulk and peripheral motion as that of the lower Pe.

We now examine the switch between the diffusive bulk and localized peripheral motion of rod. We quantify the nature by considering unique block visit by the rod using visit matrix concept (see Fig. 1(a)). We noted the average unique visit made by the rod in 50% of the total time at varying angles dividing the circular confinement into blocks (see Fig. 2(b)). For intermediate Pe, primarily the rod shows the localized peripheral movement leads to a dip in the number of unique block visit which means the rod has not visited much of blocks in bulk. Whereas for the passive, lower active force and higher Pe shows a consistent behavior for the unique block visit. As at these values, the trajectory of the rod is switching between the diffusive bulk and the localized peripheral motion and hence larger number of unique block visited.

ACKNOWLEDGMENT

SKG would like to thank MATRICS, ANRF (Project No. MTR/2022/000833) for financial support. We want to acknowledge NIT Warangal for the institute fellowship to VG and BR.

REFERENCES

1. J. Elgeti and G. Gomper, *Europhysics Letters* 85(3), 38002 (2009).
2. K. Joshi, H. M.York, C. S. Wright and S. Iyer-Biswas, *Annual Review of Biophysics* 53(2024).
3. P. C. Bressloff, and J. M. Newby, *Reviews of Modern Physics* 85(1), 135-196 (2013).
4. V. Garg, R. Mathew, R. Ibrahim, K. Singh, & S. K. Ghosh, *Iscience*, 27(4), 109348 (2024).
5. V. Garg, R. Mathew, A. Chatterjee, & S. K. Ghosh, *STAR protocols*, 6(1), 103568 (2025).
6. P. Kumar, and R. Chakrabarti, *Soft Matter* 19(35), 6743-6753 (2023).

Small Angle Neutron Scattering Study of Hydrophobic Silica Aerogels

A. A. Talkatkar[1], R. Raut Dessai[1a)], D. Sen[2]

[1]*School of Physical and Applied sciences Goa University Taleigao Plateau, Panjim, Goa 403206, India*
[2] *Solid State Physical Division, Bhabha Atomic Research Centre, Trombay Mumbai 400085, India*

[a)] *reshma@unigoa.ac.in*

Abstract. Small angle neutron scattering is well established method to probe nanostructures. Nano structural silica aerogels were prepared by ambient pressure drying method. Amorphous nature of the silica aerogel is confirmed by x ray diffraction. Fractal structure of the silica aerogel has been observed which arise as a result of aggregation and the synthesis condition. Fractal dimension was found to vary from 2.35 to 2.87 indicating highly porous nature of aerogel. With increase in surfactant concentration the correlation length (ξ) increased from 140 to 300nm.
Keywords: Silica, Aerogel, Hydrophobic, Ambient Pressure, SANS

INTRODUCTION

Aerogels exhibits three-dimensional open pore structure formed by substituting the liquid component of the gel with a gaseous element while retaining its structure [1]. Silica aerogels have many applications in various fields because of their unique properties. They are extremely lightweight and mesoporous and hence considered as a promising candidate for thermal insulation and different industry applications. The main drawback of silica aerogel is that it has less mechanical strength. The shape and size of the pores has the potential to change the bulk property of aerogel. Intrinsic property of aerogel is that it is hydrophilic in nature and has polar OH groups on the surface. These OH groups can absorb moisture from the environment. To address this issue, OH groups are replaced by silylating groups by introducing hydrophobic silica precursors like MTMS, TMCS etc. [2]. Hence hydrophobic silica aerogel is synthesized using TEOS precursor and MTMS as co-precursor by ambient pressure drying [3]. In this study, Small Angle Neutron Scattering (SANS) study on silica aerogel was used to determine the fractal dimensions of scale invariant fractal aggregates. This study focusses on synthesizing hydrophobic silica aerogel which holds potential as the next generation insulation material.

EXPERIMENTAL

Hydrophobic silica aerogels were prepared by sol gel method with TEOS and MTMS and TEOS:MTMS molar ratio of 1:1, 2:1 and 1:2 as precursors and cetyltrimethylammonium bromide (CTAB) surfactant. Chemical composition of six samples prepared is shown in Table 1. Gelation initiated after addition of ammonium and the obtained gel was soaked in ethanol and n-hexane to remove residuals. This was followed by ambient pressure drying at 50℃, 150℃, and 200℃. The samples were characterized by XRD, FTIR, Raman spectroscopy and Neutron scattering.

Rigaku X-Ray diffractometer (Cu Kα), in the step size 0.02° and the scan rate of 5° per minute was used in the scanning range 10° to 90°. Raman spectra analysis performed using laser of wavelength of 532 nm. Medium resolution small angle neutron scattering (MSANS) readings were measured at Dhruva reactor, BARC, Mumbai [4]. The experiments were conducted at room temperature, 0.003 to 0.173 nm^{-1} as the q range with neutron incident wavelength was 0.312 nm. The scattered intensities Vs momentum transfer vector q was measured.

TABLE 1. Chemical composition of Hydrophobic Silica Aerogel samples

Sample Name	A1	A2	B1	B2	C1	C2
TEOS:MTMS	2:1	2:1	1:1	1:1	1:2	1:2
CTAB (gm)	0.2	0.5	0.2	0.5	0.2	0.5

RESULTS AND DISCUSSION

The broad hump at 23 degrees in the XRD pattern is the characteristic peak of amorphous silica and was recorded in all the samples of aerogel (Fig. 1). FTIR confirmed peaks of asymmetrical stretching, symmetrical stretching, and bending vibrations in the Si-O-Si bonds and the peak at 1273 cm^{-1} ascribed to methyl group. Peaks at 1414 cm^{-1}, attributed to deformation vibrations of C-H, and at 2960 cm^{-1} to 2980 cm^{-1}, associated with stretching vibrations of C-H. These consistent peaks across all samples indicate a uniform chemical structure. \

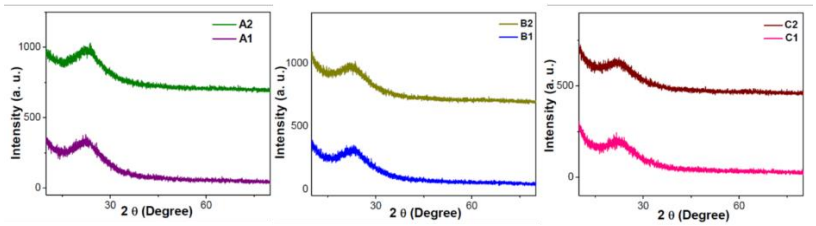


FIGURE 1. XRD plots of Hydrophobic Silica Aerogels (A1, A2, B1, B2, C1, C2)

Raman spectrum recorded from 100 cm^{-1} to 4000 cm^{-1}, Fig 2(a). Two prominent peaks noticed at 2922 cm^{-1} and 2984 cm^{-1} which are attributed to stretching vibrations of CH_2 and CH_3 groups in alkyl chain. Which is also associated with amorphous nature of silica.

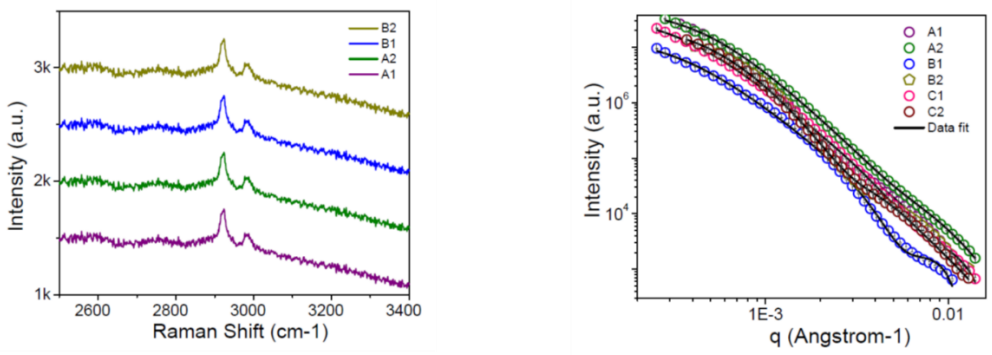


FIGURE 2. (a) Raman spectrum of sample A1, A2, B1 & B2 (b) SANS profile of silica aerogels with the fitted data (errors are smaller than the size of the symbols)

Small Angle Neutron Scattering plot and their fit on the series of silica aerogel, (Fig 2(b)) provides information on three different aspects: fractal geometry the mean size of the fractal cluster and the particle size which agglomerate together to form cluster and the fractal dimension (D_f). Power law behavior is observed at lower which is characteristic of fractal structure. Guinier model fits the Guinier function to the data directly in accordance with eq (1). The fractal model calculates scattering from fractal-like aggregates, eq (2).

$$I(q) = G \cdot exp\left[\frac{-q^2 {R_g}^2}{3}\right] + Background \quad (1)$$

$$I(q) = \phi\, V_{block}\, (\rho_{block} - \rho_{solvent})^2\, P(q)\, S(q) + Background \quad (2)$$

where ϕ is the volume fraction of the spherical particles of radius R_0, V_{block} is the volume of a single building block, $\rho_{solvent}$ is scattering length density of the solvent, and ρ_{block} is scattering length density of the building blocks, and P(q), S(q) are scattering from randomly distributed spherical particles and the interference from such building blocks organized in a fractal-like clusters. P(q) and s(q) are given by relation:

$$P(q) = \left[\frac{3(\sin(qr) - qr\cos(qr))}{(qr)^3}\right]^2 \quad (3)$$

$$S(q) = 1 + \frac{Df\,\Gamma(Df-1)}{[1+1/(q\xi)^2]^{(Df-1)/2}} \frac{sin[(Df-1)tan-1(q\xi)]}{(qR_0)^{Df}} \quad (4)$$

ξ is the correlation length and D_f is the fractal dimension, representing cluster size and the self-similarity of the structure.

In the context of the nanostructure of this aerogel, it may be inferred that the dimension of scattering centers from the Guinier region is due to the average size of pores in these gels. Such pores may or may not be linked to each other. The fractal dimensions vary from 2.35 to 2.87 which is indicative of a rather complex interconnection of porous regions. Such structures are function of both composition and preparation conditions (Table 2). Correlation length (ξ) of hydrophobic silica aerogel samples was found to be 140 nm to 300 nm. The correlation length decreases with the increase in surfactant. The densification occurs through coalescence of small particles into the larger ones thereby increasing the aggregate size, which may lead to improvement of mechanical strength of the aerogel.

TABLE 2. Structural parameter correlation length (ξ) and Fractal dimension D_f of hydrophobic silica aerogel samples estimated from Guinier and Fractal Model.

Sample Name	Particle Radius R_0(nm)	Correlation Length ξ (nm)	Fractal Dimensions D_f
A1	117.1 ± 5.8	220.1 ± 0.9	2.77
A2	57.2 ± 10.1	210.0 ± 0.8	2.63
B1	47.5 ± 0.6	294.8 ± 0.1	2.35
B2	100.3 ± 3.4	144.3 ± 0.5	2.87
C1	39.1 ± 1.8	283.4 ± 1.1	2.49
C2	101.8 ± 4.8	181.2 ± 0.7	2.82

CONCLUSION

Hydrophobic silica aerogels were synthesized via ambient pressure drying method. From Xray diffraction amorphous nature was confirmed. Structural analysis using Small Angle Neutron Scattering (SANS) revealed that the sample B_1 having 1:1 TEOS to MTMS ratio and 0.2g CTAB, exhibited the largest correlation length and smallest fractal dimension, indicating significant fractal characteristics. The mass fractal dimensions varied from 2.35 to 2.87, confirming their porous nature. Correlation length decreased with the increase in CTAB concentration leading to the densification due to the coalescence of smaller particles to form larger aggregates. The above study Indicates that the addition of surfactant leads to tuning of correlation length in aerogel. Which can strengthen the silica aerogels.

ACKNOWLEDGMENT

The authors would like to acknowledge, UGC DAE CSR for their support through funded project UGC-DAE-CSR-107 and SSPD-BARC for SANS measurements.

REFERENCES

1. J. L. Gurav, I. Jung, H. Park, E. S. Kang, and D. Y. Nadargi, vol. 2010, (2010).
2. S. Zhao, O. Emery, A. Wohlhauser, M. M. Koebel, C. Adlhart, and W. J. Malfait, vol. 160, pp. 294–302, (2018).
3. A. A. Pisal and A. V. Rao, *J. Porous Mater.*, vol. 23, no. 6, pp. 1547–1556, (2016).
4. S. Mazumder, D. Sen, and A. K. Patra, vol. 63, no. 1, pp. 165–173, (2004).

In-situ Fabrication Of ZnO@PVA Nanocomposite Film: A Flexible Free-standing Film With Antimicrobial Activity

Saiyad Akhirul Ali[1, 3, *], Sarathi Kundu[1, 3], Himadri Nath[1, 3], Aditya Narayan Konwar[2, 3] and Debajit Thakur[2, 3]

[1]*Soft Nano Laboratory (SNL), Physical Sciences Division, Institute of Advanced Study in Science and Technology (IASST), Vigyan Path, Paschim Boragaon, Garchuk, Guwahati, Assam 781035, India.*
[2]*Microbial Biotechnology Laboratory, Life Sciences Division, Institute of Advanced Study in Science and Technology (IASST), Vigyan Path, Paschim Boragaon, Garchuk, Guwahati, Assam 781035, India.*
[2] *Academy of Scientific and Innovative Research (AcSIR), Ghaziabad-201002, India*.

[*] Corresponding author: saiyadali224@gmail.com

Abstract. A flexible, free-standing PVA-ZnO nanocomposite film was prepared using a simple solution casting technique. The presence of ZnO nanoparticles (NPs) was verified through XRD, SEM, and TEM. Mechanical and antimicrobial properties were evaluated using stress-strain analysis and inhibition zone measurements on Mueller-Hinton agar plates. The PVA-ZnO films demonstrated excellent flexibility of 645% and notable antimicrobial activity against Gram-negative, Gram-positive bacteria, and fungal strains. These findings suggest the potential of such films for use in packaging and antimicrobial coatings.

Keywords: Polyvinyl alcohol, Flexible, Antimicrobial, ZnO nanoparticle, Nanocomposite film

INTRODUCTION

The development of flexible polymer nanocomposites (PNCs) has received growing interest in recent years due to their enhanced optical, mechanical, electrical, and antimicrobial properties, which result from incorporating inorganic nanostructures into polymer matrices [1]. These unique characteristics make PNCs appropriate for diverse uses such as food packaging, wearable electronics, and optoelectronics. Among various polymers, polyvinyl alcohol (PVA) has gained broad research interest due to its favorable physical, chemical, and biodegradable properties [2]. As a semi-crystalline, water-soluble, non-toxic, and economical synthetic polymer [3], PVA's properties can be tailored by doping with metal such as Au, Ag and Cu NPs and metal oxide such as CuO, and ZnO NPs, which interact with its hydroxyl groups. ZnO and CuO NPs are especially attractive due to their abundance and low synthesis cost, with ZnO being notably less toxic at higher concentrations. ZnO, a semiconductor with a 3.3 eV band gap, exhibits photooxidative, photocatalytic, and antimicrobial behavior, while also enhancing polymer mechanics when embedded in the matrix [4]. Among various fabrication techniques, chemical synthesis is favored for its high yield, energy efficiency, and nanoparticle uniformity. However, there is a growing need for eco-friendly alternatives to hazardous chemical reducing agents. PVA serves as a promising example, acting simultaneously as a reducing, stabilizing, and capping agent.

In this study, a PVA-ZnO nanocomposite film was fabricated using a straightforward solution casting approach, where water served as a green solvent and PVA acted as both the matrix and reducing agent. The resulting film was characterized by XRD, SEM, and TEM, and its mechanical behavior was evaluated using a Universal Testing Machine (UTM). To assess its broad-spectrum antimicrobial efficacy, the nanocomposite film was tested against *E. coli*, *S. aureus*, and *C. albicans*.

EXPERIMENTAL DETAILS

Polyvinyl alcohol (PVA) and zinc acetate dihydrate ($Zn(COOCH_3)_2 \cdot 2H_2O$) were sourced from Merck and Sigma-Aldrich, respectively. To prepare PVA-ZnO nanocomposite films, 10 wt% PVA was first dissolved in double-distilled water (resistivity 18.2 MΩ·cm) and stirred at 70 °C for approximately 3 hours to yield a homogeneous solution. Next, 5 wt% zinc acetate dihydrate ($Zn(COOCH_3)_2 \cdot 2H_2O$) was added into the PVA matrix and the mixture was stirred for another one hour at the same temperature to obtained the homogeneous solution. The solution was then cast onto a polystyrene Petri dish and kept to dry at normal ambient condition for 72 hours. During this process, thermal decomposition of PVA at 70 °C generates hydroxyl radicals, which reduce Zn^{2+} ions to Zn^0. These are subsequently oxidized to ZnO nanoparticles under ambient conditions.

RESULTS AND DISCUSSION

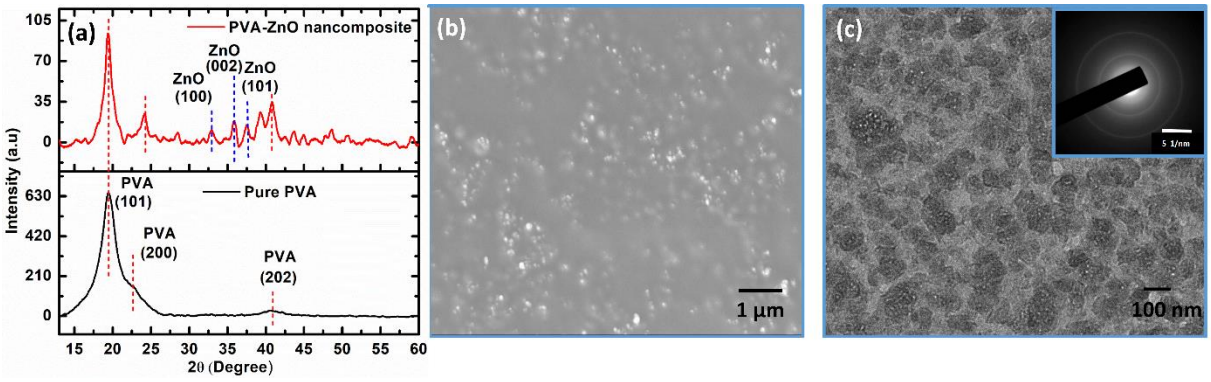
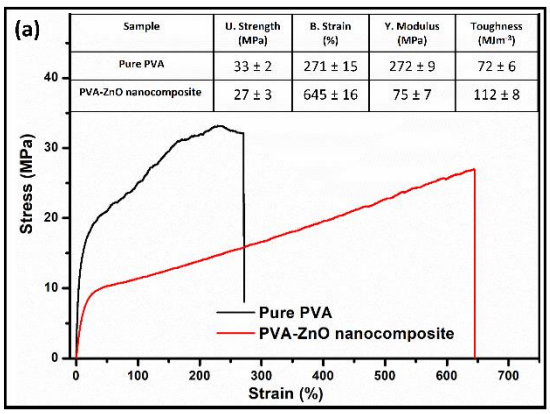


FIGURE 1. (a) XRD patterns of pure PVA and PVA-ZnO nanocomposite film. (b) SEM image showing the surface morphology of the PVA-ZnO nanocomposite film and (c) TEM image of PVA-ZnO nanocomposite solution. Inset: SAED pattern of the nanocomposite solution.

Figure 1(a) shows the XRD patterns for both pure PVA and the PVA-ZnO nanocomposite film. PVA's semi-crystalline nature is confirmed by a dominant peak at $2\theta = 19.72°$ and two weaker peaks appeared at $2\theta = 22.64°$ and 41.0°, which corresponding to the (101), (200), and (202) planes, respectively. These arise from hydrogen bonding among hydroxyl groups in the PVA matrix [5]. The nanocomposite retains these peaks, but also displays three additional reflections at 32.8°, 35.8°, and 37.4°, indexed to the (100), (002), and (101) planes of hexagonal ZnO. A noticeable decrease in the intensity of the diffraction peak at $2\theta = 19.72°$ was observed which signifies the disruption of hydrogen bonding and the formation of complexes between Zn atoms and PVA's hydroxyl groups. The SEM image in Fig. 1(b) indicates that while pure PVA exhibits a smooth surface [6], the incorporation of Zn salts leads to surface roughening, with visible ZnO nanoparticle formation. Fig. 1(c) further confirms this via TEM, which reveals nearly spherical ZnO nanoparticles. The selected area electron diffraction (SAED) inset displays crystalline ring patterns, confirming their structure. The average ZnO particle size is estimated at 130 nm.

Mechanical and antimicrobial performance of the PVA-ZnO nanocomposite was estimated using UTM analysis and agar diffusion tests on Mueller-Hinton plates. Stress-strain plots in Fig. 2(a) reveal that the tensile strength of pure PVA (33 MPa) decreases to 27 MPa upon ZnO incorporation. However, flexibility significantly improves from 271% to 645%. The nanocomposite also exhibits greater toughness and a lower Young's modulus compared to pure PVA. It is also shown in the inset of Fig. 2(a) that the nanocomposite film exhibits more toughness value and Lower Young's modulus than that of pure PVA. The modification of mechanical properties is due to the breaking of H-bonding between the PVA network and complex formation between the Zn ions and the –OH groups of PVA molecules. The antimicrobial activity of pure PVA and PVA-ZnO nanocomposite film against gram-negative and gram-positive bacteria, *E. coli* 227 and MRSA 43300 respectively, and fungi (*C. albicans* 227) are evaluated from Meuller Hilton agar plates. It can be seen from fig. 2(b) that pure PVA film does not show antimicrobial activity, whereas PVA-ZnO nanocomposite film exhibits a significant zone of inhibitions (transparent zone) against all the three microorganisms with an approximate diameter of 16 mm [7].



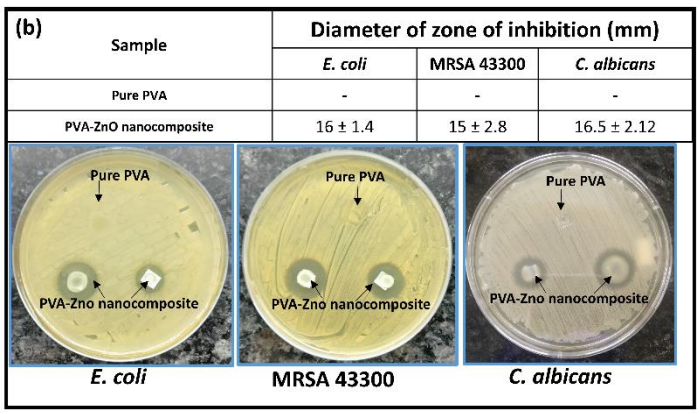


FIGURE 2. (a) Stress-strain curve of pure PVA and PVA-ZnO nanocomposite film and (b) Digital image illustrating the antimicrobial effect against different microbial strains. Inset of (a) mechanical parameter and (b) diameter of zone of inhibition.

CONCLUSION

PVA-ZnO nanocomposite film are fabricated using solution casting technique where water and PVA are used as solvent and reducing agent respectively. The free radicals of hydroxyl originated from the thermal decomposition of PVA reduces Zn^{+2} to Zn^{0}, which finally oxidized and form ZnO NPs at ambient condition. Formation of ZnO NPs inside PVA is confirmed by XRD, SEM and TEM technique. The flexibility of the nanocomposite film is observed to be about 645%. The nanocomposite film also shows excellent antimicrobial activity against different microorganisms.

ACKNOWLEDGEMENTS

Authors acknowledge DST, Govt. of India for financial support and IASST, Guwahati for experimental facilities.

REFERENCES

8. G. Armstrong, Eur. J. Phys., Vol. 36, pp. 063001 (2015)
9. M. Aslam, M. A. Kalyar and Z. A. Raza, *Polym. Eng. Sci.*, Vol. *58*, pp. 2119 (**2018)**
10. N. Hakuto, K. Saito, M. Kirihara and Y. Kotsuchibashi, *Polym. Chem.*, Vol. **11**, pp. 2469 (2020)
11. P. Sivakumar, M. Lee, Y.-S. Kim and M. S. Shim, *J. Mater. Chem. B*, Vol. *6*, pp. 4852 (**2018)**
12. A. G. El-Shamy, W. Attia and K. M. Abd El-Kader, *J. Alloys Compd.*, Vol. **590**, pp. 309 (2014)
13. S. A. Ali, S. Sau and S. Kundu, *Colloids Surf. A: Physicochem. Eng. Aspects*, Vol. **674**, pp. 131840 (2023)
14. I. M. Factori et al., *ACS Appl. Nano Mater.*, Vol. *4*, pp. 7371 (**2021)**

Cholesterol-induced Modification in Lysozyme-DMPA Mixed Langmuir Monolayer

Himadri Nath[1, 2, *], Sarathi Kundu[1, 2] and Saiyad Akhirul Ali[1, 2]

[1]*Soft Nano Laboratory (SNL), Physical Sciences Division, Institute of Advanced Study in Science and Technology (IASST), Vigyan Path, Paschim Boragaon, Garchuk, Guwahati, Assam 781035, India.*

[2] *Academy of Scientific and Innovative Research (AcSIR), Ghaziabad-201002, India*.

[*] *Corresponding author: nathhimadrii89@gmail.com*

Abstract. Langmuir monolayer of pure cholesterol, lysozyme-DMPA (LyD) and cholesterol-lysozyme-DMPA (CLyD) are formed on the aqueous subphase having pH ≈ 7.0. To investigate the effect of cholesterol on the phases and phase transition occurring with monolayer compression, Surface pressure (Π)-mean molecular area (A) isotherms are recorded from all three monolayers. Π-A isotherm reveals a distinct behavior of the CLyD monolayer than that of the LyD monolayer, with the occurrence of plateau region and collapse point comparatively at lower Π. The morphological feature captured from BAM at Π ≈ 30 mN/m shows a more compact structure of the CLyD monolayer than that of the LyD monolayer, causing the more stable nature of the CLyD monolayer at the same Π.

Keywords: Langmuir monolayer, Lysozyme, DMPA, Cholesterol, Π-A isotherm, Brewster Angle Microscope.

INTRODUCTION

Cholesterol, a vital component of cellular membrane, is amphipathic in nature with a polar head group containing a weakly hydrophilic hydroxyl (OH) group and a strongly hydrophobic region made up of four hydrocarbon rings. Such unique structure of cholesterol has enabled its interactions with other lipids and proteins, affecting the viability, fluidity, function, and structural integrity of membranes, which is essential for proper functioning of the membrane [1]. Due to their physiological importance in cell membranes, interaction of cholesterol with lipid and protein is a widely investigated topic. Various methods have been adopted for investigating interactions among membrane components, but the Langmuir-Blodgett method is unique in its ability to develop model membranes at the air-water interface, providing valuable insights into membrane mechanisms [2]. Previously reported studies on cholesterol explains that it can form stable monolayer at air-water interface [3]. Extensive literature is available on Langmuir monolayers of cholesterol/lipid and cholesterol/protein for investigating the effect of cholesterol on other components under different physiological conditions [4, 5]. However, there is still a notable gap in research for detailed understanding the cholesterol's effect on lipid-protein complex system. Three component Langmuir monolayer of cholesterol/protein/lipid, a familiar way to investigate the cholesterol's effect on lipid-protein complex system, is possible by spreading each component at air-water interface. Various phases along with phase transitions in Langmuir monolayer can be detected from Π-A isotherm while in-situ morphological feature can be observed through Brewster angle microscopy (BAM). Investigations on such phases, phase transition, morphological features, etc. will help to understand different biological processes including biomineralization, signalling, active and passive transport through the membrane, etc.

In this article, globular protein Lysozyme, cholesterol, and phospholipid DMPA (1, 2- dimyristoyl-sn-glycero-3-phosphate) are used to develop Langmuir monolayers of pure cholesterol, lysozyme-DMPA (LyD) as well as cholesterol-lysozyme-DMPA(CLyD) monolayer at air-water interface and then investigate the related phases by means of Π-A isotherms. Also, the morphological features at air-water interface are explored using BAM.

EXPERIMENTAL DETAILS

Lysozyme (Sigma-Aldrich), cholesterol (Sigma-Aldrich), and DMPA (Avanti polar lipids) were purchased. Stock solution of pure cholesterol (0.5 mg/ml in concentration) was prepared in a mixture solvent containing chloroform (Sigma-Aldrich, India), methanol (Merck, India), and water (40:20:3 in volume) [6]. Again, keeping the concentration of each compound at 0.5mg/ml both lysozyme-DMPA (LyD) solution and cholesterol-lysozyme-DMPA (CLyD) solutions were prepared in the same specific solvent solution. Three distinct monolayers that are chol monolayer, LyD monolayer as well as CLyD monolayer were formed at the interface of

water subphase, through careful spreading of desired amount of respective solution in a Langmuir trough with Hamilton syringe. Time gap of ≈ 15 min was given before compression of monolayers with speed ≈5 mm/min using double barrier. Surface pressure (Π) in each monolayer was measured using a paper Wilhelmy plate connected to a balance. All the measurements were executed with proper maintenance of room temperature at ≈ 24°C. *In-situ* visualisation of LyD and CLyD monolayers was carried out using BAM (nanofilm_EP4) with a spatial resolution of ≈ 2 μm.

RESULTS AND DISCUSSION

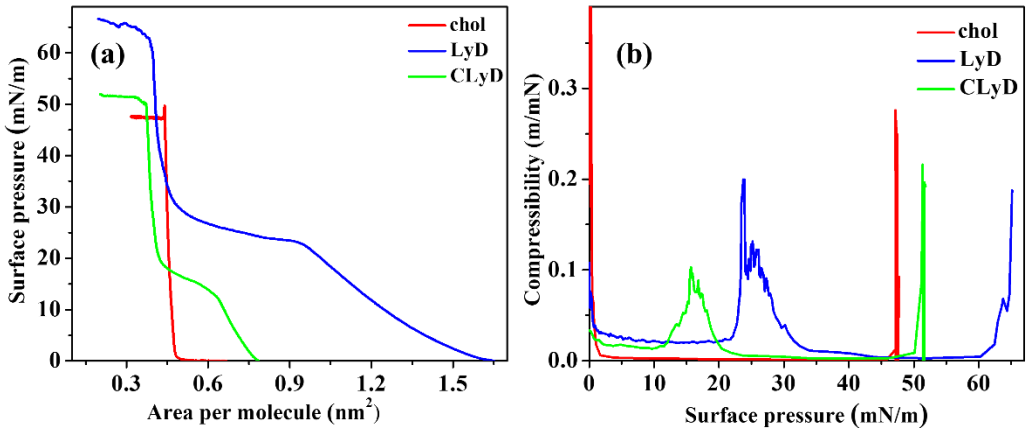


FIGURE 1. (a) Π-A isotherms and (b) isothermal compressibility (κ) curves as a function of Π, recorded from the monolayers of pure cholesterol (chol, red), lysozyme-DMPA (LyD, blue) and cholesterol-lysozyme-DMPA (CLyD, green) at pH ≈ 7.0.

Langmuir monolayers of chol, LyD, and CLyD were formed at the air-water interface of subphase pH ≈ 7.0, and the corresponding Π-A isotherms are shown in Fig. 1(a). As is seen from Fig. 1(a), Π-A isotherm of pure cholesterol shows a steep rise in Π at ≈ 0.49 nm^2/molecule, indicating a transition of the monolayer to a solid phase, which collapses at Π ≈ 47 mN/m. In contrast, the isotherm of LyD monolayer starts to rise from ≈ 1.65 nm^2/molecule almost linearly until the monolayer experiences a Π ≈ 23 mN/m, exhibiting a liquid expanded (LE) phase. Beyond this Π value, a plateau region (in Π ≈ 23-30 mN/m) followed by a steep rise in Π is observed, which collapses with additional compression at Π ≈ 63-65 mN/m. CLyD monolayer, although reflects similar appearance in Π-A isotherm, its plateau region as well as collapse pressure occurs at different Π values, exposing cholesterol-induced modification in monolayer phase transition. Occurrence of plateau and collapse point at lower Π values (≈15 mN/m and ≈ 50 mN/m respectively) can be described from the aspect of condensing effect of cholesterol [4]. For clarification of phase behaviour, isothermal compressibility, $k = -\frac{1}{A}\frac{\partial A}{\partial \Pi}$ [7], calculated from respective Π-A isotherms, are plotted as a function of Π and shown in Fig. 1(b). Comparative analysis shows that the peak of the k-Π curve, depicting the maximum compressibility value, occurs at a lower Π for CLyD than LyD monolayer. Moreover, the maximum compressibility of CLyD monolayer is comparatively less, exposing the enhancement of stiffness in the monolayer due to the presence of cholesterol molecules, which also results in collapse at lower Π in comparison to that in LyD monolayer.

Morphology of LyD and CLyD monolayers, developed at the interface of water subphase, is recorded via BAM at Π ≈ 30mN/m and is shown in Fig.2(a) and Fig. 2(b). At the same Π value, stability of both the monolayers is appraised from normalized mean molecular area-time (A/A_0-t) curves that are shown in Fig. 2(c). In-situ morphological observation clears that at Π ≈ 30mN/m LyD monolayer shows existence of different strips over homogenous pattern (Fig.2a). Meanwhile due to the presence of cholesterol in CLyD monolayer, such strips, existed

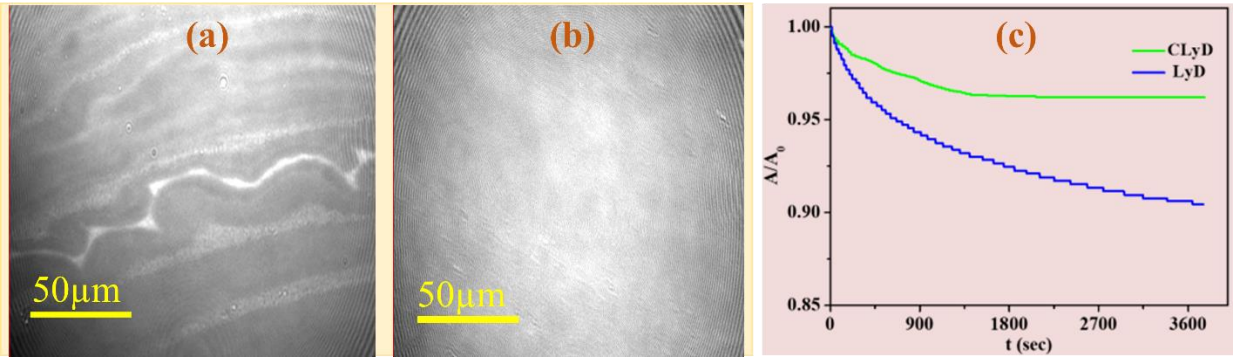


FIGURE 2. BAM image of (a) LyD and (b) CLyD monolayer recorded at $\Pi \approx 30$mN/m with spatial resolution ≈ 2 μm and (c) normalised mean molecular area-time (A/A_0-t) curves of both monolayers at $\Pi \approx 30$mN/m for 1hour.

at lower Π, merges with further compression, resulting in the formation of a homogeneous bright monolayer (Fig.2b) at $\Pi \approx 30$mN/m. From relaxation curves shown in Fig. 2(c), it is clear that at $\Pi \approx 30$mN/m CLyD monolayer is more stable than LyD monolayer with a negligible area loss of 3% and 9% respectively. The results obtained from the stability curves can be justified with the in-situ morphologies (Fig. 2). More compact structure of CLyD monolayer than LyD monolayer at $\Pi \approx 30$ mN/m is responsible for the enhancement of monolayer stability.

CONCLUSION

Pure cholesterol, LyD, and CLyD monolayers formed on an aqueous subphase of pH ≈ 7.0 were studied employing Π-A isotherm and BAM. The presence of cholesterol molecules influences the phase behaviour and enhances the film rigidity, which is mostly related to its condensing effect. Moreover, from BAM images and stability curves of both the monolayers, it is clear that at $\Pi \approx 30$ mN/m, the CLyD monolayer is more stable, having homogeneous morphology than LyD monolayer where different strip patterns are visible along with homogeneous feature. Alternation in morphological features and stability enhancement of the monolayer in presence of cholesterol is due to the interaction of cholesterol molecules with Lysozyme and DMPA molecules which alters lateral distribution of molecules in the monolayer.

ACKNOWLEDGEMENTS

H. Nath (UGC fellowship), Saiyad Akhirul Ali and S. Kundu acknowledge the financial assistance from Department of Science and Technology, Govt. of India. All authors would like to thank IASST, Guwahati for the financial and experimental facilities.

REFERENCES

1. E. E. Berring, K. Borrenpohl, S. J. Fliesler and A. B. Serfis, Chem. Phys. Lipids. Vol. 136, pp. 1–12 (2005).
2. H. Nath, R. J. Sarmah and S. Kundu, RSC advances. Vol. 13, pp. 22789-22799 (2023).
3. R. A. Demel and B. DeKruyff, Biochim. Biophys. Acta. Vol. 457, pp. 109-132 (1976).
4. A. Bañuelos-Frias, V. M. Castañeda-Montiel, E. R. Alvizo-Paez, E. A. Vazquez-Martinez, E. Gomez and J. Ruiz-Garcia, Front. Phys. Vol. 9, pp. 636149 (2021).
5. L. Zhang, C. Hao, G. Xu and R. Sun, Scanning. Vol. 2017, pp. 1542156 (2017).
6. G. D. Fidelio, B. Maggio and F. A. Cumar, Chem. Phys. Lipids. Vol. 35, pp. 231-245 (1984).
7. T. H. Chou and C. H. Chang, Colloids Surf., B. Vol. 17, pp. 71-79 (2000).

Statistical Properties of Passive, Self-Propel and Janus Particle in Ordered Crowding

Baburao Simma[1], Vrinda Garg[1], Surya K. Ghosh[1*]

[1]Department of Physics, National Institute of Technology, Warangal, Telangana, 506003, India.
[*] *Corresponding author: skghosh@nitw.ac.in*

Abstract. Transport of single molecules via passive or active processes are crucial for the functioning of biological systems. Statistical physics models are useful in understanding the underlying physical mechanism of such systems. In this study, we have discussed a comprehensive view of passive, active, and Janus particles diffusion inside non-inert ordered crowded environments. We designed the system in the underdamped limit with sticky crowders to make the scenario a biologically relevant environment having high damping with attractive centers. Our main objective here is to elucidate the diffusive dynamics of active and passive particles as the effect of stickiness and size of the crowders. The passive particle shows sub-diffusion and the self-propelled particle shows super diffusion despite being obstructed by crowders. Due to the presence of the ordered attractive centers, in the intermediate value of the packing fraction shows counterintuitive maximum diffusive behavior. Further, the strength of the active force can nullify the hindering effect of sticky crowders on the diffusion constant. In addition, we studied the dynamics of Janus particles.

Keywords: Anomalous diffusion, Langevin dynamics, Self-propelled particle.

INTRODUCTION

Understanding the complex dynamics of tracer particles in an inherently crowded cellular environment is of great interest to scientists and engineers. Its implication involving the cellular transport through biofilaments, drug delivery, chromatin dynamics in nucleus, transport in porous medium etc. [1]. Those are either passive transport resulted from thermal fluctuations, self-propelled transport due to consuming fuel from the environment [2]. Thermal fluctuations give rise to erratic movement, whereas self-propelled movement produce directive motion in persistent time and at the longer time it shows diffusive behavior with violation of Fluctuation-Dissipation theorem. Inspired by the efficient transport seen in living organisms, scientists have begun creating artificial micro- and nanoparticles capable of autonomous motion, such as Janus particles, chiral movers, and synthetic vesicles [3]. In a similar context, we examine the dynamical behavior of Brownian and active Brownian particle in an infinite lattice crowded environment. We consider two cases where first case is diffusion of passive tracer particle and second case is active particle diffusion in an environment. The tracer particle, modeled as an active Brownian particle (ABP), experiences an attractive interaction with the lattice beads. It has a spherical shape and is driven by a constant force that remains aligned with its body orientation. Langevin dynamics simulations has been implemented to examine the diffusive dynamics of tracer particle [2,3]. We analyzed the erratic behavior for parameters such as crowder size (σ_c), self-propulsion (F_a), stickiness (ε). We have calculated dynamical properties such as MSD, van hove correlation function and Diffusion constant. Passive tracer particle shows sub diffusive behavior as the stickiness increases but enhancement in the diffusion takes place as the packing fraction of lattice increases. But in the case of self-propelled tracer hopping between the lattice sites takes place as a result the sub diffusive behavior decreases with the increase in stickiness. Overall, the existing literature lacks comprehensive studies on the behavior of active tracers in uniform media containing trapping regions, with only limited computational work addressing their dynamics in polymeric environments.

MODEL

We consider a three-dimensional system of a cubic lattice every site of which occupied by the spherical obstacles as, illustrated in Fig. 1. Simulations use fixed obstacles with periodic boundaries in all directions. The packing fraction (Φ) is adjusted by varying obstacle size to reach dense configurations. A point tracer is released at the lattice center to ensure uniform spacing from neighbors. The fundamental units of length (σ), energy (ε), and mass (m) are based on Lennard-Jones parameters which define the time unit as $\sqrt{m\sigma^2/\varepsilon}$ [3].

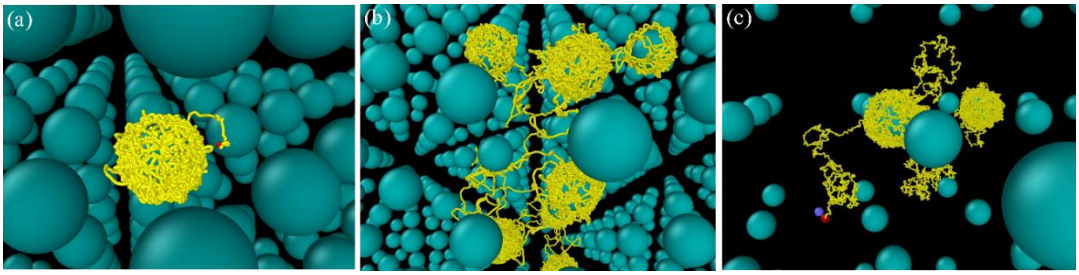


Fig 1: Schematic illustration of (a) a passive Brownian particle ($F_a = 0$) , (b) an active Brownian particle ($F_a = 6$), and (c) a Janus particle all a medium with adhesive strength ($\varepsilon = 10k_BT$) and a fixed crowder diameter (σ_c).

The interaction between the tracer particle and the periodic arrangement of obstacles is modeled using the Lennard-Jones potential to capture their attractive behavior is given,

$$V(r) = \begin{cases} 4\varepsilon\left[\left(\frac{\sigma}{r}\right)^{12} - \left(\frac{\sigma}{r}\right)^{6}\right], & if\ r \le 2.5\sigma \\ 0, & otherwise. \end{cases}$$

Here r is the distance between the tracer and crowder particle, and ε is the adhesive strength between pair of particles which interact with diameter $\sigma_{rt} = (\sigma_t + \sigma_c)/2$. The stickiness between particles of periodic array and tracer particle is implemented by full length Lennard-Jones potential [2]. The tracer dynamics, for a particle of mass mmm, are modeled using the Langevin equation given by

$$m\frac{d^2\boldsymbol{r}(t)}{dt^2} = -\gamma\frac{d\boldsymbol{r}}{dt} - \sum_j \nabla V(\boldsymbol{r} - \boldsymbol{r}_j) + \boldsymbol{f}(t) + F_a\boldsymbol{n}.$$

Here V(**r**) represents resultant potential between interacting atoms. We implemented two cases, which are Passive Brownian particles and Self-propelled particle. The former scenario is modeled by $F_a = 0$ and later $F_a \neq 0$ respectively. Our study focused at low friction coefficient consequently the dynamics is underdamped. The Thermal fluctuation taken into consideration through stochastic force $\boldsymbol{f}(t)$ that satisfies fluctuation-dissipation relations i.e., $\langle \boldsymbol{f}(t)\rangle = 0$ and., $\langle \boldsymbol{f}_\alpha(t_1)\boldsymbol{f}_{\boldsymbol{\beta}}(t_2)\rangle = 6\gamma k_BT\delta_{\alpha\beta}\delta(t_1 - t_2)$. LAMMPS has been used to carry out all the simulations [5]. The system equilibrates for 2×10^5 steps with simulation timestep $\delta t = 0.001$, and production simulations are performed for 1×10^7 steps. To facilitate analysis, simulation data were recorded at intervals of every 50-time steps throughout the study.

Results and discussion

Mean Squared Displacement

To explore the diffusion of passive Brownian particle and active Brownian particle, we have calculated Mean Squared Displacement of the tracer particle as position changes with time defined as $\Delta r^2(t) = \langle |r_i(t) - r_i(0)|^2\rangle$. The ensemble average was obtained by averaging across several independent tracer trajectories as given by $\langle \Delta r^2(t)\rangle = \frac{1}{N}\sum_{i=1}^{N}\Delta r^2(t)$ [5]. As time progress the MSD changes linearly with time in traditional diffusion, but in case of anomalous diffusion MSD changes as given as $\langle \Delta r^2(t)\rangle = t^a$. When $a < 1$, the motion is Sub diffusive, whereas $a > 1$ indicates super diffusive behavior. To investigate how crowding influences the tracer's motion, we analyze the mean square displacement (MSD) at a constant attraction strength ($\varepsilon = 9k_BT$) across various sizes of crowders, as illustrated in Fig. 2. We observed that with increasing crowder size, the tracer becomes confined to local regions of the lattice, leading to sub diffusive behavior at intermediate crowder size. But at the higher packing fraction it behaves like the free Brownian particle as channel has been created by lattice to the movement of tracer particle, as a result diffusion enhanced. Mean squared displacement coincides as a consequence of self-propulsion leads to escape from the binding sites.

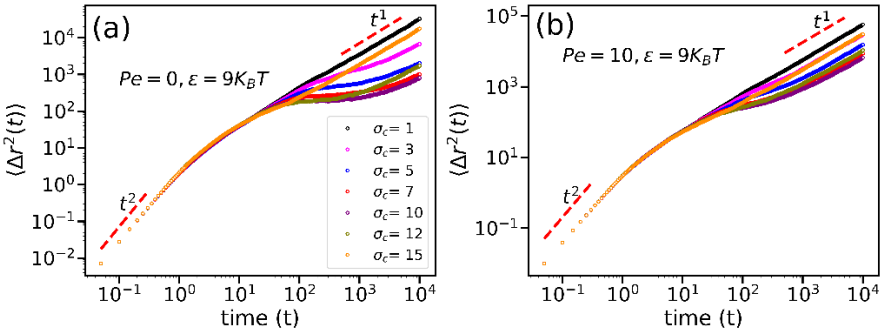


Fig 2: Mean squared displacement of the point size tracer computed at a fixed interaction strength ($\varepsilon = 9k_BT$) for various crowder sizes (σ_c).

Probability Distribution function

To have deeper understanding of dynamics we computed the van Hove correlation function, which refer to probability distribution of the tracer particle's displacement [3, 4]. It is mathematically expressed as: $P(\Delta x, \tau) \equiv \langle \delta(\Delta x - (x(t+\tau) - x(t)) \rangle$, here $x\,(t+\tau)$, $x\,(t)$ are the positions of the tracer particle along the *x*-direction at time $(t+\tau)$ and t respectively [4, 5]. Since our system is isotropic, we have similar results in all the directions, we plot $P(\Delta x, \tau)$ along with the gaussian distribution fits to the Brownian motion. It is clear from the figures that the distribution is broader for smaller crowder size and perfect gaussian. As the packing fraction increases the curve becomes sharper and non-gaussian at the intermediate pacing fraction. As self-propulsion increases the function becomes broader which can be attributed to the hopping between lattice sites.

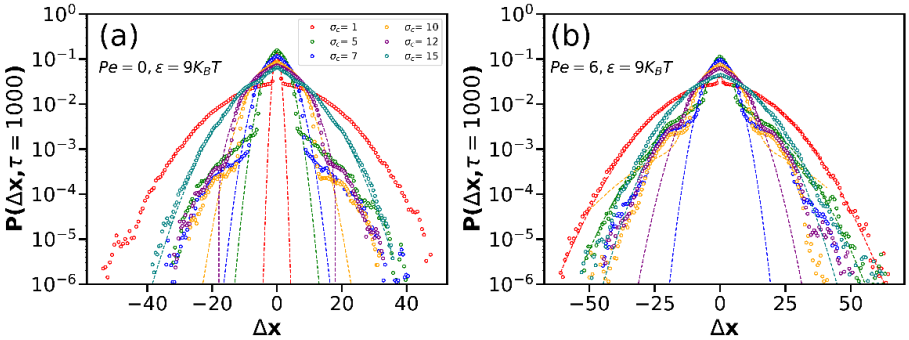


Fig3: Van Hove correlation function of the point size tracer for (a) passive Brownian particle (b) active Brownian particle, evaluated at a fixed adhesive strength ($\varepsilon = 9k_BT$) across varying crowder diameters (σ_c).

ACKNOWLEDGMENTS

SKG would like to thank MATRICS, ANRF (Project No. MTR/2022/000833) for financial support. We want to acknowledge NIT Warangal for the institute fellowship to BR and VG.

REFERENCES

1. Chen, Ying, Ran Yan, and Nanrong Zhao, *Physical Chemistry Chemical Physics* 24.12 (2022): 7415-7429.
2. Ghosh, Surya K., Andrey G. Cherstvy, Ralf Metzler, *Physical Chemistry Chemical Physics* 17.3 (2015): 1847-1858.
3. Kumar, Praveen, and Rajarshi Chakrabarti, *Physical Chemistry Chemical Physics* 25.3 (2023): 1937-1946.
4. Kumar, Praveen, Ligesh Theeyancheri, and Rajarshi Chakrabarti, *Soft Matter* 18.13 (2022): 2663-2671.Sungmin Joo, Jae-Hyung Jeon, O- chul Lee, Jae-Hyung Jeon, Soft Matter, 2020,16, 9188-9201.
5. V. Garg, R. Mathew, A. Chatterjee, & S. K. Ghosh, STAR protocols, 6(1), 103568 (2025).
6. Kim, Yeongjin, et al, *Macromolecules* 55.16 (2022): 7136-7147.

Percolation/Relaxation Behaviour Of Cold Pressed PVDF/$CoFe_2O_4$ Polymer Nanocomposites

Harsha Chouhan[1] and Maheswar Panda[1, a)]

[1]Multifunctional Polymer Nanocomposites Laboratory, Department of Physics, Dr. Harisingh Gour Vishwavidyalaya (A Central University), Sagar, M.P.- 470003, India

[a)] *Corresponding author: mpanda@dhsgsu.edu.in*

Abstract. The cold-pressed polymer nanocomposites (PNC) of PVDF and $CoFe_2O_4$ (prepared through the co-precipitation method) were prepared with the help of a hydraulic press at room temperature under 10MPa. The PNC was characterized for structural, micro-structural, & Dielectric properties respectively. Rietveld refined XRD confirmed the phase formation of $CoFe_2O_4$, and the micro/nanostructures were found from FESEM images. The percolation behaviour of the PNC is observed at a percolation threshold of f_c=0.3, which is associated with an insulator-to-metal transition (IMT) behaviour & the enhancement of dielectric parameters was explained using the MWS/interfacial polarization. The scaling laws for explaining the IMT behaviour of PNC were implemented, and the universal scaling exponents [s, s' & t] were obtained. Also, the non-Debye relaxation behaviour was found with the help of Jonscher's law for all the samples on both sides of IMT.
Keywords: Relaxation, Dielectrics, Percolation, Composites, Scaling

1.Introduction

Multiferroics is an intriguing topic of interest as it combines multiple properties within a single material, expanding its range of applications significantly, but the production of large leakage currents makes them less functional. Therefore, researchers worldwide are opting for composites instead of single-phase materials. Composites can be prepared by using ceramics and polymers. Ceramics are preferable as they possess a high dielectric constant and low energy loss, but because of their brittleness and more processing time, that makes they are less advantageous. In place of this, Polymer Nanocomposites (PNC) have the advantage due to their excellent flexibility, cost-effectiveness, and eco-friendly nature, and these materials can instantly switch electric polarization when a magnetic field is applied, therefore suitable for effective sensors and actuators. Polyvinylidene fluoride (PVDF) is a polymeric chain having the chemical formula $(CH_2CF_2)_n$, which is semicrystalline. PVDF has many phases such as α, β, δ, ε & γ. In which α & β are the most common non-polar and polar phases that can be produced during synthesis [1]. Including magnetic $CoFe_2O_4$ (CF) in PNC can boost electric, magnetic, and thermal properties and generate magnetoelectric coupling properties in PNCs. So far, researchers have examined the structural, magnetic, dielectric, and magneto-dielectric/magneto-electric properties of PVDF/CF-based particle nanocomposites. [2]. M.M. Hussein et al. have studied the structural, dielectric, and magnetic properties of CF/PVDF nanocomposites& concluded the improved magnetic properties and reduced conductivity while introducing PVDF into nanocomposites [3]. M. Koc et al. have taken PVDF/CF and examined the highest piezo/magnetoelectric coefficient found for 10%CF in the PVDF matrix [4]. Until now, researchers have focused on the structural, dielectric, magnetic, piezoelectric, and magnetoelectric properties of PVDF/CF nanocomposites. However, few have reported the percolation behaviour that arises across the Insulator Metal Transition (IMT) at a particular ferrite concentration, whenever conducting CF is introduced into the insulating polymer. In the current research, the percolation and relaxation behaviour of cold-pressed PVDF/CF PNC has been studied. Also, the scaling equations across the IMT were used to fit with the percolation phenomena that occur within the PNC.

2. Experimental Details

A Facile Co-precipitation route was employed to synthesize CF, for which Cobalt nitrate (0.001M) and Iron nitrate (0.002M) were taken and mixed with de-ionized water. The nitrate solution was placed on a magnetic stirrer for up to 2 hours at 60˚C. Then, 3M NaOH solution was added to the nitrates, while maintaining the PH 10 until a black precipitate formed. Then filter and dry the sample overnight in the oven. After that, sinter the sample for up to 5 hours at 500 ˚C using the furnace. Now, CF was ground by using a mortar and pestle. The PNC series was prepared by combining CF into PVDF in (0.05,0.1,0.2,0.3,0.4,0.5) weight fractions by the cold pressed method.

The structural investigation, such as P-XRD, was analyzed by a Rigaku D/max-200 PC diffractometer. The FTIR analysis was done through Bruker Alfa-2 in the range of 400 to 4000 cm^{-1}. The microstructures were taken by the NOVA Nano SEM 450 microscope. For dielectric measurement, pellets were formed under a pressure of 10 MPa for 10 minutes by a Hydraulic press. Then, the surfaces of the pallet were covered with silver paste & electrical measurements were carried out by sweeping the frequency from 20Hz to 2MHz, using Keysight model no E4980, a Precision LCR meter.

3.Results

3.1 Structural analysis

In Fig. 1(a), Rietveld refined XRD of CF was presented for which a pseudo-Voigt profile function was used, and Fig.1(b) shows the P-XRD of PNC. Furthermore, CF peaks are verified with JCPDS, file no. (05-0626) and PVDF are assured by the JCPDS file no. (22-1086) respectively. The pure phase formation of CF & PNC can be analyzed by the reflections, which are shown at 2θ = 18.48°, 20.18°, 26.60°, 41.41° corresponding to the planes (020), (110), (022), (221) for PVDF. Whereas, CF peaks are mentioned at 30.08°, 35.43°, 43.05°, 56.97°, 62.58° corresponding to the plane reflections at (220), (311), (400), (511) & (440). The dominancy of the (110) plane is significant, especially towards the □ phase formation inside PNC. This polar phase helps in improving the crystallinity of the sample drastically & as a result, better piezo/ferroelectric properties. Along with this, □ and □□ phases are shown with (020) & (221) planes. From Fig.1(b), it is clear that upon the addition of CF in PVDF, the cubic CF phase is growing while the PVDF phase is declining, which confirms the PNC formation. The FTIR spectra are presented in Fig. 1(c). The vibration occurring at 580cm^{-1} can be attributed to Co-O vibrations at the tetrahedral site. Various PVDF vibrations are noticed at 834cm^{-1}, 876cm^{-1}, and 1054cm^{-1}, which contribute to the β-phase vibrations. A further band at 1175 cm^{-1} will be responsible for the CF_2 stretching & also symmetric and asymmetric bands at 1395cm^{-1}& 1565cm^{-1} are related to vibrations of □□□□□□the phase of CF_2.

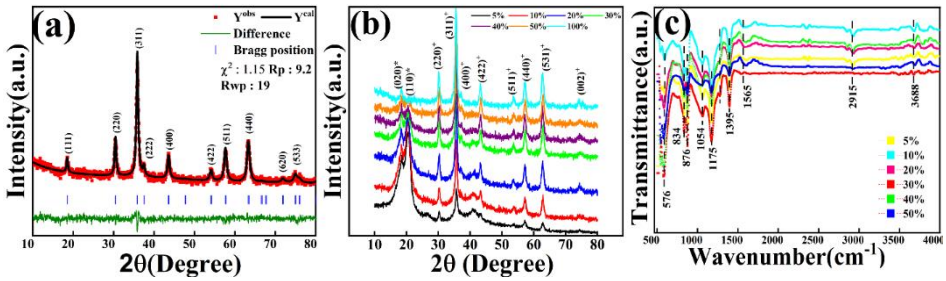


FIGURE 1. (a) Rietveld refined XRD of CF, (b) XRD spectra of PNC, (c) FTIR spectra of PNC

3.2 Microstructural analysis

The FESEM micrographs are shown in Fig.2(a-c). Evidence of spherulites in the form of spheres can be seen, and these originated in the time of α-nucleation of the PVDF. Hence, the cold-pressed method is most suitable for generating spherulites. These spherulites not only enhance porosity but also help in enhancing the surface area of PNC. The appearance of spherulites is hindered at higher fractions, which means a reduction in porosity, due to which connections are formed between the CF and PVDF matrix for percolation. The agglomeration can be seen at 0.5CF-0.5PVDF due to the enlarged magnetic interactions of magnetic domains.

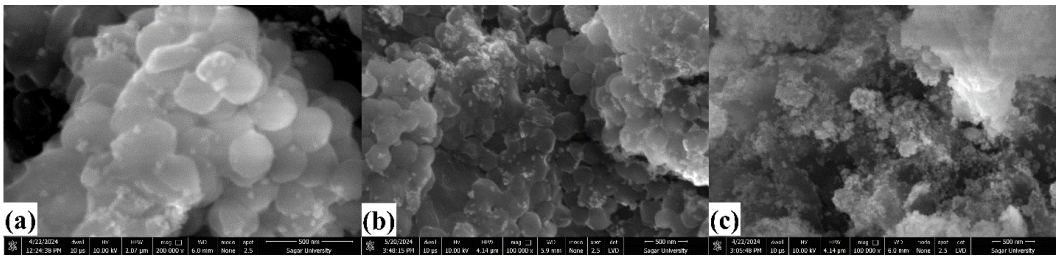


FIGURE 2. FESEM of PNC with (a) 0.05CF/0.95PVDF (b) 0.2CF-0.8PVDF (c) 0.5CF-0.5PVDF

3.3 Percolation and Scaling Behaviour

In Fig. 4(a-b), ε_{eff} & σ_{eff} are shown with ferrite fractions. For the concentration of ferrite = 0.2, there is a steady change in εeff, but for 0.3-0.5, there is an abrupt change in ε_{eff} from 105 to 420, due to the existence of IMT at fc= 0.3. This is explained by MWS polarization [5]. The ε_{eff} is fitted with the scaling equation (1) and the universal exponent.

$$\varepsilon_{eff} \propto (f_c - f_{CF})^{-s} \; for \; f_{CF} < f_c \tag{1}$$

s=1.02 ± 0.22, which is in the range of universal value, i.e., s=0.8-1. Similarly, σ_{eff} is showing abnormal change at IMT of f_c= 0.3 due to the formation of connectivity of CF within PVDF matrix. The σ_{eff} is scaled by using power law equation (2) and found the s'=0.86 ± 0.2 for (f_{CF} < fc) which is nearer to the ideal value i.e., s'= 0.8-1.

$$\sigma_{eff} \propto (f_c - f_{CF})^{-s'} \; for \; f_{CF} < f_c \tag{2}$$

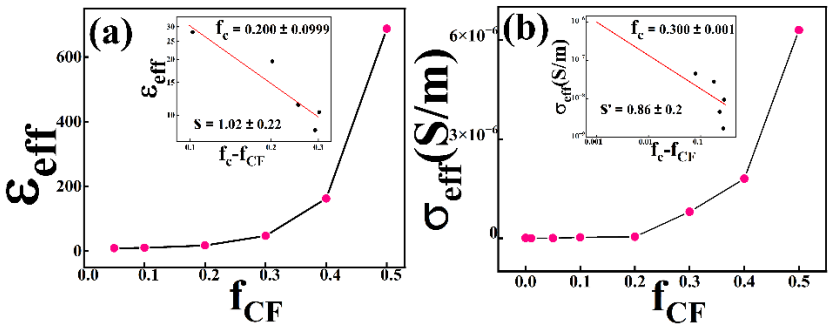


FIGURE 3. The variation of (a) ε_{eff} ~ the fraction of CF in PNC, (b) σ_{eff} ~ the fraction of CF in PNC

3.4 Electrical Spectroscopy

The dependency of dielectric constant, loss tangent &conductivity on frequencies is shown in Fig. 4. The dielectric constant shows the enhanced values from 30 (fc <0.3) to 105 (fc=0.3) due to the existence of IMT at fc=0.3 as well as loss tangent has been increased from 0.8 to 3 due to the formation of a conducting network in PNC. The Conductivity pattern was found to be constant (DC conduction) & linear (AC conduction) at lower & higher frequencies. Moreover, for percolative samples (≥0.3), electron tunneling across the barrier reduces interparticle spacing & results in the formation of a conducting network, which allows electrons to move from Fe^{2+} to Fe^{3+} within the sample at octahedral sites. The conductivity was satisfied with Jonscher's power law of equation (3), with Jonscher's exponent k = 0.8 (fc = 0.3) lying within 0-1, governing the non-Debye relaxation [6].

$$\sigma_{ac}(\omega) = \sigma_{dc} + A\omega^{k} \; (0 < k < 1) \tag{3}$$

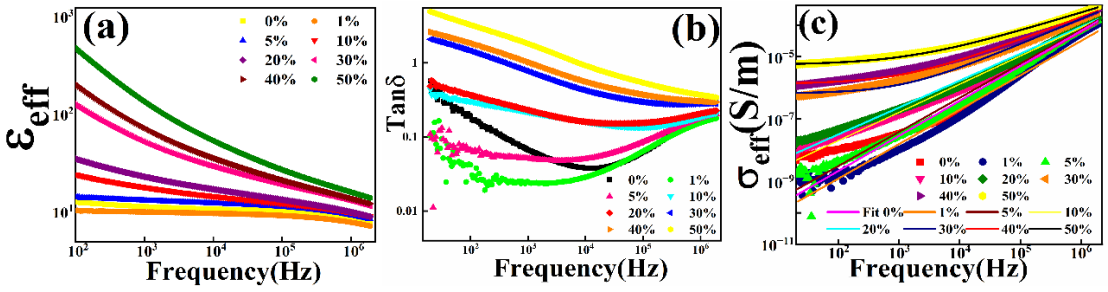


FIGURE 4. shows (a) Dielectric constant, (b) loss tangent (c) Conductivity with frequency

4. Conclusions

The PNC of PVDF/CF was synthesized through a two-step procedure of the coprecipitation route of synthesizing CF, followed by cold-pressing to prepare pellets of PNC. XRD/FTIR studies ensure phase formation. The FESEM micrographs have confirmed the spherulites/composite structures of PNC. The percolation behavior at IMT was found for $f_{CF} \geq 0.3$ & understood by implementing percolating equations around the IMT. Further, the scaling exponents are found to be in the universal region. Moreover, the enhanced dielectric constant with low loss & sharp conductivity across the IMT has been manifested to be used as an effective energy storage material &may be suitable for high-frequency applications.

REFERENCES

1. H. Chouhan, M. Panda, S. Mohanta and D. K. Shukla, J. Mater. Sci: Mater. Electron. **36**, (2025) 655.
2. T. Chakraborty, A. S. Mahapatra, S. Saha, A. Saha, A. Maity, S. Das, S. Hasan, S. Das and S. Sutradhar, Solid State Sci. **149,** (2024) 107475.
3. H. Chouhan, S. K. Behera and M. Panda, Bull. Mater. Sci. **48** (2025) 23.
4. M. Panda, Percolation, Scaling and Relaxation in Polymer Dielectrics, Springer Nature, Switzerland, 2023,1-205.

Micro-scale Dynamics in Disordered Polymers and Gels Influences Macroscale Response

Debjani Bagchi [1, a)], Shipra Bhatt [1] and Tithi Joshi [1]

[1]Department of Physics, Faculty of Science, The Maharaja Sayajirao University of Baroda, Vadodara 390002, Gujarat, India.

[a)] Corresponding author: debjani.bagchi-phy@msubaroda.ac.in

Abstract. A comparative experimental analysis of dynamics at the micro-scale is presented for polymer glasses and gels. These are disordered, off-equilibrium systems, with physical properties showing time evolution, non-Gaussian fluctuations, or jammed, heterogeneous dynamics. We show how these micro-scale dynamics affect the macroscopic properties of these systems. In the case of polymers, glassy dynamics at the micro-scale is shown to influence the macroscopic tensile response. There is a presence of caged β relaxation dynamics, in addition to α-relaxation. On the other hand, in gels, the mechanism of drug release is found to be affected by the micro-scale diffusion, measured with fluorescence recovery after photobleaching, and macro-scale diffusion, measured through release kinetics of a fluorescent molecule. Both the macro-scale and micro-scale properties are observed to be influenced by the gel network structure, which has slow ageing dynamics.

Keywords: polymer gel, glasses, diffusion, drug release, relaxation dynamics.

INTRODUCTION

Glasses and gels are disordered solids with diverse applications in daily life. Interestingly, these systems, have intriguingly similar properties. These systems are rigid like solids, but do not have translational order. Moreover, they exhibit dynamic slowing during ageing. Despite years of theoretical, simulations or experimental research, there are still many questions unanswered in the field of disordered materials, especially glassy systems. Understanding the origin of glassy behavior, which is marked by the presence of dynamic heterogeneities, dynamic slow-down and cooperatively rearranging regions on approaching the glass transition temperature has been the aim of several groups worldwide.

Simulations have shown that configurational constraints, characterized by vibrational mean-squared displacements, impact shear and bulk moduli in gels and in glasses [1]. Glasses show stiffening due to ageing, whereas gels show a transition to softening as well, from enhanced stiffness. These differences have been attributed to mechanisms minimizing free energy: structural ordering in glasses and interface reduction in gels [1]. There is an anomalous enhancement in viscosity in glasses and gels, by several orders of magnitude, with flow cessation over practical timescales until sufficient stress is applied. This behavior originates from restricted mobility of the constituents, which are dynamically arrested in disordered structures of varying length scales. As a result, these materials are thermodynamically out of equilibrium, having time-dependent evolution of their structure and the properties.

The dynamical behavior of the disordered materials influences the macroscopic properties of the material which impacts the applications of the material. The present study aims to understand the glassy behavior of polymers at the macroscopic level and its impact on the macroscopic properties. For polymer glasses, we present studies on molecular elastic properties and their relation to temperature, with the help of Raman scattering. This is analyzed with respect to macro-scale mechanical properties of the polymer glasses. In the case of gels, we have analyzed micro-scale diffusion of a fluorescent probe with respect to macro-scale drug release from gel matrix. We find dependence of properties on observation times and ageing in glasses, uncovering the underlying mechanisms.

EXPERIMENTAL RESULTS

Micro Raman spectroscopy was used to acquire the integrated Raman scattered intensity from a small (1μm radius) region of processed polyvinyl acetate (PVAc) film and non-processed PVAc, on excitation with a 532 nm laser. The samples were subjected to thermal ramps passing through the glass transition temperature. As shown in Figure 1, the PVAc films are driven away from equilibrium, and show pronounced hysteresis in Raman intensity, whereas the unprocessed samples Raman intensity is unchanged. For PVAc films, C-H stretching

modes, at the glass transition temperature, Tg, there is a crossover of Raman modes from β relaxation dynamics, fitted well by the Arrhenius equation (magenta curve), to the α relaxation dynamics fitted well by the Vogel-Fulcher-Tamann (VFT) equation (blue curve) [2]. For unprocessed samples, the VFT equation fits well, showing α relaxation dynamics.

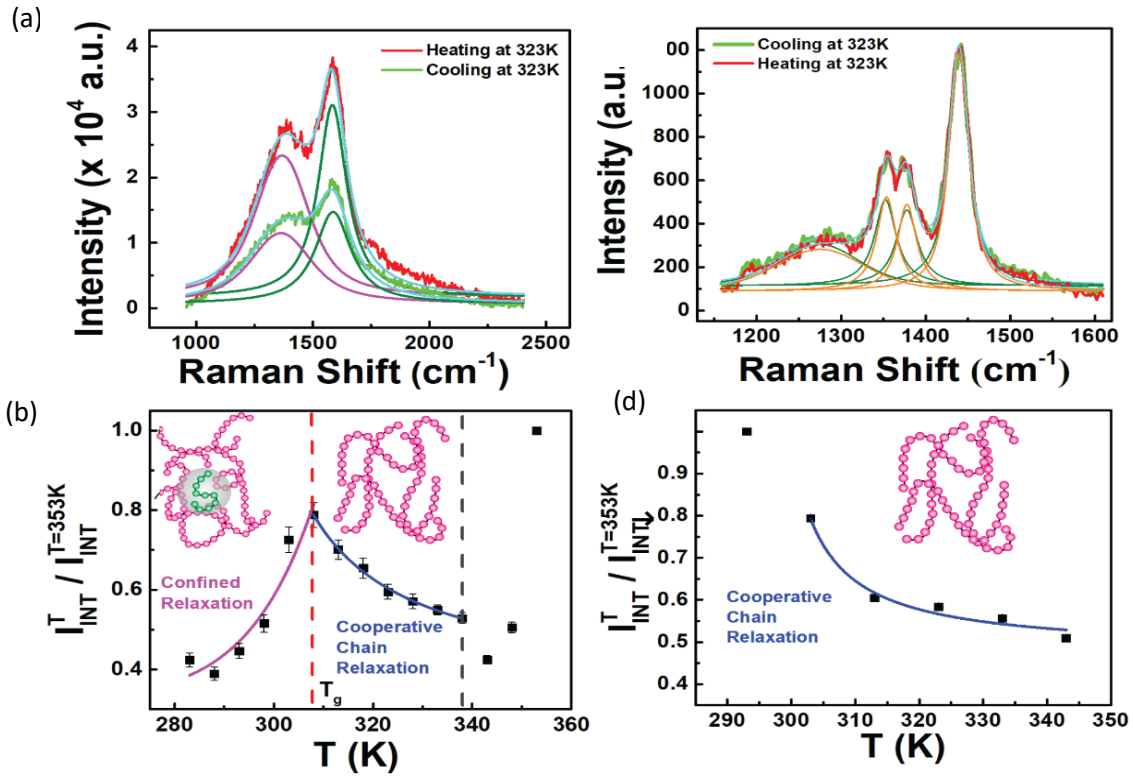


Figure 1: (a) Hysteresis in Raman peak intensity during heating and cooling ramp for PVAc film. (b) The temperature dependence during the cooling cycle of the second ramp for the integrated peak intensities of the PVAc film, normalized by the maximum peak integrated peak intensity which occurs at T=353 K. (c) No hysteresis, and almost overlapped peaks for Raman intensity from unprocessed PvAc. (d) In unprocessed PVAc, the temperature dependence of peak area, or the integrated peak intensities I, normalized by the maximum peak integrated peak intensity which occurs at T=293 K during heating cycle ramp are fitted with the VFT equation (solid lines), illustrating the presence of predominantly α relaxations in the unprocessed PVAc.

As shown in Figure 2 for polymer films, the micro-Raman intensity correlates well with the macroscopic mechanical properties [3]. Figure 2 shows high positive correlation between wavenumber of the Raman peaks to the tensile strength, illustrating that micro-scale structural dynamics do influence the macroscopic tensile properties. In case of gels, too, a strong positive correlation is observed between the micro-scale diffusion dynamics as obtained by fluorescence recovery after photobleaching (FRAP), as shown in Figure 3 to the macro-scale drug release [4]. The gel matrix stiffness was observed to depend on the matrix composition, as well as gel ageing and crosslinking, thereby affecting the diffusion dynamics and drug release. Here too, a positive correlation was observed between the mechanical properties such as shear response of the gel and drug release.

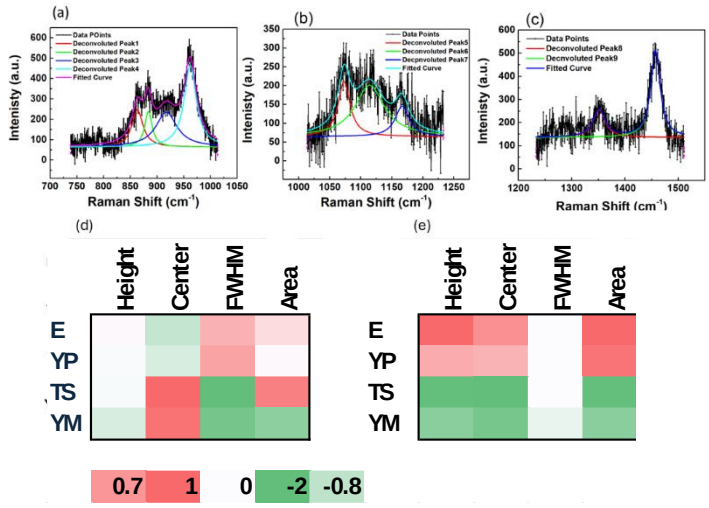


Figure 2: (a), (b), (c) Raman peaks of the films of polypropylene carbonate. (d) and (e) Correlation matrix of Pearson's correlation coefficients between Raman peak parameters and Young's modulus (YM), tensile strength (TS) and yield point (YP) of polymer films for C-C stretching vibrational mode and C-H stretching vibrational mode respectively.

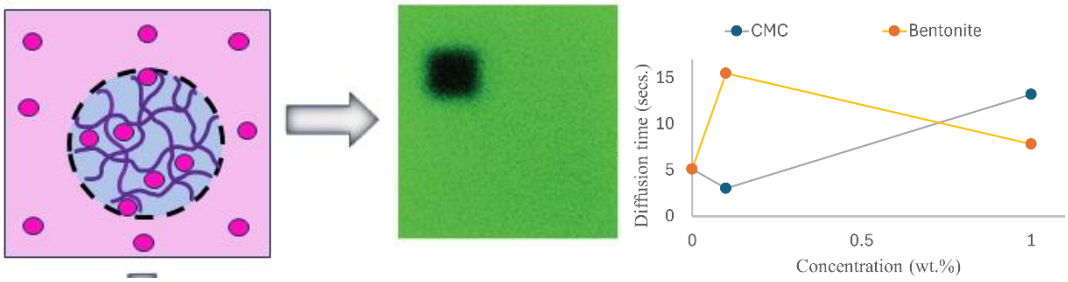


Figure 3: Diffusion dynamics of a fluorescent probe in a gel matrix modified by carboxymethyl cellulose (CMC) and Bentonite revealed from diffusion time estimates by FRAP.

CONCLUSION

The present study underlines the importance of micro-scale dynamics of disordered glassy and gel matrix in regulating the macroscopic properties of these systems. This is illustrated with the help of micro-Raman scattering and mechanical response in case of polymer glasses. In addition, a prominent interrelation is observed between diffusion dynamics and applications such as drug release in gels.

REFERENCES

1. Wang, Y., Tateno, M., & Tanaka, H. (2024). Distinct elastic properties and their origins in glasses and gels. *Nature Physics*, 1-9.
2. Bhatt, S., & Bagchi, D. (2021). Molecular and micro-scale heterogeneities in Raman modes of a relaxing polymer glass. *Journal of Physics: Condensed Matter*, *33*(32), 325101.
3. Bhatt, S., & Bagchi, D. (2024). Macroscopic mechanical properties and molecular scale thermal relaxation of a biodegradable polymer: a comparison to commonly used polyethylenes. *Journal of Physics: Condensed Matter* (under revision).
4. Joshi, T., Esther Jinugu, M., Khristi, A., Thareja, P., & Bagchi, D. (2024). Non-toxic, Printable Starch Hydrogel Composite with Surface Functionalized Silver Nanoparticles Having Wide-Spectrum Antimicrobial Property. *BioNanoScience*, 1-14.

Miscibility, Compatibility and Intermolecular Interaction Analysis of Oxypropylene Blends with Isobutene and Acrylonitrile

Mandakini Baral[1, a)], Padmaja Patnaik[1, b)], Dipan Kumar Das[1, c)] and Santanu Kumar Nayak[1, d)]

[1]*Centurion University of Technology and Management, Odisha, India*

[a)] *mandakinibarala1970@gmail.com*
[b)]*Corresponding author: padmaja.patnaik@gmail.com*
[c)] *dipandas1997@gmail.com*
[d)] *sknayak23051996@gmail.com*

Abstract. A compatibility study was conducted on polymer blends comprising oxypropylene as the base polymer with isobutene and acrylonitrile as screen polymers. Thermodynamic parameters, including Flory-Huggins interaction parameter (Chi), mixing energy (Emix), and average interaction energies, were calculated at 298 K. Results indicate poor compatibility between oxypropylene and isobutene, as evidenced by a high Chi value of 0.73326731. In contrast, the oxypropylene-acrylonitrile blend exhibited relatively better compatibility with a Chi value of 0.13832991. Oxypropylene and acrylonitrile exhibit better compatibility compared to oxypropylene and isobutene. This is likely due to a lower Chi value and a more negative Ebs avg for the oxypropylene-acrylonitrile blend.

INTRODUCTION

The development of novel polymer blends with tailored properties has been a focal point in materials science and engineering [1]. Polymer blending offers a promising approach to create materials with enhanced performance characteristics compared to their individual components. However, the successful implementation of polymer blending hinges on the understanding of intermolecular interactions and the compatibility between the constituent polymers [2].

Oxypropylene, isobutene, and acrylonitrile are versatile monomers widely employed in the production of various polymers. Blends of these polymers hold potential for applications in diverse fields such as elastomers, adhesives, and coatings. To optimize the properties and performance of these blends, a comprehensive understanding of their miscibility, compatibility, and intermolecular interactions is crucial.

This study aims to investigate the miscibility, compatibility, and intermolecular interactions between oxypropylene blends and two distinct co-monomers: isobutene and acrylonitrile. By employing advanced characterization techniques and theoretical modelling, we seek to elucidate the underlying factors governing the compatibility of these polymer systems. The insights gained from this research will contribute to the rational design of high-performance polymer blends with predictable properties.

COMPUTATIONAL METHODS

To investigate the miscibility, compatibility, and intermolecular interactions of oxypropylene blends with isobutene and acrylonitrile, computational simulations were performed using Biovia Materials Studio [3,4]. The study employed three primary modules: Forcite, Blend. Forcite was utilized for geometry optimization and force field calculations, Blend for mixing simulations. Following Computational Parameters used as follows: -

Forcite: Geometry optimization was performed with fine quality settings, including energy, force, and displacement convergence criteria. Electrostatic calculations used a cut-off distance of 15.5 Å, spline width of 1 Å, and buffer width of 0.5 Å.

Blend: Energy samples, energy bin width, cluster samples, and iterations per cluster were set to 10000, 0.2 kcal/mol, 1000, and 20, respectively. Reference temperature was 298 K.

RESULTS AND DISCUSSION

The development of novel polymer blends with tailored properties has been a focal point in materials science and engineering. Polymer blending offers a promising approach to create materials with enhanced performance characteristics compared to their individual components [5]. Here, Dassault Systems Biovia Forcite module used to optimise the geometry of Oxypropylene, Isobutene and Acrylonitrile. Then the Blend module of Biovia material

studio used to create Oxypropylene-acrylonitrile (FIGURE 1**)** and oxypropylene-isobutene (FIGURE 2) polymer blends.

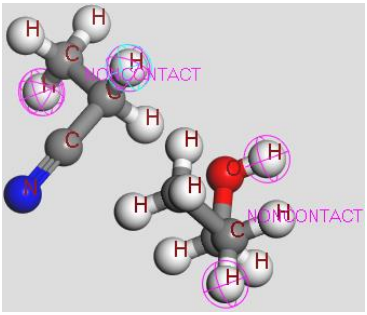


FIGURE 1. Structure of Oxypropylene-acrylonitrile

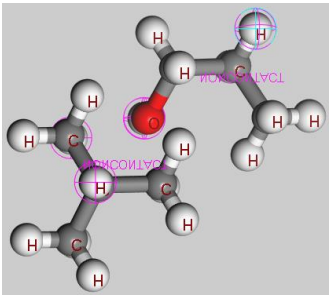


FIGURE 2. Structure of oxypropylene-isobutene

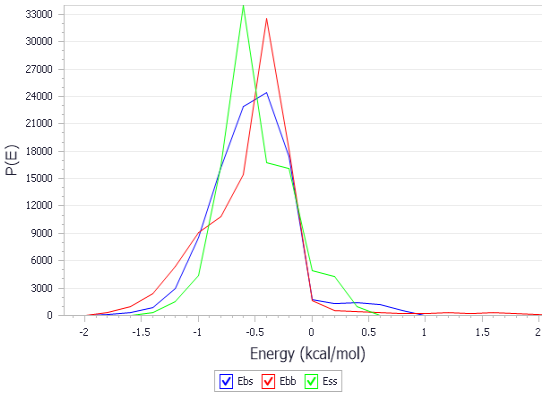


FIGURE 3. Binding energy distribution of Oxypropylene-acrylonitrile

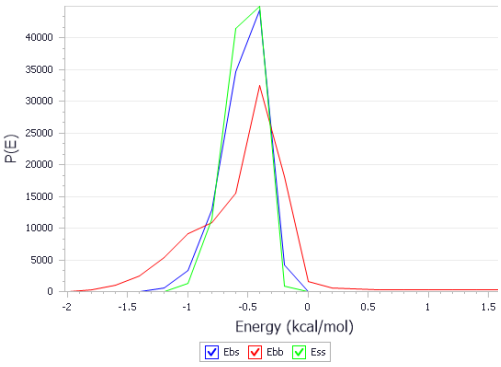


FIGURE 4. Binding energy distribution of Oxypropylene-acrylonitrile

TABLE 1. Chi value (298K), mixing energy and energy distribution parameters of base and screen

Base	Screen	Chi (298 K)	Emix (298K)	Ebb avg (298 K)	Ebs avg (298 K)	Ess avg (298 K)
oxypropylene	Isobutene	0.73327	0.43423	-0.83235	-0.60127	-0.57581
oxypropylene	Acrylonitrile	0.13833	0.08192	-0.83235	-0.72479	-0.64432

1. Compatibility Analysis

The Flory-Huggins interaction parameter (Chi) is a measure of the interaction between two polymers [6]. A lower Chi value indicates better compatibility between the polymers. Based on the Chi values in the table, we can see that: Oxypropylene and Isobutene have a poor compatibility (Chi: 0.733267). Oxypropylene and Acrylonitrile have a good compatibility (Chi: 0.138330).

2. Mixing Energy Analysis

Mixing energy (Emix) is the energy required to mix two polymers. A lower mixing energy indicates easier mixing between the polymers. The mixing energy values for both blends are relatively low (0.081917 J/mol for oxypropylene-acrylonitrile and 0.434232 J/mol for oxypropylene-isobutene). However, the oxypropylene-acrylonitrile blend has a lower mixing energy compared to the Oxypropylene-isobutene blend, suggesting that it may be easier to mix oxypropylene with acrylonitrile.

3. Interaction Energies Analysis

The interaction energies (Ebb avg, Ebs avg, and Ess avg) in FIGURE 3 and FIGURE 4 represent the average interaction energies between the base polymer (oxypropylene) and itself (Ebb), the base polymer and the screen polymer (Ebs), and the screen polymer and itself (Ess), respectively. A more negative interaction energy value

indicates a stronger attraction between the two moieties involved. In this case, a more negative Ebs value would be desirable for good adhesion between the base and screen polymers. The analysis of interaction energies reveals the following: Ebb avg (average interaction energy between oxypropylene and itself) is the same for both blends (-0.83235 J/mol). Ebs avg (average interaction energy between oxypropylene and the screen polymer) is more negative for the oxypropylene-acrylonitrile blend (-0.724796 J/mol) compared to the oxypropylene-isobutene blend (-0.601268 J/mol). This suggests a stronger attraction between oxypropylene and acrylonitrile compared to oxypropylene and isobutene. Ess avg (average interaction energy between the screen polymers) is slightly more negative for the oxypropylene-isobutene blend (-0.575814 J/mol) compared to the oxypropylene-acrylonitrile blend (-0.644319 J/mol).

Oxypropylene and acrylonitrile exhibit better compatibility compared to oxypropylene and isobutene. This is likely due to a lower Chi value and a more negative Ebs avg for the oxypropylene-acrylonitrile blend. The lower mixing energy for the oxypropylene-acrylonitrile blend suggests that it may be easier to process this blend compared to the oxypropylene-isobutene blend. The stronger attraction between oxypropylene and acrylonitrile (as indicated by the more negative Ebs avg) may lead to improved adhesion in the oxypropylene-acrylonitrile blend.

CONCLUSION

Oxypropylene and acrylonitrile exhibit a higher degree of compatibility compared to the oxypropylene-isobutene pair, as evidenced by lower mixing energies and more favourable intermolecular interactions. The Forcite module revealed that the oxypropylene-acrylonitrile blend exhibited significantly better miscibility and stronger intermolecular interactions compared to the oxypropylene-isobutene blend, as indicated by lower Chi values and more favourable binding energies. The Blend module allowed for precise modelling of polymer blend behaviour, demonstrating that the interactions within the oxypropylene-acrylonitrile blend are energetically more favourable.

REFERENCES

1. Ajitha, A. R., and Sabu Thomas. "Compatibilization of polymer blends." Compatibilization of Polymer Blends, Elsevier2019 (2020): 640.
2. Zarrintaj, Payam, Mohammad Reza Saeb, Seyed Hassan Jafari, and Masoud Mozafari. "Application of compatibilized polymer blends in biomedical fields." In Compatibilization of polymer blends, pp. 511-537. Elsevier, 2020.
3. Nayak, Santanu Kumar, Padmaja Patnaik, Dipan Kumar Das, and Mandakini Barala. "Electronic and half-metallic behaviour of manganese doped SiC Zigzag nanotubes using density functional theory." Chemical Physics Impact 8 (2024): 100417.
4. Das, Dipan Kumar, Padmaja Patnaik, Santanu Kumar Nayak, and Mandakini Barala. "Electronic and half-metallic behavior of copper-doped silicon carbide armchair single-walled nanotubes using density functional theory." International Journal of Computational Materials Science and Engineering (2024): 2450011.
5. Hosny, M. M., M. H. Abdel-Aziz, M. Sh Zoromba, and A. F. Al-Hossainy. "Design and synthesis of high-performance polymer blend solar cell." Journal of Materials Research and Technology 28 (2024): 4199-4211.
6. van Leuken, Stijn HM, Rolf ATM van Benthem, Remco Tuinier, and Mark Vis. "Theoretically predicting the solubility of polydisperse polymers using Flory–Huggins theory." Journal of Physics: Materials 7, no. 1 (2023): 015005.

Electronic and Optical Characterization of Polypyrrole Thin Films: A UV-Visible Absorption Study

Lincy K Alex[1, a)] and Lakshmi Vijayan*[1, b)]

[1]*Department of Physics, St. Aloysius College, Edathua, Kuttanad Taluk, Alappuzha, Kerala, India- 689573*
[a)] Email: lincyalex93@gmail.com
[b)] Email: lakshmivijayan@gmail.com

Abstract: Polypyrrole is a heterocyclic, positively charged conducting polymer that contains nitrogen in its oxidized form. When overoxidation occurs, polypyrrole loses its conductivity and charge. Its exceptional electrical conductivity, chemical stability, high surface area, and sensitivity to environmental changes make polypyrrole an ideal candidate for gas-sensing applications. In this study, we synthesize polypyrrole through the chemical oxidative polymerization of pyrrole monomer, using ammonium persulfate as the oxidant in varying ratios. Prepared polypyrrole thin films using the dip coating technique. We analyze the electronic transitions for different oxidant concentrations and observe an absorption peak at approximately 450 nm, corresponding to the π-π* transition. It is found that the band gap of the samples falls within the semiconducting range. Evaluated optical constants such as the absorption coefficient, extinction coefficient, refractive index, and optical conductivity for all samples and studied how these properties vary as a function of energy.

Keywords: Polypyrrole thin films, Bandgap, optical constants, chemical oxidative polymerization, Tauc's plot

INTRODUCTION

Polypyrrole (Ppy) is a conducting polymer that gained significant attention due to its electrical, optical, and mechanical properties. Extensive research on several conjugated polymers, including poly(p-phenylene), polyaniline (PANI), polypyrrole, polythiophene, polycarbazole, polyfluorene, poly (p-phenylenevinylene), and their substituted derivatives, has led to their applications in rechargeable batteries, microelectronics, sensors, electrochromic displays, and light-emitting and photovoltaic devices[1]. In this present study, we have carried out the chemical oxidative polymerization of Pyrrole. As a member of the poly-heterocycle family, Ppy has its conjugated backbone, which enables efficient charge transport and gives rise to its remarkable conductivity with a band gap energy of approximately 1.79 to 2.04 eV. Ppy exhibits semiconducting behavior, making it an attractive material for its applications, including organic electronics, energy storage, and sensing devices.

EXPERIMENTAL

Synthesized polypyrrole using the chemical oxidative polymerization technique, using ammonium persulfate (APS) as the oxidant. Prepared solutions of pyrrole monomer and APS in distilled water. Slowly add the pyrrole solution to the APS solution. Varied the oxidant-to-monomer ratio (0.1,0.2,0.3, and 0.4) by adjusting the amount of APS solution added and allowed the reaction to proceed for 2-4 hours. Casted thin Ppy film on a precleaned glass substrate by keeping it in an oxidant solution for 150 min. Washed the film to remove unwanted impurities [2].

RESULTS AND DISCUSSION

UV-Vis Spectroscopy

The absorption spectra of polypyrrole samples were recorded in the wavelength of 300 nm to 700 nm on the Thermo-Fisher equipment Fig. 1. A strong absorption peak around 400-500 nm, corresponding to the π-π transition. This peak indicates the conjugated backbone of Ppy. A weaker absorption peak around 550-600 nm is due to the n-π transition from non-bonding orbitals (n) to the lower unoccupied molecular orbital. This peak is related to the nitrogen atoms in the Ppy chain. Small humps after 600 nm indicate polaron bipolar on transitions for all the samples. The intensity of these peaks increases with a decrease in the O/M ratio.

Optical band gap

Calculation of optical band gap using formula (1). In a graph between $(\alpha h\nu)^2$ versus hν, the extrapolation of the straight line to $(\alpha h\nu)^2 = 0$ axis gives the optical band gap[3]. Figure 2 shows the Tauc's plot for the samples

$$\propto h\vartheta = A[h\vartheta - Eg]^n \quad (1)$$

where 'E_g' is an optical band gap, 'α' is the absorption of the thin film, 'A' is a constant '$h\vartheta$' is the photon energy, and 'n' is a constant. The obtained optical band-gap values have been found to increase from 1.79 eV to 2.04 eV with an increase in the O/M ratio Fig. 3.

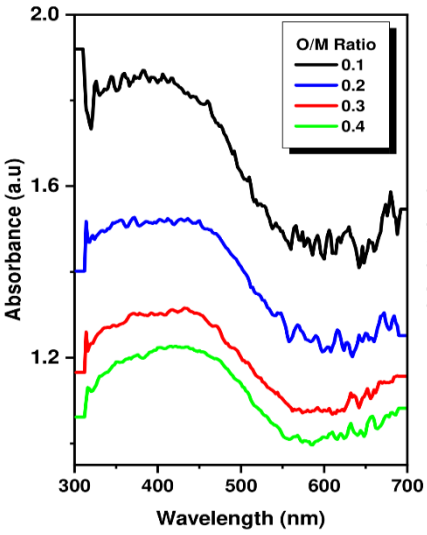


Fig 1. Absorption spectra

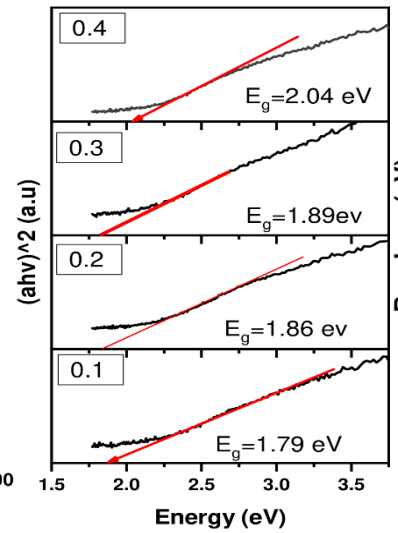


Fig 2. Tauc's Plot

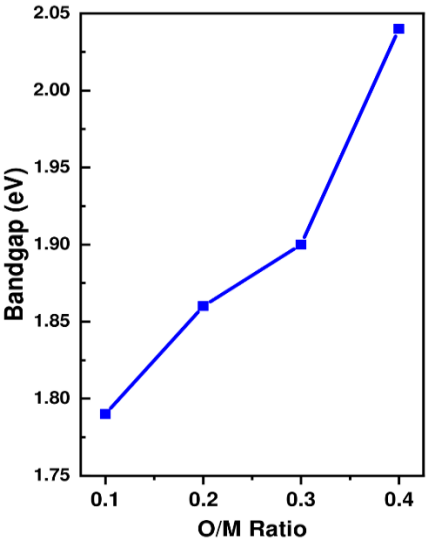
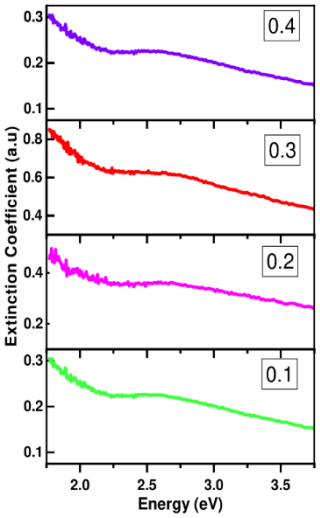
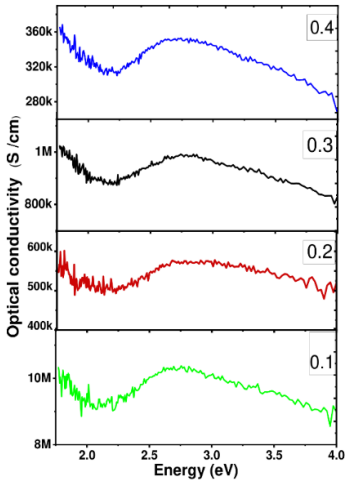


Fig 3. Bandgap vs O/M ratio

Optical constants

From the absorption coefficient, evaluated optical constants such as refractive index 'n' optical conductivity σ, and extinction coefficient 'K' of all samples as an energy (eV) function. From Figure 2, the extinction coefficient shows how strongly a chemical species absorbs light at a given wavelength[4]. Optical conductivity measures a material's ability to conduct electricity in response to light. The respective quantities show nonuniform variations from figures 4 and 5. Figure 6 shows that the refractive index decreases with an increase in the oxidant monomer ratio.





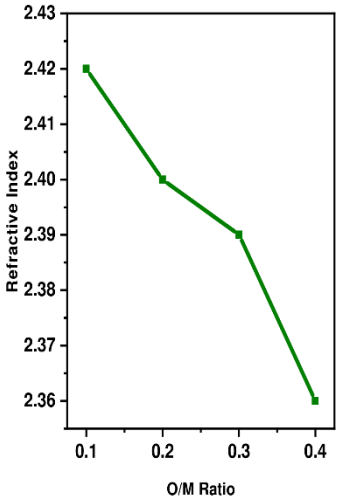


Fig 4. Extinction Coefficient vs Energy Fig 5. Optical Conductivity vs Energy Fig 6. Refractive index vs O/M ratio.

CONCLUSION

Polypyrrole thin films' electronic and optical properties depend on the oxidant-to-monomer ratio.

ACKNOWLEDGMENTS

The author is grateful to the supervisor and the research center for proper guidance and support throughout the project and to DST FIST-assisted facilities for characterization at St Aloysius College, Edathua.

REFERENCE

1. P. Chandrasekhar, *Conducting Polymers, Fundamentals and Applications: A Practical Approach*. Boston, MA, USA: Kluwer Academic, 1999.
2. V. S. Shanthala, S. N. Shobha Devi, and M. V. Mrigendra, "Optical band gap studies of polypyrrole doped with $NiZnFe_2O_4$ nanoparticles," *The Oxford College of Science, Department of Physics*, Bangalore, India, 2016.
3. R. P. Mahare, D. K. Burghate, and S. B. Kondawar, "Development of nanocomposites based on polypyrrole and carbon nanotubes for supercapacitors," *Adv. Mater. Lett.*, vol. 5, no. 7, pp. 400–405, 2014.
4. B. S. Chakrabarty, "Study of the optical properties of zinc doped polypyrrole," *M.S. University of Baroda, Applied Physics Department*, Vadodara, India, 2013.

Recycling of Medical Face Mask Waste to an Engineering Materials: A Study on the Nonwoven Polypropylene Nitrile Rubber Blend

Satyabrata Sahoo[1, a)], Smita Mohanty [1] and Sanjay K. Nayak[2]

[1] Laboratory for Advanced Research in Polymeric Materials, Central Institute of Petrochemical Engineering and Technology Bhubaneswar, Odisha 751024 India

[2] Ravenshaw University Cuttack, Odisha 753003 India.

[a]Corresponding author**:** satyabrata.sahoo@ravenshawuniversity.ac.in

Abstract. This study turns used face mask garbage into a useful resource, addressing the environmental problem associated with it. Every day, billions of single-use face masks are used worldwide, hence the COVID-19 pandemic has an influence on waste management. It might be difficult to dispose of used face masks properly without putting the environment or human health in jeopardy. This article investigates a cutting-edge method for reusing medical face masks. Using maleic anhydride as a compatibilizer, Nonwoven polypropylene (PP) fiber from masks is combined with acrylonitrile butadiene rubber (NBR) to create a PP−NBR blend. Sterilized waste was examined for pathogens, followed by characterization using differential scanning calorimetry (DSC), thermogravimetric analysis (TGA), and fourier transfer infrared spectroscopy (FTIR).

Keywords: Recycling, Face mask, Nonwoven polypropylene, Biomedical, Waste management,

Introduction: The COVID-19 epidemic has caused a sharp increase in the use of surgical face masks, resulting in billions of garbage every day. Because inappropriate disposal can contaminate soil and water and spread infectious diseases, this presents a serious environmental risk. Mask incineration is an alternative; however, it contributes to climate change by producing excessive carbon emissions and air pollution. The only practical way to reduce plastic pollution is to recycle used medical face masks. The goal of this project is to create a value-added engineering product by recycling medical face masks in an innovative way. The project investigates turning disposable masks into valuable materials by concentrating on PP/NBR blends, addressing the need for sustainable waste management as well as environmental issues.

Experimental Section

Materials:

Acrylo-nitrile butadiene rubber (nbr) was collected from the experimental lab gloves, and nonwoven polypropylene masks were extracted from the n-95 face masks. Purchases from sigma-aldrich chemicals included maleic anhydride (ma) for compatibilization, zinc oxide (zno) and stearic acid for activation, and sulfur and dicumyl peroxide (dcp) for rubber-grade chemicals. Tetramethylthiuramdisulphide (tmtd) and n-cyclohexyl-2-benzothiazolesulfenamide (cbs) were acquired from sigma-aldrich.

Formulation:

TABLE 1

Ingredients (PP/NBR Blend in php)	**90/10**	**80/20**	**70/30**	**60/40**	**50/50**
rPP	90	80	70	60	50
rNBR	10	20	30	40	50
ZnO	5	5	5	5	5
Stearic acid	2	2	2	2	2
CBC	1	1	1	1	1
TMTD	0.3	0.3	0.3	0.3	0.3
Sulfur	1.5	1.5	1.5	1.5	1.5

Characterization:

Thermal Characterization of DSC and TGA:
In a nitrogen atmosphere, rPP-NBR blends with varying compositions were studied using differential scanning

calorimetry (DSC) by utilizing the Q20 (M/s TA instruments).
The crystallinity is measured by comparing the melting enthalpy of the sample to the melting enthalpy of a 100 % crystalline sample (207 J/gm for polypropylene). [1].
Thermal degradation test was conducted using TGA Q50 (M/s TA) equipment. The procedure involved heating the samples from 40 to 800 ^{0}C at a ramp rate of 10^{0}C/min and the corresponding weight vs temperature peaks were observed.
Biological properties: Three random samples from the biomedical wastes face masks were collected for microbiological study. For the isolation and identification of bacterial species from the face masks sample, Mackonkey was utilized as selective and differential medium.

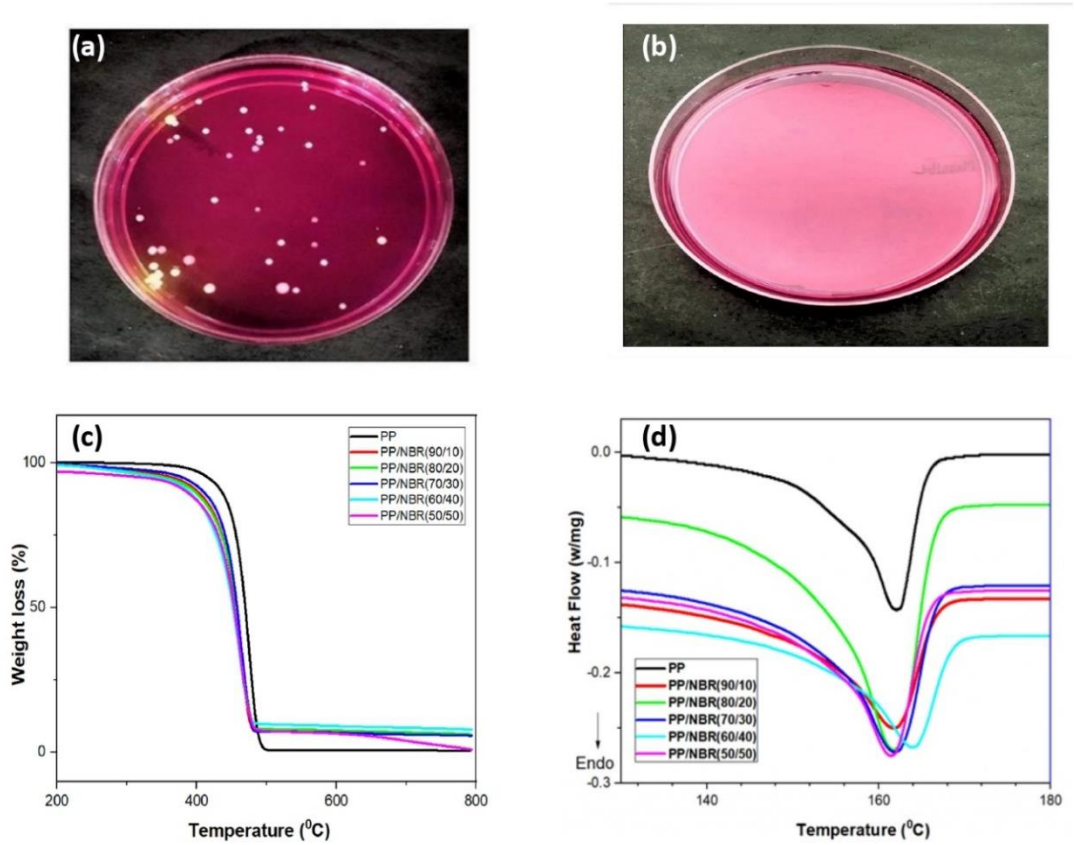


Fig 1: (a) untreated and (b) treated sample of used face masks, (c) tga and (d) dsc graph of the rpp/rnbr blends

Results and Discussion:
The study examines rPP/rNBR blends' thermal properties. As rNBR content increases, crystallization and melting temperatures slightly decrease. Enthalpy of melting and crystallinity also decrease, indicating reduced crystalline structure in higher rNBR blends.

TABLE 2:

Sample type rPP/rNBR blends	Crystallization temperature (^{0}C)	Melting temperature (^{0}C)	Enthalpy of melting ΔH_f(J/g)	Xc (%) Crystallinity	T_{10}	T_f
100/0	120.03	166.39	54.56	26.35	433	497
90/10	118.10	162	31.27	15.10	422	482
80/20	119.15	161.77	17.94	8.66	425	484
70/30	118.87	161.99	25.99	12.55	418	485
60/40	118.51	163.85	14.44	6.97	428	486
50/50	119.50	161.41	19.03	9.19	418	483

TABLE 3:

Sample rPP/rNBR	Tensile strength at yield (MPa)	Elongation at break (%)	Impact strength (j/m)	Flexural strength (MPa)
100/0	30±0.85	40.25±12	5.45±0.15	30.2±1.20
90/10	25±0.45	66.60±42	8.45±0.45	25.20±1.15
80/20	21±0.85	80.10±42	15.24±0.20	20.12±0.78
70/30	17.21±0.24	96.41±42	28.45±0.15	18.01±.01
60/40	13.4±0.93	106.80±52.56	25.24±1.05	16.35±1.35
50/50	9.84±0.93	97.45±42	22.14±2.05	15.24±.85

The mechanical properties of rPP/rNBR blends reveal notable trends with varying rNBR content. As rNBR increases, tensile strength and flexural strength decrease, indicating a reduction in rigidity. Conversely, elongation at break and impact strength significantly improve, suggesting enhanced flexibility and toughness [2].

Conclusion: The mechanical, thermal and biological characteristics of rPP/rNBR blends were investigated in this study. The enthalpy of melting, crystallinity, and crystallization temperatures all marginally decrease with increasing rNBR content, suggesting a less crystalline structure in higher rNBR blends. Mechanically, lower tensile and flexural strengths are the outcome of higher rNBR concentration, indicating a decrease in stiffness. But impact strength and elongation at break show a considerable improvement, suggesting increased toughness and flexibility. These results emphasize how strength and flexibility are traded off in rPP/rNBR mixtures. The ability to modify a material's properties for certain engineering applications is essential, since it allows for the optimization of stiffness and toughness ratios to meet performance specifications. Important information for material design and application is provided by this study.

ACKNOWLEDGEMENTS

The authors express gratitude to the Department of Science and Technology (DST), Govt. of India (Grant: DST/ TDT/WMT/Biomedical waste/2021/01(G)) for the financial support.

REFERENCES

1. A. Blanco, R. Juan, B. Paredes, C. Domínguez, and R. A. García-Muñoz, "Advancing polypropylene quantification in recycled HDPE: A comparative study of FTIR, DSC, TREF, and TGIC for enhanced plastic circularity," *Polym. Test.*, vol. 149, no. February, 2025, doi: 10.1016/j.polymertesting.2025.108855.
2. L. Lendvai, "Mechanical and morphological properties of PP/XNBR blends produced with rubber latex," *J. Polym. Res.*, vol. 30, no. 7, pp. 1–10, 2023, doi: 10.1007/s10965-023-03660-3.

Development of Sustainable Absorbent Wheat Gluten-Based Composition: Evaluation of Properties

Roshni Pattanayak[1,3 a)] Ṣwayam Pragyan Behera[2], Sukanya Pradhan[1] and Smita Mohanty[1]

[1] *School for Advanced Research in Petrochemicals (SARP), Laboratory for Advanced Research in Polymeric Materials (LARPM), Central Institute of Petrochemicals Engineering & Technology (CIPET), Patia, Bhubaneswar, Odisha, India, 751024.*

[2] *CIPET: IPT, Bhubaneswar, India*

[3] *Utkal University, Vani Vihar, Bhubaneswar, Odisha, 751004, India*

[a)]Corresponding author: roshnipattanayak@gmail.com

Abstract. The current research implies the development and its property evaluation of bio-based wheat gluten foam (WGF) absorbent material, preferably suitable for hygiene applications. Here, WGF foam exhibits an increased absorbency value in various liquid media, including distilled water, 0.9wt.% saline solution and defibrinated sheep blood media. As the mechanical stability of the neat WGF (S1) was decreased after liquid immersion, Gallic acid (GA) and Bagasse fibre powder (BFP) were used as a bio-based crosslinker and a reinforcement, respectively, to enhance its properties. The presence of only gallic acid in the foam (S2) showed absorbency of 7.8 g/g in distilled water, 9 g/g in saline and 6.3 g/g in sheep blood at 240 mins with some structural disintegration. On the other hand, the combination of BFP and GA-based wheat gluten foam (S3) showed absorbency of 8.9 g/g in distilled water, 9.4 g/g in saline and 6.5 g/g in sheep blood at 240mins time duration without disintegration. Absorbency under load test and compressive test were performed for all samples, in which S3 showed better blood absorbency of 7.5 g/g and also possessed better compressive strength of 0.35 MPa at a strain of 0.012. Through scanning electron microscopy (SEM), the porous structure of every sample was identified and around 79.863% of open cells present in the S3 composition were identified by gas pycnometers. The soil burial test was carried out to analyse the degradation behaviour of the developed samples. Additionally, they showed better thermal stability, confirmed by thermo gravimetric analysis (TGA). Thus, these findings revealed the cost-effective development of a sustainable absorbent composition, which may find effective use in hygiene applications.

Keywords: Wheat Gluten, Absorbent foam, Sugarcane bagasse fiber, Absorbency, Female hygiene application

1. INTRODUCTION

The majority of absorbents on the market today are derived from petroleum-based synthetic materials, which can absorb liquids exceeding their initial weight. Common hydrogels or absorbent particles typically absorb more than 100% (1g/g) of deionised water. However, these materials have significant drawbacks: they are made from non-renewable resources, are toxic, and non-degradable, posing health and environmental risks. Consequently, there is a growing interest in developing bio-based absorbent materials that are safer for humans and the environment. These materials have applications in agriculture, drug delivery, tissue engineering, cosmetics, wastewater treatment, and health and hygiene products.

Wheat gluten (WG) is a frequently used protein with a high molecular weight and the ability to form stable crosslinked hydrogels. It has significant mechanical strength and viscoelastic properties, making it suitable for bio-based absorbent foams that can absorb substantial amounts of fluid.

Gallic acid (GA), a naturally occurring phenolic acid found in leaves, fruits, and wildflowers, exhibits antibacterial, antioxidant, anti-inflammatory, and cytotoxic properties. Besides this, bagasse fibers (BF), a byproduct of sugarcane juicing, are often improperly disposed of, contributing to significant air pollution in India. According to the Times of India, nearly 300,000 kilograms of bagasse are produced monthly and are either dumped or burned. Utilising bagasse fibers as a reinforcing filler can leverage their mechanical stability to enhance product stability [1-5]. In the present research, gallic acid (GA) as a bio-based crosslinker and bagasse fiber powder as a reinforcement filler were used to develop a modified wheat gluten foam absorbent material, and its various characterization tests were carried out for a complete property analysis.

2. EXPERIMENTAL

2.1. Materials

Wheat gluten (Protein content ≥75g) was procured from the local e-commerce market. Gallic acid (M_w =188.14) and sodium hydroxide pellets were purchased from M/s Sigma-Aldrich, India. Bagasse fibers were collected from a local market. Distilled water was used throughout the experiment, which was prepared in the laboratory. Defibrillated sheep blood was provided generously by M/s S.R. Group, New Delhi, India. The tea bag was purchased from a local e-commerce market with a size of 5.5 x 7cm.

2.2. Methods

2.2.1. Preparation of Bagasse fiber powder

The collected bagasse fiber (BF) waste was sun-dried for three days and sterilised under UV light. It was then ground into small pieces and soaked in a sodium hydroxide solution to enhance its properties. After the alkali treatment, the fibers were rinsed with running tap water and dried in a hot air oven at 50°C for two days. The dried fibers were then finely ground using a mixer grinder for further testing.

2.3. Preparation of modified wheat gluten foam absorbent

4g of wheat gluten (WG) was added to 10ml of distilled water, and its pH was adjusted with dropwise sodium hydroxide. The mixture was stirred at 90°C and 2500 rpm until frothy. This neat wheat gluten composition (S1) was then cooled, transferred to a 2cm x 2cm x 2cm mold, frozen at -25°C for 12 hours, and lyophilised at -45°C for 20 hours. For the gallic acid-loaded wheat gluten foam (WG/GA) (S2), 40mg (0.2 wt.%) of gallic acid was added, stirred until the mixture turned green, then frozen and dried as above. Another formulation, WG/GA/BFP (S3), was prepared similarly by adding 100mg (0.7 wt.%) of bagasse fiber powder (BFP) as a reinforcement with gallic acid as the crosslinker. Foam formation was not possible above 0.7 wt.% BFP due to structural imbalances, so this amount was optimised for S3. The entire procedure is shown schematically in FIGURE 1. The whole procedure was schematically described in schematic 1.



Schamtic 1. Schematic representation of the methodology for the development of a wheat gluten-based absorbent foam sample

2.4. Characterization

The chemical analysis was conducted using a Nicolet 6700 Fourier Transform Infrared Spectroscope (Thermo Fisher, USA) with a wave number range of 4000-400 cm^{-1} and a resolution of 4 cm^{-1}. Surface morphology was examined with a Scanning Electron Microscope (EVO MA 15, Carl Zeiss, Germany) at an accelerating voltage of 10 kV. The mechanical behaviour of 2cm x 2cm x 2cm samples was tested using a Universal Testing Machine (Instron-3382, UK) with a 70N load at a compressive rate of 10 mm/min, following ASTM D1621. The density and cell content of the samples were measured using gas pycnometers (Quanta Chrome Instruments, India). Thermal behavior was analyzed with a Thermogravimetric Analyzer (Q50, TA Instruments, USA) from 25- 800°C in an inert nitrogen atmosphere at a heating rate of 10°C/min. Absorption tests were performed using the tea-bag method, and a soil burial test was conducted to assess degradation behaviour.

3. RESULT AND DISCUSSION

FIGURE 1(A) shows the FTIR spectra of neat WG foam (S1), WGF/GA (S2), and WGF/GA/BF (S3). The characteristic peaks at 3285 cm^{-1}, 2926 cm^{-1}, and 1744 cm^{-1} correspond to -OH stretching, $-CH_2$ stretching, and -COO linkage vibrations, respectively, indicating higher liquid absorption. Peaks at 1642 cm^{-1} and 1535 cm^{-1} confirm the presence of amide-I (C=O) and amide-II (N-H) groups, verifying composite formation. FIGURE 1(B) presents SEM images of the samples before absorption, while FIGURE 1(C) shows SEM images after absorption. The crosslinked porous structure is evident, facilitating higher liquid uptake compared to the neat sample. In S3, the fiber content enhances capillary action, leading to greater absorbency due to higher liquid accumulation in the open pore cells. FIGURE 1(D) visually represents the samples before and after absorption. The incorporation of gallic acid and bagasse fiber in WG (S3) increases the density and open cell percentage, resulting in higher liquid accumulation, as shown in TABLE 1.

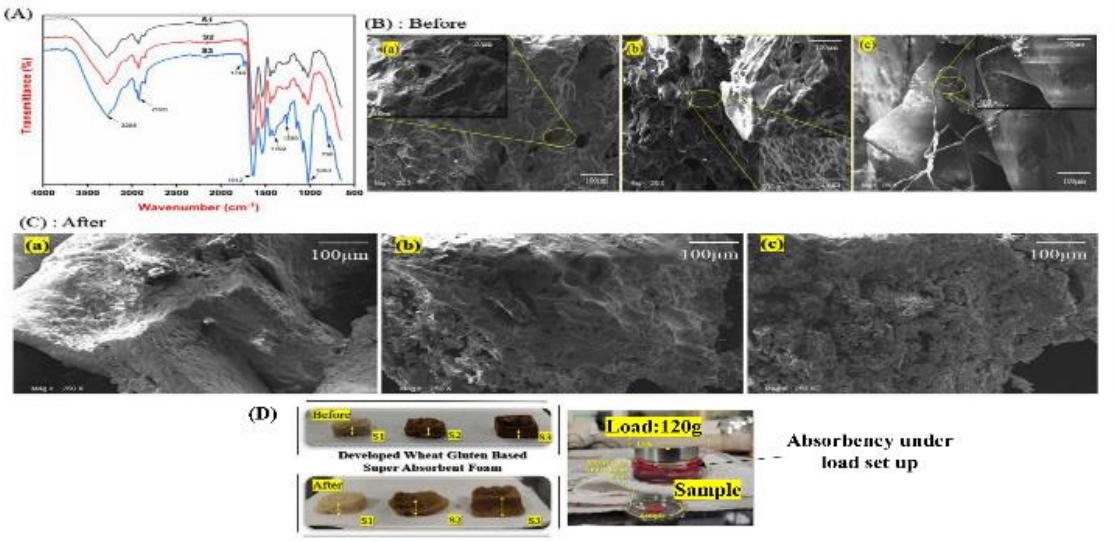


FIGURE 1. (A): FTIR of S1(neat WGF), S2 (WGF/GA) and S3 (WGF/GA/BF) and (B) SEM images: before absorbency of (a) S1, (b) S2, and (c) S3, (C) SEM images: after distilled water absorbency of (a) S1, (b) S2, and (c) S3 (D) Developed Sample

TABLE 1. Data on the density and open cell, and closed cell of the developed foam samples

Sample Name	Density(g/cc)	Open cell (%)	Closed cell (%)
S1	1.141	63.27	36.729
S2	1.375	83.824	16.174
S3	1.497	79.863	20.197

FIGURE 2 (A-C) displays the absorbency values of the developed compositions in distilled water, saline solution, and sheep blood, while FIGURE 2 (D) shows the absorbency under a 120g load. The S3 composition exhibited the highest absorbency, with values of 8.9 g/g in distilled water, 9.4 g/g in saline, and 6.5 g/g in sheep blood after 240 minutes, without disintegration. In the absorbency under load test, S3 achieved 7.5 g/g in blood. Additionally, S3 demonstrated superior compressive strength of 0.35 MPa at a strain of 0.012, as shown in FIGURE 3 (A). The cross-linked structure formed by bagasse fiber and gallic acid in the wheat gluten matrix enhanced both mechanical and thermal stability (FIGURE 3 B,C). Furthermore, the bio-based composition of S3 promoted better microorganism growth, leading to improved degradation in soil burial tests, as depicted in the morphological images in FIGURE 4.

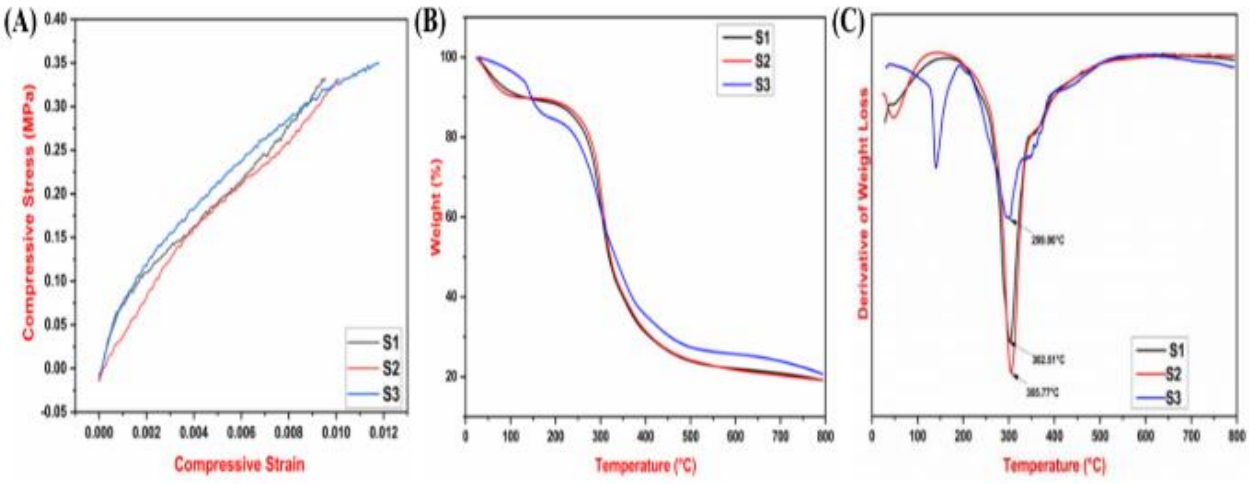


FIGURE 2. (A) Absorbency through distilled water, (B) Absorbency through saline solution, (C) Absorbency through sheep blood and (D) Absorbency under load of all developed samples.

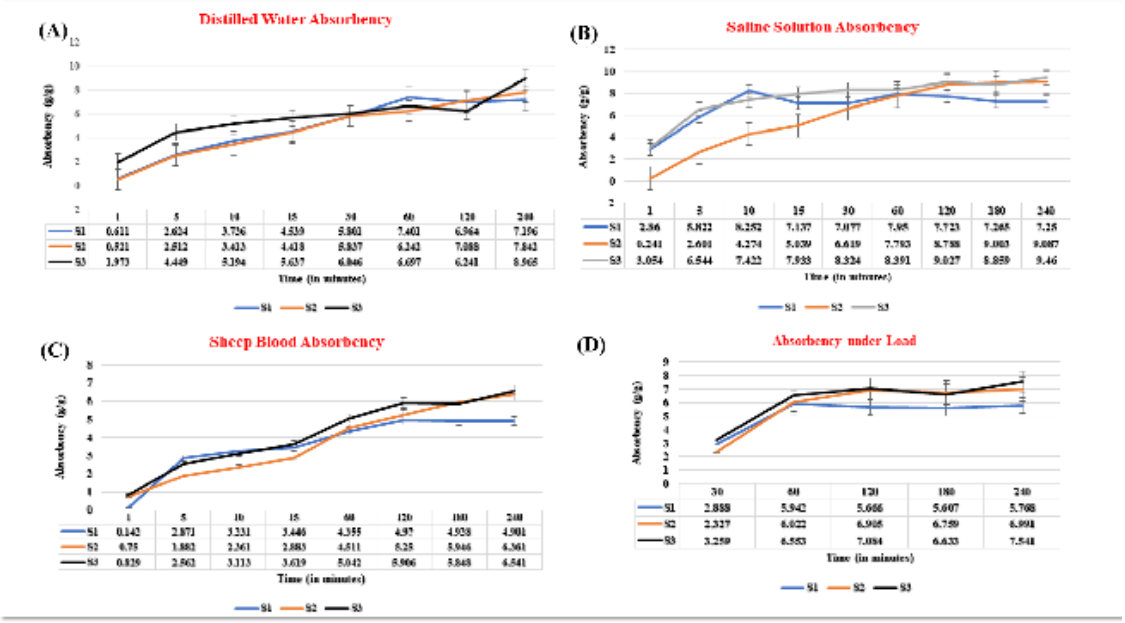


FIGURE 3. (A) Mechanical analysis of S1, S2 and S3 and (B) & (C) Thermal Analysis of (a) S1, (b) S2, and (c) S3.

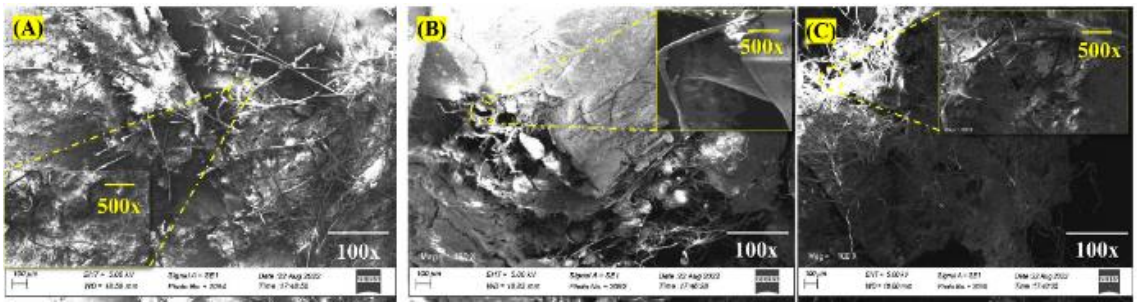


FIGURE 4. Morphological analysis of degraded samples (A) S1, (B) S2 and (C) S3.

4. Conclusion

The wheat gluten-based composition, developed using gallic acid and bagasse fiber, demonstrated superior absorbency, mechanical strength, thermal stability, and biodegradability, making it a promising sustainable solution for female hygiene applications.

ACKNOWLEDGMENTS

The authors would like to express their gratitude to the DST:INSPIRE (IF200480,2020) and Centre of Excellence (CoE), Manufacturing of Next Generation Biomedical Devices, DCPC, Govt. of India (F. No:25012/01/2020-PC-II (FTS:16020), for providing the funding to perform this experiment.

REFERENCES

1. Capezza, A. J., Muneer, F., Prade, T., Newson, W. R., Das, O., Lundman, M., ... & Johansson, E. Communications Chemistry, Vol. 4(1), pp. 52, (2021).
2. Teli, M. D., & Mallick, Journal of Polymers and the Environment, Vol. A26, pp.1393-1404, (2018).
3. A. J. Capezza, M. Lundman, R. T. Olsson, W. R. Newson, M. S. Hedenqvist, and E. Johansson, Biomacromolecules, Vol. 21(5), pp. 1709–1719 (2020).
4. Nguyen, N. T., Lin, A. B., Chang, C. T., & Hong, G. B., Molecules, Vol. 30(3), pp. 572, (2025).
5. Pattanayak, R., Jena, T., Pradhan, S., & Mohanty, S, Polymer-Plastics Technology and Materials, Vol. 62(10), pp 1290-1317,(2023).

Optimal Transport conditions of a Run and Tumble Particle in a Ratchet potential

Arjun S R[1, a)] and Ronald Benjamin[1,b)*]

[1]*Department of Physics, Cochin University of Science and Technology, Kochi, Kerala, India- 682022*
[a)] arjunsr@cusat.ac.in, [b)] rbenjamin.phys@gmail.com

Abstract. Using Brownian Dynamics simulations, we explore the optimal transport conditions of a run and tumble Brownian particle moving in an asymmetric piece-wise linear ratchet potential. The particle current can be optimized with respect to the self-propelled velocity of the run and tumble particle as well as the temperature of the thermal bath and the asymmetry parameter of the potential. However, the unidirectional motion of the particle is executed in an incoherent manner as shown by low values of the Peclet number. Additionally, the net current as well as the diffusivity degrade with the increase in the rate of tumbling events as frequent changes in orientation traps the particle at the minima of the potential.

INTRODUCTION

One of the hot topics to emerge from the study of Brownian motion first observed by Robert Brown (1828) and and later theorized by Albert Einstein (1905) is the phenomenon of Brownian motors: the generation of unidirectional transport under non-equilibrium conditions by the breaking of temporal or spatial symmetry of the system. Most studies on Brownian motors have been carried out with passive Brownian particles which exhibit the motor effect only in the presence of an external source of energy or in the presence of thermal baths at different temperatures [1]. In recent years research in the area of statistical mechanics there has been an ever-increasing focus on self-propelled particles which can execute motion without the aid of any external source. These particles are inherently out of equilibrium and therefore serve as prototypes for understanding non-equilibrium thermodynamics in the nano to micro-scale regime in the same manner that the Carnot engine model played in the development of Equilibrium Thermodynamics at the nanoscale [2]. Models of Self-propelled Brownian motors have also been introduced and various mechanical and thermodynamical aspects of their behavior have been studied. Such self-propelled Brownian motors can either be constituted by Active Brownian particles or run-and-tumble particles in a ratchet potential [3]. While in the case of Active Brownian particles, the orientational angle changes continuously, the run-and-tumble particle moves along a straight line with sudden orientational changes [4]. There have been several studies on the performance of Active Brownian particles in ratchet potentials, with focus on their transport characteristics [5]. However, comparatively fewer studies have been carried out on run and tumble type Brownian motors and the few that have been done pertain to a specific type of tumbling even where the particle does not change its orientation or changes it by 180^0 [6]. In this work we focus on a run and tumble particle where during a tumbling even the particle can reorient itself along any angle. At the tiny length scales we consider, the medium is highly viscous and so we study only the overdamped dynamics in one dimension via Brownian dynamics simulations. We observe enhancement of current at optimal values of the temperature of the heat bath, the self-propelled velocity of the run and tumble particle and the asymmetry parameter of the potential. Our simulations also show poor transport coherence of the run and tumble motor leading to unreliable transport.

THE MODEL

We consider an overdamped run-and-tumble Brownian particle suspended in a thermal bath and subjected to an asymmetric piece-wise linear potential *U(x)* of spatial period *L* such that the overdamped dynamics in one dimension is described by the following Langevin equation:

$$\dot{x} = v_0 \cos\theta - U'(x) + \sqrt{2D_T}\,\xi(t), \qquad \dot{\theta} = \sum_i \Delta\theta_i\,\delta(t - t_i) \tag{1}$$

where, v_0 is the self-propelled velocity of the run-and-tumble particle, θ is the orientation angle, D_T is the translational diffusion coefficient, t_i are random tumbling times distributed as per a Poisson distribution at the rate λ, $\Delta\theta_i$ are the tumbling angles distributed uniformly between 0 and 2π during a tumbling event and $\xi(t)$ is unbiased ($<\xi(t)>=0$) and uncorrelated $<\xi(t)\,\xi(t')>=\delta(t-t')$ Gaussian white noise. The potential *U(x)* is given by,

$$U(x) = \begin{cases} u_0 \frac{x}{\alpha}, & 0 \le x \le \alpha \\ u_0 \frac{L-x}{L-\alpha}, & \alpha \le x \le L \end{cases} \quad (2)$$

where, u_0 is the barrier height and α is the asymmetry parameter of the potential. In order to numerically solve Eqs. (1), we carry out Brownian dynamics simulations using the Euler algorithm given by,

$$x_{n+1} = x_n + \rho_n v_0 \cos\theta\, \Delta t - U'(x) + \sqrt{2D_T \Delta t} W_n\ ,\ \theta_{n+1} = \theta_n + (1-\rho_n)\Delta\Theta_n \quad (3)$$

Here, the subscript *n* denotes the nth time-step and W_n are independent Gaussian random numbers with mean zero and standard deviation one. Instead of generating the random tumbling times t_i according to a Poisson distribution, we instead introduce a parameter ρ which governs whether the particle is in the running mode ($\rho_n = 1$) or in the tumbling mode ($\rho_n = 0$) after each time-step Δt (both approaches are equivalent). It can be shown that at each time-step the probability of a run event is $e^{-\lambda}$, while the probability of a tumbling event is 1-$e^{-\lambda}$[4]. Choosing a uniform random number between 0 and 1 and comparing against the probability of either event we can choose ρ_n accordingly. In our simulations we choose $\Delta t = 0.0001$ and average over 5000-10000 independent realizations. Gaussian random numbers are generated using the Box-Mueller algorithm.

The transport characteristics determining the performance of the motor are the average particle current <*v*>, effective diffusion coefficient D_{eff} and the Peclet number, Pe, which are calculated from numerical simulations via the following equations:

$$\langle v \rangle = \lim_{t\to\infty} \left\langle \frac{x(t)-x(0)}{t} \right\rangle, \qquad D_{eff} = \lim_{t\to\infty} \frac{\langle x^2\rangle - \langle x\rangle^2}{2t}, \qquad \text{Pe} = \frac{L\langle v\rangle}{D_{eff}} \quad (4)$$

The transport is coherent if Pe>2, when drift overcomes diffusion and the motion becomes more regular.

RESULTS AND DISCUSSIONS

In Fig. 1(a) we plot <v> as a function of D_T at different values of λ. The net unidirectional motion is along the gentler side of the potential ($\alpha = 0.8$) in the forward direction as the particle can more easily overcome the weaker force towards the left than the steeper force in the reverse direction. At low values of D_T, the thermal energy is insufficient for the particle to cross the barrier and therefore it is trapped in the minima of the potential leading to a low value for the current. On the other hand, at larger values of D_T the thermal energy enables the particle to cross the barrier in the reverse direction as well and the impact of the asymmetry of the potential is reduced leading to a lower value of the current. At an optimal value of D_T, the current attains a peak. Figure 1(a) also show the current monotonically decreasing with larger values of λ. As the particle more frequently reorients itself with the increase of λ its efficiency decreases leading to a reduced current. Figure 1(b) shows the particle current as a function of v_0 at different values of the asymmetry parameter α. A completely symmetric potential ($\alpha = 0.5$) will yield no current as the necessary ingredient of a motor is broken spatial symmetry. As α increases the net current also increases and saturates as $\alpha \to 1$. We also observe that there is an optimal value of v_0 at which current reaches a maximum.

In Fig. 1c), we plot the ratio D_{eff}/D_T as a function of D_T. We observe that the ratio decreases with D_T and then saturates at a value close to one as D_T increases. The effective diffusion coefficient also monotonically increases as λ decreases. Since 1/λ represents the persistence time, as the running mode persists for longer times, the effective diffusivity also increases. Finally, in Fig.1(d), we plot the Peclet number as a function of D_T and observe that at low values of D_T, Pe hovers around 2, the critical value required for transport coherence. However, as D_T increases the transport coherence degrades due to the increase of thermal diffusion resulting in a disordered rather than regular motion.

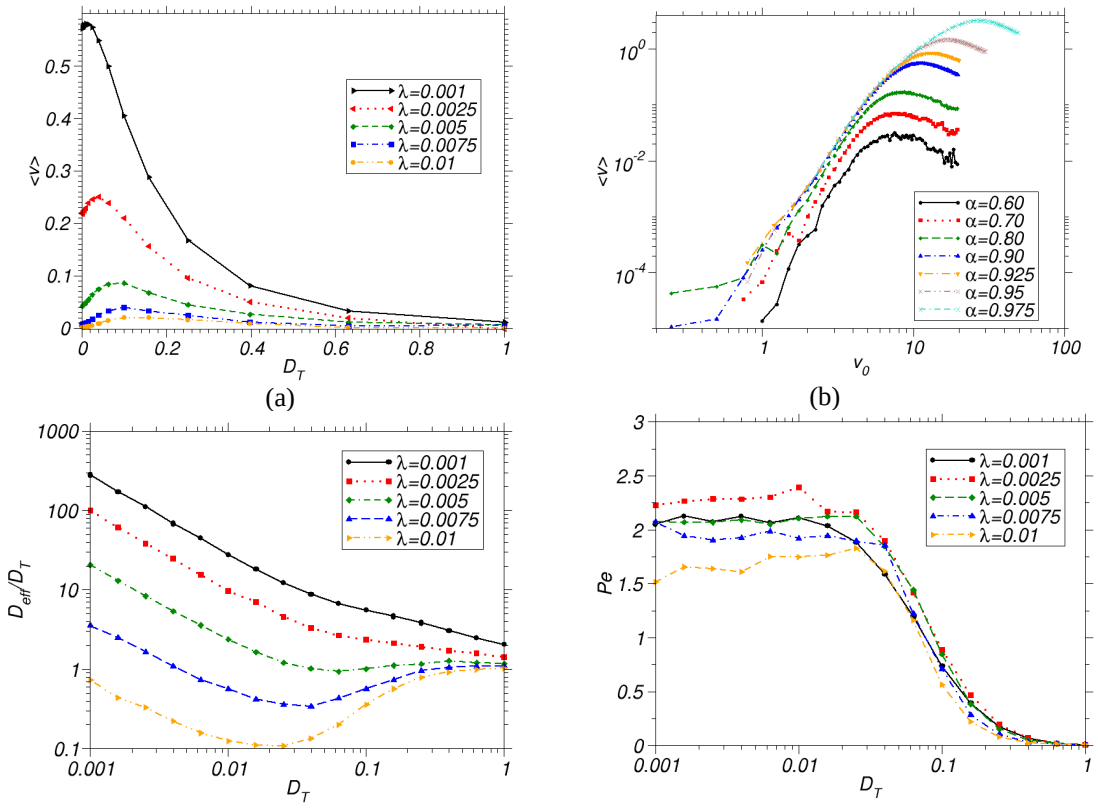


FIGURE 1. (a), (c) and (d) show the average current <v>, ratio of effective diffusion coefficient and translation diffusion coefficient D_{eff}/D_T and the Peclet number Pe respectively, as function of D_T for different values of λ. In (a), (c) and (d), the asymmetry parameter of the potential $\alpha = 0.8$ and the self-propelled velocity v_0 =5.0. (b) shows the average current <v> as a function of v_0 for different values of α. In (b) $\lambda = 0.005$ and D_T=0.10.

CONCLUSION

In this work, we have obtained the optimal transport conditions for the performance of the run and tumble Brownian motor. While the particle current can be optimized with respect to the translational diffusion coefficient and the self-propelled velocity, the maximal value of the Peclet number reaches at the most only the critical value required for coherent transport and in general the motion is irregular.

REFERENCES

1.) P. Reimann, Phys. Rep**. 361,** 57 (2002); Ronald Benjamin *Phys. Scr.* **99** 095257(2024); Ronald Benjamin and Ryoichi Kawai. Phys. Rev. E 77.5: 051132(2008).
2.) G. Volpe, G. Sylvain and G. Volpe, Am. J. Phys. **82**, 659 (2014).
3.) Reichhardt, CJ Olson, and Charles Reichhardt., *Annual Review of Condensed Matter Physics* 8.1 (2017): 51-75.
4.) A. Callegari and G Volpe, Chapter7 In: Flowing Matter. Soft and Biological Matter (eds. Toschi, F., Sega, M.) (Springer, 2019).
5.) Ai, Bao-Quan, and Feng-Guo Li. *Soft matter* 13.13 (2017): 2536-2542; Arjun S R and Ronald Benjamin, *arXiv:2211.04298* (2022).
6.) C. Roberts and Z. Zhen, Phys. Rev. E **108**, 014139 (2023).

Synthesis and Characterization of Anatase Phase Nanocrystalline-TiO_2 by Hydrothermal Method

Nidhi Garg[a*], Lori Rastogi[b], Arup Dasgupta[c]

[a]*Chemistry Division, Bhabha Atomic Research Centre, Mumbai, 400085, India*
[b]*National Centre for Compositional Characterization of Materials, Bhabha Atomic Research Centre, ECIL-Post, Hyderabad, 500062, India*
[c]*Materials and Metallurgy Group, Indira Gandhi Centre for Atomic Research, Kalpakkam, 603102, Tamil Nadu, India*

[*]Corresponding author: ngarg@barc.gov.in

Abstract. Titanium dioxide (TiO_2) nanoparticles show great promise for environmental remediation due to their photocatalytic properties and non-toxic nature. This study explores the hydrothermal synthesis of nanocrystalline TiO_2 powder with a dominant anatase phase, known for its high photocatalytic efficiency. The synthesis used a hydrothermal reaction of titanium isopropoxide with Acacia gum, followed by calcination at 500°C. Characterization through Transmission Electron Microscopy (TEM), X-ray Diffraction (XRD), and Raman Spectroscopy confirmed a particle size of 20-50 nm and the predominance of the anatase phase. TEM images showed well-dispersed nanoparticles, XRD revealed mainly anatase with minimal rutile, and Raman spectra confirmed the anatase structure. Zeta potential measurements across pH 3-10 showed a high positive zeta potential at acidic pH and a stable negative zeta potential in alkaline conditions, indicating better adsorption in alkaline environments. This study highlights the effectiveness of hydrothermal synthesis for high-quality TiO_2 nanoparticles and their potential for environmental cleanup, particularly arsenic removal from water.

1. INTRODUCTION

Titanium dioxide (TiO_2) nanoparticles have gained significant attention due to their diverse applications across industries, including as semiconductors, photocatalysts, gas sensors, and antibacterial agents, and for environmental remediation. TiO_2 is especially promising for environmental applications due to its effectiveness in photocatalytic degradation of organic pollutants and its non-toxic, chemically stable, and thermally resistant properties suitable for wastewater treatment. TiO_2 exists in three main forms: rutile, anatase, and brookite. Rutile is the stable form at room temperature, but anatase is preferred for photocatalysis due to its wider optical band gap (3.2 eV vs. rutile's 3.0 eV), and better charge carrier mobility [1]. Hydrothermal synthesis is a favored method for producing high-quality ceramic nanoparticles due to its simplicity and the ability to control particle size, phase, and composition [2].

Arsenic removal from water is a critical environmental challenge due to arsenic's classification as a carcinogen. The World Health Organization (WHO) and European Directive 98/83/EC set a maximum allowable concentration of 10 µg/L for arsenic in drinking water. While various arsenic removal methods exist, adsorption is often the most cost-effective and efficient [3]. Exploring TiO_2 as an adsorbent for arsenic removal is thus important for scaling up water treatment technologies. Here, the hydrothermal synthesis of nanocrystalline TiO_2 powder has been reported, that is characterized using TEM, XRD, and Raman spectroscopy to confirm the anatase phase. Zeta potential studies at different pH levels are performed to understand the surface chemistry of TiO_2 for adsorption applications.

2. MATERIALS AND METHODS

2.1 Synthesis of nano-TiO_2

The hydrothermal route is adopted for synthesis of nanocrystalline TiO_2 powder. First, precursor titanium isopropoxide was taken and Acacia gum was added into it. The mixture was stirred for 2h followed by high temperature high pressure heating for 1 hr in an autoclave. Sol was collected, washed and dried at 80ºC, 8h. Dried oowder was grinded and the grinded powder was calcined at 500ºC for 5h in muffle furnace. Synthesized nano0-powdere was used for further studies.

2.2 Characterization of nano-TiO_2

TEM studies were performed using a Philips CM200 ATEM using a LaB_6 filament and an acceleration potential of 200 kV. The TiO_2 powder were first dispersed in ethanol, sonicated for about 10 min, spread on a carbon coated copper grid and finally dried at 40°C. XRD patterns were recorded with a RIGAKU-ULTIMA IV diffractometer using Cu Kα radiation (1.5406 Å) in powder XRD mode, over a 2θ range of 20–70° with a 0.05° step size. Peak

positions and FWHM were determined by fitting peaks with a Voigt function, and the average crystallite size was calculated using the Scherrer formula: Size=0.9λ/βcosθ [4], where λ is the CuKα wavelength, θ the Bragg angle, and β is the FWHM corrected for instrumental broadening. Raman spectra were recorded with a Jobin Yvon HR 800 spectrometer using a 514.5 nm Ar+ ion laser.
Zeta potentials of TiO_2 nanoparticles were measured with a Zeta meter (Malvern Instruments, Malvern, UK) by phase analysis light scattering using a He-Ne laser (633 nm, 4.0 mW). Zeta potentials were calculated from electrophoretic mobility using the Smoluchowsky approximation. Measurements were done in a 0.01% (wt/vol.) TiO_2 aqueous solution at pH 6.5, adjusted to pH 3–10 with HNO_3 or NaOH. Solutions were sonicated for 1 hr and settled for 24 h before measurement.

3. RESULTS AND DISCUSSION

3.1 Characterization of synthesized nano-TiO_2

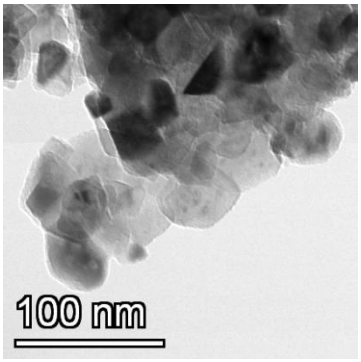


Fig. 1: TEM micrograph of nanocrystalline TiO_2 powder

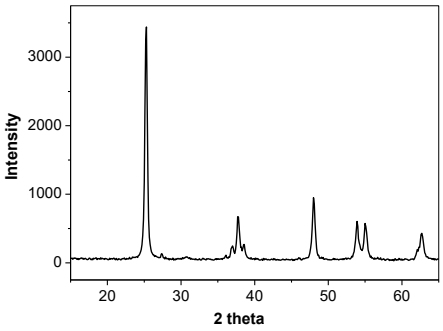


Fig. 2: XRD pattern of nanocrystalline TiO_2 powder

The visual analysis of the prepared TiO_2 nanopowder reveal the silvery white appearance. The TiO_2 nanoparticle TEM analysis (particles refer to individual crystals) is displayed in Figure 1. The bright field image reveal the crystallites range in size from 20 to 60 nm.

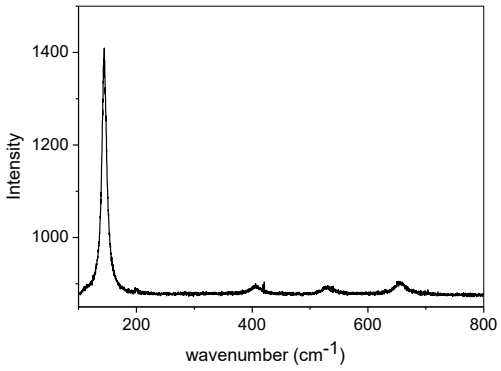


Fig. 3: Raman spectra of nano- TiO_2 powder

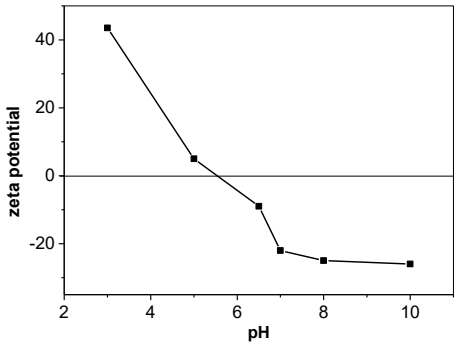


Fig. 4: Zeta potential measurements of nano-TiO_2 suspension at different pH

Fig. 2 presents the XRD analysis, confirming that the sample predominantly contains the anatase phase of TiO_2, with very weak intensity peaks also indicating the presence of the rutile phase. The diffraction peaks observed at 25.3°, 36.8°, 37.8°, 47.9°, and 62.7° correspond to the (101), (103), (004), (200), and (211) crystal planes of anatase TiO_2, respectively. The very small diffraction peak at 27° is assigned to the (110) plane of rutile phase of TiO_2 [5]. The observed peak broadening in the XRD patterns is indicative of the nanoscale dimensions of the TiO_2 particles. Particle size was calculated using scherrer formula [4] and it is calculated to be ~35 nm. Fig. 1c represents the Raman spectrum of the TiO_2 nano-powder; peaks at 144.3°, 407.1 °, 529.7 ° and 654.1 ° belong to Eg, B1g. A1g and Eg modes of anatase phase of TiO_2 [6]. Thus, TEM, XRD, and Raman analyses

confirm the successful synthesis of pure nano-TiO_2, predominantly in the anatase phase, with particle sizes ranging from 20 to 60 nm.

3.2 Zeta potential studies

The surface charge behavior of the TiO_2 nanoparticles was evaluated using zeta potential studies across a range of pH values. The nanoparticles formed a stable suspension in water, maintaining stability under varying pH conditions. At pH 3, a high positive zeta potential of +43.5 mV was recorded, indicating strong surface charge and suspension stability. This can be attributed to the adsorption of hydronium (H_3O^+) ions onto the TiO_2 surface, resulting in a surface structure of Ti–O–O–H_3O^+. The point of zero charge (PZC) for the nano-TiO_2 was found to be approximately pH 5.6, suggesting that below this pH, the surface tends to attract negatively charged species. At higher pH levels, the zeta potential becomes increasingly negative before stabilizing between pH 7 and pH 10, due to the adsorption of hydroxide ions. This stability in zeta potential at alkaline pH suggests that TiO_2 nanopowder is a promising adsorbent material in basic conditions. In contrast, at lower pH values, even small changes in pH lead to significant shifts in zeta potential, which may influence the material's adsorption efficiency. Therefore, despite having a relatively low negative zeta potential at high pH, TiO_2 exhibits strong potential as an adsorbent under alkaline conditions [7].

4. CONCLUSIONS

Nanocrystalline TiO_2 powder with pure anatase phase has been prepared with hydrothermal crystallization route. Synthesize powder is of the size of around 20-50nm by TEM investigation. XRD and Raman analysis support these findings. Zeta potential investigations at different pH signify that TiO_2 has better absorption efficiency at alkaline pH as compared to acidic pH.

ACKNOWLEDGMENTS

Authors are appreciative to A. Sukumar of NCCCM, BARC, Hyderabad and Dr. P. Chandramohan of WSCD, BARC Facilities, Kalpakkam for providing XRD and Raman data of the samples respectively. Authors are grateful to Dr. Shilpa Sawant of Chemistry Division, BARC for her guidance in carrying out experiments as well as in preparation of manuscript.

REFERENCES

1. K. Mogyorósi, I. Dékány, J. H. Fendler, Langmuir, 2003, 19, 2938–2946.
2. N. Garg, V.K Mittal, S. Bera, P Chandramohan, CR Das, S. Velmurugan, Thin Solid Films, 2013, 222-228.
3. M. Samimi, M. Zakeri, F. Alobaid, B. Aghel, Nanomaterials, 2023, 13, 60.
4. N. Garg, V.K. Mittal, S. Bera, A. Dasgupta, S. Velmurugan, Ceram. Int. 2012, 38, 2507–2512.
5. B. Li, X. Wang, M. Yan, L. Li, Mater. Chem. Phys., 2003, 78, 184-188.
6. L.V. Hong, N.T.H. Le, N.C. Thuan, N.D. Thanh, N. X. Nghia, N. X. Phuc, . Raman Spectrosc., 2005, 36, 946–949.
7. N. Garg, M.V. Balaramakrishna, Next Res., 2025, 2, 100132.

Augmented field emission properties from MoO_3 rods derived via chemical route

Anima Mahajan[1,2], Menaka Jha[2, b)], Santanu Ghosh[1, a)]

[1] *Department of Physics, Indian Institute of Technology, Hauz Khas, New Delhi -110016, India.*
[2] *Institute of Nano Science & Technology, Knowledge City, Sector-81, Mohali, Punjab- 160062, India*

***[a,b)]Corresponding Authors** Santanu.Ghosh@physics.iitd.ac.in, menaka100jha@gmail.com

Abstract. Here, we have synthesized the monoclinic phase of MoO_3 by using the micellar route. Structural analysis of MoO_3 shows the formation of monoclinic molybdenum oxide (MoO_3). Transmission electron microscopic studies of MoO_3 reveal a nanorod-like morphology having a diameter of ~100-200 nm, and a length of ~500 nm- 1 µm. Further, the obtained MoO_3 was spin-coated over an n-type silicon substrate, and a field emission study of the MoO_3 film was conducted. The observed field enhancement factor (β) and turn-on field of MoO_3 were 1.9×10^3 and 3.30 V/µm. The current study opens up new avenues for the affordable and scalable usage of MoO_3, to be employed as an electron emitter in a high-end optical and electrical device.

Introduction

Molybdenum trioxides exhibit photochromic and electrochromic properties, making them appealing for applications such as information displays, sensor devices, and smart windows[1].The presence of a 1D nanostructure is a significant characteristic that contributes to the field-emission application. Using semiconductor nanomaterials as a cold cathode lowers the necessary field for electron emission[2]. MoO_3 nanostructures, including nanoflowers, nanowires, and nanobelts, have exhibited encouraging field emission characteristics, suggesting their possible use as cold cathode materials in displays, lighting systems, and plasma generators[3], [4], [5].

Synthesis of Molybdenum trioxide and fabrication of Molybdenum trioxide film

Molybdenum trioxide (MoO_3) was synthesized using a micellar method with CTAB as a capping agent. A 0.1 M aqueous solution of ammonium molybdate (50 mL) containing 10 mM CTAB was mixed with a separately prepared 0.3 M NaOH solution (50 mL) also containing 10 mM CTAB. The NaOH solution was added slowly to the molybdate solution under continuous stirring overnight. The resulting precipitate was collected via centrifugation using methanol and dried at 70 °C overnight. For film fabrication, 25 mg of the dried MoO_3 powder was dispersed in 200 µL ethanol, sonicated for 10 minutes, followed by the addition of 200 µL ethylene glycol and further sonication. The homogeneous suspension was spin-coated onto a cleaned silicon substrate (1×1 cm²) at 3000 rpm, with 10 seconds acceleration and 60 seconds spinning. The process was repeated four times to achieve a uniform MoO_3 film, which was used as a cathode for field emission studies.

Results and Discussion

Figure 1(a) presents the X-ray diffraction (XRD) pattern of molybdenum oxide, which matches well with the monoclinic phase of MoO_3. This phase identification is corroborated by comparison with the standard JCPDS card no. 01-073-1544, corresponding to the P2/m (10) space group. Field Emission Scanning Electron Microscopy (FESEM), shown in Figure 1(b), reveals the presence of MoO_3 rods with average dimensions between approximately 500 nm and 1 µm. The rod-like morphology is further verified by Transmission Electron Microscopy (TEM) in Figure 1(c). The combined data from PXRD and TEM (Figures 1a–c) confirm the successful synthesis of high-purity, nanoscale MoO_3 rods[5].

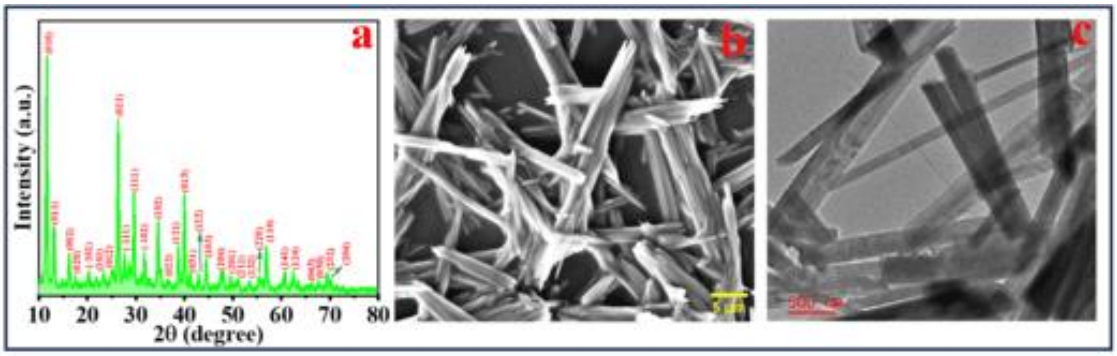


FIG. 1. (a) Powder X-ray diffraction (PXRD) pattern of MoO_3, (b)FESEM image of MoO_3, (c)TEM image of MoO_3 nanorods.

Figure 2(a-d) shows Scanning Transmission Electron Microscopy (STEM) mapping of MoO_3, which indicates both Mo and O are uniformly distributed over each other. Electron Microprobe Analysis (EPMA) mapping of MoO_3 is shown in Figure 2(e-f). For Mo and O, pentaerythritol (PET) and Rhodium Acid Phosphate (RAP) crystal detectors were used, respectively.

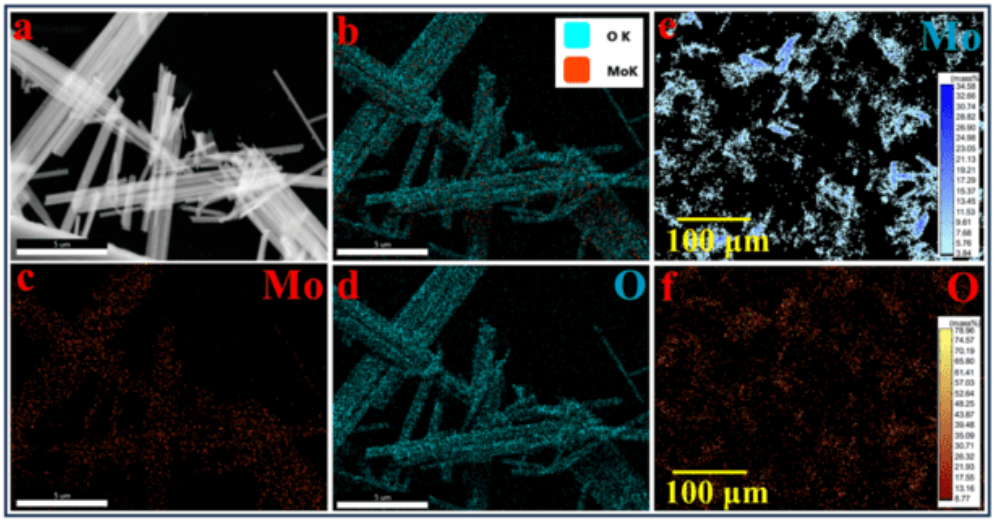


FIG. 2. (a-d) Scanning transmission electron microscopy (STEM) mapping of MoO_3. (e-f) Area selected for elemental mapping in MoO_3 using electron probe microanalysis (EPMA).

Field-emission in the quantum tunnelling phenomenon occurs when electrons traverse a vacuum barrier from an emitting material cathode to an anode under the influence of a powerful electric field of the order of 10^6–10^7 V/cm from semiconductor or conducting materials. The cathode and anode are separated by a fixed distance of 200 µm. The modified Fowler-Nordheim (F-N) equation below shows how the emission current density of semiconducting nanostructures changes with the electric field $I = Aat_F^{-2}\emptyset^{-1}(\beta E)^2 \exp\{\frac{-bv_F\emptyset^{3/2}}{\beta E}\}$. Here, 'a' and 'b' denote the first and second Fowler–Nordheim (F–N) constants, respectively; Φ represents the work function of the cathode material; A refers to the effective emission area; v_F and t_F correspond to the values of the special elliptic functions *v* and *t*; β is the field enhancement factor; and E is the externally applied electric field[6]. The FN plot slope represents the combined impact of the increased local electric field and the material work function and is given by slope=$\frac{-B\varphi^{3/2}}{\beta}$. The field emission characteristic, Figure 3 (b) demonstrates that the emitter of MoO_3 produces an emission current density of 460 µA/cm^2 at an applied field of 7.2 V/µm. The cold field emission mechanism is indicated by a straight line with a negative slope that fits the FN plot for the MoO_3 inset of Figure 2(a). The field enhancement factor value for MoO_3 is approximately 1.9×10^3

calculated by using the work function of MoO_3, 5.7 eV. The MoO_3 nanostructure emitters demonstrate a consistent emission current density of 12 µA/cm^2 for a duration of 8 hours, Figure 3(c).

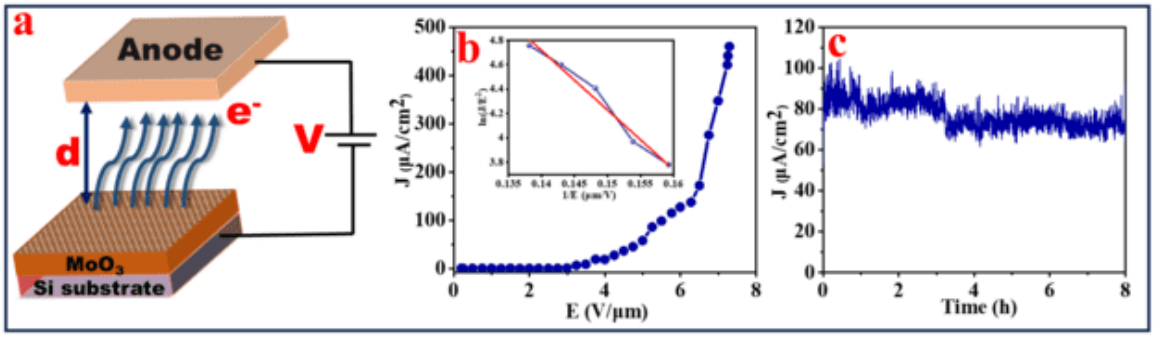


FIG. 3. (a) Schematic showing the Field emission mechanism. (b) Applied electric function as a function of emission current density (JE plot) of MoO_3 and inset shows FN plot. (c) Long-term field emission current stability indicates a stable emission current for MoO_3.

Conclusion

In the present work, we have synthesized the pure monoclinic crystalline MoO_3 nanorods by micellar route. Field emission analysis of the fabricated film demonstrated a significant current density of 460 µA/cm² along with a low turn-on electric field of 3.30 V/µm. These findings highlight the potential of such cathodes to enable the development of scalable and environmentally sustainable metal oxide-based field emitters.

Acknowledgments

The authors extend their gratitude to the Indian Institute of Technology Delhi for providing the necessary infrastructure support. Anima Mahajan sincerely acknowledges the financial assistance received through the Prime Minister's Research Fellowship (PMRF) scheme.

Reference

1. Y. B. Li, Y. Bando, D. Golberg, and K. Kurashima, "Field emission from MoO_3 nanobelts," *Appl Phys Lett*, vol. 81, no. 26, pp. 5048–5050, Dec. 2002, doi: 10.1063/1.1532104.
2. S. Deng, D. Ban, N. Xu, J. Chen, J. She, and F. Liu, "Improved field emission characteristics of large-area films of molybdenum trioxide microbelt," *J Nanomater*, vol. 2010, 2010, doi: 10.1155/2010/136860.
3. W. Q. Yang *et al.*, "Fabrication and field emission properties of needle-shaped MoO_3 nanobelts," *J Alloys Compd*, vol. 576, pp. 332–335, 2013, doi: 10.1016/j.jallcom.2013.05.221.
4. J. Zhou, S. Z. Deng, N. S. Xu, J. Chen, and J. C. She, "Synthesis and field-emission properties of aligned MoO_3 nanowires," *Appl Phys Lett*, vol. 83, no. 13, pp. 2653–2655, Sep. 2003, doi: 10.1063/1.1613992.
5. G. Wei *et al.*, "Synthesis and field emission of MoO_3 nanoflowers by a microwave hydrothermal route," *J Alloys Compd*, vol. 481, no. 1–2, pp. 417–421, Jul. 2009, doi: 10.1016/j.jallcom.2009.03.007.
6. A. Mahajan, M. Khan, G. R. Umapathy, M. Jha, and S. Ghosh, "Unraveling the Augmented Field Emission Performance of Molybdenum Disulfide-Praseodymium Sulfide (MoS_2@PrS) Heterostructure: A Combined Experimental and First Principles-Based Study," *Small*, 2408831, Jan. 2024, doi: 10.1002/smll.202408831.

Structural, Magnetic, and Raman Analysis of Strontium-Doped Nickel-Zinc Nano Ferrite

Hanamanta Badiger[1, 2a)] and B.G. Hegde[2]

[1]*Department of Physics, Jain College of Engineering Belagavi-590014, Karnataka, India.*
[2]*Department of Physics, Rani Channamma University Belagavi-591156, Karnataka, India.*

[a)]Corresponding author: hanamantabadiger93@gmail.com

Abstract. Over the past few years, significant advancements have occurred in both technology and scientific understanding within the field of nanomagnetism, particularly in Nickel-based nanoferrites ($NiFe_2O_4$), due to their unique physical and chemical properties. The present study is focused on structural, magnetic and Raman study on Strontium doped Nickel-Zinc Nano Ferrite (NZSFO). For this modified cost effective sol-gel technique is adopted. The structural analysis revealed that the synthesized NZSFO nano particles formed as a single phase and cubic spinel structure with Fd-3m space group. Using Rietveld refinement, the lattice constant and by Debye Scherrer formula, strain and crystallite size were estimated. There is an increase in the lattice constant and decreases in the crystallite size. The M-H hysteresis curve recorded at room temperature using the Vibrating Sample Magnetometer (VSM) technique. The data revealed an increase in saturation magnetization and a decrease in coercivity, indicative of super-magnetic behavior. Raman spectra displayed five Raman modes (A_{1g}, E_g, and $3F_{2g}$), confirming the purity of the samples. These properties make the material suitable for applications such as data storage and magnetic tape recording.

INTRODUCTION

Over the past few years, significant advancements have occurred in both technology and scientific understanding within the field of nanomagnetism, particularly in Nickel-Zinc ferrite ($NiZnFe_2O_4$). It has attracted and considerable attention from researchers due to its remarkable properties in the spinel ferrite family such as high Curie temperature, substantial saturation magnetization, high initial permeability, and low ferromagnetic resonance frequency compared to other ferrite materials. These attributes make $NiZnFe_2O_4$ a promising candidate for various technological applications, such as antibacterial agents, recording heads, storage devices, microwave absorbers, and high-frequency devices [1]. The chemical composition within ferrites can alter and create significant differences in the cation distribution. This distribution depends on several factors, including atomic sizes, valences, and crystal fields [2]. The substitution of divalent or trivalent metal cations into the tetrahedral or octahedral sites can significantly tune the structural and magnetic properties [3]. Many synthesis methods have been adopted to prepare nanocrystalline ferrite, such as sol-gel auto combustion method, co-precipitation method and hydrothermal method. Among these, sol-gel technique is widely employed in producing metal oxides with nanostructures because it has certain advantages such as precise control over shape and size, reproducibility, compatibility with low-temperature chemistry, high surface-to-volume ratio in products, cost-effectiveness and simple experimental setup [4]. The introducing of alkaline earth metals inside the ferrites, which play crucial roles in enhancing the magnetic and electrical properties of various materials through alloying, forming compounds with specific magnetic or dielectric properties, and serving as key components in electronic devices, permanent magnets and magnetic recording media due to its strong magnetic properties [5]. Motivated by these parameters, the present article reports the synthesis of pure phase Sr-doped Nickel-Zinc Nano Ferrite (NZSFO) by sol gel technique. We investigate their structural, magnetic, and Raman properties through various characterization techniques for magnetic storage devices applications.

EXPERIMENTAL PROCEDURE

The sol-gel method was used to synthesize $Ni_{0.5}Zn_{0.5-x}Sr_XFe_2O_4$ (X= 0.0, 0.1 and 0.2) (NZSFO) nano particles. All the precursors were taken from analytical grade. Further, stoichiometric ratio of zinc nitrate, nickel nitrate, ferric nitrate and strontium nitrate were taken into a beaker, containing 50 ml of distilled water, under constant magnetic stirring appropriate amounts of citric acid (metal nitrate to citric acid ratio was 1:1) and 2ml of ethylene glycol were added into solution. Once solution become homogeneous then transferred the beaker to hot plate (80°C). Due to vaporization process the resultant solution turns into brown viscous gel. Further, for removal of excess gel, transfer the beaker into heating mantle and heat it up to 200°C. Under the action of self-ignition, gel

becomes flint ash powder with releasing large amount of NO_2 gas. Grind the obtained powder to achieve smooth, finally sintered it at 200 °C for 5 hours in muffle furnace and cooled into room temperature, dark brown NZSFO nano powder is ready to characterize**.** To verify the phase, we utilize the Rigaku Miniflex 600 X-ray diffractometer with Cu-Kα radiation (wavelength 1.54Å). The diffraction data is collected over the 20° to 80° range with a step size of 0.01°. The Raman spectra were examined by Horiba Scientific model: Xplora plus V1.2 Multiline. The magnetic properties are examined by home built vibrating sample magnetometer (VSM) in the range of 1T to -1T [6].

RESULTS AND DISCUSSIONS

Figure 1 shows the XRD pattern of the synthesized NZSFO nano particles. It clearly indicates that, a pure single phase is obtained and shows cubic structure with Fd-3m space group and well fitted with JCPDS no 22-1086 [4]. As increasing the Sr content into NZSFO, the (311) plane peaks intensities were increased and there is a shifted towards higher angle around 0.07º. This increased intensity and orientation of peak position is due to high ionic radii of Sr ions (1.26 Å), which occupying the Zn (0.74 Å) site that leads a crystal distortion [4]. The crystallite size and micro strain were obtained by Debye Scherrer formula. The results are, crystallite size (nm) (16.94, 16.23 and 11.86) and micro strain (10^{-3}) (0.707, 0.708 and 0.710) with their respective compositions (0.0, 0.1 and 0.2). The lattice parameter is obtained by Rietveld refinement process with the help of Fullprof software. The detailed lattice parameter are (Å) (a = 8.397, 8.409 and 8.419). Additionally, the unit cell structure is obtained as shown in the Figure 2.

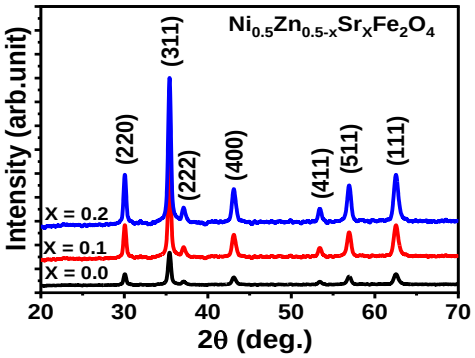


FIGURE 1. XRD Pattern of NZSFO nano particles

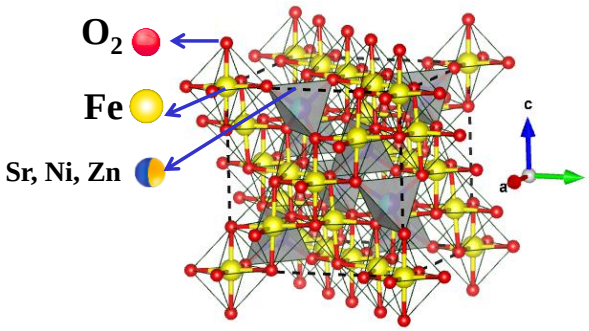


FIGURE 2. Unit cell structure of NZSFO nano particles

The magnetic hysteresis (M-H) loop of NZSFO is depicted in Figure 3, which implies ferromagnetic nature with enhancing of the magnetic saturation values. The magnetic parameters such as saturation magnetization (Ms), remnant magnetization (Mr), coercivity (Hc) and squareness ratio (S = Mr/Ms) values are estimated and these are 34.25, 44.52and 49.66 emu/gm (Ms), 6.40, 8.35, 9.30 emu/gm (Mr), 136.59, 136.33 and 135.06 O'e (Hc) and 0.186, 0.1875, 0.1872 (S) found for respective 0.0, 0.1 and 0.2 composition. The variation of these values is due to interaction between metal cation in the tetrahedral and octahedral position [4]. Additionally these values are predicted because the ionic radius of Sr is greater than Zn as discussed in XRD part. The Raman spectroscopy is utilized to obtain the information about the characteristic of the spinel space group (Fd-3m). Figure 4 represents the Raman spectra image of NZSFO nano particles. There are five optical active Raman mode such as A_{1g}, E_g and $3F_{2g}$, where A, E and F represents the dimension and g indicates the symmetry of the center of inversion [7]. Each corresponding dimension are obtained at particular bands which are at 200-250 $cm^{-1,}$ 290-355 cm^{-1}, 450-500 cm^{-1}, 520-580 $cm^{-1}$and 600-720 cm^{-1} corresponds to $F_{2g}(1)$, Eg, $F_{2g}(2)$, $F_{2g}(3)$ and A_{1g} values respectively [7]. From reported values NZSFO nano particles also shows 200 cm^{-1}, 295 cm^{-1}, 482 cm^{-1}, 577 cm^{-1} and 672 cm^{-1} of respective $F_{2g}(1)$, Eg, $F_{2g}(2)$, $F_{2g}(3)$ and A_{1g} values, that indicates the synthesized NZSFO nano particles is in spinel nature with space group Fd-3m.

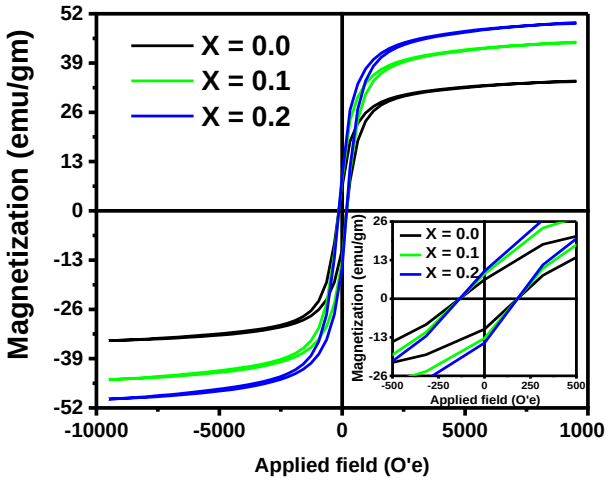


FIGURE 3. MH loop of NZSFO nano particle

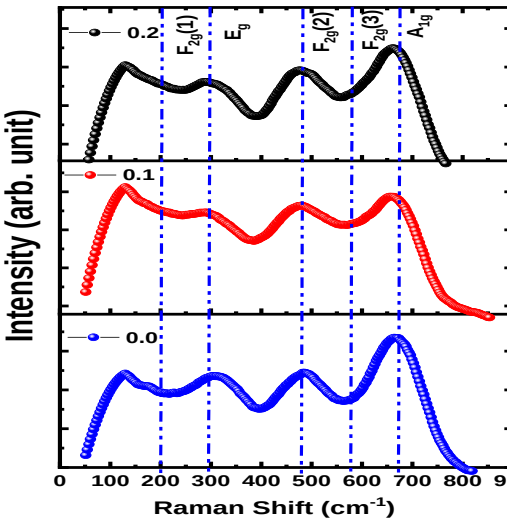


FIGURE 4. Raman spectra of NZSFO nano particle

CONCLUSION

The NZSFO is successfully synthesized by modified cost effective sol-gel technique. The structural analysis revealed that the synthesized NZSFO nano particles formed pure phase and cubic spinel structure with Fd-3m space group. From Rietveld refinement, the lattice constant were estimated and by Debye Scherrer formula, strain, and crystallite size were estimated, there is an increase in the lattice constant and decreases in the crystallite size. The M-H hysteresis curve recorded at room temperature using the Vibrating Sample Magnetometer (VSM) technique. The data revealed an increase in saturation magnetization and a decrease in coercivity, indicative of super-magnetic behavior. Raman spectra displayed five Raman modes (A_{1g}, E_g, and $3F_{2g}$), confirming the purity of the samples. These properties make the material suitable for applications such as data storage and magnetic tape recording.

REFERENCES

1. Babasaheb Ingale, Digambar Nadargi, Jyoti Nadargi, Rangrao Suryawanshi, Hamid Shaikh, Mohammad Asif Alam, Mohaseen S. Tamboli, and Sharad S. Suryavanshi, ACS Omega **8**, 30508−30518 (2023).
2. A. R. Chavan, S. B. Somvanshi, P. P. Khirade, K. M. Jadhav, RSC Adv. **10,** 25143−25154 (2020).
3. V.A. Bharati, Sandeep B, Somvanshi, Ashok V. Humbe, V.D. Murumkar, V.V. Sondur, K.M. Jadhav, Journal of Alloys and Compounds **821,** 153501 (2020).
4. Hanamanta, S. Matteppanavar and Hegde B. G, Journal of Alloys and Compounds **954**, 170031 (2023).
5. V. Jagadeesha Angadi , A.T. Kozakov, A.V. Nicolski, Y.V. Rusalev, Inas A. Ahmed, S.P. Kubrin, and Shifa Wang, Inorganic Chemistry Communications **158**, 111583 (2023).
6. Pratheek, Hanamanta Badiger, Nutan Kumari Sah, Rajeev S Joshi, Subray V Bhat and Balachandra G Hegde, Phys. Scr. **99,** 085932 (2024).
7. Carlos Andrés Palacio Gómez, César Augusto Barrero Meneses, Juan Antonio Jaén, Journal of Magnetism and Magnetic Materials **505**, 166710 (2020).

Chemical Synthesis, Characterization And Magnetic Behavior Of $NiLa_xFe_{2-x}O_4$ ($0 \leq x \leq 0.3$) Nanomaterials

Rajshekhar Balagi[1] and R. N. Panda[1, *]

[1]*Department of Chemistry, Birla Institute of Technology and Science Pilani, K K Birla Goa Campus, Zuarinagar - 403726, Goa, India*

[1,*] *Corresponding author: rnp@goa.bits-pilani.ac.in*

Abstract: By using sol gel autocombustion technique, synthesis of lanthanum (La^{3+}) substituted nickel ferrite nanomaterial ($NiLa_xFe_{2-x}O_4$, $0 \leq x \leq 0.3$) has been achieved. Materials characterization were carried out using powder XRD, FESEM, Raman spectroscopy and magnetic measurements. The materials crystallize in cubic structure having lattice parameters of 8.3269 Å, 8.3288 Å, 8.3340 Å for La content, x = 0.0, 0.1 and 0.3 respectively. The calculated crystallite sizes decrease from 42 nm down to 29 nm for $0 \leq x \leq 0.3$. FESEM studies confirm spherical nature of the particles with particle sizes of 40 nm, 28 nm and 33 nm for x = 0.0, 0.1 and 0.3 in $NiLa_xFe_{2-x}O_4$, respectively. Metal-oxygen bonds in various tetrahedral and octahedral sites were examined by Raman spectroscopic technique. Coercivity, H_c, and saturation magnetization, M_s values can be adjusted as the lanthanum (x) content gradually increases in $NiLa_xFe_{2-x}O_4$.

INTRODUCTION

The development on different methods of $NiFe_2O_4$ nanomaterial synthesis is prevalent owing to their unique magnetic behaviour [1] and technological applications [2] in science. The structural parameters of these nanomaterials can be modified in order to yield a change in their magnetic properties. One of the methods for such an approach includes substituting metal ions into the spinel ferrite structure [3]. Previous studies establish that the addition of dopants have predominant effect on the structure and properties of nickel ferrite nanomaterials [4]. The current work showcases the structural and magnetic behaviour of $NiFe_2O_4$ on substitution with different amount La^{3+} ions in the lattice. The motivation behind La^{3+} ion substitution lies on the fact that being large sized it may induce distortion in the lattice and may change net magnetic moment associated with the materials.

EXPERIMENTAL

Synthesis and Characterization of $NiLa_xFe_{2-x}O_4$ Nanomaterials

Sol gel autocombustion technique was used for synthesis as follows: Dissolution of La_2O_3 using 1 N aq. HNO_3 was carried out beforehand for subsequent use. In brief, aq. La^{3+} solution, nickel ($NiCl_2.6H_2O$) and iron salts ($Fe(NO_3)_3.9H_2O$) were taken in stoichiometric ratios and each dissolved in 50 mL of distilled water. Next, citric acid and 10 mL of 1 N HNO_3 and were added, the total volume of the solution was adjusted to 200 mL. Later, the resulting clear solution was refluxed at 80 ℃ for 2 h and let it cool to room temperature. Finally, the The mixture was subjected to evaporation at 95 ℃ to form a viscous gel and was evaporated to a swollen mass. The dried gel was crushed and subjected to heat treatment at 450 ℃ for 3 h in an air environment in a muffle furnace. The resultant product was ground and then further air-annealed at 700 ℃ for 3 h. $NiLa_xFe_{2-x}O_4$ nanomaterials were characterized using PXRD (Model: Bruker, D8 Advance X-ray diffractometer), FESEM (Model: QUANTA, FEG 250), Raman spectroscopy (LAB RAM HR Horiba France). Magnetic behaviour was studied by using VSM (Model: Quantum Design, PPMS Evercool II).

RESULTS AND DISCUSSION

X-ray Diffraction and FESEM Studies

Fig. 1 ((a)-(c)) represents X – ray diffraction (XRD) patterns of La substituted nickel ferrite nanomaterials, i.e., $NiLa_xFe_{2-x}O_4$ wherein x is 0.0, 0.1, 0.3, annealed at 700 ℃. The studies carried out through XRD confirmed the formation of pure spinel phase product for $NiLa_xFe_{2-x}O_4$ nanomaterials. XRD lines were broad which indicate nanocrystalline nature of the materials. XRD peaks correspond to various lattice planes, namely: (220), (311), (222), (400), (422), (511), (400), (422), (511) and (440) of cubic spinel lattice. The XRD lines were indexed in accordance with the entries of JCPDS card no. # 00-010-0325. For, x = 0.3, XRD pattern of (Fig. 1 (c)) $NiLa_xFe_{2-x}O_4$ shows minor extra peaks, which were identified as La_2O_3 and $LaNiO_3$. In addition, a single

minor peak (denoted as (●)) corresponding to 2θ value of 45.45° could not be identified. The calculated crystallite sizes were found to be 42 nm for x = 0.0, 22 nm for x = 0.1 and 29 nm for x = 0.3 for $NiLa_xFe_{2-x}O_4$ nanomaterials. The calculated lattice parameters exhibit an increasing trend corresponding to the progressive rise in La (x) content, in $NiLa_xFe_{2-x}O_4$, i.e., 8.3269 Å, 8.3288 Å, 8.3340 Å for of x = 0.0, 0.1 and 0.3, respectively (Table 1). The variations of lattice parameters and crystallite sizes indicates structural and magnetic changes in the synthesized nanomaterials. The FESEM micrographs reveal the morphology of the La substituted nickel ferrite ($NiLa_xFe_{2-x}O_4$) as shown in Fig. 2 ((a)-(c)). The micrographs show spherical shaped particles. FESEM particle sizes for $NiLa_xFe_{2-x}O_4$ materials were estimated using ImageJ software and found to be 40 nm, 28 nm and 33 nm for La contents, x = 0.0, 0.1 and 0.3, respectively.

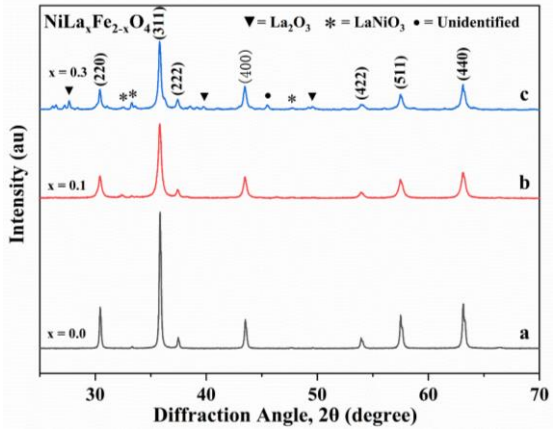


FIGURE 1. XRD patterns for $NiLa_xFe_{2-x}O_4$ nanomaterials with varying values of La content (x); (a) 0.0, (b) 0.1 and (c) 0.3.

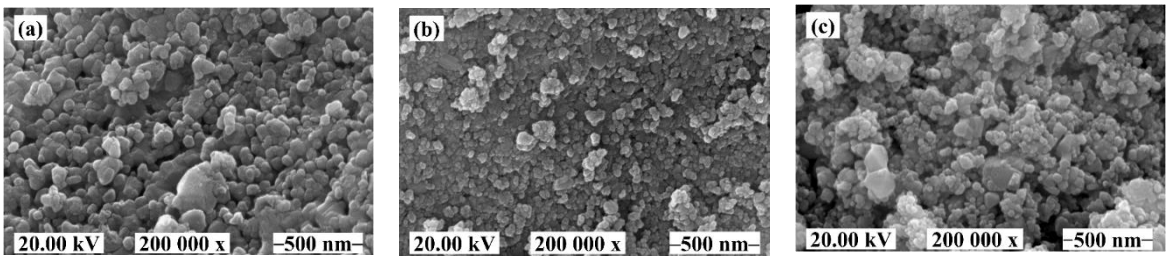


FIGURE 2. FESEM micrographs of $NiLa_xFe_{2-x}O_4$ nanomaterials with various La content (x); (a) 0.0, (b) 0.1 and (c) 0.3.

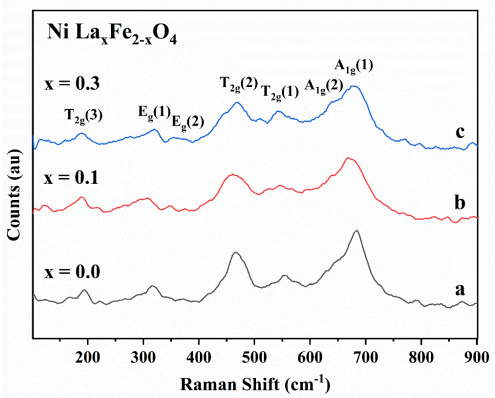


FIGURE 3. Raman spectra of $NiLa_xFe_{2-x}O_4$ with various values of lanthanum content(x); (a) 0.0, (b) 0.1 and (c) 0.3.

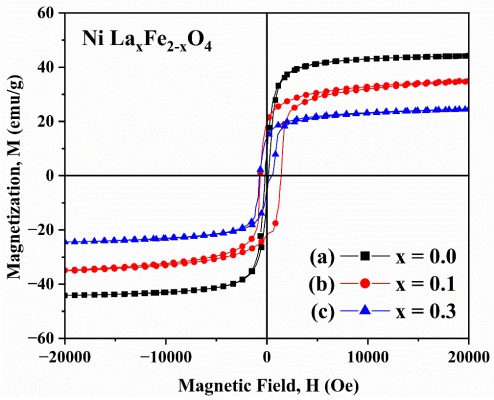


FIGURE 4. Room temperature M vs. H plots of $NiLa_xFe_{2-x}O_4$; (a) x =0.0, (b) x = 0.1 (b) and (c) x = 0.3.

Raman Studies

Fig. 3 depicts the Raman spectra of $NiLa_xFe_{2-x}O_4$ nanomaterials in the range of 900-100 cm^{-1}. A wavelength of 532 nm was used as excitation source in order to study the Raman shift. The Raman modes observed at 680 cm^{-1} and 643 cm^{-1} represent the modes $A_{1g}(1)$ and $A_{1g}(2)$ which are assigned to the symmetric stretching of Fe-O at the tetrahedral site. The Raman mode at 547 cm^{-1} and 464 cm^{-1} represent the $T_{2g}(1)$ and $T_{2g}(2)$ modes

and have been assigned to the asymmetric bending and stretching of Fe(Ni)-O bonds at octahedral sites, respectively. The Raman modes at 361 cm^{-1} and 313 cm^{-1} represent the energy bands $E_g(2)$ and $E_g(1)$, respectively. This can be interpreted as spinel symmetric bending of the Fe(Ni)-O bond. The peak at 192 cm^{-1} represents the Raman mode $T_{2g}(3)$, for the translation motion of the whole tetrahedron [5,6].

Magnetic Studies

Magnetization (M) vs. Magnetic field (H) characteristics of $NiLa_xFe_{2-x}O_4$ materials are shown in Fig. 4 (a), (b) and (c). The observed values for M_s, H_c and remanent magnetization (M_r) are summarized in Table 1. The negligibly small contribution towards M_s value due to the presence of minute quantities of non-magnetic impurities in $NiLa_{0.3}Fe_{1.7}O_4$ is acknowledged. These above mentioned parameters vary as size, shape and composition of the material changes. The values of M_s decrease from 44.69 emu/g down to 25.18 emu/g owing to increase of La content (x) in the $NiLa_xFe_{2-x}O_4$ i.e., from x = 0.0 up to x = 0.3, respectively. Similarly, the H_c values initially decrease from 155 Oe to 128 Oe for x = 0.0 to x = 0.1, respectively, However, when x = 0.3, a higher value of 173 Oe is found. These peculiarities can be attributed to the size effect predominantly (Table 1) [7]. M_r also follows the decreasing trend in $NiLa_xFe_{2-x}O_4$ materials as a result of increasing substitution of La content (x) as mentioned in Table. 1.

TABLE 1. Materials, FESEM particle size, average crystallite sizes, lattice constants, M_s, H_c and M_r of $NiLa_xFe_{2-x}O_4$.

Materials	FESEM particle size (nm)	Average Crystallite size (nm)	Lattice constants (Å)	M_s (emu/g)	H_c (Oe)	M_r (emu/g)
$NiFe_2O_4$	40	42	8.3269	44.69	155	9.33
$NiLa_{0.1}Fe_{1.9}O_4$	28	22	8.3288	36.16	128	8.32
$NiLa_{0.3}Fe_{1.7}O_4$	33	29	8.3340	25.18	173	6.97

CONCLUSION

The successful preparation of La substituted nickel ferrite has been achieved via sol-gel autocombustion method. From the XRD analysis it is clear that the product is in cubic spinel phase. The values of lattice parameters increase from 8.3269 Å to 8.3340 Å for x = 0.0 to x= 0.3 in $NiLa_xFe_{2-x}O_4$ nanomaterials. This result can be a consequence of La content with large atomic size in the $NiLa_xFe_{2-x}O_4$ crystal structure. A significant reduction in crystallite sizes was observed from 42 nm down to 29 nm with the increased La content x from 0.0 up to 0.3, respectively. FESEM studies agree well with the XRD studies. Raman studies confirm the metal-oxygen bonding in various tetrahedral and octahedral environments. The variation in M_s values from 44.69 emu/g to 25.18 emu/g occurs as a result of variation of composition, size and shape of $NiLa_xFe_{2-x}O_4$.

ACKNOWLEDGEMENTS

We acknowledge CSIF, Birla Institute of Technology and Science, Pilani K K Birla Goa Campus for powder XRD, FESEM and Raman spectroscopy measurements. For VSM measurements we thank Dept. of Phys., BITS Pilani K K Birla Goa Campus and DST, Govt. of India for DST FIST grant number SR/FST/PS-I/2017/21. R. Balagi is thankful to Anagha. B. Patil for the helpful discussion during data collection and analysis.

REFERENCES

1. W. E. Pottker, R. Ono, M. A. Cobos, A. Hernando, Jefferson F.D.F. Araujo, Antonio C.O. Bruno, S. A. Lourenço, E. Longo, F. A. La Port, Ceram. Int., Vol. 44, pp. 17290–17297 (2018).
2. K. Kombaiah, J. J. Vijaya, L. J. Kennedy, K. Kaviyarasu, Materials Chem. and Phy., Vol. 221 pp. 11-28 (2019).
3. S. E. Shirsath, B. G. Toksha, and K. M. Jadhav, Mater. Chem. and Phys., Vol. 117, pp. 163–168 (2009).
4. S. Joshi, M. Kumar, H. Pandey, M. Singh, P. Pal, J. Alloys Compd, Vol. 768, pp. 287-297 (2018).
5. O. Jankovský, V. Rach, D. Sedmidubský, S. Huber, P. Ulbrich, M. Svecova, V. Bartunek, J. Alloys Compd, Vol. 723, pp. 58-63 (2017).
6. R. S. Yadav, I. Kuřitka, J. Vilcakova, J. Havlica, J. Masilko, L. Kalina, J. Tkacz, V. Enev, M. Hajdúchová, J. Phys. Chem. Solids, Vol. 107, pp. 150–161 (2017).
7. R. S. Ningthoujam, R. N. Panda, and N. S. Gajbhiye, Mater. Chem. Phys. Vol. 134, pp. 377– 381 (2012).

Optical Characterization of Hydrothermally Synthesized Quantum Dots: Insights and Analysis

Avinash Kumar[1], Ishant Kumar[1, 2)], Sandeep Kumar[1], and Arvind K Gathania[1, *)]

[1]*Department of Physics & Photonics Science, National Institute of Technology Hamirpur, 177005 (H.P.) India*
[2)] *Rabindranath Tagore Government College, Sarkaghat, 175024 (H.P.) India*
[*)] *Corresponding Author: akgathania@nith.ac.in*

Abstract. This study reports the successful fabrication of carbon quantum dots (CQDs) from milk through the hydrothermal technique. No specialized tools or chemicals are required for a straightforward and environmentally safe process. The CQDs were approximately 7 nm in size and exhibited a nearly circular shape upon synthesis. Their primary components included nitrogen, oxygen, and carbon. They display temperature-dependent photoluminescence and broad excitation-emission spectra. They remained pretty stable with their storage time. The selective and sensitive response of luminescence quenching mechanisms makes them suitable for developing a nanosensor to detect Sn^{2+}.

Keywords: Photoluminescence, Hydrothermal, Quantum dots, Quenching, Photostability.

INTRODUCTION

Carbon Quantum Dots (CQDs): nanoparticles with sizes smaller than 10 nm, typically quasi-spherical, possess cores that range from amorphous to nanocrystalline. These dots are formed from graphene and graphene oxide sheets through sp^3 or sp^2 hybridized carbon insertion [1]. Semiconductor quantum dots and Conventional dyes were utilized before the advent of CQDs. Yet, their production involving highly toxic heavy metal ions limits their clinical applicability. This triggers a thorough scrutiny of CQDs. CQDs possess minimal toxicity, are inexpensive to produce, chemically inert, and exhibit fluorescence properties similar to their predecessors. It was by chance in 2004 that CQDs were first identified through the purification of carbon nanotubes [2]. Due to their distinctive characteristics—such as minimal toxicity, bio-friendliness, adjustable fluorescence, hydro solubility, and adaptable surface engineering CQDs have recently attracted considerable attention. They find numerous uses in areas such as medication transport, chemical monitoring, bioimaging, biosensing, nanomedicine, photoactivation, and fluorescent probes.

Employing a hydrothermal process, we produced CQDs from cow milk. CQDs are around 7 nm in size and have a quasi-spherical shape. They demonstrated outstanding photostability and temperature-dependent photoluminescence (PL). Applications for metal ion sensing were also studied. After testing their responsiveness to different metal ions, it was discovered that they were sensitive to Sn^{2+}. They may therefore be used to make a nanoprobe sensor that can detect Sn^{2+}.

MATERIAL AND METHODS

Cow milk, DI, NaOH, Na_2SO_3, H_2O_2, Anhydrous ethanol, Metal salts $SnCl_2{\cdot}2H_2O$, $CdCl_2{\cdot}H_2O$, $ZnCl_2$, KCl, $CaCl_2{\cdot}2H_2O$, NaCl, $FeCl_3$, LiCl, and $HgCl_2$.

In a 50 mL capacity autoclave reactor, 15 mL DI and 19 mL milk were allowed to react (180 °C, 2h). Permit the reactor to chill to ambient conditions. The resulting liquid blend was centrifuged for 30 minutes at 8000 rpm to eliminate any leftover solids. Next, the supernatant underwent a second filtration using a syringe filter (25 mm/0.2 μm).

RESULTS AND DISCUSSION

An assessment of CQDs morphology was done using HR-TEM, FTIR, and XPS. The resulting data are presented in Figure 1. Their shape was nearly spherical, with the average size falling between 7 and 8 nm, as disclosed in Figures 1 (a) and (b). The FTIR and XPS studies, as shown in Figure 1 (c)-(f), indicate that CQDs mainly consist of carbon, nitrogen, and oxygen and possess various related functional groups. These chemical moieties may be contributing to their excellent water solubility and reactivity.

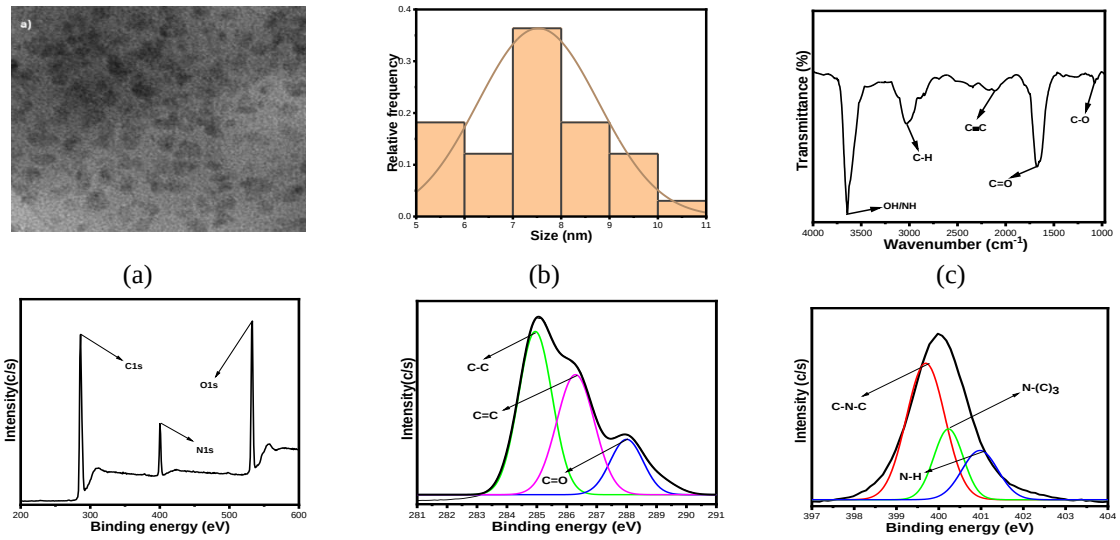


FIGURE 1. (a) HR-TEM, (b) Size, (c) FTIR, (d) XPS data, Deconvolution of (e) C 1*s* and (f) N 1*s*.

In the UV-visible presented in Figure 2 (f), two shoulder peaks were observed at 275 nm and 330 nm. The maximum at 275 nm may be linked to π-π* transitions of the C=C bond, while at 330 nm may be attributed to n-π* transitions of the C=O bond. The estimated CQDs quantum yield is 38%, meaning that CQDs can convert almost 38 % of incident light again into light of different wavelengths. In Figure 2 (a), you can find the PL excitation and emission data of CQDs. In lieu of identifiable absorption and emission peaks, CQDs have broad bands. The PL excitation wavelengths stretch from 390 to 540 nm, with a significant peak observed at 475 nm. The emission range covers 490 to 720 nm, with a peak present at 550 nm. The PL intensity was measured over a temperature range from 27°C to 77°C, with a 5°C increment between each measurement. Figure 2 (b) demonstrates that the intensity decreases as the temperature increases. The intensity reduction could be caused by increased non-radiative return to ground state at elevated temperatures, triggered by thermal activation of non-radiative trapping mechanisms.[3], [4]. Figure 2 (c) depicts the stability of CQDs with their storage time. Throughout the experiment, they were stored for five weeks, with PL intensity recorded each week. No considerable alteration in the PL was detected, pointing to the stability of CQDs. The CQDs created were used as fluorescent indicators to sense metal ions. Ca^{2+}, Fe^{3+}, K^{+}, Cd^{2+}, Na^{+}, Li^{+}, Hg^{2+}, Zn^{2+}, Pb^{2+}, and Sn^{2+}, are introduced into CQDs to examine selectivity. To 500 µL of buffer solution and 100 µL of CQDs, 5mM metal ions were added, and deionized water was used to adjust the final volume to 2.5mL. The PL spectra were recorded at 475 nm. The ratio of PL intensity (F/F_0) for CQDs with different metal ions is illustrated in Figure 2 (d), where (F_0) denotes the PL intensity without metal ions and (F) denotes the intensity with metal ions. The addition of Sn^{2+} was demonstrated to significantly decrease the intensity ratio. This points to a robust interaction of Sn^{2+} with CQDs. This led to CQDs demonstrating pronounced selectivity for Sn^{2+}. Additionally, the sensitivity to Sn^{2+} was examined by exposing CQDs to varying Sn^{2+} concentrations (0–1 mM) and observing the PL responses at 475 nm. As the concentration of Sn^{2+} rose, a decline in PL intensity was observed. This points to CQDs being reactive to Sn^{2+}. This makes the sensor ideal for the detection of Sn^{2+} in various environmental conditions. Based on UV-visible spectra (Figure 2f), the quenching mechanism can be elucidated. Peaks observed at 275 nm and 330 nm correspond to π-π* and n-π* transitions of the C=C and C=O bonds, respectively vanishes upon the addition of Sn^{2+}, suggesting an interaction between CQDs and Sn^{2+}[5]. In addition, the presence of various functional moieties may contribute to the quenching of PL intensity. These groups could enhance non-radiative recombination and metal ion chelation, thereby amplifying the quenching effect.[6].

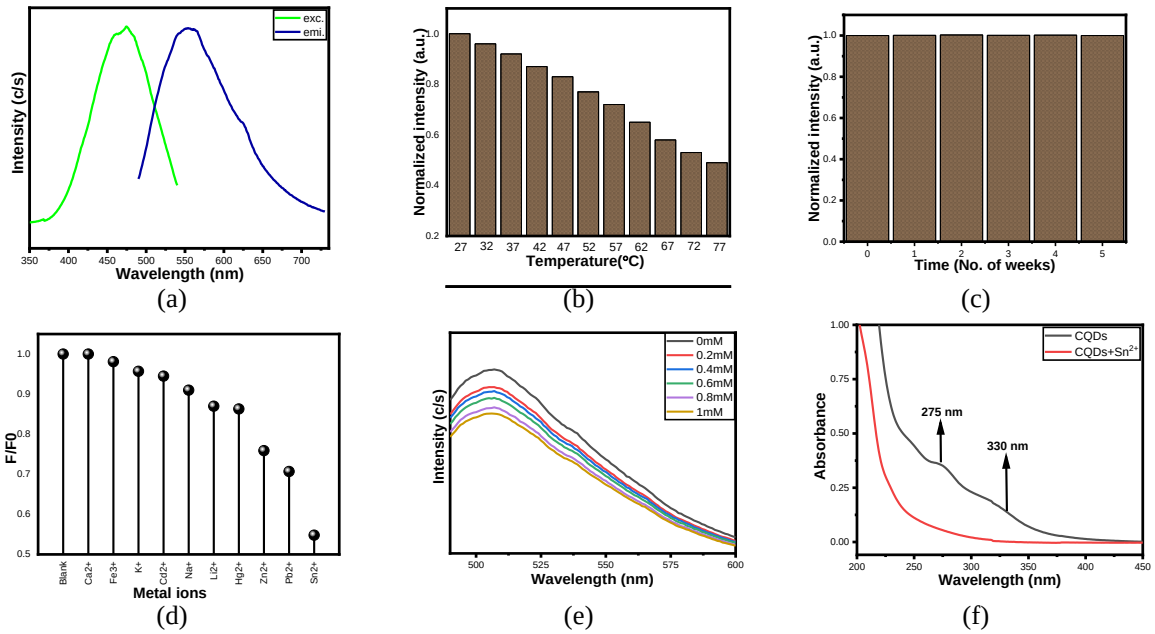


FIGURE 2. (a) Fluorescence excitation, emission spectra, (b) Normalized PL vs temperature, (c) Normalized PL vs storage time, (d) Selectivity of CQDs in different ions, (e) sensitivity towards Sn^{2+} ions, and, (f) UV-Vis data of CQDs and CQDs+Sn^{2+} ions.

CONCLUSIONS

In this work, we synthesized CQDs from cow milk utilizing the hydrothermal technique. The procedure is straightforward and environmentally friendly. This approach yields CQDs with wide excitation and emission spectra and high photostability. It also investigated how temperature influenced PL intensity. They were shown to be stable over lengthy periods of storage. Their high sensitivity and selectivity for Sn^{2+} ions make them suitable for use in the luminescence quenching process for detection. They are an excellent choice for detecting Sn^{2+} in the environment due to their outstanding properties.

ACKNOWLEDGMENT

Mr. Avinash Kumar and Mr. Sandeep Kumar thank UGC, New Delhi, and the Ministry of Education, New Delhi, for awarding the fellowship.

REFERENCE

1. S. Y. Lim, W. Shen, and Z. Gao, *Chemical Society Reviews*, **44**, (2015).
2. Y. Wang and A. Hu, *J Mater Chem C Mater*, **2**, (2014).
3. A. Kumar, I. Kumar, S. Kumar, A. Sharma, and A. K. Gathania, *Phys Scr*, **99**, (2024).
4. A. Kumar, I. Kumar, S. Kumar, and A. K. Gathania, *J Phys Conf Ser*, **2663**, (2023).
5. Y. Guo, L. Zhang, F. Cao, and Y. Leng, *Sci Rep*, **6**, 2016.
6. P. Zhu, Z. Zhu, Z. Li, Y. Xu, L. A. Belfiore, and J. Tang, *Opt Mater (Amst)*, **121**, (2021).

Graphene Nanoplatelets Reinforced Polyvinylidene Fluoride-Hexa-Fluoro Propylene Nanocomposite for Potential Electromagnetic Interference Shielding Applications

Gayathri Thanasekaran[1.], M. Vijayajayanthi[1, *]

[1]*Department of Physics, B.S. Abdur Rahman Crescent Institute of Science and Technology, Chennai,* Tamil Nadu, 600048, India

[*]Corresponding author: vijayajayanthi.cnld@gmail.com

Abstract. Graphene nanoplatelets (GNPs) based polymer nanocomposites establish themselves as an essential material for diverse applications including electromagnetic interference shielding devices. In this work, Polyvinylidene fluoride-hexa-fluoro propylene (PVDF-HFP) based nanocomposites with 10 wt% of GNPs loading were synthesized through solvent casting technique. The electromagnetic interference shielding effectiveness (EMI SE) of GNPs@PVDF-HFP nanocomposites has been investigated in the X-band (8 GHz -12 GHz) and Ku-band (12 GHz -18 GHz) frequency ranges and the obtained values are 16.25 dB and 27.16 dB, respectively. The results of this study suggest that GNPs@PVDF-HFP nanocomposite film could be a promising material for EMI shielding devices.

Keywords: Polymer nanocomposites, GNP, EMISE, X-band, Ku- band.

INTRODUCTION

In recent days, polymer nanocomposites (NCs) have been considered as fascinating materials for electromagnetic interference (EMI) shielding due to their improved properties when compared to the polymer in its pure form. NCs made by infusing nanofillers such as metal/magnetic nanoparticles, metal nanowires, carbon nanotubes, carbon fibers, graphene and its derivatives, MXene, and metal nanosheets have gained popularity in recent years. Adding nanofillers to the polymer matrix improves EMI shielding effectiveness. The excellent properties of nano materials such as high surface area-to-volume ratios, electrical conductivity, magnetic characteristics, low weight, flexibility, thermal stability, mechanical strength, and chemical stability offer superior EMI shielding effect. Furthermore, carbon-based nano materials provide plethora of advantages in diverse areas including efficient EMI shielding **[1]**. The reinforcement of nanofiller into the polymer matrix causes interfacial interaction between them, which enhances the NCs characteristic properties. In general, PVDF is a ferroelectric polymer which is studied extensively due to its remarkable ferroelectric, piezoelectric, pyroelectric, and dielectric properties. The derivative of PVDF namely PVDF-HFP provides flexibility, solubility, thermal and mechanical stability, and dielectric properties. Consequently, PVDF-HFP-based NCs have attracted considerable attention for EMI shielding applications due to their distinctive properties discussed above. **[2]**. Likewise, Graphene nanoplatelets (GNPs) find wide range of applications for instance supercapacitors, energy storage devices, flexible electronics, construction materials, composite materials, and EMI shielding. Also, GNPs have larger aspect ratio when compared to other nanofillers **[3]**. Hence, we synthesize a PVDF-HFP matrix with GNPs through solvent casting technique. This study examines the EMI shielding characteristics and thermal stability of NCs composed of GNPs embedded in a host polymer matrix.

MATERIALS AND EXPERIMENTAL METHODS

PVDF-HFP pellets (molecular weight: 400,000 g/mol) and GNPs in nano powder form (atomic weight: 12.01) were sourced from Sigma-Aldrich, India. The organic solvent N-methyl-2-pyrrolidone (NMP) was obtained from Sisco Research Laboratories India. In the present work, GNPs@PVDF-HFP NCs films were prepared by solvent casting approach. Pellets of PVDF-HFP were added to NMP and heated at 80 °C for 3 h, followed by 1 h of stirring until a clear solution formed. A 10 wt% dispersion of GNPs in NMP was subjected to ultrasonic treatment and mechanical stirring independently for one hour at ambient temperature. Subsequently, the prepared dispersion

was gradually incorporated into the PVDF-HFP polymer solution at controlled intervals. The resulting GNPs@PVDF-HFP mixture was stirred continuously overnight to ensure uniform distribution. Finally, the homogenous solution was transferred into a glass petri dish and subjected to solvent casting by heating at 80 °C for 12 hours in a hot air oven **[4]**. The prepared NCs film was peeled off from the glass petri dish and used for further investigations. Fourier transform infrared (FTIR) spectroscopy was performed on the synthesized GNPs@PVDF-HFP NCs films containing 10 wt% GNPs, covering the wavenumber range of 400–3500 cm^{-1}. X-ray diffraction (XRD) patterns of NCs film with GNPs loadings were investigated in a D8 Bruker XRD analysis was performed using Cu Kα radiation (λ = 1.5406 Å) over a 2θ range of 10°–70°, with a 0.01° step size and a 1°/min scan rate. Thermal properties of the GNPs@PVDF-HFP nanocomposite films were examined using a Labsys EVO TGA 1150 under nitrogen flow, heating at 20 °C/min up to 800 °C. A vector network analyser (Agilent E8363B) was employed to characterize S_{11} and S_{21} parameters in the X- and Ku-band microwave ranges.

EXPERIMENTAL RESULTS AND DISCUSSION

Figure 1(a) presents the FTIR spectra of pure PVDF-HFP and GNPs@PVDF-HFP composites. The characteristic absorption bands of PVDF-HFP indicate the presence of both crystalline and amorphous phases. The crystalline nature of the polymer is evident from the peaks at 610 cm^{-1}, 762 cm^{-1}, and 1070 cm^{-1}, whereas the bands at 835 cm^{-1} and 875 cm^{-1} correspond to the amorphous phase. Additional peaks include the CF_2 wagging vibration at 483 cm^{-1}, deformation vibrations at 1401 cm^{-1}, and asymmetric stretching vibrations of CH_2 and C–F groups at 3025 cm^{-1} and 2981 cm^{-1}, respectively **[2]**. In the GNPs@PVDF-HFP spectra, shifts to lower wavenumbers were observed for the peaks at 483 cm^{-1}, 610 cm^{-1}, and 875 cm^{-1}, which may result from interactions between the GNPs and the PVDF-HFP matrix, possibly due to vibrational coupling. Figure 1(b) reveals the XRD pattern for PVDF-HFP and GNPs@PVDF-HFP. The XRD characteristic peaks of PVDF-HFP at angles 2θ =18.06º and 20.08º representing the (111) and (200) planes of PVDF and the crystalline α phase of VDF. The XRD characteristic peaks of GNPs@PVDF-HFP at angles 2θ = 26.57º and 54.58º correspond to crystalline lamellae of graphite (002) and carbon crystal plane (004), respectively **[5]**. The appearance of diffraction peaks corresponding to the (002) and (004) planes suggest the presence of overlapping graphene nanoplatelets arranged in stacked, continuous layers within the PVDF-HFP matrix **[3]**.

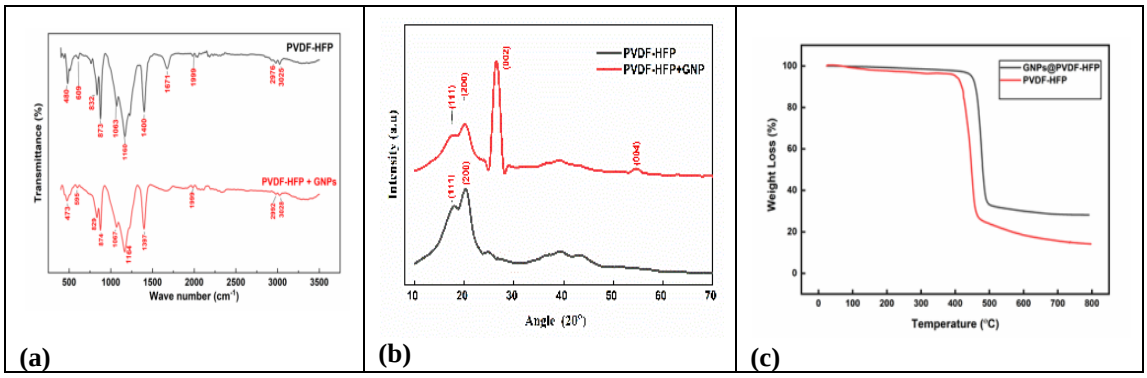


FIGURE 1. (a) FTIR spectra of PVDF-HFP and GNPs@PVDF-HFP (b) XRD patterns of PVDF-HFP and GNPs@PVDF-HFP (c) TGA of GNPs@PVDF-HFP NCs films.

Figure 1(c) presents the TGA thermographs measuring the weight loss as a function of temperature for PVDF-HFP and GNPs@PVDF-HFP. The PVDF-HFP degradation exhibits a minimal weight loss of 4% up to 403 ºC. It reveals that weight loss increases in single-step degradation which occur quickly in the temperature range of 449 ºC to 468 ºC indicating that PVDF-HFP can tolerate temperatures as high as 468 ºC in addition to a 25% weight loss. On addition of GNPs in the polymer matrix, it reveals that the GNPs@PVDF-HFP predominately stable until it attains the temperature range of 441 ºC with the weight loss of 1%. The step wise degradation starts at 452 ºC and ends at 493 ºC with 33% weight loss. The incorporation of GNPs into the PVDF-HFP matrix leads to enhanced thermal stability, as their interaction with the polymer delays the onset of thermal degradation at elevated temperatures **[6]**. The EMI shielding effectiveness (SE) of GNPs@PVDF-HFP in the X- and Ku-bands is shown in Fig. 2(a–b). The SE of GNPs@PVDF-HFP NCs reaches 16.25 dB in the X-band and increases to 27.16 dB in the Ku-band. This reveals that the GNPs in PVDF-HFP matrix increase the conductivity network that leads improved shielding effectiveness. As the contribution from SE_A (SE due to the absorption) is greater than that of SE_R (SE due to the reflection), it is evident that there occurs an absorption-dominant shielding

mechanism inside the GNPs@PVDF-HFP film. The greater shielding values in composite materials are responsible for the enhanced electron carrier transmission in electrically conductive channels.

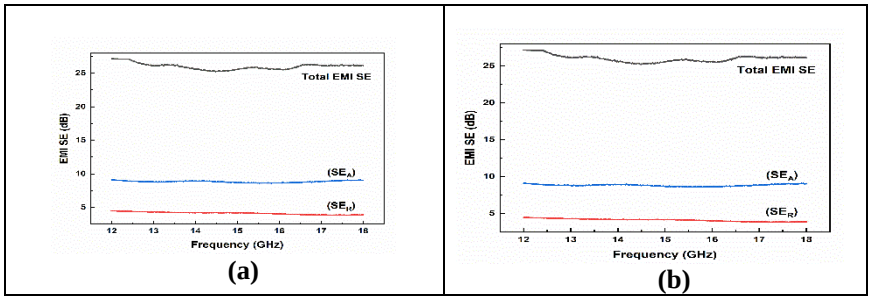


FIGURE 2. (a) EMI shielding results for GNPs@PVDF-HFP in X band (b) EMI shielding results for GNPs@PVDF-HFP in Ku band

CONCLUSION

Polyvinylidene fluoride-hexa-fluoro propylene (PVDF-HFP)-based nanocomposites (NCs) with 10 wt% GNPs loading were synthesized successfully by employing solvent casting technique. FTIR spectroscopy (Fourier-Transform infrared) has been used to investigate the interaction of GNPs within the polymer matrix. The XRD pattern of GNPs@PVDF-HFP NCs indicates uniform GNP dispersion within the PVDF-HFP matrix. Incorporation of 2D nanofillers (GNPs) causes structural changes, reflected by shifts and intensity variations in diffraction peaks, suggesting strong interfacial interactions that affect crystallinity and microstructure. The addition of GNPs increases the conductivity of GNPs@PVDF-HFPNCs resulting in greater shielding effectiveness. Furthemore, the study on shielding absorption in X band (9.33 dB) / Ku band (8.87 dB) and reflection shielding in X band (3.45 dB) / Ku band (4.23 dB) reveals that GNPs@PVDF-HFP NCs have high absorption shielding effectiveness. These findings indicate that GNPs@PVDF-HFP polymer NCs films could be a promising material for EMI shielding devices.

ACKNOWLEDGEMENT

GT would like to thank the management of B S Abdur Rahman Crescent Institute of Science and Technology for providing JRF to carry out this research work.

REFERENCES

1. L. Omana, A. Chandran, R.E. John, R. Wilson, K.C. George, N.V. Unnikrishnan, S.S. Varghese, G. George, S.M. Simon, and I. Paul, ACS Omega **7(30)**, 25921–25947 (2022).
2. Shalu, S.K. Chaurasia, R.K. Singh, and S. Chandra, J. Phy. Chem. B **117(3)**, 897–906 (2013).
3. Thanasekaran, Gayathri, M. Basheer Ahamed, Kalim Deshmukh, and Subramanian Venkatachalam. J. Appl. Polym. Sci.**140**, **45,** e54658 (2023).
4. Thanasekaran, Gayathri, and M. Vijayajayanthi. In International Conference on Emerging Multifunctional Materials and Devices for Sustainable Technologies, IEMDST 2024 pp. 52-60. Springer, Singapore, 2025.
5. Tushar Borkar, H. Mohseni, J. Hwang, T.W. Scharf, J.S. Tiley, S.H. Hong, and R. Banerjee, J. Alloys. Compd. **646**, 135–144 (2015).
6. Kim, Hyelim, and Sunhee Lee. Polym. **11**, (2019).

Influence of Electrolyte in enhancing the electrochemical performance of polyaniline-based electrodes for supercapacitor

Amisha[1], Aman Deep Acharya[1, a)], Yugesh Singh Thakur[1]

[1]Department of Physics, Lovely Professional University, Phagwara, 144411 Punjab, India

[a)] Corresponding author: acharyaphysics2011@gmail.com

Abstract

In this work, PANI nanofibers have been synthesized through the oxidative polymerization method and the effect of HCl doping on their electrochemical properties has been explored. In order to investigate the morphological and structural characteristics of the nanofibers, field emission scanning electron microscopy and X-ray diffraction were used. Galvanostatic charge-discharge and cyclic voltammetry techniques were used to evaluate the electrochemical characteristics. The cyclic voltammetry (CV) and galvanostatic charge-discharge (GCD) analysis reveals that PANI doped with 1M HCl had the highest specific capacitance 238.05 F/g and 256.25 F/g, respectively, in a 6M KOH aqueous electrolyte.

Keywords. Supercapacitor, Nanoparticles, PANI, Electrolyte, Dopant, Polymer.

1. Introduction

Conducting polymers are increasing their interest in energy storage and conversion applications like solar cells, fuel cells, batteries and supercapacitors [1]. Among all the conducting polymers polyaniline attracts lots of attention due to its moderate stability, high conductivity, low production cost, and easy synthesis [2]. Various methods have been used to synthesize PANI nanoparticles including template-assisted polymerization, seeding polymerization, interfacial polymerization, and oxidative polymerization [3]. Oxidative polymerization attracts significant interest among polymerization methods due to its cost-effectiveness, environmental friendliness, control over polymer structure, and high yield. Polyaniline has captivating electrochemical properties which makes it appropriate for various practical applications. The components of supercapacitors include electrodes, separators, current collectors, and electrolytes. Electrolyte is an essential component of supercapacitors which has a considerable impact on the electrochemical characteristics of supercapacitors [4]. Literature witnessed less exposure on how the electrochemical performance of the PANI-based electrode is affected by the ionic strength and acidity of the aqueous electrolytes [5]. The present study concentrates on the influence of acid doping concentration on polyaniline and studies their electrochemical properties in aqueous electrolyte. The different concentrations of hydrochloric acid were prepared to carry out the doping procedure on polyaniline [6].

2. Materials and method

2.1 Chemicals

For the synthesis of undoped polyaniline (PANI) and polyaniline-hydrochloric acid (PANI-HCl) anilinium hydrochloride, ammonium persulfate ($(NH_4)_2S_2O_8$), hydrochloric acid (HCl) and ethanol were brought from LOBA Chemie. All the solutions were prepared in distilled water.

2.2 Synthesis of PANI and PANI-HCl

The procedure for the preparation of PANI is briefly described below. Anilinium hydrochloride monomers and ammonium persulphate (APS) were dissolved separately in 100 ml distilled water. After preparing the above solution separately, then mix the APS solution in the anilinium hydrochloride dropwise with continuous stirring for 3 h at 0 to 5℃ to initiate polymerization. Finally, the bluish-green precipitates of undoped PANI were collected and washed numerous times through distilled water and ethanol which was dried at 70 ℃ in a vacuum oven for 12 h.

Similarly, by using the above procedure PANI-HCl was prepared by adding 1 M and 2 M hydrochloric acid (HCl) as a dopant in the anilinium hydrochloride monomer.

2.3 Characterization

Bruker Instrument Germany obtained the XRD pattern of the prepared samples. To examine the structure of the developed samples, FESEM is used. Moreover, the electrochemical characteristics of the developed electrodes are done at the electrochemical workstation (metrohm).

3. Results and discussion

3.1 XRD analysis

Figure 1, shows the diffraction patterns of undoped PANI, PANI-1 M HCl, and PANI-2 M HCl nanoparticles. The plane corresponds to (121), (113), and (322) shows high–intensity reflections at angle 2□ = 15°, 20.7° and 25.2°. From Figure 1, it's been observed that undoped PANI shows broad or low-intensity peaks. But, when 1 M and 2 M hydrochloric acid are added as dopants it exhibits narrower or high-intensity peaks compared to the undoped PANI. The prepared doped polyaniline

nanofibers show partial crystallinity, it is due to amine and imine groups due to which stronger intermolecular and intramolecular hydrogen bonds are formed [7].

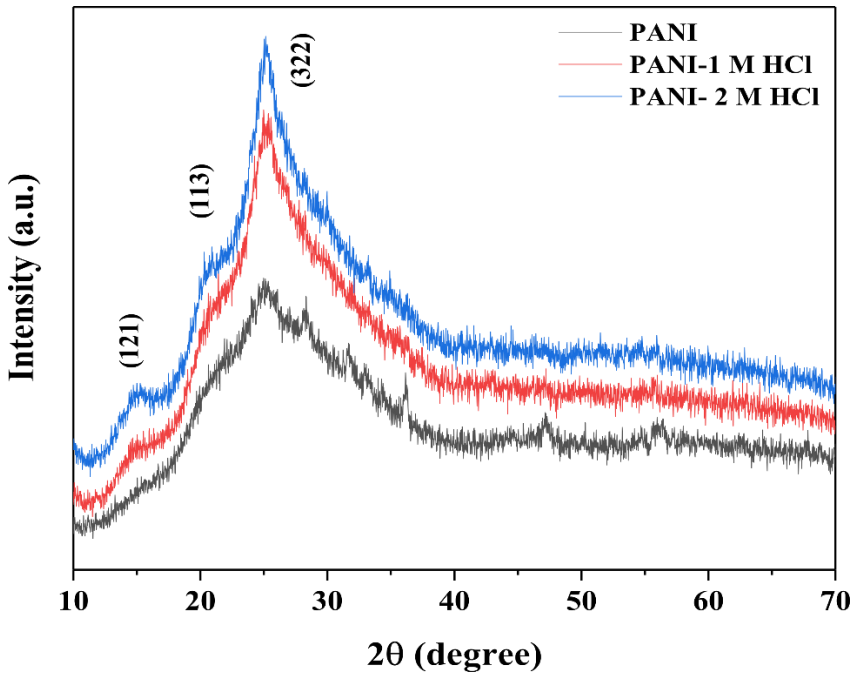


FIGURE 1. XRD diffraction pattern of PANI, PANI- 1 M HCl and PANI- 2 M HCl nanoparticles.

3.2 FESEM analysis

The surface morphology of the prepared polyaniline nanoparticles with or without dopant was analyzed with the help of FESEM as seen in Figure 2(A-C). It has been detected that the undoped PANI nanoparticles exhibit unclear morphology (see Figure 2(A). But when different concentration such as 1M and 2M of hydrochloric acid is added as a dopant the unclear morphology of PANI nanoparticles changes into randomly oriented nanofibers. Moreover, from Figure 2(C) it is seen that as the concentration of HCl increased from 1 M to 2 M, nanofiber starts to show aggregation growth due to the nucleation process.

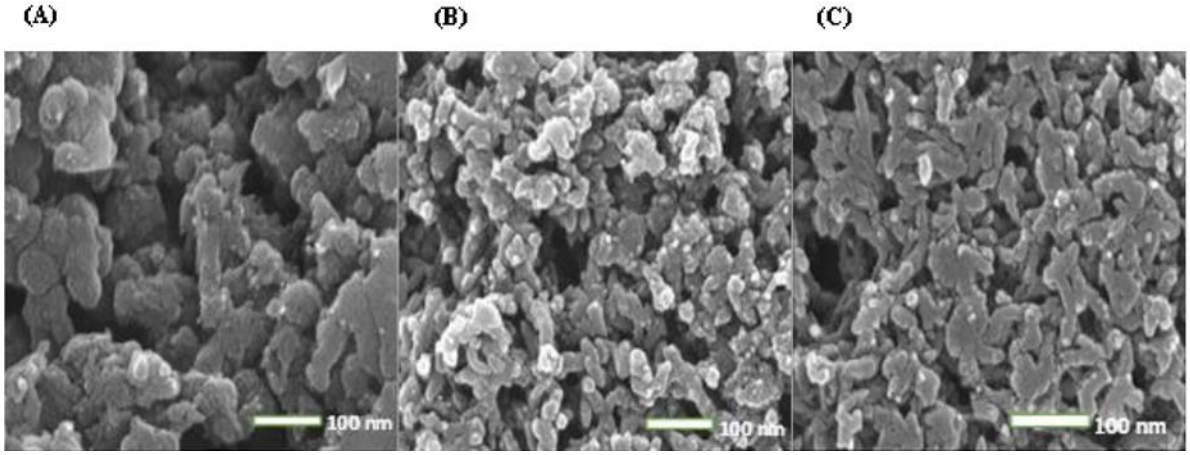


FIGURE 2. (A-C) represents the FESEM images of undoped PANI, PANI- 1 M HCl, and PANI- 2 M HCl nanoparticles.

3.3 CV analysis

A comparative study of the prepared samples is carried out by using cyclic voltammetry in a suitable potential window 0 to 0.6 V (see Figure 3A). The CV curves of PANI doped with different concentrations of hydrochloric acid and undoped PANI electrodes were analyzed in 6 M KOH at 40 mVs^{-1} scan rate. To calculate the specific capacitance of the prepared electrodes the following equation is used [2].

$$C_s = \frac{A}{2mVdv} \quad (1)$$

where, specific capacitance is represented by C_s, the area under the curve is denoted by A, m is the active mass of the electrode, scan rate is represented by v and dv denotes the potential window. The specific capacitance of undoped PANI, PANI- 1 M

HCl, and PANI- 2 M HCl are 179.67, 238.05, and 71.35 Fg^{-1} respectively. As the concentration of HCl increases, the area under the curve decreases, leading to a significant drop in the specific capacitance of PANI in 2 M HCl.

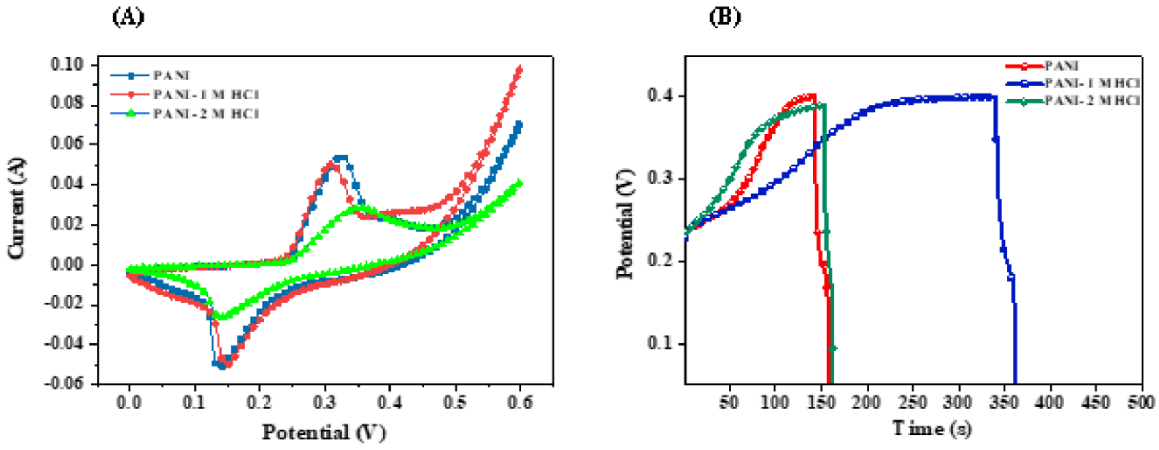


FIGURE 3. (A) CV curve of undoped PANI, PANI- 1 M HCl and PANI- 2 M HCl at 40 mVs^{-1} scan rate in 6 M KOH. (B) GCD curve of undoped PANI, PANI- 1 M HCl and PANI- 2 M HCl at 1 Ag^{-1}.

3.4 GCD analysis

At a current density of 1 Ag^{-1} and a potential window of 0 to 0.4 V, the constant current galvanostatic charge-discharge curve of all the produced PANI nanoparticles, with or without dopant, is shown in Figure 3(B). By using the equation, the specific capacitance is determined [8].

$$Csp = \frac{i \times \Delta t}{m \times V} \quad (2)$$

Δt represents the discharging time, i represents the current density, m is the mass loading, and potential window is denoted by V. The specific capacitance is 182.5, 256.25, and 113.75 Fg^{-1} for undoped PANI, PANI-1 M HCl and PANI-2 M HCl respectively. The electrochemical analysis shows that PANI- 1 M HCl provides the highest specific capacitance in 6 M KOH compared to undoped PANI and PANI-2 M HCl.

Conclusion

The oxidative polymerization method was utilized in this work to produce undoped and HCl-doped PANI. An increase in crystallinity was observed in HCl-doped PANI, as demonstrated by XRD, whereas developed nanofibers was observed by FESEM. The electrochemical investigation shows that 1 M HCl-doped PANI exhibited the maximum specific capacitance in 6 M KOH.

Acknowledgment

The authors acknowledge the Lovely Professional University (LPU) for their continuous support in order to carry out the experimental work and appreciate the financial support provided by the University Grant Commission (UGC).

References

1. Y. Shen, Z. Qin, T. Li, F. Zeng, Y. Chen, and N. Liu, *Electrochimica Acta*, Vol. 356, pp. 136841 (2020).
2. Q. Wang, J. Li, D. Wang, J. Niu, P. Du, J. Liu, and P. Liu, *Electrochimica Acta*, Vol. 349, pp. 136348 (2020).
3. R. S. Diggikar, S. P. Deshmukh, T. S. Thopate, and S. R. Kshirsagar, *ACS Omega*, Vol. 4, No. 3, pp. 5741–5749 (2019).
4. H. Zhu, S. Peng, and W. Jiang, *The Scientific World Journal*, Vol. 2013, No. 1, pp. 940153 (2013).
5. M. Z. Iqbal, S. Zakar, and S. S. Haider, *Journal of Electroanalytical Chemistry*, Vol. 858, pp. 113793 (2020).
6. N. I. A. M. Najib and S. A. Othman, *Journal of Science and Technology*, Vol. 14, No. 2, pp. 1-7 (2022).
7. T. S. Najim and A. J. Salim, *Arabian Journal of Chemistry*, Vol. 10, pp. S3459-S3467 (2017).
8. Y. S. Thakur, A. D. Acharya, S. Sharma, and S. Bisoyi, *Results in Chemistry*, Vol. 7, pp. 101259 (2024).

Impact of Site-selective Carbon Doping in Tuning the Spectral Features of Triangular-shaped Boron Nitride Quantum Dots

Aathira Haridas[1], Tushima Basak[2,*] and Tista Basak[1,*]

[1]*Mukesh Patel School of Technology Management and Engineering, SVKM's NMIMS University, Vile Parle (W), Mumbai 400056, India.*
[2]*SVKM's Mithibai College of Arts, Chauhan Institute of Science and Amrutben Jivanlal College of Commerce and Economics (Autonomous), Vile Parle (W), Mumbai 400056, India.*

[*] Corresponding author: *tista.basak@nmims.edu*
[*] Corresponding author: *Tushima.Basak@mithibai.ac.in*

Abstract. The crucial impact of site-specific carbon doping on the electronic and optical characteristics of triangular-shaped boron nitride quantum dots having armchair and zigzag terminations (ATBNQD and ZTBNQD) are explored in-depth, within the framework of density functional theory and time-dependent density functional theory. The doping of carbon at the edge of ATBNQD opens the electronic bandgap substantially as compared to its location at the centre of the quantum dot. The computed absorption profile confirm that the site-selective C-doping is more instrumental in dictating the energy of the first/highest-intensity peak in armchair/zigzag-edged triangular-shaped boron nitride quantum dots, opening up new frontiers in designing tunable futuristic devices.

Keywords: Boron nitride quantum dots, dopants, electronic properties, optical properties, time-dependent density functional theory.

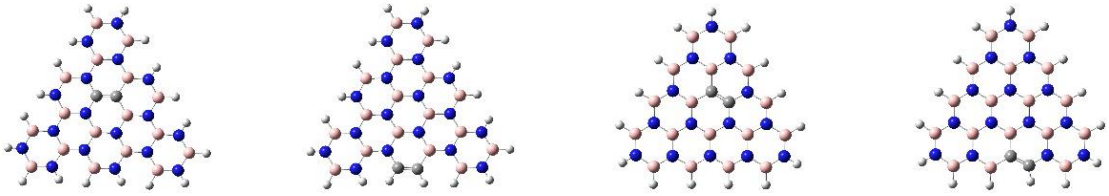
INTRODUCTION

Recently, 2D materials such as hexagonal boron nitride (hBN) exhibiting exceptional electronic and optical properties have sparked interest in scientists due to their immense applications in the field of optoelectronics [1-4]. However, the wide bandgap of the hBN monolayer significantly limits the transfer of electrons within the material [5]. This constraint can be mitigated by reducing the dimensionality of 2D hBN to 0D boron nitride quantum dots (BNQDs) [6]. The optical properties of BNQDs can be efficiently enhanced by engineering its size, shape, edge termination or introducing heteroatom dopants [7,8]. Amongst all the heteroatom dopants incorporated in BNQDs till date, carbon atom is the most preferred doping element as it accelerates the charge separation and transfer processes, which enhances the efficiency of light absorption, photoluminescence emission, energy conversion, etc. [9].

Earlier theoretical studies have revealed that C-doping introduces new acceptor states in the bandgap leading to the appearance of additional absorption peaks [9]. Also, varying concentration of carbon atoms regulates the bandgap of C-doped square-shaped BNQDs [10]. However, comprehensive studies to investigate the modulation of optical properties due to variation in the doping sites of the C-atoms in armchair and zigzag-terminated BNQDs have not yet been done. This has motivated us to explore the implication of site-specific C-doping on the optical properties related to armchair and zigzag-edged triangular shaped BNQD (ATBNQD and ZTBNQD, respectively).

METHODOLOGY AND GEOMETRICAL CONFIGURATIONS

The optimized ground-state geometries of C-doped TBNQDs are derived at density functional theory (DFT) level by applying the hybrid B3LYP functional and the 6-31G(d,p) basis set [11] as integrated in ORCA [12].



(a) (b) (c) (d)

FIGURE 1. *Portrayal of optimized ground state geometries: (a) C_C-ATBNQD, (b) C_E-ATBNQD, (c) C_C-ZTBNQD, (d) C_E-ZTBNQD systems. The blue, pink, grey and white represents N, B, C and H atoms respectively.*

The optimized geometries of hydrogen passivated triangular-shaped BNQDs (TBNQDs) having (i) armchair-edge

termination with C-dopant at centre (C_C-ATBNQD), (ii) armchair-edge termination with C-dopant at edge (C_E-ATBNQD), (iii) zigzag-edge termination with C-impurity at centre (C_C-ZTBNQD), (iv) zigzag-edge termination with C-impurity at edge (C_E-ZTBNQD), are depicted in Fig. 1 (a-d). For these geometrical configurations, the bond lengths between B-N atoms, C-C atoms, C-B atoms, and C-N atoms differ between (1.41-1.48) Å, (1.35-1.37) Å, (1.51-1.54) Å and (1.39-1.42) Å, respectively and the corresponding bond angles for all quantum dots lies in the range of 117°-125°. The optical properties of all these QDs are eventually determined by executing time-dependent density functional theory (TDDFT) with B3LYP/6-31G(d,p) for 40 excited states.

RESULTS AND DISCUSSIONS

In this paper we first evaluate the bandgap separating the highest-occupied molecular orbital (HOMO) and lowest-unoccupied molecular orbital (LUMO) of C-doped TBNQDs. Further, we analyze the modification in optical properties attributed to site-specific alteration of the C-dopant in the quantum dots.

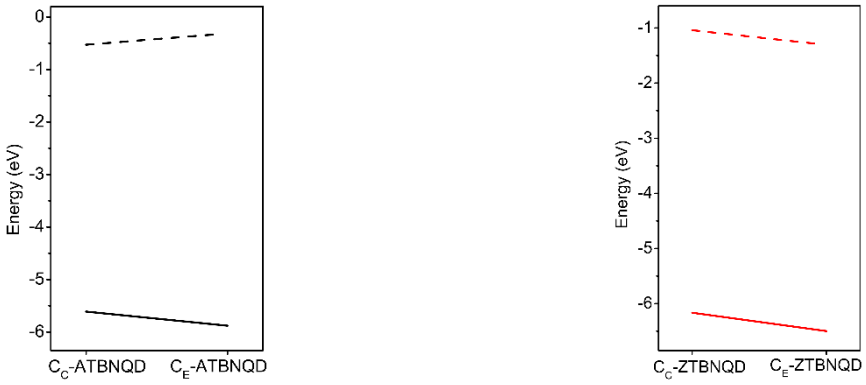
Variation in bandgap

Table 1 lists the energy gap between the HOMO-LUMO of C_C-ATBNQD, C_E-ATBNQD, C_C-ZTBNQD and C_E-ZTBNQD systems. The variation in the location of the carbon-impurity from centre to edge of zigzag-terminated TBNQDs (C_C-ZTBNQD and C_E-ZTBNQD) has no effect in modulating the electronic bandgap. This trend is in stark contrast to the substantial increase in bandgap as the position of the C-dopant is changed from centre to the edge of ATBNQD. A comparison of the bandgaps for all the configuration reveal that the magnitude of the bandgap is maximum for C_E-ATBNQD.

TABLE 1. *HOMO-LUMO gap of carbon doped TBNQDs having armchair and zigzag edge.*

System	HOMO-LUMO gap (eV)
C_C-ATBNQD	5.08
C_E-ATBNQD	5.57
C_C-ZTBNQD	5.12
C_E-ZTBNQD	5.19

In order to scrutinize the parameters influencing the variation in the electronic bandgap, the shift in the energies of the frontier molecular orbitals (HOMO and LUMO) due to change in the location of the carbon atoms from centre to edge of ATBNQD and ZTBNQD are depicted in Fig. 2.



(a) (b)

FIGURE 2. *Energy variation of HOMO, LUMO and HOMO – LUMO gap for carbon doped TBNQDs having armchair and zigzag terminated edges. The solid and dashed lines illustrate the HOMO and LUMO levels respectively.*

A critical assessment of the HOMO-LUMO plots reveals that the energy of the HOMO/LUMO level of C_C-ATBNQD is higher/lower in comparison to its energy in C_E-ATBNQD configuration, implying that the hybridization of the frontier molecular orbitals decreases as the position of the C-atom is varied from the centre to the edge of the TBNQD. However, when the atomic arrangement of the quantum dot is altered from C_C-ZTBNQD to C_E-ZTBNQD, the energies pertaining to both the HOMO and LUMO levels decreases uniformly, indicating a decreased/increased hybridization of HOMO/LUMO states. This highlights that effective bandgap tuning can be achieved by site-specific C-doping.

Variation in optical properties

We now investigate the role of C-doping at different sites of the armchair and zigzag-terminated TBNQD in governing the optical spectral features computed by adopting TDDFT approach.

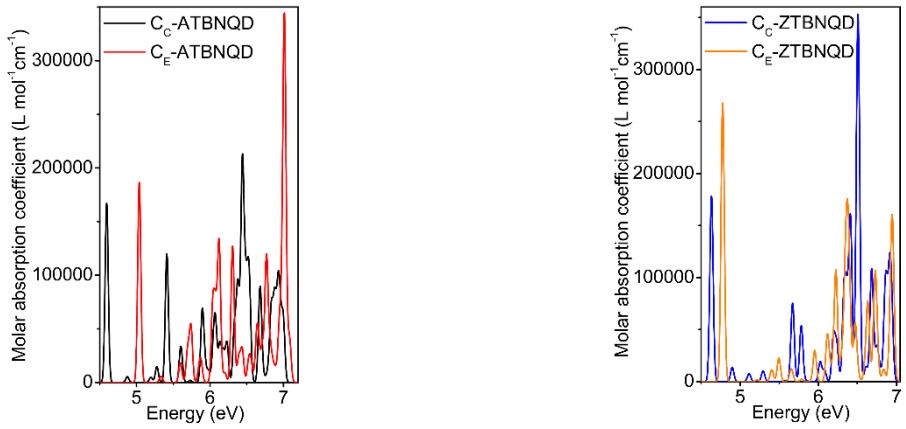


FIGURE 3. *Computed UV spectra of carbon doped TBNQDs with armchair and zigzag terminated edges.*

The remarkable characteristics observed from Fig. 3 are outlined as follows: (i) The first peak is significantly blue shifted when the C-impurity atom is shifted from the centre to the edge for both ATBNQD and ZTBNQD. However, the magnitude of this blue-shift is more conspicuous for ATBNQD in relation to ZTBNQD. (ii) The highest-intensity (HI) peak is blue/red-shifted for ATBNQD/ZTBNQD as the location of the C-dopant is altered from centre to edge of the quantum dots. However, the magnitude of this red-shift in ZTBNQD is more pronounced than the blue-shift in ATBNQD. In particular, the HI peak is the first optical peak for C_E-ZTBNQD while it is located at higher energies for C_C-ZTBNQD. This signifies that site-selective C-doping is more instrumental in tailoring the energy of the first/HI peak in ATBNQD/ZTBNQD.

CONCLUSION

In this paper, we determine the significance of site-selective carbon doping on the electronic bandgap and optical properties of the armchair and zigzag-terminated triangular-shaped boron nitride quantum dots by TDDFT methodology. Our computations highlight that the electronic band gap can be precisely modulated by changing the position of the C-atom in armchair-edged quantum dots. A critical evaluation of the spectral features of these systems reveals that C-doping at specific sites is highly effective in tailoring the energy of the first/highest-intensity peak in armchair/zigzag-edged triangular-shaped boron nitride quantum dots. Our findings emphasize the decisive role of site-selective C-doped triangular-shaped boron nitride quantum dots in the fabrication of futuristic optoelectronic devices.

REFERENCES

1. A. Gottscholl, M. Diez, V. Soltamov, C. Kasper, A. Sperlich, M. Kianinia, C. Bradac, I. Aharonovich and V. Dyakonov, Sci. Adv., Vol. 7, pp. eabf3630 (2021).
2. C. Bradac, Front. Phys., Vol. 9, pp. 641341 (2021).
3. Y. Sheng, J. Yang, F. Wang, L. Liu, H. Liu, C. Yan and Z. Guo, Appl. Surf. Sci., Vol. 465, pp. 154-163 (2019).
4. C. Zhou, C. Lai, C. Zhang, G. Zeng, D. Huang, M. Cheng, L. Hu, W. Xiong, M. Chen, J. Wang, Y. Yang and L. Jiang, Appl. Catal. B: Environ., Vol. 238, pp. 6-18 (2018).
5. H. Ouyang, W. Li and Y. Long, Electrochim. Acta., Vol. 369, pp. 137682 (2021).
6. P. Cui and J. Zhang, Catal. Commun., Vol. 174, pp. 106590 (2023).
7. T. K. Sahu, M. K. Mohanta and M. Qureshi, J. Power Sources, Vol. 445, pp. 227341 (2020).
8. S. Angizi, S. A. A. Alem, M. H. Azar, F. Shayeganfar, M. I. Manning, A. Hatamie, A. Pakdel and A. Simchi, Prog. Mater. Sci., Vol. 124, pp. 100884 (2022).
9. P. Cui and Y. Xue, FlatChem, Vol. 44, pp. 100625 (2024).
10. H. Abdelsalam, W. Osman, O. H. Abd-Elkader and Q. Zhang, Chem. Phys. Lett., Vol. 806, pp. 140025 (2022).
11. T. Basak, T. Basak and V. Roondhe, Mater. Today Commun., Vol. 39, pp. 109270 (2024).
12. F. Neese, F. Wennmohs, U. Becker and C. Riplinger, *J. Chem. Phys., Vol.* 152, pp. 224108 (2020).

Synergistic Electrochemical Performance of MoSSe@$CoMoO_4$ Composite as Advanced Supercapacitor Electrodes

Poonam Lakhiwal[1] and Santosh Kumar Mahapatra[1, a]

[1]*Department of Physics, Central University of Punjab, Bathinda*
[a)]Corresponding author: sk.mahapatra@cup.edu.in

Abstract. Supercapacitors are a potential way to meet the world's energy needs going forward. We have created a Mo-based dichalcogenide called molybdenum sulfoselenide (MoSSe) as a bifunctional electrode material for supercapacitors. Additionally, the electrically conducting active edge sites of MoSSe (MoSSe@$CoMoO_4$) have changed due to the integration of $CoMoO_4$ nanorods. The MoSSe@$CoMoO_4$ symmetric cell has a specific capacity of 127.75 Fg^{-1} at 1 Ag^{-1}, an energy density of 25.55 Wh kg^{-1}, and a power density of 600 W kg^{-1}, respectively. The results show how the proposed hydrothermally assisted synthesis can create high-performing energy storage devices.

INTRODUCTION

Energy is becoming more and more necessary for development. A constrained supply of fossil fuels favors renewable energy sources. Supercapacitors offer long-lasting, high-power density, quick charge/discharge, and environmental friendliness. Carbon, transition metal oxides, and 2D-TMDs are essential electrode materials that improve supercapacitor efficiency. The introduction of Se or S vacancies improves TMD conductivity. MoS_2's Se atoms improve charge transport by increasing edge active sites. Hydrothermal Se substitution in MoS_2 in supercapacitors still needs to be fully understood. The compound $CoMoO_4$ has garnered interest lately because of its widespread availability, cost-effectiveness, and reliable redox properties. $CoMoO_4$ exhibits strong rate capabilities while having a reduced capacitance. We produced sulfur-incorporated molybdenum selenide (MoSSe) using a one-pot hydrothermal synthesis. $CoMoO_4$ was integrated into TMD composites to explore synergistic electrochemical properties for supercapacitors. This work uses the solvothermal method and the hydrothermal approach to create the MoSSe@$CoMoO_4$ heterostructure. The produced heterostructure's electrochemical performance was then evaluated in symmetric quasi-solid-state configurations. The MoSSe@$CoMoO_4$ heterostructure exhibits a specific capacitance of 127.75 Fg^{-1} at a scan rate of 1 Ag^{-1}. MoSSe@$CoMoO_4$ has remarkable electrochemical performance, which may be explained by its two active redox sites, strong conductivity, and easily accessible ion and electron transport channels. MoSSe@$CoMoO_4$ has been shown to have an energy density of 25.55 Wh kg^{-1} and a power density of 600 W kg^{-1}.

EXPERIMENTAL SECTION

Materials

Cobalt molybdate hexahydrate ($Co(NO_3)_2 \cdot 6H_2O$) and sodium molybdate dihydrate ($Na_2MoO_4 \cdot 2H_2O$) (≥99.5% purity) were acquired from Sigma Aldrich. Thiourea (CH_4N_2S), selenium black (99% purity), hydrazine hydrate ($N_2H_4 \cdot H2O$) (85% purity), PVDF, and NMP were purchased from Loba Chemie, India. Furthermore, double-distilled (DD) water was utilized in both the synthesis of various transition metal dichalcogenides (TMDs) and in the electrochemical studies conducted.

Synthesis of $CoMoO_4$ nanorods

To synthesize $CoMoO_4$ nanorods by our facile scheme, 2.5mmol of $Co(NO_3).6H_2O$ and 2.5mmol of $Na_2MoO_4.2H_2O$ were each prepared in 25 ml of DI water [1]. Both solutions were mixed and sonicated, then transferred to 80 ml Teflon-lined autoclave and heated at 150°C for 6 hours. After cooling to room temperature, the precipitates were washed with DI water and ethanol, dried under vacuum at 60°C for 12 hours, and heat-treated at 400°C for 2 hours with a heating rate of 6°C per minute. The resulting samples were cooled to room temperature.

Synthesis of MoSSe@$CoMoO_4$

A MoSSe@$CoMoO_4$ composite was prepared via a hydrothermal synthesis route. Initially, 20 mg of $CoMoO_4$ nanorods were dispersed in a solution containing 1 mmol of sodium molybdate dihydrate ($Na_2MoO_4 \cdot 2H_2O$), 1

mmol of thiourea (CH_4N_2S), and 2 mmol of elemental selenium (Se) powder, using 10 mL of hydrazine hydrate ($N_2H_4 \cdot H_2O$) as the solvent. The mixture was magnetically stirred at 900 rpm for 1 hour at ambient temperature to ensure homogeneity. Subsequently, the resulting suspension was transferred into a Teflon-lined stainless steel autoclave and subjected to hydrothermal treatment at 240 °C for 24 hours. After naturally cooling to room temperature, the resulting product was collected by centrifugation at 8000 rpm for 20 minutes, followed by sequential washing with deionized water and ethanol. The final product was then dried at 60 °C overnight.

Results and discussions

Powder-XRD (XRD PAN analytical) was used to examine the crystallographic patterns of the as-synthesised materials. X-ray diffraction was used to examine the crystallographic structures of all produced materials, as illustrated in Figure 1. The diffraction patterns that arise for MoSSe at 13.7°, 32.4°, 38.6°, 47.9°, and 57.5° are indexed to the (002), (100), (103), (105), and (110) planes, in that order (JCPDS No: 36-1408) [2]. The XRD pattern of $CoMoO_4$ is seen in Figure 1(b). The conventional $CoMoO_4$ diffraction patterns (JCPDS No: 25-1434) and the XRD patterns of pure $CoMoO_4$ agree with each other. The lack of additional impurity peaks validated the synthesized components' purity. The MoSSe@$CoMoO_4$ composite's diffraction pattern showed both MoSSe and $CoMoO_4$ phases, demonstrating that the one-pot method was successful in forming the composite material.

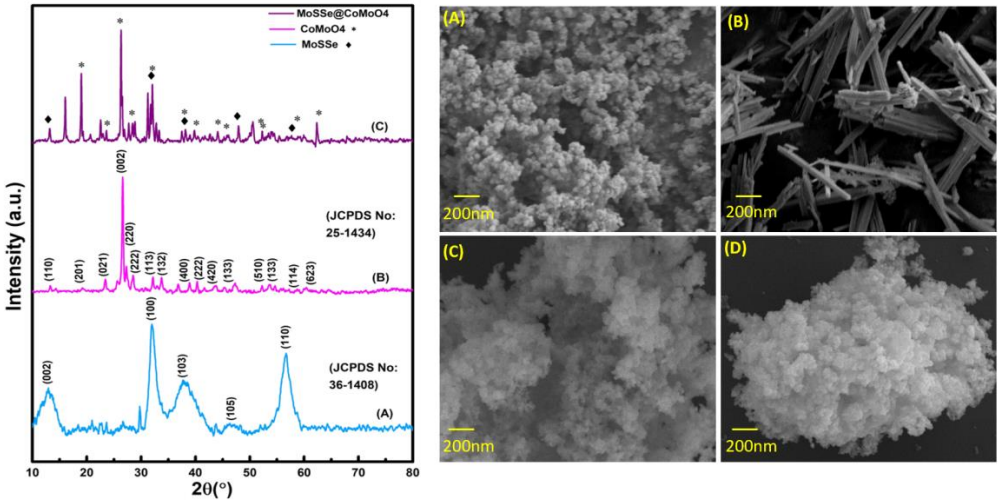


Figure 1. X-ray diffraction (XRD) spectra of **(A)** MoSSe, **(B)** $CoMoO_4$ and **(C)** MoSSe@$CoMoO_4$.

Figure 2. Field-emission scanning electron microscope (FE-SEM) images of **(A)**MoSSe, **(B)** $CoMoO_4$ nanorods and **(C and D)** MoSSe@$CoMoO_4$ nanocomposite.

A FESEM (Model: Carl Zeiss Marlin Compact) determined the materials' nanostructure and elemental composition. FESEM was used to analyze the surface morphologies of the MoSSe, $CoMoO_4$, and MoSSe@$CoMoO_4$ (Fig. 2). As seen in Fig. 2(a), Pristine MoSSe had a sphere-like form. The rough surface with spaces between intermediates was contained by the MoSSe nanospheres [3]. As seen in Fig. 2(b), the SEM images of $CoMoO_4$ exhibit rod-like morphologies. As seen in Fig. 2(c, d), the MoSSe@$CoMoO_4$ composite materials likewise preserved the spherical morphology of MoSSe. An organized hybrid arrangement can enhance electrochemical performance by providing a greater surface area that is accessible and enabling quick transport paths for the ion diffusion of the electrolyte.

Electrochemical Performance of MoSSe@$CoMoO_4$ in Symmetric Assembly

A CHI760E electrochemical analyzer was used to study symmetric supercapacitors. We conducted CV and GCD tests across -0.6 V to 0.6 V, varying scan sweeps and current densities. The electrolyte was 6 M KOH with a mass load of about 3 mg. Figure 3 represents the electrochemical studies of the generated material MoSSe@$CoMoO_4$. The typical CV profile for the MoSSe@$CoMoO_4$ electrode, obtained at various potential scan rates, is displayed in Figure 3(A). The MoSSe@$CoMoO_4$ electrode CV profiles show some redox peaks. The quasirectangular form of the MoSSe@$CoMoO_4$ composite electrode suggests the electric double layer (EDL) behavior, characterized by a rapid current response upon potential reversal. MoSSe@$CoMoO_4$'s C_{sp} value is 451.95 F/g.

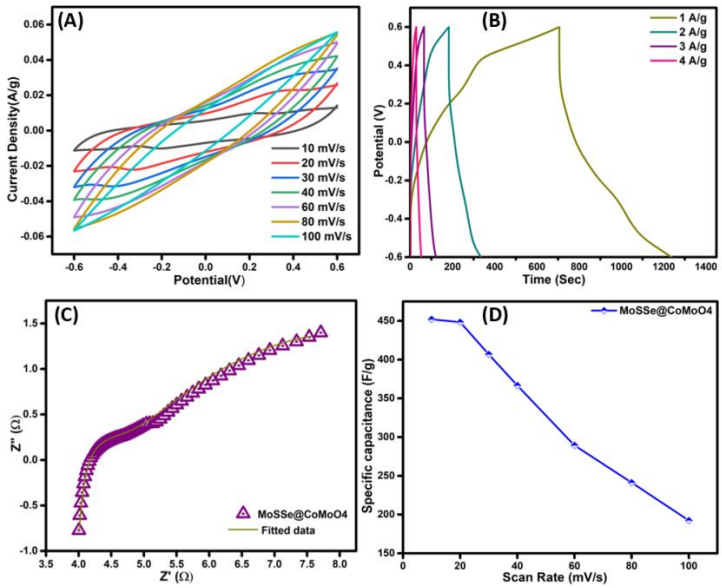


Figure 3. (A) CV profile of MoSSe@$CoMoO_4$ at different scan sweeps, **(B)** GCD profile of MoSSe@$CoMoO_4$ at different current densities, **(C)** Nyquist plot of MoSSe@$CoMoO_4$, and **(D)** Specific capacitance at different scan rates.

The charge storage capacity of all quasi-solid-state symmetric supercapacitors, made with MoSSe@CoMoO4 electrode materials, was further assessed using GCD analysis. Figure 3(B) shows the GCD curves of MoSSe@$CoMoO_4$ for a range of current densities (1–4 Ag^{-1}). The discharging time decreased with increasing current density. MoSSe@$CoMoO_4$ has a computed Csp of 127.75 Fg^{-1} at 1 Ag^{-1}. Additionally, it was found that the P_D was 600 W kg^{-1}, and the E_D was 25.55 Wh kg^{-1}. Ultimately, we can say that the MoSSe@$CoMoO_4$ electrode material improves supercapacitor performance. Figure 3(C) shows the Nyquist plot of the MoSSe@$CoMoO_4$ nanocomposite, featuring a semicircle at high frequencies and a steep line at low frequencies. The bulk resistance (Rb) and charge transfer resistance (Rct) are 4 Ω and 0.28 Ω, respectively. The low Rct value suggests efficient charge transfer and good electrochemical performance. Figure 3(D) depicts the variation of specific capacitance with scan rate, showing the highest capacitance at the lowest scan rate.

CONCLUSION

In conclusion, the MoSSe@$CoMoO_4$ composite was successfully synthesized using an efficient solvothermal method [4]. Compared to the pristine MoSSe electrode, the MoSSe@$CoMoO_4$ electrode exhibited significantly improved electrochemical performance. Specifically, it achieved a capacitance of 127.75 Fg^{-1} at 1 Ag^{-1} and demonstrated an impressive energy density (E_D) of 25.55 Wh kg^{-1} at a power density (P_D) of 600 W kg^{-1}. These results highlight the exceptional electrochemical capabilities of the MoSSe@$CoMoO_4$ binary composite, positioning it as a promising candidate for supercapacitor applications.

ACKNOWLEDGEMENTS

PL gratefully acknowledges the financial support provided by UGC through a JRF. The experimental facilities at the Department of Physics, Central University of Punjab, were utilized to conduct the experiments reported in this paper.

REFERENCES

1. Frederick Nti a, Daniel Adjah Anang b, Jeong In Han, Journal of Alloys and Compounds, Vol. 742, pp. 342e350, (2018).
2. Aruchamy Gowrisankar, Antonette Luciana Sherryn, Thangavelu Selvaraju , Applied Surface Science Advances Vol. 3, pp. 100054, (2021).
3. Lina N. Khandare , Dattatray.J. Late b , Nandu.B. Chaure , Surfaces and Interfaces Vol. 43, pp. 103533, (2023).
4. Muzahir Iqbal, Nilesh G. Saykar, Abhijeet Singh, Imtiaz Ahmed, Anil Arya, Krishna Kanta Haldar, and S. K. Mahapatra, Adv. Mater. Technol. pp. 2301797, (2024).

Room Temperature Synthesis of Ag@Au Core- Shell Nanostructures by Controlled Transmetallation Reaction

Krishnaprabha M[1, a)] and Manjunatha Pattabi[2]

[1]*Dr P Dayananda Pai- P Satisha Pai Government First Grade College, Carstreet Mangalore- 575001, India*
[2] *Department of Materials Science, Mangalore University, Mangalagangothri-574199, India*

[a)] Corresponding author: krishnaprabham@rediffmail.com

Abstract. Aqueous synthesis of Ag@Au core- hell nanostructures at room temperature is reported using controlled transmetallation (TM) reaction between silver nanoparticles (AgNPs) and gold precursor solution ($HAuCl_4$). The TM reaction is controlled using chicken egg shell membrane (ESM). The formation of Ag@Au core- shell nanostructures via TM reaction is confirmed using UV- Vis absorbance studies. The morphology of the synthesized nanostructures determined using the Transmission Electron Microscopy (TEM).

Keywords: TM reaction, ESM**,** AgNPs, Ag@Au core-shell nanostructures

INTRODUCTION

Bimetallic nanoparticles are functional nanomaterials with heterogeneous arrangement of two distinct metals like gold (Au), silver (Ag), palladium (Pd), platinum (Pt), copper (Cu) etc. which are used in wide variety of applications such as Surface Enhanced Raman Scattering (SERS), catalysis, biosensing, photodynamic therapy, diagnostics, drug delivery applications etc.[1-5] They may be alloy or core-shell or porous nanostructures and are highly desirable for the enhancement of material properties. Ag@Au core-shell nanostructures exhibiting optical properties of Ag and reactivity of Au can be synthesized using transmetallation (TM) reaction (also called galvanic replacement reaction).[3-5]. In TM reaction, the sacrificial Ag nanoparticles (AgNPs) and the Au ion (Au^{3+}) precursor solution ($HAuCl_4$) react. Usually, TM reaction is spontaneous and many research groups carried out the reaction at 100 ^oC. Shukla et. al. used dialysis tubing- an artificial semipermeable membrane to control the kinetics of TM reaction at room temperature.[3] In our earlier work of synthesizing noble metal porous nanostructures, the natural semipermeable membrane i.e, chicken egg shell membrane (ESM) was used in controlling TM reaction.[4] In our present study of synthesizing Ag@Au core-shell nanostructures, in addition to the ease of controlled addition of $HAuCl_4$ to AgNPs via ESM, ESM's reducing property[8,9] is also used to control the relative kinetics of TM reaction.

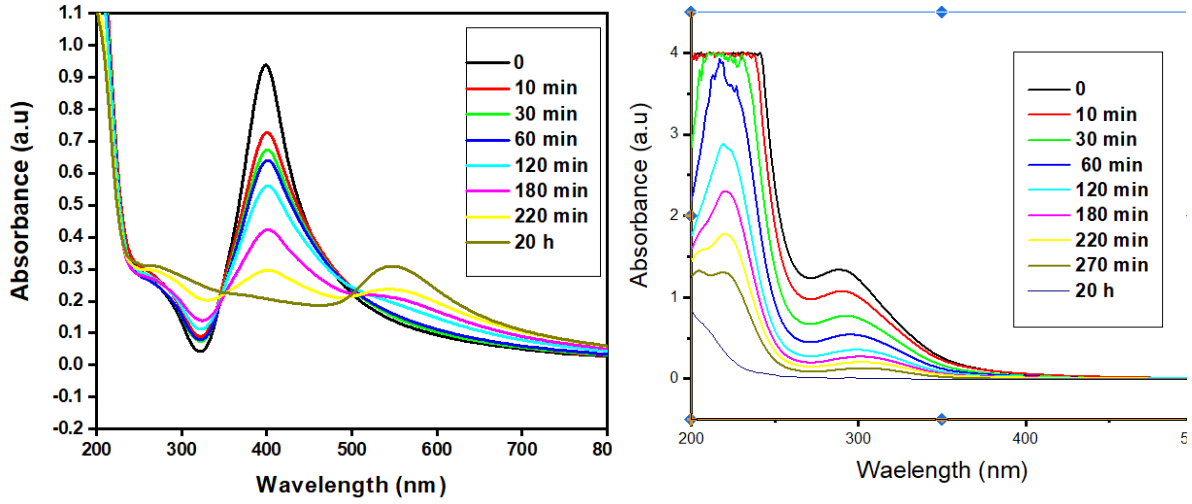
Experimental Details

Synthesis of aqueous AgNPs is carried out using the conventional borohydride method used elsewhere.[6] Briefly, in 3 min of reaction time, 10 mL of 1 mM $AgNO_3$ solution is added in a controlled manner to freshly prepared 30 mL of 2 mM $NaBH_4$ solution maintained at ice cold temperature under magnetic stirring. The yellow coloured AgNP solution is diluted 10 times to perform TM reaction. After immersing the emptied and thoroughly washed chicken egg shell in dilute HCl solution for 3 h, the ESM is carefully peeled out and cleaned using double distilled water. Desired amount of AgNP solution is taken in an open glass test tube tied with ESM at one end and then immersed in 50 mL of 0.5 mM $HAuCl_4$ solution maintained under constant magnetic stirring. The experiment is monitored by visual observation of colour changes and by taking UV- Vis readings of both AgNP and $HAuCl_4$ solutions at different time intervals using UV–1800 Shimadzu UV spectrophotometer. The same experiment is repeated by changing the pH of both AgNPs and $HAuCl_4$ solution. Micrographs and energy-dispersive X-ray spectroscopy (EDS) readings are taken using FEI Tecnai Transmission Electron Microscope (TEM). Sample for TEM imaging was prepared by depositing a drop of obtained sample on copper grids.

Results and Discussion

As the reduction potential of Ag is less than that of Au, TM reaction takes place between Au^{3+} ions and AgNPs as per the equation $3Ag\ (s) + AuCl_4^-(aq) \rightarrow 3Ag^+(aq) + Au\ (s) + 4Cl^-\ (aq)$.[4] Ag atoms act as sacrificial templates. Each Ag atom gets oxidized and gives out 3 electrons causing the reduction of Au^{3+} ions. Since Au gets deposited on the surface of AgNPs, the shape of Ag@Au core-shell nanostructures is dependent on the shape of AgNPs. TM reaction being spontaneous and can take place at any temperature needs to be slowed down and ESM is used to control the rate of TM reaction. Diffusion of $HAuCl_4$ towards AgNP solution takes place against gravitation via ESM.

Both Ag and Au nanostructures exhibit distinctive optical properties due to surface plasmon resonance (SPR). SPR occurs when the conduction electrons present on the surface of metal nanoparticles interact with incident photons. SPR of the nanoparticles is dependent on their size, shape, composition and type of solvent.[1-5] During the course of the ongoing TM reaction between AgNPs and $HAuCl_4$, the SPR properties of both solutions are studied by acquiring UV-Vis absorbance spectra at different time intervals. UV- Vis absorbance spectra of 0.1 mM Ag NP solution undergoing TM reaction with 0.5 mM $HAuCl_4$ in the presence of ESM at various times are shown in Figure 1(a).



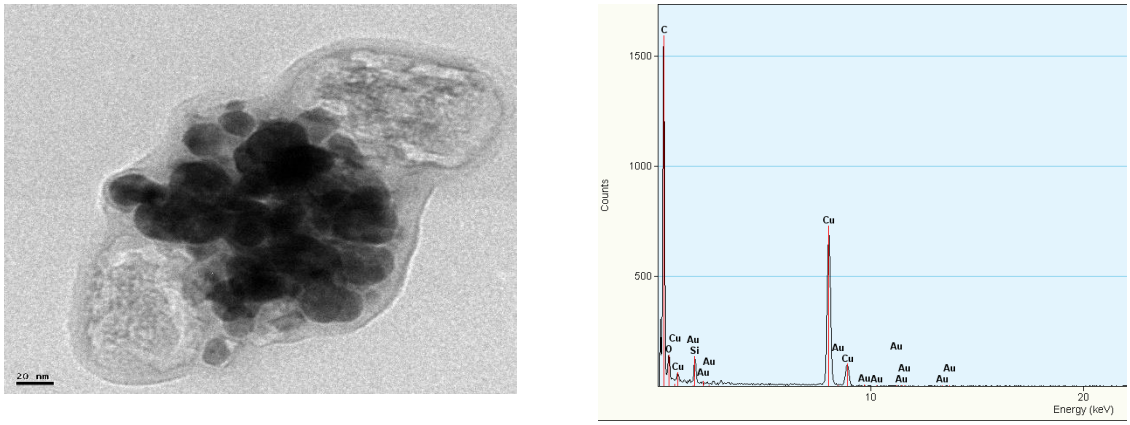
(a) (b)

FIGURE 1. (a) UV- Vis absorbance spectra of AgNPs at different periods of TM reaction. (b) UV- Vis absorbance spectra of $HAuCl_4$ solution at different periods of TM reaction.

During TM reaction, the yellow colour of AgNPs changed gradually to amber colour after 220 min, later changed to light pink shade after 270 min, whose intensity was found to increase further with time. Initially, UV-Vis absorbance spectra exhibited a single SPR peak at 401 nm corresponding to Ag. No red shift in plasmonic band corresponding to Ag is observed with increased reaction time except for the decrease in its intensity. The formation of a slight buckle at 500 nm at 120 min, later a clear SPR peak at 544 nm after 220 min is indicative of Au coating on AgNPs. Au coated AgNPs possess two distinct plasmon bands with their intensities dependent on the thickness of Au shell as reported by Mulavaney et al.[5] The readings taken at 20 h showed only one SPR peak at 548 nm and the original peak due to Ag was not found as Ag gets etched away during TM reaction. 25% of Au added is sufficient to completely etch away all the Ag metal.

Figure 1(b) represents the UV-Vis absorbance spectra of $HAuCl_4.\ 3H_2O$ solution during different periods of TM reaction. Two sharp absorption peaks at 226 nm and 311 nm are indicative of Au^{3+} ion complexes in solution.[7] The intensity of both absorption peaks is found to decrease during the TM reaction. After 20 h of TM reaction, disappearance of both the peaks confirms of the absence of Au^{3+} ion complexes in solution.

The morphology of the synthesized Ag@Au core- shell nanostructure is as shown in the TEM micrograph in figure 2(a) and the corresponding EDS spectrum is as shown in figure 2(b). Signals corresponding to elemental Au are seen in EDS spectrum thus confirming the purity of Au in the synthesized nanostructures.



(a) (b)

FIGURE 2. (a) TEM micrograph of Ag@Au core- shell nanostructure obtained after 20 h (b) EDS spectrum

The approach of controlling the kinetics of TM reaction with naturally available chicken ESM is reported by our group earlier.[4] In this study, the position of AgNPs and $HAuCl_4$ is reversed and slightly higher concentration of $HAuCl_4$ is taken. Various stages of TM reaction resulting in the formation of Ag@Au core- shell nanostructures can be observed visually. The TM reaction can be terminated at any desired time by taking out test tube containing AgNP solution from the $HAuCl_4$ solution. ESM controls the kinetics of TM reaction by helping in the controlled addition of $HAuCl_4$ addition to AgNPs. In addition, Ag^+ ions produced in TM reaction adhere on the surface of ESM itself or leach out through ESM thereby avoiding the further purification of end product. The colloid containing synthesized nanostructures were found to be stable when stored under ambient conditions. With change in pH of both AgNP and $HAuCl_4$ solution, observed a red shift in SPR peak of AgNPs (graph not shown here).

REFERENCES

1. R. Borah and S. W. Verbruggen, *J. Phys. Chem. C.*, **124(22)**, 12081-12094 (2020).
2. L Rivas, S. Sanchez- Cortes, J. V. Garcia- Ramos and M. Morcillo, *Langmuir*, **16**, 9722 (2000).
3. S. Shukla, A. Priscilla, M. Banerjee, R. R. Bhonde, J. Ghatak, P. V. Satyam and M. Sastry, *Chem. Mater*, **17**, 5000-5005 (2005).
4. M. Pattabi, M. Krishnaprabha, R. Nairy and M. Sastry, *Mater. Chem. Phys.*, **202**, 22-30 (2027).
5. P. Mulavaney, M. Greisig and A. Henglein, *J. Phys. Chem*, **97**, 7061 (1993).
6. P. V. Dong, C. H. Ha, L. T. Binh and J. Kasbohm, *International Nano Letters*, **2**, 1-9 (2012).
7. J. Z. Chan, R. R. Ali, K. Shameli, M. S. N. Salehi, K. X. Lee and E. D. M. Isa, *Conf. Series: Materials Science and Engineering*, **808**, 012036 (2020).
8. S. Pramanik, A. Saha, P. S. Devi, *RSC Adv.*, **5**, 33946-33954 (2015).
9. P. S. Devi, S. Banerjee, S, R. Chowdhury and G. S. Kumar, *RSC Adv.*, **2**, 11578-11585 (2012).

Synergistic Effect of Silver Nanoparticles on Magnetic Hyperthermia of Fe_3O_4 Nanoparticles

Ishu Attry[1], Pooja Jarora[1] and Bhupendra Chudasama[1,*)]

[1]Thapar Institute of Engineering and Technology, Patiala-147004, Punjab, India

[*]Corresponding author: bnchudasama@thapar.edu

Abstract. The relentless pursuit of effective cancer treatments has spurred considerable interest in hyperthermia for cancer as a therapeutic modality by leveraging the vulnerability of cancer cells to elevated temperatures. This study investigates the synergistic potential of Fe_3O_4 nanoparticles combined with silver nanoparticles (SNPs) for magnetic hyperthermia applications. Utilizing the superparamagnetic properties of magnetite, the research examines the heating efficiency of this nanoparticle system under an AC magnetic field. Key experimental procedures include the synthesis of Fe_3O_4 nanoparticles via co-precipitation and silver nanoparticles by chemical reduction, followed by thorough characterization using X-ray diffraction, vibrating sample magnetometry, and particle size analysis. Results indicate that the incorporation of silver nanoparticles significantly enhances the thermal response of Fe_3O_4 nanoparticles, achieving higher temperatures more efficiently. The study underscores the promising potential of this combination of nanoparticles in advancing magnetic hyperthermia as a viable cancer treatment strategy, highlighting their superior heating performance.

Keywords. Magnetic hyperthermia, Fe_3O_4 nanoparticles, silver nanoparticles, synergistic effect, heating efficiency

INTRODUCTION

Cancer, characterized by the uncontrolled growth and proliferation of abnormal cells, is a major cause of illness and death. Worldwide, an estimated 19.3 million new cancer cases and almost 10 million cancer deaths occurred in 2020 [1]. Scientists are working for the complete understanding and its control. Various methods have been put forward to treat cancer. Conventional treatments like surgery and chemotherapy have been in practice for a long time, but with limited success, and have side effects [2]. Hyperthermia could be used as cancer therapy in which cancerous tissues are exposed to temperatures of 41-45˚C, as healthy cells can sustain temperatures as high as 47˚C [3]. This can be achieved by magnetic hyperthermia. Magnetite has gained significant attention for its potential in magnetic hyperthermia due to its biocompatibility and capacity to produce heat when exposed to an AC magnetic field. This research explores the synergistic effect of SNPs on the magnetic hyperthermia performance of Fe_3O_4.

EXPERIMENTAL DETAILS

Materials and methods

For the synthesis of magnetite nanoparticles, ferrous sulphate heptahydrate ($FeSO_4 \cdot 7H_2O$), ferric chloride hexahydrate ($FeCl_3 \cdot 6H_2O$), and NaOH serve as precursors. Oleic acid is used as a surfactant. For the synthesis of SNPs, $AgNO_3$ (99.8%), diphenyl ether, oleylamine (70%), and pluronic F-127 are used. XRD patterns of the Fe_3O_4 and SNPs are recorded on Rigaku SmartLab SE diffractometer in the 2θ range of 20°-80°. Magnetic properties are examined with a Lake Shore 7404 Vibrating Sample Magnetometer at room temperature. The size distribution and hydrodynamic size of fluids are determined by the Brookhaven 90 Plus particle size analyzer. Heating efficiency of fluids is assessed on nanoTherics' magneTherm magnetic hyperthermia setup.

Synthesis of Fe_3O_4 nanoparticles and silver nanoparticles

Fe_3O_4 nanoparticles are synthesized by the co-precipitation method. For this, 0.2 mM ferric chloride and 0.1 mM ferrous sulphate are mixed with a 0.8 mM solution of NaOH under mechanical stirring. The pH of the solution is controlled and stabilized at 11. After stirring the solution for 20 minutes, black precipitates formed, which were washed several times by magnetic decantation. Further, these precipitates are coated with oleic acid [4]. SNPs are synthesized by a biphasic procedure. Initially, oleylamine-passivated hydrophobic SNPs are synthesized by the reduction of $AgNO_3$ with oleylamine. Subsequently, these water-insoluble SNPs undergo phase transfer into an aqueous medium through a ligand exchange process facilitated by the block co-polymer Pluronic F-127 [5].

RESULT AND DISSCUSSION

Figure1(a) illustrates the X-ray diffraction pattern of Fe_3O_4 nanoparticles. The five broad observed peaks are assigned to the fcc inverse spinel structure. The pattern is well-matched to the JCPDS Card No. 19-0629. Fig.1(a) also shows the X-ray diffraction pattern of SNPs. The diffraction patterns display well-resolved four broad diffraction peaks corresponding to the standard FCC structure of SNPs (JCPDS card No. 04-0783) [6]. This confirms the formation of Fe_3O_4 and SNPs without any secondary impurity phase. Fig.1(b) illustrates the magnetization curve of Fe_3O_4. The curve demonstrates superparamagnetic behavior, evidenced by very low coercivity and remanence.

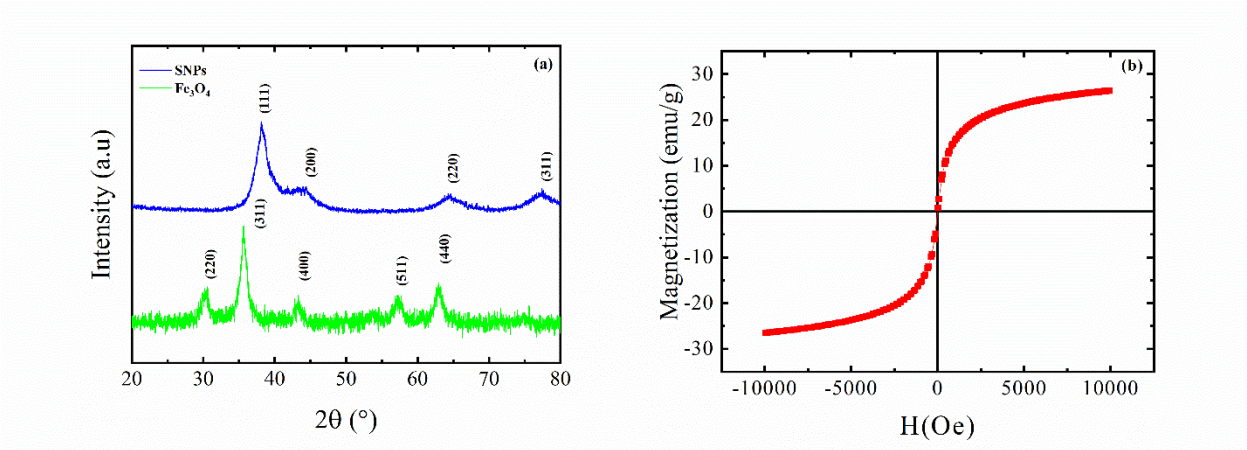


FIGURE 1. (a) X-ray diffraction pattern of SNPs and Fe_3O_4 NPs and (b) M-H loop of Fe_3O_4 nanoparticles

To evaluate the effect of dilution of Fe_3O_4 fluid with SNPs fluid and DI on their magnetic hyperthermia efficiency, temperature-time profiles are recorded as shown in Fig. 2. For this, the magnetic field frequency is fixed at 935.6 kHz, field strength 10 mT, and exposure time is kept constant at 600 sec. The highest temperature rise occurs with pure Fe_3O_4 fluid. When diluted by SNPs fluid and DI, the temperature rise decreases with increasing dilution, as shown in Fig.3(a). This change is more rapid when diluted with DI. Thus, the presence of SNPs in Fe_3O_4 fluid helps improve their hyperthermia performance at a lower concentration of Fe_3O_4 nanoparticles. The hydrodynamic size of Fe_3O_4 fluid when diluted with the SNPs fluid and DI is shown in Fig.3(b). The hydrodynamic size of Fe_3O_4 NPs is 36.7 nm. As it is diluted with SNPs fluid, the hydrodynamic size increases to 63.9 nm. In contrast Fe_3O_4 fluid diluted with DI, no significant change is observed. Thus, it is concluded that when Fe_3O_4 fluid is diluted with SNPs fluid, it induces large aggregation compared to DI water dilution, which is responsible for the observed synergy.

CONCLUSION

This study shows a potential synergistic effect of SNPs on the magnetic hyperthermia performance of Fe_3O_4 fluids. These results highlight the promising therapeutic potential of these nanoparticle systems, paving the way for more effective cancer treatment strategies with magnetic hyperthermia.

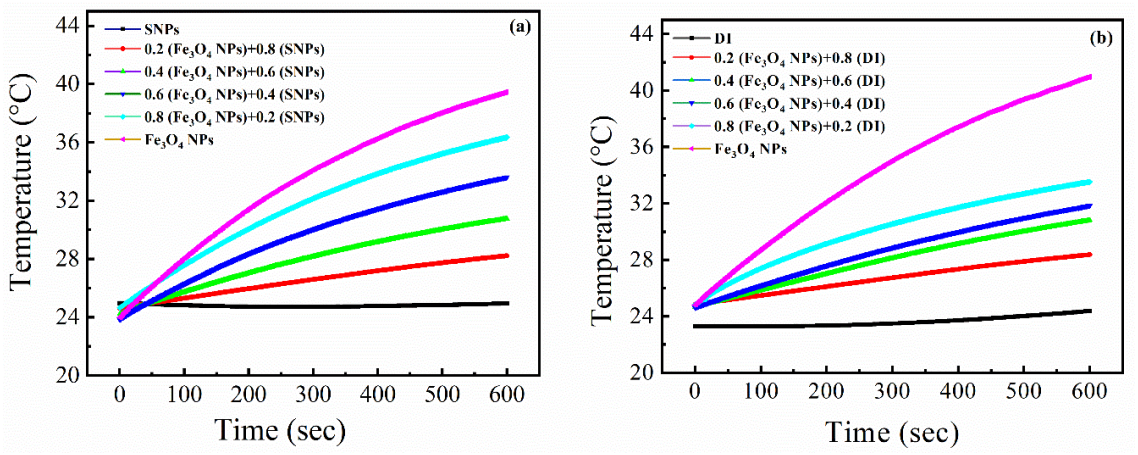


FIGURE 2. Temperature-Time plots of (a) Fe_3O_4 fluid diluted with SNPs fluid and (b) Fe_3O_4 fluid diluted with DI

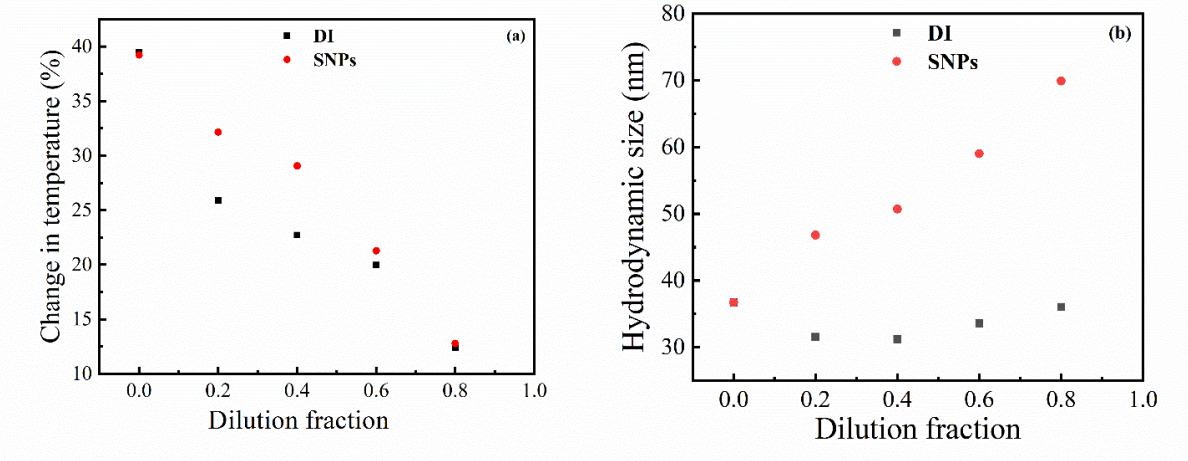


FIGURE 3. Effect of dilution on (a) % Temperature change and (b) hydrodynamic size of Fe_3O_4 fluid

ACKNOWLEDGMENTS

Authors gratefully acknowledge financial support from the DST-FIST (Grant No. SR/FST/PS-II/2018/53).

REFERENCES

1. H. Sung, J. Ferlay, R.L. Siegel, M. Laversanne, I. Soerjomataram, A. Jemal, and F. Bray, CA: ACancer Journal for Clinicians, Vol. 71, pp.209-249 (2021).
2. C.A. Cullinane, T. Borneman, D.D. Smith, D.Z.J. Chu, B.R. Ferrell, and L.D. Wagman, Cancer, Vol. 98, pp. 2266-2273 (2003).
3. B.A. Britt, M.D., DIP. ANAES. (TOR.), F.R.C.P.(C), and W. Kalow, M.D., Canadian Anaesthetists' Society Journal, Vol.17, pp. 293-315 (1970).
4. P.B. Shete, R.M. Patil, B.M. Tiwale, and S.H. Pawar, Journal of Magnetism and Magnetic Materials, Vol. 377, pp. 406-410 (2015).
5. Chandni, N. Andhariya, O.P. Pandey, and B. Chudasama, The Royal Society of Chemistry, Vol. 3, pp. 1127-1136 (2013).
6. P. Gong, H. Li, X. He, K. Wang, J. Hu, W. Tan, S. Zhang, and X. Yang, Nanotechnology, Vol. 18, 285604, (2007).

Magnetic Properties Of $CoCr_xFe_{2-x}O_4$ Nanomaterials Synthesized By Sol-Gel Autocombustion Route Using Double Fuel (Citric Acid And Glycine) Approach

Anagha B. Patil[1] and Rabi N. Panda*, [1]

[1]*Department of Chemistry, Birla Institute of Technology and Science, Pilani, K K Birla Goa Campus, Zuarinagar, Sancoale, Goa 403726, India*
**Corresponding author: rnp@goa.bits-pilani.ac.in*

Abstract. We report the synthesis of $CoCr_xFe_{2-x}O_4$ (where x = 0.0, 0.5, 0.9) nanomaterials using citric acid-glycine assisted sol-gel autocombustion route at 450 ºC. XRD studies for $CoCr_xFe_{2-x}O_4$ results in the confirmation of cubic spinel phase nanocrystalline products with the crystallite sizes (D) estimated as 25.7 nm to 26.9 nm for x = 0.0 to 0.9 in $CoCr_xFe_{2-x}O_4$, respectively. The lattice constants vary from 8.3548 Å to 8.3529 Å, for x varying from 0.0 to 0.9. Raman spectra show the Raman modes (T_{2g} (3), E_g (2), E_g (1), T_{2g} (2), T_{2g} (1), A_{1g} (2) and A_{1g} (1)) corresponding to the symmetric and asymmetric stretching vibrations along with symmetric bending vibrations in the structure of $CoCr_xFe_{2-x}O_4$. Magnetic parameters such as coercivity (H_c), magnetization (M) and remanent magnetization (i.e. M_r) were obtained from magnetic studies (MH curves). The considerable variation in the saturation magnetization values (M_s) (MH curves recorded at 300 K) was observed to be 65.88 emu/g, 40.01 emu/g and 23.08 emu/g (x = 0.0, 0.5 and 0.9, respectively) whereas the variation in values of H_c for $CoCr_xFe_{2-x}O_4$ nanomaterials was noted from 1995 Oe (x = 0.0) - 1208 Oe (x = 0.9). The high H_c values were observed in the MH curves recorded at 5 K for $CoCr_xFe_{2-x}O_4$ materials which were 10842 Oe, 7544 Oe and 5016 Oe for x= 0.0, 0.5 and 0.9, respectively.

Keywords: $CoFe_2O_4$, Sol-gel autocombustion, XRD studies, Raman spectroscopy, Magnetic properties, Cation redistribution

INTRODUCTION

In recent times amongst many other spinel ferrite nanomaterials, cobalt ferrite ($CoFe_2O_4$) is studied all over the world for its unique properties at nano-size and numerous applications [1]. $CoFe_2O_4$ is known for its remarkable magnetic properties, i.e. high coercivity (H_c) and moderate saturation magnetization (M_s) [2]. Various synthesis techniques have been used for the synthesis of $CoFe_2O_4$ nanomaterials [2] in order to achieve its specific structure and targeted properties. The magnetic properties of cobalt ferrite ($CoFe_2O_4$) nanomaterials are well studied with respect to the effect of substituent element, different synthesis techniques, alterations in various synthesis parameters [1, 2] etc. This has a large impact on particle sizes of the materials, surface properties and most importantly, drastic effect on structural properties of the materials under study [3, 4]. For instance, in case of sol-gel autocombustion method, the use of chelating agents/comlexant for binding the metal ions [5], fuel for combustion process [6], combustion and annealing temperature [7] etc. plays an important role in tuning the structural characteristics along with magnetic properties of $CoFe_2O_4$. In this work, we have reported the synthesis of Cr substituted $CoFe_2O_4$ nanomaterials ($CoCr_xFe_{2-x}O_4$) via modified sol-gel autocombustion method using double fuel i.e. glycine (G) in addition to citric acid (CA). This modification was carried out to understand the size and surface characteristics of these nanomaterials. The pure phase products were obtained at a combustion temperature of 450 ºC.

EXPERIMENTAL

Modified sol-gel autocombustion method was used to synthesize $CoCr_xFe_{2-x}O_4$ nanomaterials (x = 0.0, 0.5 and 0.9). The stoichiometric amounts of $CoCl_2{\cdot}6H_2O$, $CrCl_3{\cdot}6H_2O$ and $Fe(NO_3)_3{\cdot}9H_2O$ salts were weighed and solutions were prepared using distilled water in separate beakers. The clear salt solutions of Co^{2+}, Cr^{3+} and Fe^{3+} were collected quantitatively in a round bottom flask of 500 mL and final volume was prepared approximately 400 mL by use of distilled water. Subsequently, CA (molar ratio of metal ions (M) to citrate ions i.e. 1:3 ratio) was added in the above solution mixture in excess with continuous stirring. Similarly, glycine was added and the solution mixture was stirred till it was completely dissolved followed by the addition of 1 M HNO_3 solution. Then, similar steps were followed from this stage onwards as reported earlier by our group [8]. The combustion temperature was 450 ºC for a time period of 4 hour in muffle furnace (air atmosphere). These as-synthesized $CoCr_xFe_{2-x}O_4$ nanomaterials were characterized using X-ray diffraction (XRD) instrumentation technique (Make:

Bruker, Model: D8 Advance X-Ray Diffractometer) and Raman spectroscopy (Make: Horiba France, Model: LAB RAM HR). The VSM measurements (Make: Quantum Design, Model: PPMS Evercool II) were performed at a temperature of 300 K and 5 K with maximum applied field strength of 2 T.

RESULTS AND DISCUSSION

XRD and Raman Spectroscopy Studies

Figure 1 (a, b, c) depicts the XRD patterns for $CoCr_xFe_{2-x}O_4$ (x = 0.0, 0.5 and 0.9) materials. The formation of nanocrystalline cubic spinel structure was proved by XRD patterns with peak indexing: (220), (311), (222), (400), (422), (511) and (440) for $CoCr_xFe_{2-x}O_4$ materials (confirmed by ICDD card number 00-003-0864). XRD pattern of pure $CoFe_2O_4$ shows emergence of very minor secondary phase of α-Fe_2O_3 with 2θ at 33.26º (ICDD card number 00-001-1053). The overall variation in crystallite sizes 'D' (by Scherrer formula [4]) for (311) plane was negligible i.e. 25.7 nm, 28.1 nm and 26.9 nm for 'Cr' content: 0.0, 0.5 and 0.9, respectively. The values of 'a' shows a marginal reduction i.e. 8.3548 Å, 8.3532 Å, 8.3529 Å for x = 0.0, 0.5 and 0.9 in $CoCr_xFe_{2-x}O_4$, respectively. The changes in the values of 'D' and 'a' is negligible, probably due to the comparable ionic radii of the Fe^{3+} which is 0.67 Å and that of Cr^{3+} ions is 0.63 Å. However, the slight decrease in lattice constants can be because of lattice shrinkage taking place due to smaller size Cr^{3+} ions possibly replacing the larger size Fe^{3+} ions [9].

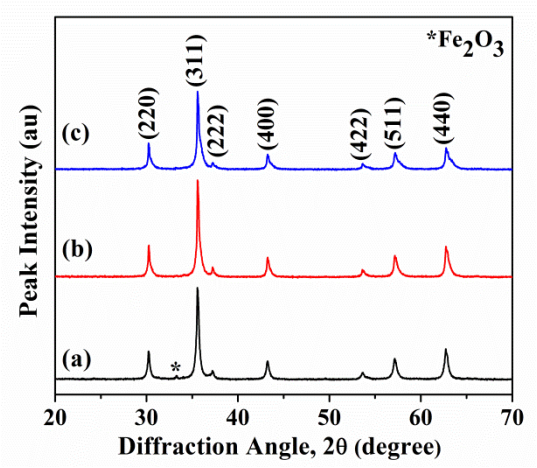


FIGURE 1. XRD patterns of $CoCr_xFe_{2-x}O_4$ materials synthesized at 450 ºC; (a) x = 0.0, (b) x = 0.5 and (c) x = 0.9

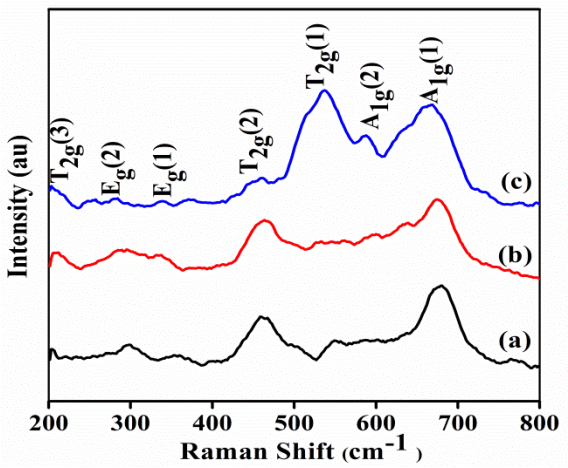


FIGURE 2. Raman Spectra of $CoCr_xFe_{2-x}O_4$ materials synthesized at 450 ºC; (a) x = 0.0, (b) x = 0.5 and (c) x = 0.9

Figure 2 (a, b, c) shows the Raman spectra for the $CoCr_xFe_{2-x}O_4$ materials. The variation noticed in the factors such as broadening, peak positions and intensities of the peaks can be related to cation redistributions in $CoCr_xFe_{2-x}O_4$. Various Raman peaks at 203 – 208 cm^{-1}, 282 – 299 cm^{-1}, 334 – 357 cm^{-1}, 460 – 464 cm^{-1}, 538 – 551 cm^{-1}, 636 – 640 cm^{-1} and 666 – 675 cm^{-1} were attributed to T_{2g} (3), E_g (2), Eg (1),T_{2g} (2), T_{2g} (1), A_{1g} (2) and A_{1g} (1) modes, respectively. These modes represent symmetric stretching of O^{2-} anion (A_{1g}), symmetric bending of O^{2-} anion (E_g) and asymmetric stretching of O^{2-} anion w.r.t. octahedral and tetrahedral and cations in the lattice (T_{2g}) [10].

Magnetic Properties of $CoCr_xFe_{2-x}O_4$ Nanomaterials

Figure 4 represents the M vs H curves (at 300 K) for the $CoCr_xFe_{2-x}O_4$ materials. The values of M_s were calculated by linear fitting of graph i.e. M plotted against ($1/H^2$). The remarkable variation in M_s was observed to be 65.88 – 23.08 emu/g for 'Cr' content 0.0 – 0.9, respectively. The changes in H_c values was observed to be 1995 Oe to 1208 Oe for x = 0.0 to 0.9. The observed values of M_r were noted to vary from 32.33 emu/g to 8.40 emu/g for x = 0.0 to 0.9 (Table 1). The squareness ratios (M_r/M_s) were also calculated varying in the range of 0.4907 to 0.3640 for x = 0.0 to 0.9. Figure 5 depicts the M vs H curves (recorded at 5 K) for $CoCr_xFe_{2-x}O_4$ materials. The values of M_s were calculated as 55.33 emu/g, 45.60 emu/g and 28.71 emu/g. Further, a striking result wherein very high values of H_c were observed, i.e. 10842 Oe, 7544 Oe and 5016 Oe for x = 0.0, 0.5 and 0.9, respectively.

TABLE 1. Variation in structural and magnetic properties (M vs H curves at 300 K and at 5 K) of $CoCr_xFe_{2-x}O_4$ materials

.Cr content, x in $CoCr_xFe_{2-x}O_4$	D (nm)	a (Å)	Magnetic parameters (300 K)			Magnetic parameters (5 K)		
			M_s (emu/g)	H_c (Oe)	M_r (emu/g)	M_s (emu/g)	H_c (Oe)	M_r (emu/g)
x = 0.0	25.7	8.3548	65.88	1995	32.33	55.33	10842	42.06
x = 0.5	28.1	8.3532	40.01	835	12.24	45.60	7544	32.33
x = 0.9	26.9	8.3529	23.08	1208	8.40	28.71	5016	18.02

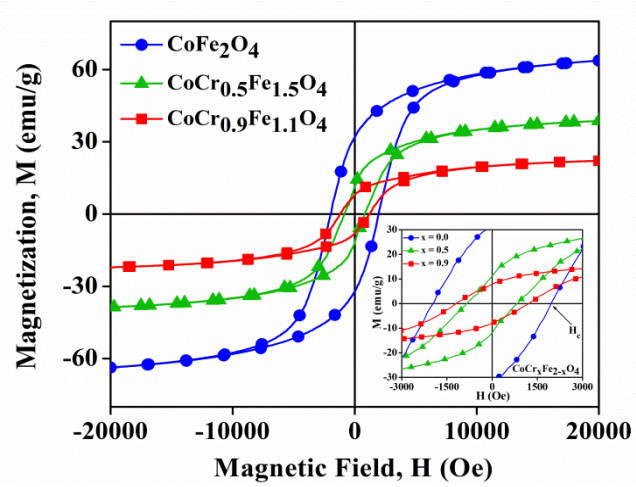


FIGURE 3. MH curves recorded at 300 K for $CoCr_xFe_{2-x}O_4$ nanomaterials (Inset: zoom-in plot for H_c)

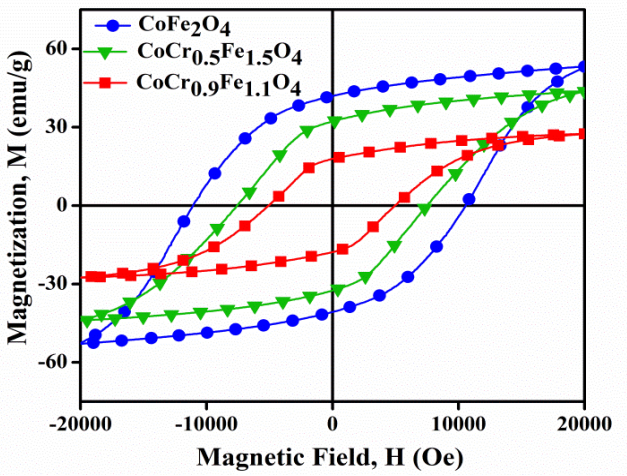


FIGURE 4. MH curves recorded at 5 K temperature for $CoCr_xFe_{2-x}O_4$ nanomaterials

The above results indicate decrease in M_s and H_c values with subsequent increase in Cr composition in $CoCr_xFe_{2-x}O_4$ nanomaterials. These alterations of M_s and H_c can be attributed to non-magnetic Cr ion insertion in the lattice, cation redistribution, size, strain and surface effects in the materials [3, 4]. In addition, there might be a presence of some amorphous fractions in the materials which could be inducing defect structures responsible for the changes occurring in magnetic parameters which could not be excluded.

CONCLUSION

The synthesis of $CoCr_xFe_{2-x}O_4$ nanomaterials was carried out successfully by sol-gel autocombustion route via double fuel approach using citric acid and glycine. The XRD analysis ascertained the product formation in cubic spinel phase. Small variation in the crystallite sizes (D) and lattice constants (a) was observed for $CoCr_xFe_{2-x}O_4$ materials. The presence of all the Raman modes ($3(T_{2g})$, $2(E_g)$, and $2(A_{1g})$) and variation in peak positions, peak broadening and peak intensities were attributed towards the cation redistribution occurring in the spinel lattice. The magnetic properties (at 300 K) wherein the significant variation in M_s values was observed from 65.88 – 23.08 emu/g for x = 0.0 to 0.9. Also, high values of H_c were observed for the magnetic measurements at 5 K i.e. 10842 Oe, 7544 Oe and 5016 Oe for 'Cr' content = 0.0, 0.5 and 0.9 in $CoCr_xFe_{2-x}O_4$, respectively.

ACKNOWLEDGMENTS

We acknowledge Department of Physics, BITS PILANI K K Birla Goa Campus and DST, Government of India for DST FIST grant number SR/FST/PS-I/2017/21 for VSM measurements required for magnetic properties study. We also thank CSIF, BITS Pilani, K K Birla Goa Campus for the provision of XRD and Raman Spectroscopy. A. B. Patil is thankful to BITS Pilani University, Pilani, for SRF fellowship.

REFERENCES

1. S. I. Ahmad, J. Magn. Magn. Mater. Vol. 562, pp. 169840-1–37 (2022).
2. S. Jauhar, J. Kaur, A. Goyal and S. Singhal, RSC Adv. Vol. 6, pp. 97694 – 97719 (2016).
3. A. B. Patil and R. N. Panda, Mater. Chem. Phys. Vol. 307, pp. 128215-1– 9 (2023).
4. A. B. Patil and R. N. Panda, **New J. Chem.** Vol. 49, pp. 109 – 123 (2025).
5. J. Venturini, R. Y. S. Zampiva, S. Arcaro and C. P. Bergmann, Ceram. Int. Vol. 44, pp. 12381–12388 (2018).
6. V.R. Bhagwat, A. V. Humbe, S.D. More and K.M. Jadhav, Mater. Sci. Eng. B. Vol. 248, pp. 114388-1–5 (2019).
7. T. Prabhakaran and J. Hemalatha, Ceram. Int. Vol. 42, pp. 14113 – 14120 (2016).
8. A. B. Patil and R. N. Panda, J. Supercond. Nov. Magn. Vol. 37, pp. 597– 608 (2024).
9. B. G. Toksha, S. E. Shirsath, M. L. Mane, S. M. Patange, S. S. Jadhav and K.M. Jadhav, J. Phys. Chem. C. Vol. 115, pp. 20905–20912 (2011).
10. R. S. Yadav, I. Kuřitka, J. Vilcakova, J. Havlica, J. Masilko, L. Kalina, J. Tkacz, J. Švec, V. Enev and M. Hajdúchová, Adv. Nat. Sci.: Nanosci. Nanotechnol. Vol. 8, pp. 045002-1–14 (2017).

Influence of Annealing Temperature on Structural, Morphological and Optical Properties of β−Ga_2O_3

Abhishek Sharma [a)1*], Kartikay[1], Tulsi[1], Saumya Chauhan[1], Shreya Thakur[1], Aman Bhalaria[1], and Vir Singh Rangra [b)1]

[1] *Department of Physics, Himachal Pradesh University, Summer Hill, 171005, Shimla*
[a)] Corresponding author; 00000abhisheksharma@gmail.com
[b)] veersinghrangra@gmail.com

Abstract. β−Ga_2O_3 nanostructures were synthesized via a solid-state combustion method and thoroughly investigated to determine the influence of annealing temperature on their structural, morphological, and optical properties. With increasing annealing temperature, the peaks in both X-ray diffraction (XRD) and Raman spectra became more defined and intense, and the full width at half maximum (FWHM) narrowed which indicates enhanced crystallinity. Elemental analysis using Energy-dispersive X-ray spectroscopy (EDS) identified gallium (Ga) and oxygen (O) as the primary constituents, with no traces of impurities detected. The optical behavior, analyzed through UV-Vis diffuse reflectance spectroscopy (DRS), revealed absorption edges in the range of 236–241 nm, and the corresponding optical band gap values for β−Ga_2O_3 nanostructures are in the range of 4.5 to 4.6 eV. Annealing at 900 °C leads to improved crystallinity and fewer defects, producing an increased absorption intensity.

Keywords. β−Ga_2O_3, Annealing temperature, PXRD, FESEM, Raman Spectroscopy, UV-Vis Spectroscopy.

INTRODUCTION

Gallium oxide has attracted considerable research attention due to its promising applications in gas sensing, catalysis, and optoelectronics [1]. Gallium oxide (Ga_2O_3) exists in five polymorphic forms—α, β, γ, δ, and ε—each exhibiting distinct structural and thermal properties [2]. Among these, β−Ga_2O_3 is the most thermodynamically stable phase, crystallizing in a monoclinic structure [3], whereas the other polymorphs are metastable and typically transform into the β-phase at elevated temperatures [4]. β−Ga_2O_3 is a direct wide bandgap semiconductor with a bandgap ranging from approximately 4.5 to 4.9 eV [5]. While β−Ga_2O_3 is the stable phase, γ −Ga_2O_3 is metastable and undergoes a phase transformation to β−Ga_2O_3 when heated above 800 °C. Due to its instability, γ−Ga_2O_3 is not typically obtained via conventional synthesis methods [6]. Building upon this understanding, we explored the potential of the solid-state combustion technique to **synthesize** nanostructured β−Ga_2O_3 by annealing, γ−Ga_2O_3 at temperatures ranging from 800 °C to 1000 °C. Gallium nitrate and urea were employed as the oxidizing agent and fuel, respectively, in stoichiometric molar ratios. To confirm the formation of the β-monoclinic phase and investigate the material's properties, we employed powder X-ray diffraction (PXRD), field emission scanning electron microscopy (FESEM), and energy-dispersive X-ray spectroscopy (EDS) for structural and morphological characterization. The lattice vibrations of β−Ga_2O_3 were studied using Raman spectroscopy, while its optical properties were further evaluated through UV-Vis diffuse reflectance spectroscopy (DRS).

METHODOLOGY

The β−Ga_2O_3 samples were synthesized using a solid-state combustion method [7], which relies on self-sustaining redox reactions. Gallium nitrate octahydrate ($Ga(NO_3)_3{\cdot}8H_2O$) and urea ($CO(NH_2)_2$), both of 99.99% purity and purchased from CDH, were employed as the oxidizing agent and fuel, respectively. These precursors were mixed in their stoichiometric molar ratios and thoroughly ground using a mortar and pestle for approximately 45-50 minutes to form a homogeneous paste. The resulting mixture was placed into a 50 mL alumina crucible and introduced into a muffle furnace preheated to 500 ± 10 °C, where it was maintained until complete decomposition occurred. After cooling to room temperature within the furnace, γ−Ga_2O_3 powder was obtained as an intermediate phase. Subsequently, this intermediate was subjected to annealing at 800 °C, 900 °C, and 1000 °C for 3 hours in a high-temperature furnace using a separate alumina crucible. Upon natural cooling to ambient conditions, the final β−Ga_2O_3 phase was achieved.

RESULTS AND DISCUSSION

The XRD patterns of the β−Ga_2O_3 samples subjected to different annealing temperatures are shown in **Fig. 1(a)**. The primary diffraction peak (-202) of the three samples aligns well with the standard card (JCPDS card no-41-1103) corresponding to the β−Ga_2O_3. No additional phases were observed, confirming the transformation of synthesized γ−Ga_2O_3 into the monoclinic phase after annealing at temperatures of 800 °C, 900 °C, and 1000 °C for 3 hours. Average crystallite size is calculated by using standard Debye-Scherrer's formula $\boldsymbol{D = K * \lambda/\beta * cos(\theta)}$[8] where β is the full-width-at-half-maximum (FWHM) of diffraction peak, θ is the Bragg angle, λ = 1.5405 Å, D is the crystallite size, and K (numerical value 0.89) is the shape factor. The increase in crystallite size observed with higher annealing temperatures is due to increased atomic mobility, which aids in

grain growth. At higher temperatures, atoms receive sufficient thermal energy to overcome diffusion barriers, resulting in fewer grain boundaries and larger crystallites.

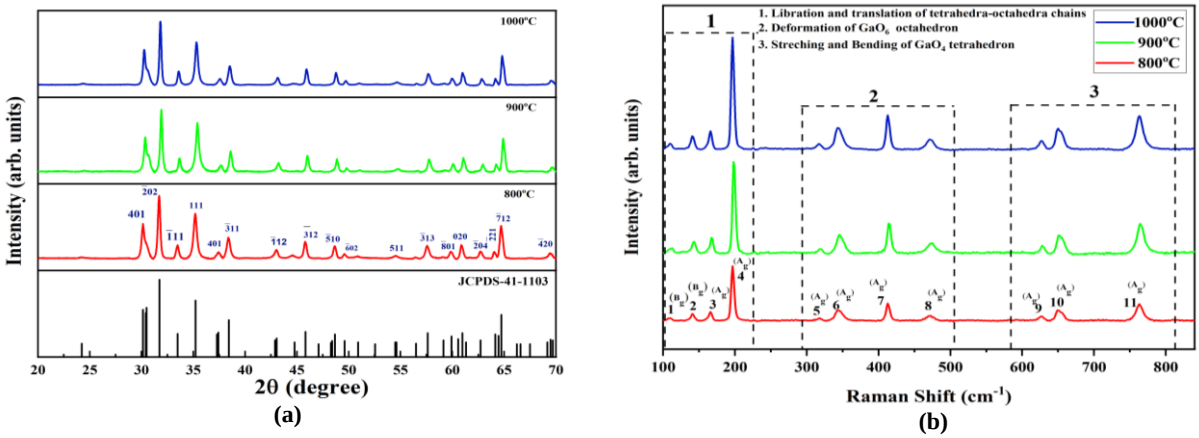


Fig. 1. (a) XRD patterns and (b) Raman spectra of β− Ga_2O_3 samples annealed at 800, 900, and 1000 °C.

Additionally, the rise in peak intensity with increased temperature indicates improved crystallinity. Elevated temperatures provide the thermal energy needed for atoms to move into more stable positions, reducing structural defects and disorder.

TABLE 1: Structural parameters of β− Ga_2O_3 annealed at 800, 900, and 1000 °C, calculated from the most intense (−202) diffraction peak.

Sample Annealing Temperature (ºC)	2θ (Degree)	FWHM (Degree)	Intensity (cps)	Crystallite size (nm)	Dislocation Density (δ*10^{-3}) nm^{-2}
800	31.69	0.2708	8461	28.22	1.25
900	31.68	0.2437	10403	31.36	1.01
1000	31.69	0.2284	12608	33.46	0.89

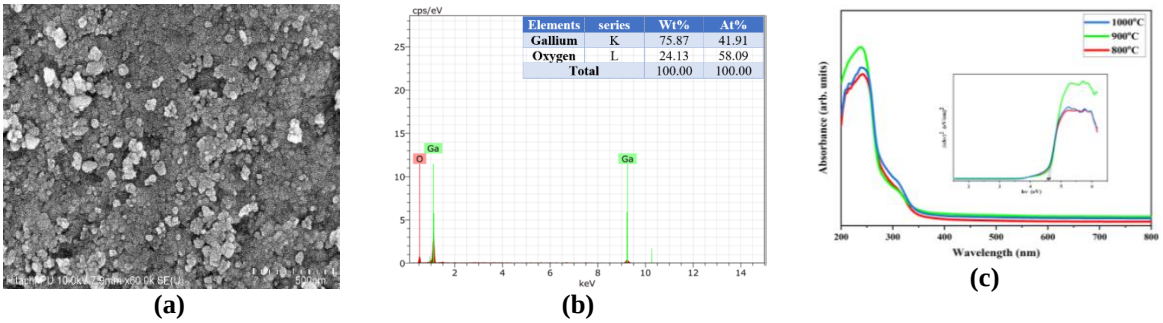


Figure 2. (a) FESEM micrograph **(b)** EDS spectra of β−Ga_2O_3 samples annealed at 900 °C **(c)** UV-Vis DRS absorbance spectra of β−Ga_2O_3 samples annealed at 800, 900, and 1000 °C (inset: tauc's plot).

Fig. 1(b) displays the room-temperature Raman spectra of β−Ga_2O_3 samples annealed at 800, 900, and 1000 °C. The Raman spectra of our samples distinctly reveals 11 vibrational peaks at 112.4, 143.4, 167.4, 198.5, 319.5, 345.2, 414.7, 474.3, 628.6, 653.2, and 764.5 cm^{-1}, aligning well with findings from another research work [9]. Three prominent high-frequency modes observed at 628.6, 653.2, and 764.5 cm^{-1} are associated with the stretching and bending vibrations of GaO_4 tetrahedra within the 500–770 cm^{-1} spectral range. Four mid-frequency modes, centered at 319.5, 345.2, 414.7, and 474.3 cm^{-1}, are attributed to distortions in GaO_6 octahedra within the 310–480 cm^{-1} range [10]. Vibrational modes below 200 cm^{-1}, detected at 112.4, 143.4, 167.4, and 198.5 cm^{-1}, are associated with the translational motion and release of tetrahedra–octahedra chain structures [10]. The Raman peak at 198 cm^{-1} for the sample annealed at 1000 °C is the most intense and exhibits the narrowest FWHM, reflecting improved crystallinity relative to the samples treated at 800 °C and 900 °C. **Fig. 2(a)** shows the electron micrographs of the β−Ga_2O_3 annealed at 900 °C. FESEM images shows spherical shaped polydisperse nanostructures with irregular morphology for all the samples. **Fig. 2(b)** displays the energy dispersive spectrum (EDS) of β−Ga_2O_3 annealed at 900 °C, revealing no impurity peaks. Ga and O are identified as the primary elements in the samples, comprising 41.91 and 58.09 atomic percentages, respectively. **Fig. 2(c)** shows UV-Vis DRS absorbance spectra of β−Ga_2O_3 samples annealed at different temperatures, revealing an absorbance edge occurring in the 236 to 242 nm range. The optical band gap was derived from the absorption data using Tauc's equation.$(\boldsymbol{\alpha h\nu})^{\boldsymbol{1/n}} = \boldsymbol{A(h\nu - Eg)}$ [11], where α denotes the absorption coefficient, *h*

stands for Planck's constant, v is the incident photon frequency, and E_g refers to the optical band gap energy and A is constant, resulting in optical bandgap of 4.5 to 4.6 eV for synthesized samples. The variation in absorption intensity with annealing temperature can be explained by changes in crystallinity and defect density. At 800 °C, lower crystallinity and a higher defect concentration result in reduced absorption intensity. In contrast, annealing at 900 °C leads to improved crystallinity and fewer defects, producing an increased absorption intensity. However, at 1000 °C, excessive grain growth and potential defect formation may cause a decrease in absorption.

CONCLUSION

In this study, β−Ga_2O_3 nanostructures were synthesized using solid-state combustion and rigorously characterized to explore the impact of annealing temperature on their structural, morphological, and optical attributes. Both XRD and Raman spectroscopy indicated that as the annealing temperature increases, there is an enhancement in diffraction peak intensity and a decrease in FWHM. FESEM micrographs shows polydisperse spherical shaped nanostructures with irregular morphology for all the annealed samples. EDS analysis confirmed that the samples primarily consist of Ga and O, without any impurities. UV-Vis DRS revealed absorption edges in the range of 236–241 nm, with the corresponding optical band gap values ranging from 4.5 to 4.6 eV**.** Moreover, the sample annealed at 900 °C exhibited better crystallinity and fewer defects, resulting in enhanced absorption intensity. These findings suggest that annealing temperature plays a crucial role in determining the crystallinity and optical properties of β−Ga_2O_3 nanostructures.

ACKNOWLEDGMENTS

Abhishek Sharma gratefully acknowledges Himachal Pradesh University for providing access to laboratory facilities, and the DST-INSPIRE program, Government of India, for awarding him the Junior Research Fellowship (Grant No. DST/INSPIRE Fellowship/2021/IF210391), which made this work possible.

REFERENCES

1. B. Fu, Z. Jia, W. Mu, Y. Yin, J. Zhang, and X. Tao, "A review of β-ga2o3 single crystal defects, their effects on device performance and their formation mechanism," Journal of Semiconductors 40, 011804 (2019).
2.F. Shi and H. Qiao, "Preparations, properties and applications of gallium oxide nanomaterials–a review," Nano Select 3, 348–373 (2022).
3. M. Higashiwaki, K. Sasaki, H. Murakami, Y. Kumagai, A. Koukitu, A. Kuramata, T. Masui, and S. Yamakoshi, "Recent progress in ga2o3 power devices," Semiconductor Science and Technology 31, 034001 (2016).
4. F. Shi and H. Qiao, "Preparations, properties and applications of gallium oxide nanomaterials–a review," Nano Select 3, 348–373 (2022).
5. S. Geller, "Crystal structure of β-ga2o3," The Journal of Chemical Physics 33, 676–684 (1960).
6. C. O. Areán, A. L. Bellan, M. P. Mentruit, M. R. Delgado, and G. T. Palomino, "Preparation and characterization of mesoporous γ-ga2o3," Microporous and mesoporous materials 40, 35–42 (2000).
7 Sharma, Abhishek, and Vir Singh Rangra. "Effect of gadolinium doping on the structural, morphological, vibrational, and optical properties of β− Ga2O3: A solid-state combustion approach." Ceramics International (2025).
8. Sharma, Abhishek, and Vir Singh Rangra. "Investigating the structural, morphological, electrical, and optical characteristics of β-Ga2O3 synthesized by solid-state combustion." Journal of Materials Science: Materials in Electronics 35.33 (2024): 2134.
9. D. Dohy, G. Lucazeau, and A. Revcolevschi, "Raman spectra and valence force field of single-crystalline β ga2o3," Journal of Solid-State Chemistry 45, 180–192 (1982).
10. J. Hu, B. Yu, and J. Zhou, "New generation beta-gallium oxide nanomaterials: Growth and performances in electronic devices," Advanced Engineering Materials 25, 2300688 (2023).
11. Muramba, V. W., Ali, A. I., & Nel, J. M. (2023). Structural and optical characterization of beta-gallium oxide. Journal of Materials Science: Materials in Electronics, 34(34), 2221.

Site-Selective Photoluminescence and Multi-Color Emission via Vis/NIR Dual Mode Excitation of Rare-Earth Doped Inorganic Nanophosphors

Ib Singh Deo[1], Mohini Gupta[1], and G. Vijaya Prakash[1,*]

[1]*Nanophotonics Lab, Department of Physics, Indian Institute of Technology Delhi, New Delhi, 110016 INDIA*

[*]Corresponding author: prakash@physics.iitd.ac.in

Abstract. Numerous possibilities open in the domain of nanophosphors when excitation is shifted from 980 nm to multiple excitation wavelengths. Multi chromaticity can be obtained by variation in chemical composition, phase, and structure, but controlling the color spectrum from a fixed composition is challenging. Here, we present an adaptable method for achieving modulated luminescence and site selectivity throughout the visible spectrum through dual-mode excitation. A series of photostable, cubic $KLaF_4$: $Er^{3+}/Yb^{3+}/Eu^{3+}$ nanoparticles bearing a size of nearly 9 nm have been synthesized through the wet chemical method. Powder X-ray diffraction and High-Resolution Transmission Electron Microscopy reflect on nanoparticles' crystallinity and nano-size distribution. Spatial photoluminescence mapping substantiates the homogeneity of doping and applicability of the nanoparticles. Thus, by utilizing the intense dual-wavelength photoluminescence signal, this work can be expanded to explore similar effects in other systems pumped by different wavelength lasers and introduces fresh opportunities for applications such as upconversion color displays, white light generation, super-resolution microscopy, and bioimaging.

Keywords: Site-selective photoluminescence, nanophosphor, rare-earth, upconversion, multi chromaticity

INTRODUCTION

The most challenging issue in materials science is the optimization, modification, and colour tunability of a photo-responsive material that can produce a diverse spectrum of colours. Identifying materials that generate different colours can transform domains, such as optical sensing, imaging, and display [1-3]. The emission wavelength is one of the most prominent characteristics of a luminous material. Modifying the excitation source or introducing optically active ions into the system makes it possible to manipulate the emission wavelength [4]. Owing to the broad spectrum of applications in material science, biology, physics, chemistry, and information technology, the search for new and promising multimodal, luminous materials is still on [5,6].

In recent years, a substantial advancement of lanthanide-doped nanomaterials has developed novel platforms for multi-chromatic emission. Surprisingly, a single lanthanide activator with ladder-like ordered energy levels can produce a variety of emission bands ranging from ultraviolet to near-infrared (NIR) wavelengths [7]. Customizing the power density under single wavelength excitation can change the emission color, which is an appealing feature of these materials.

The present work reports the site-selective luminescence from a singular system that is accomplished not by only changing the dopants but also by simultaneously exciting with various excitation wavelengths. There are only a few papers on these multiple excitations [8,9]. Nonetheless, no attempts have been made to use excitation wavelengths in the visible (405 nm) and near-infrared domains (980 nm). In this study, fluoride nano matrix has been doped with various molar percentages of rare earth (RE^{3+}) ions like Er^{3+}, Yb^{3+}, and Eu^{3+}. Yb^{3+} acts as a sensitizer, Er^{3+} is used as an activator, and Eu^{3+} is used as a spectroscopic probe. $KLaF_4$: Er^{3+}, Yb^{3+}, and Eu^{3+} have been excited under simultaneous visible (405 nm) and near infrared (NIR) wavelengths (980 nm), making it a dual excitation nanophosphor/dual mode spectral emitter, and its efficacy in site selectivity, and spatial photoluminescence mapping is being monitored.

MATERIAL SYNTHESIS

The method of synthesis used for both the undoped and doped $KLaF_4$ is the wet chemical method. In 10 ml of methanol, 1 mmol of $La(acac)_3.xH_2O$ is dissolved. 4 mmol of KF solution is added dropwise, and the solution is continuously stirred, resulting in a milky solution. The reaction is subsequently maintained at 65°C for 4 hours while being continuously agitated. The solution is brought to room temperature, centrifuged, and washed with

methanol three to four times to eliminate contaminants. For doping the precursor solution, 1 mmol of $ErCl_3.6H_20$ and 1 mmol $YbCl_3.6H_20$ are dissolved in methanol to produce their respective lanthanide solutions. These solutions are then added to the precursor solution dropwise and stirred.

RESULTS AND DISCUSSIONS

The crystal structure and phase of the host lattice $KLaF_4$ doped with RE^{3+} ions has been validated through Powder X-ray diffraction (PXRD). The Fig. 1 (a), illustrates the powder x-ray diffraction of both pure and doped $KLaF_4$ nanoparticles recorded at room temperature and indexed with the space group Fm-3m (#225). The diffraction peaks match the standard data for $KLaF_4$ (JCPDS 75-2020). The diffraction peaks' widening and relative intensity enhancement confirm the nano-dimensionality of crystallites. The decrease in the unit cell volume caused by the replacement of a large ionic radius ion (La^{3+}) by a smaller ionic radius ion (Er^{3+}, Yb^{3+}, and Eu^{3+}) in the host lattice results in the shifting of XRD reflection plane (1 1 1) towards higher diffraction angle by 1º–2º. Given the consistent profile of each diffractogram, it can be inferred that no impurity phases are present and that the dopants have been successfully incorporated into the host lattice.

The HR-TEM image is shown in Fig. 1 (b). The average sizes of the crystallites and particles, as determined by PXRD and HR-TEM, are 9.00 nm and 8.76 nm, respectively. The (1 1 1) reflection plane has a d-spacing of 0.345 nm and 0.340 nm, as determined from PXRD and HR-TEM, respectively. The particle size and d-spacing align with the PXRD data. Based on the Rietveld refinement, it was found that the pure cubic phase of $KLaF_4$ has a similar structure to the cubic CaF_2 fluorite. This refinement involves utilizing a high symmetry cation site for CaF_2 (Fm-3m) internal standards. In this case, the Ca^{2+} (4a) site is randomly filled with a combination of K^+ and La^{3+} ions and F^- ions at site 8c. The unit cell parameters a (Å) and GOF have been determined to be 5.98(50) and 1.98 S, respectively.

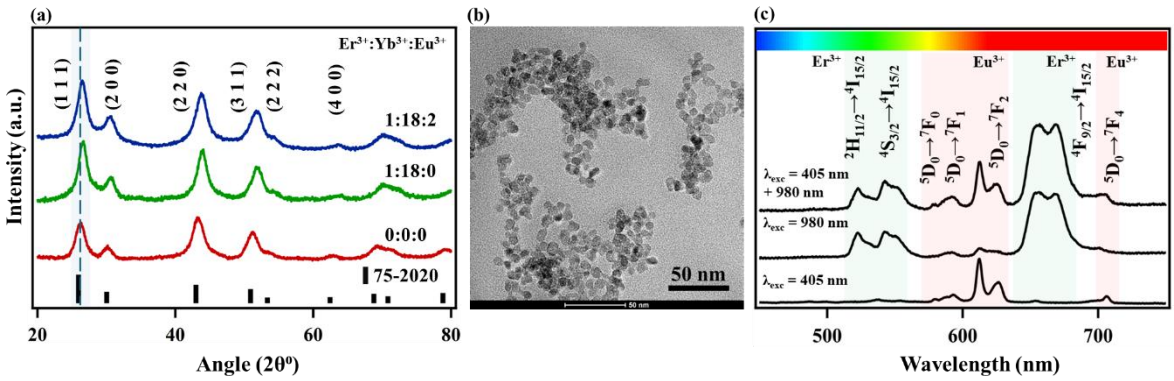


FIGURE 1. (a) PXRD patterns of undoped and doped $KLaF_4$ nanophosphors measured at room temperature, (b) HR-TEM image, (c) photoluminescence under single and dual laser excitations of $KLaF_4$: 1% Er^{3+}/18% Yb^{3+}/2% Eu^{3+}.

Site selectivity is a key strategy used to target a specific dopant site. Figure 1 (c) represents the single and dual-mode excited photoluminescence (PL) of $KLaF_4$: 1% Er^{3+}/18% Yb^{3+}/2% Eu^{3+}. Excitation at 980 nm in the near-infrared (NIR) efficiently targets the Er^{3+} sites, while 405 nm excitation preferentially impacts the Eu^{3+} sites, and dual excitation (Vis/NIR) results in an enhanced PL intensity targeting both Er^{3+} and Eu^{3+} sites.

The relationship between the laser excitation power at 980 nm and emission intensity sheds light on the localization of two-photon excitation in three dimensions. This localization minimizes potential photobleaching or photodamage of the sample that lies out of the focal point. Simultaneously manipulating the wavelength of excitation and power of the laser makes it possible to achieve site-selective excitation, which can be visualized through dual mode excitation. Under 405 nm excitation, Eu^{3+} emission peaks at 593 nm ($^5D_0 \rightarrow {}^7F_1$) and 612 nm ($^5D_0 \rightarrow {}^7F_2$) can be seen because of the radiative transition in the Eu^{3+} ion. The site-selective spectroscopic investigation of $KLaF_4$ doped with Er^{3+}, Yb^{3+}, and Eu^{3+} demonstrates upconversion (UC) phenomena under laser excitation of 980 nm. Eu^{3+}, which possesses no direct excitation under 980 nm, exhibits upconversion because of effective energy transfer from the sensitizer (Yb^{3+}) to the activator (Eu^{3+}). At approximately 524 nm ($^2H_{11/2} \rightarrow {}^4I_{15/2}$) and 543 nm ($^4S_{3/2} \rightarrow {}^4I_{15/2}$), an intense green emission corresponding to Er^{3+} is observed. Additionally, red emission of Er^{3+} and Eu^{3+} is observed at 658 nm ($^4F_{9/2} \rightarrow {}^4I_{15/2}$) and 593 nm ($^5D_0 \rightarrow {}^7F_1$), 612 nm ($^5D_0 \rightarrow {}^7F_2$), respectively. The UC emission is the result of Energy Transfer (ET) from Yb^{3+} to activator ions Er^{3+} and Eu^{3+}, as well as Ground

State Absorption (GSA) and Excited State Absorption (ESA) processes. The population of green and red emission levels increased because of non-radiative transitions of the Yb^{3+} ion ($^4F_{7/2}$). The different emissions, i.e. green and red are the result of radiative transitions $^2H_{11/2} \rightarrow {}^4I_{15/2}$ (524 nm (Er^{3+})), $^4S_{3/2} \rightarrow {}^4I_{15/2}$ (543 nm (Er^{3+})), and $^4F_{9/2} \rightarrow {}^4I_{15/2}$ (658 nm (Er^{3+})), 593 nm ($^5D_0 \rightarrow {}^7F_1$ (Eu^{3+})), 612 nm ($^5D_0 \rightarrow {}^7F_2$ (Er^{3+})). Under dual excitation, following the direct excitation of Eu^{3+} under 405 nm laser, 980 nm excitation introduces orange/red colour emission because of the presence of Er^{3+} emissions via Energy Transfer Upconversion and Back Energy Transfer between Yb^{3+}-Er^{3+} ions, as well as the Cross Energy Transfer process between Yb^{3+}-Eu^{3+} ions. Interestingly, the effective energy transfer from sensitizer (Yb^{3+}) to activators (Er^{3+} and Eu^{3+}) is evident from the enhanced Er^{3+} and Eu^{3+} emission observed under dual Vis/NIR excitation.

Hence, owing to the small size and diverse emission capabilities, these nanophosphors can be seamlessly integrated into biological systems and serve as biolabels for forensic purposes, as well as have great potential for applications such as anticounterfeiting, optical sensing, spectrum conversion in solar cells, and colour display.

ACKNOWLEDGMENTS

ISD thanks the DST-INSPIRE fellowship for her doctoral research fellowship. The authors also thank the department and the institute research facilities of IIT Delhi.

REFERENCES

1. M. Han, X. Gao, J. Z. Su, S. Nie, Nat. Biotechnol. Vol. 19, pp. 631-635 (2001).
2. M. Gupta, R. Nagarajan, C. Ramamurthy, P. Vivekanandan, G. Vijaya Prakash, Dalton Trans. Vol. 50, pp. 5197-5207 (2021).
3. A. L. Antaris, H. Chen, K. Cheng, Y. Sun, G. Hong, C. Qu, S. Diao, Z. Deng, X. Hu, B. Zhang, et al. Nat. Mater. Vol. 15, pp. 235-242 (2016).
4. M. Gupta, M. Adnan, R. Nagarajan, G. Vijaya Prakash, ACS Omega, Vol. 4, pp. 2275-2282 (2019).
5. M. Gupta, I. S. Deo, R. Nagarajan, G. Vijaya Prakash, Opt. Mater. Vol. 133, pp. 113045 (2022).
6. M. A. Triana, E. L. Hsiang, C. Zhang, Y. Dong, S. T. Wu, ACS Energy Lett. Vol. 7, pp. 1001-1020 (2022).
7. Z. Lei, X. Ling, Q. Mei, S. Fu, J. Zhang, Y. Zhang, Adv. Mater. Vol. 32, pp. 1906225 (2020).
8. X. Wang, Y. Wang, Y. Bu, J. Cheng, X. Yan, Phys. Chem. Chem. Phys. Vol. 20, pp. 22114-22122 (2018).
9. Y. Yao, C. Xu, Y. Zheng, C. Yang, P. Liu, J. Ding, T. Jia, J. Qiu, S. Zhang, Z. Sun, RSC Adv. Vol. 6, pp. 3440-3445 (2016).

AuNPs@Ag Nanodendrites for Volatile Organic Compound Detection based on Surface Enhanced Raman Scattering

V.S. Vendamani[1], S. Venugopal Rao[1,2,a]

[1]*School of Physics, University of Hyderabad, Hyderabad 500046, Telangana, India.*
[2]*Advanced Centre of Research in High Energy Materials (ACRHEM), DRDO Industry Academia - Centre of Excellence (DIA-COE), University of Hyderabad, Hyderabad, 500046, India.*

[a)]*Corresponding author:* ***soma_venu@uohyd.ac.in, somavenu@gmail.com***

Abstract. We demonstrate the fabrication and application of AuNPs decorated AgNDs for SERS-based detection of volatile organic compounds (VOC) such as acetone and ethanol. A facile electroless deposition approach has been adopted to make symmetric AgNDs with high-density hot spots. The stability and sensing capabilities were enthused to the next level by incorporating AuNPs over the AgNDs surface. The characteristic signatures of acetone and ethanol vapor at around 776 cm^{-1} and 842 cm^{-1}, correspondingly, are observed in the surface-enhanced Raman signals. The trace-level detection of acetone and ethanol in vapor-phase is important for diagnosing diabetes.

INTRODUCTION

Volatile organic compounds (VOCs) and there presents in the atmosphere is highly toxic and even carcinogenic [1, 2]. According to recent reports, >5 million premature deaths are caused worldwide every year due to indoor and outdoor VOC pollutants [3]. Thus, the monitoring of VOCs is critical in many fields, such as chemical sensing, health care diagnosis, environmental monitoring, and homeland security [4-5]. Additionally, acetone is an expansive chemical used in the printing industry and household products. Moreover, the vapor of acetone has been recognized as a significant element of environmental tobacco smoke (ETS), and it results in adversative health problems like anesthetizing the central nervous organism and damage to the pancreas, kidneys, and liver [6]. The various levels of acetone and ethanol are directly correlated to the level of plasma glucose [7]. As well as, the exhaled acetone is identified as a breath biomarker for diagnosing diabetes [8]. Nevertheless, commonly human organic systems are not capable enough to distinguish these volatile threats. Consequently, the sensitive and effective sensing of VOCs is important for securing human safety.

Raman spectroscopy is an analytical vibrational technique with great potential to get molecular structures. The drawbacks of Raman spectroscopy limited its practical implementations in VOC detection. After extensive research, surface-enhanced Raman spectroscopy (SERS) is recognized as a robust analytical technique over the existing gas/vapor sensing technology due to its high spectral resolution and lower detection limits [9-11]. SERS has been applied in sensing diverse threats of molecules with high sensitivity and rapid response. In SERS, the enormous electric field occurs at the nano region of plasmonic nanostructures, which results in the enhanced Raman signal in the order of 10^{14} [12]. The literature has demonstrated that SERS has been used for single molecular detection [16]. SERS also reportedly provides chemical fingerprints of different VOC molecules [13].

To improve the capability of SERS-based vapor sensing, we introduced three-dimensional (3D) nanostructures to fabricate SERS substrates [14,15]. Silver nanodendrites (AgNDs) are distinct plasmonic nanostructures for enhanced Raman sensing. Their abundant trunks and branches offer adequate hot-spot locations, resulting in improved detection capabilities and sensibilities. The long-term approachability of AgNDs will be improved by passivating/decorating other materials like 2D materials or functional materials, etc. In this strategy, we proposed the distribution of AuNPs over AgNDs for compelling sensibility.

EXPERIMENTAL DETAILS

The SERS-active AgNDs are prepared following a facile wet chemical process, as reported in our earlier findings [14,15]. In brief, large-scale AgND structures are obtained by immersing Si wafer into a electrolyte composed with 30 mM:4.6 M :: $AgNO_3$: H at 30 ^{0}C. The stability and sensitivity have been enriched by introducing AuNPs decoration on AgNDs by a simple galvanic deposition approach [16].

Morphological and elemental examinations are carried out by a field emission scanning electron microscopic (FESEM; Carl ZEISS, Ultra 55–5 eV for imaging, and 20 eV for EDX) instrument with energy dispersive X-ray spectroscopy. Crystalline properties were analyzed by selective area electron diffraction (SAED) studies. Further sensing abilities of AuNPs decorated AgNDs are demonstrated by the micro-Raman spectrophotometer (Horiba LabRam Raman Spectrometer) with a 532 nm excitation wavelength. The acetone and ethanol in vapor phase probed to test the sensibilities of the proposed AuNPs@AgNDs substrates. Acetone and ethanol vapors are generated simply by dwelling the sample in a 100 ml glass beaker with 1 ml of acetone/ethanol. The glass beaker was covered with parafilm and kept for complete evaporation of solvents at room temperature. Subsequently, the samples are evacuated from the beaker and covered with a glass coverslip for Raman/SERS studies.

RESULTS AND DISCUSSIONS

The morphological signatures of AgNDs is presented in Figure 1(a). The FESEM image in Fig. 1(a) shows highly symmetric and dense AgNDs, consisting of multiple branches connected to a central stem rod. The branches are in the range of 7 µm to 5 µm. The branches make an angle of 50^0-65^0 w.r.t to a central stem. Further, AuNPs are decorated on AgNDs to promote high-density hot-spot locations, resulting in a superior Raman signal, presented in Fig. 1(b). The size of overall distributed AuNPs is in the range of 30-40 nm. The elemental compositions are extracted by performing EDX measurement, which resulted in a high density of silicon, silver, gold, and a low level of oxygen, as shown in the inset of Fig. 1(b). The inverse fast Fourier transform image is depicted in Fig. 1(c), while Fig. 1(d) shows the selective area electron diffraction image. The obtained inter-planar spacing between lattice fringes of AgNDs was ~0.25 nm, which agrees with the (111) Ag's/Au's crystallographic plane. Furthermore, it proves the principal directional evolution of AgNDs towards the (111) plane.

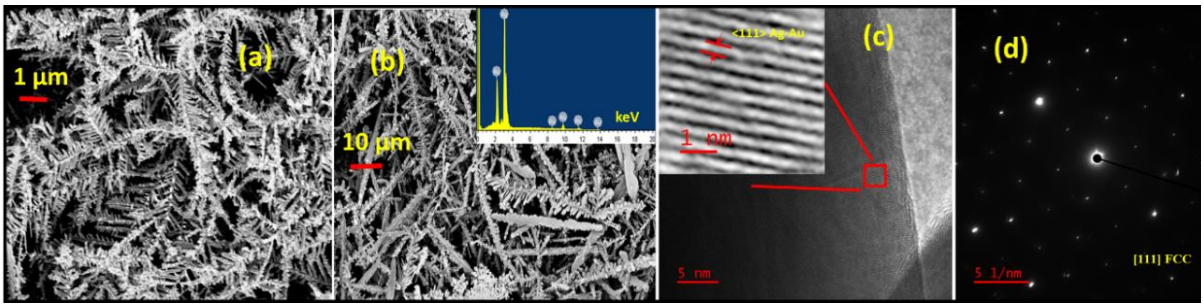


FIGURE 1. (a) Pristine Ag nanodendrites, (b) AuNPs encompassed with AgNDs (inset shows the corresponding EDX spectrum), (c) IFFT image of AuNPs@AgNDs, and (d) corresponding SAED pattern.

A reference spectrum of AuNPs@AgNDs was analyzed before the acetone/ethanol exposure. The standard spectrum of AuNPs@AgNDs is analyzed, which showed no significant peaks associated with acetone/ethanol in the air. Further, the SERS-active AuNPs@AgNDs substrates are utilized to measure acetone and ethanol vapor at low laser power. The results of acetone and ethanol vapor detection at room temperature are presented in Fig. 2. As noticed from Fig. 2(a) and (b), the Raman signatures of acetone and ethanol peaks are pointed at 776 cm^{-1} and 842 cm^{-1}, respectively. The strength of the acetone shows signature peak [shown in Fig. 2(a)] is ~52 counts at low laser power with 10 s integration time, which is the response of SERS-based VOC detection of acetone vapor. Besides, ethanol SERS-based VOC detection showed ~23 (intensity) counts. The observed background noises in the spectrum are from the glass coverslip used for sample surface protection during the Raman examination.

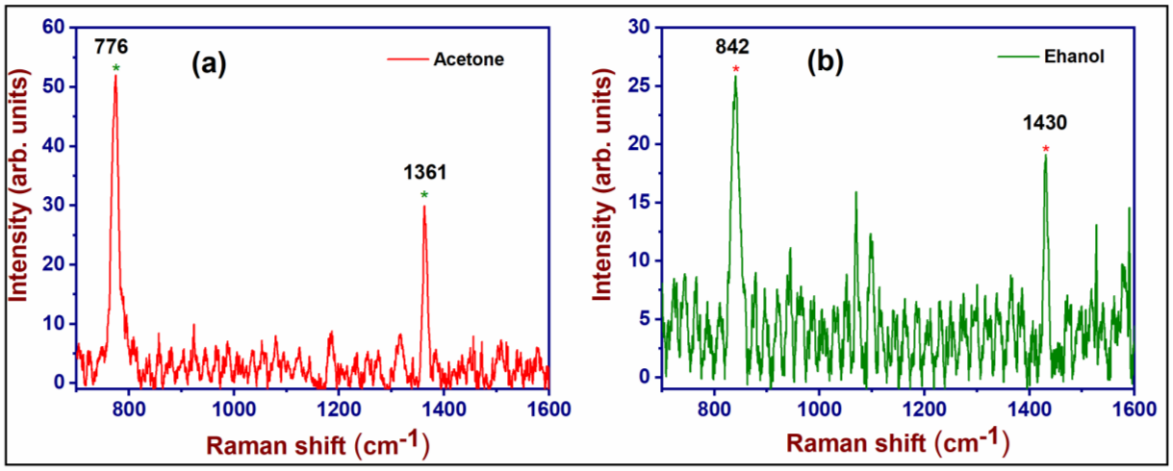


FIGURE 2. (a) Vapor-phase SERS detection of acetone, and (b) Vapor-phase detection of ethanol.

CONCLUSIONS

A study on SERS VOC sensing of acetone and ethanol vapor by AuNPs@AgNDs as a suitable plasmonic substrate is presented here. A simple wet-chemical methodology is introduced to make SERS-active substrates with superior qualities. The fingerprints of acetone and ethanol are noticed at low vapor pressure. The detection of acetone and ethanol is beneficial in the medical sector to get early alarm of diseases. Our future goal is to provide detailed quantification of the detected vapors and sensing other VOCs.

ACKNOWLEDGMENTS

VSV thanks DST for financial assistance through a WISE-PDF fellowship and research grants. We thank ACRHEM (DIA-COE) and the School of Physics, UoH, for the instrumentation facilities provided. V.R. Soma thanks IoE and UoH for financial support through the UOH/ IOE/RC1/RC1-20-016 project.

REFERENCES

1. Y. Dumanoglu, M. Kara, H. Altiok, M. Odabasi, T. Elbir, and A. Bayram, Atmos. Environ. **98**, 168-178 (2014).
2. H. Guo, S. C. Lee, P. K. K. Louie, and KF. Ho, Chemosphere. **57**, 1363-1372 (2004).
3. M. Brauer, G. Freedman, J. Frostad, A. Donkelaar, et al., A. Cohen, Environ. Sci. Technol. **50**, 79-88 (2015).
4. H.C. Menezes, L.C.A. Amorim, L.C. Zenilda, Crit. Rev. Environ. Sci. Technol. **43(1)**, 1–39 (2013).
5. U.A. Laskay, E.J. Kaleta, V.H. Wysocki, Mass Spectrum, Handb. **7**, 419 (2012).
6. Z. Zhang, and G. Li, Microchem. J. **95**, 127–139 (2012).
7. P.R. Galassetti, B. Novak, D. Nemet, C.R. Gottron, et al., Diabetes Technol. Ther. **7**, 1–39 (2005).
8. T.D.C. Minh, D.R. Blake, and P.R. Galassetti, Diabetes Res. Clin. Pract. **97**, 195–205 (2012).
9. X.M. Wang, X. Li, W.H. Liu, C.Y. Han, and X.L. Wang, Materials **14**, 388 (2021).
10. V. Snitka, D. Batiuskaite, I. Bruzaite, U. Lafont, et al., CEAS Space Journal **13**, 509–520 (2021).
11. V.H. Shabtai, H. Sharabi, A. Zaltsman, I. Ron, and A. Pevzner, Analyst **145**, 6334-6341 (2020).
12. B. Sharma, R.R. Frontiera, A.I. Henry, E. Ringe, and R.P.V. Duyne, Mater. Today **15**, 16–25 (2012).
13. S.L. Kleinman, R.R. Frontiera, A.I. Henry, et al., Phys. Chem. Chem. Phys. **15**, 21–36 (2013).
14. V.S. Vendamani, S.V.S. Nageswara Rao, A.P. Pathak, and S. Venugopal Rao, RSC Adv.10, 44747 (2020).
15. V.S. Vendamani, B. Reshma, M.M. Neethish, S.V.S.N. Rao, S. Venugopal Rao, iScience 25, 104849 (2022).
16. V.S. Vendamani, B. Reshma, and Venugopal Rao Soma, J. Alloys and Compounds **959**, 170573 (2023).

TiO_2 Nanotubes and rGO Nanocomposite Integrated Electrochemical Sensor for Cd^{2+} Ion Detection

Dasari Swarna[1], Sushma Tripathi[1], Anjana Biswas[1] and Prathibha C. [1, a)]

[1]*Department of Physics, Sri Sathya Sai Institute of Higher Learning, Anantapur, Andhra Pradesh–515001, India*

[a)]Corresponding author: cprathibha@sssihl.edu.in

Abstract. The nanocomposite of TiO_2 nanotubes and reduced graphene oxide was successfully synthesized via alkaline hydrothermal treatment. The structure and morphology of the composite were determined using XRD, Raman, and SEM characterizations. In this work, the composite was explored as an electrochemical sensor for the cadmium ion detection in water. To analyze the electrochemical performance of the composite, cyclic voltammetry (CV) was performed, whereas differential pulse stripping voltammetry (DPSV) was employed to investigate the quantitative detection of Cd^{2+} ions under optimal conditions. The nanocomposite exhibited enhanced voltametric responses in the detection of Cd^{2+} ions, compared to its components.

Key Words. TiO_2 nanotubes, rGO-TiO_2 nanocomposite, cadmium, electrochemical sensor, sensitivity

INTRODUCTION

Cadmium in its +2 oxidation state is considered a toxic heavy metal that can lead to water and environmental pollution and poses severe health risks. Its permissible limit in drinking water is 3 ppb as per the World Health Organization (WHO) guidelines, and 5 ppb according to the Environmental Protection Agency (EPA) [1]. Hence, it is crucial to detect and quantify Cd (II) ions from aquatic sources.

Protonated titanate nanotubes, with $H_2Ti_3O_7$ phase, are versatile nanomaterials used in various applications in water splitting, photo-catalysis, electronics, dye degradation, and as electrode materials for batteries and supercapacitors. One interesting characteristic of the monoclinic $H_2Ti_3O_7$ is its layered crystallographic structure, which enables researchers to modify its morphology [2]. Graphene, a two-dimensional (2D) nanostructure consisting of sp^2 hybridised atoms of carbon, has gained attention for its strong mechanical properties, excellent electrical and thermal conductivities, high specific surface areas, etc. These advantages led to the development of graphene-based sensors. By combining the beneficial properties of these two nanostructures into a nanocomposite, it is possible to achieve enhanced performance and greater properties.

MATERIALS AND METHODS

All the chemicals used in this study were of research grade and were procured from Merck.

The modified Hummers method was employed to synthesize Graphene Oxide (GO) [3], where a mixture of graphite flakes and $NaNO_3$ was introduced into H_2SO_4 and stirred in an ice bath for 2 h. Then, $KMnO_4$, H_2O_2, and distilled water were added. Further, it was washed with HCl and centrifuged for 30 min. The supernatant was heated to obtain GO. Hydrogen tri-titanate nanotubes($H_2Ti_3O_7$) were synthesized by the alkaline hydrothermal method [2]. The process involved dispersing 80g of NaOH in 200 mL of distilled water, adding 3.5g of TiO_2-anatase, and stirring for 1h to obtain $Na_2Ti_3O_7$. The dispersion was transferred to a 250 mL stainless-steel autoclave lined with Teflon and subjected to heating at 130 °C for 20 h in a hot-air oven. After filtration, the precipitate was thoroughly washed with distilled water, ethanol, and 0.1 M HCl, then dried at 80 °C for 16 hours to yield hydrogen titanate nanotubes (HTNTs) as a white powder. A nanocomposite of rGO and TiO_2 was further synthesized by dispersing HTNT and rGO in a 1:2 ratio into a Milli-Q water and ethanol mixture [4]. To exfoliate GO and achieve homogeneity, the solution was ultrasonicated and stirred for 30 min. The suspension, sealed in a Teflon-lined autoclave, was heated at 100 °C for 8 h in a hot-air oven. The resultant was filtered, rinsed with Milli-Q water and ethanol, and dried in an oven for 10 h at 60 °C to obtain the rGO-TiO_2 nanocomposite.

Preparation of modified electrode for the electrochemical detection of cadmium ions

The synthesized nanocomposite was ultrasonically dispersed in N-Methylpyrrolidone (NMP), containing polyvinylidenefluoride (PVDF) as a binder. A 4 µL aliquot of the suspension was drop-cast onto the surface of a clean glassy carbon electrode (GCE), which was then dried for 8 h in a vacuum oven. Similarly, the sensing electrodes were also prepared with HTNT and rGO for electrochemical studies.

RESULTS AND DISCUSSION

Material Characterisation

The phase of the developed materials was determined using X-ray diffraction studies, performed using an XpertPro PANalytical X-ray diffractometer. Fig. 1 depicts the XRD spectra of rGO, HTNT, and rGO-TiO_2 nanocomposite. The intense peak at 9.86^0 (001) of the HTNT diffractogram represents its layered structure. The peaks at 24.29^0, 28.27^0, and 43.37^0 were indexed to the (110), (310), and (114) crystallographic planes, respectively, and are characteristic peaks of $H_2Ti_3O_7$ (ICSD #98-023-7518). In contrast, the XRD peaks of the composite material located at 25.28^0, 37.80^0, 37.80^0, 48.16^0, 53.90^0, 55.02^0, 62.66^0, 68.74^0, 70.32^0, and 75.05^0 correspond to the anatase-TiO_2 (ICSD #98-017-2914), implying that HTNT has undergone a phase change to anatase-TiO_2 on hydrothermal treatment during the nanocomposite synthesis, and hence the name rGO-TiO_2.

Due to the low rGO content in the rGO–TiO_2 nanocomposite, the characteristic (002) peak at 25.60° [5] is not prominently visible in the XRD pattern, which is consistent with the SEM–EDX results (Fig. 2(c)). It can also be due to the fine dispersion of rGO in the composite[4], and thus overlaps with the (011) strong peak of anatase-TiO_2 at 25.28^0.

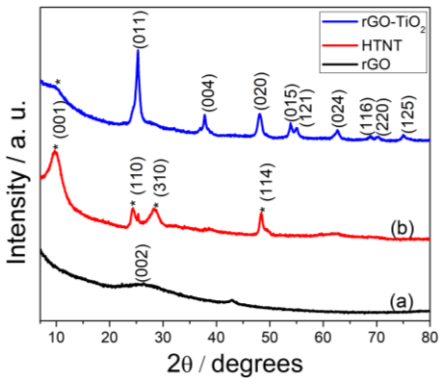


FIGURE 1. XRD patterns

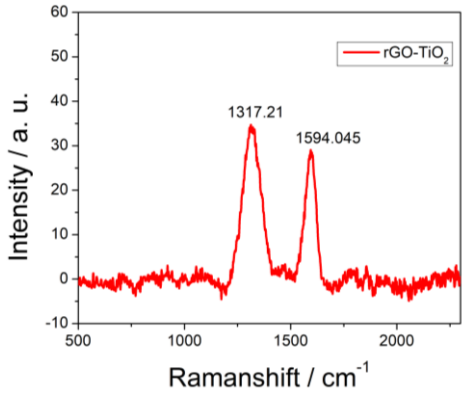


FIGURE 2. Raman spectrum of rGO-TiO_2 composite

Fig. 2 depicts the Raman spectrum of rGO-TiO_2 nanocomposite. The incorporation of rGO in the nanocomposite was indicated by the D- and G-bands observed at 1317.21 and 1594.05 cm^{-1}, respectively. The D-band corresponds to the breathing modes of carbon rings, with six C-atoms, that are activated by defects, and the G-band represents the in-plane vibrations of sp^2-hybridized carbon atoms in the rGO domains [5].

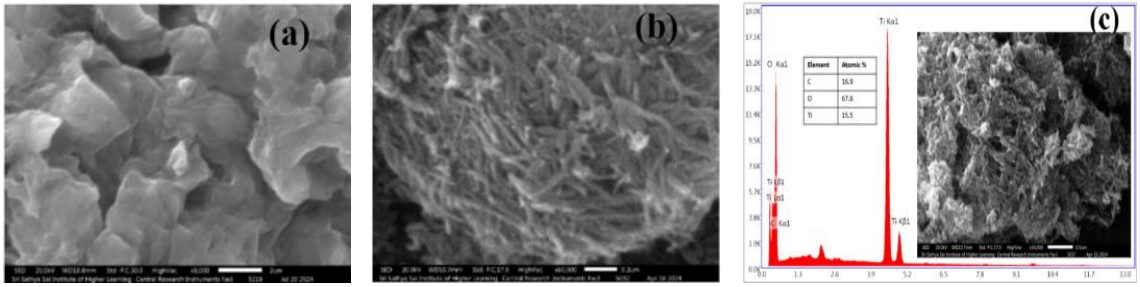


FIGURE 3. SEM plots of (a) GO, (b) HTNT, and (c) rGO-TiO2 composite

Joel IT-300 SEM, paired with EDX, was used for scanning electron microscopy (SEM) and EDX analysis. SEM images revealed flake-like morphology of rGO (Fig. 3(a)), while HTNT exhibited a fibrous nature (Fig. 3(b)). The presence of the C, O, and Ti elements in the EDX spectrum of rGO-TiO_2 composite confirmed the successful integration of rGO and TiO_2 in the composite (Fig. 3(c)).

Application: Electrochemical detection of Cd^{2+} ion in water

The electrochemical studies of the bare and modified GCEs were performed using a three-electrode setup, containing GCE as the working electrode, Ag/AgCl as the reference electrode, and a platinum wire as the counter electrode. Fig. 4(a) depicts the cyclic voltammograms (CVs) recorded between 0 and 1.0 V. Curve *b* of GCE modified with TiO_2 showed lower redox currents than the bare GCE (curve *a*), whereas the rGO and rGO/TiO_2 modified GCEs showed higher redox currents (curves *c* and *d*). This suggested that the addition of rGO enhanced the electrode's surface area and the conductivity of TiO_2 nanotubes by improving the electron transfer.

Differential pulse stripping voltammetry (DPSV) was employed for the quantification of Cd^{2+} ions. As in Fig. 5(a), the rGO/TiO_2/GCE exhibited significantly higher peak current of 23.94 µA, compared to 6.39µA of rGO/ GCE. Additionally, the oxidation potential shifted from -0.496 V to -0.508 V. This enhancement in peak current, along with the negative shift in oxidation potential, provides evidence of the electrocatalytic activity [6] of rGO-TiO_2 for Cd^{2+} oxidation.

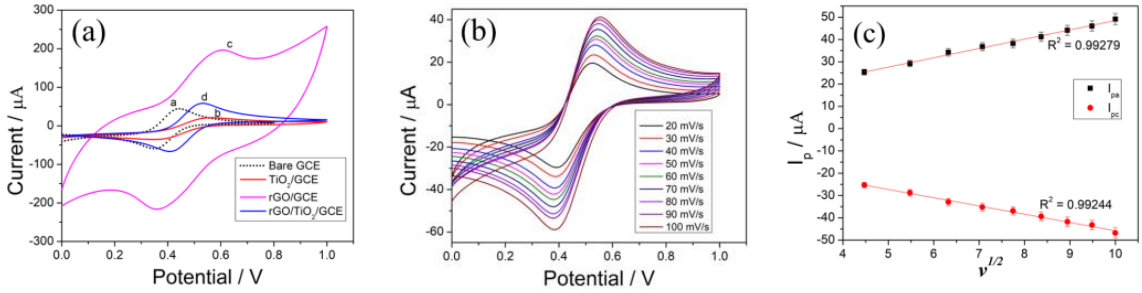


FIGURE 4. CV response in 5mM $K_3Fe(CN)_6$ with 0.1 M KCl (a) of bare and modified GCEs, (b) of GCE modified with rGO-TiO_2 composite at various scan rates, and (c) its corresponding calibration plot

CVs of rGO/TiO_2/GCE by increasing the scan rate from 20-100 mV/s, as shown in Fig. 4(b). The CVs exhibited an increase in both oxidation and reduction currents with increasing scan rate. As shown in Figure 4(c), a linear correlation between peak currents and the square root of the scan rate indicates a diffusion-controlled electrode process [7].

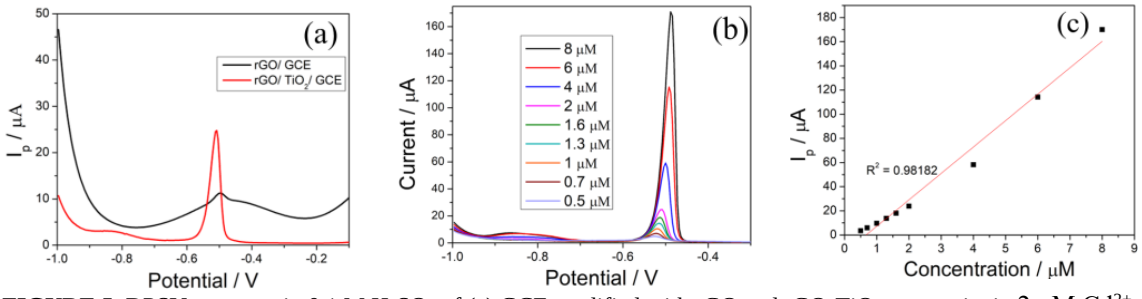


FIGURE 5. DPSV response in 0.1 M H_2SO_4 of (a) GCE modified with rGO and rGO-TiO_2 composite in 2 µM Cd^{2+} ions, (b) GCE modified with rGO-TiO_2 composite at various concentrations of Cd^{2+} ions, and (d) its corresponding calibration plot.

The DPSV experiment was optimized with deposition for 240 s at -1.0 V while stirring the solution, and a quiescence for 20 s. The stripping voltammogram was recorded from -1.0 to -0.1 V, using 50 mV amplitude, 20 ms sample width, 0.5 s pulse period, and 60 ms pulse width. Fig. 5(b) depicts the stripping response of rGO/ TiO_2/ GCE upon successive additions of various concentrations of Cd^{2+}, in 0.1 M H_2SO_4 supporting electrolyte, in the range of 0.5 to 8 µM. The stripping peak current increased with increasing concentration (C) of Cd^{2+} ions, with calibration equation (Fig. 5(c): I (µA) = 21.87 C (µM) – 14.6055, with R^2 = 0.9818.

CONCLUSION

The study investigated the synthesis of a nanocomposite of TiO_2 nanotubes and reduced graphene oxide via hydrothermal treatment of hydrogen titanate nanotubes and graphene oxide. XRD studies confirmed the nanocomposite formation. The obtained composite exhibited the fibrous nature of HTNTs and the flake-like nature of GO. The study also investigated the electrochemical sensing properties of the synthesized nanocomposite by employing DPASV to detect the cadmium ions. The synthesised composite showed a linear response in the range 0.5µM to 8µM concentration of Cd^{2+} ion, with a sensitivity of 21.87 µA/µM.

ACKNOWLEDGEMENT

The authors would like to thank the Central Research Instruments Facility, Prashanthi Nilayam, and Central Research Laboratory, Anantapur, Andhra Pradesh, for providing necessary synthesis and characterization facilities.

REFERENCES

1. S. Maity, ChemElectroChem. **10.3** (2023).
2. A. Biswas and C. Prathibha, Mater. Adv. **3**, 5947–5963 (2022).
3. D. C. Marcano et al., ACS Nano **4**, 4806–4814 (2010).
4. F. Vajedi and H. Dehghani, Mater. Sci. Eng. B **243**, 189–198 (2019).
5. P. Chithaiah, M. M. Raju, G. U. Kulkarni, and C. N. R. Rao, Beilstein J. Nanotechnol. **11**, 68–75 (2020).
6. Y. Fan, K. J. Huang, D. J. Niu, C. P. Yang, and Q. S. Jing, Electrochim. Acta **56**, 4685–4690 (2011).
7. I. Diédhiou, A. Sebei, M. Fall, S. Ben Aoun, R. Zarrougui, and N. Raouafi, Electroanalysis **35**, 1–13 (2023).

Tuning of Structural and Magnetic Properties of $MnFe_2O_4$ Nanoparticles Through Cerium Ion Substitution

Bhaskar Pandey[1, *], R. C. Srivastava[1] H. K. Verma[1] and C. S. Joshi[1]

[1]Department of Physics, G. B. Pant University of Agriculture and Technology, Pantnagar, Uttarakhand, 263145
[*]Corresponding author: bhaskar2000pandey@gmail.com

Abstract. The present study explores the influence of Cerium (Ce) doping on the structural and magnetic properties of $MnFe_2O_4$ nanoparticles (NPs). These nanoparticles were synthesized successfully using the citric acid-assisted sol-gel auto-combustion method. Structural, functional, and magnetic characteristics were studied using X-ray diffraction (XRD), Fourier transform infrared (FTIR) spectroscopy and vibrating sample magnetometer (VSM), respectively. Pristine and Ce-doped NPs both exhibited a pure spinel structure with the Fd3m space group. Lattice parameter and Crystallite size were found in the range of 9.9±0.1 to 13.6±0.2 nm and 8.366±0.007 to 8.395±0.0003 Å, respectively. FTIR spectra showed the presence of characteristic bands corresponding to tetrahedral and octahedral lattice vibrations. Magnetic parameters were found to decrease with the addition of Ce ions, which was further decreased with an increase in the concentration of Ce ions. The variation resulted through larger ionic radii and lower magnetic moment of Ce in comparison to Fe.

Keywords
Spinal Ferrite; Sol-Gel Synthesis; Structural Properties; Magnetic Properties; Rare Earth Doping

INTRODUCTION

Manganese ferrite ($MnFe_2O_4$) is a magnetic ceramic material known for its versatile properties, including significant magnetic behaviour, high electrical resistivity, high thermal and chemical stability [1].It exhibits supercapacitive properties, making it suitable for energy storage applications [2]**.** Additionally, it is utilized in catalysis and high-frequency devices owing to its low eddy current losses. It also finds applications in biomedical fields, as it serves as a contrast agent in magnetic resonance imaging (MRI) [3]. The properties of spinel ferrite are well influenced by the synthesis methods. Sol-gel auto-combustion techniques provide the advantage of precise control over particle size and morphology, thereby enhancing performance of $MnFe_2O_4$ for specific applications. Doping with rare earth ion can alter the elastic, magnetic, structural, optical, and electrical properties [3]. Manganese ferrite nanoparticles (NPs) are mixed spinel ferrites in which Mn^{2+} and Fe^{3+} ions are randomly distributed in tetrahedral and octahedral voids. Ce-doping in spinel ferrites resulted in alteration in various properties such as structural, magnetic, dielectric, optical and photocatalytic degradation efficiency. This led to make it a promising material for various applications in different fields. Additionally, incorporation of cerium improves structural stability and conductivity of spinel ferrite, broadening its potential use in environmental remediation and energy storage devices. The current study investigates how doping with Ce ions affects the structural and magnetic properties of $MnFe_2O_4$ NPs.

MATERIALS AND METHODS

Ce-doped manganese ferrite nanoparticles were synthesized using the sol-gel auto-combustion method. $Mn(NO_3)_3.6H_2O$, $Ce(NO_3)_3.9H_2O$ and $Fe(NO_3)_3.9H_2O$ were used as reactants. $C_6H_8O_7$. H_2O was added as fuel, and ammonium hydroxide [NH_4OH] was used as an oxidant. Metal nitrates and the fuel were weighed in stoichiometric ratios, and each was dissolved separately in double-distilled water. The resulting solutions were then combined and heated on a magnetic stirrer to ensure uniform mixing. When the temperature reached approximately 40 °C, NH_4OH was added dropwise to adjust and maintain the pH at 7 or above 7. The solution was subsequently heated to 90 °C while being continuously stirred. After 4 to 5 hours of continuous stirring, it transformed into a gel-like dense solution. Now, stirring was stopped and the gel was heated up to 120°C until spontaneous ignition occurred. This results in a fluffy and highly voluminous product. The samples were grinded using mortar and pestle to get fine powdered samples. Subsequently, the samples were annealed at 400°C for 2 hours in a muffle furnace. After annealing, cerium-doped manganese ferrite nanoparticles were obtained.

RESULTS AND DISCUSSION

The structural properties of Ce-doped manganese spinel ferrites ($MnCe_xFe_{2-x}O_4$) with (x = 0-0.15, 0.025) were examined using X-ray Diffraction (XRD). XRD patterns were obtained at room temperature across a 2θ range of 20° to 80°. Figure 1(a) shows the XRD patterns of Ce-doped $MnFe_2O_4$. The XRD analysis confirmed that all the samples showed sharp, intense, and characteristic peaks of spinel ferrite having face-centered cubic (FCC) lattice with highly crystalline nature [4]. No extra phase was observed after doping of Ce^{3+} ions in the samples. Various structural parameters, including lattice constant (a), crystallite size (D), unit cell volume (V), and X-ray density (ρ_x), were determined using standard equations (1), (2), and (3) and tabulated in Table 1. The value of lattice constant was found in the range from 8.366 ± 0.007 Å to 8.395 ± 0.0003 Å. The lattice constant was observed to increase slightly as the dopant concentration increased. This is attributed to the larger ionic radius of Ce^{3+} ion (1.04 Å) as compared to the Fe^{3+} ion (0.64 Å). Debye-Scherrer formula (2) was used to calculate the crystallite size of synthesized NPs, and the values are reported in Table 1. The range was found to be 9.9±0.1 to 13.6±0.2 nm. The size was continuously decreased with an increase in Ce^{3+} ion concentration because of the larger size of Ce^{3+} ion compared to Fe^{3+} ion. The incorporation of rare earth Ce^{3+} ions causes lattice distortion, which restricts grain growth, and consequently reduces the crystallite size [5].

$$a = \frac{\lambda\sqrt{(h^2+k^2+l^2)}}{2sin\theta} \quad (1)\ D = \frac{k\lambda}{\beta\cos\theta} \quad (2) \quad \rho_x = \frac{nM}{N_a V} \quad (3)$$

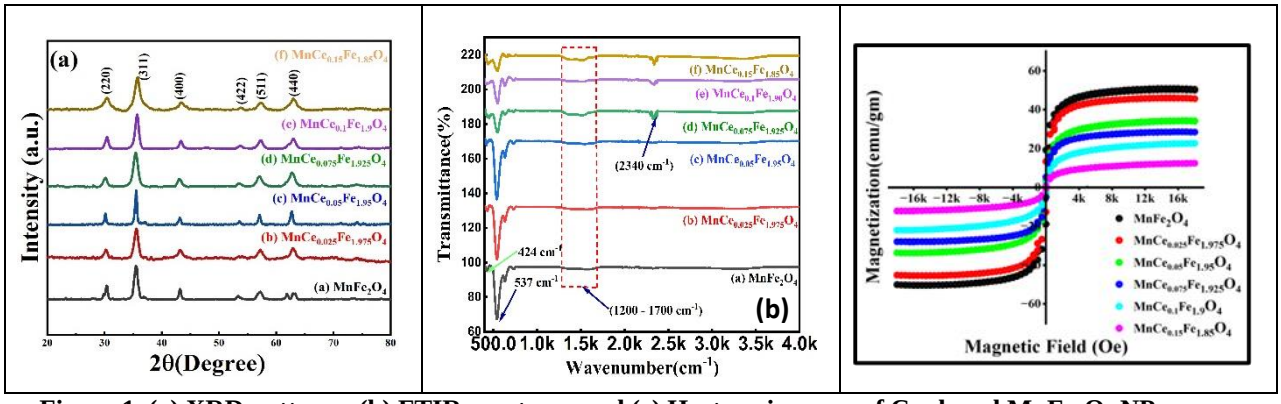


Figure 1. (a) XRD patterns, (b) FTIR spectrum and (c) Hysteresis curve of Ce-doped $MnFe_2O_4$ NPs.

FTIR spectroscopy was used to analyze the functional groups present in the synthesized samples. The FTIR spectra of $MnCe_xFe_{2-x}O_4$ (x = 0.000-0.150, 0.025) NPs were recorded in the range of 400 to 4000 cm^{-1} at room temperature. FTIR spectra of synthesized NPs are shown in Figure 1(b). A broad absorption band appearing in the range of 530 cm^{-1} to 550 cm^{-1} and 410 cm^{-1} to 430 cm^{-1} was attributed to the stretching vibrations of metal–oxygen (M–O) bonds ascribed at the tetrahedral and octahedral sites, respectively. The replacement of Fe^{3+} ions with Ce^{3+} ions is responsible for the slight shift and broadening of absorption bands observed with increasing Ce^{3+} doping [6]. The absence of any additional absorption bands below 800 cm^{-1} confirmed that Ce^{3+} ions were successfully substituted in place of Fe^{3+} ions. Bands observed in the range of 1650–1510 cm^{-1} and 1400–1280 cm^{-1} correspond to asymmetrical and symmetrical vibrations of metal-carbon bond [4].

Table 1. List of structural parameters for Ce-doped $MnFe_2O_4$ nanoparticles.

Sample Composition	Crystallite size D (nm)	Lattice constant (Å)	Volume (~Å^3)	X-ray density (g/cm^3)
$MnFe_2O_4$	13.6±0.2	8.366±0.007	585.54	5.22
$MnCe_{0.025}Fe_{1.975}O_4$	10.2±0.2	8.371±0.004	586.59	5.27
$MnCe_{0.05}Fe_{1.95}O_4$	14.3±0.3	8.3770±0.0006	587.85	5.30
$MnCe_{0.075}Fe_{1.925}O_4$	11.6±0.1	8.3782±0.0001	588.06	5.35
$MnCe_{0.1}Fe_{1.9}O_4$	10.9±0.1	8.3790±0.0004	588.27	5.40
$MnCe_{0.15}Fe_{1.85}O_4$	9.9±0.1	8.395±0.0003	591.65	5.46

The magnetic properties of Ce^{3+} substituted $MnFe_2O_4$ NPs were studied using vibrating sample magnetometer (VSM) at room temperature. Room temperature magnetization versus external field for Ce^{3+} substituted $MnFe_2O_4$ is shown in Figure 1(c). All the NPs exhibited their characteristic ferrimagnetic hysteresis loops. The magnetic behavior of ferrites is influenced by many factors such as lattice imperfections, the type and concentration of dopant ions and the distribution of cations between tetrahedral (A site) and octahedral (B site) voids. The

superexchange interaction between cations occupying the A and B sites is stronger than that occurring between A-A or B-B sites. Rare earth metal cations possess larger ionic radii (ranging from 0.90 to 1.10 Å) compared to Fe^{3+} ions, which have an ionic radius of 0.64 Å. So, RE cations prefer to occupy B sites and lead to alteration in cation distribution and hence in structural and magnetic properties of spinel ferrite.

The M-H curves of the samples obtained from VSM data are shown in Figure 1(c). Different magnetic characteristics for Ce-substituted Manganese ferrite NPs are listed in Table 2. The saturation magnetization (M_s) decreased from 49 emu/g to 12 emu/g as the Ce^{3+} ion concentration increased from x = 0.00 - 0.15 with step size of 0.025. This is plausibly because of highly magnetic Fe^{3+}(5.92 μ_B) ions are replaced by less magnetic Ce^{3+}(1.73 μ_B) ions [7]. Similar trends were observed in the values of coercivity (H_c), remanence magnetization (M_r), and squareness ratio ($S=M_r/M_s$). These lowered values of Ms, M_r, and H_c confirmed the soft magnetic nature of pure and doped MnF NPs. Further, the magneto-crystalline anisotropy constant (K) was estimated with the help of equation (4) and calculated values are listed in Table 2.

$$K = \frac{1}{0.96} H_c M_s \quad (4)$$

Table 2. Values of magnetic parameters for Ce-doped $MnFe_2O_4$ NPs.

Chemical Composition	M_S (emu/g)	M_R (emu/g)	H_C (Oe)	Squareness ratio	K ($\times 10^4$ erg/g)
$MnFe_2O_4$	49	19	289	0.38	1.5
$MnCe_{0.025}Fe_{1.975}O_4$	46	13	252	0.28	1.2
$MnCe_{0.05}Fe_{1.95}O_4$	34	5	156	0.15	0.6
$MnCe_{0.075}Fe_{1.925}O_4$	29	4	88	0.14	0.3
$MnCe_{0.1}Fe_{1.9}O_4$	22	2	75	0.09	0.2
$MnCe_{0.15}Fe_{1.85}O_4$	12	1	73	0.08	0.09

CONCLUSION

Ce-doped $MnFe_2O_4$ NPs were successfully synthesized through sol-gel auto-combustion method. Pristine as well as Ce-doped NPs were found in pure spinel phase with Fd3m space group. Crystallite size and lattice parameters were found in the range of 9.9±0.1 to 13.6±0.2 nm and 8.366±0.007 to 8.395±0.0003 Å, respectively. Lattice constant and crystallite size were found to be increased with increasing concentration of Ce ion in manganese ferrite NPs. FTIR spectra showed the presence of characteristic bands corresponding to tetrahedral and octahedral lattice vibrations. All magnetic characteristics were found to be decreased with addition of Ce ions. Therefore, it is concluded that the Ce ion substitutions have significant effect on structural and magnetic properties of $MnFe_2O_4$ NPs. The variation resulted through larger ionic radii and lower magnetic moments of Ce in comparison to Fe. So, Ce ion doping could be useful for the fine-tuning of characteristics of $MnFe_2O_4$ NPs and can be used for material engineering as per requirements of specific application. However, it will require precise control of doping concentration.

ACKNOWLEDGEMENT

The authors express their gratitude to IIC, Indian Institute of Technology Roorkee for providing access to XRD and VSM characterization facilities. Authors would also like to acknowledge CIF, Lovely Professional University, Chandigarh for providing FTIR facility.

REFERENCES

1. Y. Yang, L. Liu, H. Zhu, N. Bao, J. Ding, J. Chen, and K. Yu, ACS Appl. Mater. Interfaces, 12, 16609 (2020).
2. V. Vignesh, K. Subramani, M. Sathish, and R. Navamathavan, Colloids Surfaces A Physicochem. Eng. Asp., 538, 668 (2018).
3. S. Debnath, K. Deb, B. Saha, and R. Das, J. Phys. Chem. Solids, 134, 105 (2019).
4. C. S. Joshi, R. C. Srivastava, and A. Joshi, https://doi.org/10.1177/02670836241234197 (2024).
5. A. Joshi, R. C. Srivastava, R. Dhyani, and C. S. Joshi, J. Magn. Magn. Mater., 578, 170812 (2023).
6. M. M. Baig, S. Zulfiqar, M. A. Yousuf, M. Touqeer, S. Ullah, P. O. Agboola, M. F. Warsi, and I. Shakir, Ceram. Int., 46, 23208 (2020).
7. K. Kukli, M. Mikkor, A. Šutka, M. Kull, H. Seemen, J. Link, R. Stern, and A. Tamm, J. Magn. Magn. Mater., 498, 166167 (2020).

An Electrospinning Approach Towards the Production of Bio Degradable Mulch Films

Sayana K V[1], Vishwanath T[1, *]

[1]*Department of Materials Science, Mangalore University, Mangalagangothri, India*

[*] Corresponding author: vishutcg@gmail.com

Abstract

The advent of plastic technology marked a significant revolution in the field of agriculture. Among its many applications, mulch films have played a crucial role in improving crop yield and protection. These films contribute to increasing soil and air temperatures, protecting plants from various environmental stresses, enhancing water retention, suppressing weed growth, and ultimately reducing the excessive dependence on agrochemicals. Traditionally, synthetic polymers derived from non-renewable resources have been used for these purposes due to their low cost, ease of processing, mechanical strength, and barrier properties. However, their resistance to degradation poses serious ecological and economic challenges during disposal. This study explores the development and potential of biodegradable mulch films, particularly those based on starch–polylactic acid (PLA) bio composites, as an effective and eco-friendly alternative to conventional plastic mulch films.

Keywords: Mulch film, biopolymer, electrospinning, Nanofibers, polymer composite.

Introduction

The application of plastics in agriculture, commonly referred to as plasticulture, has revolutionized farming practices by enhancing both the quantity and quality of crop yields. Owing to their distinctive properties—such as ease of processing, thermal stability, resistance to chemical degradation, antimicrobial resistance, and excellent mechanical and barrier characteristics—plastics have been widely adopted in agricultural systems[1]. Various forms of plastic materials are utilized, including soil cover films, seedling bags, and water-retentive films designed to reduce soil erosion and improve moisture conservation.

Mulching, which involves covering the soil surface with a layer of material, plays a significant role in reducing water loss, suppressing weed growth, and increasing crop productivity[2]. Since its introduction in the 1950s, mulch technology has been globally recognized for enhancing soil microclimate, nutrient retention, and physical soil properties. Given the decline in available agricultural land and the growing demand for food, improving crop productivity through methods like mulching has become increasingly essential—particularly in drought-prone or urban/suburban regions where cultivable land is limited.

Traditionally, synthetic polymer-based mulches have been the material of choice due to their cost-effectiveness and durability. However, their non-biodegradable nature poses challenges related to disposal, secondary pollution, and increased pesticide contamination in landfills[3]. In response to these environmental concerns, the development of biodegradable mulch films (BDMs) has emerged as a promising alternative. Unlike conventional polyethylene (PE)-based films, BDMs can be either plowed back into the soil or composted after the growing season, where microbial action breaks them down into carbon dioxide, methane, water, or biomass.

Natural polymers offer several advantages for BDM production, including low cost, renewability, non-toxicity, biodegradability, and biocompatibility. However, their application also presents limitations—particularly brittleness and poor moisture barrier properties. Among natural biopolymers, starch stands out as one of the most widely used materials for manufacturing biodegradable thermoplastic films. It is often combined with polymer matrices such as poly(vinyl alcohol) (PVA), polylactic acid (PLA), and poly(butylene succinate) (PBS) to enhance film performance[4–5].

The present study aligns with the goals of sustainable agriculture by focusing on the development of an environmentally friendly biodegradable mulch film with minimal chemical input during fabrication. The electrospinning technique was employed to produce fibrous, structured films that mimic fabric-like characteristics, offering potential improvements in mechanical properties and degradation behavior.

Materials and methodology

Starch was procured from NICE Chemicals Pvt. Ltd., Kochi, India. Polylactic acid (PLA), along with acetone and dimethylformamide (DMF), was obtained from Sisco Pvt. Ltd., Maharashtra, India.

The polymer solution for electrospinning was prepared by dissolving polylactic acid (PLA) and starch, each at 5 wt.%, in a binary solvent system comprising acetone and dimethylformamide (DMF) in a 60:40 (v/v) ratio. The solvents were added to a pre-weighed amount of the polymers, and the mixture was magnetically stirred at 50 °C for 4 hours to ensure complete dissolution. The resulting blend solution, in an optimized PLA-to-starch ratio of 80:20, was then loaded into a 5 mL plastic syringe for electrospinning. Electrospinning was carried out under the following conditions: an applied voltage of 15 kV, a flow rate of 0.030 mL/min, a tip-to-collector distance of 10 cm, and a collector rotation speed of 300 rpm. The nanofibers were collected on a layer of cotton fixed onto a rotating drum collector.

Characterisations

The thermal properties of the electrospun films were analyzed using Differential Scanning Calorimetry (DSC) and Thermogravimetric Analysis (TGA), performed on a PerkinElmer STA600 thermal analyzer. Mechanical properties were evaluated using a Universal Testing Machine (UTM) according to the ASTM D882 standard, which is employed to determine the tensile properties of thin plastic films and fibers.
To assess plant compatibility and the service life of the nanofiber mat, the films were placed over potting soil in rectangular vases. Small holes were made in the film for seedling placement. The vases were kept indoors and irrigated through controlled water-dropping methods. After the harvest period, the biodegradable films were collected, washed, dried, and analyzed to observe their structural and compositional changes post-degradation.

Results and Discussion

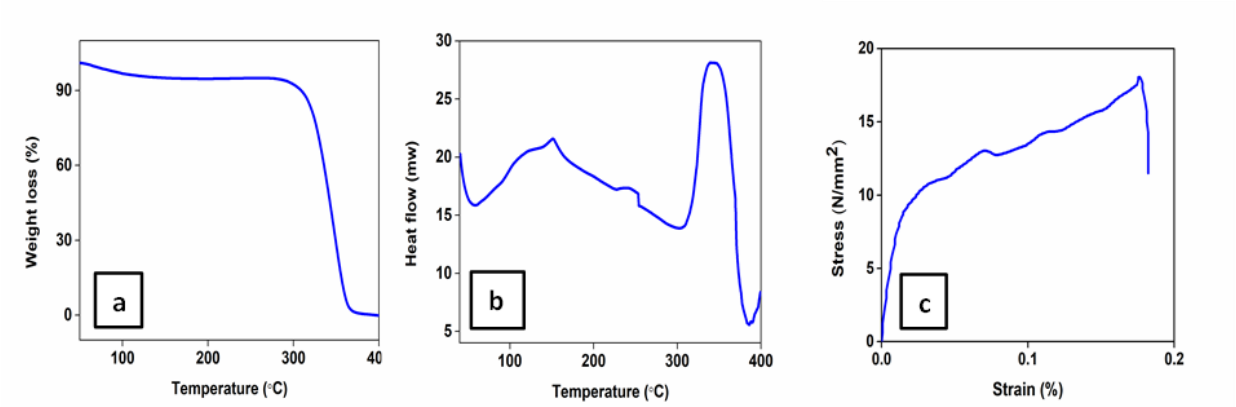


FIGURE 1. (a) TGA curve of PLS film, (b) DSC curve of PLS film, (c) Stress-Strain plot of PLS film

The thermal stability of the PLA–Starch (PLS) mulch film was evaluated using TGA, as shown in **Figure 1(a)**. A slight weight loss was observed around 78–80 °C, attributed to the evaporation of physically adsorbed moisture. A more pronounced weight loss beginning at approximately 285 °C corresponds to the thermal decomposition of the composite matrix, primarily indicating the onset of PLA degradation.

The DSC thermogram in **Figure 1(b**). of the PLS mulch film revealed a glass transition temperature (Tg) at 59 °C. A distinct melting endotherm was observed at 159 °C, which is slightly lower than the melting point of pure PLA, likely due to the interaction with starch in the composite matrix. Additionally, a sharp exothermic peak at 343 °C indicated the thermal degradation of the film beyond 300 °C. Mechanical performance was assessed via a stress–strain analysis showed in **Figure 1(c)**. The PLS film exhibited a tensile strength of 17.7 MPa and an elongation at break of 18.2%. Notably, the lamination of multiple electrospun nanofiber layers enhanced the tensile strength while reducing elongation, suggesting

improved durability and mechanical stability—key attributes for its use as a mulch film in agricultural applications.



FIGURE 2. The seedling stages of plants on mulch environment. (a) Mulch film before use, (b) Seeds sown covered with mulching, showing initial sprouting, (c) Plant growth after 10 days with visible seeding emergence through the mulch layer.

Figure 2. illustrates the stages of seed germination and subsequent plant growth in an environment covered with the PLS mulch film. The mulch films remained intact in the soil for up to 20 weeks, maintaining their structural and functional integrity throughout this period. Weekly monitoring revealed healthy plant growth, with no visible negative impact from the mulch material on germination or development. After the 20-week period, the mulch films began to exhibit signs of degradation, including weight loss and fragmentation, indicating the onset of bio decomposition. These results demonstrate that the developed biodegradable mulch films provided sufficient durability during the crop cycle while ensuring gradual degradation post-use, supporting their potential for sustainable agricultural applications.

Conclusion

In this study, biodegradable mulch films were successfully developed using a PLA–starch-based composite system. A key strategy for producing environmentally friendly mulch films involves the formulation of multiphase materials—such as polymer blends or reinforced composites—that address internal limitations while meeting international performance standards. The bio-based composite described here comprises two distinct biodegradable phases: a continuous polymer matrix and a reinforcing phase. Starch served as the reinforcing component, enhancing the mechanical strength and stiffness of the PLA matrix. The incorporation of starch significantly improved the film's tensile strength and durability, both of which are essential for mulching applications where materials must retain integrity under mechanical and environmental stress. The developed biocomposite exhibited adequate flexibility and coverage, allowing it to function effectively as a soil cover while withstanding specific load conditions. Additionally, the PLA–starch blend improved water vapor barrier properties, helping to retain soil moisture throughout the cultivation period. Field observations confirmed that the starch component contributed to resistance against physical deterioration during extended exposure. The mulch films were found to be 100% biodegradable and environmentally safe, eliminating the need for removal after the harvest season. After prolonged soil contact, slight increases in film thickness were observed, likely due to soil particle absorption and surface residue accumulation. Laminating the electrospun nanofiber layers into a single sheet via hot pressing further enhanced the strength and stability of the mulch film. As the starch content increased from 10% to 40%, the resulting films became stiffer and more rigid—indicating that formulation tuning can tailor material performance for specific agricultural needs. Overall, the findings demonstrate that the PLA–starch (PLS) mulch film maintains its functional and structural properties over prolonged outdoor use, supporting its potential as a sustainable and viable alternative to traditional petroleum-based polymer mulches in agricultural applications.

References

1. M. Menossi, M. Cisneros, V. A. Alvarez, and C. Casalongué, Agronomy for Sustainable Development, *41*(4), 53, (2021).
2. C. S. Andrade, M. D. G. Palha and E. Duarte, J Berry Res, 4, 193–202, (2014).
3. K. Kong, and G. R. Ziegler, Food Hydrocolloids, 36, 20-25, (2014).
4. J Sunthornvarabhas, P Chatakanonda, K. Piyachomkwan and Sriroth K, Materials Letters, 65(6), 985-7, (2011).
5. Z. Tan,Y. Yi, H. Wang, W. Zhou, Y. Yang and C. Wang, Appl Sci., 6(5), 147, (2016).

Temperature Dependent Tunable Optical Property Analysis of In_2Se_3 Thin Films

Mukesh Mishra[1, 2,*] and AgniKumar G Vedeshwar[1]

[1]*Thin film lab, Department of Physics and Astrophysics, University of Delhi, Delhi, India 110007*
[2]*Shri R K Parikh Arts and Science College Petlad Anand Gujarat 388550*

[*]Corresponding author: mukeshmishra@petladcollege.org.in

Abstract. In this research work, we performed the systematic analysis of the effect of annealing temperature and annealing time period on the optical properties of In_2Se_3 films deposited on glass slide by using thermal vapor deposition setup. Initially at room temperature, the deposited films are amorphous in nature. Here in this part of research our aim to estimate the nature of variation of optical band gap of 30 nm thin film of In_2Se_3 by varying the annealing temperature and annealing time period. To evaluate the band gap of heat-treated In_2Se_3 samples; we did the UV-visible absorption spectra analysis of these films and we find out that the optical band gap of In_2Se_3 films increases as we increase the heating temperatures and heating time period. The effects of heating temperatures and heating time period are more prominent when we treating films at temperature higher than 100 °C and for a time period of more than 5 min. The observed band gap turnability of In_2Se_3 by varying different heating parameters shows that it can be useful for various application purposes.

INTRODUCTION

The superior material properties of two dimensional nanosheets like nature of III-VI group semiconductor In_2Se_3 material possess many applications in the field of solar cells, photodiodes and phase change memories and many more just like other well-known two-dimensional nanosheets possessing high surface area and tunable material property etc. [1-4]. The In_2Se_2 nanosheets can be prepared by using, exfoliation of layers from their bulk materials via chemical methods or mechanical exfoliation or thermal evaporation process etc. [1-7]; among these methods we opted the thermal evaporation deposition method for the deposition of thin films of In_2Se_3 on glass slide at vacuum in controlled way with less effort and low cost. To estimate the effect of annealing temperature and annealing time period on the optical properties, the deposited In_2Se_3 films are heated at different temperature and for different time periods by using hot plate and these heats treated In_2Se_3 films are characterized by using UV-visible absorption spectrometer.

EXPERIMENTAL METHOD

The thin films of In_2Se_3 material of thickness 30 nm were deposited by opting thermal vapor deposition (HIND-HIVAC) setup with attachment of Quartz Crystal Digital Thickness Monitor Model-101 to monitor the rate of deposition and film thickness at a vacuum of ~ 10^{-6} torr. For this purpose, indium (III) selenide (In_2Se_3) powder purchased from Alfa Aesar (99.99 %, 12056-07-4) was kept into molybdenum boat and heated up to melting point by slowly to controlled the rate of deposition under vacuum chamber, so that formed vapor of In_2Se_3 moved upward to get deposited on the glass slides placed above the boat at room temperature. After the deposition of In_2Se_3 film of thickness 30 nm, these films were heated for 5 min at different temperatures 50 °C, 60 °C, 80 °C, 100 °C, 120 °C, 150 °C, 200 °C with the help of hot plate to see the effect of heating temperature on the In_2Se_3 films. Deposition of In_2Se_3 on glass slide with thickness 30 nm was heated at temperature 80 °C for time period 1 min, 2 min, 3 min, 4 min, 5 min, 6 min, and 7 min with the help of hot plate to see the effect of heating time period on the properties of In_2Se_3 films. The deposited and heat-treated In_2Se_3 films are analysis by using UV-visible absorption spectrometer to estimate the nature of band gap (E_g-value) variation with heating temperature and heating time period.

CHARACTERIZATIONS

The rate of deposition and film thickness of In_2Se_3 film was confirmed by Quartz Crystal Digital Thickness Monitor Model-101 attached with the TVD setup. UV-visible absorption spectrometer (HITACHI U-3900H) was used to evaluate the band gap of heat-treated In_2Se_3 film for optical behavior analysis.

RESULTS AND DISCUSSIONS

The optical absorption measurement of In_2Se_3 film can determines the magnitude and type (direct or indirect) of the band gap quite accurately. The UV-visible absorption spectra of heat-treated In_2Se_3 films are shown in Figure 1.

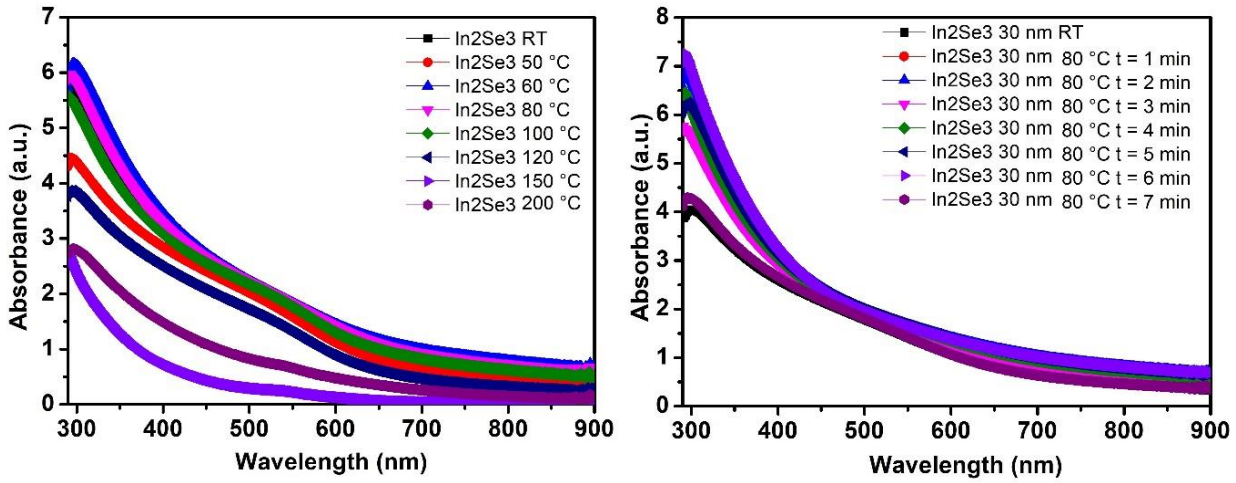


FIGURE 1. UV-visible absorption spectra of heat treated In_2Se_3 films deposited on glass slide.

The relation between absorbance (A) and absorption coefficient (α) for a non-reflecting films of thickness 't' near absorption region is,

$$\alpha = 2.303\frac{A}{t} \quad (1)$$

For parabolic bands, the absorption coefficient (α) is related to the band gap in direct transition by

$$\alpha h\nu = constt.(h\nu - Eg)^n \quad (2)$$

The values that n for direct allowed transition is 1/2, for direct forbidden n = 3/2 (in quantum mechanical sense) transition, n takes value 2 for indirect allowed transition, 3 for indirect forbidden transition.
To find out the band gap nature and band structure, of the materials, the proper analysis of the value of n which gives the best linear fit for the plot the graph between $(\alpha h\nu)^{1/n}$ and hν in the absorption edge region. We have tried the plot between $(\alpha h\nu)^{1/2}$ and hν and linear fitted with the correlation factor (R^2) better than 0.99 and only few are shown in Figure 2, for the illustration and determination of band gap (E_g-value) and its nature from measured absorption spectra [7-9]. The E_g-value along with correlation factor are listed in Table 1.

TABLE 1. The band gap value and R^2 value of In_2Se_3 thin films having thickness 30 nm (Set-A) heated at temperature: T= 50 °C, 60 °C, 80 °C, 100 °C, 120 °C, 150 °C, 200 °C for time period of 5 min and (Set-B) heated at temperature: T= 80 °C, for time period of 1 min, 2 min, 3 min, 4 min, 5 min, 6 min, 7 min on hot plate.

Set-A (In_2Se_3 30 nm, heating time period - 5 min)			**Set-B (In_2Se_3 30 nm, heating temperature - 80 °C)**		
Temperature (T)	**E_g-value (eV)**	**R^2-value**	**Time period (t)**	**E_g-value (eV)**	**R^2-value**
T= RT	0.856	0.998	t = 0 min	0.887	0.998
T= 50 °C	0.915	0.995	t = 1 min	0.857	0.986
T= 60 °C	0.853	0.995	t = 2 min	0.864	0.982
T= 80 °C	0.842	0.996	t = 3 min	0.852	0.995
T= 100 °C	0.866	0.997	t = 4 min	0.861	0.990
T= 120 °C	1.002	0.994	t = 5 min	0.852	0.987
T= 150 °C	1.871	0.993	t = 6 min	0.875	0.981
T= 200 °C	1.136	0.996	t = 7 min	0.910	0.998

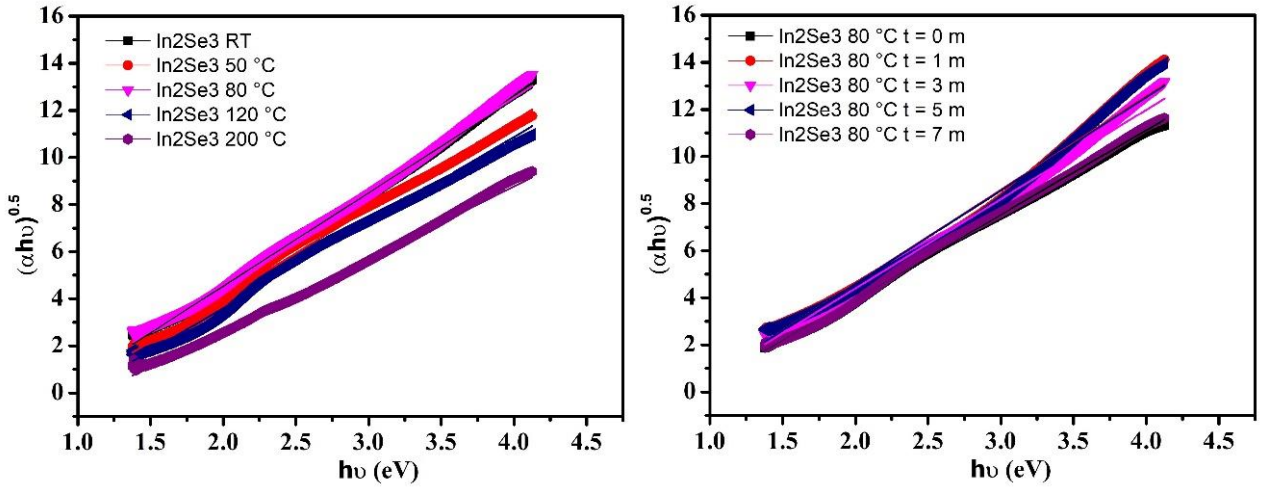


FIGURE 2. The linear fitted graph plot of $(\alpha h\nu)^{1/2}$ versus hν value for the heat treated In_2Se_3 thin film.

The systematic analyses of UV-visible absorption spectra and from the plot of $(\alpha h\nu)^{1/2}$ versus hν value with linear fitting estimate the band gap of heat-treated In_2Se_3 films (in Table 1) confirmed the indirect band gap nature for In_2Se_3 films and the optical band gap increases with increasing heating temperature and similar behavior observed when we analyze with the heating time periods at constant temperature.

CONCLUSIONS

In conclusion, In_2Se_3 thin films of 30 nm have been successfully deposited on glass slide by using thermal evaporation setup under high vacuum ~ 10^{-6} torr, after that heat treated at different temperature and for different time periods. The systematic analyses of UV-visible absorption spectra of treated films confirmed the indirect type band gap for In_2Se_3 films. The optical band gap increases with increasing heating temperature and similar behavior observed, when we analyze with the heating time periods at constant temperature. We hope this report is interesting and could well be the motivation for the further exploration of similar layer structured materials.

ACKNOWLEDGMENTS

Authors MM and AGV are thankful to University of Delhi, India for carrying out all measurements. One of the authors MM is thankful to UGC, India for providing financial support as Kothari fellowship [PDF/PH/2017-18/00059].

REFERENCES

17. C. H. de Groot, and J. S. Moodera, J. Appl. Phys. **89**, 4336 (2001).
18. M. Ishikawa, and T. Nakayama, Jpn. J. Appl. Phys. **37**, L1122-L1124 (1998).
19. S. M. Poh, S. J. R. Tan, H. Wang, P. Song, I. H. Abidi, X. Zhao, J. Dan, J. Chen, Z. Luo, S. J. Pennycook, A. H. C. Neto, and K. P. Loh, Nano Lett., **18**, 6340-6346 (2018).
20. W. Feng, F. Gao, Y. Hu, M. Dai, H. Liu, L. Wang, and P. A. Hu, ACS Appl. Mater. Interfaces, **10**, 27584-27588 (2018).
21. N. Balakrishnan, E. D. Steer, E. F. Smith, Z. R. Kudrynskyi, Z. D. Kovalyuk, L. Eaves, A. Patanè and P. H. Beton, 2D Mater., **5**, 035026 (2018).
22. H. Peng, D. T. Schoen, S. Meister, X. F. Zhang, and Y. Cui, J. Am. Chem. Soc., **129**, 34-35 (2007).
23. N. Balakrishnan, C. R. Staddon, E. F. Smith, J. Stec, D. Gay, G. W. Mudd, O. Makarovsky, Z. R. Kudrynskyi, Z. D. Kovalyuk, L. Eaves, A. Patanè and P. H. Beton, 2D Mater., **3**, 025030 (2016).
24. M. Küpers, P M. Konze, A. Meledin, J. Mayer, U. Englert, M. Wuttig, and R. Dronskowski, Inorg. Chem., **57**, 11775-11781 (2018).
25. C.-H. Ho1, Sci. Rep. **4**, 4764; DOI:10.1038/srep04764 (2014).

Cross-sectional Transmission Electron Microscopy Study of As-grown CuO nanowire Sample Synthesized by Thermal Oxidation Method

Pabitra Sahu[1,a)], Himanshu Srivastava[1,2], Mahendra Babu[1], Pragya Tiwari[1,2] and A.K. Srivastava[1,2]

[1]*Accelerator Physics and Synchrotrons Utilization Division, Raja Ramanna Centre for Advanced Technology, Indore - 452013, India*
[2]*Homi Bhabha National Institute, Training School Complex, Anushakti Nagar, Mumbai 400094, India,*
[a)] *Corresponding author: spabitra@rrcat.gov.in*

Abstract. Cross-sectional Transmission Electron Microscope (XTEM) investigation of as-grown CuO nanowires sample, synthesized by thermal oxidation method, has been carried out to find out the origin of the growth mechanism that may be present in the underlying oxide layers on which the nanowires grow. The TEM measurement invariably showed the presence of twin bands almost everywhere in the CuO layer and the nanowires grow at the junction of these twin bands. The as-grown samples were also analyzed by the Scanning Electron Microscope (SEM).

INTRODUCTION

Owing to their high surface to volume ratio, quantum size effect and large range of band gaps, metal oxide nanowires have found diverse applications such as gas sensors, efficient electrodes in solar cells, field emission devices, optoelectronic devices and high density devices [1]. Among the various methods of synthesis of these class of nanowires, the thermal oxidation or annealing is a relatively simpler method and widely popular for synthesizing high quality metal oxide nanowires. The size and shape of the nanowires in this method can be controlled by manipulating the synthesis parameters like oxidation temperature and time [2]. CuO nanowires have been a representative system for the thermal oxidation method, as the initial reports and many subsequent important studies on this synthesis method have been devoted to this system.

Despite the simplicity of the method, the underlying growth mechanism is still not fully understood and is under investigation. A. Kumar *et al* [2] suggested the growth of nanowires is a result of the relaxation of stress developed at oxide layer interfaces during oxidation. S. Rackauskas *et al [3] in his work proposed twin boundary driven nanowire growth stating that the edge of twin boundary ridge facilitate the anisotropic nanowire growth. The presence of twin boundary in CuO nanowires is confirmed by H. Srivastava in his work [4]. Further, the stress observed by the in-situ energy dispersive X-ray diffraction (EDXRD) study of the growth of nanowires did not support the stress relaxation in the* underlying CuO layer [5].

The underlying CuO layer and its relation to the nanowires may hold important clues regarding the growth mechanism. A cross-sectional Transmission Electron Microscope (XTEM) investigation of as-grown nanowire sample may thus provide important insight and can test the growth mechanisms proposed in the existing literature. In our work, we have grown CuO nanowires from pure copper foil via thermal oxidation in moist oxygen environment with optimized growth parameters as suggested by H. Srivastava in his work [4] and devised a method to prepare XTEM sample of very brittle CuO nanowires. The as-grown sample (AGS) was studied with Scanning Electron Microscope (SEM) and XTEM.

EXPERIMENTAL METHOD

The substrates of the size 1 cm x 1 cm were cut from a commercial grade 99.9% pure copper foil of 0.3 mm thickness, procured from M/s Sigma Aldrich Chemicals and was used for the nanowire growth. The substrates were cleaned in dilute HCl solution, ultra-sonicated in methanol for 10 minutes and were then kept on an alumina boat and loaded into horizontal quartz tube of single zone resistive furnace. Moist oxygen was introduced inside quartz tube by flowing oxygen at a rate of 250 sccm per minute by a Mass Flow Controller (MFC) through a 1 ft water column. The furnace was heated to 550°C and kept at this temperature for 1 hr before allowing natural

cooling up to the room temperature and the samples were thereafter removed from the furnace. The AGS was observed in a Philips XL30CP scanning electron microscope (SEM) operated at 30 kV.

The AGS becomes very brittle due to complete oxidation. The usual XTEM sample preparation requires several steps of mechanical polishing. To preserve the as-grown oxide structure during XTEM sample preparation, the sample is first fixed by encapsulating the whole sample in an epoxy glue. Subsequently, the usual steps of XTEM sample preparation like cutting the sample in a cross-section geometry after fixing in a brass rod, mechanical thinning, dimple grinding and finally ion-milling were carried out. The XTEM sample was studied by a Thermofisher make Talos F200X G2 TEM operated at working voltage of 200 kV.

RESULT AND DISCUSSION

SEM micrograph of AGS synthesized at the optimized condition is shown in Fig. 1. The nanowires grown have high growth density, length in the range of few tens of μm and diameter varying from 50 to 120 nm. Figure 2 shows the XTEM results of AGS. Figure 2(b) shows bright field image of a CuO nanowire with underlying CuO oxide layer at its base. Selected area diffraction pattern (SADP) was collected from the oxide layer at the base of nanowire (Fig. 2(a)). The single crystal diffraction pattern was indexed to [431] zone axis of monoclinic phase of CuO (JCPDS Card No. 48-1548). BF (Fig. 2(b)) and DF (Fig. 2(c)) image from $(01\bar{3})$ reflection clearly show alternative sharp dark and bright bands, indicating the presence of twin bands near the base of nanowire. Corresponding HRTEM image of area across twin boundary is shown in Fig 2(d).

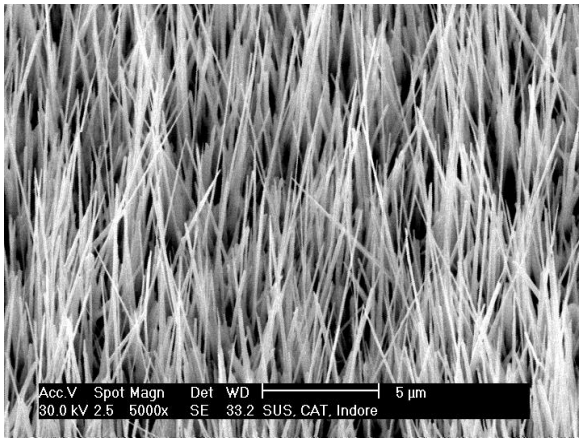


FIGURE 1. SEM micrograph of AGS

Twin bands in CuO layer were also observed at another site as evident from the BF and DF image shown in Fig. 2(e) and Fig. 2(f) respectively. The nanowires were invariably seen to grow at the junction of the twin boundary, thus supporting the observation of S. Rackauskas [3]. The widespread twin structure observed in CuO layer seems to be an inherent outcome of the thermal oxidation of Cu foil. The growth of the nanowires at the twin junction is preferred, as it serves as the low energy site for the addition of ions such as Cu^{2+} and O^{2-} , thereby accelerating the anisotropic growth of the nanowires in the direction of the junction. A similar XTEM study of the samples in prepared in different synthesis condition would put more light on the growth mechanism and is a part of the ongoing work.

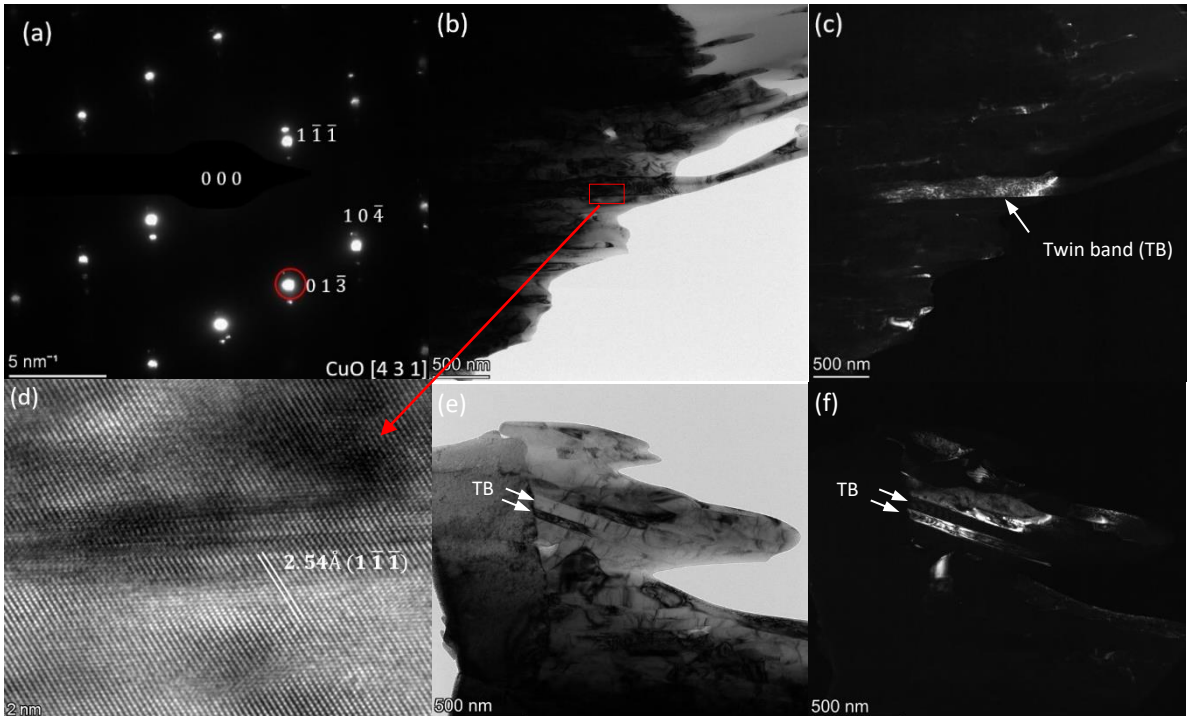


FIGURE 2. TEM result of AGS. (a) SADP recorded from oxide layer base of nanowire. (b) BF and (c) DF image from $(0\,1\,\bar{3})$ reflection of SADP shows alternating contrast indicating presence of twin band in oxide layer. (d) HRTEM image of area across the twin boundary. (e) BF and (f) DF image taken from oxide layer at different site invariably shows twin bands.

CONCLUSION

The cross-sectional TEM investigation of as-grown sample of CuO nanowires synthesized by thermal oxidation method was carried out. The results show the formation of twin bands throughout the CuO layer. The nanowires grow at the twin band junction. This supports the twin mediated growth of the nanowires in this system.

ACKNOWLEDGEMENTS

The authors are thankful to Dr. Tapas Ganguli for his valuable guidance throughout the work and Shri Shubham Mingwal for his help in the growth of the sample.

REFERENCES

1. J.G. Lu, P. Chang and Z. Fan, *Mater. Sci. and Engg*. R **52**, 49 (2006).
2. Kumar A, Srivastava AK, Tiwari P, Nandedkar RV *J. Phys.: Condens. Matter* **16** 8531 (2004)
3. Rackauskas S, Jiang H, Wagner JB, Shandakov SD, Hansen TW, Kauppinen EI, Nasibulin AG *Nano letters* **14.10**: 5810-5813 (2014).
4. Srivastava H, "Growth and Characterizations of Metal Oxide Nanowires" Ph.D. Dissertation, HBNI (2018)
5. Srivastava H, Ganguli T, Deb SK, Sant T, Poswal HK, Sharma SM *Journal of Applied Physics* **114**, 144303 (2013).

Investigation of the effect of gamma irradiation on the structural and magnetic properties of Ni-Co ferrite/ graphene oxide nanocomposite

H. K. Verma[1 a)], R. C. Srivastava[1], C. S. Joshi[1] and G. C. Joshi[1]

Department of Physics, CBSH
G. B. Pant University of Agriculture and Technology, Pantnagar, Uttarakhand, 263145

[*]E-mail- hkverma1103@gmail.com

Abstract. This study investigates the structural and magnetic characteristics of $Ni_{0.5}Co_{0.5}Fe_2O_4$/graphene oxide (NCF/GO) nanocomposites exposed to ^{60}Co gamma radiation at doses of 25 and 50 kGy. Structural and magnetic behavior was analyzed using powder XRD, FTIR, and VSM techniques. The crystallite size, ranging between 22 and 42 nm, showed a dose-dependent increase after gamma irradiation. FTIR spectra of NCF/GO nanocomposite showed the presence of absorption bands correspond to both NCF and GO, which confirmed the successful formation of nanocomposite. The peak intensity of absorption bands in FTIR spectra was found to be reduced after gamma irradiation, which was father reduced with increase in dose. The saturation magnetization and coercivity were observed in the range of 57-48 emu/g and 787-776 Oe, respectively. The saturation magnetization and coercivity were decreased after gamma irradiation.

INTRODUCTION

Interaction of radiation with matter causes alteration in various properties of matter and continuously becoming center of attraction of researcher both theoretically and practically. The rise in various types of defects inside the target material after irradiation changes physical and chemical properties of material. Gamma rays possess strong penetrating ability and interact with substances by causing ionization through the photoelectric effect, Compton scattering, or pair production. Their deep penetration allows them to affect materials throughout their volume.[1]. The changes in various properties after gamma irradiation depends on dose rate, irradiation time and absorption of radiation by material.

Spinel ferrites are regarded as a key group of functional materials owing to characteristics like high resistivity, superior saturation magnetization, robust chemical stability, high coercivity, and impressive mechanical strength, . These characteristics make ferrites suitable for various applications, including high-density magnetic storage, ferro-fluids, high-frequency devices, catalysts, and microwave devices etc. Cobalt ferrite is a partially inverse spinel ferrite, while nickel ferrite exists in completely inverse spinel structure. Nickel ferrite has higher electrical resistivity and lower eddy current losses. Addition of cobalt in nickel ferrite can modify properties which increase its suitability in various applications [2]. Composites are one of the most innovative and versatile engineering materials. A unique two-dimensional graphene oxide (GO) has excellent physical and chemical properties and is being recently explored as a radiation absorbing material. The various oxygen functional groups present in GO, specifically, hydroxyl (-OH), carbonyl (C=O), epoxide (-O-), and carboxyl (-COOH), make it chemically active and enhance its ability to interact with other substances. The addition of GO into ferrites modify results in a new class of material combining the properties of both [3, 4]. This investigation aims to examine the changes in structural, compositional, and magnetic characteristics of NCF/GO nanocomposites induced by gamma irradiation.

MATERIALS AND METHODS

NCF/GO nanocomposite with 20 weight percentage of GO was synthesized through ultra- sonication method. NCF and GO were prepared separately via sol-gel auto combustion and modified hummers method, respectively. Appropriate amounts of GO and NCF powder were dispersed individually in doubly ionized water and under ultrasonicated for 30 min to obtain homogeneous dispersion. Both the solutions were mixed and kept under constant stirring at ~60 ˚C for 2 h. Finally, resulting mixture was dried in a hot air oven at 80 ˚C. The dried mixture was finely ground using mortar-pestle. Black-coloured powder of NCF/GO nanocomposites was obtained.

Irradiation experiment was performed in an irradiator (gamma cell) with ^{60}Co isotope as a source of energetic gamma radiation. The synthesized NCF/GO nanocomposite was subjected to gamma irradiation at different doses of 25 and 50 kGy. The effective dose rate of ^{60}Co source at the time of exposure was 5.413 kGy/h and the chamber

temperature was 34.3˚C. Both the irradiated and unirradiated nanocomposites were analyzed at room temperature using XRD, FTIR, and VSM techniques.

RESULTS AND DISCUSSION

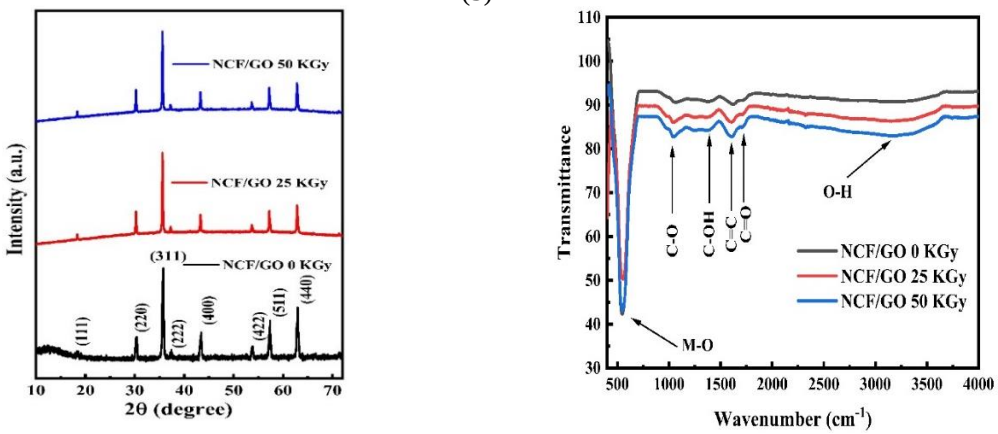
The XRD patterns for pristine and gamma irradiated NCF/GO nanocomposites are presented in Fig. 1(a). The reflection planes corresponding to NCF were clearly observed. However, reflection planes for GO in NCF/GO were not observed. This was attributed to the exfoliation and completely homogeneous dispersion of GO layers in the nanocomposite sample. The crystallite size D was calculated through Scherer's formula (1)

$$D = \frac{k\lambda}{\beta cos\theta} \quad (1)$$

where, k is a shape factor and has a value of 0.9 for spherical shaped nanoparticles and λ is wave length of X rays (1.5406 Å, Cu Kα radiation). β and θ are full width at half maximum (FWHM) and peak position in radians, respectively for most intense (311) peak. The interplanar spacing 'd' and lattice parameter 'a' were also estimated from equation

$$2d\sin\theta = n\lambda \quad (2)$$

$$a = d\sqrt{h^2 + k^2 + l^2} \quad (3)$$



(a) **(b)**

Figure 1 (a) XRD and (b) FTIR patterns of NCF/GO nanocomposite irradiated at 25 kGy and 50 kGy.

The crystallite size increased after gamma irradiation, reaching 42 nm compared to 22 nm for the unirradiated sample. The increase of crystallite size with irradiation is due to the formation of Fe^{2+} ions, which is having large ionic radii (0.74 Å) compared to the Fe^{3+} ion having ionic radii (0.67 Å). This causes to move the Fe^{2+} ions from A-site to the B-site. This is responsible for the increasing tendency of crystallite size[5]. Table 1 summarizes the crystallite size, lattice parameter, interplanar spacing, and unit cell volume. It is evident from the data that both the lattice constant and the unit cell volume increased as a result of gamma irradiation.[6]. Results of XRD Patterns suggest that gamma radiation influences the structural parameters of synthesized samples.

Table 1 Values of different structural parameters for NCF/GO nanocomposites irradiated at gamma dose at 25 kGy and 50 kGy.

Samples	2θ (Degree)	D (nm)	d-spacing (Å)	a (Å)	V (~Å^3)
NCF/GO 0 KGy	35.696 ± 0.002	22.3 ± 0.6	2.51 ± 0.01	8.33 ± 0.06	579
NCF/GO 25 KGy	35.614 ± 0.005	40.7 ± 0.5	2.51 ± 0.01	8.35 ± 0.01	583
NCF/GO 50 KGy	35.603 ± 0.004	42.0 ± 0.2	2.51 ± 0.01	8.35 ± 0.01	583

Figure 1(b) presents the FTIR spectrum of the NCF/GO nanocomposite, highlighting two distinct peaks at 543 cm^{-1} and 431 cm^{-1}. The absorption at 543 cm^{-1} corresponds to the Co/Ni–O stretching vibrations in the tetrahedral

sites, while the 431 cm^{-1} band is associated with Fe–O vibrations in the octahedral sites. These peaks are indicative of the typical vibrational modes found in NCF structures.[7]. The absorption bands at 1044, 1389, 1615 and 1707 cm^{-1} are attributed to the C–O–C epoxy and C–O alkoxy groups, C–OH hydroxyl functional group, aromatic C=C and C=O (in carboxyl or carbonyl group) respectively. The vibrational bands of GO powder confirms the presence of GO in nanocomposite [8]. The FTIR spectra exhibits absorption bands of both NCF and GO, confirming the successful formation of NCF/GO nanocomposite. After gamma irradiation, no observable shift was occurred in peak position of absorption bands of FTIR spectra. However, peak intensity of absorption bands got reduced after gamma irradiation[9, 10].

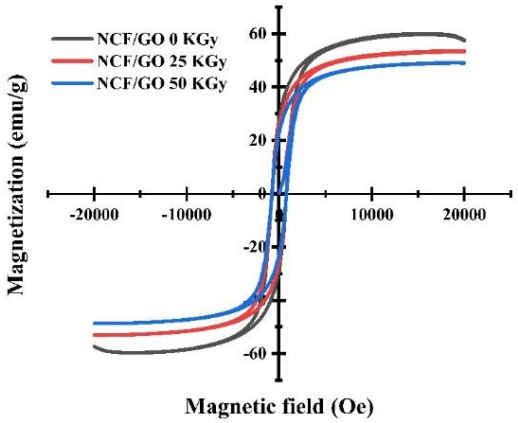


Figure 2 Magnetic hysteresis curves of NCF/GO nanocomposite irradiated at gamma dose at 25 kGy and 50 kGy.

Magnetic properties of NCF/GO nanocomposite were analyzed with the help of VSM at room temperature. The values of saturation magnetization (M_S), remanence magnetization (M_R) and coercivity (H_C) are summarized in Table 1. The saturation magnetization (MS) of the pristine NCF/GO sample was measured at 57 emu/g. A gradual reduction in magnetization was observed with increasing gamma radiation dose, potentially due to alterations in superexchange interactions like A–A, B–B, and A–B. Coercivity, determined from the magnetic hysteresis loop, also showed a decreasing trend with higher radiation exposure.[5].

The squareness ratio (S), is the ratio of remanence magnetization (M_R) to saturation magnetization (M_S). A higher squareness ratio indicates that material has strong tendency for magnetic domains to return in their preferred orientation. From Table 2, it is evident that increasing gamma radiation dose led to a reduction in the squareness ratio.[11, 12]. The following relation was employed to determine the value of anisotropy constant (K).

$$K = \frac{M_S \times H_C}{0.96} \quad (4)$$

Table 2 Values of magnetic parameters for NCF/GO nanocomposites irradiated at gamma dose of 25 kGy and 50 kGy.

Samples	M_S (emu/g)	M_R (emu/g)	Hc (Oe)	$S = \frac{M_R}{M_S}$	K (erg/g)
NCF/GO 0 KGy	57	28	787	0.491	4.72×10^4
NCF/GO 25 KGy	53	25	781	0.471	4.31×10^4
NCF/GO 50 KGy	48	22	776	0.458	3.80×10^4

CONCLUSIONS

The NCF/GO nanocomposite was effectively prepared using the ultra-sonication method and exposed to gamma radiation from a ^{60}Co source. The formation of the nanocomposite was validated using XRD and FTIR analyses. Structural parameters such as crystallite size, lattice constants, interplanar distance, and unit cell volume were examined from the XRD data. Crystallite size determination showed values ranging from 22 nm to 42 nm.

The lattice parameter was obtained in the range of 8.335–8.356 Å. The structural parameters increase with increase in dose of gamma radiation. The saturation magnetization of the sample decreased from 57 emu/g to 48 emu/g as the dose of gamma radiation increase upto 50 kGy An increase in gamma radiation dose led to a reduction in coercivity, remanent magnetization, and the squareness ratio of the samples. This gamma irradiation with suitable dose may be used to tailor the properties of the materials according to its use.

ACKNOWLEDGMENT

The authors would like thanks Institute instrumentation center (IIC), Indian Institute of Technology, Roorkee for providing XRD, FTIR and VSM. Radiation & Isotopic Tracers Laboratory (RITL), G.B. Pant University of Agriculture and Technology, Pantnagar is acknowledged for providing gamma irradiation facility.

REFERENCES

1. Maqbool M (2017) Interaction of gamma rays and X-rays with matter. An Introd to Med Phys 43–61
2. Debnath S, Das A, Das R (2021) Effect of cobalt doping on structural parameters, cation distribution and magnetic properties of nickel ferrite nanocrystals. Ceram Int 47:16467–16482
3. Nawaz M, Islam MU, Nazir MA, et al (2021) Transport properties in spinel ferrite/graphene oxide nanocomposites for electromagnetic shielding. Ceram Int 47:25505–25513
4. Wang G, Ma Y, Wei Z, Qi M (2016) Development of multifunctional cobalt ferrite/graphene oxide nanocomposites for magnetic resonance imaging and controlled drug delivery. Chem Eng J 289:150–160
5. Srinivasamurthy KM, Manjunatha K, El-Denglawey A, et al (2021) Dosimetry induced modifications in structural, magnetic and Mössbauer spectroscopy studies of 60Co γ-irradiated Co0. 5Ni0. 5Fe2O4. Radiat Phys Chem 189:109781
6. Reddy BC, Manjunatha HC, Vidya YS, et al (2021) Synthesis and characterization of multi functional nickel ferrite nano-particles for X-ray/gamma radiation shielding, display and antimicrobial applications. J Phys Chem Solids 159:110260
7. Nandan B, Bhatnagar MC, Kashyap SC (2019) Cation distribution in nanocrystalline cobalt substituted nickel ferrites: X-ray diffraction and Raman spectroscopic investigations. J Phys Chem Solids 129:298–306
8. Al-Gaashani R, Najjar A, Zakaria Y, et al (2019) XPS and structural studies of high quality graphene oxide and reduced graphene oxide prepared by different chemical oxidation methods. Ceram Int 45:14439–14448
9. Ansón-Casaos A, Puértolas JA, Pascual FJ, et al (2014) The effect of gamma-irradiation on few-layered graphene materials. Appl Surf Sci 301:264–272
10. Hosseini MA, Malekie S, Ebrahimi N (2020) The analysis of linear dose-responses in gamma-irradiated graphene oxide: Can FTIR analysis be considered a novel approach to examining the linear dose-responses in carbon nanostructures? Radiat Phys Chem 176:109067
11. Kaur N, Kaur M (2018) Envisioning the composition effect on structural, magnetic, thermal and optical properties of mesoporous MgFe2O4-GO nanocomposites. Ceram Int 44:4158–4168
12. El-Khawas EH, Azab AA, Mansour AM (2020) Structural, magnetic and dielectric properties of reduced graphene oxide/La0. 9Bi0. 1FeO3 nanocomposites. Mater Chem Phys 241:122335

Antibacterial and Photocatalytic activities of g-C_3N_4/STO for biomedical and Water treatment application

Tusharkanta Nayak[1,2, a], Debashish Nayak[1], Deviprasad Sahoo[1], T M Naren Vidaarth[3], Smita Mohanty[1], and Akshaya K Palai[1]

[1]*School for Advanced Research in Petrochemicals (SARP), Laboratory for Advanced Research in Polymeric Materials (LARPM), Central Institute of Petrochemicals Engineering & Technology (CIPET), Patia, Bhubaneswar, Odisha, India- 751024*

[2]*Ravenshaw University, Cuttack, Odisha, India-753003*

[3]*K. S. Rangasamy college of technology, Tiruchengode, Namakkal.Tamil Nadu.India-637215*

[a)] *Corresponding author: tushar.nayak@ravenshawuniversity.ac.in*

Abstract

Here the production of Graphitic carbon nitride (g-C_3N_4) and its doping with strontium titanate nanopowder ($SrTiO_3$) (STO), as well as the methodical investigation of photocatalytic dye degradation of Rhodamine B (RhB) dye, have been investigated. Both the morphological and structural analyses verified that the produced materials had formed correctly. its antibacterial characteristics were examined using the Muller-Hinton technique. At last Excellent degradation efficiencies over a 0-60 minute period were achieved by the photocatalytic degradation of g-C_3N_4/STO by breaking down Rhodamine B under UV light. According to these findings, g-C_3N_4/STO is appropriate for industrial applications including biological and water treatment.

Introduction

A layered metal-free semiconductor nanomaterial with photocatalytic characteristics graphitic phase carbon nitride (g-C_3N_4) has been developed for use in environmental remediation. Its larger absorption spectrum, stronger photostability, and improved charge separation efficiency set it apart from other graphite-like photocatalysts. Strontium titanate (STO), a perovskite ceramic, has undergone extensive investigation due to its outstanding dielectric, ferroelectric, and piezoelectric characteristics. This material offers exciting avenues for research, particularly because of the interplay between its photoluminescence properties and its morphological structure. STO demonstrates remarkable compatibility with human body cells, particularly osteoblasts, and exhibits notable antibacterial activity. Due to its remarkable antibacterial properties and its compatibility with biological systems.

The combination of g-C_3N_4 and $SrTiO_3$ has shown remarkable antimicrobial properties. The production of reactive oxygen species (ROS) during the photocatalytic process is essential for their antimicrobial effects. The ROS have the ability to harm the cellular components of microorganisms, ultimately causing their inactivation and demise. The versatile properties of g-C_3N_4 and $SrTiO_3$ make them ideal materials for tackling both environmental and public health challenges. These materials have the ability to degrade dyes and also exhibit antimicrobial properties, making them highly effective in various applications. Exploring the combination of g-C_3N_4 and $SrTiO_3$ has been found to enhance their photocatalytic and antimicrobial efficiencies. Composite materials that combine g-C_3N_4 and $SrTiO_3$ have demonstrated enhanced performance by effectively separating photogenerated charge carriers and expanding the range of absorption.

This research focuses on optimizing these materials for various applications, with the goal of creating a cleaner and healthier environment. By exploring the potential of g-C_3N_4 and $SrTiO_3$ in photocatalytic dye degradation and antimicrobial activities, we are paving the way for sustainable solutions to address water pollution and microbial contamination.

Experimental Analysis

Synthesis of g-C_3N_4/STO powder:

Strontium titanate (STO) was synthesized through a solid-state reaction. Equal proportions of strontium carbonate and titanium dioxide were ball-milled for 24 hours and then calcined at 1100 °C for 5 hours. To produce g-C3N4/STO nanocomposites, melamine (5 g) was dissolved in 30 mL of DI water, and 10% STO powder was gradually added while stirring. This mixture was heated at 120 °C for 12 hours to remove water. The dried samples were processed into a powder and placed in an alumina crucible, then heated in a muffle furnace to 550 °C over

three hours at a rate of 2.5 °C per minute. The resulting yellow substance was ground, washed with ethanol and deionized water, and air-dried at 60 °C for six hours before analysis. A similar procedure was used to produce pure g-C_3N_4 without STO.

Result and discussion:

The structural analysis as well as the crystallinity nature of developed composite g-C_3N_4 /STO and also individual materials analyzed by X-ray diffraction. In XRD analysis the developed materials show diffraction peaks 27.7º, 32.48º, 39.98º, 46.48º, and 57.79º. The determined peaks correspond with the planes of crystallography (002), (110), (111), (200), and (211), respectively.For individual g-C_3N_4 and STO also shown in **Fig. 1(a)**. referenced by JCPDS file no. 01-087-1526 and 00-005-0634.

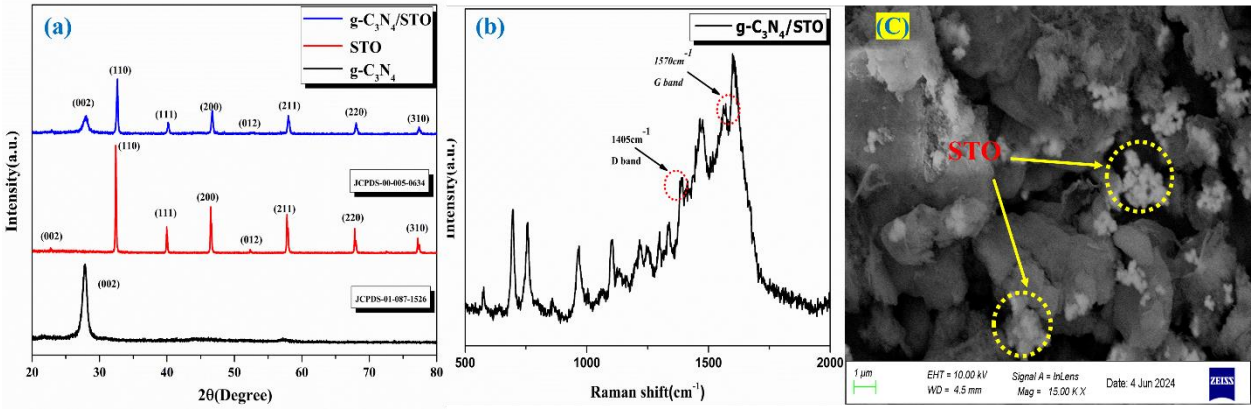


***Fig. 1**. (a) XRD pattern of synthesized* g-C_3N_4 */STO powder, and g-C3N4/STO, (b)Raman shift of* g-C_3N_4 *STO (c) FESEM images of g-*C_3N_4

Fig. 1(b) shows the Raman analysis for the Developed composite, Raman active derived at laser source 356nm and in shift resulting at 1405cm^{-1} for the D band and 1570cm^{-1} for the G band. It sharp indicating the formation of g-C_3N_4 based composite. The morphology analysis of the developed g-C_3N_4 /STO composite by the FESEM images is shown in Fig.1(c). the incorporation of STO materials sharp indicated yellow points in fig.1c. it confirmed the incorporation of STO which shows better antibacterial and photocatalytic properties.

The photocatalytic performance of g-C_3N_4 /STO particles over RhB dye degradation is projected in **Fig. 2(a).** As the irradiation time increased from 0 to 60 minutes, there was a noticeable decrease in the absorption intensity at 554 nm for RhB, which can be attributed to the impact of nanocatalysis. After the irradiation process, it was indicated that the g-C3N4/STO combination achieved a determined degradation percentage of 30% for RhB within an interval of 1 hour. Based on the characteristics of the dyes, it is evident that varying levels of dye degradation take place.

It also noted that the maximum degradation efficiency with more time of degradation. The photocatalytic efficiency (η) was calculated according to the equation derived from the graph.

$$degradation\ (\%) = \frac{C - C_0}{C} \times 100$$

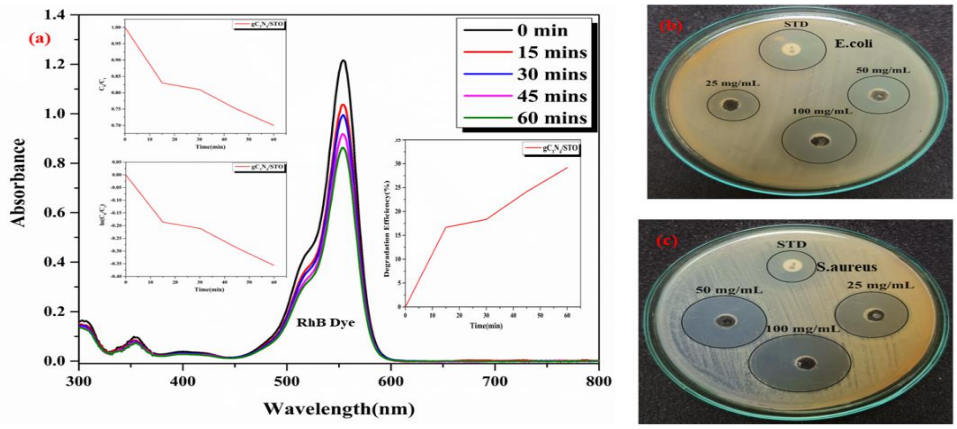


Fig. 2. (a) *Absorbance of degraded RhB dye by* g-C_3N_4*/STO (b)Antibacterial test images of* g-C_3N_4*/STO particle against E.coli Bacteria, and (c) Antibacterial test images of* g-C_3N_4*/STO particle against S aureus bacteria.*

The antibacterial activity of g-C_3N_4/STO in bacteria was determined using the Muller-Hinton method. Tests were conducted on Escherichia coli (E. coli) and Staphylococcus aureus (S. aureus) bacteria, as shown in **Fig. 2(b).** Figure demonstrates the antibacterial activities of g-C_3N_4/STO. It was noted that during an incubation period of 12 hours at a temperature of 37°C, based on the findings, it is evident that the antibacterial activity experiences a notable increase when the concentration of g-C_3N_4 STO is at 25, 50, and 100 µg/mL. The Zone inhibits various concentrations of g-C_3N_4/STO which follows a comparison with the standard Streptomycin 25. The Inhibitory Zones of 25 mg, 50 mg, and 100 mg of g-C_3N_4/STO for E. Coli bacteria are 21 mm, 25 mm, and 27 mm, and 17 mm, 19 mm, and 25 mm for S. aureus bacteria, respectively.

Conclusion

A powder of g-C3N4 was successfully synthesised, followed by an XRD analysis to characterise its structural properties. Utilising the Mueller-Hinton method, an important clear zone was observed when assessment the g-C3N4 /STO material against Escherichia coli and Staphylococcus aureus, demonstrating its possible antibacterial characteristics. In addition, the powder of g-C_3N_4/STO exhibits remarkable catalytic properties. The degradation rates of RhB dye can reach approximately 30% within a period of 60 minutes, making it suitable for various biomedical applications. g-C_3N_4/ STO is commonly employed in the textile industry to facilitate the degradation of dyes for various industrial applications. The value demonstrates innovation and is appropriately aligned with various biomedical applications. The remarkable antibacterial properties of these advanced materials hold significant promise for the enhancement of healthcare technology.

Acknowledgment

T. Nayak and all contributing authors wish to express their gratitude to the Centre of Excellence (CoE) on ‘Manufacturing of Next Generation Bio-Medical Devices’ from DCPC Govt. of India (F.No:25012/01/2020-PC-II (FTS:16020) for the financial support provided to carry out this research.

REFERENCES

1. Tunç Parlak, T., Apaydin, F., & Yildiz, K. *Journal of Thermal Analysis and Calorimetry*, *127*, 63-69 (2017).
2. Nayak, D., & Choudhary, R. B.. *Spectrochimica Acta Part A: Molecular and Biomolecular Spectroscopy*, *289*, 122-162 (2023)
3. Vidaarth, T. N., Surendhiran, S., Jagan, K. S. G., Savitha, S., Balu, K. S., Karthik, A., & Kalpana, B. *Journal of Photochemistry and Photobiology A: Chemistry*, *448*, 115349 (2024).
4. K. Sharifian, V. Mahdikhah, and S. Sheibani, Journal *Ceramic. International*.,. 47, 16, 22741–22752 (2021).

Reduced Graphene Oxide Using Graphene by Modified Hummer Process

Nileema Patil[1], J. R. Mahajan*
[1]*Deccan Education Society's, Kirti M. Doongursee College of Arts, Science and Commerce (Autonomous), Dadar(W), Mumbai-28, University of Mumbai, Maharashtra, India.*
Corresponding Author: mahajanjrm@gmail.com.

Abstract:
From last two decades Graphene(G) related materials attracted more attention of researchers due to their non presidential properties and applications. Different methods are employed for the preparation of graphene-related materials. Reduced graphene oxide (rGO) was prepared by modified Hummer's method using graphene as a starting material. Annealing temperature was fixed for reduced graphene oxide. X-ray Diffraction and Raman Spectroscopy characterized the graphene and prepared reduced graphene oxide.
Keywords: Reduced graphene oxide, Hummer's method, Graphene oxide, Raman spectroscopy and Xray diffraction.

1 Introduction:

From the discovery of graphene in 2004 it becomes a part of frontier research due to its extraordinary properties. Being a single atomic layer material, it has high specific surface area, high thermal and electronic conductivity, high mechanical property, flexibility. Graphene based polymers exhibits superior toughness and strength to original polymers. Graphene coated metals and GO, r-GO coated metals have high anti-corrosion performance. G/GO/r-Go and their composites exhibit application in supercapacitors. [1]

Reduced graphene oxide is prepared by different methods based on chemical routes, thermal method or electrochemical means. r-GO may be obtained by last treating graphene oxide (GO) with H_4N_2. H_2O (hydrazine hydrate) for 24 h at 100 °C. Exposure of GO to hydrogen plasma for some seconds and strong pulse light of xenon flashtubes. Heating GO in distilled water at varying temperatures for different times. [1,2]

This study reveals, a modified Hummer's method can be effectively used to prepare r-GO, which involves graphene as the starting material.

2 Experimental:

Chemicals and Material used: Graphene nanoplatelets (6-8nm thick) was purchased from TCI (Tokyo Chemical Industry), Sulfuric acid (H_2SO_4, about 98%pure), Phosphoric acid (H_3PO_4, about 88%pure), Potassium permanganate ($KMnO_4$, about 98%pure), Hydrochloric acid (HCL about 37%pure), all these chemicals were purchased from sigma Aldrich, hydrogen peroxide (H_2O_2 about 30%,) and Deionised water (DIW).

2.1 Method for producing reduced graphene oxide: -

r-GO was typically made from pure graphene nanoplatelets as the precursor material. using the modified Hummer process. Here, a volume ratio of 9:1 between sulfuric acid (27 ml) and phosphoric acid (3 ml) was used, and the mixture was agitated for at least 30 minutes. The next step was to whisk in 0.225 g of graphene powder to the mixing fluid.
Potassium permanganate ($KMnO_4$) was progressively added, 1.32 g at a time. Then the solution was made to stirred in an ice bath that was less than 10 degrees Celsius for 60 minutes. When this ice bath was removed, the solution temperature went up to 45°C. The coloration started changing after 5 hours of stirring to a deep green. Excess $KMnO_4$ was removed by adding 0.675 ml of hydrogen peroxide (H_2O_2) dropwise while stirring for 10 minutes. It was permitted to cool after the exothermic reaction.
Next, the mixture was centrifuged at 5000 rpm for 10 minutes, and the precipitate was washed with HCl and deionized water. A 24-hour oven drying process at 90 °C was used to create the r-GO powder from the washed r-GO pellet. Fig (A) showing flowchart for how the reactions work to make rGO.

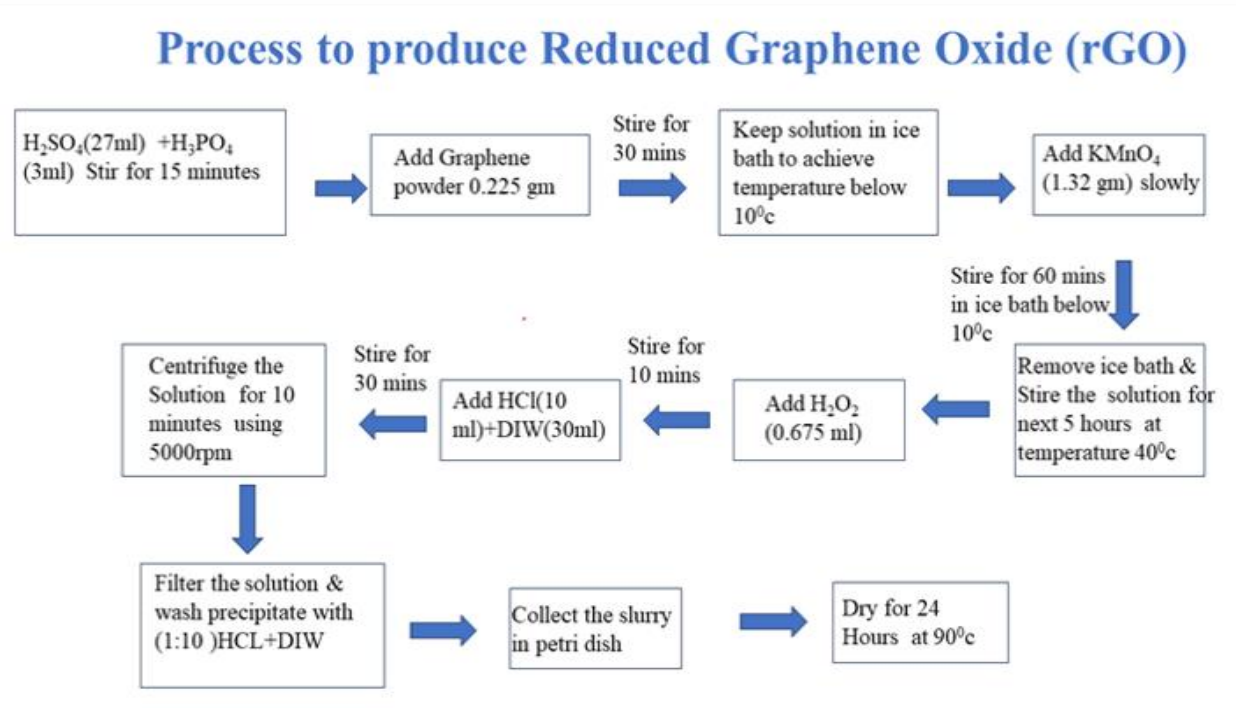


Fig. A. Flowchart showing how the reactions work to make rGO

Results and Discussion:

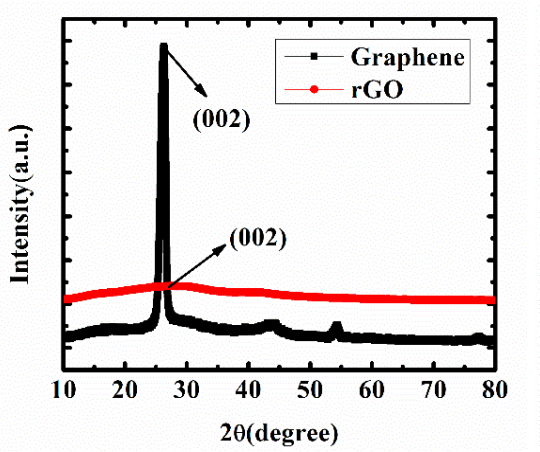
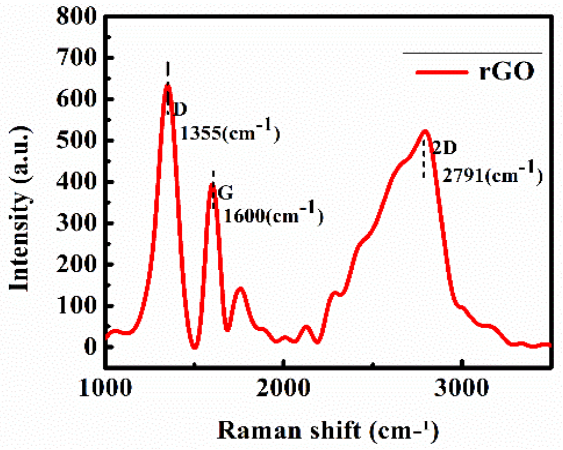


Fig (B): X-ray diffraction of Graphene and Reduced Graphene oxide (JCPDS 00-065-1528)



Fig(C): Raman Spectroscopy of Reduced Graphene oxide

Fig B. Shows the X-ray diffraction pattern of graphene and reduced graphene oxide. For graphene a sharp peak at (002) is due to graphene. A broadening of peak of (002) is due to reduced graphene oxide formation [3,6]. This validates the GO component when compared to the conventional X-ray diffraction curve of GO (JCPDS 00-065-1528).[7]

Fig(C) shows that sample consists of two prominent peaks at 1355 cm^{-1} and 1600 cm^{-1}. The peak around the 1355 cm^{-1} is due to band D. The band D reveals the presence of defects, like -distribution in the sp^2 bonding, because of heptagon and pentagon rings, vacancies, edge effects can be seen. The defects also arrive due to formation of wrinkle and the presence of functional groups, in this case $\frac{I_D}{I_G} > 1$ [4,5].

Conclusion

In present study the efforts were taken to form reduced graphene oxide from pure graphene. Fron X-ray diffraction and Raman spectroscopy it was revealed that reduced graphene oxide is formed.

Acknowledgement

We are thankful to our parent institute for providing research funding to carry out this research

References

1. Zhiyuan Liu, Rahul Navik[a], Hunjun Tan, Qixuan Xiang, Wahyudiono, Motonobu Goto, Rodolfo Morales Ibarra, Yaping Zhao,(2022) Graphene-based materials prepared by supercritical fluid technology and its application in energy storage. The J. of Supercritical Fluids,188: 105672. https://doi.org/10.1016/j.supflu.2022.105672.
2. Tarko Fentaw Emiru, Delele Worku Ayele, (2,017) Controlled synthesis, characterization and reduction of graphene oxide: A convenient method for large scale production, Egy J of Basic and App Sciences 4:74-79. http://dx.doi.org/10.1016/j.ejbas.2016.11.002.
3. Ghulam Yasin, Muhammad Arif, Muhammad Shakeel, Yuchao Dun, Yu Zuo,Waheed Qamar Khan, Yuming Tang, Ajmal Khan, and Muhammad Nadeem, (2018) Exploring the Nickel–Graphene Nanocomposite Coatings for Superior Corrosion Resistance: Manipulating the Effect of Deposition Current Density on its Morphology, Mechanical Properties, and Erosion-Corrosion Performance, Adv. Eng. Mater., 1701166:1-12, https://doi.org/10.1002/adem.201701166.
4. Kurniasari1, A Maulana, A Y Nugraheni, D N Jayanti, S Mustofa, M A Baqiya and Darminto (2017) Defect and Magnetic Properties of Reduced Graphene Oxide Prepared from Old Coconut Shell, IOP Conf. Series: Materials Science and Engineering 196: 012021, https://doi.org/10.1088/1757-899X/196/1/012021.
5. Kudin, K.N., Ozbas, B., Schniepp, H.C., Prud'homme, R.K., Aksay, I.A. and Car, R. (2008) Raman Spectra of Graphite Oxide and Functionalized Graphene Sheets. Nano Letters, 8, 36-41. https://doi.org/10.1021/nl071822y.
6. G. Sreenivasa Kumar, N. Ramamanohar Reddy, B. Sravani, L. Subramanyam Sarma,T. Veera Reddy, V. Madhavi, S. Adinarayana Reddy, (2019) Ultra-Range Bimetallic Pt–Pd Nanospheres Deposited on Reduced Graphene Sheet as Efficient Electrocatalyst Towards Electrooxidation of Methanol, Journal of cluster sci, 0123456789: https://doi.org/10.1007/s10876-019-01752-z.
7. Le Ngoc Long, Pham Trung Kien, Tran Van Khai, (2019). Synthesis of MoS2/Graphene nanocomposite by facile ultrasonic assisted hydrothermal method. Vietnam Journal of Science and Technology 57: 703-713, https://doi.org/10.15625/2525-2518/57/6/13955.

Increased Defect Sites and Enhanced Fluoride Adsorption by Nanocomposite of Silver Oxide and Hydrogen Tri Titanate Nanotubes

Prathibha C. [1, a)], Anjana Biswas[1], Dasari Swarna[1], Sushma Tripathi[1]

[1]*Department of Physics, Sri Sathya Sai Institute of Higher learning, Anantapur, Andhra Pradesh–515001, India*

[a)]Corresponding author: cprathibha@sssihl.edu.in

Abstract. A nanocomposite of hydrogen tri titanate nanotube and silver oxide was developed using a twostep simple synthesis route. The composite formation was confirmed through XRD and TEM characterizations. Further optical properties of the nanocomposite were examined by the UV-Visible spectroscopy. The data was further utilised to calculate the Urbach energy. The increased Urbach energy of the composite indicated a higher number of defect sites which further contributed to enhanced absorption properties. Further the nanocomposite was explored for adsorption of fluoride from water. The adsorbent capacity for the fluoride was 165 mg/g which is 3 times higher than that of hydrogen tri titanate nanotubes.

Keywords: Layered structure, hydrothermal, optical property, fluoride adsorption, surface area

INTRODUCTION

Developing nanocomposites is one of the efficient ways to fabricate materials with superior properties. This can be better achieved by selecting a material with a layered structure which allows the intercalation and surface decoration of the other material. Therefore, in this work Hydrogen tri titanate nanotube with a versatile layered structure was selected for the nanocomposite formation with silver oxide nanoparticles (AgTNC). The composite was developed using a simple two step procedure. The nanocomposite was synthesized with the aim of combining the attractive properties of two different materials into a single material which will offer superior properties compared to the individual counterparts. The synthesized adsorbents properties were thoroughly investigated and analysed by advanced characterization tools. Further the developed composite was explored for removal of hazardous contaminant fluoride from water through adsorption[1]. Batch adsorption studies were performed to evaluate the fluoride removal efficiency of the material.

MATERIALS AND METHODS

All the chemicals used in this work are of research grade and procured from Merck.

Silver oxide and Hydrogen tri titanate Nanotube Composite (AgTNC)

The nanocomposite was prepared by following a simple two-step synthesis route. In step 1, the hydrogen titanate nanotubes (HTNT) were synthesised by the alkaline hydrothermal method with anatase titanium dioxide as the precursor. In the second step nanocomposite with silver oxide was synthesized by treating HTNT with 0.1M of silver nitrate (AgN) solution via wet chemical route. The reaction mixture of silver nitrate solution and the synthesised HTNT was prepared and stirred for 20 h at 75 °C. At this stage the silver oxide nanoparticles form and homogeneously adhere to the nanotube surface. The resultant was filtered and dried in a hot air oven at 80°C overnight. The product thus formed is silver oxide and tri titanate Nanotube Composite (AgTNC) and was greyish in colour. Along with the nanocomposite formation, other phenomena may take place, is the incorporation of silver ions into the layered spaces of the titanate structure. Lastly, when the material is heated overnight, during the drying process, the nanoparticles bind themselves efficiently to the nanotube surface.

RESULTS AND DISCUSSION

Material Characterisation

The phase of the synthesized material, AgTNC, was confirmed with the XRD. From the fig. 1, AgTNC is composed of peaks corresponded to both monoclinic $H_2Ti_3O_7$ and cubic Ag_2O. The peaks at 2θ values 23.8°, 29.7° and 48.6° corresponding to the (h k l) planes (1 1 0), (3 1 0) and (0 2 0) respectively of the $H_2Ti_3O_7$ phase (ICSD # 98-023-7518), whereas the peaks at 34.7° and 61.2° correspond to the (1 1 1) and (3 1 1) planes of the Ag_2O phase (ICSD# 98-017-4090) [2,3]. The presence of both the phases confirmed the formation of the composite. Further, the (2 0 0) peak of the $H_2Ti_3O_7$ positioned around 2θ = 10°, representing the interlayer spacings, this feature disappeared in AgTNC due to the incorporation of Ag(I) ions into the interlayer spaces. Furthermore, the larger size of Ag(I) ions caused greater disruption of the crystallinity by interfering with the interlayer structure of HTNT. Due to the same reason, the (110) peak also has a substantial reduction in its intensity [4].

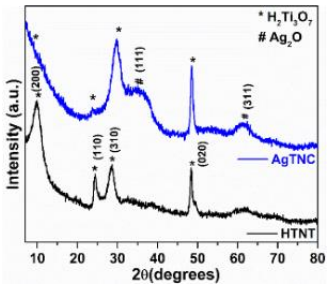


FIGURE 1. XRD of AgTNC

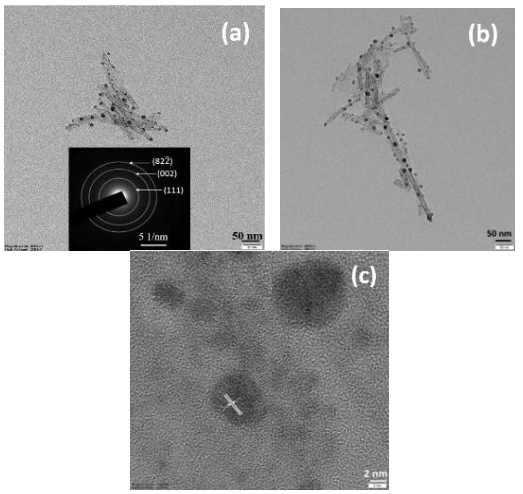


FIGURE 2. (a) and (b) are TEM images; (c) is HRTEM image of AgTNC

The TEM image, SAED pattern and HRTEM image of AgTNC are shown in fig. 2(a) – (c). From the figure, AgTNC was composed of nanotubes that are loaded with Ag(I) nanoparticles which are in spherical shape. These nanoparticles comprises the Ag_2O phase of the composite material. The phase modification was further confirmed using the lattice fringes obtained in the HRTEM images of the nanoparticles.

The size of the Ag_2O nanoparticles were in between 3.5 nm to 9.5 nm with an average particle size of 8.9 nm[5]. Further the lattice fringes in nanoparticles as observed the HRTEM images of AgTNC had the d-spacing of 0.33 nm which corresponds to the (1 1 0) plane of the Ag_2O phase[5]. The SAED pattern of AgTNC, shown as inset image in fig. 2(a), corresponded to both the Ag_2O and $H_2Ti_3O_7$ phases. The obtained results are in concurrence with the XRD data, discussed in the above section.

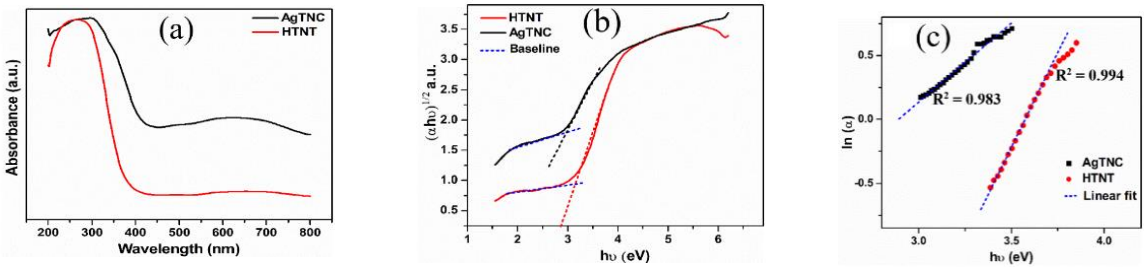


FIGURE 3. (a) UV-Vis absorbance spectra, (b) Tauc plot and (c) linear plot of ln α vs hν for calculation of Urbach energy

Urbach energy was employed as a tool to estimate the defect sites. The optical behaviour of the synthesized AgTNC was investigated using UV-Visible spectroscopy. The absorbance as a function of wavelength is illustrated in fig. 3(a). The figure reveals that HTNT exhibits an absorbance peak within the 200–300 nm region, followed by a pronounced transition, characteristic of an indirect allowed transition associated with the titanate nanostructure.The absorbance peak broadens towards a higher wavelength region which could be ascribed to the nanosized materials. The absorbance data was further examined using the Tauc relation. The Tauc plot of $(\alpha h\nu)^{1/2}$ vs $h\nu$ for calculation of indirect band gap for both AgTNC and HTNT is shown in fig. 3(b). The indirect band gap for AgTNC was found to be 2.93 eV whereas for HTNT it was 3.23 eV. Therefore, intercalation of Ag and decoration of Ag_2O nanoparticles resulted in formation of intermediate transition pathways, which resulted in the reduction in the optical band gap.

Further, the optical absorption data was used for quantification of defect sites present in AgTNC by estimating Urbach energy [6]. The linear plot of ln α vs hν is shown in fig. 3(c). The inverse of the slope of the linear fit gives the Urbach energy. The linear fit to the experimental data had R2 values of 0.994 and 0.983 respectively for HTNT and AgTNC. The Urbach energy (Eu) for HTNT and AgTNC were calculated to be 0.838 eV and 0.934 eV respectively. Therefore, the composite formation increased the Urbach energy, serving as evidence of the increased defect sites in AgTNC compared to HTNT. These defect sites behave as active sites for fluoride adsorption thereby increasing the material's adsorption efficiency.

Application: Fluoride removal efficiency of AgTNC

The developed nanocomposite was explored for its fluoride removal efficiency. AgTNc was tested for a wide range of fluoride concentrations from 2 mg/L – 200 mg/L. Fixed amount of AgTNC with a dosage of 1 g/L was mixed to these solutions seperately, at pH 2 and contact was maintained for 2 h. The adsorption capacity was measured and the variation of this parameter with the initial concentration of fluoride is shown in fig. 4(a). This experimental result was further analysed with the two popular adsorption isotherm model, Langmuir and Freundlich. As observed from the fig. 4(b), both the isotherms fit the experimental data well with $R^2 \sim 1$. The maximum Langmuir adsorption capacity of AgTNC, at pH 2, was 165 mg/g,

higher than HTNT adsorption capacity 58 mg/g at pH 2 [7]. Therefore, the formation of nanocomposite (AgTNC) resulted in 3 times enhancement of the fluoride adsorption capacity.

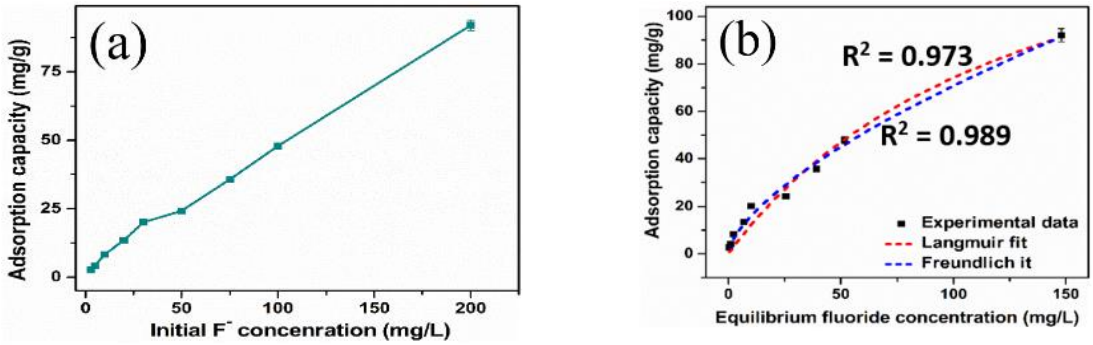


FIGURE 4. (a) Variation of adsorption capacity with initial fluoride concentration (pH = 2, dosage = 1g/L, contact time = 2 h), (b) Adsorption isotherms fit to the experimental data

CONCLUSION

This can be better achieved by selecting a material with a versatile layered structure which allows the intercalation and surface decoration of the other material. The nanocomposite of silver oxide and HTNT, that is AgTNC, exhibited enhanced adsorption properties. The fluoride removal efficiency of Ag TNC was 3 times higher than that of HTNT. The enhanced adsorption properties of the composite are a synergic effect of increased number of defect sites, the tubular morphology of HTNT and the layered structure of HTNT which allowed the intercalation of Ag ions.

ACKNOWLEDGEMENT

The authors would like to thank the Central Research Instruments Facility, Prashanthi Nilayam and Central Research laboratory, Anantapur, Andhra Pradesh, for providing necessary synthesis and characterization facilities.

REFERENCES

[1] P. Chinnakoti *et al.*, "Titanate nanobelts–a promising nanosorbent for defluoridation of drinking water," *Sep. Sci. Technol.*, vol. 55, no. 6, pp. 1023–1035, 2020, doi: 10.1080/01496395.2019.1580733.

[2] S. Akel *et al.*, "Ag/ag2O as a co-catalyst in tiO2 photocatalysis: Effect of the co-catalyst/photocatalyst mass ratio," *Catalysts*, vol. 8, no. 12, pp. 1–19, 2018, doi: 10.3390/catal8120647.

[3] Q. T. Pham, B. T. Huy, and Y. I. Lee, "New highly efficient electrochemical synthesis of dispersed Ag2O particles in the vicinity of the cathode with controllable size and shape," *J. Mater. Chem. C*, vol. 3, no. 29, pp. 7720–7726, 2015, doi: 10.1039/c5tc01274k.

[4] D. A. Sales *et al.*, "Synthesis of silver-cerium titanate nanotubes and their surface properties and antibacterial applications," *Mater. Sci. Eng. C*, vol. 115, p. 111051, 2020, doi: 10.1016/j.msec.2020.111051.

[5] A. Biswas and C. Prathibha, "Metal ion-intercalated layered hydrogen tri-titanate nanotubes: synthesis, characterization and their use in ultrafast and enhanced removal of hazardous contaminant fluoride from water," *Mater. Adv.*, vol. 3, no. 14, pp. 5947–5963, 2022, doi: 10.1039/d2ma00434h.

[6] B. Choudhury and A. Choudhury, "Oxygen defect dependent variation of band gap, Urbach energy and luminescence property of anatase, anatase-rutile mixed phase and of rutile phases of TiO2 nanoparticles," *Phys. E Low-Dimensional Syst. Nanostructures*, vol. 56, pp. 364–371, 2014, doi: 10.1016/j.physe.2013.10.014.

[7] P. Chinnakoti, R. K. Vankayala, A. L. A. Chunduri, L. R. Nagappagari, S. V. Muthukonda, and V. Kamisetti, "Trititanate Nanotubes as highly efficient adsorbent for fluoride removal from water: Adsorption performance and uptake mechanism," *J. Environ. Chem. Eng.*, vol. 4, no. 4, pp. 4754–4768, 2016, doi: 10.1016/j.jece.2016.11.007.

Exploring the Electronic and Optical Properties of Armchair SiC (8,8) SWNTs Using First-Principles Calculations

Nibedita Nayak[1, a)], Santanu Kumar Nayak[1, b)] ,Dipan Kumar Das[1, c)] and Padmaja Patnaik[1, d)]

[1]*Centurion University of Technology and Management, Odisha, India*

[a)] *Corresponding author: nibeditanayak@cutm.ac.in*

[b)] *sknayak23051996@gmail.com*

[c)] *dipandas1997@gmail.com*

[d)] *padmaja.patnaik@gmail.com*

Abstract.Single-walled silicon carbide (SiC) nanotubes have been of immense interest for their distinctive properties and their probable applications in optoelectronic devices, light-emitting diodes (LEDs), energy storage materials, and photovoltaic systems. In the present work, density functional theory (DFT) along with the universal force field method was utilized to verify the electronic aswellas optical features of armchair (8,8) SiC nanotubes by first-principles calculations. The results of the simulation show that the armchair (8,8) SiCNT has indirect band gap semiconductor characteristics. The optical properties of absorption spectra, reflectivity, conductivity, and refractive index were characterized in different spectral regions.

INTRODUCTION

Non-carbon nanotubes, or SiCNTs, are made of hexagon-shaped links between silicon and carbon atoms. These particular kinds of nanotubes are cylinder-shaped nanostructures made of single-layer silicon and carbon atoms folded into sheets (2D silicon carbide) [1-2]. Similar to carbon nanotubes, silicon carbide (SiC) nanotubes are one- dimensional tubular structures [3,4]. The diameter, thickness, and chirality of the tube determine its nature and electrical characteristics in SiC nanotubes. Strong covalent bonding allows SiC nanotubes to have more stable physical characteristics than carbon nanotubes, as well as superior electrical and magnetic capabilities [5]. Based on the pair of indices, SWCNTs are categorised into three distinct groups (n, m). Similar to carbon nanotubes, single-walled SiC nanotubes show three different forms of structure: m = n for armchair, m = 0 for zigzag, and m and n different for chiral structure.

In this paper, we present the theoretical confirmation of optical properties like conductivity, reflectivity, absorption spectra, and refractive index, electronic properties like band structure, density of states (DOS) and partial density of states (PDOS), which are computed and plotted for the armchair (8,8) SiC nanotube.

COMPUTATIONAL METHODS

A comprehensive study of the electronic and optical properties of SiC (8,8) nanotubes was carried out with the help of the computational scheme of DFT utilizing the BIOVIA Materials Studio. 340 eV of cutoff energy , plane-wave basis set was used to accurately describe the electronic wave functions, while ultrasoft pseudopotentials were adopted in order to effectively describe the core-ion valence interactions by solving the Kohn-Sham equations, the study delved into the intricacies of the electronic structure of these nanotubes. Furthermore, the optical properties were meticulously explored, providing invaluable insights into their potential applications in the realms of nanotechnology and optoelectronics

RESULTS AND DISCUSSION

Electronic properties

SiC (8,8) nanotubes' band structure plot indicate an indirect bandgap of 2.471 eV. The plot shows that the valence and conduction bands are separated, and there are several energy levels available for electron occupation. Dos plot shows more electrons in the valance band compared to the conduction band, indicating the characteristics of a semiconductor. The energy differential between the top of the valence band and the bottom of the conduction band, or bandgap, establishes the electrical characteristics of a material and its possible uses in optoelectronic devices.

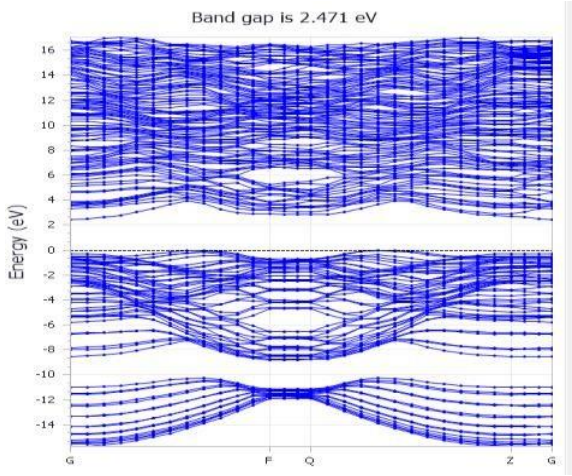


FIGURE 1. Band structure of SiC (8,8) Nanotubes

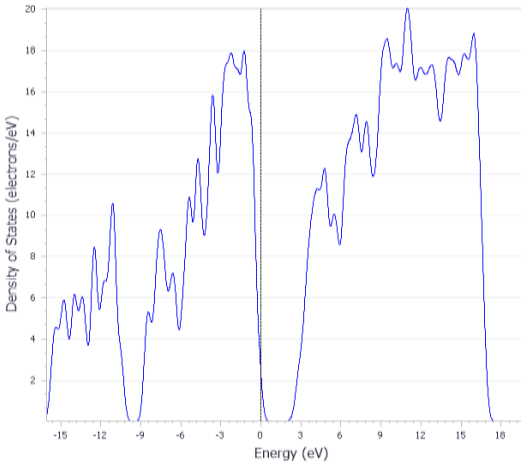


FIGURE 2. DOS of SiC (8,8) Nanotubes

Optical Properties

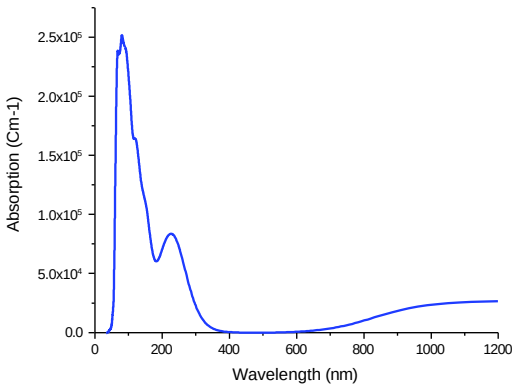


FIGURE 3. Optical absorption of SiC (8,8)

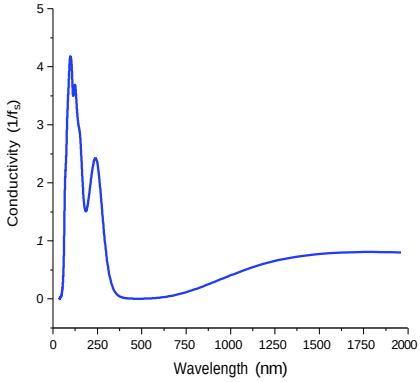


FIGURE 4. Conductivity of SiC (8,8)

In order to comprehend SiC nanotubes' behaviour with light and investigate possible optoelectronic applications, it is imperative to investigate their optical characteristics. These characteristics, which include refractive index, absorption, and reflection, provide information about the electrical structure and behaviour of the nanotube in various light settings. Through comprehension of these attributes, scientists can create innovative apparatuses, including lasers, solar cells, and sensors, that capitalise on the distinct optical features of SiC nanotubes.

SiC (8,8) nanotubes exhibit a significant UV absorption peak between 100 and 200 nm, indicating strong electronic transitions and interactions with high-energy radiation, while showing decreased absorption in the visible spectrum and a gradual increase in the NIR range. Their conductivity is highest in the UV region (100-400 nm), decreases in the visible range (400-700 nm), and further diminishes in the NIR (700-2500 nm). These properties suggest potential applications in UV sensors, optoelectronic devices, and photocatalysis, leveraging their ability to efficiently generate charge carriers and exhibit high conductivity under UV illumination.

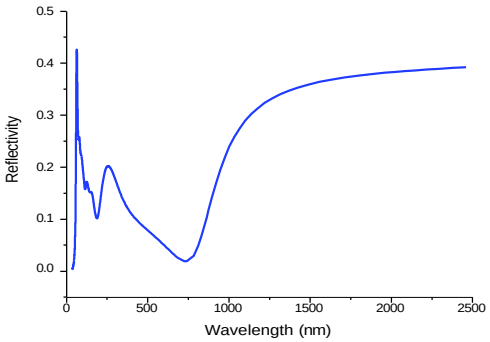


FIGURE 5. Reflectivity of SiC (8,8)

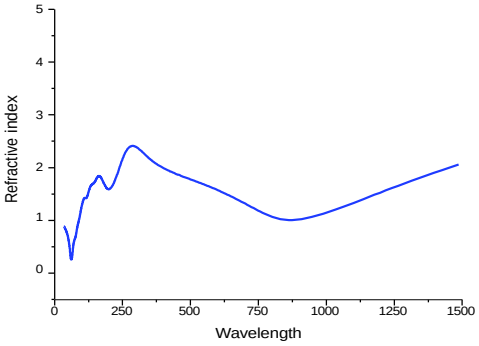


FIGURE 6. Refractive index of SiC (8,8)

SiC (8,8) nanotube have minimal reflectance between 500 and 1500 nm, indicating strong light absorption, increasing reflectivity in the NIR region, and significant UV reflectivity as a result of their interaction with high- energy photons. Their refractive index varies noticeably with wavelength; it rises quickly in the ultraviolet, fluctuates in the visible spectrum, peaks in the near-infrared, and then rises steadily in the visible spectrum. Their potential utility in UV filtering, light-absorption technologies like photocatalysis and solar energy harvesting, and NIR applications like heat management and infrared imaging is highlighted by their sensitivity to various photon energies and electronic transitions. Furthermore, the nonlinear variation in refractive index indicates uses for the technology in nonlinear optics, such as modulation, optical switching, and frequency conversion.

CONCLUSION

The study of SiC (8,8) nanotubes demonstrates their potential in advanced applications due to their unique optical and electronic properties. The indirect bandgap of 2.471 eV displayed by the nanotubes verifies that they are semiconducting. They exhibit strong visible to near-infrared light absorption, high UV conductivity, and considerable UV absorption. Their use for UV filtering, photocatalysis, solar energy harvesting, thermal management, and infrared imaging is highlighted by their variable reflectivity and refractive index. Their adaptability in a variety of technical domains is further demonstrated by their nonlinear refractive index behaviour, which offers prospective applications in nonlinear optics, such as optical switching and frequency conversion

REFERENCES

1. Pham-Huu, Cuong, Nicolas Keller, Gaby Ehret, and Marc J. Ledoux. "The first preparation of silicon carbide nanotubes by shape memory synthesis and their catalytic potential." Journal of Catalysis 200, no. 2 (2001): 400-410.
2. Nayak, Santanu Kumar, Padmaja Patnaik, Dipan Kumar Das, and Mandakini Barala. "Electronic and half-metallic behaviour of manganese doped SiC Zigzag nanotubes using density functional theory." Chemical Physics Impact 8 (2024): 100417.
3. Pan, Yuewu, Pinwen Zhu, Xin Wang, and Subei Li. "Preparation and characterization of one-dimensional SiC–CNT composite nanotubes." Diamond and related materials 20, no. 3 (2011): 310-313.
4. Das, Dipan Kumar, Padmaja Patnaik, Santanu Kumar Nayak, and Mandakini Barala. "Electronic and half-metallic behavior of copper-doped silicon carbide armchair single-walled nanotubes using density functional theory." International Journal of Computational Materials Science and Engineering (2024): 2450011.
5. Rathinavel, S., K. Priyadharshini, and Dhananjaya Panda. "A review on carbon nanotube: An overview of synthesis, properties, functionalization, characterization, and the application." Materials Science and Engineering: B 268 (2021): 115095.

Degradation studies of Dichlorvos Pesticides using Copper Nanoparticles

Chetan Pant[1], Divyanshu Pant[1], Deepak Chauhan[1] and Puja Goel[1,*]
[1]Department of Physics, G. B. Pant University of Agriculture and Technology, Pantnagar, Uttarakhand, 263145.

[*]Corresponding author: pujagoel.bpp@gbpuat.ac.in

Abstract: In this study, a stable copper nanoparticle (CuNP) suspension was prepared using isopropanol as the solvent and oleic acid as a surfactant. X-ray diffraction (XRD) was used to determine particle size and phase composition. UV-Vis analysis showed a broad peak between 243–261 nm with maximum absorbance around 249 nm and weak absorbance between 325–380 nm, indicating good suspension stability. To study pesticide degradation, various concentrations (1–100 ppm) of dichlorvos (DDVP) were treated with the Cu nanosuspension, and color changes were observed over time. UV-Vis spectra of treated samples showed a redshift in the plasmon peak, indicating pesticide breakdown. A decrease in the energy band gap, calculated using the Tauc plot method, confirmed the photocatalytic activity of Cu–Cu_2O cocatalysts. FTIR analysis further supported DDVP degradation by showing the disappearance of characteristic peaks at 1150 cm^{-1} (P=O) and 870 cm^{-1} (C–O).

Keywords: CuNPs, Band gap, Photocatalytic activity, pesticide degradation

INTRODUCTION

Dichlorvos (DDVP) is an organophosphate widely used as an insecticide for eradication of household pests [1]. Dichlorvos has a strong water solubility and a propensity to remain in water. European Union (E.U., 2007) proposed that total allowable concentration of all pesticides be 0.5 µg/L, and the maximum acceptable concentration level of any pesticide be 0.1 µg/L. However, the documented range of DDVP incidence in surface water worldwide is 0.0014–5.6300 µg/L. Therefore, the remediation of rising concentration of DDVP in wastewater and natural resources is an emerging issue that needs to be tackled before it poses a risk to public health. Conventional methods of pesticide degradation such as chemical oxidation, ozonation, photocatalysis each have their own limitations therefore there is a need to have an alternative method for effective disintegration of these pesticides from soil and water resources. In the past few years, metal nanoparticles such as Silver nanoparticles (AgNPs) and Gold nanoparticles (AuNPs) have been recognized as highly promising catalysts for pesticide disintegration however they are comparatively costly which may pose a limit on their large-scale practical application. In view of this, we have chosen CuNPs as a potential alternative as they are cost-efficient and possess well-established anti-fungal, anti-bacterial, catalytic and electrical properties.
In this work, a specified amount of isopropanol solvent and surfactant, such as oleic acid, were added to prepare a stable suspension of copper nanoparticles. This suspension was then tested for its effectiveness in DDVP mineralization in various concentrations.

MATERIALS AND METHOD

CuNPs (Sigma-Aldrich Chemical Co.) were dispersed in isopropanol (Merck & Co.) with oleic acid (Fisher Scientific Chemicals) to prepare a nanosuspension. After trying different ratios of CuNPs, isopropanol, and oleic acid, one sample with optimum stability, was selected for further experiments, containing 2 mg of CuNPs dispersed in 25 mL of isopropanol with 35 µL of oleic acid. Dichlorvos (HPM Chemical & Fertilizers Ltd.) solutions (1-100 ppm) were prepared in acetonitrile (Merck & Co.), then combined with fixed copper nanosuspension amounts for degradation studies.
The UV-Vis spectroscopy was used to characterize the copper nanosuspension and the reaction products of CuNPs and dichlorvos pesticides. XRD diffraction was carried out to estimate the particle size and phase analysis of Cu nanopowder. The degradation of dichlorvos was also analysed using the energy band gap analysis of CuNPs treated DDVP samples. FTIR spectra of Cu nanosuspension and all the reaction products in the degradation process were taken in the scanning range of 4000-600 cm^{-1}, to study the functional groups before and after the degradation process.

RESULTS AND DISCUSSION

The XRD spectra of CuNPs is shown in Fig 1(a). The peak observed at 2θ value of 36.5^0 corresponds to (111) reflection of Cu_2O which suggests the oxidation of CuNPs. Two more peaks due to Cu (111) and Cu (200) reflections are also observed. The peak due to Cu (111) has much higher intensity than Cu (200) peak which indicates that the (111) plane is closed packed. These three peaks are assigned on matching their values as per the standard JCPDS card no. 04-0836 for the pure FCC metallic Cu [2]. The average size of nanoparticles was calculated using Debye-Scherrer's equation

$$D = \frac{k\lambda}{\beta cos\theta}$$

Where D is the crystalline size of nanoparticles, k is the Scherrer's constant, λ denotes the wavelength, θ is Bragg's diffraction angle, and β denotes the full width at half maximum. From the most intense reflection from Cu (111) in XRD pattern the average size of nanoparticles was found to be around 33 nm.
UV-Vis spectra of prepared Cu nanosuspension after 60 days, recorded in 200-900 nm range is shown in Fig 1(b) A very broad peak is obtained in the 243-261 nm range with maximum absorbance at around 249 nm with a very weak absorbance in 325-380 nm range. The absorption at 249 nm was attributed to Cu^+ ions and absorption at 325-380 nm range was attributed to charge transfer bands of O − Cu − O complex of Cu_2O [3]. Even after sixty days, the nanoparticles didn't sink or modify in the suspension which implied the stability of nanosuspension is extremely high and the nanoparticles are well distributed

in isopropanol. This suggests that while oleic acid, used as a surfactant, is effective in stabilizing the nanosuspension, it does not adequately prevent the oxidation of Cu nanoparticles [4].

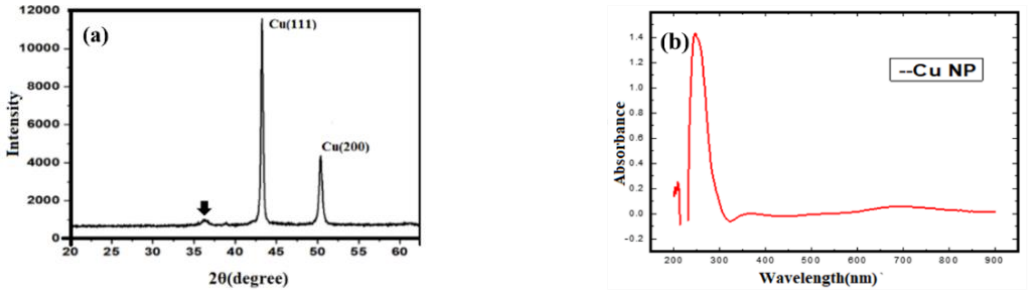


Fig. 1. (a)XRD spectra of CuNPs and (b) UV-Vis spectra of Cu nanosuspension

The change in maximum absorbance peak at different times for all concentrations of the DDVP sample is depicted in Fig 2(a). The maximum absorbance peak shifted towards a higher wavelength with the passage of time. For 1 ppm concentration the peak observed after 24 hours at 331 nm which raised to 337 nm after 72 hours, then shifted at 348 nm for 8 days later. The shifting of peaks indicates the coordination of dichlorvos on CuNPs surface, which causes degradation product. It is clear from the plot that the amount of degradation of dichlorvos increased with the increasing reaction time.

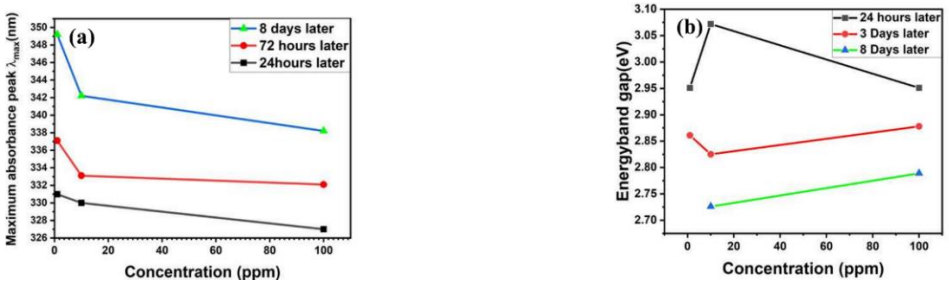


Fig. 2. (a) Variation of λ_{max} with respect to variation of dichlorvos concentrations at different time intervals (b) Time variation of energy band gap with different concentrations of DDVP

In this study, energy band of Cu_2O in reaction product was determined by the Tauc-plot method at different time intervals. It was observed that for the same concentration of the DDVP, band gap vary with reaction time. The variation of energy band gap with different concentrations for different reaction times is shown in Fig 2(b). The energy band gap has been found to decrease as the reaction time increases for all concentrations of the reaction product. Cu_2O layer acts as an electron-trap for hot electrons generated by CuNPs through interband and intraband transitions. However, when time elapses, band gap of Cu_2O decreases which allow hot electrons from CuNPs to be transferred to the surrounding Cu_2O layer conduction band to enhance its activity which in turn assist the co-ordination of DDVP on Cu NPs surface.

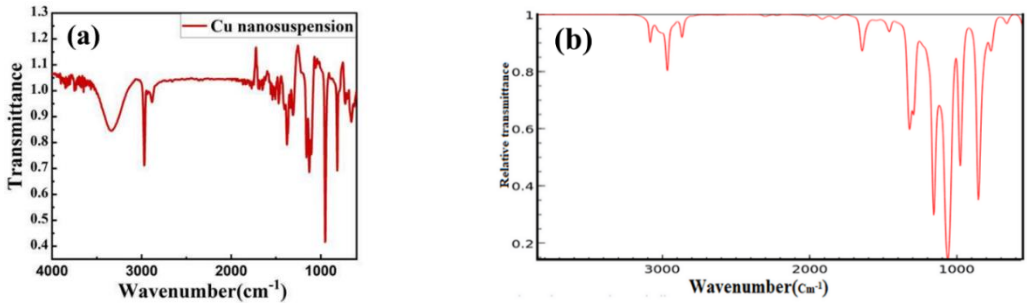


Fig. 3. FTIR spectra of (a) Cu nanosuspension and (b) dichlorvos

The FTIR spectra of Cu nanosuspension is shown in Fig 3(a). The spectra exhibit peaks in the range of 600-800 cm^{-1} which is due to the formation of CuO in the sample and can be attributed to bending mode vibration of Cu−O−Cu [5]. The peaks observed at 1128 cm^{-1} and 816 cm^{-1} are due to the stretching of C −O and C−C−O stretching respectively. These peaks are characteristic of isopropanol. Due to C−C bond vibrations, the peak is observed at 950 cm^{-1}. The peaks due to C −O and C−C−O stretching are more intense than the C − C vibration peak because of polarization caused by oxygen [6]. The stretching of C−H bond created four peaks at 1469 cm^{-1}, 1377 cm^{-1}, 1310 cm^{-1} and 1307 cm^{-1}. These peaks show the layering of oleic acid in Cu nanosuspension. The bands shown from 1771 cm^{-1} to 1507 cm^{-1} are due to C=O vibration [7]. These bands also indicate the bonding of Cu and carboxylate ion and confirm the coating of copper nanoparticles by oleic acid. The peak observed at 2968 cm^{-1}, 2936 cm^{-1} and 2883 cm^{-1} due to C−H stretching indicates the aliphatic tail of oleic acid. A wide peak observed at 3083-3901 cm^{-1} represents the −OH group absorbed on CuO nanoparticles [8].

The FTIR spectra of pure dichlorvos, taken from NIST Chemistry Web Book is shown in Fig 3(b) The peak observed at 670 cm^{-1} is due to the stretching of C–Cl. The C–O stretching exhibits two peaks at 870 cm^{-1} and 1310 cm^{-1} [9]. The peaks at 1630 cm^{-1} observed due to C=O bond stretching [10]. Due to P=O bond vibrations, comparatively intense peaks arise at 1070 cm^{-1} and 1150 cm^{-1}. The peak at 2950 cm^{-1} is found due to $-CH_2$ group vibration [10].
FTIR spectra of reaction products (Cu nanosuspension+ dichlorvos) in the range of 500 – 2500 cm^{-1} is shown in Fig 4(a). The peak present in pure dichlorvos spectra at 670 cm^{-1} due to C − Cl stretching has vanished after adding Cu nanosuspension which indicates the removal of Chlorine in the reaction products. The intensity of the Cu − O − Cu bending peaks observed at 627 cm^{-1} to 704 cm^{-1} is heavily suppressed which implied the interaction between the DDVP and nanoparticles. The peak observed at 816 cm^{-1} in nanosuspension spectra due to C − C − O stretching also decreased in intensity after adding DDVP.

In DDVP spectra, the peaks observed at 1150 cm^{-1} and 870 cm^{-1} due to P=O and C − O vibrational bonds respectively were absent in reaction products. This further indicates the degradation of these bonds of dichlorvos. One new peak at 1093 cm^{-1} was found due to CH_2 scissoring [11]. The FTIR spectra of reaction products in the range of 2500-4000 cm^{-1} are shown in Fig 4(b). The peak observed due to C-H stretching at 2950 cm^{-1} slightly shifted to 2970 cm^{-1} in reaction products. A new wide peak due to the creation of −OH bond was also observed in reaction products spectra.

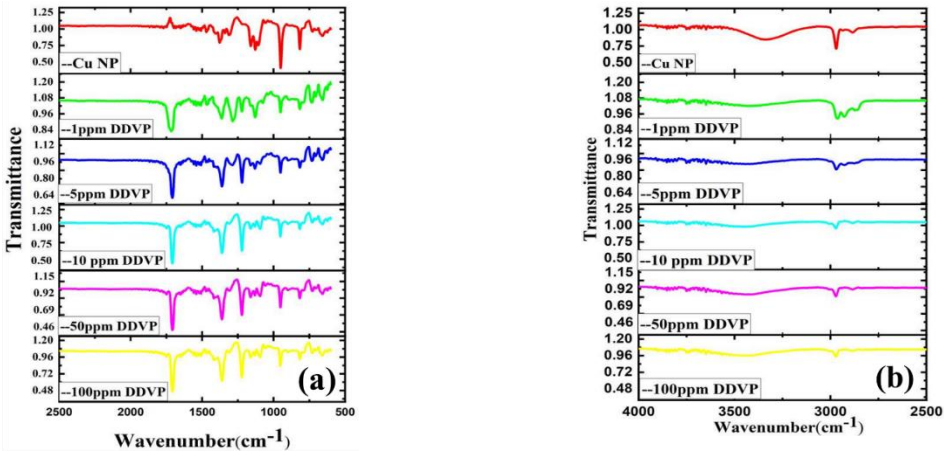


Fig. 4. FTIR spectra of DDVP + CuNPs (a). in 2500 - 500 cm^{-1} range and (b) in 4000 - 2500 cm^{-1} range

CONCLUSION

CuNPs were dispersed in isopropanol using oleic acid as a surfactant to prepare a suspension under ambient conditions. FTIR, UV-Vis, and XRD studies confirmed the stability of CuNPs in nanosuspension. The degradation of dichlorvos pesticide was studied by adding copper nanosuspension to varied concentration of DDVP solution. UV-Vis analysis depicted a shift in the absorption maxima to the longer wavelength side over time, suggesting the formation of reaction products resulting from the degradation of DDVP. In addition to this, a decrease in the energy bandgap over time, as recorded using the Tauc-Plot method, indicated the photocatalytic activity of Cu- Cu_2O cocatalysts in the degradation of DDVP. Furthermore, absence of P=O, C–O and C-Cl vibrational bonds as well as decrease in intensity of Cu-O-Cu bond in FTIR spectra of reaction products confirms the degradation of the organic bonds of dichlorvos.

ACKNOWLEDGMENT

The authors sincerely thank, Department of Biochemistry and Department of EVS, G.B.P.U.A.T. for providing UV-Vis and FTIR facilities respectively.

REFERENCES

1. A. Kumar and N. Verma, Chemical Engineering Journal 351, 428 (2018).
2. T. Theivasanthi and M. Alagar, Archives of Physics Research 1, 112 (2010).
3. Z. Kaminskiene, I. Prosyevasa, J. Stonkute, and A. Guobiene, Acta Phys Pol A 123, 111 (2013).
4. P.K. Khanna, P. More, J. Jawalkar, Y. Patil, and N. Koteswar Rao, Journal of Nanoparticle Research 11, 793 (2009).
5. D. Berra, S.E. Laouini, B. Benhaoua, M.R. Ouahrani, D. Berrani, and A. Rahal, *green synthesis of copper oxide nanoparticles by pheonixdactylifera l leaves extract* (2018).
6. B. Smith, (2017).
7. D. Mott, J. Galkowski, L. Wang, J. Luo, and C.J. Zhong, Langmuir 23, 5740 (2007).
8. N. Jardón-Maximino, M. Pérez-Alvarez, R. Sierra-Ávila, C.A. Ávila-Orta, E. Jiménez-Regalado, A.M. Bello, P. González-Morones, and G. Cadenas-Pliego, J Nanomater 2018, (2018).
9. T. Alka and B. Anita,Int. **J**. Environ. Sci. 3(11):41-6 (2014).
10. C.H. Cheng, J. Lehmann, J.E. Thies, S.D. Burton, and M.H. Engelhard, Org Geochem 37, 1477 (2006).
11. P. Goel and M. Arora, Journal of Nanoparticle Research 24, 1 (2022).

Phonon Confinement and Size Effect in the Raman Modes of $K_{0.5}Na_{0.5}NbO_3$ Lead-free Ceramics

Manish Saha[1, 2], Saket Asthana[1, a)] and Manish K. Niranjan[2, b)]

[1]*Advanced Functional Materials Laboratory, Department of Physics, Indian Institute of Technology Hyderabad, Kandi, Telangana-502284, India*
[2]*Theoretical Nanoscience Group, Department of Physics, Indian Institute of Technology Hyderabad, Kandi, Telangana-502284, India*

Corresponding author: [a)]asthanas@phy.iith.ac.in, [b)]manish@phy.iith.ac.in

Abstract. The relationship between grain size and Raman modes in lead-free ceramics $K_{0.5}Na_{0.5}NbO_3$ (KNN) is investigated through a comprehensive examination of the effects of different synthesis methods on Raman spectroscopy. KNN ceramics are synthesized through the conventional solid-state and hydrothermal methods to obtain different grain sizes. The phonon confinement effect (PCE) explains the grain size effect on the changes in the Raman spectra. Asymmetric broadening and intensity variation observed in Raman peaks of KNN samples is corelated with grain size and PCE. To illustrate the correlation between experimental Raman data and PCE predictions, the present study incorporates effects such as grain and crystallite size distribution. The computed Raman spectrum obtained from density functional theory (DFT) shows strong agreement with the experimental spectrum.

Keywords: KNN, lead-free piezoelectric, Raman spectra, Phonon confinement effect, first-principles calculations

INTRODUCTION

$K_{0.5}Na_{0.5}NbO_3$ (KNN) has emerged as a leading piezoelectric material among lead-free alternatives due to its high Curie temperature and excellent piezoelectric performance [1]. In addition to the solid-state method, the hydrothermal approach is employed due to its advantages, including compositional uniformity, stoichiometry, lower sintering temperature, controlled stoichiometry and better photocatalytic property as well [1]. Raman spectroscopy is a valuable tool for examining the structural characteristics of finite size of nanoparticles because the changes in Raman modes with decreases in grain/particle size can be clearly observed. However, the effects of grain size on Raman modes and electron-phonon interactions are still not fully understood [2]. Raman modes study provides essential information about structure, composition, homogeneity of a material, chemical bonding and surface modes, thereby revealing the effects of the finite size of the nanoparticles. As the grain/particle size decreases, the increasing surface to volume ratio can significantly impact on material properties [1]. The reduction in particle size contributes to changes in lattice vibrations, which in turn causes shifts in Raman spectral features. The crystal structure of KNN consists of orthorhombic $Amm2$ symmetry with ten atoms per unit cell, results in the presence of 27 optical phonon modes [3].

EXPERIMENTAL DETAILTS

$K_{0.5}Na_{0.5}NbO_3$ ceramics are prepared using two different synthesis procedures: a hydrothermal method and a conventional solid-state method, indicated as KNN-H and KNN-S, respectively. The synthesis process and Raman characterization technique are described in detail elsewhere [1,3]. First-principles calculations are carried out using the plane-wave formalism within the density functional theory (DFT) framework, as implemented in the PWscf package and further details are mentioned in elsewhere [3].

RESULTS AND DISCUSSION

Fig.1(a) illustrates the Raman spectra of KNN-S and KNN-H. Three characteristic Raman peaks at 852, 609 and 259 cm^{-1} are attributed to the internal vibrations of the NbO_6 octahedron. To better visualize the differences between the KNN-H and KNN-S spectra, the intensity variation and broadening a peak (259 cm^{-1}) with respect to the grain-size is presented in the form of contour plot (see Fig. 1(c)), showing the intensity of the mode versus Raman shift and grain size. Comparing two Raman spectra KNN-S and KNN-H, it is clear that the band broadening increases and a relative decrease in intensity with decreasing particle/grain size**;** as reflected in Fig. 1(a) and (c). However, the bands shifting is insignificant, and so it is not considered further in this study. Phonon confinement effect (PCE) provides a suitable explanation for the observed Raman modes [4,5]. According to PCE, in an infinite crystal, only phonons near the Brillouin Zone (BZ) center ($q \sim 0$) contribute to the Raman spectrum due to momentum conservation with incident light and resulting in sharp Raman peaks. Whereas, phonons can be confined in space by defects or crystal boundaries in a nanocrystal or finite crystal. As a result, uncertainty in the phonon momentum, allowing phonons away from the BZ-center ($q \neq 0$) to influence the Raman spectrum. The uncertainty increases with decreasing grain size (i.e., in KNN-H), which in turn causes the Raman peak to broaden asymmetrically more as the particle/grain size decreases. This implies the contribution of off-center phonons in KNN-H is increased. Intensity variation of the Raman peaks can be attributed to changes in the chemical bonds between atoms within the material. The lower density in KNN-H could induce defects [1] might cause certain bonds to break and/or lead to the formation of new bonds. This suggests that changes in the elements of the polarizability tensors associated with the vibrational modes involving these bonds, which results the changes in the intensity of the corresponding peaks [6]. For one-phonon Raman scattering at the BZ-center, the first-order Raman intensity $I(\omega)$ arising from PCE is expressed as [5]:

$$I(\omega) \cong \int_{BZ} \frac{|C(\boldsymbol{q_0},\boldsymbol{q})|^2}{[\omega-\omega(\boldsymbol{q})]^2-(\Gamma_0/2)^2} d^3\boldsymbol{q} \qquad (1)$$

where $C(q_0, q)$ represents the Fourier transform coefficients associated with the confinement function, while $\boldsymbol{\Gamma_0}$ is the natural linewidth of the zone-center Raman mode and $\boldsymbol{\omega(q)}$ represents the phonon dispersion relation. $\boldsymbol{q_0}$ corresponds to the phonon wave vector for an infinite crystal. Therefore, these Raman spectra are correlated with the grain / crystallite size and crystalline quality assessed by XRD (X-ray diffractometer) and SEM (Scanning electron microscopy); where the crystallite size (D), grain size and relative density for KNN-S and KNN-H are (64 and 39 nm), (2.072 and 0.895 μm) and (96 % and 94 %) respectively [1]. According to the Heisenberg uncertainty principle, the uncertainty in the wave vector for a vibration is expressed as $\Delta q = \pi/D$**,** where $q = |q|$**.** The magnitude of the BZ boundary wave vector is given by $|k_{BZ}| = \pi/a$, where a is the lattice constant [5]. For instance**,** KNN-H and KNN-S would cause of uncertainty of $\Delta q_x \approx 1$ % and 0.6 % respectively, relative to the zone-center phonon wave vector and the size of the BZ (i.e., $\Delta q_x/k_x = a/D$); where $a = 3.9437$ and 3.9451 Å for KNN-H and KNN-S respectively [1]. Fig. 1(d) represents a schematic diagram of PCE on the Raman spectra for KNN samples. The computed Raman spectrum in Fig. 1(b) agrees well with the experimental results shown in Fig. 1(a). According to the irreducible representation of C_{2v}^{14} point group, the optical phonon modes at the zone-center (Γ-point) are represented as [3]:

$$\Gamma \equiv 9A_1 \oplus 9B_1 \oplus 7B_2 \oplus 2A_2 \qquad (2)$$

All modes are Raman-active and non-degenerate. It is important to note that, the ab-initio calculated mode frequencies presented here correspond to zero temperature (T=0 K), while the experimental results correspond to room temperature (T=300 K). The shift in mode frequency with increasing temperature (from 0 K to 300 K) due to anharmonicity from phonon–phonon coupling and three-phonon processes [3].

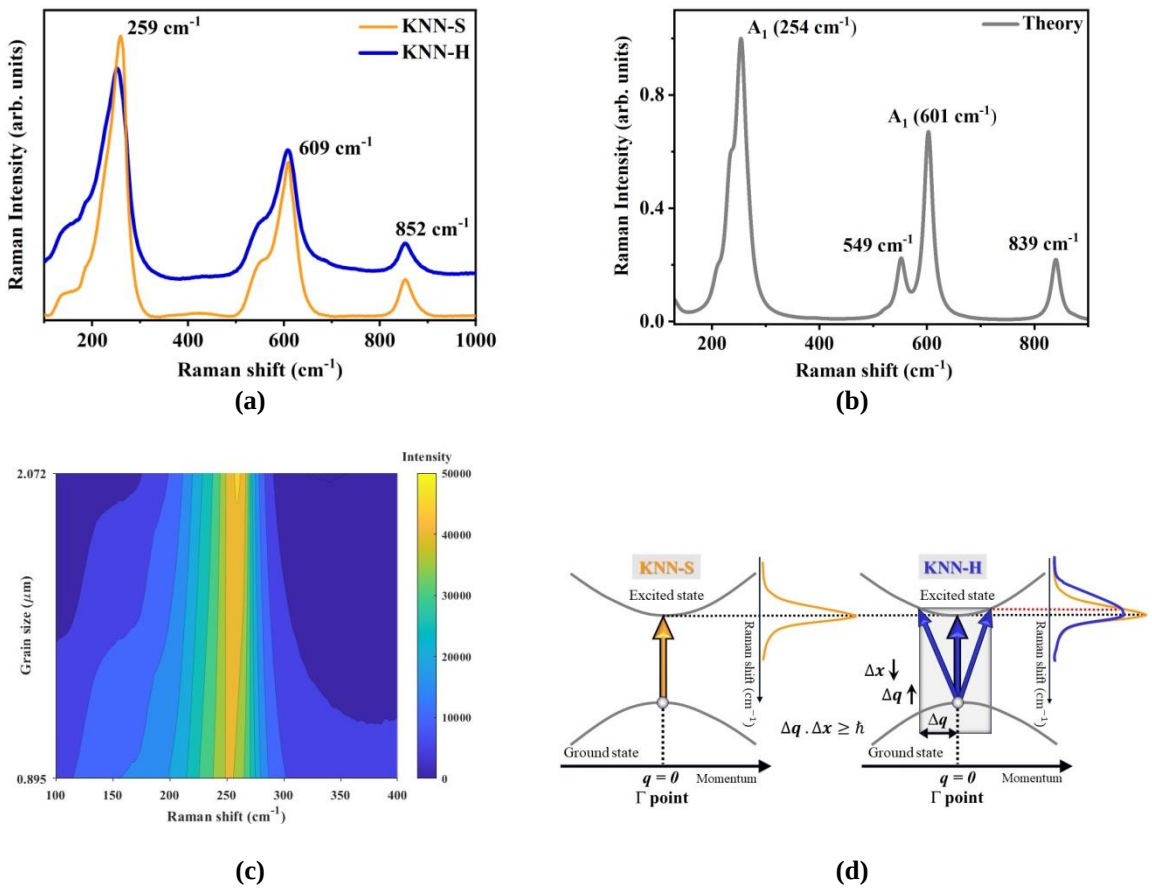


FIGURE 1. (a) Room temperature Raman spectra of KNN-S and KNN-H ceramics. **(b)** Computed Raman spectra of KNN. **(c)** Contour plot of Raman intensity versus frequency and grain size. **(d)** Schematic diagram of the phonon confinement effect on the Raman spectra for KNN-S and KNN-H.

CONCLUSION

In conclusion, the Raman spectra of KNN prepared by hydrothermal and solid-state method is studied. The correlation between intensity and broadens of the Raman mode versus grain size is established and comprehensively explained by PCE. KNN-H shows higher wavevector uncertainty than KNN-S ceramic due to smaller grain size**.** The computed Raman modes agree well with the experimental results.

ACKNOWLEDGMENTS

This work is supported by UGC-DAE (CRS/2021– 22/03/553) and DST-FIST (SR/FST/PSI-215/2016).

REFERENCES

1. M. Saha, P.P. Cho, C. Subrahmanyam, M.K. Niranjan, S. Asthana, J. Mater.Sci. Mater.Electron. **34**, 2214,(2023).
2. Choi, Hyun Chul, Young Mee Jung, and Seung Bin Kim, Vibrational spectroscopy **37(1)**, 33-38, (2005).
3. M. Saha, M.K. Niranjan, S. Asthana, J. Phys. Condens. Matter. **36,** 425703 (2024).
4. Zuo, J., Xu, C., Liu, Y. and Qian, Y., Nanostructured materials, **10**, 1331-1335, (1998).
5. Osswald, S., Mochalin, V.N., Havel, M., Yushin, G. and Gogotsi, Y., Physical Review B-Condensed Matter and Materials Physics, **80**, 075419, (2009).
6. Cançado, L.G., Jorio, A., Ferreira, E.M., Stavale, F., Achete, C.A., Capaz, R.B., Moutinho, M.D.O., Lombardo, A., Kulmala, T.S. and Ferrari, A.C., Nano letters, **11**, 3190-3196, (2011).

Mixed State of rGO/GO in The Removal of Cadmium Ion from Water

Sushma Tripathi[1], Dasari Swarna[1], Anjana Biswas[1] and Prathibha C. [1, a)]

[1]*Department of Physics, Sri Sathya Sai Institute of Higher Learning, Anantapur, Andhra Pradesh-515001, India*

[a)]Corresponding author: cprathibha@sssihl.edu.in

Abstract. The green and facile approach to synthesize a two dimensional nano-hybrid of reduced graphene oxide(rGO) /graphene oxide (GO) was successfully achieved. The material characterization confirmed the mixed state of rGO/GO. The preparation using inexpensive source – sugar, from local markets and the high yield along with a very short synthesis time makes it possible to scale up the procedure. Further, the developed material was employed in removal of hazardous contaminant, cadmium, from water. It was possible to achieve 70 % of Cd^{2+} removal from 1 L of water with the use of 1g of the material. The production cost of 1g of material is as low as 20 paise, making the method highly cost effective. Therefore, this work reports an economic and efficient material for removal of toxic contaminant, cadmium ion, from water, serving as a pathway to develop nanomaterial based filters for removal of cadmium.

Keywords: green, cost effective, reduced graphene oxide, adsorption, fluoride

INTRODUCTION

Water contamination is one of the major problems in the world due to the explosion of population and immature handling of technologies at industrial level. The dreadful effect of water contamination is majorly due to the presence of heavy metal ions. Heavy metal ions are not biodegradable and they can easily enter the food chain causing very serious health problems even leading to death [1].Cadmium is one of the heavy metal ions which has adverse effects on human health when exposed for a longer time period. According to the World Health Organization (WHO) and the Environmental Protection Agency (EPA), the permissible limit of cadmium in drinking water is 3 ppb and 5 ppb, respectively [2]. Hence, it is important to remove cadmium from contaminated drinking water.

Carbon rich material in adsorption phenomena has been known for millennia, however there is a need for improving its efficiency [3]. Reduced graphene oxide and graphene oxide are the modified forms of the carbon rich material having high surface area, low mass, and numerous functional groups such as carboxyl, epoxy and hydroxyl groups that provide attachment sites for ion exchange. Reduced graphene oxide has attracted many researchers because of the similarity with pristine graphene [4]. The production of large scale of graphene oxide and reduced graphene oxide with Hummer's method and other chemical reduction methods has not become a strategically global method. However, the rapid method for the synthesis of rGO nanosheet by thermal decomposition of sugar without adding any solvent and hazardous chemicals has gained attraction in removal of cadmium ions from water.

MATERIALS AND METHODS

Common sugar was procured from the local market. Cadmium nitrate tetrahydrate ($Cd(NO_3)_2.4H_2O$) and Ionic strength adjuster (ISA) were procured from Sigma Aldrich and ThermoScientific, USA respectively. All the experiments were carried out using Milli-Q water.

The mixed state rGO/GO was prepared by heating the crystalline sugar (5 g) in a pre-heated muffle furnace at 400 ± 10 °C [4]. Sugar taken in the Borosil glass beaker was directly introduced into the muffle furnace for nearly about 9 min. This resulted in puffed foam and the final product was obtained by crushing the puffed foam using mortar and pestle into a fine powder.

Adsorption studies

The adsorption experiments were performed in polypropylene bottles. The stock solutions of various concentrations were prepared by dissolving a calculated amount of cadmium nitrate tetrahydrate ($Cd(NO_3)_2.4H_2O$) in Milli-Q water. In order to prepare 100 mg/L of cadmium ion solution, 274.4 mg of $Cd(NO_3)_2.4H_2O$ was dissolved in 1000 mL of Milli-Q water. The functioning solutions were further prepared by serial dilution of the

stock solution. For the adsorption measurement, fixed dosage of adsorbent was added to various cadmium concentrations. The adsorbent was retrieved by filtration. The cadmium ion content was measured before and after adsorption by Orion cadmium ion sensing meter. Ionic Strength Adjuster was added to each sample in 1:50 ratio before recording the measurement.

RESULT AND DISCUSSION

The phase of the sample was identified by analysing the XRD data obtained by using the PANalytical X'Pert Pro system with Copper K_α source (λ= 1.5406 Å), room temperature X-ray diffractometer. The crystallinity and amorphous nature of synthesized material was studied with the help of XRD spectra, shown in fig. 1. The XRD peak at 17.19° corresponded to the mixed state between reduced graphene oxide and graphene oxide. The shift in the peak towards the higher theta value was also reported by B. Aragaw . This might be due to the strong π-π interactions between the planes of GO and rGO [8]. In addition, the peak shown in the fig. 1 is wide, indicating the amorphous nature of the material [5].

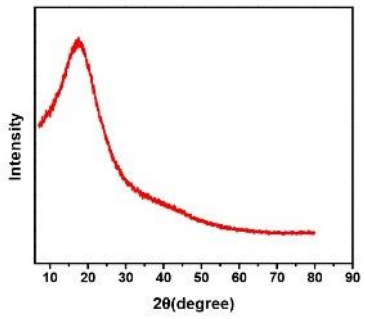


FIGURE 1. XRD Pattern

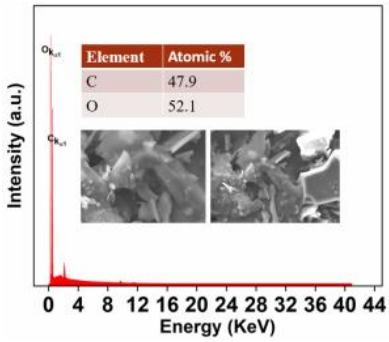


FIGURE 2. SEM Image

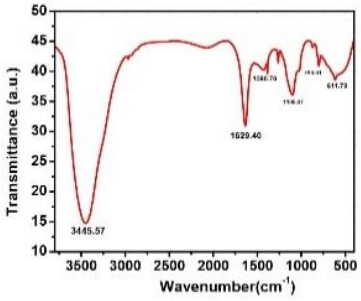


FIGURE 3. FTIR Spectra

The analysis surface morphology and elemental composition was carried by using the Jeol IT-300 Energy Dispersive X-ray Spectroscopic Facility. The low magnification SEM images (fig. 3) of the synthesized rGO/GO revealed its nanosheet-like structure of rGO and flake-like structure of GO [4]. The EDS was also employed to evaluate the chemical composition of the synthesized material. The result from EDS showed that the product contains only carbon and oxygen indicating the purity of the material. As depicted in fig. 2, the carbon composition is greater than GO but lesser than rGO [9]. Thus, it confirms that the synthesized material is a mixed state of rGO / GO.

The available functional groups of the synthesized material were obtained using the Perkin Elmer Spectrum 2 Fourier transform infrared instrument, from the FTIR spectra (fig. 3). The intense peak at 3445.57 cm^{-1} corresponded to the stretching vibration of the hydroxyl group present in the material [5]. The peak at 1629.40 cm^{-1} corresponded to vibration of aromatic rings (C=C and C=O) [6]. The band at 1629.40 cm^{-1} represented alkane-nature and also suggested that sp^2 structure of carbon atoms remains as expected [7]. The peaks at 1380.70 cm^{-1} and 1100.07 cm^{-1} were linked with the -C-C bending [6] and (C-O-H) bonding [8], respectively.

Application: mixed state of rGO/GO in the removal of cadmium in water

The adsorption capacity is a measure of the amount of cadmium ion adsorbed per gram of the material used for adsorption. It is calculated by the formula:

$$q_e = \frac{(C_i - C_e)V}{m} \quad (mg/g)$$

where, C_i and C_e are the initial and final cadmium concentrations respectively, V represents the volume (L) and m is the mass of adsorbent (g).

Isotherm Studies on Cadmium adsorption by rGO/GO mixed state

To analyze the efficiency of inexpensively synthesized rGO/GO in removal of heavy metal ion, cadmium, experiments were conducted in batch mode. In a typical experiment, adsorbent with a dose of 1 g/L was added to 10 mg/L of cadmium solution adjusted to different pH .The solution was maintained in contact with the adsorbent for a contact time of 5 h. As shown in the fig. 4(a) the maximum adsorption capacity was obtained at pH 4 and it decreased towards higher pH.

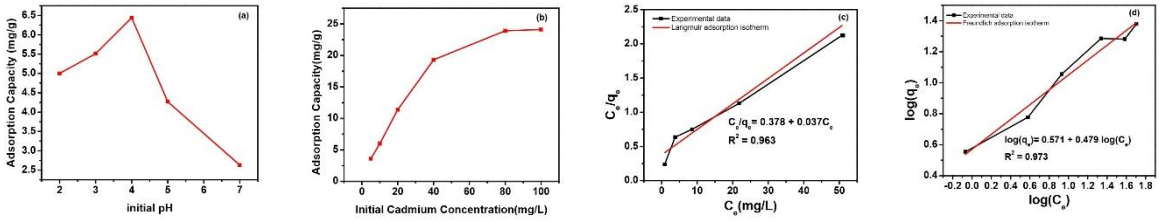


FIGURE 4. Cadmium adsorption studies using nano-hybrid rGO/GO (a) variation of adsorption capacity with pH of the solution (b) variation of adsorption capacity with initial cadmium concentration (c) Langmuir Isotherm (d) Freundlich Isotherm

Further, to evaluate the efficiency of the material in treating low and high concentrations of cadmium, the experiments were conducted with an adsorbent dosage of 1 g/L and initial cadmium concentration ranging from 1 to 100 ppm at pH 4 with a contact time of 5 h. The data obtained was plotted and shown in fig. 4(b). As the figure depicts, the adsorption capacity increased with increment in initial cadmium concentration, nearly reaching a saturation value at higher cadmium concentration. This indicated that developed material was suitable for treating both low and high concentration of cadmium. Further, this data was employed to model two famous adsorption isotherms Langmuir and Freundlich in order to get an insight into adsorption mechanism. From the fig. 4(c) and 4(d), it is evident that both the isotherms modelled the data with R^2 value close to 1. This indicated the adsorption mechanism to be a combination of physisorption and chemisorption. The maximum adsorption capacity of nano-hybrid rGO/GO, calculated from Langmuir fit of experimental data was 26.87 mg/g which is much higher compared to many carbon based materials reported in the literature [10].

CONCLUSION

A mixed state rGO/GO was successfully obtained by a simple, fast, and direct thermal decomposition method. The method produced a material with a cost as low as 20 paise per gram, significantly lower than any other available method, which costs at least Rs. 1 per gram. The characterizations employed confirmed the developed material to be the mixed state of rGO/GO. Furthermore, this study also investigated the suitability of the material for adsorption of cadmium ion in the batch system. It was possible to bring down 5 ppm cadmium concentration to a final concentration of 1.4 ppm, using as low as 1 g/L of the material. Thus, this work confirms that rGO/GO is a cost effective and efficient nanomaterial that can be easily scaled up for the removal of excessive cadmium from water.

ACKNOWLEDGEMENT

The authors gracefully like to thank the Central Research Instruments Facility, Prasanthi Nilayam and Central Research laboratory, Anantapur, Andhra Pradesh, for providing the synthesis and characterization facilities.

REFERENCES

1. S. Bagheri, A. Esrafili, M. Kermani, J. Mehralipour, and M. Gholami, Jounal of Molecular liquid, **9** (2020).
2. S. Maity, S. Deshmukh, S. S. Roy, and B. B. Dhar, ChemElectroChem, **10** (2023).
3. E. Worch, Adsorption Technology in Water Treatment (De Gruyter, Boston, 2012), p.p 12.
4. P. Chithaiah, M. M. Raju, G. U. Kulkarni, and C. N. R. Rao, **11**, 68–75 (2020).
5. S. Wu, L. Kong, and J. Liu, Res. Chem. Intermed., **42**, 4513–4530 (2016).
6. C. Bhan, J. Singh, N. Sahu, and J. R. Koduru, Environ. Sci. Pollut. Res., **30**, 87483–87499 (2023).
7. V. Sarmiento, M. Lockett, E. G. Sumbarda-ramos, and V. Oscar, Molecules, **28,** 1–18 (2023).
8. B. A. Aragaw, J. Nanostructure Chem., **10**, 9–18 (2020).
9. S. Azizighannad and S. Mitra, Sci. Rep., **8**, 1–8 (2018).
10. Y. Bian, Z. Y. Bian, J. X. Zhang, A. Z. Ding, S. L. Liu, and H. Wang, Appl. Surf. Sci., **329**, 269–275 (2015).

Synthesis of polymer functionalized manganese iron oxide nanoparticles by using thermal decomposition method in magnetically activated hyperthermia therapy

Satish S. Phalake, Vishwajeet M. Khot*

Department of Medical Physics, Centre for Interdisciplinary Research, D. Y. Patil Education Society (Deemed to be University), Kolhapur, MS, India, 416 006

* Corresponding author: E-mail: wish.khot@gmail.com

Abstract

Magnetic hyperthermia, utilizing magnetic nanoparticles (MNPs), shows significant potential as an adjunct cancer treatment due to MNPs ability to generate heat when exposed to an alternating magnetic field (AMF). In this study, manganese iron oxide nanoparticles were synthesized via the thermal decomposition method. The resulting nanoparticles, confirmed to have a cubic spinel structure through X-ray diffraction, transmission electron microscopy, Fourier transform infrared spectroscopy, and vibrating sample magnetometry, were monodisperse with an average size of 22.75 ± 0.17 nm and excellent cubic morphology. The specific absorption rate (SAR) of the nanoparticles were 154.67 W/g at a clinical field maximum of 352.2 Oe and a frequency of 277 kHz. The m-PEG functionalized MNPs exhibited highest specific absorption rate (SAR) of about 342.08 W/g at the same field. These results highlight the potential of enhanced magnetic heating efficiency of functionalized manganese iron oxide nanoparticles, suggesting promising advancements in hyperthermia as an alternative cancer therapy.

Keywords: Magnetic hyperthermia, Magnetic nanoparticles, Nanoclusters, Thermal decomposition etc.

Introduction

In resent year magnetic nanoparticles (MNPs) have received great attention over the past several decades due to their potential use as multifunctional biomedical applications such as drug delivery, biosensing, magnetic resonance imaging, and cancer treatment [1–5]. Magnetic hyperthermia, which utilizes MNPs, shows great promise as an adjunct therapy for cancer treatment due to the MNPs inherent ability to dissipate heat when exposed to an alternating magnetic field (AMF). Spinel ferrites are crucial magnetic materials because of their unique combination of electrical and magnetic properties. Notably, manganese iron oxide nanoparticles exhibit a mixed spinel structure, with Mn^{2+} and Fe^{3+} ions occupying both A and B sites simultaneously. This distinctive lattice arrangement enhances their magnetic properties, making them highly suitable for advanced biomedical applications [6]. The synthesis of manganese iron oxide nanoparticles by different methods like coprecipitation, hydrothermal, and thermal decomposition. For practical biomedical applications, iron oxide nanoparticles need surface modification with non-toxic and biocompatible stabilizers. Methoxy-polyethylene glycol (m-PEG) is a promising coating option due to its highly hydrophilic nature, which enhances biocompatibility, colloidal stability, and the SAR of MNPs [7,8]. In the present investigation, manganese iron oxide nanoparticles were prepared by a promising thermal decompositions method and functionalized with m-PEG. The structural and magnetic properties of m-PEG functionalized MNPs were investigated to understand their self-heating mechanism under an AC magnetic field.

Result and Discussion

The phase identification and purity of materials were confirmed by X-ray diffraction (XRD) measurements. **Fig.1a** shows the XRD patterns of $MnFe_2O_4$ and m-PEG $MnFe_2O_4$ NCs. The characteristic broad diffraction peaks confirmed crystallinity of NPs and their reflection planes (220), (311), (400), (422), (511), (440), (622) indicates presence of all the diffraction peaks obtained are well-matched with JCPDS card nos. 00-010-0319 for both sample and spinel cubic structure is confirmed (space group Fd3m). The crystallite size of synthesized MNPs was determined by using Scherrer's formula, the average crystallite size of MNPs was found to be 18.08 nm. The synthesized MNPs show uniform size distribution as measured by transmission electron microscopy (TEM) and morphologies of the as synthesized magnetic nanoparticles are shown in **Fig. 1b** The MNPs have a cubic shape and exhibiting a narrow size distribution well fitted by a log-normal distribution function with a mean value of 22.75 ± 0.17 nm. The particle size distribution of the nanoparticles was determined by generating a histogram of diameters from TEM images using ImageJ software (**Fig. 1b**). TEM images also revealed variations in the aggregation state of the samples.

Fig. 1c shows the FTIR spectra of the as-synthesized Fe_3O_4 NCs. The strong absorption bands at 451 and 576 cm^{-1} are associated with the vibration of Fe–O bonds. The absorption band at 781 cm^{-1} arises from the C–H stretching vibration. The bands at 1386 cm^{-1} and 1632 cm^{-1} occurred from the C-H and C=O bond vibrations in surfactant molecules. Absorption bands at 2920 cm^{-1} and 3416 cm^{-1} are attributed to the C–H and O-H band vibration [9]. The presence of m-PEG layer on MNPs surface was characterized after coating m-PEG shown in fig. c. The absorption band at about 458 and 571 cm^{-1} is due to Fe–O stretching vibration for the Fe_3O_4 nanoparticles. The intensity of this peak is reduced as compared to as synthesized MNPs due to m-PEG coating on the MNPs and it confirm the polymer m-PEG grafted on the surface of MNPs [10].

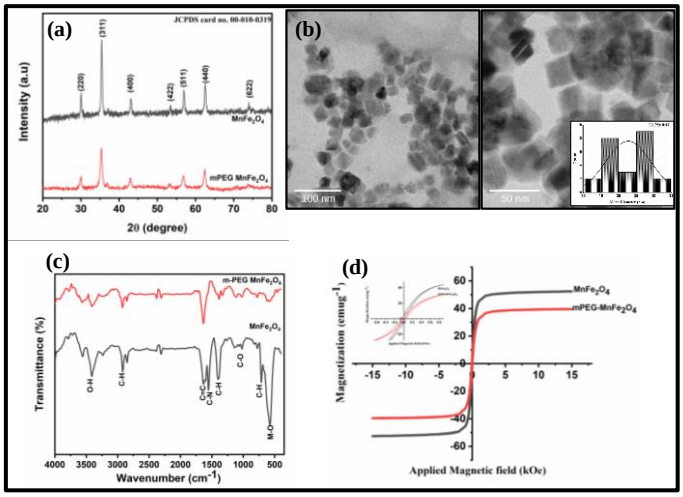


Figure 1 (a) XRD patterns, (b) TEM images, (c) FT-IR spectrum, (d) M-H curves of the $MnFe_2O_4$ and and m-PEG $MnFe_2O_4$ NCs with an inset image showing the coercivity values

The magnetism of MNPs was characterized by VSM at room temperature, and the results are shown in **Fig.1d**. The hysteresis loop profiles of both MNPs exhibit significant coercivity (H_c) and remnant magnetization (M_r). However, the M_s values of as synthesized $MnFe_2O_4$ and m-PEG $MnFe_2O_4$ are 52.76 $emug^{-1}$ and 39.86 $emug^{-1}$ respectively.

Induction heating study:

The ability of MNPs to generate heat inductively in an AC field was assessed by measuring the SAR, which quantifies the amount of heat produced by the MNPs per gram. The SAR was calculated using the following equations: $SAR = C\left(\frac{dT}{dt}\right)\left(\frac{M_s}{M_m}\right)$. The magnetic heating properties of the samples were tested at room temperature by exposing 1 mL of NCs solution in water to an alternating magnetic field of different amplitudes (H_{max} = 13.3, 20, and 26.6 kA/m) and frequencies (f_{AC} = 277 kHz) for at least 600 s. The concentration of the solutions was fixed at 1, 2 and 5 mg/mL shown in **Fig. 2 (a-f).**

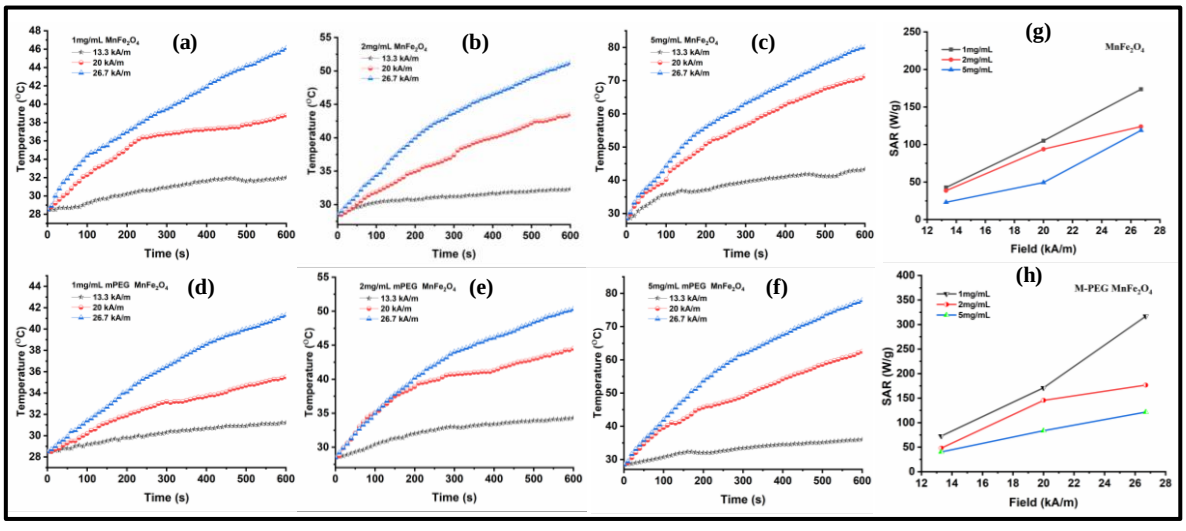


Figure 2. Temperature vs. time curves for $MnFe_2O_4$ (a-c) and m-PEG $MnFe_2O_4$ (d-f) nanoparticles and SAR value $MnFe_2O_4$ (g) and m-PEG $MnFe_2O_4$ (h)

The measurements performed in water were designed specifically to evaluate how the magnetic and structural properties of the synthesized samples affect their heating performance. SAR values calculated in physiological media are shown in Fig. 2 g, h. For the uncoated particles, the SAR value 154.67 W/g with an increase in the field from 13.3 - 26.6 kA/m and for coated NPs is 342.08 W/g. The magneto-crystalline anisotropy energy (K_{eff}) of m-PEG MNPs also played a significant role in achieving high SAR, with particle magnetic moments affecting the K_{eff}. As a result, the strong magnetic moment in the current state enhanced particle-particle interactions, boosted exchange coupling energy, and increased the effectiveness of magnetic hyperthermia [11,12].

Conclusions

The magnetic manganese iron oxide nanoparticles synthesized through the thermal decomposition method and coating with m-PEG. The impact of coating on structural and morphological properties has been studied in both cases. The excellent magnetic properties with small coercivity and remanence are typical of soft ferrimagnetic characteristics. It is thus shown that the synthesized m-PEG-coated manganese iron oxide nanoparticles, after being coated with the biocompatible m-PEG polymer, are promising candidates for applications in biomedicine, particularly in magnetic particle hyperthermia.

Acknowledgment: Authors, Satish Phalake are gratefully thanks for to Chhatrapati Shahu Maharaj Research Training and Human Development Institute (SARTHI), Government of Maharashtra, India for awarding the Junior Research Fellowship (JRF).

References

1. AC Maldonado, G. Goya, *ACS nano.* 2023 Aug 22;17(16):15217-8.
2. H. Huang, S. Delikanli, H. Zeng, D. Ferkey, A. Pralle, *Nat. Nanotechnol.*, 2010 Aug;5(8):602-6.
3. S. Stanley, J. Gagner, S. Damanpour, M. Yoshida, J. Dordick, J. Friedman, *Science*. 2012 May 4;336(6081):604-8.
4. R. Chen, G. Romero, M. Christiansen, A. Mohr, P. Anikeeva, *Science*. 2015 Mar 27;347(6229):1477-80.
5. N. Frey, S. Peng, K. Cheng, S. Sun, Chem. Soc. Rev., 2009;38(9):2532-42.
6. C. Kalaiselvan, et.al., *Coord. Chem. Rev.*, 2022 Dec 15; 473:214809.
7. S. Grancharov, et.al, *J. Phys. Chem. B*, Jul 7;109(26):13030-5.
8. A. Lu, E. Salabas, F. Schüth, *Angew. Chem. Int. Ed.,* 2007 Feb 12;46(8):1222-44.
9. X. Cao, B. Zhang, F. Zhao, L. Feng, *J. Nanomater.* 2012;2012(1): 607296.
10. S. Khoee, A. Kavand, *J. Nanostructure Chem.* 2014 Sep;4:1-6.
11. I. Rubio, et.al, ACS *Appl. Mater. Interfaces* 2020, 12 (25), 27917–27929.
12. L. Del Biancoet.al, *Nanoscale* 2019, 11 (22), 10896–10910.

Hydrothermally Synthesized Titanium Dioxide Nanorods Assembled in Rice Ball Morphology for Application in Ultraviolet Light Detection

Vishakha Zimba, Brahmamaya Sahu, N. Meghana, Jhasaketan Nayak*

Oxide Semiconductor Laboratory, Department of Physics, Indian Institute of Technology (Indian School of Mines) Dhanbad, India

* Corresponding author's email: nayakj@iitism.ac.in

Abstract

Titanium dioxide nanorods were synthesized by a single step hydrothermal process using titanium butoxide precursor. Field emission scanning electron microscopy showed that the nanorods were self-assembled to form porous microspheres resembling rice balls. The optical properties of nanorods were studied by diffuse reflectance spectroscopy and their bandgaps were estimated using the Tauc's plots. Ultraviolet light sensing activities were studied by illuminating the doctor bladed TiO_2 nanorod films with a 16 W, 312 nm UV lamp. The results indicate that our TiO_2 nanorods can be utilized in the field of ultraviolet sensors.

Keywords

Titanium dioxide; hydrothermal synthesis; ultraviolet light sensing; Optical bandgap; Tauc's plot

1. Introduction

Titanium dioxide nanocrystals attract immense research interest due to their wide applicability in visible light photocatalysis [1], water splitting [2], dye sensitized solar cells [3], and biosensors [4]. There are three crystalline phases for TiO_2: (i) anatase, (ii) brookite and (iii) rutile, among which rutile TiO_2 is characterized by its outstanding chemical and thermodynamic stability [5]. Nonreversible transition from anatase to rutile phase has been observed in TiO_2 due to thermal treatment above 600 °C [6]. Performance of TiO_2 nanomaterials depends on their compositions, morphologies, sizes, crystal structures, surface areas and porosities. There are several physical and chemical methods for the synthesis of TiO_2 nanoparticles such as laser ablation [7], ball milling [8], sol-gel synthesis [9], and hydrothermal treatment [10] in acidic and basic medium. Among them, hydrothermal treatment is considered to be most attractive because in this method, the synthesis parameters such as temperature, pressure and precursor concentration can be easily controlled during the reflux reaction in a closed chamber. Moreover, hydrothermal method is considered to be one of the most efficient techniques for synthesis of highly pure nanocrystals because of its simplicity and low cost nature.

Looking at the versatility of nanostructured titanium dioxide, we have synthesized TiO_2 nanorods by a single step hydrothermal method. Effects of variation of hydrothermal reaction temperature on various physico-chemical properties of TiO_2 nanorods have been systematically studied. Ultraviolet light sensing capabilities of TiO_2 nanorods have been evaluated and correlated with variation of synthesis temperature.

2. Experimental

2.1.Materials and Methods

Titanium (IV) butoxide ($C_{16}H_{36}O_4Ti$, 97%), ethyl alcohol (C_2H_6O, 99.9%), hydrochloric acid (HCl, 37%), sulfuric acid (H_2SO_4, 98%), ethyl cellulose ($C_{20}H_{38}O_{11}$, 48.0–49.5%), and α-terpineol ($C_{10}H_{18}O$, 96%) were purchased from Merck and used without further purification.

In a typical synthesis, 30 mL of HCl was added dropwise to 30 mL of ethanol under continuous stirring at room temperature until a clear solution formed. Titanium (IV) butoxide was then added dropwise to this solution, followed by 30 minutes of stirring. The resulting mixture was transferred to a stainless steel autoclave and subjected to hydrothermal treatment at temperatures ranging from 110 °C to 170 °C for 24 hours.After cooling to room temperature, the resulting white precipitate was washed with deionized water and ethanol, then dried overnight at 80 °C. The dried product was ground using a mortar and pestle to obtain fine white TiO_2 powders.

The powders synthesized at 110 °C, 130 °C, 150 °C, and 170 °C were labeled S110, S130, S150, and S170, respectively.Viscous pastes were prepared by dispersing the TiO_2 powders in a solution containing ethyl cellulose, ethanol, and α-terpineol, following a previously reported method [33]. The pastes were applied to ultrasonically cleaned FTO-coated glass substrates using the doctor blade technique. The resulting films, a few microns thick, were thermally annealed in an inert atmosphere at 450 °C for 30 minutes. The films derived from S110, S130, S150, and S170 powders were designated as TF110, TF130, TF150, and TF170, respectively.

3. Results and discussion

3.1Morphologies of TiO_2 nanocrystals

In the FESEM images (Fig. 2), it is observed that the TiO_2 nanorods either form agglomerates or are assembled in rice ball morphologies. In S110, nanorod bundles with diameters more than 100 nm are present whereas S130 contains nanoseeds smaller than 50 nm and irregular shaped agglomerates of nanorods thicker than 100 nm. In S150 and S170, a large number of TiO_2 nanorods having diameter less than 50 nm and length more than 100 nm are assembled to form porous spherical structures resembling rice balls. Densely packed nanorods can be visualized in the high resolution images of S150 and S170 which indicate a higher porosity and hence a larger surface area of the powders.

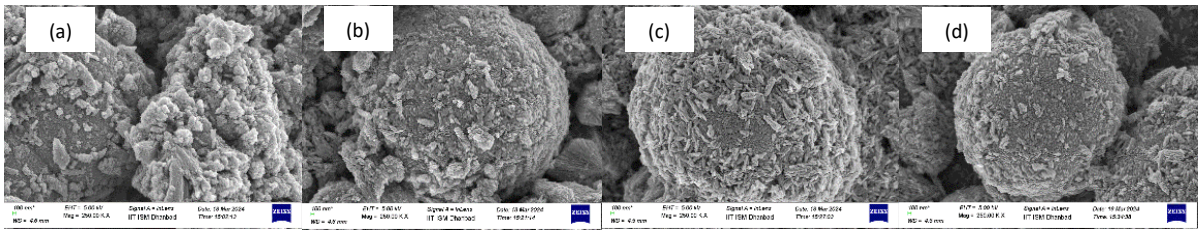


Fig. 2 FESEM images of TiO_2 nanocrystals: (a) S110, (b) S130, (c) S150, (d) S170 .

3.2 Bandgap estimation from UV-Vis DRS and Tauc's plots.

As shown in Fig. 3a, the diffuse reflectance in the visible region (400-700 nm) ranges from 60-90% for our TiO2 nanopowders. The reflectance of S170 has the highest magnitude in the visible region whereas S110 reflects the lowest amount of light. This could be attributed to a greater volume density of TiO2 nanorods in S150 and S170 that diminishes the transmittance, and again, visible light cannot be absorbed by TiO2, having a band gap wider than 3.0 eV. The direct band gap energies were estimated from Tauc's plot (Fig. 3b) and were 3.57 eV, 3.60 eV and 3.46 eV for S110, S150 and S170, respectively. We would like to mention that the reflectance results for S130 was almost the same as that for S110 and was skipped to avoid redundancy

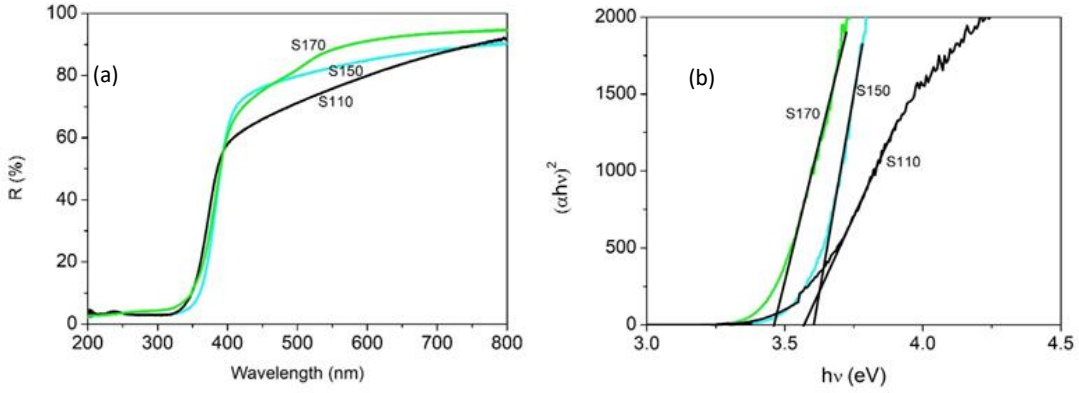


Fig. 3 (a) Diffuse Reflectance spectra for TiO2 nanocrystals synthesized at 110-170 °C. (b) Tauc's plot.

3.4 Ultraviolet light sensing properties of TiO_2 nanorods

As shown in Fig. 4a, the surface photocurrent of TiO_2 film jumps to a higher value under ultraviolet (UV) light irradiation for 10 s at an applied bias of 5.0 V. The dark current is shown for comparison. Every nanorod film was illuminated with ultraviolet light for 10 s and the decaying photocurrent current was measured for sufficiently

long time after the UV light was switched off (Fig. 4b). Persistent photoconductivity was observed for all nanorod films presumably due to point defects such as oxygen vacancies in TiO_2 [11,12]. Photocurrent decay parts were fitted by exponential function (Fig. 4c) given by [13,14];

$$I = I_0 + C_1 \, exp \, exp \left[-\left(\frac{t}{\tau}\right)^{\alpha} \right] \quad (1)$$

Where, I_0 is the steady state photo current, t is the time, C_1 is the scaling constant, τ is the decay time constant and α is the decay exponent. The values of α and τ with an error of ±0.5 %, obtained from the fitting of the decay curves for all four samples. The decay exponent α remains the same for all five samples whereas the decay time constant τ decreases with an increase in synthesis temperature. The decay time constants for the best fits were determined to be 10.91 s, 8.98 s, 5.29 s and 1.54 s for the TiO_2 films TF110, TF130, TF150 and TF170 respectively. A higher value of decay time constant shows persistent photoconductivity which is attributed to charge trapping at point defects and grain boundaries. The rate of decay of photocurrent depends on volume density of surface defects and grain boundaries present in TiO_2 nanorod films. When the UV light is switched off, a sharp decrease in the photocurrent is observed initially due to carrier recombination. As the time progresses, thermal release of trapped electrons into the conduction band of TiO_2 takes place that effectively slows down photocurrent decay. Similarly, the grain boundaries act as potential barriers that impede carrier recombination process. A slower photocurrent decay for TF110 and TF130 indicate a larger number of defects and grain boundaries. With an increase in synthesis temperature, nanorod density increases for TF150 and TF170 that results in a faster carrier recombination and hence the time constant decreases.

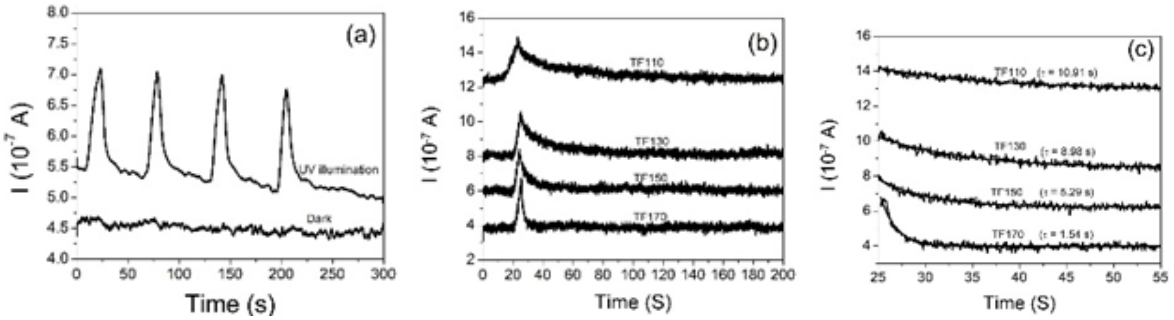


Fig.4 (a) Ultraviolet light response of TiO2 nanorod film showing short photocurrent pulses (10 s), (b) photocurrent pulses (100 s) for four different TiO2 nanorod films, (c) exponential fitting for the photocurrent decay curves.

4. Conclusions

Hydrothermally synthesized titanium dioxide nanorods having diameter less than 50 nm and length more than 100 nm are observed to be self-assembled in porous spherical structures resembling rice balls. The bandgap estimates from the Tauc's plots derived from the UV DRS data were 3.57 eV, 3.60 eV and 3.46 eV for S110, S150 and S170, respectively. The synthesized TiO_2 nanostructures show excellent ultraviolet response with persistent photoconductivity. Therefore the obtained TiO_2 nanorods can be implemented in the field of ultraviolet photodetector and sensor applications.

Acknowledgements

The authors gratefully acknowledge the Department of Physics and the Central Research Facility at IIT(ISM) Dhanbad for providing research support, characterization facilities, and financial assistance throughout the course of this work.

References

[1] M.B. Kanoun, F. Ahmed, C. Awada, C. Jonin and P.-F. Brevet, Int. J. Hydrogen Energy **51**, 907–913 (2024).

[2] S.M. Thabet, H.N. Abdelhamid, S.A. Ibrahim and H.M. El-Bery, Sci. Rep. **14**, 10115 (2024). 0.

[3] P. Gnida, P. Jarka, P. Chulkin, A. Drygała, M. Libera, T. Tański and E. Schab-Balcerzak, Materials (Basel) **14**, 1633 (2021).

[4] T. Kavetskyy, O. Smutok, O. Demkiv, Y. Kukhazh, N. Stasyuk, E. Leonenko, A. Kiv, Y. Kobayashi, A.

Kinomura, O. Šauša, M. Gonchar and E. Katz, Bioelectrochemistry **147**, 108215 (2022) .
[5] S.J. Smith, R. Stevens, S. Liu, G. Li, A. Navrotsky, J. Boerio-Goates and B.F. Woodfield, Am. Mineral. **94**, 236–243 (2009).
[6] S. Bakardjieva, J. Šubrt, V. Štengl, M.J. Dianez and M.J. Sayagues, Appl. Catal. B Environ. **58**, 193–202 (2005).
[7] K.S. Khashan, G.M. Sulaiman, F.A. Abdulameer, S. Albukhaty, M.A. Ibrahem, T. Al-Muhimeed, and A.A. AlObaid, Appl. Sci. **11**, 4623 (2021).
[8] D. Ursu, C. Casut, D. Albulescu, M. Vajda, C. Mosoarca and M. Miclau, Coatings **14**, 283 (2024).
[9] O. Sadek, S. Touhtouh, M. Rkhis, R. Anoua, M. El Jouad, F. Belhora and A. Hajjaji, Mater. Today Proc. **66**, 456–458 (2022).
[10] K. Kucio, V. Sydorchuk, S. Khalameida and B. Charmas , J. Alloys Compd. **862**, 158011 (2021).
[11] D. Comedi, S.P. Heluani, M. Villafuerte, R.D. Arce and R.R. Koropecki, J. Phys. Condens. Matter. **19**, 486205 (2007).
[12] R.S. Chen, C.A. Chen, H.Y. Tsai, W.C. Wang and Y.S. Huang , Appl. Phys. Lett. **100,** 123108 (2012).
[13] C. Itoh and A. Wada, Phys. Status Solidi. **2**, 629–632 (2005).
[14] T. Bando, K. Koshino, C. Itoh and Y. Shinozuka, , Phys. Status Solidi C. **6**, 105–107 (2009).

Enhanced Room Temperature Ammonia Gas Sensing in La Doped ZnO Nanorods

Manami Midday [1, 2, a)], Abhinav Mahapatra [1, 2], Priyanshi Tiwari [1, 3], R.S. Ajimsha [1], Pankaj Misra [1,2, a)]

[1]*Nano-Electronic Materials & Devices Lab., Photonic Materials Technology Section, Raja Ramanna Centre for Advanced Technology, Indore, 452013, India*
[2]*Homi Bhabha National Institute, Training School Complex, Anushakti Nagar, Mumbai, 400085, India*
[3]*Department of Chemistry, Institute for Excellence in Higher Education, Bhopal ,462016, India*

[a)]Corresponding author: manamimidday@gmail.com, pmisra@rrcat.gov.in

Abstract. The detection of ammonia is critical for industrial safety and clinical diagnostics due to its adverse health effects even at low concentrations. Heater-free detection of ammonia at room temperature is essential for sensor miniaturization and energy conservation. We have fabricated room temperature Zinc Oxide(ZnO) nanorods based ammonia gas sensor and enhanced its performance using Lanthanum(La) doping. Indium Tin Oxide (ITO) inter-digitated electrodes (IDE) were fabricated on glass substrates via UV photolithography. A ZnO seed layer (200 ± 5 nm thick) was deposited on the ITO-IDE at room temperature using RF magnetron sputtering with an $Ar:O_2$ ratio of 5:3. ZnO nanorods were synthesized on ZnO-seeded ITO IDE substrates using hexamethylenetetramine and zinc nitrate hexahydrate as precursors. 0.5% La doping was achieved by incorporating lanthanum chloride heptahydrate into the ZnO nanorods via hydrothermal growth process conducted at 95 °C. Structural characterizations using x-ray diffraction shows a strong peak at 34.8° which shows a c-axis oriented growth of ZnO in hexagonal wurtzite phase and morphological characterization using field emission scanning electron microscopy (FESEM) confirmed the presence of vertically aligned ZnO nanorods. Exposure to 250 ppm ammonia gas decreased resistance of ZnO nanorods based sensor from ~ 0.19 MΩ to ~ 59 kΩ while the resistance of the 0.5 % La doped ZnO nanorods from ~ 4.6 kΩ to ~ 0.89 kΩ. The 0.5 % La doped ZnO nanorods based sensor exhibited a faster response time of ~ 13 s, and an enhanced responsivity of ~ 85 %. The low-cost, biocompatible, and compact ZnO-based ammonia gas sensors with high responsivity demonstrate immense potential for room temperature ammonia sensing applications.

INTRODUCTION

Ammonia (NH_3) is a toxic chemical widely utilized in various industries, heavy water plants, chemical laboratories, agriculture, medical diagnostics and numerous other applications[1]. This colorless gas can cause severe health issues even in small concentrations so it is very crucial to detect ammonia at lower concentration. Commercially available chemiresistive NH_3 gas sensors based on metal oxide semiconductors are usually operated at high temperature to achieve reversibility and fast response which results in shorter life time of sensors and portability issues. Room temperature ammonia gas sensors are crucial as they eliminate the need for external heating, reducing energy consumption and safety risks associated with high temperatures[2] making them reliable for real-time monitoring[3]. Various metal oxide semiconductors such as SnO_2, TiO_2, ZnO, WO_3, CuO etc., and their nanostructures with different morphologies have been used for NH_3 sensing. Among these, ZnO nanostructures are preferred due to their excellent sensing response, good thermal and chemical stability, low cost, easy preparation, and non-toxicity. ZnO is an intrinsic n-type semiconductor with wide bandgap of 3.37 eV and rugged wurtzite crystal structure[4]. Lanthanum (La), a rare earth element, has been shown to increase the oxygen vacancy related defects in zinc oxide (ZnO)[5]. Consequently, the incorporation of La into ZnO is expected to improve its gas sensing characteristics. A. Jansi et al. reported that a ZnO film with 3 wt.% La doping demonstrates a sensing response of ~ 55 and response/recovery time of (39 s/11 s) for detecting 100 ppm of NH_3 at room temperature[6]. Devarajan et al. reported La doped ZnO films prepared by dropcasting method which exhibited a response and time of recovery time of 80 s and 10 s respectively with a gas sensor response of 70 %[7]. In this present study, pure ZnO and 0.5 % La doped ZnO nanorods were grown on Indium Tin Oxide (ITO) inter-digitated electrodes (IDE) patterned on glass substrates using UV photolithography for room temperature ammonia gas sensing.

EXPERIMENTAL DETAILS

For the fabrication of ZnO nanorods based gas sensor, an ITO-coated glass substrate was cleaned using soap water followed by sequential ultrasonication in acetone, propanol, DI water, and drying with a nitrogen gun. ITO Interdigitated electrodes (IDEs) patterns were obtained using UV photolithography with the line width 200 ± 10 µm and line spacing of 150 ± 10 µm as shown in Fig. 1 (a). A ZnO seed layer was deposited onto the IDE-patterned ITO substrates via RF sputtering. The chamber was evacuated to a base pressure of 5×10^{-6} mbar before deposition. Argon and oxygen were then introduced into the chamber with Ar:O_2 ratio of 5:3 and the deposition was carried out at an RF power of 100W. A series of depositions were carried out to optimize the thickness of ZnO thin film (200 ± 5 nm) with total deposition time of 30 minutes. A portion of the electrode was masked for electrical connections. Subsequently, ZnO nanorods were synthesized via hydrothermal method. This involved dissolving 50 mM of zinc nitrate hexahydrate and 50 mM of hexamethylene tetramine (HMTA) in 100 ml of DI water, followed by continuous stirring at room temperature to achieve a homogeneous solution. To prepare 0.5 % La doped ZnO nanorods, Lanthanum chloride heptahydrate along with zinc nitrate hexahydrate and hexamethylene tetramine were used as precursors. The substrate with the deposited ZnO seed layer was floated on the solution and placed in an electric oven at 95 °C for 3 hours. Finally, the substrate was further heated at 110 °C for 10 minutes. Gas sensing characterization of the devices was performed using a setup with controlled gas dilution and insertion arrangements as shown in Fig. 1(b). For the measurement of the ammonia gas sensing studies, the fabricated gas sensor was placed into the sample holder, and two electrical connections were made using gold-plated tungsten probe tips. A rotary vacuum pump was then used to evacuate the sensing chamber to a pressure of 2×10^{-2} mbar. Current versus time data at room temperature for 250 ppm NH_3 concentrations was measured using an SMU interfaced with a computer.

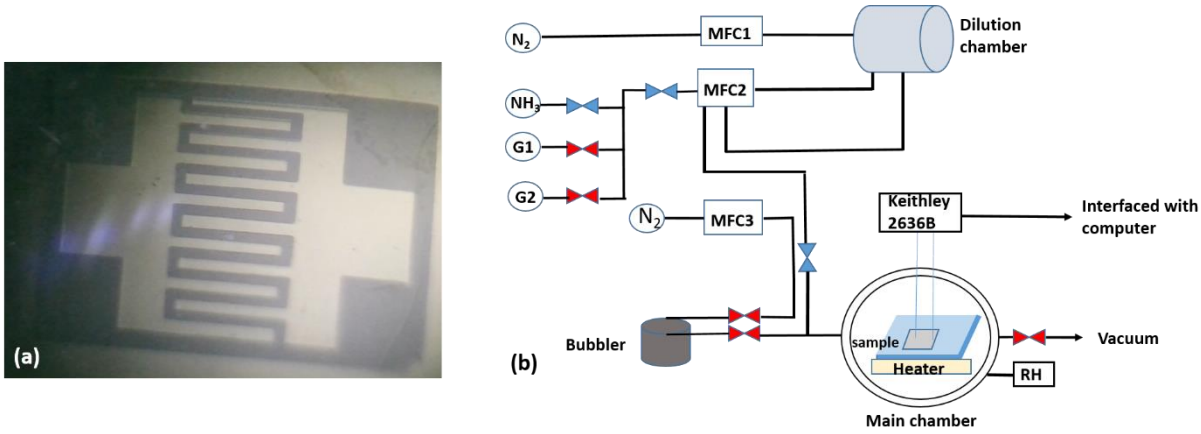


FIGURE 1. (a) ITO interdigitated electrodes on glass substrate fabricated using UV photolithography **(b)** Schematic of gas sensing characterization set up

RESULTS AND DISCUSSION

The morphological analysis of as grown ZnO nanorods and 0.5% La doped ZnO nanorods was performed using field emission scanning electron microscopy (JEOL-JSM7610). The FESEM images of ZnO and 0.5% La doped ZnO nanorods shown in Fig. 2 (a) and (b). It revealed the hexagonal morphology with uniform, vertically aligned and highly dense nanorods over the substrate. The diameter of the pure ZnO nanorods was found to be ~ 85 nm using ImageJ software while for 0.5% La doped ZnO nanorods grown under similar conditions, the diameter was ~ 116 nm. To confirm the phase purity of ZnO and 0.5% La doped ZnO nanorods, X-ray diffraction (XRD) measurement was conducted using a Bruker D8 Advance diffractometer with Cu-Kα radiation at a wavelength of 1.5405 Å. The XRD pattern of the ZnO nanorods is shown in Fig. 2 (c) which showed a peak at $2\theta = 34.80^\circ$ corresponding to ZnO (002) family of planes confirming the c-axis oriented growth of ZnO and La doped ZnO nanorods in hexagonal wurtzite structure (JCPDS Card No. 36-1451) [8] without any impurity phase. No measurable peak shift was observed with lanthanum doping in ZnO as shown Fig. 1 (c).

Photoluminescence spectroscopy studies of ZnO nanorods was carried out using 325 nm He-Cd laser as an excitation source. The as grown ZnO nanorods showed strong and distinct emission peaks at ~ 370 and 580

and 640 nm as shown in Fig. 2 (d). The sharp peak centered at ~ 370 nm corresponds to near band edge (NBE) emission, which reflects the crystallinity of the grown ZnO nanorods[9]. The broad peak at ~ 580 nm also known as deep level emission signifies the presence of point defects such as oxygen vacancies or zinc interstitials in the ZnO nanorods[10]. The red emission band observed at 640 nm is associated with the presence of oxygen and zinc antisites[11]. In these spectra, the peak at 580 nm is higher than the peak at 370 nm, suggesting that the grown nanorods have a large number of defects e.g., oxygen vacancies or zinc interstitials.

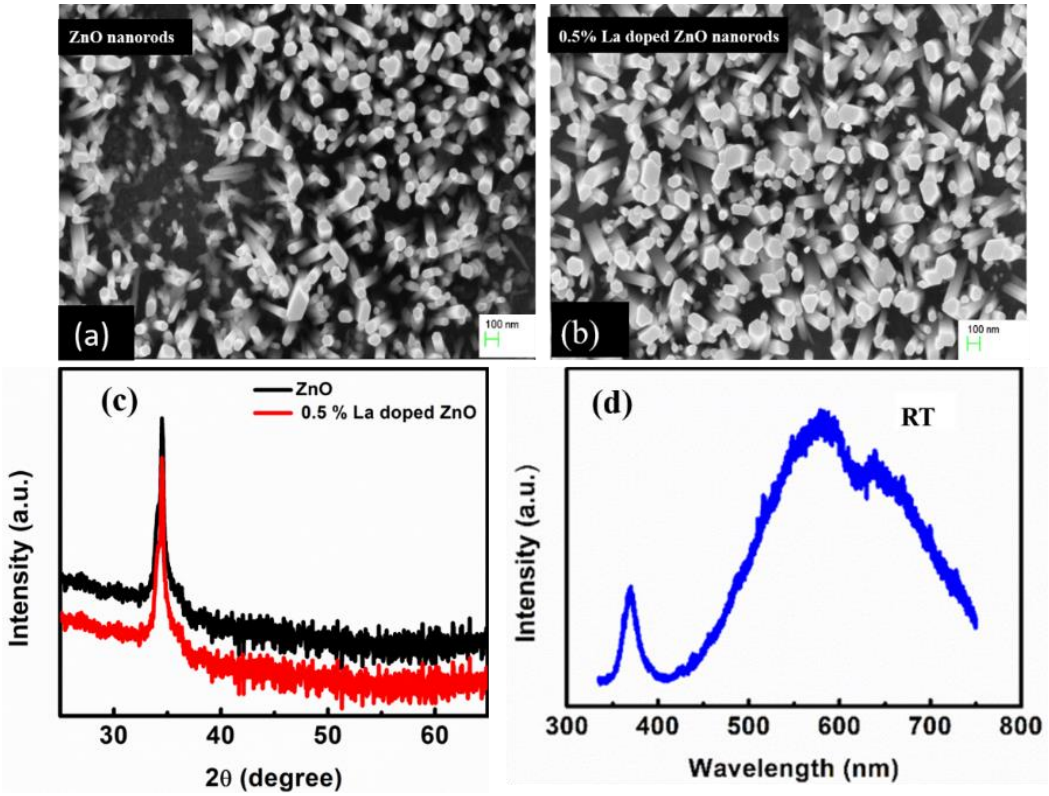


FIGURE 2. **(a)** FESEM image of ZnO nanorods **(b)** and 0.5% La doped ZnO nanorods **(c)** XRD patterns of ZnO nanorods and 0.5% La doped ZnO nanorods, **(d)** Photoluminescence spectra of ZnO nanorods

It is known that the presence of oxygen vacancies or oxygen defect states in ZnO facilitates adsorption of oxygen at the surface of the ZnO[5]. The oxygen molecules from ambient adsorbed on the ZnO nanorods capture electrons from the conduction band of ZnO to form adsorbed oxygen ion (O^-/O_2^-) on the surface leading to formation of electron depletion region near the surface and increase in resistance of ZnO at equilibrium. When NH_3 gas is introduced, the NH_3 molecules react with the absorbed oxygen ion species on the ZnO nanorods to produce N_2, H_2O and an e^- . The released electrons are transferred back to the conduction band of ZnO nanorods resulting decrease in the width of electron depletion region, thus the current is increased and resistivity is decreased. When the NH_3 gas is removed from the environment, the adsorbed ammonia molecules desorb from the ZnO nanorods surface. The electrons that were donated to the ZnO are withdrawn again by the formation of oxygen ions as discussed above, resulting in increase in resistance, allowing the sensor to return to its baseline state. ZnO nanorods having large surface to volume ratio and oxygen vacancies provide more oxygen adsorption and increased sensor response. The electrical characteristics of the ZnO and 0.5% La: ZnO NR sensors on exposure of 250 ppm NH_3 vapour at room temperature are shown in Fig. 3 (a) and (c) respectively. The baseline current of sensors was measured at fixed bias of 3V in the vacuum chamber at an ambient pressure of ~2 x 10^{-2} mbar without exposing sensor to the ammonia gas. The current was again measured by introducing 250 ppm of NH_3 at room temperature. It can be seen in Fig. 3 (a) and (c) that the current value of the sensors containing pure ZnO and 0.5% La: ZnO increased significantly on exposure of the ammonia gas. It can also be noted that values of base line current of sensors and variation in current on exposure to NH_3 gas at fixed bias of 3 V is much larger in 0.5% La:ZnO NR sensors compared to pure ZnO NR sensor which is expected as the doping of rare earth ion La in ZnO produces more oxygen vacancies in ZnO lattice.

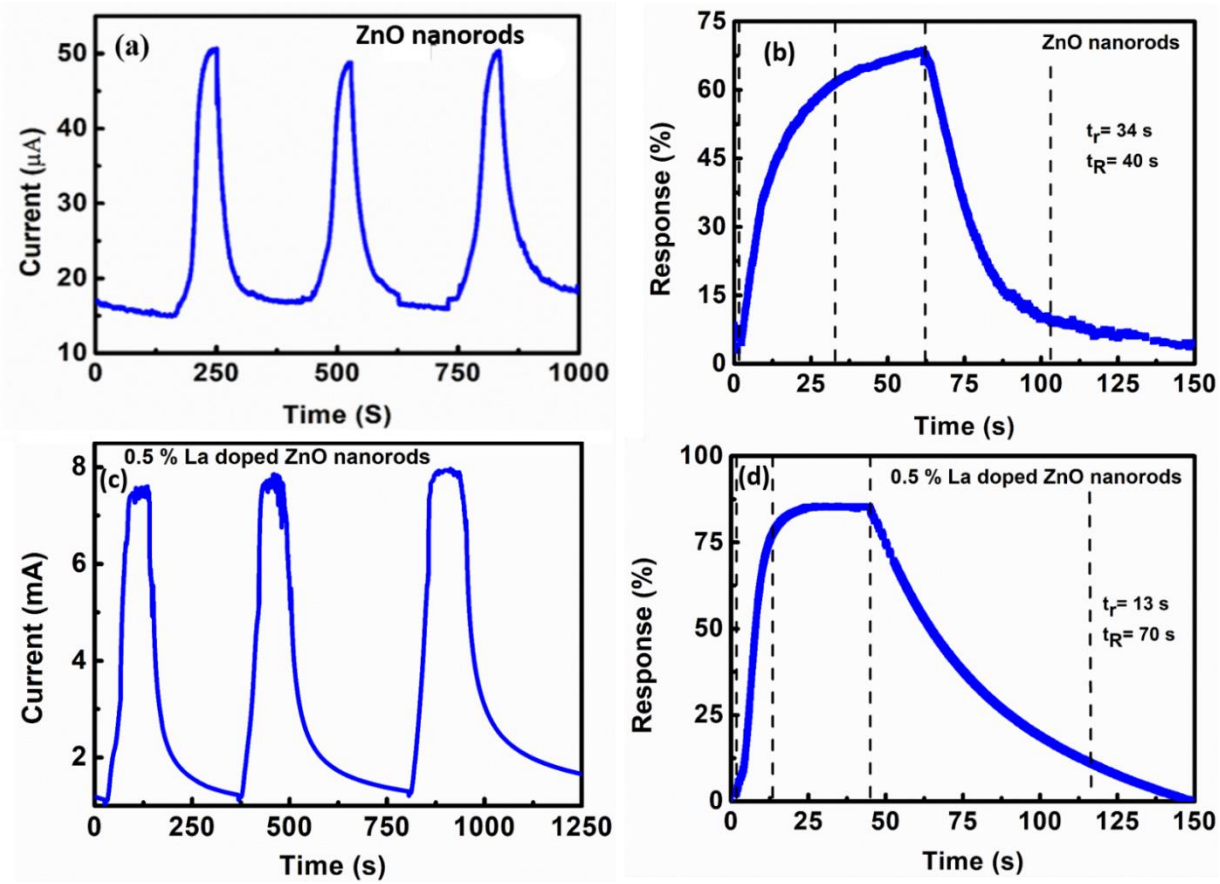


FIGURE 3. (a) Current signal repeatibility and **(b)** Gas sensing response curve for ZnO nanorods under 250 ppm NH_3,**(c)** Current signal repeatibility and **(d)** Gas sensing response curve for 0.5 % La doped ZnO nanorods under 250 ppm NH_3

The sensor response or responsivity of a gas sensor was calculated by using expression $\frac{R_a - R_g}{R_a} \times 100$ %, [12] where R_a is the resistance of the sensor in air and R_g is the resistance in presence of the gas. The room temperature response of sensor based on ZnO nanorods was found to be ~ 67 % with a response time of ~ 34 s and recovery time of ~ 40 s as shown in Fig. 3 (c). The sensor response at room temperature for same NH_3 concentration increased to a value of ~ 85 % in case of 0.5 % La doping and response time decreases to ~ 13 s whereas the recovery time is increased to ~ 70 s. As discussed above, the lanthanum doping in ZnO tends to increase oxygen vacancies which inturn increases free electron concentration in ZnO[13] leading to enhanced adsorption of ammonia on ZnO surface and improved sensor response. The observed increase in recovery time in case of 0.5% La doped ZnO NR sensor may primarily be attributed to strong adsorption of ammonia molecules on 0.5% La doped ZnO NR surface which may lead to slow desorption of ammonia from the sensor surface at room temperature, making it more challenging for the sensor to return to its baseline state after the removal of the NH_3 gas.

CONCLUSIONS

We have fabricated and studied the room temperature NH_3 sensing properties of ZnO and La doped ZnO nanorod based gas sensors. The sensors were fabricated on ITO interdigitated electrodes of the line width 200 ± 10 µm and line spacing of 150 ± 10 µm prepared through UV- photolithography on glass substrates. ZnO seed layer of thickness 200 ± 5 nm was deposited by RF magnetron sputtering at room temperature. Pristine ZnO nanorods and 0.5% La doped ZnO nanorods were grown over seed layer by hydrothermal method. The XRD result shows a strong peak at 34.8° which confirms the c-axis growth of ZnO in hexagonal wurtzite phase. FESEM studies demonstrated the vertically aligned growth of ZnO nanorods. Room temperature ammonia gas sensing characteristics of the as fabricated sensors was studied by introducing 250 ppm of NH_3 gas in the sensing chamber. It was observed that 0.5 % La doping in ZnO nanorods increases the sensor response from ~ 67 to 85 % with decrease in response time from ~ 34 to ~ 13 s. Our studies show that La doped ZnO nanorods may be an appropriate material for detecting NH_3 at room temperature.

ACKNOWLEDGMENTS

One of the authors Ms. Manami Midday acknowledges Homi Bhaba National Institute , Mumbai and RRCAT for the financial support and would like to thank Dr. A.K. Das and Dr. Vikas Kumar Sahu of NEMDL, RRCAT for extending RF sputtering for thin films deposition. Authors would like to thank Dr. Pooja Gupta and Mr. Momin, SUS, RRCAT for XRD measurements, Mrs. Rashmi Singh and Mr. Abhijit Chowdhury of NFML, PMTS, RRCAT for FESEM measurements. Authors are thankful to Dr. Sunil Verma, Head, Photonic Materials Technology Section, RRCAT, Indore for constant support, fruitful discussions and encouragement.

REFERENCES

1. Y. Tu, C. Kyle, H. Luo, D.-W. Zhang, A. Das, J. Briscoe, S. Dunn, M.-M. Titirici, and S. Krause, ACS Sens. **5**(11), 3568–3575 (2020).
2. T. Wang, G. Liu, D. Zhang, D. Wang, F. Chen, and J. Guo, Applied Surface Science **597**, 153564 (2022).
3. A. Mirzaei, M.H. Lee, H. Safaeian, T.-U. Kim, J.-Y. Kim, H.W. Kim, and S.S. Kim, Sensors **23**(21), 8829 (2023).
4. P. Nakarungsee, S. Srirattanapibul, C. Issro, I.-M. Tang, and S. Thongmee, Sensors and Actuators A: Physical **314**, 112230 (2020).
5. M. Al-Hashem, S. Akbar, and P. Morris, Sensors and Actuators B: Chemical **301**, 126845 (2019).
6. A.J. Santhosam, K. Ravichandran, Mohd. Shkir, and M. Sridharan, J Mater Sci: Mater Electron **31**(16), 13240–13248 (2020).
7. D. Alagarasan, S.S. Hegde, R. Naik, P. Murahari, H.D. Shetty, S. Prasad Hb, F. Maiz, and M. Shkir, Optical Materials **147**, 114705 (2024).
8. H. Aydın, F. Yakuphanoglu, and C. Aydın, Journal of Alloys and Compounds **773**, 802–811 (2019).
9. R. Jansi, M.S. Revathy, A. Vimala Juliet, M.A. Manthrammel, and M. Shkir, Ceramics International **50**(17), 29419–29427 (2024).
10. A. Galdámez-Martinez, G. Santana, F. Güell, P.R. Martínez-Alanis, and A. Dutt, Nanomaterials (Basel) **10**(5), 857 (2020).
11. S.S. Shinde, P.S. Shinde, R.T. Sapkal, Y.W. Oh, D. Haranath, C.H. Bhosale, and K.Y. Rajpure, Journal of Alloys and Compounds **538**, 237–243 (2012).
12. V.N. Mishra, and R.P. Agarwal, Microelectronics Journal **29**(11), 861–874 (1998).
13. A. Tabriz, N. Shahzad, S. Nadeem, S. Mehmood, N. Iqbal, G. Ali, and M.I. Shahzad, Materials Proceedings **17**(1), 9 (2024).

Exploring Gold Nanoparticle Morphologies for Enhanced Surface-Enhanced Raman Scattering (SERS) Applications

Sneha Senapati[1, *], Arvind Kaushik[2] and J.P. Singh[2]

1. *School of Interdisciplinary Research (SIRe), IIT Delhi, New Delhi-110016, India*
2. *Department of Physics, IIT Delhi, New Delhi-110016, India*

[*]Corresponding author: sssenapatisneha@gmail.com

Abstract. The impact of gold nanoparticle shape on Surface Enhanced Raman Scattering (SERS) was investigated using a probe molecule. Although SERS is extensively researched for usage in detecting and imaging, the design and optimization of suitable substrates continue to pose a problem. To improve comprehension and optimization of the SERS process in nanoparticles, gold nanospheres, nanotriangles, and nanostars of comparable dimensions were produced and studied via High-Resolution Transmission Electron Microscopy (HRTEM). Different concentrations of BPE were dropcast on these gold nanostructures. The SERS effect was observed developing in the following sequence among suspensions with equal nanoparticle and dye concentrations: nanospheres < nanotriangles < nanostars. This pattern unequivocally illustrates that the quantity of local field hotspots can be regulated to enhance SERS efficiency. The anisotropic nanostructures are attributed to local surface plasmon "hotspots," establishing a clear relationship between surface roughness and SERS signal intensity.

Keywords: SERS, Raman, gold nanoparticles, chemical method, BPE molecule

INTRODUCTION

Gold nanoparticles (GNPs) are highly valued in biomedical applications due to their biocompatibility and superior optical properties. SERS has emerged as a particularly promising technique in this field, offering exceptional sensitivity for chemical and bioanalytical sensing and imaging. While extensive research has explored the SERS effects using various molecules, nanoparticle shapes, and concentrations, identifying the critical parameters for optimizing effective and reproducible SERS remains challenging. Reliable quantitative comparisons are essential for the rational design of new nanomaterials to enhance SERS performance [1–6].

The orientation-dependent properties of metal nanoparticles are essential in determining SERS impact. Anisotropic nanoparticles, such as nanostars, nanotriangles, and nanorods, offer distinct benefits compared to isotropic geometries like nanospheres because they can generate localized surface plasmon resonances (LSPRs). The LSPRs create regions of intense electromagnetic fields known as "hotspots," resulting in enhanced Raman signals [7–10]. The morphology of these anisotropic nanoparticles affects the spatial arrangement and strength of the hotspots. For example, the pointed points and edges of nanostars and nanotriangles generate more powerful electromagnetic fields compared to the smoother surfaces of nanospheres, thereby directly improving the performance of SERS. Moreover, the nanoparticles' anisotropic characteristics enable more precise adjustment of their optical properties to align with the excitation wavelength of the Raman laser, hence enhancing the SERS effect. As a result, anisotropic nanoparticles are extremely efficient in chemical and biological sensing applications, offering enhanced sensitivity and specificity[11–13].

To harness these benefits, numerous synthetic procedures have been developed to control the size and shape of metal nanoparticles. The production of gold nanospheres, nanotriangles, and nanostars with a certain degree of size and shape uniformity has become routine. This study aims to detail the synthesis and HRTEM imaging of these nanoparticles and to compare their relative efficiencies for SERS using BPE as a probe molecule. By doing so, we seek to elucidate pathways for optimizing SERS probes, ultimately enhancing their performance in various applications.

EXPERIMENTATION

Au nanospheres: Gold (III) chloride trihydrate ($HAuCl_4 \cdot 3H_2O$) from Sigma Aldrich was dissolved in deionized (DI) water to create a 0.5 mM $HAuCl_4$ solution. Sodium citrate ($Na_3C_6H_5O_7$) at a concentration of 1%

was then added to this $HAuCl_4$ solution and brought to a boil, serving both as a reducing and stabilizing agent. The solution's color gradually changed from pale yellow to deep red, signifying the formation of gold nanospheres.

To prepare Au nanotriangles, 0.25 mM $HAuCl_4$ solution was prepared by dissolving $HAuCl_4 \cdot 3H_2O$ in DI water. To this solution, 1 mM silver nitrate ($AgNO_3$) from Fischer Scientific was added, followed by 0.1 M ascorbic acid ($C_6H_8O_6$) from Fischer Scientific, and the mixture was stirred gently, remaining colorless to form the growth solution. Next, the previously prepared gold seed solution was added to the growth solution, followed by the addition of 0.1% hydrogen peroxide (H_2O_2). The mixture was gently stirred for 10-15 minutes at room temperature, during which the color of the solution changed gradually, indicating the formation of gold nanotriangles. The final mixture was centrifuged at 10,000 rpm for 15 minutes to separate the gold nanotriangles from any excess reagents [8].

To prepare gold nanostars, a 1.25 mM solution of gold (III) chloride trihydrate ($HAuCl_4$) was first prepared. To this solution, a 0.01 M solution of silver nitrate ($AgNO_3$) in deionized water was added, followed by the addition of a 0.1 M ascorbic acid ($C_6H_8O_6$) solution, creating the growth solution for gold nanostars. Subsequently, 50 µL of a previously prepared gold nano seeds solution was introduced into the growth solution. The mixture was stirred gently for 10-15 minutes at room temperature, during which the solution's color gradually changed, indicating the formation of gold nanostars. To purify the nanostars, the solution was centrifuged at 10,000 rpm for 15 minutes to separate the gold nanostars from the excess reagents [14,15].

The performance of the gold nanostructures in Surface Enhanced Raman Scattering (SERS) was assessed using various concentrations of BPE as the probe molecule. A stock solution of 1 mM BPE was prepared in ethanol and subsequently diluted to obtain lower concentrations. The gold nanostructures were dropcast onto clean silicon substrates and allowed to air-dry. Approximately 20 µL of the BPE solution was then applied to the gold nanostructure-coated substrates and spread evenly to dry.

The SERS spectra were collected using a Renishaw In Via Compact Raman Spectrometer with a 785 nm laser. The laser was configured to emit at a power of 15 milliwatts, with an exposure time of 15 seconds per measurement. Data collection included two sets of measurements, with a total of 5 to 10 spectra acquired from different locations on the same substrate to ensure reproducibility and accuracy.

RESULTS AND DISCUSSIONS

Characterization of Au nanostructures

HRTEM was utilized to visualize the morphology and distribution of nanospheres, nanotriangles, and nanostars. Figures 1(a-d) present electron microscopy images of nanospheres, demonstrating a uniform size range of approximately 20 to 30 nm. The presence of lattice fringes within the nanospheres indicates their crystallinity. The measured interplanar spacing of the crystal lattice fringes, shown in Figure 1(c), is around 0.22 nm. This spacing corresponds to the (111) planes of gold (Au), confirming the crystal structure when compared to standard crystallographic data. Figure 1(d) displays the SAED pattern of the nanospheres, characterized by a series of concentric rings or spots, further indicating the high crystallinity of these structures.

Similarly, Figures 1(e-h) present HRTEM images of gold nanotriangles, highlighting their uniformity and size, which range from approximately 50 to 60 nm. The clear lattice fringes observed within the nanotriangles indicate a high degree of crystallinity. The interplanar spacing of these fringes, as shown in Figure 1(g), measures around 0.23 nm. This value corresponds to the (111) planes of gold (Au), as confirmed by standard crystallographic data. Figure 1(h) shows the SAED pattern of the nanotriangles, characterized by a series of concentric rings or spots, which further confirms the high crystallinity of these nanostructures.

Figure 1 (i-l) shows the morphology and crystallinity of Au nanostars, with a size of around 50 to 60nm. The 3D structure shows the edges of stars clearly (Figure 1(j)). Same the interplanar spacing was found to be around 0.23nm (Figure 1(k)). And SAED pattern shows highly crystalline structures (Figure 1 (l)).

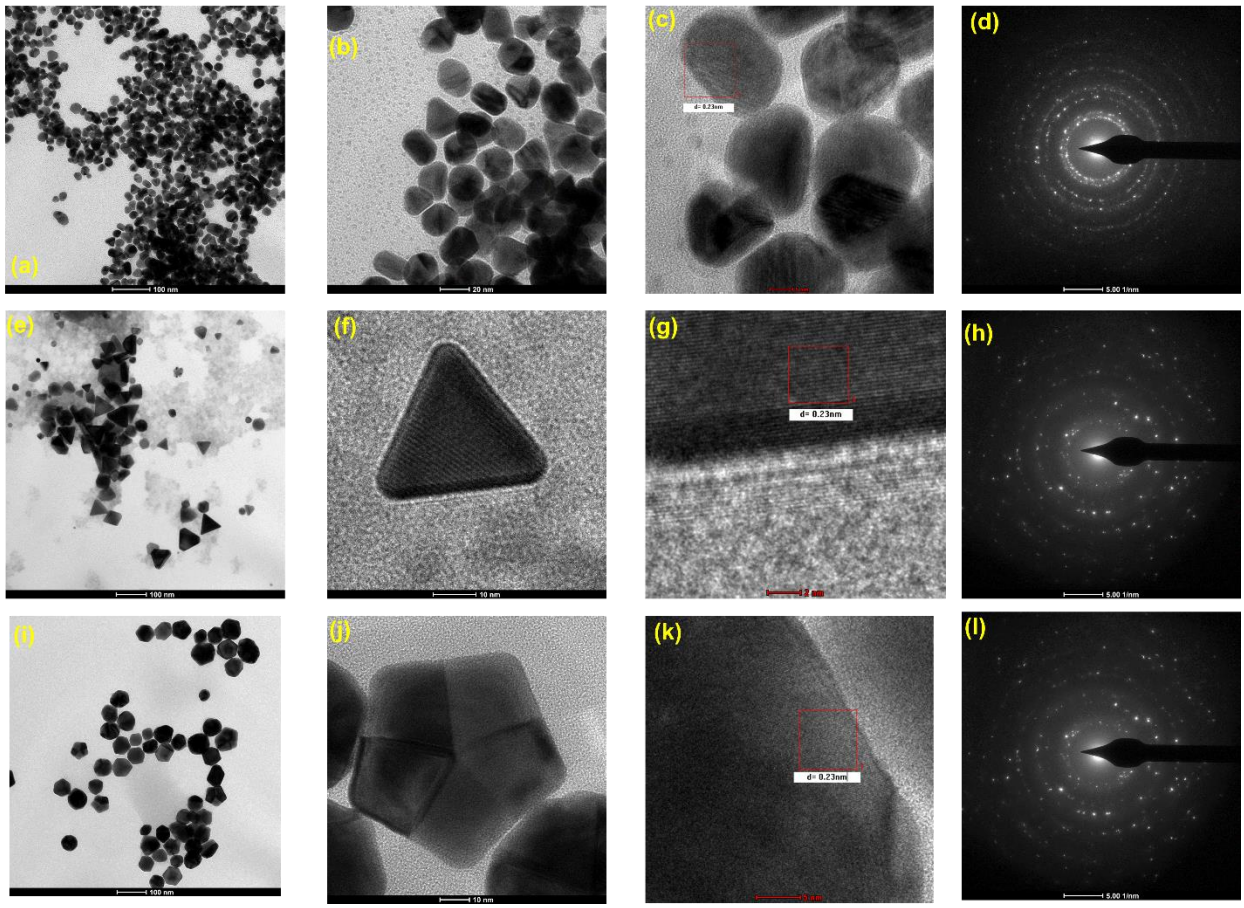


FIGURE 1. (a-d) HRTEM images of Au nanospheres (e-h) images showing the size, morphology, fringes and SAED pattern of Au nanotriangles (i-l) shows the morphology, distribution, size and crystallinity of Au nanostars.

SERS measurements

Figure 2 clearly illustrates the SERS enhancement of BPE probe molecule for the three different Au nanostructures i.e. nanospheres, nanotriangles and nanostars. For the concentration 10^{-12} M of BPE highest enhancement was observed in case of Au nanostars compared with nanospheres and nanotriangles. The unique structure of gold nanostars, with their sharp tips and multiple branches, creates numerous LSPR hotspots. These hotspots are areas where the electromagnetic field is significantly enhanced, leading to stronger Raman signal amplification. While gold nanospheres and nanotriangles also exhibit LSPR, their geometries do not generate as many or as intense hotspots as the nanostars. Nanospheres have smooth surfaces, and nanotriangles have fewer sharp features compared to nanostars [8]. The anisotropic nature of nanostars, with their extended tips and rough surfaces, enhances the surface roughness significantly. This increased roughness contributes to a greater number of SERS-active sites. The entire spectrum of BPE molecules exhibits distinct peaks within the frequency range of 600 to 1800 cm^{-1}. Spectral assignment was given to the BPE peaks which corresponded with the literature. Peak around 1600 cm^{-1} (typically between 1580-1620 cm^{-1}) is associated with the C-C stretching vibrations in the phenyl rings. Peak around 1200 cm^{-1} corresponds to the C-H bending or in-plane bending vibrations of the pyridine rings. Peak around 1000cm^{-1} is attributed to the C-N stretching vibrations within the pyridine rings [15,16].

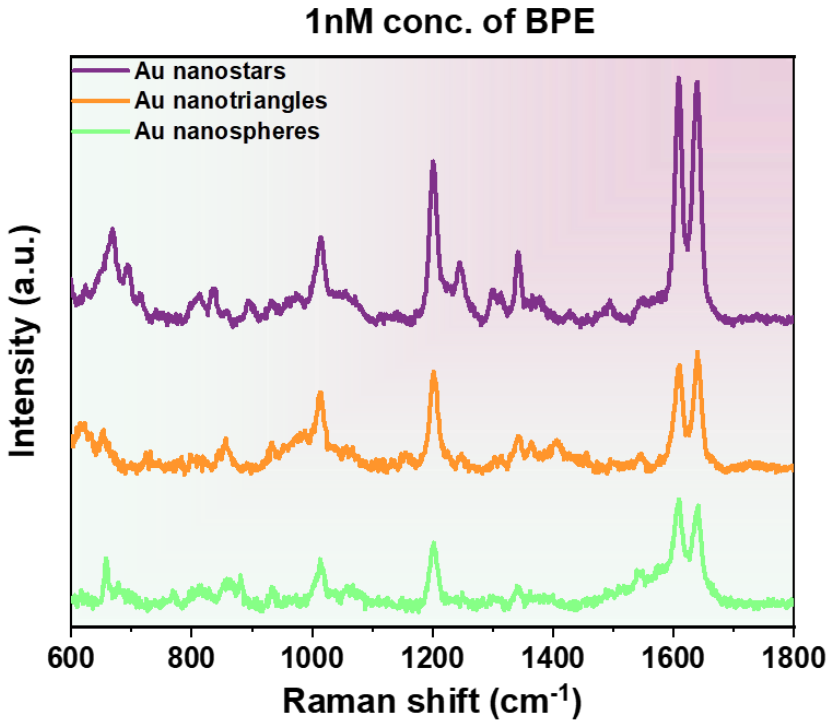


FIGURE 2. (a-d) SERS of BPE on Au nanostars, nanotriangles and nanospheres respectively for the concentration 1nM.

CONCLUSION

This study demonstrated that gold nanostars achieve superior SERS enhancement for BPE compared to gold nanospheres and nanotriangles. The enhanced performance of nanostars is attributed to their unique morphology, which creates numerous localized surface plasmon resonance hotspots and significantly intensifies the Raman signal. This underscores the importance of nanoparticle shape in optimizing SERS efficiency for sensitive chemical and biological detection.

ACKNOWLEDGEMENT

The authors further express gratitude to the Central Research Facilities (CRF) and the Nanoscale Research Facility (NRF) for granting access to the characterization facilities. The author expresses sincere gratitude to MHRD for financial support.

REFERENCES

1. S. Senapati, A. Kaushik, M. Kaur, S. Rana, N. Singh, S. S. Kulkarni, J. P. Singh, *Appl Surf Sci* **2025**, *709*, 163814.
2. A. Kaushik, S. Senapati, N. Agrawal, S. A. Ali, S. Habib, J. P. Singh, *Spectrochim Acta A Mol Biomol Spectrosc* **2025**, *339*, 126298.
3. S. Senapati, A. Kaushik, J. P. Singh, in *AIP Conf Proc*, American Institute Of Physics, **2025**.
4. S. Yadav, S. Senapati, S. S. Kulkarni, J. P. Singh, *J Photochem Photobiol B* **2023**, *239*, 112629.
5. S. Yadav, S. Senapati, S. Kumar, S. K. Gahlaut, J. P. Singh, *Biosensors (Basel)* **2022**, *12*, DOI: 10.3390/bios12121115.
6. S. Yadav, S. Senapati, D. Desai, S. Gahlaut, S. Kulkarni, J. P. Singh, *Colloids Surf B Biointerfaces* **2021**, *198*, 111477.
7. A. Kaushik, P. Bisht, S. Senapati, J. P. Singh, *Surfaces and Interfaces* **2024**, *52*, DOI: 10.1016/j.surfin.2024.104951.
8. A. Kaushik, S. Kapoor, S. Senapati, J. P. Singh, *Colloids Surf B Biointerfaces* **2025**, *252*, DOI: 10.1016/j.colsurfb.2025.114676.

9. A. Kaushik, J. Singh, R. Soni, J. P. Singh, *ACS Appl Nano Mater* **2023**, *6*, 9236.
10. S. Senapati, M. Kaur, N. Singh, S. S. Kulkarni, J. P. Singh, *ACS Appl Nano Mater* **2024**, DOI: 10.1021/acsanm.4c00008.
11. S. Rana, J. Yadav, S. Senapati, R. H. Horng, J. P. Singh, *Appl Mater Today* **2024**, *41*, DOI: 10.1016/j.apmt.2024.102485.
12. A. Kaushik, S. Senapati, J. P. Singh, in *AIP Conf Proc*, American Institute Of Physics, **2025**.
13. A. Kaushik, P. Bisht, S. Senapati, J. P. Singh, *Surfaces and Interfaces* **2024**, *52*, 104951.
14. P. Senthil Kumar, I. Pastoriza-Santos, B. Rodríguez-González, F. Javier García De Abajo, L. M. Liz-Marzán, *Nanotechnology* **2008**, *19*, DOI: 10.1088/0957-4484/19/01/015606.
15. E. Nalbant Esenturk, A. R. Hight Walker, *Journal of Raman Spectroscopy* **2009**, *40*, 86.
16. F. Tian, F. Bonnier, A. Casey, A. E. Shanahan, H. J. Byrne, *Analytical Methods* **2014**, *6*, 9116.

Solution-Processed CdTe Nanoparticle Memory Device

Himanshu Marothya[1, a)], Atul Sachan[1], Vishwas Acharya[1] and Sandip Mondal[1]

[1]Indian Institute of Technology Bombay, Mumbai 40076, Maharashtra, India

[a)] Corresponding author: himanshu.marothya@iitb.ac.in

Abstract. In this study we introduce a memory device utilizing Cadmium Telluride (CdTe) Nanoparticles (NPs) as charge charge-storing unit, the whole device is processed at a temperature below 300 ºC. This low-temperature annealing process not only ensures compatibility with flexible and temperature-sensitive substrate but also reduce production cost and thermal budget. The CdTe NPs are spin coated over the dielectric layer (i.e. ALPO), creating discrete charge trapping sites that enhance charge retention of the memory device. A significant memory window of more than 16 V was observed for a voltage sweep of 25 V. This indicate a substantial difference in both program and erase states, and this can be utilized for multi-bit storage. This work demonstrates the feasibility of low-temperature processed CdTe NPs-based memory devices. The device offers promising route for development of high performance non-volatile (NV) memory technology with enhanced scalability.

INTRODUCTION

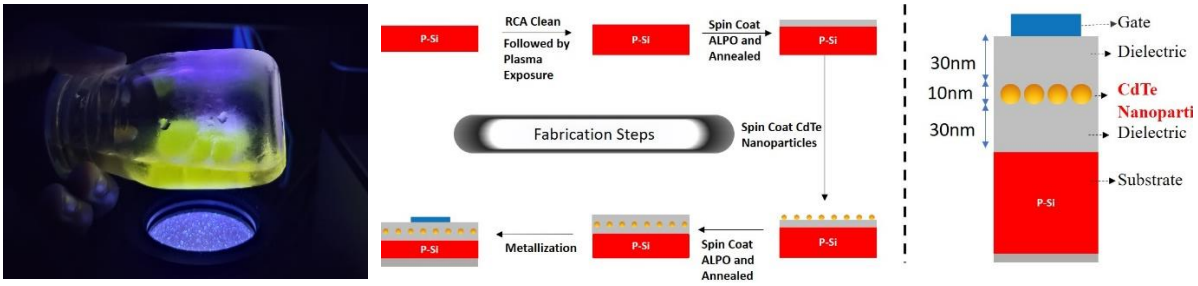
The continuous advancement in NV memory technology demands innovative approaches to material processing and device fabrication. NV memories especially NAND flash memory is the most widely used memory device for data storage in modern devices. Traditional NV memory devices use high-temperature processes that lead to high thermal budget, limited substrate compatibility and high production cost. To address these challenges in traditional NV memory devices this study introduces a fully solution-processed memory device utilizing CdTe NPs as charge storing medium, the entire device is fabricated and processed at a temperature below 300 ºC. CdTe NPs are chosen because of their exceptional electronic properties, including high dielectric constant, stable charge trapping capabilities and tunable bandgap. These properties make CdTe NPs suitable for low-temperature processing. The device architecture involves CdTe NPs layers sandwiched between two ALPO [1] dielectric layers. The use of ALPO as dielectric material ensures efficient charge trapping and retention which is crucial for reliable NV memory operation. Electrical characterization was done by performing several Capacitance Voltage (CV) sweeps for different voltages. A significant memory window of ~16 V was observed under a voltage sweep of ±25 V at 500 kHz AC frequency. This large memory window indicates a clear distinction in program and erase states of the memory device and shows the potential of CdTe NPs for multi-bit memory devices. This study highlights the feasibility of fully solution-processed CdTe NP-based memory devices that offer a cost-effective and scalable approach for next-gen NV memory devices. Also, a processing temperature of less than 300 ºC improves the compatibility with temperature-sensitive substrates and flexible substrates that require low processing temperatures.

MATERIAL SYNTHESIS AND DEVICE FABRICATION.

CdTe NP Growth: We used the hydrothermal process to grow CdTe NPs of below 7 nm radius [2]. In a typical synthesis procedure to make CdTe NP, 4 ml of cadmium chloride solution ($CdCl_2$, 0.04 mol L^{-1}) was diluted in ~36 ml of DI water to achieve the desired concentration. Following this 100 mg of trisodium citrate dihydrate ($C_6H_5O_7Na_3.2H_2O$) was added to the solution. After this, 4 ml of sodium tellurite solution (Na_2TeO_3, 0.01 mol L^{-1}), 0.033 mL of mercaptopropionic acid (MPA), and 50 mg of sodium borohydride ($NaBH_4$) was introduced sequentially into a mixture under continuous magnetic stirring. The precursor's solution is made in such a way that the molar ratio of Cd^{2+}/MPA/Te was maintained at 1:2.4:0.25 to ensure the proper stoichiometry for NP growth. The resulting precursor solution was then transferred into a Teflon-lined stainless-steel autoclave with volume of 50 mL. This sealed tight autoclave was subjected to thermal treatment at 180 ºC for 45 mins resulting in ~5 nm radius CdTe-NPs. After synthesis, the autoclave was allowed to cool to room temperature before opening it. The synthesized CdTe NPs with an approximate concentration of 10^{19} NPs /L, were retrieved in an aqueous form that was later used to make a memory device. Fig. 1a. illustrates the excitation of NPs under UV light, as UV light is incident on the sample, it turns green.

Device Fabrication: A two-terminal Metal (Al) -Insulator (ALPO)-Semiconductor (CdTe) -Insulator (ALPO)-Semiconductor (Si)-MISIS device is fabricated using successive spin coating on a silicon wafer as shown in Fig. 1b. First, an RCA cleaned and plasma exposed silicon wafer is taken and first layer of ALPO dielectric is spin

coated over it, after this the wafer is annealed at 275 ºC for 1 min and plasma exposed for 8 mins, then the CdTe-NP layers are spin coated and then annealed for 1 min at 275 ºC, then the sample is exposed to oxygen plasma. Next, the last layer of ALPO is spin-coated over the CdTe layer. Once this stack is prepared the sample is annealed at 300 ºC for 60 mins, and then gate metal is deposited using a thermal evaporator.

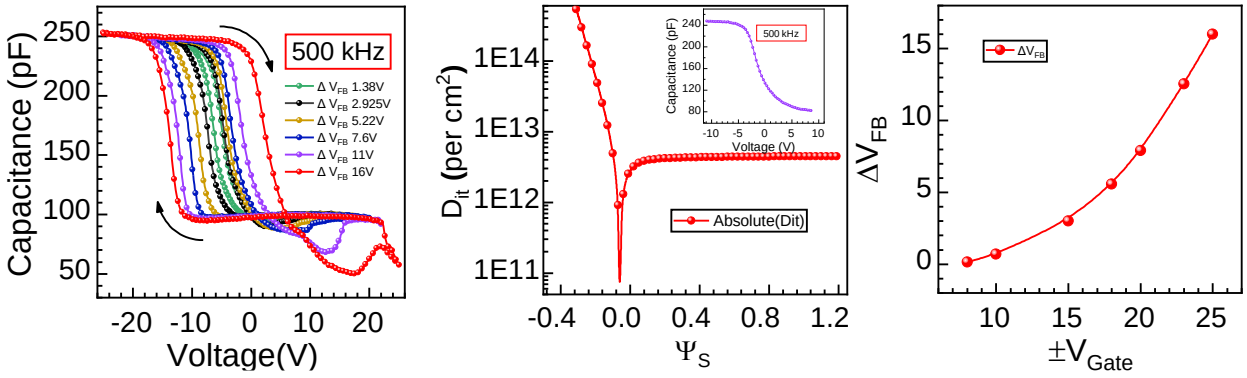


(a) (b)

FIGURE 1. (a) Color of grown CdTe-NPs under UV excitation, that turns the solution green(b) Fabrication steps of the MISIS device.

RESULTS & DISCUSSION.

The CdTe-based MISIS device was analyzed using CV measurements at various frequencies with an amplitude of 50 mV using the CV measurement system, as shown in Fig. 2a. We sweep voltages at different magnitudes and observed that at 500 kHz the memory window increases as we go from ±12 V to ±25 V showing a maximum window ΔV_{FB} ~16 V at ±25 V. Below ±12 V the ΔV_{FB} is insignificant.



(a) (b) (c)

FIGURE 2. (a) Capacitance Voltage (CV) curve for device with gate electrode diameter of 600 µm at frequency 500 kHz for various applied voltage sweeps. (b) D_{it} plot using the terman method inset shows the CV curve of device(c). Variation of memory window with applied voltage sweep.

Figure. 2b. shows the D_{it} plot obtained from terman method, the x-axis shows the surface potential and the y-axis shows the interface states per unit area, at 0.2 V of surface potential the D_{it} is around $4x10^{12}$ cm^{-2}, whereas, the Fig. 2c. shows that as the applied voltage is increased the memory window ΔV_{FB} also increases.

When measuring the C-V curve, starting from a negative voltage, the C-V shift to the right indicates an increase in threshold voltage, suggesting electron injection when a negative voltage is applied. Fig. 3a shows the device's band diagram in equilibrium condition (assuming zero work function difference in metal and semiconductor), with no band bending and nearly zero electric field. Applying a negative voltage to the gate, while keeping the substrate grounded, causes electrons to tunnel through the dielectric and become trapped in the NP layer, increasing the device's threshold voltage, referred to as the program state as shown in Fig. 3b. Conversely, applying a positive gate voltage allows the electrons stored in the NP layer to tunnel back to the gate, decreasing the threshold voltage and achieving the erase state as shown in Fig. 3c.

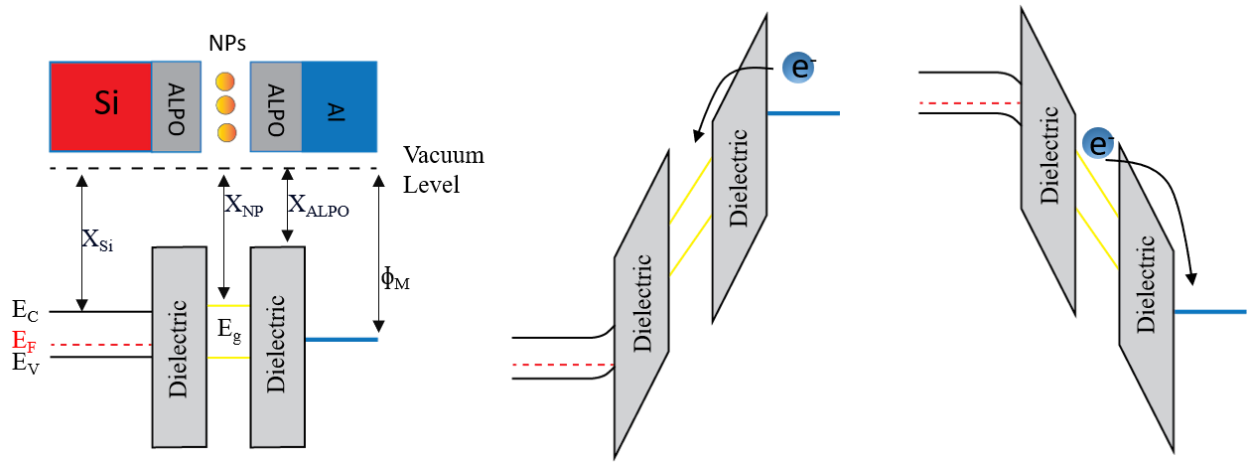


FIGURE 3. (a) Energy band (EB) diagram of MISIS device in equilibrium state when no voltage is applied to the gate (b) EB diagram of MISIS device when the applied gate voltage is negative (Program) (c) EB diagram when the applied gate voltage is positive (Erase).

CONCLUSION

This study demonstrates a fully solution-processed method for fabricating non-volatile (NV) memory devices using Cadmium Telluride (CdTe) nanoparticles (NPs) as charge storage elements, processed at 300 °C. The integration of CdTe NPs and aluminum phosphate (ALPO) dielectric layers results in a robust memory device with a 16 V memory window under ±25 V sweep, suitable for multi-bit storage. This low-temperature processing reduces thermal budget and costs while enhancing compatibility with flexible and temperature-sensitive substrates, offering a scalable solution for next-generation NV memory devices.

ACKNOWLEDGMENTS

The authors wish to thank the Indian Institute of Technology Bombay Nanofabrication Facility for providing the essential fabrication and characterization facilities for this study.

REFERENCES

1. S. Mondal and V. Venkataraman, Low temperature below 200 °C solution processed tunable flash memory device without tunneling and blocking layer. *Nat Commun* **10**, 2143 (2019).
2. J. Khatei, K.S.R. Koteswara Rao, Hydrothermal synthesis of CdTe QDs: Their luminescence quenching in the presence of bio-molecules and observation of bistable memory effect in CdTe QD/PEDOT:PSS heterostructure, *Materials Chemistry and Physics*,Volume 130, Issues 1–2 (2011).

Zinc Ferrite/Polyaniline Nanocomposites for High-Capacity Energy Storage

B. M. Bangalkar[a], R N. Kambale[a], Y. S. Waghode[a], S Habibuddin[a], V. A. Bambole[a]*

a Department of Physics, University of Mumbai, Vidyanagari Campus, Kalina, Santacruz (E) Mumbai 400098, India.

***Email**: bhagyashri.bangalkar@physics.mu.ac.in, vaishali.bambole@physics.mu.ac.in,

Abstract:

Recently transition metal oxides as capacitive electrodes are finding place in supercapacitor. However, low specific energy and poor electrical conductivity are main drawbacks for energy storage applications. We report, Zinc ferrite nanoparticles (ZnF) and ZnF/polyaniline (ZnF/PANI) in the form of a nanocomposite as a better substitute for supercapacitor electrode. These nanocomposites were prepared by sol gel auto-combustion and in-situ polymerization method and characterized by XRD. The XRD pattern revealed the single phase of highly crystalline ZnF nanoparticles and crystalline-amorphous nature of nanocomposite. The surface morphology was studied by SEM which shows cubic structure of ZnF nanoparticles and formation of core-shell of nanocomposite. Capacitance was measured by electrochemical measurements to examine the impact of introducing PANI in ferrite nanoparticles. The specific capacitance value increased due to high conductivity of PANI.

Key words: ferrite nanoparticles, polyaniline, nanocomposites, electrochemical, specific capacitance.

1.Introduction

The rapid use of conventional energy resources causes environmental damage, fossil fuel shortages, and an increase in the cost of petroleum products. To address these pressing concerns, the development of clean, sustainable, and renewable energy storage technology is necessary. [1]. Hence, evolution of durable and highly efficient energy storage devices is indispensable. Batteries, fuel cells, and supercapacitors are believed to compensate for the anticipated future energy demands[2]. Supercapacitors have demonstrated their capacity to store energy efficiently, providing a range of benefits including high power densities, large specific capacitance, rapid charging and discharging times, extended cycle life, and clean electrochemical energy storage. One popular option for an environmentally friendly energy storage device is the supercapacitor [3] According to the recent report nanocomposite based on conducting polymers and metal oxides overcome the limitations of the supercapacitors such as low energy density low cyclic stability and high cost.[4] The Novelty of the present study is the simple green technique for the synthesis of ferrite and polymer nanocomposite for enhancing the super capacitive activity.

2. Experimental

2.1 The synthesis of $ZnFe_2O_4$ ferrite nanoparticles

ZnFe2O4 ferrite (ZnF) powder was prepared using a sol-gel auto-combustion technique. The detailed procedure is as follows. Stoichiometric amounts of $Zn(NO_3)_2{\cdot}6H_2O$,and $Fe(NO_3)_3{\cdot}9H_2O$ were each dissolved in deionized water, followed by the addition of a specific quantity of lemon juice to the metal nitrate solution. These cationic solutions were then combined and stirred continuously for one hour to ensure homogeneity. Ammonium hydroxide was gradually added dropwise to adjust the pH to approximately 7.0. Subsequently, the mixed solution was heated to 90°C with constant stirring to form a dried gel, which underwent self-propagating combustion until all the gels were fully burnt, resulting in dry precipitate. Finally, $ZnFe_2O_4$ crystalline powder was obtained by calcining obtained precipitate at 600°C for 4 hours [5].

2.2 Synthesis of ZnFe2O4/PANI nanocomposite

Zinc ferrite nanoparticles/polyaniline (ZnF/PANI) nanocomposite was synthesized using an in-situ polymerization method. Initially, a specified amount of ZnF ferrite nanoparticles was dispersed in 70 ml of 1 M HCl solution and stirred for 90 minutes to achieve a uniform dispersion. Subsequently, 2 ml of aniline (AN) monomer was added to the ferrite solution, followed by stirring for an additional two hours. A solution of 4.98 g of ammonium persulfate (APS) in 40 ml of 1 M HCl was then prepared. This APS solution was gradually added to the ferrite mixture under continuous stirring for two hours[6]. The resulting green solution was left to polymerize for 12 hours at temperatures ranging from 0°C to 5°C. The mixture was then filtered, thoroughly washed with 1 M HCl and double-distilled water, and finally dried in a vacuum oven at 60°C for 48 hours.

3 Result and Discussion

3.1 Structure and Morphology

Fig. 1(a) shows the X-Ray diffraction pattern of ZnF ferrite nanoparticles and ZnF /PANI nanocomposite. PANI shows the amorphous nature in a partially crystalline state having two diffraction peak $2\theta = 30°$ and 35.6° in nanocomposite XRD pattern [7], [8]. The ZnF ferrite nanoparticles and composites showed the polycrystalline

nature. From Fig.1, we can see that between ZnF ferrite nanoparticles and ZnF /PANI composite, there is no significant difference in crystalline nature, except the intensity. The average crystallite size (D) of ZnF ferrite nanoparticles has been calculated from XRD data using Scherer's equation.

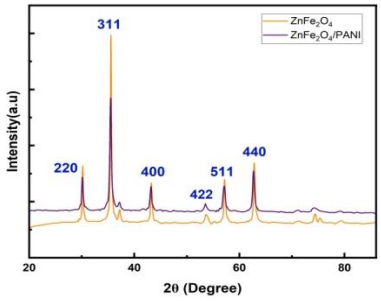


Fig. 1 (a) XRD of ZnF and ZnF/PANI

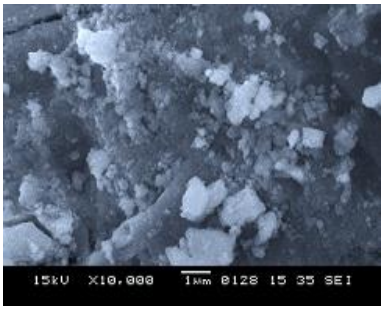


Fig. 1 (b) SEM image of ZnF nanoparticles

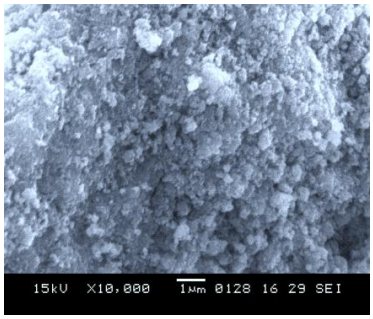


Fig. 1 (c) SEM image of ZnF/PANI nanocomposite

The SEM images of ZnF ferrite nanoparticles and the ZnF /PANI nanocomposite are presented in Fig. 1(b) and 1(c). In Fig.1 (b), the Zinc ferrite nanoparticles exhibit a cubic structure. Fig. 1(c) illustrates the polyaniline coating on ZnF ferrite nanoparticles, where the nanoparticles are uniformly dispersed within the polymer matrix [9].

3. 2 Electrochemical characterization

The electrochemical performance of the synthesized ZnF and ZnF /PANI electrodes was investigated at room temperature using a 2 M KOH electrolyte solution through cyclic voltammetry (CV). The CV plots of the prepared ferrite nanoparticles and nanocomposite electrodes in a three-electrode configuration at various scan rates (5 mV/s, 10 mV/s, 20 mV/s, 40 mV/s, 60 mV/s, 80 mV/s, and 100 mV/s) are presented in Fig. 2 (a) and (b). In Fig. 2 (a), pronounced oxidation/reduction peaks are observed for the ZnF nanoparticles, indicating their pseudocapacitive properties related to electrochemical reactions at the electrode-electrolyte interface. The CV curves of the nanocomposites in Fig. 2(b) show peaks attributable to the faradaic processes of both ZnF and PANI components. The specific capacitance and surface area of the ZnF /PANI nanocomposite are enhanced due to the improved conductivity of the composite. The inclusion of ZnF in the PANI matrix results in a continuous conductive network that facilitates ion transport and redox reactions [10], [11]. Additionally, ZnF ferrite improves the electro-chemical performance of the ZnF /PANI supercapacitor electrode by minimizing charge transfer resistances and enhancing the interfacial contact between ZnF /PANI and electrolyte. The specific capacitance and energy density were computed using following equations,

Specific capacitance(F/g), $C_s = \frac{\int IdV}{v\ x\ m\ x\ \Delta V}$ ..... (1)

where, I- Integral area - Scan rate (mVs^{-1}), m is mass of the composites and ΔV is window potential

Energy density, E (Wh/kg) $E = \frac{0.5\ x\ C_s\ \Delta V^2\ x\ 1000}{3600}$ ..... (2)

The maximum specific capacitance values calculated for ZnF nanoparticles and ZnF /PANI nanocomposite are 200.76Fg^{-1} and 285.78 Fg^{-1}, respectively, at a scan rate of 5 mV/s. The energy density values for ZnF nanoparticles and ZnF /PANI nanocomposite are 6.97 Wh/kg and 9.92Wh/kg, respectively.

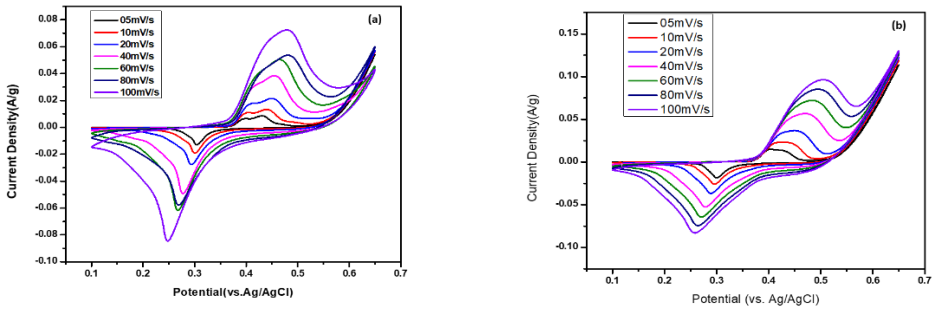


Fig. 2 C V curves of (a) ZnF ferrite nanoparticles (b) ZnF /PANI nanocomposite at different scan rates and potential.

4. Conclusion

Zinc ferrite nanoparticles and Zinc ferrite/polyaniline nanocomposites were successfully synthesized using the sol-gel auto-combustion and in-situ polymerization methods. X-ray diffraction patterns confirmed the spinel cubic structure of the ZnF ferrite and the amorphous nature of polyaniline. The average particle size of the synthesized ferrite nanoparticles, determined from XRD and SEM images was approximately 15nm. The maximum specific capacitance values for the ZnF ferrite nanoparticles and ZnF /PANI nanocomposite were calculated to be 200.76Fg^{-1} and 285.78 Fg^{-1}, respectively, at a scan rate of 5 mV/s. The ZnF /PANI nanocomposite and ZnF ferrite nanoparticles have energy densities of 6.97 Wh/kg and 9.92Wh/kg respectively. These findings imply that the materials that were produced are good choices for the anode electrodes of supercapacitors.

REFERENCES

[1] H. Jiang, P. S. Lee, and C. Li, "3D carbon based nanostructures for advanced supercapacitors," Jan. 2013. doi: 10.1039/c2ee23284g.

[2] J. Tao *et al.*, "Solid-state high performance flexible supercapacitors based on polypyrrole-mno2-carbon fiber hybrid structure," *Sci Rep*, vol. 3, Jul. 2013, doi: 10.1038/srep02286.

[3] S. M. Pawar *et al.*, "Nanoporous CuCo 2 O 4 nanosheets as a highly efficient bifunctional electrode for supercapacitors and water oxidation catalysis," *Appl Surf Sci*, vol. 470, pp. 360–367, Mar. 2019, doi: 10.1016/j.apsusc.2018.11.151.

[4] Q. A. Alsulami, A. Rajeh, M. A. Mannaa, S. M. Albukhari, and D. F. Baamer, "Preparation of highly efficient sunlight driven photodegradation of some organic pollutants and H2 evolution over rGO/FeVO4 nanocomposites," *Int J Hydrogen Energy*, vol. 46, no. 54, pp. 27349–27363, Aug. 2021, doi: 10.1016/j.ijhydene.2021.05.211.

[5] R. N. Kambale, K. M. Sagar, S. M. Patange, S. E. Shirsath, K. G. Suresh, and V. A. Bambole, "Excellent Microwave Absorbing Properties of Nd3+-Doped Ni–Zn Ferrite/PANI Nanocomposite for Ku Band," *Physica Status Solidi (A) Applications and Materials Science*, vol. 219, no. 8, Apr. 2022, doi: 10.1002/pssa.202100505.

[6] M. Beygisangchin, S. A. Rashid, S. Shafie, A. R. Sadrolhosseini, and H. N. Lim, "Preparations, properties, and applications of polyaniline and polyaniline thin films—a review," *Polymers (Basel)*, vol. 13, no. 12, Jun. 2021, doi: 10.3390/polym13122003.

[7] R. D. Balikile, A. S. Roy, S. C. Nagaraju, and G. Ramgopal, "Conductivity properties of hollow ZnFe2O4 nanofibers doped polyaniline nanocomposites," *Journal of Materials Science: Materials in Electronics*, vol. 28, no. 10, pp. 7368–7375, May 2017, doi: 10.1007/s10854-017-6425-5.

[8] K. I. Ajeel and Q. S. Kareem, "Synthesis and Characteristics of Polyaniline (PANI) Filled by Graphene (PANI/GR) nano-Films," in *Journal of Physics: Conference Series*, Institute of Physics Publishing, Jul. 2019. doi: 10.1088/1742-6596/1234/1/012020.

[9] J. Stejskal *et al.*, "Coating of zinc ferrite particles with a conducting polymer, polyaniline," *J Colloid Interface Sci*, vol. 298, no. 1, pp. 87–93, Jun. 2006, doi: 10.1016/j.jcis.2005.12.034.

[10] A. G. Tabrizi, N. Arsalani, Z. Naghshbandi, L. S. Ghadimi, and A. Mohammadi, "Growth of polyaniline on rGO-Co3S4 nanocomposite for high-performance supercapacitor energy storage," *Int J Hydrogen Energy*, vol. 43, no. 27, pp. 12200–12210, Jul. 2018, doi: 10.1016/j.ijhydene.2018.04.129.

[11] M. Fu, W. Chen, X. Zhu, and Q. Liu, "One-step preparation of one dimensional nickel ferrites/graphene composites for supercapacitor electrode with excellent cycling stability," *J Power Sources*, vol. 396, pp. 41–48, Aug. 2018, doi: 10.1016/j.jpowsour.2018.06.019.

Green Route Synthesis of CuO Nanoparticles utilizing Trema Micrantha Leaf Extracts

Vrushali Raut[1, a)], Jui Tambe[1] and Trupti Chavan[1]

[1]*Deparment of Chemistrty, Karmaveer Bhaurav Patil college, Vashi Navi Mumbai*

[a)]Corresponding author: vru4raut@gmail.com

Abstract. The green chemistry approach for synthesizing nanoparticles has shown great potential as an alternative to the expensive and environmentally harmful chemical methods. In this study, copper oxide nanoparticles (CuO NPs) were synthesized using a green method that utilized the water extract of Trema Micrantha (*Jamaican Nettletree*) leaf as both reducing and stabilizing agents, with copper (II) nitrate trihydrate salt serving as the precursor. Green CuO NPs were characterized using powder XRD and Scanning electron microscope (SEM) images. CuO NPs with several potential uses, particularly in the biomedical field.

INTRODUCTION

Green chemistry has become a top priority of research, necessitating extra efforts to implement sustainable methods. The goal was to produce desired products while minimizing and eliminating waste materials. Metal nanoparticles (NPs) have garnered considerable attention in scientific research and industrial applications. Copper oxide (CuO) nanoparticles are in high demand for both fundamental research and industrial applications due to their exceptional properties. CuO Nps have numerous significant applications in catalysis, sensor, solar cell, thermal conductivity, superconductor, water treatment, battery, hydrogen production, and transistors.[1, 2] The cost of CuO is relatively low and it is much less toxic compared to other metal oxide nanoparticles. Various traditional methods have been used to produce CuO NPs, these methods include chemical reduction, Thermal Decomposition, electrochemical Method, precipitation Method, microwave- assisted synthesis, hydrothermal methods, Sonochemical Synthesis, and Sol-Gel Method. Researchers are concentrating more on green synthesis among these methods, which are environmentally friendly, non-toxic, cost-effective, simple for large-scale production, and biocompatible for synthesizing CuO NPs.[3, 4] Green synthesis using microorganisms and plant extracts has been widely reported.[5,6] In the green synthesis method plant extracts have significant attention including cost-effectiveness, ease of process, abundant availability, safety,



FIGURE 1. Image of *Trema Micrantha* leaf.

their role as precipitating, reducing, and capping agents, lack of special storage requirements and enhanced stability.[7, 8]

In this paper, we recorded an inexpensive and efficient method for the synthesis of CuO nanoparticles utilizing powdered Trema Micrantha (*Jamaican Nettletree*) leaves and copper salt as a precursor. Trema Micrantha is a shrubs and small trees within the Cannabaceae family and Trema genus. Trema Micrantha is known for its various medicinal properties, including anti- inflammatory, anti-arthritic and analgesic activity in rodents. The green method provides several advantages, including simplicity, low cost, non-toxic materials, and high phase purity.[9]

EXPERIMENTAL DETAILS

Materials

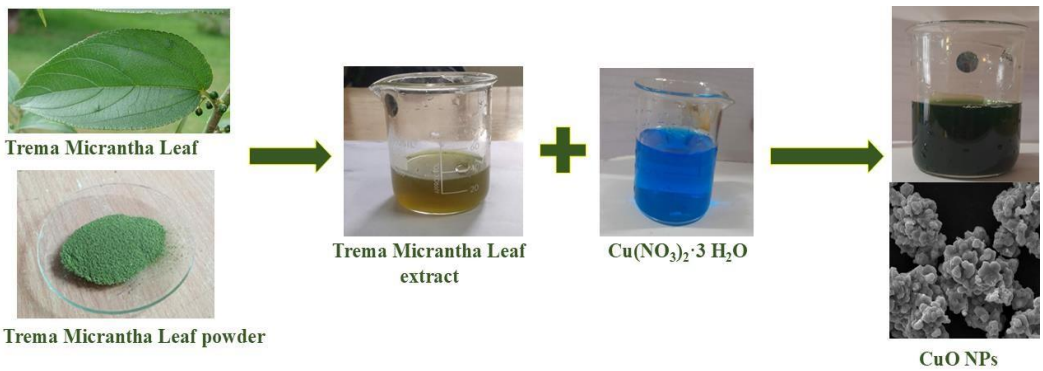
$Cu(NO_3)_2 \cdot 3\ H_2O$ was purchased from Sigma Aldrich and fresh Trema Micrantha (*Jamaican Nettletree*) leaves were collected from Karmaveer Bhaurao Patil College, Vashi, Navi Mumbai, India. Deionized (DI) water was used for all experimental works.

Preparation of Trema Micrantha (*Jamaican Nettletree*) *leaves extract*

Leaves were collected and washed multiple times with deionized water. They were then sun-dried for a day and further dried at 100°C for 24 h. The dried leaves were ground into a moderately fine powder. 6 gm of dried powder was placed in a glass container with 100 ml deionized water mixed well and t heated in a water bath at 60°C for 30 min. The resulting extract was filtered, and the filtrate was stored in the refrigerator for future use.

Synthesis of CuONPs

CuO NPs were synthesized by gradually adding 20 mL of leaf extract dropwise to 20 mL of a 2 mM cupric nitrate solution. The mixture was boiled with constant stirring at 60°C for 45 min. During heating, the colour of the solution changed from blue to dark brown due to surface plasmon resonance excitation, indicating the formation of CuO NPs as hydrogen was donated from the leaf extract. The resulting precipitate was washed with water and ethanol to remove impurities, then dried at 100°C for 10 h. The product was then calcined in a muffle furnace at 450°C for 2 hours. After calcination, a black powder was produced, which was kept at room temperature in a desiccator for further characterization.



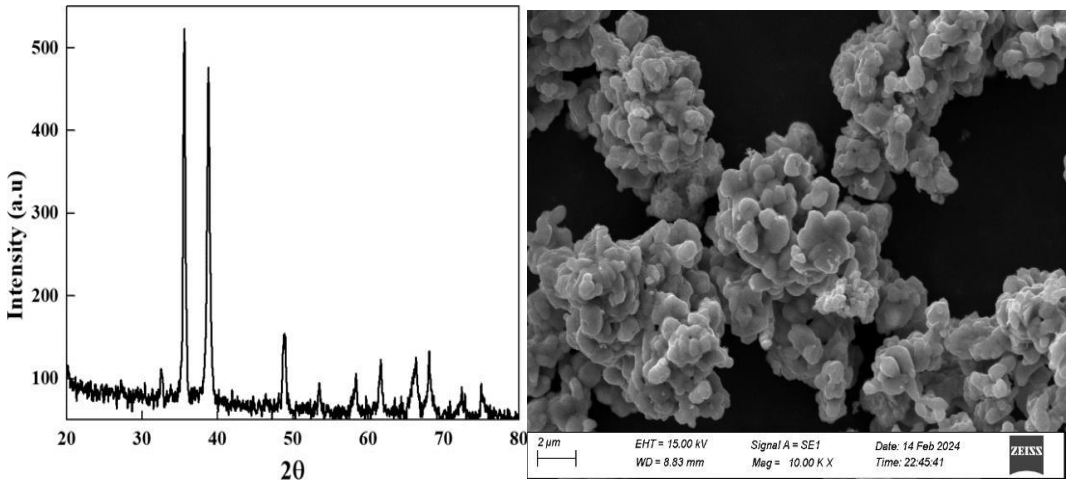
SCHEME 1. Synthesis of **CuO NPs** using Trema Micrantha leaf.

Materials characterization

Powder X-ray diffraction (PXRD) patterns were recorded using Ultima IV, Rigaku Corporation, Japan, Cu Kα X-ray wavelength: 1.5406 Å from Punyashlok Ahilyadevi Holkar Solapur University, Solapur, Maharashtra, India. Scanning electron microscope (SEM) images from Karmaveer Bhaurao Patil College, Vashi, India.

RESULT AND DISCUSSION

CuO nanoparticles (NPs) were synthesized using Trema Micrantha leaf extracts. In the nanoparticle synthesis process, plant extracts can function as both reducing and capping agents. The leaves of the selected plant species are widely used in herbal medicine due to their medicinal phytochemical content. Synthesized CuO Nps using *Trema Micrantha* leaf was analyzed using XRD diffractogram (Fig.2a) exhibits peaks at 2θ values of 32.52°, 35.52°, 38.76°, 48.8°, 53.68°,
58.24°, 61.6°, 66.36°, 68.18° and 75.12° were associated with lattice planes (hkl) follows as (−110), (002), (111), (−202), (020), (202), (−113), (022) and (004), respectively.[10] The scanning electron microscope (SEM) analysis indicated that the particles exhibit a spherical shape, as illustrated in Fig.2b. The measured particle size was 350 ± 150 nm, aligning with previously reported findings.



(a) (b)

FIGURE 2. (a) XRD of CuONps using *Trema Micrantha* leaf. (b) Scanning electron microscope of CuONps using *Trema Micrantha* leaf.

CONCLUSIONS

Compared to chemical and physical synthesis, green synthesis of nanoparticles is considered safer and more environmentally friendly. Using plant extracts for this process is straightforward, easy to perform, cost-effective, highly efficient, and sustainable. We successfully synthesized CuO NPs using Trema micrantha leaves without utilizing toxic, hazardous materials or surfactant templates. CuONps have a broad range of applications, including catalysis, medicine, water treatment, dye degradation, textile engineering, bioengineering, sensors, imaging, biotechnology, electronics, optics, and various other biomedical fields. Plants contain special substances that facilitate and accelerate the synthesis process. Using plants for green nanoparticle production is an intriguing and growing element of nanotechnology, with substantial implications for environmental sustainability and nanoscience developments.

ACKNOWLEDGMENTS

The authors are thankful to Rashtriya Uchchatar Shiksha Abhiyan (RUSA), Karmaveer Bhaurao Patil College, Vashi, Navi Mumbai, India.

REFERENCES

1. B. Murugan, Md Z.Rahman, I. Fatimah, J. A. Lett, J. Annaraj, N. H. M. Kaus, M. A. Al-Anber, S. Sagadevan, Inorg. Chem. Commun. 155, 111088 (2023).
2. M. Sorbiun, E. S. Mehr, A. Ramazani, A. M. Malekzadeh, Nanochem Res. **3**, 1-12 (2018).
3. Ahmad, Naveed, and S. Sharma, Green and Sustainable Chem. **2**, 141-147 (2012).

4. Salem, Salem S. Fouda, Biological Trace Element Research, 199, 344-370 (2020).
5. E. Derakhshani, M. Asri and A. Naghizadeh, Bio. Nano. Sci. **13**, 212–218 (2023).
6. A. Bhardwaj, Ritika and A. K. Singh, Plant Nano Biology **8**, 100076 (2024).
7. M. Nasrollahzadeh, S. M. Sajadi and M. Maham, RSC Adv. **5**, 40628–40635 (2015).
8. P. K. Pantawane, B. A. Mehere, R. K. Chahande, A. K. Potbhare, Mater. Today **29**, 934-938 (2020).
9. R. Barbera, A. Trovato, A. Rapisarda, S. Ragusa, Phytother. Res. **6**, 146-148 (1992).
10. S. Jillani, M. Jelani, N. Ul Hassan, S. Ahmad and M. Hafeez, Mater. Res. Express **5**, 045006 (2018).

Study of Structural, Morphological and Optical Properties of CuS Nanomaterials

Priya Chandra[a], K. S. Ojha

Department of Physics, National Institute of Technology, Raipur- 492010, C. G., India

[a)]Corresponding author: chandrapriya31051998@gmail.com

Abstract. Copper sulphide (CuS) nanomaterials have been synthesized using a hydrothermal method, with ethylene-diamine-tetraacetic acid (EDTA) employed as a surfactant to examine its influence on the properties of CuS. The produced nanomaterials were characterized through X-ray diffraction, scanning electron microscopy, energy dispersive X-ray spectroscopy, Fourier-transform infrared spectroscopy, UV-visible spectroscopy and photoluminescence spectroscopy. The result suggests that the CuS nanomaterials exhibit a hexagonal crystal structure. The energy bandgap is calculated as 1.48 eV. Photoluminescence emission peaks were observed in both UV and visible regions. The study highlights the significant impact of EDTA on the structural and optical properties of CuS nanomaterials and suggests their potential applications in optoelectronics, including light-emitting devices, sensors and photovoltaic technology.

Keywords: CuS, hydrothermal method, EDTA, surfactant

1. INTRODUCTION

Transition metal sulphides, such as CuS, MoS, CoS, FeS, NiS, ZnS, CdS have gained significant attention in various applications, such as thermoelectric energy harvesters, water purification, supercapacitors, solar cells and batteries [1-3]. Among them, CuS is a distinctive p-type semiconductor suitable for various applications due to its tunable characteristics and non-toxicity. These characteristics include various crystal structures, adjustable stoichiometric composition and a direct energy band gap of 1.2-2.0 eV [4]. Studying these materials at nanoscale is crucial due to the induction of quantum confinement effects, higher surface-to-volume ratio, elevated melting point and improved optical absorption [5]. These nanomaterials can be produced by various techniques such as self-assembly, sputtering, chemical vapor deposition, electro-deposition technique, sol-gel technique, wet chemical technique, ball milling, hydrothermal and solvothermal method [6]. Among these methods, the hydrothermal method has a simple aqueous method requiring less chemicals uses and elevated temperature and pressure conditions [7].

Khan et al. [8] synthesized CuS nanomaterials via wet chemical coprecipitation method and reported the interaction of CuS nanomaterials with bovine serum albumin, human serum albumin and collagen proteins in the presence of various surfactants such as dodecyl-trimethyl-ammonium-bromide, cetyl-trimethyl-ammonium-bromide and Tween 80. Rabkin et al. [9] reported the control of localized surface plasmon resonance of CuS nanomaterials and different morphologies by manipulating the surfactants. Selvi et al. [10] studied cetyl-trimethyl-ammonium-bromide capped CuS and CdS nanoparticles and reported a red shift in their photoluminescence and enhanced optical properties. these literature shows that the surfactants can often be employed to tune the properties of CuS nanomaterials. Ethylene-diamine-tetraacetic-acid (EDTA) is a versatile chelating agent and surfactant that can also tune the properties of CuS nanomaterial [11, 12]. This article presents the hydrothermal synthesis of CuS nanomaterials using EDTA as surfactant and investigates the influence of EDTA surfactant on structural, morphological and optical properties of CuS nanomaterials.

2. PREPARATION OF CuS NANOMATERIALS

0.5 M copper acetate (Sigma Aldrich, 99.9% purity), 1.5 M thiourea (Sigma Aldrich, 99.99% purity) and 0.107 M EDTA (Sigma Aldrich, 98% purity) were dissolved in 20, 20 and 10 ml of distilled water, respectively [3]. These solutions were then combined and stirred continuously until a black solution was formed. Then the solution was transferred into a 100 ml Teflon-lined stainless-steel autoclave. The autoclave was heated at 180°C for 24

hours in an oven. Then the autoclave was allowed to cool gradually. The final solid precipitate was thoroughly washed with deionized water and then dried at 60°C for four hours and used for further characterization**.**

3. RESULTS AND DISCUSSION

3.1 Structural study

The structural analysis was conducted using Bruker D8 Advance A25 Powder X-Ray Diffractometer (XRD) to examine the crystal structure and crystallite size of the synthesized EDTA-capped CuS nanomaterials, as illustrated in Fig. 1. The XRD pattern of the CuS nanomaterials displays distinct peaks corresponding to the (102), (103), (006), (104), (105), (106), (107), (112) and (108) diffraction planes, located at 29.2°, 31.6°, 32.3°, 35.6°, 39.7°, 42.3°, 46.8°, 49.9° and 53.5°, respectively. These peaks confirm the successful formation of covellite CuS with a hexagonal crystal structure (space group: P63/mmc) [13,14]. The broadening of the XRD peaks suggests that the crystallite size is in the nanometer range and the high peak intensity indicates that the material has good crystallinity. The crystallite size was calculated using the Debye–Scherrer equation, yielding an approximate value of 8.5 nm for the synthesized EDTA-capped CuS nanomaterials.

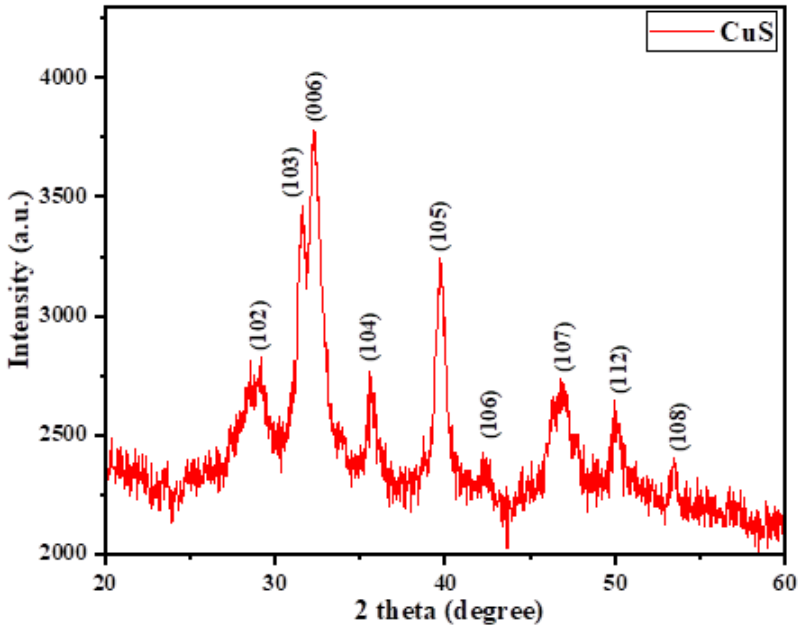


FIGURE 1. XRD spectrum of CuS nanomaterials

3.2 Morphological and compositional analysis The morphology of the CuS nanomaterial was examined using a Zeiss EVO-18 scanning electron microscope (SEM), with energy-dispersive X-ray spectroscopy (EDX) used for elemental analysis. SEM images reveal that the CuS nanomaterial has an irregular shape, as shown in Fig. 2(a) [15]. The EDX spectrum, represented in Fig. 2(b), confirms the presence of copper (Cu) and sulphur (S) in the sample, along with trace amounts of carbon (C) and oxygen (O), which may be attributed to environmental contamination. Fig. 2(c) presents a bar graph with a quantitative analysis of these elements, detailing their weight percent and atomic percent in the CuS

nanomaterial, indicating a Cu:S atomic ratio of approximately 1:1. Additionally, elemental mapping displayed in Fig. 2(d) illustrates the uniform spatial

3.3 distribution of these elements within the sample.

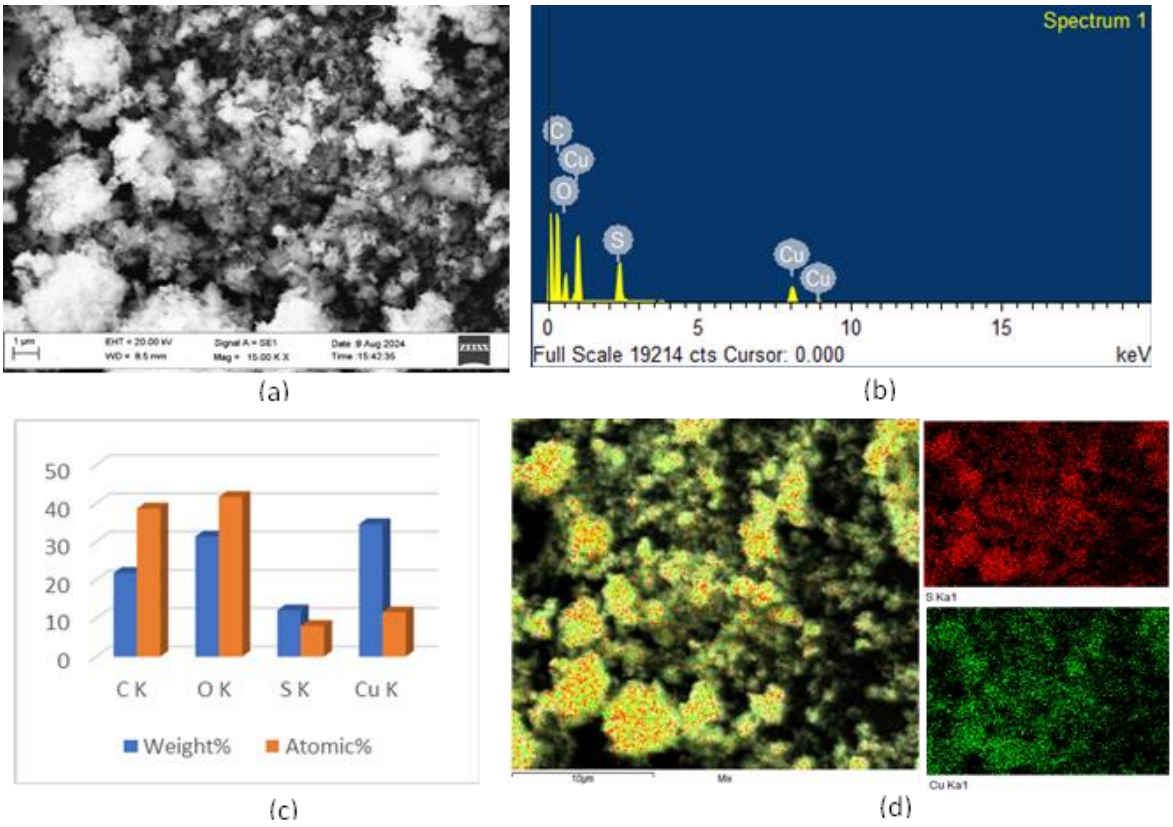


FIGURE 2. (a) SEM image, (b) EDX spectra, (c) quantitative analysis of elements present and (d) elemental mapping for CuS nanomaterial.

3.3 FTIR analysis

The FTIR spectrum was recorded using a Bruker FTIR spectrometer over a wavenumber range of 4000 to 400 cm^{-1} shown in Fig. 2 (a). A characteristic band observed at 3455 cm^{-1} corresponds to the vibrational mode of the hydroxyl (-OH) group and the band at 1626 cm^{-1} is attributed to the -OH bending mode, signifying the presence of trace amounts of water adsorbed on the sample [16]. A band at 1108 cm^{-1} is related to the asymmetric stretching of the carbonyl (C=O) group. The characteristic peak observed at 609 cm^{-1} attributed to the Cu-S stretching modes [14]. These FTIR results confirm the existence of Cu−S bonds, along with hydroxyl (OH) and carbonyl bonds, which may be due to EDTA on the surface of the CuS nanomaterial.

3.4 UV-Vis study

To investigate the optical properties of the synthesized material, UV-visible spectroscopy was conducted using a Shimadzu UV-1800 spectrophotometer. A small quantity of the sample was dissolved in water and subjected to ultrasonic treatment to ensure even dispersion of the particles within the solution. The absorption spectrum, along with the Tauc plot, is presented in Fig. 2 (b). The absorption edge occurs around 450 nm, as shown in Fig. 2(b). The energy band gap was calculated to be approximately 1.48 eV for the EDTA-capped CuS nanomaterials.

3.5 PL analysis

To examine the emission properties of the nanomaterial at room temperature, a Shimadzu spectrofluorophotometer (RF-5301 PC) was used. The photoluminescence (PL) spectrum of the fabricated sample

is presented in Fig. 2 (c). The PL emission peaks have been observed at excitation wavelength 320 nm and subsequently deconvoluted using Gaussian fitting, revealing distinct peaks at 362 nm, 549 nm, 725 nm and 798 nm. The peak at 362 nm arises in the long UV range, which is likely due to electronic transitions occurring near the band edge. The green emission band, observed at 549 nm, is likely attributed to material defects, possibly caused by an excess of sulfur. These defects create trap states within the energy levels, which influence the electronic transitions, leading to the observed emission at this wavelength. The additional peaks at 725 nm and 798 nm suggest further electronic transitions, potentially involving deeper trap states or other defect-related emissions [17].

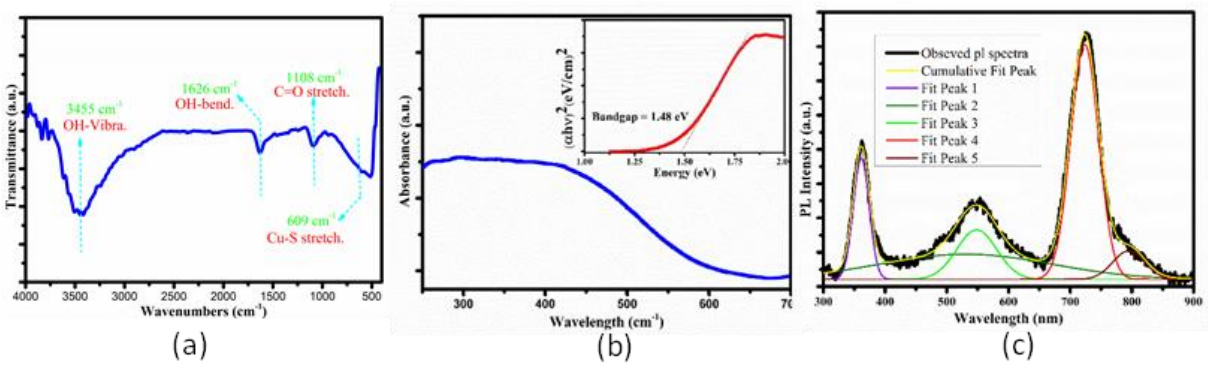


FIGURE 3. (a) FTIR spectrum (b) UV-Vis spectrum with Tauc plot (c) PL spectra for CuS nanomaterial

4. CONCLUSION

CuS nanomaterial was successfully produced by a hydrothermal process with EDTA as a surfactant. The structural, morphological and optical characteristics of the CuS nanomaterial were thoroughly investigated. The XRD and SEM analysis revealed that the prepared nanomaterial exhibited a hexagonal structure having an irregular morphology. Elemental investigation shows the presence of Cu and S in the nanomaterial, with trace amounts of C and O. FTIR spectroscopy provided insights into the chemical bonding and surface functional groups, identifying characteristic Cu−S bonds and highlighting the surface chemistry. The UV-Vis absorption spectra indicated an energy band gap of approximately 1.48 eV. The PL spectroscopy revealed distinct emission peaks in both UV and visible regions, reflecting the electronic structure and potential defect states within the CuS nanomaterials.

REFERENCES

1. J.M. Mazurków, A. Kusior, A. Mikuła and M. Radecka, Appl. Surf. Sci. 606 (2022).
2. M. Wang, L. Zhang, Y. He and H. Zhu, J. Mater. Chem. A **9**, 5320–5363 (2021).
3. K. Ramakrishnan, B. Ajitha and Y. Ashok Kumar Reddy, Sensors Actuators A Phys. 349 (2023).
4. M. Hammadi, E.H. Hummadi and R. Sabah, J. Pharm. Negat. Results 13, 76–81 (2022).
5. Z.H. Mahmoud, N.S. Ahmed, W. Shamkhi and O. Dha'a, Earthline J. Chem. Sci. 141–149 (2020).
6. N. Baig, I. Kammakakam, W. Falath and I. Kammakakam, Mater. Adv. 2 1821–1871 (2021).
7. Y. Guo, Y. Gao, B. Guo, Y. Luo, G. Zhao, J. Sun, W. Li, R. Wang and C. Zhao, Carbon Neutrality 3 (2024).
8. S.M. Khan, S. Bhatkalkar, D. Kumar, A. Ali, S. Sharma and S. Sachar, J. Mol. Liq. **369,** 120881 (2023).
9. A. Rabkin, O. Friedman and Y. Golan, J. Colloid Interface Sci. **457,** 43–51 (2015).
10. S.S.T. Selvi, J.M. Linet and S. Sagadevan, J. Exp. Nanosci. 13 130–143 (2018).
11. L. Rani and R.P. Chauhan, Surfaces and Interfaces **33**, 102306 (2022).
12. K. Vijai Anand, J. Clust. Sci. **32,** 155–161 (2021).
13. J. Jung, H. Jin, S. Woong, M. Choi, D. Vidyasagar, J. Hyeok, R. Bo, Y. Yun, S. Han, I. Sun, J. Eun and S. Lee, J. Mater. Res. Technol. **28** 1875–1882 (2024).
14. I. Savarimuthu and M.J.A.M. Susairaj, ACS Omega 7, 4140–4149 (2022).
15. U. Mureed, Z. Saddique and K. Asad, Acta Chemica Malaysia **7**(2), 64-68 (2023).
16. S. Riyaz, A. Parveen and A. Azam, Perspect. Sci. 8, 632–635 (2016).
17. S.H. Chaki, J.P. Tailor and M.P. Deshpande, Adv. Sci. Lett. **20,** 959–965 (2014).

Thorough Structural Analysis of MACE-grown SiNWs and Its Future Prospectives

Anand Kumar[1], Avadhesh Kumar Sharma[1], Kapil Saxena[2*]
[1]*Department of Applied Sciences and Humanities, Invertis University, Bareilly, 243001, Uttar Pradesh, India*

[2]*Department of Applied Sciences and Humanities, Kamla Nehru Institute of Technology, Sultanpur, 228118, Uttar Pradesh, India*
Corresponding author: kapil.saxena@knit.ac.in

Abstract. This research offers an in-depth structural analysis of Metal-Assisted Chemical Etching (MACE) grown silicon nanowires (SiNWs) and explores it in the terms of their potential future applications. A MACE is a powerful technique that enables the growth of SiNWs through a chemical etching process facilitated by metal catalysts. The structural characteristics of SiNWs, including their diameter, length, aspect ratio, morphology, and crystallinity, were thoroughly examined using various analytical techniques such as field emission scanning electron microscopy (FESEM), X-ray diffraction (XRD), and Fourier-transform infrared spectroscopy (FTIR). The study highlights the influence of metal catalysts and etching conditions on the structural properties of the nanowires. Additionally, the potential applications of MACE method SiNWs in fields such as electronics, energy storage, and sensor technology are discussed. The findings underscore the versatility of MACE-grown SiNWs and suggest promising directions for future research and technologies.

Keywords: SiNWs, MACE method, Crystallinity, and FTIR.

INTRODUCTION

SiNWs have emerged as pivotal material in the realm of nanotechnology, exhibiting remarkable potential across various applications, including photovoltaics, sensors, and nanoelectronics[1,2]. The unique properties of SiNWs, such as their high aspect ratio (surface area-to-volume ratio), quantum confinement effects, and tunable electrical and optical characteristics, make them ideal candidates for next-generation devices. Among the various fabrication methods like vapor-liquid-solid process, chemical vapor deposition, thermal evaporation, and laser ablation, MACE method has gained significant attention due to its simple processibility, cost-effectiveness, and ability to produce high-density and vertically aligned SiNWs with controlled dimensions and morphology[3,4].

This research focuses on a comprehensive structural analysis of MACE method-grown SiNWs, examining the influence of etching parameters on their morphology, crystallinity, chemical bonds and functional groups present in SiNWs[5]. By employing advanced characterization techniques such as FESEM, XRD, and FTIR, we aim to elucidate the relationship between the fabrication conditions and the resulting structural features of SiNWs[6,7]. Understanding these correlations is crucial for optimizing the MACE process to achieve desired nanowire characteristics tailored for specific applications. Furthermore, the future prospects of MACE-grown SiNWs are discussed by highlighting their potential integration into emerging technologies. With the continuous advancement of nanoscale fabrication techniques, SiNWs are poised to play a significant role in the development of storage devices, gas sensors, photodetectors, and high-performance devices, paving the way for innovative solutions in energy, electronics, and beyond[3,8].

EXPERIMENTAL DETAILS

The SiNWs were grown by using the MACE method as shown in Fig.1. A p-type silicon wafer was cleaned by acetone and then immersed in a deposition solution of 4.6 mol/L HF and 0.02 mol/L $AgNO_3$ upto 1 minute. Then Ag-decorated wafer was immersed in an etching solution of 4.6 mol/L HF and 0.8 mol/L H_2O_2 up to 35 minutes, where local dissolution and oxidation of silicon were catalyzed by the metal layer, resulting in vertically aligned SiNWs with residual Ag particles. Lastly, to clean the Ag particles, the SiNWs were submerged in a mixture of HNO_3 and DI water (ratio 1:1) for a period of 10 minutes, yielding clean vertically aligned SiNWs The etching parameters, including metal thickness, solution concentration, and etching time, were optimized to control nanowire morphology. After etching, the nanowires were characterized using FESEM offers high-resolution surface imaging, XRD identifies crystalline structures, and FTIR analyzes chemical bonds and functional groups.

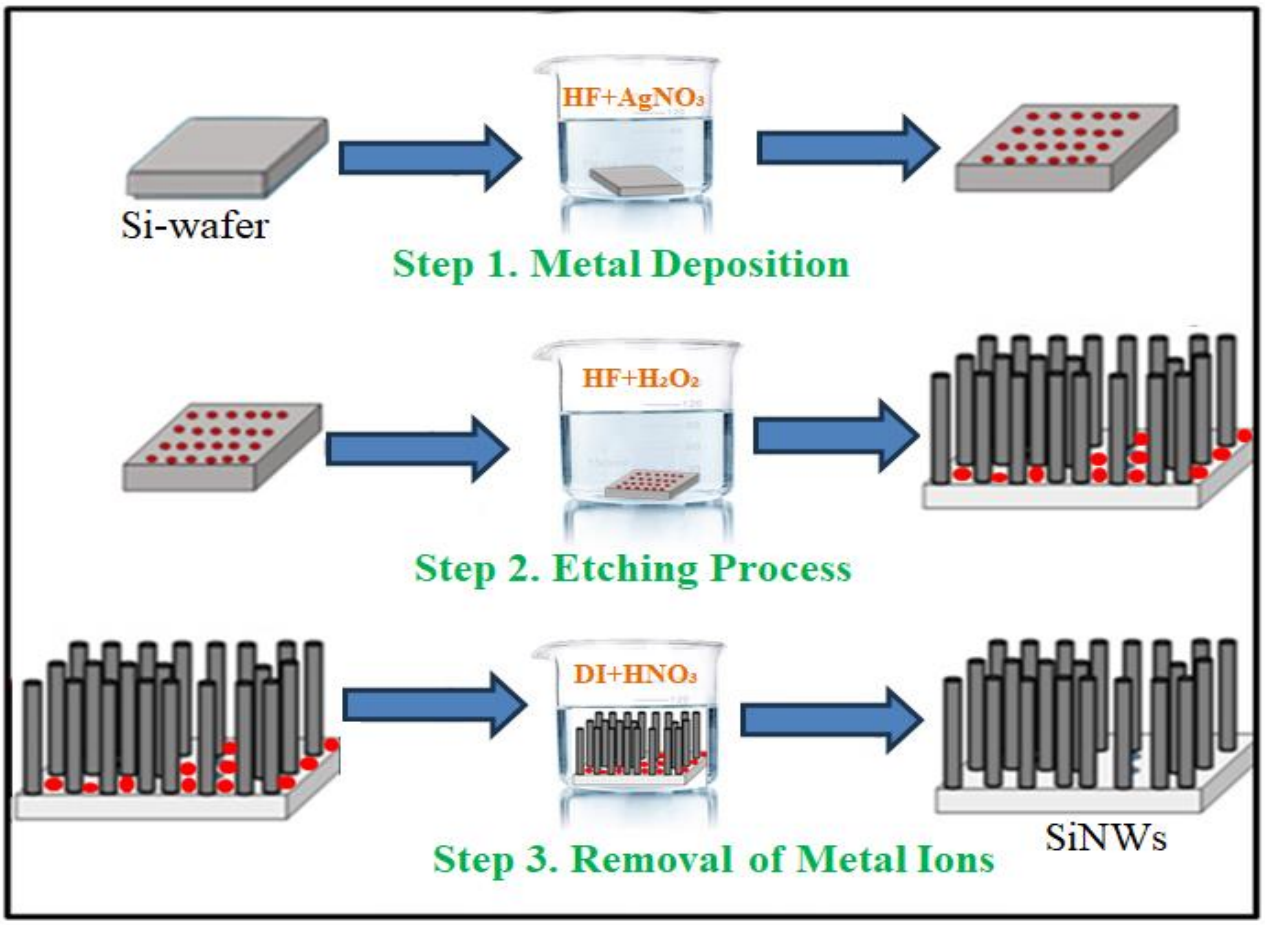


FIGURE: 1. Schematic illustration of the MACE process for the growth of SiNWs.

RESULTS AND DISCUSSION

The FESEM image (Top view and lateral view) reveals dense and vertically aligned SiNWs as shown in Fig. 2(a). Moreover, the nanowires exhibit a uniform and dense distribution, with diameters ranging from tens to hundreds of nanometers. The magnified lateral inset image provides a closer view of the nanowires, showing that they possess smooth and well-defined vertical profiles. The nanowires appear to have a high aspect ratio, indicating significant length relative to their diameter. The overall structure suggests effective etching, with minimal tapering and consistent wire morphology across the sample.

The XRD pattern of the SiNWs is shown in Fig. 2(b). It possess the distinct peaks corresponding to the (111), (220), and (311) crystallographic planes, indicating a high degree of crystallinity with a cubic diamond structure. The sharp and intense (111) peak at approximately 28.4° suggests that the nanowires are highly oriented and well-crystallized. The crystallite size (D) of the SiNWs is 40.96 nm , has been calculated by using the Scherrer formula, $D = \frac{k\lambda}{\beta \cos\theta}$ [9] with a shape factor K = 0.9, X-ray wavelength λ = 0.15418 nm, and an FWHM (β) of 0.2° for the (111) peak. This nanoscale crystallite size is particularly advantageous in various applications, such as in photovoltaics, where high crystallinity enhances charge carrier mobility, in sensors, where the high aspect ratio improves sensitivity, and in nanoelectronics, where small crystal sizes can lead to improved performance in devices.

The Fig. 2(c) represents the FTIR spectrum of the p-type SiNWs that demonstrates key absorption peaks characteristic of silicon and its surface chemistry. The significant absorption band observed around 600 cm^{-1} corresponds to the Si–Si stretching mode, indicating the presence of crystalline silicon in the nanowires. The prominent peak near 1100 cm^{-1} is attributed to the Si–O–Si stretching vibrations, suggesting that the nanowire surfaces have been oxidized, forming a thin layer of silicon oxide. Additionally, the broad absorption in the region between 2200 cm^{-1} and 2400 cm^{-1} may be due to the presence of Si–H bonds, indicating hydride termination on the silicon surface. The gradual increase in transmittance beyond 2400 cm^{-1} suggests that the material is largely transparent to IR radiation at higher wavenumbers, typical of SiNWs with a thin oxide layer.

These materials characterizations are ideal for applications requiring high surface area, such as in sensors, photovoltaics, and other nanoscale devices. And high crystallinity enhances charge carrier mobility, and confirms the nanowires composition and surface chemistry, which are crucial for applications in electronics where surface properties significantly influence performance.

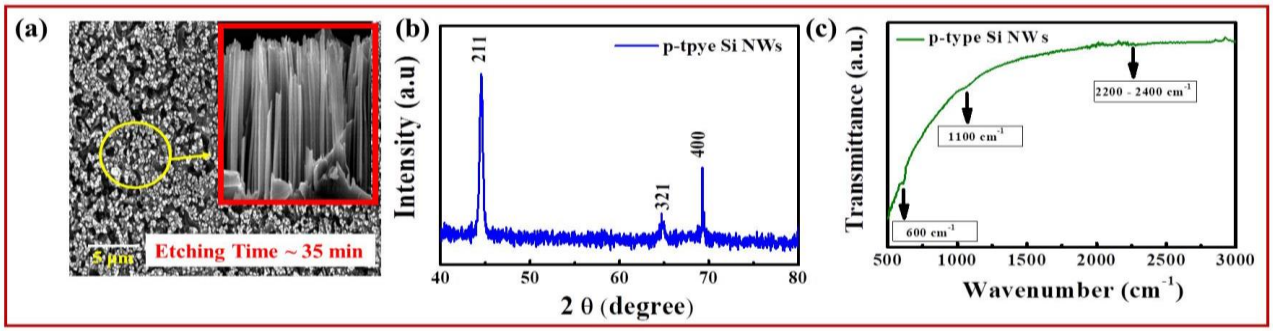


FIGURE: 2. Comprehensive characterization of SiNWs: (a) FESEM image (Top view and lateral view) illustrating the uniform and vertically aligned nanowire structures. (b) XRD pattern confirming the crystalline structure with a prominent (111) orientation. (c) FTIR spectrum revealing the presence of Si–Si, Si–O–Si, and Si–H bonds, indicating surface oxidation and hydride termination.

CONCLUSION

A thorough investigation of the MACE method-grown SiNWs has been presented in this work, which reveals their high potential for cutting-edge technologies. The FESEM analysis confirms a high-density array of vertically aligned nanowires with smooth and well-defined profiles, indicative of effective etching and consistent morphology. The XRD analysis further demonstrates a high degree of crystallinity with a calculated crystallite size of 40.96 nm, which is particularly beneficial for enhancing performance in photovoltaic cells, sensors, and nanoelectronic devices. The FTIR spectrum confirms the presence of crystalline silicon, surface oxidation, and hydride termination, reinforcing the nanowires suitability for applications where surface chemistry is critical. Looking forward, these well-grown SiNWs could offer promising opportunities in the development of high-efficiency photovoltaic devices, ultra-sensitive sensors, and advanced nanoelectronics. Moreover, the combination of their high aspect ratio, excellent crystallinity, and well-controlled surface chemistry opens new avenues for their integration into portable and wearable electronics. Additionally, further refinement in their synthesis and functionalization could lead to their application in quantum computing and other fields requiring precision at the nanoscale. The continued exploration and development of SiNWs will undoubtedly play a crucial role in advancing nanotechnology and its applications across various scientific and industrial domains.

ACKNOWLEDGMENT

Authors acknowledge Department of Applied sciences and Humanities, Invertis University, Bareilly provided lab facilities to fabricate SiNWs.

REFERENCES

1. M. J. Lo Faro, A. A. Leonardi, C. D'Andrea, D. Morganti, P. Musumeci, C. Vasi, F. Priolo, B. Fazio, and A. Irrera, J Mater Sci: Mater Electron **31**, 34 (2020).
2. V. Kashyap, H. Pawar, C. Kumar, N. Chaudhary, and K. Saxena, Frontiers in Materials **9**, 1022317 (2022).
3. C.-Y. Hsu, A. M. Rheima, Z. sabri Abbas, M. U. Faryad, M. M. Kadhim, U. S. Altimari, A. H. Dawood, A. dhari jawad al-bayati, Z. T. Abed, R. S. Radhi, A. S. Jaber, S. K. Hachim, F. K. Ali, Z. H. Mahmoud, G. Behzadi pour, and E. Kianfar, South African Journal of Chemical Engineering **46**, 286 (2023).
4. S. Li, W. Ma, Y. Zhou, X. Chen, Y. Xiao, M. Ma, W. Zhu, and F. Wei, Nanoscale Res Lett **9**, 196 (2014).
5. B. P. Azeredo, J. Sadhu, J. Ma, K. Jacobs, J. Kim, K. Lee, J. H. Eraker, X. Li, S. Sinha, N. Fang, P. Ferreira, and K. Hsu, Nanotechnology **24**, 225305 (2013).
6. A. Bathla, C. Narula, and R. P. Chauhan, J Mater Sci: Mater Electron **29**, 6225 (2018).
7. F. Flory, L. Escoubas, and G. Berginc, JNP **5**, 052502 (2011).
8. V. Kashyap, H. Pawar, I. Sihmar, C. Kumar, A. Kumar, S. Kumar, N. Chaudhary, N. Goyal, and K. Saxena, Appl. Phys. A **130**, 238 (2024).
9. N. R. B. Coleman, N. O'Sullivan, K. M. Ryan, T. A. Crowley, M. A. Morris, T. R. Spalding, D. C. Steytler, and J. D. Holmes, J. Am. Chem. Soc. **123**, 7010 (2001).

Mechanical property evaluation of Alloy 690 at different strain rates and temperatures

Sagar Chandra[1,a)], Sudhanshu Sharma[1], Ather Syed[2], N Naveen Kumar[3], Mahendra K Samal[2], Vivek M Chavan[1]

[1]*Reactor Technology Division, Bhabha Atomic Research Center, Mumbai-400085, India*
[2]*Reactor Safety Division, Bhabha Atomic Research Center, Mumbai-400085, India*
[3]*Materials Science Division, Bhabha Atomic Research Center, Mumbai-400085, India*

[a)]Corresponding author: sagarc@barc.gov.in

Abstract. Mechanical behaviour of Ni-based Alloy 690 is characterized under different conditions (25^0C – 900^0C and 0.0033 s^{-1} – 3500 s^{-1} strain rate). Universal testing machine (UTM) is used to perform quasi-static tests under tension and Split Hopkinson pressure bar (SHPB) test setup is utilized for performing dynamic compression experiments at different temperatures. It is observed that thermally activated deformation mechanisms are prevalent at all the deformation conditions investigated here. However, the flow curve of tensile experiments at 0.0033 s^{-1} strain rate and 800^0C display a gradual decrease of stress following initial yield. Microstructural examination using scanning electron microscope (SEM) of the deformed samples at 0.0033 s^{-1} strain rate and 800^0C reveals dynamic recrystallization in the alloy, which is not present in the samples deformed in compression at high strain rates and high temperatures. This signifies a change in dynamic recrystallization temperature of Alloy 690 with increase in strain rate.

INTRODUCTION

Ni-based superalloys are very attractive for their remarkable mechanical properties, particularly at high temperatures [1]. During high temperature deformation of Ni-based alloys, complex microstructure changes and consequent evolutions are inevitably involved, such as dynamic recrystallization and recovery [2]. Such microstructural changes can significantly alter the mechanical properties of crystalline materials and alloys [3]. In view of this, this work investigates the mechanical properties of Alloy 690 deformed at varying strain rates and temperatures. The mechanical behavior is discussed in conjunction with the deformed microstructure of the alloy.

MATERIALS AND EXPERIMENTS

Uniaxial tension and compression experiments are performed under different test conditions on Ni-based Alloy 690. Specimens of Alloy 690 are obtained from the plate (200 mm X 200 mm X 5 mm dimensions) and the chemical composition of materials is: 60.4 wt% Ni, 29.5 wt % Cr, 9.38 wt % Fe, 0.44 wt% Si, 0.34 wt % Mn and 0.022 wt % C. Initial and final microstructures are observed using SEM and EBSD (electron back-scattered diffraction) techniques. The SEM is field emission gun (FEG) SEM and is integrated with EDS and EBSD detectors. Characterization is performed using a scan step size of around 5 µm and 20.0 kV operating voltage.

In this work, SHPB is utilized to perform compression experiments on Alloy 690 at different rates of loading and varying temperatures (Fig. 1(a)). Adiabatic heating leads to ~65-80^0C temperature rise and this rise is less at higher temperatures. Therefore, adiabatic heating has been neglected in our study. Displacement control mode is utilized to carry out tensile quasi-static tests on Alloy 690 at 10^{-4} s^{-1} and 300 K, 423 K , 573 K, 873 K and 1073 K temperatures (Fig. 1(b)).

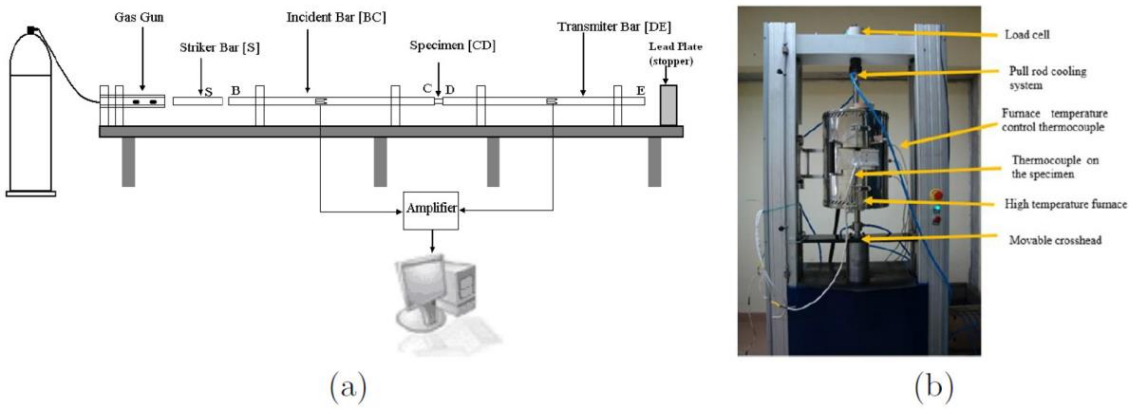


FIGURE 1. (a) A typical schematic of SHPB used to perform uniaxial dynamic compression experiments on Alloy 690. (b) Universal testing machine employed for quasi-static tensile testing of the material.

RESULTS AND DISCUSSION

Fig. 2(a) displays the deformation response of Alloy 690 deformed at 10^{-4} s^{-1} under uniaxial tension. The yield stress decreases with rise in temperature. For instance, the yield stress is around 345 MPa at 300 K, 310 MPa at 423 K, 270 MPa at 573 K and around 220 MPa at 873 K. The flow stress after yielding also displays a decreasing tendency with increase in temperature. This implies that major deformation mechanism in this material is dislocation glide, which is thermally activated in these investigated conditions (quasi-static tensile loading at different temperatures of 300 K – 873 K). It may be noted that all these observations are in accordance with the previous experimental findings on Alloy 690 [4,5]. At a higher temperature of 1073 K at quasi-static rate, the flow curve exhibits continuous softening after the initial peak (Fig. 2(a)). The continuous softening after initial yielding is a signature of dynamic recrystallization (DRX) which manifests itself in the form of continuous softening in Ni-based superalloys having a relatively low stacking fault energy [6]. Microstructure in Fig. 2(b) for the sample deformed at 1073 K is a typical signature of DRX as has also been confirmed by previous studies [6].

Fig. 3 displays the representative stress-strain curves and microstructure of Alloy 690 compressed at 3500 s^{-1} at 300 K, 773 K and 1173 K temperatures. The blue regions in the EBSD maps show the grains that have recrystallized and the red regions show the deformed grains that have undergone plastic deformation and stored distortion energy. Yellow regions depict the substructure that has not undergone complete recrystallization and has a relatively lower stored energy than the red zones. It can be inferred from Fig. 3(b-d) that dynamic recrystallization has not readily occurred, in comparison to deformation at quasi-static rate at 1073 K, at higher strain rates even at higher temperatures of 1173 K. This implies that rate of deformation plays a crucial part in the microstructure evolution and DRX behaviour of Alloy 690. This is because the whole process of DRX can be considered to comprise of the nucleation of corresponding nuclei and subsequent grain growth of these recrystallized grains. At lower strain rates, the total amount of DRX is relatively higher. This phenomena can be attributed to longer applied deformation time at quasi-static rates of loading which cause a relatively larger time for migration of grain boundaries [7,8]. At strain rates of ~3500 s^{-1}, this time for deformation induced migration of grain boundaries is reduced. Hence, lower fraction of DRX grains is encountered in such cases even though the applied deformation temperature is higher. Hence, the reduction in deformation time due to higher applied strain rates restricts the DRX grain growth and therefore, increases the work hardening ability of the material [8]. This is evidenced by the hardening behaviour exhibited by Alloy 690 as can be conceived curves displayed in Fig. 3(a).

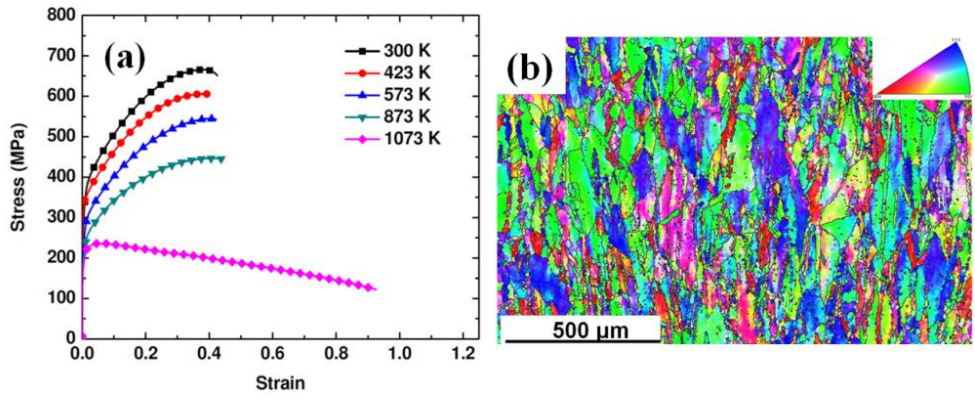


FIGURE 2. (a) Quasi-static uniaxial tensile curves of Alloy 690. (b) Deformed EBSD map of Alloy 690 at 1073 K at these strain rates.

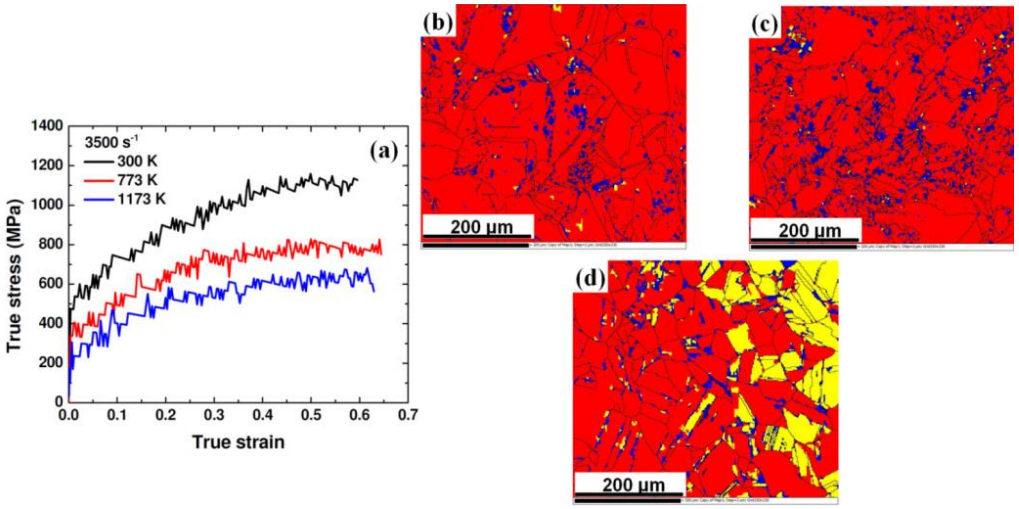


FIGURE 3. (a) Deformation response of Alloy 690 deformed at 3500 s^{-1} strain rate at different temperatures. EBSD maps of Alloy 690 deformed at (b) 300 K, (c) 773 K and (d) 1173 K.

SUMMARY

This work investigates the effect of loading rate and deformation temperature on the mechanical behavior of Ni-based Alloy 690. Uniaxial compression and tension experiments are performed at different temperatures and the obtained stress-strain curves are used to infer the internal deformation mechanisms. While thermally activated deformation mechanisms are prevailing in Alloy 690 at lower temperatures, deformation at high temperatures is accompanied by DRX in the material. The amount of DRX grains reduces with an increase in strain rate, which can be attributed to reduction in time for deformation induced migration of grain boundaries at higher rates of loading.

REFERENCES

18. A. A. Hopgood and J. W. Martin, Mater. Sci. Eng. **82,** 27-36 (1986).
19. Qu Z, P. Zhang P, S. Liang, Y. Lai, J. Wang, J. Jan and R. Bai, J. Mater. Research Tech. **18**, 2112-2124 (2022).
20. K. Huang, K. Marthinsen, Q. Zhao and R. Loge, Prog. Mater. Sci. **92,** 284-359 (2018).
21. P. Sengupta, C. Kaushik, G. Kale, D. Das, K. Raj and B. Sharma, J. Nucl. Mater. **392,** 379-385 (2009).
22. J. Blaizot, T. Chaise, D. Nelias, M. Perez, S. Cazottes and P. Chaudet, Int. J. Plast. **80,** 139-153 (2016).
23. H. Jiang, J. Dong, M. Zhang, L. Zheng and Z. Yao, J. Alloys Comp. **647,** 338-350 (2015).
24. S. Mandal, M. Jayalakshmi, A. Bhaduri and V. Sarma, Metall. Mater. Trasc. A **45,** 5645-5656 (2014).
25. X. Chen, Y. Lin, D. Wen, J. Zhang, M. He Mater. Des. **57,** 568-577 (2014).

Study of effect of loading rate on plastic deformation behaviour and fracture toughness of SA516Gr70 steel

Sudhanshu Sharma[1,a)], Ather Syed[2], Mahendra K Samal[2], Vivek M Chavan[1]

[1]*Reactor Technology Division, Bhabha Atomic Research Center, Mumbai-400085, India*
[2]*Reactor Safety Division, Bhabha Atomic Research Center, Mumbai-400085, India*

[a)]Corresponding author: sudhansh@barc.gov.in

Abstract. Mechanical properties of metals are known to vary with rate of deformation. For evaluation of component integrity and stress analysis, properties at high loading rates are mandatory. Radioactive material shipping cask is such a structure which has to clear the regulatory requirement of 9m drop test. FE analyses of such structures are carried out to determine the worst drop orientation. As such drop tests are an impact event, numerical simulation requires data at deformation rates that are of 2 to 3 order above with respect to quasi-static deformation rate. Considering this, deformation and fracture studies of SA516 Gr. 70 steel has been carried out at deformation rate of 500 mm/min in this work. SA516Gr.70 steel is a pressure vessel that is also used for outer shell of lead-shielded cask. The material has ferritic-pearlitic structure and finds a wide application for fabrications of casks for transport of radioactive materials in nuclear industry, pressure vessels and piping etc.

INTRODUCTION

Dealing with radio-active material is a regular activity for various sectors such as nuclear industry for refueling of nuclear reactors and research purpose, in health care sector for diagnosis and treatment of diseases, in other industries for radiographic inspection etc. Safe handling of the radio-active material is very necessary as it can cause irreparable and fatal damage to human body. To ascertain safety of public and professionals, the radio-active materials are kept in specially designed containers. For nuclear industry these specially designed containers are known as cask. These casks are used for handling and transportation of radio-active materials such as spent fuel, irradiated materials or specimen etc. The SA516Gr.70 steel is used for fabrication of outer shell of shipping cask apart from its use as nuclear piping material [1, 2]. In recent years the application of such ferritic steel for fabrication of monolithic radio-active material transportation cask is also increasing. The radio-active material shipping cask has to clear various normal and hypothetical accident condition requirements for certification by regulatory body before it can be put to use [3,4]. One of the important requirements is the structure should maintain its integrity under the condition of drop from a height of 9m on unyielding surface. Such design requirements are necessary to avoid the release of radio-active material in public domain, in case of any accident. These drop tests are carried out in different cask orientations such as horizontal drop, edge drop, corner drop etc. so as to determine the most damaging drop orientation and cask has to survive the drop in terms of structural integrity [5].

As conducting multiple tests in different orientations to determine the most damaging drop orientation is a costly affair, Finite Element (FE) method is used to simulate the drop tests at different drop orientation and determine the worst drop orientation. In case of failure in the worst orientation, the design is modified and reanalyzed to check the integrity of modified structure. The process is repeated till the integrity is ensured for the worst drop orientation through simulation. Once the most damaging drop orientation is known and the integrity is confirmed through FE simulation, the drop test is carried out in actual for the damaging drop orientation to check if the structural integrity is secured or not.

As, under the 9 m drop condition, the loading rates on the structure are high and to simulate such impact event the material property under high strain rate loading are needed as input parameter. The simulation results will be more accurate and reliable if the material property parameters provided as input are of same loading rate as the cask has seen in the drop tests. Based on the above requirements, in this work, tests were conducted at high loading rate on SA516 Gr. 70 steel to study the deformation and fracture behaviour.

MATERIALS AND EXPERIMENTS

To determine the mechanical properties of SA516 Gr. 70 steel, tensile and fracture tests were conducted. The alloying elements in the material are listed in Table 1. The base material was in the form of billet of dimensions 500mm (L)*110mm (W)*85 mm(H) in rolled and normalized condition.

TABLE 1. Alloying elements in SA516 Gr.70 steel (%wt)

Element	C	Mn	Si	P	S	Ni	Cr	Cu
(wt %)	0.24	1.14	0.2	0.016	0.022	47 ppm	30 ppm	180 ppm

Threaded end specimen with circular gauge cross-section (Ø-3mm X 9 mm (L)) were used for tensile experiments and for fracture test, Side Edge Notch Bend (SENB) specimen having dimension 55mm*10mm*5mm were used with crack at the edge having a/W ratio of 0.5. Both tensile and fracture tests were conducted using conventional testing machines. The tensile experiments were carried out at a deformation rate of 500mm/min at different temperatures ranging from RT to (minus) -125^{o}C and fracture tests were also conducted at deformation rate of 500mm/min and test temperature of (minus)-100^{o}C.

EXPERIMENTAL RESULTS

The data gathered from the tension test were processed to evaluate the stress-strain curve. The stress-strain curve for different temperatures are shown in Fig. 1. It was found that as temperature decreases, the material yield strength and flow stress increases, showing loss of material ductility. The yield and ultimate strength determined from a quasi-static test was noted to be 300 MPa and 485 MPa respectively. On comparison stress-strain curves it can be observed that there is a remarkable rise in the yield and flow stress of the material at 500mm/min with respect to the quasi-static properties.

Five number of identical fracture tests were conducted at -100 ^{o}C at loading rate of 500mm/min. The load deformation data obtained from the test were shown in Fig. 2. Though the loading rate and test temperature were same for each test, the load deformation behaviour of the material is varying a lot. The variation in deformation is form nearly 0.2mm for tests 1 to 0.7mm for test 5 and load is changing form 2.75kN to 3.25kN. It can be inferred from the load deformation curves presented that there is some amount of ductile crack propagation before unstable crack growth. Thus, the overall energy absorbed by the specimen before fracture is different for each test. This variation in load and deformation response is because the ferritic steel shows Ductile to Brittle Transition Temperature (DBTT) behaviour and the current test temperature fall in DBTT regime.

As the loading rate are high unloading compliance test are not possible. Hence the tests are carried out in monotonic loading till the specimen fractures. The unstable crack growth is preceded by ductile crack growth, the J-fracture toughness parameter has been evaluated at the point of unstable crack growth for each test. The J-fracture toughness parameter is sum of the elastic J (Je) and Plastic J (Jp). The Je can be evaluated using the maximum load and Jp can be evaluated by plastic area under load deformation curve. The procedure followed to determine the J integral is as per ASTM 1820[6]. The critical values of J integral at final fracture are listed in the Table 2.

TABLE 2. Fracture toughness value evaluated for different tests at -100^{o}C

Test No.	J_C (N/mm)
1	51.01
2	103.68
3	128.00
4	137.78
5	144.5

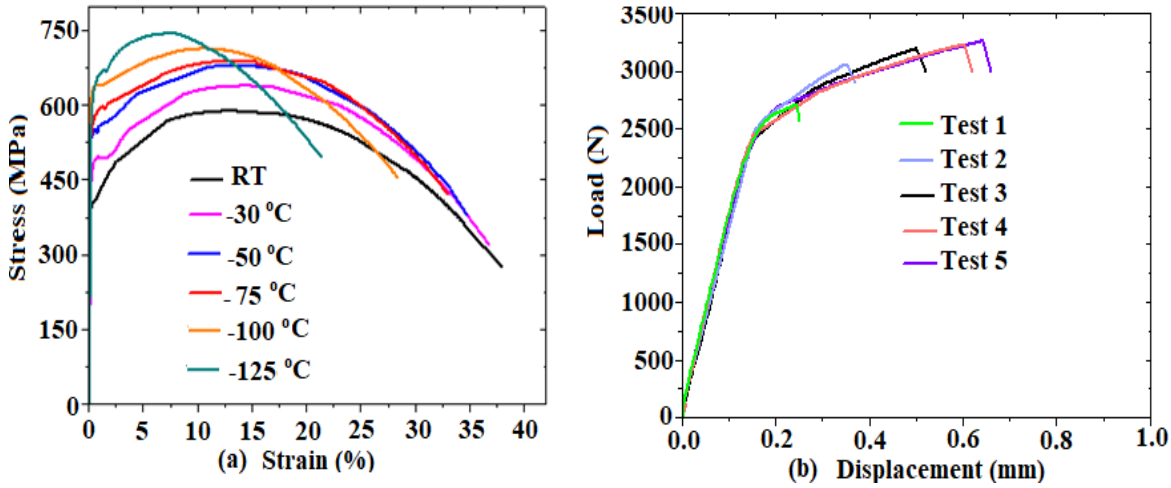


FIGURE 1. (a) Stress-strain data of SA516Gr.70 steel for the loading rate of 500mm/min and different temperatures. (b) Load-deformation graphs for SE(B) specimen fracture tests as 500 mm/min loading rate at -100ºC.

SUMMARY

The load-deformation behaviour of SA516Gr.70 steel has shown expected behaviour. There is a loss of ductility with decrease in temperature with an increase in flow and yield strength of the material. As the deformation rate was high, it was not possible to evaluate the J-R curve and hence, single value fracture toughness was determined at the point of unstable crack growth. The fracture tests were conducted at (minus)-100ºC that falls in the DBTT regime, hence large variation in fracture toughness of the material was observed. This is so because at low temperatures both the ductile and brittle fracture mechanisms are active. If the applied load is sufficient to reach critical stress in the presence of an existing flaw, sudden unstable crack growth can happen but if the critical stress is not reached, the ductile crack growth keeps increasing with void nucleation and growth mechanism. Owing to this phenomenon, large variation in J value at final fracture is observed. The random distribution of flaw is responsible for the variation in the critical fracture toughness values.

REFERENCES

1. J. H Yoon, B S Lee, and J H Hong, Int. J. of Pressure Vessels and Piping **76,** 663-670 (1999).
2. C. S. Seok, K. L. Murty, Int. J. of Pressure Vessels and Piping **76,** 945–953. (1999).
3. AERB Safety Code No. AERB/NRF-TS/SC-1, ' Safe Transport of Radioactive Material'.
4. IAEA, 'Regulation for the safe transport of radioactive material' Safety Guide TS-R-1.
5. J. V. Mane, S. Sharma, V. M. Chavan, D. C. Kar, R. G. Agrawal, Cage design, impact analysis and experimental testing of teletherapy source transportation flask. Transactions, SMiRT 21, 2011, New Delhi, India', (2016).
6. ASTM Standard E 1820-01, Standard test method for measurement of fracture toughness. 03.01: 1-21(2000).

On the Optical Response of a MgZnO/ZnO HEMT

Saheb Chakraborty[1,2], Radha Raman Pal[1] and Sutanu Dutta[3,*]

[1]*Department of Physics, Vidyasagar University, Paschim Medinipur, West Bengal, India*
[2] *Department of Physics, Garhbeta College, Paschim Medinipur, West Bengal, India.*
[3] *Department of Electronics, Vidyasagar University, Paschim Medinipur, West Bengal, India.*
[*]*Corresponding author: sutanu@mail.vidyasagar.ac.in*

Abstract. This article analyzes and reports the optical sensitivity of a MgZnO/ZnO-based high electron mobility transistor. An analytical equation of threshold voltage is established under optical illumination considering a new theoretical approach. Further, a new theoretical model of the drain current of a HEMT has been developed considering the modulation of sheet carrier density. It is observed that the saturated drain current has been shifted by 14.7 % from the dark drain current when no gate bias is applied. In addition, the threshold voltage shows a significant sensitivity to optical illumination.

Keywords: MgZnO/ZnO HEMT; MODFET; Optical study; OPHEMT; Threshold voltage; Drain current.

INTRODUCTION

In the era of modern technology, High Electron mobility transistor (HEMT) has played an important role for the last few decades. Among the various types of HEMTs, ZnO-based HEMTs have shown considerable interest in recent times. Because, ZnO has some excellent material properties like wide band gap (3.37 eV), large breakdown field (3MV/cm), large exciton binding energy (60meV) and very high saturation velocity of electrons (3.2×10^5 m/s) [1-5]. Several theoretical and experimental studies has been executed previously to study the characteristics of ZnO-based HEMTs [6-10]. But, there is a lack of proper work in the literature to study the optical response of MgZnO/ZnO HEMTs. The threshold voltage have been modulated due to the generation of electron-hole pairs (EHPs) in the MgZnO region under the optical illumination. The sheet carrier concentration of the 2DEG layer has been changed with the optical illumination. The previous literature developed so far did not address this issue and the theoretical background of optical sensitivity concerning drain current and threshold voltage remains unexplored. In our work, we have incorporated these issues of contemporary interest to model the device current and switching on potential and developed simple analytical expressions of these parameters probably for the first time in the literature. This work thus presents a novel and innovative approach to study the optical sensitivity of the MgZnO/ZnO HEMTs.

MODEL DEVELOPMENT

The proposed structure of a MgZnO/ZnO HEMT with optical illumination is represented in FIGURE 1(A). The band diagram of the heterojunction has been represented in FIGURE 1(B). The barrier potential of the metal-semiconductor junction has been represented as $q\emptyset_b$. The band gap between MgZnO and ZnO has been represented by ΔE_c. d_1 and d_0 denote the thickness of the doped MgZnO region and the undoped MgZnO region respectively. Δd represents the thickness of the 2DEG layer. The expression of the threshold voltage of the device has been derived from FIGURE 1(B) as [11]

$$V_t = \emptyset_b - \frac{\Delta E_c}{q} - V_p \quad (1)$$

V_p is pinch-off voltage. The gate junction has been illuminated with the incident radiation with optical flux ($\varphi(y) = \varphi\alpha_1\tau e^{-\alpha_1 y}$) [12]. φ is the incident optical flux density at the gate interface, α_1 is the absorption coefficient in the MgZnO layer and τ represents the relaxation time of excess electrons.

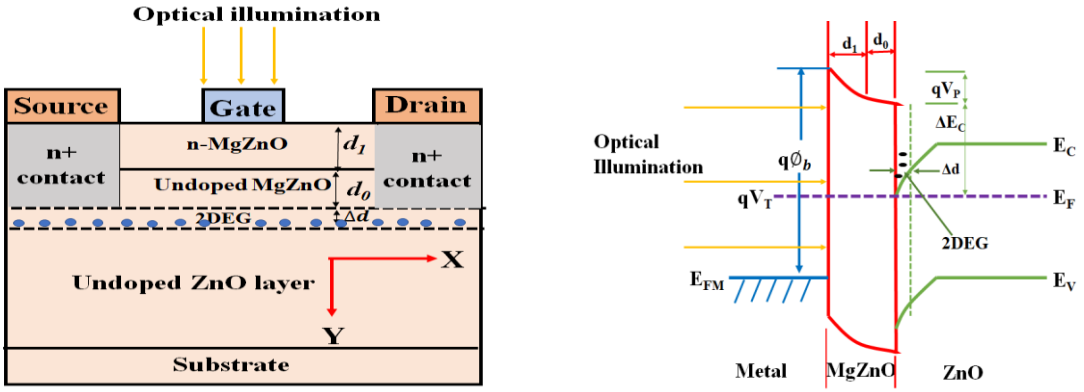


FIGURE 1. (A) Structure of MgZnO/ZnO HEMT; **(B)** Band structure of MgZnO/ZnO heterostructure.

We have assumed that the gate metal is transparent to the incident radiation and the energy of the incident photons is greater than the band gap energy of MgZnO. The photons will transfer the energy of the valence band electrons of MgZnO and transfer it to the conduction band.The distribution profile of total charge density is corrected as after illumination

$$N(y) = q\{N_d + \varphi\alpha_1\tau e^{-\alpha_1 y}\} \quad (2)$$

The pinch-off voltage is derived as

$$V_p = \frac{q}{\epsilon}\left\{\int_0^{d_1} N(y)ydy + \varphi\alpha_1\tau\int_{d_1}^{d_1+d_0} e^{-\alpha_1 y}dy\right\} \quad (3)$$

Putting the value of *N(y)* in equation (3) and evaluating the integration, the value of pinch off voltage is given by

$$V_p = \frac{q}{\epsilon}\left[\frac{N_d d_1^2}{2} + \frac{\varphi\tau}{\alpha_1}(1-e^{-\alpha_1 d_1}) - \varphi\tau e^{-\alpha_1 d_1}\left\{(d_1+d_0)e^{-\alpha_1 d_0} - \frac{1}{\alpha_1}(1-e^{-\alpha_1 d_0})\right\}\right] \quad (4)$$

Where, N_d and ε represents the doping concentration and relative permittivity respectively in the doped MgZnO region.

After travelling through the MgZnO barrier layer the incident optical flux density has been reduced to

$$\varphi'(y) = \varphi'\alpha_2\tau e^{-\alpha_2 y} \quad (5)$$

Where, φ' is given by $\varphi' = \alpha_2\tau e^{-\alpha_1(d_1+d_0)}$ and α_2 is the absorption coefficient of ZnO. This optical flux will again generate EHPs in the 2DEG layer and the sheet carrier concentration has been modulated as

$$n_{so} = n_s + \Delta d\varphi'\alpha_2\tau e^{-\alpha_2 y} \quad (6)$$

Here, n_s represents the sheet carrier concentration of the 2DEG layer before illumination [13].

Integrating equation (6) with respect to *y*, n_{so} can be rewritten as

$$n_{so} = n_s + \varphi'\tau(1-e^{-\alpha_2\Delta d}) \quad (7)$$

The modulated drain current with optical illumination at the gate can be written as [9]

$$I_d = qn_{so}Z\frac{[\mu_0 V_d L^3 + C_1 v_s V_d{}^4]}{[L^4 + a\,C_2 V_d L^3 + C_1 V_d{}^4]} \quad (8)$$

Here, Z represents the channel width, V_d represents the drain voltage and v_s is the saturation velocity of electrons in the ZnO layer.

The relationships between mole fraction and the several material parameters of the device are given as

$$\epsilon = 8.75 + 1.08x \quad (9)$$

$$E_g^{Mg_xZn_{1-x}O} = 3.37 + 2.14x \quad (10)$$

$$\emptyset_b = 5.81x^2 - 3.12x + 1.12 \quad (11)$$

Where, N_d=3×10^{24} /m^3, L=0.1µm, μ_0=332 cm^{2}V^{-1}S^{-1}, d_1 =17 nm, d_0 =3nm, Δd= 5nm, E_g^{ZnO}=3.37 eV, v_s=3.2×10^5 m/s, α_1=7×10^6 m^{-1}, α_2=13×10^6 m^{-1}, τ=5×10^{-4} s and φ=1×10^{13} cm^{-2}s^{-1}.

RESULTS AND DISCUSSIONS

The drain current with drain voltage variation for different gate bias has been depicted in FIGURE 2(A). The drain current has been increased with drain voltage and the drain current becomes saturated after a specific drain voltage. However, with optical illumination at the gate junction generates new EHPs and the current is greater with optical illumination due to these excess electrons.

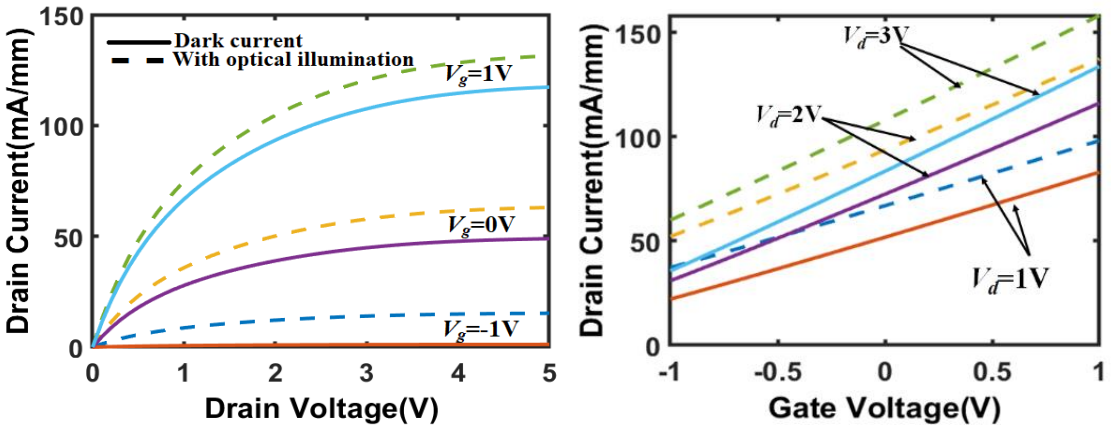


FIGURE 2(A). I_d–V_d plot for different V_g; **(B)** I_d–V_g plot for different V_d.

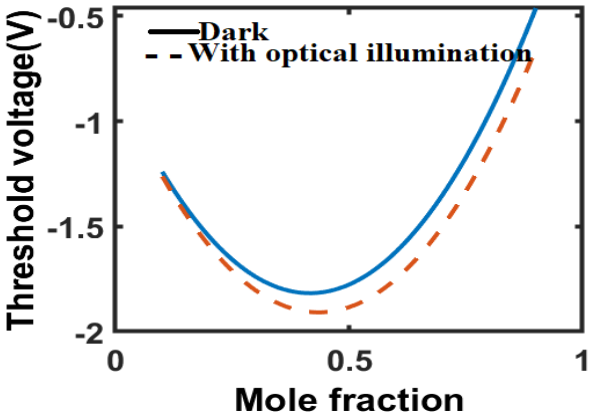


FIGURE 3. Variation of threshold voltage with mole fraction.

The drain current vs gate voltage for different drain voltages is illustrated in FIGURE 2(B). It is observed that if the gate voltage rises then the drain current also rises and is greater for larger drain voltage. It is also observed from FIGURE 2(B) that the drain current is larger with optical illumination due to excess EHPs.

FIGURE 3 illustrates the threshold voltage vs mole fraction variation. It is seen that the threshold voltage reduces initially with '*x*' and after a certain value '*x*' threshold voltage enhances. It is due to the fact that the Wurtzite MgZnO is converted into the Rocksalt structure after a particular value of the mole fraction [14]. It is also observed that the threshold voltage is lower with optical illumination and hence higher gate bias is necessary for switching on the device. Thus, this is consistent with FIGURE 2(A) and 2(B).

REFERENCES

1. D. C. Look, J. Electron. Mater. **35,** 1299–1305 (2006).
2. M. A. Khan, P. Kumar, G. Siddharth, M. Das and S. Mukherjee, IEEE Trans. Electron Devices **66** 5097-5102 (2019) .
3. R. Singh, M. A. Khan, S. Mukherjee and A. Kranti, IEEE Trans. Electron Devices **64**, 3661-3667 (2017).
4. H. P. Zhou, M. Xu, W. Z. Shen, Phys. Rev. B Condens. **403**, 3585-3588 (2008).
5. D. Liu, J. Comput. Electron **22**, 603-611 (2023)
6. Y. K. Verma, V. Mishra and S. K. Gupta, J. Circuits Syst. Comput. **29**, 2050009 (2020)
7. Y. K. Verma, V. Mishra, and S. K. Gupta, Silicon **13**, 91–107 (2021).
8. S. Chaudhary, P. Kumar, M. A. Khan, A. Kumar and S. Mukherjee, Eng. Res. Express **4** 025007 (2022).
9. S. Chakraborty, R. R. Pal, and S. Dutta, J. Korean Phys. Socy **84**, 313-322 (2024).
10. S. Chakraborty, R. R. Pal, and S. Dutta, Indian J. Pure Appl. Phy **62**, 285-291 (2024).
11. S.M. Sze, *Semiconductor Devices Physics and Technology* (Wiley India Publication, 2011), pp.246.
12. S. Dutta, Opt. Eng. **58**, 117102-117102 (2019)
13. N. Dasgupta, A. Dasgupta, Solid State Electron. **36**, 201-203(1993).
14. Y. H. Zan, S. L. Ban, Superlattices and Microstructures **150**, 106782(2021).

On the Thermal Sensitivity of a GaN MODFET for High Field application

Prabir Kumar Shit[1,2], Radha Raman Pal[2], and Sutanu Dutta[3]*
[1]*Department of Physics, Garhbeta College, West Bengal, 721127, India*
[2]*Department of Physics, Vidyasagar University, West Bengal,721102, India*
[3]*Department of Electronics, Vidyasagar University, West Bengal,721102, India*
[*]Corresponding author: sutanu@mail.vidyasagar.ac.in

Abstract. This paper represents a temperature dependent theoretical model of a GaN Modulation Doped Field Effect Transistor (MODFET) operated at high electric field, under electron velocity saturation. To assess the device's DC properties, including drain current and threshold voltage, as a function of mole fraction and ambient temperature, a straightforward analytical model has been created. The choice of AlGaN mole fraction and environmental temperature changes are shown to have a substantial impact on the device current. The device's performance is evaluated according to the N-AlGaN layer's thickness and doping concentration. The thermal sensitivities of drain current and threshold voltage are calculated in order to study the thermal effect more precisely.
Keywords: GaN MODFET, Thermal effect, Thermal sensitivity of drain current, Thermal sensitivity of threshold voltage

INTRODUCTION

GaN MODFETs are becoming highly attractive and interesting devices for high-power, high temperature and microwave frequency applications in recent years [1-2]. This is due to some inherent properties of GaN such as its wide band gap (3.4 eV), high breakdown field ($2 \times 10^6 V/cm$), high mobility of electrons (2000 cm^2/v-s), high saturation velocity of electrons ($2.5 \times 10^7\ cm/s$), outstanding thermal conductivity (1.3 w/cm/k), etc [3]. The additional feature, such as lattice matching of GaN with the large band gap materials such as AlN and AlGaN enables its-self as a promising material for hetero-structure electronics [4]. Some workers have studied GaN based devices in their work earlier [2-5]. All such models and theoretical approaches are complex and do not consider the device operation for high electric fields, particularly when electron velocities are saturated. A basic mathematical model of a GaN MODFET within the context of electron velocity saturation is presented in this paper. In addition, the performance of the device with ambient temperature is explored. Here, the analytical formulations of the DC parameters- such as threshold voltage and drain current- are computed, and their relationship to ambient temperature is examined. In addition, in order to study the impact of temperature on the device more precisely, the thermal sensitivities of various DC parameters are calculated and studied. The previous models developed so far did not consider electron velocity saturation at high drain field, which in our opinion is more relevant and realistic. At the same time, the impact of various device parameters such as thickness, mole fraction and doping concentration of N-AlGaN layer and impact of ambient temperature cannot be ignored. Overall, our work includes all these above issues and provides a useful, inclusive, realistic and simple mathematical formulation for various device parameters of a GaN MODFET.

MODEL DEVELOPMENT

Let us consider the structure of a GaN MODFET in FIGURE 1(a) and band structure of the heterojunction in FIGURE 1(b). Here d_1, d_0 and Δd are the doping thickness, the thickness of undoped AlGaN layer and the thickness of the 2DEG layer formed at the interface between the undoped GaN and undoped AlGaN respectively.

The threshold voltage (V_T) of the device is given by [6].

$$V_T = \emptyset_{bn} - \frac{\Delta E_c}{q} - \frac{qN_d d_1^2}{2\varepsilon} - \frac{\sigma_{pz} d}{\varepsilon} \quad (1)$$

Where $\boldsymbol{\varepsilon}$ is the dielectric constant of AlGaN layer, d=(d_1+d_0+Δd) is the space between the conducting channel and the Schottky gate. $\emptyset_{bn}$ is the Schottky barrier height of the metal-semiconductor junction at the gate. ΔE_c is the difference of the energy band gaps between GaN and AlGaN, σ_{pz} is the total polarization charge density. N_d is the doping concentration and V_p is the pinch-off voltage of the device.

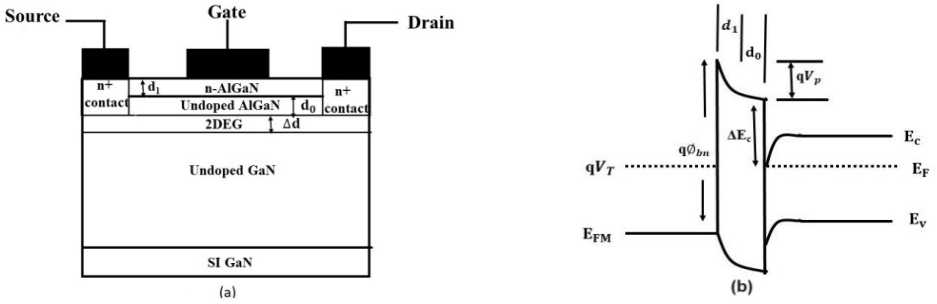


FIGURE 3. (a) Cross-sectional view of a GaN MODFET, (b) Energy band structure of the hetero-junction under the gate.

The drain current of a MODFET under electron velocity saturation is given by [7]

$$I_d = Z v_s \frac{\varepsilon}{d}[V_g - V_T - \frac{V_d}{2}] \quad (2)$$

The material parameters such as saturation electron velocity, relative permittivity, the energy band gap of GaN, and the energy band gap of AlGaN dependent on the temperature and their functional forms are given by [8-10].

$$\left.\begin{aligned} v_s &= 2.87 \times 10^7 - 9.8 \times 10^3 T \\ \varepsilon &= \varepsilon_0[1 + 10^{-4}(T - 300)] \\ E_g^{GaN} &= E_g^{GaN} - 2\alpha_B^{GaN} \exp\left(\frac{\theta_B^{GaN}}{1-T}\right) \\ E_g^{AlGaN} &= E_g^{AlGaN} + \Delta E_g - 2\alpha_B^{GaN} \exp\left(\frac{\theta_B^{GaN}}{1-T}\right) \\ \emptyset_{bn} &= \emptyset_{bn0}(0°C) + \frac{\alpha_B T^2}{T_B + T} \end{aligned}\right\} \quad (3)$$

Where, $v_{sat} = 2.87 \times 10^5\ m/s$, $\Delta E_g = 0.082\ eV$, $\alpha_B^{GaN} = 0.112\ eV$, $\theta_B^{GaN} = 386\ K$, $E_g^{GaN}(0) = 3.5\ eV$, $\emptyset_{Bn0} = 1.07\ eV$, $\alpha_B = -0.32 \times 10^{-2}\ V/°C$, $T_B = 1.67 \times 10^2$ °C. The thermal Sensitivity of Threshold Voltage (S_{V_T}) and the thermal sensitivity of drain current (S_{I_d})of the device can be calculate as follows

$$S_{V_T} = \frac{2\alpha_B T}{T_B + T} - \frac{\alpha_B T^2}{(T_B + T)^2} + \frac{qN_d d_1^2}{2\varepsilon^2}\frac{d\varepsilon}{dT} + \frac{\sigma_{pz} d}{\varepsilon^2}\frac{d\varepsilon}{dT} \quad (4)$$

$$S_{I_d} = \frac{I_d}{v_{sat}}\frac{dv_s}{dT} + \frac{I_d}{\varepsilon}\frac{d\varepsilon}{dT} - z v_s \frac{\varepsilon}{d}\frac{dV_T}{dT} \quad (5)$$

RESULTS AND DISCUSSIONS

Equation (2) shows the functional dependence of the drain current on various material and device parameters of a GaN MODFET. The critical field required for electron velocity saturation for GaN is $E_c = 2 \times 10^5$ V/cm, and it can be obtained at the drain bias $V_d = 2$ V having channel length lower than $0.1\mu m$. For the applied voltage $V_d = 2$ V or more, the electron velocity gets saturated and the device follows the velocity saturation model. The value of the device parameters are as follows $d_1 = 17\ nm$, $d_0 = 3\ nm$, $\Delta d = 0.1\ nm$, $z = 75\ \mu m$, $N_d = 10^{24} m^{-3}$ and $x = 0.15$. FIGURE 2 shows how the drain current changes with the drain voltage over a range of gate voltage values. The figure shows that while the drain current rises with gate bias, it falls with drain voltage. This is due to the fact that after velocity saturation is reached, the electron velocity does not increase further with drain field. On the contrary, with the increase of drain bias the 2D charge density at GaN and AlGaN interface (n_s) decreases. As a result drain current decreases. But with the increase of V_g, n_s increases and the drain current increases.

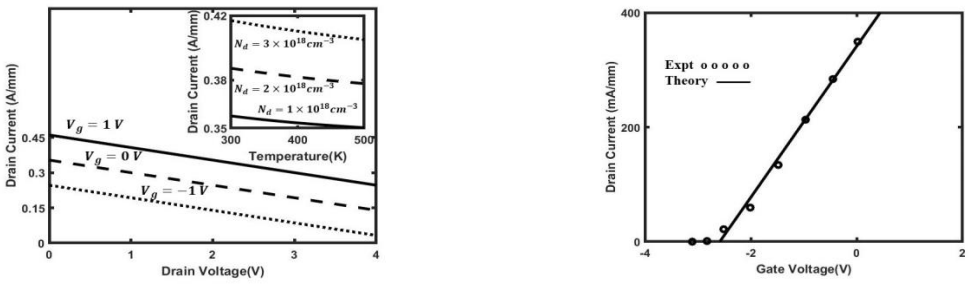
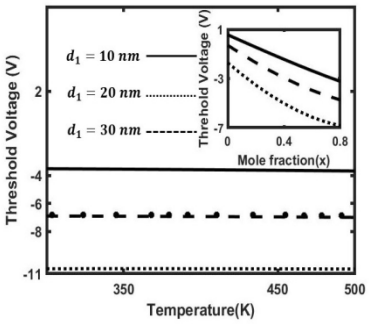


FIGURE 4. I_d vs V_d curve for different V_g. I_d vs T curve for different d_1 is shown in the inset of FIGURE 2. **FIGURE 3** I_d vs V_g curve for V_d = 3V.

The inset of FIGURE 2 illustrates how the drain current changes with temperature for a range of N-AlGaN layer doping concentrations. The graphic makes it clear that at higher temperatures, the drain current drops. This is because at increasing temperatures, the velocity of the saturated electrons decreases. Additionally, it is noted that when N_d grows, so the device current rises as a result of the pinch off voltage increasing with N_d, the threshold voltage decreasing, and ultimately the sheet carrier concentration rises. FIGURE 3 illustrates how the drain current varies with gate bias. It is seen from the figure that the drain current increases with gate voltage, which is consistent with FIGURE 2. In order to validate this work, we compare our results obtained from theoretical computation with the experimental data reported earlier by Rashmi et al. [11], where the drain current was measured for different gate bias. It is observed that our computed data satisfactorily match with experimental data reported earlier as shown in FIGURE 3. The device's threshold voltage is expressed as a function of mole fraction and other device parameters in Equation (1). FIGURE 4 illustrates how the threshold voltage changes with temperature for varying d_1. As can be seen from the figure, the device's threshold voltage gradually rises with temperature. Once more, it is seen that when d_1 rises, the threshold voltage falls. This is because, for large d_1, the value of pinch-off voltage increases and threshold voltage reduces. We again compare our results with the experimental data reported by Egawa *et al.*[12] where they measured threshold voltage of the device for d_1=20 nm for a temperature range 300K to 500K and interestingly it also matched well with our computed data. The circular dots shown in FIGURE 4 represents the experimental data of threshold voltage reported in ref [12].

The inset of FIGURE 4 illustrates how the threshold voltage changes with mole fraction for various d_1. It is observed from the figure that threshold voltage of the device decreases with increasing mole fractions. This is due to the enhancement of ΔE_c with 'x' at the GaN/AlGaN interface. FIGURE 5 illustrates how the drain current's thermal sensitivity varies with mole fraction for varying d_1. It is seen from the figure that S_{I_d} is independent of d_1 and its value approaches to zero for lower values of x. The inset of FIGURE 5 illustrates how the threshold voltage's thermal 215ensitivityy varies with mole fraction for various d_1. The graphic illustrates that S_{V_T} grows as x increases. At smaller values of x, S_{V_T} approaches zero. Once more, S_{V_T} rises as d_1 does. However, the dependency of S_{V_T} on d_1 decreases at low mole fraction values.



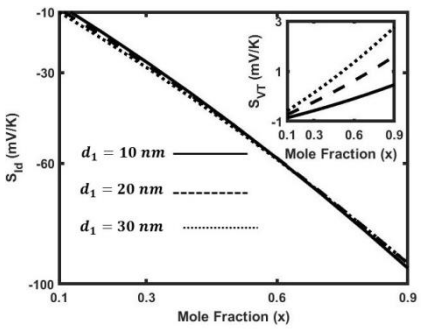


FIGURE 4. V_T vs T and V_T vs x for different d_1. **FIGURE 5.** S_{Id} with x and S_{V_T} with x for various thicknesses of the N-AlGaN layer.

REFERENCES

1. I. Saidi,M. Gassoumi,H. Maaref,H. Mejri,and C. Gaquiere, J ApplPhys, **106**, 1-7 (2009).
2. P. K. Shit, R. R. Pal andS. Dutta, Indian J Pure ApplPhys, **60**395-400 (2022).
3. P. Gangwani, R. Kaur, S. Pandey,s. Halder, M. Gupta andR. S. Gupta, SuperlatticeMicrostruct, **44** 781-793(2008).
4. T. Kuech,R. T. Collins, D. L. Smith andC. Mailhoit, J ApplPhys, **67**, 2650-2652 (1990).
5. M. J. Murphy, K. Chu, H. Wu, W. Yeo, W. J. Schaff, O. Ambacher, L. F. Eastman, T. J. Eustis, J. Silcox, R. Dimitrov and M. Stutzmanm, ApplPhys Lett,**75** 3653-3655 (1999).
6. P. Ganwani, S. Pandey, S. Haldar, M. Gupta andR. S. Gupta, Solid State Electron, **51** 130-135 (2007).
7. P. Shit, R.R. Pal andS. Dutta, AIP ConfProc, **2369** 020139 1- 4 (2021).
8. M. K. Chattopadhyay andS. Tokekar, Solid State Electron, **50** 220-227 (2006).
9. S. Kabra, H. Kaur, S. Halder, M. Gupta andR. Gupta, Solid State Electron, **52** 25-30 (2008).
10. Z. Xiaoling, L. Fei, L. Changzhi, X. Xuesong, L. Ying andS. N. Mohammad, J Semicond,**30** 034001-(1-7) (2009).
11. Rashmi, S. HaldarandR. S. Gupta, Microw Opt Technol Lett, **29**117-123 (2001).
12. T. Egawa, G. Y. Zhao, H. Ishikawa, M. UmenoandT. Jimbo, IEEE transElectron Devices, **48** 603-608 (2001).

A Method of aligning CNTs in nanocomposite polymer films

Bhakti Hirani[1*] and P.S. Goyal[2]

[1]Department of Biotechnology, Pillai College of Arts, Commerce and Science, New Panvel Maharashtra, India – 410206
[2]Department of Electronics, Pillai College of Engineering, New Panvel, Maharashtra, India – 410206

*Corresponding author: bhaktih90@gmail.com

Abstract A new method of aligning CNTs in polymeric films involves mixing of CNTs and magnetic nanoparticles to the polymer solution and casting the polymer film/ membrane in presence of a moderate magnetic field, has been developed. Polysulfone – MWCNTs films were synthesized and the alignment of MWCNTs was examined by carrying out water permeability and dielectric studies. Water permeability was higher for membranes casted in magnetic field and it increased with an increase in magnetic field.

Keywords Alignment of CNTs, Magnetic nanoparticles, Polysulfone-MWCNT nanocomposites membranes, Membrane casting machine, Water permeability, Dielectric Constant.

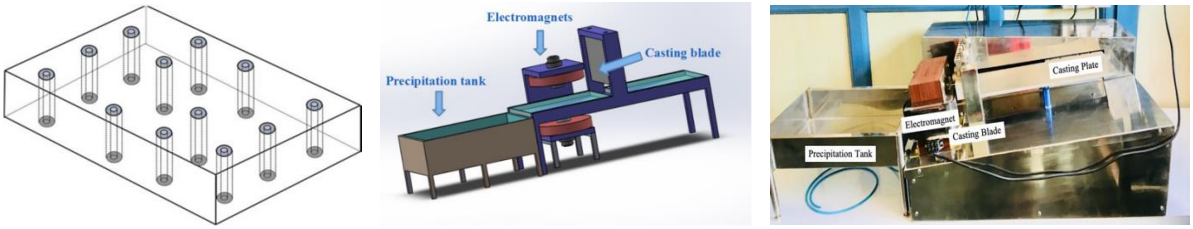
1. Introduction

The alignment of carbon nanotubes (CNTs) in nanocomposites is of interest for optimizing the properties of technologically useful materials, e.g., reinforced composites, electronic components and optical materials [1]. Several different methods have been used for aligning CNTs and they have their merits and demerits [2]. This paper reports a new method of aligning CNTs in the nanocomposite films. It involves mixing of CNTs and magnetic nanoparticles to the polymer solution and casting the polymer film/ membrane in presence of magnetic field. Magnetic forces align spins of the magnetic particles along the direction of magnetic field, and their alignment in turn, causes alignment of CNTs. The importance of this method emerges from the fact that it involves aligning of hollow tubes using moderate magnetic fields. The above method has been used to synthesize Polysulfone (PSf) – Multiwall Carbon Tubes (MWCNT) nanocomposite films/ membranes with nanotubes aligned in a direction perpendicular to the film surface (Figure 1A) [3]. The water permeability and dielectric studies shows that the degree of alignment of MWCNTs is higher for the films casted in presence of magnetic field as compared to those casted in absence of magnetic field.

2. Experimental

2.1 Membrane Casting Machine

Membranes are porous polymeric films, and are routinely used for water treatment [4]. Usually they are synthesized by "Phase inversion" method, which involves casting of a thin film of suitable polymer solution and submerging it in water [5]. This viscous liquid film precipitates in form of a thin polymer sheet on submerging in water, and it is referred to as membrane. A bench-top membrane casting machine (Size 90 cm x 40 cm x 30 cm) has been indigenously designed and fabricated [6, 7]. Figures 1B. and 1C. are schematic representation and the photograph of the casting machine respectively. The machine consists of a casting plate, a casting blade, an electromagnet, and a water tank. The synthesis of membrane involves pouring of polymer solution on the casting plate, allowing the plate to pass underneath a casting blade and then between two magnetic poles and finally submerging the plate in water tank. The machine allows casting of about 100 mm x 100 mm polymer film in presence of a magnetic field, which can be varied in the range of 0 – 1600 Gauss. The thickness of the polymer film can be controlled in range of 50 µm to 500 µm with an accuracy of ± 10 µm. The operation of the machine has been automated.



(A) **(B)** **(C)**

FIGURE 1A. Artistic view of the carbon nanotubes-based nanocomposite membrane [3], **FIGURE 1B.** Schematic drawing of a membrane casting machine and **FIGURE 1C.** Photograph of indigenously developed Bench-top Membrane Casting Machine that allows casting of membrane in the presence of magnetic field.

2.2 Synthesis and characterization of Polysulfone-MWCNTs Nanocomposite Membranes

Polysulfone (PSf) membranes with and without MWCNTs were synthesized using above machine [7]. The dope (Pure PSf) was prepared by dissolving 25 gm of PSf beads and 7.5 gm of polyvinyl pyrrolidone (PVP) in 87.5 ml of N methyl - 2 - pyrrolidone (NMP) and agitating the solution vigorously for 2 days. In case of PSf/ MWCNTs membranes, 0.1 gm of MWCNTs and 1.0 gm of Fe_3O_4 nanoparticles were added to the above solution and the solution was sonicated for 15 minutes to disperse carbon nanotubes in the solution. MWCNTs (Outer Diameter ~ 6 – 13 nm, length ~ 2.5 – 20 µm) were procured from M/s. United Nanotech Innovations Pvt. Ltd. India and Fe_3O_4 nanoparticles (Size ~ 12 nm) were synthesized in our laboratory. Control PSf membrane and four PSf/ MWCNT membranes corresponding to four different magnetic fields (0, 1000G, 1200 G and 1500G) were casted. The time of exposure to magnetic field was 5 seconds for all the above PSf/ MWCNT membranes. An additional PSf / MWCNT membrane was casted under 1500 G field with an exposure time of 10 seconds. The thickness of all the membranes was about 100 µm. The above membranes were characterized with regards to alignment of MWCNTs, by carrying out water permeability using an indigenously developed membrane testing skid [8] and dielectric studies using an impedance analyser (NoVo control Alpha AT) at UGC DAE CSR, Mumbai [9].

3. Result and Discussion

Results of water permeation studies for the six membranes are tabulated in Table-1. The permeated water flux for control PSf membrane was F = 96 L M^{-2} H^{-1} [9] and that for PSf/ MWCNT-1 (sample 2) 145 L M^{-2} H^{-1}. The fact that PSf/ MWCNT-1 was casted without exposure to magnetic field, it is reasonable to believe that MWCNTs are aligned randomly in the membrane.

Table 1. Water permeability of the Polysulfone-MWCNT Nanocomposite Membranes

Sample No.	Membrane	Evaporation time (Sec.)	Magnetic field (Gauss)	Average permeated water flux water ($LM^{-2}H^{-1}$)
1.	Pure PSf	5 Sec	No field	96
2.	PSf / MWCNT – 1	5 Sec	No field	145
3.	PSf / MWCNT – 2	5 Sec	1000 G	145
4.	PSf / MWCNT – 3	5 Sec	1200 G	341
5.	PSf / MWCNT – 4	5 Sec	1500 G	577
6.	PSf / MWCNT – 5	10 Sec	1500 G	820

The increase in water permeability in going from control PSf membrane to PSf/ MWCNT-1 membrane is connected with the fact that MWCNTs provide additional pathways to water-flow in PSf/ MWCNT-1, over and above the paths provided by the pores in the conventional PSf membrane. The most important result in Table 1. is that permeated water flux for PSf/ MWCNT membranes (samples 3, 4, 5 and 6) casted in presence of magnetic field are higher than that for the membrane (sample 2) casted in absence of magnetic field. It is seen that higher is the field, higher is the permeated flux. The value of F increases from 145 L M^{-2} H^{-1} to 577 L M^{-2} H^{-1}, when the magnetic field is increased from 0 to 1500 Gauss. It suggests that nanotubes align in magnetic field and the degree of alignment increases with increase in magnetic field. It is noted that degree of alignment or permeated water flux did not saturate at H = 1500 G. It was seen that the degree of alignment of nanotubes can be improved by exposing the film to magnetic field for a longer time. Independent of above, it is seen (Samples 5-6) that permeated

water flux increases from 577 L M^{-2} H^{-1} to 820 L M^{-2} H^{-1} when evaporation-time τ is increased from 5 sec to 10 sec for a fixed magnetic field of 1500 Gauss. Thus, the degree of alignment of MWCNTs can be improved by exposing the film to magnetic field for a longer time. It is interesting to note that permeability of PSf membrane can be increased by a factor of about 10 by adding ~0.1% of MWCNTs to the PSf and by suitably aligning the nanotubes. Figure 2 shows the variation of real part of dielectric constant (ε`) with frequency for control PSf membrane, PSf/ MWCNT -1 membrane and PSf/ MWCNT - 5 membrane (Samples 1, 2 and 5). It may be mentioned that for present discussions the data for frequencies > 1000 Hz are relevant, as the sharp increase in permittivity at low frequencies is superius and arises due to the electrode polarization effects. It is seen that at high frequencies, ε` shows negligible change in going from Sample - 1 to Sample - 2. This is related to the fact that, both, PSf and PSf/ MWCNT-1 membranes are isotropic. The increase in dielectric constant in going from Sample - 2 to Sample – 5 is related to the fact that unlike that in PSf/ MWCNT-1, nanotubes are aligned in PSf/ MWCNT-5 [10]. That is, dielectric studies also show that MWCNTs are aligned in the membranes casted in presence of magnetic field.

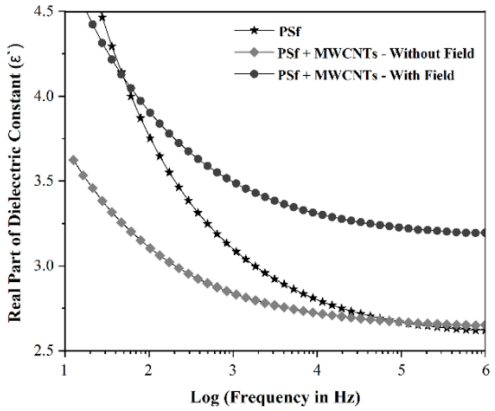


FIGURE 2. Variation of real part of dielectric constant (ε`) vs frequency for PSf/ MWCNT membranes.

4. Conclusion

A new method of aligning CNTs embedded in polymer films has been developed. A membrane casting machine, where one can cast membranes in presence of magnetic field has been designed and fabricated indigenously. Polysulfone – MWCNT nanocomposite membranes under varying magnetic fields have been synthesized. The membranes casted in presence of magnetic field showed higher water permeability as compared to those casted in absence of magnetic field. It is seen that water permeability of PSf membrane can be increased by a factor of about 10 by adding ~ 0.1% of MWCNTs to the PSf and by suitably aligning the nanotubes.

Acknowledgement

We thank Soumitra Kar for his invaluable advice and useful suggestions in designing the membrane casting machine. We acknowledge Divya Padmanabhan and Abhishek Narse's help in designing the electromagnet and Biswajit Panda`s help in synthesis of magnetic nanoparticles. The financial support from BRNS (Grant no.: 37(2)/14/04/2015-BRNS) is acknowledged.

References

1. Y. Lan, Y. Wang and Z. F. Ren, Advances in Physics, Vol. 60, pp. 553-678 (2011).
2. K. Lakoubovskii, Central European Journal of Physics, Vol. 7(4), pp. 645-653 (2009).
3. B. J. Hinds, N. Chopra, T. Rantell, R. Andrews, V. Gavalas and L. G. Bachas, Science, Vol. 303, pp. 62-65 (2004).
4. R. W. Baker, Overview of membrane science and technology in Membrane Technology and Applications, 2nd ed., West Sussex: John Wiley & Sons, 2004, pp. 1-7.
5. P. van de Witte, P. J. Dijkstra, J. W. A. van den Berg, and J. Feijen, Journal of Membrane Science, Vol. 117, pp. 1-31 (1996).
6. Goyal P S and Hirani B (2020). A method for manufacturing a membrane (Indian Patent No. 560533) The Patent Office, Government of India
7. B. Hirani and P. S. Goyal, Synthesis and water permeation studies of polysulfone based composite membranes having vertically aligned CNTs (2021). https://doi.org/10.48550/arXiv.2105.10473
8. B. Hirani, P. S. Goyal, S. Kar and R. C. Bindal, (2017). International Conference on Environment Management and Sustainability, January 6-7, 2017, Nerul, Navi Mumbai, India, Published by: SIES- Indian Institute of Environment Management, 2017.
9. B. Hirani, P. S. Goyal, D. Shrivastava and S. K. Deshpande, Dielectric properties of Polysulfone carbon nanotube composite membranes (2022). https://doi.org/10.48550/arXiv.2201.04957
10. H. Ravishankar, J. Christy and V. Jegatheesan, *Membranes*, Vol. *8*(3), pp. 77-89 (2018).
11. A. Sharma, B. Tripathi and Y. K. Vijay, Journal of Membrane Science, Vol. 361, pp. 89-95 (2010).

Fabrication and Application of P(VDF-TrFE) Copolymer Films for X-ray Detection in Synchrotron Radiation Sources.

S.R. Kane[1, a], S. Satapathy[2, 3], Ajit Kumar Singh[1], P.K.Jha[4], P.K.Mehta[4]

1. Accelerator Physics and Synchrotrons Utilization Division, Raja Ramanna Centre for Advanced Technology, Indore 452013, India.

2. Homi Bhabha National Institute, BARC Training School Complex, Anushaktinagar, Mumbai 400 094, India

3. Laser Biomedical Applications Division, Raja Ramanna Centre for Advanced Technology, Indore 452013, India

4. Department of Physics, The M S University of Baroda, Vadodara -390002, India

Keywords: Pyroelectric, Synchrotron radiation, PVDF, P(VDF-TrFE), X-ray, Detector

Corresponding author: rksanjiv@rrcat.gov.in

Abstract: This paper explores the use of P(VDF-TrFE) thin films for detecting X-rays produced by a synchrotron radiation source. Upon exposure to X-rays, pyroelectric materials exhibit localized heating, resulting in a voltage signal proportional to the temperature change. Enhancing the properties of PVDF with relaxor ferroelectrics like TrFE improves the piezoelectric coefficients and material efficiency. These co-polymer films were prepared using solution casting and characterized through X-ray diffraction (XRD) and polarization-electric field (P-E) loop tracer. XRD measurement carried out at Indus-2, confirmed the presence of β-phase, essential for piezoelectric applications. These films showed decreased voltage responsivity with increasing chopping frequency, in the line with other thermally thick IR detectors. This study highlights the potential of pyroelectric detectors for high-intensity synchrotron environments, for addressing the saturation challenges faced by traditional detectors.

INTRODUCTION

A pyroelectric material, either in crystal form or as thin film form, is a good thermal transducer which is based on its pyroelectric effect. When a pyroelectric detector is exposed to radiation, it absorbs the radiation, causing its temperature to rise. This rise in temperature changes the spontaneous polarization with respect to time , and thus, a photocurrent is generated [1, 2]. Poly(vinylidene fluoride) (PVDF) film has excellent piezoelectric and pyroelectric properties, but it exhibit relatively low piezoelectric coefficient compared to inorganic or single crystals [3]. To enhance the piezoelectric coefficient, relaxor ferroelectrics like TrFE, HEP, and CTFE, are added to PVDF. This enhances its dielectric and piezoelectric properties by stabilizing the ferroelectric phase and reducing the coercive field. These additives broaden the temperature range of phase transitions and improve flexibility and process ability, thereby making the material more efficient and versatile for applications in sensors, actuators, and flexible electronics.

Pyroelectric sensors operate as thermal transducers by converting the incident radiation into a measurable quantity like charge, voltage, or current as an output, similar to other radiation detectors. Pyroelectric detectors have faster response among thermal detectors but are limited to a specific temperature range. Most studies have explored the response of pyroelectric materials in the form of crystals [4, 5] or thin films [6, 7]for infrared radiation.

In this paper, we describe the fabrication process of P(VDF-TrFE) thin films and their characterization using polarization-electric field (P-E) testing and X-ray diffraction (XRD) analysis. The suitability of these films as X-ray detectors was evaluated using the synchrotron radiation facility at Indus-2.

EXPERIMENTAL DETAILS

Martin et al. [8]. have discussed various effective methods and processing techniques such as mechanical stretching of the α-phase, melting under high pressure, application of an external electric field, ultra-fast cooling, and solution casting for synthesizing the β-phase of P (VDF-TrFE). In this work, we used solution casting with a doctor blade to prepare the films. A P(VDF-TrFE) (70:30) solution in N,N-dimethylformamide (DMF) was stirred

at 70°C for 2 hours, and then heated to 140°C for complete dissolution and homogenization. The resulting films, 30-100 µm thick, were tape cast at room temperature and dried for 24 hours before being peeled off for further studies. The β-phase, identified using XRD analysis, exhibits piezoelectricity due to its dipolar conformation, making it suitable for sensors applications. XRD analysis confirmed β-phase with peaks at $2\theta = 20^{\circ}$, corresponding to the 110 and 200 reflections. [9] Other peaks with smaller intensity are also present at different angles (35.1^0 and $40.8^{0)}$ because of the crystallinity and phase composition. The peak at $2\theta=18^0$ is from α phase but its contribution is very less.

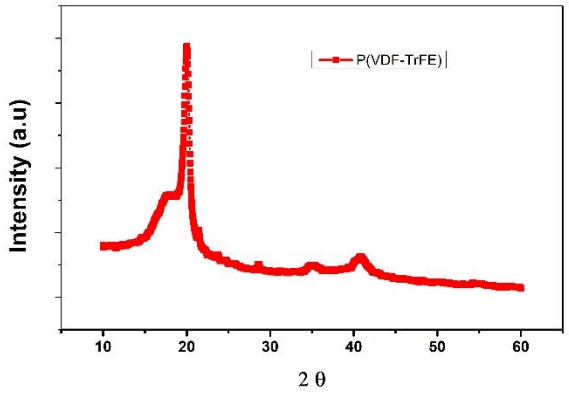


Fig. 1 XRD Pattern of P(VDF-TrFE) film

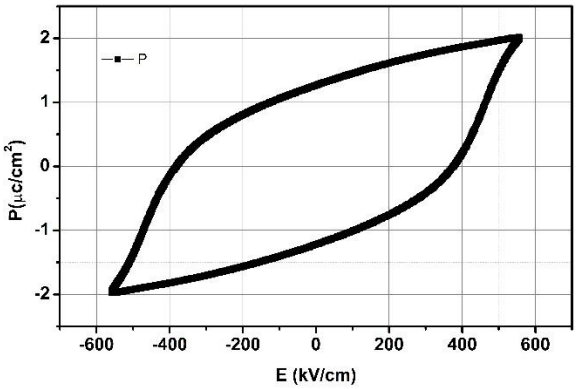


Fig.2 PE loop of 50-micron P(VDF-TrFE) film

The polarization-electric field (P-E) loop is crucial for evaluating the ferroelectric properties of PVDF-TrFE films. It reveals key characteristics such as remnant polarization (P_r), coercive field (E_r), and energy dissipation, which are essential for applications in sensors, actuators, and non-volatile memory devices. For sensor application High P_r and low E_c are desirable for sensitive and efficient sensors. Figure 2 shows the P-E loop for the 50-micron thick film. From this figure, it is clear that the P-E loop with nonzero remnant polarization indicates favorable ferroelectric properties.

In this paper, we investigate the response of the pyroelectric composite films with various thicknesses ranging from 30 to 100 microns in the hard X-ray region. The basic structure of a single-element pyroelectric radiation sensor, shown in Figure 3, includes a thin pyroelectric chip with silver electrodes on both sides. These 100-micron-thick electrodes, formed with silver conducting paste, absorb radiation, while the chip's exposed side faces synchrotron radiation and the opposite side is attached to a 1mm thick oxygen-free copper plate acting as a heat sink and it is grounded. When a pyroelectric material or its conducting coating absorbs X-rays, it experiences localized heating, which generates a voltage signal due to the change in temperature with respect to time. This voltage signal can be used to detect the presence of X-rays and to determine the incident X-ray energy. In our experiment, we utilized the Indus-2 [10]synchrotron X-ray radiation source to measure the voltage response of pyroelectric detectors. All measurements were conducted at the Microprobe X-ray fluorescence beamline (µ-XRF) beamline (BL-16) at the Indus-2 synchrotron radiation facility. The optics of the beamline comprises of a Double-Crystal Monochromator (DCM) with Si (111) symmetric and asymmetric crystals and a pair of Kirkpatrick–Baez focusing mirrors. The beamline operates in the energy range of 5 keV to 25 keV [11]. Our findings highlight the potential of pyroelectric detectors in high-intensity synchrotron environments.

We have examined the voltage response of P(VDF-TrFE) films of varying thickness to a constant X-ray power of 0.5 µW, with chopping frequencies from 2 Hz to 70 Hz. The minimum and maximum voltage signal level is given in table-1.

Table 1: "Voltage response of P(VDF-TrFE) films of different thicknesses."

Sample Thickness	Minimum Voltage level (mV)	Maximum Voltage level(mV)
30 µm	0.41	9.29
50 µm	0.38	8.25
70 µm	0.26	6.26
100 µm	0.17	4.78

The results shown in figure 4 indicate that that the voltage response of P(VDF-TrFE) films decreases with increasing film thickness due to reduced thermal diffusion efficiency and higher thermal mass, thereby reducing the temperature gradient and subsequent pyroelectric voltage generation.

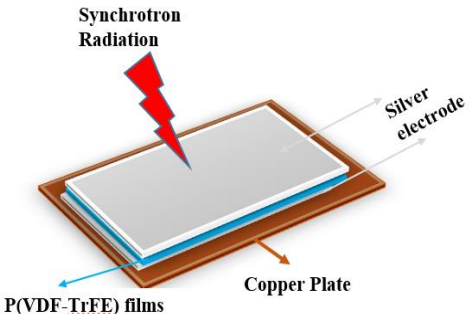


Fig. 3: The structure of a Pyroelectric Detector

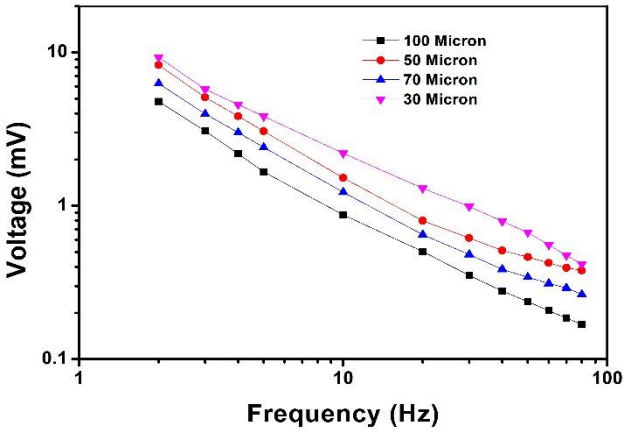


Fig. 4 : Voltage response of P(VDF-TrFE)

CONCLUSION

In this study, we evaluated the voltage response of P(VDF-TrFE) films of different thickness ranging from 30 to 100 microns to X-rays generated from synchrotron radiation. Notably, the voltage responsivity decreased with increasing chopping frequency, consistent with the behavior observed in thermally thick detectors used for infrared applications. This finding underscores the potential of pyroelectric detectors, beyond their extensive use in infrared detection and energy harvesting, as efficient X-ray detectors. These detectors can be particularly effective in the high-intensity environments of synchrotron facilities, where conventional detectors often face issues due to saturation.

ACKNOWLEDGMENTS

The authors acknowledge the assistance of Dr. Pooja Gupta, Ms. Sampa Sutradhar and Mr. Sawan Kumar Bhakar in conducting the experiment and analyzing the data. They also express their gratitude for the kind support and guidance provided by Dr. S.V. Nakhe, Director of RRCAT, in this work.

REFERENCES

1. A. Rogalski, Infrared detectors, II ed., CRC Press, 2011, pp. 138-153.
2. S. B. Lang, "Pyroelectricity: A 2300-year history," Ferroelectrics, vol. 7, 231–34 (1974).
3. X. Zhang, W. Xia, J. Liu, "PVDF based and its Copolymer Based Piezoelectric Composites: Preparation Methods and Applications," J. Electron. Mater., vol. 51,5528–5549 (2022).
4. R. W. Whatmore, "Pyroelectric ceramics and devices for thermal infra-red detection and imaging," Ferroelectrics, vol. 118, 241—259 (1991).
5. S. Liu and D. Long, "Pyroelectric detectors and materials," Proc. IEEE, vol. 66,14-16 (1978).
6. Z. Liang, S. Li, Z. Liu, “High responsivity of pyroelectric infrared detector based on ultra-thin (10μm) LiTaO3," J. Materia. Sci.: Mater. in Electro., vol. 26,5400-5404 (2015).
7. M.-H. Lee, H. R. Hwang, "Effect of buffer layer on the voltage responsivity of the pyroelectric thermal sensors prepared with PZT ceramics," SPIE Proceedings, vol. 3061,170-178 (1997).
8. M. Pedro Libânio, S. Lanceros-Mendez, "Electroactive phases of poly (vinylidene fluoride): Determination, processing and applications," Prog. Polym. Sci., vol. 39, 683-706 (2014).
9. M. Kim, S. Lee, "Solvent-controlled crystalline beta-phase formation in electro spun P(VDF-TrFE) fibers for enhanced piezoelectric energy harvesting," APL Materials, vol. 8, 071109 (2020).
10. S. K. Deb, G. Singh and P. D. Gupta, "Indus-2 Synchrotron Radiation Source: current status and utilization," J. Phys.: Conference Series, vol. 4254, 072009 (2013).
11. M. K. Tiwari, P. Gupta, A. K. Sinha, S. R. Kane, A. K. Singh, S. R. Garg, C. K. Garg, G. S. Lodha and S. K. Deb, "A microfocus X-ray fluorescence beamline at Indus-2 synchrotron radiation facility," J. Synchrotron Radiat, vol. 20, 386-389 (2013).

Development of Nanocomposite Films having Low Dielectric Constant for Microelectronics Applications

Deepali Shrivastava[*1], P S Goyal[2], S K Deshpande[3]

[1] Department of Chemistry, Pillai College of Engineering, New Panvel - 410206
[2] Department of Electronics, Pillai College of Engineering, New Panvel - 410206
[3] UGC-DAE Consortium for Scientific Research, Mumbai Centre, BARC, Mumbai- 400085
*Corresponding author deepali@mes.ac.in

Abstract. High performing polyimide films are finding increased use for packaging in semiconductor industry. Pure polyimide (PI) films, which are otherwise ideally suited for the above purpose, have high dielectric constant of $\kappa = 3.4$. It is of interest to prepare polyimide films having low dielectric constant (say $\kappa \leq 2.5$) and low levels of water absorption. We have synthesized polyimide /silicic acid (SA) and polyimide/ polyethylene glycol (PEG) nanocomposite films and it was observed that dielectric constant of nanocomposites is much lower than that of pure polyimide. Results of FTIR, dielectric and water uptake studies on above nanocomposite films are reported. It was seen that the dielectric constant for PI-PEG films was 1.17 and 1.29 for additive concentrations of 1% and 5% respectively.

Key Words- Polyimide, Silicic acid, Polyethylene glycol Dielectric constant, Nanocomposite.

INTRODUCTION

The materials having low dielectric constant (say $\kappa \leq 2.5$) are of special interest for fabrication and smooth functioning of microelectronic devices, especially when one reduces the sizes of the devices [1, 2]. In addition to low dielectric constant (κ), it is important that the above materials are mechanically strong and they have good adhesion to metals. Several materials have been explored for the low-k application [3, 4]. Polyimides (PIs) are among the most promising candidates for their use in microelectronic devices as they satisfy above requirements of strength and adhesion [5]. However, dielectric constant of normal PI is about 3.4 and it is not suitable for microelectronic applications [6]. Fluorinated PIs are having dielectric constant (κ) of about 2.4, are better, but cannot be used as they give out fluorine vapors at high temperatures [7]. This paper deals with synthesis and characterization of polyimide /silicic acid and polyimide / polyethylene glycol nanocomposite films. The nanocomposite films are prepared by blending polyimide precursor Polyamic Acid (PAA) with Silicic Acid (SA) and Polyethylene Glycol (PEG) and then imidizing the blend by thermal curing. It is seen that dielectric constant of polyimide decreases on addition of Silicic acid or PEG to PI films.

EXPERIMENTAL SECTION

Materials and Synthesis of nanocomposite polyimide films having Silicic and PEG as modifiers

The Polyamic acid (PAA) solution in NMP (N-methyl -2- Pyrrolidone), having Product No. 575828-1L was purchased from Sigma Aldrich. Polyethylene Glycol (PEG) 99% pure, Mol. Weight. 4000 was also bought from Sigma Aldrich. Silicic acid 99% pure was bought from Lancaster, All chemicals were used as supplied. The dope for the nanocomposites were prepared by blending polyimide precursor PAA with silicic acid or polyethylene glycol as modifiers. The blends were mixed and stirred for half an hour using a magnetic stirrer. The above blends were then casted on glass substrate and subjected to suitable "time-temperature curing profile" for conversion of PAA into polyimide [8]. It involved curing the samples for one hour at each of the successive temperatures of 70 °C 100° C, 150° C, 200° C, 250° C and 300° C. Finally the films were kept at 350° C for 2hrs. In addition to pure PI films, PI-Silicic and PI-PEG films were prepared for additive concentrations of 1% and 5%. The samples were designated as PI, PI-Silicic-1, PI-Silicic-5, PI-PEG-1 and PI-PEG-5 respectively. The thicknesses of the films were approximately 50µm as measured using optical interference-based methods**.**

Characterization

It is important to find out if PAA has got imidized by thermal curing or not. This was examined by carrying out Infra-red absorption studies. Measurements were made on all nanocomposite films in the range of 450 cm^{-1} to

4000 cm $^{-1}$ using 3000 Hyperion Microscope having Vertex 80 FTIR System (Bruker, Germany) at SAIF, IIT Bombay.

The second important parameter for characterization is the dielectric constant of the nanocomposite films. The real part of dielectric constants *(ε')* of PI, PI-Silicic and PI-PEG were measured in frequency range of 100Hz to 5MHz using an impedance analyzer (Novo control model Alpha AT), with the nanocomposite films sandwiched between gold plated electrodes in a parallel plate capacitor configuration.

The water absorption behavior is another parameter that decides the suitability of the films for microelectronics applications. Water absorption tests were performed on above nanocomposites as per ASTM D570 guidelines. The test sample (3 X 3 cm) was first kept at 110^{o} C for 2 hours so as to evaporate water etc. if any. The sample was then kept in double distilled methanol for 48 hours at 23^{o} C so that pores in the sample get filled with methanol. The weight of sample containing methanol was designated as W. This sample was dried of methanol by keeping the sample at 110^{o} C for 2 hours and weighed again. This weight of dry sample having empty pores, was referred to as W_D. Finally, the samples were immersed in double distilled water. Weight of these wet samples were taken at regular intervals until equilibrium condition was reached. This weight of wet sample having water filled pores was referred as W_W. These data were used to compute the percentage water absorption.

RESULTS AND DISCUSSIONS

Figure 1 shows the FTIR absorption spectra for Pure PI, PI-Silicic-1 and PI-PEG-5. The peaks at 1776 cm $^{-1}$ and 1376 cm $^{-1}$ for Pure PI are characteristic peaks of an imide ring and correspond to asymmetric stretching vibration of carbonyl (C=O) and stretching vibration of C-N of imide ring respectively [4, 8, 9] .The 1650cm $^{-1}$ peak corresponding to precursor PAA is absent suggesting that PAA has been fully imidized [4]. The presence of 1776 cm $^{-1}$ and 1376 cm $^{-1}$ for peaks for PI-Silicic-1 and PI-PEG-5 indicate that PAA is converted to polyimide even in presence of Silicic or PEG modifier. It is noted that 1376 cm $^{-1}$ peaks for PE-PEG-5 is much broader as compared to that for other samples. We believe this is connected with absorption of water by the PI-PEG samples [10]. It seems the water absorption in PI-PEG is more as compared to that for pure PI or PI-Silicic samples.

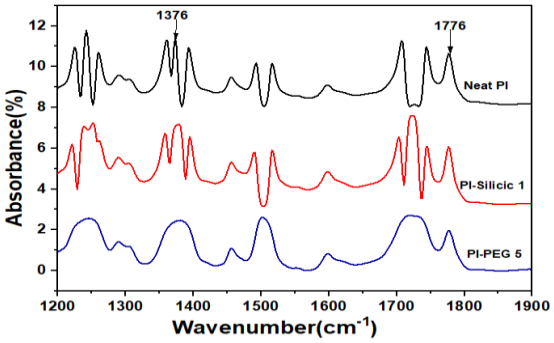


FIGURE1. IR absorption spectra for (a) Neat PI, (b) PI-PEG 5 (c) PI-Silicic 1

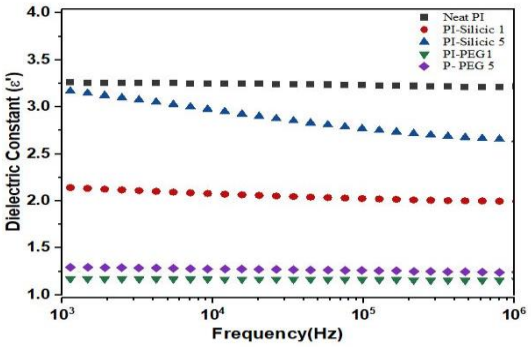


FIGURE 2. Real part of for dielectric constant (ε') as a function of frequency for different concentrations of additives

It was observed that dielectric constant (ε') was quite large at low frequencies because of electrode polarization effects, arising due to charge accumulation at the interface between the electrodes and the sample. This effect diminishes at frequencies ≥1000Hz since the charges are unable to respond to these frequencies. In view of above, data are plotted from 1000Hz to 1 MHz in Fig 2. The measured values of ε' are in very good agreement with the literature. The reported literature data for dielectric constant of solid neat polyimide is 3.26 at 1 KHz [11]. Our value of ε' at 10 KHz is 3.26. It is seen that there is significant decrease in real part of dielectric constant (ε') for polyimide films having Silicic or PEG clusters in the polyimide matrix, especially, for additive concentration of 1%. The values of ε' for PI-PEG 1 and PI-PEG 5 are 1.17 and 1.29 respectively. It is believed that decomposition of flexible chain of oligomer PEG leave micro porous structures in the matrix and that reduces the dielectric constant. It is known that PEG decomposes at 175^{0}C [12]. The observed values of ε' = 2.14 for PI-Silicic 1, is again lower than those for neat polyimide i.e. 3.26 at 1 KHz. The dielectric behavior of PI-Silicic 5 is somewhat erratic. There is large variation in ε' with frequency, which is not the case with other samples. We believe this erratic behavior of PI-Silicic5 is connected with large water uptake by the sample.

The water absorption studies were carried out all samples, namely, films of PI, PI-Silicic and PI-PEG. For each system, measurements were repeated on 5 independent samples and the results reported in Table 1 are the average

values. It is noted that except PI-Silicic 5, water absorption behavior of all other samples are similar. The above results are in agreement with literature. Ding and co-workers had reported water absorption values Polyimide to be 3.54% [13]. Which is not very different from our value of 2.26%. It is interesting that water uptake by PI-Silicic 1 is quite low.

TABLE 1 Water Uptake by Polyimide films with and without additives

Sample	Neat PI	PI-Silicic1	PI-Silicic 5	PI- PEG1	PI-PEG 5
% age Water Uptake	2.26	1.56	5.88	2.98	3.12

CONCLUSION

The films of Polyimide/ Silicic Acid and Polyimide/ Polyethylene Glycol nanocomposites have been synthesized. It is shown that dielectric constant of polyimide films can be decreased by adding SA or PEG to PI films. The measured values of ε' for PI, PI-Silicic 1, PI-Silicic 5, PI-PEG 1 and PE-PEG 5 nanocomposites at a frequency of about 10^6 Hz are 3.21, 2.00, 2.65, 1.15 and 1.24 respectively. That is, as compared to Silicic acid, Polyethylene Glycol is much more effective in reducing the dielectric constant of Polyimide. PI-Silicic 5 nanocomposite showed abnormally high water absorption. The reasons for this are not clear. It is noted that, both, the dielectric constant and water absorption are low for PI-PEG nanocomposites and hence they are better choice for microelectronic applications.

ACKNOWLEDGEMENTS

We thank Priam V Pillai and Sandeep M Joshi for useful discussions and encouragement. One of us (DS) would like to thank Department Science and Technology, Government of India for financial assistance under project SR/WOS-A/CS-127/2017

REFERENCES

1. D. Shamiryan, T. Abell, F. Iacopi, and K. Maex, Mater. Today, Vol. 7, pp. 34–39 (2004).
2. R. M. Wallace, Dielectric Materials for Microelectronics, Springer International Publishing, 2017.
3. P. S. Alegaonkar, V. N. Bhoraskara, P. Balaya, and P. S. Goyal, Appl. Phys. Lett., Vol. 80, pp. 28 (2002).
4. C. Huang, J. Li, G. Xie, F. Han, D. Huang, F. Zhang, B. Zhang, G. Zhang, R. Sun, and C.-P. Wong, Macromol. Mater. Eng., Vol. 304, pp. 1900505 (2019).
5. J. A. Kreuz and J. R. Edman, Adv. Mater., Vol. 10, pp. 1229 (1998).
6. A. Zulkifli, "Polymeric Dielectric Materials," in Polymeric Dielectric Materials, Chapter 1, INTECH Open Source, 2012.
7. B. Xu, R. Feng, T. Zhao, L. Zhou, Y. Ju, J. Chen, Q. Zhang, L. Dong, and Feng, Eur. Polym. J., Vol. 202, pp. 112627 (2024).
8. J. Zhang, B.-K. Zhu, H.-J. Chu, and Y.-Y. Xu, J. Appl. Polym. Sci., Vol. 97, pp. 20 (2005).
9. C. A. Pryde, J. Polym. Sci., Part A, Vol. 27, pp. 711 (1989).
10. P. Lv, Z. Dong, X. Dai, Y. Zhao, and X. Qiu, RSC Adv., Vol. 7, pp. 4848 (2017).
11. S. Ando, K. Sekiguchi, M. Mizoroki, T. Okada, and R. Ishige, Macromol. Chem. Phys., Vol. 219, pp. 1700354 (2018).
12. J. Hedrick, R. DiPietro, Y. Charlier, and R. Jerome, High Perform. Polym., Vol. 7, pp. 133 (1995).
13. Ding M. Polyimides Series in Chemistry; (Science Press 2006), pp 528−530.

First Results of Single Grating Based Multi-contrast X-ray Imaging Technique at Imaging Beamline of Indus-2

Balwant Singh [1, 2, *)], Ashish K. Agrawal[1, 2], Yogesh S. Kashyap[1, 2], Payal Singhai[1] and Mayank Shukla[1, 2]

[1]*Technical Physics Division (TPD), Bhabha Atomic Research Centre, Trombay, Mumbai, 400085, India*
[2]*Homi Bhabha National Institute (HBNI), Anushaktinagar, Mumbai, 400094, India*

[*)] Corresponding author: balwants@rrcat.gov.in; balwantsci@gmail.com

Abstract. We report here the development of a single grating based multi-contrast imaging (SGBI) technique at X-ray imaging beamline of Indus-2 synchrotron source which uses scattering and refraction of the beam as an image signal. This simultaneously generates absorption, dark-field and differential phase contrast images of the sample from a single set of acquired data. Multi-contrast images of the sample provide complementary structural details which are not possible with conventional absorption based techniques. We illustrate here detection of low density and high density features of the sample simultaneously with enhanced contrast. The qualitative and quantitative structural characterization of different samples has also been presented to show the potential of the developed setup.

Keywords: Synchrotron, Grating, Multi-contrast, Dark-field image, Differential phase image

INTRODUCTION

Conventional X-ray imaging techniques based on absorption have been widely used in security scanning, material research, quality control of components from automobile industry and in bio-medical diagnostic imaging since their discovery. But, it offers limited contrast and high dose for soft tissues, advance polymer composites etc. It further fails to exploit the full potential of the synchrotron sources, recent developments in X-ray optics and detector technologies. In view of it, phase contrast X-ray imaging (PCI) techniques, which use beam deflection as an image signal, have been developed such as Propagation Based Imaging (PBI), Diffraction Enhanced Imaging (DEI), Grating Interferometer (GBI) etc.[1]. These techniques differ largely in terms of experimental setup, data collection, analysis methods and sensitivity but provide quantitative measure of wave-front deflection from the samples.Some of them offer multi-contrast X-ray images of the sample from a single set of acquired data. And hence provide the complementary structural details with enhanced contrast at lower dose to the sample, in contrast to conventional methods. This underlying advantage motivated us to develop a single absorption grating based multi-contrast X-ray imaging (SGBI) technique at the Imaging Beamline, Indus-2. We discuss here the basic principle, instrumentation, data acquisition and extraction of the multi-contrast images, qualitative and quantitative analysis of multi-contrast images for different samples.

BASIC PRINCIPLE AND EXPERIMENTAL SETUP

The schematic layout of the SGBI setup is shown in the Fig.1 (a). Grating is used as a standard periodic mask to modulator the incident wave front.The masked beam illuminates the sample and is being recorded by a high resolution detector capable of resolving the grating lines. One has to acquire sample image with grating and grating image only to extract the multi-contrast images of the sample. The spatial harmonic analysis algorithm in Fourier space is used to extract the multi-contrast images from the acquired data [2]. The acquired grating pattern in frequency space contains a number of discrete separated harmonic peaks and the sample with grating image represents convolution of the object and grating spectra in frequency space. Thus, relative change in amplitude and phase of the grating harmonic spectra with and without sample need to be analyzed. The primary harmonic peak is used to retrieve the conventional absorption image. Whereas, the first harmonic is used to extract the dark field image from the relative change in amplitude and relative shift in phase gives the differential phase contrast image of the sample [3].We have used a single absorption grating (period 10 μm), 18 keV and 14 keV beam energy to expose samples, a high resolution microscope detector system integrated with PCO-2000 camera (pixel~7.4 μm) to acquire the experimental images at Imaging Beamline. Detailed description of the beamline is given somewhere else [4].

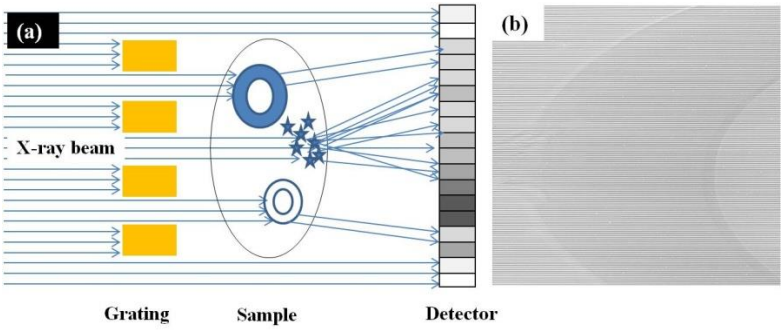


FIGURE 1. (a) Schematic of the SGBI setup at beamline and (b) An acquired sample image with grating.

RESULTS AND DISCUSSION

To demonstrate the technique, we have carried experiment on a standard polypropylene tube of well defined geometry as a phantom and extracted the multi-contrast X-ray images from the acquired data. The acquired tube image with grating is shown in Fig. 1(b) and the extracted multi-contrast images are shown in Fig. 2 (a-c).

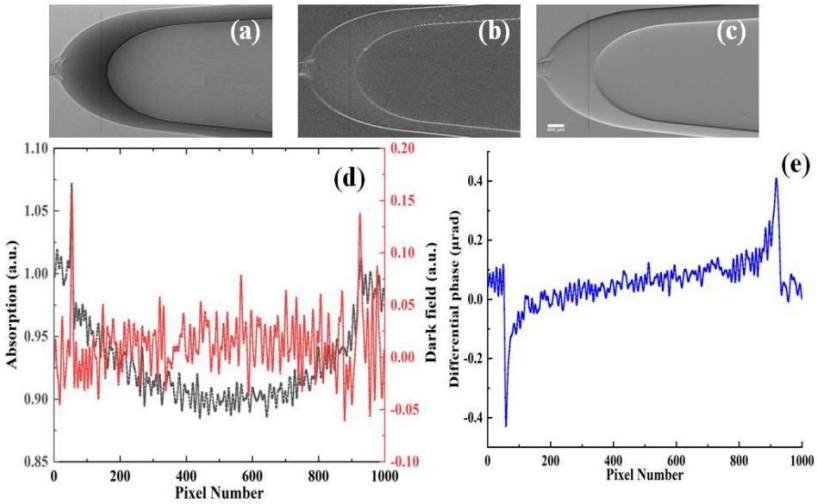


FIGURE 2. Multi-contrast X-ray images of polypropylene tube (a) Absorption, (b) dark field and (c) differential phase contrast image. (d) and (e) shows the line plot across the black line in respective images.

These multi-contrast X-ray images depict the visual difference qualitatively among underlying contrast mechanism. Whereas, the line plot across black line is shown in Fig. 2(d) & (e) illustrate the quantitative absorption, dark field and differential contrast signal for the sample. The differential phase image, relative to conventional absorption image, provides the enhance contrast for fine structures in wall thickness of the tube and strong edge contrast has been produced by the sharp edges in dark field image. These results clearly demonstrate the proof of concept and capability of the single grating based multi-contrast X-ray imaging setup developed at the Imaging beamline (BL-04), Indus-2.

Fig. 3 shows the multi-contrast X-ray images of an electrical wire. The absorption contrast image presents the average details. The dark field image clearly segments the metallic wires whereas the differential phase contrast image provides the strong contrast for the outer and inner polymer sheath and irregularities in the polymer sheath. This result clearly shows the potential benefits of the technique to identify defects in multi-layered structures with wide density (&/ Z variation) variation simultaneously. In nut, it provides complementary details of the specimen for complete and accurate structural characterization of samples. Feather of a bird is imaged as a representative of biological sample, results are shown in Fig.4. The absorption contrast image clearly shows the micro-structures of the feather. The shaft/rachis having central tubular structure, vane/barbs and millions of barbules oriented opposite in the upper and lower barbs are also visible. The strong dark-field signal from region of rachis confirms the porous micro-structure of medulla or in-homogeneity on sub resolution scale. Whereas, the differential phase image provides contrast for the central tubular structure of rachis, cortex around rachis and barbs. It confirms that complex biological systems can also be studied by using SGBI technique [5].

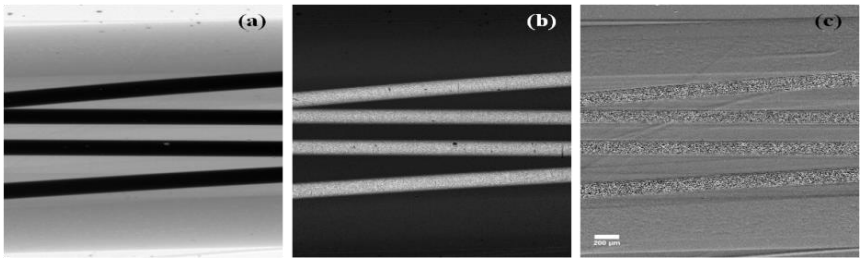


FIGURE 3. X-ray image of an electrical wire showing metallic conducting wire and polymer sheath .(a) Absorption contrast image, (b) Dark field image and (c) Differential phase contrast image.

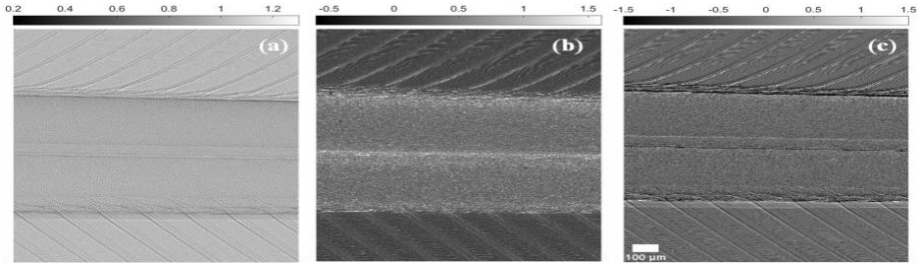


FIGURE 4. (a) Absorption contrast image, (b) Dark field and (c) Differential phase contrast image of a bird feather.

ACKNOWLEDGMENTS

I would like to thank Dr. L. M. Pant (Head TPD, BARC) for his consistent support in research and development activity at the X-ray Imaging Beamline and also I would like to thank scientists from Accelerator Control and Beam Diagnostic Division (AC&BDD) Indus-2, RRCAT to provide the stable beam during the experiment.

REFERENCES

1. Laurene Quenot, Syvain Bohic et.al, *Applied Science* 12, 9539(2022).
2. Eric E. Bennett, Rael Kopace et.al, *Med. Physics* 37, 6047-6054(2010).
3. Matias Kagias, Zhentian Wang et.al, *Physical review Letters* 116,093902 (2016).
4. A. K. Agrawal, B. Singh et.al, *J. Synchrotron Rad* 22, 1531–39(2015).
5. Ryo Hosono, Tomoki Kawabata, et.al, *Optics Express* 26, 21044(2018).

Vertically Aligned Hexagonal $MoSe_2$ Nanoflakes for Supercapacitor Applications

Akshay Tomar, Prachi Gurawal, and Ramesh Chandra*

Nano Science Lab, Institute Instrumentation Centre, Indian Institute of Technology Roorkee, Roorkee, 247667, India

*ramesh.chandra@ic.iitr.ac.in

Abstract. Transition metal diselenides (TMDSs) have been discovered to be great for storing capacities and have a distinct place in supercapacitor research due to their extreme hydrophilicity, honeycomb arrangement, and large surface area. This work used DC-magnetron sputtering to deposit molybdenum diselenide nanoflakes on stainless steel (SS) substrate at room temperature in a regulated vacuum level. The structural, morphological, and compositional analysis of the thin film was performed by XRD, Fe-SEM, and XPS. The TMDSs film of $MoSe_2$ deposited over SS was evaluated as an active electrode material in 1M Na_2SO_4 aqueous electrolyte at varying scan speeds. At a scan speed of 20 mV s^{-1}, $MoSe_2$ nanoflakes resulted in a good specific capacitance of 182.2 F g^{-1}, along with ~97 % capacitive retention even after 5000 cycles.

Keywords: Energy storage, transition metal dichalcogenides, supercapacitors, sputtering, nanoflakes.

Introduction

The rapid increase in energy demand over the past decade, driven by economic growth, population expansion, and urbanization, poses significant challenges, often leading to heightened pollution and greenhouse gas emissions. Fossil fuel dependence in the chemical, transportation, and power industries exacerbates these issues, straining energy systems and worsening air quality. To address these challenges, there is a growing shift towards renewable energy sources, i.e., wind, hydro, and solar power.[1] Although being intermittent, these sources lead to fluctuations between energy production and consumption. Energy storage systems provide an effective solution to grid instability by storing surplus energy generated during low demand and supplying it during high demand, thereby minimizing power outages and enhancing overall energy reliability. Recent advancements focus on improving energy storage technologies through novel materials and synthesis methods that offer precise control over structural and chemical properties. Transition metal dichalcogenides (TMDCs), composed of a transition metal (such as W, Ti, or Mo) positioned between two chalcogen atoms (such as S, Se, or Te), found promising materials for energy applications based on their substantial theoretical capacity, cost-effectiveness, and the natural abundance of their constituent elements. TMDCs have shown potential in energy storage applications, including solar cells, lithium-ion batteries, and hydrogen evolution reactions.[2] Among the various synthesis techniques, the wet chemical method is commonly used for fabricating supercapacitor materials. Alternative methods, such as atomic layer deposition and chemical vapor deposition, offer benefits but often struggle with controlling structure and purity. The sputtering method, however, excels in producing highly crystalline and pure single crystals of TMDs.[3,4] This straightforward and scalable approach avoids the use of extraneous precursors, leading to high-quality materials suitable for advanced energy storage applications.

Experimental Details

Synthesis of $MoSe_2$ thin film electrode

DC magnetron sputtering was used to create $MoSe_2$ thin films, which were deposited on a SS substrate. As the cathode, a 99.9% pure $MoSe_2$ disc was employed to produce a thin coating of $MoSe_2$. The working pressure was kept at 10 mTorr after the sputtering chamber had initially been emptied to a base pressure of 3×10^{-6} Torr. The deposition process was conducted with a target-to-substrate distance maintained at 5 cm, using argon (Ar) gas at a flow rate of 20 SCCM as the sputtering medium. A constant DC power of 75 W was applied, and the thin film was deposited over 5 minutes at a substrate temperature of 200 °C.

Materials characterization

Bruker AXS D8 Advance X-ray diffractometer was used to investigate the phase composition and crystal structure of the $MoSe_2$ thin-film electrode. FE-SEM (Zeiss FE-SEM) was utilized to analyze the morphology of the sample surface. XPS (PHI Versa probe III) was used to show the electronic structure and composition of the elements present in the film. An aqueous solution of 1M Na_2SO_4 was employed as the electrolyte for the electrochemical characterization, which was carried out using an electrochemical workstation (Autolab). As a reference, working and counter electrode, Ag/AgCl, electrode materials, and Pt wire were employed.

Results and discussion

XRD analysis was performed to determine the phase composition of the $MoSe_2$ thin film, as illustrated in Figure 1a. Distinct diffraction peaks were observed at 13.6°, 33.3°, 37.8°, and 57.8° corresponding to the (002), (101), (103), and (008) planes of $MoSe_2$, respectively. These reflections are in good agreement with the 2H-type hexagonal phase of $MoSe_2$ and match the standard data from JCPDS card No. 00-038-1388.

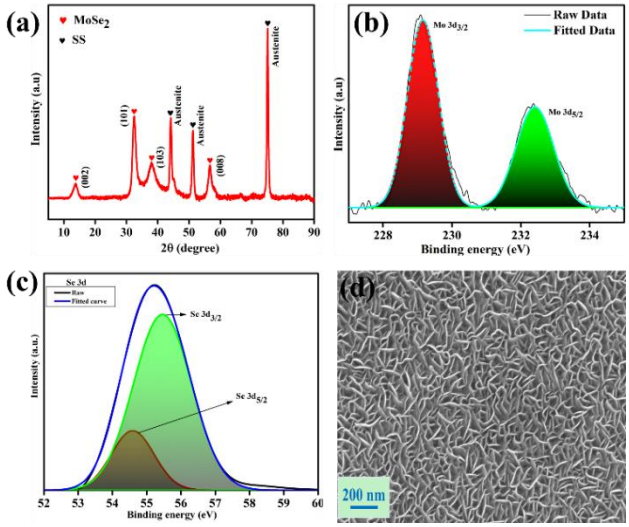


FIGURE 1. Crystallography and elemental analysis of the $MoSe_2$ nanostructures: (a) XRD pattern and XPS high-resolution spectrum of (b) W 4f and (c) Se 3d, (d) nanoflakes type surface morphology obtained from FESEM.

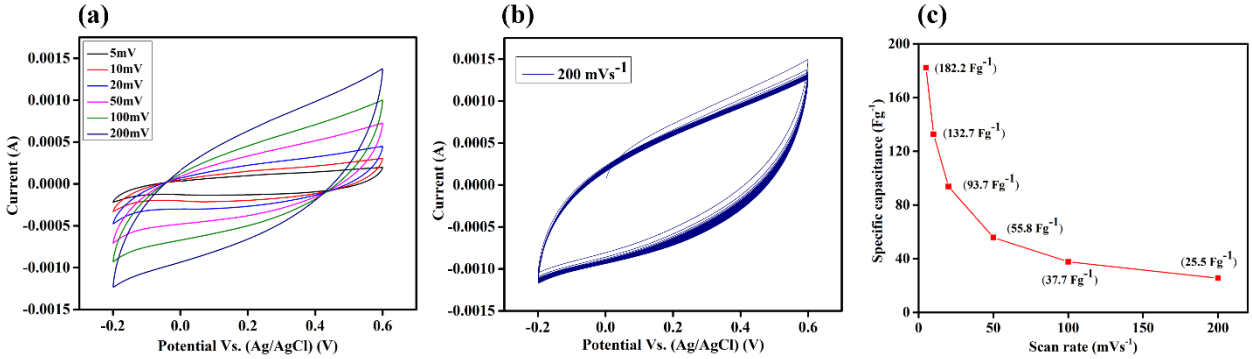


FIGURE 2. Electrochemical performance of $MoSe_2$ nanoflake-based electrode (a) CV curves at various scan speeds, (b) 5000 CV cycles at 200 mVs^{-1}, (c) Calculated specific capacitance by CV curves as a function of scan rate.

Chemical state and surface composition of the fabricated thin films were analyzed using X-ray photoelectron spectroscopy (XPS). The high-resolution XPS (HR-XPS) spectrum of Mo 3d (Figure 1b) displays two different peaks at binding energies of 232.3 and 229.2 eV that correspond to Mo $3d_{3/2}$ and Mo $3d_{5/2}$, respectively. This confirms Mo in the +4-oxidation state, indicating the formation of Mo-Se bonds. In the Se 3d region (Figure 1c), the deconvoluted peaks at 55.4 and 54.7 eV correspond to Se $3d_{3/2}$ and Se $3d_{5/2}$, confirming the -2-oxidation state of selenium. The surface morphology of the deposited $MoSe_2$ thin film, presented in Figure 1d, reveals a uniform

coverage of nanoflakes across the stainless steel (SS) substrate. This nanoflake-like architecture results in a porous structure with a large surface area, which facilitates enhanced interaction between the electrolyte and electrode, providing more active sites for ion transport and charge storage. Such a structural design is beneficial for improving the electrochemical performance of the electrode. Electrochemical measurements were performed in 1 M Na_2SO_4 aqueous electrolyte to evaluate the energy storage capabilities of the $MoSe_2$ thin film electrode, as illustrated in Figure 2. As shown in Figure 2a, CV curves show a quasi-rectangular shape at scan speeds from 5 to 200 mV s^{-1} within a potential window of -0.2 to +0.6 V, indicating capacitive behavior and good reversibility. The long-term electrochemical stability is demonstrated in Figure 2b, showing consistent CV profiles over 5000 cycles at 200 mV s^{-1}. Figure 2c shows the variation of specific capacitance (C_s) and scan rate. As the scan rate increases, a distortion in the CV curve shape is observed, suggesting limited ion diffusion and reduced interaction at higher current densities. At lower scan rates, the integral area under the CV curve increases, indicating higher charge storage. Specifically, the $MoSe_2$ electrode results in a specific capacitance of 182.2 F g^{-1} at 5 mV s^{-1}, which decreases to 25.5 F g^{-1} at 200 mV s^{-1} due to decreased ion accessibility and shorter diffusion time at higher scan rates.

Conclusion

The DC magnetron sputtering technique was used to form the $MoSe_2$ nanoflakes, which have a large surface area and were analyzed as an electrode material. The $MoSe_2$ nanoflakes' compact and smooth surface and equally distributed active material are confirmed by the morphological and surface analyses. The low degree of crystallinity of the $MoSe_2$ nanoflakes electrodes was further revealed by the XRD analysis. In the 1M Na_2SO_4 electrolyte of the $MoSe_2$ nanoflakes, the electrochemical performance is studied, and the working potential windows are well within the 0.8 V range. For the $MoSe_2$ nanoflakes, an excellent specific capacitance of 182.2 Fg^{-1} at 5 mVs^{-1} was measured. Good cyclic stability is maintained by developed electrodes. Our research has confirmed that sputtering is an excellent methodology for the formation of electrodes as well as an important process for supercapacitor applications because of its potential to provide electrode materials with nanostructures, crystalline nature, and more surface area while maintaining stoichiometry on a large scale. As a result, the current study provides a simple and unique method for producing high-performance energy storage devices.

Acknowledgments

The author, Akshay Tomar, would like to thank the IIT Roorkee and the Ministry of Education (MoE) for providing the research fellowship.

References

(1) Choudhary, N.; Singh, S.; Malik, G.; Bhardwaj, S.; Sharma, S.; Tomar, A.; Issar, S.; Chandra, R.; Maji, P. K. Chemically Tuned Cellulose Nanocrystals/Single Wall Carbon Nanosheet Based Electrodes for Hybrid Supercapacitors. *Sustainable Energy Fuels* **2024**. https://doi.org/10.1039/D4SE00286E.

(2) Tomar, A.; Issar, S.; Choudhary, N.; Kodan, S.; Chandra, R. Design of High-Performance Symmetric Supercapacitor Based on WSe_2 Nanoflakes for Energy Storage Applications. *Energy & Fuels* **2024**, *38* (14), 13425–13435. https://doi.org/10.1021/acs.energyfuels.4c02345.

(3) Arora, A.; Chander, P.; Tomar, A.; Kodan, S.; Chandra, R.; Malik, V. K. Investigating the Electrical Transport and Photoresponse Properties of WSe_2 and a Thermally Engineered $SrTiO_3$-Based Heterojunction. *ACS Appl Electron Mater* **2024**, *6* (5), 3186–3196. https://doi.org/10.1021/acsaelm.3c01819.

(4) Singh, S.; Gurawal, P.; Malik, G.; Kaur, D.; Chandra, R. Temperature-Dependent Wetting and Other Physical Characteristics of Sputtered Grown WO_3 Thin Films. *Bulletin of Materials Science* **2024**, *47* (3), 137. https://doi.org/10.1007/s12034-024-03243-y.

(5) Wang, H.; Kong, D.; Johanes, P.; Cha, J. J.; Zheng, G.; Yan, K.; Liu, N.; Cui, Y. $MoSe_2$ and WSe_2 Nanofilms with Vertically Aligned Molecular Layers on Curved and Rough Surfaces. *Nano Lett* **2013**, *13* (7), 3426–3433. https://doi.org/10.1021/nl401944f.

Mathematical Modeling of Vertical Focusing Monochromator

Venkateswara Rao G[1, a)], A.D.Patil[2] and Sameer Bhatt[3]

[1,2,3] Centre for Design and Manufacture, Bhabha Atomic Research Centre, Mumbai-400085

[a)]vgumma@barc.gov.in

Abstract. Vertical neutron Focusing Monochromator (VFM) with focusing range of 1m to ∞ contains 13 No. of single crystal Cu/Ge mirrors, arranged vertically to form a virtually seamless concave reflecting surface to the incoming neutron beam to accurately focus the same to higher intensity on sample to conduct physics experiments. These mirrors independently rotate about backlash free frictionless hinges as modules of different gradients to form concave mirror. These mirrors are actuated by synchronized cams with various gradients mounted on motorized single common shaft. Mathematical model to derive the cam profiles for various gradients, development of relations between common shaft actuation (i/p) and focusing distance (o/p), work space optimization for sensitive working of instrument and augmentation of the range of instrument are presented in this paper.

INTRODUCTION

Vertical neutron Focusing Monochromator (VFM) is used for focusing the neutron beam on sample to carry out neutron beam-based material characterization experiments. It monochromatizes and accurately focuses the neutron beam to higher intensity at specific focusing point where experimental sample is positioned to carryout physics studies. Focusing range of the instrument is 1m to ∞. This instrument contains 13 No. of hinged horizontal single crystal Cu/Ge mirrors arranged vertically in a straight line and are positioned perpendicular to the incoming neutron beam as shown in figure1(a). These mirrors independently rotate about backlash free hinges to form virtual concave mirror surface. The mirror at the center is fixed and other 6 mirrors each above and below the center (symmetric configuration), are rotated with different gradients to focus the neutron beam as shown in figure1(b). To rotate the mirror, follower link with ball tip is mounted on each mirror. The ball tip of the follower link is rested on the profile of cam element. Each mirror is actuated by unique cam and profiles and gradients of each cam depends on location of mirror. Cams are mounted on single common shaft for automated actuation as shown in figure 1(a). Rotation of cams causes rocking of follower levers which in turn rotates all mirrors by different angles, yet with common focusing point. The gradient of cams increases from center mirror to outside mirror. The mirror at 6^{th} position has highest gradient while the mirror at 1^{st} position has the lowest gradient. Positive engagement of the ball tip, to eliminate backlash, is ensured by the stiffness of frictionless hinges of mirror.

The principle of mirror focusing is shown in figure 1(b). It is assumed that the incoming neutron beam reflects in normal direction to the mirror surface that is facing the neutron beam and the normal was taken from the center of mirror for this mathematical model. The divergence of the neutron beam is not considered in this mathematical modeling.

MATHEMATICAL MODEL

The instrument is symmetric about the centerline as shown in figure 1(b). 'R' is the focusing distance in m. 'p' is the uniform vertical mirror pitch in m. 'n' is the position of mirror (0-fixed mirror, 1 to 6 for rotating mirror). 'np' distance between center line and center of n^{th} mirror. 'θ' is the angle between mirror normal with center line at any given instant. '$\theta_{max,n}$' is rotation angle of n^{th} mirror at extreme end of instrument focusing range i.e. at 1m. When θ is zero, the focusing distance will be ∞. θ_{max} will be highest for the mirror at 6^{th} position and lowest for mirror at 1^{st} position. 'l' is distance between hinge center and ball tip axis in m. It is assumed that axis of follower ball intersects and perpendicular to the axis of shaft. 'r' is the radial distance from center of cam to the point of contact of follower ball in m. 'ϕ' is the angle of rotation of common shaft i.e. cam in rad. Cam is mounted on the common shaft through a grub screw. Hence, profile of cam is restricted to 320º (1.78π) of cam circumference only.

From figure 1(b),

$$sin\theta = \frac{np}{\sqrt{R^2+(np)^2}};\ cos\theta = \frac{R}{\sqrt{R^2+(np)^2}};\ \theta_{max,n} = \tan^{-1}(np) \quad (1)$$

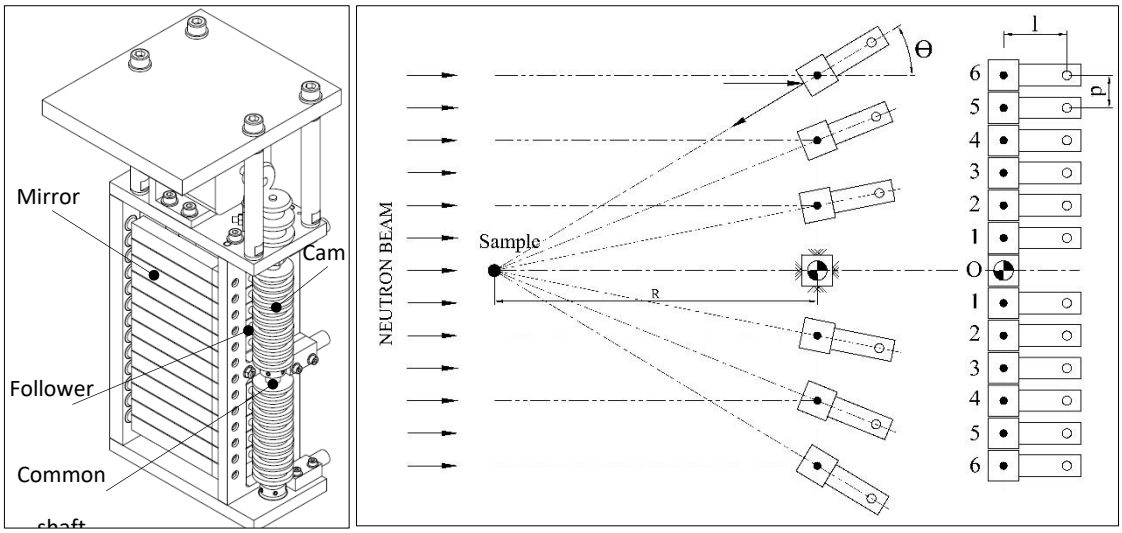


FIGURE 1. (a) 3D model of vertical focusing monochromator (b) Principle of neutron focusing of mirror for mathematical modelling

The model will be analyzed in polar coordinate system. As the follower lever rotates about hinge, the axis of follower shaft no longer intersects the axis of shaft. To accommodate this, a correction was introduced in the cam rotation. 'ϕ_{eff}' is effective cam rotation and 'r_{eff}' is radial distance at actual point of contact between cam and follower. The equation of cam profile in polar coordinate system is as follows,

$$z = l * \sin\theta;\ \phi_{eff} = \phi - tan^{-1}(\tfrac{l - l*cos\theta}{r});\ r_{eff} = \sqrt{r^2 + (l - l*cos\theta)^2} \quad (2)$$

Assuming a linear relationship between 'θ' and 'ϕ' i.e. ϕ = C*θ. Then, the constant 'C' can be obtained by applying boundary conditions.

Boundary conditions: ϕ = 0 then θ = 0; ϕ = 320º then θ = θ_{max};

Then the relationship between 'θ' and 'ϕ' shall be,

$$\phi = \left(\tfrac{1.78\pi}{\theta_{max}}\right) * \theta \quad (3)$$

Cam profile of eq.(2) is modified be as follows,

$$z = l * \sin\theta;\ \phi_{eff} = \left(\tfrac{1.78\pi}{\theta_{max}}\right) * \theta - tan^{-1}(\tfrac{l - l*cos\theta}{r});\ r_{eff} = \sqrt{r^2 + (l - l*cos\theta)^2} \quad (4)$$

Relation between focusing distance and common shaft rotation for n^{th} mirror,
from eq. (1) and (3),

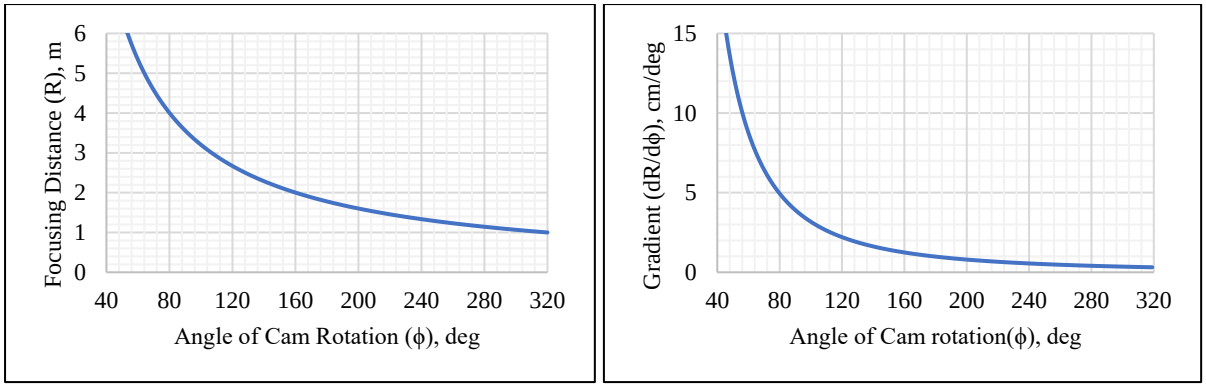
$$\phi = \left(\tfrac{1.78\pi}{tan^{-1}(np)}\right) * tan^{-1}(\tfrac{np}{R}) \quad (or) \quad R = \tfrac{np}{tan\left(\frac{tan^{-1}(np)*\phi}{1.78\pi}\right)} \quad (5)$$

RESULTS AND ANALYSIS

The cam profile as per eq.(4) have focusing distance (R) and angle of cam rotation (ϕ) as per eq.(5). The relationship between R and ϕ is nonlinear. To analyze the sensitivity of the instrument in practical working range of R:1m to 6m, graphs are plotted for mirror at 6^{th} position as shown in fig.2. The following values of variables are considered for plotting the graphs of figure (2),

l = 20.5mm; p = 10.5mm; r = 10mm; n=6.

Figure 2(a) shows, there is steep change of focusing distance during initial cam rotation but after half rotation (around 160º) the change is gradual. Generally, instruments operated in this zone for better resolution.



(a) (b)

FIGURE 2. (a) Relation between focussing distance and angle of cam rotation (b) Relation between gradient and angle of cam rotation.

The resolution of the instrument shall be quantified by dR/dϕ (gradient) vs ϕ graph as shown in figure 2(b). From the graph, it is clear that in the focusing range of 1m to 2m (ϕ =160º to 320º), the gradient dR/dϕ is 1cm/deg. With the commercially available motors, achieving of 0.5deg resolution is quite easy. Hence the fig. 2(b) confirms a focusing resolution of 5mm can be achieved easily.

This mathematical modelling enables the selective customization/optimization of vertical focusing monochromator based on application for augmentation of sensitivity, resolution and workspace by modifying the profiles of cam or dimensions of kinematic links or both.

ACKNOWLEDGEMENTS

The authors acknowledge the contribution of Mr. Tanmay Mohan Devli, Trainee, 67th Batch of BARC Training school for carrying out literature survey and alternative analytical approaches.

REFERENCES

1. User Manual, Seimens NX12.
2. Help/Manual, Microsoft Excel-2021.

Visible-light Effect on CV-Characteristics in Transparent MOS Device

Moumita Indra[1,2,*] and Sandip Mondal[1]

[1]*Department of Electrical Engineering, Indian Institute of Technology (IIT) Bombay, Mumbai, Maharashtra, India*

[2]*Theory Division, Saha Institute of Nuclear Physics (SINP), Kolkata, West Bengal, India*

[*]Corresponding author: moumitaindra@ee.iitb.ac.in / moumita.indra@saha.ac.in

Abstract. The core of today's semiconductor technology lies in solution-processed charge trapping Metal-Oxide-Semiconductor (MOS) structures, often hindered by high interface state densities. A spin-coated transparent MOS device has been fabricated on a silicon substrate using ALPO and IGZO. The effect of light illumination on the devices at different frequencies has been measured. A significant shift of CV curve is observed in the inversion region under the illumination of light. The shift of the capacitance due to illumination of light are varied from 32.5 pF to 1.8 pF for the AC signal frequency of 100 kHz to 1MHz. These findings enhance the understanding of light's interaction with MOS structures, crucial for optimizing optoelectronic and memory devices.

Keywords. Transparent MOS device, ALPO, IGZO, Capacitance-Voltage (CV), Light Illumination, Shift on CV curve.

INTRODUCTION

Transparent Metal-Oxide-Semiconductor (MOS) devices that incorporate light-enhanced features are a major improvement in semiconductor technology, with the potential to be used in transparent electronics, opto-electronics, and sensing [1]. Traditional MOS devices are fundamental for integrated circuits due to their reliability, scalability, and manufacturability [2]. However, their opacity restricts their use in transparent electronics. Integrating light-enhanced characteristics into transparent MOS devices overcomes this limitation by exploiting the interaction between light and semiconductors, paving the way for transparent displays, smart windows, wearable devices, and beyond. It is well known that capacitance-voltage (CV) characteristics of MOS provide information regarding the charge at the oxide-semiconductor interfaces. Grove et. al. [3] have shown that the transition from high-to-low frequency CV curves can be obtained by increasing the carrier recombination generation rate. A way to accelerate this process is by exposing the device to illumination. It has been shown that, under strong inversion, the capacitance tends to shift toward its low-frequency value as the intensity of illumination increases. This behaviour arises from two main effects: (a) enhanced generation and recombination of minority carriers in the inversion layer, and (b) a reduction in the width of the space-charge region, which leads to a decrease in surface potential. The photosensitive characteristics of the MOS device is studied in details by Pierret and Sah [4]. The characteristics of the MOS-capacitor subjected to steady state illumination depend upon the test frequency, light wavelength, incident light orientation (back or front), the band-to-band communication, and to a lesser degree on the majority carrier conductance [5]. It is demonstrated that there is a large shift of flat-band voltage (V_{FB}) due to illumination of white light during the capacitance voltage measurement on HfO_2 based MOS devices [6]. Luo et. al. reported the memory window is enhanced with light in high-k MOS non-volatile memories [7]. Singh et. al. [8] shown that CV curves measured without light were usually of high-frequency type, whereas those measured under illumination were of low-frequency type.

This work investigates the impact of illumination on the CV characteristics and highlights the advantages of the light-enhanced transparent MOS device. It also outlines the fabrication steps, employing Aluminium Oxide Phosphate (ALPO) and Indium-Gallium-Zinc-Oxide (IGZO) as dielectric materials. Since IGZO and ALPO both are entirely transparent oxides, memory devices constructed from them hold great promise for flexible and transparent electronics. Such device will offer intriguing opportunities for novel ideas in transparent electronics in the near future by employing the unique characteristics of the transparent materials and combining light and semiconductor physics together.

EXPERIMENTAL PROCEDURE

The inorganic dielectric precursor solutions ALPO [$Al_2O_{3-3X}(PO_4)_{2X}$] and IGZO [$In_2Ga_2ZnO_7$] is synthesized following the earlier works [9, 10]. We used ALPO + IGZO as dielectric layers in our MOS structure following a step-by-step fabrication process as describes below. We utilized low-doped p-type silicon (Si) wafers (resistivity:

4.0-7.0 Ω·cm, thickness: 275 µm, doping concentration ~ 4×10^{15} cm^{-3}) that were initially cleaned using the RCA method. Following this, the samples underwent a 60-second oxygen plasma treatment using a Plasma Asher. Then ALPO was applied via spin coating at 4000 RPM for 30 seconds. This step was repeated to form a double-layered ALPO film. Post-deposition, the samples were annealed at 275 °C. Subsequently, a single IGZO layer was spin-coated over the ALPO stack and annealed at 110 °C. Finally, 50 nm thick Indium Tin Oxide (ITO) top contacts (circular shape having diameter 450 µm) were deposited through a shadow mask using a Sputter Orion system. The bottom metal contact of Aluminum (Al) of thickness 50 nm was deposited by thermal evaporator. CV measurements were carried out by applying voltage sweeps and pulses, using small AC signals at different frequencies of 100 kHz, 500 kHz, and 1 MHz. CV characteristics of the MOS capacitor were recorded by cyclically sweeping the voltage from −V to +V and back to −V, with the sweep amplitude progressively increased from ±10 V to ±20 V. We performed the same CV measurements keeping the light of the probe station both ON and OFF condition. We observed a drastic change in the CV characteristics with and without light illumination to the device. The value of the capacitance in the inversion region (C_{min}) is dependent on the frequency of the ac-signal as well as changing with illumination of light. We have presented some of the data in different ac-signal frequencies. We have noted the shift of the capacitance minima (ΔC_{min}) due to light illumination in different frequencies of the ac signal and also observed the variation of threshold voltages (V_{th}).

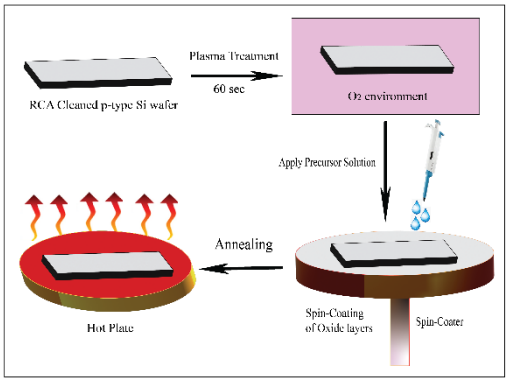


FIGURE 1. Schematic diagram of device fabrication steps: RCA Cleaning of wafer, Plasma treatment for further cleaning, Spin-Coating of precursor solutions, Annealing.

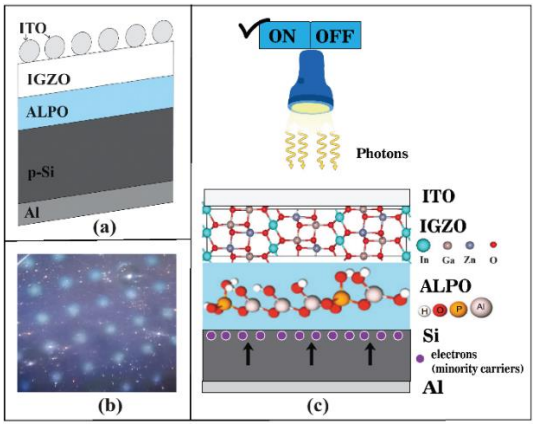


FIGURE 2. (a) Schematic diagram of device layers, (b) Top-view of the spin-coated MOS device. (c) Zoomed view of the structure and cartoon image of the mechanism to the device in presence of light.

RESULTS & DISCUSSION

There are three main regions of interest for operating the MOS capacitor: accumulation, depletion and inversion [12]. Minority carrier response to the ac gate voltage is irrelevant in the accumulation and depletion regions because minority carrier density is minimal in comparison to majority carrier density at the silicon surface. The MOS capacitor's steady-state CV characteristics are governed by minority carrier response in the inversion region mainly. When the gate electrode is opaque and free from defects, minority carriers generated within a diffusion length near the gate edge can contribute to forming an inversion layer, provided the gate bias is sufficiently strong. The response time of the light generated inversion layer will depend on the light intensity. When light is illuminated onto a MOS device with a p-type semiconductor substrate, it can induce charges in the inversion region due to the generation of electron-hole pairs within the substrate. The MOS capacitor on p-substrate exhibits a standard curve shape for CV measurements, with an accumulation capacitance at −V (C_{acc}) and a depletion capacitance at +V (C_{dep}) with a deep depletion at a higher positive voltage. In this case, the C_{acc} at −V represents the capacitance of oxide layer (C_{OX}) and the C_{dep} at +V is the series capacitance of oxide layer and the depletion region in p-Si (C_{min}). Some of the CV curves are shown in Fig 3 with light (red colored) and without light (black colored) illumination.

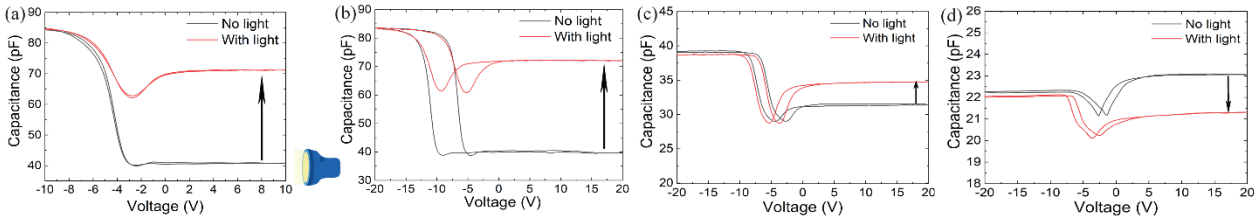


FIGURE 3. CV characteristics of the device with or without visible light at different voltage sweeps and at different ac signal frequencies. Panel (a), (b) represent CV data at frequency 100 kHz with voltage sweeps ±10 V and ±20 V respectively whereas the two panels (c) and (d) representing CV data for frequency 500 kHz, and 1 MHz respectively at voltage sweep ±20 V.

We found that the threshold voltage is varied with the frequency of the ac signal but it has not much effect on light illumination. The hysteresis window (ΔV_{FB}) is observed at higher voltage sweep only (±20 V). It reduces with increase in frequency of ac signal but there is no significant role of light illumination. The shift of the capacitance minima (ΔC_{min}) due to light illumination is very prominent in different frequencies. At lower frequencies it is shifted upwards but at high frequency it goes downwards in presence of light. We can conclude that when light is illuminated to the MOS structure, minority carriers (here electrons) are generated in the Si-Oxide interface [11] and they respond quickly at lower frequencies to modulate the capacitance characteristics of the device. But at higher frequencies there is lesser number of generations of minority carriers and they are not able to respond at that small time domain.

CONCLUSION

This study covers the effect of light illumination in MOS device and how it affects the device characteristics. Light illumination on memory devices is very significant because there is a need to use semiconductor devices in radiation-prone industrial, space, and military applications. We can conclude that illumination of light can modulate the electrical characteristics of MOS device in a drastic way. The CV characteristics can be tuned by the variation of the intensity and wavelength of light.

ACKNOWLEDGMENTS

The authors want to acknowledge Indian Institute of Technology Bombay Nanofabrication (IITBNF) Facility for providing the facilities for the fabrication and characterization of the set of devices.

REFERENCES

1. Shunhao Ge et. al., Nanomaterials, Vol. 13, pp. 1141 (2023).
2. Van Rossum, M., MOS Device and Interconnects Scaling Physics. In: Shacham-Diamand, Y., Osaka, T., Datta, M., Ohba, T. (eds) Advanced Nanoscale ULSI Interconnects: Fundamentals and Applications. Springer, New York, 2009.
3. A. S. Grove, B. E. Deal, E. H. Snow & C. T. Sah, Solid State Electron Vol. 8 (2), pp. 145 (1965).
4. R. F. PIERRET and C. T. SAH, Solid-State Electronics, Vol. 13, pp. 269-288 (1970).
5. R. F. PIERRET and C. T. SAH, Solid-State Electronics, Vol. 13, pp. 289-302 (1970).
6. Sandip Mondal, AIP Conf. Proc. 1942, 060007-1–060007-4; https://doi.org/10.1063/1.5028777.
7. Bingqing Luo, Chen-Han Lin, and Yue Kuo, ECS Trans. Vol. 41 (3) pp. 93-100 (2011).
8. J.P. SINGH AND R.S. SRIVASTAVA, IETE Journal of Research, 26:10, 546-549 (2015).
9. S. Mondal et. al., IEEE Transactions on Electron Devices, vol. 68, no. 3, pp. 1190-1195 (2021).
10. Marco Moreira et. al., Nanomaterials, Vol. 9, pp. 1273 (2019).
11. Yasuhisa Omura et. al. Jordan Journal of Electrical Engineering, Vol. 8 (1), pp. 1-16 (2022).
12. E. H. Nicollian and J. R. Brews, “MOS (Metal Oxide Semiconductor) Physics and Technology”, John Wiley & Sons, New York, 1982.

Comparative Study of BF_3 Based Neutron Detectors with Cylindrical and Cuboid Geometry Using COMSOL and FLUKA Software

Arkaprabha Bhowmik[1,2], Shraddha S Desai[*,1], Shylaja Devan[1], Mala N. Rao[1,2]

[1]Solid State Physics Division, *Bhabha Atomic Research Centre*, Trombay Mumbai 400085

[2]Homi Bhabha National Institute, Trombay Mumbai 400085
[*]*Corresponding author: ssdesai@barc.gov.in*

Abstract. Neutron proportional counters commonly use coaxial cylindrical geometry for advantage of symmetry in electric field distribution and for use in isotropic neutron field. In case of BF_3 filled neutron detectors, electron attachment plays role in high pressure compatibility that determines the sensitivity of a detector. Detectors with complex geometry such as square cross section and array of multitubes is useful to suppress recombination. The square geometry is analyzed for electric field distribution and neutron detection sensitivity. Multiphysics software COMSOL is used for defining detector geometry in 2D mode and simulate electric field distribution in sensitive region of detector. Data obtained from simulations will reflect the shape of pulse height distribution resulting from neutrons. FLUKA software is used to accurately simulate the neutron sensitivity of a detector with coaxial and square cross section geometry of interest. A comparative analysis of multitube-based cylindrical and parallelepiped geometry for BF_3 filled neutron detectors is presented.

Keywords: Proportional Counters,BF_3 detectors, COMSOL multiphysics, FLUKA, FLAIR, cylindrical geometry, Cuboid geometry

INTRODUCTION

In-house developed neutron detectors are used for neutron scattering facilities at Dhruva reactor. BF_3 based cylindrical neutron proportional detectors are used in counting and position sensing mode. These detectors are used to monitor neutron beam flux and to record neutron scattering data at angular positions. BF_3 as neutron detection material has challenges due to its electronegative properties [1-3]. Recombination in drift region can be suppressed by increasing drift voltage and reducing drift length. Smaller diameter may lower sensitivity, whereas multiple such array of tubes can be advantageous. Square cross section geometry is suitable than circular one due to no dead region being lost during stacking. The square cross section needs to be analyzed for electric field distribution in drift and avalanche region and compared with the circular one. The higher volume in square geometry resulting in to gain in detection sensitivity is also analyzed.

Electric field distribution is simulated using COMSOL multiphysics software [4] for both circular and square cathode geometries. The neutron sensitivity is simulated using FLUKA software [5]. Flair interface is used for the purpose. The simulated values for circular and square cathode are compared with the mathematical calculations.

SIMULATION METHODS

COMSOL Multiphysics software for electric field distribution

COMSOL multiphysics is a FEM based software, used to study the electric field distribution in 2D planar mode. Gas filled neutron detectors operate in the proportional region. Gas multiplication is crucial to achieve the higher electric field in the vicinity of the anode wire. The field lines are mapped to get an idea about the pulse shape. The variation of electric field strength with radial distance is obtained for circular and square cross sections of cathodes. Diagonal distance is also considered for electric field distribution and field lines. BF_3 gas is taken as a medium and the bias voltage is 2 kV. Fig 1a shows the plot of electric field distribution between anode and cathode for circular geometry of 5 mm radius and square of 10 mm x 10 mm, anode (tungsten wire) diameter is 25 µm. Black and red lines show electric field in circular and square geometry respectively and blue line shows the data along diagonal from square geometry. Fig 1b and 1c show the electric field line distribution in circular and square cross section.

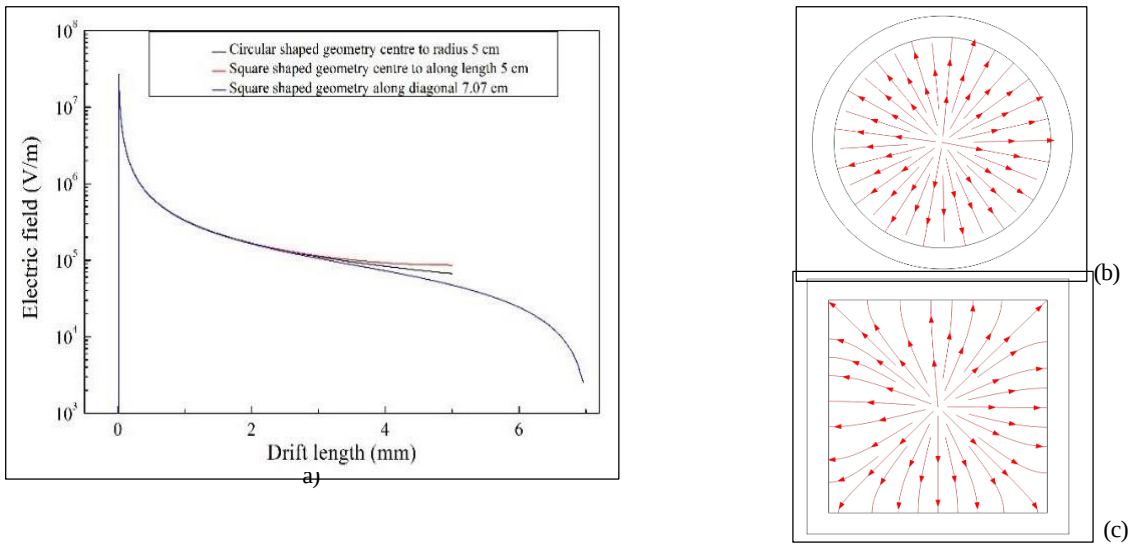


FIGURE 1: a) Electric field variation with distance from anode to cathode (zero on x-axis corresponds to surface of anode wire), Bias: 2000 V. Electric field line distribution.in (b) circular cross section and c) square cross section

FLUKA SOFTWARE FOR NEUTRON TRANSPORT

FLUKA is a crucial computational tool employed for simulating radiation transport and particle physics. Flair, equipped with a user-friendly graphical interface (GUI), simplifies the setting up of simulations. Different parameters such as the type and energy of beam particles, beam position, detector geometry, material properties, physics of interactions are defined. The input files are generated for cylindrical and cuboid geometry. Thermal neutron beam of 25 meV is directed along the z-axis with a spread of surface 1 cm² centered at the origin, without any beam divergence. BF_3 is the detection material. Thermalized neutrons undergo nuclear reactions with ^{10}B, produce alpha particles and ^{7}Li. The output files show extensive data of interactions and results of simulation are obtained.

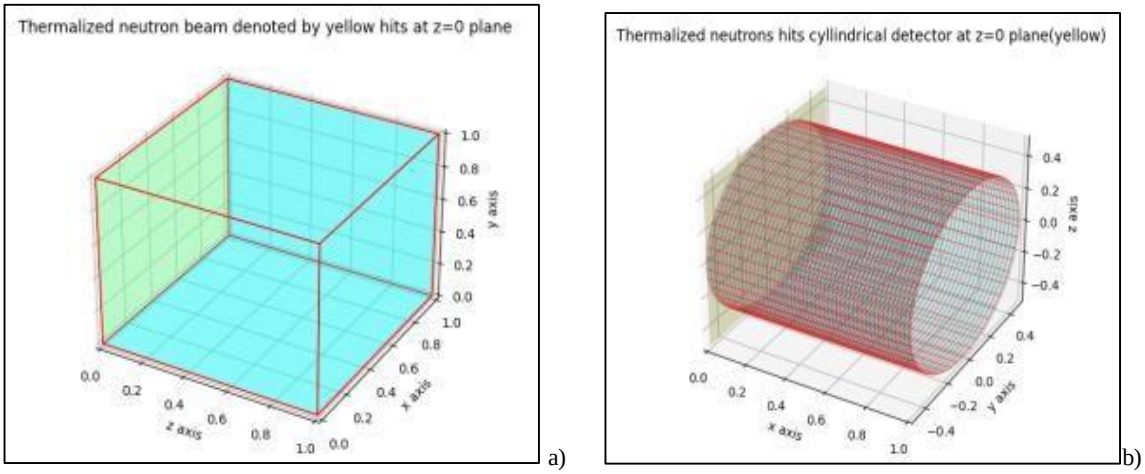


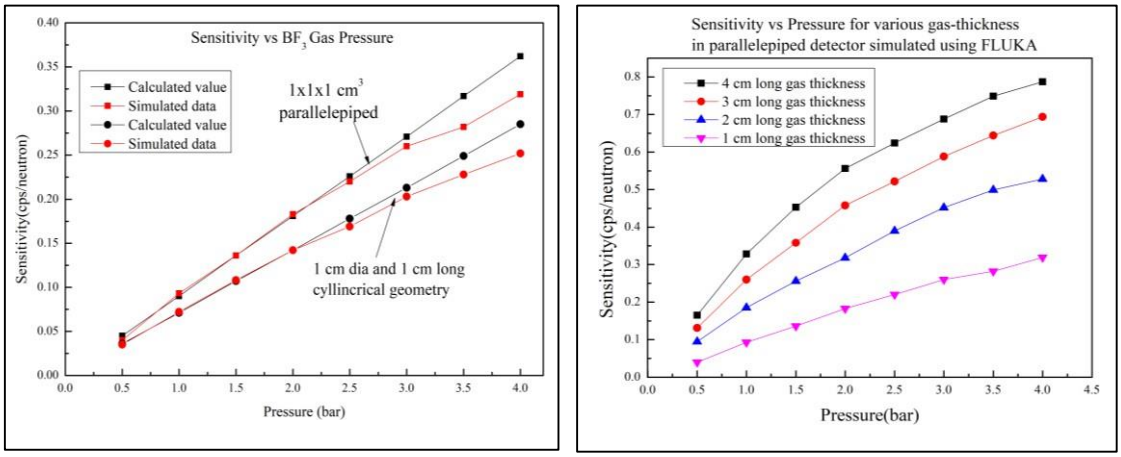
FIGURE 2: FLUKA models of BF_3 filled detector a) Cuboid geometry b) Cylindrical geometry

RESULTS AND DISCUSSION

From Fig 1b and 1c, it is evident that COMSOL output data of the square cross section geometry has a nearly identical electric field distribution to the circular cross section proportional counter. Differences near the corners are due to the increased anode cathode distance along diagonal. The density of electric field lines near the corners is lower and is expected that field will be lower by factor of □2 as compared to normal distance. It is expected to broaden the pulse within acceptable

limit, with gain in efficiency.

FLUKA program output is used to estimate the sensitivity of the detector, and is analyzed by measuring the number of alpha particles produced per neutron in volume of the detector. A comparative study is made amongst cylindrical and cuboid detectors as per models shown in Fig 2a and 2b at various gas pressures from 0.5 bar to 4 bar under identical source-to-detector geometry. The results are plotted in Fig 3a and compared to mathematical calculation of sensitivity. Sensitivity is calculated using the formula $NV\sigma /1.128$, where N is number density of ^{10}B atoms, V is detector volume, and σ is the thermal neutron nuclear reaction cross section for ^{10}B (~3840 barns). Fig 3b denotes the variation of sensitivity with length of a parallelepiped detector from 1 cm to 4 cm, which also denotes the path length of neutron in the sensitive region.



(a) (b)

FIGURE 3: a) Sensitivity with different BF_3 pressure b) Sensitivity vs pressure for various gas thicknesses in parallelepiped

The neutron sensitivity is also plotted against the gas pressures. Fig 3a shows that sensitivity increases on changing the geometry from cylindrical to cuboid, which is expected for neutron detector. The simulated curve aligns with the calculated curve at lower pressures up to ~ 2 bars, beyond which the slope decreases for simulated value. This formula is accurate at lower pressures, but at higher pressure, results approach saturation, which is an observation evident from simulation. Fig 3b illustrates the variation of detector sensitivity with pressure at various gas thicknesses. The plot shows that increasing gas thickness and pressure enhances sensitivity, but gain is not linear.

CONCLUSION

COMSOL and FLUKA analysis of detector geometries indicate that a square cross section geometry has a nearly identical electric field distribution to the circular cross section proportional counter. Square cross-sectional parallelepiped can serve as a proportional counter for neutron detection. FLUKA analysis indicates that increasing gas thickness and pressure improves neutron detection sensitivity. The cuboid geometry enhances detector sensitivity and thus can also be utilized in array of multitube configuration.

REFERENCE

1. Boron trifluoride detectors, Thomas Wilpert, Neutron News 23 (2012) 14.
2. Shraddha S Desai, and Mala N Rao, AIP Conf. Proc. 1832 (2017) 060014
3. Glenn F. Knoll (1979). Radiation Detection and Measurement. Second edition
4. https://www.comsol.com
5. http://www.fluka.org/flair

Design of Enclosure Chamber of Large 2D PSD for SANS Diffractometer at Dhruva Reactor

Shraddha S Desai[*,1], Saurabh Gupta[2], V K Shrivastava[2], Mala N Rao[1,3], V K Aswal[1]

[1]*Solid State Physics Division, Bhabha Atomic Research Centre Trombay Mumbai 400085*
[2]*Division of Remote Handling and Robotics, Bhabha Atomic Research Centre Trombay Mumbai 400085*
[3]*Homi Bhabha National Institute, Anushaktinagar, Mumbai 400094*
[*]*Corresponding author: ssdesai@barc.gov.in*

Abstract. Small angle neutron scattering experiments require efficient neutron detectors forcovering scattering angle of interest. Isotropic scattering samples are often analyzed using linear 1D position sensitive detector (PSD) intercepting the diameter of the scattered spectrum. Multiple 1D PSDs in fan-like arrangement are must to observe the signature of anisotropic scattering samples, with significant dead regions, however 2D PSD shows the advantage of covering entire area of scattered neutron indicating better statistics as well as access to smaller Q (large length scale). A 2D PSD for neutron scattering is being developed as an import substitute. It has sensitive area of 640 mm × 640 mm and is based on multiwire geometry, ^{3}He gas filled and delay line position encoding. Scaling up of the hardware enclosure considering neutron transmission and permeability of ^{3}He gas are challenges. Design features of gas enclosure chamber, neutron detection efficiency, position encoding and position resolution would determine the success of the 2D PSD development. In this work, the design of enclosure chamber for vacuum and high-pressure tolerance is presented.

INTRODUCTION

Neutron scattering experiments carried out at National Facility for Neutron Beam Research, Dhruva reactor are supported with indigenously developed neutron detectors ranging from small beam monitors to array of 1-Dimensional position sensitive detectors (1D PSD). 2-Dimensional position sensitive detector (2D PSD) shows the advantage of continuous sensitive area of scattered neutron indicating better statistics, data of asymmetric spectrum and access to smaller wave vector transfer Q and reduction experimental time making judicious use of neutron beam time. 2D PSD based on multiwire proportional counter [1-4] is a detector with multiple anode wires covering the sensitive region and combination of orthogonal multiwire cathodes, enclosed in a gas volume. 2D PSD is being developed with design based on multiwire sense grids and delay line position encoding. Simultaneous *x* and *y* position information of scattered neutrons would enhance data collection statistics and reduce experimental beam time. Design of 2D PSD includes consideration for enclosure chamber, vacuum-pressure capability, sensitive area, neutron detection efficiency, position resolution, count rate capability pulse processing and data acquisition. All these factors contribute to the successful functioning of the PSD. Assembly of multiwire grids depends on choice of wires, tension on wires, pitch of wires, method of winding, as well as accuracy of wires and grid alignment. Choice and mounting of delay components need consideration for long term stability and functioning of 2D PSD. Multiwire grids are heart of PSD and have exhaustive design features being discussed elsewhere. The design features of 2D PSD enclosure chamber need utmost care as it holds the costly and precious ^{3}He gas at high pressure. All above factors are considered for long life of PSD. The availability of this PSD will make the SANS facility [5-8] productive in a multi-fold manner.

DESIGN OF 2D PSD

An indigenous design and development of a large area 2D PSD (sensitive area 640 mm × 640 mm), is taken up, using the experience from small area neutron beam imaging 2D PSD [9-11]. The overall dimensions of 2D PSD are 850 mm × 850 mm. It will be mounted on a 5 m long translation stage with 300 mm of x translation to vary the source to detector distance and consequently the variable 2θ angular coverage over the sensitive area. Fill gas ^{3}He at 3 bar and Kr at 1.5 bar with 40 mm neutron path length along incident beam to result in the estimated neutron detection efficiency 75% at 5.6 Å. Multiwire grids are array of wires with spacing ~5 mm pitch, which is equivalent to the position resolution. Enclosure chamber holds 3 multiwire grids, central anode is sense grid for avalanche formation of primary charge cloud and the amplified charge is seen by two orthogonal position sensing grids. Each wire in

position grid is separated by fixed time delay, which separates pulses from each wire by time of arrival. LC bridge determines the time resolution and count rate capability of the PSD.

DESIGN OF 2D PSD ENCLOSURE CHAMBER

The 2D PSD enclosure chamber is designed for weldless structure and consists of bottom plate holding all three grids. Top plate is with neutron transmission window. Fig 1a shows the schematic design of internal structure of the chamber with all accessories mounted and Fig 1b shows the schematic assembly of the chamber mounted with vacuum port and connectors. Hermitically sealed connectors make electrical contacts with sense and readout grids inside vacuum compatible chamber. Top plate is designed suitable for neutron transmission window by thinning the plate in the sensitive area. NPT threaded couplings make the mounting ports of vacuum connectors and readout electrodes compatible to high vacuum and high pressure.

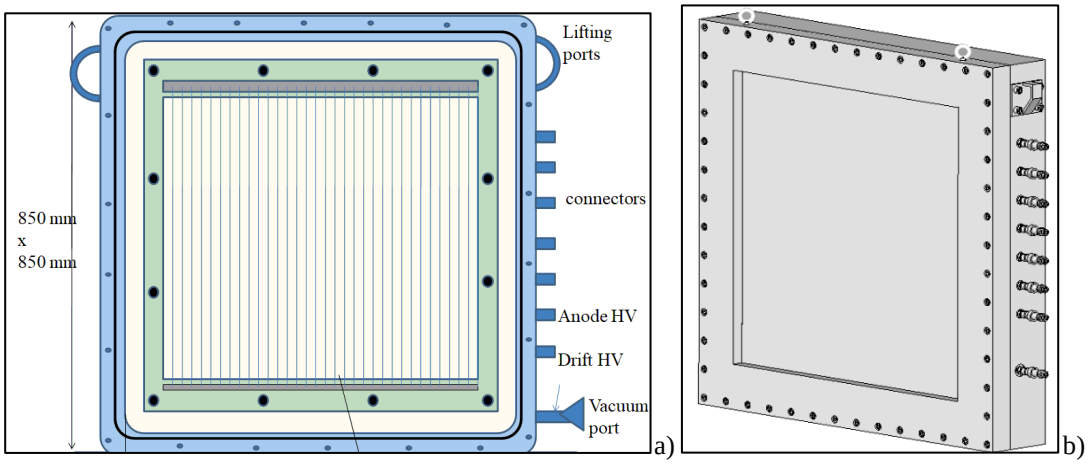


FIGURE 1. Schematic design of multiwire based 2D PSD for SANS Diffractometer with delay line position encoding, a) Front view showing internal grid assembly and b) Assembled enclosure mounted with connectors

SIMULATION OF STRESS AND DEFLECTION AT HIGH PRESSURE

Dimensions and geometry of the enclosure chamber are simulated using Finite Element Method (FEM) for stress and deflection under vacuum and high-pressure conditions of 5.5 bar. The inner area of the plate is exposed to pressure and the outer area has been fixed. The maximum stress in the plate is below the yield stress and is limited to very small area [12, 13]. The FEM results for stress and deflection are shown in Fig 2 a and 2b and are found to be within the acceptable limit. The von Mises stress reduces from maximum value of 154 N/mm^2 to 75 N/mm^2 in the span of less than 10 mm. Since the pressure inside the chamber is constant, fatigue will not play role and thus it is not considered. The stress apart from the local zone is well below the yield stress as indicated in Fig 2a. The deflection is maximum at the centre of the plate which is expected and this maximum value is 1.8 mm. The increase in neutron path length at centre by 2 mm results in rise of efficiency at the position from 75% to 76%. This rise in efficiency is marginal and within acceptable limit, however this central area is covered with beam stop, being a direct beam position.

The chamber material is chosen as Al 6061 T6, which has better neutron transmission, good mechanical strength and good corrosion resistance property [14]. Both the plates are hold together with Viton Oring that has radiation resistant property along with good chemical and temperature compatibility [15] and 52 SS screws for the vacuum and high pressure. The whole assembly can be lifted with the help of bottom plate lifting lugs. Top plate weighs 70 kg and overall weight is ~200 kg, fabrication and handling would need proper machine handling equipment for skillful mounting of chamber accessories. Initially entire assembly of grids and high voltage connectors are to be tested with X-rays using Ar+CH_4 gas. The top cover with gridded holes of 3 mm diameter and 20 mm pitch are machined in matrix form for X-ray transmission. It is to be secured with vacuum compatible 50 µm thick Al foil.

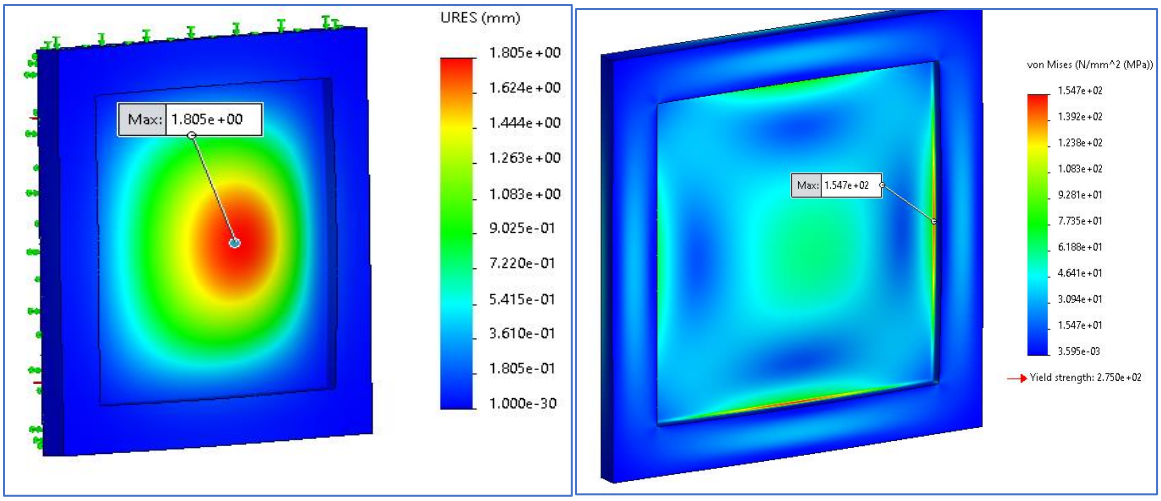


FIGURE 2 a) Variation of net deflection and b) Variation of von Mises Stress across Top Plate at 5.5 bar

CONCLUSION

Design features of the 2D PSD for neutrons as an import substitute are presented. 2D PSD is being developed with design based on multiwire sense grids and delay line position encoding. Simultaneous *x* and *y* position information of scattered neutrons would be obtained. The availability of 2D PSD will enhance data collection statistics and reduce experimental beam time. The chamber has been fabricated as per the design and found compatible for the vacuum 10^{-6} Torr and high pressure of 5.5 bar.

ACKNOWLEDGMENTS

We are thankful to Dr S M Yusuf, Shri K. Madhusoodanan and Dr D C Kar for support and encouragement.

REFERENCES

1. G. Charpak and F. Sauli, Nucl. Instrum. Methods 162, 277 (1979)
2. F. Sauli, CERN Scientific Report, RD/233 (1977)
3. P. Convert, J.B. Forsyth (Eds.), Position-Sensitive Detection of Thermal Neutrons, Academic Press (1983)
4. Radiation Detection: Concepts, Methods, and devices, Douglas McGregor, J K Shultis, CRC Press 2021 p 391
5. V K Aswal and P S Goyal, Current Science, **79,** 947 (2000)
6. D. Ray and V.K. Aswal, J. Phys.: Condens. Matter **26**, 035102 (2014)
7. Sugam Kumar, D. Saha and V.K. Aswal, Phys. Rev. Mater. 7, 015601 (2023)
8. Sugam Kumar and V.K. Aswal, Soft Matter 20, 5553 (2024)
9. Shraddha S Desai *Journal of Physics*: Conference Series **528** (2014) 012037
10. Shraddha S. Desai And Mala N. Rao, AIP Conf. Proc. 1447, 491 (2012).
11. Shraddha S Desai, , AIP Con Proc 2265, 030200 (2020)
12. ASME, Boiler and Pressure Vessel Code: Section VIII Rules for Construction of Pressure Vessels, Div 1 (2017)
13. ASME Boiler and Pressure Vessel Code: Section II – Materials: Part B – Nonferrous Material Specifications
14. J. R. Granada, Journal of Nucl Mat, Vol 277, Issues 2–3, 2000, Pages 346-350,
15. A. Zenoni, et al, Rev Sci Instrum. 2017 Nov;88 (11) 113304.

Conceptual design of an innovative shock absorber for possible application in Dhruva reactor

J. V. Mane[a)], S. Sharma, J. S. Misal, K. K. Verma, S. Chandra, V. M Chavan

Reactor Technology Division, Bhabha Atomic Research Center, Mumbai-400085, India

[a)]Corresponding author: jvmane@barc.gov.in

Abstract. *The innovative concept of extrusion tube as a part of existing shut-off rod (SOR) of Dhruva reactor assembly is developed here. This modification in SOR will absorb drop energy under postulated event of drop of SOR into the guide tube without damaging the tube. Effectiveness of SOR under postulated drop event is evaluated using explicit FE simulations of entire SOR assembly and verified experimentally in Drop Weight Tower machine. It is found that the modified SOR is functioning in intended manner and guide tube remains in elastic condition throughout the postulated event of SOR drop into the guide tube, irrespective of working of existing emergency springs inside the guide tube. New concept of modified SOR can be used as SOR in Dhruva reactor.*

INTRODUCTION

Dhruva is a thermal 100MW reactor for research purposes and contains fuel in the form of metallic natural uranium. Heavy water acts as moderator, coolant and reflector. The primary fast shutdown system of this reactor is Shut-Off Rods (SOR) [1]. During normal reactor operation a set of nine shut-off rods containing neutron absorber assemblies of Cadmium are kept ready above the top of fuel elevation in the reactor core. On a reactor trip signal, these rods simultaneously drop down into reactor core region under gravity. Under very unlikely accident condition, if free fall of SOR occurs due to snapping of its wire rope, SOR will hit the emergency spring located at the bottom of guide tube. For better shock absorbing capabilities, a conceptual design of shock absorber as a part of existing SOR assembly is proposed here which will absorb drop energy under postulated event of SOR drop into guide tube without damaging the guide tube. Experiments and Finite Element (FE) simulations are used synergistically to arrive at appropriate design incorporating concept of extrusion tubes. In this concept, drop energy will be absorbed by plastic deformation of tube and inherent friction.

EXPERIMENTAL AND NUMERICAL METHODOLOGY

Constraint in developing modified SOR is that its neutronic characteristic should remain same. Therefore, modification is possible only in lower part of SOR with available length of 120 mm and maximum diameter of 60 mm. To absorb energy efficiently, extrusion tube type concept is postulated here through explicit FE simulations. Numerous FE simulations are carried to arrive at the final concept of modified SOR sub assembly of Dhruva reactor. Fig. 1(a) displays the conceptual design arrived through existing design and preliminary FE simulations [2]. All the structural components (made of SS-304) of modified part of SOR except extrusion tube (made of Al-6061) are meshed with solid hexahedral elements and extrusion tube is meshed with shell elements. Appropriate boundary conditions are defined as shown in Fig. 1(a). An initial velocity of 8.27 m/s (to absorb 900J of impact energy with 26 kg mass) is assigned to the mass on top of modified part of SOR to mimic experimental conditions. Material properties utilized in FE simulations are displayed in Table 1.

Drop Weight Tower (DWT) machine (Fig. 1(b)) is utilized to experimentally verify the concept of modified SOR. The setup consists of anvil, striker and mass carriage assemblies to achieve drop velocities ranging from 1 m/s – 20 m/s through varying heights of 0.1 m – 3.0 m. A drop height of 2.25 m is set with 40.55 kg mass to absorb 900 J of equivalent energy. Force vs time plots obtained from transducers and the final deformed shape of the Al tube are noted from the experiments and compared with FE simulations to authenticate the validity of proposed design.

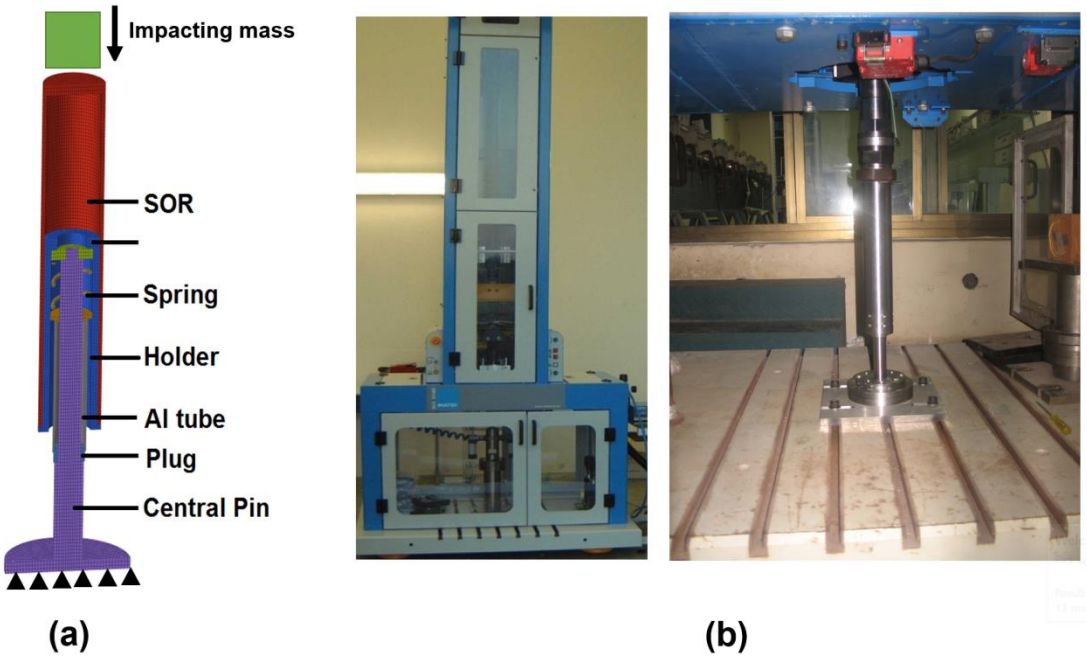


FIGURE 1. (a) Cut-view of the three-dimensional FE model of modified SOR assembly. The impacting mass mimics a drop energy of 900 J. (b) DWT setup used to perform experiments on the modified SOR assembly.

TABLE 1. Material properties utilized in FE simulations.

Material	E (GPa)	ν	Density (kg/m^3)	Yield stress (MPa)	Tangent modulus (MPa)
Al-6061	68.9	0.3	2710	306	430
SS-304	200	0.3	7800	205	772.9

RESULTS AND DISCUSSION

The obtained results in the form of force vs time plots are displayed in Fig. 2(a). An important point to be noted from these figures is that the peaks in force vs time graphs, which signify the reaction force during impact, are quantitatively similar in both situations. The first peak in force is observed at around 100 kN in experiments (Fig. 2(a)) while the corresponding value is around 95 kN in numerical simulations. Similarly, the second peak exists at 125 kN force in experiments and 123 kN in numerical computations (Fig. 2(a)). This observation validates that the energy absorption phenomena during drop event simulated from FE simulations is commensurate with the actual phenomena occurring during real impact test.

To further validate this, Fig. 2(b) displays the comparison of geometrical deformation in extrusion tube obtained from experiments and FE simulations. Zoomed inset in Fig. 2(b) highlights the deformation of the extrusion tube. Notably, the height of extrusion of tube in both cases is similar, viz. 32.8 mm in experiments and 32.3 mm in FE simulations (vertical distance between node IDs 3019 and 4679 in Fig. 2(b)). Similarity in magnitudes of peak reaction forces during impact and the final deformed shapes of extrusion tube observed during experiments and numerical simulations validates the proposed concept. Therefore, the modified SOR with extrusion tube presents a promising opportunity to absorb the kinetic energy during impact of SOR without damaging the guide tube.

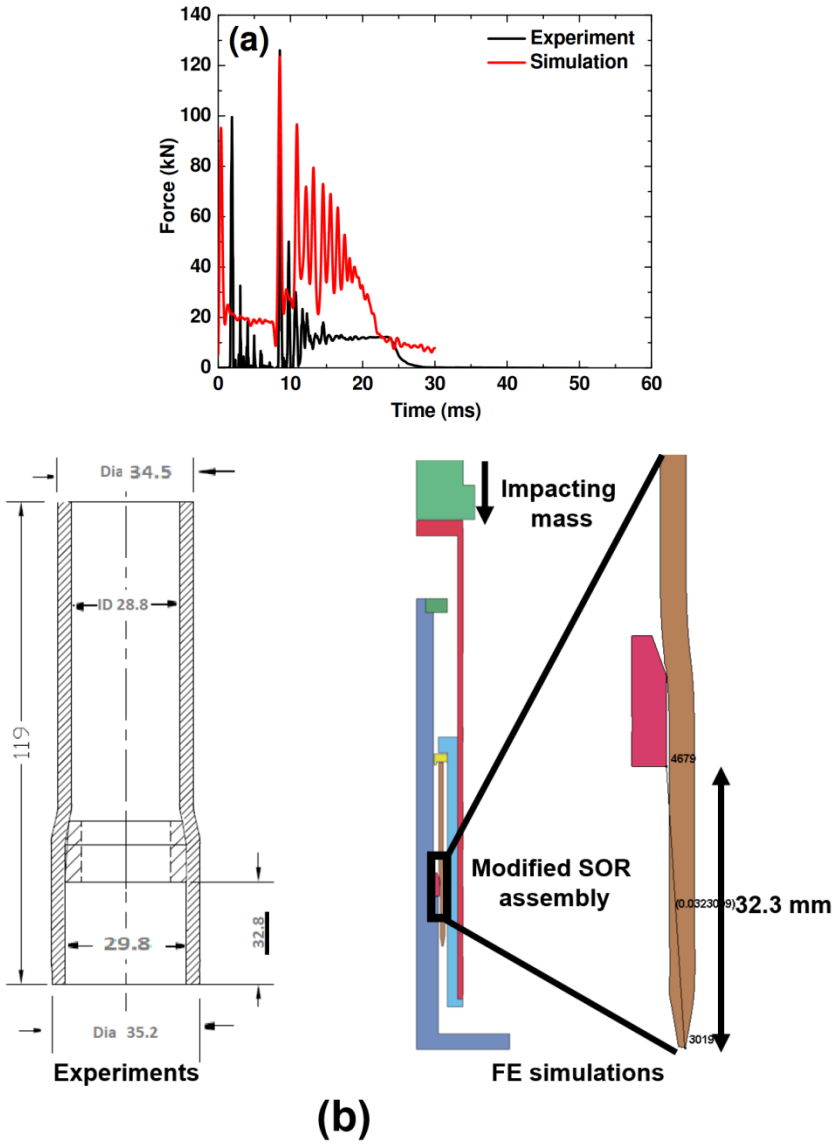


FIGURE 3. (a) Force-time plots and (b) deformed geometries obtained from simulations and experiments.

SUMMARY

In this work, FE simulations of a conceptual innovative design of shock absorber for SOR of Dhruva reactor are carried out and compared with actual test drop in DWT machine. It is observed that the modified SOR with extrusion tube is able to efficiently absorb the kinetic energy upon impact without damaging the guide tube. Similarity in magnitudes of peak reaction forces and deformed geometrical parameters of the extrusion tube between experiments and simulations validate the proposed design of modified SOR, which can be used in DHRUVA reactor.

REFERENCES

1. DHRUVA Safety Report, Vol. I & II, Design Description, 1984.
2. J. V. Mane, S. Sharma, S. Rai, V. M. Chavan, R. J. Patel, “Analytical and experimental studies for the incident of drop of absorber rod of shut-off rod mechanism of Dhruva," Divisional report RTD/ATDS/19/2013, August 2013.

Sealed D-T Neutron Generator for Borehole Logging and Bulk Material Characterization

Prashant Singh[1, 2, a)], Mayank Shukla[1, 2], Tushar Roy[1], M.R. More[1], Shefali Shukla[1], Ravi Baribaddala[1] and Yogesh Kashyap[1, 2]

[1]*Neutron & Synchrotron Radiation Physics Section, Technical Physics Division, BARC, Mumbai.*
[2]*Homi Bhabha National Institute, Anushaktinagar, Mumbai.*

[a)] Corresponding author: prashants@barc.gov.in

Abstract. The paper presents design, operational principles and applications of a compact neutron generator, developed indigenously, which provides a reliable source of fast neutrons for material characterization. The sealed D-T neutron generator offers enhanced safety, portability, and operational efficiency compared to traditional neutron sources. It enables real-time, in-situ measurements of elemental compositions and densities of geological formations and bulk materials. This paper also describes two different applications of this neutron generator. In the first application, we have used Prompt Fission Neutron (PFN) technique for precise identification and quantification of uranium deposits by measuring the prompt fission neutrons. The second application highlights bulk material characterization using neutron-induced gamma-ray spectroscopy, such as in coal to quantify moisture and carbon content, and determine its gross calorific value. Both these experiments were carried using indigenously developed 14.1 MeV D-T neutron source with yield of 5x10^7 n/sec operated in pulsed mode.

INTRODUCTION

D-T neutron generators produce neutrons through the fusion reaction of deuterium (D) and tritium (T), which yields a neutron and helium-4[1]. The device comprise of an ion source, deuterium gas reservoir, a compact linear DC accelerator and neutron production target. We have used cold cathode Penning ion source to generate D+ ions, due to its compact size, minimal auxiliary power sources requirement and no maintenance needs, making it ideal for a sealed device. The deuterium ion beam is accelerated in a DC field upto -80 kV and subsequently hitting on tritium target to produce mono energetic neutrons by fusion reaction. The neutron has energy of ~14.1 MeV, making D-T neutron sources highly effective for applications requiring deep penetration such as borehole logging and bulk material characterization.

In this paper we have described Prompt Fission Neutron (PFN) analysis technique for uranium ore assay in borehole. This is a direct uranium logging technique that effectively quantifies uranium in areas of radioactive disequilibrium [2]. Unlike traditional gamma-ray methods, PFN analysis is less influenced by the presence of other radioactive elements or varying rock densities, leading to more accurate and reliable results. We conducted set of experiments in borehole to check the reliability of neutron generator and were able to identify the uranium content at various depths. Neutron generators have advantage of rapid characterization, making them suitable for online monitoring. This paper also describes Pulsed Fast Thermal Neutron Activation technique to determine moisture content and gross calorific value of coal by measuring its elemental composition. Traditionally, moisture content in coal has been measured using gravimetric methods, which involve drying samples and measuring weight loss. These methods are time-consuming, labor-intensive, and may not provide real-time data. The 14.1 MeV neutrons from D-T source interact with the hydrogen atoms present in the water molecules within the coal matrix, and associated characteristic gamma is detected by Bismuth Germanate (BGO) detector. A moisture content of at least 2% by weight was observed, with a relative error margin of 0.4%.

SEALED D-T NUETRON GENERATOR

Fusion based neutron sources are relatively cheaper, compact and portable. Fusing isotopes of hydrogen produces neutrons. ${}_1^2H + {}_1^3H \rightarrow {}_0^1n\,(14.1\,MeV) + {}_2^4He$, ${}_1^2H + {}_1^2H \rightarrow {}_0^1n\,(2.45\,MeV) + {}_2^3He$ (1)

The neutron generator includes a compact cold cathode penning ion source, a compact high voltage (upto -80kV DC) accelerating drift tube electrode and a neutron target assembly. Deuterium ions produced in the ion source are extracted through an aperture and accelerated to produce neutrons by hydrogen isotope fusion. The D+ ions were accelerated to maximum energy of 80keV. A plot of neutron dose and acceleration voltage is shown in **FIGURE 1** with maximum dose of ~170 µSv/hr corresponding to a neutron yield of 5x10^7 n/sec at -80kV acceleration and ion source operated in pulsed mode at 2.2kV, 300µsec and 500Hz.

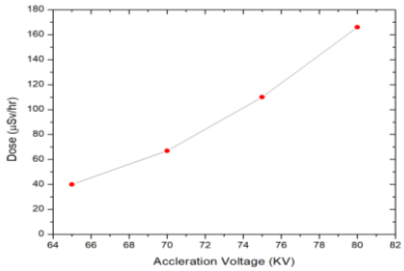
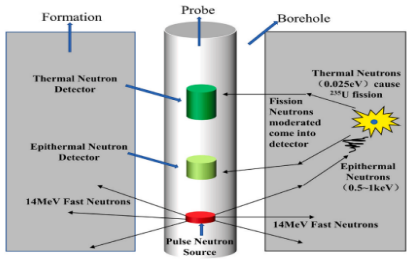


FIGURE 1. Neutron Dose vs Acceleration Voltage

APPLICATION for BOREHOLE LOGGING for URANIUM EXPLORATION

The PFN analysis technique leverages the unique properties of fission neutrons produced during the fission of uranium-235 to find uranium content in geological formations. Fast neutrons from D-T source gets moderated by interaction with formation material into thermal neutrons (with an energy of about 0.025 eV). The thermal neutrons produce fission in 235U and the prompt fission neutrons produced are detected using an epithermal neutron detector (see **FIGURE 2**) This buildup of fission neutrons prolong the extinction time of the epithermal neutron [3, 4] as shown in **FIGURE 3**. The epithermal neutron counts measured id directly proportional to the U-235 content present in the ore.



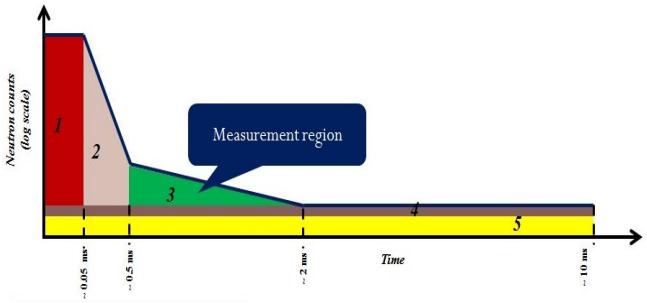
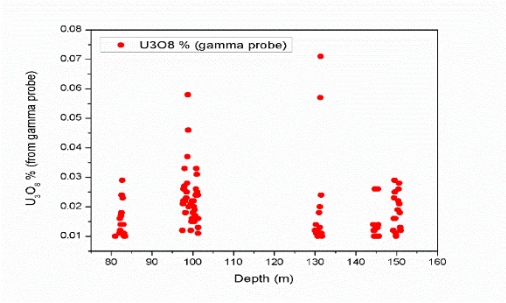
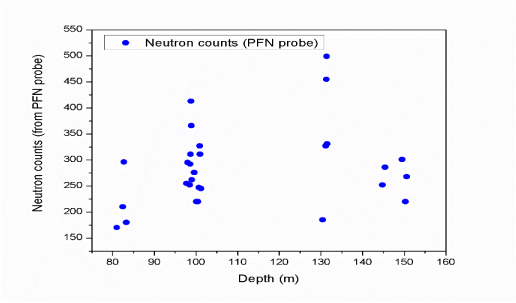


FIGURE 2. Borehole logging method using PFN, **FIGURE 3.** Timing of source, epithermal and thermal neutrons

PFN logging probe developed using indigenously produced sealed neutron generator has been tested at inclined





(a) (b)

FIGURE 4. (a) U_3O_8 content (%) at different depth measured by gamma probe (b) neutron count by PFN probe (55°) HQ size (78mm diameter) borehole at site. Probe was lowered in the borehole upto the depth of ~ 160 meters using steel wire rope winch assembly. Activity data using gamma logging at various depths was also recorded as

shown in **FIGURE 4(a)**.The corresponding neutron counts recorded using PFN logging probe is shown in **FIGURE 4(b)**. It corroborated with the gamma activity obtained at various depth position using gamma logging.

APPLICATION for BULK MATERIAL CHARACTERIZATION

The PFTNA method [5] integrates the benefits of both Fast Neutron Activation (FNA) and Thermal Neutron Activation (TNA). In this technique, a pulse of fast neutrons, generated by a D-T source, interacts with the sample through inelastic scattering (n, n'γ). Once the pulse ends (FIGURE 5), the neutrons are thermalized and interact with the sample via neutron capture (n, γ). Two distinct gamma spectra, captured using a BGO detector, are recorded over time and analyzed to determine the elemental composition. With PFTNA, it's possible to identify elements activated through both fast (C, O, N, Si, Fe, Al) and thermal (H, S, Al, Fe, Si) processes.

For PFTNA, the coal sample is exposed to a pulsed D-T neutron source with an output of 5 × 10^7 neutrons per second. The gamma spectra of the sample are collected at a right angle to both the neutron source and the detector during both the pulse ON and OFF phases. This is accomplished using a 3″ x 3″ BGO detector, which records time-stamped data to differentiate between gamma rays originating from inelastic scattering and those from neutron capture. The data shown in FIGURE 6 and FIGURE 7 illustrates the moisture content, carbon content, and gross calorific value of the coal, all measured using the PFTNA technique.

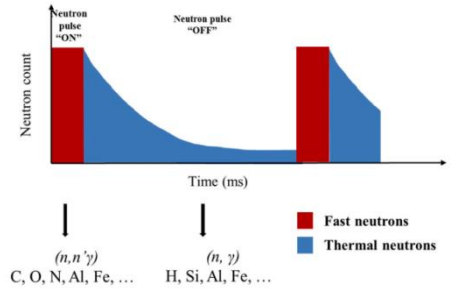


FIG 5. Timing of neutron pulse

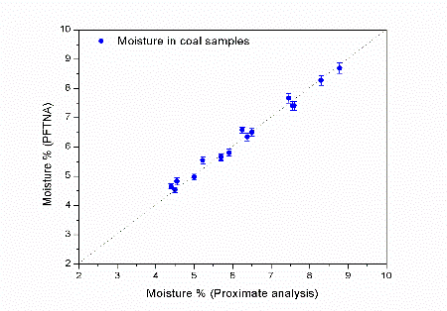
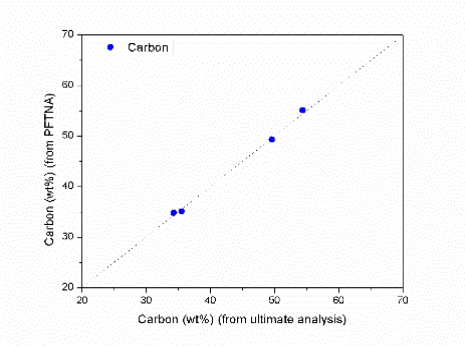
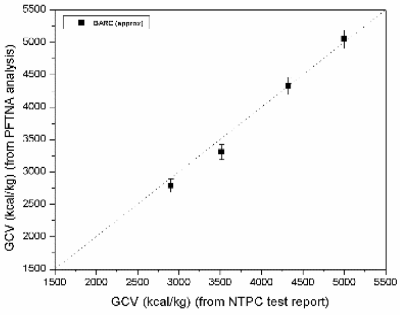


FIG 6. Comparison of moisture content by PFTNA and proximate analysis



(a)



(b)

FIGURE 7. Comparison of (a) carbon content by PFTNA and ultimate analysis (b) gross calorific value of coal by PFTNA and test report by NTPC.

REFERENCES

1. IAEA Radiation Technology Reports Series No. 1, 2012.
2. A. Jan Czubek, *Pulsed neutron method for uranium well logging*, Geophysics 37, (1971) 160.
3. Z. Feng, L. Tian, Q. Zhang, C. Qian, Seg Technical Program Program Expanded Abstract 2016.
4. D.R. Humphreys, R.W. Barnard, H.M. Bivens, Int. J. Appl. Radiat. Isot. 34 (1983) 261-268.
5. Sang H., Wang F., Liu L., Nucl. Instrum. Methods Phys. Res. B 239, 202-208

Temperature dependent electrical transport properties of W/WS_2 junction

Prachi Gurawal[1], Somdatta Singh[1], Akshay Tomar[1], Vivek K. Malik[2], and Ramesh Chandra[1*]

[1]*NSL, Institute Instrumentation Centre, Indian Institute of Technology Roorkee, Roorkee 247667, Uttarakhand, India*
[2]*Department of Physics, Indian Institute of Technology Roorkee, Roorkee 247667, Uttarakhand, India*
**Corresponding author: ramesh.chandra@ic.iitr.ac.in*

Abstract. Transition metal dichalcogenides (TMDs) comprising of layered structures and tunable band gaps, have been majorly explored over the last decade. Among them, tungsten disulfide (WS_2) particularly stands as an intriguing material for optoelectronic and electronic device applications. Herein, have synthesized a WS_2 thin film on n-type silicon (100) utilizing the magnetron sputtering for uniform and homogeneous nano-pebble growth, followed by fabrication of tungsten (W) contacts on the WS_2 film (W/WS_2) in circular geometry using a shadow mask. To study the current conduction mechanism, current-voltage (I-V) characteristics of the W/WS_2 junction have been measured for a temperature range of 270-350 K. The results indicate that current transport is not solely governed by thermionic emission. Schottky parameters extracted from the I-V-T measurements reveal that the ideality factor decreases while the barrier height increases with temperature. Furthermore, the standard deviation from homogeneity has been used to evaluate the deviations from thermionic emission.

Keywords: Sputtering, tungsten disulfide, thin film, circular geometry, thermionic emission.

INTRODUCTION

Transition metal dichalcogenides (TMDs), from a class of two-dimensional (2D) nanomaterials, possess distinctive characteristics and potential applications. The electrical behavior of these materials spans from semiconductor to metallic. In-plane covalent bonds and out-of-plane weak Van der Waals forces are present between the TMDs layers. These materials consist of a layer of transition metal (such as Mo, W, etc.), sandwiched between two chalcogenide layers, such as sulfur, selenium, or tellurium [1],[2]. Among TMDs, tungsten disulfide (WS_2) is one of the most researched owing to its interesting electronic and optical properties. In its bulk form, WS_2 has an indirect band gap of 1.35 eV, while its monolayer exhibits a direct band gap of 2.05 eV. Theoretical calculations suggest that WS_2 is likely to exhibit higher carrier mobility than MoS_2, as a consequence of its lower effective mass, making it a promising material for device applications. However, there have been limited studies on WS_2 compared to MoS_2 [3][4]. In particular, quantum transport studies of WS_2 are constrained by the scarcity of high-quality devices with reliable contacts at cryogenic temperatures [5]. The type of contact, i.e., Schottky or Ohmic, depends upon the difference between the metal work function and electron affinity, as well as the type of semiconductor.

In this report, we have synthesized the WS_2 thin film using the DC magnetron sputtering on n-type silicon substrate. Thereafter, a metal-semiconductor-metal (MSM) symmetric junction is fabricated using tungsten (W) metal as contacts in circular geometry (1 mm diameter). Following this, the electrical transport at the metal-semiconductor interface is investigated by the current-voltage (I-V) characteristics.

EXPERIMENTAL

The DC magnetron sputtering was used to synthesize uniform WS_2 thin film on a silicon (Si) substrate with (100) orientation. A WS_2 target of 2-inch diameter and 99.9% purity was used in the sputtering, acting as a cathode, and Si substrate placed 4.5 cm away from the target, which acted as an anode. The chamber was evacuated through a turbo molecular pump and a rotary pump. Thereafter, pure argon gas is purged in the chamber with a 20 sccm flow rate to form plasma. The deposition was performed at 8 mTorr working pressure and 60 W power for 10 min at a temperature of 200 ℃. The cross-section of the thin film for 10 min was used to estimate deposition rate, which is found to be ~0.78 nm/sec. The electrical measurements were performed on a WS_2 film, for 30 s deposition time, with circular W-metal contacts over it, fabricated using a shadow mask.

RESULTS AND DISCUSSION

The X-ray diffraction (diffractometer, Rigaku) pattern of WS_2 thin film is obtained to analyze the structural properties shown in Fig. 1(a). The diffraction peaks observed at an angle 12.80°, 35.23°, 62.85°, and 73.8° corresponding to the (002), (102), (107), and (203) planes (JCPDS ICDD No. 01-084-1398), respectively, affirm the single-phase grown WS_2 film. Fig. 1(b) shows the schematic representation of the circular W-metal contacts over the surface of the WS_2 thin film.

The surface features of WS_2 thin film are imagined employing field emission scanning electron microscopy (FE-SEM, Apreo ThermoFisher). The dense nano-pebble structure is observed with a thickness of 472 nm for 10 min deposition, as depicted in Fig. 1(c). The EDX analysis depicts homogeneous growth of WS_2 thin film and uniform distribution of constituent elements. Fig. 1(d-g) shows the SEM image, overlay (mixed color), W (red color), and S (yellow color) of the WS_2 thin film.

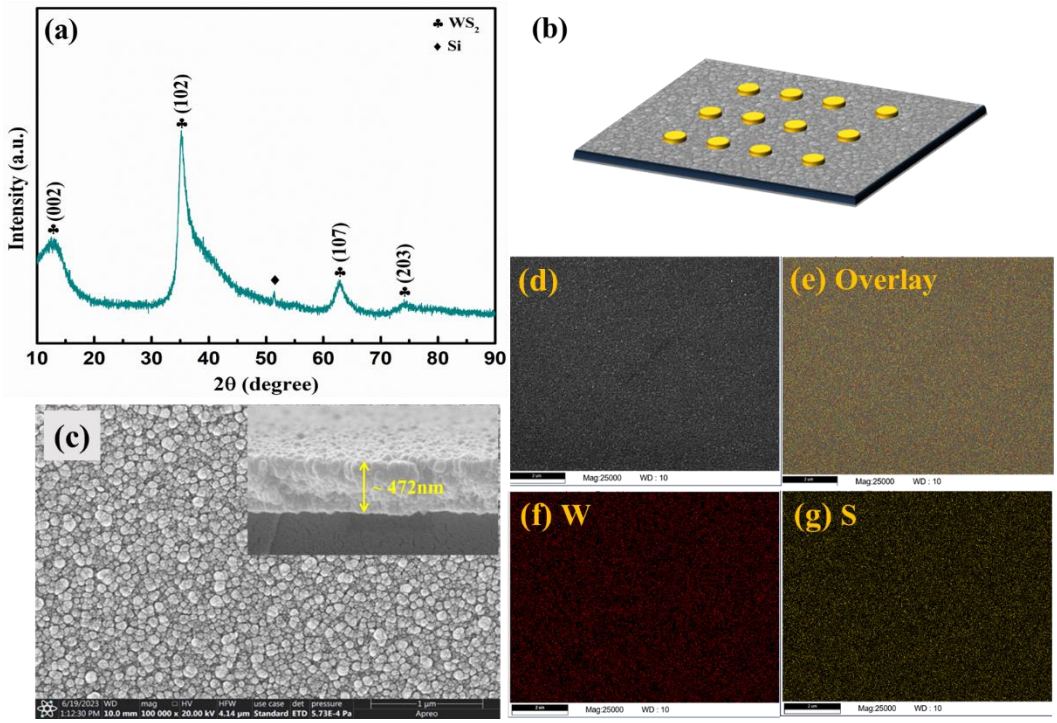


FIGURE 1. (a) The diffraction pattern of WS_2 thin film, (b) Schematic of metal W contacts on the WS_2 thin film, (c) the nano-pebble surface image with thickness in the inset, (d-g) the SEM image, overlay, W and S elements of WS_2 thin film.

In the thermionic emission model, the current conduction across the junction is described by the equation $\boldsymbol{I = I_o[exp(qV/nkT) - 1]}$ in which the saturation current is presented by $\boldsymbol{I_o = AA^* exp(-q\varphi_B/kT)}$, where $\boldsymbol{A}$ is the

contact area (~0.785x10^{-2} cm^2) of metal, $\boldsymbol{A^*}$is the Richardson's constant, $\boldsymbol{k}$ is the Boltzmann constant, $\boldsymbol{n}$ is the ideality factor [6]. The semi-logarithmic plot of I-V characteristics is shown in Fig. 2(a) for the temperature range 270 K to 350 K. The ideality, barrier height, and saturation current value are determined using the thermionic equation's forward I-V characteristics. The ideality factor and Schottky barrier height (SBH) expressions are as follows;

$$\boldsymbol{n = q/kT(dV/dlnI)}$$

and $$\boldsymbol{\varphi_B = (kT/q)ln(AA^*T^2/I_o)}$$

Fig. 2 (b) shows that the ideality factor decreases and SBH increases with the temperature from 270 K to 350 K. The room temperature values of the ideality factor and SBH are found to be 2.35 and 0.64 eV, respectively. Fig. 2(c) presents the Richardson plot [$\boldsymbol{ln(I_o/T^2) = ln(AA^*) - q\varphi_B/kT}$] showing non-ideal behavior, as the fitting is not linear. The slope of this plot gives SBH (φ_B) and intercept provide a value of Richardson constant (A^*). The determined values of φ_B and A^* from fitting 1 are 0.179 eV and 2.07x10^{-6} A/cm^{2}K^2 in temperature range 350 – 300 K while from fitting 2 in temperature range 290 – 270 K values obtained are 0.28 eV and 1.32x10^{-6} A/cm^{2}K^2, respectively.

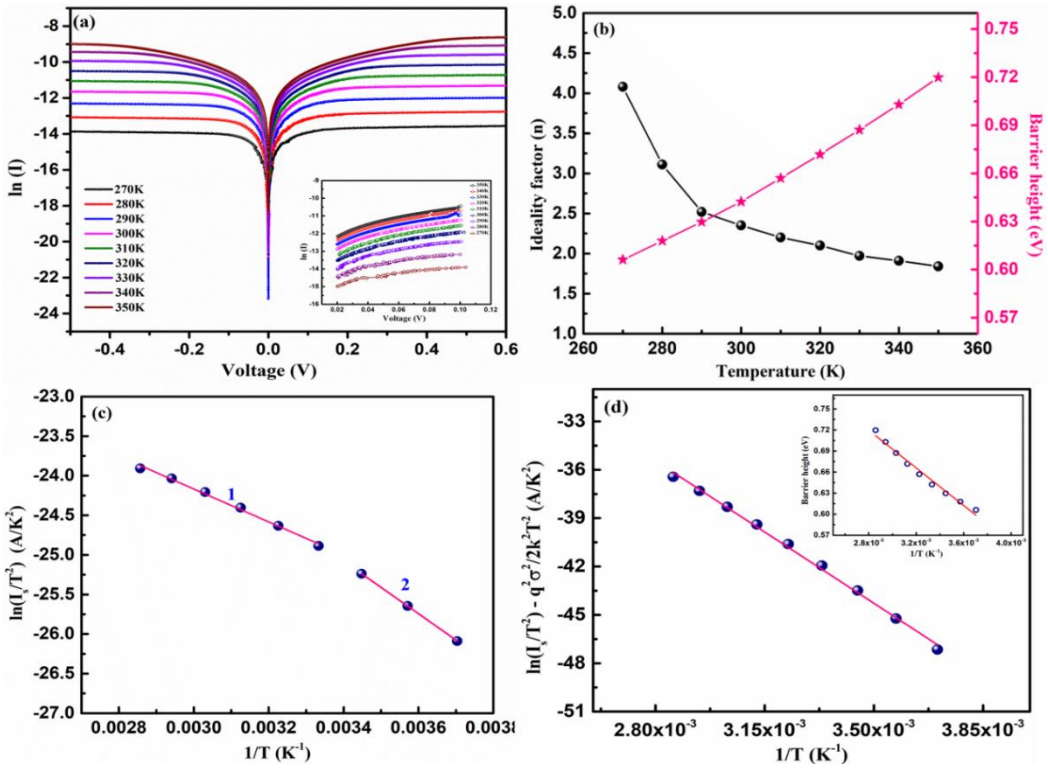


FIGURE 2. (a) The I-V characteristics curve, (b) Varying ideality factor and barrier height with respect to temperature, (c) Richardson plot, (d) Modified Richardson plot, from temperature 270-350K.

The departure from ideal behavior in the Richardson plot is explained by considering local inhomogeneity at the interface with the Gaussian distribution of the SBH. For this, the apparent barrier height was calculated with temperature shown in the inset of Fig. 2(d), which is found to be 1.0942 eV along with standard deviation of 0.151 eV. Both these terms were used to analyze the modified Richardson plot $\boldsymbol{ln(I_o/T^2) - (q^2\sigma^2/2k^2T^2) = ln(AA^*) - q\overline{\varphi_B}/kT}$ (Fig. 2d), having a linear fit with SBH and Richardson constant value of 1.08 eV and 117.7 A/cm^{2}K^2, respectively, in the temperature range of 270 –350 K.

CONCLUSION

In this study, we have investigated the electrical properties of W/WS_2 junction over a temperature range of 270 – 350 K. For this study, we have synthesized WS_2 thin films using a DC sputtering technique and subsequently fabricated tungsten contacts in a circular geometry. Our findings indicate that the Schottky barrier junction does not exhibit ideal behavior. At room temperature, the ideality factor and SBH are calculated to be 2.35 and 0.65 eV, respectively. Modified Richardson plots, which are fitted with straight lines, reveal an effective barrier height of 1.08 eV and a Richardson constant of 117.7 A/cm²-K². Deviation from thermionic emission was assessed by measuring the standard deviation from homogeneity.

ACKNOWLEDGMENTS

The author would like to acknowledge University Grants Commission (UGC) for financial support to carry out this work via grant no. 1617/(CSIRNETJUNE2019).

REFERENCES

[1] Neetika, S. Kumar, A. Sanger, H.K. Chourasiya, A. Kumar, K. Asokan, R. Chandra, V.K. Malik, Influence of barrier inhomogeneities on transport properties of Pt/MoS2 Schottky barrier junction, J Alloys Compd 797 (2019) 582–588. https://doi.org/10.1016/j.jallcom.2019.05.028.

[2] P. Gurawal, S. Singh, G. Malik, R. Adalati, M. Madaan, V.K. Malik, R. Chandra, Correlative morphology effects on surface characteristics of hydrophilic h-MoS2 thin films, Mater Chem Phys 341 (2025). https://doi.org/10.1016/j.matchemphys.2025.130870.

[3] W. Zhang, Z. Huang, W. Zhang, Y. Li, Two-dimensional semiconductors with possible high room temperature mobility, Nano Res 7 (2014) 1731–1737. https://doi.org/10.1007/s12274-014-0532-x.

[4] A. Kormányos, V. Zólyomi, N.D. Drummond, G. Burkard, Spin-Orbit Coupling, Quantum Dots, and Qubits in Monolayer Transition Metal Dichalcogenides, Phys Rev X 4 (2014) 11034. https://doi.org/10.1103/PhysRevX.4.011034.

[5] K. Cho, J. Pak, J.-K. Kim, K. Kang, T.-Y. Kim, J. Shin, B.Y. Choi, S. Chung, T. Lee, Contact-Engineered Electrical Properties of MoS2 Field-Effect Transistors via Selectively Deposited Thiol-Molecules, Advanced Materials 30 (2018) 1705540. https://doi.org/10.1002/adma.201705540.

[6] I. Jyothi, V. Janardhanam, J.-H. Kim, H.-J. Yun, J.-C. Jeong, H. Hong, S.-N. Lee, C.-J. Choi, Electrical and structural properties of Au/Yb Schottky contact on p-type GaN as a function of the annealing temperature, J Alloys Compd 688 (2016) 875–881. https://doi.org/10.1016/j.jallcom.2016.07.292.

Efficient Transmission Gate with Charge Plasma Doping: A Simulation Study

Gagan[1, *], Himanshu Marothya[1] Devender Kumar Soni[2] and Vishwas Acharya[1]

[1]*Department of Electrical Engineering, IIT Bombay, Mumbai, Maharashtra, India – 400076*

[2]*Department of Electronic Science, Kurukshetra University, Kurukshetra, Haryana, India – 136119*

[*] Corresponding author: gaganyadav838@gmail.com

Abstract: In this article, we present design and simulation study of a novel transmission gate that utilizes charge plasma doping to eliminate the requirement for physical doping. In contrast to conventional CMOS transmission gates, which normally require two transistors for the NOT gate and another two for signal transmission, our proposed design functions with just two silicon blocks. This design significantly streamlines the structure while still retaining its functionality. We employed Silvaco ATLAS to run detailed device-level and mixed-mode simulations to assess the performance and features of the proposed doping-less transmission gate. The voltage transfer characteristics (VTC) curve, transient analyses of the NOT gate, and transient and mixed-mode analyses of the final transmission gate are all important studies. Additionally, we present the carrier concentration profiles induced by charge plasma doping. The results demonstrate that our doping-less design not only reduces the complexity and transistor count but also achieves robust performance, making it a promising candidate for future integrated circuit applications.

Keywords: *Transmission gate, charge plasma doping, mixed-mode analyses, design flexibility, reconfigurable architecture*

INTRODUCTION

The advancement in integrated circuits technology demands continuous innovation to enhance performance, reduce complexity, silicon footprint efficiency and power consumption minimization. Additionally, stringent doping requirements are bottlenecks for achieving optimal device performance and scaling in advanced semiconductor manufacturing processes. One fundamental component of modern digital circuit technology is the transmission gate that can control the digital input whenever the control pulse is enabled. Traditional implementation of transmission gate logic using CMOS technology requires four distinct MOSFETs, two for inverter and the other two for signal transmission. This architecture is effective but at the same time, it introduces design complexities and increases transistor count, which results in reduced efficiency and scalability.

In this study, we propose a novel transmission gate design that eliminates the need for doping by utilizing the electro-statistically induced doping. Charge plasma or electrostatic doping was first introduced by Raymond J. E. Hueting et.al in 2008 [1-2]. In their study, Raymond utilized the charged plasma doping to demonstrate a p-n junction, by selecting the appropriate work functions and layer thickness, that induced electron plasma on one side of silicon and hole plasma on the other side. Using a similar approach, we create regions of required charge carriers without traditional doping methods, we choose the 3.9eV work function Hafnium metal for electron plasma and the 5.93eV work function Platinum metal to induce hole plasma [3], later these charge plasma regions are used as the source and drain of the devices. The proposed transmission gate design operates with only two silicon blocks, significantly simplifying the structure while maintaining the functionality of conventional design. We evaluate device performance, focusing on critical parameters such as voltage transfer characteristics (VTC) curve and transient responses of the inverter as well as the transmission gate through mixed-mode analyses.

SIMULATION SETUP AND DEVICE DESIGN

The proposed device design is featured in Fig. 1a which involves a “plus” like structure [4], which is divided by a thin 10nm wide SiO_2 layer to reduce the device-to-device interference. All simulation study is done using the Silvaco

ATLAS TCAD tool. The whole fin is 30nm wide and all the source and drain contacts are "L" shaped. One side of all contact is separated from the silicon with a thin oxide that is used to induce charge plasma doping and the other end of "L" shape contact is direct in contact of metal with the underlying silicon to efficiently collect charge carriers from the source and drain regions. Fig. 1b shows induced charge carriers due to the difference in work-function between metal and silicon underneath the dielectric layer. Near the oxide-silicon interface, the carrier concentration is highest at ~10^{19} per cm^3, these high-concentration regions serve as source and drain regions for four different transistors. In Fig. 1c we have shown the equivalent circuit symbol of the proposed device that is used to analyze this "plus" structure, the upper half of the device serves as two N-type MOSFETs and the lower half serves as two P-type MOSFETs.

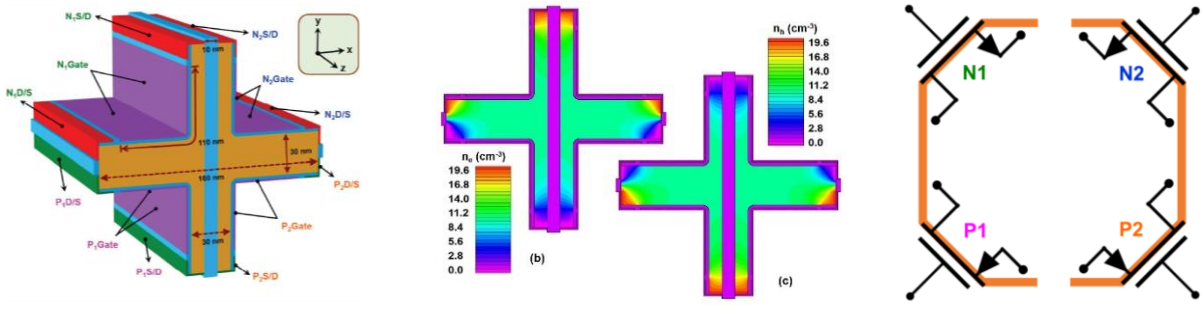


FIGURE 1. (a) Proposed device structure in three dimensions: The upper half comprises two charge plasma induced NMOS transistors, and the lower half contains two charge plasma induced PMOS transistors, all four gates are L-shaped. (b) 2-D contour plots along XY-plane for distribution of electron and hole concentration. (c) Equivalent circuit symbol for proposed device design.

RESULTS & DISCUSSION

Fig. 2a shows the connections that are used to carry circuit-level simulations, the gate of N1 and P1 transistors are shorted to get a common inverter input "A". The Source terminals of P2 and N2 transistors are shorted to get a common signal input "IN", and the Drain terminals of P2 and N2 transistors are shorted to obtain a common output "OUT" of the proposed transmission gate. Fig. 2b shows the equivalent CMOS schematic for a transmission gate involving an inverter, an NMOS (N2) and a PMOS (P2) connected in parallel. Transient analysis for the inverter realized from the proposed device architecture here is shown in Fig. 2c, where "A" is the input pulse to the inverter and "$\bar{A}$" is the output, I_{Leak} is the dynamic leakage current of the inverter, which only flows when the output transitions from one state of another.

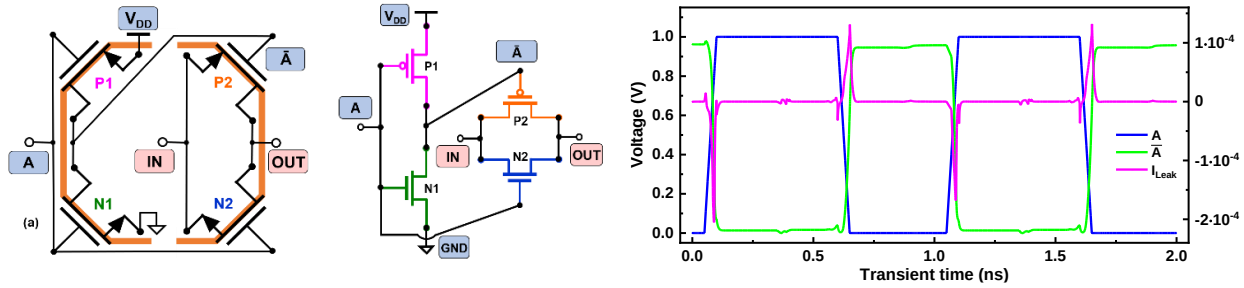
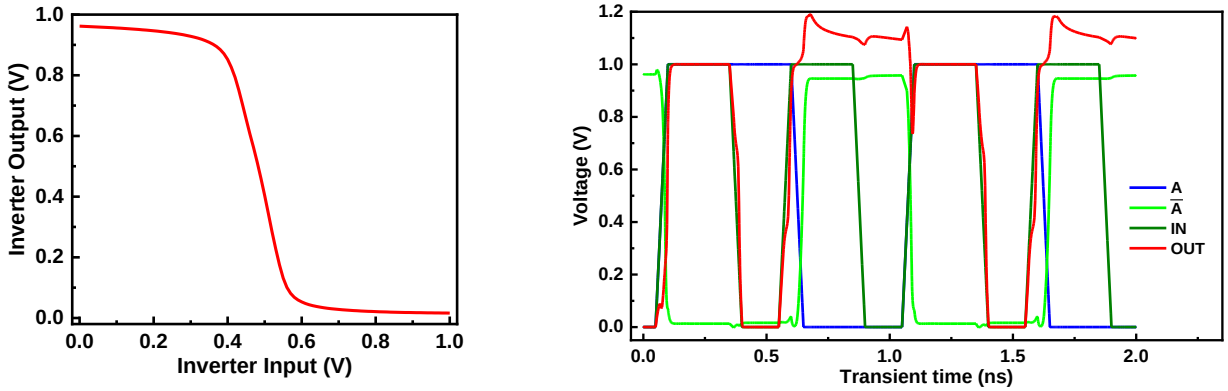


FIGURE 2. (a) Circuit of proposed transmission gate showing all the internal and external connections. (b)The equivalent circuit contains two transistors (P1 and N1) to realize an inverter and two transmission transistors (P2 and N2) in parallel, P1 and P2 are P-type MOSFETs whereas, N1 and N2 are N-type MOSFETs. (c) Transient analysis of the inverter circuit made from the proposed device, "A" is the input, "$\bar{A}$" is the output and I_{Leak} shows the leakage current.



(a) (b)

FIGURE 3. (a) VTC for the realized inverter circuit. (b) Transient analysis of the obtained transmission gate circuit realized from the proposed device architecture. "IN" and "OUT" represents the signal at the sorted source and sorted drain terminals respectively.

VTC characteristics for the inverter are shown in Fig. 3a, where sharp transition for the output switching between HIGH and LOW states within 0.1V is obtained. For transmission gate analyses, Fig. 3b shows the transient analysis for the input signal "IN" followed as "OUT" when the control input "A" is enabled (HIGH), whereas, for "A" as low, signal "OUT" does not follow "IN" signifying the high-impedance state of the realized transmission gate.

CONCLUSION

This study demonstrates a novel architecture of transmission gate without traditional doping instead, we employed charge plasma doping that induces charge carrier in silicon by the virtue of metal-semiconductor workfunction difference with a dielectric layer in between. This design employs only two silicon blocks, making it simpler than the traditional four-transistor design. Simulations were carried out by the Silvaco ATLAS tool and results show that the design performs well, while keeping all the needed functionality while reducing complexity and the number of transistors. This makes the proposed device-design a promising and efficient option for future ICs.

REFERENCES

1. R. J. E. Hueting, B. Rajasekharan, C. Salm and J. Schmitz, "The Charge Plasma P-N Diode," in IEEE Electron Device Letters, Vol. 29, no. 12, pp. 1367-1369, (2008).
2. B. Rajasekharan, R.J.E. Hueting, C. Salm, T. van Hemert, R.A.M. Wolters, J. Schmitz, "Fabrication and characterization of the charge-plasma diode," in IEEE Electron. Device Letters, Vol. 31, no. 6, pp. 528–530, (2010).
3. D. R. Lide, CRC Handbook on Chemistry and Physics, 89th ed. New York, NY, USA: Taylor & Francis, pp. 12– 114 (2008).
4. Gagan, Akansha Aggarwal, Unified multifunctional-reconfigurable architecture for device-circuit co-design, Microelectronics Journal, Vol. 151, 106329, ISSN 1879-2391, (2024).

micro-Kelvin Laboratory at BARC for Physics Research at Ultra Low Temperature

Neetesh Cheeta[1, a)], Anil Kumar[2], D Sarkar[1,3], K Dutta[1], S K Gamre[1], K M Rajbhoj[1], I B Thapa[1], R Pradeep[1], H H Patil[1], D Karmakar[1,3], Jagannath[1,3], L M Pant[1,3]

[1]*Technical Physics Division, Bhabha Atomic Research Center, Mumbai, 400085*
[2]*Department of Condensed Matter Physics, Tata Institute of Fundamental Research Mumbai, 400005*
[3]*Homi Bhabha National Institute, Mumbai,400094*
[a)]Corresponding author: Neetesh Cheeta (neeteshc@barc.gov.in)

Abstract. We report the measurement of an ultra-low temperature of 480 microkelvin (μK) in our laboratory after using the technique of adiabatic nuclear demagnetization on a 5 kg Copper block, which was attached to a dilution refrigerator through a superconducting switch made from aluminum. This experiment represents a significant advancement in low-temperature physics, demonstrating the efficacy of nuclear demagnetization techniques and the stability of superconducting switches in maintaining ultra-low temperatures. Accomplishment of such a stable environment of ultra-low temperature has the potential of implementation and utilization in future low-temperature experiments and applications relevant in the field of quantum computing.

Keywords : Adiabatic Nuclear Demagnetization, Nuclear Refrigeration, Dilution Refrigerator, milli-Kelvin temperature, micro-Kelvin temperature

INTRODUCTION

Physics at ultra-low-temperatures ranging from millikelvin (mK) to microkelvin (μK) possesses the accessibility of a series of quantum phenomena like superconductivity, superfluidity, magnetism and quantum phase transitions, hitherto masked by the thermal noise in the range of the temperatures of tens of Kelvin (K). At temperatures close to absolute zero (0 K or -273.15°C), rather than the classical physics, quantum mechanical processes become more prevalent, which allows the study of panoply of quantum phenomena. As also proven by prior measurements, attaining such temperatures requires innovative cooling techniques and has the potential of achieving breakthroughs in the understanding of the fundamental quantum properties of matter.

Reaching ultra-low temperatures is crucial for various scientific advancements and technological applications. In addition to the study of fundamental physics, it also enables the development of highly sensitive quantum devices including magnetic and superconducting sensors, Josephson junctions, single-photon emitters and so on. Each of these systems has a useful impact in the advancement of quantum computing. Ultra-low temperature helps in reducing the thermal scattering of electrons and ions, which is vital for precise measurements and the operation of quantum devices.

One of the key processes of achieving an ultra-low temperature is nuclear demagnetization, which involves aligning the nuclear spins of a material in a high magnetic field, followed by a reduction of the applied field to zero in an adiabatic and closed manner to obtain a lower temperature. This technique takes advantage of the fact that the nuclear spins have much lower magnetic moments compared to the electronic spins, allowing the room for an extremely low temperature.

The entire facility was shifted from TIFR and relocated at New Helium Plant in Technical Physics Division, Physics Group, BARC[1].

EXPERIMENTAL SETUP

Dilution Refrigerator: The dilution refrigerator employed in our experiment is a modified DRS 1000 model, which has a extra space at the bottom for mounting of adiabatic nuclear stage. This system is supplied by Leiden Cryogenics [2]. The system comprises of three primary components: 1.Dilution Refrigerator insert(DRS), 2. Gas Handling System(GHS), and the ^{4}He reservoir. The ^{3}He reservoir is installed within the GHS along with all vacuum pumps. This Refrigerator boasts significant cooling power, around 1000 μW at 100mK temperature. In the absence of the adiabatic nuclear demagnetization stage which is made from copper,

the system achieves cools to nearly 4.5 mK. The 1 K pot is maintained by a scroll pump, while mixture circulation is facilitated by two turbo pumps, which are cooled by chilled water and backed by another scroll pump.

Copper Block: The Copper(Cu) stage utilized in our experiment, has a mass of approximately 5 kg, which corresponds to 80 moles of Cu having 5cm diameter and 30cm length. The stage is constructed from 4N purity NOSV type alloy of electrolytic Copper (suitable for cryogenic measurements), exhibits a residual resistivity ratio more than 400. Heating due to eddy current is kept to minimum by gold plating and splitting it to 36 slits as shown in fig 1. Adiabatic demagnetization stage is such placed tha atleast $3/4^{th}$ part of the stage remain in 75% of the peak magnetic field. Also the superconducting coil is designed in a such way that residual field outside the coil remain in acceptable limits.

Aluminum Superconducting Switch: Superconducting heat switch serves as controlled thermal connection between mixing chamber and copper nuclear stage. For fabrication aluminum (6N pure) and copper (4N pure) foils (width 1.3cm, thickness 0.2mm overlapping 1cm) were pressed to weld together. Afterword's in a Vacuum chamber it is heated for half a day at 400°C temperature. To minimize eddy current heating and thermal conductivity, 30 foils were used, aligned parallel to the magnetic field. For thermal conduction it is kept in normal state with the help of applied magnetic field, and for thermal insulation it is kept in superconducting state by removing the applied magnetic field. For magnetic field a switch field coil is used made with Nb-Ti wires(thickness 75µm) having 7269 loops around copper matrix with proper shielding to reduce fringing fields.

PRINCIPAL OF ADIABATIC NUCLEAR DEMAGNETIZATION

Adiabatic nuclear demagnetization is a cooling technique used to achieve ultra-low temperatures, often in the microkelvin range. Every nucleus with a non-zero spin has a magnetic moment. In the presence of an external magnetic field, these nuclear spins align with or against the field, creating different energy levels. The entropy of the nuclear spin system depends on the alignment of these spins. At high temperatures or low magnetic fields, the spins are randomly oriented, corresponding to high entropy. At low temperatures or high magnetic fields, the spins align more with the field, reducing entropy.

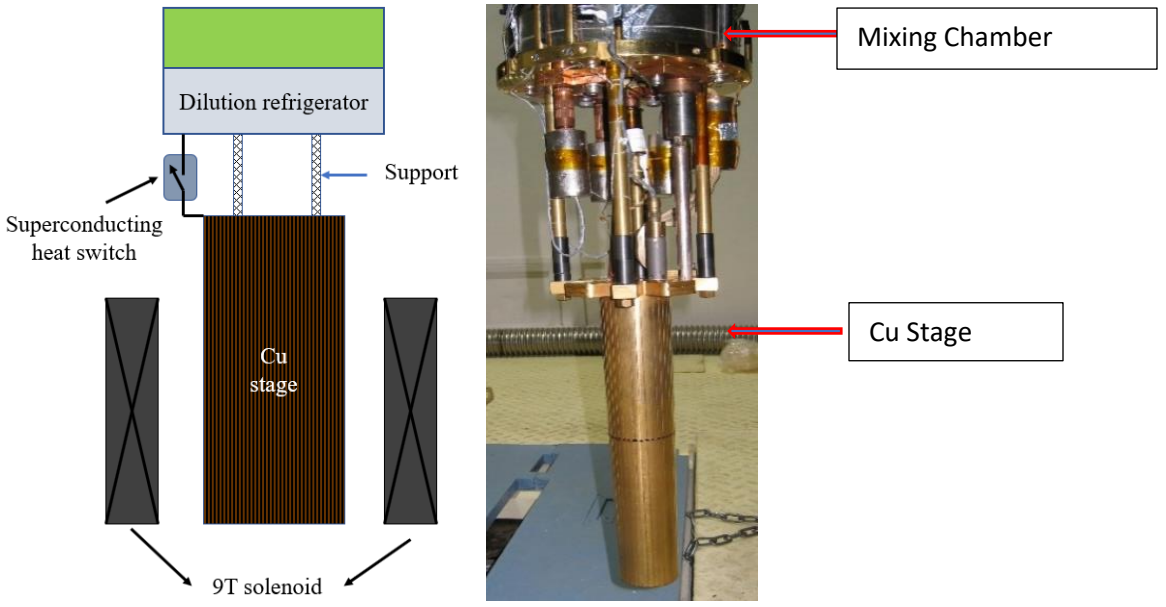


FIGURE 1: Schematic diagram for adiabatic nuclear demagnetization and actual image of Copper stage

The process begins with the material, often a high-purity metal like Copper, being placed in a strong magnetic field at low temperatures, achieved using a dilution refrigerator. This strong magnetic field aligns the nuclear spins and thus significantly reduces their entropy. During this stage, the system is in thermal equilibrium with the dilution refrigerator, meaning the electron and nuclear spins are at the same temperature. Once the nuclear spins are well-aligned, the material is thermally isolated from the dilution refrigerator. The magnetic field is then gradually reduced in an adiabatic process, such that no heat is exchanged with the

surroundings and the process is quasi-static. As the magnetic field decreases, the energy levels of the nuclear spins move closer together. Thus, to maintain the adiabatic condition (constant entropy), the temperature of the nuclear spin system must decrease.

EXPERIMENTAL PROCESS

The experimental procedure commenced with overnight pumping of the inner vacuum chamber (IVC) and helium-3 line to achieve a high vacuum. Following this, a comprehensive ultra-high vacuum leak testing was performed on all vacuum lines. The positive and negative pressure tests were conducted on the 1K flow to detect any potential capillary blockages. Helium exchange gas was then introduced into the still and IVC at a pressure of 20 mbar. The 1K pot was pressurized with helium gas at 1.8 bar to ensure proper operation. Liquid nitrogen was transferred into the cryostat and allowed to cool the system overnight. After this, the liquid nitrogen was removed, and the cryostat was pumped for 1 hour and purged with helium gas to prepare it for the next phase. Helium gas was filled into the cryostat at atmospheric pressure and connected to a recovery system. Subsequently, liquid helium was transferred into the cryostat.

To remove the residual helium (He) exchange gas, the IVC was pumped overnight. The SORB heater was then heated incrementally from 10 to 30 mA over 1.5 hours for maintaining the vacuum level, as IVC pumping is to be turned off. Then 1K pot pumping is started Following this, condensation of He^3 was initiated once the temperature dropped below 2K. After helium-3 was fully condensed, the condensation of He^4 began. The system was kept in normal circulation for 24 hours, during which temperatures below 10 mK were achieved. With continued circulation, the temperature further decreased to below 6 mK after one day. This temperature is transferred to Cu stage Via a Superconducting Heat switch.

To reach even lower temperatures, the Copper stage was magnetized with a 9T magnetic field using a high current power supply, a process that took 7 to 8 hours. After magnetization, the persistent heater current was removed, and the lead current was ramped down to zero over approximately 2 hours. During this process, the Copper stage temporarily heated up to 180 mK. A waiting period of three days allowed the Copper stage temperature to lower to 45 mK. After this, adiabatic nuclear demagnetization was performed with an appropriate ramping rate over 12 hours, achieving a minimum temperature of 480 μK on the Copper stage.

Measurement of temperature: To measure the temperature of the Copper nuclear stage, we employ a platinum NMR thermometer mounted directly on it. This setup includes a bundle of 4000 platinum wires, each with a diameter of 20 μm and a length of approximately 8 mm. These wires work in tandem with an NMR (Nuclear Magnetic Resonance) excitation coil, which is precisely constructed with 770 windings of 25 μm diameter Copper wire. The coil has an inductance of 1.3 mH. Measurement of the temperature is based on the dependence of spin-lattice relaxation time on the system's temperature, utilizing this property to determine the precise temperature of the Copper stage.

RESULT AND DISCUSSION

In this experiment, we successfully achieved a stable temperature of 480 μK using the adiabatic nuclear demagnetization of a 5 kg Copper block. This experiment marked a significant improvement, setting a new benchmark for achievable temperatures. The stability of the temperature of 480 μK over time highlighted the reliability and precision of the experimental setup, including the high purity of the Copper block, the effective use of the dilution refrigerator and the performance of the superconducting switch.

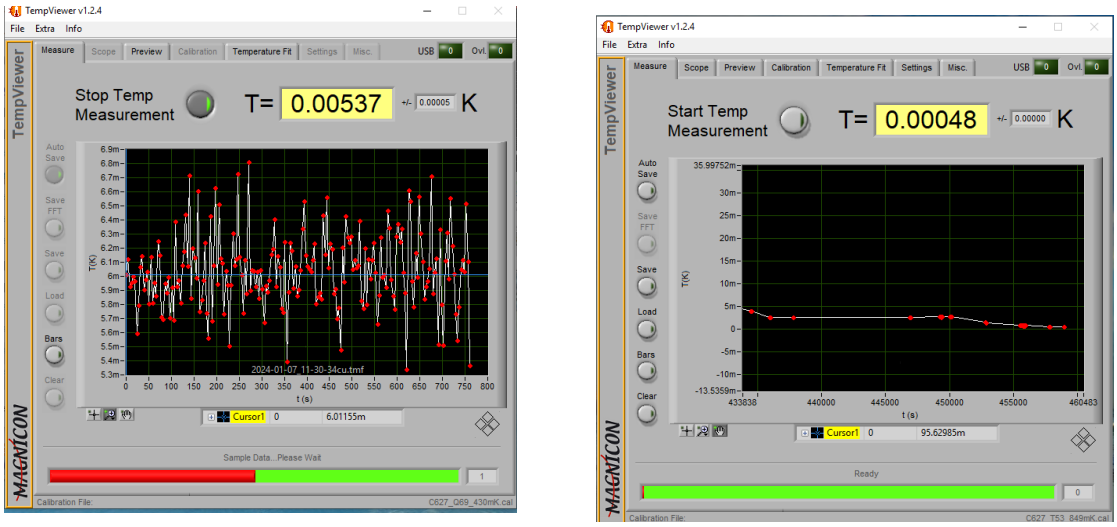


FIGURE 2: Ultra low temperature measured on mixing chamber on 7th Jan 2024 (left), (b) Ultra low temperature measured on Cu stage upon adiabatic demagnetization On 21st may 2024(right)

Overall, our results confirmed the viability of using the process of adiabatic nuclear demagnetization for reaching and sustaining temperatures in the μK-range, opening new possibilities for research in quantum materials and low-temperature physics. It provides a platform for studying phenomena that require ultra-low temperatures and contributes to the development of new technologies.

ACKNOWLEDGEMENT

we acknowledge the support of Shri G T Zinzuvadiya and Shri Sunil Kumar for night shift duty.

REFERENCES

1. Setting up a micro-Kelvin Laboratory at Bhabha Atomic Research Center, Mumbai, Neetesh Cheeta, Anil Kumar, D Sarkar, K Dutta, Jagannath, L M Pant, presented in SSPS 2023, Vizag.
2. Setting up of a micro-Kelvin refrigerator facility at TIFR: H. R. Naren, R. S. Sannabhadti, Anil Kumar, V. Arolkar, Arlette de Waard, G. Frossati and S. Ramakrishan, CURRENT SCIENCE, 2011, 101

Analysing the changes observed in Neutron diffraction peaks of $Cs_6H(HSO_4)_3(H_2PO_4)_4$ crystal as it undergoes Deterioration

Rajul Ranjan Choudhury[1,2* a)] and R. Chitra[1 b)]

[1)] *Solid State Physics Division, Bhabha Atomic Research Center, Trombay Mumbai, India 400085.*
[2)] *Homi Bhabha National Institute, Mumbai, India 400085.*
[a)] Corresponding author: *rajul@barc.gov.in*, [b)] *rchitra@barc.gov.in*

Abstract. Single crystal neutron diffraction investigation on superprotonic crystal $Cs_6H(HSO_4)_3(H_2PO_4)_4$ belonging to $CsHSO_4$–CsH_2PO_4–H_2O solid solution system was undertaken by us earlier, it was found that the crystal underwent a spontaneous deterioration after a few days of data collection most likely due to change in ambient condition. Structure for the crystal was obtained before as well as after deterioration and it was found that the unit cell of the crystal had contracted due to strengthening of the O-H---O hydrogen bonds of the crystals. We report here how the above mention change in the hydrogen bonding affected the diffraction intensities as well as peak shapes for the crystal, Williamson-Hall analysis is performed to estimate the lattice strains introduced due to this change in hydrogen bonding network. Finally the changes in the potential energy contour of the O-H---O hydrogen bonds have been modeled and expected consequences of these changes on proton conduction discussed.

Keywords: Single crystal, Diffraction, Peak shape, Hydrogen bonds, Williamson-Hall analysis

INTRODUCTION

Proton conduction in crystals belonging to $CsHSO_4$–CsH_2PO_4–H_2O solid solution system has been studied extensively since many of these crystals exhibit superprotonic properties at elevated temperatures. Many new crystals belonging to this family have been grown [1] with the aim to get proton conductors having highly stable superprotonic phase as found in the $CsHSO_4$ [2], and high conductivity, as found in CsH_2PO_4 [3]. $Cs_6H(HSO_4)_3(H_2PO_4)_4$ (here after abbreviated as Cs6) is one such crystal crystallized from aqueous solutions of $CsHSO_4$ and CsH_2PO_4 in the molar ratio of 2 : 3 [1]. We had previously performed Single crystal neutron diffraction investigation on Cs6 crystal under ambient condition [4], since single crystal neutron diffraction experiments take days to complete one has to monitor the crystal stability throughout the data collection, this is usually done by repeatedly recording a selected strong reflection after a fixed interval of time, during the data collection of Cs6 it was observed that after about a month's data collection the intensity of the selected standard as well as its peak position started changing. Taking this as an indication of spontaneous deterioration of the crystal, complete data was recollection after the intensity as well as peak position of the standard reflection stabilized to a new value. Hence two crystal structure of Cs6 were obtained, first using data collected prior to structure change and second using the data collected after the change. Comparison of the two structures revealed that the change in crystal structure was mainly due to the shrinkage of the unit cell resulting from the change in the geometry of strong asymmetric O-H---O hydrogen bond connecting the SO_4 and PO_4 groups within the crystal [4]. Since the above mentioned structural change not only resulted in shifting of the diffraction peaks but also a change in the intensity as well as FWHM of the peaks, we performed peak shape analysis of few of the selected strong diffraction peaks before and after the deterioration in order to study the lattice strains developed within the single crystal due to spontaneous deterioration, we report here the results of this analysis along with discussion on what might be the cause of this structure change and its likely influence on proton conduction in Cs6.

PEAK SHAPE ANALYSIS

We have selected 11 strong diffraction peaks as shown in Figure-1 for our analysis, Table -1 gives details like the hkl values, peak positions (2θ), d values, Gaussian peak widths (w), integral peak widths (β) etc for these peaks both before (top line) and after (bottom line) deterioration. Using this data we performed Williamson-Hall analysis which is an integral breadth (β) based method used to estimate average coherent particle size and average internal strain. According to this methods a linear fit between βCos(θ) Vs 4Sin(θ) data points from a crystalline diffraction pattern gives average particle size as intercept and average internal strain (ε) as the slop. Figure-2a shows the results for Cs6

crystals, it is observed that there is an increase in the average internal strain within the Cs6 crystal from 0.237 to 0.396 as it undergoes deterioration.

The abrupt change in the unit cell of Cs6 during the neutron single crystal data collection appears to be due to surface dehydration. Panithipongwut [5] had studied dehydration of $Cs_6(H_2SO_4)_3(H_{1.5}PO_4)_4$ (another way of writing the chemical formula of $Cs_6H(HSO_4)_3(H_2PO_4)_4$) and found that under conditions of low humidity, the dehydration reaction transformed the compound to $Cs_6(H_{2-0.5x}SO_4)_3(H_{1.5}PO_4)_{4-x}$, also having cubic structure, but with a smaller unit cell (here x = 0-1 indicates the degree of dehydration).

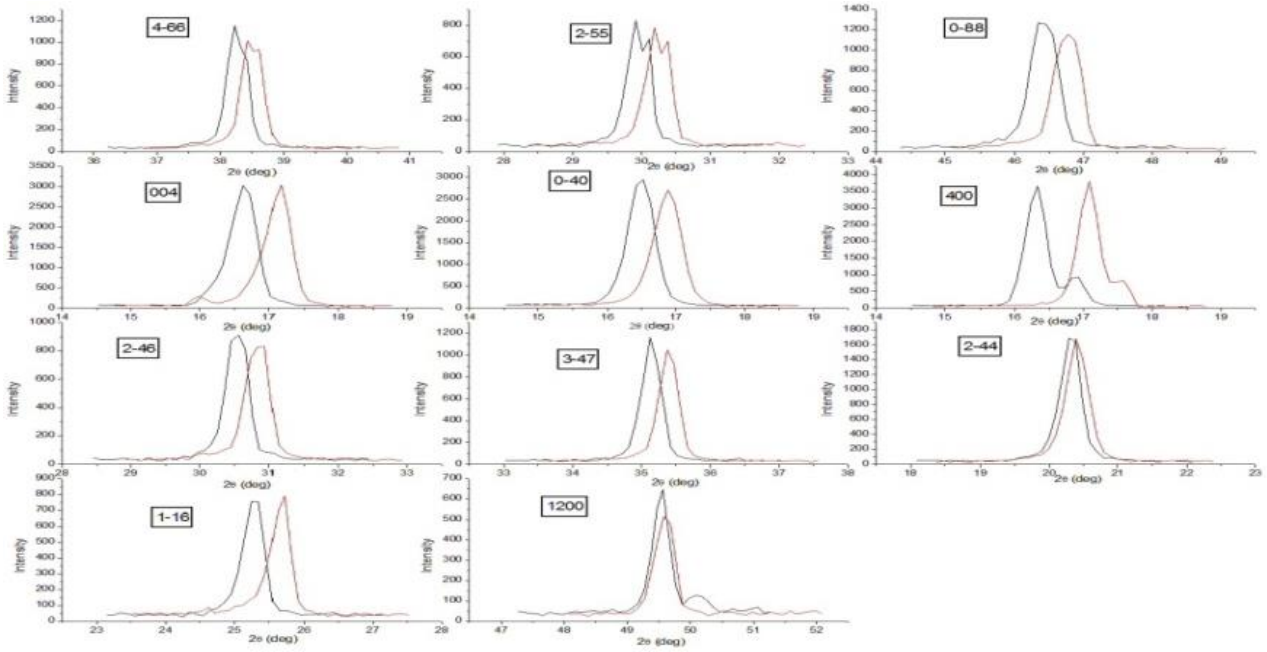


Figure-1 Selected strong diffraction peaks of Cs6 before (black) and after (red) deterioration

TABLE-1 hkl values, peak position (2θ), d values, Gaussian peak width (w), integral peak width (β) for selected peaks of Cs6 before (top line) and after (bottom line) deterioration

	H K L	2θ	d	w	β	Δ(d)	Δ (d)/d
1	0 -4 0	16.49	3.473	0.381	5.926	0.078	0.0224
		16.87	3.395	0.407	6.273		
2	0 0 4	16.62	3.446	0.399	5.984	0.102	0.0295
		17.13	3.344	0.374	5.812		
3	4 0 0	16.31	3.511	0.301	5.321	0.156	0.0444
		17.07	3.355	0.312	5.015		
4	2 -2 4	20.31	2.825	0.301	5.263	0.013	0.0046
		20.40	2.812	0.331	5.321		
5	1 -1 6	25.27	2.277	0.304	6.351	0.034	0.0149
		25.66	2.243	0.281	6.231		
6	2 -5 5	29.95	1.927	0.333	6.097	0.017	0.0088
		30.23	1.910	0.353	6.542		
7	2 -4 6	30.53	1.891	0.309	6.072	0.017	0.0089
		30.83	1.874	0.334	6.701		
8	3 -4 7	35.13	1.650	0.281	4.924	0.012	0.0072
		35.39	1.638	0.283	5.111		
9	4 -6 6	38.27	1.519	0.318	5.407	0.008	0.0052

		38.50	1.511	0.335	5.893		
10	0 -8 8	46.42	1.264	0.385	6.777	0.009	0.0071
		46.76	1.255	0.383	6.479		
11	12 0 0	49.53	1.189	0.267	6.871	0.002	0.0016
		49.59	1.187	0.307	7.024		

HYROGEN BOND ENERGY CALCULATION

Hydrogen bonds interactions play the most important role in the proton conduction in Cs6, any change in the hydrogen bond geometry is expected to have a significant effect on its proton conduction. In order to obtain the hydrogen bond energy, we have used Diabatic state model [6], it gives the potential energy for an X-H---Y bond as

$E\pm(r,R) = ½[V1(r)+V2(R-r)] \pm ½[(V1(r)-V2(R-r))^2+4\Delta(R)^2]^{1/2}$

R is X---Y distance, r is X-H distance, V1(r) is Morse potential for free X-H bond and V2(R-r) is Morse potential for free H-Y bond, Δ(R) is the coupling energy term. The O-H—O hydrogen bond in Cs6 is between PO_4 and SO_4 groups that have different Hydrogen donating powers. Since SO_4 group is more acidic than the PO_4 group the H atom in O-H—O hydrogen bond of Cs6 is located nearer to PO_4 group. The asymmetry in the hydrogen donating power of free donor & acceptor groups is modelled by taking Morse potential parameter (b2=2.16) for SO_4 group to be slightly smaller than the Morse potential parameter (b1=2.21) for PO_4 group, hence even though both X-H and Y-H bonds are same (X-H = Y-H = O-H) in the case of O-H—O hydrogen bond of Cs6 we have used slightly different Morse potential parameters for them. This resulted in a potential energy surface that is slightly asymmetric with minimum energy (Emin) lying closer to PO_4 (figure-2b). Potential energy Minima before & after deterioration are -145.6 Kcal/mol and -150.5 Kcal/mol respectively. Zero-point energy E0 for the H atom is obtained using FINDIF which is a Windows-based application written by A. M. Halpen of Indiana state university, E0 values before and after deterioration are -142.1 Kcal/mol and -146.7 Kcal.mol respectively, effective barrier height encountered by H atoms is defined as Veff=V(barrier)-E0, it is found to be 7.4 Kcal/mol and 4.1 Kcal/mol before and after deterioration. We can define the hydrogen bond energy (Ehb) as the extra stabilizing energy experienced by the H atom covalently bonded to donor O atom due to the presence of an acceptor O atom, hence Ehb=Emin-E(O-H), where covalent bond energy E(O-H) is given as E(O-H)=-132 Kcal/mol. Ehb values before and after deterioration are -13.5 Kcal/mol and -18.5 Kcal/mol respectively, in order to break these hydrogen bond, one has to supply energy equal to -Ehb.

Proton transport in Cs6 takes place by the Grotthuss mechanism which is a two-step process, step-1) hopping of proton from donor to acceptor atom step-2) rotation of the acceptor group by breaking of the existing H-bonds and making new ones. Both the steps involve energy expenditure but the step that requires higher energy is usually the rate limiting step. In case of Cs6 crystals the energy (~Veff) required by H atom to hop from donor to acceptor atom is smaller than the energy required to break the hydrogen bond (-Ehb). Hence step-2 which involves breaking of existing H-bonds is most likely the rate limiting step for proton conduction in Cs6. Above calculations show that the Deterioration results in reduction of Veff but increase in Ehb. Since step-2 is the rate limiting step for proton conduction in Cs6, we expect that deterioration resulting in increase in Ehb will lead to reduced rate of proton conduction in Cs6 crystals.

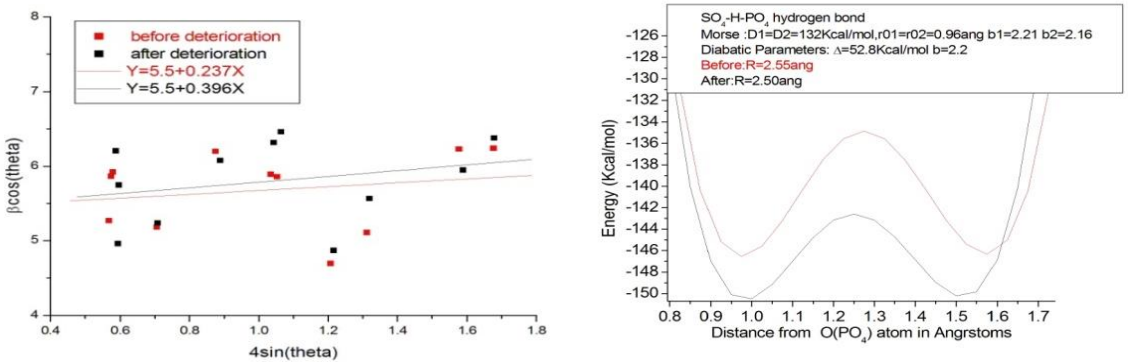


Figure-2 (a) Williamson-Hall plots for Cs6 before (red) and after (black) deterioration (b) potential energy surface for O-H—O hydrogen bond in Cs6 before (red) and after (black) deterioration

REFERENCES

1. I. P. Makarova, V. V. Grebenev, V. A. Komornikov, and E. V. Selezneva Crystallography Reports, 2016, 61, pp. 918–922
2. A. I. Baranov, L. A. Shuvalov, and N. M. Shchagina, Pis'ma Zh. Eksp. Teor. Fiz., 1982, 36 (11), pp. 381.
3. A. I. Baranov, V. P. Khiznichenko, V. A. Sandler, and L. A. Shuvalov, Ferroelectrics, 1988, 81, pp. 183.
4. R. R. Choudhury, R. Chitra, I. P. Makarova, E. V. Selezneva and V. A. Komornikov, Bull. Mater. Sci. (2021) 44:108
5. C. Panithipongwut https://thesis.library.caltech.edu/7778/1/ChatrCompletedThesis.pdf.
6. R. H.McKenzie, Chemical Physics Letters , 535, (2012) 196

Investigating the Role of Strontium on the Bioactivity of Silicate Glass and the Effect of Doping Fe

S. Rane[1] and R. Raut Dessai[1,*]
[1]*School of Physical and Applied Sciences, Goa University, Taleigao Plateau, Panjim, Goa 403206, India*
[*]*reshma@unigoa.ac.in*

Abstract. The Bioactive glasses are playing crucial role in bone tissue engineering as they are used as temporary template for tissue regeneration. With regards to their design some issue still remains unfolded. Strontium is one of the trace elements that plays role to slow the breakdown of old bone. In the present study strontium silicate glass doped with Fe is synthesized by conventional melt quenching technique. The glass doped with Fe exhibited higher relative percentage of Q^2 silica species indicating formation of silanol (Si-OH) groups and enhanced bioactivity. In vitro study soaking pellets of glass powder in simulated body fluid for 3 ,7 and 21 days showed appearance of Hydroxyapatite (HAp) crystals. Crystalline phases of HAp became more prominent in samples soaked for 21 days, enhancing their bioactivity. Enhancement of bioactivity can be achieved by tailoring the composition of Fe and Sr to meet specific performance in biomedical applications.

Keywords: Glass, Bioactivity, Strontium, Raman spectra, Hydroxyapatite, Melt quenching

INTRODUCTION

With the increase in geriatric population in the world, the number of bone and joint related problems are also on the rise hence there is a constant demand for newer and newer biomaterials for bone degeneration. Bioactive glasses (BGs) and glass ceramics (GCs) are widely used as implantable material for various bone disorders and for bone tissue regeneration. Biocompatibility and bioactivity have long been recognized as crucial for implants in bone recovery, dating back to the 1960s when synthetic materials were first explored for medical use. Bioactive glass is a specialized biomaterial that stimulates bone regeneration and integrates with surrounding tissue. The bioactivity of glasses is determined by the rate of Hydroxyapatite (HAp) formation on their surface [1]. The composition of bioactive glasses is critical to their performance, consisting of a silica-based system with additions of sodium, calcium, and phosphate. Many varieties of bioactive glasses are being explored starting from the silicate glass to borate and phosphate glasses. These elements work synergistically to facilitate the formation of HAp layer upon exposure to biological fluids. Strontium and iron are among the elements extensively studied in the glass composition. Strontium is well known for its role in bone health to stimulate bone growth which could be beneficial for patients having bone-related disorders [2]. Strontium can be substituted for calcium due to its chemical similarity and having similar biological functions. Iron is essential for the growth, proliferation, and differentiation of bone cells. It has been studied that incorporating Iron into the glass may slightly reduce its in-vitro bioactivity [3]. In the present work strontium silicate glasses have been synthesized by conventional melt quenching method to study the effect of strontium and Iron on the bioactivity of the glass.

EXPERIMENTAL

A series of strontium silicate glasses were synthesized by melt quenching method using 99% pure analytical grade mixture of SiO_2, $CaCO_3$, Na_2CO_3, K_2CO_3, $MgCO_3$, P_2O_5, $SrCO_3$ and Fe_2O_3. The glass batches were melted in alumina crucible at temperature 1400°C, holding temperature at 800°C for 1 hour to decompose calcium carbonate. The molten material was rapidly air quenched; the resulting glass beads were annealed in a preheated furnace at 350°C for 1 hour to alleviate strains, with subsequent gradual cooling to room temperature. Simulated body fluid (SBF) was prepared by Kukobo method [4] and the pellets of glass powder soaked in SBF at body temperature of 37ºC for the duration of 3,7 and 21 days. X-ray diffraction pattern before and after soaking in SBF, were obtained from Rigaku SmartLab X-ray diffractometer with CuK_α target of wavelength 1.5405 Å. The scan was carried out in the 2θ range of 20º to 80º , with a step size of 0.02º and 5º/min speed. Raman spectra of the glass beads were recorded on a Horiba LabRAM HR Raman spectrophotometer in the range 500 to 1200 cm^{-1} wavenumber using a diode laser of wavelength 532 nm. Glass transition temperatures obtained by Differential thermal analyzer Shimadzu DT4 instrument and the densities of the glass were determined by water displacement method.

RESULTS AND DISCUSSIONS

The amorphous nature of glass was confirmed by the appearance of broad hump at 31° and absence of crystalline peaks in X-ray diffraction patten Fig 1(a). The glass transition temperatures (T_g) and the density of the glass samples are shown in Table-1. With increase in strontium concentration the glass transition temperature decreases. This indicated that the incorporation of Sr into the glass matrix leads to the weakening of the glass network structure, thereby lowering T_g. The glass sample containing iron (Fe) exhibited higher T_g values compared to those devoid of Fe. This observation implies that the inclusion of Fe enhances the structural stability of the glass network, resulting in elevated T_g values. Densities of the different glasses were found to be in the range 2.76 to 2.79. The glasses devoid of Fe exhibit a more compact nature compared to those containing Fe, highlighting the significant impact of iron on the structural arrangement in the glass matrix, which has direct implication on pore structure of glass.

TABLE 1. Glass transition temperature and density values of the glass

Glass Sample	Glass Transition Temperature	Density (g/cc)
BG-3Sr	872°C	2.7876 ± 0.0017
BG-5Sr	870°C	2.7915 ± 0.0016
BG-7Sr	867°C	2.7933 ± 0.0016
BG-3Sr0.5Fe	871°C	2.7659 ± 0.0017

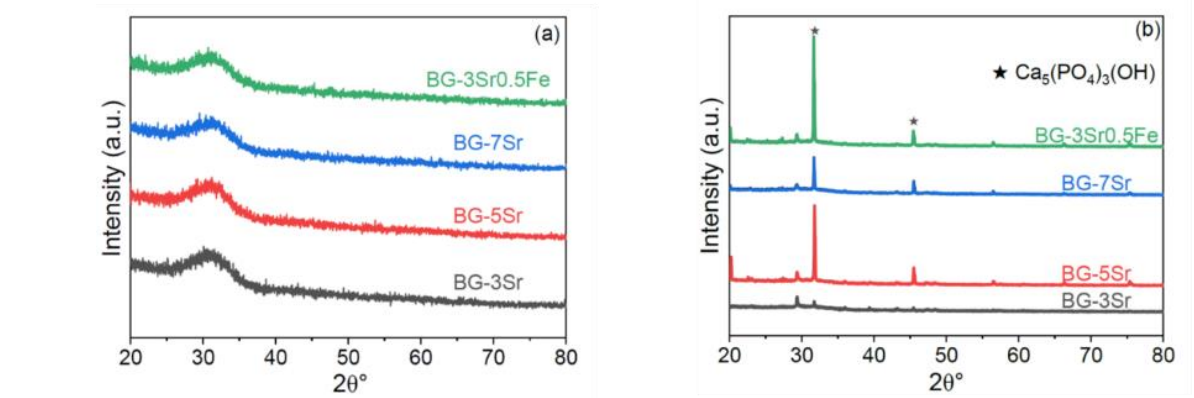


FIGURE 1. XRD plots of glass samples (a) as synthesized (b) samples soaked in the SBF solution for 21 days

Deconvolution of Raman bands allow the identification of specific Si-O vibrations and structural groups attributed to different Q^n silica units within the glass shown in Fig. 2. In silicate glass, the structure is primarily composed of a network of silicon-oxygen tetrahedra. The connectivity and arrangement of these tetrahedra are characterized by the Q^n notation, n represents the number of bridging oxygens attached to a silicon atom. In a Q^4 unit, all four oxygen atoms are bridging, forming a fully interconnected tetrahedral network. In contrast, Q^3, Q^2 and Q^1 units have 3, 2, and 1 bridging oxygen respectively, with the remaining oxygen(s) being non-bridging. The Q^0 unit has no bridging oxygens, representing a completely isolated tetrahedron. The distribution of these Q^n units influence the glass's physical properties. The deconvoluted peaks of glass sample BG-3Sr and BG-3Sr0.5Fe are shown in Fig. 2(a) and Fig. 2(b). The relative percentages of various silica species present in a sample are determined by analyzing the relative areas of the deconvoluted Raman peaks and are shown in bar graph in Fig. 2(c). Experimental evidence suggests that the abundance of Q^2 silica species plays a pivotal role in promoting the bioactivity. It is observed that the BG-3Sr0.5Fe sample exhibits the highest number of Q^2 silica species, indicating a potentially enhanced bioactivity. The prevalence of Q^2 silica species is linked to the formation of silanol (Si-OH) groups upon glass dissolution, facilitating interactions with biological fluids and promoting the deposition of hydroxyapatite (HAp) on the glass surface. Thus, the higher proportion of Q^2 species in the BG-3Sr0.5Fe sample suggests a greater tendency for bioactivity.

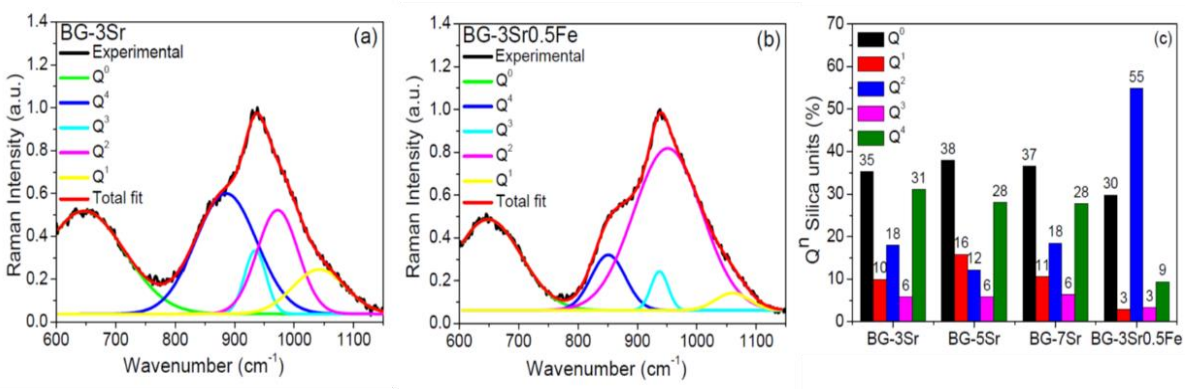


FIGURE 2. Deconvolution of peaks in Raman Spectra showing various Q^n silica units in (a) BG-3Sr, (b) BG-3Sr0.5Fe (c) Bar graph showing relative percentages of Q^n silica units

For in vitro bioactivity study samples were kept in incubator at temperature 37°C for 3, 7 and 21 days. Crystalline peaks of HAp started appearing after 7 days of soaking the sample in SBF. The presence of crystalline HAp, in bioactive material is recognized for the onset of bioactivity within the glass matrix upon exposure to the SBF solution. X-ray diffraction of the samples soaked for 21 days are shown in Fig. 1(b) showing formation of HAp crystals. The characteristics peaks observed at 29°C, 31°C and 45°C indicative of the formation of hydroxyapatite (HAp) ($Ca_5(PO_4)_3OH$) crystals (JCPDS#: 9-0432) [5]. The formation of crystalline HAp highlights the bioactivity of the glass compositions, suggesting their potential applications in bone tissue engineering and regenerative medicine.

CONCLUSIONS

Strontium silicate glass doped with Fe were synthesized by melt quenching method and studied for in vitro bioactivity by soaking the pellets into simulated body fluid. Amorphous nature of glasses confirmed by X-ray diffraction and their glass transition temperature was found to be between 867 - 872°C. In vitro studies showed formation of HAp, crystalline peaks of calcium phosphate. The samples soaked for 21 days showed higher bioactivity. The role of Q^2 silica units in promoting bioactivity was studied showing higher Q^2 species in Fe doped sample. These findings indicate that varying strontium and iron concentrations in the composition can modulate bioactive glass properties; density, glass transition temperature as well as bioactivity. The structural stability, and formation of hydroxyapatite after exposure to SBF suggests suitability of these glasses for biomedical applications.

ACKNOWLEDGMENTS

The authors gratefully acknowledge the Principal of Govt. College of Arts, Science and Commerce Khandola, Marcela, Goa for providing TG -DTA Instrument facility.

REFERENCES

1. M. T. Islam, R. M. Felfel, E. A. Abou Neel, D. M. Grant, I. Ahmed and K. M. Z. Hossain, *Journal of Tissue Engineering* **8**, 1-16 (2017).
2. E. Bonnelye, A. Chabadel, F. Saltel, and P. Jurdic, *Bone* **42**, 129–138 (2008).
3. F. Kermani, A. Vojdani-Saghir, S. M. Beidokhti, S. Nazarnezhad, Z. Mollaei, S. Hamzehlou, A. El-Fiqi, F. Baino, S. Kargozar, *Transl Oncol* **20**, 101397 (2022).
4. T. Kokubo and H. Takadama, "Simulated Body Fluid (SBF) as a Standard Tool to Test the Bioactivity of Implants," in *Handbook of Biomineralization: Medical and Clinical Aspects*, edited by E. Bäuerlein (Wiley-VCH, Weinheim, 2007), Vol. 1, pp. 97–108.
5. U. Pantulap, I. Unalan, K. Zheng, and A. R. Boccaccini, *Journal of Porous Materials* **31**, 685–696 (2024).

Growth of Single Crystal Diamond Substrates Via Welding-Assisted Microwave Plasma Enhanced Chemical Vapor Deposition

Khyati Upadhyay[1], Abhay Dasadia[1,*], Jordan Moshcovitis[2] and Vanaraj Solanki[3]

[1]*A. D. Patel Institute of Technology, C.V.M University, New Vallabh Vidyanagar-388121, Gujarat, India*
[2]*MMC Research PTY LTD, Melbourne, VIC 3000, Australia*
[3]*Dr. K.C. Patel R&D Centre, Charotar University of Science and Technology, Changa-38821, Gujarat, India*
* Corresponding author: abhaydasadia@adit.ac.in

Abstract. Lab grown single crystal diamonds (SCDs) exhibit exceptional hardness, extensive optical transparency across a wide range, and remarkably high thermal conductivity, making them reliable materials for incorporation into devices operating at high frequency, temperature, and power. Optimized synthesis methods are crucial for expanding the potential applications of high-quality single crystal diamonds. This research focuses on reducing the thermal contact resistance between diamond seeds and the molybdenum holder by employing welding material. The quality of the diamond substrates produced was evaluated using Raman spectroscopy. The first-order Raman peak, observed near 1332.64 cm^{-1} in the spectra, confirms the diamond phase in the grown crystals. Additionally, the peak intensity ratio I_d/I_g shifts to lower values, indicating reduced growth of graphitic carbon and suggesting that the grown single crystal diamonds possess high quality.

Keywords. single crystal diamonds**,** microwave plasma enhanced chemical vapour deposition (MPCVD), thermal contact resistance, welding method, copper foil

INTRODUCTION

Efficient synthesis techniques are essential for producing high-quality single crystal diamonds with properties tailored for advanced technological applications, such as quantum computing, high-precision optics, and cutting-edge electronics. Quality of the diamond including its purity, structural perfection, and optical characteristics directly impacts its performance and suitability for these demanding applications. Therefore, developing reliable synthesis methods for high-quality single crystal diamonds is vital to unlocking their full potential across various industries [1]. One promising approach to achieve superior diamond quality involves the strategic use of welding material during the growth process to suppress the formation of graphitic carbon at the bottom of the diamond seeds. This technique aims to improve the chemical vapor deposition process specifically microwave plasma chemical vapor deposition by integrating welding material with SCD substrates that are nearly identical in size. This integration helps maintain the substrate temperature at the optimal growth point, which is critical for ensuring high-quality, optical-grade single crystal diamonds with minimal nitrogen impurities [2-3]. A significant challenge during growth is the gradual increase in substrate temperature over time, primarily caused by the formation of graphitic carbon layers between the substrate and the holder. These carbon layers act as thermal barriers, increasing thermal contact resistance and destabilizing the temperature control essential for consistent diamond growth. Consequently, reducing thermal contact resistance becomes a key factor; implementing measures to improve thermal contact ensures stable substrate temperatures throughout the growth process, leading to more uniform and higher-quality diamond films [4].These advancements in growth techniques particularly the careful management of thermal conditions and the suppression of unwanted carbon phases are crucial steps toward the reliable fabrication of high-performance single crystal diamonds suitable for cutting-edge technological applications.

1. EXPERIMENTS

Homoepitaxial growth is carried out using the Seki Diamond MPCVD system (Model SDS 6K), which functions at a frequency of 2.45 GHz under pressures ranging from 100 Torr to 200 Torr. For the growth process, commercially available (100)-oriented CVD-grown SCD seeds measuring 10 mm × 10 mm × 0.5 mm are employed. Through careful real-time monitoring, the ideal growth conditions for producing high-quality single crystal diamond substrates are determined, supported by detailed analysis.

Subsequently, high-quality growth of SCDs was achieved by arranging the seeds on a substrate holder along with copper foils. In order to reduce thermal contact resistance, the 14-micron thin copper foil (welding material) was inserted between the seed and molybdenum holder [2]. Fig. 1 shows a schematic of welding assisted growth technique. Copper (Cu) foils having dimensions 8 mm × 8 mm × 0.014 mm were used to fill the interface between the seed substrate and the molybdenum holder, which enabled heat flow at the contact interface. During the welding process, the temperature at the bottom surface of the seed substrate is lower than that at the upper surface of the seed substrate. When the seed substrate temperature reaches the growth temperature, the substrate temperature still needs to be progressively raised until the substrate temperature drops suddenly by about 50°C to 100°C, indicating that the welding material has melted successfully [4].

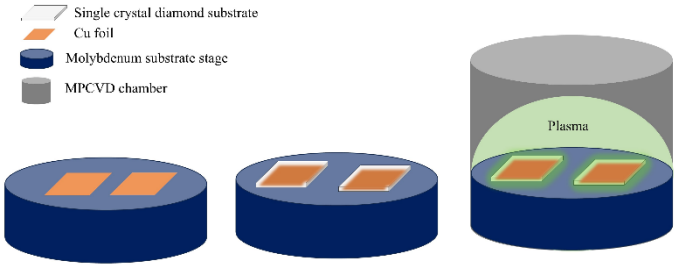


FIGURE 1. Schematic representation of welding-assisted growth technique

2. RESULT & DISCUSSION

2.1 Growth Parameters

After completing the growth process, a summary of the different growth parameters for the samples is presented in Table 1. The growth of the single crystal diamond during a 175 hour process cycle is depicted in Fig. 2, offering an insightful visual overview of the growth progression and the quality achieved over the duration.

TABLE 1. Summary of growth parameters

Growth parameter	Value
Microwave power	5-6 kw
Gas pressure	150-180 Torr
Substrate temperature	900-1150 ˚C
H_2	400-500 sccm
CH_4	5 %
Process cycle	175 h
Obtained thickness	1.60 mm
Average growth rate	9-10 µm/h

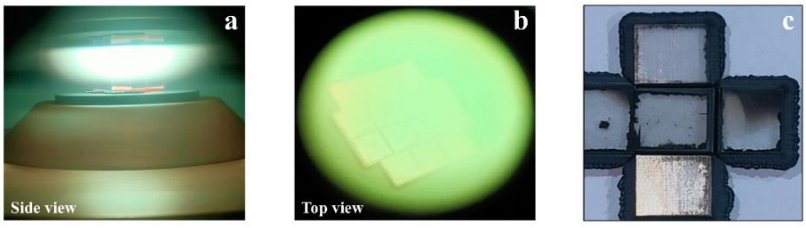


FIGURE 2. The observed growth of single crystal diamond over a 175 hour process cycle is shown in (a) side view, (b) top view, and (c) the resulting single crystal diamonds synthesized during the 175 hour cycle

2.2 Raman spectroscopy

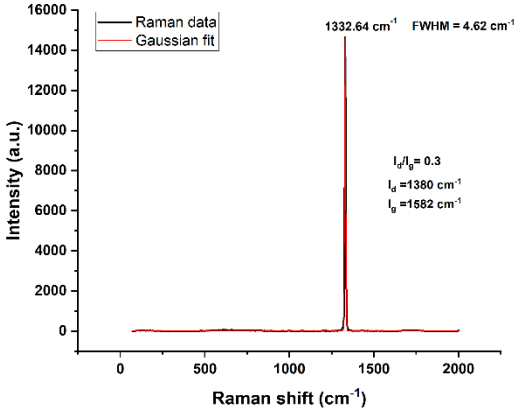


FIGURE 3. Raman spectra of grown single crystal diamond recorded using a 532 nm excitation laser wavelength

Figure 3 illustrates the Raman spectra of the synthesized single crystal diamond, obtained using the Horiba Micro-Raman Xplora Plus Model with a 532 nm laser excitation. The spectra display peaks around 1332 cm^{-1}, identified as first-order Raman peaks, with a full width at half maximum (FWHM) ranging between 5 cm^{-1} and 10 cm^{-1}. The lack of peaks in the 1500 cm^{-1} to 1550 cm^{-1} region serves as strong evidence for the formation of a pure diamond phase free from non-diamond carbon components [5]. A prominent peak at 1332.64 cm^{-1} (FWHM 4.62 cm^{-1}) corresponds to the vibrational modes of sp^3-bonded carbon atoms. Gaussian fitting of the Raman spectra shows that the peak approximately at 1350 cm^{-1} is associated with the D-band, whereas the peak near 1530 cm^{-1} relates to the G-band. The ratio of the peak intensities, I_d / I_g, is approximately 0.3, with I_d at 1380 cm^{-1} and I_g at 1582 cm^{-1}, both peaks shifting toward lower frequencies. These observations indicate a reduced presence of graphitic carbon, suggesting that the grown single crystal diamond is of high quality [6].

3. CONCLUSION

Fluctuations in substrate temperature during the synthesis of single crystal diamonds are responsible for poor quality and the deposition of non diamond carbon instead of homoepitaxial growth. To address this issue, the welding method was employed, and the quality of the grown SCDs was evaluated. In the Raman spectra, the peak near 1332.64 cm^{-1}, called the first-order Raman peak, with an I_d/I_g ratio of 0.3, indicates the growth of a high-quality diamond phase.

ACKNOWLEDGEMENT

The authors gratefully acknowledge the support of the Sophisticated Instrumentation Centre for Applied Research and Testing (SICART) in Vallabh Vidyanagar, Gujarat, India, for providing the necessary instrumentation to analyze the optical properties of the synthesized SCDs. Additionally, we extend our thanks to ABD Diamonds Pvt. Ltd., GIDC Vatva, Ahmedabad, for their support in conducting the experimental work related to the growth of the SCDs.

REFERENCES

1. O. Kitzler, A. Sabella, B. F. Johnston, A. McKay, and R. P. Mildren, Conference on Lasers and Electro-Optics/Pacific Rim, 28 August - 1 September, 2011, Sydney, Australia, Optica Publishing Group, 2011.
2. K. Upadhyay, A. Dasadia, S. V Bhatt, M. P. Deshpande, Functional Diamond, Vol. 4, pp. 2350967 (2024).
3. K. Upadhyay, A. Dasadia, J. Moshcovitis, Journal of Superhard Materials, Vol. 47, pp. 107-113 (2025).
4. Bo. Yang, S. Shen, L. Zhang, Q. Shen, R. Zhang, Y. Zhang, Z. Gang, and S. Liue, Journal of Applied Crystallography, Vol. 55, pp. 240-246 (2022).
5. J. Wagner, C. Wild, P. Koidl, Applied Physics Letters, Vol. 59, pp. 779-781 (1991).
6. S. Zhang, X.T. Zeng, H. Xie, P. Hing, Surface and Coatings Technology, Vol. 123, pp. 256-260 (2000).

Single Crystal Growth of Sn doped Ca_2RuO_4 using Optical Floating Zone Technique

N. Budania[1,2,*], B. C. Sahoo[1], A. Jain[1,2], S. M. Yusuf [1,2]

[1]*Solid State Physics Division, Bhabha Atomic Research Centre, Mumbai 400085, India*
[2]*Homi Bhabha National Institute, Anushaktinagar, Mumbai, 400094, India*

* neelamb@barc.gov.in

Abstract. We present the single crystal growth of Sn doped 4*d* transition metal oxide Ca_2RuO_4, a single layer compound of Ruddelsden-Popper (RP) series. In the literature, this series of single crystals have been synthesized using techniques such as flux method and optical floating zone technique. Here, we employ the optical floating zone technique by utilizing RuO_2 as a self-flux to grow single crystal, while analyzing the challenges encountered in the midst of the growth process such as molten zone formation & stabilization, and gas mixing ratio. Further after the growth, evolution of those grown crystals with time were tracked for 6-7 days. The grown crystals were characterized by powder x-ray diffraction, back-reflection x-ray LAUE, energy dispersive x-ray analysis (EDX), and x-ray rocking curve analysis. The crystals cleaved surface are examined by optical light microscope. The grown crystals crystalize in orthorhombic structure (*Pbca*) with distorted RuO_6 octahedra, where Ru atoms are placed at *4a* special Wyckoff-position site.

1. INTRODUCTION

The float-zone (FZ) crystal growth technique is highly rated for its ability to produce crystals with high purity, higher homogeneity, and larger size crystals, compared to other single crystal growth techniques, such as chemical vapour transport (CVT), Bridgman, the Czochralski method, hydrothermal, and flux growth[1]. The journey of this technique started in the mid-20th century, and over the years, the FZ furnace features have evolved in an exponential way with modifications in the heating source, precise temperature control, and motorized control system. However, FZ technique has its own difficulties; the quality of the crystals depends on various parameters that need to be optimized, which includes the purity of polycrystalline feed/seed rods, growth speed, rotation rate of seed and feed rod, growth chamber environment, gas pressure, analysis of phase diagrams, and molten zone stability[1]. In the present work, we have addressed these challenges for growing single crystal of a compound belonging to Ruddelsden Popper (RP) series. The RP $A_{n+1}B_nX_{3n+1}$ series of 4*d* transition metal oxides (TMOs) has been extensively studied due to its rich and complex properties. The plethora of phenomena in these materials is driven by lattice distortion, strong spin-orbit coupling (SOC), Jahn-Teller distortion, and coulombic repulsion [2]. Ca_2RuO_4 (CRO) is a RP series with n=1 compound, crystallizes in orthorhombic (*Pbca*) structure[3] having magnetic atom Ru at square lattice corner positions which exhibits antiferromagnetic ordering below 110K. The physical and magnetic properties of CRO are significantly influenced by modification in its crystal structure by external pressure, chemical pressure and electric voltage [4]. In the quest to understand the intrinsic properties of these materials, high quality and pure single crystals are required. Here, we report the single crystal growth of $Ca_2Ru_{0.95}Sn_{0.05}O_4$ with a detailed analysis of challenges encountered during crystal growth.

2. EXPERIMENTAL

We have employed the optical floating zone (OFZ) technique for single crystal growth. The single crystals of $Ca_2Ru_{0.95}Sn_{0.05}O_4$ were grown by the OFZ technique using floating zone furnace (Crystal System Co., Japan, model **FZ-T-10000-H-VII-VPO-PC**), equipped with four elliptical mirrors and halogen lamps of power 1500W. We have used RuO_2 as self-flux in order to overcome the high evaporation of ruthenium during the growth due its high volatile nature [2]. The detailed procedure for crystal growth will be discussed in more detail in the later part of the paper. The surface of the grown crystals were examined by an optical light microscope (OLM) and scanning electron microscope (SEM) (Hitachi/Oxford SEM/EDX Instrument). The chemical composition analysis was carried out using energy dispersive x-ray spectrometry (EDX). Further, the orientation and alignment of crystal planes were investigated by using back reflection x-ray LAUE technique. Rocking curve analysis using x-ray source was performed to check the

mosaicity of the grown crystals. Few of the crystals were crushed into fine powder for the purpose of x-ray powder diffraction. The phase purity and crystal structures were determined using Rietveld refinement analysis of x-ray powder diffraction data.

3. SINGLE CRYSTAL GROWTH

Single crystal growth (SCG) requires significant effort, with numerous preparatory steps prior to the growth process [2]. SCG involves following procedure: i) synthesis of highly pure polycrystalline samples, ii) the formation of feed and seed rods, and iii) mounting of the rods in the furnace.

In oxide materials, 3*d* TMOs have been extensively explored due to the relative ease of their synthesis compared to 4*d*/5*d* TMOs. Ruthenates, in particular, give challenges due to the high vapor pressure of RuO_2, leading to off-stoichiometry at high temperatures, which prevents the formation of the desired phase [4,5]. Raw chemicals $CaCO_3$ (Sigma-Aldrich), RuO_2 (Alfa-Aesar), and SnO_2 (Sigma-Aldrich) with purity 99.99%, were mixed in stoichiometric proportions with 5 – 20 % excess of RuO_2. The mixture was grounded homogeneously for 4 hours and fired at 1250°C–1400°C for 15–30 hours inside the box furnace in presence of atmospheric air, and then cooled down to room temperature. Due to significant evaporation of RuO_2, additional 5–10% RuO_2 was incorporated into the polycrystalline sample. The mixture was grounded for 2 hours prior to shaping into rods. The rod was formed by compressing the polycrystalline powder inside a cylindrical rubber balloon placed in a hollow cylindrical steel tube, pressurized hydrostatically to 70 MPa using a cold isostatic press machine (Crystal System Co., Japan). The typical dimensions of feed (seed) rod are 100 * 6 mm (20 * 6 mm) for length and diameter, respectively. The rod size was controlled by selecting appropriate balloon and steel tube size. The compressed rod, inside the rubber balloon, was gently taken out by cutting the balloon with scissors. The rod was sintered at 1000°C for 30 hours in air, and then cooled down to room temperature. The feed rod was suspended from the upper shaft using nickel wire, and the seed rod was mounted on the seed holder connected to the lower vertical shaft of the OFZ furnace. The crystal growth chamber was made up by setting up the 5 mm thickness hollow cylindrical quartz tube to allow the crystal growth under controlled environment condition (e.g., atmospheric, high pressure, vacuum). Satoru Nakatsuji and his group have reported the effects of varying gas mixture ratio of Ar to O_2 on the crystal growth of Sr doped CRO [5]. In our case, we initiated the growth with 100% Ar gas environment, but the feed did not melt even at the highest power of furnace. This occurred because Ar gas creates a reducing environment, converting RuO_2 into Ru metal [5]. In contrast A. Jain *el al.* has reported the effect of O_2 gas as oxidizing agent for Li to Li_2O, a white powder deposited on the quartz tube and surface of feed rod for single crystal growth of $LiCoO_2$[6]. To address this, numerous attempts RuO_2 have been made to optimize parameters, including the gas ratio (Ar + O_2), the quantity of self-flux RuO2, and the temperature. Finally, the optimized gas ratio of Ar : O_2 was 9:1, with an overall pressure of 9 bar. In this growth, RuO_2 was used as a self-flux, placed between the feed and seed rods as depicted in Fig.1 (a). This approach helped to minimize the RuO_2 evaporation and preserve the correct Ca_2RuO_4 phase composition.

The growth was initiated with focusing halogen lamp light reflected by elliptical mirrors, on flux RuO_2 placed between the feed and seed rod. When the power reached to the 66% of lamp power, the Ru flux began to melt, as well as evaporation of RuO_2. The evaporated RuO_2 black powder condensed at the surface of quartz tube and blocking the path of lamp light focused on molten zone. The melted RuO_2 flux helped in molten zone formation by compensating the loss of RuO_2 in feed and seed rod. The molten zone formed at 88% power of lamps. To ensure the homogenous mixing of feed, seed and flux in molten zone, only the counter rotation of feed and seed rod was maintained for 30 minutes. The feed and seed rods were translated down with heating of remaining upper part of the feed rod. The seed holder, connected to the cooling system, was allowing steadily solidifying the molten zone. The solidified material is known as crystal. The maintained growth parameters were translational rate 20 mm/hr, and rotation rate of seed and feed rod were 30 and 20 rpm with opposite rotation direction. The crucial part was to maintain the molten zone, which was overcame by manual lowering of feed rod to molten zone and increasing the lamp power. The grown crystals were approximately 1– 6 cm in size, however due to structural transition, they shattered into smaller crystals.

4. RESULT AND DISCUSSION

Many crystal growth attempts were made to optimize the crystal growth parameters. The grown crystals were of various length ranging from1 to 6 cm, as shown in Fig.1 (c). During the growth, evaporated RuO2 condensed on the quartz tube which blocked the light that needed to be focused on the feed for the molten zone, due to this blockage the molten zone dried which was monitored by manually pulling down the feed or increasing the power of lamps. CRO compound has metal to insulator transition (structural), which gives rise to cracks in the crystal and leads to cleaving

of the grown crystal rod into small mm-sized crystals with a shining surface within 6-7 days, as depicted in Fig.1 (d). Figure 1(e) shows the optical microscope image of (001) cleaved surface of rectangular plate type crystal having size 300*200 µm. The qualitative analysis of chemical composition was done by EDX measurement. The experimental chemical concentration of Sn, Ru and Ca are well matched with the theoretical values. Figure 1(f) represents the EDX pattern, energy vs. concentration of Ru, Ca, and Sn; here the O has been omitted due to limitation of x-rays to the precise detection of lower atomic-number (Z) element oxygen. The orientation of the naturally cleaved surface has also been verified by back-reflection x-ray LAUE technique with a tungsten target (Proto-COS LAUE with 0.2 mm beam size). Inset of Figure 1(g) shows the LAUE pattern taken along the [00L] axis on the shiny surface of naturally cleaved crystals. Figure 1(g) depicts the x-ray rocking curve on a crystal mounted in (hhl) scattering plane by θ scanning in the range 6 - 10° at a fixed 2θ. The Full Width at Half Maximum (FWHM) for (002) reflection is 0.19 degrees, calculated by Gaussian fit. To verify the phase purity, x-ray diffraction measurement was carried out using a Cu Kα target x-ray source at room temperature on grounded crystals. The Rietveld analysis on diffraction pattern shows Figure 1(h) that compound crystallizes in orthorhombic crystal structure with space group Pbca (61) with lattice parameters a = 5.425 Å, b = 5.53 Å, c = 11.87 Å, and $\alpha = \beta = \gamma = 90°$.

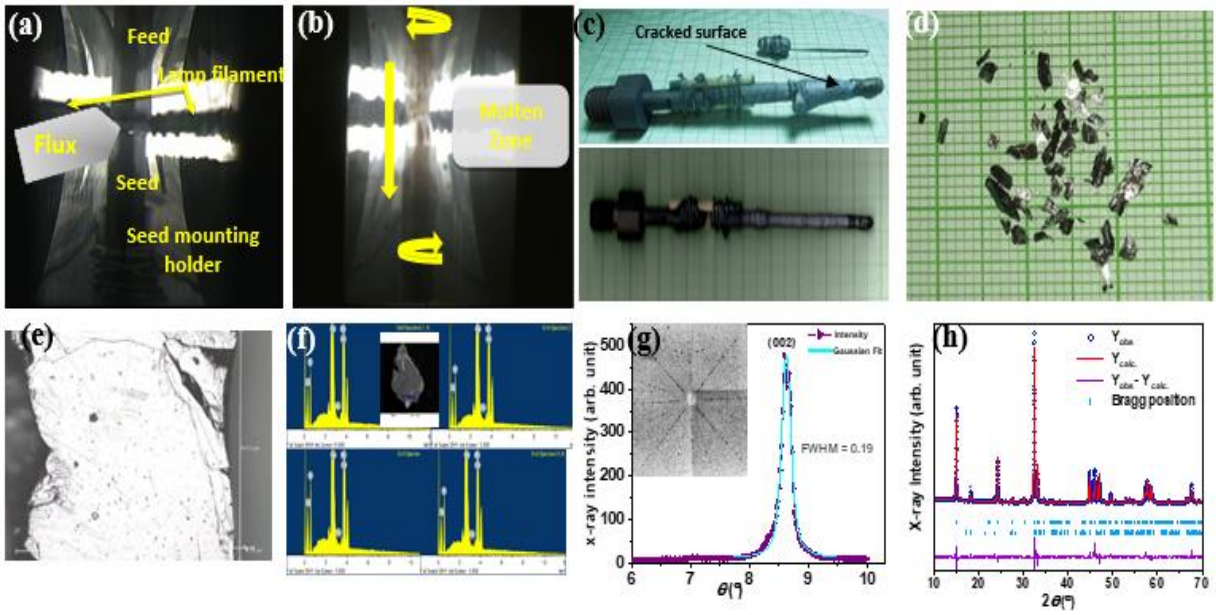


FIGURE 1*(a) Image of growth chamber at the initiation of growth with RuO_2 flux as sandwiched in feed and seed rod,* ***(b)*** *Image during the growth, molten zone is stable with counter rotation of feed and seed with vertical translation motion of feed and seed rod,* ***(c)*** *The grown crystals just after the growth,* ***(upper)*** *one cm grown crystal and,* ***(lower)*** *4.5 cm grown crystals.* ***(d)*** *Image of spontaneous cleaved crystals with (00L) plane, after the 7 days of growth.* ***(e)*** *Optical microscope image of naturally cleaved surface (00L) plane.* ***(f)*** *EDX pattern taken on 0.8*0.5 mm rectangular plate shape of crystal,* ***(inset)*** *SEM image of crystal,* ***(g)*** *X-ray rocking curve of (002) reflection,* ***(inset)*** *back reflected x-ray LAUE pattern along the [00L] axis ,* ***(h)*** *Rietveld refined x-ray diffraction pattern.*

5. CONCLUSION

We have successfully grown the single crystals of Ca2Ru0.95Sn0.05O4 using the optical floating zone technique by optimizing the amount of self-flux RuO2, the ratio of Ar to O2 gas mixture, and the quantity of excess RuO2. The obtained crystal rod has cracks which spontaneously cleave along the ab-plane into mm-sized crystals. We conclude that the evaporating nature of RuO2 makes this growth challenging. These challenges can be resolved by using RuO2

as self-flux and by adding the RuO2 during the rod formation. In addition, the spontaneous cleaving of the grown crystal is independent of the growth length crystals rod.

ACKNOWLEDGMENTS

N. Budania acknowledge to DAE for sponsor her scholarship to carry out her thesis project work.

REFERENCES

1. S. M. Koohpayeh, D. Fort, and J. S. Abell, Progress in Crystal Growth and Characterization of Materials **54**, 121 (2008).
2. T. Takayama, J. Chaloupka, A. Smerald, G. Khaliullin, and H. Takagi, Journal of the Physical Society of Japan **90**, 062001 (2021).
3. S. Nakatsuji, S.-i. Ikeda, and Y. Maeno, Journal of the Physical Society of Japan **66**, 1868 (1997).
4. B. Brunetti, P. Scardala, and V. Piacente, Materials Chemistry and Physics **83**, 145 (2004).
5. S. Nakatsuji and Y. Maeno, J Journal of Solid State Chemistry **156**, 26 (2001).
6. A. Jain, A. Mohan, and S. M. Yusuf, Journal of Crystal Growth **536**, 125578 (2020).

Soft X-ray Energy Calibration in BL-03, Indus-2 with an In-house Grown Potassium Acid Phthalate Crystal

Shruti Gupta[1, a)], Rajkumar Gupta[1], Praveen K.Yadav[1] Amit Saxena[2], Rajeev Bhatt[2, 3], Indranil Bhaumik[2, 3], and Mohammed H. Modi[1, 3]

[1]*Accelerator Physics and Synchrotrons Utilization Division, Raja Ramanna Centre for Advanced Technology, Indore 452013 INDIA.*
[2]*High Energy Lasers and Optics Division, Raja Ramanna Centre for Advanced Technology, Indore 452013 INDIA.*
[3]*Homi Bhabha National Institute, Anushakti Nagar, Mumbai 400094 INDIA.*

[a)] Corresponding author: guptashruti@rrcat.gov.in

Abstract. Photon energy calibration of soft x-ray monochromator is of the utmost importance for precise measurements at a synchrotron beamline. Conventional methods based on absorption edge measurements using gas cells or metal foils, face limitations such as limited energy points, contamination issues and associated experimental difficulties. Potassium acid phthalate (KAP) crystal has sufficiently large d-spacing (1.3315 nm) and therefore can be used for photon energy calibration in the soft x-ray region. In the present study we have calibrated the soft x-ray reflectivity beamline, BL-03 at Indus-2, having photon energy range of 100 eV to 1500 eV, using an in-house grown KAP crystal. We have measured the angular positions of Bragg peaks corresponding to unknown incident photon energies and then applied the Bragg law to determine the actual values of incident photon energy. Below 800 eV energy region, higher order Bragg peaks are used to overcome the limitations caused by lattice spacing of the KAP crystal.

INTRODUCTION

Photon energy calibration is an important requirement for precise analysis of experimental data in any x-ray and synchrotron radiation facility. Factors such as instrumental drift, beam shift, component degradation, and thermal effects can lead to shift in energy values, necessitating regular recalibration of beamline monochromator. The periodic calibration is essential for high-precision experiments across various scientific disciplines, including materials science, chemistry, biology, etc. to yield consistent and reproducible results. Furthermore, the calibration process helps in optimizing beamline performance, which in turn helps in determining the maximum photon flux and spectral range. Several methods exist for calibrating the soft x-ray photon energy.One common method involves using gas cells, where the absorption edges of gases like nitrogen, oxygen, or neon etc. serve as reference points for energy calibration [1]. Another method employs metal foils with well-defined absorption edges to calibrate photon energy [2]. While these methods are useful, they have limitations such as limited energy points, effect of potential contamination, and associated experimental difficulties in maintaining gas cells or fabricating ultra-thin foils.

Acid phthalate crystals, such as potassium acid phthalate (KAP), rubidium acid phthalate (RbAP), and thallium acid phthalate (TlAP) crystals, offer several advantages. Due to their large d-spacing and excellent reflectivity, these crystals are useful in calibrating photon energies above 500 eV. Zastrau et al. [3] demonstrated the near identical reflectivity performance of a KAP crystal after exposure to ambient conditions over many years with one which was cleaved just before the measurement. Such excellent surface stability of these crystals makes them suitable for long-term calibration applications in a beamline. Loisel et al. [4] developed a compact spectrometer using a single KAP crystal, achieving a broad spectral range of 0.8-13 keV, thereby demonstrating the versatility of these crystals. In the present study, we used a KAP, which has the molecular formula $C_6H_4(COOH)(COOK)$. It has an orthorhombic unit cell with a=0.9605 nm, b= 1.3315 nm and c=0.6473 nm. Most applications of KAP utilize the perfect cleavage along the (010) plane because it has one of the largest d spacing (1.3315 nm), thus allowing the diffraction in the soft x-ray energy range [5]. Measuring the reflectivity of the crystal at an unknown monochromatic wavelength, λ yields a diffraction peak at the theta (θ) position where it satisfies the following Bragg condition [6],

$$n\lambda = 2d \sin\theta \sqrt{1 - \frac{2\delta}{\sin^2\theta}} \quad (1)$$

Equation (1) can be rewritten as to find the angular position of the Bragg peak as

$$\sin\theta = \frac{n\lambda}{4d}\left(1+\sqrt{1+\frac{16d^2\delta}{n^2\lambda^2}}\right) \quad (2)$$

In hard x-ray regime where $\delta \sim 0$, and equation (1) reduces to

$$n\lambda = 2d\sin\theta \quad (3)$$

This simple approach has been used to calibrate the incident photon beam energy at the soft x-ray reflectivity beamline, BL-03, at Indus-2 using a KAP crystal having a well-defined periodicity d = 1.3315 nm.

EXPERIMENTAL DETAILS

Single crystal of KAP is grown by solution growth method using in-house developed high stability crystal growth setup. A [010] plate is cleaved from the grown crystal and used for the calibration of the soft x-ray reflectivity beamline BL-03 at Indus-2 synchrotron radiation source, RRCAT, Indore. This beamline operates in constant angle deviation mode and covers an energy range of 100 – 1500 eV using a varied line spacing plane grating monochromator (VLS-PGM) [7]. The energy range is efficiently covered by three different gratings: G-1 with 1200 lines/mm covers 400-1500 eV (0.83-3.1 nm), G-2 with 400 lines/mm covers 150-600 eV (2.07-8.26 nm), and G-3 with 150 lines/mm covers 100-225 eV (5.51-12.4 nm). The beamline provides a moderate energy resolution of 1000–5000 and photon flux ~ 10^9 – 10^{11} photons/s. The whole beamline operates in ultra-high vacuum (~10^{-9} mbar) environment. The experimental station at the beamline is a high vacuum reflectometer coupled with soft x-ray fluorescence setup, which are separated from the beamline by means of a suitable differential pumping system.

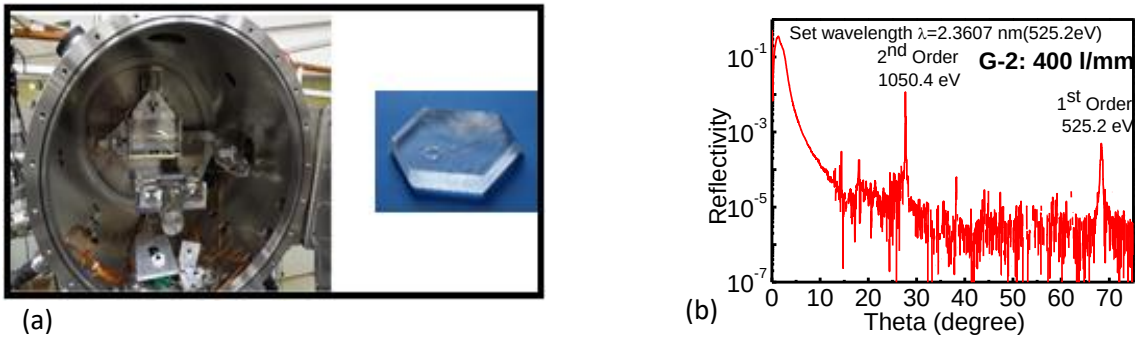


FIGURE 1. (a) Reflectometer chamber of soft x-ray reflectivity beamline and image of the in-house grown KAP crystal (b) Angle dependent reflectivity curve of the KAP crystal for incident wavelength 2.36 nm (525.3 eV).

Reflectivity measurements of the KAP crystal were performed in the reflectometer station of the beamline, shown in Fig. 1(a), at three different wavelengths for each grating energy range. The chamber consists of two axes (θ-2θ) goniometer with x, y and z sample scanning stages. Measurements were performed in θ-2θ mode, where the KAP crystal was loaded on the θ stage and the Si photo diode detector on the 2θ stage. The θ-2θ reflectivity scan of the KAP crystal taken at 2.36 nm (525.3 eV) incident wavelength obtained using G-2: 400 lines/mm grating is shown in Fig. 1(b). First order diffraction peak corresponding to the set wavelength of 2.36 nm (525.3 eV) appears at 68.3˚ Bragg angle, whereas its 2nd order (1050.4 eV) appears at 27.6˚ Bragg angle.

RESULTS AND DISCUSSIONS

For energy calibration of the beamline grating G-1 (1200 lines/mm), the angle dependent reflectivity measurements of the KAP crystal were performed at three different wavelengths (photon energies): 0.985 nm (1258.7 eV), 1.1837 nm (1047.4 eV), and 1.478 nm (838.8 eV). Fig. 2(a) shows the angular scan of the Bragg peaks corresponding to these wavelengths. The measured Bragg peaks were fitted with Gaussian profiles to determine their precise angular positions (θ values). The □ values of the KAP crystal at these wavelengths obtained from the Center for X-ray Optics (CXRO) database [8], ranges from 2×10^{-4} to 5×10^{-4}. Thus considering their negligible contribution in equation (2), we have used equation (3) to calculate the actual wavelengths.

For the beamline grating G-2 (400 lines/mm), the angle dependent reflectivity measurements were performed at 1.966 nm (630.6 eV), 2.3607 nm (525.2 eV), and 2.954 nm (419.7 eV), with □ values of KAP crystal varying between 8×10^{-4} and 1.7×10^{-3}. To minimize the effect of delta value on □ theta shift, the λ/2 harmonics of the actual wavelength were used for calibration. Fig. 2(b) shows the angle dependent Bragg peaks corresponding to these λ/2 harmonics, and the actual wavelengths were calculated using equation (3).

Similarly, for the beamline grating G-3 (150 lines/mm), the angle dependent reflectivity measurements of the KAP crystal were conducted at 4.786 nm (258.9 eV), 5.928 nm (209.1 eV), and 7.829 nm (158.3 eV), having □ values ranging from 2.8×10^{-3} to 9.4×10^{-3}.

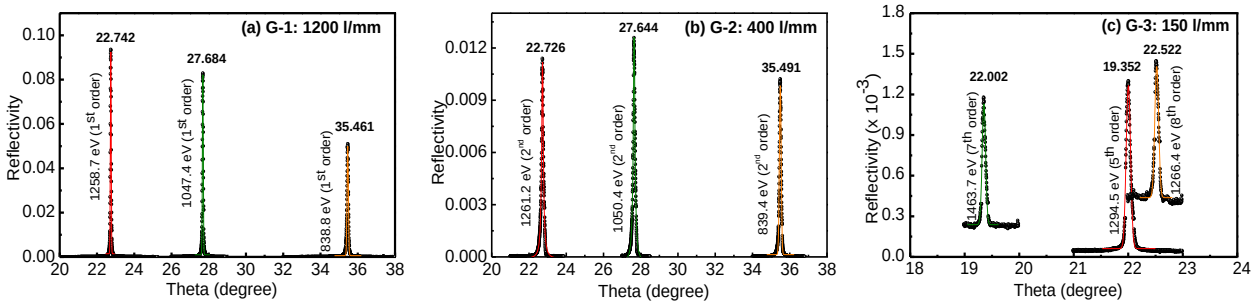


FIGURE 2. (a) Reflectivity curves of the KAP crystal for three different photon energies set using the beamline monochromator for gratings (a) G-1: 1200 lines/mm (b) G-2: 400 lines/mm (c) G-3: 150 lines/mm.

Here, □ values corresponding to the 5th, 7th and 8th harmonics (i.e., λ/5, λ/7, and λ/8) were considered to cover low energy range of the beamline as shown in Fig. 2(c).The higher harmonic contamination, which is a known issue in grating monochromators, has been used in this work to calibrate the low energy range that is covered by G-2 (400 lines/mm) and G-3 (150 lines/mm) gratings. The linear calibration curve using three measured points for G-1, G-2 and G-3 are shown in Fig. 3(a)-(c).

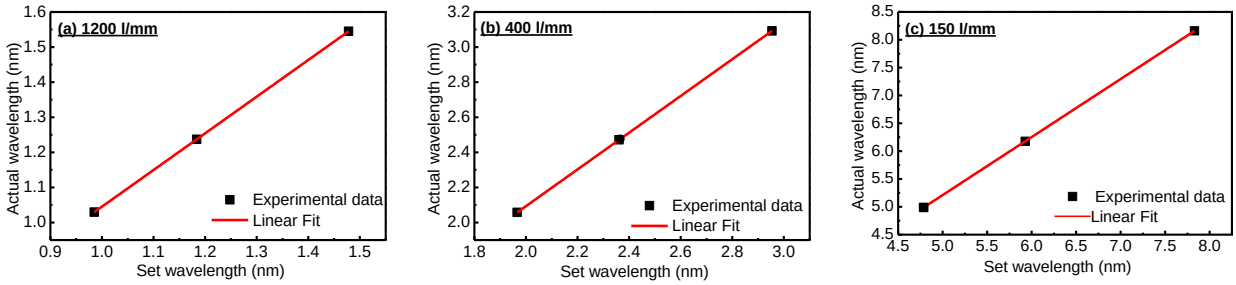


FIGURE 3. Energy calibration curves obtained using measured Bragg peak positions for three values of incident wavelengths for (a) G-1: 1200 lines/mm (b) G-2: 400 lines/mm (c) G-3: 150 lines/mm gratings of the beamline monochromator.

CONCLUSIONS

We have used an inhouse grown potassium acid phthalate (KAP) crystal for photon energy calibration of the soft x-ray reflectivity beamline of Indus-2. The large d-spacing and good reflectivity of KAP crystal enabled us to perform energy calibration in broad energy range from 800 eV to 1500 eV using 1st order Bragg peaks and below 800 eV region using higher order Bragg peaks.

ACKNOWLEDGMENTS

Authors would like to thank Dr. Tapas Ganguli, Head APSUD and Shri Rakesh Kaul, Head LTD for their kind support and keen interest in this activity.

REFERENCES

1. A. Preobrajenski et al., J. Synchrotron Radiat. **30**, 831-840 (2023).
2. A. Joseph et al., AIP Conference Proceedings **1512**, 498 (2013).
3. U. Zastrau and E. Foerster, J. Instrum. **9**, P09008 (2014).
4. G. P. Loisel et al., Rev. Sci. Instrum. **89**, 10F117 (2018).
5. M. Wu et al., Appl Opt. **60**, 558-570 (2021).
6. E. Spiller, *Soft X-ray Optics* (SPIE Optical Engineering Press, Washington USA, 1994), pp.101-107.
7. M. H. Modi et al., Rev. Sci. Instrum. **95**, 023904 (2024).
8. B.L. Henke, E.M. Gullikson, and J.C. Davis, At. Data Nucl. Data Tables **54**, 181-342 (1993).

Evaluation of Light Induced Metastable Defects in $Se_{90}Ag_6Sb_4$ Amorphous Chalcogenide Thin Films by Space Charge Examination

Anjani Kumar[1, a)], S. Shukla[2], Prince K. Singh[3] and Rajeev Gupta[4]

[1]*Department of Physics, Indian Institute of Information Technology Bhopal – 462003, India.*
[2]*Department of Physics, School of Basic Sciences, U.I.E.T., C.S.J.M. University, Kanpur-208024, India.*
[3]*Department of Electronics and Communication Engineering, Indian Institute of Information Technology Bhopal – 462003, India.*
[4]*Materials Science Programme, Indian Institute of Technology, Kanpur-208016, India.*

[a)]Corresponding author: *anjanikumar51284@gmail.com*

Abstract. A well-known Space charge analysis (SCA) is employed for the analysis of defect density for different illumination time, and quantitatively found Light induced metastable defects (LIMD) on the $Se_{90}Ag_6Sb_4$ thin films of Amorphous Chalcogenide Materials (ACMs). The outcomes show that density of defect states (DOS) raises with illumination time i.e. generation of LIMD took place. On the basis of LIMD suitability of optoelectronic applications can be explored further

INTRODUCTION

Chalcogenide materials in amorphous form have fascinated much enthusiasm because of their spacious technological advancement applicability in the recent technological important fields of energy generations, photonics, optics & electronics [1-2].

The Amorphous chalcogenide materials (ACMs) found to be suitable candidates for high field conduction studies due to low conductivity and negligible small joule heating [3-4]. Last few decades various research groups motivated towards the electrical properties of ACMs and interpreted their experimental results by heating effects, Poole-Frankel effect, and Space Charge Limited Conduction (SCLC) [3, 4]. Space Charge analysis (SCA) is one of most important analysis due to inadequate knowledge of electronic structures of ACMs and have more experimental freedom [4].

Shim et.al. [5] have studied Se-based ACMs and published that these are extra convenient in comparison of unalloyed Selenium due to their giant photosensitive properties, more prominent hardness, giant crystallization effect and lower aging impact. Se-Sb ACMs are favored over Se-Te ACMs because a small addition of Sb is sufficient to crystallize pure a-Se [6].

The study of selenium based ternary glassy systems are more important in research point of view in the fields of optoelectronics, basic sciences, cell-based device applications, optical components, optical memories, microlenses, waveguides, electrochemical and natural sensors, solid electrolytes, and batteries etc. [7] As of late it has been observed that assortment of photoinduced phenomena happens in ACMs [8]. Numerous past studies have demonstrated that Ag-based ACMs indicate most prominent applications in optoelectronic and assortment of photoinduced impacts are seen in these technological important materials [9].

To quantify DOS in ACMs, several techniques have been pre-owned which have completely precedence and their respective confinements. Due to difficulties in forming a p-n junction, spectroscopic techniques could not be used to estimate the density of states (DOS) in ACMs. The SCLC technique [10] has commonly been employed for quantitative experimental estimation of the density of states (DOS) in ACMs.

In perspective of above mentioned, this study announces the quantitative assessment of light-induced meta stable defects (LIMD) in thin films of ACMs $Se_{90}Ag_6Sb_4$ by using SCLC analysis. Thus, for this, white light of

intensity 1500 lux exposed to the above-mentioned thin films of ACMs from 0 to 6 hours. The DOS increment with exposure time demonstrates that additional DOS are made as increment of light illumination time.

EXPERIMENTAL METHOD

The whole process of $Se_{90}Ag_6Sb_4$ ACMs [3,7] thin film preparation is given by process flow given below through weighing, sealing, quenching, crushing and vacuum evaporation technique [3,7]. The amorphous character of ACMs is affirmed by the absentia of diffraction peak in XRD. For the measurements of SCA the thin films of ACMs of $Se_{90}Ag_6Sb_4$ are arranged in a uniquely composed high temperature metallic sample holder containing vacuum of 10^{-3} Torr. First annealing for one hour then I-V characteristics under d. c. voltage (0-440V) at various fixed temperatures (300K - 450K) have been done for all thin films of ACMs. For exposure of white light, sample holder containing transparent window is used. For avoiding thermal impacts of light source, proper care is already taken.

RESULTS AND RELATED DISCUSSIONS

I-V properties are investigated with respect to temperatures in ACMs thin films of $Se_{90}Ag_6Sb_4$ prior and after prolonged illumination of white light. An Ohmic and super-ohmic conduction phenomenon is seen at electric fields below $10^{\wedge 3}$ V/cm and approximately $10^{\wedge 4}$ V/cm, respectively. ln(I/V) versus V curves have been plotted in the high-field conduction region, and observed to be linear both, before and after prolonged illumination with white light, as depicted for a- $Se_{90}Ag_6Sb_4$ thin films. The slopes (S) of ln(I/V) versus V curves exhibit temperature-dependent characteristics. At low voltages, the number of infused charge carriers is lower than the number of charge carriers generated thermally, thereby enabling ohmic conduction. At very high voltages, the dominance of the infused charge carrier thickness may lead to conduction being predominantly governed by a trap-limited space-charge-limited current (SCLC) mechanism in this particular-region. On account of a uniform distribution of localized states of density g_0, the current (I) at specific voltage (V) is written by:

$$I = (2\ e\ A\ \mu\ n_0\ V/\ d)\ [\exp\ (SV)] \qquad (1)$$

S is also given by:

$$S = 2\ \varepsilon_r\varepsilon_0 / e\ g_0\ k\ T\ d^2 \qquad (2)$$

In above equations, symbols have their usual meanings.

According to Eqs. (1) and (2), the ln(I/V) versus V curves are expected to form straight lines. As temperature increases, the slope S of these curves decreases. The slopes, estimated in their current form, are plotted as functions of temperature before and after prolonged exposure to white light for a- $Se_{90}Ag_6Sb_4$. It is intelligible from this figure that the slope (S) of ln I/V versus V curves is reversed relative to the temperature for every present sample of ACMs. The particular-outcomes show the existence of SCLC in present samples of ACMs.

Thin films of ACMs accommodate a giant DOS that offer ascent to extensive numeral of localized defect states. These giant localized defect states worked as carrier trappers and behind trapping the inoculated charge from electrodes, they get to be charged and accordingly anticipated that would develop a space charge. These developments of space charge then assume the crucial part in their solution of SCLC mechanism.

The density of states (DOS) is quantitatively determined from the slope of S versus 1/T plots. For the calculations, the relative dielectric constant (ε_r) is assumed to be 70 for all the ACM samples. The calculated values of DOS for various illumination times are presented in Tables 1 and shown in Figure 1 as a function of illumination time for thin films of $Se_{90}Ag_6Sb_4$ ACMs. It is intelligible from the present figures that the DOS (g_0) raises with the rise of time white light illumination.

The results are explained as, on long illumination of band gap light, Staebler-Wronski worked on hydrogenated amorphous silicon debases upon light absorbing and passes to a metastable state [11] which was described because on the basis of formation of light induced metastable defects states in such type of specific materials. Biegelsen and Street [12] have also detected light induced ESR signal, extrinsic absorption below the band gap energy and non-radiative recombination in ACMs and clarified these outcomes in terms of the creation of giant DOS.

It have [13] have detected a time-dependent decrease in photocurrent during light illumination in thin films of ACMs and clarified these specific outcomes in respect of light induced metastable defects. Shimakawa et al. and Elliott and Shimakawa have developed a model to elucidate the formation of light-induced metastable defects in

amorphous chalcogenide materials (ACMs). In their model, self-trapped excitons play a crucial role in creating these defects, forming intimate valence alternation pairs (IPs) that are stable at low temperatures, specifically below 200 K.

The experimental investigations of LIMD of present samples of ACMs are interesting research in the field of science and technology for searching materials as optoelectronic applications because of light induced metastable defects.

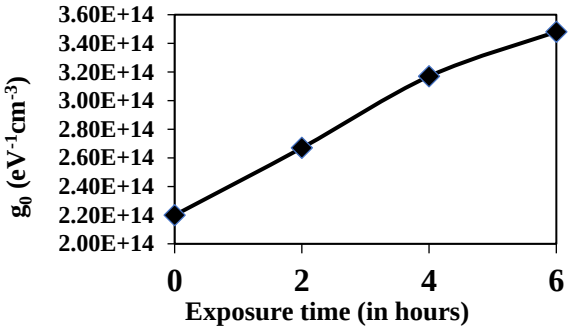


FIGURE 1. Variation of g_o with illumination time in thin-films of $Se_{90}Ag_6Sb_4$ACMs.

TABLE 1. g_o in thin films of $Se_{90}Ag_6Sb_4$ACMs before and after prolonged illumination of white light.

Illumination time (hrs)	Slope of S vs. 1/T curves	g_o (eV^{-1} cm^{-3}) x 10^{14}
0	4.150	1.10
2	3.444	1.35
4	3.053	1.52
6	2.735	1.70

CONCLUSIONS

Light induced defects have quantitatively investigated by well-known SCLC analysis in present $Se_{90}Ag_6Sb_4$ samples of ACMs. A microscopic model suggested by Shimakawa and collaborators have been used to explain the formation of light induced metastable defects due to prolonged illumination of white light.

REFERENCES

[1] M. H. R. Lankhorst, B. W. S. M. M. Ketelaarsand R. A. M. Wolters, Nat. Mater.4, 347 (2005).
[2] A. V. Kolobov, P. Fons,A. I. Frenkel,A. L. Ankudinov,J. Tominagaand T. Uruga, Nat. Mater. 3, 703 (2004).
[3] K. Yilmaz, M. Parlak and C.Ercelebi, J. Mat. Sci. 15,225 (2004).
[4] R. SINGH, S.K. TRIPATHI AND S. KUMAR, J. NON-CRYSTALLINE SOLIDS 352, 3230 (2006).
[5] J. Y. Shim, S. W. Parkand H. K. Baik,Thin Solid Films 292, 31 (1997).
[6] K. S. Bindra,N. Suri and R. Thangaraj, Chalcogenide Lett.3, 133 (2006).
[7] Anjani Kumar, S. Shukla, R.K. Shukla and Rajeev Gupta,AIP Conf. Proc.2115, 030264 (2019).
[8] *M. Wuttig and N. Yamada, Nat. Mat.6, 824 (2007).*
[9] M. A. Alvi, S. A. Khan, and A. A. Al-Gamdi, J. Lumin.132, 1237 (2012).
[10] Pravin Kumar Singh and D.K. Dwivedi, Ferroelctrics520, 256-273 (2017).
[11] D. L. STAEBLER AND C. R. WRONSKI, APPL. PHYS. LETT. 31, 292 (1977).
[12] *D. K. Biegelsenand R. A. Street, Phys. Rev. Lett. 44, 803 (1980).*
[13] K. Shimakawa,A. Kondo,K. Hayashi, S. A. Kahori,T. Katoand S. R. Elliot, J. Non-cryst. Sol. 164, 387 (1993).

Silicon Surface Energy Modification Using UV, IR Laser and RF Plasma Exposure

Bijay Verma*[1,a)], Praveen K. Yadav[2], Manoj Kumar Singh[1], Mohammed H.Modi[2] and A.K. Choubay[3]

[1] Department of Physics, Central University of Haryana, Mahendragrah, India.
[2]Soft x-ray Application Section, Raja Ramanna Centre for Advanced Technology, Indore, India.
[3]Engineering Design and Manufacturing Division, Raja Ramanna Centre for Advanced Technology, Indore, India.

[a)] Corresponding author: *bijay220893@cuh.ac.in*

***Abstract*:** To enhance adhesion of Au on silicon substrate, systematic surface energy modification techniques such as IR laser, ultraviolet (UV-172 nm) irradiation, and radio frequency (RF) oxygen plasma exposure were employed. The effects of these treatments are analyzed by measurement of water drop contact angle using goniometer and x-ray reflectivity. The water drop contact angle variation and measured surface energy show UV and oxygen plasma treated increases surface energy while IR laser treated decreases surface energy. Hard x-ray reflectivity measurements provided structural (surface roughness, thickness, density) and optical parameters (optical constants: δ and β) of pristine and surface treated substrates.
Keywords: Soft X-ray, Surface energy, Surface treatment, Reflectivity, optical constants,

INTRODUCTION

The X-ray mirrors are based on the principle of total external reflection on grazing angle incidence geometry. The angle of grazing incidence depends on material as well as the incidence wavelength and it should be less than the critical angle of that material at given wavelength [1]. The x-ray mirror production falls under the category of extreme manufacturing. This process typically involves achieving slop errors within the nanorad range on a scale of a meters length and achieving surface roughness below 1 nm. The x-ray mirrors are made of two parts (i) substrate and (ii) coating material used for reflection. The material selection for synchrotron mirrors is mainly determined by substrate properties such as good optical machinability, long-term stability, resistance to high heat load and UHV compatibility [2]. In Indus-2 the heat load in the bending magnet beam-line is nearly 20 watt/mrad at 200 mA ring current and 2.5 GeV energy [3]. For this type of heat load silicon substrate based mirror is the suitable choice. The coating material needs good thermal and chemical stability and good adhesion to the substrate material. Due to noble characteristics and high atomic number, gold (Au) is found suitable material for reflective coating for x-ray mirror, but Au on silicon does not have good adhesion. As a result it peels off from silicon substrate. For good adhesion, a chromium (Cr) layer is generally put in between the Au and silicon substrate. This layer gives good adhesion to the Au layer but due to heat load on mirror surface by synchrotron beam this Cr layer diffuse into the Au layer resultant the reflectivity of mirror affected by interface diffusion and Cr near edge absorption [4-5]. So, instead of adding Cr layer, surface energy of Si substrate is modified by rf oxygen plasma, deep UV (172 nm) and infrared (IR) laser irradiation of Si substrate. The exposed samples with different techniques are characterized by x-ray reflectivity and x-ray photoelectron spectroscopy techniques. The surface energy is measured by water drop contact angle measurement. After surface analysis the exposed sample and a pristine sample is coated with Au thin film of approximately 300 Å thicknesses.

EXPERIMENTAL DETAILS

Before exposure all the Si substrates are cleaned by ultra-sonication in acetone bath for 20 minutes. Three cleaned Si substrate is exposed to the 172 nm UV radiations (Xe excimers lamp) for 1 hour, 2 hours and 3 hours respectively. 172 nm radiations can crack hydrocarbons as well as breaks the O=O (2.57 eV) bond to form oxygen radicals. Three samples are exposed to rf oxygen plasma. The plasma chamber consist of two electrodes at 65 mm separation connected with 13.56 MHz rf power supply. Vacuum of the order of 10^{-6} mbar in the chamber was achieved by combination of rotary and turbo molecular pump O_2 is supplied at 20 SCCM as a process gas. RF feed power is maintained at 10 Watt to the electrodes. This excites the O_2 gas molecules between the electrodes and forms oxygen plasma. The plasma interacts with the substrates surface placed between the electrodes and surface modification takes

place by interaction of oxygen ions/radicals or electrons to the Si surface. The samples are exposed for 1hour, 2 hours and 3 hours respectively. In case of IR laser (1064 nm) irradiation, three silicon substrates is treated with power of 50W, 70W and 100W. The pulse frequency of 10 KHz with pulse duration of 80 ns is scanned at 2 m/sec. During exposure Si substrate are kept at off focus to protect the damage. The changes in the surface are studied by water drop goniometer (Ossila enabling science) and x-ray reflectivity characterization using Brukar (D-8 discover) machine.

A 300 Å thick Au layer was deposited on pristine, IR laser (100 W), oxygen plasma irradiated (3 hours), UV irradiated (3 hours) Si substrates by RF magnetron sputtering without any adhesive layer. 4 inch gold sputtering target of 99.99% purity was used for deposition. Argon gas of 6N purity is used as sputtering gas and 5 SCCM flow rate was used to maintain 10^{-2} mbar pressure during deposition.

RESULT AND DISCUSSION

The contact angles are measured and surface energy is calculated by Young's equation i.e. $\gamma_{Lv}\cos\theta = \gamma_{sv} - \gamma_{sL}$ using theoretical value of liquid-vapor pressure of water as 72.8 mN/m in standard conditions [6]. It is observed that the plasma exposed and UV irradiated surface becomes hydrophilic while laser treated surface becomes hydrophobic

TABLE 1. Contact angle and surface energy measured by water drop goniometer.

Samples	Contact angle	Surface energy (mj/m^2)
Pristine Silicon	38.56	42.37
UV treated for 1 hr.	18.83	49.89
UV treated for 2 hrs.	17.26	53.40
UV treated for 3 hrs.	11.73	52.62
O_2 plasma treated for 1 hr.	11.39	52.47
O_2 plasma treated for 2 hrs.	11.87	51.87
O_2 plasma treated for 3 hrs.	13.33	50.38
Laser scanned at 50 W	58.07	21.66
Laser scanned at 75 W	44.75	34.86
Laser scanned at 100 W	47.34	29.95

The measured reflectivity spectra by hard x-ray (1.54 Å) are fitted by Parratt recursive formalism [7]. For fittings Si bulk optical constants δ and β are kept 7.3 x10^{-6} and 1.59 × 10^{-7} respectively. The best fitted top surface optical constants and layer thickness and roughness are tabulated in table-2. After surface treatments the surfaces are coated with 300 Å Au layer. The gold coated mirror samples shows 70% reflectivity in soft X-ray region but it is observed that Au layer still have poor adhesion. The tape removes more than 80 % of the gold from the surface. For further study we will try it for increasing exposure time and in-situ coating.

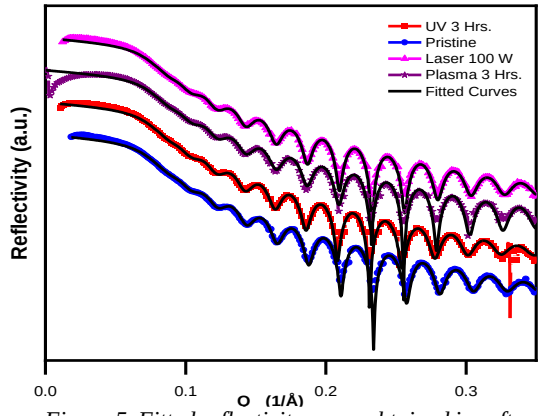


Figure 5. Fitted reflectivity curve obtained in soft x-ray region by Au coated samples

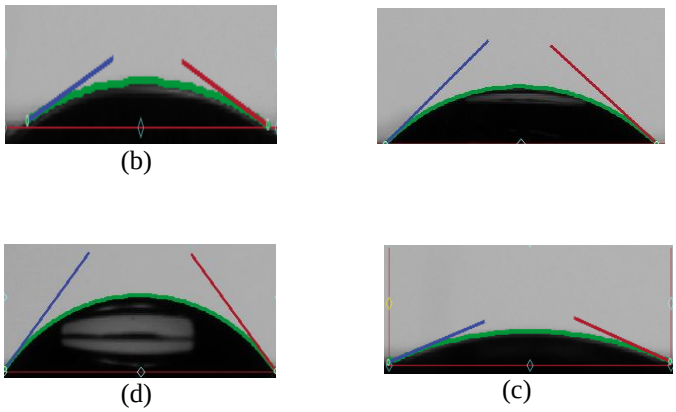


Figure 2.Contact angles measured for (a) Pristine Silicon (b) UV treated Silicon (c) Plasma treated Silicon (d) Laser treated Silicon

TABLE 2. Measurement of dispersive coefficient (δ), absorptive coefficient (β), roughness (σ) and thickness (d) of top layer and bulk layer of all the samples.

Samples	**Bulk**			**Top layer**			
	δ (10^{-6})	β (10^{-7})	σ(Å)	d(Å)	δ(10^{-6})	β(10^{-7})	σ(Å)
Pristine Silicon	7.30	1.59	8.5	30	0.98	1.15	3.0
UV treated for 1 hr.	7.30	1.59	8.5	30	1.04	1.20	3.0
UV treated for 2 hrs.	7.30	1.59	9.5	34	1.01	1.15	6.0
UV treated for 3 hrs.	7.30	1.59	9.5	35	1.05	1.15	4.3
O_2 plasma treated for 1 hr.	7.30	1.59	7.5	25	1.06	1.15	3.5
O_2 plasma treated for 2 hrs.	7.30	1.59	8.7	30	1.02	1.15	3.5
O_2 plasma treated for 3 hrs.	7.30	1.59	7.8	30	1.02	1.15	3.0
Laser scanned at 50 W	7.30	1.59	8.5	30	1.00	1.09	5.5
Laser scanned at 75 W	7.30	1.59	8.2	35	1.00	1.09	6.0
Laser scanned at 100 W	7.30	1.59	9.0	35	1.06	1.09	3.8

CONCLUSION

The objective is to understand the possibility of development of gold coated mirror for beam-line without using any adhesion promoter. This is done here by modifying the substrate surface energy by techniques such as oxygen plasma exposure, UV (172 nm) exposure and IR (1064 nm) laser treatment. In UV and plasma exposure, surface energy increases (Hydrophilic) while in case of laser treatment surface energy decreases (Hydrophobic). The characteristic changes may be taking place due to cleaning of hydrocarbons and formation of oxides at surface. After surface treatment dispersive coefficient and the absorptive coefficient both slightly changes with respective to the pristine one. 70% of reflectivity is observed by gold coated samples. The adhesion of the gold onto the substrate is then studied using tape test. After increasing surface energy the adhesion of gold is still not found so good. So it can be concluded that, applied techniques modified surface energy but it is not sufficient for good adhesion of Au on Si substrate. Despite this, these types of mirrors can be used in synchrotron beam-line with ultra-high vacuum environment.

ACKNOWLEDGMENTS

I am deeply appreciative Dr. Sunita Srivastava (Head, Department of Physics, Central University of Haryana) and Dr. C. Mukherjee whose collaborative spirit and intellectual exchanges have enriched my research journey beyond the measure. My sincere thanks go to, Mr. R. K. Gupta, Mr. Pushkardeep, and Mrs. Shruti Gupta of soft x-ray application lab at RRCAT.

REFERENCES

1. Attwood, David. Soft x-rays and extreme ultraviolet radiation: principles and applications. Cambridge university press, 2000.
2. Howells, Malcolm R., and Roger A. Paquin. "Optical substrate materials for synchrotron radiation beam lines." Advanced Materials for Optics and Precision Structures: A Critical Review. Vol. 10289. SPIE, 1997.
3. Deb, S. K., Gurnam Singh, and P. D. Gupta. "Indus-2 Synchrotron Radiation Source: current status and utilization." Journal of Physics: conference series. Vol. 425. No. 7. IOP Publishing, 2013..
4. Rahman, Mohammad Mahbubur. Solar selective characteristics and local electronic bonding states of 3d transition metal oxide and metal nitride based thin film coatings. Diss. Murdoch University, 2016.).
5. Singhapong, Wadwan, et al. "Multilayer Optics for Synchrotron Applications." Advanced Materials Technologies (2024): 2302187..
6. Saleh, Khashayar, et al. "Dry water: From physico-chemical aspects to process-related parameters." Chemical engineering research and design 89.5 (2011): 537-544.
7. Parratt, L. G. (1954). Surface studies of solids by total reflection of X-rays. Physical review.

Modifications Of The Structural, Electronic Structure and Magnetic Properties of $PrVO_3$ Thin Films By 100 MeV Au Ion Irradiation

Shivank Kalia[1,*], Pankaj Bhardwaj[2], Varun Ranade[3], Keun Hwa Chae[3], Rajesh Kumar[1] and Ravi Kumar[2]

[1] *Department of Physics and Photonics Science, National Institute of Technology, Hamirpur 177005, India*
[2] *Department of Materials Science and Engineering, National Institute of Technology, Hamirpur 177005, India*
[3]*Advanced Analysis Center, Korea Institute of Science and Technology, Seoul 02792, Republic of Korea*

[*] Corresponding author: shivankkaliap@gmail.com

Abstract. This study explores the impact of ion irradiation on $PrVO_3$ thin films, examining structural, electronic structure, and magnetic properties. X-ray diffraction (XRD) reveals stress induction and lattice distortion due to ion track formation. X-ray absorption near edge structure (XANES) confirms the stability of the V^{3+} oxidation state, and extended X-ray absorption fine structure (EXAFS) analysis indicates changes in bond distances affecting the VO_6 octahedra. Magnetization measurements demonstrate reduced saturation magnetization and increased coercivity due to defect formation and partial amorphization.

Keywords: Rare earth vanadates, Swift heavy ion irradiation, Strain, X-ray absorption spectroscopy, Tracks.

INTRODUCTION

In recent years, rare-earth vanadate perovskites have garnered significant scientific interest owing to their intricate interplay of spin-orbital interactions and lattice dynamics, primarily influenced by weak Jahn-Teller effects [1,2]. Among these materials, $PrVO_3$ stands out for its distinctive properties: it crystallizes in a distorted *Pbnm* space group and undergoes a structural phase transition from orthorhombic to monoclinic at 185 K, accompanied by a magnetic transition to a C-type antiferromagnetic (AFM) state from a paramagnetic phase at 140 K [3,4]. Recent investigations have demonstrated the sensitivity of its structural and magnetic characteristics to external pressure and stress/strain induced by various means [5,6]. However, the influence of swift heavy ion irradiation on these properties has remained largely unexplored. Swift heavy ions, characterized by high kinetic energy, can induce substantial modifications in materials through electronic excitation and ionization processes, potentially altering their structural, electronic, and magnetic behaviours. In this study, we explore the effects of swift heavy ion irradiation on the structural, electronic structure, and magnetic properties of $PrVO_3$ thin films.

EXPERIMENTAL DETAILS

For the deposition of a $PrVO_3$ thin film, a polycrystalline $PrVO_4$ target was prepared using a solid-state reaction method. The thin film deposition was performed utilizing Pulsed Laser Deposition (PLD) using a KrF excimer laser at a laser fluence of 2 J/cm^2 and a repetition rate of 2 Hz. The $PrVO_3$ film was deposited on a $LaAlO_3$ substrate under conditions of 750°C and an oxygen partial pressure of 10^{-6} mbar. Following deposition, the film was cooled to room temperature while maintaining the same conditions. Additionally, a piece of the film was sectioned and irradiated with

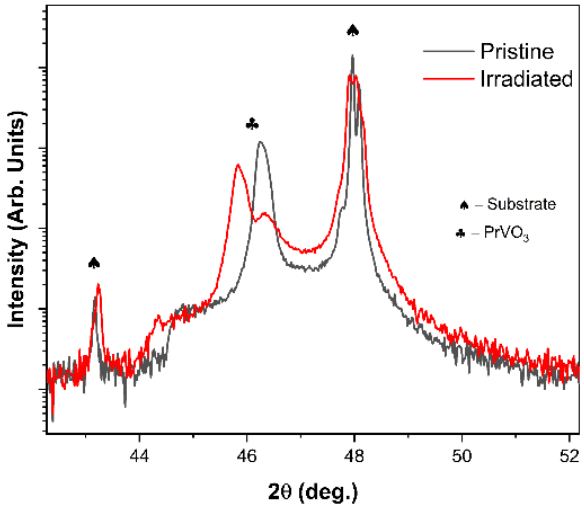


Figure 6. XRD patterns of pristine and irradiated $PrVO_3$ thin films.

100 MeV Au^{8+} ions at a fluence of 5×10^{11} ions/cm^2. Structural characterizations were conducted using an Empyrean Panalytical X-ray diffractometer. Surface topography was studied using an Agilent 5500 atomic force microscope. X-ray absorption near edge structure (XANES) and extended X-ray absorption fine structure (EXAFS) spectra were acquired at the 10D beamline at PAL, South Korea, and the 1D KIST PAL beamline, South Korea, respectively. Magnetic studies were conducted using an MPMS3 SQUID VSM.

RESULTS AND DISCUSSIONS

Structural Analysis

Figure 1 displays the XRD scans for pristine and irradiated $PrVO_3$ thin films. When $PrVO_3$ thin film is grown on a $LaAlO_3$ substrate, the grown film is in-plane compressively strained. It is evident that upon irradiation, the (002) Bragg peak shifts to a lower angle, indicating the induction of stress within the film. The calculated out-of-plane lattice constants for the pristine and irradiated samples are 3.916 Å and 3.957 Å, respectively. For the irradiated sample, there is also a notable growth of a component at a higher 2θ, which leads to out-of-plane compression. This phenomenon may be attributed to the presence of irradiation-induced damaged tracks. These damaged tracks can induce local out-of-plane compression, resulting in out-of-plane expansion in the undamaged regions. Such a transformation might be due to the sufficient overlap of these damaged tracks [7]. The complex interplay of these structural changes highlights the significant impact of ion irradiation on the thin film's lattice structure.

Local Electronic Analysis using XANES

Figure 2(a) displays the X-ray absorption spectra at the V $L_{3,2}$ and O-*K* edges for pristine and irradiated $PrVO_3$ thin films. Both spectra show identical energy positions in their line profiles. The features observed in the photon energy ranges of 510-518 eV and 518-526 eV correspond to transitions from V $2p_{3/2}$ and V $2p_{1/2}$ to unoccupied V *3d* states, respectively. The features between 526-530 eV arise from the mixing of O *2p* states with V *3d* states, while those between 530-536 eV are due to the mixing of O *2p* states with Pr *5d* states. Additionally, the broad features around 540 eV result from the mixing of O *2p* states with V *4sp* states. These observed features are consistent with previous XAS spectra of vanadate-based perovskite materials, confirming the +3 oxidation state of V in both thin films [8].

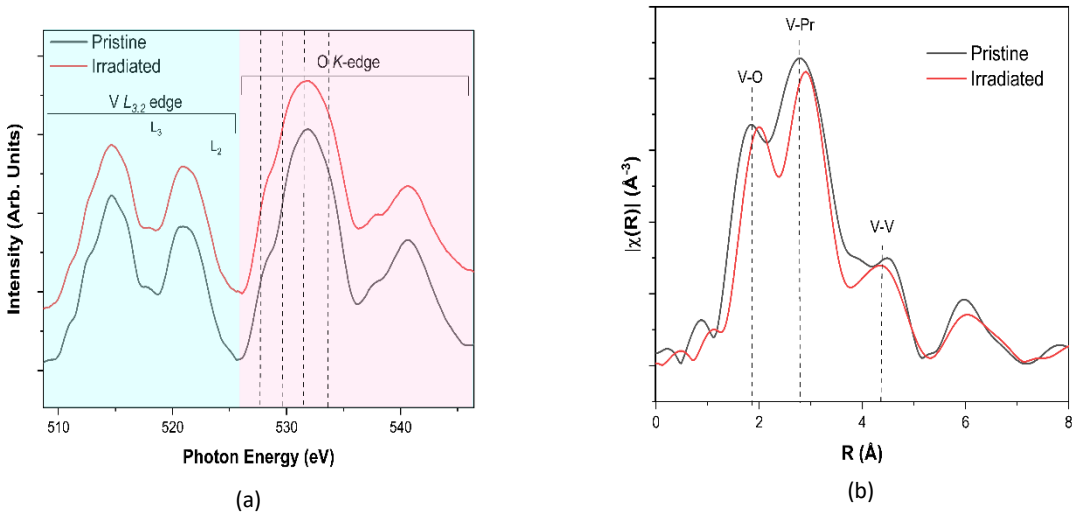


Figure 7. (a) V $L_{3,2}$- edge and O K-edge X-ray absorption spectra of pristine and irradiated $PrVO_3$ thin films. (b) Comparison of magnitudes of Fourier transforms spectra of the V K-edge for pristine and irradiated $PrVO_3$ thin films.

Local Structural Analysis using EXAFS

To investigate the effect of irradiation on structural changes in the local geometry of $PrVO_3$ thin films, we have performed EXAFS analysis on the V K-edge. Figure 2(b) depicts the bond distances of vanadium atoms from the first neighbour oxygen atoms, nearby praseodymium atoms and vanadium atoms. It can be seen that with irradiation, the
V-O and V-Pr bond distances increase from 1.85 Å and 2. 77 Å for pristine to 2.02 Å and 2.90 Å for irradiated $PrVO_3$ thin film. While the V-V bond distance decreases from 4.49 Å for pristine to 4.33 Å for irradiated $PrVO_3$ thin film. The change in V-V and V-O bond distances indicates the alternations in VO_6 octahedra, affecting the superexchange interactions between V- atoms.

Magnetic Analysis

To investigate the magnetic properties of pristine and irradiated $PrVO_3$ thin films, we performed magnetization measurements as a function of the applied field at 5K. As shown in the figure 3, the saturation

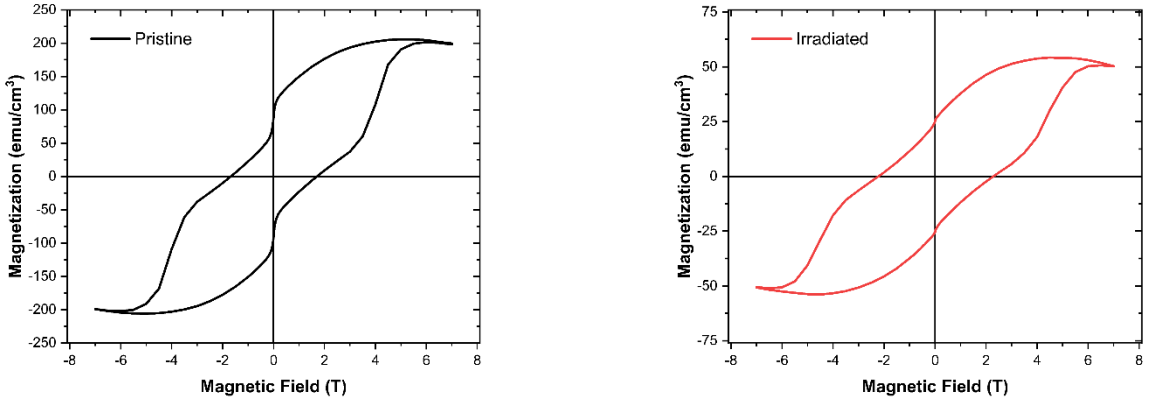


Figure 3. Isothermal magnetization curves for pristine and irradiated $PrVO_3$ thin films at 5K.

magnetization decreases significantly from 200 emu/cm^3 for the pristine sample to 51 emu/cm^3 for the irradiated sample, while the coercivity increases from 1.690 T for the pristine film to 2.225 T for the irradiated $PrVO_3$ thin film. This decrease in saturation magnetization can be attributed to irradiation-induced defect formation and partial amorphization of the thin film. The defects disrupt the magnetic ordering by interfering with the exchange interactions between magnetic ions, while amorphization breaks down the long-range magnetic order, both contributing to the reduction in magnetization. Additionally, these structural changes can enhance the pinning of magnetic domains, leading to an increase in coercivity.

CONCLUSIONS

In conclusion, we have studied the impact of ion irradiation on the structural, electronic structure, and magnetic properties of $PrVO_3$ thin films. XRD analysis reveals stress induction and lattice distortion due to ion track formation. XANES spectra confirm the preservation of the V^{3+} oxidation state, while EXAFS analysis indicates alterations in bond distances, affecting the VO_6 octahedra. Magnetization measurements demonstrate a decrease in saturation magnetization and an increase in coercivity resulting from defect formation and partial amorphization.

ACKNOWLEDGMENTS

R.K. would like to thank UGC, New Delhi for support in the form of User Funded Research project UFR No. 72301. The authors are thankful to the accelerator group of Inter-University Accelerator Centre, New Delhi for providing the 100 MeV Au ion beam.

REFERENCES

[1] S. Miyasaka, Y. Okimoto, M. Iwama, and Y. Tokura, Phys. Rev. B - Condens. Matter Mater. Phys. **68**, 1 (2003).
[2] M. H. Sage, G. R. Blake, C. Marquina, and T. T. M. Palstra, Phys. Rev. B - Condens. Matter Mater. Phys. **76**, 1 (2007).
[3] L. D. Tung, Phys. Rev. B - Condens. Matter Mater. Phys. **72**, 1 (2005).
[4] M. Reehuis, C. Ulrich, P. M. Abdala, P. Pattison, G. Khaliullin, J. Fujioka, S. Miyasaka, Y. Tokura, and B. Keimer, Phys. Rev. B **94**, 1 (2016).
[5] D. Kumar, A. David, A. Fouchet, A. Pautrat, P. Boullay, C. U. Jung, and W. Prellier, ACS Appl. Mater. Interfaces **12**, 35606 (2020).
[6] D. Kumar, A. Fouchet, A. David, A. Cheikh, T. S. Suraj, O. Copie, C. U. Jung, A. Pautrat, M. S. Ramachandra Rao, and W. Prellier, Phys. Rev. Mater. **3**, 1 (2019).
[7] S. B. Ogale et al., J. Appl. Phys. **84**, 6255 (1998).
[8] S. Kalia, V. Ranade, K. H. Chae, F. Singh, R. Mishra, R. J. Choudhary, R. Kumar, and R. Kumar, , J. Alloys Compd. **1010**, 177998 (2025).

Fabrication of Al_2O_3 Nanopore By Anodization Technique for SERS Application

Najmeh H. Dehkordi[1] and Rajeshkumar S. Hyam [1,a)]
[1] *School of Physical and Applied Sciences, Goa University, Taleigao, Goa, India. 403206*

[a)]*Corresponding author: rajesh.hyam@unigoa.ac.in*

Abstract. The synthesis of anodic aluminum oxide (AAO) nanostructures and their morphology has generated significant attention in the field of nanotechnology. The fabrication procedure of anodic aluminum oxide involves a controlled electrochemical process known as anodization. This process transforms aluminum into a highly ordered nanostructured oxide material which is suitable for Surface Enhanced Raman scattering (SERS). In this work a pure Aluminum foil was two step anodized with voltage variation of 40 to 60 volts for six hours at 1-step and one minute for 2nd step. Samples were then coated with plasmonic gold nanoparticles with spin coating technique and drop cast with different R6G concentration to study the SERS signal. Scanning Electron microscopy and Raman spectroscopy characterization was performed on samples to study their morphology and SERS properties of samples.

KEYWORDS: Anodic Aluminum oxide, Anodization technique, plasmonic Gold nanoparticles, Rhodamine 6G, SERS

INTRODUCTION

Surface-enhanced Raman scattering (SERS) is an optical effect that significantly enhances Raman signals for molecules on nanostructured substrates. It provides detailed chemical composition information, enabling the detection of minute quantities, potentially down to single molecules in an analyte. Practical SERS substrates require stability, reproducibility, cost-effectiveness, and easy production [1]. Various fabrication methods focus on colloidal solutions or films with Au and Ag nanoparticles, but these often lack reproducibility and sufficient hot-spot volume density [2]. Among non-lithographic techniques, the use of anodic aluminum oxide (AAO) templates for patterned nanoparticle arrays has gained attention [3]. Anodization, discovered in 1857 [4], creates durable, corrosion-resistant oxide layers with controllable nanopore structures. AAO has applications in nanotechnology, biosensing, and drug delivery, offering large surface areas and uniform pore sizes that enhance SERS signal amplification. AAO-based SERS biosensors are capable of detecting biomolecules with high sensitivity and specificity. It promises significant advancements in biomedical research, diagnostics, and environmental monitoring, thus allowing for ultra-low concentration of analyte detection [5].

EXPERIMENTAL

To fabricate self-ordered nanoporous anodic aluminum oxide (AAO), aluminum foils (1.2 cm × 4 cm, 0.5 mm thickness, purity 99%) were employed as the anode, while a platinum sheet (2 cm × 2 cm) functioned as the cathode, positioned parallel to each other with a 2 cm separation. The aluminum foil and platinum sheet were degreased in an ultrasonic bath with ethanol for 30 minutes. To eliminate surface roughness and irregularities, the aluminum foil was electropolished in a mixture of perchloric acid ($HClO_4$) and ethanol (C_2H_5OH) (at a 1:4 volumetric ratio) for 60 s at room temperature with an applied voltage of 20 volts. The samples were then washed with distilled water and dried. A two-step potentiostatic anodization process was used to prepare the samples. The first step of anodization was performed using 0.3M oxalic acid ($H_2C_2O_4$) for 360 minutes at 15°C, with a varied voltage ranging from 40 volts to 60 volts. To remove the first step of anodization, the samples were immersed in a mixture containing 1.8 wt/g chromic acid and 6 mL phosphoric acid for 3 h at a temperature of 65°C. The second step of anodization was performed under the same conditions as the first step, with a duration of 1 min. A star-shaped plasmonic AuNP coating was applied to the sample surfaces using a spin-coating technique at a speed of 1500 rpm for 60 s. Rhodamine 6G (R6G) at concentrations of 0.1 mM, 0.01 mM, and 0.001 mM was then drop-cast onto the samples to study their surface-enhanced Raman scattering (SERS) signal [6].

RESULTS AND DISCUSSION

To examine the surface morphology of the fabricated sample, the scanning electron microscopy (SEM) characterization technique was utilized. Figure 1 presents an SEM image of the two-step anodized sample S3, which was subjected to an applied voltage of 60 volts. The SEM image clearly illustrates the effect of the applied voltage during anodization on the pore diameter and growth. Uniform self-ordered pores were formed on the

surface of S3, with an average pore diameter of 65 nm. Sample S3 was divided into three pieces, designated as aS, bS, and cS. To investigate the surface-enhanced Raman scattering (SERS) tunability of the samples, they were spin-coated for 60 seconds with gold nanoparticles at a concentration of 1 mM. Subsequently, rhodamine 6G (R6G) at concentrations of 0.1 mM, 0.01 mM, and 0.001 mM was drop-cast onto the surfaces of samples aS, bS, and cS, followed by Raman spectroscopy analysis at a wavelength of 532 nm. The SERS intensity of the samples is depicted in Figure 2. The Raman peaks of R6G molecules were detected at 787 cm^{-1} and 1363 cm^{-1} for all three different R6G concentrations. The sample cS, which was drop-cast with 0.001 mM R6G, exhibited higher intensity at 787 cm^{-1} and 1363 cm^{-1} compared to samples aS and bS. The advantage of this method is that it allows for the fabrication of self-ordered SERS substrates through two-step anodization without the use of lithographic techniques.

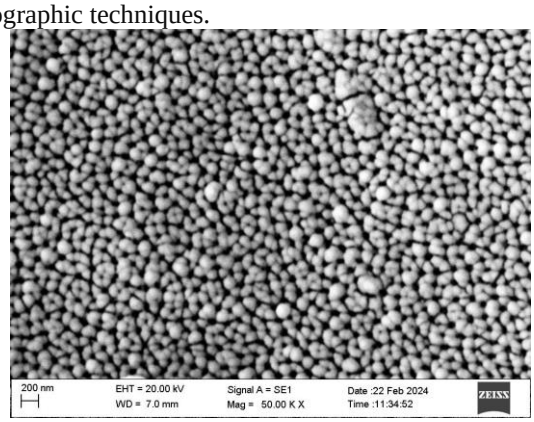


FIGURE 8. SEM image of S3 sample which was anodized with applied voltage of 60 volts.

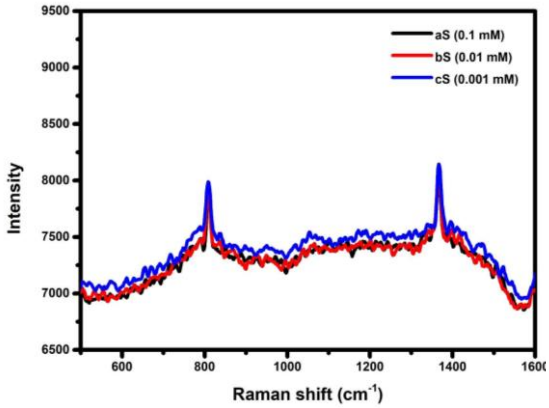


FIGURE 2. Raman spectroscopy graph of aS (0.1 mM) and bS (0.01 mM) and cS (0.001 mM) R6G concentration.

CONCLUSION

This study aimed to investigate the Surface-Enhanced Raman Scattering (SERS) signals from porous anodic aluminum oxide (PAAO) substrates prepared under varying anodization conditions. Scanning Electron Microscopy (SEM) images of samples fabricated at different voltage levels, determined that Sample S3, anodized at 60 volts, exhibited an average pore diameter of 65 nm, rendering it suitable for SERS applications. The concentration of Rhodamine 6G (R6G) on the surface of Sample S3 was varied, and it was observed that a concentration of 0.001 mM resulted in the highest SERS signal intensity. Several factors, including the length of the anodic aluminum oxide (AAO) pores, the thickness of the gold nanoparticles layer coated on the AAO substrate, and the concentration of R6G, can influence the SERS signals. Enhancing all these parameters is expected to improve the intensity of the SERS signals.

ACKNOWLEDGMENTS

This work was supported by the School of Physical and Applied Sciences, Goa University and Indian Council for Cultural Relations (ICCR). Special thanks to Dr. Sudhir Cherukulappurath laboratory for providing plasmonic gold nanoparticles.

REFERENCES

1. A Ruiz-Clavijo, O Caballero-Calero, M Martín-González, Nanoscale **13**, 2227-2265, (2021).
2. Dukhyun Choi, Yeonho Choi, Soongweon Hong, Taewook Kang, Luke P. Lee, Small **6**, 1741-1744, (2010).
3. Chengyuan Li, Yilin Ni, Jingjing Gong, Ye Song, Tianle Gong, and Xufei Zhu, Nanoscale **4**, 322-333, (2022).
4. H. Masuda and K. Fukuda, Science **268**, 1466-1468, (1995).
5. Silu Feng and Weiwei Ji, Frontiers in Nanotechnology **3**, 678275, (2021).
6. Mikhail Pashchanka, Sherif Okeil, and Jorg J. Schneider, ACS **124**, 25931-25943, (2020).

Towards Sustainable Construction Materials: CO_2 Sequestered M-Sand-Cement Blocks

Md Zamil Hasan Shovon, Vasanthmani I., Arunachaleshwar V, Malavika Sunil and B. M. Jaffar Ali*.
Department of Green Energy Technology, Pondicherry University, Kalapet, Pondicherry 605014.
* jaffarali.get@pondiuni.ac.in

Abstract. This study delves into the impact of carbon dioxide (CO_2) curing on cement blocks, specifically looking at their microstructure, mechanical strength, and CO_2 uptake. The cube and cylindrical shaped cement blocks were made to test the CO_2 uptake capacity at 0.25 bar and consequent effect on its compression strength. CO_2 curing of cement-M sand blocks were carried at two different water to cement ratios (w/c), namely 0.48 and 0.35 at 0.25 bar pressure. Analysis of CO_2 uptake by mass gain method on an ASTM standard block reveal about 12.5 wt.% uptake while retaining a compression strength of 22.1 MPa. We gather evidence from thermal analysis and XRD data that enhanced formation of calcium carbonate takes place when subjected to CO_2 curing. Furthermore, a significant amount of microstructure densifications was observed from SEM analysis. The results indicate that CO_2 curing in M-sand-cement block sequester significant amount of carbon without compromising on the structural strength of the material block. Therefore, CO_2 curing of M-sand - cement blocks offer a sustainable way of utilizing construction materials by mitigating over-all carbon footprint of its production process.
Keywords: CO_2 curing, Water to cement ratio, Carbonation curing, Accelerated carbonation, Compression strength, Cement block, CO_2 curing reactor, Calcium carbonate precipitation.

INTRODUCTION

Around 8.0% of carbon dioxide (CO_2) emissions come from manufacturing cement and concrete [1][2]. Predictions state that between 2030 and 2050, CO_2 emissions from cement and concrete production may contribute more than 10% of all CO_2 emissions worldwide [3]. To reduce concrete's adverse impact on global carbon footprint, researchers have focused on developing new cement types having low carbon footprints, like magnesium silicates, calcium sulfoaluminate belite binders, and geo-polymers [4]. Also, significantly replaced cement in concrete production with additional materials, namely, fly ash, granulated blast furnace slag, and silica fume [5]. Recent research on CO_2 curing on construction materials to absorb and store the CO_2 in sand-cement block has been shown to be another promising option realize carbon neutrality [6]. It was found that when there is an excess ambient CO_2 available, the carbonation process wins over the hydration reaction in concrete/ cement-sand mixtures, leading to significant CO_2 assimilation [7][8]. The interaction between cement and calcium-modified silica gel quickly forms from clinkers or cement that hydrates with CO_2 [9]. Thus, formed calcium carbonate ($CaCO_3$) can fill in and make the microstructure matrix denser thereby, in addition to CO_2 sequestration, it also enhances the strength and durability of cement-based products. In the recent time, M-sand replacing the conventional river sand, assume greater significance in examining its viability in CO_2 sequestration in place of river sand. The focus of this research thus has been to sequester carbon dioxide in M-sand - cement blocks and investigate its effect on the mechanical properties.

MATERIALS AND METHOD

Sample Preparation: The experiment employed Portland Pozzolanic Cement (PPC), Dalmia, M-sand, and water were mixed to built standard cement cubes of 70×70×70 mm^3 and cylinders of D/H 20 mm × 30 mm as per ASTM standard. A 99.9 % pure CO_2 gas was used to create the CO_2 atmosphere. The cement to M-sand ratio (c/s) in wt.% for both cylindrical and cube samples are 1:2.75 (c/s). Two types of specimens were prepared with the w/c ratio specified 0.485 and 0.35. All standard 70mm cubes were prepared with 0.35 w/c ratio as reasoned in the results section. The cement, M-sand, and water were meticulously mixed by hand to produce a homogeneous mixture, filled the cylindrical and cube mold with two layers, 32 tamps were added using a rod for even compaction between layers. After the casting process, the specimens were left undisturbed for 24 h at room temperature prior to CO_2 curing. Process parameters, namely, temperature, pressure and time are varied to arrive at optimal CO_2 uptake. **Water Curing:** To compare CO_2 uptake capacity of specimens cured at two different w/c ratios (0.485 and 0.35), samples were subjected to conventional water curing (also called ponding) by immersing them in a water container for 7 days (d). Two of the eight produced cylindrical specimens were selected for ponding. **CO_2 curing process:** An airtight cylindrical vessel with a single intake and a pressure safety valve was chosen as the controlled environment for curing the cement blocks under CO_2. A sealed enclosure facilitates the regulated CO_2 exposure to the blocks. The cylindrical samples are subjected to carbonation for 6, 12, 24 h and at pressure of 0.25 bar. All the cube samples were subjected to carbonation for 6 h and at pressure of 0.25 bar. **CO_2 curing reactor:** An autoclave chamber has been retrofitted as an airtight vessel appropriate for CO_2 curing. Additionally, a pressure gauge used to monitor the vessel's internal pressure dynamics. **Calculation of CO_2**

Capture Capacity: Two approaches were used to determine the carbon sequestration of M-sand/cement mixture or mortar that has undergone carbonation. The mass gain method determined the mortar's CO_2 uptake following early-age carbonation curing. The cement dry mass was the basis for this procedure. Cement mortar samples were weighed using a digital balance, designated $\mathbf{m_1}$ before curing and, again, after carbonation, which was designated $\mathbf{m_2}$. The volume of water produced during the carbonation curing process was measured and recorded as water. Finally, the CO_2 uptake computation is provided by Eq.1. The mass gain method provided a direct way to detect the formation of carbonation by curing [10].

$$\boldsymbol{CO_2\ uptake}\ (\%) = \frac{\boldsymbol{m_2 - m_{water} - m_1}}{\boldsymbol{m_{cement}}} \times \mathbf{100}\ \% \quad (1)$$

where m_{water} was the water mass extracted from the inside of the curing chamber, m_{cement} was the sample's dry cement mass determined by the mix design, and m_1 and m_2 were the sample masses before and following carbonation, respectively. Since calcium carbonate can breakdown between 550 °C and 1000 °C, samples were heated to this temperature to monitor mass loss. Thus, the CO_2 content of a cubic mortar samples was further investigated using the thermal analysis method. A 5 g of specimen powder drawn from different distinct depths (0-10 mm) from all faces of cubic samples and heated to 105, 550, and 1000 °C. After each heating regime, the residual mass was calculated and CO_2 uptake calculated using thermal mass loss method using Eq. 2.

$$\boldsymbol{CO_2\ uptake}\ (\%) = \frac{\boldsymbol{m_3 - m_4}}{\mathbf{m_0}} \times \mathbf{100}\% \quad (2)$$

Where $\mathbf{m_3}$ is residual mass of sample at 550°C, $\mathbf{m_4}$ is residual mass measured at 1000°C and $\mathbf{m_0}$, is the mass of mortar multiplied by the cement ratio based on the mix design (0.26667).

RESULT AND DISCUSSION

Optimal w/c ratio and CO_2 curing time: Following Eq.1, CO_2 uptake was quantified for small cylindrical samples. Results of experiments of CO_2 uptake as a function of two ratios of w/c carried out on small cylindrical specimen, determined for various CO_2 curing time is given in Fig.1(a). The M-sand/cement mortar exhibited 10.5 to 12.5 wt.% sequestration of CO_2. It was observed that for w/c of 0.35, consistently high CO_2 uptake as a function of curing time is shown. Hence, 0.35 ratio is considered for further evaluation. Further, since there appears to be marginal increase in CO_2 uptake beyond 6h curing time, optimal curing time is taken as 6 h for further investigations.

Effect of CO_2 Uptake on Compressive Strength: Results of analysis of compressive strength of the M-sand/cement blocks prepared under ASTM standard size of 70mm cube evaluated at w/c ratio of 0.35 under 6 h curing is summarized in Fig.1(b). As control experiments, 7 d water cured samples were compared. The results reveal that both water cured and CO_2 sequestered M-sand/Cement blocks exhibit near equal compressive strength characteristics. It underscores the fact that CO_2 curing did not compromise on the structural strength of the cement blocks, at the same time, it has assimilated more than 10 wt.% CO_2 in the block under 6 h accelerated curing process.

Analysis of XRD Pattern: The diffraction patterns for 6 h CO_2 cured and only water cured samples were obtained and analysed. Major peaks of the component of M-sand/cement mortar material, namely, quartz, calcite, di-calcium silicate (C_2S), and portlandite ($Ca(OH)_2$) were identified as shown in Fig.1(c). It is observed that the amounts of calcite peaks were distinctly larger in the 6h CO_2 cured samples compared to the water-cured samples. On the other hand, the portlandite peaks were significantly lower in the former. Therefore, the XRD data indicate that CO_2 curing significantly improves the micro-morphology of the cured blocks, leading to the enhancement of the physical and mechanical qualities.

Thermal deconstruction of M-sand/cement block: The thermal deconstruction of cement mortar leading to mass loss, is provided in Fig.1(d). Results of both CO_2 sequestered and only water cured samples are given in Fig.1(e). The uptake of CO_2 is derived from the mass loss method pertains to the deconstruction of carbonate in the sample. It was demonstrated that a substantial amount of the portlandite (CH) is efficiently utilized during the CO_2 curing process, evident from the formation of calcium carbonate crystals which manifest break down at high temperature leading the substantial loss of mass (Fig.1(d)). The CO_2 content percentage was calculated using Eq.1. It is noted that 6 h CO_2 cured block showing a mass loss of 14.01 wt.%, whereas the conventional water cured block had a considerably lower percentage of mass loss. This difference suggests a significant amount of carbon dioxide sequestration was achieved by the CO_2 curing technique.

SEM Evidence for the Fixation of Carbon: Fig. 2 presents the SEM images of the 6 h CO_2-cured sample and compared with SEM pictures of 7 d water-cured specimen at w/c ratio of 0.35 for comparison study. There is a noticeable difference in the microstructures of the two specimens shown in Fig.2(a-d) upon comparison. It is

evident from the 6 h CO_2 cured sample that cubic $CaCO_3$ aggregates on the pores' surface and that some C-S-H-like products are present within these pores, leading to a denser structural configuration. Overall, SEM analysis shed light on the differing microstructural characteristics of the two curing techniques, bringing out the complex interactions between mechanical strength, pore shape, and hydration products.

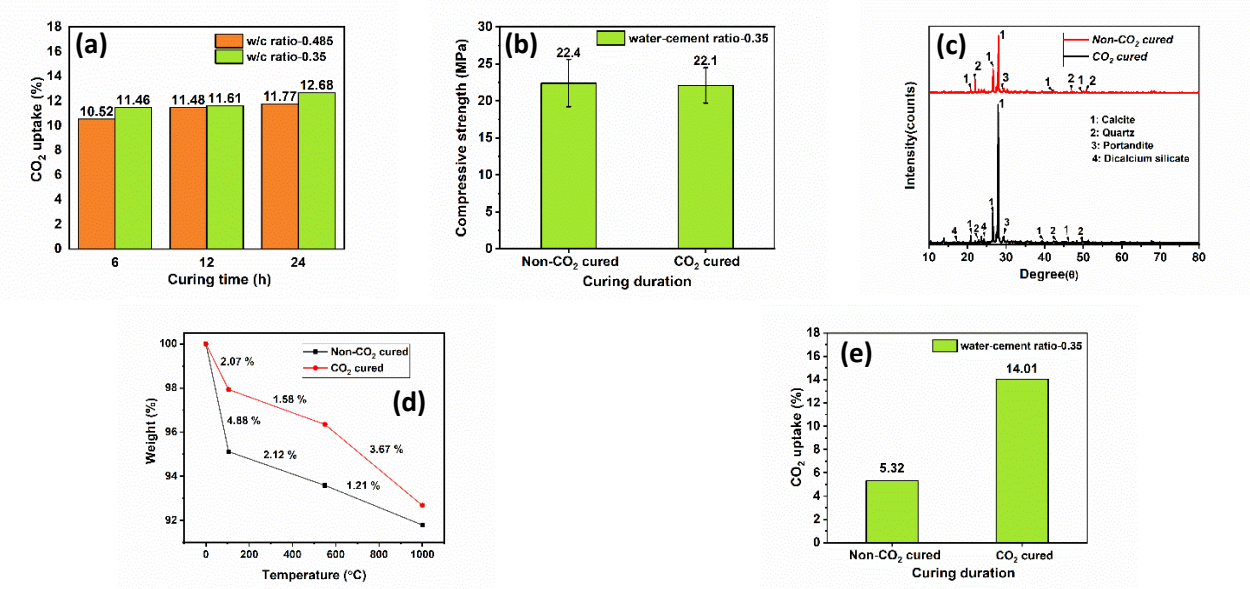


FIGURE 1. (a) Quantification of CO_2 sequestration by mass gain at fixed 24 h precuring; (b) Compressive strength specimen for different curing time; (c) XRD patterns of cement blocks CO_2 cured and water cured sample; (d) Weight loss analysis by thermal deconstruction; (e) Evaluation of CO_2 sequestration by mass loss.

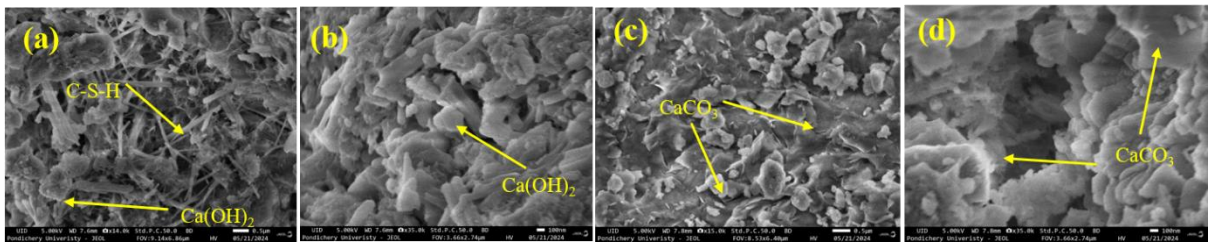


FIGURE 2: SEM images of (a-b) 7 d water cured sample; (c-d) 6 h CO_2 cured sample.

CONCLUSION

In this study, CO_2 uptake in M-sand/cement mortar containing PPC and M-sand (an alternative material for river sand) has been examined. The w/c ratio of 0.35 found to be optimal in retaining better compressive strength and maximal CO_2 uptake. Study of specimen's microstructure morphologies by SEM show appreciable densification which was corroborated by the results of thermal analysis and XRD pattern. The CO_2 absorption in cement blocks found to be as high as 11.4 wt.%, at an optimal 6 h of CO_2 curing. Higher curing duration appears to have very low or marginal increase in CO_2 sequestration. Cement blocks cured with CO_2 for 6 h had compressive strengths comparable to those cured with conventional water for 7 d, indicating that the CO_2 curing process did not affect the material's strength. Overall, these findings highlight the possibility of CO_2 curing as a sustainable way to improve the qualities of cement mortar without affecting its functionality and strength.

REFERENCE

[1] N. Lippiatt, T. C. Ling, and S. Y. Pan, *Journal of Building Engineering*, vol. 28, p.101062 (2020).
[2] B. Lothenbach, K. Scrivener, and R. D. Hooton, *Cem. Concr. Res.*, vol. 41, pp. 1244–1256 (2011).
[3] N. Müller and J. Harnisch, *Report for the WWF–Lafarge Conservation Partnership.* (2008).
[4] L. J. Vandeperre, M. Liska, and A. Al-Tabbaa, *Cement and Concrete Composites*, vol. 30, pp. 706–714 (2008).
[5] M. I. A. Khokhar, E. Roziere, P. Turcry, F. Grondin, and A. Loukili, *Cement and Concrete Composites*, vol. 32, pp. 377–385 (2010).
[6] J. G. Jang, G. M. Kim, H. J. Kim, and H. K. Lee, *Construction and Building Materials*, vol. 127, pp. 762–773 (2016).
[7] T. Chen and X. Gao, *Journal of CO2 Utilization*, vol. 34, pp. 74–86, (2019).
[8] H. Mehdizadeh, X. Shao, K. H. Mo, and T. C. Ling, *Cement and Concrete Composites*, vol. 133, (2022).
[9] B. Šavija and M. Luković, *Construction and Building Materials*, vol. 117, pp. 285–301 (2016).
[10] D. Zhang and Y. Shao, *Construction and Building Materials*, vol. 113, pp. 134–143 (2016).

Trap Dynamics in ALPO Capacitive Devices

Atul Sachan*, Sandip Mondal

Department of Electrical Engineering, IIT Bombay, Mumbai 400076, India

*Corresponding author: 22D0521@iitb.ac.in

Abstract. Charge-trapping oxides are essential for non-volatile memory storage in electronic devices such as smartphones, laptops, industrial robots, and self-driving cars. However, the performance of memory technology often degrades due to the interface state density between the oxide and the semiconductor. In this work, we demonstrate fully solution-processed Aluminum Oxide Phosphate (ALPO) devices, which exhibit unique memory-like behavior due to intrinsic trap levels. These intrinsic traps cause a distinct hysteresis in the capacitance-voltage (CV) traces, highlighting the devices' memory-like characteristics. Our ALPO devices show a charge storage capacity of 1.765×10^{13} cm^{-2}, a low leakage current density of 7.81×10^{-9} A/cm^2, and a low interface trap density (Dit) of 9.1×10^{10} $cm^{-2}eV^{-1}$, which are critical for high performance. Thermal treatment alters trap density and influences electrical performance, affecting voltage and leakage current. The interplay between carrier transport and electric field effects, driven by interface trap density and gate voltage, offers valuable insights into MOS capacitor behavior. This research underscores the potential of ALPO in enhancing electronic device efficiency and scalability.

Keywords. Aluminum Oxide Phosphate (ALPO), Interface Trap Density (D_{it}), Capacitance-voltage (CV).

INTRODUCTION

Flash memory is a type of non-volatile data storage system based on transistor technology that has become crucial to modern electronic devices. Non-volatile flash memory is an essential component in modern electronic devices due to its operating simplicity and seamless integration into NAND or NOR array designs. Predominantly made of silicon-oxide-nitride-oxide-silicon (SONOS), this memory technology is the dominant paradigm in modern computer memory systems, utilizing discrete locations for storing electric charges within silicon-rich silicon nitride layers [1-3]. Despite its effectiveness, the fabrication of sol-gel dielectrics often requires high-temperature processing to achieve low-leakage solid-state films. Various materials, including TiO_2, ZrO_2, HfO_2, and Al_2O_3, have been explored as alternatives. However, leakage currents remain a persistent issue, potentially limiting their application in memory devices. A new cost-effective, all-inorganic precursor solution-processable Aluminum Oxide Phosphate (ALPO) has recently been introduced as a promising solution to this problem [4-6]. ALPO has been previously utilized to fabricate entirely solution-processed thin-film transistors (TFTs), and it shows exceptional properties in two-terminal memory devices optimized for trapping and blocking layers, such as low leakage current density. The energy distribution of electronic traps (E_{IL}) within dielectric materials situated between tunneling and blocking layers is crucial for the performance of charge-trapping flash memory systems. Traditional dielectrics like Si_3N_4, HfO_2, ZrO_2, and TiO_2 contain numerous intrinsic traps (approximately $>10^{12}$ cm^{-2}), formed through high-temperature processing and ultrahigh vacuum procedures. However, low-temperature solution-processed dielectrics (200°C) with a considerable number of deep-level traps ($>10^{12}$ cm^{-2}) and minimal leakage currents (10^{-6} A/cm^2) are necessary for flexible electronics [7-9]. ALPO dielectric-based tunable flash memory, manufactured using sol-gel technology, offers controlled traps ($N_T > 10^{13}$ cm^{-2}) at low temperatures, making it ideal for these applications.

DEVICE FABRICATION AND EXPERIMENTAL SETUP

Material Growth: The Aluminum Oxide Phosphate (ALPO) precursor solution was synthesized using a well-defined procedure to ensure the desired composition and properties. The synthesis began by preparing a solution in water with a resistivity of 18 MΩ cm. The main component, Aluminum Hydroxide [$Al(OH)_3$] powder (99%, Alfa Aesar, USA), was dissolved in this high-purity water. To achieve the correct chemical environment, two mole equivalents of Hydrochloric Acid (HCl, AR Grade, Thermo Fisher Scientific, USA) were added to the solution. Following this, an appropriate amount of Phosphoric Acid (H_3PO_4, ExcelaR Grade, Thermo Fisher Scientific, USA) was introduced to obtain a

phosphorus-to-aluminum (P/Al) ratio of approximately 0.5, resulting in a final precursor concentration of 0.5 M (Molarity). The mixture was thoroughly stirred and heated at 90°C for 24 hours to ensure complete dissolution and proper reaction between the components. This process allowed the ALPO precursor solution to form, characterized by its specific chemical composition [$Al_2O_{3-3}X(PO_4)_2X$]. The controlled synthesis conditions, including the precise ratios of reactants and the extended heating period, were crucial for obtaining a homogenous and stable precursor solution suitable for further processing into charge-trapping oxide layers for non-volatile memory devices.

Device Fabrication: Two-terminal MOS devices (Al/ALPO/p-Si) were fabricated on piranha-cleaned [H_2SO_4:H_2O_2] lightly doped p-silicon substrate (doping of 4.11×10^{15} cm^{-3}). The ALPO solution was spin-coated at 3500 rpm for 30 sec to form the gate dielectric. The films were then heated at 275 °C for 1 minute. This process was repeated 3 times to achieve the desired thickness of around 91 nm. The sample was exposed to oxygen plasma for 8-11 minutes at 0.5 mbar pressure before deposition of each layer. A 200 nm top aluminum gate was deposited by thermal evaporation at 10^{-6} mbar pressure with a shadow mask. Before the deposition of the top aluminum gate, the ALPO films were annealed at 300 °C for 2 hr at normal room temperature.

RESULT & DISCUSSION

The ALPO-MOS devices (Al/ALPO/p-Si) were analyzed using capacitance-voltage (CV) measurements at a high frequency of 1 MHz with a small signal amplitude of 0.050 V as shown in Fig. 1a. We observed a change in flat band voltage (ΔV_{FB}) of approximately 11.4 V for a gate oxide thickness of around 91 nm and 5 V for a thickness of about 32 nm, with constant sweep voltage. The ΔV_{FB} per unit thickness relative to gate oxide thickness remains nearly constant because the electric field is inversely related to the oxide thickness as shown in Fig. 1b. In Fig. 1c, the notable increase in ΔV_{FB} from 2.35 V to 11.5 V is due to the rising sweep voltage from ±5 V to ±15 V, which amplifies the electric field. This heightened electric field enhances charge injection into deep-level traps, resulting in a larger ΔV_{FB} and an expanded hysteresis window. Consequently, the trapped charge density increases from 6.834×10^{11} cm^{-2} to 3.016×10^{12} cm^{-2}, attributed to the increased electric field that promotes more charge injection into the deep-level defects within ALPO [10].

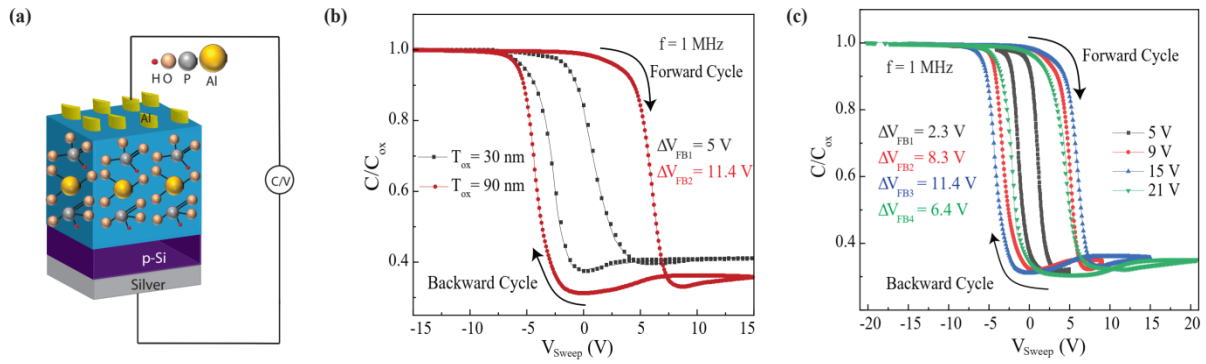


FIGURE 1. (a) Schematic of ALPO-MOS device (Al/ALPO/Si), (b) At a constant voltage supply of 15V, there is a significant amount of change in the hysteresis window from 5V to 11.4V for oxide thickness (T_{ox}) of around 30 nm (B) and 90 nm (R), (c) HFCV curve for ALPO-MOS device is plotted at different sweep voltages shows a significant amount of change in the ΔV_{FB}.

At room temperature, the leakage current density varies from 7.718×10^{-9} A/cm² to 3.718×10^{-8} A/cm² as the thickness of the gate oxide decreases. This variation occurs because, as the oxide layer becomes extremely thin (typically a few nanometers or less), electrons can tunnel directly through the barrier between the semiconductor and the gate electrode. This tunneling is a quantum mechanical phenomenon

where electrons have a probability of passing through the barrier even if they do not possess sufficient energy to overcome it in a classical sense. As the barrier thickness reduces, the likelihood of tunneling increases, resulting in higher leakage currents as shown in Fig. 2a. To understand the underlying mechanisms of the ALPO-MOS devices, we examined the band diagram with ALPO's electron affinity and band gap values of E_A (ALPO) = 1.365 eV and E_g (ALPO) = 7.63 eV, respectively as shown in Fig. 2b. Under zero gate bias, the system reaches equilibrium with the Fermi level aligned with the mid-gap energy levels. When a negative gate voltage ($V_g < 0$) is applied, the energy bands bend, depleting charges near the Si-ALPO interface and causing charge injection into deep-level traps as shown in Fig. 2c. Conversely, during inversion with a positive gate voltage ($V_g > 0$), the stored charges are ejected from the Si-ALPO interface to the metal gate, which results in the removal of charges from the deep-level traps as shown in Fig. 2d.

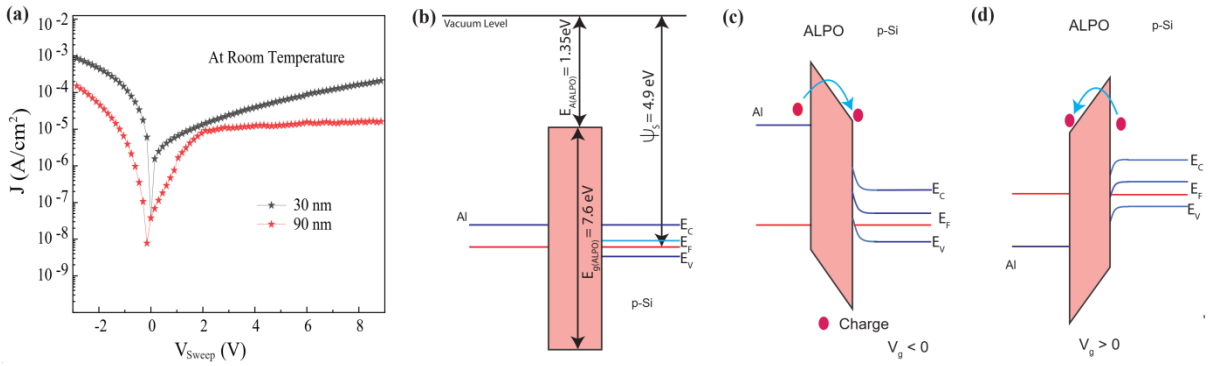


FIGURE 2. (a) At different gate oxide thickness variation in J is observed at constant sweep voltage, (b) Alignment of energy band diagram for ALPO-MOS structure at $V_g = 0$, (c) Band bending in the ALPO-MOS interface when $V_g < 0$ is applied, (d) Band bending in the ALPO-MOS interface at inversion when $V_g > 0$.

CONCLUSION

In conclusion, the solution-processed ALPO dielectric films demonstrate a large amount of memory hysteresis in CV curve which corresponds to an enormous amount of charge trapping within the dielectric medium. This research has investigated Aluminum Oxide Phosphate (ALPO) as a promising dielectric material for non-volatile memory devices. The study explored factors influencing the memory window, including trap density and thickness, utilizing the Termann method to calculate the interface trap density (Dit). ALPO exhibited a remarkable hysteresis response and low leakage current, positioning it favorably among non-volatile memory materials. The unique properties of ALPO, such as its ability to form stable, low-leakage films at low processing temperatures and its efficient charge-trapping capabilities, underscore its potential to advance non-volatile memory technology. These findings suggest that ALPO could become a compelling candidate for future applications in non-volatile memory devices, addressing current limitations and enhancing the performance and scalability of electronic systems.

ACKNOWLEDGMENTS

The authors would like to express their gratitude to the Indian Institute of Technology Bombay Nanofabrication Facility for providing the facilities for the fabrication and characterization of the set of devices.

REFERENCES

1. JS. Meena, SM. Sze, U. Chand, TY. Tseng, Nanoscale Research Letters, vol. **9**, no. 1, pp. 1-33 (2014)
2. SH. Liu, WL. Yang, CC. Wu, TS. Chao, in IEEE Electron Device Letters, vol. **33**, no. 10, pp 1393-1395 (2012)
3. S. Mondal, Venkataraman, Nature Communication **10**, 2143 (2019)
4. S. Mondal, T. Paul, A. Ghosh and V. Venkataraman, in IEEE Electron Device Letters, vol. **41**, no. 5, pp 717-720 (2020)
5. S. Mondal, A. Kumar, IEEE Transactions on Electron Devices, vol. **68**, no. 3, pp 1190-1195 (2021)
6. A. Sachan, S. Mondal, IEEE Electron Devices Technology and Manufacturing Conference, pp. 1-3 (2024)
7. W. Xu, H. Li, JB. Xu, L. Wang, in ACS applied materials and interfaces, vol. **10**, no. 31, pp. 25878-25901 (2018)
8. A. Sachan, S. Mondal, in DRC, Maryland, U.S.A (2024)
9. Z. Cui, D. Xin, T. Kim, J. Choi, J. Cho, J. Yi, ECS Journal of Solid-State Science and Technology, vol. **10**, no. 12, pp. 125002 (2021)
10. S. Mondal, Venkataraman, Appl. Phys. Lett., vol. **114**, no. 17, (2019)

Effect of Stacking of Layers and Variation of Ag Layer Thickness in (Cu, Al)-SnO_2/Ag Layer on Optical and Electrical Properties

Anju Dutt[1, 2, a)], Harpreet Singh[1, 2], Sangeeta[1, 2], Anand Kumar[2]

[1]*Department of Physics, Kurukshetra University, Kurukshetra, Haryana 136119, India*
[2]*Department of Physics, Institute of Integrated and Honour Studies, Kurukshetra University, Kurukshetra, Haryana 136119, India*

[a)]Corresponding author E-mail: anju.iihs@kuk.ac.in

Abstract: The CuAl co-doped SnO_2 single layer, (CuAl)-SnO_2/Ag bilayer of different thicknesses, and (CuAl)-SnO_2/Ag/(CuAl)-SnO_2 multilayer thin films were successfully deposited by the e-beam evaporation method on a glass substrate. The current study examines how varying the thickness of Ag affects the structural, optical, and electrical properties of CAT/Ag thin films. Layer stacking significantly impacts both the electrical and optical characteristics of materials. With layer stacking in the multilayer configuration, both optical transmittance and electrical conductivity increase, reaching maximum values of 84.75% and $3.09 \times 10^4\ \Omega^{-1}cm^{-1}$, respectively. Additionally, increasing the thickness of the silver (Ag) layer further enhances these properties, resulting in an optical transmittance of 57.02% and an electrical conductivity of $1.16 \times 10^4\ \Omega^{-1}cm^{-1}$.
Keywords: Transparent Conducting Oxides, Stacking, Electrical and Optical properties. Silver layer thickness

INTRODUCTION

Transparent conductive oxides (TCOs) are materials that exhibit excellent electrical and optical properties simultaneously, making them ideal for optoelectronic devices. Tin Oxide (SnO_2) is an n-type transparent oxide semiconductor with a direct and wide bandgap, offering significant potential for optoelectronic applications. Semiconductors from the II-VI group are known for their high conductivity and optical transparency, making them valuable for energy storage applications [1]. Recent research has focused on SnO_2-based TCO multilayer thin films due to their high demand in optoelectronics [2].

In this study, we fabricated CuAl co-doped SnO_2 single-layer, CuAl-SnO_2/Ag bilayer, and trilayer CuAl-SnO_2/Ag/CuAl-SnO_2 thin films on glass substrates using the e-beam evaporation technique. We investigated their structural, optical, and electrical properties. The study discusses the impact of increasing the number of layers and the variation in properties with changes in Ag thickness in the CuAl-SnO_2/Ag layer.

EXPERIMENTAL PROCEDURE

The glass substrates were cleaned ultrasonically using liquid soap, distilled water, acetone, and isopropyl alcohol. To prepare the (Cu-Al)-SnO_2 pellets, a powder mixture containing 2 mol% of Cu, 2 mol% of Al, and 98 mol% of SnO_2 was ground in a mortar and pestle for 2 hours. The resulting pellets were then sintered at 950°C. These CuAl-SnO_2 pellets, along with chunks of Ag metal, were used as target materials for thin film deposition.

The samples CuAl-SnO_2 single layer, CuAl-SnO_2/Ag (8 nm), CuAl-SnO_2/Ag (12 nm), CuAl-SnO_2/Ag (16 nm), CuAl-SnO_2/Ag (20 nm), and CuAl-SnO_2/Ag (16 nm) /CuAl-SnO_2, were synthesized with different Ag thicknesses e.g., 8 nm, 12nm, 16 nm, and 20 nm, and are abbreviated here as CAT, CA1, CA2, CA3, CA4, and CAT/Ag/CAT, respectively. The CAT layer was deposited by taking voltage, current, and substrate temperature at 5KV, 40mA, and 200°C, respectively. The Ag layer was deposited by taking voltage, current, and substrate temperature at 5KV, 7mA, and 30°C. The entire deposition process in the e-beam evaporation chamber was conducted under ultra-high vacuum conditions, i.e., 2×10^{-5} mbar pressure at 0.3 (ang/sec) deposition rate with the substrate rotation rate of 10rpm.

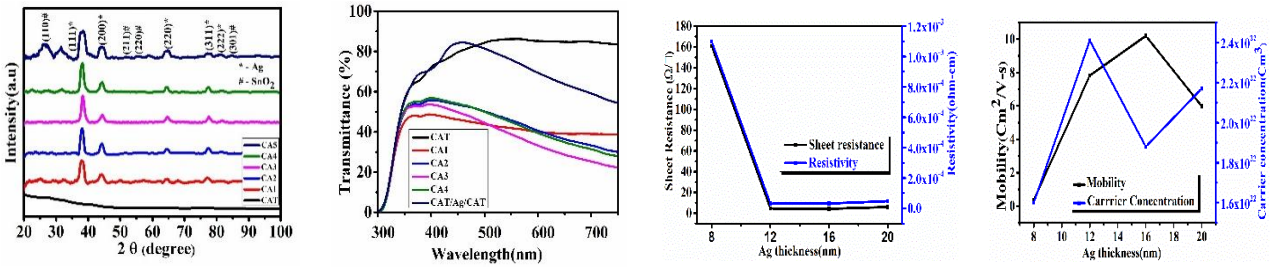
RESULTS AND DISCUSSIONS:

The Glancing Angle X-ray Diffraction (GXRD) spectra of CAT, CAT/Ag (8 nm, 12 nm, 16 nm, 20 nm), and CAT/Ag/CAT are shown in Fig. 1(a). The CAT thin film sample exhibits an amorphous nature. For CAT/Ag (8 nm, 12 nm, 16 nm, 20 nm) and CAT/Ag/CAT, the Ag peaks were observed at 38.29°, 44.24°, 64.60°, and 77.47°, corresponding to the (111), (200), (220), and (311) planes, respectively matches the face centred cubic structure of Ag (JCPDS file no. 04-0783) [3], and (110), (211), (220), and (301) at 27.4°, 51.8°, 55.6°, and 84.9 °

respectively, match the tetragonal rutile structure of SnO_2 (JCPDS file no. 41- 1445) [4]. The crystallite size was determined using the Debye-Scherrer equation [5]:

$$D = \frac{K\lambda}{\beta Cos\theta} \quad (1)$$

Where λ is the wavelength of the incident X-ray used, β is the full-width half maxima, K is the Scherrer constant and takes 0.9 value, and θ is the diffraction angle in radians. It is found to be 6.90 nm and 6.55 nm



(a) (b) (c) (d)

FIGURE 1*:* (a) GXRD pattern of CA1, CA2, CA3, and CA4 (b) UV-Vis. spectra of CAT, CA1, CA2, CA3, CA4, and CAT/Ag/CAT (c) Variation of sheet resistance and resistivity with Ag thickness in CAT/Ag thin film (d) Variation of Carrier concentration and mobility with Ag thickness in CAT/Ag thin film.

forCAT/Ag, and CAT/Ag/CAT, respectively.

The transmittance of the thin films was analyzed using UV-visible spectroscopy. Figure 1(b) presents a comparison of the UV-visible spectra for the CAT layer, CAT/Ag layers with thicknesses of 8 nm, 12 nm, 16 nm, and 20 nm, and the CAT/Ag/CAT thin film. All samples exhibited maximum transmittance in the 400-550 nm wavelength range. The transmittance percentage values for CAT, CA1, CA2, CA3, CA4, and the multilayer CAT/Ag/CAT thin films are provided in Table 1.

TABLE 1: Values of %Transmittance, Surface roughness, Particle size, and Figure of merits of CAT, CA1, CA2, CA3, CA4, and CAT/Ag/CAT

Sr no:	Thin film	%T	RMS Surface Roughness (nm)	Particle Size (nm)	Figure of merit (Ω^{-1})
1	CAT	86.44	0.72	55.793	1.26×10^{-3}
2	CA1	48.90	15.85	100.286	1.19×10^{-6}
3	CA2	55.86	18.78	72.546	1.9×10^{-4}
4	CA3	53.87	1.75	44.809	4.0×10^{-4}
5	CA4	57.02	15.35	77.84	2.1×10^{-4}
6	CAT/Ag/CAT	84.75	1.11	52.08	4.48×10^{-2}

It is observed that transmittance decreases as Ag layers are stacked on the CAT layer, likely due to the high reflectivity of the Ag layer and surface plasmon resonance. Stacking the CAT layer on top of the CA3 thin film improved transmittance, probably because forming a continuous layer on the Ag surface reduced surface roughness, as shown by the AFM data in Fig. 2. As a result, the CAT/Ag/CAT multilayer thin film reaches a maximum transmittance of 84.75%. For the CAT/Ag bilayer, transmittance initially rises with increasing Ag thickness from 8 nm to 12 nm but drops at 16 nm. At lower Ag thicknesses, Ag nuclei form discontinuous islands, which decrease light scattering and lower transmittance. At an Ag thickness of 20 nm, the layer becomes nearly continuous, reducing scattering and increasing transmittance to 57.02%.

The topography of various thin films was analyzed using Atomic Force Microscopy (AFM), and the 3D AFM images are displayed in Fig. 2. As shown in Table 2, the RMS value of surface roughness increases from 0.72 nm to 1.75 nm with the stacking of the Ag layer. However, when an additional CAT layer is stacked on top, the surface roughness decreases to 1.11 nm. The improved smoothness of the CAT/Ag/CAT multilayer thin film reduces the scattering of incident light, thereby increasing transmittance. In the CAT/Ag bilayer, surface roughness increases from 15.85 nm to 18.78 nm as the Ag thickness increases from 8 nm to 12 nm. At 16 nm Ag thickness, a significantly lower roughness value of 1.75 nm is observed. However, at 20 nm Ag thickness, the surface roughness increases to 15.35 again.

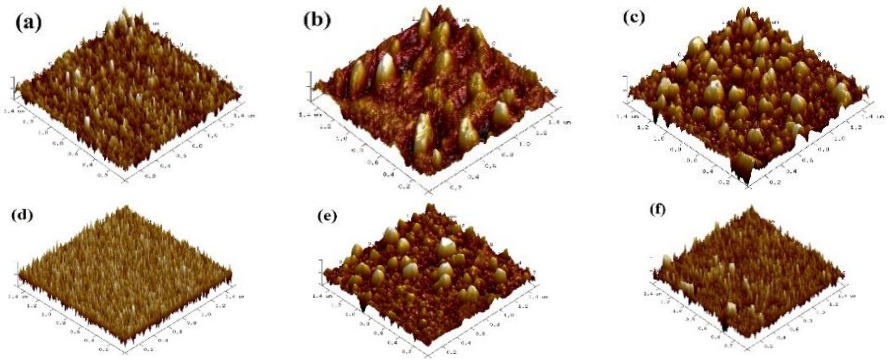


FIGURE 2: AFM 3D images of (a) CAT, (b) CA1, (c) CA2, (d) CA3, (e) CA4, and (f) CAT/Ag/CAT thin films

The electrical properties of the thin films were examined using the Hall Effect Measurement. Figure 1(c) illustrates the changes in sheet resistance and resistivity with different Ag thicknesses, while Figure 1(d) depicts the carrier concentration and mobility as functions of Ag thickness. The CAT/Ag/CAT multilayer thin film achieved good conductivity, with a value of $3.09\times10^4\ \Omega^{-1}cm^{-1}$. The CA3 sample, which has a greater Ag thickness than the CA1 and CA2 samples, exhibited the highest conductivity and higher carrier concentration, i.e., $4.32\times10^4\ \Omega^{-1}cm^{-1}$ and 4.98×10^{22} /cm^3, respectively. The conduction mechanism for these thin films follows the Volmer-Weber model [2], where the Ag layer grows on the amorphous CAT layer. In this model, conduction in the continuous layer occurs through the metal, facilitated by the migration of carriers from the low work function Ag layer to the higher work function CAT layer. The continuous CAT/Ag (16 nm)/CAT multilayer film shows enhanced conductivity, reaching $3.09\times10^4\ \Omega^{-1}cm^{-1}$.

The figure of merit evaluates the performance of transparent conducting thin films. The Haccke's formula for calculating FOM [6] is given by:

$$\Phi = (T)^{10}/R_{sh} \quad (2)$$

Where R_{sh} is the sheet resistance of the thin film and T is the average transmittance. The figure of merit for CAT/Ag/CAT and CA3, i.e., $4.48 \times 10^{-2}\ \Omega^{-1}$ and $4.0 \times 10^{-4}\ \Omega^{-1}$, respectively, has obtained a maximum FOM as shown in Table 1.

Conclusions:

Various thin films, including CuAl co-doped SnO_2, CAT/Ag with thicknesses of 8 nm, 12 nm, 16 nm, and 20 nm, and CAT/Ag/CAT, were successfully deposited using the e-beam evaporation method. The structural, optical, and electrical properties of these thin films were evaluated. The study focused on the impact of layer stacking on optical and electrical properties, revealing that the multilayer thin film and CA3 thin film achieved high transmittance and high conductivity. Consequently, we conclude that CAT/Ag (16 nm) and CAT/Ag/CAT can be used as transparent conducting electrodes in optoelectronic devices.

ACKNOWLEDGMENTS

The author extends gratitude to the Ion Beam Centre at Kurukshetra University, Kurukshetra, for providing the AFM and UV facilities. Also, acknowledge the Central Instrumentation Laboratory at Guru Jambheshwar University, Hisar, for the GXRD facilities. The author thanks MNIT, Jaipur, for the e-beam synthesis facilities.

REFERENCES

1. J. Jie, W. Zhang, I. Bello, C. S. Lee, & S. T. Lee, Nano today, 5(4), 313-336 (2010).
2. S. Yu, W. Li. L. Zhang, D. Xu, H. Dong, & Y. Jin, Thin Solid Films, 552, 150-154, (2014).
3. A. S. Lanje, S. J. Sharma, & R. B. Pode, J. Chem. Pharm. Res, 2(3), 478-483 (2010).
4. J. Li, C. Chen, J. Li, S. Li, & C. Dong, Journal of Materials Science: Materials in Electronics, 31, 16539-16547 (2020).
5. A. L. Patterson, Physical Review, 56(10), 978 (1939).
6. G. Haacke Journal of Applied Physics, 47(9), 4086-4089 (1976).

Structural and Optical Properties of Reactively Sputtered Nanostructured NiO Thin Films for NO_2 Gas Detection

Debarati Bhattacharya[*1,6], Amrita Das[1], Sipra Choudhury[2], Swapan Jana[1], Kailasa Ganapathi[3], Vijay Karki[4], S.K. Ghosh[5], and Surendra Singh[1, 6]

[1]*Solid State Physics Division, Bhabha Atomic Research Centre, Mumbai 400085, India*
[2]*Radiation and Photochemistry Division, Bhabha Atomic Research Centre, Mumbai 400085, India*
[3]*Technical Physics Division, Bhabha Atomic Research Centre, Mumbai 400085, India*
[4]*Fuel Chemistry Division, Bhabha Atomic Research Centre, Mumbai 400085, India*
[5]*Materials Processing and Corrosion Engineering Division, Bhabha Atomic Research Centre, Mumbai 400085, India*
[6]*Homi Bhabha National Institute, Anushaktinagar, Mumbai 400094, India*

[*]Corresponding author: debarati@barc.gov.in

Abstract. NiO thin films were fabricated by reactive magnetron sputtering using different O_2/Ar gas flow ratios, for toxic gas detection. The films deposited at room temperature without further annealing were analyzed to be crystalline. The influence of various gas flow ratios on the structural, optical and morphological properties of the films was examined through measurements made with several sensitive techniques namely XRR, GIXRD, FESEM, SIMS and UV-visible spectroscopy. It was found that these nanostructured films were sensitive to NO_2 gas detection at room temperature. Apart from exhibiting a fairly good sensor response, the fabricated NiO films were observed to undergo complete recovery between sequential gas doses of increasing concentration.

INTRODUCTION

The detection of toxic gases in our environment is vital to control the rising levels of atmospheric pollution. Research activity in the field of thin film gas sensors and detectors is directed towards this end. Nanostructured semiconducting metal oxides, like NiO, exhibit superior gas sensing ability [1] owing to their unique characteristics of high selectivity, good thermal stability and fast recovery rate. The parameters used during deposition of thin films for gas sensor materials have a great impact on the detection efficiency of the final product. The formation of NiO films for gas sensors through sputtering techniques have been studied using variation in the O_2/Ar gas flow ratios. Most of the reported studies on these films utilize some form of heat treatment to achieve crystallinity as with substrate heating [2] or post deposition annealing [3]. This paper reports a facile formation of nanostructured NiO thin films by reactive D.C. magnetron sputtering without the aid of heat treatment. The films were tested for their response to various gases and were found to be sensitive to the detection of NO_2 gas.

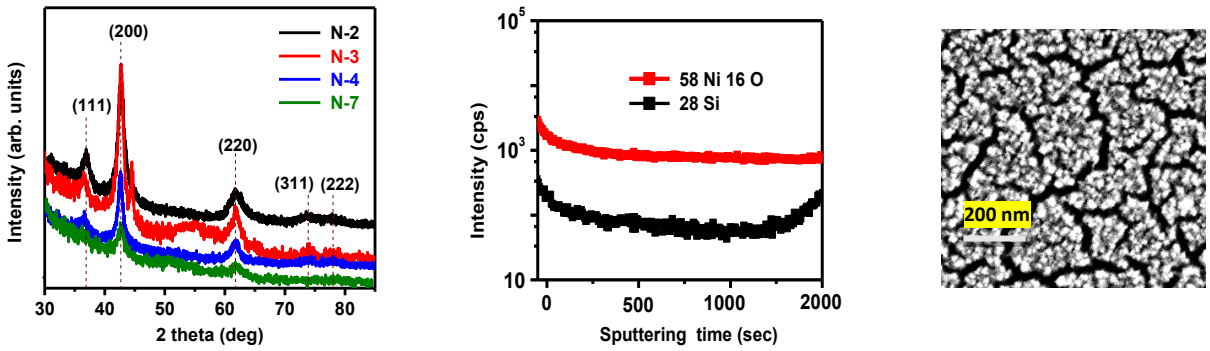
EXPERIMENTAL DETAILS

NiO thin films on Si, glass and quartz substrates were prepared by reactive sputtering in an indigenous magnetron sputter deposition system [4]. Base vacuum used was of the order of 2×10^{-4} Pa and the target to substrate distance was kept fixed at 84 mm. High purity (99.99%) Ni target was sputtered with ~100 W D.C. power in pure O_2 partial pressure onto the room temperature substrates held in sputter-up mode. Substrates were rotated at 4 rpm to ensure the formation of uniform films. The Argon gas flow was maintained constant at 20 sccm and the flow of oxygen gas was varied to yield working pressures of 1.6 Pa, 2.9 Pa, 4.1 Pa and 7.3 Pa. The corresponding NiO thin films obtained with these arrangements are designated as N-2, N-3, N-4 and N-7 respectively for this study. These films were investigated for their structural and optical properties through several sensitive techniques: Grazing incidence X-ray diffraction (GIXRD), Secondary ion mass spectrometry (SIMS), Field enhanced scanning electron microscopy (FESEM) and UV-visible spectroscopy.

STRUCTURAL AND OPTICAL CHARACTERIZATION

The thickness of the sputtered films used for this study were derived from X-ray reflectivity measurements (not shown here) to be in the range of 20 - 40 nm. These as-deposited thin films were examined through GIXRD

measurements and found to be invariably nanocrystalline as shown in Fig. 1 (a). The peak positions of all the films were identified and indexed as shown in this figure indicating the formation of polycrystalline NiO. The uniform distribution of the NiO films over the substrates was determined through SIMS and FESEM measurements. We have selected to display the characteristics of the NiO film, N-3 (36 nm thick), for all further analyses in this study. Figure 1 (b) shows the homogeneous concentration profile of N-3 throughout its depth as obtained from SIMS measurement. The specific distribution of grains in the surface morphology of N-3 was derived from FESEM scan recorded at 2 kV with a magnification of 75 kX and is shown in Fig. 1(c).



(a) (b) (c)

FIGURE 1. (a) GIXRD patterns of NiO thin films grown with variation in O_2/Ar gas flow ratios, (b) SIMS profile of N-3 showing uniform distribution of NiO, (c) FESEM image showing unique morphology of N-3.

The optical properties of films were obtained through UV-visible spectroscopy. The absorbance spectra were recorded and the values of absorption coefficient α with respect to photon energy hν were obtained. The related Tauc plot for N-3 can be seen in Fig. 2 which provided the value of band gap energy E_g. The inset of Fig. 2 shows the strong absorption of this film below 400 nm of the spectral range.

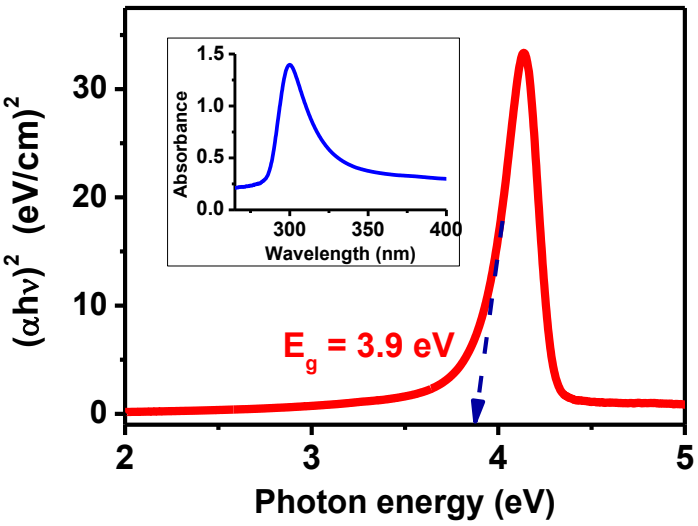


FIGURE 2. Tauc plot showing estimation of band gap energy E_g of N-3 corresponding to the formation of NiO. The inset shows the UV-visible absorption spectrum of the same film wherein a strong absorption peak was observed in the UV region.

The main parameters (viz. grain size and optical band gap energy) obtained from the structural and optical characterization of the NiO thin films deposited using different working pressures, are listed in Table 1. It was observed that low working pressures prompted the formation of larger grains in the NiO films.

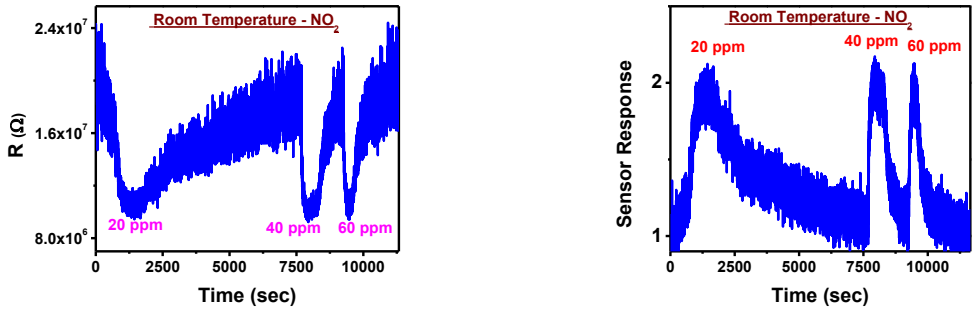
TABLE 1. Structural and optical parameters of reactively sputtered NiO thin films

NiO film	Working vacuum: O_2+Ar gas (Pa)	Grain size (nm) from GIXRD	E_g (eV) from UV-visible spectroscopy
N-7	7.3	7	3.1
N-4	4.1	10	3.4
N-3	2.9	11	3.9
N-2	1.6	15	3.8

Band gap values of the films were seen to be higher for those deposited with low oxygen flow.

GAS SENSING CHARACTERISTICS

The NiO thin film N-3 was repetitively exposed to NO_2 gas of different concentrations (20, 40 and 60 ppm). Figure 3 (a) shows the related changes in resistance of the film which decreased with the application of oxidizing gas, owing to the p-type nature of the film. It was observed that the film responded to NO_2 at room temperature with a sensor response of about twice the ratio of the resistance values in air and gas (Fig. 3 (b)). Another noteworthy observation was that the film could recover completely after withdrawal of gas and before injection of the next higher dose.



(a) (b)

FIGURE 3. (a) Resistance values of N-3 exposed to varying gas doses measured at room temperature, (b) Response and recovery of N-3 recorded for increasing NO_2 concentrations (in ppm).

CONCLUSIONS

A facile synthesis route of reactive sputtering with variation in O_2/Ar gas flow ratios was used to prepare crystalline NiO thin films without additional heat treatment. The nanostructured films were characterized for their structural and optical properties. The uniform and homogeneous thin films were used for effective sensing of NO_2 gas at room temperature for several concentrations. The fabricated NiO thin films exhibited a good sensor response and were also observed to undergo complete recovery between sequential gas doses of increasing concentration.

REFERENCES

1. S. Kailasa Ganapathi, Manmeet Kaur, Ranjit Singh, Vishwa Inder Singh, A. K. Debnath, K. P. Muthe, and S. C. Gadkari, ACS Applied Nano Materials, Vol. 2, pp. 6726-6737 (2019).
2. Wei Xu, Xin Mao, Nan Zhou, Qing-Yu Zhang, Bo Peng, and Yu Shen, Vacuum, Vol. 196, pp. 110785-(2022).
3. M. Predanocy, I. Hotovýa, and M.Čaplovičová, Applied Surface Science, Vol. 395, pp. 208–213 (2017).
4. Debarati Bhattacharya, A. Biswas, K.G. Bhushan, M. Swain and S. Basu, Solid State Physics, Proceedings of the 55th DAE Solid State Physics Symposium, December 26-30, 2010, Manipal, India, AIP Conf. Proc. 1349, 487-488 (2011).

Interfacial Free Energy of Solid on Solid *fcc* Cu/*fcc* Pb Interface: A Molecular Dynamics Study

Ankosh D. Deshmukh[1, 2, *], Abhik Choudhury[3], Saswata Bhattacharyya[4], Gandham Phanikumar[5], M. P. Gururajan[6] and Vaishali Shah[1, *]

[1]*Department of Scientific Computing Modeling and Simulation, Savitribai Phule Pune University, Pune, Maharashtra 411007, India*
[2]*Department of Physics, Savitribai Phule Pune University, Pune, Maharashtra 411007, India*
[3]*Department of Materials Engineering, Indian Institute of Science, Bangalore, Karnataka 560012, India*
[4]*Department of Materials Science and Metallurgical Engineering, IIT Hyderabad, Hyderabad, Telangana 502284, India*
[5]*Department of Metallurgical and Materials Engineering, IIT Madras, Chennai, Tamil Nadu 600036, India*
[6]*Department of Metallurgical Engineering and Materials Science, IIT Bombay, Powai, Mumbai, Maharashtra 400076, India*

[*]Corresponding author: ankoshdeshmukh50@gmail.com ; vaishali@unipune.ac.in

Abstract. We have used classical molecular dynamics simulations to compute the solid on solid interfacial energy of Cu(001)/Pb(001) and Cu(111)/Pb(111) interfaces. Interfacial energy is difficult to obtain via experiments and different theoretical methods have been applied in published literature to estimate it. However, a majority of these theoretical calculations with either ab-initio or classical simulations report the interfacial energy only at 0 K although experiments are performed on alloy interfaces at finite temperatures. In this paper, we present a simple methodology to obtain the interfacial energy at any finite temperature of interest. We have applied it to calculate the interfacial energy of two Cu/Pb interfaces at 583 K (310 ºC) for which experimental results are available. Our calculated finite temperature interfacial energy although underestimated is in much better agreement with the experimental values.

Keywords. Interface energy, Cu/Pb interface, molecular dynamics, anisotropy, interface orientation.

INTRODUCTION

Copper-lead system has various applications in the electronics and automotive industry. In the electronic industry, the copper-lead alloy is used to design various electrical components like connectors, battery terminals, relays, and switches, heat sinks for electronic components, and in thermal interface materials to improve the heat transfer efficiency. In automotive industry, copper-lead alloy is used in bushing, sleeves, bearing materials, radiators and heat exchangers in automotive and industrial machines due to its high fatigue resistance, good thermal conductivity, corrosion resistance and anti-friction properties. In the defense sector, it is used to make bullets and other ammunition components due to its malleability and density that provides optimal ballistic performance. Hence, understanding the interfacial energy and properties of copper-lead alloy is essential for its effective application across these industries. Experimentally, it is difficult to obtain the interface energy due to limitations of probe ability, sensitivity, resolution of measurement techniques and presence of contaminants and defects in surfaces.

A few theoretical studies on interfacial energy of Cu alloys are available in the literature. In the classical molecular dynamics simulations at 0 K on Cu(111)/Nb(110) solid-solid interface an interface energy value of 0.54 J/m^2 [1, 2] and of 0.32 J/m^2 for Cu(111)/Ni(111) semi-coherent interface [3] has been reported. The incoherent and immiscible solid on solid *fcc*/*bcc* Nishiyama-Wassermann (NW) interface of Cu/Nb with an interfacial energy of 0.45 J/m^2 and Cu/W interface with interfacial energy of 0.64 J/m^2 has been studied with classical molecular dynamics by Bodlos *et al* [4]. Besides these, there are other solid-solid interface studies reported in literature on non-copper alloys using either classical or DFT simulations, wherein, the interfacial energy is reported for 0 K. Majority of these studies do not provide a comparison with experimental data to be able to evaluate the quantitative accuracy of these results. In this paper, we have computed the solid-solid interface energy of *fcc* Cu(001)/*fcc* Pb(001) and *fcc* Cu(111)/*fcc* Pb(111) interface at 0 K and 583 K and compared it with the available experimental results [5, 6] at 583 K.

COMPUTATIONAL AND SIMULATION DETAILS

Classical molecular dynamics simulations using the Large-Scale Atomistic/Molecular Massively Parallel Simulator (LAMMPS) [7] were performed for bulk structure optimization and NPT ensemble calculations, with the embedded atom method (EAM) potential developed by Hoyt *et al* [8]. We used the conjugate gradient method for lattice minimization calculations of all structures with the stopping tolerance for energy and force set to 10^{-25} and 10^{-25} eV/Å, respectively. The *fcc* Cu(001), Cu(111), Pb(001), and Pb(111) surfaces were generated using the optimized lattice parameters. We then performed NPT simulations using a Nosé-Hoover thermostat [9, 10] set at 583 K with damping parameter of 0.1 ps and barostat [11] at zero bar pressure with damping parameter of 1 ps allowing for anisotropic volume fluctuations with a time step of 1 fs on *fcc* Cu and Pb bulk. After equilibration, the Cu and Pb structures spanned the NPT ensemble phase space for 400 ps. The lattice parameters obtained from these simulations were used to create the structure of *fcc* Cu(001)/*fcc* Pb(001) and *fcc* Cu(111)/*fcc* Pb(111) interface at 583 K. To generate structures with minimum lattice mismatch along the x- and y-direction of the interface, simulation cell dimensions of 5.445 x 5.445 x 5.082 nm^3 for Cu(001) (15x15x14 unit cells) surface with 5.442 x 5.442 x 4.948 nm^3 for Pb(001) (11x11x10 unit cells) surface and 6.674 x 3.853 x 8.809 nm^3 for Cu(111) (15x15x14 unit cells) surface with 6.666 x 3.848 x 8.570 nm^3 for Pb(111) (11x11x10 unit cells) surface were required. The thickness of 10.03 nm for Cu(001)/Pb(001) and 17.37 nm for Cu(111)/Pb(111) interface was used. NPT simulations were performed on the respective surface and interface structures at 583 K and 0 bar pressure as described earlier here. The solid on solid interfacial energy (γ) was calculated as [12]:

$$\gamma_{Pb-Cu} = \frac{E^{\text{int}}_{Pb-Cu} - E^{\text{surf}}_{Pb} - E^{\text{surf}}_{Cu}}{2A}$$

where, E^{int}_{Pb-Cu} is the total energy of the Cu/Pb interface structure, E^{surf}_{Pb} is total energy of Pb slab, E^{surf}_{Cu} is total energy of Cu slabs, and *A* is the surface area of the interface at the temperature of interest. The factor of 2 in the denominator accounts for the two identical interfaces in the interface structure shown in Fig. 1.

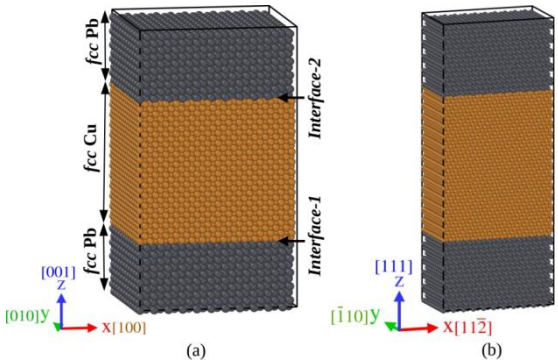


FIGURE 1. Simulation cell of (a) Cu(001)/Pb(001) and (b) Cu(111)/Pb(111) interface structure consisting of two interfaces. The interface structure is periodic in x-, y-, and z- direction. Structure visualizations were performed with open source Ovito [13].

RESULTS AND DISCUSSION

On structural optimization, we obtained a lattice constant of 3.615 Å for bulk Cu, which is in good agreement with the experimental value of 3.61 Å [14, 15]. For Pb, our calculated lattice constant of 4.910 Å agrees well with the experimental value of 4.95 Å [15]. These optimized lattice parameters were used to generate the Cu(100), Cu(111), Pb(100) and Pb(111) surfaces and the interface structures with the Burgers orientation relationship (BOR): (i) Cu[100]//Pb[100], Cu[010]//Pb[010], and Cu[001]//Pb[001] shown in Fig. 1(a) and (ii) Cu[11$\bar{2}$]//Pb[11$\bar{2}$], Cu[$\bar{1}$10]//Pb[$\bar{1}$10], and Cu[111]//Pb[111] shown in Fig. 1(b).

Classical molecular dynamics NPT simulations were performed on Cu and Pb bulk to obtain the lattice parameters at 583 K (310 °C). The thermal expansion at this temperature leads to Cu bulk having a lattice parameter of 3.651 Å and Pb bulk of 4.981 Å. These lattice parameters were used to create the Cu and Pb surfaces with (100) and (111) orientations and to generate the interfaces with the BOR shown in Fig. 1. The interface energy is the quantity associated with interface stability and is defined as an excess energy per unit area. It depends on the structural strain, chemical bonding at the interface [16] and helps to understand the strength of atomic bonding at the interface as against the interlayer atomic bonding in the respective bulk materials [12].

We have calculated the interfacial energy for Cu/Pb interfaces at 0 K and at 583 K. At 0 K our calculated interfacial energy of Cu(001)/Pb(001) is 547 mJ/m^2 and of Cu(111)/Pb(111) is 336 mJ/m^2. At 583 K, our calculated interfacial energy of Cu(001)/Pb(001) is 712 mJ/m^2 (0.71 J/m^2) which is closer to the experimental value of 926 mJ/m^2 evaluated at 310 °C by Rao *et al* [5]. The interfacial energy of Cu(111)/Pb(111) interface is 343 mJ/m^2 (0.34 J/m^2) which is only marginally improved but still underestimated from the experimental value

of 1016 mJ/m^2. While the interface energy values at 583 K are improved than that of 0 K, and are in agreement with the observed interface energy anisotropy with respect to different surface orientations, they disagree with the experimental observation of the interface energy of Cu(111)/Pb(111) being larger than that of Cu(100)/Pb(100). Our interface anisotropy trend agrees with the interface energy trends observed in theoretical calculations on another Cu alloy. In Cu(001)/Ag(001) an interface energy of 530 mJ/m^2 and in Cu(111)/Ag(111) of 231 mJ/m^2 has been reported [17]. We hope this study will motivate theoretical investigations for obtaining the interface energy at finite temperatures of other industrially relevant alloys and also motivate experimental investigations to validate the anisotropy trends in them.

CONCLUSION

A majority of theoretical studies, generally calculate and report the interfacial energy at 0 K and provide no validation with experimental data. This work describes a simple methodology to obtain the interfacial energy at finite temperatures. Using the methodology, we performed classical molecular dynamics simulations on two solid on solid interfaces of *fcc* Cu with *fcc* Pb to calculate their interfacial energy at 583 K for which experimental data is available. Our results show that the interfacial energy values at 583 K although somewhat underestimated have a better agreement with the experimental results.

ACKNOWLEDGMENTS

ADD, AC, SB, GP, MPG, and VS gratefully acknowledge funding support from the National Supercomputing Mission (NSM), India. ADD wishes to acknowledge the Government of Maharashtra for MAHAJYOTI Fellowship (MAHAJYOTI/Ph.D. Fellowship/2821(28)/2024-25). We acknowledge use of HPC facilities at IISc Bangalore, IIT Kharagpur, NIT Trichy under NSM and at the Department of Scientific Computing Modeling and Simulation (SCMS), SPPU Pune.

REFERENCES

1. M. J. Demkowicz, R. G. Hoagland, and J. P. Hirth, Phys. Rev. Lett., Vol. 100, pp. 136102 (2008).
2. M. J. Demkowicz, J. Wang and R. G. Hoagland, Interfaces Between Dissimilar Crystalline Solids, in Dislocations in Solids, edited by J. P. Hirth, Amsterdam: Elsevier, 2008, Vol. 14, pp. 141–207.
3. S. Shao, J. Wang, A. Misra and R. G. Hoagland, Sci. Rep., Vol. 3, pp. 2448 (2013).
4. R. Bodlos, V. Fotopoulos, J. Spitaler, A. L. Shluger and L. Romaner, Materialia, Vol. 21, pp. 101362 (2022).
5. G. Rao, D. B. Zhang and P. Wynblatt, Acta. Metall. Mater., Vol. 41, pp. 3331–3340 (1993).
6. V. Timoshenko, V. Bochenko, V. Traskine and P. Protsenko, J. Mater. Eng. Perform., Vol. 21**,** pp. 575–584 (2012).
7. S. Plimpton, J. Comput. Phys., Vol. 117**,** pp. 1–19 (1995).
8. J. J. Hoyt, J. W. Garvin, E. B. Webb, and M. Asta, Model. Simul. Mater. Sci. Eng., Vol. 11**,** pp. 287–299 (2003).
9. S. A. Nosé, J. Chem. Phys., Vol. 81, pp. 511–519 (1984).
10. W. G. Hoover, Phys. Rev. A, Vol. 31, pp. 1695–1697 (1985).
11. G. J. Martyna, D. J. Tobias and M. L. Klein, J. Chem. Phys., Vol. 101, pp. 4177–4189 (1994).
12. S. V. Dudiy and B. I. Lundqvist, Phys. Rev. B, Vol. 69, pp. 125421 (2004).
13. A. Stukowski, Model. Simul. Mater. Sci. Eng., Vol. 18, pp. 15012 (2009).
14. C. Kittel, Introduction to Solid State Physics, USA: John Wiley & Sons, 1953, pp. 26.
15. N. W. Ashcroft and N. D. Mermin, Solid State Physics, USA: Harcourt College Publishers, 1976, pp. 70.
16. J. Li, Y. Q. Yang, L. L. Li, J. H. Lou, X. Luo and B. Huang, J. Appl. Phys., Vol. 113, pp. 023516 (2013).
17. S. A. Dregia, Thesis, Carnegie Mellon University, Pittsburgh, Pa, USA, 1989.

Ultra-Broadband Resistive Microwave Meta Absorber for Stealth Technology

Priyanka[1], Himanshu B. Baskey[2], Prashant S. Alegaonkar[1,a]

[1]Department of Physics, School of Basic Sciences, Central University of Punjab, Bathinda-151401, Punjab, India

[2]Stealth & Camouflage Division, Defence Material Store R & D Establishment, DRDO, Kanpur, UP 208013, India

[a] Prashant S. Alegaonkar: prashant.alegaonkar@cup.edu.in

Abstract. This work demonstrates a novel ultra-broadband microwave metamaterial absorber that consists of an FSS resistive pattern that is made of 280 Ω/□ resistive ink imprinted on an FR4 dielectric interlayer with $0.029\lambda_L$ thickness. The complete design was grounded with the help of a conducting copper plate. Simulation results revealed that a -10 dB reflection loss is found from 4-24 GHz with a high resonance peak of 17.9 GHz. Moreover, at resonance frequency, maximum reflection loss -29.9dB was achieved. The proposed absorber is angularly stable for 0^0-50^0 and polarization insensitive for 0^0-90^0. The absorber is well-suited for various X-band applications including communication devices, radar systems, and stealth technologies. Research suggests that the proposed metamaterial absorber is a feasible option for reducing electromagnetic waves in the X-band due to its compact size and exceptional performance.

INTRODUCTION

Over the years, researchers have become increasingly interested in a unique substance called Metamaterial. This substance has distinct qualities such as phase and antiparallel group velocities, which have captured the attention of researchers in the field of microwave engineering. They have thoroughly analyzed its potential applications in filter design, cloaking technologies, antenna design development, absorbers[1], and superlenses[2]. Metamaterial absorbers (MMAs) are structured to efficiently absorb electromagnetic radiation within a specific range of frequencies. These resources can be applied in many different contexts, such as the usage of metamaterial (MMA) microwave absorbers in covert technologies. The Salisbury screen[3], an early model of an absorber, was constructed using a single-layer resistive sheet mounted on a metal surface with a thickness of a quarter wavelength. In contrast, the broadband Jaumann absorber[4], with its wider absorption range, has gained more popularity compared to the narrow-band property of the Salisbury screen. The absorber has a broader absorption range due to its use of multiple resistive sheets spaced at quarter-wavelength intervals. Numerous research studies have investigated different approaches to balancing the absorber's wide absorption capability with a smaller construction, even if increasing the absorber size is necessary to achieve this broad range. FSS-based resonating structures can be created using various techniques, including capacitive circuit analog absorbers and circuit analog procedures[5-8]. In this study, a resistive FSS-based absorber was demonstrated. The pattern was printed on a 2.2 mm FR-4 interlayer mounted on a conducting ground plane. A -10 dB reflection loss was observed in the operating frequency range of 4 to 24 GHz, with a resonance frequency of 17.9 GHz. The proposed design was angularly stable up to 50^0 and polarization insensitive up to 90^0. To pattern the FSS layer, a 280 Ω/□ resistive ink was used. Furthermore, performance evaluations for surface current distribution for the TE mode were conducted to gain insight into the reflection loss mechanism.

DESIGN AND SIMULATION STUDIES OF THE PROPOSED ABSORBER

The design was simulated in CST Microwave Studio software using a frequency domain solver. A periodicity boundary condition was applied in the xy direction, while an open space boundary condition was used in the z-direction. The absorption performance of the absorber was performed using the following equation [1]:

$$A = 1 - |S_{11}^2| - |S_{21}^2| \quad (1)$$

The terms S_{11} and S_{21} represent the reflectance and transmittance coefficients, respectively. If the absorber is terminated with a metallic ground plane, the transmittance coefficient becomes zero, i.e., $|S_{21}^2| = 0$ thus, equation (1) can be written as:

$$A = 1 - |S_{11}^2| \quad (2)$$

RESULTS AND DISCUSSION

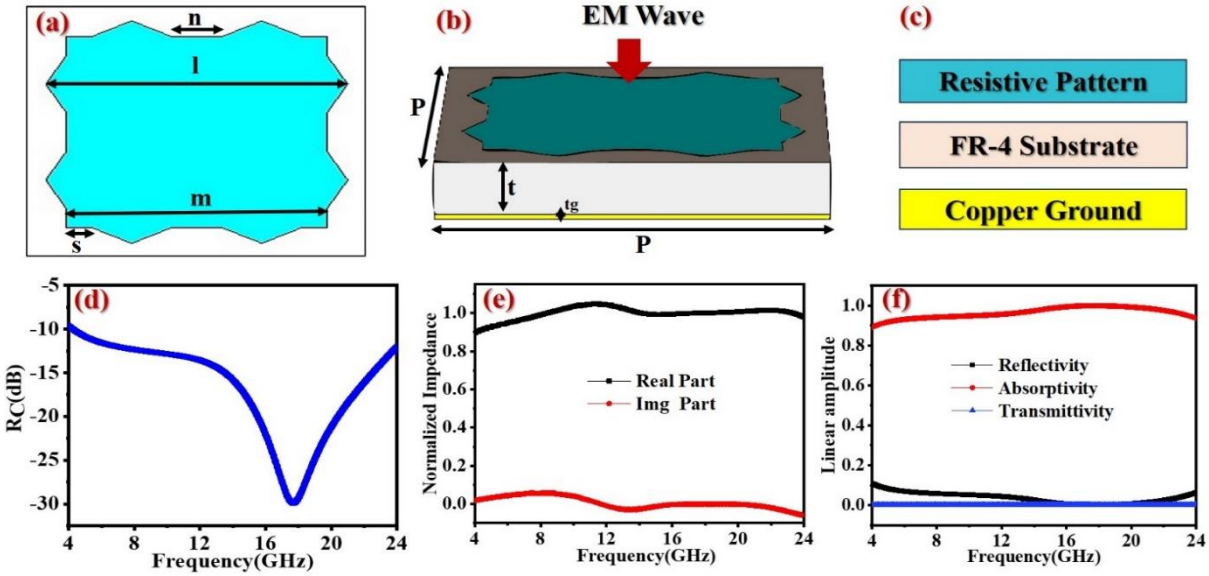


FIGURE 1. (a) FSS overlayer resistive pattern of the proposed absorber with dimensions, (b) 3-D view of the structure including interlayer and ground with thickness parameters, (c) color code of each layer, (d) real and imaginary normalized impedance of the absorber, (e) reflection loss performance, and (f) linear amplitude of reflectivity, transmissivity and absorptivity of the absorber.

Figure 1 (a) displays the geometry of the cell of the proposed absorber with an FSS pattern made of resistive ink with 0.02 mm thickness. The parameters of the geometry were as follows: l = 15.03 mm, m = 12.96 mm, n = 2.59 mm, and s = 1.30 mm. Figure 1 (b) depicts the 3-dimensional y-z orientation of the cell of the absorber with a length (p) of 17 mm. It was composed of a resistive ink pattern with a sheet resistance of 280 Ω/□, which was imprinted on an FR-4 interlayer having a permittivity (ε) of 4.4, loss tangent (tanδ) of 0.02 with a thickness (t) of $0.029\lambda_L$ ('λ_L denotes the corresponding thickness of lowest operating frequency). The substrate is mounted on a copper ground plane with a thickness (tg) of 0.035 mm. The color code for each layer of the absorber is shown in Fig. 1(c). To achieve higher gain and wider bandwidth, the design parameters need to be tuned. Choosing the right absorber is important for increasing the efficiency and bandwidth. In Fig. 1(d), the absorption performance of the absorber is depicted for the 4 – 24 GHz frequency range, spanning the C, X, Ku, and K bands of the electromagnetic spectrum with a bandwidth of approximately 20 GHz. The maximum loss of -29.9 dB has been achieved at 17.9 GHz. The graphs in Fig. 1(e) confirm the absorption capability of the structure, as the real and imaginary impedance values in the operating range are close to one and near zero, respectively. This indicates that the structure is resonating. When the structure resonates, it traps incoming waves and functions as an absorber. Figure 1(f) shows the losses of the wave in terms of absorptivity, reflectivity, and transmissivity. The absorber can absorb over 90% of waves in the 4-24 GHz range at a resonance frequency of 17.2 GHz, with a fractional bandwidth (FBW) of 166%. At this frequency, the reflection and transmission values are almost zero.

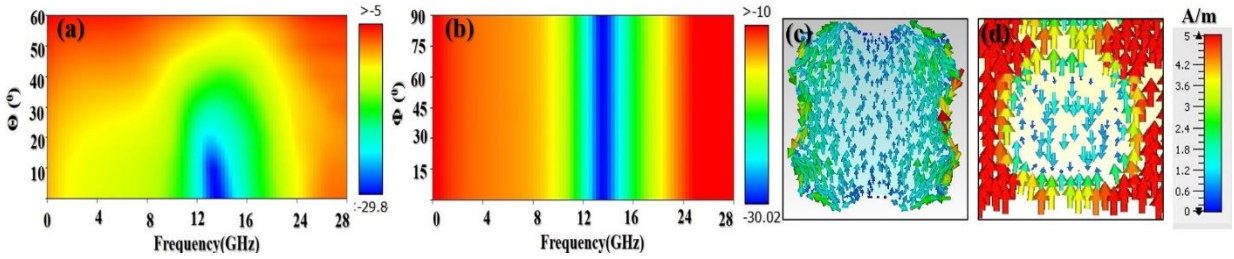


FIGURE 2. Reflection loss performance of the absorber (a) by changing the angle of incidence from 0^0- 60^0, (b) by varying rotation angle from 0^0-90^0, for TE mode. Surface current density (c) for front surface, (d) for rare surface at 17.9 GHz for TE mode (Scale bar for each parametric profile is shown on the left-hand side).

A high-quality absorber should possess a broad bandwidth and exhibit sensitivity to both the angle of incidence and rotation. In Figure 2(a) and (b), the reflection loss of the absorber for the TE mode is illustrated for various oblique incidences. It is observed that for most TE modes, 90% absorption occurs when the angle of incidence ranges from 0° to 50°. Interestingly, the reflection loss performance remains unchanged at different oblique angles for TE mode up to 50^0. Figure 2(b) shows the R_C data of the absorber at different rotation angles. The consistent loss is attributed to the fourfold symmetry of the top layer, with the polarization angles varying from 0° to 90° in 15° increments over the 4 – 28 GHz frequency range. Overall, this wide-band microwave absorber demonstrates stability for polarization and performs effectively across a wide range of incident angles. The absorption process of the proposed structure is explained by illustrating the distribution of surface currents at the overlayer and ground layers at the absorption frequency of 17.9 GHz. In Fig. 2(c) and (d), it is clear that the top layer of the surface shows a higher current distribution compared to the bottom layer. This suggests that the resistive surface of the top layer is the main contributor to broadband absorption. Additionally, there is a magnetic excitation produced by currents flowing in opposite directions on the overlayer and bottom surfaces, creating a circulating loop around the incoming magnetic field. On the other hand, electric excitation primarily occurs due to the electric field exciting the resistive pattern on the top layer. To achieve high absorption over a given period, it is essential for both electric and magnetic excitations to occur simultaneously.

CONCLUSION

This study introduces a new ultra-broadband microwave metamaterial absorber. The absorber includes an FSS overlayer made of 280 Ω/□ resistive ink imprinted on FR4 dielectric interlayer with a thickness of $0.029\lambda_L$ with ε of 4.4 and a tanδ of 0.02. It was grounded with the help of a conducting copper plate. The simulation results showed that there is a -10 dB reflection loss across the frequency range of 4-28 GHz, with a resonance frequency of 17.9 GHz. Additionally, at the resonance frequency, the highest R_C loss of -29.9 dB was achieved. The proposed absorber is stable for angles between 0-50^0 and is insensitive to polarization for angles between 0-90^0. The absorber is suitable for various X-band applications, such as radar systems and stealth technologies.

ACKNOWLEDGMENTS

All authors are thankful to the financial support provided by UGC, India, and the laboratory facilities provided by CIL, the Vice Chancellor, Dean, Director, and Divisional head of the respective university/institute.

REFERENCES

1. N. I. Landy, S. Sajuyigbe, J. J. Mock, D. R. Smith, and W. J. Padilla, "Perfect metamaterial absorber," *Physical review letters*, vol. 100, no. 20, p. 207402, 2008.
2. X. Zhang and Z. Liu, "Superlenses to overcome the diffraction limit," *Nature materials*, vol. 7, no. 6, pp. 435-441, 2008.
3. W. W. Salisbury, "Absorbent body for electromagnetic waves," 1952.
4. L. J. Du Toit, "The design of Jauman absorbers," *IEEE Antennas and Propagation Magazine*, vol. 36, no. 6, pp. 17-25, 1994.

5. S. Ghosh, S. Bhattacharyya, Y. Kaiprath, and K. Vaibhav Srivastava, "Bandwidth-enhanced polarization-insensitive microwave metamaterial absorber and its equivalent circuit model," *Journal of Applied Physics*, vol. 115, no. 10, 2014.
6. A. P. Sohrab and Z. Atlasbaf, "A circuit analog absorber with optimum thickness and response in X-band," *IEEE Antennas and Wireless Propagation Letters*, vol. 12, pp. 276-279, 2013.
7. Priyanka, S. Mohanty, P. S. Alegaonkar, and H. B. Baskey, "Design and Manufacturing of a Hexapattern Frequency Selective Surface Absorber for Aerospace Stealth Application," *ACS Applied Materials & Interfaces*, vol. 15, no. 30, pp. 37107-37115, 2023.
8. Y. Tayde, M. Saikia, K. V. Srivastava, and S. A. Ramakrishna, "Polarization-insensitive broadband multilayered absorber using screen printed patterns of resistive ink," *IEEE Antennas and Wireless Propagation Letters*, vol. 17, no. 12, pp. 2489-2493, 2018.

Effect of Post Deposition Annealing Temperature and Duration on Structure of DC Sputtered Sn Films

Damu V. Rupnar[1,2], D. Goyal[1], M. Kaur[1], P. Sarawade[2], Niranjan S. Ramgir[1]*

[1]*Gas Sensing Devices Section, Technical Physics Division, Bhabha Atomic Research Center, Mumbai 400 085*
[2]*Department of Physics, University of Mumbai, Kalina, Mumbai, 400 098*

[a)]Corresponding author: niranjanpr@yahoo.com

Abstract. We report the systematic study on the growth and characterization of SnO_2 thin films deposited using DC sputtering method. The quality of the deposited film is governed by the choice of different process parameters that includes sputtering power, deposition pressure, substrate, substrate temperature, deposition duration, post deposition annealing temperature and duration, carrier gas etc. To realize polycrystalline thin films of SnO_2 from Sn targets, the post deposition temperature and duration is found to play the important role. Accordingly, in the present work SnO_2 films deposited using Sn target, 25 W power, base vacuum of 2 x 10^{-5} mbar, substrate (glass) temperature of 100°C, deposition time of 15 min were investigated in detail to find the optimum post deposition annealing temperature and duration. XRD results indicate that the post deposition annealing temperature of 450°C and duration of 2 h resulted in the formation of polycrystalline SnO_2 films.

INTRODUCTION

Metal oxide semiconductor thin films have been studied extensively owing to their excellent chemical, mechanical, optical and electrical properties[1]. Of the family, SnO_2 and ZnO have been widely exploited for the development of sensors for toxic and hazardous gases. They offer numerous advantages like control over morphology, non-stoichiometry, ease of synthesis and wealth of interesting nanostructures. SnO_2, in particular offer advantages like wide band gap of ~ 3.6 eV, oxygen non-stoichiometry and thereby tunable surface reactivity. Accordingly, it has found application in different fields like transparent conducting films, antireflection coatings, catalysts, and gas sensors[2].

SnO_2 thin films can be deposited employing different physical and chemical methods. These include spray pyrolysis, spin coating, hydrothermal method, thermal evaporation and sputtering[3, 4]. Each of these techniques has its own advantages and disadvantages. The choice of the deposition method is mainly governed by the availability, economics and the quality of the resulting thin films. Of the different methods, DC sputtering involves use of ionized gas molecules to sputter the target material molecules into the plasma which subsequently are deposited onto the substrate. It offers numerous advantages that include low cost, high level of control, high deposition rates, high uniformity and better adhesion due to involvement of high energies. It however, also suffers from drawbacks like target material limited to metals, excessive heating of target and requirement of high carrier gas pressure. All these makes it an ideal choice for the realization of metallic thin films. Thermal oxidation of these films is then subsequently carried out to realize oxide films. This method takes advantage in depositing metal with low melting points and the ease with which the oxidation can be carried out. Accordingly, in the present work, we report the deposition of Sn films employing DC sputtering method and the effect of post deposition annealing temperature and duration on the quality of the deposited films i.e., formation of SnO_2.

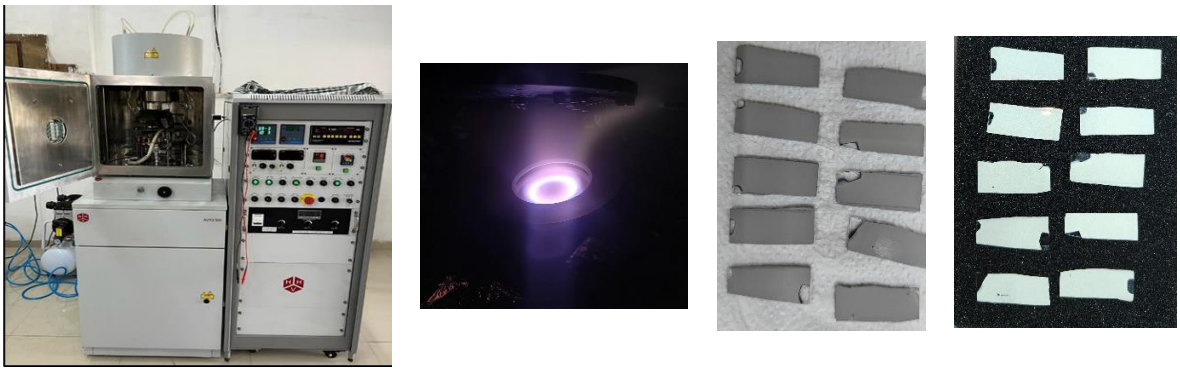
EXPERIMENTAL

DC sputtering technique with 2-inch Sn target 99.99% pure having 4 mm thickness was used for the deposition of the SnO_2 films. Prior to deposition the glass substrates of size ~1 sq. inch was cleaned using ultrasonication in trichloroethylene, methanol and acetone. The deposition was carried out at a base vacuum of 2 x 10^{-5} mbar, power of 25 W, substrate temperature of 100°C, with source to substrate distance of 5 cm and Ar flow rate of 20 sccm, Films with thickness in the range from 180 to 6500 nm were grown by variation in deposition time from 5 min to 3 h. The thickness of the film was determined by weight difference method. For 15 min deposition, the Sn film of ~ 450 nm was grown. The as deposited films (A1) were then subjected to post deposition annealing at different temperatures of 250, 350 and 450°C for 2 h under oxygen flow of 60 sccm and assigned as A2, A3 and A4, respectively.

XRD studies were carried out using a bench top X-ray diffractometer (M/s Bruker GmbH, D2 phaser, 2nd Generation with XET detector) using Cu-Kα radiation (λ = 1.5405 Å) at room temperature. The XRD data were collected from 2θ = 20° to 80° with step size of 0.02° and count time 0.2 sec for each step.

RESULTS AND DISCUSSION

Figure 1 shows the actual photograph of the DC sputtering system used for the deposition of the SnO_2 thin films along with the plasma that is generated during deposition process.



(a) (b) (c) (d)

FIGURE 1. (a) Actual photograph of the DC sputtering system used for the deposition of the SnO_2 thin films and (b) Plasma generated during the deposition process and photograph of the (c) as deposited film and (d) film annealed at 450°C for 2 h.

Figure 2 shows the XRD spectra recorded for as deposited films and those annealed at different temperatures. As is evident from the figure, all the peaks for as deposited sample (A1) matches with those corresponding to crystalline planes of the tetragonal structure of elemental Sn. With increase in the annealing temperature the peaks corresponding to Sn are found to disappear and those corresponding to SnO phases were found to appear. SnO usually grows faster under the humid condition than in dry air. Now, at higher annealing temperature of 450°C SnO is subsequently found to transform into SnO_2. For A4 sample, the peaks match well with the tetragonal SnO_2 phase (cassiterite). At 450°C, tetragonal rutile structure of SnO_2 is found to be the dominant phase (A7). We have also studied the effect of annealing time as shown in figure 2 (b). With increase in time, the metallic Sn phase is found to totally disappear while a small signature of SnO at 2θ value of 30° is still visible. The thickness of oxide films, as function of the annealing time, usually follows a parabolic law. Because, a strong interaction between Sn and the energetic oxygen takes place at the surface, the top surface of the film is characterized predominantly by the presence of SnO_2 while SnO as expected is known to form in the deeper regions of the film.

Thus, our results clearly indicate that employing Sn as a target material and using DC sputtering technique and subsequent thermal oxidation it is possible to grow SnO_2 on glass substrates. SnO_2 is considered to be one of the best metal oxide semiconductors for gas sensing applications. Accordingly, the present film is under investigation for its potential as gas sensing material.

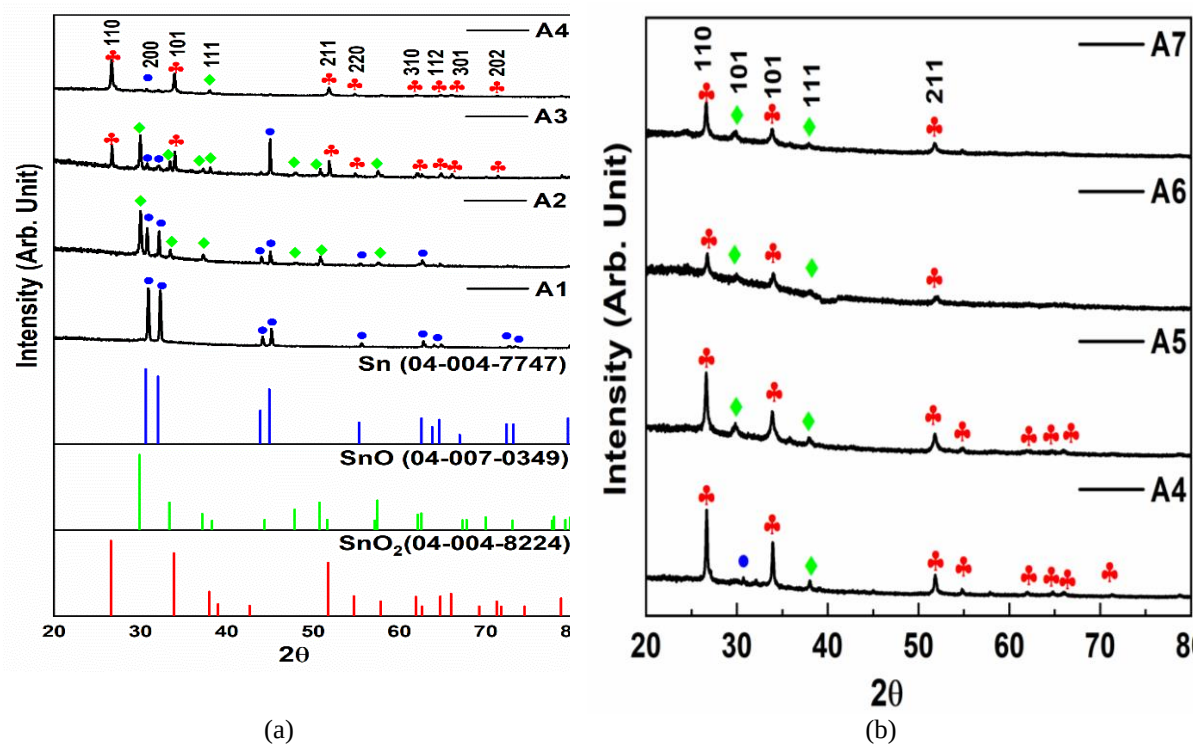


FIGURE 2. (a) XRD spectra recorded for as-deposited Sn films (A1) and those annealed at temperature of 250 (A2), 350 (A3) and 450°C (A4), respectively. (b) XRD spectra recorded for samples annealed at 450°C for 2 (A4) , 3 (A5), 4 (A6) and 5 h (A7), respectively.

ACKNOWLEDGMENTS

Deepak Goyal thank the Department of Science and Technology, Government of India, for Inspire fellowship (INSPIRE Reg. No. IFA22-ENG341). Authors thank Dr. S. Bhattacharya for his help with XRD measurements. Shri Pushkar Deo is also acknowledged for his help with deposition.

REFERENCES

1. N. S. Ramgir, K. R. Sinju, B. B. Bhangare, A. K. Debnath, J. Mater. Nanosci., (2022) 9 (2), 79-90.
2. N. S. Ramgir, V Patnaik, A Patel, A K. Debnath, D K Aswal, S K Gupta, Asian J. Phy., 24 (2015) 1541-1548.
3. F.H. Aragón, J.C.R. Aquino, N.C.S. Gomes, J.D. Ardisson, S.W. da Silva, D.G. Pacheco-Salazar, J.A.H. Coaquira, J. Euro. Ceram. Soc. 37 (2017) 3375–3380.
4. H. Xiong, B.L. Zhu, J.Q. Zhang, J. Wu, X.W. Shi, W.Q. Sun, J. Alloy. Compd. 997 (2024) 174970.

Structural and Optical Properties of NiO Thin Films Deposited Using Ni Pellet by PLD Technique with Varying Laser Energy

Kartikey Bhardwaj[1,*], Vipul Rastogi[1] and Anirban Mitra[1]
[1]*Department of Physics, Indian Institute of Technology Roorkee, Roorkee – 247667, Uttarakhand, India*
[*] kartikey_b@ph.iitr.ac.in

Abstract: In this work, NiO thin films were deposited by ablation of Ni pellet using a pulsed laser deposition technique with varying laser energy. The polycrystalline nature of deposited thin films are confirmed by the X-ray diffraction technique, and the transmittance is approximately 60 – 80 % in the visible region. The Band gap of the films is 3.45 – 3.62 eV, and the extinction coefficient shows good and approximately constant transparency in the visible region and higher absorption in the UV region.

Keywords: Pulsed laser deposition, Extinction coefficient, Absorption coefficient, Spectroscopic ellipsometer, Metal oxides.

INTRODUCTION

Nickel oxide is a transparent hole-selective material with magnetic, electrical, and optical properties. It is a p-type semiconductor with a band gap in the range of 3.15 to 4 eV, antiferromagnetic below 523 K, and a cubic (NaCl) crystal structure with a lattice parameter of 0.4195 nm [1], [2]. P-type transparent metal oxides are becoming more and more crucial parts of electrochromic devices, solar cells, display systems, and transparent optoelectronic devices [3]. NiO has drawn a lot of interest because of its superior chemical and physical characteristics, affordable production costs, high substrate adaptability, lack of toxicity, and abundance of storage options [4]. In this study, we demonstrated how the varying laser energy affects the structural and optical properties of NiO film.

EXPERIMENTAL SECTION

The NiO thin films are fabricated on a glass substrate using the pulsed laser deposition technique by ablation of Ni pellet. Films were grown using Nd: YAG laser with a wavelength of 355 nm, and the substrate and target distance was 4.5 cm. We have made four samples with varying laser energies: 75 mJ/p, 100 mJ/p, 150 mJ/p, and 200 mJ/p. During the deposition, the substrate temperature was 400^{O}C, and the oxygen pressure in the chamber was 50 mTorr. The crystalline quality of these samples was examined by in-plane XRD tests conducted with a Rigaku XRD system. The Shimadzu UV spectrometer model UV-1800 was used to measure the transmittance of the deposited films. Using the Tauc plot and transmittance data, we were able to determine the bandgap of these deposited films. A variable angle spectroscopic ellipsometer (Model: M-2000, J. A. Woollam Co.) is used to calculate the extinction coefficient and refractive index. Utilizing software called Complete Ease, the data is examined using a three-layer model.

RESULT AND DISCUSSION

The crystalline nature of deposited films has been examined using X-ray- Diffraction, with reference to JCPDS data file no. 00-047-1049, the obtained XRD peaks for NiO were matched to their appropriate planes. The XRD spectra exhibit peaks at 2θ angles of of 79.41°, 75.42°, 62.88°, 43.28°, and 37.25°, which are attributed to the (222), (311), (220), (200), and (111), planes respectively. This pattern suggests that the NiO films are polycrystalline with a cubic structure and demonstrate a preferred orientation along the (200) lattice planes. Crystalline size in thin film was calculated using Debye-Scherrer's equation [5].

$$\boldsymbol{D = \frac{k\,\lambda}{\beta\,cos\theta}}$$

where $\boldsymbol{\lambda}$ is the radiation wavelength (0.154 nm), θ-bragg's angle, β is the full-width half maximum of diffraction peaks, k is the shape factor (0.9), and D is the crystalline size. The crystalline size and FWHM of all four prepared films are tabulated in Table 1.

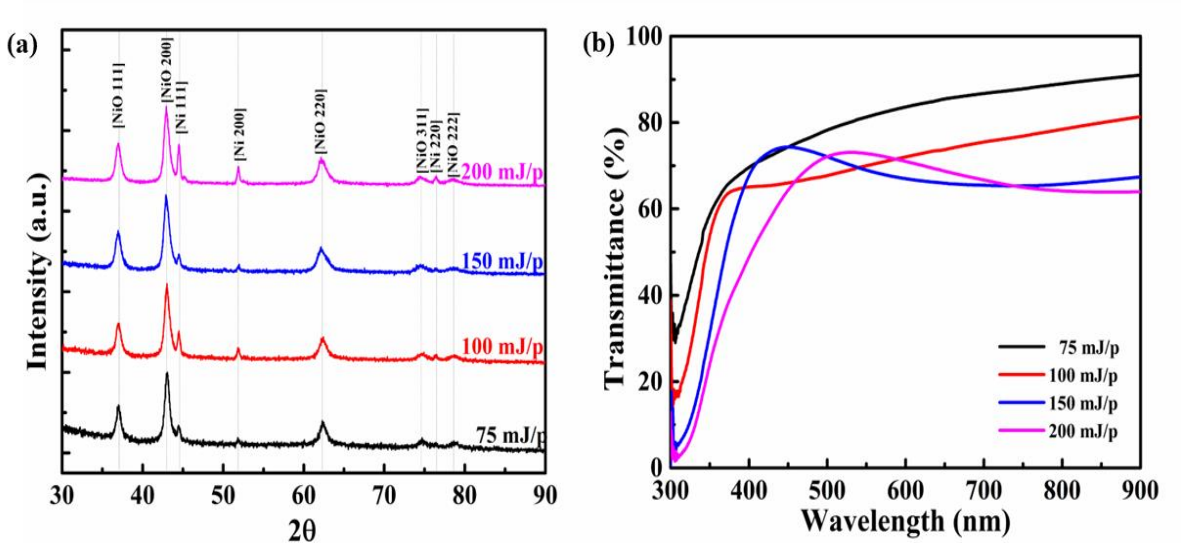


Figure 1. (a). XRD, (b) Transmittance of prepared NiO films with varying laser energy

Table 1. Parameters extracted from XRD through the intense peak data

Samples	2*theta	FWHM	Crystalline Size	Lattice Parameter(nm)
75 mJ/p	43.06	0.757	11.286	0.4197
100 mJ/P	43.052	0.831	10.273	0.4197
150 mJ/p	42.99	0.89	9.589	0.4202
200 mJ/p	42.99	0.843	10.125	0.4202

Figure 1(b). shows the optical transmittance spectra of NiO films for wavelengths between 300 and 900 nm, which are affected by laser energy, an important factor in film fabrication. The films exhibit approximately 60 – 80% transmittance in the visible spectrum. The notable cutoff observed around 350 nm in the ultraviolet range is caused by NiO's band edge absorption. To calculate the absorption coefficient (α), the following formula was employed [6].

$$\boldsymbol{\alpha = \frac{1}{d} ln(\frac{1}{T})}$$

Where *d* represents the film thickness, and *T* is the transmittance. Figure 2(a) shows the absorption coefficient of the film deposited under varying laser energy. The cross-section images were taken by FESEM to determine the thickness of the deposited films. The thickness of deposited films is 63 nm, 74 nm, 92 nm, and 105 nm, corresponding to laser energy 75 mJ/p, 100 mJ/p, 150 mJ/p, and 200 mJ/p. According to the Tauc plot, the relationship between the band gap (*Eg*) and the absorption coefficient (α) can be described by the equation [7]:

$$\boldsymbol{(\alpha h\nu) = A(h\nu - E_g)^n}$$

Where, hv is the photon energy, E_g is the band gap, A is a constant, n is a quantity that varies depending on the kind of electronic transition, and α is the absorption coefficient. Since NiO has a direct band gap, the Tauc plot of $(\alpha h\nu)^2$ versus $h\nu$ is anticipated to display a linear relationship. According to the Tauc relation, the extrapolation of this linear plot to the energy axis allows for the determination of the material's band gap. In **Figure 2(b),** it can be seen that the fitted curve intersects the Energy axis around 3.48 eV, 3.59 eV, 3.58 eV, and 3.61 eV corresponding to the NiO film deposited at laser energy 75 mJ/p, 100 mJ/p, 150 mJ/p, and 200 mJ/p.

The optical properties of NiO films deposited with varying laser energy were investigated using spectroscopic ellipsometry. Spectra were collected in the UV-visible range from 300 nm to 900 nm (1.38 eV to 4.13 eV) using a J. A. Woollam Co. M-2000 XI spectroscopic ellipsometer. We measured the ellipsometric parameters, Ψ and Δ, at an incidence angle of 65°. Ψ represents the ratio of the amplitudes of the reflected light in p- and s-polarizations, while Δ denotes the phase difference between these polarizations before and after reflection. To fit the spectroscopic ellipsometry (SE) data for the NiO film, we employed a three-layer model consisting of a glass substrate, a NiO film, and a rough surface layer. Multiple oscillators were

used in the modeling process because a single oscillator was insufficient to account for the various electronic transitions within the NiO thin films, which contribute to the optical absorption observed in the ultraviolet region.

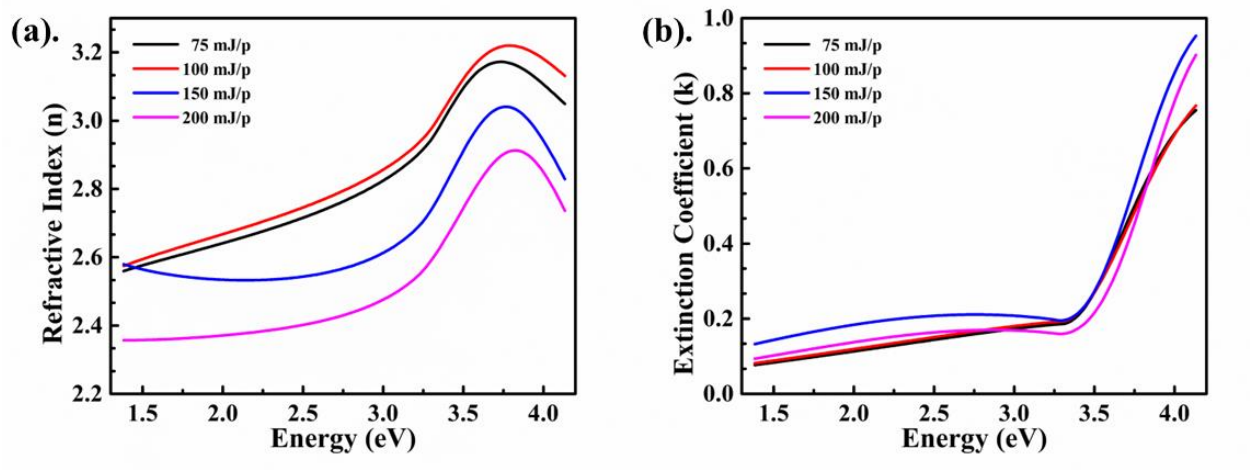


Figure 3. (a). Refractive index, (b). The extinction coefficient of deposited film at different laser energy

Figure 3 illustrates the real and imaginary parts of the refractive index of the NiO thin film as a function of energy, as measured by ellipsometry. The extinction coefficient is notably low and roughly constant in the visible range, indicating that all the deposited films exhibit good transparency. Conversely, a higher extinction coefficient in the UV region signifies increased absorption, which occurs at energies above the band gap.

ACKNOWLEDGMENTS

Kartikey Bhardwaj would like to acknowledge MHRD India and IIT Roorkee for the senior research fellowship. Anirban Mitra gratefully acknowledges the financial support provided by SERB, DST under Grant No. CRD/2021/001709, dated 01-03-2022, which facilitated the expenditure required to conduct the experiments

REFERENCES

1. F. A. F. Lahiji *et al.*, “Growth and optical properties of NiO thin films deposited by pulsed dc reactive magnetron sputtering,” *Journal of Vacuum Science & Technology A*, vol. 41, no. 6, Dec. 2023, doi: 10.1116/6.0002914.
2. X. Y. Zhang *et al.*, “Modulation of the conductive behavior of NiO thin film deposited by HiPIMS through varying the O2 flow ratio,” *Ceram Int*, vol. 48, no. 23, pp. 34668–34677, Dec. 2022, doi: 10.1016/j.ceramint.2022.08.054.
3. Kingsley O. Egbo *et al.*, “Room temperature sputtered Cu doped NiO1þd: p-type conductivity, stability of electrical properties and p-n heterojunction,” *Journal of Alloys and Compounds* 835 (2020) 155269, doi.org/10.1016/j.jallcom.2020.155269
4. Xiao-Ying Zhang *et al.*, “Modulation of the conductive behavior of NiO thin film deposited by HiPIMS through varying the O2 flow ratio,” *Ceramics International*, doi.org/10.1016/j.ceramint.2022.08.054
5. U. Holzwarth and N. Gibson, “The Scherrer equation versus the ‘Debye-Scherrer equation,’” *Nature Nanotechnology*, vol. 6, no. 9. Nature Publishing Group, p. 534, 2011. doi: 10.1038/nnano.2011.145.
6. M. T. Dejpasand, H. R. Dizaji, and M. H. Ehsani, “Tunable Structural and Optical Properties of Cadmium Telluride (CdTe) thin Films with Substrate Temperature,” *Procedia Materials Science*, vol. 11, pp. 114–118, 2015, doi: 10.1016/j.mspro.2015.11.122.
7. P. Makuła, M. Pacia, and W. Macyk, “How To Correctly Determine the Band Gap Energy of Modified Semiconductor Photocatalysts Based on UV-Vis Spectra,” *Journal of Physical Chemistry Letters*, vol. 9, no. 23. American Chemical Society, pp. 6814–6817, Dec. 06, 2018. doi: 10.1021/acs.jpclett.8b02892.

Low interface trap states in Solution Processed Silicon-Graphene oxide stacked MOS Device

Vishwas Acharya*, Atul Sachan, Sandip Mondal

Department of Electrical Engineering, IIT Bombay, Mumbai 400076, India

*Corresponding author: vishwasacharya59@gmail.com

Abstract. Graphene Oxide (GO) is a promising material for next-generation electronic devices. GO's exceptional electrical, mechanical, and thermal properties, along with its ability to form stable, low-leakage films at low processing temperatures, make it a strong candidate for enhancing device performance and scalability. This study explores the interface characteristics of GO in metal-oxide-semiconductor (MOS) structures, revealing low interface trap densities (D_{it}),) of 5.3×10^{11} $cm^{-2}eV^{-1}$ at 500 KHz and 7.3×10^{11} $cm^{-2}eV^{-1}$ at 1 MHz, comparable to high-quality SiO_2 dielectrics. The leakage current density of GO in metal-oxide-semiconductor (MOS) structures is 12×10^{-9} $A.cm^{-2}$ at 1 V. The low interface states are highly essential towards integrating GO for commercial device applications.

Keywords. Graphene Oxide, Interface Trap Density (D_{it}), Capacitance-voltage (CV).

INTRODUCTION

The good quality of the interface between silicon and silicon dioxide (SiO_2) is the main factor contributing to silicon's supremacy in the electronics industry. An approximate midgap interface trap density of 10^{10} $cm^{-2}eV^{-1}$ is characteristic of SiO_2 gate dielectrics of superior quality. In comparison, the trap densities, which range from 10^{11} to 10^{12} $cm^{-2}eV^{-1}$, are much higher at the interface between silicon and high-κ (high dielectric constant) materials [1,2]. All potential semiconductor systems naturally aim to have an interface as good or better than Si/SiO_2, since a good interface is necessary for every type of electrical and optoelectronic device that arises. Typically, the semiconductor-insulator interface is characterized by an examination of the interface state density (D_{it}). The silicon band gap contains the so-called Pb centers, which are mostly responsible for the interface states in the silicon dangling bonds at the Si/SiO_2 interface [3,4]. On the other hand, poorly understood native defects give rise to interface states in high mobility substrates such as III-V materials or Ge. Depending on the semiconductor, the majority of these states fall into the valence or conduction bands [3,4].

Due to its exceptional electrical, mechanical, thermal, and optical qualities as well as its large specific surface area, graphene and graphene-based materials have attracted the interests of scientists. These special qualities hold a lot of potential for a variety of uses in sensors, energy storage, nanoelectronics, and capacitors [5,6]. In order to realize these uses, high-quality graphene sheets must be produced on a large scale in an efficient and productive manner.

To investigate the characteristics of the graphene oxide MOS interface, the CV measurement has been performed on Al/GO/p-Si MOS capacitor, as illustrated in Figure 1. The CV curve has been used to estimate the interface state density [7]. We have evaluated the interfacial characteristics and determined the D_{it} using the terman method [8,9].

DEVICE FABRICATION AND EXPERIMENTAL SETUP

Material Growth: In this work, we have synthesized the solution processed graphene oxide by modified Hummers method. In which, 108 ml (H_2SO_4) and 12 ml (HNO_3) are combined and stirred in a 9:1 volume ratio for a few minutes. Subsequently, 1 g of graphite powder was added to the mixture and constantly mixed. After that, 6 grams of potassium permanganate ($KMnO_4$) was progressively added to the solution. The liquid turned dark green after vigorously stirring it for six hours. After adding 1 mL of hydrogen peroxide (H_2O_2) dropwise, this solution was agitated for 10 minutes to eliminate the excess $KMnO_4$. We allowed it to cool at room temperature for a while since an exothermic reaction happened. Afterwards, 10 ml of HCl and 30 ml of deionized water (DIW) were added to the solution.

Following that, an instantaneous centrifugation at 5,000 rpm was applied to the mixture. Cleaning the residuals three times with HCl and DIW followed by decanting of the supernatant. After that the GO solution was cleaned and dried in an oven for 24 hours at 90°C to produce graphene oxide powder.

Device Fabrication: The graphene oxide based two terminal MOS devices were fabricated through sol-gel method. We prepared the Graphene oxide solution by dissolving the 1 mg graphene oxide powder in 1 ml of deionized water and sonicate it for 4 hours in ultra sonicator water bath. The commercial silicon (doping of 4×10^{15} cm^{-3}) was used a substrate. We took 2-inch RCA cleaned Silicon wafer and exposed them to oxygen plasma exposer for 10 minutes at 20 watts to remove the residual organic substance and to make them hydrophilic. Then the graphene oxide solution was spin coated on the cleaned substrate at 2000 rpm for 30 seconds and immediately kept on hot plate at 90 ^{O}C for 1 minute. There after we deposited the Al electrode with thermal evaporator at 10^{-6} mbar pressure with a shadow mask.

RESULT & DISCUSSION

The GO-MOS devices (Al/GO/p-Si) were subjected to capacitance-voltage (CV) measurements at high frequencies of 500 KHz and 1 MHz, using a small signal amplitude of 50 mV, as illustrated in Fig. 1b. The high-frequency CV curve demonstrated a noticeable stretch-out due to interface traps, distorting the curve shape. This stretch-out indicates a uniform distribution of interface trap levels across the silicon bandgap, highlighting the significant impact of these traps on the behavior and performance of semiconductor devices, as shown in Fig. 2(a) and Fig. 2(b).

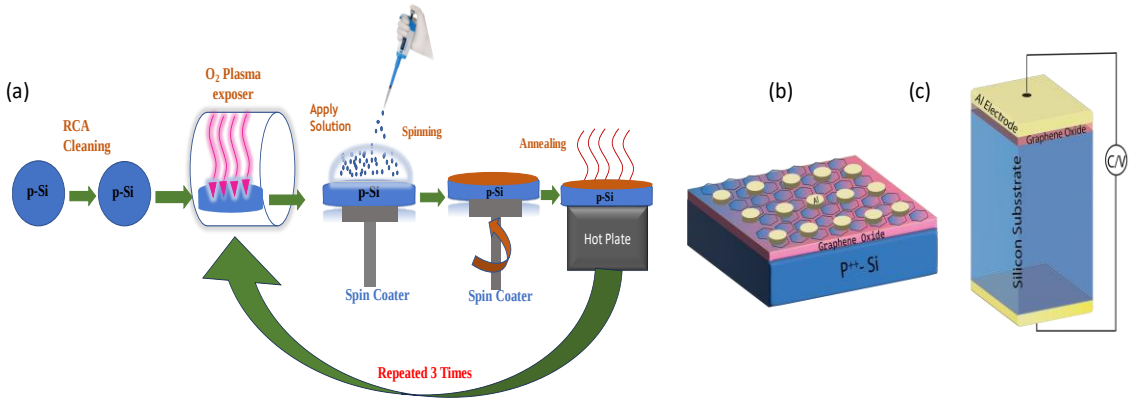


FIGURE 1. (a) Schematic of device Fabrication process using solution-processed GO on silicon wafer. (b) Schematic of GO-MOS device (Al/GO/Si) Architecture. (c) Probed device for CV measurement.

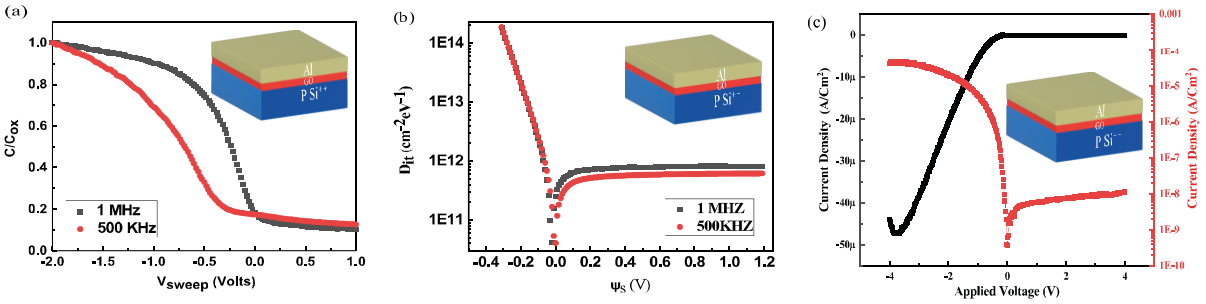


FIGURE 2. (a) CV characteristic of Al/GO/Si MOS device at different frequencies (b) D_{it} calculation using terman method, (c) leakage current density vs applied field

The density of interface traps (D_{it}) was determined at room temperature using the Termann Method, based on high-frequency CV measurements. The results are displayed in Fig. 2(b) as a function of ψ_s (band bending). To calculate the derivative $d\psi_s/dV_G$, either graphical or numerical differentiation of the ψ_s vs. V_G (Gate Voltage) curve was performed. Following this, the interface capacitance $C_{it}(\psi_s)$ was calculated using equation (1):

$$C_{it}(\psi_s) = C_{Ox}\left\{\left(\frac{d\psi_s}{dV_G}\right)^{-1} - 1\right\} - C_s(\psi_s) \qquad (1)$$

Where C_{ox} is the maximum capacitance per unit area obtained from the high-frequency CV curve, and C_s is the silicon surface capacitance per unit area, which varies with band bending ψ_s. Once C_{it} is determined using equation (1), the interface trap density D_{it} can be calculated using equation (2):

$$D_{it} = C_{it}/q \qquad (2)$$

Notably, the GO oxide exhibits a D_{it} value of 5.3×10^{11} $cm^{-2}eV^{-1}$ at 500 KHz and 7.3×10^{11} $cm^{-2}eV^{-1}$ at 1 MHz in the mid-gap region, indicating an interface state density comparable to thermally grown SiO_2 and even lower than Si oxides produced at lower temperatures using techniques such as chemical vapor deposition (CVD) and atomic layer deposition (ALD). The leakage current density of GO in metal-oxide-semiconductor (MOS) structures at 1V is 12×10^{-9} $A.cm^{-2}$.

CONCLUSION

In conclusion, Graphene Oxide (GO) has demonstrated significant potential in electronic applications. The study found that solution-processed GO films exhibit relatively low interface trap densities, around 5.3×10^{11} $cm^{-2}eV^{-1}$ at 500 KHz and 7.3×10^{11} $cm^{-2}eV^{-1}$ at 1 MHz, which are promising compared to traditional high-κ materials. The unique electrical, mechanical, thermal, and optical properties of GO, combined with its capability to form stable, low-leakage films at low processing temperatures, position it as a strong candidate for future use in electronics. The leakage current density of GO in metal-oxide-semiconductor structures at 1 V is 12×10^{-9} $A.cm^{-2}$.These findings suggest that GO could address current challenges in device performance and scalability, paving the way for advancements in sensors, energy storage, and nanoelectronics. As research progresses, the scalable production of high-quality graphene materials will be crucial to realizing the full potential of GO in various technological applications.

ACKNOWLEDGMENTS

The authors would like to express their gratitude to the Indian Institute of Technology Bombay Nanofabrication Facility for providing the facilities for the fabrication and characterization of the set of devices.

REFERENCES

1. Dev, D., Krishnaprasad, A., Kalita, H., Das, S., Rodriguez, V., Calderon Flores, J., ... & Roy, T. (2018). High quality gate dielectric/MoS2 interfaces probed by the conductance method. *Applied Physics Letters*, *112*(23).
2. Wilk, G. D., Wallace, R. M., & Anthony, J. (2001). High-κ gate dielectrics: Current status and materials properties considerations. *Journal of applied physics*, *89*(10), 5243-5275.
3. Robertson, J. (2009). Model of interface states at III-V oxide interfaces. *Applied Physics Letters*, *94*(15).
4. Chelikowsky, J. R., & Cohen, M. L. (1979). Self-consistent pseudopotential calculation for the relaxed (110) surface of GaAs. *Physical Review B*, *20*(10), 4150.

5. Mei, X., & Ouyang, J. (2011). Ultrasonication-assisted ultrafast reduction of graphene oxide by zinc powder at room temperature. *Carbon*, *49*(15), 5389-5397..
6. Fan, Z. J., Kai, W., Yan, J., Wei, T., Zhi, L. J., Feng, J., ... & Wei, F. (2011). Facile synthesis of graphene nanosheets via Fe reduction of exfoliated graphite oxide. *ACS nano*, *5*(1), 191-198.
7. Kundu, T., Garg, R., Chowdhury, N., & Misra, D. (2005). The Chalkboard: Electrical Techniques for the Characterization of Dielectric Films. *The Electrochemical Society Interface*, *14*(3), 17.
8. A. Sachan and S. Mondal, "Solution Process Charge Balancing Capacitive Devices," 2024 Device Research Conference (DRC), College Park, MD, USA, 2024, pp. 1-2, doi: 10.1109/DRC61706.2024.10605258. keywords: {Indium gallium zinc oxide;Logic gates;Dielectrics;Aluminum oxide}.
9. A. Sachan and S. Mondal, "Probing Dit and Memory Window of Solution Processed Oxide," 2024 8th IEEE Electron Devices Technology & Manufacturing Conference (EDTM), Bangalore, India, 2024, pp. 1-3, doi: 10.1109/EDTM58488.2024.10511573.

Theoretical Insights Towards Interfacial Engineering And Device Optimization Of $CH_3NH_3SnI_3$ Perovskite Solar Cells By SCAPS-1D

Arushi Sharma[1,*)], Himanshu[2)], Ekta Yadav[1)], Kamlesh[1)] and M.S. Dhaka[1)]

[1] *Department of Physics, Mohanlal Sukhadia University, Udaipur- 313001 India*
[2]*University Centre for Research & Development, Chandigarh University, Mohali, 140413, India*
[a)]Corresponding author: anshu26667@gmail.com

Abstract: Perovskite solar cells (PSCs) possess the capability to revolutionize the solar energy landscape with their high efficiency and low production costs, establishing them as prime contenders for next generation solar technology. However, their effective sustainable utilization is hindered due to major challenges viz. use of toxic Lead and rapid degradation issues. Addressing these obstacles is crucial to unlocking the full potential of PSCs and ensuring their practical widespread use. In pursuit of this objective, this study examines the impact of interfacial engineering in Lead free PSCs by introducing graphene interlayer which typically promotes hole extraction and reduces hole recombination. The Lead free, Tin based PSCs having device configurations as FTO/SnO_2/$MASnI_3$/Cu_2O/Au and FTO/SnO_2/$MASnI_3$/Graphene/Cu_2O/Au have been simulated by using SCAPS-1D program. The presented research highlights the impacts of absorber thickness and total defect density (N_t) on performance of Sn based PSCs. Incorporating graphene into the optimized device boosted the PCE from 22.42% to an impressive 25.06%. This improvement is mainly due to reduced recombination losses and better suppression of interfacial non-radiative recombination. These findings demonstrate the potential of incorporating a graphene interlayer to develop cost effective, high efficiency Lead free Tin based PSCs comprising of graphene interlayer to address the defects and control the non radiative recombination.

Keywords: Perovskite solar cells; Stability; Numerical simulation; Graphene; SCAPS-1D.

Introduction

In the classification of emerging solar photovoltaic technologies, the PSCs are experiencing substantial interest owing to their scalable fabrication, low production costs, excellent optoelectronic features, and low-temperature processing routes. Due to the remarkable enhancement in efficiency from 3.8% to 27% over the past decade, PSCs have garnered significant attention as they keep pace with the rapid advancements in solar cell technologies. However, for continued improvements in efficiency, efficient charge carrier generation, extraction, and transport, together with stability under diverse conditions, are critical factors [1]. The methylammonium Tin iodide ($CH_3NH_3SnI_3$ or $MASnI_3$) is a significant Lead free light harvesting absorber perovskite material which provides appreciable PCE to associated PSCs owing to its higher light absorption coefficient, tunable optical properties, suitable bandgap and effective charge separation virtues along with higher stability and cost effectiveness. The SnO_2 is considered as a crucial contender for electron transport layers which improves performance and longevity by providing high electron mobility, reducing recombination losses, and maintaining strong chemical stability. Its optical transparency and solution-processability further boost efficiency, making it versatile for a variety of perovskite materials. Additionally, the shift toward inorganic hole transport materials (HTMs) like Cu_2O addresses the limitations of organic HTMs, offering high hole mobility, stability, and cost-effectiveness, along with simple processing for scalable manufacturing [2]. Since the PSCs suffer from use of toxic Lead (Pb), degradation issues, and therefore to address the same, current work explores the device designing and optimization of $MASnI_3$ absorber based PSCs by elaborating the significance of absorber thickness, defect density and interlayer modifications on device's performance by utilizing SCAPS-1D code. The present work also investigates the effectiveness of utilizing graphene as a surface passivation material since, it hinders the interfacial recombination leading to higher performance of the associated PSC devices.

Numerical simulation and device modeling

This study utilizes, the solar cell capacitance simulator-one dimensional (SCAPS-1D - version 3.3.0.11), developed by Burgelman's team using LabWindows/CVI at University of Gent, to perform numerical simulations of $MASnI_3$ based perovskite solar devices since, it offers more flexibility on device design [3]. The Pb-free Sn-based PSCs configured with device architecture as glass/FTO/SnO_2/$MASnI_3$/Cu_2O/Au are simulated. Figure 4(a) and 4(b) depict the model PSC without graphene and with graphene interlayer, respectively. Table 1 provides the key physical parameters of constituent layers for the purpose of numerical simulation which performed at standard conditions [4].

Table 1. Several physical parameters related to distinct constituent layers utilized in the simulation process.

Parameters	Unit	FTO [5]	SnO_2 [6]	Graphene [5]	$MASnI_3$ [2]	Cu_2O [6]
Layer Thickness (W)	nm	500	100	50	Vary	200
Bandgap energy (E_g)	eV	3.5	3.6	1.8	1.3	2.17
Electron affinity (χ)	eV	4	4	3.92	4.1	3.2
Relative permittivity (ε_r)		9	9	10	8.2	7.1
Effective Conduction band density of states (N_c)	cm^3	2.2×10^{18}	3.7×10^{18}	1×10^{21}	1×10^{18}	2.5×10^{18}
Effective Valence band density of states (N_v)	cm^3	1.8×10^{19}	1.8×10^{19}	1×10^{21}	1.8×10^{18}	1.8×10^{19}
Electron mobility (n)	cm^2/Vs	2×10^{1}	1×10^{2}	1×10^{9}	1.6×10^{0}	2×10^{2}
Hole mobility (p)	cm^2/Vs	1×10^{1}	2.5×10^{1}	1×10^{1}	1.6×10^{0}	8.6×10^{3}
Donor Density (N_D)	cm^{-3}	2×10^{19}	1×10^{17}	0	0	0
Acceptor Density (N_A)	cm^{-3}	0	0	9×10^{21}	1×10^{16}	1×10^{18}
Defect density (N_t)	cm^{-3}	1×10^{15}	1×10^{15}	1×10^{15}	1×10^{15}	1×10^{15}

Results and Discussion

• Effect of absorber layer thickness on device performance

Herein, the absorber thickness has been altered from 350 nm to 850 nm in steps of 100 nm to examine its impact on photovoltaic characteristics, where obtained parameters are graphically demonstrated in Fig. 2 (A) and 2(B) and listed in Table 2 as well. A boost in carrier concentration resulted in an upsurge in the open circuit voltage (V_{oc}) and short circuit current density (J_{sc}), which climbed from 0.8501 V to 0.8522 V and from 27.59 mA/cm² to 29.21 mA/cm², respectively.

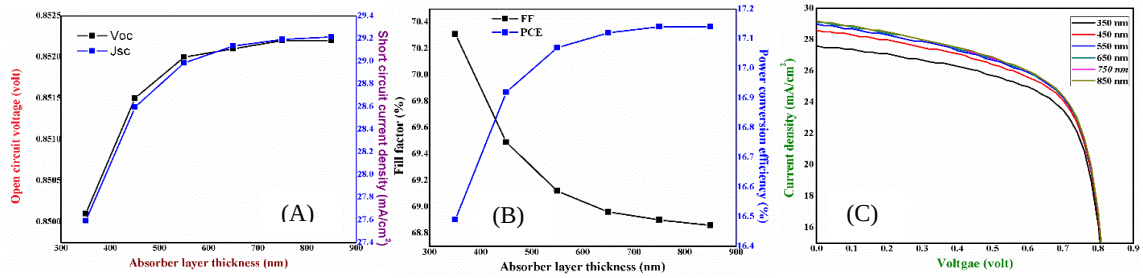


Fig. 2 Pictorial presentation of (a) V_{oc} and J_{sc}, (b) FF and PCE, and (c) J-V curve with varied absorber layer thickness.

Table 2. Variation in absorber layer thickness, defect density and its impact on various performance parameters.

Thickness (nm)	V_{oc} (mvolt)	Jsc (mA/cm^2)	FF (%)	PCE (%)	Defect density (cm^{-3})	V_{oc} (mvolt)	Jsc (mA/cm^2)	FF (%)	PCE (%)
350	850.1	27.59	70.03	16.49	$\mathbf{10^{12}}$	908.3	31.41	78.61	22.42
450	851.5	28.59	69.49	16.92	$\mathbf{10^{13}}$	906.5	31.37	78.42	22.30
550	852.0	28.98	69.12	17.07	$\mathbf{10^{14}}$	892.6	31.05	76.70	21.26
650	852.1	29.13	68.96	17.12	$\mathbf{10^{15}}$	852.2	29.19	68.90	17.14
750	852.2	29.19	68.90	17.14	$\mathbf{10^{16}}$	749.5	23.81	60.95	10.88
850	852.2	29.21	68.86	17.14	$\mathbf{10^{17}}$	617.6	11.96	48.79	3.60

Conversely, as thickness grew, the fill factor (FF) dropped from 70.31% to 68.86%, probably due to increased series resistance (R_s), whereas the PCE increased from 16.49% to 17.14% despite a decline in FF. The performance evaluation revealed that 750 nm is the optimum thickness for the absorber layer. The simulation results indicate that as the intensity of incident light is increased, the charge carriers are incessantly produced, leading nearly constant current density at low voltages, with the maximum J_{sc} occurring at zero voltage, as illustrated in Fig. 2(C). An increase in applied voltage led to substantial charge carrier recombination both within the absorber and at the interfaces in the simulated $MASnI_3$-based PSCs, thus capping the V_{oc} near 0.8 V [7,8].

• Effect of absorber layer defect density on device performance

This work comprehensively examines how changing the absorber defect density (N_t) from 10^{12} cm^{-3} to 10^{17} cm^{-3} affects device performance, employing the Shockley-Read-Hall (SRH) recombination model to elucidate its influence on the performance of PSCs. The J-V curve and the relationships between V_{oc}, J_{sc}, FF and PCE with N_t are portrayed in Fig. 3. It is evident that rising defect density within the absorber layer clearly indicates a decline in PV performance. This degradation is attributed to an increase in carrier recombination within device on increasing N_t [9]. An absorber defect density of 10^{12} cm^{-3} was identified as optimal, achieving V_{oc} 0.9083 V, J_{sc} 31.41 mA/cm^2 , FF 78.61%, and PCE 22.42% (refer Table 2).

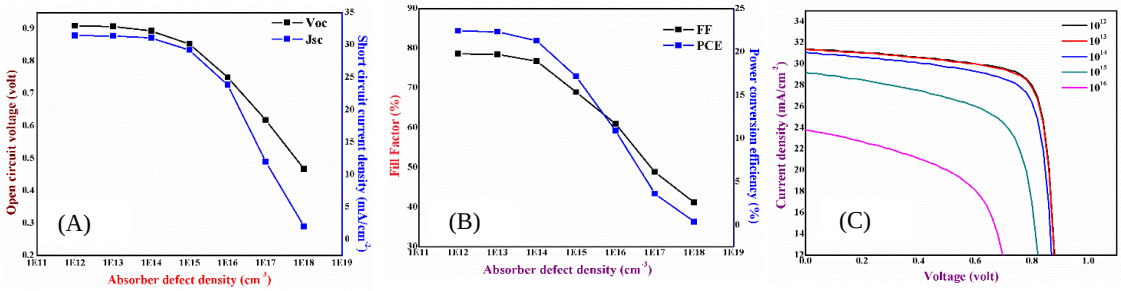


Fig. 3 Pictorial presentation of (A) V_{oc} and J_{sc}, (B) FF and PCE, and (C) J-V curves under different absorber defect densities.

• Effect of graphene interfacial layer on device performance

Since incorporation of graphene interlayer is a crucial approach for boosting device performance, therefore, the surface passivation graphene interlayer is introduced in optimized devices as shown in Fig. 4. As compared to a device without graphene, the device with graphene layer exhibits better PV performance with V_{oc} 0.9083 V, J_{sc} 33.05 mA/cm^{-2}, FF 83.91% and PCE 25.06% while the optimized device without graphene layer showed lower performance parameters viz. V_{oc}, J_{sc}, FF and PCE of 0.9083 V, 31.41 mA/cm^{-2}, 78.61% and 22.42%, respectively, Fig. 4 shows the J-V plots, where passivating the perovskite surface with graphene has a pronounced positive effect on device performance.

The improved J_{sc} is due to faster charge transfer at the perovskite/graphene interface, caused by the reduction in defect states at this interface. This enhancement likely stems from the greater charge extraction efficiency offered by the graphene modification layer [6].

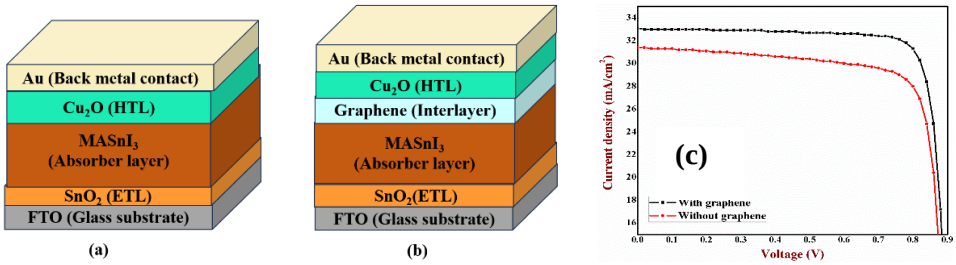


Fig. 4. The device architecture of $MASnI_3$ based PSC, (a) structure deprived of graphene interlayer, (b) structure with graphene interlayer, and (c) J-V characteristic for the optimized PSCs with and without graphene interlayer.

CONCLUSIONS

In summary, present work examined the significance of $MASnI_3$ absorber layer defect density and thickness on PSC device performance using SCAPS-1D, where an optimized absorber thickness of 750 nm and defect density of 10^{12} cm^{-3} were achieved and optimized device yielded V_{oc} 0.9083 V, J_{sc} 31.41 mA/cm², FF 78.61%, and PCE 22.42%. Incorporating functionalized graphene as an interlayer between the absorber layer and HTL further resulted into enhancement in device performance. The graphene modified device achieved a V_{oc} 0.9036 V, J_{sc} 33.05 mA/cm², FF 83.91%, and PCE 25.06%. The findings emphasize the potential for substantial performance improvements through optimizing absorber layer defect density and thickness, along with implementing interface modifications.

ACKNOWLEDGEMENTS

The authors are thankful to Prof. M. Burgelman, University of Gent Belgium for providing SCAPS-1D code facility.

REFERENCE

[1] M.K. Hossain, G.F.I. Toki, D.P. Samajdar, M. Mushtaq, M.H.K. Rubel, R. Pandey, J. Madan, M.K.A. Mohammed, Md. R. Islam, Md .F. Rahman, H. Bencherif, ACS Omega, Vol. 8, pp. 22466-22485 (2023).
[2] H. Alipour, A. Ghadimi, Opt. Mater., Vol. 120, pp. 111432 (2021).
[3] M. Burgelman, K. Decock, S. Khelifi, A. Abass, Thin Solid Films, Vol. 535, pp. 296-301 (2013).
[4] T.O. Ahmed, T.T. Ibrahim, O.E. Oladimeji, J.D. Koffa, Braz. J. Phys., Vol. 54, pp. 42 (2024).
[5] E. Danladi , A.C. Egbugha, N.N. Tasie, C.U. Achem, I.S. Haruna, L.O. Ezeh, J. Ind. Chem. Soc., Vol. 100, pp. 101001 (2023).
[6] Y. Raouia, H.E. Zahraouyc , N. Tahiric , O.E. Bounaguid , S. Ahmada, S. Kazima, Sol. Energy, Vol. 193, pp. 948-955 (2019).
[7] F. Anwar, R. Mahbub, S.S. Satter, S.M. Ullah, Int. J. Photoenergy, Vol. 1, pp. 846310 (2017).
[8] H.J. Du, W.C. Wang, J.Z. Zhu, Chinese Phys. B, Vol. 25, pp. 108802 (2016).
[9] H. Heo, S.H. Im, C.S. Lim, J.A. Chang, H. Kim, A. Sarkar, M. Grätzel and S.Il Seok, Nat. Photonics, Vol. 7, pp. 486-491 (2013).

Synthesis of Tungsten Carbide Thin Film by Ion Beam Sputtering

Rajnish Dhawan[1*], Abhay Bhisikar[1] , Maheswar Nayak[1,2]

[1]Accelerator Physics and Synchrotrons Utilization Division, Raja Ramanna Centre for Advanced Technology, Indore, INDIA
[2]Homi Bhabha National Institute Training School Complex Anushakti Nagar, Mumbai, 400094, India
[*]*Corresponding Author E-mail:**rajnish@rrcat.gov.in***

Abstract: Thin films of tungsten carbide (WC) have been deposited on single crystal silicon wafers by Ion Beam Sputtering (IBS) technique using WC target. The effect of ion beam energies in the range of 800-1200 eV on the structure and morphology of thin films were investigated using X-ray reflectivity (XRR) and grazing incidence X-ray diffraction (GIXRD) techniques. It is observed that roughness of film decreases with increasing the ion beam energy up to 1000 eV. With further increase of energy, the roughness increases. At the optimum beam energy of 1000 eV, the minimum roughness of WC film, of ~2.5 Å is achieved with mass density of 14.50 g/cc (93% of bulk density), required for x-ray optics application. The observed variations of structure and morphology of WC film with ion beam energy have been discussed.

Keywords: Thin film, Ion beam sputtering, XRR, Beam Energy, GIXRD

INTRODUCTION

Nano-scaled thin film of tungsten carbide (WC) is a potential candidate for soft gamma-ray multilayer optics application [1]. In addition, WC thin film has been widely used in many other applications due to its useful properties such as chemical resistance, high thermal stability and mechanical hardness [2–4]. The properties of the WC film depend on technique used for fabrication. Earlier, different deposition techniques have been used to deposit the WC thin films such as chemical vapour deposition [5], plasma enhanced chemical vapour deposition (PE-CVD) [6], pulsed laser deposition [7], and sputtering methods [8–10, 1]. For x-ray multilayer optics application, the layer thickness is in nano-meter scale with mandatory abrupt interfaces [1]. For abrupt interfaces, the interfacial roughness should be in atomic scale with high mass density contrast at the interface. Here, we attempt to optimize the process parameters using ion beam sputtering (IBS) system in a systematic study, to obtain the achievable low roughness and high mass density in nano-scaled WC films.

EXPERIMENTAL DETAILS

Five samples of WC thin films are deposited on silicon wafer substrate of size 20 mm x 20 mm at room temperature, using in-house developed ion beam sputtering deposition system with Kaufman Ion Source. High purity argon gas (99.999%) is used as sputtering gas. We used commercially available 4.0 inch (diameter) and 8.0 mm thick sputtering targets of WC of purity 99.99%. Pre-sputtering of the target is also done for 30 min to remove any unwanted layer on the target. Before deposition, the sputtering chamber is evacuated to the base pressure of ~ 2×10^{-7} mbar. High purity (99.999%) argon sputtering gas is introduced into the vacuum chamber through a mass flow controller with a constant flow of 2.5 std cm^3/min. During the sample deposition, pressure in the chamber is maintained between ~4×10^{-4} mbar to ~5×10^{-4} mbar with 3 std cm^3/min Ar gas flow. The typical roughness of the bare substrates was ~ 4-5 **Å** as determined by XRR measurements. Before deposition, all substrates are cleaned with isopropyl alcohol. To understand the influence of ion beam energy on structure and morphology of the WC films, five samples [(S1), (S2), (S3), (S4), and (S5)] are deposited at beam energies 800 eV, 900 eV, 1000 eV, 1100 eV and 1200 eV at room temperature. Characterizations of all the samples are done using XRR and GIXRD techniques. Before the measurements are carried out, alignment of both theta and two-theta axis within 0.002° is carried out using standard alignment procedures. All the XRR measurements are performed with a step size of 0.01° in theta axis and GIXRD measurements are done in 0.03° step size with scan speed 0.5 (step/sec) with incident angle 0.6°. Figure 1(a) and 1(b) show the internal and external view of Ion beam sputtering system respectively, specifically indicateng the ion gun, target material and substrate.

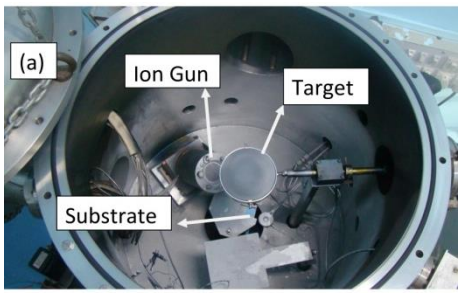


Figure 9: (a) IBS internal view



Figure 1: (b) IBS external view

RESULTS AND DISCUSSIONS

To understand the effect of ion beam energy on microstructure and morphology of WC thin films, WC thin films are deposited at various beam energies at constant Ar gas flow of 2.5 std cm^3/min. These samples are marked as S1, S2, S3, S4 and S5. Figure 2(a) shows the measured XRR data up to high q_z value along with the best fit profiles of five samples of WC films. Parratt's formalism [11] is used to model XRR measured data and refraction corrections are taken into account using Nevot-Croce model [12]. XRR is a non-destructive and sensitive technique to find out thickness, surface roughness and density of different layers of the thin films. The XRR curves in fig 2(a) are shifted vertically for the sake of clarity. The measured XRR data indicates well defined interference oscillation pattern up to higher q_z values that indicates qualitatively good quality of the fabricated thin films. The microstructure parameters (thickness, roughness and density) obtained from the best fit XRR data is shown in Table.1.

Table 2: Parameters of WC thin films deposited at different beam energies

S.no	Sample	Beam energy (eV)	Thickness (Å)	Roughness (Å)	Density (g/cc)	Deposition rate (Å/min)	Crystallite grain size (nm)
1	S1	800	357	4.2	14.3 (91% of bulk)	25	1.2
2	S2	900	353	6.0	14.3 (91% of bulk)	27	1.2
3	S3	1000	356	2.5	14.5 (93% of bulk)	29	1.1
4	S4	1100	347	6.3	14.4 (92% of bulk)	30	1.1
5	S5	1200	345	7.0	14.6 (93% of bulk)	31	1.0

It is clearly observed that both roughness and mass density changes as ion beam energy varies. As ion energy increases from 800 to 900 eV, roughness of the films increases from 4.2 to 6.0 **Å** with density remaining nearly constant at ~ 14.3 g/cc. However, as ion energy further increases to 1000 eV, roughness decreases to a minimum value of 2.5 **Å** with increasing density to ~14.5 g/cc. As ion energy is further increased to 1200 eV, roughness starts increasing to a maximum value 7.0 **Å** with density slightly increasing to 14.6 g/cc. Thus, it is observed that at the optimum ion energy of 1000 eV, WC film grows as smooth films with a reasonable high density. Scattering length density (SLD) profiles of WC films fabricated at different ion energies, which is derived from the best fit XRR data, along with that of ideal WC film (bulk density and zero roughness) for comparison. Figure 2(b) shows the variation of the SLD profile thickess in all the films. SLD trends follow the variation in the film densities with ion beam energies. To investigate the crystalline structure and crystallite grain size, GIXRD measurements of all the samples are done as shown in Figure 2(c).

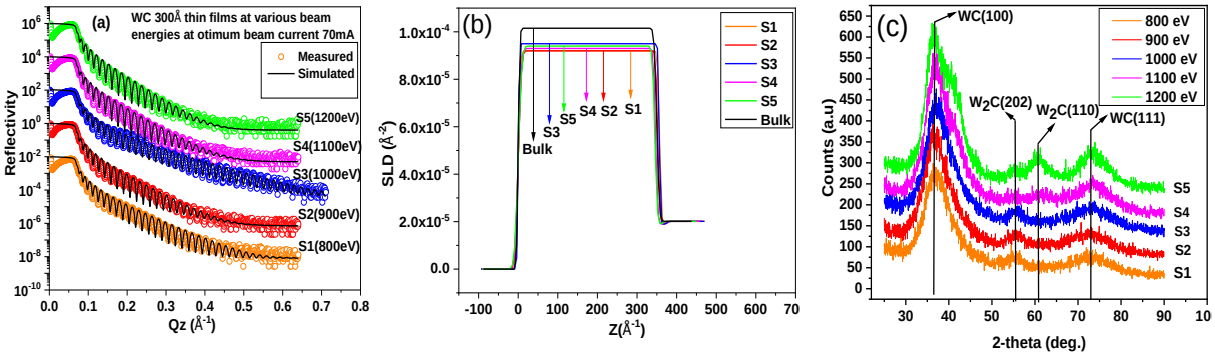


Figure 2: (a) XRR measured data (open circles) and fitted profile (solid line) of WC thin films S1, S2, S3,S4 and S5 deposited at different beam energies from 800 eV to 1200 eV. (b) Corresponding scattering length density profiles obtained from the best fit XRR data. (c) GIXRD measured data of WC thin films.

GIXRD data indicate that the WC films are polycrystalline. The high intensity diffraction peak at $2\theta = 36^{\circ}$ corresponds to the WC (100) hexagonal phase. In addition, the other diffraction peaks at $2\theta = 55.3^{\circ}$, 60.8°, and 72.9° correspond to W_2C (202), W_2C (110) and WC (111), respectively are also observed. It is noted that W_2C (110) peak is missing in samples S1, S2 and S3, but clearly visible in samples S4 and S5. The average crystallite size calculated for WC (100) diffraction peak by using the Scherrer formula as given in Table 1. The average values of crystallite sizes are ~1.2 nm for S1 and S2 and ~1.1 nm for S3, S4 and S5.

CONCLUSIONS

In this study the influence of ion beam energy (800-1200 eV) at constant argon flow rate of 2.5 sccm on the surface roughness, density and crystallite size of the WC films deposited by ion beam sputtering technique are investigated. X-ray reflectivity studies reveal that the roughness of the films get significantly modified (7.0 to 2.5 Å) with change in ion beam energy, while mass density changes from 91-93% of bulk value. Low surface roughness of 2.5 **Å** and high density (93% of bulk value) WC thin film is achieved at the optimum value of ion beam energy of 1000 eV. This observation of reduction in substrate roughness of thin film as compared to the substrate at a certain deposition condition is interesting and further understanding of this process is underway.

ACKNOWLEDGMENTS

Authors would like thank to Dr.S.K.Rai for his valuable support in XRR and GIXRD measurements using hard X-ray Bruker D8 diffractometer setup.

REFERENCES

1 M. Fernández-Perea et al. Phys. Rev. Letts. 111, 027404 (2013).
2. J. Esteve, G. Zambrano, C. Rincon, E. Martinez, H. Galindo, P. Prieto, , Thin. Sol. Film. 373 (2000) 282 – 286.
3. K.A. Beadle, G. Rahul, M. Anoop, G.C. Jingguang, G.W. Brian, Thin. Sol. Film. 516 (2008) 3847 – 3854.
4. E. Raekelboom, K. Abdelouahdi, C. Legrand-Buscema, Thin. Sol. Film. 517 (2009) 1555 – 1558.
5. D.W. Skaf, A. W. Warner, N.R. Dollahon, G. H.Fargo,. 33 (1994) 393 – 402.
6. W. Precht, A. Czyzniewski, Surf. Coat. Technol. 174 – 175 (2003) 979 – 978.
7. S. Ghaisas, J. Appl. Phys. 70 (1991) 7626.
8. M.D. Abad, M.A. Muñoz-Márquez, S. El Mrabet, A. Justo, J.C. Sánchez-López, . 204 (2010)3490 – 3500.
9. P.C. Jiang, J.S. Chen, J. Vac. Sci. Technol. 21 (2003) 616.
10. N. Radi´, B. Pivac, F. Meinardi, Th. Koch, Mater. Sci. Eng A. 396 (2005) 290 – 295
11. L.G. Parratt Phys. Rev. 95 (1954) 359
12. L.Nevot and P Croce. Rev.Phys.Appl. 15,761, (1980)

Fabrication and Characterization of Thin Film Coating on Large Area for Development of X-ray Mirrors

Faiyaz Mollick[1,2*], Jitendra Kumar[2], Maheswar Nayak[1,2*], P.K. Gauttam[2], V. K. Raghuwanshi[2], S. R. Kane[2], Pooja Gupta[1,2] and Nageswara Rao Pothana[2]

[1]Homi Bhabha National Institute, Training School Complex, Anushakti Nagar, Mumbai, 400094, INDIA
[2]Accelerator Physics and Synchrotron Utilization Division, Raja Ramanna Centre for Advanced Technology, Indore, 452013, INDIA

[*]*Corresponding author: fmollick@rrcat.gov.in*
[*]*Corresponding author: mnayak@rrcat.gov.in*

Abstract. Development of mirrors for hard x-ray micro/nano focusing requires large size optical coating with length of the order 300 mm on figured surfaces. To fabricate such mirrors, an ultra-high vacuum ion-assisted electron beam evaporation system is indigenously developed with an automated substrate rotation facility. Small-sized (20 mm × 20 mm) dummy Si substrates were placed at different locations over the area of ~300 × 100 mm^2 to analyze the structure and thickness uniformity of the coating. The process parameters were systematically varied to tailor the surface roughness, film density and uniformity of coating. Nickel thin films (average thickness ~42.5 nm) deposited at the optimized deposition parameters has a maximum thickness non-uniformity of ~4.4%, with mass density ~99% of bulk value and average roughness ~1.2 nm. The calculated maximum slope error due to thickness non-uniformity is ~37 nano radian.

Key words: X-ray Mirror; X-ray Reflectivity; Thin Film Coating; Large-size mirrors; Electron Beam Evaporation.

INTRODUCTION

X-ray reflective mirrors are used to manipulate x-rays for wide range of applications in science and technology. It works on the principle of total external reflection in case of thin film mirrors and by Bragg reflection in case of crystals as well as periodic multilayers [1]. The Kirkpatrick-Baez (KB) mirror is among the most commonly used optical elements using either thin film or periodic multilayer coating, for hard x-ray micro/nano focusing applications. Thin film KB mirror operates below the critical angle, which is typically on the order of a few milliradian for hard x-rays. Due to this low angle of incidence, the x-ray footprint on the substrate is very large and mirrors with length typically in the range ~200-500 mm are required [2,3]. In order to preserve the photon brilliance, coherence and the propagating wavefront, high-precision mirrors with slope error of the order of a fraction of micro radian to tens of nano radians, are essential for use at beamlines on a modern synchrotron radiation source or free electron laser [4]. Even slight deviations in mirror shape can significantly distort the coherence and wavefronts of reflected beams [5]. Achieving such low slope error in the substrates of large optics (~ 500 mm long) poses significant fabrication challenges. In addition to the slope errors arising from substrate, the thickness non-uniformity of the coating, can also significantly contribute to the resultant slope errors of the mirror. To fabricate large-area x-ray mirror for future applications at beamlines in Indus synchrotrons, an ultra-high vacuum ion-assisted electron beam evaporation system with an automatic substrate rotation facility, has been indigenously developed. The primary focus is to fabricate large-area x-ray thin film mirrors by controlling the lateral variations in coating thickness. The process parameters are systematically varied to tailor the uniformity and microstructure of the coating. Small-sized (20 mm × 20 mm) Si (100) substrates were placed at different locations within the area of 300 × 100 mm^2.The micro-structural characteristics of the Ni coating at different locations were studied systematically using hard x-ray reflectivity (XRR) measurement & atomic force microscopy (AFM), and the results are discussed.

EXPERIMETAL METHOD

The uniformity of coating thickness over a large deposition area is studied using an indigenously developed ultra-high vacuum ion-assisted electron beam evaporation deposition system coupled with an automated substrate rotation facility. The deposition chamber is cylindrical in shape, with a height of 120 cm and a diameter of 70 cm. It is designed to have a large source to substrate distance (~750 mm) to obtain a uniform

distribution of the evaporated ad-atoms. The main chamber houses two multi-crucible 6 kW electron guns. One electron gun has three crucibles, each with a volume of 15 cm^3; and the other electron gun has four crucibles each with a volume of 7 cm^3. The main deposition chamber is connected to two 1500 liter/sec turbo molecular pumps (TMP) via pneumatic gate valves. A low energy ion gun is installed in the main chamber for ion-assisted deposition, which helps in reducing the surface roughness and increasing the density of the coatings. The substrates are loaded through a load lock chamber, which is pumped by a 250 liter/sec TMP. The nominal thickness of the coated film is measured during deposition using a quartz crystal monitor. An automated substrate rotation subsystem, is specially designed along with proper masking arrangement and installed inside the main deposition chamber. This chamber can accommodate substrate with maximum dimension of 300 mm × 100 mm × 40 mm (length × width × thickness), up to a maximum weight of 5 kg. In the present work, Ni films have been deposited and analyzed. The chamber base pressure and the pressure during deposition were ~ 3.2×10^{-8} mbar and ~3.2×10^{-4} mbar, respectively. To maximize film density and minimize surface roughness, a detailed study was carried out to investigate the influence of various process parameters on film properties. To study the thickness uniformity of coating over a large area, small-sized dummy Si (100) substrates were placed at different locations within the entire area and depositions were carried out at different substrate rotation speeds, to determine the optimum substrate rotation speed. At first, the thickness uniformity was studied over an area of 200 × 60 mm^2 followed by a larger area of 300 × 100 mm^2. The Bruker D8 advanced diffractometer was used to measure the XRR data at Cu K_α radiation, λ = 1.54Å for microstructural analysis (thickness, roughness and density) of the film. The surface morphology of the coating was further characterized using AFM.

RESULT AND DISCUSSION

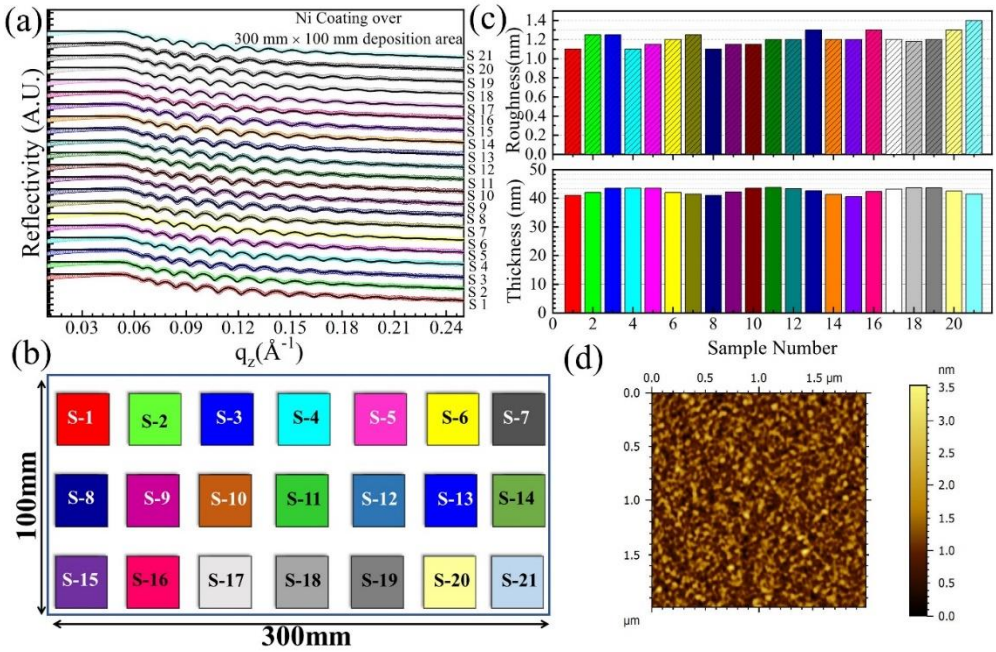


FIGURE 1. (a) XRR experimental data and fitted profiles of 21 Ni thin films fabricated on small Si wafers placed at different positions. (b) Different positions of Ni films within 300 × 100 mm^2 deposited area. (c) Roughness and thickness distribution of the Ni films. (d) Representative AFM result of sample No. 5 over the area of 2 μm × 2 μm

The deposition parameters for which the Ni films have the least surface roughness and maximum density are: electron gun supply voltage: ~7 kV, electron emission current: ~140 mA; substrate rotation speed: 1-2 rpm; ion anode voltage: 110 V, ion current: 3 mA and Ar flow rate: 4.5 sccm. The obtained deposition rate is 1.2 nm/min. To develop the large-area mirror, we have studied the thickness uniformity and microstructure over a large-area. Figure 1(a) shows the measured XRR data and best-fitted profile of 21 samples, located at different positions (sample numbers with position are given schematically in Fig. 1(b)) within 300 × 100 mm^2 deposited area. XRR data are fitted using Parratt's formalism [6] implemented in the PARRATT 32 software, to obtain the coating thickness, roughness and the density. As shown in Fig. 1(c), the surface roughness varies randomly across the samples, whereas the thickness varies systematically along the length. Over the length of 300 mm, the

thickness of the coating increases from one end to the center. Thereafter, the thickness of coating again decreases from the center to the other end. Further, it is observed that the variation of the thickness is nearly same along the width of the area. The average thickness of the Ni coating is 42.5 nm with the maximum deviation of thickness from the mean to be ~4.4% (1.9 nm), standard deviation ~1.0 nm, absolute mean deviation ~0.9 nm and coefficient of variation ~2.44%. The maximum slope error arising only from the coating considering the maximum thickness variation across the length (1.9 nm) is ~37 nano radian. Roughness varies from 1.1 nm to 1.4 nm with average mass density around 8.8 g/cc (99% of the bulk density). The roughness obtained from XRR results are correlated with AFM measurements performed on sample no. 5 over an area of 2 □m × 2 □m, as shown in Fig. 1(d). AFM measurements performed in two different positions of area 2 □m × 2 □m and 5 □m × 5 □m shows variations in roughness from 0.3 nm to 0.4 nm, respectively. The differences of roughness values obtained using XRR and AFM is due to fact that AFM measures in a local area, whereas XRR provides average information of the complete area on the sample that is illuminated by the incident x-ray beam. The role of substrate roughness on the observed film roughness will be subsequently investigated. It may be noted that these results can be extended to other metals like Pt and Au also, which are commonly used in x-ray mirrors, because the thickness uniformity is expected to be nearly similar under the identical deposition conditions for these different metals.

CONCLUSION

The large-area reflective mirror plays a pivotal role in the design of synchrotron beamlines. We have developed an ion assisted electron beam evaporation system equipped with an automated substrate rotation facility, capable of uniform deposition over a maximum area of 300 × 100 mm². We have studied the thickness uniformity and microstructure of the Ni coating (thickness ~42.5 nm). The average density of the films is 99% of the bulk value, with surface roughness varying from 1.1 nm to 1.4 nm. The maximum thickness variation of the coating is ~4.4%. The maximum slope error arising only from the coating non-uniformity is ~37 nano radian. Our upcoming research will focus on investigating non-uniformity on a figured surface.

ACKNOWLEDGMENTS

The authors gratefully acknowledge Dr. Tapas Ganguli, RRCAT for useful technical discussions during progress of work. They also express their gratitude to Dr. S. K. Rai, RRCAT for valuable input during XRR measurements. F. M. acknowledges financial support from HBNI, Mumbai.

REFERENCES

1. E.A. Spiller, Soft X-ray optics, SPIE. Press, 1994.
2. Michael Störmer, C. Horstmann, D. Häussler, E. Spiecker, F. Siewert, F. Scholze, F. Hertlein, W. Jäger and R. Bormann, Advances in X-ray/EUV Optics and Components III, Single-layer and multilayer mirrors for current and next-generation light sources, September,2008, San Diego, California, United States, SPIE. Press,2008.
3. Q. S. Huang, H. D. Huang, Q. Y. Wu, J. Yu, Z. Zhang, Z. S. Wang, Advances in Manufacturing, Vol. 12, pp. 177-184 (2024).
4. H. Jiang, J. Xie, Y.He, Z. Jiang, D. Liang, H. Yu, and Aiguo Li, Opt. Express Vol. **32**, pp. 13597-13613 (2024)
5. H. Yumoto, H. Mimura, T. Koyama, S. Matsuyama, K. Tono, T. Togashi, Y. Inubushi, T. Sato, T. Tanaka, T.Kimura, H. Yokoyama, J. Kim, Y. Sano, Y. Hachisu, M. Yabashi, H.Ohashi, H. Ohmori, T. Ishikawa and K. Yamauchi., Nature Photon, Vol.**7**, pp. 43–47 (2013).
6. Lyman G. Parratt, Physical review, Vol. **95**, pp. 359-369 (1954).

WS_2-Ag Nanocomposite-based SERS Substrates with an Ultralow Detection Limit for Pesticide Thiram

Arvind Kaushik[1, *], Sneha Senapati[2], J.P. Singh[1]

1 *Department of Physics, IIT Delhi, New Delhi-110016, India*
2 *School of Interdisciplinary Research, IIT Delhi, New Delhi-110016*

* Corresponding author email: askaushik07@gmail.com

Abstract. Two-dimensional transition metal dichalcogenides (TMDCs) exibhit unmatched optical and electronic properties that make them highly suitable as SERS substrates, primarily by promoting efficient interfacial charge transfer with adsorbed analytes and thereby enhancing the chemical contribution to Raman signal enhancement. Here, vertically aligned WS_2 flakes were grown on a silicon (Si) substrate via the pulsed laser deposition (PLD) method. Subsequently, silver nanoparticles (Ag NPs) were deposited onto the WS_2 surface using thermal evaporation. The WS_2-Ag composite sample was characterized by FESEM, Raman and XRD. The composite of WS_2-Ag is investigated as a potential SERS substrate for detection of harmful pesticide thiram. Thiram is a common pesticide used as animal repellant in agricultural industry with many harmful effects on human health. Thiram is known to be highly toxic and life threatening to aquatic life. The WS_2-Ag composite SERS substrate effectively detects the toxic thiram up to the 10^{-13} M concentration.

Keywords: SERS, 2D, Nanocomposite, PLD, Pesticide, Thiram, Sensing.

INTRODUCTION

The field of surface enhanced Raman spectroscopy (SERS) majorly depends on noble metal nanoparticles (NPs) attributing to their strong localized surface plasmon resonance (LSPR) that produces the large enhancements in the Raman signals of the analyte [1]. However, metal NPs solutions are mostly unstable, and NPs tends to agglomerate with time decreasing their performance [2]. Recently, 2D materials have shown good results in many applications including SERS [3]. The 2D materials have a large family comprising of many promising materials for research applications. WS_2 is the prominent member of the metal chalcogenides family with superior optoelectronic properties [4]. WS_2 has layered structure which makes it suitable for adsorbing the analyte molecules and thus producing the charge transfer effect for SERS signal enhancement [5]. WS_2 can be synthesized easily using common methods such as hydrothermal, chemical vapor deposition etc. Normally, these methods produce certain impurities in the final product, thus reducing the performance of WS_2 based devices. Therefore, physical route must be explored to synthesize the impurity free morphology optimized WS_2.

EXPERIMENTAL

WS_2 flakes were synthesized by the PLD technique employing an Nd:YAG laser with 70 mJ energy. The deposition parameters were optimized to synthesize the vertical flake-like structures on silicon wafer of (1 cm × 1 cm) 1 cm^2 area. The deposition pressure was optimized to 9×10^{-2} mbar maintaining a constant flow of inert argon gas through a mass flow controller. The WS_2 target for PLD was prepared by grinding and pressing the WS_2 powder purchased from Sigma Aldrich Co., USA. Following the successful synthesis of vertical WS_2 flakes, thermal evaporation was employed in order to decorate the WS_2 flakes with Ag NPs. The nanocomposite of WS_2-Ag was characterized by FESEM, Raman, and XRD.

RESULTS AND DISCUSSION

The WS_2 flake morphology was confirmed by the FESEM characterizations. Figure 1(a-b) presents the morphological features of WS_2, and WS_2-Ag samples captured with FESEM. The WS_2 flakes have an average thickness of 15-20 nm measured using the ImageJ software from FESEM images. The EDX spectroscopy was carried out to confirm the presence of respective elements in the WS_2-Ag composite. Figure 1c illustrates the collective elemental distribution in the composite sample. Whereas figure 1(d-f) represents the presence of W, S along with Ag in the composite sample of WS_2-Ag. Thus, confirming the formation of WS_2-Ag composite for SERS applications.

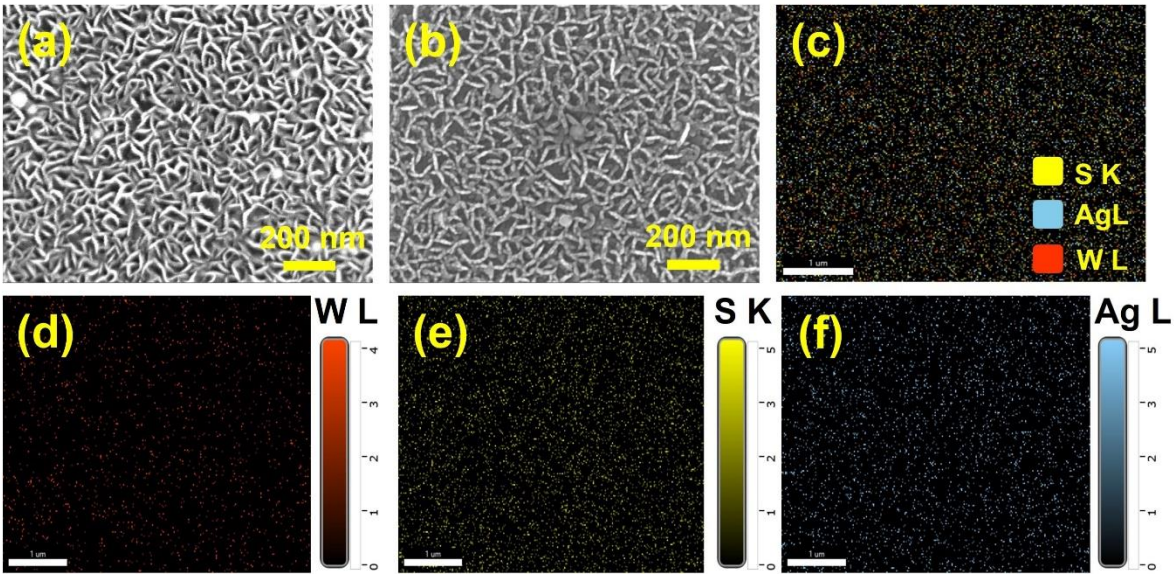


FIGURE1. (a-b) Morphological images of WS_2 and WS_2-Ag composites captures with FESEM. (c-f) EDX spectroscopy mapping of respective elements in the WS_2-Ag composite sample.

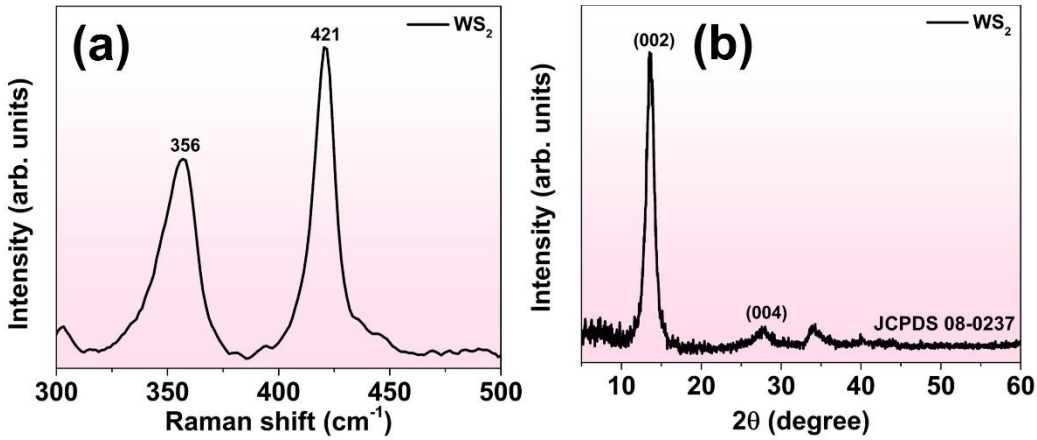


FIGURE 2. (a-b). Raman and XRD spectra of the synthesized WS_2 flakes depicting the 2H phase and presence of few layers in the prepared sample.

The XRD and Raman spectra are plotted in figure 2(a-b) confirms the 2H phase of WS_2 samples. The corresponding peaks are assigned to their vibrations in the Raman spectra. The difference of 65 cm^{-1} between the peak positions of $E_2{}^{1g}$ and A_{1g} further confirms the few layers of prepared WS_2 flakes. The prominent peaks in the XRD pattern are indexed to (00l) reflections that exhibit the characteristics of specific orientation of WS_2 flakes along the c axis direction.

SERS MEASUREMENTS

To explore the SERS performance of WS_2-Ag composite, Thiram, a popular pesticide molecule, was used as an analyte. The synthesized WS_2-Ag substrate of 1 cm^2 was cut into four equal parts of 0.25 cm^2 each. The thiram solution was then deposited over the WS_2-Ag substrate through a pipette. The substrate was allowed to dry for approximately one hour. As thiram solution was prepared in ethanol, the substrate dried quickly. The SERS measurements were performed using the 532 nm laser. The SERS response of thiram molecule is presented in figure 3 for decreasing concentrations. The corresponding peaks of thiram are well matched with the earlier reports [6]. The prominent peaks observed in the SERS spectra of thiram are 560, 939, 980, 1146, 1382, 1443 and 1512 cm^{-1}. The 560 cm^{-1} peak is ascribed to the stretching (ν) of S–S bond, 939 cm^{-1} is assigned to the stretching (ν) of CH_3N and ν(C=S), 980 cm^{-1} to the asymmetric stretching of CSS, 1146 cm^{-1} to the rocking (ρ) modes of CH_3 (ρ(CH_3)) and ν(N–CH_3). The most enhanced peak at 1382 cm^{-1} is ascribed to the deformation of CH_3 ($\delta_s(CH_3)$) and ν(CN) and 1512 cm^{-1} peak to the ν(C=N) and δ(CH_3) [7].

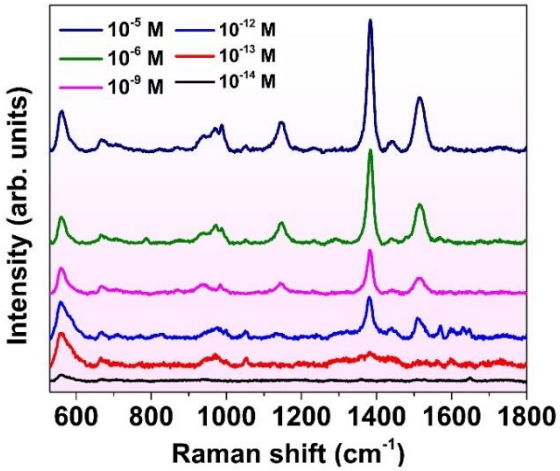


FIGURE 3. SERS spectra of pesticide thiram molecules on WS_2-Ag composite SERS substrate.

The 1382 cm^{-1} peak, along with a few other bands such as 980 cm^{-1} can easily be detected in 10^{-13} M concentration. Therefore, WS_2-Ag composite substrate successfully detects the trace level concentration of 10^{-13} M of thiram molecule. Therefore, 10^{-13} M is the experimental limit of detection for thiram pesticide that can be detected with WS_2-Ag composite SERS substrate.

The electromagnetic (EM) enhancement from 'hot spots' formed by the electric field enhancement between two Ag NPs is responsible for the significant increase in the Raman peak intensity of the RhB dye for the nanocomposite SERS substrate. Along with EM enhancement from Ag NPs, WS_2 flakes produce the SERS signal enhancement through charge transfer mechanism between thiram molecules and WS_2 sample. Charge transfer between the SERS substrate and probe molecule is identified as chemical enhancement. Therefore, the utilization of both the chemical and EM enhancing mechanisms in the nanocomposite SERS substrate yields exceptional SERS performance for pesticide detection.

CONCLUSION

This study involves the preparation of a nanocomposite SERS substrate by adorning the vertical WS_2 flakes with Ag NPs. The WS_2-Ag composite SERS substrate effectively detects thiram molecules at ultralow concentrations of up to 10^{-13} M. Therefore, it can be confidently stated that composites of metal nanoparticles and 2D materials have the potential to serve as a feasible alternative due to their high sensitivity, facile fabrication techniques, and long-term stability.

ACKNOWLEDGMENT

The authors gratefully acknowledge the Central Research Facility (CRF) at IIT Delhi for access to the key characterization facilities that supported this work.

REFERENCES

[1] A. Kaushik, P. Bisht, S. Senapati, J.P. Singh, Surfaces and Interfaces, 52, 104951 (2024).
[2] A. Kaushik, S. Kapoor, S. Senapati, J.P. Singh, Colloids Surf B Biointerfaces, 252, 114676 (2025).
[3] A. Kaushik, J. Singh, R. Soni, J.P. Singh, ACS Appl Nano Mater, 6, 9236–9246 (2023).
[4] C. Cong, J. Shang, Y. Wang, T. Yu, Adv Opt Mater, 6, 1700767 (2018).
[5] Y. Song, H.-C. Huang, W. Lu, N. Li, J. Su, S.-B. Cheng, Y. Lai, J. Chen, J. Zhan, Food Chem, 344, 128570 (2021).
[6] N.C.T. Martins, S. Fateixa, H.I.S. Nogueira, T. Trindade, Analyst, 149, 244–253 (2024).
[7] M.B. Bhavya, R. Prabhu B., B.M. Shenoy, P. Bhol, S. Swain, M. Saxena, N.S. John, G. Hegde, A.K. Samal, Environ. Sci. Nano, 7, 3999–4009 (2020)

Surface studies of Non-evaporable F thin film

Nidhi Gupta[1,a)], Kaushik Dutta[1], Jagannath[1,2]

[1]*Technical Physics Division, Bhabha Atomic Research Center, Mumbai, 400085*
[2]*Homi Bhabha National Institute, Mumbai,400094*
[a)]Corresponding author: Nidhi Gupta (*nidhigup@barc.gov.in*)

ABSTRACTIn order to achieve extreme high vacuum (XHV), non-evaporable getter (NEG) deposited byMagnetron sputter deposited thin film nowadays is considered as a suitable candidate. Its application in achieving XHV in various applications and instruments like vacuum pipe, particle accelerator, large Synchrotron Sourcesmake themthe most promising option as vacuum pump. In the present article, the authors report the Zr,Ti,V thin film deposition and behavior at different activation temperature. In addition, XPS characterization were performed to explore the change in elemental composition of the film surface.

Introduction

Non-evaporable Getter pumping is apowerful techniquetoachieve extreme high vacuum [1]. Elements like Ti, V, Zr, Hf, Nb, Feare promising candidates acting as getter for pumping residual gasses.Alloy prepared from these elements enhances pumping propertiesby increasing adsorption and reduction of activation temperature [2].NEG coating last for several cycles without anyhuman intervention in the vacuum .

Material selection for NEG

Materials with high oxygen diffusivity are favorable for gettering action. The transition metals of IV B and V B group, generally alloy of Zr, Ti, Hf, Fe, Co, Al, Ni and V are used as NEG materials. Among these Zr- and Ti- based alloy are extremely explored because of their ability to efficiently trap hydrogen molecules during activation process. In the present work, ternaries alloy of titanium, zirconium, vanadium has been synthetized and characterized.

Thin film deposition and Experimental Details:

DC-Magnetron sputtering technique was used for deposition of NEG thin film. Stainless steel substrate of typical size 300 × 250 mm^2 was cleaned and pure 1 mm diameter Zr, Ti, V (2:1:1) wires were twisted together to serve as the cathode.

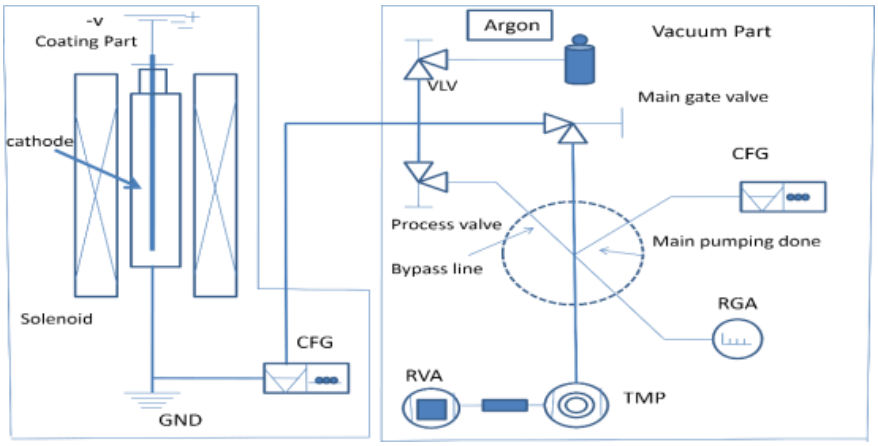


FIGURE1: Setup for NEG deposition

Then system and target are heated at 120˚C for baking. Then the system is cooled to room temperature in order to get good deposition and morphology.A vacuum of 2×10^{-8}Torris obtained by a combination of rotary, turbo and sputter ion pump.Ar-gas was used as sputtering gas.DC power supplyis used for initiating Discharge.There was a distance of 50mm between the target and the substrate.Cathode voltage of- 550V is applied on the target and several deposition cycles were performed. Quartz crystal thickness monitor is used for film thickness .

RESULTS

Data was analyzed using X – ray photo electron spectrometer which has VG make analyzer. For this sample was mounted using a sample manipulator which has sample heating arrangement upto 1000 ºC.
First the data is recorded at room temperature. Peaks namely, 3d 5/2 of Zr,2p3/2 of V,Ti 2p3/2and O1s are obtained at182eV, 458eV, 516 eVand 529.2eV, respectively. Then film is heated at 80ºC for two hours. Then XPS data wasrecorded and no shift in peak positions obtained at this temperature.
The film was heated to 200ºC for two hours and shift in binding energy is obtained for Zr element. The film was further heated to 300ºC for two hours. This time change in peak position of V is obtained.The film composition forTi, V and Zr has been found matching with XPS data(area under the curve) deposited in a 1:1:2 ratio.

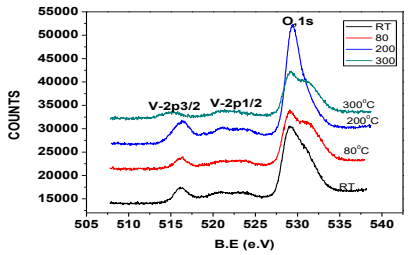


Fig 2: XPS peak for Vanadium and Oxygen

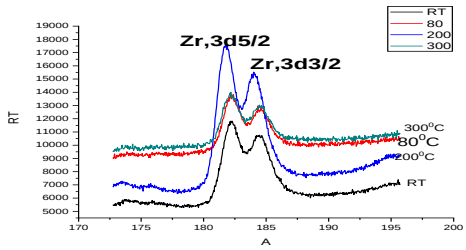


Fig 3: XPS peak for Zirconium

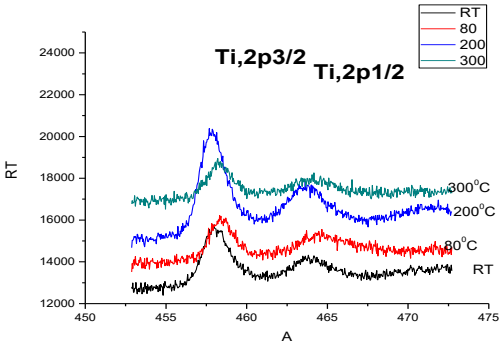


Fig 4: XPS peak for Titanium

Conclusion

The alloy coating of Zr/Ti/V was deposited by DC magnetron sputtering system. Activation temperature around 200°C is first observed in Zr element from the XPS data and it confirmed the conversion of oxide film to metallic film on baking. The surface morphology and grain size were studied using SEM and elemental composition confirmed by XPS measurements.

Reference

1. C. Benvenuti, P. Chiggiato, F. Cicoira, and V. Ruzinov, Vacuum,50(1998) 57.
2. R.K. Sharma, Jagannath, S. Bhattacharya, R.B. Tokas, K.G. Bhushan, Shashwati Sen, S.C. Gadkari and S.K. Gupta, Journal of Alloys and Compounds651, 375-381 (2015).

Molecular Engineering and Investigation of Novel Donor Molecule Based on [D-π-D] Type Architecture

Ankit Kargeti[*1,3], Shamoon Ahmad Siddiqui[2], Tabish Rasheed[3]

[1]Department of Physics, Mohan Babu University, Tirupati, Andhra Pradesh 517102, India
[2]Department of Physics, Integral University, Lucknow, Uttar Pradesh 226026, India
[3]School of Engineering and Technology, BML Munjal University, Gurugram, Haryana 122413, India
[*]*Corresponding author: ankitkargeti@gmail.com*

Abstract. The Density functional theory (DFT) calculations have been performed on [D-π-D] type molecular structural model for designing the efficient donor moiety for dye sensitized solar cell application. The dye sensitized solar cell designed by Gratzel et al., in 1991 with ruthenium complex photosensitizer opened the new way of designing the organic solar cells. For this purpose, here in the paper, one novel donor molecule is designed and modelled on Gauss view interface. The designed molecule is named [Triphenylamine-Thiophene-Fluorene] as molecular system M1. The designed molecule was optimized under the framework of density functional theory using B3LYP hybrid functional and 6-31G(d,p) basis set level on GAUSSIAN 16W Software package. Further, the important electronic and chemical parameters like HOMO-LUMO energy gap, ionization potential, electron affinity are calculated. The excited state properties like absorption spectra, oscillator strength and excited state energy of the transition are calculated by utilizing the time dependent density functional theory along with CAM-B3LYP functional at same basis set level. The highest absorption maxima for the designed molecular complex was observed at 337.28 nm and open circuit voltage was reported to be 2.72 eV. From these photovoltaic calculation results, it is confirmed that the designed molecular complex which is based on D-π-D structure will be suitable for DSSC application. **Keywords:** Photosensitizer; DSSC; Donor- π- Donor; Absorption spectra; DFT; TDDFT.

INTRODUCTION

The dye sensitized solar cell was first introduced by Gratzel et al., in 1991 was based on ruthenium dye complex and had showed efficiency around 10%[1]. Since then, various photosensitizers were developed and showed improved photovoltaic performances. The commonly utilized molecular complexes are based on donor-π -acceptor [D-π-A] model where donor and acceptor units are connected through the bridging molecule[2]. The other models reported to be [D-π-A-A], [D-D-π-A], [D-π-π-A][3]–[5]. Therefore, here in this paper we designed novel donor molecular complex based on the Donor-π–Donor i.e., [D-π-D] architecture which can be utilized in dye sensitized solar cell and as hole transporting material in perovskite solar cells[6]. Here, the chosen donor units are triphenylamine and fluorene whereas thiophene is the bridging unit which connects both the donor sides. Recently published articles on dye sensitized solar cells have shown that the efficiency is increased from 10 to 16% [7]which can further be improved because the other organic solar cells like perovskite solar cells have shown improved results in terms of efficiency[8]. Therefore, search for novel organic semiconducting molecules which show higher efficiency is continuous. The optimized molecular complex is shown below in Figure 1.

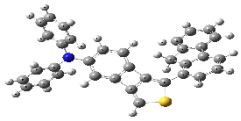


FIGURE 1. Optimized geometry of the Molecular system M1 [Triphenylamine-thiophene-fluorene] at B3LYP/6-31G(d, p) level of theory.

Computational Methodology

The molecular system M1 [Triphenylamine-thiophene-fluorene] was optimized under the framework of density functional theory (DFT) [9], [10] with B3LYP/6-31G(d,p) level[11] on GAUSSIAN 16W software package[12]. Further the excited state properties of the dye molecule were calculated by utilizing the TD-DFT method with CAM-B3LYP/6-31G(d,p) level of theory. Further various parameters have been calculated and analyzed in the results section.

Results and Analysis

Charge transfer properties of the molecular system M1[triphenylamine-thiophene-fluorene]

Frontier molecular energy orbitals where the highest occupied molecular orbital (HOMO) and lowest unoccupied molecular orbital (LUMO) represent the spatial distribution of the charges as shown in Figure 2 (A) and (B) below. HOMOs are mostly spread over the Triphenylamine and thiophene units while LUMOs are mostly spread over the Fluorene part. This suggests us that triphenylamine is more electron rich as compared to the fluorene molecule which is because of the presence of the Nitrogen atom in the triphenylamine unit. LUMOs are mostly spread over the fluorene unit which confirms that electron distribution is asymmetric in the whole molecule. Further, the HLG gap energy is calculated to be 3.61 eV which lies in the semiconducting region for the designed molecule and reported in Table 1 below.

(A) (B)



FIGURE 2. (A) HOMO charge distribution for the system M1. (B) LUMO charge distribution for the system M1.

TABLE 1. HOMO-LUMO energy along with ionization potential and electron affinity calculated in eV.

Molecule	HOMO (eV)	LUMO (eV)	HLG (eV)	I.P. (eV)	E.A. (eV)
M1	-4.89	-1.28	3.61	4.89	1.28

Absorption spectra and Photovoltaic properties

For the suitable application in DSSC, the role of absorption spectra is very critical. For the designed molecular system M1, it shows the absorption maxima at 337.28 nm which lies in the UV region and corresponding to this absorption maxima the oscillator strength reported to be 0.544 which suggests us that this molecule is having good transition probability at this wavelength. Further the excitation energy of the transition is reported to be 3.67 eV. The absorption wavelength is reported in Table 2 below.

The change in free energy of electron injection (ΔG^{inject}) to the semiconductor TiO_2 is defined as, ΔG^{inject} = (- E_H - 4.0 eV) where $E_{dye^*}{}^{ox}$ =-E_H is the excited state oxidation potential and -4.0 eV stands for conduction band (C.B.) edge of the TiO_2 semiconductor. It is calculated as: $\Delta G^{inject} = E_{ox}{}^{dye^*} - |E_{CB}{}^{TiO_2}|$

$E_{dye}{}^{*ox}$ is approximated as the difference between the ground state oxidation potential of the dye and the absorption maxima energy: $E_{dye}{}^{*ox}$ = (- E_H) - λ_{max}.

And the difference between the energy of the LUMO (E_L) of the dye and the energy of the conduction band edge of TiO_2 is regarded as the open circuit voltage, eV_{OC} = E_L —(— 4.0). It is calculated as below:

The light harvesting efficiency (LHE) for the dye molecule is calculated by using the following formula:

$$LHE = 1 - 10^{-f}$$

From Table 1, it is seen that the designed molecular units M1 have deeper HOMO energy level i.e., it lies at -4.895 eV and Redox couple of the iodide solution -4.80 eV, which confirms that designed molecular systems will have fast charge regeneration. The LUMO level for this system lies at -1.284 eV which is basically at an upper level than the conduction band edge of the TiO_2 at -4.0 eV. These results explicitly favour the charge transfer from the LUMO level of the dye to the TiO_2 conduction band.

TABLE 2. Three excited states for absorption wavelength (nm), oscillator strength (f) and excitation energy $\lambda_{max}{}^{ICT}$ in eV.

	Three Excited states for absorption wavelengths (λ_{max}) (nm)	Oscillator strengths (f)	Excitation energy $\lambda_{max}{}^{ICT}$ in (eV)
First excited state	337.28 (Maximum)	0.544	3.67
Second excited state	324.28	0.087	3.82
Third excited state	272.64	0.269	4.54

TABLE 3. Calculated maximum absorption wavelength (λ_{max}) in (nm), charge injection energy ΔG^{inject} in (eV), Oxidation potential for excited state of the dye E_{OX}^{dye*} in (eV), regenerating driving force $\Delta G^{(reg)}$ in (eV) and open circuit voltage V_{oc} in (eV).

Molecule	Maximum Absorption (λ_{max}) (nm)	LHE (eV)	ΔG^{inject} Energy (eV)	E_{OX}^{dye*} Energy (eV)	$\Delta G^{(reg)}$ (eV)	Open-circuit voltage V_{oc} in (eV)
M1	337.28	0.72	-2.78	1.22	0.09	2.72

From Table 2 and 3, the ΔG^{inject} (change in free energy of the charge injection) value is -2.78 eV which is negative value i.e., the charge injection into the conduction level of the semiconducting material would be favourable here. The other photovoltaic properties like Light harvesting efficiency (LHE) value for the designed system is reported as 0.72 eV, the intramolecular charge transfer energy is reported to be 3.676 eV. Further the open circuit voltage for the system M1 is 2.72 eV, which shows that the designed system has high open circuit voltage values. Therefore, in conclusion it can be inferred that designed molecular system could be useful in designing efficient photosensitizers for the dye sensitized solar cells.

Conclusion

In this study of novel molecular system based on [D-π-D] model, it is found that the designed system M1 [Triphenylamine-thiophene-fluorene] has shown the low HLG energy value at 3.61 eV. From the space charge distribution plots of HOMO and LUMO, it was found that charge is delocalized over the triphenylamine and thiophene unit mostly. The Photovoltaic performance is checked for this molecule where the absorption maxima was observed at 337.28 nm and the light harvesting efficiency was reported to be 0.72 eV, this shows that the designed molecule has absorption in the UV-Visible region which can be utilized for DSSC application. Therefore, the designed molecule based on [D-π-D] molecular architecture would be suitable as donor unit for DSSC application.

References

[1] M. G. Brian O' Regan, "A low-cost, high efficiency solar cell based on dye-sensitized colloidal TiO2 films," *Nature*, vol. 353, pp. 737–740, 1991, doi: doi.org/10.1038/353737a0.

[2] B. E. Hardin, H. J. Snaith, and M. D. McGehee, "The renaissance of dye-sensitized solar cells," *Nat. Photonics*, vol. 6, no. 3, pp. 162–169, 2012, doi: 10.1038/nphoton.2012.22.

[3] A. Kargeti, R. S. Dhar, S. A. Siddiqui, and N. Saleh, "Design and Exploration by Quantum Chemical Analysis of Photosensitizers Having [D−π-π-A]- and [D-D-triad-A]-Type Molecular Structure Models for DSSC," *ACS Omega*, vol. 9, no. 10, pp. 11471–11477, 2024, doi: 10.1021/acsomega.3c08165.

[4] T. Rasheed, A. Kargeti, and S. A. Siddiqui, "Design of two novel dyes having maximum absorption in infrared region: A DFT investigation," *Mater. Today Proc.*, vol. 68, no. xxxx, pp. 2715–2719, 2022, doi: 10.1016/j.matpr.2022.06.267.

[5] S. A. Siddiqui, "In silico investigation of the coumarin-based organic semiconductors for the possible use in organic electronic devices," *J. Phys. Org. Chem.*, vol. 32, no. 3, pp. 1–10, 2019, doi: 10.1002/poc.3905.

[6] S. Cells, "Novel Anthracene HTM Containing TIPs for Perovskite Solar Cells," 2021.

[7] Y. Cui *et al.*, "Over 16% efficiency organic photovoltaic cells enabled by a chlorinated acceptor with increased open-circuit voltages," *Nat. Commun.*, vol. 10, no. 1, pp. 1–8, 2019, doi: 10.1038/s41467-019-10351-5.

[8] S. Paek *et al.*, "Donor-pi-Donor Type Hole Transporting Material: Marked pi-Bridge Effects on Optoelectronic Properties, Solid-State Structure, and Perovskite Solar Cell Efficiency," *Chem. Sci.*, 2016, doi: 10.1039/C6SC01478J.

[9] P. Hohenberg and W. Kohn, "Inhomogeneous Electron Gas," *Phys. Rev.*, vol. 136, 1964.

[10] W. Kohn and L. J. Sham, "Self-Consistent Equations Including Exchange and Correlation Effects," *Phys. Rev.*, vol. 140, 1965.

[11] A. D. Becke, "A new mixing of Hartree-Fock and local density-functional theories," *J. Chem. Phys.*, 1993, doi: 10.1063/1.464304.

[12] M. J. Frisch *et al.*, "Gaussian 16," *Gaussian, Inc., Wallingford CT,*. 2016.

Ab initio Study of Intermediate Band Solar Cell Material: V Substituted $MgSnP_2$

G. Kruthika[3], and P. Ravindran[1, 2, *]

[1]*Department of Physics, Central University of Tamil Nadu, Thiruvarur, Tamil Nadu, 610101, India*
[2]*Simulation Center for Atomic and Nanoscale MATerials (SCANMAT), Central University of Tamil Nadu, Thiruvarur, Tamil Nadu, 610101, India*
[3]*Department of Physics, Srinivasa Ramajunan center, SASTRA-Deemed to be university, Kumbakonam, Tamil Nadu, 612001, India*

[*]Corresponding author: raviphy@cutn.ac.in

Abstract. Intermediate band semiconducting materials have potential to use in high efficiency solar cell devices. Herein, we studied the optoelectronic properties of pure and V substituted $MgSnP_2$ using first principle density functional theory calculations. From our calculations, we found that $MgSnP_2$ is a direct band gap material with band gap value of 1.17 eV and V substitution creates intermediate band. Moreover, optical absorption spectra reveal that V substitution increase optical absorption at visible range compared with that of $MgSnP_2$ and silicon. Thus, it is understood that $MgSn_{0.94}V_{0.06}P_2$ has potential to use in intermediate band solar cells.

INTRODUCTION

Intermediate band solar cell (IBSC) was proposed by Luque and Martí in 1997 as a structurally simple yet highly efficient photovoltaic concept[1]. By introducing a new band between the valence band (VB) and conduction band (CB), optically excited low energy electrons from the VB to CB is absorbed by the successive transition from VB to IB (Intermediate band) and IB to CB. There are no known natural IB materials, but many IB materials have been produced artificially, using quantum dots, highly mismatched alloys or deep level impurities. Introducing deep level impurities in some bulk materials creates the IB between VB and CB[2]. The class of chalcopyrite materials with II-IV-V_2 structure type, (II – Mg, Ca, Sn, IV – Si, Ge, Sn, V – P, As, Sb) span a range of optoelectronic, spintronic and photovoltaic applications, because of their unique physical properties[3]. This study deals about the effect on optoelectronic property through vanadium substitution in $MgSnP_2$ structure.

KEYWORDS. $MgSnP_2$, Intermediate band solar cell, Optoelectronic properties, chalcopyrite, Density Functional Theory.

COMPUTATIONAL DETAILS

First principle calculations were performed with Vienna *Ab initio* Simulation Package (VASP)[4]. The electron-ion interaction was described using the projected augmented wave method[5]. Structural relaxation and electronic band structure calculations were carried out by the generalized gradient approximation. The Brillouin zone was sampled using Monkhorst–pack scheme with 10×10×5 and 8×4×2 $\boldsymbol{k}$–points for parent structure with 8 atoms and supercell structure with 64 atoms, respectively. The energy cut-off for the plane wave basis set was fixed at 330 eV. The geometry optimization was performed by full relaxation of all internal atomic positions as well as unit cell volume and shape until the total energy converges to 10^{-4} eV/atom, and forces on all atoms was less than 0.01 eV/Å. The optical absorption spectrum of the material was plotted by calculating the frequency dependent dielectric function $\varepsilon(\omega) = \varepsilon_1(\omega) + i\varepsilon_2(\omega)$.

RESULTS AND DISCUSSION

The structural relaxation is carried out with the primitive cell of $MgSnP_2$ having 8 atoms. Figure 1. shows the optimized crystal structure of $MgSnP_2$. This compound crystallizes in chalcopyrite structure with the space group of I-42d (No.122) and $CuFeS_2$ structure type. The equilibrium lattice constant of relaxed structure is 5.949 Å and c/a ratio is 1.967. The tetragonal distortion (c/2a) value is 0.983. Usually in the chalcopyrite materials two cations are bonded with one anion. Here the anion (P) is bonded with two

Mg ions and two Sn ions. For V substituted $MgSnP_2$, we have constructed 1×2×2 supercell which has 64 atoms. 1 out of 16 Sn atom is replaced with V atom. After the V substitution, the bond length value between Mg and P increases to 2.565Å from 2.554 Å and the bond length between Sn and P decreases to 2.534Å from 2.546 Å.

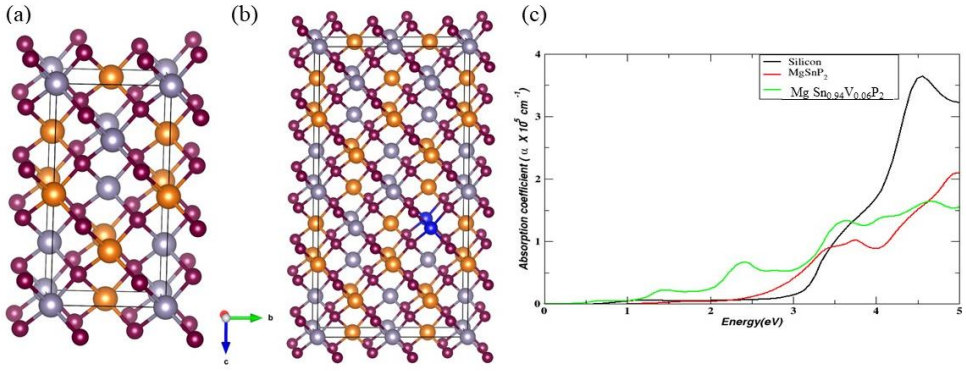


FIGURE 1. Crystal structure of (a) $MgSnP_2$ and (b) $MgSn_{0.94}V_{0.06}P_2$. The orange, ash gray, blue and maroon balls represent Mg, Sn, Vand P atoms, respectively. (c) The optical absorption coefficient spectra computed from the dielectric function of Silicon, $MgSnP_2$ and $MgSn_{0.94}V_{0.06}P_2$

The optical properties of $MgSnP_2$, $MgSn_{0.94}V_{0.06}P_2$ and silicon were computed and the results are displayed in Fig.1(c). The $\propto(\omega)$ remain zero for certain energy values for which the material is transparent. The vanadium substituted compound is having higher value of absorption coefficient in the visible part of the solar spectrum than $MgSnP_2$ and silicon. Moreover, the contribution of transition from the VB to IB, starts at E= 0.45 eV and the transition from the IB to CB, starts at E= 0.65 eV. Further, the usual transition from VB to CB is observed to start at E= 1.40 eV.

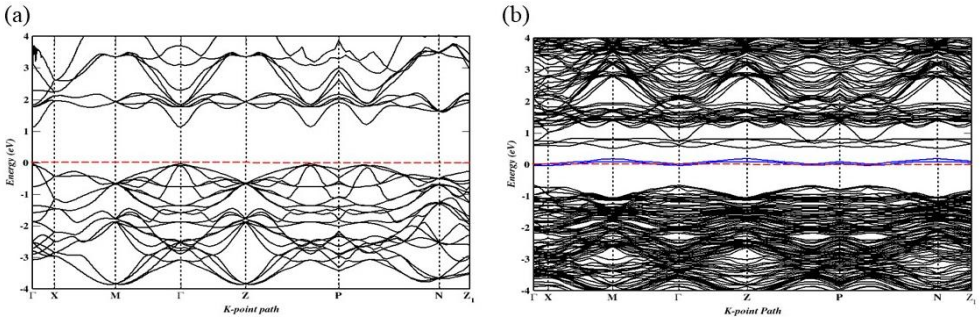


FIGURE 2. The calculated band structure of (a) $MgSnP_2$ and (b) $MgSn_{0.94}V_{0.06}P_2$

Figure 2(a) and (b) show the band structure of pure $MgSnP_2$ and $MgSn_{0.94}V_{0.06}P_2$, respectively. From the Fig. 2(a), it is found that $MgSnP_2$ exhibits direct band gap with band gap value (E_g) of 1.17 eV. From the Fig. 2(b), the presence of partially filled narrow IB between VB and CB is observed. The band gap between VB and IB is 0.624 eV with direct band featured at Γ point, and the band gap between IB and CB is 0.354 eV with direct band featured at M point of the Brillouin zone. Width of the IB is 0.20 eV. Hence, the total band gap value is 1.178 eV. Thus, the material would result in high solar energy conversion efficiency. Due to the presence of dispersed bands at band edges, this material is predicted to possess high carrier mobility.

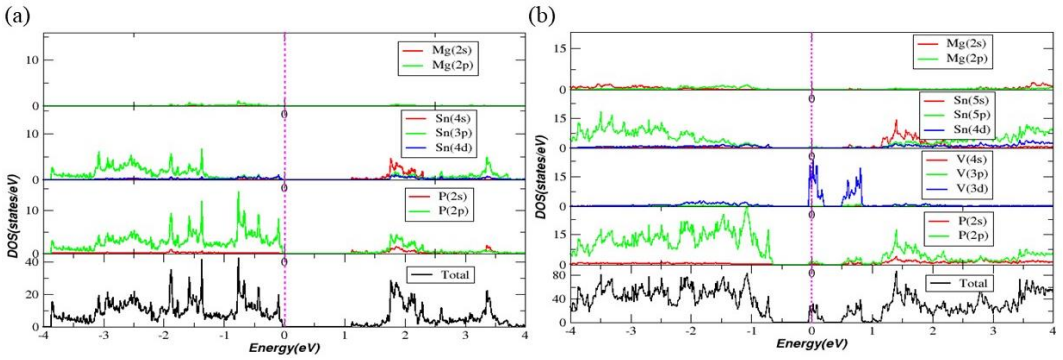


FIGURE 3. The calculated total and partial density of states for (a) $MgSnP_2$ and (b) $MgSn_{0.94}V_{0.06}P_2$

In order to understand the character of the electrons at the band edges, the total (TDOS) and projected density of states (PDOS) are calculated and displayed in Fig.3(a) and (b), respectively for $MgSnP_2$ and $MgSn0.94V_{0.06}P_2$. The PDOS of $MgSnP_2$ show that P-*2p* orbital mainly contributes to VB maximum with low contribution from both Sn-*3p* and P-*2s* states. Whereas, CB edge is originating from Sn-*4s* and P-*2p* states. From Fig.3(b), it is observed that the VB is mostly contributed by P-*2p* states, similar to $MgSnP_2$ and V-*3d* states mostly contributes to the IB.

CONCLUSIONS

The structural, electronic and optical properties of $MgSnP_2$ and $MgSn_{0.94}V_{0.06}P_2$ are studied using GGA functional. $MgSnP_2$ has the direct band gap with E_g value of 1.17 eV. $MgSn_{0.94}V_{0.06}P_2$ has partially filled narrow IB with E_g value of 1.178 eV. This band gap is within the visible part of the solar spectrum and hence it is suitable for photovoltaic cells. TDOS and PDOS of $MgSn_{0.94}V_{0.06}P_2$ shows IB, and is mainly contributed by the V-3*d* electrons. The optical absorption spectra show that $MgSn_{0.94}V_{0.06}P_2$ has higher value of optical absorption in the visible part than the pure $MgSnP_2$ and silicon. From the above analysis, we have concluded that V substituted $MgSnP_2$ is a promising intermediate band solar cell material.

ACKNOWLEDGMENTS

GK acknowledges UGC for DSK-PDF via grant no. F.4-2/2006(BSR)/PH/18-19/0015.

REFERENCES

1. I. Ramiro and A. Martí, Prog. Photovolt. Res. Appl., Vol. 29, pp. 705-713 (2021).
2. J. Li, M. Chong, J. Zhu, Y. Li, J. Xu, P. Wang, Z. Shang, Z. Yang, R. Zhu, and X. Cao, Appl. Phys. Lett., Vol. 60, pp. 2240-2242 (1990).
3. V. Kumar, S.K. Tripathy, V. Jha, and B.P. Singh, Phys. Lett. A, Vol. 378, pp. 519-523 (2014).
4. G. Kresse and D. Joubert, Phys. Rev. B, Vol. 59, pp. 1758-1775 (1999).
5. P.E. Blöchl, Phys. Rev. B, Vol. 50, pp. 17953-17979 (1994).

Molecular dynamic study of dental material TEGDMA with 1% gold nanoparticles

B N Amruth[1, 2*], H Somashekarappa[2], M Maurya[3], M B Nandaprakash[1] and R Somashekar[4]

[1]Department of Physics, Karnataka State Open University, Mysore 570006, Mysore, Karnataka, India
[2]*Department of Physics, Yuvaraja's College, University of Mysore 570006,* Mysore, Karnataka, India
[3]*Department of public health, JSS Dental College, Mysore 570015,* Mysore, Karnataka, India
[4]*Department of Studies in Physics, University of Mysore, Mysore,* Mysore, Karnataka, India

[*]Corresponding author: **amruthbn4120@gmail.com**

Abstract : We have conducted a molecular dynamics study on TEGDMA with 1% Au nanoparticles. Physical parameters such as lattice energy, heat capacity, zero-point energy, self-energy, dipole moment, and elastic constants were determined, phonon density of states and compared with pure TEGDMA. Additionally, IR spectra were simulated and contrasted with those of pure TEGDMA. Significant differences were observed between these two materials, and an effort has been made to interpret these differences in terms of the nature of interactions in this research work.

INTRODUCTION

Triethylene glycol dimethacrylate (TEGDMA) is a commonly used resin monomer in dental materials due to its excellent mechanical properties and ease of polymerization. However, its inherent brittleness and potential for shrinkage during polymerization present significant challenges for its application in high-performance dental composites [1]. To address these issues, researchers have explored the incorporation of nanoparticles into TEGDMA matrices to enhance their physical properties [2]. Gold (Au) nanoparticles have garnered significant interest in recent years due to their unique optical, electronic, and catalytic properties [3]. When integrated into polymer matrices, Au nanoparticles can impart improved mechanical strength, enhanced thermal stability, and modified electrical properties to the host material [4]. This makes Au nanoparticles a promising candidate for reinforcing TEGDMA-based composites. Our study investigates the impact of incorporating 1% Au nanoparticles into TEGDMA using molecular dynamics simulations. Previous research has demonstrated that the addition of nanoparticles can significantly alter the physical properties of polymer matrices [5], but a comprehensive understanding of the specific interactions between TEGDMA and Au nanoparticles is still lacking. We aim to determine and compare physical parameters such as lattice energy, heat capacity, zero-point energy, self-energy, dipole moment, and elastic constants of TEGDMA with and without Au nanoparticles. Furthermore, we will simulate IR spectra to elucidate the differences in molecular interactions between the two systems. This research is essential as it provides insights into the nature of interactions at the molecular level, which can help in designing better dental composites with enhanced properties. By understanding these interactions, we can optimize the concentration and distribution of nanoparticles to achieve desired material characteristics, ultimately leading to improved performance and durability of dental materials.

Materials and Methods

Using ChemDraw software, we drew TEGDMA with 1% Au nanoparticles. The necessary SMILES notation is CC(=C)C(=O)OCCOCCOCCOC(=O)C(=C)C.Au.

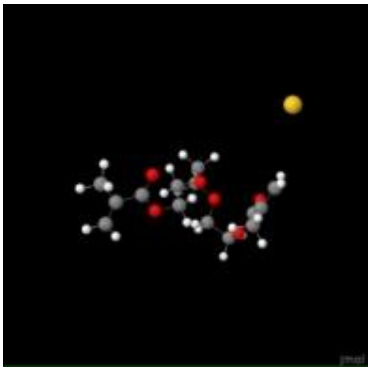


Figure 1. 3D structure for TEGDMA-Au system

Calculation for 1% Gold by Weight:

To achieve 1% gold by weight, we use TEGDMA ($C_{13}H_{22}O_6$) molecular weight = 254 g/mol and Gold (Au) atomic weight = 197 g/mol which gives total weight=254+n×197 and Gold weight = 0.01×(254+n×197). With this **for 1%,** 0.01×(254+n×197)=n×197 and this gives equation:2.54+1.97n=1.97n n≈0.013. Since we cannot have a fraction of an atom, rounding to the nearest whole number results in approximately 1 gold atom for 1%.
With this SMILES notation, we created a .pdb file for the 3D structure with appropriate fractional coordinates (x, y, z) for each atom. Using this as a starting point, we wrote an input file for computing physical parameters using the General Utility Lattice Program (GULP)[6].
Further, using Gaussian statistics, we computed the IR spectra of the TEGDMA-Au system. We also wrote a LAMMPS[7] input script to compute viscosity, surface tension, cohesive energy, and heat capacity of the TEGDMA-Au system. These scripts and files are available upon request.

RESULTS AND DISCUSSIONS

The computed physical parameters for TEGDMA-Au system are given in Table 1 along with pure TEGDMA. Here it should be emphasized that the results corresponds to a convergence state with a stable system as determined by ELATE online program. Otherwise one cannot generate the spatial variations of the moduli of the tegdma-Au system.

Table 1: Computed physical parameters of Au in TEGDMA and pure TEGDMA

Physical Parameter	TEGDMA-Au	TEGDMA(8)
Refractive index	1.38	1.12(experimental 1.4595)
Zero point energy(eV)	0.012	0.105
Electronegativity(eV)	6.39	6.6 (For O-O atoms value is 3.5[9])
Self energy(eV)	-0.78	-0.64
Youngs modulus(GPa)	0.00083	0.133(Experimental=2.37GPa)[9]
Bulk Modulus(GPa)	0.0015	0.105
Shear Modulus(GPa)	0.0006	0.236
S-wave velocity(km/s)	0.339	2.16
P-wave velocity(km/s)	0.68	2.88
Lattice energy (eV)	-0.90	-0.87
Dipole moment(Debye)	2.95	0.829
Specific heat	81.1Cal/mol-K	71.41cal/mol-K
Entropy	172.8cal/mol-K	169.35cal/mol-K

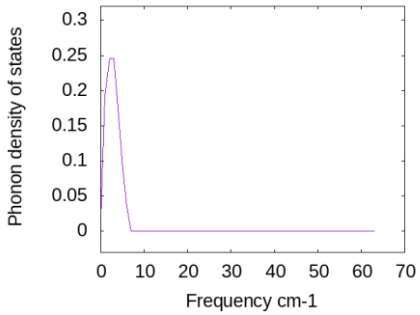
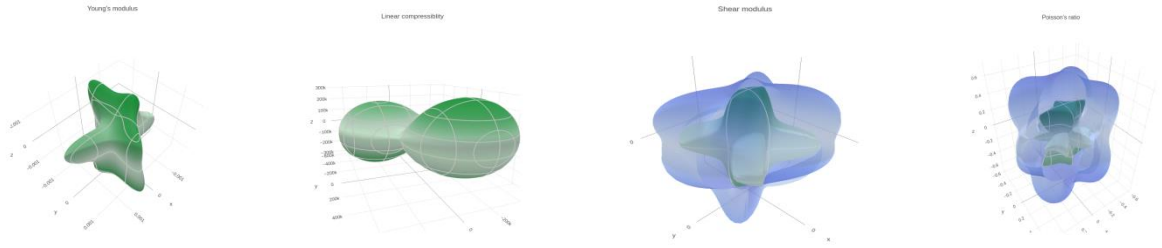


Figure 2 shows he frequency variation of the phonon densityof states in the case of TEGDMA-Au system.

Specifically, this observation may suggest that certain molecular bonds or interactions within the TEGDMA-Au structure are vibrating at less than 10 cm^{-1} frequency which like damping the groups specific chemical groups, such as C-H, C-C, or C=O bonds, which are present in the pure TEGDMA. Furthermore, the distribution of density of states at different frequencies can also reveal important information about the material's thermal conductivity, mechanical properties, and overall stability. Electronegativity is a fundamental concept in chemistry; however, its an elusive quantity to evaluate experimentally. Experimental values for O-O surface atoms have been reported [9]. We have computed 3-dimensional spatial variation of Youngs, Linear, Shear moduli and Poisson ratio for TEGDMA-Au complex and it is given in Figure 3 using ELATE program[10].



(a) (b) (c) (d)

Figure 3: (a) Youngs modulus, (b) Linear modulus, (c) Shear modulus and (d) Poissson ratio, spatial variations

A comparison with spatial variation of these moduli of TEGDMA [ref] and TEGDMA-Au indicate that the presence of Au do alter the magnitude and shape of these curves. Further, Table 1 do indicate that there are changes in several parameters when Au is present in the complex because of change in the electropotentials in the neighboring regions. We have also simulated Infrared spectra (IR) of TEGDMA-Au complex and it is compared with pure TEGDMA in Figure 4 using WebMo method [11].

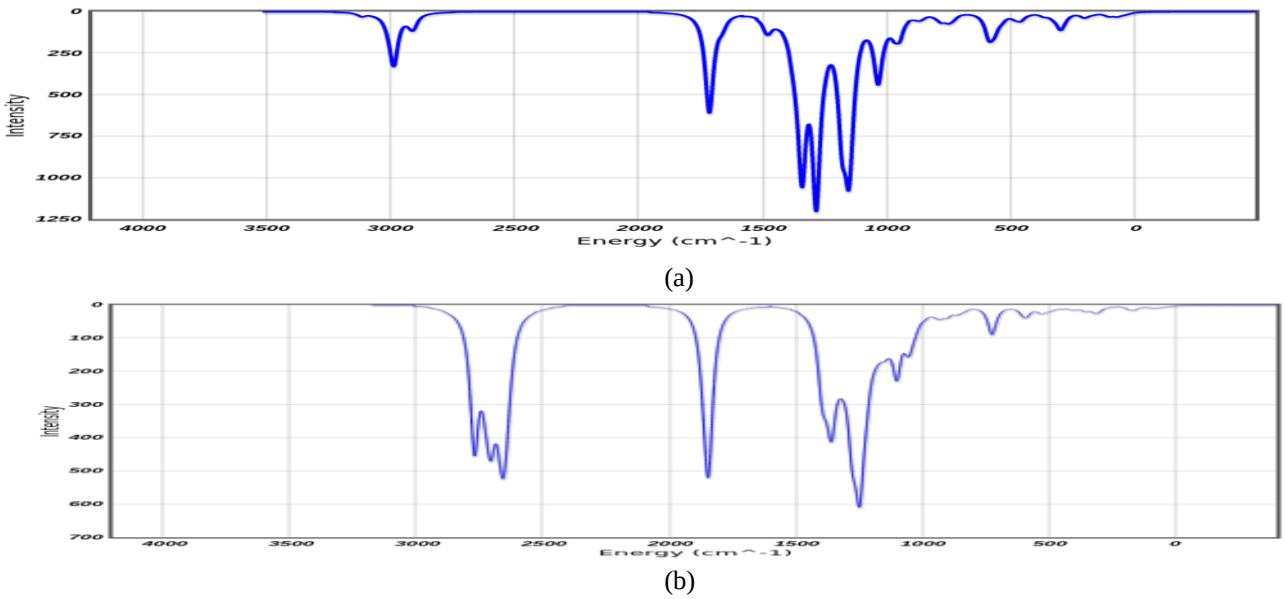


Figure 4: Computed IR spectra of (a) TEGDMA and (b) TEGDMA-Au system.

An observation of the Figure 4 indicate that there are changes in the region 2500 to 3000 cm-1 which is damping of vibrational modes of C-H bonds due to the presence of Au atoms in the neighbourhood.

CONCLUSIONS

In the molecular dynamic study of TEGDMA-Au, a dental complex material, the following observations emerge:

1. Changes in physical parameters in TEGDMA-Au complex system when compared to pure TEGDMA is due to change in the gradient of electro-potentials seen by the atoms present in the molecule. These properties can significantly impact the overall performance and durability of dental restorations.
2. Spectral studies shed light on the possible chemical transformations and reaction kinetics of TEGDMA-Au complex system.
3.The physical properties of TEGDMA-Au play an important role in dental composites. Research focused on parameters such as lattice energy, electronegativity, elastic constants, spatial dependence of moduli, refractive index, and dipole moment provide valuable information on how TEGDMA-Au affects these properties.

REFERENCES

1. Ferracane, J. L. (2001). Materials in Dentistry: Principles and Applications. Lippincott Williams & Wilkins.
2. Sun, B., Zhang, M., Shen, J., He, Y., & Huang, J. (2014). Recent advances in organic-inorganic nanocomposites for dental restorations. *Journal of Applied Polymer Science, 131*(15), 40561.
3. Daniel, M. C., & Astruc, D. (2004). Gold nanoparticles: Assembly, supramolecular chemistry, quantum-size-related properties, and applications toward biology, catalysis, and nanotechnology. *Chemical Reviews, 104*(1), 293-346.
4. Lu, W., Senapati, D., Wang, S., Tovmachenko, O., Singh, A. K., Yu, H., & Ray, P. C. (2010). Effect of surface coating on the toxicity of gold nanorods in human skin keratinocytes. *Chemical Physics Letters, 487*(1-3), 92-96.
5. Balazs, A. C., Emrick, T., & Russell, T. P. (2006). Nanoparticle polymer composites: Where two small worlds meet. *Science, 314*(5802), 1107-1110.
6. J.D.Gale,1997. J.Chem Society-Faraday Transactions. 93,629-637.
7. LAMMPS - a flexible simulation tool for particle-based materials modeling at the atomic, meso, and continuum scales, A. P. Thompson, H. M. Aktulga, R. Berger, D. S. Bolintineanu, W. M. Brown, P. S. Crozier, P. J. , Veld, A. Kohlmeyer, S. G. Moore, T. D. Nguyen, R. Shan, M. J. Stevens, J. Tranchida, C. Trott, S. J. Plimpton, Comp Phys Comm, 271 (2022) 10817.
8. Understanding of dental material Triethylene Glycol Dimethacrylate (TEGDMA) using molecular dynamics method ;B N Amruth 1 , M Maurya 2 , M B Nandaprakash 1 , H Somashekarappa 3,* , S G Jayaprakash 4 and R Somashekar 5, communicated to IOP journal (2024).
9. Electronegativity determination of individual surface atoms by atomic force microscopy Jo Onoda, Martin Ondráček, Pavel Jelínek, and Yoshiaki Sugimoto1 Nat Commun. 2017; 8: 15155.
10. EELATE: an open-source online application for analysis and visualization of elastic tensors Romain Gaillac, Pluton Pullumbi and François-Xavier Coudert , J.Phys. Condensed Matter, 28. (27) 275201 (2016) https://progs.coudert.name/elate.
11. .Polik, WF, Schmidt, JR. WebMO: Web-based computational chemistry calculations in education and research. WIREs Comput Mol Sci. 2021;e1554. https://doi.org/10.1002/wcms.1554.

Electronic Structure and Thermoelectric Properties of Single-layer 1D and 2D MoS_2

Poulami Biswas[1,*] and Molly De Raychaudhury[1]

[1]Department of Physics, West Bengal State University, Barasat, Kolkata 700126, India

*poulamibiswas1999@gmail.com

Abstract. We have studied the structural, electronic, and thermoelectric (TE) properties of monolayer (ML) MoS_2 in 1-dimensional (1D) and 2-dimensional (2D) structures using first-principles method based on density functional theory and followed by semi-classical Boltzmann transport theory. The monolayer 2D MoS_2 exhibits a band gap of 1.66 eV, whereas the 1D MoS_2 is metallic. The transport properties such as the Seebeck coefficient, thermal conductivity, electrical conductivity, power factor (P.F.), and thermoelectric figure of merit (ZT) of ML 1D/2D MoS_2 were computed at temperatures 300 K and 800 K. The 2D MoS_2 is found to be more suitable for thermoelectric applications than 1D MoS_2.

Keywords: Semiconducting, direct band gap, Seebeck coefficient, power factor, figure of merit

INTRODUCTION

After the discovery of graphene and its outstanding properties and applications [1], there has been a concerted effort in the search for new 2d materials that replicate graphene's advantages without its drawbacks. Transition metal dichalcogenides (tmds) represent one such class of 2d materials discovered over the last decade [2]. Tmds are layered structures held together by weak van der waals forces between the layers and there is a strong covalent bonding between the atoms within each layer. Hence structurally tmds are much like graphene. This capability enables tmds to form thin layers such as monolayers (ml), bilayers (bl), and few layers, each displaying unique properties due to their low dimensionality as in graphene. Among tmds, mo$\mathbf{S_2}$ is predominantly studied for application purposes because of its natural abundance. The band gap issue of graphene can be addressed by mo$\mathbf{S_2}$, which possesses a band gap [3] comparable to silicon. Theoretical calculations indicate that bulk mo$\mathbf{S_2}$ has an indirect band gap of 1.20 ev, while monolayers (ml) exhibit a direct band gap of 1.66 ev. The band gap of tmds vary depending on its thickness, thereby making them well-suited for applications in optoelectronic devices [4]. The band gap and low dimensionality play significant roles in enhancing the thermoelectric (te) properties of te materials [5].

nowadays, thermoelectric technology has received a lot of attention as an alternative to fossil fuels. Thermoelectric materials enable the direct conversion of thermal energy to electrical energy and vice versa. The energy conversion efficiency of te materials at a given temperature is defined by a dimensionless quantity called the thermoelectric figure of merit (zt). The figure of merit of a te material at a given temperature t is given by zt = $\boldsymbol{\sigma S^2}$t/κ ,where $\boldsymbol{\sigma}$, s, κ = $\boldsymbol{\kappa_e}$ + $\boldsymbol{\kappa_l}$ represent the electrical conductivity, the seebeck coefficient and the total thermal conductivity (which includes both electronic component of thermal conductivity ($\boldsymbol{\kappa_e}$) and lattice thermal conductivity ($\boldsymbol{\kappa_l}$)) respectively. Here we have studied the thermoelectric properties of ml mo$\mathbf{S_2}$ at two different temperatures. These transport properties are determined using boltzmann transport theory under constant relaxation time ($\boldsymbol{\tau}$) approximation as implemented in the boltztrap2 code [6].

COMPUTATIONAL DETAILS

We performed first-principles electronic structure calculations within the framework of density functional theory (dft) using projected augmented wave (paw) pseudopotentials, as implemented in the plane wave-based vienna ab initio simulation package (vasp) program [7]. The generalized gradient approximation (gga) is used as an exchange-correlation functional, following the perdew-burke-ernzerhof (pbe) formalism. To calculate the ground state crystal structure 4 × 4 × 1 and 10 × 1 × 1 monkhorst-pack mesh are used for 2d and 1d mo$\mathbf{S_2}$ respectively. Along with optimized lattice parameters, a denser mesh of 15 × 15 × 1 k-points for 2d and 15 × 1 × 1 k-points for 1d are used for the calculation of electronic properties. The cutoff energy is set to 344.914 ev, which is sufficient to achieve self-consistent (scf) energy. We apply the condition that the scf cycle will converge when the energy difference between two consecutive cycles is less than $\mathbf{10^{-4}}$ ev. The electronic transport properties are determined using semi-classical boltzmann transport theory (bte) within the relaxation time approximation. Boltztrap2 is used for interpolating band structures and calculating semi-classical transport coefficients. These transport coefficients are evaluated based on the group velocity of the band electrons [8]. We have computed all the thermoelectric properties of mo$\mathbf{S_2}$ based 1d/2d structures by using boltztrap2 code with constant relaxation time approximation at two distinct temperatures 300k and 800k.

RESULTS AND DISCUSSION

We have calculated the ground state crystal structure, electronic structure and the thermoelectric properties of mono-layer 1d and 2d mo$\mathbf{S_2}$. Mo$\mathbf{S_2}$ has a layered structure and with each layer made up three hexagonal atomic layers consisting of sulfur-molybdenum-sulfur atoms (p$\mathbf{6_3}$/mmc, space group no. 194). The lattice constant used for mo$\mathbf{S_2}$ are a = b = 3.19 Å and c = 13.38 Å. These lattice parameters are used to make a ml 3 × 3 × 1 supercell with sufficient amount of vacuum of thickness 11.83 Å in 'c'

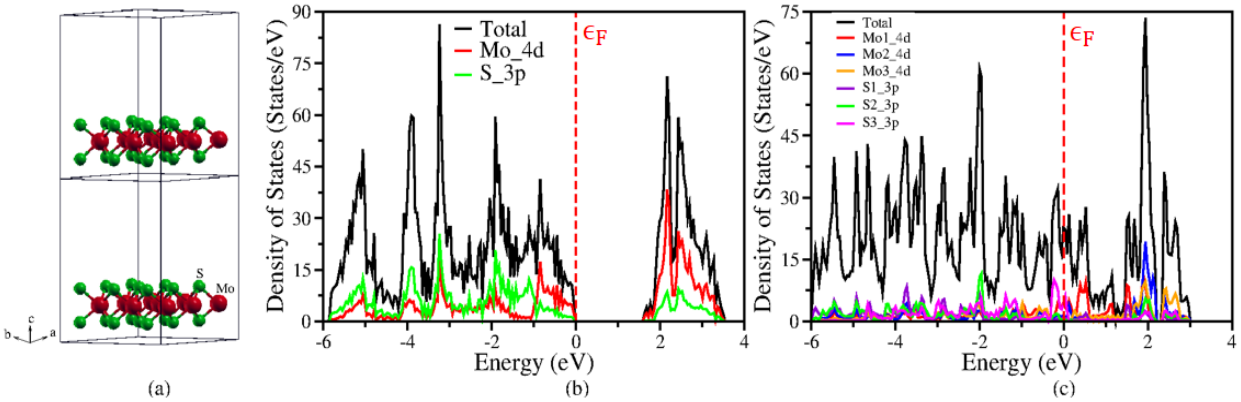


FIGURE 1. (a) Crystal structure of monolayer MoS_2 (supercell 3 × 3 × 1) with two unit cell along Z direction (b) TDOS and PDOS plots of ML 2D MoS_2 (c) TDOS and PDOS plots of ML 1D MoS_2.

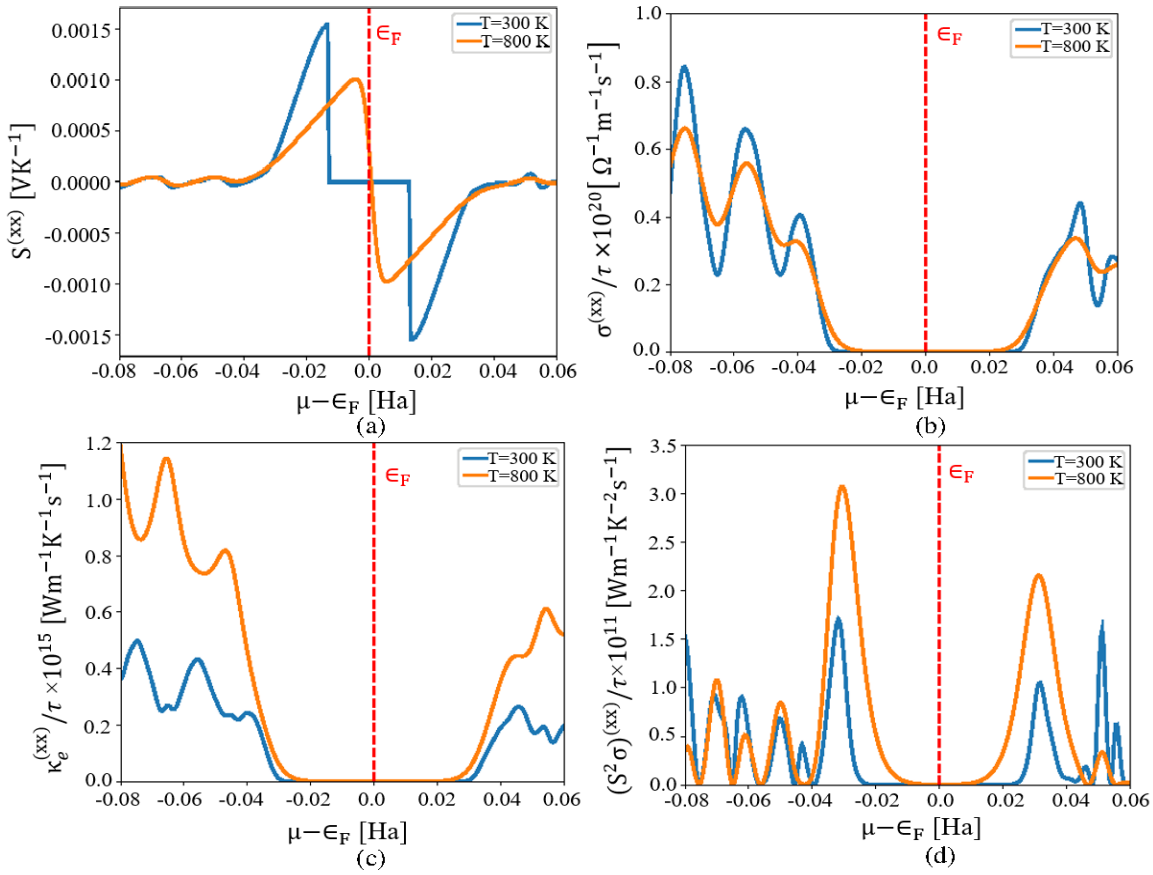


FIGURE 2. (a) Seebeck coefficient (S) (b) Electrical conductivity per unit relaxation time (σ/τ) (c) Electronic thermal conductivity

per unit relaxation time (κ_e/τ) (d) Power factor per unit relaxation time ($S^2\sigma/\tau$) as a function of Chemical potential for ML 2D MoS_2 at 300K and 800K. [1 Ha =27.2114079 eV]

Direction for 2d, 7.11 Å in 'b' and 11.83 Å in 'c' directions both for 1d mo$\mathbf{S_2}$ structures. The 1d mo$\mathbf{S_2}$ has a finite width 8.17 Å along 'b' direction. The relaxed 1d and 2d structures are used for the calculation of electronic properties. We have calculated the density of states (dos) for both 1d and 2d mo$\mathbf{S_2}$. The resulting total density of states (tdos) and partial density of states (pdos) of both 2d and 1d mo$\mathbf{S_2}$ are shown in fig. 1. The monolayer mo$\mathbf{S_2}$ based 2d structure has a direct band gap 1.66 ev whereas 1d structure behaves like a metal [9] due to the surface atoms appear from confinement in the 'b' direction. Owing to the finite width of 1d mo$\mathbf{S_2}$ in 'b' direction, the states of surface atoms mo and s are responsible for closing the band gap.

BoltzTraP2 computes the electronic transport properties mainly the Seebeck coefficient (S), electrical conductivity for constant relaxation time (σ/τ), thermal conductivity due to electrons for constant relaxation time (κ_e/τ), power factor for constant relaxation time ($S^2\sigma/\tau$) and figure of merit ($ZT = S^2\sigma T/\kappa$) but it assumes the phonon contribution to thermal conductivity (κ_l) to be negligible. In these calculation we have used $\tau = 1 \times 10^{-14}$ s. The negative range of chemical potential denotes p-region while the positive range of chemical potential denotes n-region. Seebeck coefficient gives the information about the nature of dominant charge carriers present in the materials. The variation of Seebeck coefficient, power factor, electrical and thermal conductivity with chemical potential ($\mu - \epsilon_F$), where ϵ_F is the Fermi energy for 2D MoS_2 [10] has been shown in Fig. 2. Here we presented only the 'xx' component of thermoelectric parameters because the other diagonal components shows nearly similar results to the 'xx' component. From the Fig. 2, we have found that 2D MoS_2 has a maximum Seebeck coefficient (S) of -1552 μV/K at 300K in n-region, which matches well with the experimental results [11]. We conclude that the predominant carriers at 300 K are of n-type. But at 800K, the maximum value of Seebeck coefficient is 1004 μV/K for p-region. Both the Seebeck coefficient and electrical conductivity decrease with rising temperature. For 2D MoS_2, P.F shows a maximum value of 17.07 $\mu WK^{-2}cm^{-1}$ at 300 K and 30.75 $\mu WK^{-2}cm^{-1}$ at 800K. On the other hand, the electrical part of thermal conductivity (κ_e/τ) increases with increasing temperature. In order to achieve a larger figure of merit, we choose the highest value of power factor ($S^2\sigma/\tau$) along with minimum value of thermal conductivity (κ_e/τ). Although no theoretical perimeter is set for highest value of ZT, it is yet a challenge to obtain the higher value of figure of merit by varying three transport parameters S, σ, κ_e. From our theoretical calculations, we observe that single layer 2D MoS_2 has a highest ZT value 0.389 at 800K. The thermoelectric properties of 1D MoS_2 has also been studied. The metallic MoS_2 based 1D structure shows large electrical conductivities at both 300K and 800K but its Seebeck coefficients are very low resulting in a small ZT value 0.097 at 800K.

CONCLUSION

The structural and electronic properties of monolayer 1D and 2D MoS_2 were investigated using first-principles electronic structure calculations based on density functional theory (DFT), implemented in the plane-wave-based Vienna Ab initio Simulation Package (VASP). Monolayer 2D MoS_2 exhibits semiconductor behavior, whereas the 1D form behaves as a metal. Loss of the band gap is purely due to surface states arising on account of confinement in the 2nd dimension. Thermoelectric properties were evaluated using semi-classical Boltzmann transport theory under the relaxation time approximation, employing the BoltzTraP2 code. The semiconducting nature of 2D MoS_2 makes it promising as a thermoelectric material by enhancing its Seebeck coefficient.

ACKNOWLEDGMENTS

We are grateful to the department of science and technology, government of india, for their financial support vide dst inspire fellowship, sanction order no. Dst/inspire fellowship/2021/if210716. We also thank government of west bengal, india for providing infrastructural support.

REFERENCES

1. Ferrari, Andrea C., Jannik C. Meyer, Vittorio Scardaci, Cinzia Casiraghi, Michele Lazzeri, Francesco Mauri, Stefano Piscanec et al. Physical review letters 97, no. 18 (2006): 187401.
2. C. Ataca, H. Sahin, and S. Ciraci, J. Phys. Chem. C 116, 8983 (2012).
3. Mak, Kin Fai, Changgu Lee, James Hone, Jie Shan, and Tony F. Heinz. Physical review letters 105, no. 13 (2010): 136805.
4. Lopez-Sanchez, Oriol, Dominik Lembke, Metin Kayci, Aleksandra Radenovic, and Andras Kis. Nature nanotechnology 8, no. 7 (2013): 497-501.
5. Hasdeo, Eddwi H., Lukas Krisna, Muhammad Y. Hanna, Bobby E. Gunara, Nguyen T. Hung, and Ahmad RT Nugraha. Journal of Applied Physics 126, no. 3 (2019).
6. Madsen, Georg KH, Jesús Carrete, and Matthieu J. Verstraete. Computer Physics Communications 231 (2018): 140-145.
7. Kresse, Georg, and Jürgen Hafner. Physical review B 47.1 (1993): 558.
8. Madsen, Georg KH, and David J. Singh. Computer Physics Communications 175.1 (2006): 67-71.
9. Junghare, Rajesh C., and Ganesh C. Patil. In Proc. of TechConnect World Innovation Conference and Expo, co-located with the Nanotech-2019 and AI TechConnect. 2019.
10. Ramanathan, Amall A., and Jamil M. Khalifeh. IEEE Transactions on nanotechnology 17.5 (2018): 974-978.
11. Wu, Jing, et al.Nano letters 14.5 (2014): 2730-273

Thermodynamic Properties of Small Aluminum Clusters

Amit Kumar,[1, a)] Balasaheb J. Nagare,[2] Raman Sharma,[1] and Dilip. G. Kanhere[3]

[1]*Department of Physics, Himachal Pradesh University, Summer Hill, 171005, Shimla, India.*
[2]*Department of Physics, University of Mumbai, Kalina Campus, Santacruz (E), 400098, Mumbai, India.*
[3]*Department of Scientific Computing, Modeling, and Simulations, Savitribai Phule Pune University, Ganeshkhind, Aundh, 411 007, Pune, India.*

[a)]Corresponding author: amitkumarcuhp@gmail.com

Abstract. We utilized a DNN-based deep potential (DP) approach to study the thermodynamics of small aluminum clusters. We have computed heat capacity and melting temperatures of Al_{25}, Al_{33}, Al_{39}, and Al_{44} clusters using multiple histogram technique. Simulations using molecular dynamics were performed at 24 separate temperatures for each cluster. Obtained results have an accuracy very close to the density functional theory (DFT). Our results show excellent agreement with the experimentally reported melting temperatures and heat capacity curves for all the investigated clusters

INTRODUCTION

Machine learning (ML) approaches have become invaluable for generating accurate and computationally efficient potential energy surfaces (PES). When combined with molecular dynamics (MD), ML-based potentials can achieve accuracy that closely mirrors the original density functional theory (DFT) data used for training. Once developed, these ML potentials enable fast MD simulations while maintaining fidelity to the high-quality reference calculations. Sun et. al. [1] has used high-dimensional neural networks potential (HDNNP) to examine the structures of small platinum clusters. Chiriki et. al. [2] has investigate the thermodynamic properties of small sodium clusters using a neural network potential. The accuracy and reliability of the ML-based deep potential have been verified by Fronzi et al. [3] in predicting the properties of gold nanoparticles. Martin and collaborators have provided enough experimental data for aluminum clusters. They reported melting temperatures and heat capacities for clusters containing between 16 and 342 atoms [4]. The DP model has been successfully used by us to investigate the thermodynamics of aluminum clusters [5].

The abundance of experimental data, combined with the proven accuracy of the DP model, motivated us to study the thermodynamic properties of small aluminum clusters i.e., Al_{25}, Al_{33}, Al_{39}, and Al_{44}. All MD simulations have been performed using LAMMPS with the DP model. Computed melting temperatures and heat capacity curves are consistent with the experimental data. To gain deep insights into the thermodynamical behavior of the aluminum clusters under investigation, we have analyzed the mean squared displacements (MSD) and Lindemann melting criterion (δ_{rms}).

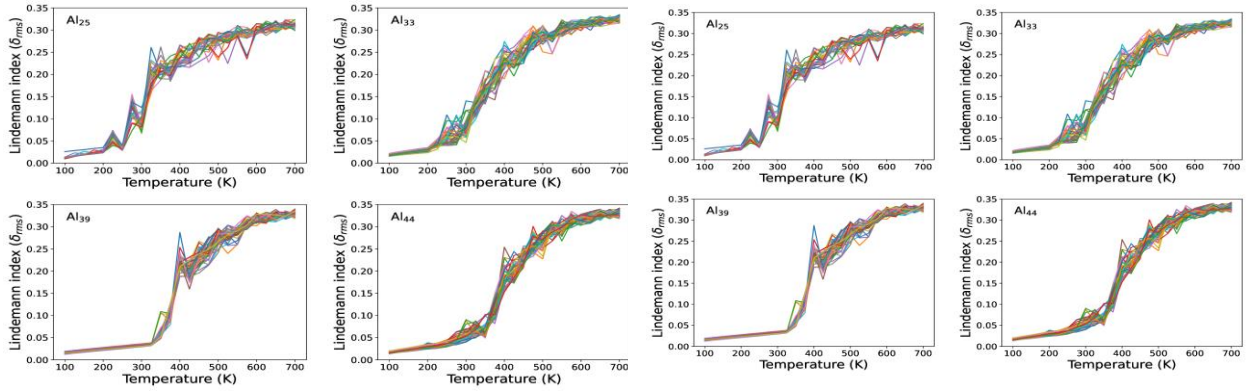
METHODOLOGY AND COMPUTATIONAL DETAILS

We have used machine-learned DP model based on DeePMD methodology [6], developed by Tuo et. al. [7], to investigate thermodynamic properties of aluminum clusters, i.e., Al_{25}, Al_{33}, Al_{39}, and Al_{44}. A brief overview of DeePMD method is given below. In ML methods, a local neighborhood approximation is used which assumes that only a small neighborhood within a sphere of radius r_c contributes to the energy E_i and force $\mathbf{F}_i$. In this approximation, the total energy of the system is given by, $E = \Sigma E_i$, where E_i is atomic energy of the i^{th} atom and is determined by the local environment. It is characterized by all the coordinates $\{\mathbf{R}^i_j\}$, where j run over all atoms within r_c. The DP model incorporates a variety of descriptors, such as local frame, two- and three-body embeddings from DeepPot-SE, attention-based mechanisms, and hybrid approaches. The training dataset used consisted of energy and forces of aluminum clusters with N = 10, 11, 13, 19, 23, 25, 26, 55, and 147. It includes 10,000 configurations in total. The input data has been generated by using VASP with GGA exchange correlation potential. A cutoff radius of 9 Å with a fitting and embedded network of layer sizes {240, 240, 240} and {25, 50, 100} have been used, respectively. The model is well-validated for ground state and a few low lying energy structures. The errors in the predicted energy and reference values were around 0.1 eV. To calculate heat capacity curves and melting temperatures we used multiple histogram approach. Histograms were constructed from molecular dynamics simulations performed at 24 different temperatures (100 K to 700 K) for each cluster, using

a time step of 2 fs and the Nosé–Hoover thermostat. Each simulation was performed for 400 thousands iterations per temperature.

RESULTS AND DISCUSSION

We have computed the heat capacity and melting temperature of Al_{25}, Al_{33}, Al_{39}, and Al_{44} clusters. Computed heat capacity is determined from the multiple histogram method. Obtained heat capacity curves along with the available experimental results are given in Fig. 1a . There is an excellent agreement between experimental and computed heat capacity curves for all the clusters. Determined symmetry, lowest energy, and melting temperatures for all the clusters under investigation are given in Table 1.

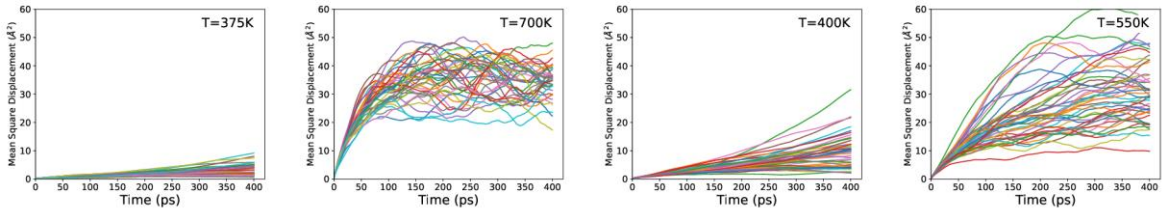


(a) Computed and experimental heat capacity curves for Al_{25}, Al_{33}, Al_{39}, and Al_{44}.

(b) Lindemann melting criterion for individual atoms, $\delta_{rms}(i)$ of Al_{25}, Al_{33}, Al_{39}, and Al_{44}.

FIGURE 1. Heat capacity curves and δ_{rms} for Al_{25}, Al_{33}, Al_{39}, and Al_{44}.

The form of heat capacity curves is largely determined by the characteristics of the ground-state geometry. Symmetric and ordered geometries lead to relatively narrow melting peaks whereas disordered geometries give rise to broader peaks in the heat capacity curve. Out of these 4 clusters, Al_{39} is ordered and has higher symmetry (C_{4v}), as compared to other clusters, which results in a narrower peak in the heat capacity curve. The remaining three disordered clusters exhibit low symmetry, which results in a broader peak in their heat capacity curves. To have deep insights into the behavior of these clusters, we have examined MSD and δ_{rms} of individual atoms. Obtained results for MSD and δ_{rms} are reported in Fig. 2 and 1b, respectively.



Al_{39} Al_{44}

FIGURE 2. MSDs for Al_{39} and Al_{44} at different temperatures.

All the atoms in Al_{39} exhibit collective diffusive motion seen in Fig. 1b, leading to a more pronounced peak in the heat capacity curve. In contrast, the other three clusters undergo continuous melting, displaying a broader spread in the $\delta_{rms}(i)$ curve over a wide temperature range, leading to a more gradual behavior in the heat capacity curve.

TABLE 1. Symmetry, lowest energy per atom, Melting temperatures of aluminum clusters obtained from the DP model.

Cluster size	Symmetry	Energy (eV/atom)			Melting Temperature (K)	
		VASP	DP	ΔE	Experiment	DP
25	C_3	-3.00	-3.08	0.08	850.00	-
33	C_2	-3.09	-3.14	0.05	567.00	-
39	C_{4v}	-3.11	-3.17	0.06	710.00	708.00
44	C_1	-3.15	-3.18	0.03	660.00	666.00

The MSDs for Al_{39} and Al_{44} clusters at various temperatures are presented in Fig. 2. At 375~K in Al_{39}, there is no signature of diffusive motion, and MSD values are closer to 5 $Å^2$. In contrast, for Al_{44}, a few atoms have crossed MSD values greater than 10 $Å^2$. This collective motion of atoms in Al_{39} leads to a sharper peak compared to Al_{44}. Since the heat capacity curve for Al_{25} and Al_{33} are almost flat which signifies continuous melting of the cluster. So, it is not possible to predict the sharp melting point. Experimental values for these clusters are based upon theoretical models which are not supposed to be reliable. Further, in our previous work, we noticed that none of the clusters have melting points very close to bulk[5].

CONCLUSION

We used a machine-learned DP model to calculate the heat capacities and melting temperatures of four aluminum clusters, Al_{25}, Al_{33}, Al_{39}, and Al_{44}, using the multiple histogram technique. The calculated melting points show strong agreement with experimental findings. Overall, the shapes of the calculated heat capacity curves closely match the experimentally measured ones. From the MSD and Lindemann melting criterion, we conclude that there is continuous melting behavior in all the clusters except Al_{39} under investigation.

ACKNOWLEDGMENTS

Amit Kumar gratefully acknowledges the financial assistance provided by the CSIR-UGC, Government of India, through the Junior Research Fellowship (JRF) program. The authors also thank the Department of Physics at Himachal Pradesh University, Shimla, for access to the HPC cluster and the Param Shavak computing facility used.

REFERENCES

1. G. Sun and P. Sautet, "Toward fast and reliable potential energy surfaces for metallic Pt clusters by hierarchical delta neural networks," J.Chem. Theory Comput. **15 (10)**, 5614–5627 (2019).
2. S. Chiriki and S. S. Bulusu, "Modeling of dft quality neural network potential for sodium clusters: Application to melting of sodium clusters(Na_{20} to Na_{40})," Chem. Phys. Lett. **652**, 130–135 (2016).
3. M. Fronzi, R. D. Amos, and R. Kobayashi, "Evaluation of machine learning interatomic potentials for gold nanoparticles—transferabilitytowards bulk," Nanomaterials **13**, 1832 (2023).
4. C. M. Neal, A. K. Starace, and M. F. Jarrold, "Melting transitions in aluminum clusters: The role of partially melted intermediates," Phys.Rev. B **76**, 054113 (2007).
5. A. Kumar, B. J. Nagare, R. Sharma, and D. G. Kanhere, "Understanding melting behaviour of aluminum clusters using machine learned deepneural network potential energy surfaces," The Journal of Chemical Physics **161,** 174301 (2024).
6. H. Wang, L. Zhang, J. Han, and W. E, "Deepmd-kit: A deep learning package for many-body potential energy representation and moleculardynamics," Computer Physics Communications **228**, 178–184 (2018).
7. P. Tuo, X. Ye, and B. Pan, "A machine learning based deep potential for seeking the low-lying candidates of al clusters," The Journal ofChemical Physics **152**, 114105 (2020).

Structural and Optoelectronic Properties of Monolayer $ScBiS_3$ under Pressure: A First Principle Approach

Riddhi Desai*[1(a], Yashasvi Naik[1(b], H. P. Patel[(c] and P. B. Thakor[1(d]

[a,b,d]*Department of Physics, Veer Narmad South Gujarat University, Surat-395007, Gujarat, India.*
[c]*School of science, Birsa Munda tribal university, Rajpipla-393145, Gujarat, India.*

[a)]Corresponding author: desairiddhii.phy@gmail.com

Abstract. The optoelectronic properties of the $ScBiS_3$ monolayer have been systematically investigated under varying pressures up to 16 GPa using ab initio simulations based on density functional theory (DFT). With the increasing pressure band gap of monolayer decreasing and at the 16GPa the band gap becomes zero and material turns into metal. By examine the optical properties of material at various pressure, we have been observed that at 16GPa material stat absorption from infrared region which make it suitable for the application in infrared photonic technologies and systems.

INTRODUCTION

The discovery of graphene has triggered intensive investigations into 2D materials [1]. Such as III-group chalcogenides, Janus, halides, Mxenes, and v-group chalcogenides[2] because of its prominent electronic and optical properties like high carrier mobility and stability which finds its applications in various advanced field including optoelectronic, photo catalytic, photovoltaic [3]. Bi2S3 and their heterostructures shows the high thermoelectric performance and use as photodetector [4]. Which gain the interest in research. In our previous work, a new ternary chalcogenide monolayer, $ScBiS_3$, was developed by substituting one Bi atom in Bi_2S_3 with a Sc atom.[5]. There are numerous methods to modify the properties of materials including the application of Strain, doping and defects etc. Pressure is crucial factor in thermodynamics that can also tune the properties of materials. By applying pressure, it is possible to transform materials from insulators to metal and Semiconductor to metal and vice versa. The different properties of Janus WSeTe monolayers [6] have been studied under the pressure, the effect of pressure on Sc_2CBr_2 monolayer [7] have been also studied. The Sc_2CBr_2 monolayer turned into metal at 16GPa. In this work, we employ first principles Simulations to assess the role of pressure in tuning the optoelectronic properties of monolayer. The purpose of our research is to by applying various pressure to the ScBiS3 monolayer its band gap reduced gradually and potentially enhancing the optical properties.

COMPUTATIONAL METHODS

In this work, we compute the optoelectronics characteristics of $ScBiS_3$ monolayer under the pressure by first principles simulations using quantum espresso[8], with the generalized gradient approximation (GGA). Electron ion interactions have been carried out by the projected augmented wave type pseudo potential[9]. The electron density was established at 550 Ry, and the energy cutoff was fixed at 55 Ry. The force relaxation limit was set at 1×10^{-3} Ry/Bohr Ry/Bohr and total energy at 10^{-6} Ry. The accurate electronic properties have been obtaining by Heyd-Scusenia Ernzerhof (HSE06) hybrid functional. K-point grid of 4x4x1 used for the structural optimization. The optical nature of monolayer has been acquired from independent-particle approximation within the framework of the Yambo simulation suite[10]. To avoid any interaction between neighboring atoms, Vacuum of 20A° is applied along the z direction.

RESULTS AND DISCUSSIONS

GEOMETRIC STRUCTURE AND STABILITY

Geometrical structure of ScBiS3 monolayer and phonon spectra for SCBiS3 monolayer have been depicted in figure 1. Lattice Constant, band gap, and cohesive energy with different pressure are detailed in table 1

TABLE 1 lattice parameter, band gap(eV) and cohesive energy of $ScBiS_3$ monolayer

	0GPa	4GPa	8GPa	12GPa	16GPa
Lattice constant a_0	3.84	3.65	3.50	3.38	3.28
Bandgap	2.66	2.51	1.70	0.78	0.00
Cohesive energy eV	-3.65	-3.34	-2.99	-2.65	-2.33

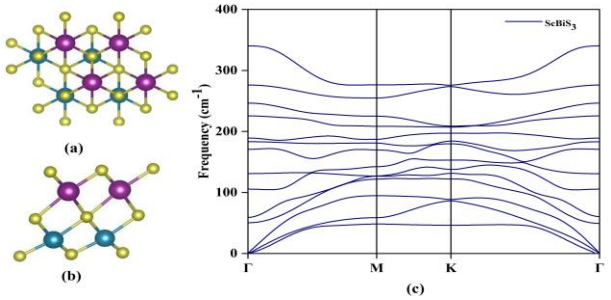


Figure 10(a) (a) Planar view (b) Lateral view (c) phonon at 0GPa of monolayer

The stability of the material was determined based on the interatomic interaction energy obtained from the equation below

$$E_{cohesive} = \frac{E_{total} - n_{Sc}E_{Sc} - n_{Bi}E_{Bi} - n_S E_S}{\text{Number of atoms}}$$

Here, E_{total} is the total energy of monolayer $ScBiS_3$, E_{Sc}, E_{Bi}, E_S, indicated the energy of individual atoms. The negative cohesive energy secure energetic stability of monolayer. Kinetic stability of ScBiS3 monolayer has been assure by the phonon spectra.

BANDGAP MODULATION UNDER PRESSURE

Electronic behavior and PDOS of $ScBiS_3$ monolayer have been obtained by HSF06 functional. Which is introduce in figure 2(a). The energy gap of $ScBiS_3$ monolayer without pressure is 2.66eV which Shows Semiconductor behavior of material. From the PDOS OF $SCBiS_3$ monolayer it has been shown that d orbit of Sc atom shows major contribution in conduction band and p orbit of s atom shows major contribution in Valance

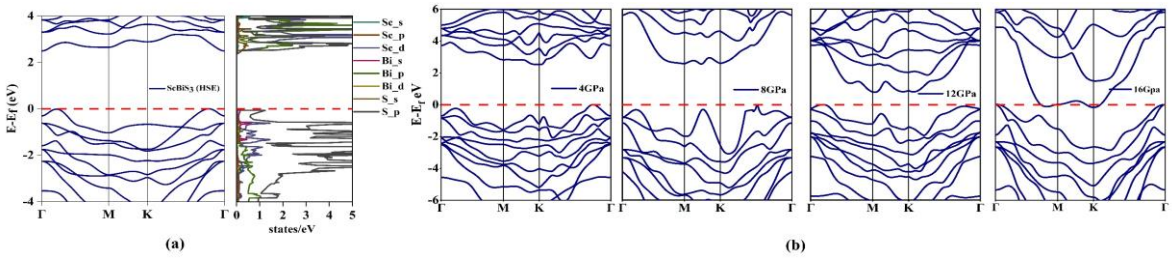


Figure 11(a)band structure and PDOS(b)band structure with pressure for ScBiS3 monolayer

band followed by the p orbit of Bi atom.

As pressure increases, the top of the valence band and the bottom of the conduction band shift closer to the Fermi energy. As shown in figure 2(b). as pressure increases band gap of monolayer decreases at the pressure of 16GPa material became metal with zero band.

OPTICAL CHERECTERISTICS

Figure 3(a, b) indicate the real and imaginary portion of ScBiS3 monolayer. From the figure 4(a) the highest value of dielectric constant is appearing at 2.96 eV for zero pressure, 2.68 eV for 4GPa, 2.44 eV for 8GPa, 2.56 eV for 12 GPa and 1.20 eV for 16GPa pressure. Figure 4(b) of $ScBiS_3$ monolayer shows that with increasing

pressure the first peak of Imaginary part is shifted towards the infrared region, which suggests its application in infrared optoelectronic devices and technologies. Figure 4(c) shows the absorption spectra for $ScBiS_3$ monolayer with various pressure. Material start absorption from visible region and shifting towards UV region for Zero pressure. For higher pressure of 12GPa and 16GPa material start absorption from infrared region and get its highest peak in UV region.

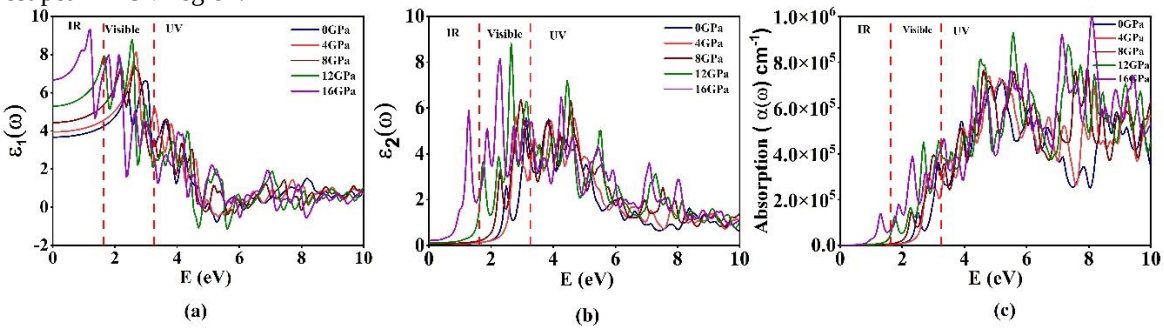


Figure 12(a) Real component (b) Extinction part and(c) absorption coefficient of $ScBiS_3$ monolayer

CONCLUSIONS

Under the pressure the optoelectronic properties of $ScBiS_3$ monolayer have been studied, using quantum espresso. The pressure significantly affects the electronic properties of $ScBiS_3$. With the increasing pressure energy gap of monolayer decreased and material becomes metal at 16GPa. The optical behavior under applied pressure demonstrates that the compound exhibits absorption in the infrared range, making it a strong candidate for application in infrared photonic systems such as sensor, detector etc.

ACKNOWLEDGMENTS

This work was supported by the knowledge consortium of Gujarat (KCG) for granting the SHODH-Scheme of Developing High quality research Fellowship for supporting this research. (Student Ref. No.-2022017442)

REFERENCES

[1] K.S. Novoselov, A.K. Geim, S. V Morozov, D. Jiang, Y. Zhang, S. V Dubonos, I. V Grigorieva, A.A. Firsov, Electric Field Effect in Atomically Thin Carbon Films, Science (80-.). 306 (2004) 666–669. https://doi.org/10.1126/science.1102896.

[2] P.R. Parmar, S.J. Khengar, D. Mehta, Y. Naik, R. Desai, H.R. Mahida, P.B. Thakor, Theoretical exploration of PtSSe/ZrS2 Van der Waals heterostructure for solar energy conversion, Phys. B Condens. Matter. 689 (2024) 416165. https://doi.org/https://doi.org/10.1016/j.physb.2024.416165.

[3] Y. Naik, D. Mehta, P.R. Parmar, P.B. Thakor, First-principles calculations to investigate structural and electronic properties of novel halides ZrIX (X = Cl, Br) for photovoltaic application, Phys. B Condens. Matter. 673 (2024) 415499. https://doi.org/https://doi.org/10.1016/j.physb.2023.415499.

[4] M. Ge, C.-L. Yang, M.-S. Wang, X.-G. Ma, Two-dimensional PtI2/Bi2S3 and PtI2/Bi2Se3 heterostructures with high solar-to-hydrogen efficiency, Colloids Surfaces A Physicochem. Eng. Asp. 666 (2023) 131286. https://doi.org/https://doi.org/10.1016/j.colsurfa.2023.131286.

[5] R. Desai, Y. Naik, P.R. Parmar, P.B. Thakor, A First principles investigation for structural and optoelectronic properties of oxygen functionalized ScBiS3 monolayer, Interactions. 245 (2024) 133. https://doi.org/10.1007/s10751-024-01964-4.

[6] I. Oreibi, J. M. Al-ıssawe, A class of two-dimensional WSeTe monolayers under pressures with novel electronic and optical properties, Turkish Comput. Theor. Chem. 7 (2023) 12–19. https://doi.org/10.33435/tcandtc.1161253.

[7] N. Modi, Y. Naik, S.J. Khengar, D.B. Shah, P.B. Thakor, Pressure Induced Structural, Electronic and Optical Properties of Sc2CBr2 MXene Monolayer: A Density Functional Approach, Comput. Theor. Chem. 1232 (2024) 114466. https://doi.org/https://doi.org/10.1016/j.comptc.2024.114466.

[8] P. Giannozzi, S. Baroni, N. Bonini, M. Calandra, R. Car, C. Cavazzoni, D. Ceresoli, G.L. Chiarotti, M. Cococcioni, I. Dabo, A.D. Corso, S. De Gironcoli, S. Fabris, G. Fratesi, R. Gebauer, U. Gerstmann, C. Gougoussis, A. Kokalj, M. Lazzeri, L. Martin-samos, N. Marzari, F. Mauri, R. Mazzarello, S. Paolini, A. Pasquarello, L. Paulatto, C. Sbraccia, A. Smogunov, P. Umari, Q UANTUM ESPRESSO : a modular and open-source software project for quantum simulations of materials, (2009). https://doi.org/10.1088/0953-8984/21/39/395502.

[9] P.E. Blöchl, Projector augmented-wave method, Phys. Rev. B. 50 (1994) 17953–17979. https://doi.org/10.1103/PhysRevB.50.17953.

[10] A. Marini, C. Hogan, M. Gr, D. Varsano, yambo : an ab initio tool for excited state calculations, (n.d.).

Tuning MXene Monolayer via -OH Functionalization: DFT Insights into Structural and Optoelectronic Properties

Nidhi Modi[1, a)], Yashasvi Naik[2], S. J. Khengar[2], D. B. Shah[1], and P. B. Thakor[2]

[1]*Department of Physics, Sir P.T. Sarvajanik College of Science, Athwalines, Surat, Gujarat, 395001, India.*
[2]*Department of Physics, Veer Narmad South Gujarat University, Udhna-Magdalla Road, Surat, Gujarat, 395007, India.*

[a)] Corresponding author: nidhimodi2000@gmail.com

Abstract. The present study represents the effect of functional groups (-O and -OH) on the structural and optoelectronic properties of Y_2C and ScYC monolayers. Both Y_2C and ScYC monolayers have been functionalized with -O and -OH group to form Y_2CO_2, $Y_2C(OH)_2$, $ScYCO_2$, and $ScYC(OH)_2$ monolayers. Among all, except $ScYCO_2$, all the monolayers are kinetically stable confirmed by phonon dispersion relation. Y_2C monolayer with oxygen functionalization on both the surfaces (Y_2CO_2) shows insulating nature with indirect bandgap 3.67 eV, while Y_2C and ScYC monolayer with -OH functionalization ($Y_2C(OH)_2$ and $ScYC(OH)_2$) shows semiconducting nature with direct bandgap 1.12 eV and 1.09 eV, respectively. Optical properties suggest that -OH functionalized monolayers show absorption in visible as well as in IR regions. Overall findings suggest application of $Y_2C(OH)_2$ and $ScYC(OH)_2$ monolayers in optoelectronic devices.

INTRODUCTION

Two-dimensional (2D) materials such as graphene[1] are highly intriguing due to their unique properties and extensive applications. Among these, MXenes are particularly notable, being carbides, nitrides, and carbo-nitrides of d-block elements. Ti_3C_2 MXene, synthesized by Y. Gogotsi et al. in 2011[2], follows the chemical formula $M_{n+1}X_n$, where M represents a d-block element and X can be C, N, or both. These materials are derived from ternary MAX phases, where the A group element is selectively removed through treatments like HF acid etching or sonication[3]. Most pristine MXenes exhibit metallic properties initially. Modifying the band structure of 2D layers is achievable through various methods; one effective approach is surface functionalization. Recent studies have explored the impact of -O and -OH functional groups on M_2C (M = Zr, Sc, Mo, Hf) MXenes[4]. Additionally, double transition metal MXenes (MM'C), obtained by substituting one metal atom with another, have also been subject to functionalization[5]. This prompts investigation into the effects of surface terminations (-O and -OH) on monolayers of Y_2C and ScYC within the density functional theory framework.

COMPUTATIONAL METHODOLOGY

In this study, all calculations were performed using Quantum Espresso[6] within the framework of density functional theory. The Heyd-Scuseria-Ernzerhof (HSE06) hybrid functional was employed to account for the exchange-correlation effects in electron interactions, utilizing the Wannier90 code[7]. The Projector Augmented Wave (PAW) pseudopotential has been applied by setting the force convergence threshold and energy convergence threshold at 10^{-6} Ry/Bohr and 10^{-6} Ry, respectively. To address van der Waals interactions between the pristine monolayer and the functionalized atoms, we used Grimme's DFT-D3 scheme. The k-point sampling was done using a 6×6×1 k-grid as per the Monkhorst-Pack method[8], with a 20 Å vacuum layer to prevent interactions between periodic layers. The Yambo code, along with norm-conserving pseudopotentials[9], was used to calculate the optical properties.

RESULTS AND DISCUSSIONS

Optimization and the Stability of Structures

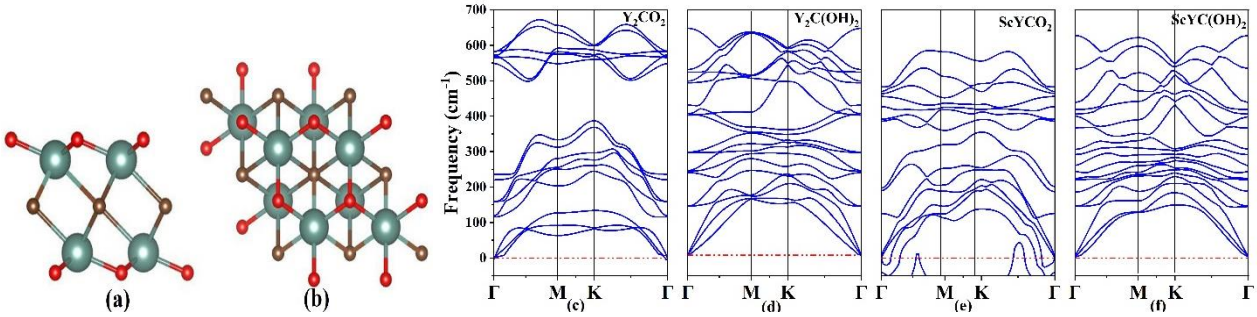


FIGURE 13. (a) Side view; (b) Top view of Y_2CT_2 (T = O, OH) monolayers; (c, d, e and f) Phonon dispersion curve of Y_2CO_2, $Y_2C(OH)_2$, $ScYCO_2$ and $ScYC(OH)_2$ monolayers

The side and top views of the hexagonal Y_2CT_2 and $ScYCT_2$ (T = O, OH) monolayers are depicted in fig.1(a and b). The pristine Y_2C and ScYC MXene monolayers possess hexagonal symmetry. One of the Y atoms is substituted by the Sc atom to form $ScYCT_2$ monolayer. Green, brown, and red spheres are Y, C, and T atoms, respectively. The side view reveals that the carbon atom is positioned between two transition metal elements. The cohesive energies (equation [10]) of these monolayers are -2.45 eV, -2.73 eV, -0.69 eV, and -3.24 eV, respectively for Y_2CO_2, $Y_2C(OH)_2$, $ScYCO_2$ and $ScYC(OH)_2$ monolayers, confirm their energetic stability due to their negative values. Additionally, the kinetic stability of the monolayers has been assessed through the simulation of phonon dispersion curves, indicating that all Y_2CO_2, $Y_2C(OH)_2$, and $ScYC(OH)_2$ monolayers except $ScYCO_2$ are kinetically stable due to all positive frequencies. Hence in this research work, all the stable monolayers have been studied.

Tuning the Optoelectronic Properties via Surface Functionalization

All the functionalized monolayers exhibit hexagonal symmetry. Therefore, the Γ-M-K-Γ path was used for the stable monolayers Y_2CO_2, $Y_2C(OH)_2$, and $ScYC(OH)_2$, as shown in fig.2 (a, b, and c). Upon oxygen functionalization, the Y_2C MXene transforms into an insulator (Y_2CO_2) with an indirect bandgap of 3.67 eV as shown in Fig.2 (a) as valance band maxima (VBM) situated at Γ point and conduction band minima (CBM) located at M point. When hydrogen is added along with oxygen to both surfaces, $Y_2C(OH)_2$ becomes a direct bandgap semiconductor with a bandgap of 1.12 eV. The ScYC monolayer is unstable after oxygen functionalization ($ScYCO_2$), but it becomes a direct bandgap semiconductor with a 1.09 eV bandgap when hydrogen is added along with oxygen to both surfaces ($ScYC(OH)_2$). For both -OH functionalized monolayers $Y_2C(OH)_2$, and $ScYC(OH)_2$, CBM and VBM are situated at the same Γ point as depicted in Fig. 2 (b and c) and hence make them direct band gap semiconductors.

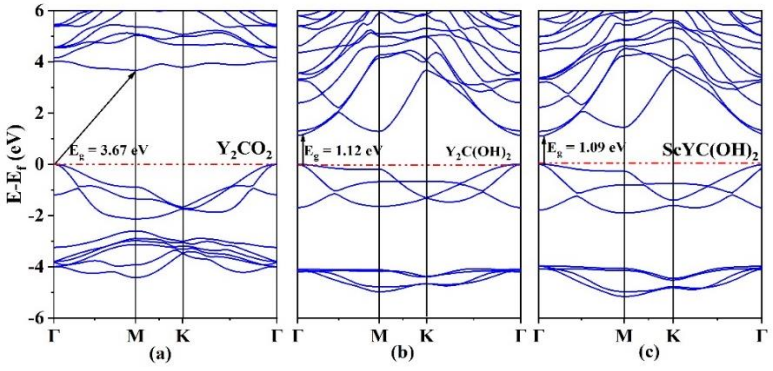


FIGURE 14. (a, b and c) Electronic Band Structures of Y_2CO_2, $Y_2C(OH)_2$ and $ScYC(OH)_2$ monolayers

The absorption behavior of the material was analyzed using the complex dielectric function. The static dielectric constant values (real part at zero energy) for Y_2CO_2, $Y_2C(OH)_2$, and $ScYC(OH)_2$ are 3.4, 4.3 and 4.5, respectively as shown in Fig.3(a). The imaginary part exhibits peaks in the Visible as well as in UV region. For the Y_2CO_2 monolayer, absorption begins in the ultraviolet region. Upon hydrogenation, the absorption spectrum red-shifts, with some peaks appearing in the visible region for both -OH functionalized $Y_2C(OH)_2$, and

$ScYC(OH)_2$ monolayer. Hence, there is an enhancement in optical absorption due to -OH functionalization as shown in Fig.3(c). Therefore, the -OH functionalized monolayers, $Y_2C(OH)_2$ and $ScYC(OH)_2$, demonstrate higher efficiency for optoelectronic applications.

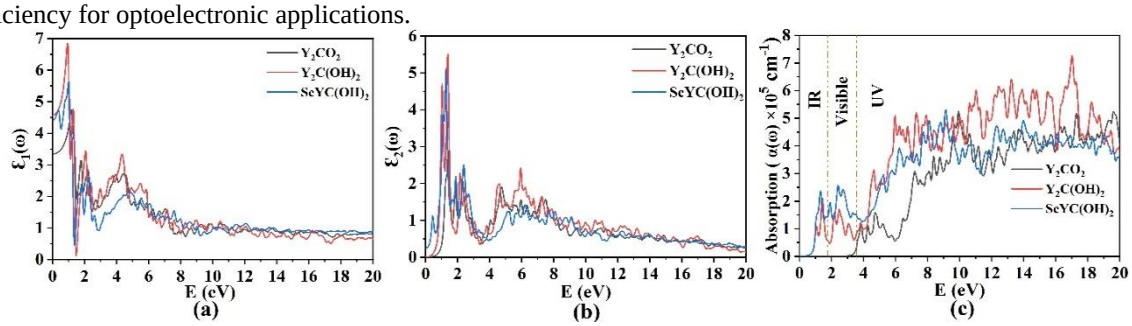


FIGURE 15. (a) Real part, (b) Imaginary part and (c) Absorption coefficient of Y_2CO_2, $Y_2C(OH)_2$ and $ScYC(OH)_2$ monolayers

CONCLUSIONS

The electronic bandgap, structural stability, and optical performance of these monolayers have been adjusted through surface functionalization. Except for $ScYCO_2$, all other monolayers Y_2CO_2, $Y_2C(OH)_2$, and $ScYC(OH)_2$ are confirmed to be kinetically stable based on their phonon dispersion curves. Y_2CO_2 is an insulator with an indirect bandgap of 3.67 eV, while the addition of hydrogen along with oxygen results in $ScYC(OH)_2$ and $Y_2C(OH)_2$ becoming semiconductors with direct bandgaps of 1.12 eV and 1.09 eV, respectively. The -OH group induces a redshift in the absorption behavior of these monolayers due to absorption peaks in the visible region as well as in IR regions. These results indicate that -OH functionalization enhances the suitability of Y_2C and ScYC monolayers for optoelectronic applications due to the direct bandgap and absorption in both the infrared and visible regions.

ACKNOWLEDGEMENTS

This work was supported by the Knowledge Consortium of Gujarat (KCG) for granting the SHODH-ScHeme Of Developing High quality research Fellowship for supporting this research. [Student Ref. No. – 2022017421 (Nidhi Modi), 2022017442 (Yashasvi Naik), 2021017467 (S. J. Khengar)]

REFERENCES

[1] A.H. Castro Neto, F. Guinea, N.M.R. Peres, K.S. Novoselov, A.K. Geim, The electronic properties of graphene, Rev. Mod. Phys. 81 (2009) 109–162. https://doi.org/10.1103/RevModPhys.81.109.

[2] M. Naguib, M. Kurtoglu, V. Presser, J. Lu, J. Niu, M. Heon, L. Hultman, Y. Gogotsi, M.W. Barsoum, Two-Dimensional Nanocrystals Produced by Exfoliation of Ti 3 AlC 2, (2011) 4248–4253. https://doi.org/10.1002/adma.201102306.

[3] M. Khazaei, A. Ranjbar, K. Esfarjani, D. Bogdanovski, R. Dronskowski, S. Yunoki, Insights into exfoliation possibility of MAX phases to MXenes, Phys. Chem. Chem. Phys. 20 (2018) 8579–8592. https://doi.org/10.1039/c7cp08645h.

[4] E. Pakizeh, M. Mohammadi, A. Mostafaei, Effect of Hydrogen concentration on the structural, electronic and optical properties of 2D monolayer MXenes: DFT study, Solid State Commun. 369 (2023) 115214. https://doi.org/10.1016/j.ssc.2023.115214.

[5] K. Xiong, Z. Cheng, J. Liu, P.-F. Liu, Z. Zi, Computational studies on functionalized Janus MXenes MM′CT 2 , (M, M′ = Zr, Ti, Hf, M ≠ M′; T = –O, –F, –OH): photoelectronic properties and potential photocatalytic activities , RSC Adv. 13 (2023) 7972–7979. https://doi.org/10.1039/d3ra00303e.

[6] P. Giannozzi, S. Baroni, N. Bonini, M. Calandra, R. Car, C. Cavazzoni, D. Ceresoli, G.L. Chiarotti, M. Cococcioni, I. Dabo, A.D. Corso, S. De Gironcoli, S. Fabris, G. Fratesi, R. Gebauer, U. Gerstmann, C. Gougoussis, A. Kokalj, M. Lazzeri, L. Martin-samos, N. Marzari, F. Mauri, R. Mazzarello, S. Paolini, A. Pasquarello, L. Paulatto, C. Sbraccia, A. Smogunov, P. Umari, Q UANTUM ESPRESSO : a modular and open-source software project for quantum simulations of materials, (2009). https://doi.org/10.1088/0953-8984/21/39/395502.

[7] G. Pizzi, V. Vitale, R. Arita, S. Blügel, F. Freimuth, G. Géranton, M. Gibertini, D. Gresch, C. Johnson, T. Koretsune, J. Ibañez-Azpiroz, H. Lee, J.M. Lihm, D. Marchand, A. Marrazzo, Y. Mokrousov, J.I. Mustafa, Y. Nohara, Y. Nomura, L. Paulatto, S. Poncé, T. Ponweiser, J. Qiao, F. Thöle, S.S. Tsirkin, M. Wierzbowska, N. Marzari, D. Vanderbilt, I. Souza, A.A. Mostofi, J.R. Yates, Wannier90 as a community code: New features and applications, J. Phys. Condens. Matter. 32 (2020). https://doi.org/10.1088/1361-648X/ab51ff.

[8] H.J. Monkhorst, J.D. Pack, Special points for Brillonin-zone integrations, 13 (1976) 5188–5192. https://doi.org/http://prb.aps.org/pdf/PRB/v13/i12/ p5188_1.

[9] D.R. Hamann, M. Schlüter, C. Chiang, Norm-Conserving Pseudopotentials, Phys. Rev. Lett. 43 (1979) 1494–1497. https://doi.org/10.1103/PhysRevLett.43.1494.

[10] N. Modi, Y. Naik, S.J. Khengar, P.H. Jariwala, D.B. Shah, P.B. Thakor, Theoretical investigations of asymmetric functionalized Y2C-based MXene monolayers, Solid State Commun. 372 (2023) 115303. https://doi.org/https://doi.org/10.1016/j.ssc.2023.115303.

A DFT study of electronic, optical and mechanical properties of $LiBaBr_3$ perovskite for opto-electronic applications

Anuradha[1,a], Sunil Kumawat[1] and Gunjan Arora[1]

[1]*Department of Physics, University College of Science, Mohanlal Sukhadia University, Udaipur, 313001 Rajasthan, India.*

[a)] Corresponding author: anuradhabarala82@gmail.com

Abstract. We present ab initio calculations to determine the electronic, optical, and mechanical characteristics of $LiBaBr_3$ opto-electronic material. Opto-electronic simulations for lead-free perovskite compound are done using Perdew-Burke-Ernzerhof approach. The electronic band structure computations for $LiBaBr_3$ revealed a band gap of 2.895 eV with indirect nature. Moreover, the dielectric constant and absorption coefficient of $LiBaBr_3$ are reported that suggest its possible utilization in opto-electronic devices.

INTRODUCTION

A large amount of energy expenditure has attracted researchers to focus on renewable energy sources. Researchers have done extensive researches on material, which show their potential in significant opto-electronic applications. Halide perovskites are a class of materials that are used in opto-electronic devices [1, 2]. In cubic ABX_3 structure, B and X form a corner shared octahedral BX_6 in three dimensions where, the A-site cation is present in the cage formed by the octahedral and surrounded by 12 evenly spaced anions [3].

Metal halide perovskites, AMX_3 where A/M = rare-earth/alkali-earth, X = Br, Cl, F, I) show promising optical properties. The direct/indirect band gap characteristics of these compounds can be controlled by various chemical adjustments [4]. For the study of potential applications of $Li(Be,Mg)F_3$ perovskite compounds in opto-electronic and UV protection devices, ab-inito calculations have been utilized to evaluate the electronic structure and optical absorption characteristics of these compounds [5,6]. Perdew-Burke-Ernzerhof (PBE) methodology have been precisely applied in the current work for the study of structure of energy bands and partial and total density of states (DOS) and optical properties of $LiBaBr_3$ perovskite. Additionally, we have deduced mechanical characteristics for the verification of mechanical stability of this compound.

COMPUTATIONAL DETAILS

PBE approach is employed in this study, which is implemented using the WIEN2k code, to explore the mechanical, electronic and optical properties of $LiBaBr_3$ crystallizing in cubic structure [7, 8]. First of all, the lattice parameter for $LiBaBr_3$ is taken as 6.2792 Å for space group Pm-3m (221) [4]. The energy optimization tool is used to improve its value for greater precision. Until the strain and stress on every atom were zero, the structural optimization procedure was continuously carried out. Murnaghan's equation of state, (displayed in Fig. 1 (a)), was used to plot the volume vs total energy curves to calculate the optimized lattice parameters [9]. We calculated the opto-electronic characteristics of $LiBaBr_3$ using 1000 k-points and the mechanical properties with 3000 k-points.

RESULTS AND DISCUSSION

Electronic properties

The motion of electrons through a substance is characterized by its electronic properties. The electronic properties of $LiBaBr_3$ compound are computed in the form of energy bands and DOS using PBE potential, along the first BZ, (shown in Fig. 1 (b and c)).

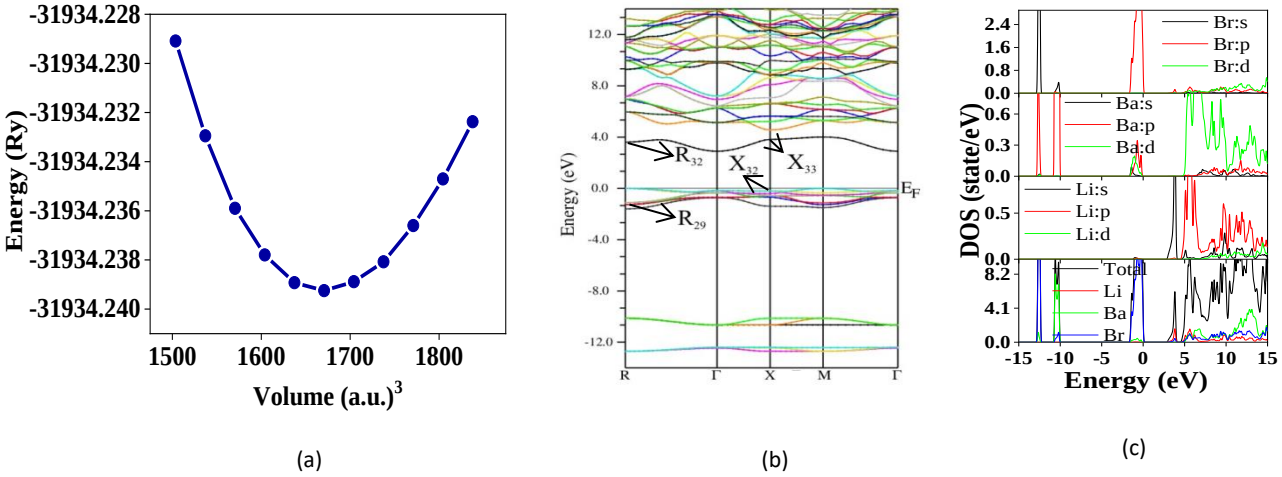


FIGURE 1. (a) Energy v/s volume optimization, (b) band structure and (c) density of states curves for $LiBaBr_3$ computed using PBE approach.

The results indicate that $LiBaBr_3$ shows an indirect band gap, since the maxima of valence band (VB) and minima of conduction band (CB) fall at the points M and Γ of the BZ, respectively. Band gap of $LiBaBr_3$ is found as 2.895 eV, which is very near to that reported by Kaleemullah et al. [4], as 2.905 eV. We now explain the partial and total DOS curves. Bands at energy -12 eV are mostly produced by the Br-s state, whereas bands around -10 eV are formed by the mixing of the Ba-p and Br-s states. Electronic states namely Ba-p, Ba-d, and Br-p are responsible for bands in the topmost valence region (-2 to 0 eV). Slightly above the Fermi energy level the bands are generated by Li-s state. The Li-s, Li-p, Li-d and Ba-d states are the main sources for the creation of the bands in the energy above 4 eV.

Optical properties

We have verified the potential usage of $LiBaBr_3$ in photovoltaic and opto-electronic applications by analyzing its optical properties. Moreover, the optical characteristics of a material are determined by dielectric tensor [10]. Fig. 2 (a and b) displays the energy-dependent $\varepsilon_1(\omega)$ and $\varepsilon_2(\omega)$ for $LiBaBr_3$.

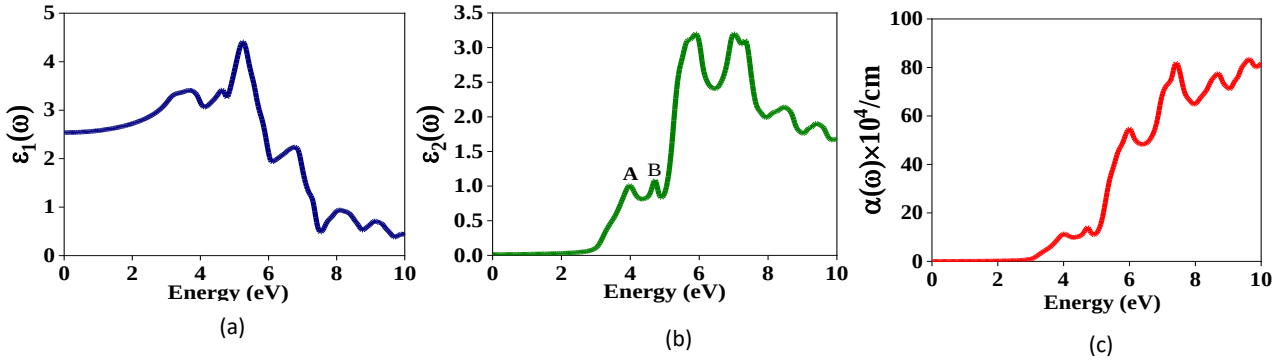


FIGURE 2. (a) Real part of dielectric constant, $\varepsilon_1(\omega)$, (b) imaginary part of dielectric constant, $\varepsilon_2(\omega)$, (c) absorption, α (ω), of $LiBaBr_3$ computed using PBE theory.

The threshold energy is determined as 2.884 eV in the spectrum of $\varepsilon_2(\omega)$, represents the electronic transitions between the VB and the CB and it, is in close proximity to the computed energy gap of $LiBaBr_3$. Different inter band transitions can be used to explain the peaks detected in the $\varepsilon_2(\omega)$ spectrum. When electrons transit from the p state of Ba and Br atoms to the Li-s state, for instance, peak A at 3.975 eV is created (Fig. 2(b)). This transition corresponds to the electron movement from X_{32} to X_{33} band (Fig. 1(b)). As an electron moves from the Ba-d state to the Li-s state, which corresponds to the R_{29} to R_{33} band transition, the peak B at energy 4.7166 eV is created.

The absorption spectrum $\alpha(\omega)$, of any compound is widely acknowledged as the most important factor to consider while thinking about its opto-electronic and photovoltaic applications. To compute this, one can utilize $\varepsilon_1(\omega)$ and $\varepsilon_2(\omega)$ [10]. The absorption coefficient computed using PBE potential is demonstrated in Fig. 2 (c).

Mechanical properties

The mechanical stability of $LiBaBr_3$ is investigated by calculating the elastic constants C_{ij} using the PBE potential. For the cubic crystal structure, the mechanical stability criteria are given by elastic constants as $C_{11} > 0$, $C_{44} > 0$, $C_{11} > C_{12}$ and $(C_{11}+2C_{12}) > 0$ [11]. Values calculated for C_{11}, C_{12}, C_{44} and elastic moduli viz. bulk modulus (B), and shear modulus (G) are 36.756, 3.699, 1.598, 14.718 and 5.036 GPa, which prove mechanical stability and ductile nature for $LiBaBr_3$.

CONCLUSION

In the current study, PBE potential is used to investigate the opto-electronic properties of lead-free halide perovskite $LiBaBr_3$. Based on the band structure designs, we observed that $LiBaBr_3$ possesses an indirect band gap of 2.895 eV. Suitable band gap, reasonably excellent absorption spectra (0–5 eV) and environmental friendly nature of lead-free $LiBaBr_3$ perovskite is recommended for the application of photovoltaic and opto-electronic devices.

ACKNOWLEDGEMENTS

We are grateful to Prof. P. Blaha for facilitating us with the WIEN2k code. This work is financially supported by the University Grants Commission (UGC), New Delhi through junior research fellowship (No. 201610150226) awarded to Anuradha. Fundings from the research project RUSA 2.0, MHRD, New Delhi (No. F.30 (16)SPD/RUSA/2016/178), sanctioned to GA are also highly acknowledged.

REFERENCES

1. N.K. Tailor, A. Listorti, S. Collela and S. Satapathi, Adv. Mater. Technol. **8** 2200442 (2023).
2. H. Wang, C. Zhang, W. Huang, X. Zou, Z. Chen, S. Sun, L. Zhang, J. Li, J. Cheng, S. Huang, M. Gu, X. Chen, X. Guo, R. Guia and W. Wang, Phys. Chem. Chem. Phys. **24** 27585-27605 (2022).
3. Q. A. Akkerman and L. Manna, ACS Energy lett. **5** 604-610 (2020).
4. N.S. Kaleemullah, M.S. Hussain, V. Ashwin, G. Ajay and M.M.S. Sirajuddeen, Chem. Phys. Impact **8** 100545 (2024).
5. M.K. Shahzad, S. Hussain, M. Riaz, H. Sattar, G. A. Ashraf, W. Azeem, S.M. Ali and M. Alam, Heliyon **10** e29143 (2024).
6. K.E. Babu, K. Neeraja, D. Deenabandhu, A.M. Vijaya Ratna, V.V. Kumar, K.B. Kumari, P. Taddesse, G.T. Aregai, M.V.K. Mehar, B.V. Babu, K. Samatha and V. Veeraiah, J. Phys. Conf. Ser. **1495** 012010 (2020).
7. P. Blaha, K. Schwarz, G.K.H. Madsen, D. Kvasnicka and J. Luitz, An Augmented Plane Wave Local Orbitals Program for Calculating Crystal Properties, 2001.
8. J.P. Perdew, K. Burke and M. Ernzerhof, Phys. Rev. Lett. **77** 3865-3868 (1996).
9. V. Nayak, S. Banger and U.P. Verma, AIP Conf. Proc. **1591** 1095-1097 (2014).
10. Z. Jin, Y. Wu, S. Li, S. Chen, W. Zhang, Q. Wu and C. Zhang, Mater. Res. Express **6** 125116 (2019).
11. H. Benmhidi, H. Rached, D. Rached and M. Benkabou, J. Electron. Mater. **46** 2205-2210 (2017).

A DFT Study on Optoelectronic Properties of $GaAlS_2$ Homo-bilayer

Disha Mehta[1, a)], Yashasvi Naik[1], Nidhi Modi[2], P. R. Parmar[1], and P. B. Thakor[1]

[1]*Department of Physics, Veer Narmad South Gujarat University, Surat, Gujarat, 395007, India.*
[2]*Department of Physics, Sir P. T. Sarvajanik College of Science, Surat, Gujarat, 395001, India*

[a)]Corresponding author: dishamehta47@gmail.com

Abstract. In the present study, the optoelectronic behaviour of $GaAlS_2$ homo-bilayer has been explored using a density functional approach. The calculation of adhesive energy and phonon validates the energetic and dynamic stabilities of the $GaAlS_2$ bilayer. The band gap of bilayer $GaAlS_2$ homo-bilayer is 2.30 eV which shows its indirect semiconductor nature. The optical behaviour indicates a significant enhancement in the absorption of the $GaAlS_2$ homo-bilayer compared to the $GaAlS_2$ monolayer. There is a significant increment observed in the reflectivity of the $GaAlS_2$ homo-bilayer. The outcomes suggest that $GaAlS_2$ homo-bilayer is a promising applicant for optoelectronic devices, UV detectors and UV absorbers.

INTRODUCTION

The successful experimental fabrication of graphene [1] as a two-dimensional (2D) material has sparked significant interest in the field of 2D materials, leading researchers to explore the utilization of 2D materials in optoelectronic devices due to their compelling potential. 2D materials exhibit diverse forms in bulk, characterized by layers that are tightly bonded internally but exhibit weak attraction between adjacent layers [2]. This characteristic facilitates the separation of monolayer (ML) from its bulk form [3]. The interactions between adjacent layers substantially affect the electronic characteristic of the material, underscoring the importance of studying bilayers (BL) in depth [4]. Recently, Radha Somaiya and their team have explored the $SiSe_2$ bilayer as a potential applicant for optoelectronic devices [3]. Chenhai Shen et al. have investigated the optoelectronic characteristic of the PbI_2 bilayer and analyzed the stacking effect on it [4]. These studies motivated us to investigate the optoelectronic properties of $GaAlS_2$ homo-bilayer. The $GaAlS_2$ monolayer has been investigated in our previous study [5]. The recent study includes a comparison of the electronic and optical characteristics between $GaAlS_2$ monolayer and homo-bilayer.

COMPUTATIONAL METHODS

Density Functional Theory (DFT) was employed to theoretically study the homo-bilayer of $GaAlS_2$ using the Quantum ESPRESSO software [6]. The computation was performed using the Projector Augmented Wave (PAW) [7] type pseudopotential. The Heyd Scuseria Ernzerhof (HSE06) functional has been employed to accurately determine the band structure. The van der Waals correction DFT-D3 [8] has been utilized to incorporate the interlayer interaction of the bilayer. The system was optimized with a force tolerance of 1×10^{-3} Ry/Bohr and an energy cut-off of 1×10^{-3} Ry. A Monkhorst pack grid [9] consisting of 6×6×1 k-point was taken to represent the first Brillouin zone. The interaction of the $GaAlS_2$ bilayer with other layers vanished by establishing a vacuum of 20 Å. The optical characteristics were computed by using Yambo software [10].

RESULTS AND DISCUSSIONS

Structure

Figure 1 (a) demonstrates the side view of $GaAlS_2$ monolayer. The hexagonal unit cell of the $GaAlS_2$ monolayer contains 4 atoms. Figure 1 (b and c) displays side view stacking AA and AB of $GaAlS_2$ homo-bilayer. The interlayer distance between the adjacent layers of AA stacking is 3.56 Å which indicates the weak interaction between two layers while the inter layer distance for AB stacking is 3.20 Å. Hence, in our further study, we have neglected the AA stacking and considered AB stacking for all calculations. Figure 1 (d and e) illustrates the top and bottom view of AB stacking of the $GaAlS_2$ bilayer. The lattice constant of the $GaAlS_2$ bilayer is 3.58 Å. The

energetic and dynamic stability of the $GaAlS_2$ bilayer is verified from the calculation of adhesive energy and phonon curve. The value of adhesive energy for the $GaAlS_2$ bilayer is -1.03 eV calculated from the equation mentioned in our previous study [5], indicating that the $GaAlS_2$ homo-bilayer is energetically stable. Figure 1 (f) represents the phonon curve of the $GaAlS_2$ bilayer. All positive frequencies in the phonon curve validate the dynamical stability of the $GaAlS_2$ bilayer.

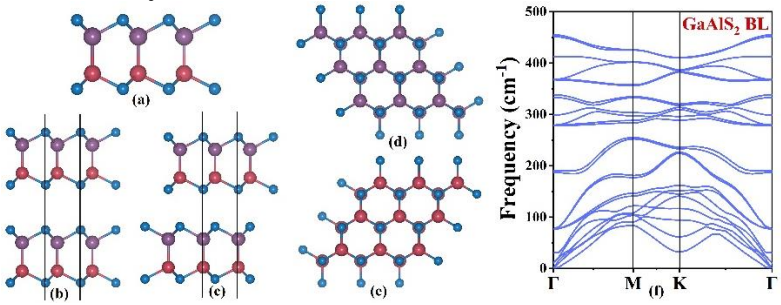


Figure 16. (a) Side perspective of ML $GaAlS_2$, (b) AA stacking of $GaAlS_2$ bilayer, (c) AB stacking of bilayer; (d and e) top and bottom perspective of $GaAlS_2$ bilayer; (f) phonon curve of $GaAlS_2$ bilayer

Optoelectronic performance

Figure 2 (a and b) depicts the band structure and partial density of states (PDOS) of ML $GaAlS_2$ while Figure 2 (c and d) displays the band structure and PDOS of $GaAlS_2$ homo-bilayer. The HSE functional has been used to get accurate values of the band gap. The bandgap of ML $GaAlS_2$ and homo-bilayer is 2.87 eV and 2.30 eV. There is a slight decrement in the band gap of the $GaAlS_2$ bilayer compared to its monolayer. The PDOS of the $GaAlS_2$ bilayer signifies that the valance band contain the dominant contribution of the S atom while the conduction band possess a significant contribution of Ga, Al and S all atoms.

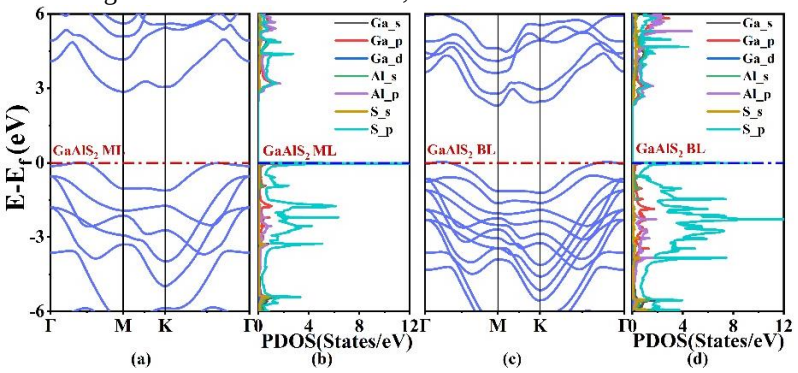


Figure 17. (a) Band structure, (b) PDOS of ML $GaAlS_2$; (d) band structure, (e) PDOS of bilayer $GaAlS_2$

Figure 3 (a, b, c, and d) depicts the real part, imaginary part, absorption coefficient, and reflectivity of $GaAlS_2$ monolayer and bilayer. The real part indicates that the static dielectric constant (SDC) of the $GaAlS_2$ bilayer is 5.19. The SDC increases for the bilayer in comparison with the monolayer. The interband transitions are analyzed from the imaginary portion of the complex dielectric function calculated from the equation mentioned in our previous study [5]. The interband transitions increase for the $GaAlS_2$ bilayer with the res shift compared to its monolayer. The absorption coefficient is calculated from the equation mentioned in our previous study [5]. The absorption starts from the visible region and goes maximum in the ultraviolet (UV) region similar to monolayer. There is a noticeable increment in the absorption of the $GaAlS_2$ bilayer in the visible region and a significant increment in the UV region compared to its monolayer. The static reflectivity of the $GaAlS_2$ bilayer is 12.27% while the maximum reflectivity is 28.13%. Hence, the $GaAlS_2$ homo-bilayer is a promising candidate for optoelectronic devices, UV detectors and UV absorbers.

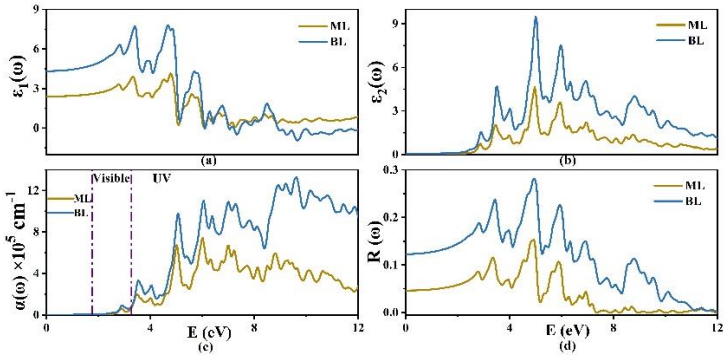


Figure 18. (a, b, c, and d) Real part, imaginary part, absorption coefficient, and reflectivity of $GaAlS_2$ monolayer and bilayer

CONCLUSIONS

In the present research, the optoelectronic performance of the $GaAlS_2$ homo-bilayer has been explored by utilizing first principles calculations. The $GaAlS_2$ bilayer is energetically and dynamically stable bilayer confirmed by the calculations of adhesive energy and phonon spectra. The indirect band gap of the $GaAlS_2$ bilayer is 2.30 eV which indicates its semiconductor behaviour. There is a slight decrement in the band gap of the $GaAlS_2$ bilayer compared to its monolayer. The optical performance indicates a significant enhancement in absorption and reflectivity of the $GaAlS_2$ bilayer compared to the $GaAlS_2$ monolayer. The findings suggest the promising application of $GaAlS_2$ homo-bilayer in optoelectronic devices, UV detectors and UV absorbers.

REFERENCES

[1] A.A.F. K. S. Novoselov, A. K. Geim, S. V. Morozov, D. Jiang, Y. Zhang, S. V. Dubonos, I. V. Grigorieva, Electric Field Effect in Atomically Thin Carbon Films, Indian J. Biochem. Biophys. 16 (1979) 61–65.

[2] K.S. Novoselov, D. Jiang, F. Schedin, T.J. Booth, V. V Khotkevich, S. V Morozov, A.K. Geim, Two-dimensional atomic crystals, 102 (2005) 10451–10453.

[3] R.N. Somaiya, Y. Sonvane, S.K. Gupta, Van der waals SiSe2 homo-bilayers for optoelectronics applications, Superlattices Microstruct. 152 (2021) 106858. https://doi.org/https://doi.org/10.1016/j.spmi.2021.106858.

[4] C. Shen, G. Wang, Electronic and optical properties of bilayer PbI2: a first-principles study, J. Phys. D. Appl. Phys. 51[1] R.N. (2018) 35301. https://doi.org/10.1088/1361-6463/aa9cd5.

[5] D. Mehta, N. Modi, S.J. Khengar, P.H. Jariwala, P.B. Thakor, A GaAlS2 Janus Monolayer as a Promising Candidate for Optoelectronic Devices, Mater. Today Proc. (2023) 2–5. https://doi.org/10.1016/j.matpr.2023.01.341.

[6] P. Giannozzi, S. Baroni, N. Bonini, M. Calandra, R. Car, C. Cavazzoni, D. Ceresoli, G.L. Chiarotti, M. Cococcioni, I. Dabo, A.D. Corso, S. De Gironcoli, S. Fabris, G. Fratesi, R. Gebauer, U. Gerstmann, C. Gougoussis, A. Kokalj, M. Lazzeri, L. Martin-samos, N. Marzari, F. Mauri, R. Mazzarello, S. Paolini, A. Pasquarello, L. Paulatto, C. Sbraccia, A. Smogunov, P. Umari, Q UANTUM ESPRESSO : a modular and open-source software project for quantum simulations of materials, (2009). https://doi.org/10.1088/0953-8984/21/39/395502.

[7] P.E. Blöchl, Projector augmented-wave method, Phys. Rev. B. 50 (1994) 17953–17979. https://doi.org/10.1103/PhysRevB.50.17953.

[8] S. Grimme, J. Antony, S. Ehrlich, H. Krieg, A consistent and accurate ab initio parametrization of density functional dispersion correction (DFT-D) for the 94 elements H-Pu, J. Chem. Phys. 132 (2010) 154104. https://doi.org/10.1063/1.3382344.

[9] J.D.P. Hendrik J. Monkhorst, Special points for Brillouin-zone integrations, J. Mater. Chem. A. 7 (2019) 2156–2164. https://doi.org/10.1039/c8ta11250a.

[10] A. Marini, C. Hogan, M. Gr, D. Varsano, yambo : an ab initio tool for excited state calculations, (n.d.).

MgClBr vdW homobilayer as a promising UV-light detector

Yashasvi Naik [1, a)], Disha Mehta[1], H. R. Mahida[2], Riddhi Desai[1], and P. B. Thakor[1]

[1]*Department of Physics, Veer Narmad South Gujarat University, Surat, Gujarat, India. 395007.*
[2]*Navyug Science College, Surat, Gujarat, India. 395009*

[a)] *Corresponding author: yashasvinaik18@gmail.com*

Abstract. In this study, the optoelectronic characteristics of a newly predicted MgClBr homo-bilayer have been examined using Density Functional Theory. Two different stacking configurations, AA and AB are considered for the calculation. To confirm its thermal and dynamical stability, both AIMD simulations and phonon spectrum analysis have been conducted, demonstrating that it is stable in both aspects. The MgClBr HBL shows the insulator nature with wide bandgap of 5.91 eV, using HSE06 functional. Additionally, the absorption spectrum covers a broad range of spectrum. The obtained static refractive index is 1.42 for MgClBr HBL. However, there is a significant absorption in the UV region. This highlights its potential for use in opto-nano devices applications and UV-light detectors.

INTRODUCTION

Many two-dimensional (2D) systems can be exfoliated from their bulk forms due to weak interlayer attractions, allowing them to be cleaved into monolayers. Graphene, derived from graphite, stands out for its linear electronic band structure, exceptional thermal conductivity, and high carrier mobility [1]. Examining such layered configuration helps us to understand monolayer (ML) and bilayer (BL) behavior. These 2D materials, with their layer-controlled direct energy gap, and unique in-plane anisotropy, makes them suitable for thermoelectric applications. Over hundreds of members from the 2D system are studied extensively, including, TMDs, MXenes, Halides, etc. Among which, Halide is gaining the large attention due to their intriguing electronic, magnetic and topological properties. Huang et al. has systematically explored Halides such as MX (X = Cl, I, Br; M = Cu, Ag) MLs. Mahida et al has theoretically MgF_2 and $MgCl_2$ [2], and found its potential application in nano-optoelectronic devices. Materials with a wide bandgap can be limited in their applications, but this can be tuned by doping, applying strain or electric fields, and altering the number of material layers [3]. Recently, Kasipour et al. has theoretically studied the CuI ML and BL [4]. MgClBr ML has been examined previously, which shows excellent properties useful in various domain [5]. Due to MgClBr ML's excellent properties, we have constructed a MgClBr homo-bilayer (HBL) to study its behavior. To the best of our knowledge, there are no research papers on MgClBr HBL. In this study, we thoroughly examine the optoelectronic properties of MgClBr HBL by utilizing first-principles density functional theory (DFT).

COMPUTATIONAL DETAILS

In this research, all the simulations have been performed within the DFT [6] framework by Quantum Espresso software. The Projected-Augmented-Wave type pseudopotential is used to describe electron-ion interaction. To obtain an accurate bandgap, a hybrid functional HSE06 given by Heyd-Scuseria-Ernzerhof is utilized. The DFT-D3 method given by Grimme has been utilized to provide an accurate representation for the Vander Waals (vdW) interactions [7]. A thick vacuum of 20 Å is given in a perpendicular direction in order to prevent interactions between two layers. The energy and force threshold are set to 10^{-6} Ry and 10^{-4} Ry/Bohr, respectively, to obtain structural optimization and system convergence. The Monkhorst-Pack k-point grid is fixed at 6×6×1 and plane wave energy cut-off are fixed at 600 Ry. The optical properties are obtained by using the Norm-conserving pseudopotential and frequency-dependent complex dielectric function $\varepsilon(\omega)$.

RESULTS AND DISCUSSIONS

Geometric Structure, Stability and Electronic property

Figure 1(a and b) depicts the two distinct stacking configuration AA and AB in the top and side view. The lattice parameter is 3.74 Å and 3.75 Å for AA and AB stacking, respectively. The interlayer distance is 3.30 Å and 3.26 Å for AA and AB stacking, respectively. The AA stacking is excluded because of its larger interlayer distance. So, the AB stacking is the most stable due to its smaller interlayer distance, which signifies the stronger interlayer interactions. The data of MgClBr ML is shown here for the comparison. In order to confirm the energetic stability of MgClBr HBL, the binding energy E_b is obtained from the equation, $E_b = E_{HBL} - 2E_{ML}$ [8]. Where E_{HBL} and E_{ML} corresponds to overall energy of MgClBr HBL and ML, respectively. The obtained negative binding energy is -1.01 eV for AB stacking, which confirms that MgClBr HBL is energetically favorable. Further, the dynamic stability is ensured from phonon spectra as it has no imaginary frequency present (Figure 1(e)). Moreover, the thermal stability at 300 K is confirmed by AIMD calculation because it shows no structural deformation and less energy variation, depicted in Figure 1(c). The AIMD simulation is performed for 3.5 ps with a time interval of 1fs.

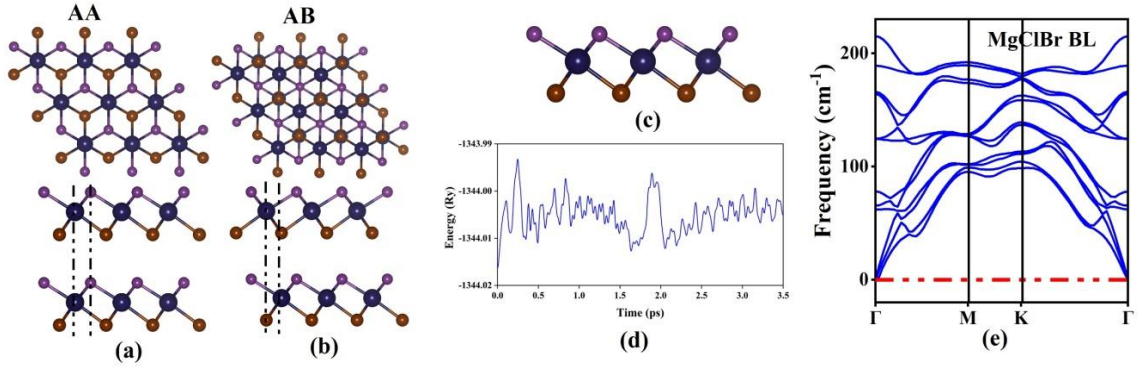


Figure 19. (a, b) Top, side view of MgClBr BL, (c)Side view of MgClBr ML, (d & e) AIMD and Phonon spectra of MgClBr BL

Figure 2(a and b) illustrates the band diagram of MgClBr ML and BL, respectively, at HSE level. The band diagram is obtained along highly symmetric direction 'Γ-M-K-Γ'. MgClBr BL and MgClBr ML has a wide bandgap of 5.91 eV and 6.08 eV, respectively. Both displays the direct "Γ-Γ" type bandgap. This shows that the bandgap can be tuned by increasing the number of layers. The Projected Density of States (PDOS) is also examined to get better insight into the electronic properties. It is clear from the figure that VBM is dominated by Br-p and Cl-p state while the CBM is influenced by Mg-s state. Furthermore, to study the charge localization of MgClBr HBL, the Electron Localization function (ELF) has been examined as in Figure 2(d). In which, red indicates the highest electron concentration, while blue indicates the lowest. The electrons are mainly localized around the Cl atoms and less around Br atoms. The negligible electron localization between layers suggests that only vdW bonds exist between them.

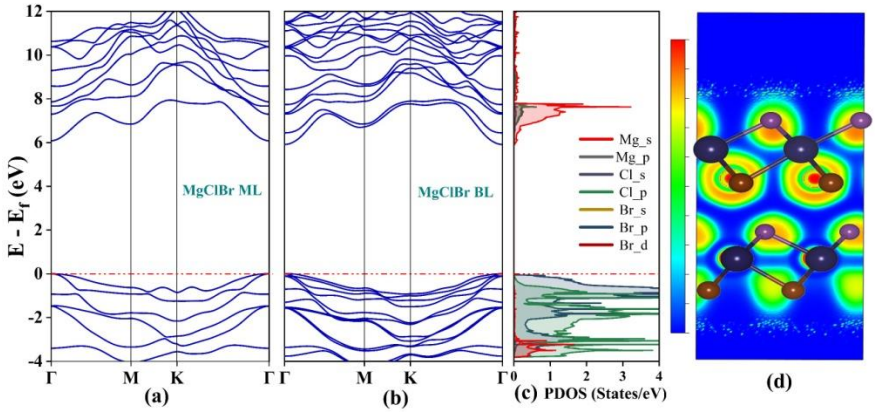


Figure 20. Band diagram of (a) MgClBr ML (b) MgClBr HBL (c) PDOS of MgClBr of HBL (d) ELF of MgClBr HBL

Optical Properties

The optical response is calculated from the dielectric function (that is the function of frequency) $\varepsilon(\omega)$ given as $\varepsilon(\omega) = \varepsilon_1(\omega) + i\varepsilon_2(\omega)$. Here, $\varepsilon_1(\omega)$ and $\varepsilon_2(\omega)$ corresponds to the real and imaginary portion, respectively. The real part in Figure 3(a) shows that the static dielectric constant (SDC) of MgClBr HBL and ML is 2.02 and 1.48, respectively. The increment in SDC of $\varepsilon_1(\omega)$ implies that lower exciton binding energy which leads to an effective

hole and electrons separation. The dielectric function's imaginary portion is related to the interband transition, which is shown in Figure 3(b) exhibits several distinct peaks. Further, the relation between absorption coefficient and energy is displayed in Figure 3(c) [9]. The highest peak is observed at 7.51 eV and 7.74 eV for MgClBr HBL and MgClBr ML, respectively. It is seen from the figure that absorption of MgClBr HBL is enhanced from MgClBr ML. So, by comparing the absorption curve of both, it is seen that MgClBr HBL has better absorption performance. So, MgClBr HBL has great potential for efficient optoelectronic-nanoelectronics devices and photovoltaic application. Figure 3(d) shows the refractive index (RI) for MgClBr HBL and MgClBr ML. The RI at 0 eV is static Refractive index (SRI) which is 1.42 and 1.21 for MgClBr HBL and MgClBr ML. So, the MgClBr HBL has higher RI compared to MgClBr ML. The materials with high RI can be used as coating material in nano devices.

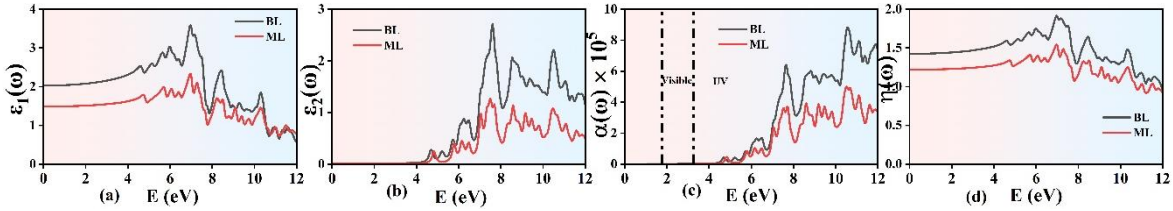


Figure 21. (a) Real Part, (b) Imaginary Part, (c) Absorption coefficient (d) Refractive index of MgClBr HBL and BL

CONCLUSIONS

The structural, and optoelectronic properties of MgClBr HBL have been investigated within the DFT framework by utilizing vdw correction and HSE06 functional. The dynamic and thermal stability of MgClBr HBL is verified from the obtained positive phonon spectra and AIMD calculation. The MgClBr HBL possesses a direct wide bandgap of 5.91 eV from HSE functional. The ELF is also examined for the MgClBr HBL. The optical properties show that MgClBr ML has comparatively low absorption in UV region, while MgClBr HBL has noticeable enhanced absorption in UV range than the MgClBr ML. So, the MgClBr HBL exhibits higher potential compared to its ML, that makes them well-suited for next generation nanoelectronics-optoelectronic devices and UV-light detector and emitters.

ACKNOWLEDGMENTS

This work was supported by the Knowledge Consortium of Gujarat (KCG) for granting the SHODH-ScHeme of Developing High quality research Fellowship for supporting this research. (Student Ref. No.– 2022017442, 2022017448).

REFERENCES

[1] A. Linggawati, K. Arifin, R.M. Yunus, Effect of External Electric Field Applied to Bilayer Graphene Bandgap: Density Functional Theory Study, International Journal of Integrated Engineering 14 (2022) 193–197. https://doi.org/10.30880/ijie.2022.14.02.023.

[2] H.R. Mahida, D. Singh, Y. Sonvane, MgF 2 monolayer as an anti-re fl ecting material, 252 (2017) 22–28. https://doi.org/10.1016/j.ssc.2017.01.005.

[3] A. Batool, Y. Zhu, X. Ma, M.I. Saleem, C. Cao, DFT study of the structural, electronic, and optical properties of bulk, monolayer, and bilayer Sn-monochalcogenides, Applied Surface Science Advances 11 (2022) 100275. https://doi.org/10.1016/j.apsadv.2022.100275.

[4] A. Kasipour-Rastekenari, H. Alavi-Rad, Intrinsic electronic and optical properties of monolayer and Bilayer CuI under many-body effects, Vacuum 215 (2023) 112357. https://doi.org/10.1016/j.vacuum.2023.112357.

[5] Y. Naik, D. Mehta, P.R. Parmar, P.B. Thakor, Impact of Strain on Electronic and Optical Properties of MgClBr Monolayer: First-principle Calculation, Comput Theor Chem 1228 (2023) 114278. https://doi.org/https://doi.org/10.1016/j.comptc.2023.114278.

[6] W. Kohn, A.D. Becke, R.G. Parr, Density Functional Theory of Electronic Structure, 0 (1996) 12974–12980. https://doi.org/https://doi.org/ 10.1021/jp96066.

[7] S. Grimme, J. Antony, S. Ehrlich, H. Krieg, A consistent and accurate ab initio parametrization of density functional dispersion correction (DFT-D) for the 94 elements H-Pu, J Chem Phys 132 (2010) 154104. https://doi.org/10.1063/1.3382344.

[8] R.N. Somaiya, Y. Sonvane, S.K. Gupta, Van der waals SiSe2 homo-bilayers for optoelectronics applications, Superlattices Microstruct 152 (2021) 106858. https://doi.org/10.1016/j.spmi.2021.106858.

[9] Y. Naik, D. Mehta, P.R. Parmar, P.B. Thakor, First-principles calculations to investigate structural and electronic properties of novel halides ZrIX (X = Cl, Br) for photovoltaic application, Physica B Condens Matter 673 (2024) 415499. https://doi.org/https://doi.org/10.1016/j.physb.2023.415499.

Quantum Computation of Small Atomic Clusters Using Subspace-Search Variational Quantum Eigensolver

Kaushik Das[1*], Narender Paul[2] and Ashok Kumar[1*]

[1]*Department of Physics, Central University of Punjab, Bathinda, Punjab, India 151401*
[2]*Department of Physics, Govt. Degree College Ani, Kullu, H.P., India 172026*
[*]*Corresponding authors: kd733585@gmail.com; ashokphy@cup.edu.in*

Abstract. The subspace-search variational quantum eigensolver (SSVQE) algorithm is used on various atomic clusters of Be, B and C atoms to find their ground state and 1st excited state energy values. Various approximations such as active space and freeze core have been used to reduce the quantum qubit in the computation. The approximations affect the energy values for quantum mechanically big clusters (C_4, B_4, etc.) This work also shows the use of the application of SingleExcitation and DoubleExcitation to build the ansatz. The final calculated energy values are compared with those calculated by the Hartree-Fock and DFT methods. The findings show that, when the ansatz and optimization are properly customized to the given situation, the SSVQE algorithm can consistently and accurately find both ground and excited state energies. This research highlights SSVQE's potential as a formidable tool for quantum simulations on upcoming quantum technology, providing a mechanism to achieve more accurate and thorough quantum chemistry and material science computations.
Keywords: SSVQE, energy values, ansatz, active space approximation, freeze core approximation

INTRODUCTION

In materials research, quantum computation is becoming a powerful instrument that makes it possible to simulate and analyse complex molecule structures[1]. The use of the Subspace-Search Variational Quantum Eigensolver (SSVQE) to calculate the electronic states of different molecules has recently been utilized for different systems [2]. Our goal is to improve molecular simulations' accuracy and efficiency over traditional methods by utilising quantum techniques. The recent past studies illustrate the promise of quantum computing in furthering materials science research by showing notable advances in quantum hardware and algorithms. The research also advances knowledge of applications of quantum computation in material science and chemistry. In this study, we demonstrate the performance of the SSVQE algorithm by benchmarking it against classical techniques such as Hartree-Fock and Density Functional Theory on various molecular clusters such as Be_2, Be_3, Be_4, B_2, B_3, B_4, C_2, C_3, C_4. The implications of this research pave the way for more sophisticated quantum simulations in the future.

METHODOLOGY

For the simulation, Pennylane framework is used[3] utilizing the SSVQE algorithm which is an extension of Variational Quantum Eigensolver (VQE) algorithm[4]. First the molecular Hamiltonian is constructed in terms of second quantization as:

$$H = \sum_{i,j} h_{i,j} a_i^\dagger a_j + \frac{1}{2}\sum_{ijkl} h_{ijkl} a_i^\dagger a_j^\dagger a_k a_l \quad \textbf{(1)}$$

Here a_i is annihilation and $a_i^\dagger$ is creation operator, h_{ij} and h_{ijkl} are first and second integral, respectively. Then molecular Hamiltonian is decomposed to qubit Hamiltonian as a linear combination of tensor products of Pauli matrices as:

$$H = \sum_j C_j \otimes \sigma_i^{(j)} \quad \textbf{(2)}$$

Where, C_j is a coefficient and σ_i is Pauli operator. As per the algorithm, a parameterized circuit $U(\theta)$ (ansatz) is applied to orthogonal input states $\{|\psi_i>\}$. To find all excited states up to k^{th} state, single optimization weighted SSVQE is used by minimizing the loss function which is given as:

$$L_\omega(\theta) = \sum_{j=0}^{k} w_j < \psi_j|U^\dagger(\theta)HU(\theta)|\psi_J > \quad \textbf{(3)}$$

Where, the weight w_j can have any value in (0,1). A suitable optimizer (e.g. Adam, Adagard, GradientDescent etc) is used during the simulation process.

RESULTS AND DISCUSSIONS

Using this method on various molecules, the ground and 1st excited state energy values are calculated. The ansatz quantum circuit used in the study is given in Figure 1.

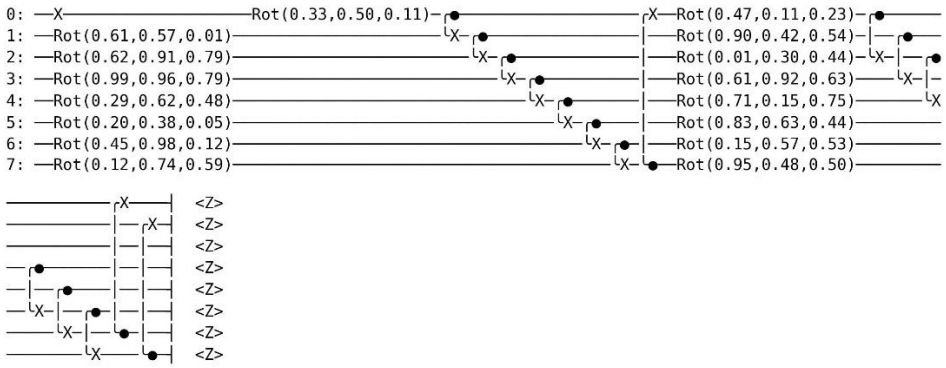


FIGURE 1. Ansatz quantum circuit having number of layers 2.

The clusters which are used in this simulation are Be_2, Be_3, Be_4, B_2, B_3, B_4, C_2, C_3, C_4 atoms. The freez core and active space approximation is used for various atomic clusters to obtain ground state and 1st excited state energy (Table 1). The restrictions like employing Slater-type basis sets and lowering the active space cause the error margin to rise and use of these approximations may affect the accuracy but at the same time the number of qubits for computation reduced greatly. Despite these accuracy for small atomic clusters are good enough (Table 2). The results are compared with the calculated data of HF and DFT studies collected from the database, CCCBDB[5]. Here, SSVQE algorithm is used because SSVQE is perfect for investigations that need both ground and excited state energies because of its ability to compute numerous eigenstates at once. Table 2 also indicates the accuracy of the SSVQE algorithm when benchmarked against the DFT and HF data. The Figure 2 shows that after 200 iterations the energy value of Be_2 atomic cluster is converges.

TABLE 1. Ground State and 1st excited state energy values of clusters of Be, B and C atoms.

System	Basis-sets	Active space	No. of qubits	Ground state energy (Ha)	1st excited energy (Ha)
Be_2	sto-3g	CAS(4,5)	10	-28.5468	-28.5474
	6-31g	CAS(4,5)	10	-28.8941	-28.8941
	6-311g	CAS(4,5)	10	-28.9030	-28.9030
Be_3	Sto-3g	CAS(6,5)	10	-36.5461	-36.5372
	6-31g	CAS(6,5)	10	-36.9236	-36.9125
	6-311g	CAS(6,5)	10	-36.9352	-36.9214
Be_4	Sto-3g	CAS(8,6)	12	-47.5024	-47.4139
	6-31g	CAS(8,6)	12	-47.9654	-47.9632
	6-311g	CAS(8,6)	12	-46.9658	-47.9641
B_2	Sto-3g	CAS(2,4)	8	-47.6426	-47.5592
	6-31g	CAS(2,4)	8	-48.2388	-48.2129
	6-311g	CAS(2,4)	8	-48.2367	-48.2254
B_3	Sto-3g	CAS(6,8)	16	-65.1694	-65.1624
	6-31g	CAS(6,8)	16	-65.2654	-65.2273
B_4	Sto-3g	CAS(8,8)	16	-75.6875	-75.6430
C_2	Sto-3g	CAS(4,4)	8	-73.0312	-73.0179
	6-31g	CAS(4,4)	8	-73.8631	-73.5321
C_3	Sto-3g	CAS(6,6)	12	-105.8845	-105.8712
	6-31g	CAS(6,5)	10	-105.9820	-105.9631
C_4	Sto-3g	CAS(8,8)	16	-140.4615	-140.4402

TABLE 2. Comparison of calculated energy from quantum computing with DFT and HF energy values.

System	HF (Ground state)(Ha)	DFT (Ground state)(Ha)	HF(1st excited state)(Ha)	DFT(1st excited state)(Ha)	SSVQE (Ground state)(Ha)	SSVQE(1st excited state)(Ha)
Be_2	-28.703	-28.629	-28.703	-28.629	-28.546	-28.547
B_2	-48.3503	-48.3283	-48.3503	-48.3283	-47.6426	-47.6412
C_2	-74.4220	-74.4463	-74.4220	-74.4463	-73.0312	-73.0179
C_3	-111.9066	-111.8625	-111.9066	-111.8625	-105.8845	-105.8712
C_4	-149.2456	-149.1736	-149.2456	-149.1736	-140.4615	-140.4402

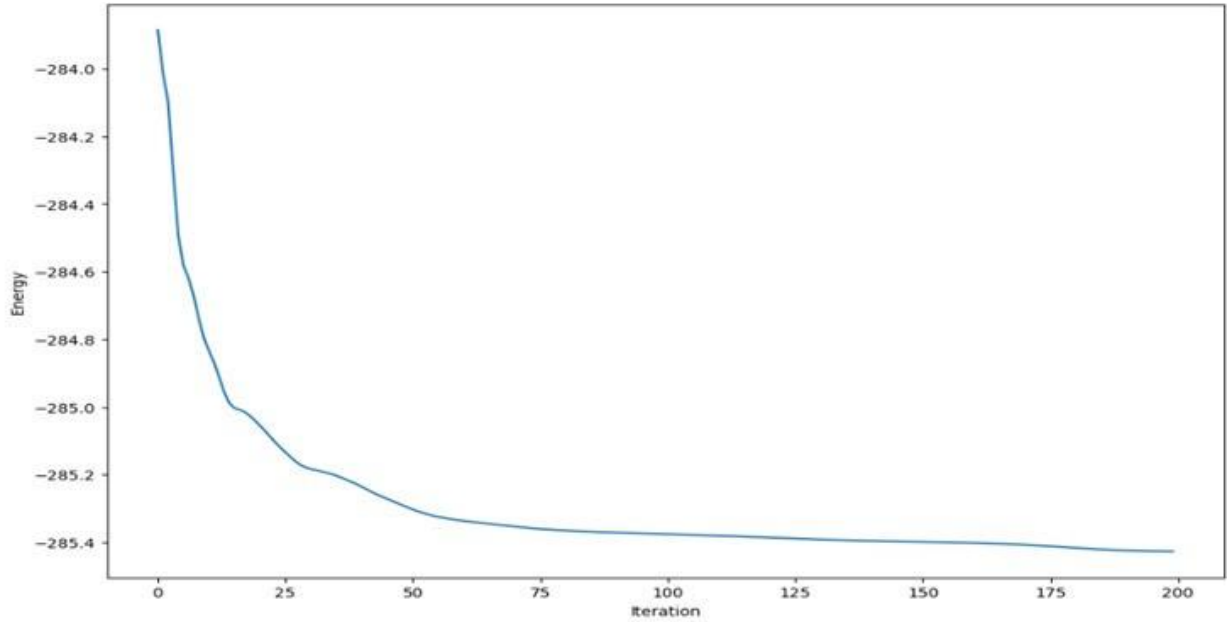


FIGURE 2. Energy convergence of Be_2 after certain iterations

CONCLUSIONS

In summary, Subspace-Search Variational Quantum Eigensolver algorithm is applied on the various atomic clusters to find the ground state and 1st excited state energy values. The approach works well in atomic cluster simulations, where knowledge of the excited states can reveal details like stability, optical features, and reaction routes. SSVQE can calculate energies with great accuracy by employing a variational technique, and as quantum hardware advances, its scalability will enable it to be used for bigger molecular systems in future.

ACKNOWLEDGEMENTS

Helpful discussions with Catalina Albornoz Anzola and Anibal Thiago Bezerra are highly acknowledged.

REFERENCES

1. RC de Souza Pimenta , AT Bezerra, *Phys Scr*. **98**, 045804 (2023).
2. K M Nakanishi, K Mitarai , K Fujii, *Phys Rev. Research*, **1**, 033062 (2019).
3. V Bergholm, J Izaac, M Schuld, C Gogolin, S Ahmed, V Ajith, et al. PennyLane: Automatic differentiation of hybrid quantum-classical computations. 2018, arxiv.org/abs/1811.04968
4. A Peruzzo , J McClean, P Shadbolt, MH Yung, XQ Zhou, PJ Love et al. *Nat. Commun.*, **5**, 4213 (2014).
5. CCCBDB database: https://cccbdb.nist.gov

CdS-Janus van der Waals Heterostructure for Green Hydrogen Fuel Production

G. Tejaswini[1], Anjana E Sudheer[1], M. Vallinayagam[2,3], M. Posselt[4], S. Mani Prakash[1], and D. Murali[1*]

[1] *Indian Institute of Information Technology Design and Manufacturing Kurnool 518008, Andhra Pradesh, India*
[2]*IEP, TU Bergakademie Freiberg, Akademiestraße 6, 09599 Freiberg, Germany*
[3]*Fakultät Maschinenbau/ Energietechnik/Physik, Hochschule für Technik und Wirtschaft Dresden, Friedrich-List-Platz 1, 01069 Dresden, Germany*
[4]*Helmholtz-Zentrum Dresden-Rossendorf, Institute of Ion Beam Physics and Materials Research, Bautzner Landstraße 400, 01328 Dresden, Germany*

[*] Corresponding author: dmurali@iiitk.ac.in

Abstract. Photocatalysis is one of the promising methods to produce green hydrogen by splitting the water molecule under solar irradiation. There are a large number of studies available on the CdS based photocatalyst due to its unique photocatalytic properties. However, CdS in its pristine form has a drawback of photoinstability due to photocorrosion effect. To improve the performance of the pristine CdS, a 2D-2D van der Waals heterostructure has been constructed with the Janus monolayer In_2SeTe. Due to their structural asymmetry, Janus materials have some peculiar properties associated with them. The properties of the constructed heterostructure have been investigated using Density Functional Theory. The geometrical and electronic properties of the designed heterostructure have been investigated systematically. The favorable staggered type band edge alignment and the intrinsic electric field in the heterostructure are suggesting the CdS-In_2SeTe as an excellent photocatalyst for hydrogen production.

INTRODUCTION

The continuous depletion of the fossil fuels into the environment is causing the global climate changes. So, there is an urgent need to find a substitute for the fossil fuels to solve the global energy and environment problems. The production of hydrogen by using solar energy and a semiconducting material is the best method with zero carbon emissions. However, the efficiency of the pristine bulk materials are far from ideal. Among different bulk materials, CdS is one of the most widely investigated photocatalytic material for green hydrogen production. Many studies on different dimensional CdS have been conducted by the researchers to improve the efficiency. In this study we have employed the technique of heterostructure construction to improve the efficiency of the CdS monolayer (ML). We have designed the CdS-In_2SeTe van der Waals heterostructure and investigated its photocatalytic properties. The reason for choosing Janus material is that, these materials have unique photocatalytic properties due to the polarization in the material which is arising due to the broken symmetry in their geometry. The built-in polarization in the Janus materials will be helpful in effective charge carrier separation. Thus, we have constructed the CdS-In_2SeTe heterostructure and investigated its basic geometrical and electronic properties.

COMPUTATIONAL DETAILS

The calculations are performed using Density Functional Theory (DFT) implemented in Vienna Ab-initio Simulation Package (VASP). Projected augmented wave pseudopotentials are used in calculations [1]. The PBE functional of the Generalized Gradient Approximation (GGA) is used to consider the exchange-correlation interactions. During the structural optimization the forces on each atom are converged to 0.001 eV/Å and the total energy is converged up to a threshold of 10^{-6} eV. A kinetic energy cut off of 650 eV and a 16 ×16×1 k-point grid is used for all the calculations. A vacuum of around 20 Å has been provided for all the structures to prevent the interaction between the neighboring layers. Tkatchenko-Scheffler method is used for van der Waals corrections.

RESULTS AND DISCUSSION

Before going for the design of the CdS-In_2SeTe interface, the structural and electronic properties of the CdS and In_2SeTe monolayers (MLs) have been explored. CdS ML is a planar structure with optimized lattice constant of 4.23 Å. The Cd-S bond length is 2.44 Å [2]. The pristine Janus In_2SeTe ML contains four atomic sublayers with two In layers sandwiched between the Se and Te atomic layers. The In2SeTe ML can be obtained from the relaxed structure of InSe (InTe) ML by substituting one layer of Se (Te) atoms with Te (Se) atoms. The optimized lattice constants of In_2SeTe ML is observed to be 4.20 Å with the bond distances 2.77 Å (In-In), 2.70 Å (In-Se) and 2.83 Å (In-Te) [3]. From the GGA level electronic structure calculations the band structure and projected density of states (PDOS) of the pure MLs have been studied. The CdS ML is found to be a direct band gap semiconductor with both the valence band maxima (VBM) and conduction band minima (CBM) at the center of the Brillouin zone. The observed band gap is 1.65 eV. From the PDOS, it is observed that the VBM of CdS ML is composed of Cd-d and S-p orbitals and the CBM originates from Cd-s and S-p orbitals. The In_2SeTe ML is also found to have a direct band gap of 1.16 eV with the positions of both VBM and CBM at the high symmetry Γ point. The CBM of In_2SeTe ML is dominated by s-orbitals of In whereas the VBM is dominated by p-orbitals of Te with partial contribution from p-orbitals of the In and Se atoms. All these observed geometrical information and electronic structure information results of the MLs are in good agreement with the reported results.

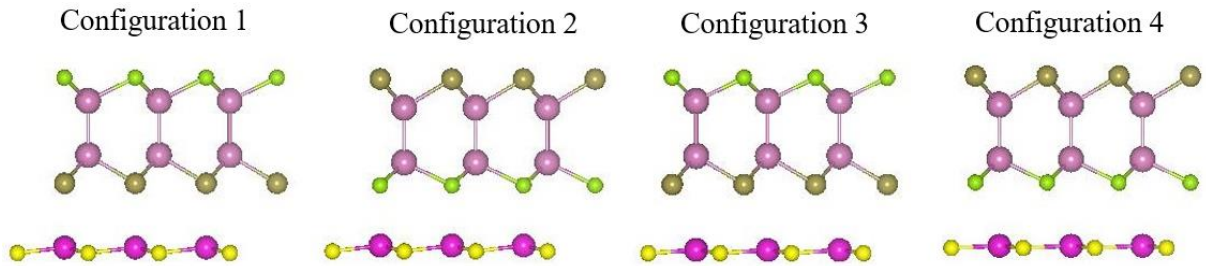


FIGURE 1. Four different stacking configurations of the CdS-In_2SeTe heterostructure

From the lattice constants of the both MLs, the observed lattice mismatch is 0.71% which is calculated using the formula $(a_{CdS} - a_{In2SeTe})/a_{In2SeTe}$ %. This ultra-low lattice mismatch between the MLs is favorable to construct the heterostructure. The structural optimization of the CdS-In_2SeTe heterostructure is done by keeping the volume of the unit cell as constant. The mean of the lattice parameters of pristine CdS and In_2SeTe MLs (4.215 Å) is taken as the lattice constant for the designed van der Waals heterostructure. Thus, both the MLs will be strained by an equal amount. As shown in Fig. 1, four different stacking configurations have been designed. From the four configurations the one with the lowest energy has been chosen for further studies. To ensure the energetic stability of the heterostructure, we have calculated the binding energy E_b using the formula

$$E_b = E_{Total}\,(CdS - In_2SeTe) - E_{Total}\,(CdS) - E_{Total}\,(In_2SeTe)$$

Where $E_{Total}\,(CdS - In_2SeTe)$, $E_{Total}\,(CdS)$ and $E_{Total}\,(CdS - In_2SeTe)$ are the total energies of the heterostructure, isolated CdS and In_2SeTe MLs respectively. The binding energy of the heterostructure is found to be -0.309 eV. The negative value of E_b is indicating the energetic stability of the structure.

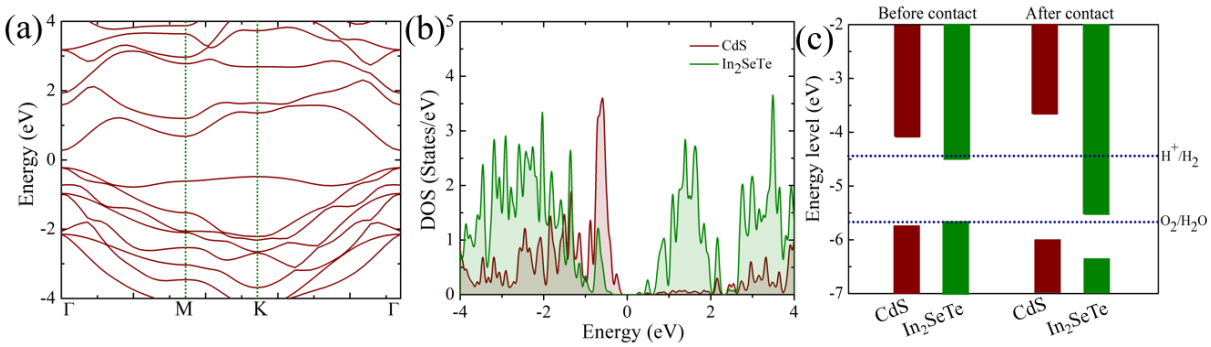


FIGURE 2. (a) The electronic band structure and (b) LDOS of the CdS-In_2SeTe heterostructure. The fermi-level is set to zero. (c) the band edge alignment before and after the construction of the of the CdS-In_2SeTe heterostructure. The blue dotted lines represent the standard hydrogen reduction and oxidation potentials.

From the GGA level electronic band structure calculations we found that the constructed heterostructure has a direct band gap of 0.49 eV which is shown in Fig. 2 (a). The layer resolved density of states has been calculated to understand the contribution of the layers at VBM and CBM and presented in Fig. 2 (b). From this study it is observed that, the VBM and CBM of the CdS-In_2SeTe heterostructure are dominated by CdS and In_2SeTe MLs respectively which is suggesting the type–II band edge alignment in the heterostructure. To understand this more clearly, the band edge alignment of the MLs has been analyzed before and after the construction of the heterostructure, which is as shown in Fig. 2 (c).

Before the contact the CdS and In_2SeTe MLs have type-I band edge alignment, in which there is a chance of quick recombination of the charge carriers. This is because, the accumulation of electrons and holes will be in the same material. In this case in In_2SeTe ML. After the construction of the heterostructure we can clearly observe a band alignment of type-II or staggered type which will be helpful for the photocatalytic water splitting. Here, the electrons passage will be from CBM of CdS to CBM of In_2SeTe and the hole passage will be from VBM of In_2SeTe to VBM of CdS. Therefore, the hydrogen evolution reaction will take place on the surface of the In_2SeTe and the oxygen reduction reaction will take place on the surface of the CdS. The built-in electric field in the heterostructure, and the favorable type-II band edge alignment are making the CdS-In_2SeTe heterostructure a prominent photocatalyst for hydrogen production.

CONCLUSION

In this work, we have systematically investigated the structural and electronic properties of CdS and In_2SeTe MLs. The negligible lattice mismatch between the MLs is making them eligible to construct the heterostructure. The stability of the constructed CdS-In_2SeTe is confirmed by the negative value of the binding energy. The heterostructure has shown a direct band gap of 0.49 eV with type-II band edge alignment. The built- in electric field and favorable band edge alignment are indicating the potential applications of the CdS-In_2SeTe heterostructure in photocatalytic green hydrogen production.

REFERENCES

1. P. E. Blöchl, *Phys. Rev. B* **50**, 17953–17979 (1994).
2. P. Garg, S. Kumar, I. Choudhuri, A. Mahata, and B. Pathak, J. Phys. Chem. C **120**, 7052-7060 (2016).
3. X. H. Li, B. J. Wang, H. Li, X. F. Yang, R. Q. Zhao, X. T. Jia, S.H. Ke, New J. Chem. **44**, 16092-16100 (2020).

Study of Mechanical Properties of Nanowires (Ni, Cu, Ag) using Classical Molecular Dynamics Simulations

Mohd Hassanain[1]* and Narender Paul[2] and Ashok Kumar[1*]

[1]*Department of Physics, Central University of Punjab, Bathinda, Punjab, India 151401*
[2]*Department of Physics, Govt. Degree College Ani, Kullu, H.P., India 172026*
*Corresponding authors: mhshabiree@gmail.com; ashokphy@cup.edu.in

Abstract: This study investigates the mechanical properties of various nanowires using classical molecular dynamics simulation. This study mainly focuses on variation of diameter of various nanowires and to observe the size effect on stress strain curve. The primary aim is to obtain stress strain curve of various nanowires and observe their mechanical properties response during application of tensile stress. The result reveals that the mechanical properties of the nanowires are size dependent and it is significant varying with the size. The study provides an insight about various nanowires like nickel, copper and silver contributing to the understanding of nanomaterials for the application in various fields such as light sensors, gas sensors, resonators etc.

INTRODUCTION

In current time nondimensional materials have emerged as research field due to their distinct physical and chemical properties which is completely different from the bulk counterpart. The nanomaterials have shown tremendous potential features in small devices as compared to their bulk properties. One of the important nanomaterials are nanowires and they have shown potential in light sensors, gas sensors, high resolution tip for atomic force microscopes (AFM), resonators etc. [1-2]. The researchers are putting tremendous effort to understand deformation of nanowires and to bridge the gap between experimental and theoretical results [3]. When the size of nanowire reached near atomic scale, there is absence of dislocation in the structure resulting a stable structure of nanowire and revealing the strength in metallic nanowires [4]. Planar defects in nanowires create stress concentrations that can initiate plastic deformation and act as barriers or pathways for dislocation movement, altering the material's mechanical response [5]. There is various computational way such as first principles calculations, to study the mechanical properties of nanowires for FCC metallic structure including its scale effect, however, one cannot use large number of atoms in the calculations due to computational constraints. In this work we have utilized classical molecular dynamics to simulate Ni, Cu and Ag nanowires and study their mechanical properties.

COMPUTATIONAL METHOD

Molecular dynamics simulations are performed using Large Atomic/Molecular Massively Parallel Simulator **(**LAMMPS) software [6]. The structure of silver, copper and nickel are simple since it consists of single type of atom so the structure of these nanowires' material can be generated easily using LAMMPS input script. The Embedded atomic method (EAM) potential employed to model the interaction between the atoms in nanowire. EAM potential effectively describe the metallic bonding and collective describe both pair interaction energy and embedding energy for an atom within electron density. Initial velocities are assigned to the atoms according to Gaussian distribution function to achieve the target temperature 300 K. The equilibration process applied in Nose-Hoover and NPT ensemble to control temperature and pressure and this ensemble allow the system to stabilize at target temperature and pressure. The Nose-Hoover thermostat used to maintain the temperature of system at 300 K and the tensile stress applied at the nanowires of strain rate 0.001/ps along z-axis which means after every pico second the length of simulation box along z-axis will increase 0.001% of actual length of simulation box resulting the deformation in nanowire.

RESULTS AND DISCUSSIONS

The topology of Copper nanowires at initial zero-time step and after 1,60,000 time steps is shown in Figure 1. After 1,60,000 time steps, nanowire show breakage of bonds. The strain versus stress curves at the diameter of 6

nm and 10 nm is shown in Figure 2 and Figure 3, respectively. When the diameter is increased from 6 nm to 10 nm, the stress that can be bear by the nanowires increases from 9GPa to 15 GPa.



(a) At timestep = 0 (b) After timestep 160000

FIGURE 1: Structure of Copper nanowire with an average diameter of 6 nm.

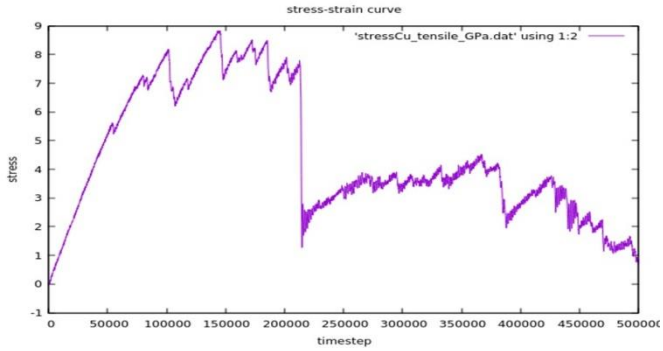


FIGURE 2: Stress-Strain curve for Copper nanowire having average diameter of 6 nm.

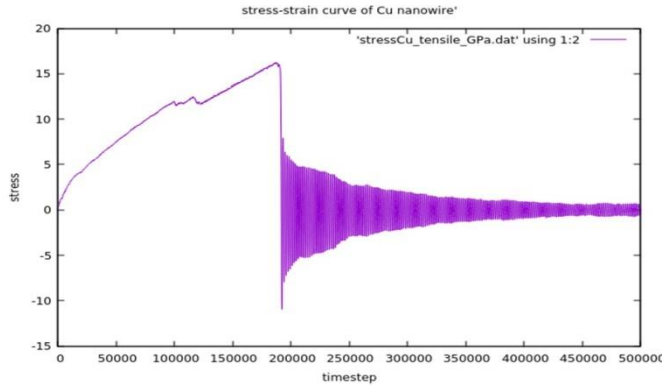


FIGURE 3: Stress-Strain curve for Copper nanowire having average diameter of 10 nm.

TABLE 1: Mechanical properties of various nanowires of an average diameter of 6 nm.

Parameters	Nickel	Copper	Silver
Atoms	4600	10000	5071
Stress(GPa)	9.2	9	4.7
Timestep	130000	225000	160000

TABLE 2: Mechanical properties of various nanowires of an average diameter of 10 nm.

Parameters	Nickel	Copper	Silver
Atoms	8000	17000	8000
Stress(GPa)	9	15	4.8
Timestep	120000	195000	95000

Table 1 and Table 2 show a complete observation of the mechanical properties of various nanowires—Nickel, Copper and Silver of different diameters 6 nm and 10 nm showing insights into their stress bearing and structural stability over time. According to the stress data, Nickel, Copper, and Silver can endure maximum stresses of 9.2 GPa, 9 GPa, and 4.7 GPa, respectively, for nanowires with average diameters of 6 nm. Nickel exhibits the greatest stress endurance of 6 nm diameter nanowires with a time step record of 130,000. Copper has the largest time step of 225,000, indicating higher lifespan under stress, while having a somewhat lower stress tolerance. Silver is almost breaking time step at 160,000, but being less stress resistant as compared to nickel.

CONCLUSIONS

The molecular dynamics simulation has been performed by using LAMMPS software to investigate the mechanical properties of Ni, Cu and Ag nanowires. The EAM form of potential model is used to describe correctly the metallic bonds in various nanowires. The simulation setup consists of generation of structure, potential, thermal equilibration and tensile loading. The mechanical properties are found to be dependent of the diameter of the nanowires. The studied nanowires may have potential applications in mechanical sensors.

ACKNOWLEDGEMENTS

The computational facility at the Department of Physics at the Central University of Punjab is used to obtain the results presented in this paper.

REFERENCES

1. K. Gall, J. Diao and M. L Dunn, The strength of gold nanowires, *Nano Letters*, **4** ,2431–2436 (2004)
2. C. M Lieber, Nanoscale science and technology: building a big future from small things, *MRS Bulletin*, **28**, 486–491 (2003).
3. M. N. Esfahani and B. E. Alaca, A review on size- dependent mechanical properties of nanowires, *Advanced Engineering Materials*, **21**, 1900192 (2019)
4. S. Wang, Z. Shan and H. Huang, The mechanical properties of nanowires, *Advanced Science*, **4,** 1600332 (2017).
5. G. Feng, W. D Nix, Y. Yoon and C. J. Lee, A study of the mechanical properties of nanowires using nanoindentation, *Journal of Applied Physics*, **99**, 074304 (2006).
6. LAMMPS Molecular Dynamics Simulator: https://www.lammps.org/#gsc.tab=0

Structural, Electronic and Thermal Stability of Janus Silicene monolayers: First-Principles Study

Kamal Dev[1, a)], Manish Patial[1], Ishan Kaundal[1], Kritika Thakur[2], Arun Kumar[1]

[1]*Post graduate govt. College Bilaspur, Himachal Pradesh, India, 174001*

[2]*Swami Vivekanand Govt. College Ghumarwin, Bilaspur, Himachal Pradesh, India, 174021*

[a)]Kamal Dev: kamaldevmnd@gmail.com

Abstract. This study employs first-principles density functional theory to investigates the structural, electronic, and thermodynamic stability of Janus silicene monolayers functionalized with chlorine atoms on one side and hydrogen or lithium atoms on the other, referred to as Si_2HCl and Si_2LiCl, respectively. Our findings reveal that the presence of hydrogen and lithium atoms increases the Si-Si bond length compared to pristine silicene, indicating significant covalent bonding interactions. Electronic band structure and density of states analyses show that Si_2HCl has a direct band gap of 1.92 eV, making it suitable for optoelectronic applications, while Si_2LiCl exhibits a narrower band gap of 0.42 eV, advantageous for applications requiring higher electrical conductivity. Phonon dispersion calculations confirm the kinetic stability of these Janus structures, evidenced by the absence of imaginary phonon modes and high phonon frequencies.

INTRODUCTION

Two dimensional (2D) Janus monolayers have considerable attention due to their unique properties and potential applications in photocatalysis, gas-sensors, electronic devices, drug delivery, and antibacterial treatments [1-3]. 2D monolayers of Xenes family such as graphene, borophene, stanene etc. have been both theoretically and experimentally explored, offering novel ways to tune the electronic structures [4, 5]. Silicene, a 2D allotrope of silicon with a honeycomb structure like graphene, offering new opportunities for fabricating 2D Janus monolayers including outstanding properties, such as Dirac cones, quantum spin Hall effects, high mobility, and compatibility with existing silicon-based microelectronics. However, the lack of a significant band gap restricts its application in futuristic nanoelectronics. Several approaches, including hydrogenation, halogenation, oxidation, and cycloaddition reactions, have been explored to achieve specific properties [6, 7]. For instance, fully hydrogenated silicene shows a large indirect band gap, while halogenated silicene has a direct band gap, although its performance under visible light limits its use in optoelectronic devices. Therefore, new strategies are necessary to develop silicene materials with moderate band gaps suitable for these applications. Recent research explores novel materials known as Janus derivatives [8], where different elements occupy opposite sides of a single layer, offering exciting properties due to their broken crystal symmetry. This broken symmetry can lead to tailored functionalities and potentially superior properties compared to their pristine counterparts. This study utilizes first-principles density functional theory (DFT) calculations to provide a comprehensive analysis of the structural, electronic, and optical properties of silicene and its Janus derivatives (Si_2HCl and Si_2LiCl). We aim to gain a deeper understanding of these materials' atomic arrangements, binding energies, band gap, and dynamical stability. The obtained results will shed light on their potential applications in energy storage and beyond, paving the way for advancements in emerging fields.

COMPUTATIONAL DETAILS

The first-principles calculations in this study were performed using the SIESTA code [9], employing a split-valence triple-zeta polarized (TZTP) basis set. An energy shift of 20 meV was applied to the basis functions. The exchange-correlation effects were treated using the Generalized Gradient Approximation (GGA) with the Perdew-Burke-Ernzerhof (PBE) functional. A Monkhorst-Pack k-point grid of 7 × 7 × 1 was used for Brillouin zone sampling. The electronic structure was solved using diagonalization with parallelization over k-points, and the electronic temperature was set to 300 K. Structural optimizations were conducted using the conjugate gradient (CG) method, with a maximum force tolerance of 0.001 eV/Å and a maximum displacement of 0.1 Å per step.

The calculations included the determination of the density of states (DOS) and projected density of states (PDOS), as well as the optical properties with a broadening of 0.2 eV. The phonon dispersion was analyzed to confirm the thermal stability of the materials.

RESULT AND DISCUSSION

To model the janus monolayers, we functionalized the silicene with chlorine atoms on one side and hydrogen/lithium atoms on the other is referred to as Si_2HCl and Si_2LiCl. The optimized structure of both monolayers are presented in figure 1(a,b) and lattice constants, bond length and energy gap are summarized in table.1. The optimized lattice constants for pristine silicene, Si_2HCl and Si_2LiCl are found to be 3.891 Å [10], 3.892 Å [8], and 3.783 Å respectively. The presence of hydrogen and lithium atoms in the Janus structures leads to an increase in the Si-Si bond length compared to pristine silicene. This elongation suggests that the bonding interactions in the Janus structures have a significant covalent character, as these additional atoms alter the electronic structure and bonding nature of the silicene lattice. Furthermore, the average bond lengths between Si-X (X = H, Li) and Si-Cl are approximately the same.

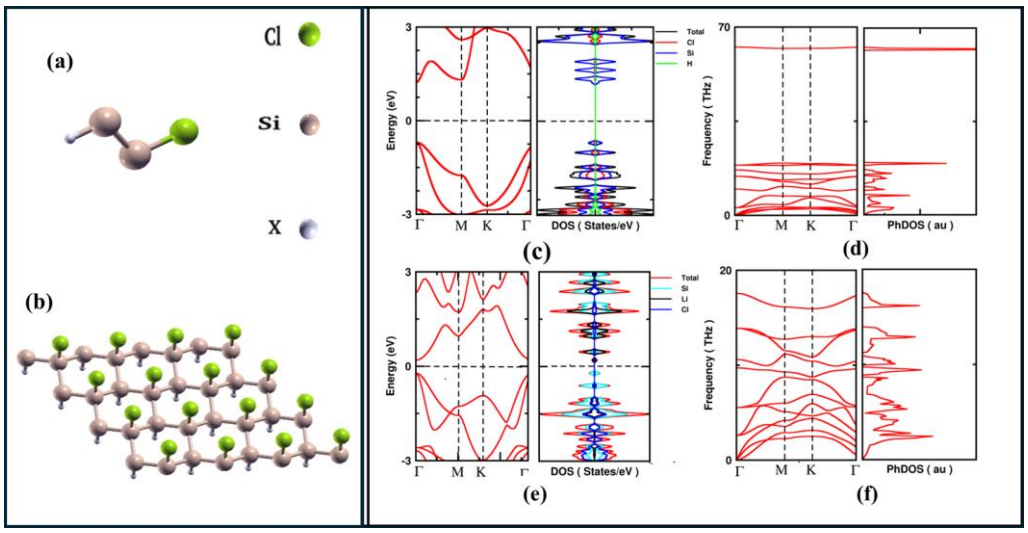


FIGURE 22: The optimized structure of janus silicene monolayers Si_2XCl where X = H, Li (a, b), electronic band structure and density of states along with their phonon dispersion relation for Si_2HCl and Si_2LiCl in (c,d) and (e,f) respectively.

Furthermore, we calculate the structural stability of the janus monolayers by calculating the binding energy (E_b) using the formula:

$$E_b = \frac{E_{total} - (nE_X + mE_{Cl})}{n+m} \qquad (1)$$

Where, E_b is the total energy of janus monolayer, E_X and E_{Cl} are the total energy of X = H, Li and chlorine atom. The calculated binding energy was found to be -4.00 eV for silicene, -3.59 eV for Si_2HCl, and -3.34 eV for Si_2LiCl as reported in the table-1. Higher binding energy represents the thermodynamical stability of the monolayers.

The electronic band structure and total/projected density of state analysis (as shown in Figure 1) revealed band gaps of 1.92 eV for Si_2HCl and 0.42 eV for Si_2LiCl, demonstrating the semiconducting nature of these materials (Table1). The introduction of hydrogen and lithium atoms significantly modifies the electronic properties of silicene, making these Janus materials suitable for various electronic applications. The sizable band gap of Si_2HCl makes it a potential candidate for optoelectronic devices, while the narrower band gap of Si_2LiCl is advantageous for applications requiring higher electrical conductivity.

Table 3: Lattice constant, bond lengths between Si-Si (d_{Si-Si}), Si-X(d_{Si-X}), Si-Cl (d_{Si-Cl})], binding energy (E_b) and band gap (E_g) of studied systems

Monolayers	Lattice Constant (Å)	Bond Length (Å)			E_b (eV)	E_g (eV)
		d_{Si-Si}	$d_{Si-X\ (X=H,Li)}$	d_{Si-Cl}		
Silicene	3.891	2.289	--	--	-4.00	0.2[6]
Si_2HCl	3.892	2.357	1.509	2.087	-3.59	1.92
Si_2LiCl	3.783	2.418	1.509	2.088	-3.34	0.42

To confirm the stability of janus monolayers, we have calculated the phonon spectra using density-functional perturbation theory [10]. As figure 1(d, f), illustrated the absence of imaginary phonon modes in both Si_2XCl (X = H, Li) monolayer indicates structural stability. Furthermore, the highest phonon frequency at the Γ point, approximately 68 THz for Si_2HCl and 18 THz for Si_2LiCl suggests that these Janus silicene structures exhibit good kinetic stability.

CONCLUSION

This study provides a detailed analysis of silicene and Janus materials Si_2HCl and Si_2LiCl using first-principles DFT calculations. Our study shows that functionalization with hydrogen and lithium atoms significantly alters the electronic and structural properties of silicene, resulting in stable monolayers with potential applications in electronics and optoelectronics. Si_2HCl, with its sizable band gap, is a promising candidate for optoelectronic devices, while the smaller band gap of Si_2LiCl may be beneficial for electronic applications requiring higher conductivity. The absence of imaginary phonon modes in the calculated phonon spectra further shows the structural and kinetic stability of these Janus monolayers. This work provides a foundation for future exploration of Janus silicene derivatives in various technological applications.

ACKNOWLEDGEMENTS

Authors would like to thank the SIESTA team for providing the open-source code and the Post graduate Govt. College Bilaspur, Himachal Pradesh for providing the computational research laboratory.

REFERENCES

1. K-H Roh, C. D. Martin and J. Lahann, Nat. Mater. **4**, 759 (2005).
2. A. Kirillova, C. Schliebe, G. Stoychev, A. Jakob, H. Lang, A. Synytska, ACS Appl. Mater. Inte **7**, 21218 (2015).
3. M. Meilikhov, S. Furukawa, K. Hirai, R. A. Fischer and S. Kitagawa, Angew. Chem., Int. Ed. **52**, 341 (2013).
4. K. Narender, B. Hyeounhu, L. Hoonkyung, H. Tanveer, A. Abu, S. V. Chandra, T. Nacir, ACS Appl. Nano Mater. **7(7)**, 6873–6884 (2024).
5. S. Khan, N. Kumar, T. Hussain, N. Tit, Journal of Power Sources, **580**, 233298 (2023).
6. D. Anjna, K. Narender, T. Abu, K. Arun, S. Amarjeet. P. K. Ahluwalia. ACS Omega **7(44)**, 40054–40066 (2022).
7. N. Kumar, M. Sharma, R. Pandey, N. Tit, International Journal of Hydrogen Energy, **70**, 510-521 (2024).
8. M. Sun , Q. Ren, S. Wang, J. Yu and W. Tang, Journal of Physics D **44,** 445305 (2016).
9. J.M. Soler, E Artacho, J.D. Gale, A García, J Junquera, P Ordejón, & D Sánchez-Portal. *Journal of Physics: Condensed Matter*, ***14***(11), 2745 (2002).
10. F. Gimbert, C.C. Lee, R. Friedlein, A. Fleurence, Y. Yamada-Takamura and T. Ozaki, Physical Review B **90**, 165423 (2014).

Experimental and DFT studies on Cubic Structured ε-FeSi Semiconductor

Hanna Shirin P H[1,a)], Hashir P[1], P P Pradyumnan [1]

[1]*Department of Physics, University of Calicut, Malappuram-673635,Kerala, India*
[a)]Corresponding author: hannashirinph@gmail.com

Abstract. In the present work we experimentally synthesized cubic structured FeSi using planetary ball mill. The structural and electrical properties were compared with DFT results.The obtained FeSi phase is confirmed using X-ray diffraction and electrical conductivity studies are conducted using Hall measurement of the sample at different temperatures. To gain deeper insights into the electronic structure of FeSi, computational method called density functional theory(DFT) calculations are conducted within generalised gradient approximation(GGA) framework using Quantum ESPRESSO software. Additionally, the density of states(DOS) and projected density of states(PDOS) of FeSi are carefully evaluated to understand the electronic distribution within the material.The obtained values of band gap and lattice parameter show consistency with previous works.

INTRODUCTION

Iron Silicide (FeSi) is a narrow band semi-conductor and shares some unusual similarity in properties with some rare earth compounds called kondo insulators [1]. There are previous works for nickel and magnesium based silicides produced by ball milling technique but there have been no cited works were ball milling or mechanical alloying be used for the production of cubic-FeSi. In this work we synthesized ε-FeSiusing planetary ball milling and the formation is confirmed using X-ray diffraction.For studying the electrical property, Hall measurement of the sample is done. DFT calculations of FeSi are done using Quantum Espresso software within generalised gradient approximation(GGA). Using DFT calculations we obtained bandgap and lattice parameter. Electronic band structure of FeSi along with the density of states(DOS) and projected density of states(PDOS) are graphically represented.

METHODOLOGY

Elemental iron (98% Spectrochem Pvt. Ltd) and silicon(-100 mesh, 99.9% Thermo Fisher Scientific) powders were used as starting materials for the synthesis of iron silicide (FeSi). About 4g of powder mix and steel balls of total weight 80g is taken. Ball to powder ratio is maintained at 20:1. The milling is conducted under vacuum at 82kPa using a rotary pump. These powders are milled in a 4 Jar Planetary Ball mill operating at a speed of 200rpm. The milling was conducted for different times up to 36hr. After 12hr, 24hr and 36hr a small amount of milled powder is removed for XRD characterization. We used RigakuMiniflex 600 diffractometer with source Cu(kα) with wavelength of X-rays as 1.5405A˚. The data obtained is plotted between 2θ and intensity in Origin Pro software. Crystallite size of the sample taken after ball milling of 12hr, 24hr, 36hr is calculated using Scherrer formula. For the study of electrical property, Hall measurement of the sample is done. Required amount of sample is taken and pelletised using hydrolic press and the thickness of pellet is measured to be 1.70mm. Hall measurement was done from temperature ranging from 300K - 500K. Conductivity, carrier concentration of FeSi is measured for different temperatures and carrier mobility is calculated.

The electronic properties of FeSi were studied within the density functional theory (DFT) framework with generalised gradient approximation used as exchange correlation function. Input parameters like celldm, ecutwfc, ecutrho, k points are optimised. The optimized new values of the input parameters are then used to run SCF calculations to obtain the Fermi energy. NSCF file is run to obtain valance band maximum and conduction band minimum values. From the difference between these values we will get more accurate bandgap. For calculating the bandstructure of FeSi, which is cubic in nature we used k-path $\Gamma - X - M - \Gamma - R - X|M - R$specified in the previous work by WahyuSetyawan and Stefano Curtarolo[2]. The energy cutoff for wave function is 90Ry and the electronic charge density is evaluated up to the kinetic energy cut-off of 900 Ry. Brillouin-zone integrations were performed using a $3 \times 3 \times 3$ k-point mesh. Integration up to the Fermi surface was done with the smearing technique.

RESULTS AND DISCUSSION

Figure 1 shows the XRD patterns of FeSi particles at different milling times. By comparing the peak positions with JCPDS No. 01-076-1748 it could be concluded that new diffraction peaks of 36hr XRD (110), (210), (211) completely coincide with JCPDS card. Hence we can confirm the formation of Iron Silicide (FeSi) by planetary ballmilling.The crystallite size of the samples are calculated using scherrer formula and is 10.1nm, 8.5nm and 7.3nm corresponding to the milling times 12hr, 24hr and 36hr respectively, this shows that the size of particles reduces with milling time.

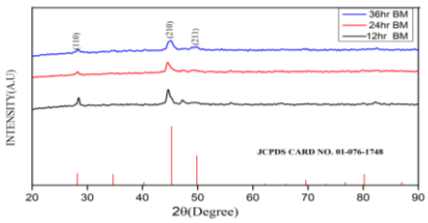


FIGURE 1. Comparison of XRD pattern of FeSi obtained at different ball milling time with JCPDS data

From the experimental data obtained from hall measurement, it is seen that as temperature increases the carrier concentration of the sample increases. Figure 2(a) shows the linear increment of electrical conductivity with temperature which exposes the semiconductor behavior of ε-FeSi and the positive value of conductivity shows the p type behavior of the sample. Mobility of the charge carriers are calculated for different temperatures and it decreases with temperature. Inverse dependence between carrier concentration and mobility is shown in the fig 2(b).

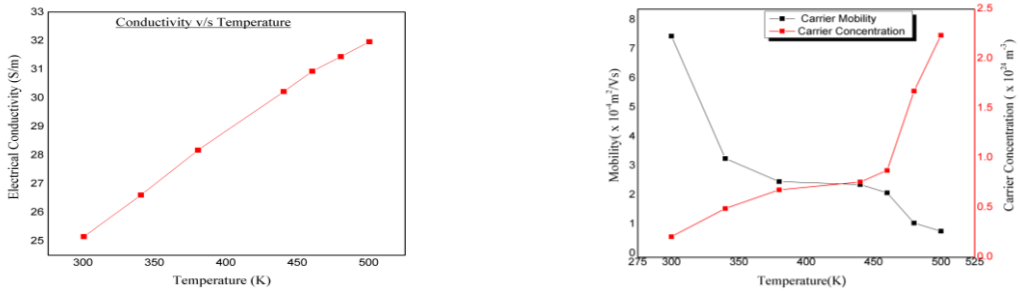


FIGURE 2. (a) Shows the variation of Electrical conductivity with temperature of FeSi (b) Temperature dependence of mobility and carrier concentration.

For the electronic structure studies using DFT, SCF calculation isinitially done. From NSCF output we get highest occupied level= 16.9120ev and lowest occupied level= 17.1690ev. The band gap obtained = 0.2574 ev. This obtained value of bandgap energy is consistent with previous work [3] which is 0.392ev and we can conclude that, FeSi is a narrow band semiconductor. Also the obtained lattice constant value 4.408Aº is consistent with previous work which is 4.44Aº. The electronic structure obtained using DFT calculations is shown in fig (3).From fig 3, we see that the conduction band and valence band are very close to each other and the high symmetric point corresponding to X shows the direct bandgap value of 0.2574ev which is already obtained from NSCF calculation output.

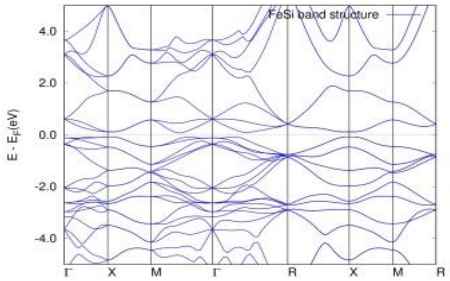


FIGURE 3. Band structure of FeSi obtained using DFT calculations.

Figure 4(a) shows the calculated density of states (DOS) using DFT and we can say that the density of states of the valence band is greater than the conduction band. From the calculated PDOS (fig 4 (b)) the contribution of d-orbitals of Fe is the greatest followed by p- orbital of Si. The obtained results show that the Fe d- orbitals are very close to the Fermi level. The contribution of Fe d-orbitals is higher in the upper valence band and lower conduction band after that there is appreciable contribution of Si p- orbitals.



(a) (b)

FIGURE 4.(a) Density of states (DOS) of FeSi obtained using DFT (b) Projected density of states (PDOS) of FeSi

CONCLUSION

In this work we successfully synthesized cubic ε-FeSi by planetary ball mill technique. The electrical properties obtained from the Hall measurement ensure the p type semiconductor behaviour of the sample. The slow increment of electrical conductivity with temperature shows the electrically stable nature of the sample and may be used as current regulator. The DFT study of the ε-FeSi sample is performed with the aid of Quantum ESPRESSO simulation software. The cubic FeSi structure shows the p type as well as low band gap property which is confirmed using DFT. The obtained bandgap value and lattice constant is consistent with previous works. The electronic structure, DOS and PDOS of FeSi is also represented graphically using quantum ESPRESSO software. Hence our experimental and DFT studies are in good agreement with each other.

ACKNOWLEDGMENTS

The authors gratefully acknowledge UGC-SAP, FIST and DST SERB Government of India for allowing the research facilities at the Department of Physics, University of Calicut, and Central Sophisticated Instrumentation Facility (CSIF), university of Calicut for characterization facilities.

REFERENCES

1. Transport and optical properties of FeSi L. Degiorgi a'*, M. Hunt a, H.R. Ott a, Z. Fisk b aLaboratoriumfiirFestkOrperphysik, ETH-Ziirich, CH-8093 Ziirich, Switzerland W. Setyawan and S. Curtarolo,
2. “High-throughput electronic band structure calculations: Challenges and tools,” Computational materials science, vol. 49, no. 2, pp. J. Piamba, C. Ortega, R. Hern´andez-Bravo, J. G. Carmona, J. Tabares, G. P. Alc´azar, and J. Alvarado Orozco,
3. “Theoretical and experimental study of fesi on magnetic and phase properties,” Applied Physics A, vol. 126, pp. 1–9, 2020.

Investigation of native defects on the PbIBr Janus monolayer: A DFT study

Aditya Shankar[1], Anjana E Sudheer[1], G. Tejaswini[1], D. Murali[1, *], M. Posselt[2]

[1] *Indian Institute of Information Technology Design and Manufacturing Kurnool 518008, Andhra Pradesh, India*
[2]*Helmholtz-Zentrum Dresden-Rossendorf, Institute of Ion Beam Physics and Materials Research, Bautzner Landstraße 400, 01328 Dresden, Germany*

[*] Corresponding author: dmurali@iiitk.ac.in

Abstract. The growth of any material especially two-dimensional layers involves unavoidable defects. These point defects will have a significant effect on the geometry, electronic and optical properties of the structure. Herein, we investigate the influence of point defects on the electronic properties of the Janus monolayer PbIBr using first-principles based Density Functional Theory (DFT) calculations. The formation energy of the point defects I, Br and Pb in PbIBr has been calculated. Using the calculated formation energy, we found the concentration the three different defects as a function of temperature. Later, to understand the electronic properties of the defected structures we have calculated electronic density of states (DOS) and observed the evolution of the defect states in the band gap region.

INTRODUCTION

From the past few years 2D Janus materials are being explored for various applications such as photocatalysis, photovoltaics, optoelectronics and thermoelectrics. Among all the Janus structures post transition metal halide structures are recently predicted and explored because of their unique structural and electronic properties. The experimental growth of these two- dimensional materials can be done using the technique of chemical vapor deposition. The growth of high-quality crystalline samples also involves minute defects due to the atomically thin layered structure and more exposed surface. The presence of these defects will influence the electronic, magnetic and optical properties of the materials. It was also reported that, defects can be introduced deliberately to tune the properties of the materials. In the present study we have studied the role of halide defects in the PbIBr Janus structure.
First, we have analyzed the defect formation energy and after that the electronic properties of the defective system are calculated and compared with the pristine system.

COMPUTATIONAL DETAILS

All the Density Functional Theory (DFT) calculations are performed using Vienna Ab-initio Simulation Package (VASP) with projector augmented wave (PAW) pseudopotentials. Exchange-correlations are treated by Perdew–Burke-Ernzerhof (PBE) Functional of the Generalized Gradient Approximation (GGA). The van der Waals corrections are incorporated using DFT-D2 method of Grimme. A kinetic energy cut-off of 650 eV and a k-point grid of 16×16×1 is used for structural optimization of Janus structure. In the process of optimization, the forces on each atom and total energy are converged up to 0.001 eV/ Å and 10^{-6} eV/cell. A vacuum layer of around 20 Å is provided along the Z direction to prevent interactions between the neighboring layers. A 4×4×1 supercell is used to investigate the defect study. VASPKIT software is used for extracting data from VASP-generated output files. VESTA has been used for geometry visualization.

RESULTS AND DISCUSSION

Recently, we have designed and explored Pb based Janus structures for photocatalytic, photovoltaics, optoelectronic and thermoelectric applications[2]. From the designed six Janus structures, in the current study, we have chosen PbIBr and analyzed the effect of point defects on the structure. The optimized lattice constant of the PbIBr monolayer is 4.49 Å. The Pb-I and Pb-Br bond lengths are measured to be 3.24 and 3.06 Å respectively. The thickness of the layer is 3.6 Å. After this, we have introduced a single point defect of Pb, I and Br separately and the structural optimization has been performed by allowing only the ions in the lattice to move. The optimized

structures of pristine I, Br, Pb defected PbIBr monolayers are presented in Fig. 1. From the optimized defect structures, we can observe that The structure with Br defect distorted more compared to the I and Pb defected structures. Later, the defect formation energy has been calculated using the following equation[1]

$$\Delta E_f = E_{def} - E_{host} - \sum_j n_j \mu_j$$

Where, E_{def} and E_{host} are the total energies of the structure with and without defect, n_j is the number of removed atoms and μ_j is the chemical potential of the corresponding atom.

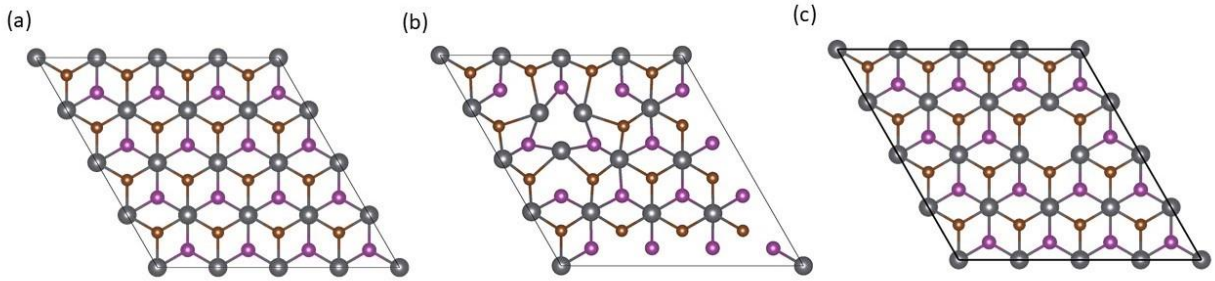


FIGURE 1. (a) The atom resolved density of states of the pristine Janus monolayer, (b) I, (c) Br and (d) Pb defected structures.

The defect formation energies for I, Br and Pb defected structure are calculated to be 2.32, 2.76 and 4.23 eV. From these values we can say that in the synthesis of the PbIBr monolayer, the I defect is more like to be present. From the calculated defect formation energies, we have calculated the concentration of defects as function of temperature using the following equation

$$c_i^d = c_i^0 \exp(-\frac{\Delta E_i^d}{KT})$$

Here, c_i^0 is the number of sites available for defects on the respective sublattice per volume and ΔE_i^d is the defect formation energy of the corresponding defect. The concentration of I, Br and Pb defects with respect to the variation in temperature as shown in Fig. 2. From this we can observe that, the concentration of I defect is very much high compare to the Br and Pb defects in the PbIBr monolayer.

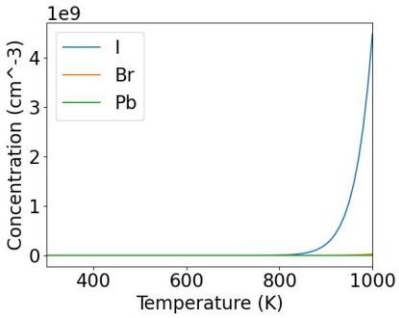


FIGURE 3. The concentration of defects as a function of temperature.

Next, we have calculated the atom resolved DOS of the defected structures and presented in Fig. 3. The band gap of the pristine PbIBr structure is 2.75 eV. In the DOS of I defected structure, the valence states are shifted towards the negative energy region and the defects states are coming in the band gap region. The same scenario is observed in the case of Br defected structure. There are no much defect states observed in the case of the structure with Pb defect.

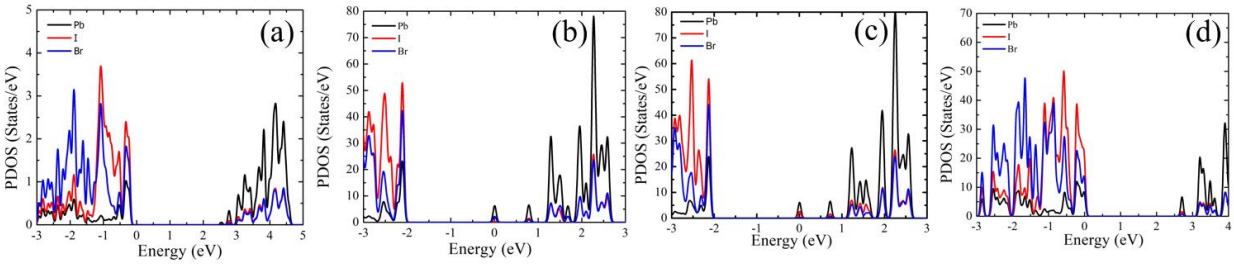


FIGURE 3. (a) The atom resolved density of states of the pristine Janus monolayer, (b) I, (c) Br and (d) Pb defected structures.

CONCLUSION

In summary, we have performed density functional theory calculations to the properties of the defected PbIBr Janus structure. Three vacancy defects of I, Br and Pb has been introduced in the structure and calculated their formation energies. To understand the concentration of defects at higher temperatures, using the defect formation energies we have calculated the defect concentration and found, I defect is more likely to be present in the PbIBr monolayer. Later, the electronic density of states of the pristine Janus layer and the defected structures have been compared and found the presence of the defect states in the band gap region which will alter the electronic properties.

REFERENCES

1. P. Erhart and K. Albe, *J. Appl. Phys.* **104**, 044315 (2008).
2. E. S. Anjana, G. Tejaswini, M. Posselt and D. Murali, *Comput. Mater. Sci.* **243**, 113123 (2024).

A Review of Theoretical Approach to Study the Anomalous Behaviour of Strongly Correlated Heavy Fermion System

Namita Shadangi[1, a)], Prayasha Satpathy[1]

[1](*School of Physics, Gangadhar Meher University, Sambalpur, Odisha, India.)*

[a)] *Corresponding author: namita.shadangi@gmail.com*

Abstract. Here we try to review our theoretical approach to study the anomalous behavior of heavy fermion system. As heavy fermion system shows low temperature anomalous behavior such as large effective mass, by lowering temperature decrease in electrical resistivity and non-dependence of magnetic susceptibility with temperature and linear dependence with temperature. Here considering the Periodic Anderson Model and using Zubarev technique for Double time temperature dependent Green function method we evaluate electron self- energy and spectral density. In order to explore the low temperature anomalies such as elastic constant, resistivity has been explored with long wavelength (q=0), finite 'q' and finite 'T'. Putting $\omega \rightarrow \omega+i\eta$, the electron self-energy evaluated with imaginary and real part which can be utilized to calculate the elastic constant and resistivity. f electron moment at low temperature interacts with each other and electron in the conduction band strongly resulting in a highly correlated electron state which shows the anomalies in heavy fermion systems. Therefore, we consider electron-phonon interaction in the system Hamiltonian and investigate its effect on elastic constant and resistivity. The impact of different system parameters including 'd' refers the location of f- level, 'r'- electron-phonon coupling strength and 'g'- the coupling constant on the anomalies has been inspected.

Keywords: Heavy fermion system, electron-phonon interaction, self-energy, spectral density, elastic constant.

INTRODUCTION

The widely recognized intermetallic compounds having incomplete 4f or 5f electrons shells which display unusual characteristics at extremely low temperatures are the heavy fermion (HF) systems. These HF compounds at low temperature are characterized by a significantly increased effective mass, which is nearly one hundred times greater than the effective mass of a normal electron. Due to the f electron localization the peculiarities observed in these systems which at higher temperatures shows the weak interaction of f and conduction electron assembly with standard masses. The strong interaction of f- electron moments with conduction electrons and among themselves becomes prominent with decrease in temperature. strongly interconnected with both conduction electrons and each other. This creates a highly correlated electron state with remarkable anomalies in electronic, magnetic and lattice properties [1,2] in heavy fermion systems such as UBe_{13}, $CeCu_2Si_2$, U_2Zn_{17}, UCd_{11}, $CeAl_3$ and $CeCu_6$. Specifically, the resistivity in these systems peaks at a temperature denoted as T^*, typically below 40K, followed by a significant decrease. This decrease is attributed to a coherent interaction emerging among different sites within these materials.

FORMALISM

The system Hamiltonian for strongly correlated heavy fermion system using Periodic Anderson Model (PAM) [3], can be given as

$$H = H_0 + H_p + H_{e-p} \tag{1}$$

Here H_0 is the electronic Hamiltonian, also called the Anderson lattice Hamiltonian, $H_{e\text{-}p}$ is the Hamiltonian related to the electron-phonon interaction term and H_p is the Hamiltonian for phonons and are expressed as,

$$H_0 = \sum_{k\sigma} \varepsilon_k \, C^{\dagger}_{k\sigma} C_{k\sigma} + E_0 \sum_{k\sigma} f^{\dagger}_{k\sigma} f_{k\sigma} + \gamma_0 \sum_{k\sigma} (f^{\dagger}_{k\sigma} C_{k\sigma} + C^{\dagger}_{k\sigma} f_{k\sigma}) + \frac{U}{2} \sum_{k\sigma} n^f_{i\sigma} \, n^f_{i,-\sigma} \tag{2}$$

$$H_p = \sum_q w_q \, b^{\dagger}_q \, b_q \tag{3}$$

$$H_{e-p} = \sum_{kq\sigma} [f_1(q)(C^{\dagger}_{k+q,\sigma} f_{k\sigma} + f^{\dagger}_{k+q,\sigma} C_{k\sigma}) + f_2(q)(f^{\dagger}_{k\sigma} f_{k\sigma})] \left[b_q + \, b^{\dagger}_{-q} \right] \tag{4}$$

Where $C_{k\sigma}^{\dagger}$ & $f_{k\sigma}^{\dagger}$ are the creation operator and $C_{k\sigma}$ & $f_{k\sigma}$ are the annihilation operator for conduction and f electron having momentum and spin k and σ respectively. E_0 is the position of f level, ε_k is the conduction band electron energy, $n_{i\sigma}^{f} = f_{k\sigma}^{\dagger} f_{k\sigma}$ is the f electron number operator and γ_0- strength of 'f' electron and conduction electron hybridization constant. For phonon $b_q^{\dagger}$ the creation and b_q the annihilation operator with frequency ω_q and wave number q, U- onsite coulomb repulsion $f_1(q)$ and $f_2(q)$- coupling constant.

Using Zubarev [4] technique with Green function having double time temperature dependency, the Green function for phonon represented as

$$D_{qq'}(t-t') = \ll A_q(t);\, A_{q'}(t') \gg = -i\theta\,(t-t') < \left[A_q(t);\, A_{q'}(t')\right] > \tag{5}$$

Here

$$A_q = b_q + b_{-q}^{+} \quad and \quad B_q = b_q - b_{-q}^{+}$$

Where A_q, B_q represents the momentum and displacement of the lattice with q^{th} Fourier components.

The Hamiltonian (eq. 1) used by applying Fourier transform to the Green function evaluated as

$$D_{qq'}(\omega) = \delta_{-qq'} \left(\frac{\omega_q}{\pi}\right) \left[\omega^2 - \omega_q^2 - 4\pi\omega_q \chi_{qq'}(\omega)\right]^{-1} \tag{6}$$

Here χ (q,ω,T), the self-energy of phonon is calculated using the equation of motion with Fourier transform.

$$\chi(q,\omega,T) = \frac{\mathcal{N}(\varepsilon_f)}{\pi} |f_1|^2 \left[\left\{ \int d\varepsilon_k \frac{(\varepsilon_k - E_0)\{2(\varepsilon_k - E_0) - qv_f\}}{D(y_1 - y_2)} \left[\left\{ \left(\frac{f_1}{f_2}\right) \frac{2\gamma_0}{(\varepsilon_k - E_0)} + 1 \right\} + \left(\frac{f_1}{f_2}\right)^2 \frac{{\gamma_0}^2}{(\varepsilon_k - E_0)^2} \right] T_y \right\} + \frac{qv_f}{D} (\omega - \varepsilon_k + E_0) \left[\left\{ \left(\frac{f_1}{f_2}\right) \frac{2\gamma_0}{(\varepsilon_k - E_0)} + 1 \right\} + \left(\frac{f_1}{f_2}\right)^2 \frac{{\gamma_0}^2}{(\varepsilon_k - E_0)^2} \right] \right] \tag{7}$$

Here,

$$D = \left\{ \left(\varepsilon_f - E_0\right)^2 + 4{\gamma_0}^2 - \omega^2 \right\} \tag{8}$$

$$T_y = -4 \exp \frac{(\varepsilon_k - E_0)}{2kT} \sinh \sqrt{(\varepsilon_k - E_0)^2 + \frac{4{\gamma_0}^2}{2kT}} \tag{9}$$

The electron self-energy $\chi(k,q,\omega)$ is calculated for $\omega \to \omega + i\eta$. The real and imaginary part has been obtained using the dimensionless parameters r = $\left(\frac{f_1}{f_2}\right)$ where f_1 represents interaction strength of phonon with hybridization band and f band electron, g = $\frac{\mathcal{N}(\varepsilon_f)}{\omega_q} |f_1|^2$ is the effective coupling constant, d = $\frac{E_0}{\gamma_0}$ position of f level, p = $\frac{qv_f}{\gamma_0}$ (v_f is the fermi velocity), b = $\frac{\gamma_0}{2kT}$ inverse temperature, x = $\frac{\varepsilon_k}{\gamma_0}$ the fermi level, c = $\frac{\omega}{\gamma_0}$ and t = $\frac{\eta}{\gamma_0}$ [5].

$$Re\ \chi(k,q,\omega) = \left[\left\{ \frac{\{4 - c^2 + (x-d)^2\}\{(x-d) - p\}}{\{(x-d)^2 + 4 - c^2 - 4t^2c^2\}\{(x-d)^2 + 4\}^{1/2}} \left[\frac{r^2}{(x-d)^2} + \frac{2r}{(x-d)} + 1 \right] \right\} e^{-(x+d)b} \sin h\,\{(x-d)^2 + 4\}^{1/2}] + \frac{p\,[(c+d-x)\{(x-d)^2 + 4 - c^2\} - 2t^2c]}{\{(x-d)^2 + 4 - c^2 - 4t^2c^2\}} \left[\frac{r^2}{(x-d)^2} + \frac{2r}{(x-d)} + 1 \right] \right] \tag{10}$$

As the reduced elastic constant,

$$\hat{C} = \frac{C}{C_0} = 1 + 4g\, Re\ \chi(k,q,\omega) \tag{11}$$

where C is the elastic constant with interaction and C_0 is the bare elastic constant.
The value of reduced elastic constant can be calculated for different values of g and d from the above expression.

The imaginary part of $\chi(k,q,\omega)$ is directly proportional to the resistivity and evaluated as,

$$Im\,\chi(k,q,\omega) = \int\left[\frac{2ct(x-d)\{(x-d)-p\}}{\{[c^2-t^2-(x-d)^2+4]^2-4c^2t^2\}]\{(x-d)^2+4\}^{1/2}}\sinh[b(x-d)^2+4]^{1/2}\right]dx + \int\left[\frac{2ct(x-d)\{(x-d)-p\}}{\{[c^2-t^2-(x-d)^2+4]^2-4c^2t^2\}]\{(x-d)^2+4\}^{1/2}}\frac{2r}{(x-d)}e^{-b(x+d)}\sinh[b(x-d)^2+4]^{1/2}\right]dx + \int\left[\frac{2ct(x-d)\{(x-d)-p\}}{\{[c^2-t^2-(x-d)^2+4]^2-4c^2t^2\}]\{(x-d)^2+4\}^{1/2}}\frac{r^2}{(x-d)^2}e^{-b(x+d)}\sinh[b(x-d)^2+4]^{1/2}\right]dx \quad (12)$$

Now

$$Resistivity\ (\rho) = 1 + 16gIm\chi(k,q,\omega) \quad (13)$$

The elastic constant and resistivity with variation of temperature by changing the system parameters r, g, d and p has been estimated.

RESULT AND DISCUSSION:

The various outcomes are shown in Fig.1which gives the change in reduced elastic constant with the f level. Taking d= -2, -4 and -6, the reduced elastic constant is plotted for r= 0.01, c= 0, p= 0.25 and g= 0.01. Its found that more the f level away from the fermi level the elastic constant goes on decreasing which happens as the f electron interact with phonon weakly due to phonon softening.

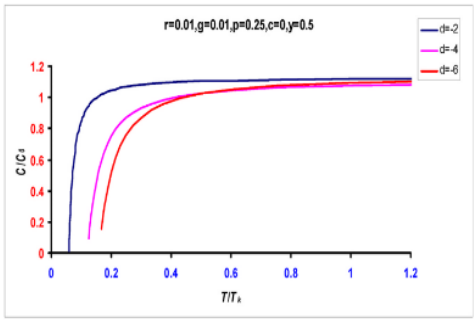


FIGURE 1. The reduced elastic constant $\hat{C}$ w.r.t temperature T= T/T_k with changing value of d from -2 to -6

In Fig.2 a set of curves has been plotted between resistivity verses temperature at different values of d=-4 to -2, 0,2 to 4 with other parameter fixed.

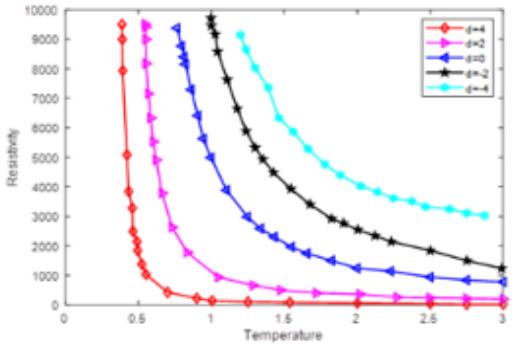


FIGURE 2. The resistivity w.r.t temperature variation with changing value of d from -4 to 4

At extremely low temperature along with a peak the resistivity value increases with decrease in temperature and then as T approaches to zero, resistivity decreases. The low-temperature resistivity anomaly in itinerant heavy electrons is due to scattering from impurities, localized spin fluctuations, and interactions among the electrons themselves. As the temperature drops, the coupling between the local moments and the conduction electrons strengthens. When the value of d is negative, it suggests that the f-level is positioned further from the Fermi level. This configuration causes an increase in resistivity with rising temperature, indicating that the electrons are highly localized because the f-level is deep within the core. At low temperatures, the lack of sufficient phonons means that interactions between conduction electrons and spin fluctuations have a minimal impact on resistivity. This low-temperature resistivity behaviour is similar to that observed in experimental studies of various heavy fermion systems such as UBe_{13} [6], $CeCu_6Si_2$, UZn_{17}, UCd_{11}, $CeAl_3$, and $CeCu_6$.

ACKNOWLEDGEMENT

I wish to convey my sincere appreciation to Gangadhar Meher University, Sambalpur, Odisha, for their financial assistance and support.

REFERENCES

1. P. A. Lee *et al.*, Comments Cond. Matt. Phys., Vol. 12, pp. 99 (1986).
2. Z. Fisk, D. W. Hess, C. J. Pethick, D. Pines, J. L. Smith, J. D. Thompson, and J. O. Willis, Science, Vol. 239, pp. 33 (1988).
3. P. W. Anderson, Phys. Rev., Vol. 124(1), pp. 41 (1961).
4. D. N. Zubarev, Sov. Phys. Usp., Vol. 3, pp. 320 (1960).
5. B. Parida, J. Sahoo, N. Sahu, and P. Nayak, Indian J. Phys., Vol. 84(10), pp. 1333–1339 (2010).
6. C. Hewson, *The Kondo Problem to Heavy Fermions*, Cambridge Univ. Press, (1995).

Investigating the mechanism of magnetic moment suppression in Quaternary Heusler alloy CoCrVAl

Ataur Rahman[1] and Jagdish Kumar[1, *]

[1]Department of Computational Sciences, Central University of Punjab, Bathinda-151401, India

** Corresponding author: jagdish.kumar@cup.edu.in (J. Kumar)*

Abstract. The alloy CoCrVAl (CCVA) has been investigated using the framework of *density functional theory*. Within the full *potential linearized augmented plane wave* (FP-LAPW) method the pristine alloy shows ferrimagnetic ground state with total magnetic moment of ~1.0 Bohr magneton, however a recent experimental study has found that there is no resultant magnetic moment in this alloy. To investigate the origin of such inconsistency, we have employed *coherent potential approximation* (CPA) based Korringa-Kohn-Rostoker method to investigate the energetics and magnetic properties of this alloy. Our results find that the intermixing of cobalt and chromium atoms in the crystal can suppress the magnetic moment yielding in zero resultant magnetism.

KEYWORDS: Coherent Potential Approximation, Antisite Disorder, Density Functional Theory, Sprkkr, Generalized Gradient Approximation, Quaternary Heusler Alloy, First-Principles Calculation

INTRODUCTION

Quaternary Heusler Alloys (QHA's) have captured significant interest of researchers in recent years due to their interesting magnetic and electronic properties such as high curie temperature, half-metallic nature, Dirac like dispersions, and shape memory effects [1, 2, 3, 4]. Based on the element's position of the four sites, Heusler alloys are classified into two broad categories called ternary Heusler alloy XYZ which crystallizes in the $C1_b$ structure and Full Heusler alloy X_2YZ or XX`YZ (equi-atomic) which crystallizes in the $L2_1$ structure. X and Y are transition-metal elements and Z is a main group sp element. The QHA are prone to antisite disorder due to their similar electronegativity.

In a recent experimental study, Paul et al. [5] have investigated CoCrVAl which crystallizes in face centered cubic structure. Their investigations found that despite the presence of magnetic Cr and Co in the crystal, there is no resultant magnetic moment on the unit cell as shown by different magnetic measurements. The density functional theory-based calculations on this crystal have shown that the unit cell must exhibit a magnetic moment of ~0.9-1.0μ_B which is in contrast to experimental results. To investigate this mismatch, we have performed density functional theory-based calculations to investigate the origin of suppression of magnetic moment on the unit cell. We have employed *coherent potential approximation* based SPRKKR code to explore the effect of inter-elemental disorder on the magnetic moment of the crystal. Our results show that the intermixing of cobalt and chromium can significantly result in suppressing the magnetic moment on the unit cell and hence zero resultant magnetism.

COMPUTATIONAL METHODS

First-principles calculations for alloys have been performed using two distinct approaches: FP-LAPW for the pristine structure as implemented in the ELK Code [6] and Spin Polarised Relativistic Korringa-Kohn-Rostoker Coherent Potential Approximation (SPR-KKR-CPA) formalism as implemented in the Munich SPR-KKR software [7]. For the pristine alloy, the value of the muffin-tin radii of Co, Cr, V & Al is 2.1 Bohr. The structures are relaxed till the stress tolerance of 10^{-5} Ha/Bohr^3 and 10^{-5} Hartree/Bohr for force tolerance. For the ground state energy calculations, a grid of 6 × 6 × 6 k-points has been taken for the BZ integrations and the band structure calculations were performed using a denser grid of 10 × 10 × 10 k-points. The electronic band structure is calculated along the Γ-L-K-W-X-U-Γ path in the first IBZ. The bulk modulus of the studied alloy has been calculated by fitting the energy vs volume data into different equations of state as implemented in the *eos* utility of the ELK Code. The phonon dispersion calculations of the ferromagnetic structure have been performed within the supercell method with a q-point of 2 × 2 × 2. For the disordered alloys, full relativistic & spin-polarised calculations with angular momentum (l_{max})= 3 & 20 × 20 × 20 k-points. The tolerance value for the CPA cycle is 10^{-5} Ry. GGA-PBE exchange correlational functional have been employed for all the calculations [8].

The quaternary Heusler alloy (QHA) CCVA shown in **Figure 1** (a), forms in the LiMgPdSn prototype with *F-43m* (spacegroup no. 216) with Co occupying 4d (0.75, 0.75, 0.75), Cr at 4c(0.25, 0.25, 0.25), V at 4b(0.5, 0.5, 0.5), and Al at 4a (0, 0, 0) Wyckoff positions. This is the type 1 structure and the subject of our study in this work.

RESULT AND DISCUSSION

Among the three non-degenerate structures of the QHA CCVA, type 1 structure is energetically most stable as can be found from energy versus lattice constant plots shown in Figure 1(b). The ground state properties like lattice constant(a_0), Bulk modulus(B_0) and magnetic moment(μ_B) of the pristine structure are listed in **Table 1**. Our results show that in pristine state, the Co and Cr align ferromagnetically whereas V aligns oppositely leading to the ferrimagnetic unit cell. To ensure that there is no local minimum in the magnetic structure, we performed fixed spin moment (FSM) calculations by fixing total magnetic moment on the unit cell. It is found that the 1μB is the lowest energy ground state of the system as shown in Figure 1 (c). To check the dynamical stability of the pristine CCVA unit cell we did lattice dynamics calculations and found that the structure is dynamically unstable and exhibits imaginary frequencies. This indicates that the pristine CCVA might not be stable. The band structure plots for pristine unit cell shows that pristine CCVA is close to being a half metal as the fermi level for one of the spins is close to a band gap whereas for other spin the bands are crossing fermi level. The imaginary phonon frequencies and no magnetic moment observed in experiments by Paul et al. motivated us to study the disordered structure for CCVA and investigate the mechanism for suppression of magnetism.

Table 1. Calculated ground state properties of pristine CoCrVAl.

Lattice constant (Å)	Bulk Modulus (GPa)	Magnetic Moment (μB)					$E_{NM} - E_{FM}$ (meV)
		Co	Cr	V	Al	Total	
5.76	197.5	-0.3	-0.93	0.34	0.0	~1.0	8.5

Experimentally, CCVA is reported to have a magnetic moment of 0.0012μB/fu [2] unlike the expected by DFT calculations on pristine CCVA unit cell. For QHAs, the B2 type disorder is suspected in which atoms at X & X` sites and Y & Z' sites are intermixed. In the context of CCVA such disorder can lead to Co/Cr intermixing and Al/V intermixing. Therefore, we have investigated the effect of antisite disorder on the magnetic characteristics of the CoCrVAl as a function of the concentration of x & y in site 1 & site 2 respectively.

The results for total energy and magnetic moment values of the unit cell as a function of disorder concentration are plotted in Figure 2 (a) and (b). Our results show that as per the total energy plots, energy for Al/V intermixing is lower in comparison to Co/Cr disorder. However, the impact of Co/Cr intermixing on magnetic moment is critical and as small as 10% intermixing of Co/Cr is sufficient to suppress the magnetic moment totally.

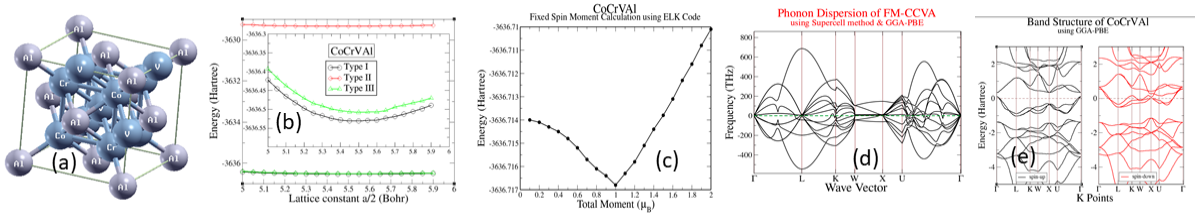


Figure 1. (a)Type 1 primitive unit cell of CCVA, (b). Energy-vs-lattice constant graph for all types, (c) Fixed spin moment calculation, (d) Lattice dynamics, (e) spin-polarised Band structure for CCVA.

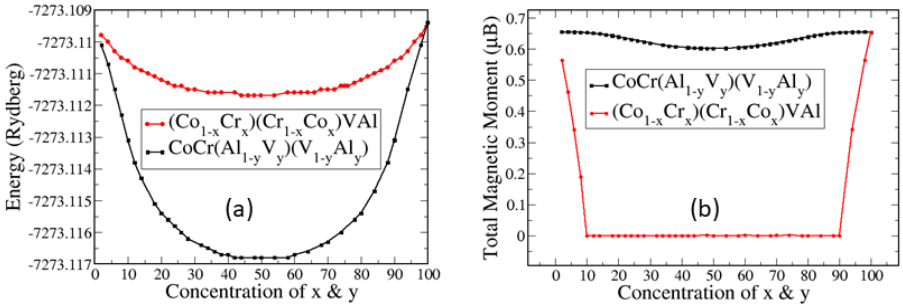


Figure 2: (a) total energy versus concentration of intermixing of co/cr sites and al/v sites and (b) magnetic moment versus concentration of intermixing.

These results indicate that the experimentally observed zero magnetic moment might be caused due to intermixing of co/cr atoms at x and x' sites. The intermixing of al/v atoms at y and z sites is not very critical to magnetism but can lead to lowering in energy. However, more combinations of intermixing including disorder at both x/x' and y/z simultaneously may throw some more light on energetics and magnetism of this alloy.

CONCLUSIONS

In conclusion, we have investigated the ccva quaternary heusler's alloy to explain the microscopic origin of experimentally observed results on magnetism. The density functional theory based calculations on pristine unit cells show that pristine ccva is ferrimagnetic with resultant magnetic moment of ~1.0 bohr magneton. However, the pristine ccva is indicated unstable dynamically by lattice dynamics calculations. The coherent potential approximation-based calculations show that the intermixing of atoms at x/x' and y/z sites have a crucial impact on energetics and magnetism of this alloy. The intermixing of co/cr can rapidly suppress magnetism on the unit cell and should be responsible for explaining the experimental observation of no resultant magnetism on the unit cell.

ACKNOWLEDGMENTS

The authors would like to thank the developers of elk code and munich spr-kkr code for making it available for the researchers. The computational facility is available in the department of computational sciences, cup, bathinda is also acknowledged**.**

REFERENCES

1. K. Elphick, W. Frost, M. Samiepour, T. Kubota, K. Takanashi, H. Sukegawa, S. Mitani & A. Hirohata, *Heusler alloys for spintronic devices: review on recent development and future perspectives*, Science and Technology of Advanced Materials, Vol. 22, pp. 235–271 (2021).
2. R. Chellakumar, T. S. D. Malar, A. N. Rawther, and K. Ravichandran, *Soft Ferromagnetic Co_2MnAl Full Heusler Alloy Particles with High Curie Temperature for Spintronics Device Applications*, Journal of Superconductivity and Novel Magnetism, Vol. 36(2), pp. 547–557 (2023).
3. F. Heusler, W. Starck, and E. Haupt, *Magnetisch-chemische Studien*, Verh. Dtsch. Phys. Ges., Vol. 5, pp. 219–232 (1903).
4. G. D. Liu, J. L. Chen, Z. H. Liu, X. F. Dai, G. H. Wu, B. Zhang, and X. X. Zhang, *Martensitic transformation and shape memory effect in a ferromagnetic shape memory alloy: Mn_2NiGa*, Applied Physics Letters, Vol. 87, 262504 (2005).
5. S. Paul, B. Bandyopadhyay, M. K. Chattopadhyay, and K. G. Suresh, *Griffiths phase-like behaviour in CoCrVZ (Z= Al, Ga) Heusler alloys*, Journal of Magnetism and Magnetic Materials, Vol. 598 (2024).
6. K. Dewhurst, S. Sharma, L. Nordström, F. Cricchio, F. Bultmark, H. Gross, and C. Ambrosch-Draxl, *The ELK Code (8.8.26)*, https://elk.sourceforge.io/ (2023).
7. H. Ebert, et al., *The Munich SPR-KKR package, version 8.6*, https://www.ebert.cup.uni-muenchen.de/ (2022).
8. J. P. Perdew, K. Burke, and M. Ernzerhof, *Generalized Gradient Approximation Made Simple*, Physical Review Letters, Vol. 77(18), p. 3865 (1996).

Enhancement of Relaxor Properties in NKBT via BMN Additive

Ranjan Kumar Sahu[1, a], Saket Asthana[1]

[1]*Advanced Functional Materials Laboratory, Department of Physics, Indian Institute of Technology Hyderabad, Kandi, Sangareddy 502284, Telangana, India*

[a)] Corresponding author: ph20resch11021@iith.ac.in

Abstract: Perovskite solid solutions of $(1–x)Na_{0.2}K_{0.3}Bi_{0.5}TiO_3–xBiMg_{2/3}Nb_{1/3}O_3$, abbreviated as (1–x)NKBT–xBMN, were manufactured using the solid-state process. The samples with x = 0 and x = 0.10 are referred to as 0 BMN and 10 BMN, respectively. X-ray diffraction analysis confirmed the development of a single phase perovskite structure across all configurations. Surface morphology studies showed an increase in grain size with the incorporation of BMN. Dielectric characterization revealed typical relaxor behavior in NKBT–BMN ceramics, with widened phase transition peaks that evolved into a temperature-steady permittivity profile as BMN content increased. The observed increase in the diffuseness parameter further validates the relaxor nature of the system. These findings highlight the potential of lead-free NKBT–BMN ceramics for use in dielectric capacitors suited for modern electronic applications.

Keywords: Ferroelectrics; Relaxor; Dielectrics; Lead-Free; Ceramics

INTRODUCTION

The rapid progress in power electronics has created a pressing demand for dielectric materials that combine elevated energy storage density, little dielectric loss, and excellent temperature constancy, making them suitable for next-generation pulsed capacitor applications. Considering the growing importance of environmental sustainability, lead-free piezoelectric materials are becoming crucial[1]. Recent studies have identified relaxor perovskites based on $Na_{0.2}K_{0.3}Bi_{0.5}TiO_3$ (NKBT) as capable candidates for dielectric capacitor applications outstanding to their slim hysteresis loops and broad type dielectric curve. As a result, enhancing the relaxor properties of NKBT is a significant focus for researchers across multiple scientific fields[2]. The development of new material systems for dielectric capacitors is of critical importance. Among emerging candidates, the lead-free perovskite relaxor ferroelectric system $0.7BaTiO_3–0.3BiScO_3$ (BT–BS) has attracted considerable attention. In compositions with an optimal amount of $BiScO_3$, the sharp dielectric peak typically associated with the paraelectric–ferroelectric phase transition becomes significantly broadened, evolving into a temperature-independent permittivity plateau—indicative of relaxor behavior. Interestingly, the temperature corresponding to the maximum dielectric constant (Tm) initially decreases from around 120 °C in pure $BaTiO_3$ as the BS content increases, but beyond a certain concentration, Tm begins to rise again, resulting in a characteristic "U"-shaped trend[3]. The overall dielectric behavior of thin films is often limited by their thinness, failing to meet certain requirements. However, there has been no reported dielectric analysis of the NKBT-BMN system. Thus, the NKBT-BMN system may exhibit promising relaxor-type behavior, making it suitable for various applications. This study focuses on the dielectric behavior of relaxor ferroelectric NKBT–BMN ceramics. A systematic investigation was carried out to understand the effect of varying BMN content on the processing conditions, microstructural features, and dielectric performance of the NKBT–BMN system. Furthermore, the relaxation characteristics were analyzed with an emphasis on their potential for practical applications.

EXPERIMENTAL DETAILS

Synthesis of materials:

The (1–x)NKBT–xBMN ceramic models were manufactured by means of the solid state reaction process. High-purity precursor materials—Na_2CO_3 (99.9%), K_2CO_3 (99.8%), Bi_2O_3 (99%), TiO_2 (99%), MgO (99%), and Nb_2O_5 (99%)—all sourced from Sigma-Aldrich, were used for the preparation. To remove any absorbed moisture, the powders were pre-dry at 200 °C for 20 hours. After drying, the precursors were balanced conferring to the desired stoichiometric ratios and thoroughly mixed using a mortar and pestle with isopropyl alcohol (IPA) as a milling medium. The resulting mixture was formerly calcined at 800 °C for 3 hours. Subsequent calcination, the powder was ground again and mixed with a 2 wt.% polyvinyl alcohol (PVA) binder solution. Pellets were formed using a hydraulic press below a pressure of 4 tons. These green pellets were subsequently sintered by 1100 °C for 4 hours in an alumina crucible under ambient air. The sintered ceramics were then ready for further structural and microstructural characterization.

Characterization of materials:

The phase transparency and crystal structure of the samples were observed by means of X-ray diffraction (XRD), executed on a high-resolution Rigaku SmartLab diffractometer with Cu Kα radiation (λ ~ 0.15405 nm). The grain morphology and microstructural features were analyzed using a Supra-40 Zeiss scanning electron microscope (SEM). For electrical characterization, the sintered pellets were layered with silver paste and then dry at 200 °C for 2 hours to ensure good electrode contact. Dielectric properties were measured over a array of temperatures and frequencies using a Wayne Kerr 6500B impedance analyzer, with the setup associated to a temperature-controlled oven.

RESULT AND DISCUSSION

Figure 1a depicts the XRD designs of NKBT–BMN samples recorded in the 2θ range of 20° to 80°. The formation of a well-defined perovskite phase suggests that there was little to no evaporation of volatile components during processing, indicating a complete reaction facilitated by the issue of CO_2 from the carbonate-based precursors. Notably, the clear splitting of the (200) diffraction peaks confirm the tetragonal symmetry of the structure. Microstructural observations shown in Figures 1b and 1c reveal that the sintered ceramics exhibit a dense and compact microstructure, with no visible porosity. Grain size analysis, fitted using a Gaussian distribution, indicates average grain sizes of approximately 0.473 µm and 0.50 µm for the respective samples. A slight increase in grain size with higher BMN content suggests that BMN addition promotes better densification in the NKBT–BMN ceramic system[4].

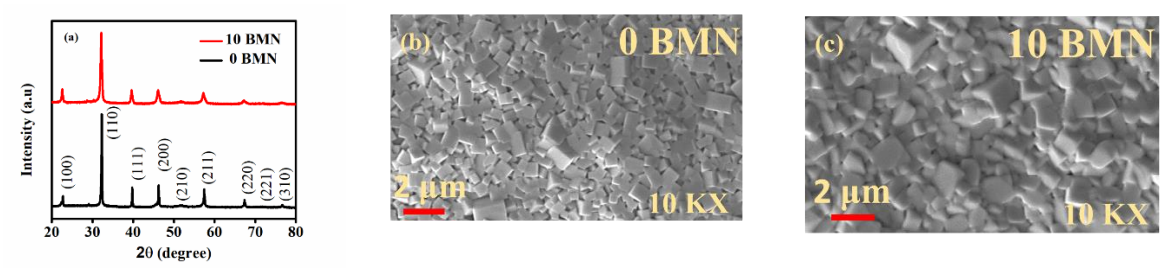


FIGURE 1. (a) X-ray diffraction and (b,c) Surface micrographs of 0 BMN and 10 BMN.

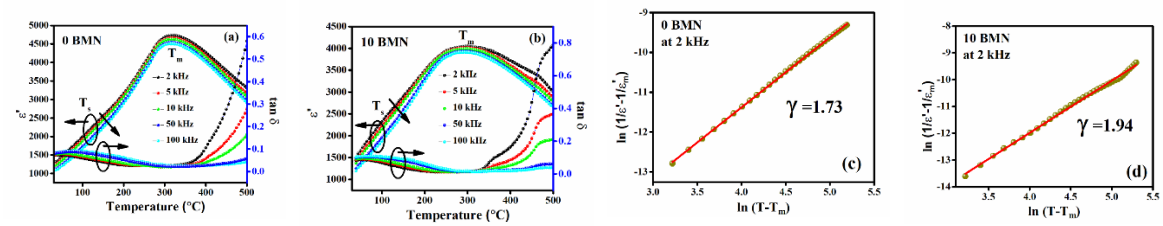


FIGURE 2. (a,b) Representation of dielectric curves and **(c,d)** diffusive factors of 0 BMN and 10 BMN.

FIGURE 2 illustrates the variation of the dielectric continuous at different temperatures for frequencies of 2 kHz and 100 kHz. The dielectric plots indicate that, for a given frequency, the highest rate of the dielectric constant decreases as the concentration of BMN increases. The temperature-dependent dielectric permittivity (ε') and loss (tan δ) for compositions with 0% and 10% BMN are displayed in Figure 2(a) and 2(b), respectively, across various frequencies. In general, the presence of different cations in the lattice introduces compositional inhomogeneities, which underwrite to the construction of polar nanoregions (PNRs). These PNRs generate a quenched random confined electric field, disrupting the long-range ferroelectric order and resulting in a short-range polar structure under suitable conditions. A notable feature in relaxor ferroelectrics, unlike conventional ferroelectrics, is the strong frequency dispersion near the first broad dielectric anomaly (denoted as Ts). For the 0% BMN composition (Figure 2a), the ε'-T plot shows two distinct humps at higher frequencies: one around 75 °C (Ts) and another near 320 °C (Tm). The frequency-dependent nature of the first peak and the corresponding dispersion in the tan δ curve confirm the relaxor behavior due to the occurrence of PNRs. With the incorporation of BMN, Ts shifts to a higher temperature (~95 °C), while the temperature of

the second dielectric peak (Tm) decreases to around 295 °C. This shift suggests that BMN influences the dynamics and distribution of PNRs, thereby modifying the dielectric response of the system. The altered Curie-Weiss law is utilized to examine the relaxor performance in NKBT-BMN at a frequency of 2 kHz, expressed as [5]:

$$\frac{1}{\varepsilon'} - \frac{1}{\varepsilon'_m} = \frac{(T - T_m)^\gamma}{C}$$

In the altered Curie–Weiss law, $\boldsymbol{\varepsilon'_m}$ represents the maximum dielectric constant, **C** is the Curie–Weiss constant, and **γ** is the diffuseness parameter. For conventional ferroelectrics, γ typically 1, however for ideal relaxor ferroelectrics, it tends toward 2. The γ values for different compositions are illustrated in Figures 2c and 2d, showing an increase from 1.73 for 0% BMN to 1.94 for 10% BMN. This rising trend in γ indicates a more diffuse phase transition, confirming in enhancement of relaxor behavior with BMN substitution. The improved relaxor characteristics are primarily attributed to A-site cationic disorder, which disturbs long-range ferroelectric order and promotes the development of polar nanoregions (PNRs).

CONCLUSION

In this study, BMN-modified NKBT ceramics were effectively manufactured using the conventional solid-state sintering process. X-ray diffraction investigation confirmed the tetragonal crystal structure, while surface morphology revealed well-defined grains with uniform distribution. The dielectric measurements showed clear evidence of a diffused phase transition, which became more pronounced with growing BMN content—indicating enhanced relaxor behavior. Notably, the temperature corresponding to the supreme dielectric constant (Tm) shifted as of 320 °C to 295 °C with BMN substitution, suggesting improved thermal stability suitable for capacitor applications. The increasing value of the diffuseness parameter (γ) further supports the evolution of a strong relaxor character in the system.

ACKNOWLEDGEMENTS

Authors SA and RS gratefully acknowledge the support from UGC-DAE (Project No. CRS/2021-22/03/553) and SERB (Grant No. CRG/2020/001509), India, for facilitating this research. RS extend thanks to the Ministry of Education (MoE), Government of India, intended for the financial support provided.

REFERENCES

1. Rödel, J. *et al*. Perspective on the Development of Lead-free Piezoceramics. *Journal of the American Ceramic Society* **92**, 1153–1177 (2009).
2. Sahu, R. K. & Asthana, S. Improved recoverable energy storage density, breakdown strength, and relaxor nature in eco-friendly K+1-ion rich NBT ferroelectrics. *Journal of Alloys and Compounds* **929**, 167340 (2022).
3. Ogihara, H., Randall, C. A. & Trolier-McKinstry, S. High-Energy Density Capacitors Utilizing 0.7 $BaTiO_3$ –0.3 $BiScO_3$ Ceramics. *Journal of the American Ceramic Society* **92**, 1719–1724 (2009).
4. Wang, T., Jin, L., Li, C., Hu, Q. & Wei, X. Relaxor Ferroelectric $BaTiO_3$ –$Bi(Mg_{2/3}Nb_{1/3})O_3$ Ceramics for Energy Storage Application. *J. Am. Ceram. Soc.* **98**, 559–566 (2015).
5. Sahu, R. K. & Asthana, S. Enhanced energy storage performance, breakdown strength, and thermal stability in compositionally designed relaxor Eu3+ substituted Na0.2K0.3Bi0.5TiO3. *Journal of Energy Storage* **91**, 112020 (2024).

Insight into the electrical properties of Ni doped $SrBi_2Nb_2O_9$ Aurivillius ceramics prepared through microwave sintering method

Anurag Pritam [a,b*]

[a] *Department of Physics, School of Natural Sciences, Shiv Nadar Institution of Eminence, Greater Noida, India.*
[b] *Tyndall National Institute, University College Cork, Ireland*

Corresponding author: anurag.pritam64@gmail.com

Abstract Polycrystalline $Sr_{0.8}Ni_{0.2}Bi_{1.95}La_{0.05}Nb_2O_9$ (NSBN) ceramics were synthesized via a single step microwave sintering method. Frequency dependent electrical measurement demonstrates a high dielectric constant and low dielectric loss, irrespective of temperatures. AC conductivity investigation directs the polaron abetted conduction mechanism which closely follows Jonscher power law. Complex impedance spectroscopy (CIS) techniques have been incorporated to examine the intra- and intergranular contributions to the overall impedance in NSBN. Moreover, the non-Debye type relaxation mechanism and the NTCR behavior were confirmed from the impedance and modulus study. These findings highlight the potential of NSBN ceramics as an eligible candidate for high temperature industrial applications.

Keywords: Dipolar polarization, ionic conductivity, dispersion behavior, Koops's theory, and impedance spectroscopy

INTRODUCTION

Bismuth layered structured ferroelectrics (BLSFs), first discovered by B. Aurivillius in 1949 served as a perfect alternative for lead-based ferroelectrics mostly due to its exceptional fatigue characteristics, high curie temperature, incomparable ferroelectric, pyroelectric, and piezoelectric property, which make them suitable for numerous industrial applications such as NvRAMs, tunable capacitors, etc. BLSFs possess a structural formula $(Bi_2O_2)^{2+}(A_{m-1}B_mO_{3m+1})^{2-}$ where A-site is taken by mono, dia, and trivalent ion (K^+, Ca^{2+}, Ba^{2+}, Bi^{3+}, etc.), B-site is occupied by transitional elements like (Ti^{4+}, Nb^{5+}, Ta^{4+}, Mo^{6+}, etc.) and m is an integer which denotes the number of BO_6 octahedral sandwiched between the $(Bi_2O_2)^{2+}$ layers [1-3]. Among diverse BSLFs, the m=2 group $SrBi_2Nb_2O_9$ (SBN) and its solid solution have seized substantial attention due to their extraordinary control of rattling space on the dielectric and ferroelectric properties. However, these properties can be further enhanced by performing appropriate doping of the suitable elements [4-5].
In the present work, we demonstrate the dielectric relaxation mechanism and electrical transport phenomena in $Sr_{0.8}Ni_{0.2}Bi_{1.95}La_{0.05}Nb_2O_9$ (NSBN) ceramics prepared through single step microwave sintering method.

EXPERIMENTAL DETAILS

The stoichiometric ratios of Bi_2O_3, NiO, $SrCO_3$, La_2O_3, and Nb_2O_5 were extensively wet milled for 25 hours in a planetary ball mill in lab grade ethanol medium. The obtained slurry was blended with a PVA binder and pressed into cylindrical pellets measuring 10.8 mm in diameter and 2 mm in thickness. These pellets were then sintered in an alumina crucible at 1000 °C for 5 hours using a microwave furnace operating at a frequency of 3.5 GHz. [4]. Temperature and frequency dependent dielectric, AC conductivity, impedance, and modulus spectroscopy were examined using a high-frequency LCR meter.

RESULTS AND DISCUSSION

1.1 Dielectric study

Fig.1(a) depicts the frequency-dependent variation of the real part of dielectric constant at a temperatures range of 50-600 °C. A notably high dielectric constant is observed at low frequency, which considerably declines with increasing temperature, irrespective of the temperature. This behavior can be primarily attributed to interfacial polarization and non-insignificant contribution from ionic conductivity referred as low-frequency dielectric dispersion [5-7]. It can be observed that the dielectric constant increases with the increasing temperature, particularly in low frequency regions. This trend is probably due to the impression of dipolar polarization which

becomes more prominent due to its inversely proportional relation with the temperature. The inset of **Figure 1(a)** depicts variation of loss tangent with frequency which mirrors the pattern of dielectric constant which can be attributed to ionic polarization and enhanced mobility of charge carriers within the NSBN matrix. Such behavior is extensively witnessed in BLSFs [6].

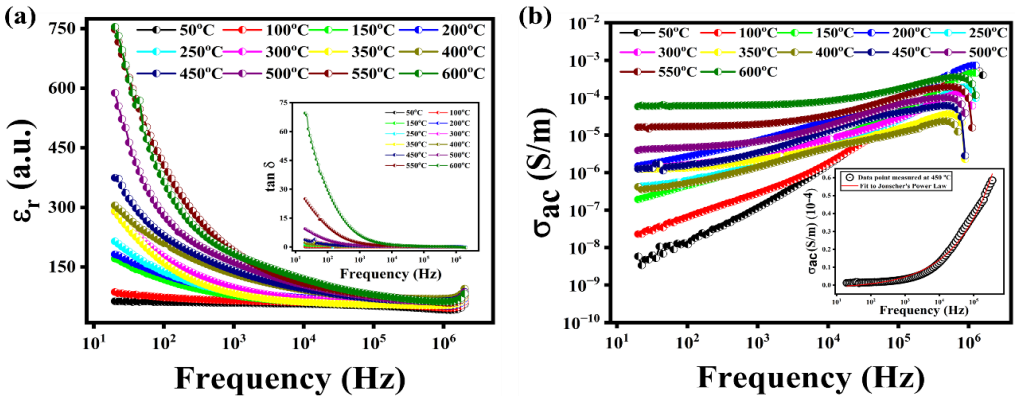


FIGURE 1 Frequency dependent variation of (a) real part of dielectric constant (b) ac conductivity of NSBN ceramics at several temperatures.

3.2 AC conductivity analysis

The conduction mechanism and transport properties of the NSBN ceramics can be known by probing it through an electrical conductivity study, which can be calculated using the equation below.

$$\sigma_{ac} = 2\pi f \varepsilon_o \varepsilon' tan\delta \quad \ldots\ldots\ldots\ldots\ldots\ldots (1)$$

Where f, εo, ε', and $tan\delta$ represent the frequency, permittivity in a vacuum, permittivity of the medium, and dielectric loss respectively. **Fig.1(b)** shows the frequency-dependent ac conductivity behavior of NSBN composition at several temperatures. A very feeble response was observed at low frequency regime perhaps due to non-equilibrium habitation of the trap charges; however, the conductivity drastically increases with the increasing frequency and can be elucidated based on polaron hopping [7]. Further, the AC conductivity of the NSBN perfectly obeys Jonscher's formulation, using the equation below

$$\sigma = \sigma_{d.c.} + A\omega^s \quad \ldots\ldots\ldots\ldots\ldots\ldots\ldots\ldots (2)$$

where σ is the total conductivity of the system, $\sigma_{d.c.}$ represents the conductivity affecting the frequency-independent DC part, A is a pre-exponential factor, ω is the angular frequency, and n ($0<n<1$) is a dimensionless exponent that enunciates the degree of interaction between nearby lattice and mobile ions. The Jonscher's fitting of experimental AC conductivity data at 50 °C is shown in the **inset of Fig.1(b)**. The value of n lies typically between 0.5 to 0.8

3.3 Complex Impedance Spectroscopy (CIS)

CIS is one of the prevailing tools to know the influence from grains, grain boundaries, and interfacial contribution to the total impedance of compositions. The frequency dependent variation of real and imaginary components of impedance of NSBN ceramics is shown in **Fig. 2(a)** and **2(b).** The Z′ and Z″ both display a strong dispersion in low frequency regions and decrease drastically with increasing frequency, eventually merging in high frequency regions. This type of behavior arises due to the release of space charge from the system, implying an increase of conductivity in the prepared composition. A sharp decrease in Z' was observed for the higher temperature measurement, which concludes a NTCR (negative temperature coefficient of resistance) behavior, which is notably equivalent to semiconductors. An asymmetrical peak broadening of Z″ was observed in the **inset of Fig.2(b)**, which designates multiple relaxation mechanisms in NSBN composition. Additionally, a shifting of Z‴ peak is observed with the increasing temperature and frequency, implying that the relaxation mechanism is spread over a wide range of frequencies [4].

The Cole-Cole plot of NSBN ceramics is shown in **Fig.2(c)**, A linear response was recorded at low temperatures, which transformed into the semicircular one, thus demonstrating a localized and nonlocalized charge-assisted conduction mechanism in composition. A single semicircle was observed for all measurements thus implying a grain contribution to the total impedance of the system. M′ vs. M″ plot is shown in **Fig. 2(d),** depicts a non-Debye type conduction mechanism. Shifting of M′ peaks towards the y-axis were observed, which implies enhanced grain conductivity in the SBN matrix due to Ni doping [8-10].

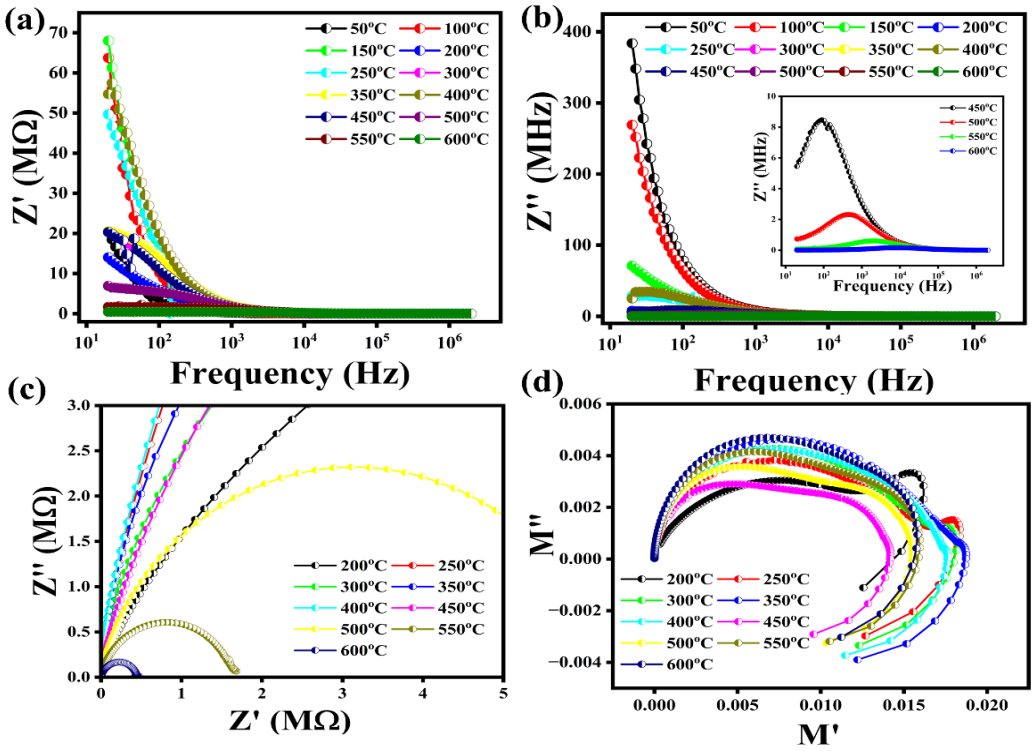


FIGURE 2 Frequency dependent variation of (a) real (b) imaginary component of impedance at several temperatures (c) Cole-Cole plot measured at different temperatures (d) Cole-Cole (Argand) modulus plot of NSBN composition

CONCLUSION

We have successfully synthesized novel $Sr_{0.8}Ni_{0.2}Bi_{1.95}La_{0.05}Nb_2O_9$ (NSBN) ceramics using single step microwave sintering method. Temperature and frequency dependent dielectric measurements suggest high dielectric constant and low loss, obeying Maxwell-Wagner type relaxation and Koop's theory. AC Conductivity analysis indicates that the conduction mechanism is governed by long range polaron hopping and perfectly obeys Jonsher's power law, with the frequency exponent *n* ranging between 0.5-0.7. CIS reveals that the electrical response is primarily governed by grain contributions, while modulus spectroscopy reveals non-Debye type relaxation behavior. These comprehensive results demonstrate that the synthesized NSBN ceramics hold strong potential for advanced energy storage applications.

ACKNOWLEDGMENT

Anurag Pritam (AP) gratefully acknowledges the Irish Research Council (IRC) for awarding him a postdoctoral fellowship at the Tyndall National Institute, University College Cork, Ireland. He also extends his sincere thanks to the Shiv Nadar Foundation for their financial support throughout the duration of his Ph.D. studies

REFERENCES

1. A. Pritam, Material *Materials Science and Engineering: B* 303 (2024): 117297.
2. A. Mohapatra, Aparajita, and R. N. P., *Journal of Materials Science: Materials in Electronics* 26: 3035-3043 (2015).
3. A. Pritam, S. Kumar. V. Shrivastava, S.S. Roy and K. Szacilowski, *Materials Chemistry and Physics*, 316,129089 (2024).
4. A. Pritam, Ceramics International 50, 48343-48353 (2024)
5. A Pritam and V. Shrivastava, *Physica B: Condensed Matter* 593, 412320 (2020)
6. A. Pritam et al. *Applied Physics A* 130, no. 5: 342 (2024).
7. A. Pritam and V. Shrivastava " *Physica status solidi (b)* 257, no. 3,1900450 (2020).
8. A. Pritam, G. Abdi, S. Hussain and M. Sikora, Ceramics International, 0272-8842 (2025)
9. V. Shrivastava, A. Pritam, A. Joshi, *Journal of Materials Science: Materials in Electronics* 29, 17388-17396 (2018)
10. A. Pritam and V. Shrivastava, *Physica B: Condensed Matter* 593, 412320 (2020).

Wind Energy Harvester Based on Electrospun CNT/DNA Doped Poly(vinylidene fluoride co hexafluoropropylene) Composite Nanofibers

Priti Sundar Barman[1], Prakriti Adhikary[1*]

[1]*Department of Physics, University of North Bengal, Raja Rammohunpur, District: Darjeeling-734013, West Bengal, India*

E-mail: prakriti@nbu.ac.in*

Abstract. Composite nanofibers (NFs) of CNT and DNA doped electrospun poly(vinylidene fluoride-co-hexafluoropropylene) [P(VDF−HFP)] are prepared for designing the ultrasensitive wearable piezoelectric harvester (WPH). The fabricated piezoelectric harvester from the composite ES(CD-HFP) NFs mat demonstrates better output performance with an open circuit voltage output of ~12 V under a pressure amplitude of ~14 kPa and output power of 5.6 μW. A wind blower associated with the composite nanofibers (NFs), a wind velocity of ~8.5 m/s showing a maximum of ~4.5 V of open-circuit output voltage, and the ability of successfully charging up capacitors promising for developing wind energy harvesting applications.

INTRODUCTION

Among the various energy harvesting systems, converting mechanical energy into electric power is a recent emerging technology in self-powered electronic devices. In some applications, piezoelectric polymer especially PVDF and its copolymers, like P(VDF−HFP) and P(VDF−TrFE) have significant advantages over ceramics due to their low density, low stiffness, flexibility, and mechanical robustness, including toughness and high strains to failure. Copolymer P(VDF−HFP) is a ferroelectric polymer that exhibits four main crystalline polymorphs in α-, β-, γ-, and δ-phases. The focus of interest is the β- and γ-phases manifesting spontaneous polarization showing piezoelectricity whereas the α-phase is electrically non-active.[1, 2] We selected the copolymer P(VDF−HFP) as the host material doped with DNA and CNT for the present study to see the cooperative effect of those fillers for the nucleation of electro-active β- and γ-phases to enhance the piezoelectric response.[3] It is realized that one of the most economical and environmentally friendly methods for fabricating large-scale piezoelectric harvesters (PH) is the integration of various external fillers into a polymer matrix. The piezoelectric response of about ~12 V by the constant finger tapping and the current signal with the load resistances of the fabricated wearable piezoelectric harvester (WPH) from the composite ES(CD-HFP) NFs mat might be superior for designing piezoelectric sensors, actuators, and vibration-based energy harvesters. The open-circuit output voltage of about ~4.5 V under the wind flow and the capacitor charging ability within a very short period of the fabricated WPH by ES(CD-HFP) NFs composite might be superior as a power source for portable electronics.

EXPERIMENTAL SECTION

To prepare the solution, we have used P(VDF−HFP) pellets (Mw~275000), N, N-dimethylformamide (DMF) (Sigma-Aldrich), Deoxyribonucleic acid (DNA) and Carbon nanotube (CNT) (Alpha-Asser). For the solution 12 wt% (w/v) of P(VDF−HFP) pellets were immersed in a (6:4) volume ratio of DMF/acetone for 12 hours of continuous stirring at 60 °C. Then, (~ 0.004 wt% (w/v)) of CNT and DNA were mixed with the prepared solution and stirred for 6 h followed by ultrasonic dispersion for an additional 30 m at 60 °C to prepare the ES(C-HFP), and ES(CD-HFP) NFs. The Electrospinning of the above copolymer was performed at a 10 kV DC bias by placing 10 ml of solution and applied to a metallic needle of ~0.8 mm tip diameter at constant flow rate of ~1 ml h^{-1} and plate collector wrapped with an Al foil placed 10 cm apart to collect the electrospun fibers. Fourier transform infrared spectroscopy (FT-IR) (Bruker Tensor II) with a spectral resolution of 4 cm^{-1} was used for the characterizations. A diffractometer (Empyrean, D8 Advance) with CuK_{α} radiation of (λ = 1.54 Å) running at 40 kV voltage and 40 mA current was used to take the X-ray diffraction (XRD) pattern. The electrospun fibers' morphologies were imaged by the Field Emission Scanning Electron Microscopy (FE-SEM) (JEOL, JSM-IT100) operated at 20 kV and accelerating voltage of 200 kV. The NFs mats prepared from CNT mixed P(VDF−HFP) solution are termed ES(C-HFP), and ES(CD-HFP) for both CNT and DNA mixed P(VDF−HFP) solution respectively. A digital storage oscilloscope (DSO) (Agilent, DSO3102A) was used to record the piezoelectric output and capacitor charging voltage data of NFsPEH, fabricated by the ES(CD-HFP) composite nanofiber (NFs) mat.

RESULTS AND DISCUSSION

The FT-IR spectra (Fig. 1(a)), show the characteristic mode of the well-known phases of the two composites. After the CNT and DNA fillers are introduced prominent characteristic peaks at 1233 and 1277 cm^{-1} appeared as the signature of β-phase and γ-phase respectively.[4, 5] The intense peak at 840 cm^{-1} also indicates the signature of the β- and γ-phases.[5] Thus, the external fillers utilized in the P(VDF−HFP) solution, play an essential role in crystallographic phase transformation (*i.e.*, α → γ/β phase). The intensity of absorption at the 840 cm^{-1} band is selected in order to calculate the samples' electro-active phase (F_{EA}) %. The following equation can be used for the calculation of F_{EA} *i.e.*,

$$F_{EA} = \frac{A_{EA}}{\left(\frac{K_{840}}{K_{764}}\right)\times A_{NEA}+A_{EA}} \times 100\% \qquad (1)$$

where A_{EA} is the intensity of absorbance at 840 cm^{-1}, A_{NEA} is the intensity absorbance at 764 cm^{-1}, K_{840} is the absorption coefficient at 840 cm^{-1}, and K_{764} is the coefficient of absorption at 764 cm^{-1}. The values are K_{840} = 7.7×10^4 cm^2 mol^{-1} and K_{764} = 6.1×10^4 cm^2 mol^{-1}. The interactions between the fillers CNT and DNA with P(VDF−HFP) molecules increase the β-phase nucleation. The estimated F_{EA} for ES(C-HFP) is about 97%. On the other hand, the value of F_{EA} is attained more than 99% for the composite ES(CD-HFP). This result indicates that CNT and DNA fillers are acceptable for designing piezoelectric-based devices. XRD pattern of the ES(CD-HFP) composite NFs (Fig. 1(b)) represents the presence of β-phase at $2\theta \sim 21°$ (110/220).[5, 6] Overall crystallinity in the composite ES(CD-HFP) NFs is found to be (χ_c~55%). The FE-SEM image (Fig. 1(c)) illustrates the surface morphology of the electrospun ES(CD-HFP) NFs mat respectively. A histogram of the fiber diameter is displayed in the inset of Fig. 1(c) and the composite is composed of randomly oriented NFs with an average diameter of around 200 nm. In addition, the presence of DNA attached to the NFs is also clearly observed.[5]

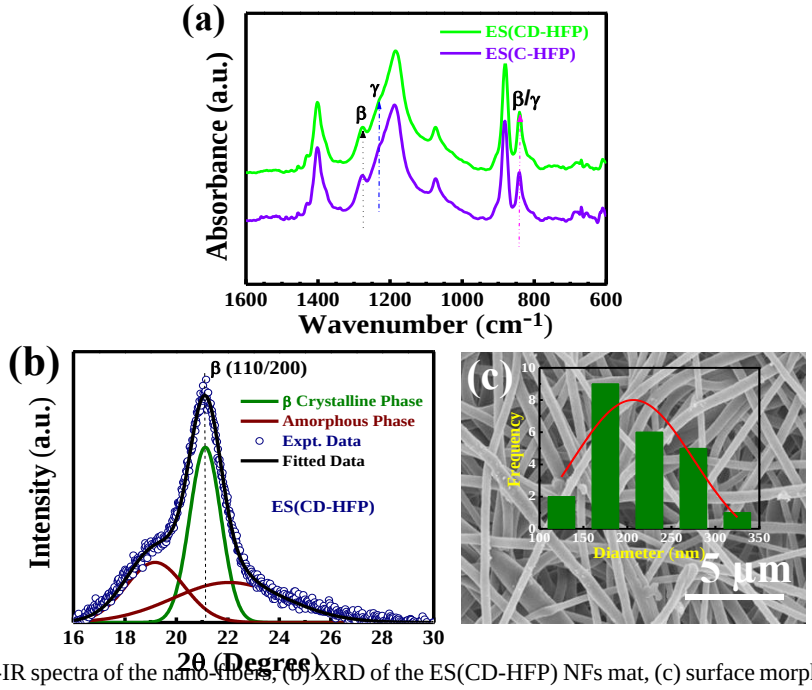


FIGURE 1. (a) FT-IR spectra of the nano-fibers, (b) XRD of the ES(CD-HFP) NFs mat, (c) surface morphology of the ES(CD-HFP) NFs mat. The statistical distribution of the related fibers' diameters is shown in the inset of Figure 1(c).

The NFs-based piezoelectric harvester's (NFsPEH) mechanical energy harvesting capability (Fig. 2(a)) has been assessed by impacting repetitive stress amplitude (σ_a) of ~14 kPa by constant finger tapping on the surface of the WPH of ES(CD-HFP) composite NFs mat.[7, 8] The variation in the output voltage and the corresponding current signal through the outer resistor (R_L) of the ES(CD-HFP) mat (Fig. 2(b)) shows gradual rises and decreases with increasing load resistance. At a typical value of around 10 MΩ of resistance, the instantaneous power ($W = \frac{V^2}{R_L}$), where R_L is the external load resistance, can reach up to 5.6 μW (inset of Fig. 2(b)). We have also harvested wind energy from the prepared NFsPEH by fixing the WPH and blowing the wind at a different velocity. It showed a maximum of ~4.5 V open-circuit output voltage (Fig. 2(c)) and is also capable of successfully charging up the capacitors of 1 μF and 4.7 μF capacitances separately through a full-wave bridge circuit within a very short period, *i.e.*, 50 s and 170 s (Fig. 2(d)) when the wind flow velocity was ~8.5 m/s, promising for developing a wind energy harvesting applications.

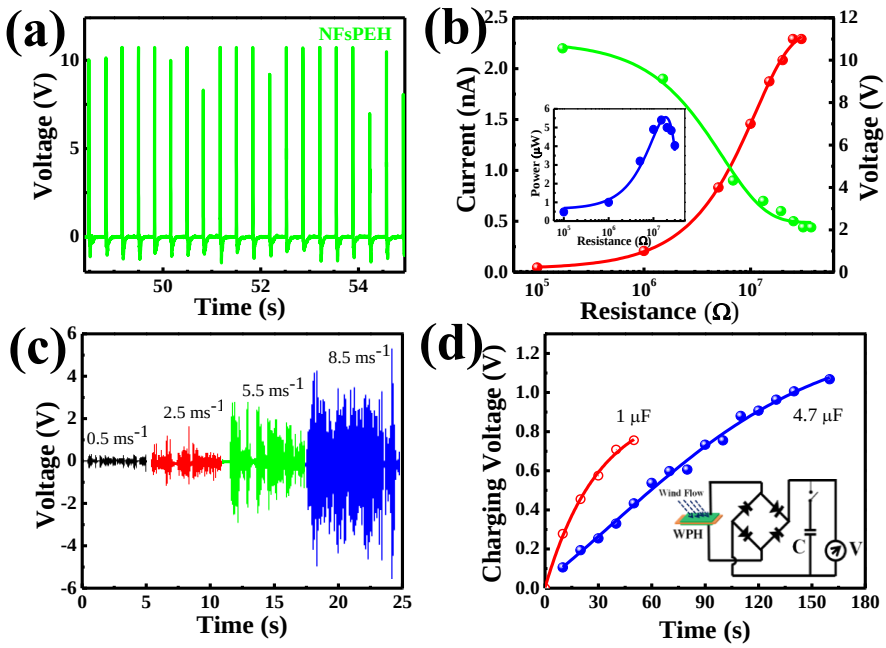


FIGURE 2. (a) ES(CD-HFP) nanofibers (NFs) mat-fabricated NFsPEH open-circuit output voltage during repeated finger-touch motion, (b) output open-circuit voltage and theoretical current amplitude, the inset figure represents instantaneous output power over the load resistances, (c) NFsPEH's open-circuit voltage caused by wind blowing at a different velocity, and (d) Charging response of capacitors (1 μF and 4.7 μF) as a function of time and the inset displays the equivalent circuit schematic

CONCLUSIONS

In conclusion, this work emphasized inducing a large proportion (~99%) of the electroactive phases in ES(CD-HFP) nano-fibers (NFs) based composite. The energy harvesting ability of fabricated NFsPEH showed a better response of about ~12 V under repeated finger-touch motion and ~4.5 V open-circuit output voltage with the capacitor charging ability by the wind flow drives WPH as a power source for portable electronics as well as offer a number of promising applications in piezoelectric energy harvesting-based security monitoring, noise detection, and health care monitoring.

ACKNOWLEDGMENTS

The research facilities provided by North Bengal University's Department of Physics are acknowledged by the authors. Priti Sundar Barman acknowledges the West Bengal government's Swami Vivekananda Merit-cum Means Scholarship (WBSVMCM; Applicant ID: WBP211629445105).

REFERENCES

1. S. Garain, S. Jana, T. K. Sinha and D. Mandal, ACS Appl. Mater. Interfaces, Vol. 8, pp. 4532–4540 (2016).
2. H. Parangusan, D. Ponnamma and M. A. A. Al-Maadeed, Sci. Rep., Vol. 8, pp. 754–766 (2018).
3. A. Anand, D. Meena, and M. C. Bhatnagar, Journal of Alloys and Compounds, Vol. 843, pp. 156019–156029 (2020).
4. P. Saxena, and P. Sukla, Advanced Composites and Hybrid Materials, Vol 4, pp. 8–26 (2021).
5. A. Tamang, S. K. Ghosh, S. Garain, Md. M. Alam, J. Haeberle, K. Henkel, D. Schmeisser and D. Mandal, ACS Appl. Mater. Interfaces, Vol. 7, pp. 16143−16147 (2015).
6. S. Zhang, B. Zhang, J. Zhang, and K. Ren, ACS Appl. Mater. Interfaces, Vol. 13, pp. 32242–32250 (2021).
7. M. M. Alam, S. K. Ghosh, A. Sultana, and D. Mondal, ACS Sustainable Chem. Eng., Vol. 6, pp. 292−299 (2018).
8. F. Meng and J. Hu, Polymers, Vol. 16, pp. 1728−1738 (2024).

Comparative Simulation of Piezoelectric Output at Different Inclinations in ZnO, $BaTiO_3$, and PZT-4 Nanorods for the Development of Tactile Sensors

Laishram Anamika Devi[1], Aparna Singh[2], and Pramod Kumar[3,*]

[1]*Center for Research in Nanotechnology and Science (CRNTS), Indian Institute of Technology Bombay, Mumbai 400076, India*

[2] *Department of Metallurgical Engineering & Materials Science, Indian Institute of Technology Bombay, Mumbai 400076, India*
[3]*Department of Physics, Indian Institute of Technology Bombay, Mumbai 400076, India*

[*]Corresponding author: pramod_k@iitb.ac.in

Abstract. This study investigates the potential of three piezoelectric materials Zinc Oxide (ZnO), Barium Titanate ($BaTiO_3$), and Lead Zirconate Titanate (PZT-4) by varying the inclination angle of a cylindrical nanorod. The peak value of the piezoelectric potential of ZnO and $BaTiO_3$ nanorods are observed at 60° inclination angles with value 62.336 mV and 29.024 mV, respectively whereas in PZT-4 it is observed at 30° inclination angle with value 21.341 mV. Among these materials, ZnO nanorods exhibit higher piezoelectric potential at all relative inclination angles. The vertical nanorods in all the materials show less piezoelectric output, which contrasts with the existing assumption where maximum piezoelectric potential response should be observed in vertical nanorods due to higher d_{33} piezoelectric coefficient along the vertical direction. The values of piezoelectric coefficients and dielectric constant vary due to the anisotropic nature of the material. The higher piezoelectric output in inclined nanorods of all the material suggests increased normal stress and shear stress contribution. These results can be used for the development of efficient, highly sensitive, and better-performing tactile sensors.

Keywords: Zinc oxide, Barium Titanate, Lead Zirconate Titanate, Finite Element Method, Tactile sensors, Piezoelectricity.

INTRODUCTION

Self-powered micro-electromechanical technologies such as tactile sensors [1], flexible electronic skin [2], nanogenerators [3], and energy-harvesting devices [4] have become highly in demand in recent years. These devices can harvest energy from their ambient surroundings, thus removing the requirement for external power supply and batteries. These devices contribute to a more sustainable environment-friendly solution for environmental issues. These emerging self-powered technologies are inevitably dependent on piezoelectric materials. The development of these technologies requires to study of the performance of various piezoelectric materials such as Zinc Oxide (ZnO) [5], Barium Titanate ($BaTiO_3$) [6], Quartz [7], Aluminum Nitride (AlN) [8], Lithium Niobate ($LiNbO_3$) [9], and Lead Zirconate Titanate (PZT), etc. [9]. PZT is considered to have the highest piezoelectric coefficient among these materials but is toxic. ZnO is a promising candidate for the development of self-powered technologies due to its biocompatibility and environment-friendly, high c-axis piezoelectric coefficient d_{33}, high exciton binding energy of 60 meV and a wide direct band gap of 3.4 eV. An electromechanical phenomenon called Piezoelectricity happens when the electric charges are generated by applying a mechanical force and vice-versa. The key phenomenon for making self-powered sensing devices is the effect of direct piezoelectricity. Achieving efficient, robust performance in these devices is highly dependent on the material properties such as piezoelectric coefficients, dielectric constant, geometrical structure of the piezoelectric materials, and device design. The piezoelectric response of various materials can be simulated by COMSOL simulation using the finite element method (FEM). Owing to the increased piezoelectric response of the piezoelectric coefficient d_{33}, vertical nanorod geometry has been chosen and researched in the literature for the creation of piezoelectric devices. However, the piezoelectric potential of inclined nanorod geometry is rarely studied in the literature. Therefore, we have simulated and compared the piezoelectric output potential for vertical and inclined nanorod geometries in ZnO, $BaTiO_3$, and PZT-4 piezoelectric materials for studying the effect of various piezoelectric coefficient and dielectric constants.

SIMULATION DETAILS

The piezoelectricity is an electromechanical phenomenon where the electric dipoles or charges are generated by a mechanical force and vice-versa. Mathematically, the piezoelectric effect is constituted by coupled constitutive equations to relate the mechanical deformation to the electric field. The direct piezoelectric effect is the phenomenon that occurs in self-powered devices. The coupled constitutive equation that the mechanical and electrical variables in direct piezoelectric effect can be written as (where i, k = 1,2,3 and j = 1, 2, ……6) [10].

$D = d\,S + \varepsilon^{S} E$ (Strain-Charge form)

$T = c^{E}S - d^{t}E$ (Stress-Charge Form)

where $\boldsymbol{D}$ is the electric charge density displacement vector (C m^{-2}), $\mathbf{d}$ is the piezoelectric coefficient or piezoelectric strain coefficient for direct effect (C N^{-1}), $\boldsymbol{T}$ is the mechanical stress (N m^{-2}), $\boldsymbol{\varepsilon^{S}}$ is the permittivity at constant stress (F m^{-1}) at constant mechanical strain, $\mathbf{E}$ is the electric field strength (V m^{-1}), $\mathbf{c^{E}}$ is the elasticity matrix or stiffness (Nm^{-2}) at the constant electric field and ^{t} denotes the transpose [10]. Here we study and compare the piezoelectric potential of three piezoelectric materials ZnO, $BaTiO_3$, and PZT-4 in the COMSOL Multiphysics simulation for different geometries vertical and inclined single cylindrical nanorod geometry by FEM. Cylindrical vertical nanorods at a 90° angle and inclined nanorods with the same diameter of 500 nm and length of 5 µm at 30°, 60°, and 70° angles are designed in the software. A fixed constraint is applied at the bottom of the NR in both vertical and inclined geometry. In the case of vertical nanorod geometry, a pressure of 50 kPa is applied on the top area whereas in the inclined geometry, the same pressure is applied on the top as well as on the facial portion which faces the direction of the applied pressure as boundary load. The electrically grounded is provided at the bottom part of the single NR, and a floating potential is calculated from the top as part of the electrostatic boundary conditions. The study was done in stationary mode, and the simulations were carried out for the three different materials.

RESULT AND DISCUSSSIONS

The simulation results show that as the angle of inclination of the single cylindrical nanorod varies from the substrate, there is variation in the piezoelectric potential at a constant applied pressure and aspect ratio. The variation of piezoelectric potential and von Mises stress for ZnO, Ba$\mathbf{TiO_3}$, and PZT-4 inclined at 90° and 60° angles from the substrate, are shown in Figures 1 and 2 respectively. Figure 2 (g) shows the piezoelectric potential varies to the angle of inclination. ZnO and Ba$\mathbf{TiO_3}$ nanorod exhibits higher piezoelectric potential at an inclination angle of 60° whereas PZT-4 exhibits at an inclination angle of 30°.

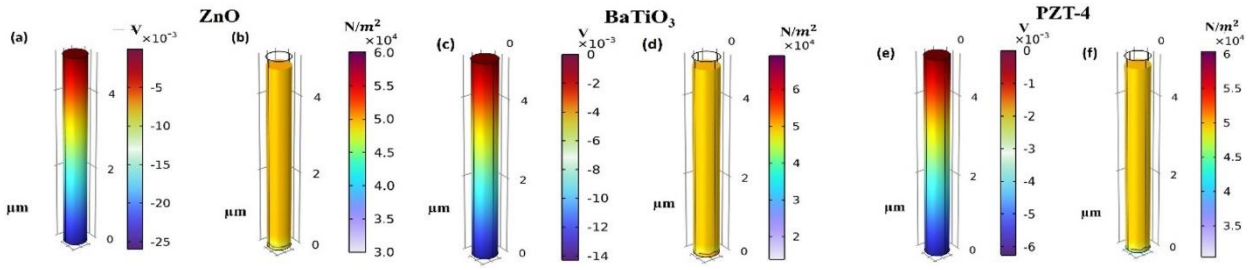


Figure 1: The cylindrical vertical nanorods (a),(c), and (e) show the piezoelectric potential, and (b),(d) and (f) show the von Mises stress for ZnO, $BaTiO_3$,and PZT-4 respectively.

The reason for exhibiting variation in piezoelectric potential at different inclination angles of nanorods is that these materials show anisotropic piezoelectric coefficients and anisotropic dielectric constants. The piezoelectric potential in ZnO and $BaTiO_3$ found to increase initially from 30° to 60° then decreases from 70° to 90°. The peak value is observed at 60° inclination angle which is 62.336 mV for ZnO and 29.024 mV for $BaTiO_3$ due to the experience of the larger normal stress and contribution from shear stress whereas in PZT-4, the peak value is observed at 30° inclination angle of value 21.341 mV which may be the result of combined contribution from various piezoelectric coefficients and dielectric constants within the nanorod leading to a more significant piezoelectric response compared to other angles[11]. Among these materials, ZnO exhibited higher piezoelectric potential due to the material's higher anisotropic piezoelectric coefficient and lower anisotropic dielectric constant properties, as shown in Figure 2(g).

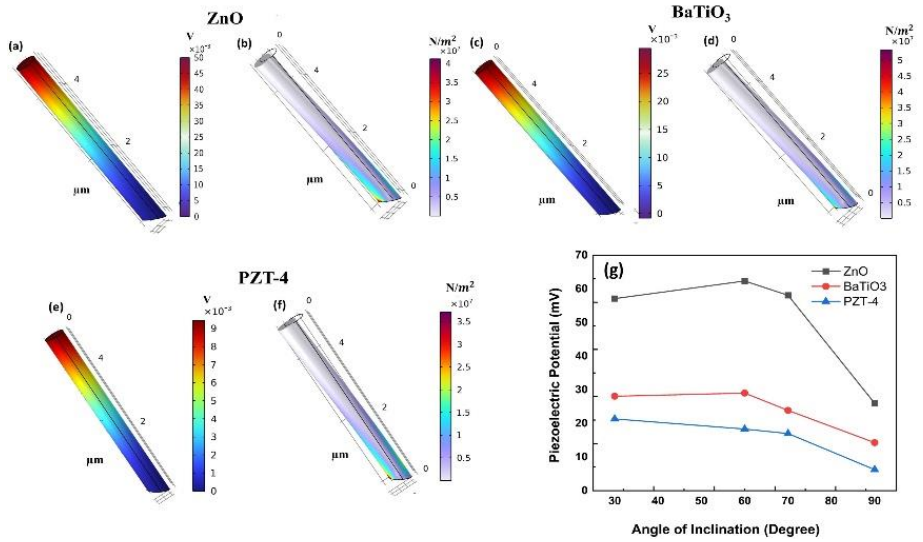


Figure 2: The cylindrical nanorods inclined at 60° (a), (c), (e) show the piezoelectric potential, (b), (d), (f) show the von Mises stress, and (g) show piezoelectric potential versus angle of inclination of nanorod for ZnO, $BaTiO_3$, and PZT-4 respectively.

CONCLUSION

In conclusion, we have compared the piezoelectric potential of three materials ZnO, $BaTiO_3$ and PZT-4 by COMSOL Multiphysics Simulation. According to the simulation results, the peak value of the piezoelectric potential of ZnO and $BaTiO_3$ are observed at 60° inclination angles with values 62.336 mV and 29.024 mV respectively, whereas PZT-4 is observed at 30° inclination angle of value 21.341 mV. When the nanorods are inclined due to the experience of combined normal and shear stress induces all the piezoelectric coefficients and dielectric constants leading to the higher peak values. According to these simulated results, the inclined nanorod growth is preferred over vertical growth which will be a cost-effective material growth structure for optimizing the sensitivity and functionality of self-powered tactile sensors.

ACKNOWLEDGEMENT

The authors acknowledge the Indian Institute of Technology Bombay (IIT Bombay) for the research fellowship.

REFERENCES

1. Y. Zhang, G. Lu, M. Chen, Y. Liu, & R.Yao, IEEE Sens. J., Vol *22*(13), 12613-12621 (2022).
2. W. Deng, L. Jin, B. Zhang, Y. Chen, L. Mao, H. Zhang, & W. Yang, Nanoscale, Vol *8*(36), 16302-16306 (2016).
3. M. Bah, T.S.Tlemcani, S.Boubenia,C. Justeau, N.Vivet, J.M.Chauveau, & Alquier, D. Nanoscale Adv.,Vol 4(4), 1125-1135 (2022).
4. A.Yang,Y. Qiu, D.Yang, K. Lin, & S. Guo, RSCAdv.,Vol 11(6), 3363-3370 (2021).
5. S. Xu, Y. Qin, C. Xu, Y.Wei, R.Yang , & Z.L.Wang, Nat. Nanotechnol, Vol 5(5), 366-373 (2010).
6. A.Koka, Z. Zhou, & H.A. Sodano, EES,Vol 7(1), 288-296 (2014).
7. J. W. Lee,B. Lee, J.W. Kim, & B.K. Ju, IEEE Sens. J, Vol 20(22), 13277-13283 (2020).
8. N.A.F. Zaki,A.A. Aziz, N. Khairudin, & N. Burham, In 2021 IEEE Regional Symposium on Micro and Nanoelectronics (RSM) (2021, August). (pp. 38-41). IEEE, 2021.
9. S. Bai, Q. Xu, L. Gu, F. Ma, Y. Qin, & Z.L. Wang, Nano Energy, Vol 1(6), 789-795 (2012).
10. R. Ahmed, & P. Kumar, Phys. Scr., Vol 99(2), 025930 (2024).

New Oxygen Deficient Double Perovskite Ceramic Compound: $YSrCuFeO_5$

Rashmi Rekha Sahoo*[,1,a)], R.N.P. Choudhary[1]

Multifunctional Research Laboratory, Siksha 'O' Anusandhan (deemed to be) University, Department of Physics, Bhubaneswar,Odisha, 751030, India.

[a)] srashmirekha1@gmail.com

Abstract**.** The ability to intricately design, manipulate and develop new materials by structure-property modification at various scales has launched a completely new era of materials fabrication. In the present communication we have reported the (structural, dielectric, impedance and conductivity) behaviour of a new oxygen deficient double perovskite $YSrCuFeO_5$ of the general formulae $A_nB_nO_{3n-1.}$ It has been synthesized using cost-effective mixed-oxide solid-state reaction route. Room temperature X-ray diffraction studies reveal the overall phase and further analysis suggests tetragonal symmetry with lattice parameters a = 3.8318(4)Å, c = 7.6063(4)Å and volume = 111.68(Å)^3. Microstructure study using scanning electron micrograph (SEM) confirms the formation of compact and homogeneously distributed grains with distinct grain boundaries with an average grain size of 1.32 µm. The crystallite size of the sample is calculated from the Williamson-Hall plot and is found to be 63.9 nm. To decipher the transport property of the compound frequency dependent conductivity study has been carried out in accordance to universal Jonscher power law. Non-overlapping small polaron tunneling (NSPT) and correlated barrier hopping (CBH) conduction mechanisms are prevalent in the sample. Complex impedance spectroscopy study suggests negative temperature coefficient of resistance (NTCR) behaviour and the deviation of the center of the semicircular loops from the real abscissa suggests Non-Debye type relaxation.

Keywords: *Dielectric analysis; conductivity; X-ray diffraction; Microstructure; Jonshers law*

1. INTRODUCTION

Oxygen deficient perovskites of the general formulae $A_nB_nO_{3n-1}$ where n can take values from n=1,2,3,4.. find major applications in the field of fuel cells pertaining to their ability to efficiently convert chemical energy into electrical energy. Huge applications of perovskites can be ascribed to their structural stability and high tolerance. The aforementioned ability favors the formation and feasibility of perovskites with different possible combination of constituents with enhanced thermal, electrical and impedance behaviour. As a result of this double perovskites are most often used as cathode materials, in gas sensors and thermoelectrics[1]. The novel compound $YSrCuFeO_5$ falls on the category of oxygen-deficient double perovskites; considering that in $YSrCuFeO_5$, n = 2 [2]. In this structure, the A site hosts a rare-earth element, while Fe and Cu ions occupy the B site. The $YSrCuFeO_5$ structure can also be represented using the $AA'BB'O_{6-\delta}$ notation, where A sites are mainly filled by rare-earth elements and B sites by transition metals [3].With the perspective of exploring the multifunctional aspects of this material understanding its structural, dielectric and frequency response of charge carriers we have analysed its conductivity and impedance charecterstics in this communication.

2. EXPERIMENTAL TECHNIQUES: (SYNTHESIS & CHARECTERIZATION)

$YSrCuFeO_5$ has been prepared by conventional ceramic processing route. The high purity oxides and carbonate such as Y_2O_3, CuO, $SrCO_3$, Fe_2O_3 have been used for preparation of the sample. The abovementioned selected precursors were thoroughly ground using an agate mortar and pestle for 2 hours in air, followed by an additional 2 hours in methanol to ensure a homogeneous mixture of the target compound. The resulting mixture was calcined at 950 °C and subsequently sintered at 1000 °C. Phase formation was confirmed via X-ray diffraction (XRD) analysis using a Rigaku Ultima-IV diffractometer. After calcination, the powder samples obtained was cold-pressed into circular pellets (~12 mm diameter, ~1–2 mm thickness) using a hydraulic press under a pressure of 4.5×10^5 N/m². To facilitate reliable electrical characterization, a thin layer of conductive silver paste was applied to establish ohmic contacts. Prior to measurement, they were heated at 150 °C for 2 hours to remove moisture. Dielectric measurements were conducted using (N4L, PSM1735) LCR meter from 1 kHz to 1 MHz frequency range.

2.1 STRUCTURAL AND MICRO-STRUCTURAL ANALYSIS:

Figure.1(a). presents the room-temperature XRD data of the synthesized sample. The indexing of the respective data sets is performed using the " POWDMULT" software. The sample is found to crystallize in tetragonal crystal system with a = 3.8318(4)Å, c = 7.6063(4)Å and volume = 111.68(Å)^3 with the estimated standard deviation in the parenthesis. The crystallite size is calculated using Williamson-Hall relation given as: $\beta\cos\theta = 4\varepsilon_{st}\sin\theta + \frac{k\lambda}{T}$ is found to be 63.9 nm. The scanning electron micrograph presented in the Fig1(b). suggests the presence of well defined grain with distinct grain boundaries .The average grain size is determined from the histogram shown as inset of Fig.1(b) and is found to be 1.32 µm. The presence of all the constituent elements is further confirmed from the energy dispersive X-ray spectroscopy spectrum presented in Fig.1(c).

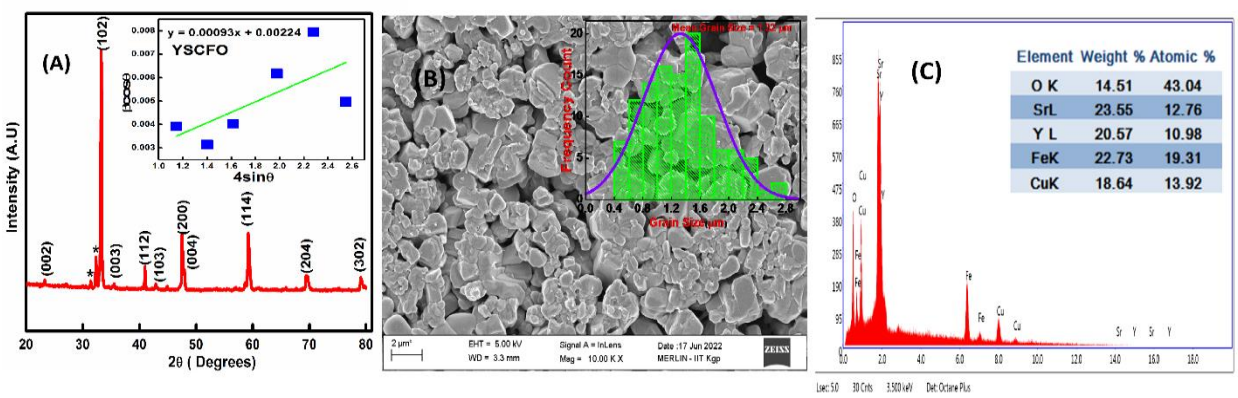


FIGURE 1. X-ray diffractogram (WH Plot inset) of YSCFO sample along with SEM and EDAX images.

2.2 TRANSPORT CHARECTERISTICS:

Conductivity study is very much crucial in determining the transport behavior of the charge carriers and hence their mobility. The frequency dependent plots (Fig. 2(a)) of ac conductivity are plotted within the temperature ranges of 25 to 300 °C and fitted with Jonschers equation $\sigma_{ac} = \sigma_{dc} + A\omega^s$. The terms σ_{ac} and σ_{dc} are conductivities pertaining to the ac and dc component respectively. s is the frequency exponent typically ranging from 0 to 1 and A is the polarizability strength. The exponent 's' provides insights into the interactions among dipoles involved in the polarization mechanism. We observe that the trend followed by s as a function of temperature (Fig. 2(a)).inset) suggests, initially the compound exhibits NSPT (value of frequency exponent s increase with temperature) and then follows CBH (value of frequency exponent s decreases with temperature). When the value of s < 1 translational 'motion is exhibited ; whereas when s>1 localised hopping in the viscinity of the neighbourhood is observed [4].The expression for s in case of NSPT and CBH model is given as:

$$s = 1 - \left[\frac{4}{\frac{1}{\omega\tau_0} - \frac{W_H}{k_B T}}\right] \text{ and } s = 1 - \frac{6k_B T}{W_m - k_B T \ln(1/\omega\tau_0)} \quad \text{---------- (1)}$$

where, W_H is the activation energy associated with polaron hopping and Wm is the binding energy governing electron transfer across neighbouring sites . CBH is a high temperature phenomenon and is also observed for the sample.

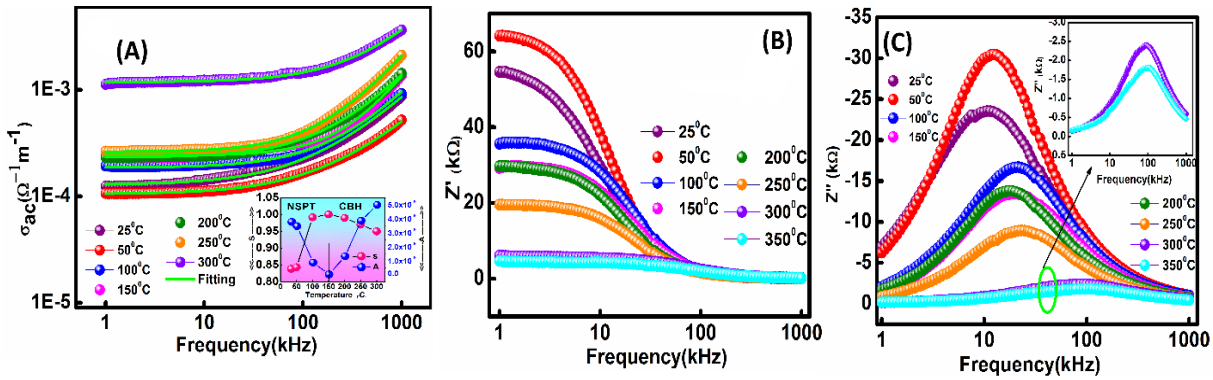


FIGURE 2. a) Frequency-variant ac conductivity plot (inset shows temperature variance of A and s) b) Frequency-dependent real part of impedance (Z') plot. c) Frequency-sensitive imaginary part of impedance (Z") plot.

2.3 IMPEDANCE SPECTROSCOPIC ANALYSIS AND NYQUIST PLOT : One of the significant non-evasive methods of microstructure and electrical property evaluation is analysis of the complex impedance spectroscopy plots.The nature of the different electroactive regions with their varying values of resistance and capacitance and its impact on the type of relaxation behaviour observed can be correlated and ascertained.The application of ac input signal across the silver paint electroded YSCFO pellet and the output response obtained and formulated as $Z^* = Z' + j\,Z''$ where $Z' = \frac{R}{1+(\omega\tau)^2}$ and $Z'' = \frac{-\omega R\tau}{1+(\omega\tau)^2}$. The imaginary part of impedance curves (Fig. 2 (c) depict presence of asymmetric peaks that keep shifting with frequency suggesting a spread of relaxation times and thus confirm non-Debye type relaxation in the compound. Figure. 3 (a) shows the nyquist plots of the sample and confirms the NTCR effect along with non-Debye relaxation behavior also evident from depression angle measured at 50 °C shown in Fig. 3.

TABLE 1. Details of obtained fitting parameters grain and grain boundary resistance and capacitance ranging from 25 °C to 350 °C.

Temperature	Model	Rg	Q	Cg	Rgb	Q	Cgb
25 °C	**(RQC)**	5.905E+004	3.408E-009	1.385E-010			
50 °C	**(RQC)**	6.661E+004	4.965E-010	1.128E-010			
100 °C	**(RC)(RQC)**	2.666E+002		9.541E-010	3.695E+004	3.222E-009	1.789E-010
150°C	**(RC)(RQC)**	1.062E+004		1.114E-009	1.964E+004	7.236E-010	1.121E-011
200 °C	**(RC)(RQC)**	2.315E+004		4.130E-010	6.768E+003	2.243E-008	2.541E-010
250°C	**(RC)(RQC)**	1.432E+004		4.741E-010	5.657E+003	2.542E-008	5.261E-019
300 °C	**(RC)(RQC)**	2.640E+003		6.467E-010	3.318E+003	1.928E-008	5.903E-017
350 °C	**(RC)(RQC)**	2.208E+003		7.040E-010	2.389E+003	4.533E-008	7.291E-022

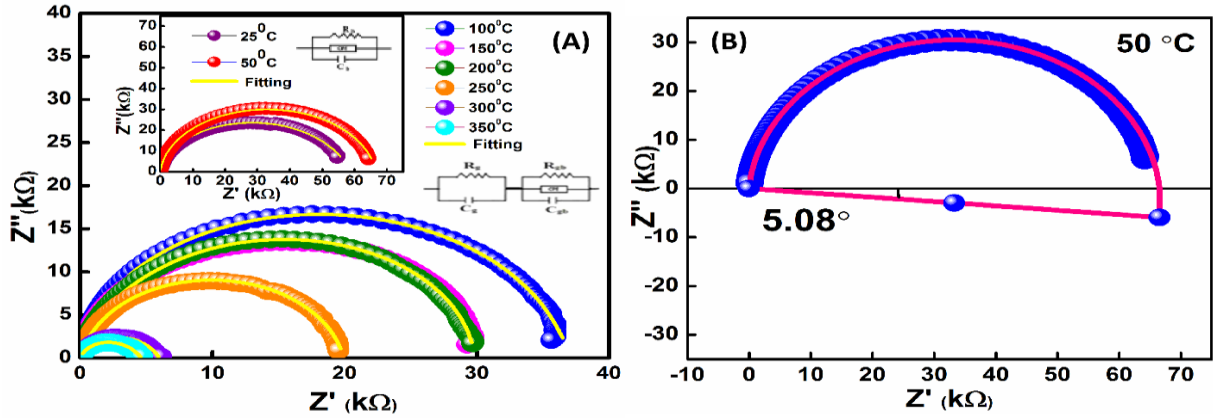


FIGURE 3. Nyquist plots of YSCFO compound along with the depression angle plot measured at 50 °C.

CONCLUSION:

The present study reports the formation of $YSrCuFeO_5$ compound in tetragonal symmetry. The scanning electron micrograph presents the microstructure of the sample along with the conformity of all the elements presence from EDX reports. The conductivity analysis suggests the presence of both tunneling and hopping mechanisms present in the samples. The Nyquist fitting of the impedance graphs clearly depicts the grain effect predominance at lower temperature and higher frequencies along with both bulk and interface effects at higher temperatures. The degree of deviation from the Debye type behavior is also calculated as a measure of deviation measured at 50 °C.

ACKNOWLEDGEMENT:

The authors acknowledge IIT Kharagpur CIF for SEM characterization and the author Rashmi Rekha Sahoo would acknowledge DST, GOI for INSPIRE fellowship.

REFERENCES:

1. A.I. Klyndyuk, Layered Perovskite–Like Oxides 0112 Type: Structure, Properties, and Possible Applications. In Advanced in Chemistry Research; Taylor, J.C., Ed.; Nova Science Publishers: New York, NY, USA, pp. 59–105 (2010).
2. M.T.Anderson, J.T. Vaughey, and K.R. Poeppelmeier, Structural similarities among relaxation in the double perovskite YBaCuFeO5. Journal of Physics: Condensed Matter, 29(14), p.145801 (1993).
3. M.K.Srivastava, X.S.Qiu, Y.Y. Chin, S.H.Hsieh, Y.C.Shao, Y.H. Liang, C.H. Lai, C.H. Du, H.T. Wang, J.W. Chiou, and Y.C Lai ,The effect of orbital-lattice coupling on the electrical resistivity of $YBaCuFeO_5$ investigated by X-ray absorption. Scientific reports, 9(1), pp.1-11 (2019).
4. D. Triyono, S. N Fitria, & U. Hanifah, Dielectric analysis and electrical conduction mechanism of $La_{1-x}Bi_xFeO_3$ ceramics. RSC advances, 10(31), 18323-18338 (2020).

Investigation of structural and dielectric studies of Ho substituted Nd_2CoMnO_6 Double Perovskite compounds

Nibedita Nayak[1] and S. Ravi[2*]

[1,2]*Department of Physics, Indian Institute of Technology Guwahati, Guwahati-781039, India*

[*] Email: sravi@iitg.ac.in

Abstract. In this work, an in-depth examination of the $(Nd_{1-x}Ho_x)_2CoMnO_6$ (x = 0.0 – 0.3) series is carried out, focusing on their structural, electrical properties. The materials are synthesized using the conventional solid-state method, X-ray diffraction (XRD) confirmed the single phase formation of all samples. Detailed structural analysis through Rietveld refinement revealed that all compositions adopt monoclinic symmetry within the $P2_1/n$ space group. To probe their electrical behaviour, impedance spectroscopy is performed across a range of frequencies (10^2-10^6 Hz) and temperature (303K-423K). The frequency-dependent results indicate that space charge polarization plays a significant role at lower ranges in the dielectric response, while the temperature dependence points to a negative temperature coefficient of resistance. Further insights into the conduction mechanism are obtained by analysing the AC conductivity data with Jonscher's Power Law, suggesting the large polaron tunnelling model of conduction mechanism. Finally, the activation energy corresponding to both the relaxation phenomena and the conduction process are calculated using the Arrhenius relation, providing a deeper understanding of the movement of charge carriers dynamics in the present study.

Keywords. Double perovskites, Dielectric relaxation, Arrhenius relation, Ac conductivity, Jonscher's power law,

1. INTRODUCTION

Double perovskites (DPs), denoted by the formula $R_2MM'O_6$ (with R being a rare-earth element and M/M' being transition metals), are highly valued for their wide range of structural, magnetic, and electrical properties. In ideal DPs, oxygen ions should align at a 180˚ angle relative to the transition metals within the MO6/M'O6 octahedra. However, in practice, deviations from this ideal alignment, along with octahedral distortions and tilting, are common and lead to a variety of functional properties. Extensive research has been conducted on DP compounds with Co^{2+} as M and Mn^{3+} as M', focusing on their magnetic and dielectric properties. For example, La_2CoMnO_6 shows a ferromagnetic transition close to room temperature (around 235 K) and possesses both magnetic and dielectric properties that make it suitable for microwave dielectric resonators [1]. Similarly, Y_2CoMnO_6 features a low leakage current, positioning it as a potential candidate for electronic devices [2]. Other CoMn-based DPs also demonstrate noteworthy magnetic and dielectric properties, indicating their potential for use in high-temperature applications [3]. DP materials are recognized for their inherent dielectric properties, making them highly suitable for use in microwave technologies and various advanced electronic applications. In this work, we explored Nd_2CoMnO_6 compounds with partial substitution of Ho to gain deeper insight into their behavior. In addition to the structural characterization, dielectric studies, especially their complex impedance spectroscopy and conductivity analysis are studied for the synthesized compounds.

2. EXPERIMENTAL TECHNIQUES

A series of $(Nd_{1-x}Ho_x)_2CoMnO_6$ (x = 0.0 – 0.3) compounds are synthesized through the standard solid-state synthesis approach. Oxide of the required elements are taken as starting material. They are manually ground in a mortar and pestle for 3 hours to ensure fine and consistent mixing. The homogenized mixture is subjected to a preliminary heat treatment for 6 hours at 800°C. After cooling, the pre-sintered material is compacted into disc-shaped pellets (diameter: 10mm, thickness: <2mm) using a hydraulic press. The formed pellets are then sintered for a duration of 48 hours at 1200°C to ensure proper phase formation.

Phase identification of the synthesized samples is carried out using powderX-ray Diffraction (XRD) at room temperature, employing a TTRAX III diffractometer (Rigaku) with a Cu Kα radiation source (wavelength = 1.5406 Å). The microstructural features of the sample surfaces are investigated through Field Emission Scanning Electron Microscope (FESEM) using a ZEISS Sigma 300 system. Elemental composition analysis is performed via Energy Dispersive X-ray (EDX) system. Dielectric behavior is measured using an LCR meter (Model 4300) over a frequency range from 10^2 Hz to 10^6 Hz and within a temperature range of 303–423 K.

3. RESULTS AND DISCUSSIONS

Room-temperature XRD patterns of all samples are shown in Fig. 1 (a), confirming their single phase formation. To extract more structural information, Rietveld refinement has been performed for all the samples and the fitted plot for x = 0.3 sample along with the observed data is shown in Fig. 1 (b). Additionally, the (hkl) planes are also mentioned in the figure which aligns with the monoclinic symmetry with $P2_1/n$ space group. As the substitution amount of Ho increases in the compounds, both lattice parameters and unit cell volume gradually decrease. This behavior results from the replacement of larger Nd^{3+} ions with smaller Ho^{3+} ions, leading to a more compact crystal structure. The deviation of angle β from 90° provides an additional evidence for the monoclinic nature of the structure. The average crystallite size, calculated using Scherer's formula [4], decreased from 35.5 ± 3.0 nm for the x = 0.0 sample to 27.0 ± 1.9 nm for the x = 0.3 sample.

The surface characteristics of the samples are examined through FESEM micrographs, with Fig. 1 (c) displaying the micrograph of the x = 0.2 sample. Grain size distribution is analysed by generating a histogram of the observed grains, followed by fitting the data with a log-normal distribution. This analysis yielded average grain sizes ranging from 2.33 ± 0.07 μm for the x = 0.0 to 1.25 ± 0.03 μm for the x = 0.3, indicating a reduction in grain size with increasing x content.

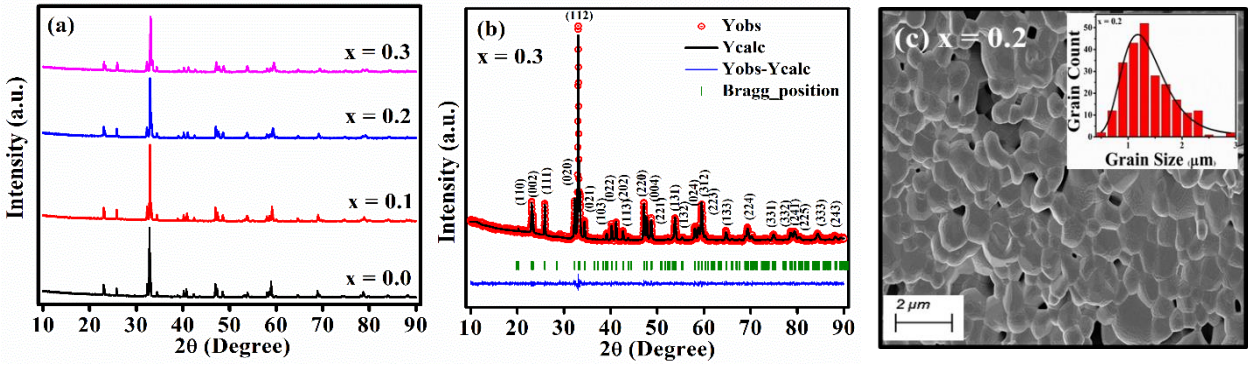


FIGURE 1. (a) XRD patterns of all the samples, (b) Rietveld refined XRD plot of x = 0.3 sample, (c) FESEM micrographs of x = 0.2 sample with inset figure of grain size distribution.

We measured both the real (Z') and imaginary (Z'') parts of the impedance over a frequency range of 10^2 – 10^6 Hz and a temperature range of 303K to 423K. The Z' plot at a specific temperature shows a plateau at lower frequencies and then decreases at higher frequencies. The higher Z' values at lower frequencies are primarily due to space charge polarization. As the temperature increases, Z' values decrease, indicating a negative temperature coefficient of resistance (NTCR) [5]. To understand the relaxation process of charge carriers in the samples, we measured the frequency variation of Z'' at different temperatures, shown in Fig. 2 (a) for the x = 0.3 sample. At each temperature, a pronounced peak appears in the plots at a specific frequency (f_{max}), indicating relaxation behaviour of charge carriers at grain boundaries. The relaxation peak in the Z'' plots shifts toward higher frequencies as the temperature rises, which is attributed to thermally activated charge carriers in the samples. This relaxation process was further analysed using the Arrhenius equation ($f_{max} = f_0 \exp(-E_a/K_BT)$). The activation energy (Ea) was calculated from the plot of the logarithm of f_{max} against the inverse of the temperature, varying from 0.07 eV for the x = 0.0 sample to 0.10 eV for the x = 0.3 sample.

Using the values of Z' and Z'', we calculated the real (ε') and imaginary (ε'') parts of the complex dielectric constant [6]. Fig. 2 (b) shows the frequency variation of ε' for the x = 0.3 sample over a temperature range of 303K to 423K. The ε' values are found to be in the range of 10^4 – 10^5 at lower frequencies. The higher dielectric constant values at low frequencies are primarily due to the significant impact of space charge polarization.

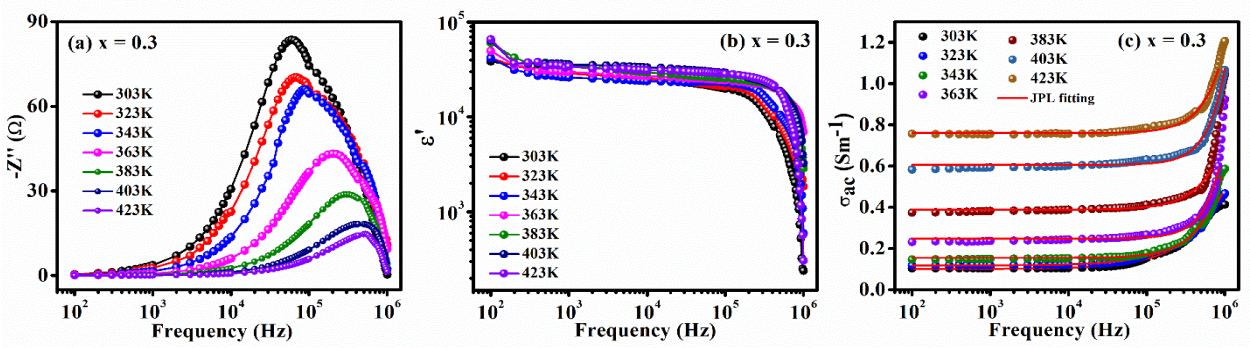


FIGURE 2. Frequency variation of the imaginary part of impedance (a), dielectric constant (b), and ac conductivity with Jonscher power law fitting (c) measured across various temperatures for x = 0.3 sample.

Additionally, to gain insight into the conduction process, we calculated the AC conductivity (σ_{AC}) of all the samples using the values of ε''. By analyzing the trend of σ_{AC}, we fitted these plots with Jonscher's power law, as described in [6].

$$\sigma_{AC} = \sigma_{DC} + B\omega^{n} \qquad \text{i)}$$

The DC conductivity (σ_{DC}) remains unaffected by frequency variations (up to almost 10^5 Hz) but exhibits an increase with rising temperature, suggesting the thermal activation enhances charge carriers' mobility with the samples. Conversely, the frequency dependent term ($B\omega^n$) is governed by the parameters B and n. The variation of n with temperature serves an important indicator for analyzing the nature of conduction process. To better understand the conduction mechanism, the activation energy (E_a) is determined by applying the Arrhenius relation ($\sigma_{DC} = \sigma_0 \exp(-E_a/K_BT)$) to the DC conductivity values obtained from equation (i). The E_a values range from 0.06 eV for the x = 0.0 sample to 0.09 eV for the x = 0.3 sample. An increase in E_a with higher Ho doping concentration is observed, which can be attributed to the reduced hopping of charge carriers. The fitting results suggest that the conduction process involves a charge carrier hopping mechanism and thermal activation of charge carriers [7]. Comparing the activation energy (E_a) values for the relaxation dynamics with those for the conduction mechanism, it is observed that E_a values are nearly comparable [8].

ACKNOWLEDGMENTS

The authors acknowledge the Central Instrument Facility (CIF), IIT Guwahati for for access to XRD, and FESEM facilities.

REFERENCES

1. R. X. Silva, A. S. de Menezes, R. M. Almeida, Journal of Alloys and Compounds **661**, 541-552 (2016).
2. R. Das, R. N. P. Choudhary, Ceramics International **47**, 439-448 (2021).
3. W. Z. Yang, X. Q. Liu, H. J. Zhao, & X. M. Chen, Journal of magnetism and magnetic materials **371**, 52-59 (2014).
4. A.L. Patterson, Physical Review 56, 978–982 (1939).
5. I. N. Bhatti, I. N. Bhatti, Physica B: Condensed Matter **610**, 412943 (2021).
6. D. Mazumdar, I. Das, Physical Chemistry Chemical Physics **23**, 5596-5606 (2021).
7. A. Hadded, J. Massoudi, E. Dhahri, K. Khirouni, B.F.O. Costa, RSC Adv. **10**, 42542–42556 (2020).
8. F. Hcini, S. Hcini, M.A. Wederni, B. Alzahrani, Phys. B Phys. Condens. Matter. **624** 413439 (2022).

Tailoring the Electrical Properties of [0.98KNLNS-0.02BNZSH] Lead-Free Ceramics through Variation in Sintering Temperature

Aditi[1, a)], Amit Kumar[2], V.Kumar [1]

[1)]Department of Physics, Institute of Integrated and Honors Studies (IIHS), Kurukshetra University, Kurukshetra-136119, India
[2)]Department of Physics, Kurukshetra University, Kurukshetra-136119, India

[a)] Corresponding author E-mail: aditikhatkar77@gmail.com

Abstract: In this work, $0.98[((K_{0.4}Na_{0.6})_{0.94}Li_{0.06})(Nb_{0.96}Sb_{0.04})O_3]-0.02[(Bi_{0.5}Na_{0.5})(Zr_{0.8}Sn_{0.1}Hf_{0.1})O_3]$, [0.98KNLNS-0.02BNZSH] KNN based ceramic have been synthesized through the solid-state sintering method. The effect of sintering temperature on structural, bulk density and dielectric properties has been investigated systematically. The XRD analysis reveals a tetragonal phase for 1050˚C, while it is observed to be a co-existence of rhombohedral–tetragonal (R–T) phase for sample sintered at 1075˚C, and orthorhombic-tetragonal (O-T) for 1100˚C. The optimum electrical properties such as Curie temperature (T_c) ~400°C, maximum dielectric constant (ε_m) ~5090, dielectric loss (tanδ) ~0.3, piezoelectric parameter (d_{33}) ~120pC/N and the bulk density ~4.77g/cm^3 have been obtained for ceramic pallet sintered at 1075˚C and an enhanced thermal stability coefficient also observed for the sample sintered at 1075°C.

INTRODUCTION:

Lead Zirconium Titanate [Pb $(Zr_xTi_{1-x})O_3$]-based ceramic's excellent electrical qualities have led to their widespread use in various scientific and technological applications, including sensors, transducers, actuators and piezoelectric transformers [1-8]. However, the lead ingredient present in these ceramics has harmful effects on human health and on environment. Therefore, in recent decades, there has been a renewed attention on the development of lead free piezo-electric ceramics due to the need for sustainable global development and environmental protection concerns over the use, re-cycling, and disposal of lead based piezoelectric ceramics. A Large electro-mechanical coupling coefficient, good ferro-electric properties, and a high Curie temperature make $K_{0.5}Na_{0.5}NbO3$ (KNN), a promising candidate for lead free piezoelectric ceramics [2]. Without a doubt, choosing the best sintering procedure is crucial to produce KNN-based ceramics with excellent electrical properties [3-4]. It is commonly predictable that the electrical properties include extrinsic contribution dominated by densification of ceramic sample. Meanwhile, the intrinsic contribution is mainly attributed to ceramic's lattice and crystalline structure [5]. The densification of ceramics can be increased by providing an optimum sintering temperature. The sintering process has an effective impact at various electrical properties. Therefore, in this work, effect of sintering temperature on the properties of solid-state solution of a new composition $0.98[((K_{0.4}Na_{0.6})_{0.94}Li_{0.06})(Nb_{0.96}Sb_{0.04})O_3]-0.02[(Bi_{0.5}Na_{0.5})(Zr_{0.8}Sn_{0.1}Hf_{0.1})O_3]$ has been studied.

SYNTHESIS METHOD:

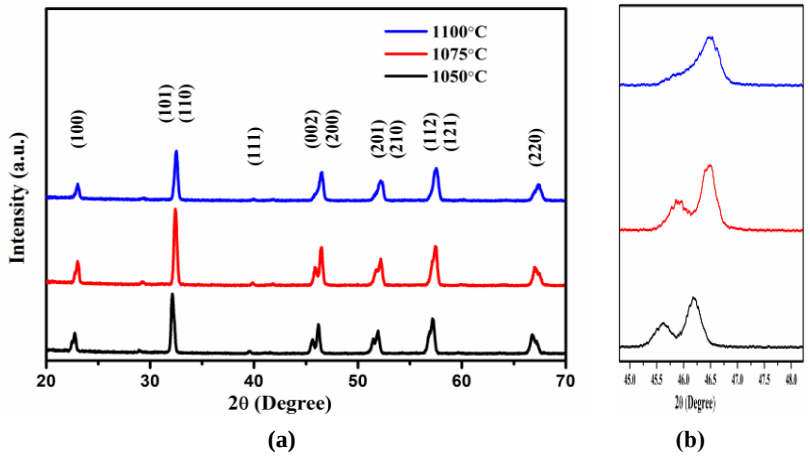
$0.98\ [((K_{0.4}\ Na_{0.6})_{0.94}Li_{0.06})(Nb_{0.96}Sb_{0.04})O_3]-0.02[(Bi_{0.5}Na_{0.5})(Zr_{0.8}Sn_{0.1}Hf_{0.1})O_3]$ ceramics used in this investigation were made using a conventional ceramics method. Starting raw materials included K_2CO_3, Na_2CO_3, Li_2CO_3, Sb_2O_5, Nb_2O_5, Bi_2O_3, SnO_2, ZrO_2 and HfO_2, oxide and carbonate powers of reagent grade. The mixing and grinding procedures were conducted for 3h with mortal-pestle in the presence of anhydrous IPA. The mixed powder was calcined at 850˚C for 6h after dehydration of powder. The calcined powder was again milled for 3h using a mortar and pestle, dried for 30 minutes at 130˚C, and mixed with 5wt% polyvinyl alcohol. After that, powder was compressed under 65 MPa into disk pellets of diameter 10 mm and thickness of ~1 mm and pallets heat at 500˚C to remove the binder solution. Subsequently, the ceramic pellets were sintered for 3h at 1050˚C, 1075˚C, and 1100˚C, respectively, at the heating rate of ~ 4-5 ˚C/min.

The sample was covered with silver paste on both sides, and it was burned for 1hour at 280°C to serve as an electrode for electrical property measurements [3]. Archimede's method was used for measuring bulk density of the ceramic pellets. Using a Cu K-alpha radiation (Rigaku Ultima-IV, Germany), step size of 0.02˚, X-ray powder diffraction analysis was used for structural properties. The di-electric characteristics were measured using an

impedance analyzer (Wayne Kerr-6500B, U.K.) in the temperature range room temperature to 450˚C. For piezo-electric properties, ceramic pellets have been poled under DC electric field (~2.5kV/mm) in silicon oil for 20 minutes. After 24h of poling, the piezo-electric properties were measured using YE2730 d_{33} meter.

RESULTS AND DISCUSSION:

The room-temperature XRD pattern of 0.98KNLNS-0.02BNZSH ceramic sintered at temperatures 1050˚C, 1075˚C and 1100˚C) are represented in Fig. 1(a). Peak near the 45˚ splits into two diffraction peaks in all the sintered samples. The peak intensity ratio for these peaks is observed to be 1:2 for the pellet sintered at 1050˚C, which indicates a pure pervoskite structure i.e. tetragonal phase for this sample [4]. The further analysis of peaks position and peak intensity shows that the mixed R-T phase is exist for the sample sintered at 1075˚C and mixed O-T phase sample sintered at 1100˚C [5-6]. An amplified view of XRD patterns for 2Θ = 44˚~48˚ is shown in Fig. 1(b).



(a) (b)

FIGURE 1. (a) X-Ray diffraction patterns of the 0.98KNLNS-0.02BNZSH ceramic pellets sintered at 1050 ◦C, 1075◦C and 1100 ◦C for 2θ ranging from 20˚ to 70˚ (b) enlarged pattern for 2θ ranging from 44˚ ~ 48˚.

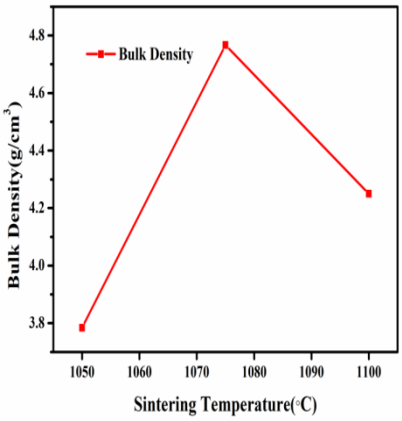


FIGURE 2. Plot of Bulk density versus sintering temperature for the samples sintered at 1050˚C, 1075˚C and 1100˚C.

Figure2 shows the behavior of bulk density of the ceramic sample with the variation in sintering temperature. It is clear from this figure that the bulk density of specimens is maximum (~ 4.77 g/cm^3) for sample sintered at 1075˚C. However, above 1075˚C, the value of density begins to drop, which can be attributed to the presence of many distinct pores in grain boundaries [3-5].

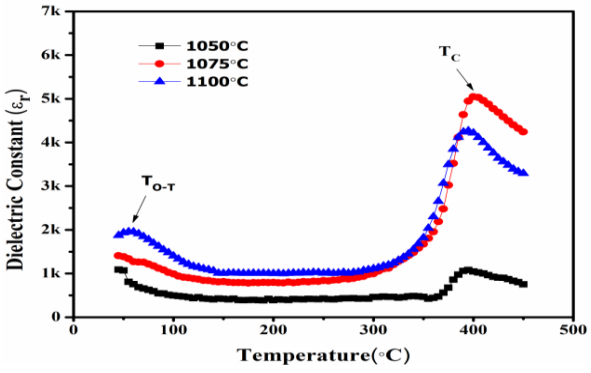


FIGURE 3. Variation of di-electric constant with temperature for 0.98KNLNS–0.02BNZSH ceramics sintered at 1050˚C, 1075˚C and 1100˚C, respectively at 100Hz.

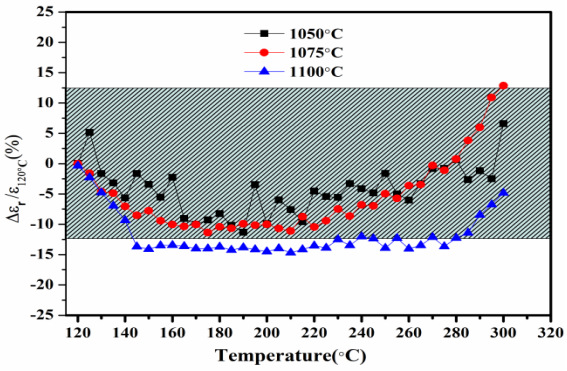


FIGURE 4. Temperature dependence of temperature stability coefficient of dielectric permittivity.

Figure 3 depicts the dielectric constant spectra in temperature range from 45˚C–450 °C and at frequency 100Hz for KNN based ceramic samples sintered at different temperatures. Fig.3 shows that from temperature 290˚C onward, the relative dielectric permittivity rises rapidly and peaked at the temperature that corresponds to the Curie- temperature (T_C), which is the temperature at which the ferro-electric to para-electric phase transition takes place.

This figure also indicates that in the temperature from 45˚C to 450 °C, two dielectric peaks, one corresponds to the transition temperature T_{o-T} of the ortho-rhombic phase to the tetragonal phase at low temperature (55˚C) and the other corresponds to Curie temperature (T_C ~ at 395˚C) observed for the ceramic sintered at 1100˚C.
However, for the pellets sintered at (1050˚C and 1075˚C) the dielectric peak at low temperature shifted toward room temperature [7]. Further, the Curie temperature (Tc) is observed to be ~395˚C for both samples sintered at 1050˚C and 1100˚C but, there is huge difference in relative permittivity for both the samples. The Curie temperature and the maximum relative permittivity for sample sintered at 1075˚C are 400˚C and 5090, respectively, which may be assigned to the co-existence of rhombohedral–tetragonal (R–T) phase for this sample [8].
Figure 4. shows the temperature dependence of temperature stability co-efficient of permittivity in the range 115˚C -300˚C. This figure demonstrates an enhanced temperature stability coefficient of permittivity (±12.5) for the ceramic pellet sintered at 1075˚C.
The piezo-electric measurement has been done for the samples sintered at (1050˚C, 1075˚C ,1100˚C) and the observed values of d_{33} for these samples are 90pC/N,120pC/N,55pC/N, respectively.

CONCLUSIONS

$0.98\{((K_{0.4}Na_{0.6})_{0.94}Li_{0.06})(Nb_{0.96}Sb_{0.04})O_3\}-0.02\{(Bi_{0.5}Na_{0.5})(Zr_{0.8}Sn_{0.1}Hf_{0.1})O_3\}$ ceramic sample have been prepared using the solid-state reaction method. The influence of sintering temperature on the structural phases, bulk density and dielectric measurements have been discussed comprehensively. The optimum electrical properties (e.g., bulk density-4.77g/cm^3, tanδ ~0.3, T_C ~400°C and d_{33} ~120pC/N) have been observed for the ceramic pellet sintered at 1075˚C due to the contribution of the R-T phase boundary region. Thermal stability co-efficient of permittivity also improved for the ceramic pallet sintered at 1075˚C. In summary, this type of ceramic material possessing a high T_C and enhanced bulk density and high relative permittivity will be a promising candidate for scientific and technological applications.

ACKNOWLEDGMENTS

The authors express their sincere gratitude to Ion Beam Centre, Department of Physics, Kurukshetra University, Kurukshetra for their kind support during XRD and Dielectric measurements. This work is financially supported by University Grant Commission, New Delhi in the form of Junior Research Fellowship (UGC-JRF).

REFERENCES

1. Wu, J., Wang, Y., Xiao, D., Zhu, J., & Pu, Z. Applied physics letters, 91(13)(2007).
2. Jiten, C., Gaur, R., Laishram, R., & Singh, K. C. Ceramics International, 42(12), 14135-14140(2016).
3. Jiang, L., Li, Y., Xie, L., Wu, J., Chen, Q., Zhang, W., & Zhu, J. Journal of Materials Science: Materials in Electronics, 28, 8500-8509(2017).
4. Wen, R., Zhou, L., Zou, X., Luo, L., Jiang, N., Zheng, Q. & Lin, D. Journal of Materials Science: Materials in Electronics, 26, 8341-8349(2015).
5. Chen, Q., Gao, T., Lang, R., Tan, Z., Xing, J., & Zhu, J. Journal of the European Ceramic Society, 43(6), 2442-2451(2023).
6. Lv, X., Li, Z., Wu, J., Xi, J., Gong, M., Xiao, D., & Zhu, J. Materials & Design, 109, 609-614(2016).
7. Wu, J., Xiao, D., Wang, Y., Wu, L., Jiang, Y., & Zhu, J. Journal of the American Ceramic Society, 91(7), 2385-2387(2008).
8. Sharma, J. P., & Kumar, D. Materials Science and Engineering: B, 301, 117182(2024).

Ce and Bi Doped BCZT Based Lead-Free Ceramic: A Material with High Dielectric Constant

Bhawna[1,2*], Sapna Kumari[1], V. Kumar[1]

[1]*Department of Physics, Institute of Integrated and Honors Studies (IIHS), Kurukshetra University, Kurukshetra,136119, India*
[2]*Department of Physics, Kurukshetra University, Kurukshetra,136119, India*
[*]*Corresponding author: bhawna.iihs.scholar@kuk.ac.in*

Abstract-In this study, perovskite-type ($Ba_{0.95}Bi_{0.02}Ca_{0.02}$) ($Zr_{0.02}Ce_{0.0005}Ti_{0.9795}$) O_3 (BBCZCeT) lead-free ceramic has been synthesized by the conventional solid-state reaction method. The X-ray diffraction (XRD) technique was used to analyze the structural properties of the ceramic. The XRD analysis confirms that the synthesized material has a pure perovskite structure and no other phase or impurity is present. The dielectric study of ceramic shows that incorporation of Ce and Bi in BCZT results in a high dielectric constant of ~33182 and low dielectric loss of 0.17056 at 100 Hz at a reduced sintering temperature of 1360°C. Also, the phase transition peak is broadened, and near-relaxor behavior is observed.

Keywords: Lead-free ceramics, dielectric properties, phase transition, Curie temperature, perovskite, relaxor, BCZT

INTRODUCTION

Due to their numerous uses, including energy-storage capacitors, microwave applications, and gate dielectrics in field-effect transistors, materials having a high dielectric constant are greatly sought after [1]. For many years, lead-based systems such as lead zirconium titanate (PZT) have been the most utilized materials in these applications because of their exceptional dielectric and piezoelectric constant. However, there is a great deal of concern about the high toxicity of lead oxide, which drives up the need for alternatives, i.e., lead-free ceramics [2-6]. The Barium titanate ($BaTiO_3$) based systems have good dielectric and piezoelectric properties. However, the current use of electroceramic components requires increasing control of the materials to get properties that match the properties needed for real-life applications. This can be done by using different synthesis techniques and adding/doping appropriate chemical species. With this motivation, various BT-based ceramic systems have been developed and studied. Among these, BCZT, obtained through the doping of calcium (Ca) at A-site and zirconium (Zr) at B-site in $BaTiO_3$, has been found to have excellent electrical properties, which are even comparable to the PZT systems in some cases [3]. M. Maraj et al. reported that doping in BCZT has the potential to modify the dielectric constant to achieve a suitable adjustable constant [4]. Othmani et al. doped BCZT with Bi at the A-site and discovered that a high value of maximum dielectric constant (11508) is achieved at T_m of 270K at 1kHz [5]. Also, it is observed that cerium exhibits various electronic properties in a variety of oxidative and reductive situations, so it is a highly effective tool for improving ceramics electrical properties [6]. The objective of this work is thus to understand the influence of Bi and Ce doping on the electrical properties of BCZT ceramics.

EXPERIMENTAL PROCEDURE

In the present study, ($Ba_{0.95}Bi_{0.02}Ca_{0.02}$) ($Zr_{0.02}Ce_{0.0005}Ti_{0.9795}$)$O_3$ ceramic was prepared using a solid-state reaction route. For this, $BaCO_3$, $CaCO_3$, ZrO_2, TiO_2, CeO_2, and Bi_2O_3 (all of high purity) were taken as raw materials. Starting powders were dried in the oven at 180°C/1h before weighing to remove moisture and then ground for 5h in the presence of acetone. After desiccating the slurry, it was calcined for 3h at 1200°C. Pellets were then obtained by pressing at 30 kg/cm2(~3MPa), followed by the grinding process with the addition of a few drops of 6 wt.% polyvinyl

alcohol (PVA), and finally sintered at 1360°C. The structure examination of the sintered samples was carried out through the X-Ray diffraction technique using the instrument Rigaku Ultima-IV, Germany (Cu-Kα radiation of wavelength 1.5406 Å). For dielectric measurements, the Wayne Kerr 6500B Precision Impedance Analyzer is used. To carry out the measurements of the dielectric study, both sides of the pellet were coated with silver paste, and then the pellets were fired at 260 °C for 1h.

RESULTS AND DISCUSSION

STRUCTURAL ANALYSIS

To reveal the crystallographic information of the sample, XRD spectra have been recorded between a 2θ range of 20°-70°, at room temperature, and are shown in Fig. 1. The well-defined and intense (hkl) peaks have been observed in the XRD pattern, which indicates the good crystallinity of the sample. The observed peaks have been accurately identified and are matched to the crystallographic structure. The careful analysis indicates that the ceramic has a pure perovskite structure, and no traces of a secondary phase are observed, which confirms that Bi and Ce ions dissolve into the host lattice BCZT and form a solid solution.

The (002) and (200) peak intensities can be compared to identify the perovskite phase structure. The ratio (I_{002}/ I_{200}) is approximately 2:1 in the orthogonal phase and switches to 1:2 in the tetragonal phase. In the present study, this ratio is ~0.5, indicating that the sample has a pure tetragonal phase at room temperature, which favors the results of the dielectric study.

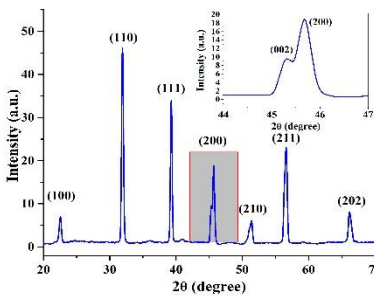


Fig.1-Room temperature X-ray diffraction pattern of BBCZCeT; inset: enlarged view of peak splitting in the 2θ range of 44°-47°

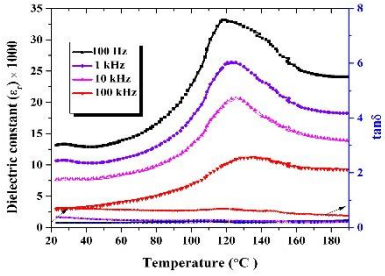


Fig.2-Temperature dependence of ε_r and tanδ for BBCZCeT ceramic, at different frequencies

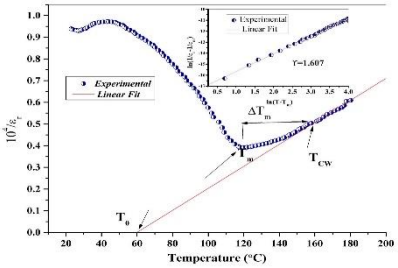


Fig.3- Plot of $10^4/\varepsilon_r$ vs T and ln $(1/\varepsilon_r - 1/\varepsilon_m)$ vs ln$(T-T_m)$ at 1kHz for BBCZCeT ceramic.

ELECTRICAL ANALYSIS

Fig. 2 represents the dielectric constant (ε_r) and dielectric loss (tanδ) as a function of temperature (T) for BBCZCeT ceramics recorded at different frequencies, in the temperature range of 20°C to 180°C. The maximum dielectric constants observed are 33182, 26409, 20604, and 11188, corresponding to frequencies of 100 Hz, 1 kHz, 10 kHz, and 100 kHz, respectively. Because of the ferroelectric transition of BBCZCeT ceramics, one dielectric anomaly associated with the tetragonal to cubic phase transition at Tm can be easily identified. Furthermore, T_m is shifting to a higher temperature side with frequency, which reveals a relaxor-like behavior and may be assigned to the presence of polar nano regions [7]. Also, tanδ is almost constant corresponding to a specific frequency, and increases with increasing frequency. The Curie–Weiss law governs the dielectric constant of typical ferroelectrics above the Curie temperature as:

$$\frac{1}{\varepsilon_r} = \frac{T-T_0}{C} \quad -(1)$$

where T_0 denotes the Curie-Weiss temperature and C is the Curie–Weiss constant. We obtain T_0 = 60°C and ΔT_m = 38°C from the plots of 10^4/εr vs. T, corresponding to the dielectric data recorded at 1 kHz (Fig. 3, Curie-Weiss law). Here, $\Delta T_m = T_{CW}-T_m$ is a parameter used to study the deviation from the Curie-Weiss law. To further study the dielectric behavior, the modified Curie-Weiss law is used, [9] which is given by the expression

$$\frac{1}{\varepsilon_r} - \frac{1}{\varepsilon_m} = \frac{(T-T_m)^{\Upsilon}}{C} \quad -(2)$$

where ε_m denotes the maximum permittivity, and T_m denotes the temperature corresponding to the maximum permittivity. The degree of diffuseness is indicated by the value of γ, which has a range of 1 (normal ferroelectrics) to 2 (ideal relaxor ferroelectrics). The inset in Fig. 3 displays the plot of ln $(T-T_m)$ against ln $(1/\varepsilon_r-1/\varepsilon_m)$ to determine the value of γ. The value of γ is obtained to be 1.607, indicating a near relaxor behavior for the BBCZCeT ceramic.

CONCLUSION

A perovskite-type $(Ba_{0.95}Bi_{0.02}Ca_{0.02})(Zr_{0.02}Ce_{0.0005}Ti_{0.9795})O_3$ (BBCZCeT) lead-free ceramic has been synthesized by the conventional solid-state reaction method. Structural studies confirm a pure perovskite tetragonal structure at room temperature in the synthesized material. Dielectric studies (at 100Hz) show that the material has a very high dielectric constant of 13214 and 33182, at room temperature and T_m, respectively, along with a low dielectric loss. The degree of diffuseness (γ) is found to be 1.607, which indicates characteristics of relaxor behavior to some extent. Such a high dielectric constant with low dielectric loss is required in the downsizing of passive components like filters and resonators, since the size of the resonator is proportional to $\sqrt{\varepsilon_r}$. Thus, the higher the dielectric constant, the smaller the size of the needed component. Additionally, the fabrication of capacitors and gate dielectric materials requires a material with a high dielectric constant.

ACKNOWLEDGMENTS

The author would like to acknowledge the Council of Scientific and Industrial Research (CSIR), New Delhi, for providing financial support in the form of a junior research fellowship and the Ion Beam Centre, Kurukshetra University, Kurukshetra, for their support in XRD and dielectric measurements.

REFERENCES

1. Hari Singh Nalwa, Handbook of Low and High Dielectric Constant Materials and Their Applications, Vol. 2 (Academic Press, 1999)
2. Kumari, S., Kumar, A., Kumar, V., Dubey, S.K., Goyal, P.K., Kumar, S., ... & Arya, A., Journal of Materials Science: Materials in Electronics, 32(12), 16900-16915(2021)
3. Frattini, A., Di Loreto, A., de Sanctis, O., & Benavidez, E., Procedia Materials Science, 1, 359-365(2012)
4. Maraj, M., Wei, W., Peng, B., & Sun, W., Materials, 12(21), 3641(2019)
5. Othmani, N., Amouri, A., Benabdallah, F., Sassi, Z., Seveyrat, L., Lebrun, L., ... & Khemakhem, H., Ceramics International, 46(14), 22592-22605(2020)
6. Chen, X., Xue, Y., Zhang, B., Zhao, P., Liu, Y., Bai, X., ... & Xie, Y., Ceramics International, 48(13), 18730-18738(2022)
7. Fan, H., & Ke, S., Science in China Series E: Technological Sciences, 52(8), 2180-2185(2009)
8. Singh, R., & Ulrich, R. K., The Electrochemical Society Interface, 8(2), 26(1999).
9. Ji, X., Wang, C., Zhang, S., Tu, R., Shen, Q., Shi, J., & Zhang, L., Journal of Materials Science: Materials in Electronics, 30, 12197-12203(2019)

Synthesis and Characterization of Eco-friendly $NiFe_2O_4$ Octahedrons Spinel Ferrite for Multi-Faceted Applications

DHARTI J. TANK[1], VED B. BHARADVA[1], CHETNA C. CHAUHAN[2] AND ABHISHEK A. GOR[1,*]

[1]*Department of Physics, School of Energy Technology, Pandit Deendayal Energy University, Gandhinagar 382426, Gujarat, India*

[2]*Institute of Technology, Nirma University, Ahmedabad-382481, Gujarat, India*

[*]*Corresponding Author*: *Abhishek.Gor@sot.pdpu.ac.in*

Abstract In this work, we explore structural, morphological, Raman and optical properties of Green Synthesized Nickel Spinel Ferrite $NiFe_2O_4$ (NFO) using Azadirachta indica (Neem tree) leaves extract. The heat treatment method was utilized for green synthesis and the sample was calcined at 1100°C for 4 hours. The XRD confirms the formation of cubic spinel phase of polycrystalline NFO. The morphology was examined using SEM, which shows the formation of octahedrons, with the average particle size distribution at around 500 nm. FT-IR was used to confirms the presence of iron oxide and metal oxide bonds at the octahedral and tetrahedral sites. UV-Vis's spectroscopy is utilized for optical properties which shows that it has a strong absorbance peak in visible region. From Kubelka-Munk function the band gap is measured at 2 eV. Raman spectra confirm 5 Raman active modes.

INTRODUCTION

NFO is a fascinating material with a unique crystal structure, wide potential applications, high magnetic permeability, high resistivity, and high curie temperature which can be utilized for variety of potential applications [1]. Spinel Ferrites have a very good dielectric and magnetic permeability properties in high and low temperature regions. Spinel Ferrite has a crystal structure – AB_2X_4 [(A-Mg, Cr, Mn, Fe, Co, Ni, Cu, Zn, Cd, Sn), (B-Al, Ga, Ti, In, V, G, Mn, Fe, Co, Ni), (X-O, S, Se)]. Figure1(a) displays the crystal structure of NFO.NFO has an inverse spinal structure. Spinel exhibit a strong ferrimagnetism because they possess electrons of metal and oxygen ions on lattice sites with opposite spin arrangement. In, inverse spinal structure, A^{+2} octahedral and B^{+3} is half tetrahedral and half octahedral structure. The distribution of cations in the spinel structure plays a critical role in determining the material's behavior. Here Ni^{2+} cations occupy octahedral positions and Fe^{3+} cations are distributed in both tetrahedral and octahedral positions. This specific arrangement contributes greatly to the unique properties of NFO. There are many ways to synthesize nickel ferrite, including the solid-state method [2], co-precipitation method [3], sol-gel method, and green synthesis method. In the green synthesis process, as reported many extracts have been used, such as clove extract [4], brassica oleracea var, capitate (green cabbage) [5], and hibiscus rosasinensis extract [6]. Here the Green Synthesis is done using Neem (Azadirachta indica) leaf extract, as the extract contain flavonoid and aromatic compounds which works as reducing and caping agent. To prepare NFO, such method is commercially viable and environmentally friendly.

METHODOLOGY

2.1 Preparation of nickel ferrite

The NFO nano powder was prepared by using a cost-effective safe and environment-friendly green synthesis technique. The method includes: To soak and clean the Neem leaves in distilled water to get rid of all kind of impurities. Then the leaves are boiled for some time and they are cooled and filtered through Wattman filter. And then the extract is added into the solution of Ferric Nitrate ($Fe(NO_3)_3.9H_20$) and Nickel nitrate ($Ni(NO_3)_2.6H_20$) salts, the constant stirring in a magnetic stirrer and the speed is adjusted accordingly. The extract is obtained after evaporating all the remaining water. The extract contains numerous phytochemicals, including amino acids, vitamins, minerals, terpenoids, flavonoids, sterols, glycosides, and alkaloids. Azadirachta indica's secondary metabolites serve as reducing, capping, and stabilizing agents for the nanoparticles. Metal salt is converted to metal oxide nanoparticles when it is treated with Azadirachta indica extract.[7]

RESULTS AND DISCUSSION

3.1 X-RAY DIFFRACTION ANALYSIS

The X-ray diffraction of NFO spinel ferrite was carried out using Rigaku MiniFlex600c at room temperature. The results were obtained in the 2θ range of 20 to 80. Understanding the material's phase purity and structure can be accomplished through X-ray diffraction method. Figure1(b) displays the nickel ferrite nanoparticle XRD pattern which shows highly crystalline and pure phase with sharp NFO peaks. The obtained data was analyzed using PowderX Software. All the reflections in the XRD pattern belong to the FCC type of cubic spinel structure having lattice constant [cubic: a=b=c] is 8.431 Å and volume[$(a)^3$] is 599.29 $Å^3$.

It can be observed from the values of the structural parameters that match well with the reported values [8][9]. The analysis of the XRD pattern proved that prepared nickel ferrite possesses a single-phase Cubic Spinel Structure.

3.2 FT-IR ANALYSIS

The FT-IR spectroscopy technique also characterized the prepared NFO. Figure1(c) represents nickel ferrite's FT-IR spectra, which show one absorption band near 600 cm^{-1}. The tetrahedral bonds have the effect of substantially increasing the frequency for vibrations (v_1), while vibrations at right angles (v_2) would change frequency only slightly if small bending force constants are assumed. [10]. The force constant of the octahedral ($K_{octa} = v_1$) and the tetrahedral ($K_{tetra} = v_2$) site have been estimated for v_1 and v_2 by using the suggested [11] (v_1=584, v_2=396): $K=4\pi^2\times C^2\times M \times v^2$ [Where; K: force constant, *v:* corresponding wave number, *M*: atomic mass ($NiFe_2O_4$=234.4 g/mol), *C:* speed of light (free space).]. So, the force constant is $K_{octa} = 2.83 Nm^{-1}$ *and* $K_{tetra} = 1.30 Nm^{-1}$.

3.3 RAMAN ANALYSIS

The Raman mode is also characterized by NFO crystal. The Raman spectra showcase 5 Raman Modes and it conforms the structural analysis of XRD. Due to symmetric stretching of oxygen in tetrahedral AO_4 group, the A_g symmetry mode is about 701cm^{-1}. Due to symmetric bending of oxygen with respect to cation E_g symmetry mode is about 329 cm^{-1}. Due to asymmetric stretching $F_{2g}(2)$ is at 484$cm^{-1}$and due asymmetric bending of oxygen $F_{2g}(3)$ is at 583cm^{-1} which is corresponding to vibration of octahedral group. $F_{2g}(1)$ is about 210cm^{-1}. The Raman modes confirm the XRD peaks. Figure1(d) shows the Raman modes with symmetric and asymmetric modes [11].

3.4 FESEM ANALYSIS

The FESEM technique also characterized the prepared NFO. Figure1(e) represents the FESEM of nickel ferrite and Figure1(f) shows the histogram showing particle size distribution. By doing FESEM we can get the particle size distribution of the crystal structure [10] as well as we can see the octahedral shape of NFO. The particle size of nickel ferrite crystal is 500 nm.

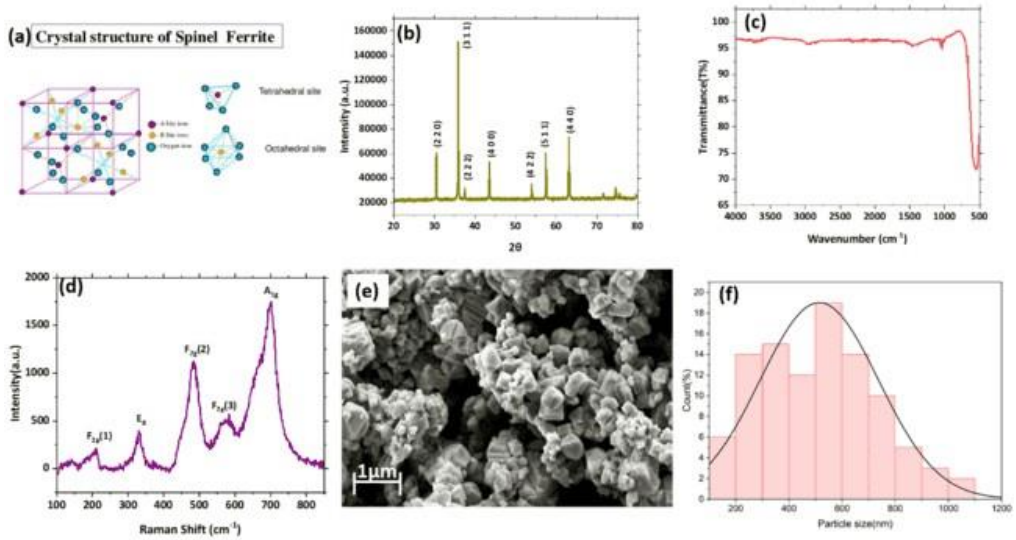


FIGURE (1): (a)Crystal structure of spinal ferrite, (b) XRD, (c) FT-IR, (d) RAMAN, (e) FESEM, (f) Particle Size Distribution

3.5 UV-VIS ANALYSIS

The optical band gap Eg was estimated by plotting the square of the Kubelka-Munk function and gives absorption band gap energies at 2 eV. Figure 2(a) shows the absorbance and Figure2(b) shows the energy bandgap. From the data we can see as we move from near infrared to visible spectra there is a sharp peak in absorbance at around 700nm then there is a drop in the absorbance in the UV range of around 300nm. The optical band gap was calculated by the relation of Tauc's Relation;

$(\alpha hv)^{1/n}=A(hv-E_g)$

[Where; A: Constant, E_g: band gap of the material, n: depends on the transition type (For direct allowed transition the parameter n=2 and for indirect allowed transition n= ½).]

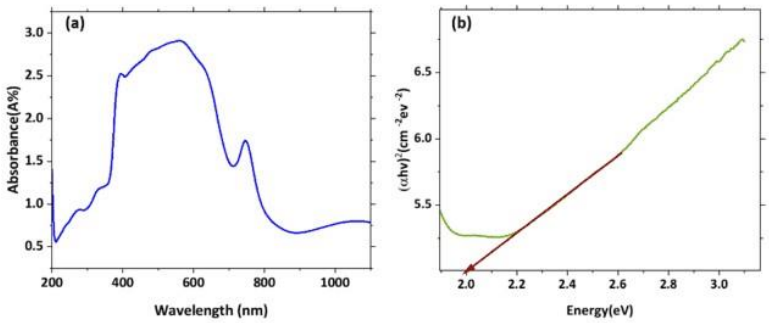


FIGURE (2): (a) Absorbance, (b)Energy Bandgap

CONCLUSION

The present work describes the properties, crystalline nature of NFO particles prepared by green synthesis using neem extract. The XRD shows the formation of cubic spinel phase of polycrystalline with lattice parameter a=b=c= 8.431 Å. The octahedrons morphology of synthesized NFO is found from SEM, with the average particle size distribution at around 500 nm. FT-IR confirms the presence of iron oxide and metal oxide bonds at the octahedral and tetrahedral sites i.e. ν_1=584 cm^{-1}, ν_2=396 cm^{-1} respectively. UV-Vis's spectroscopy shows that it has a strong absorbance peak at 800 nm and there is sharp rise in absorbance at 650 nm wavelength in visible region. From Kubelka-Munk function the band gap is measured at 2 eV. Raman spectra confirm 5 Raman active modes with most dominant A_{1g} symmetry mode at 701cm^{-1}.

ACKNOWLEDGMENTS

This research was supported by financial support from the department of physics, school of energy technology, pandit deendayal energy university. We thank srdc, pandit deendayal energy university for important measurements.

REFERENCES

1. Bhagat, B., et al. Chemistry–An Asian Journal 19.2 (2024): e202300841.
2. Zhang, Zhigang, et al Physica E: Low-Dimensional Systems and Nanostructures 45 (2012): 122-129.
3. Kazi, Subiya, et al. Materials Today: Proceedings 73 (2023): 448-454.
4. Kulkarni, G. D., et al. Journal of Physics: Conference Series. Vol. 1644. No. 1. IOP Publishing, 2020.
5. Bilal, Ahmed, et al. Materials Chemistry and Physics 290 (2022): 126483.
6. Putri, J., and Y. Stiadi. Rasayan Journal of Chemistry 12.4 (2019).
7. Moradnia, Farzaneh, et al. Journal of Cleaner Production 288 (2021): 125632.
8. Kounsalye, Jitendra S., et al. AIP Conference Proceedings. Vol. 1832. No. 1. AIP Publishing, 2017.
9. Chauhan, Lalita, A. K. Shukla, and K. Sreenivas Ceramics International 41.7 (2015): 8341-8351.
10. Naik, M. Madhukara, et al.Nanotechnology for Environmental Engineering 8.1 (2023): 143-151.
11. Ž Lazarević, Z., et al. Journal of Applied Physics 113.18 (2013).

Fabrication and Characterization of Barium Hexaferrite Film Based Device for Neuromorphic Applications

Ved B. Bharadva[1] and Dharti J. Tank[2], Abhishek A. Gor[1*]

[1]*Department of Physics, School of Energy Technology, Pandit Deendayal Energy University, Gandhinagar 382426, Gujarat, India*
[*]*Corresponding Author*: *Abhishek.Gor@sot.pdpu.ac.in*

Abstract: Hexaferrites, due to their unique magnetic and electrical properties, show great promise in multifunctional devices. This paper aims to study the electrical properties of Gold//Barium Hexaferrite//Graphite devices deposited on Alumina substrate—furthermore, structural analysis of the $BaFe_{12}O_{19}$ film by XRD and Raman spectroscopy at room temperature. The electrical characteristics are measured using Keithley SMU 2604B.The memristor device Alumina//Gold//Barium Hexaferrite//Graphite show bipolar analog switching behavior with an on/off ratio of 4.3.

INTRODUCTION

Neuromorphic computing is suggested to be the next computing breakthrough, with the current limitations of the von Neumann architecture, brain like memory devices can efficiently process large sums of data efficiently. Memristors are one or this brain inspired memory devices which can mimic synaptic functions by resistive switching. Ferroelectric memristors are voltage-controlled memory devices with good stability, long endurance periods and fast switching, Hexaferrite memristors also have great magnetic properties whose influence on its resistive switching behaviors can be studied. Barium hexaferrite exhibits high magnetic anisotropy, meaning it requires a significant amount of energy to change the direction of its magnetic moment. [1] This property is crucial for ensuring stable and long-lasting resistance states in memristor devices, which is essential for reliable memory storage. It also has high magnetic Coercivity, hence it does not easily lose its resistance state after writing it in memory. The magnetic behavior of Barium Hexaferrite is direction-dependent, influenced by the crystal orientation. This anisotropy can be leveraged to design memristors with tailored switching characteristics, enhancing their performance in neuromorphic computing and other advanced applications. The alumina substrate is used due to its high thermal stability. Hence after fabrication of the device, its performance can be tuned by sintering it at various temperatures. Gold is also chemically stable at high temperatures and has good conductivity, hence it is used as the bottom electrode. Graphite dots are used as the top electrode as it is easy to apply, and the large surface area of graphite paint improves the performance of the device.

METHODOLOGY

2.1 Device Fabrication

The substrate was prepared by first cleaning with acetone, ultrasonicated and ozonized to remove any organic impurities and make the surface more hydrophilic. Gold bottom electrode was deposited on alumina using thermal evaporation at 4.8 x 10^{-6} torr with 0.7 V Voltage and 110 mA current; the thickness was measured to be 130 nm[2].

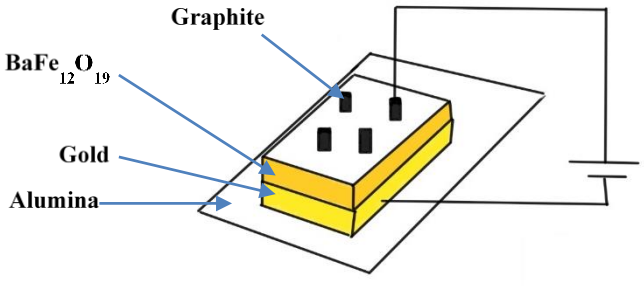


FIGURE (1) Diagram of Device

The Barium Hexaferrite films was deposited on gold deposited alumina substrate by RF sputtering technique. The target used was a high purity Barium Hexaferrite powder pelleted into a 2-inch diameter target. The Barium Hexaferrite powder was synthesized and characterized beforehand for its properties [2]. For the RF sputtering a planar magnetron sputtering unit (12" MSPT) by Hind High Vacuum Pvt. Ltd. was used. To ensure a high purity film, a residual pressure of 10^{-6} torr was maintained in the vacuum chamber. Sputtering was done at 30˚ C with substrate to target distance at 7 cm, substrate rotation was 6 rotations

per minute. Graphite paint was used as the top electrode to form small islands and the device was allowed to settle for 8 hours at 25˚C.

RESULTS AND DISCUSSIONS

3.1 X Ray Diffraction Analysis

The X-Ray data for Barium Hexaferrite is shown below in fig (2). The Diffraction pattern of the film was obtained using Rigaku MiniFlex600c at room temperature. 2θ range from 20˚ to 80˚ was observed at 25˚C room temperature at 0.1˚/sec. The XRD pattern shows crystalline structure. Using PowderX analysis software the miller indices were calculated using Rietveld refinement method, these are (006), (107), (009), (114), (109), (212), (215), (1 1 13), (307) and (315). The Barium Hexaferrite belongs P63 MMC space group with a hexagonal crystal system[3].

$$a = b = 5.423\text{Å}, c = 21.303\text{Å}$$

$$\alpha = \beta = 90^{\circ}, \gamma = 120^{\circ}$$

The volume of unit cell (V_{cell}) was calculated to be 542 $Å^3$ using the formula,

$$V_{cell} = a^2 b \sin 120^{\circ}$$

The calculated values of the structural parameters fit the reported values well, confirming the phase purity of the film.

3.2 Raman Analysis

E_{1g} band at 164 cm^{-1} the presence of whole spinel block, A_{1g} band is observed at 216 cm^{-1} due to O-Fe-O bridge. A_{1g} bands at 340cm^{-1}, 511cm^{-1} and 618cm^{-1} confirms octahedral (FeO_6) structure and the prominent A_{1g} band at 731 cm^{-1} shows presence of tetrahedral (FeO_4) structure. Raman spectra of Barium Hexaferrite at room temperature is shown in fig (3) below

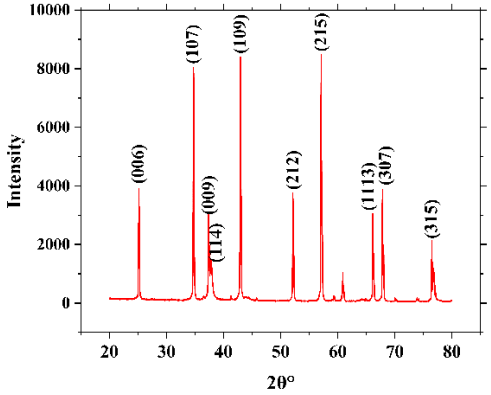


FIGURE (2) X- Ray Diffraction Pattern

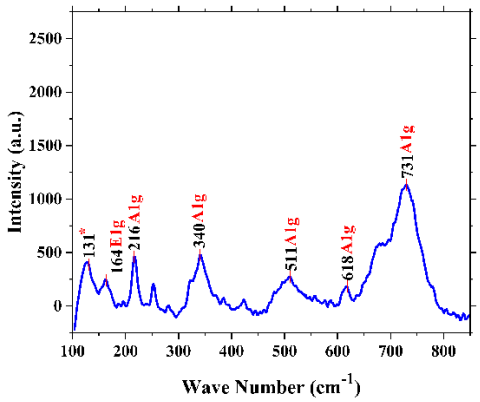


Figure (3) Raman Spectra

3.3 Electrical Characterization

The electrical characteristics of the device were studied using Keithley SMU 2604B. The I-V data was observed on kickstart application providing a voltage sweep from 0V to 1.5V, 1.5V to -1.5V and -1.5V to 0V. The current compliance was kept at 0.5 mA, measure window of 20ms and 0.01s measure delay.

The device shows bipolar resistive switching characteristics. The set voltage is observed to be 1V and reset voltage is observed at -1V. The maximum on/off ratio was observed to be 4.4. The device shows ohmic behavior in positive first quadrant from 0V to 1V and negative third quadrant form 0V to -0.9V during the sweep.

The device shows non-linear behavior in the positive first quadrant from 1V to 1.5V. This nonlinearity is fitting with Schottky emission[5] with goodness of fit 0.962, the equation is given by

$$\ln(I) = c + k\sqrt{V}$$

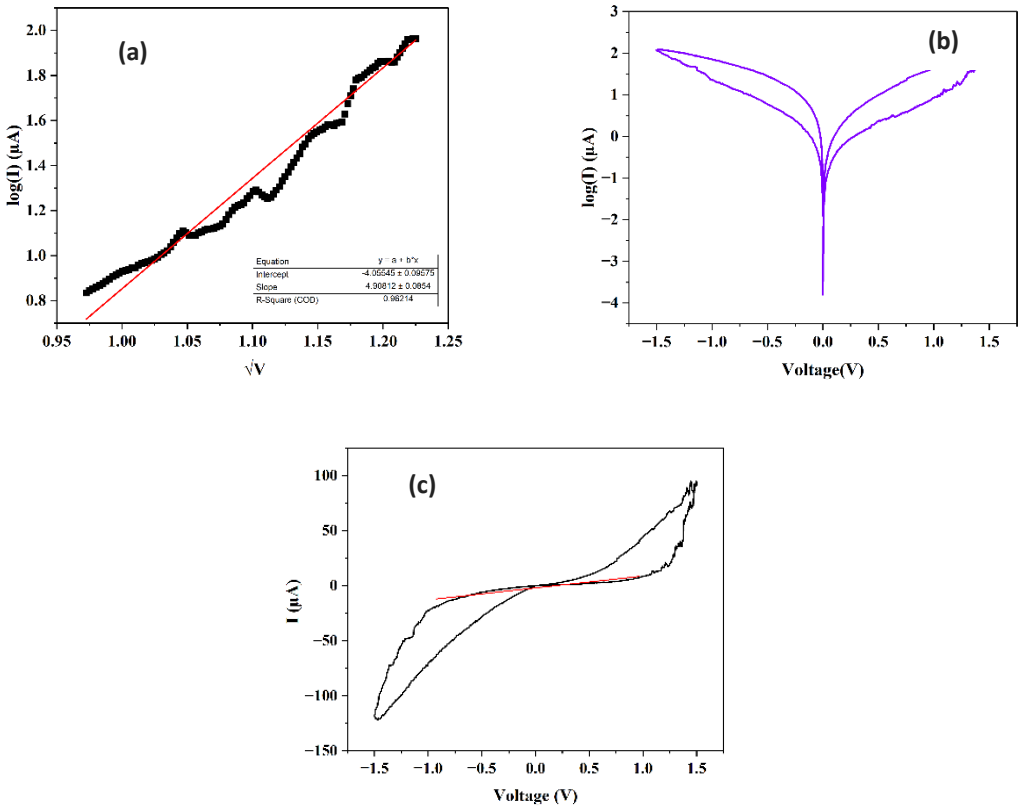


Figure (4) (a). Schottky Regime, (b). log I vs V plot, (c). I vs V plot

Conclusion

Preparation of Graphite/Barium Hexaferrite/Gold /Alumina devices using RF sputtering results in high quality films with pure phase formation, as seen by the XRD and Raman spectra also, the electrical characterization of the device shows promising result with fast bipolar switching and a large on/off ratio. This change in the resistive states of Barium Hexaferrite can be used to create neuromorphic devices with tunable resistive states

Acknowledgments

This research was supported by financial support from the department of physics, school of energy technology, pandit deendayal energy university. We thank srdc, pandit deendayal energy university for important measurements.

References

1. Babu, V., and P. Padaikathan Journal of magnetism and magnetic materials 241.1 (2002): 85-88.
2. Gor, Abhishek A., et al. Journal of Materials Science: Materials in Electronics 35.8 (2024): 584.
3. Gor, Abhishek A., et al. Materials Today Communications 37 (2023): 107214.
4. Kreisel, J., G. Lucazeau, and H. Vincent. Journal of Solid State Chemistry 137.1 (1998): 127-137.
5. Munjal, Sandeep, and Neeraj Khare. Scientific reports 7.1 (2017): 12427.

Near Room Temperature Dielectric Relaxation in Lead Free $0.67BiFeO_3$-$0.33BaTiO_3$ (BF-33BT) Piezoceramic

Samanway Mohanta[1*], Koushik Dey[1,2], A. Tripathy[1], Ashutosh Anand[3], D. Kumar[4], V. G. Sathe[1], D. K. Shukla[1]

[1]*UGC-DAE Consortium for Scientific Research, Indore (452001), India.*
[2]*GREMAN UMR 7347. University de Tours, CNRS, INSA-CVL, 16 rue Pierre et Marie Curie, 37071 Tours, France.*
[3]*Guru Gobind Singh Indraprastha University, New Delhi (110078), India.*
[4]*Central University of Punjab, Punjab (151401), India.*

[*] Corresponding author: *samanwaymohanta@gmail.com*

Abstract. Among lead free perovskite piezoelectric, $BiFeO_3$ based piezoceramics have garnered enormous attention for exhibiting high T_C as well as room temperature antiferromagnetism. Particularly, $BiFeO_3$-$BaTiO_3$ solid solutions have become potential candidates as these exhibit morphotropic phase boundary (MPB) and high T_C value. Here, we report dielectric spectroscopy of BF-33BT ($0.67BiFeO_3$-$0.33BaTiO_3$), a MPB composition in a broad temperature (100-520 K) and frequency (10 Hz to 1 MHz) range, which shows ferroelectric relaxation around room temperature, manifested from dispersion in relative dielectric permittivity and a broad peak in loss tangent (tanδ). Origin of the ferroelectric relaxation has been identified as temperature dependent contributions of grain boundaries in polarization at low frequencies, which is dominant at higher temperatures and freezes slightly below room temperature.
Keywords: Ferroelectric, Dielectric spectroscopy, Nyquist plot, Vogel-Fulcher model, Jonscher's power law.

INTRODUCTION

Due to the toxicity and worldwide restrictions on lead, research interests in lead free piezoceramics in last decades have grown extensively. $BiFeO_3$ is the only single-phase lead free multiferroic material simultaneously exhibiting antiferromagnetic ordering (with a Neel temperature around 643 K) and robust ferroelectric behavior (with a curie temperature around 1103 K) [1]. To suppress the leakage current issues and achieve high piezoelectricity in $BiFeO_3$, solid solution with another ferroelectric perovskite material is an effective approach [2]. Particularly, $BiFeO_3$-$BaTiO_3$ solid solution has emerged as a potential candidate for the above purposes, besides, interestingly it also exhibits morphotropic phase boundary (MPB) nearby $0.67BiFeO_3$-$0.33BaTiO_3$ (BF-33BT) composition [2]. At room temperature, the parent compounds $BiFeO_3$ and $BaTiO_3$ ($T_C \approx 400$ K) [3] exhibit rhombohedral (R3c) and tetragonal (P4mm) structures, respectively. The BF-33BT composition is found to exhibit pseudo cubic (Pm-3m) structure. At very high temperatures (~770 K), a huge value (~10,000) of relative dielectric permittivity is seen around the para to ferro transition [4].

Impedance spectroscopy is an effective method for examining the dynamics of bound and mobile charges in the bulk (grain) and interface regions of materials. It is particularly useful for determining the contributions of the electrode interface, grain, and grain boundary to the electric polarization. [4]. Most of the dielectric and impedance spectroscopy studies on BF-33BT has focused on high temperatures. H. Singh *et al.,* [5] and H. Zhang *et al.*,[3] performed impedance spectroscopy for explaining the relaxor ferroelectricity in BF-BT based perovskite ferroelectrics at high temperature regions. However, there is rarely any report on dielectric spectroscopy of BF-BT compounds in low temperature regions. Here, we report the solid-state synthesis of BF-33BT, and its dielectric spectroscopy in wide temperature (100-520 K) and frequency (10 Hz to 1 MHz) range. To understand the origin behind the ferroelectric relaxation observed near room temperature, complex impedance spectroscopy (CIS) and ac conductivity analysis has been employed.

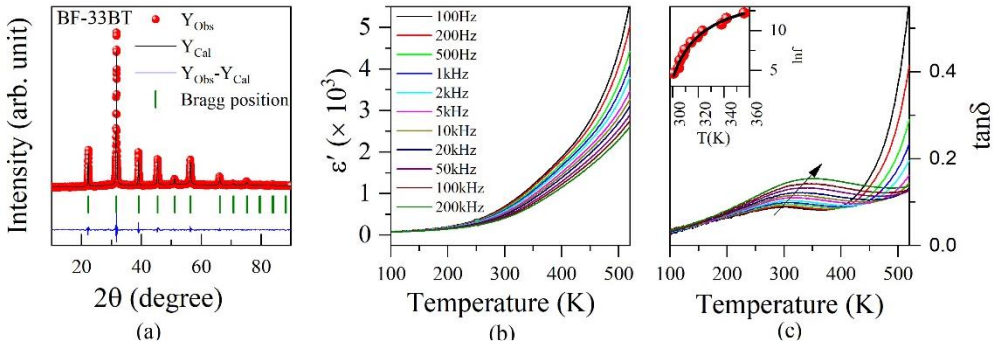


FIGURE 1. (a) Rietveld fitted powder XRD pattern of the BF-33BT at room temperature. **(b)** Temperature dependence of relative dielectric permittivity and **(c)** loss of BF-33BT, at increasing frequency values. Insets of Fig. (c) shows the fitting of the Vogel-Fulcher model of the maxima in temperature dependent loss tangent with varying frequencies.

EXPERIMENTAL SECTION

Utilizing high purity powders of Bi_2O_3 (99.99%), $BaCO_3$ (99.95%), TiO_2 (99.90%), and Fe_2O_3 (99.99%), the BF-33BT ceramic was synthesized via a traditional solid state reaction process. All of the powders, along with an additional 5% Bi_2O_3, were mixed and grind in an acetone medium for approximately 12 hours using a motor pestle. The well mixed powder was ball-milled for approximately twenty-four hours at 200 rpm, once more in an acetone medium. The finely mixed powder was calcined for 6 hours at 1033 K. For about twelve hours, the calcined powder was ball-milled once again. The final powder had been mixed with 2 weight percent polyvinyl alcohol (PVA) and compressed using a uniaxial press into a disc about 8 mm in diameter. The pellet was sintered in a covered crucible for two hours at 1293 K. The polished pallet's two sides were coated with silver electrodes, which were then burned for two hours at 873 K. Using Cu Kα radiation and a scan step of 0.02°, X-ray diffraction (XRD) was recorded using a Bruker D2 phaser x-ray diffractometer. Temperature dependent dielectric measurements were carried out by utilizing HIOKI LCR meter (IM 3536) and CRYOCON temperature controller in a home developed insert for measurements from liquid Nitrogen temperature up to high temperatures (~ 525K).

RESULTS AND DISCUSSION

XRD pattern of BF-33BT at room temperature is shown in the Fig. 1(a). XRD data testifies a phase pure synthesis of BF-33BT ceramic. Rietveld analysis of X-ray powder diffraction data confirms the Pm-3m (pseudo-cubic) space group. Fig. 1(b) shows frequency dispersion in relative dielectric permittivity (ε′), for frequency values between 100 Hz to 200 kHz, in a wide temperature window (100 K - 520 K), and Fig. 1(c) shows the dielectric loss (tanδ) at some of the frequencies with increasing temperature, where a broad peak is clearly seen. The Vogel-Fulcher model typically provides the best explanation for these behaviors, which show that the broad loss maxima shift to higher temperatures with rising frequencies [6]. The Vogel-Fulcher model states that the frequency dependent on peaking temperature is as, $f = f_0 \exp [-E_a / k (T-T_f)]$, where T is the temperature where dielectric loss got maximize and k is the Boltzmann constant, and fitted values are found to be as follows: freezing temperature (T_f) is ~ 276.172 K, the attempt frequency (f_0) is ~ 6.3 MHz, activation energy (E_a) is ~ 23.9 meV, and the relaxation time is ~ 0.16 μs. The inset of Figure 1(c) displays the Vogel-Fulcher fit indicating the freezing of grain boundary contributions (discussed in next section) below 276 K.

An efficient method for determining the type of relaxation and distinguishing the various contributions (to the polarization mechanism) that may originate from the grain, the grain boundary, and the electrode interface is the Nyquist plot. The Nyquist plots are shown in Fig. 2(a), at different temperatures (100-520 K) for wide frequency ranges 4 Hz to 1 MHz. Figure 2(a) shows the creation of semicircular arcs, whose pattern essentially stays the same between 100 and 400 K, confirming the presence of dominant grain effect in polarization. However, at temperatures above 400 K semicircles start to flatten which clearly indicate appearance of contributions from grain boundary in addition to grains. Fig. 2(b) shows the frequency dependency of imaginary impedance (Z'') at a few chosen temperatures. With increase in frequency the value of Z'' decreases up to 400 K. With further increase in the temperature, we observed a clear hump like behavior of Z'' at low frequency region which indicates the grain boundary contribution in polarization below a frequency 1 kHz.

FIGURE 2. (a) Nyquist plot at selected temperatures for BF-33BT. Inset shows Nyquist plot at 520K. (b)The variation of Imaginary part of impedance with frequency of BF-33BT at different temperature. (c) Frequency dependent ac conductivity at increasing temperature of of BF-33BT. Inset shows variation of A with temperature.

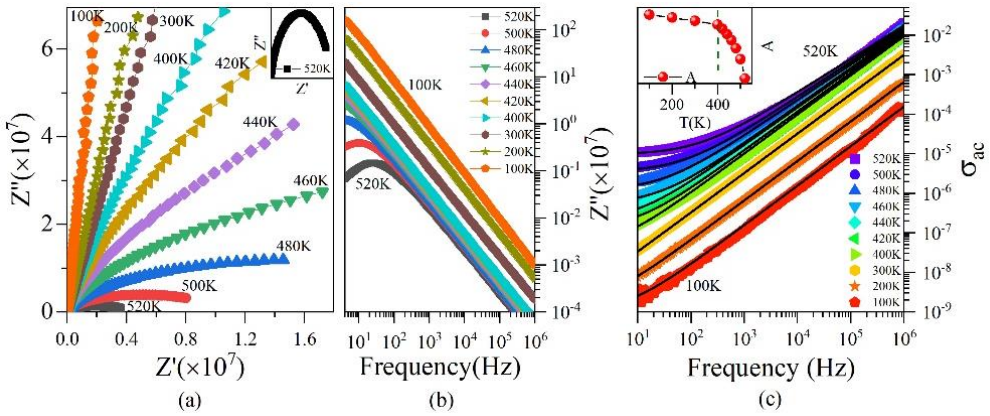


FIGURE 2. (a) Nyquist plot at selected temperatures for BF-33BT. Inset shows Nyquist plot at 520K. (b)The variation of Imaginary part of impedance with frequency of BF-33BT at different temperature. (c) Frequency dependent ac conductivity at increasing temperature of of BF-33BT. Inset shows variation of A with temperature.

Relative contributions of translational motion of ions or the charge carriers within a lattice coming from grain and grain boundaries can be identified in ac conductivity analysis. Figure 2(c) illustrates the log-log plot of the change in ac conductivity (σ_{ac}) with frequency. Up to 400 K, σ_{ac} exhibits a linearly increasing behavior with frequency. The σ_{ac} versus frequency graphs show a low slope (almost flat) region below 1 kHz and a somewhat sharper slope above 1 kHz for temperatures above 400 K. Thus, the graphs show that the grain boundary effect has no effect on the conduction processes at temperatures up to 400 K. Moreover, as the temperature rises the grain as well as grain boundary both contributes to the conduction processes. To understand this behavior, σ_{ac} is fitted by Jonscher's power law [6] which is given by, $\sigma_{ac} = \sigma_{dc} + A\omega^n$, where, the direct current conductivity contribution at low frequencies is represented by the first term, the dispersive trend of σ_{ac} is determined by the exponent power (n), and the strength of polarizability in the sample is determined by the pre-exponential factor (A) in the second term. The variation of A with temperature is shown in inset of Fig. 2(c). Values of A decreases rapidly above the temperature 400K, this unambiguously shows a shift from contributions of the grain border alone to those of both the grain and the boundary.

CONCLUSIONS

The BF-33BT ceramic has been successfully synthesized utilizing a traditional solid state reaction method. A single-phase synthesis of BF-33BT with pseudo-cubic crystal structure was confirmed by Rietveld fitted XRD pattern. Based on temperature dependent dielectric spectroscopy analysis we found that the grain boundary contributions freeze below around 276 K. The frequency dependent impedance spectroscopy confirmed that the grain boundary effect contributes with grain effect in ferroelectric polarization only at high temperatures below a certain frequency, this is also supported by ac conductivity analysis. Thus, we conclude here that for BF-33BT at low temperatures, below 400 K, the grain boundary contribution to ferroelectric polarization is minimum which finally freezes around 276 K.

REFERENCES

1. G. Catalan and J.F. Scott, Advanced Materials, 21, 2463-2485 (2009).
2. D. Wang, G. Wang, S. Murakami, Z. Fany, A. Feteiraz, D. Zhoux, S. Sun, Q. Zhao and I. M. Reaney, Journal of Advanced Dielectric, 8, 1830004 (2018).
3. K. Dey, A. Tripathy, S. R. Sahu, H. Srivastava, A. Sagdeo, J. Strempfer and D. K. Shukla, Physical Review B 105, 174202 (2022).
4. H. Zhang, W. Joa, K. Wanga, K. G. Webber, Ceramics International, 40, 4759–4765 (2014).
5. H. Singh, A. Kumar and K.L. Yadav, Materials Science and Engineering B, 176, 540–547(2011).
6. A. A. Bokov and Z. G. Ye, J. adv. Dielectrics., 02, 1241010 (2012).

Multiferroicity and Magneto-capacitance in

$BaTi_{1-x}Fe_xO_{3-\delta}$(x= 0, 0.02, 0.1, 0.15 and 0.2)

Arunangsu Banerjee[1,*] and Subhajit Sarkar[1]

[1]Department of Physics, West Bengal State University, Barasat, West Bengal 700126, India.

* Corresponding author: arunangsubanerjee.hrpv@gmail.com

Abstract

$BaTi_{1-x}Fe_xO_{3-\delta}$ (x= 0, 0.02, 0.1, 0.15 and 0.2) ceramics were synthesized by solid state reaction route. Presence of oxygen vacancies in three charge states were found in all the samples and the densities of oxygen vacancies increased with increase in doping.The findings of the room temperature Mössbauer spectroscopic studies in corroboration with the magnetic field dependence magnetization studies revealed the coexistence of ferromagnetic and antiferromagnetic orderings among Fe^{3+} ions along with the isolated paramagnetic Fe^{3+} ions. Oxygen vacancies played the key role in introducing magnetic orderings among the Fe^{3+} ions. The magnetic orderings were individually scrutinized through Mössbauer spectroscopic studies revealing the hyperfine parameters for the magnetic orderings perhaps for the first time for this system. Magneto-capacitance increased with increase in doping, became 41% for 10% doping and thereafter decreased with further doping.

INTRODUCTION

In recent years, multiferroics are subjected to intensive studies. In single-phase ABO_3 structured multiferroics, a ferroelectric material is taken as a host material wherein magnetization is incorporated by doping with transition elements at the A or B sites. However, higher doping is usually restricted as it gives rise to significant decrease in ferroelectricity due to formation of secondary phase unsuitable for the spontaneous electric polarization. In case of Fe doped $BaTiO_3$, numerous reports about the dielectric and magnetic studies can be found in literature. However, the results of the magnetic studies of the compound in different reports are found conflicting rather insufficient [1-2]. Attempts were pursued to reveal the magnetic orderings individually in Fe doped $BaTiO_3$ systems by Mössbauer spectroscopic technique [2-3]. However, no sextet pattern was observed in the spectra and they tried to explain the non-observance of the sextet patterns by their own ways [2-3]. In the present work, apart from the structural, dielectric and magnetization studies, we focused on the magnetic hyperfine analysis of the magnetic interactions among the magnetic ions. We successfully observed the sextet patterns for the ferromagnetic (FM) and antiferromagnetic (AFM) orderings and comprehensively scrutinized the hyperfine parameters of the magnetic interactions for the first time for this system. High value of magneto-capacitance (MC) (about 42%) of the system in $BaTi_{0.90}Fe_{0.1}O_{3-\delta}$ is an indicative of reasonable magnetoelectric coupling of the system.

EXPERIMENTAL

$BaTi_{1-x}Fe_xO_3$ (x= 0, 0.02, 0.1, 0.15 and 0.2) were prepared by solid state reaction using TiO_2, $BaCO_3$ and Fe_2O_3 (99% from Sigma Aldrich, USA). The X-ray diffraction (XRD) patterns were recorded using X-ray diffractometer (Bruker D8 Advance) with Cu-K (1.5418 Å). Photoluminescence (PL) Spectroscopic method (Perkin-Elmer LS-55) was used to detect PL emission. For monitoring fluorescence in visible region, the excitation wavelength was selected at 440 nm, and emission was recorded from 480 nm to 700 nm at a scan rate of 250 nm/min. Dielectric measurements were carried out by LCR Meter (IM 3650, Hioki Japan). Mössbauer spectroscopic measurements in transmission geometry were carried out at room temperature with a 1024-channel Mössbauer spectrometer with 25 mCi ^{57}Co source in Rh matrix. Magnetic measurements of the samples were carried out in a SQUID magnetometer (MPMS, Quantum Design, USA). Room temperature MC was measured by LCR Meter (IM 3650, Hioki Japan) attached with a DC electromagnet.

RESULTS AND DISCUSSION

Figure 1[A] shows the Rietveld refinement of XRD patterns. The un-doped and 2% Fe doped samples formed in tetragonal phase. On the other hand, tetragonal and hexagonal phases were observed in 10%, 15% and 20% doped samples. The amount of hexagonal phase increased with increase in doping. Figure 1[B] shows the room temperature PL spectra of the samples in the visible region. The broad peaks are attributed to the oxygen vacancies. They were fitted into three peaks at around 581 nm, 606 nm and 628 nm respectively. They are assigned to oxygen vacancies in three charge states namely, neutral, singly ionized and doubly ionized oxygen vacancies respectively. Figure 1[C] depicts the dielectric constant against temperature measured at 1 kHz. The Curie temperature of the un-doped sample is around 140^0C and shifted towards the higher temperature with increase in doping. A peak at around 40^0C was observed for every sample which is attributed to the Maxwell-Wagner (M-

W) polarization. The reason behind the M-W polarization was the space charge polarization at the grain boundary region resulting in formation of grain boundary capacitance wherein grain interiors act as electrodes and the grain boundary as dielectric. Oxygen vacancies act as the donors of the free electrons that are accumulated at the grain boundary region leading to the space charge polarization. Fig.1[D] shows the M-H curves at room temperature. The samples exhibited FM hysteresis loop near the origin with non-saturating linear magnetization. The linear magnetization is attributed to the paramagnetic and AFM components along with FM component. Magnetization increased with doping up to 15% and thereafter decreased for 20% doping because of AFM orderings more than the FM orderings among the Fe^{3+} ions.

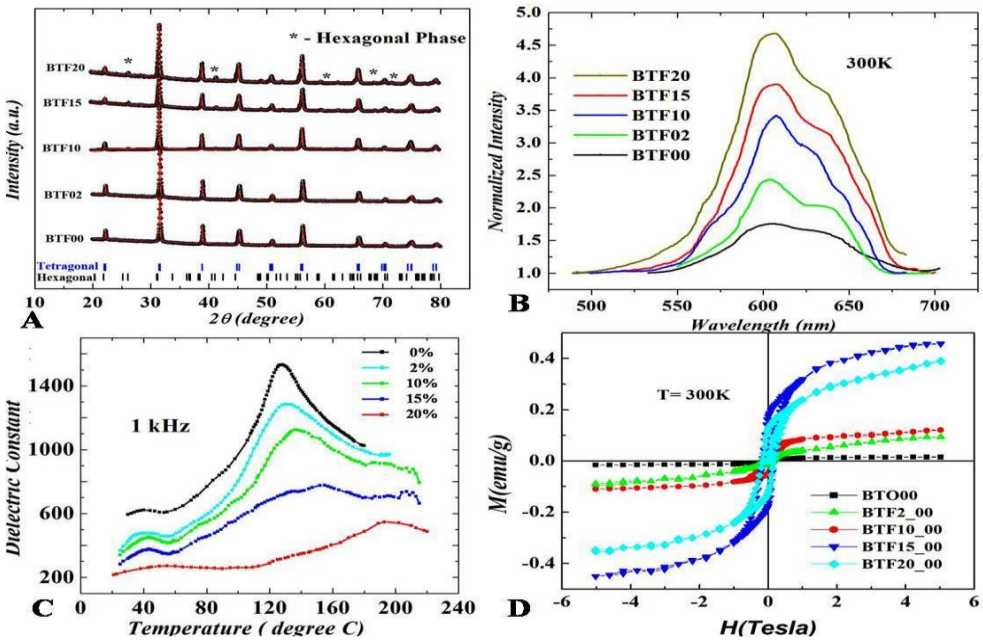


Figure 1: [A] Rietveld refinement XRD patterns [B] photoluminescence spectra in the visible region and [C] temperature dependence of dielectric constant and [D] M-H curves of $BaTi1\text{-}xFexO_{3\text{-}\delta}$ (x= 0, 0.02, 0.1, 0.15 and 0.2).

The doublets in fig.2 are attributed to the Quadrupole Splitting of Fe^{3+} ions in octahedral and pentahedral cages of Ti. Fittings resulted in hyperfine fields 512kOe (sextet1), 478kOe (sexte2) and 418kOe (sextet3) respectively except for 2% doped sample wherein the sextet of hyperfine field 421kOe was absent. The sextet1 is assigned to AFM ordering between the Fe^{3+} ions mediated by oxygen atoms or neutral oxygen vacancies. On the other hand, the sextet2 and sextet3 are assigned to FM interactions between Fe^{3+} ions situated at the Ti sites of tetragonal and hexagonal phases. The analysis of sextet patterns in the Mössbauer spectra shows that AFM ordering is dominated over FM orderings with increase in doping concentration which was also reflected in the field dependence of magnetization curves. Hence, the results of the magnetization measurements corroborate nicely with the Mössbauer studies.

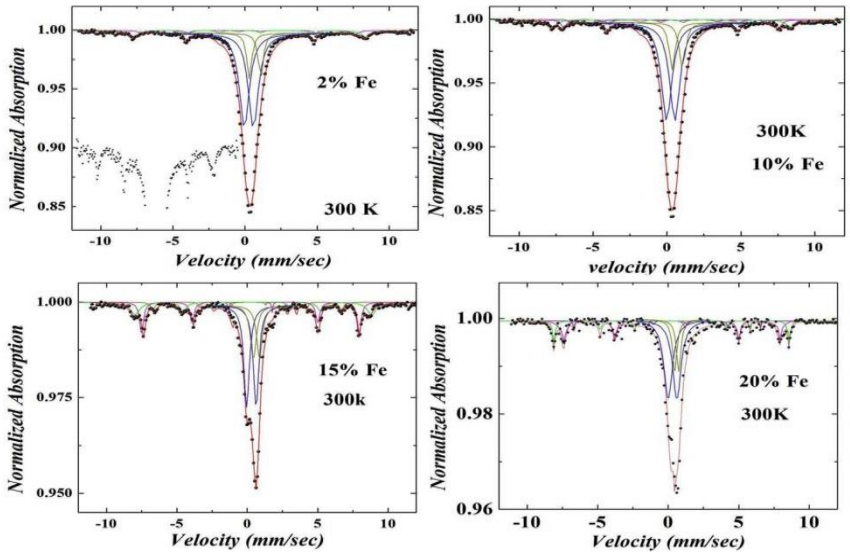


Figure 2: Mössbauer spectra of $BaTi_{1-x}Fe_xO_{3-\delta}$ (x= 0.02, 0.1, 0.15 and 0.2).

Fig 3 shows room temperature MC measured at 1 kHz. When the magnetic field was applied, a strain was produced due to domain wall motion. The strain in turn produced a stress in the material resulting in change in electric polarization of the samples. The value of MC increased with doping up to 10% doping and there after decreased with further doping. The decrease in MC for 15% and 20% doped samples might be due to the substantial decrease in ferroelectricity as shown in fig 3.

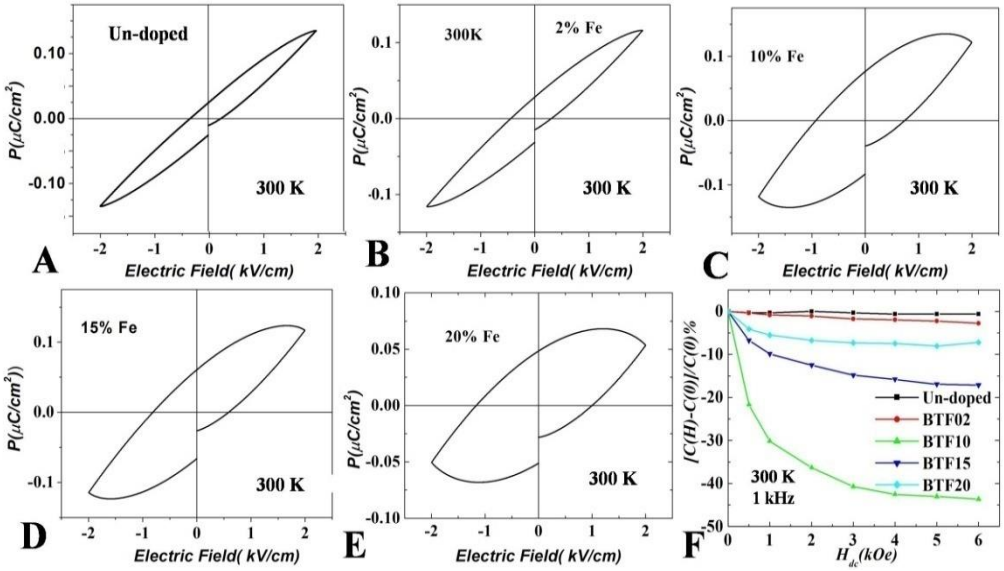


Figure 3: [A-E] P-E loops of $BaTi_{1-x}Fe_xO_{3-\delta}$ (x= 0, 0.02, 0.1, 0.15 and 0.2) recorded at room temperature. [E] Room temperature magneto-capacitance of $BaTi_{1-x}Fe_xO_{3-\delta}$ (x= 0, 0.02, 0.1, 0.15 and 0.2).

CONCLUSIONS

A comprehensive study on the oxygen vacancy mediated magnetic orderings and magneto-capacitance was carried out on $BaTi_{1-x}Fe_xO_{3-\delta}$ (x= 0, 0.02, 0.1, 0.15 and 0.2) ceramics synthesized by solid state reaction route. Presence of peaks in the visible region of Photoluminescence spectra confirmed oxygen vacancies in three charge states.Thermo-dielectric studies exhibited ferroelectricity with Curie temperature at about 130^0C. Substantial decrease in dielectric constant occurred with increase in doping. The samples exhibited interfacial polarization near room temperature that indicates formation of grain boundary capacitance due to space charge polarization. Magnetization was found to enhance with increase in oxygen vacancies as a result of increase in Fe doping up to 15% and thereafter deceased on further doping. Oxygen vacancies played the key role in introducing magnetic

orderings. Magnetic orderings were studied separately using Mössbauer Spectroscopic technique perhaps for the first time for this system. MC increased with increase in amount of Fe. MC in 10% Fe doped sample was found to be 41% which is significantly higher than the earlier reports. Through this work, we proposed that the material could be considered as a promising candidate for MC applications.

AKNOWLEDGEMENT

This work was partially carried out using the facilities of UGC-DAE CSR, Kolkata Centre.

REFERENCES

1. L. Yang a, H. Qiu, L. Pan, Z. Guo, M. Xu, J. Yin and X. Zhao, Journal of Magnetism and Magnetic Materials, Vol. 350, pp. 691–694 (2014).
2. F. Lin, D. Jiang, X. Ma and W. Shi, Journal of Magnetism and Magnetic Materials, Vol. 320, pp. 691–694 (2008).
3. F. Lin, D. Jiang, X. Ma and W. Shi, Physica B, Vol. 403, pp. 2525–2529 (2008).

Variation In Dielectric Properties Of Sm^{+2} Doped Lead Titanate Prepared By High Energy Ball Milling

Sona Kumari[1], R.K.Chaudhary[2] and S.K.Sinha[3]

[1]*RTC Institute of Technology, Anandi Ormanjhi, Ranchi, Jharkhand, India*
[2]*NIT Jamshedpur, Jharkhand, India*
[3]*B.I.T..Mesra Patna Campus*

[a)] *Corresponding author: sona_kumari@rtcit.ac.in*
[b)] *sonakumariphy@gmail.com*

Abstract. Our aim and expectation is that modification of rare earth element as Sm^{+2} will be more dependent on the radii difference. Sumarium has selected as source of the guest ion. Such type of the studies has been reported hardly as such lead titanate having perovskite structure has been selected as host lattice. Powder form of the ceramic has been fabricated by using High Energy ball Milling (HEBM) method. Undoped lead titanate has minimum dielectric constant and increases gradually (with increasing rate of doping) by 5% of Sm^{+2} doped sample. From the figure it also appears that Tc shift to higher temperature side for 5% Sm^{+2} sample of doping concentration. Electrical conductivity measurements are reported. Doping with Sm^{+2} result in a marked reduction in particle size and unit cell volume of pure lead titanate. Partial substitution of the Sm^{+2} on the B- site suggested.

Keywords: Lead titanate, high energy ball milling, dielectric constant, Curie Temperature , conductivity and dielectric loss etc.

INTRODUCTION

Literature survey made to the extent possible studies of structural, microstructural, electrical and electromechanical properties of lead titanate ceramics doped with rare earth metal Samarium(Sm^{+2}). It reveals results of such studies with a little discussion in the case of (Sm^{+2}) doped in the host lattice of lead titanate ceramics. Samarium being off valent with lead ions of lead titanate ceramics and also having a larger radii difference with lead ions compared to that between gadolinium and lead ions, It is expected that host lattice ion may produce enhancement in the electrical properties and doping of samarium ions into the lattice of lead titanate having ABO_3 structure will produce interesting results for ,microstructural , electrical and electromechanical properties of lead titanate ceramics [1-5].

Electrical measurement

Variation of dielectric constant (ϵ) and dielectric loss ($\tan\delta$) measured at 1 kHz for 1 wt.%, 3 wt.% and 5 wt.% samarium doped lead titanate ceramics as a function of temperature have been placed at Figure no. 1 - 4, show that the dielectric constant starts increasing from about 100^0 C reaches the value 1100 at around 260^0 C and reaches the maximum value of about 2600 at 475^0 C . It is also observed from this figure that the dielectric constant increases more rapidly with concentration of samarium dopant.[6-9]. Figure : 3. presents the variation of dielectric constant as a function of temperature from 400^0 C to 500^0 C.. The figure shows that dielectric constant maxima are shifting towards low temperature side with the increase in dopant concentration[10-13].

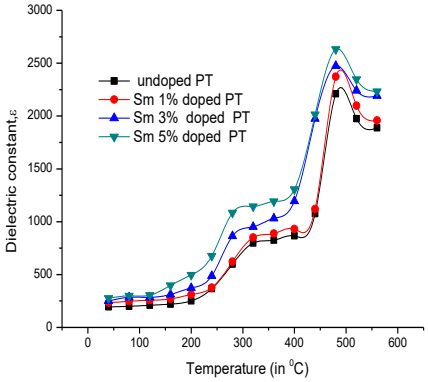


Fig 1. Dielectric constant as a function of temperature of samarium doped lead titanate ceramics.

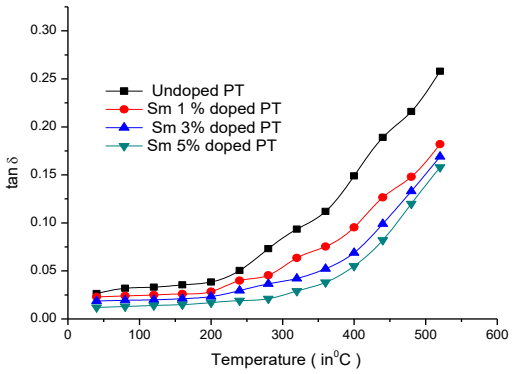


Fig 2. Dielectric loss (tanδ) as a function of temperature of samarium doped lead titanate ceramics .

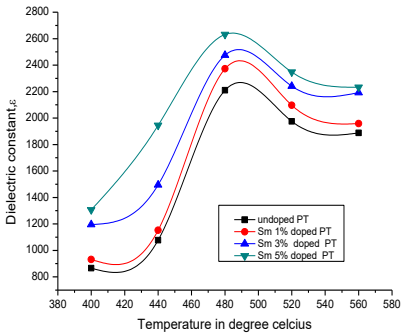


Fig 3. Variation of dielectric constant maxima as a function of temperature of samarium doped lead titanate ceramics

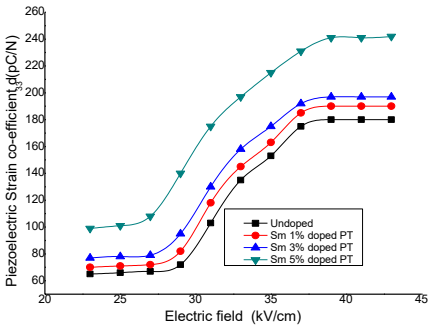


Fig 4. Variation of piezoelectric stain as a function of electric field of samarium doped led titanate ceramics

Electromechanical Properties

The variation of piezoelectric coef

ficient with polling field for Sumerium doped in lead titanate lattice for 1 wt.%, 3 wt.% and 5 wt.% have been presented in Figures : 1. These figures show that the piezoelectric coefficient i.e. charges developed per unit force with the application of electric field producing strain in the material increases with the concentration of doping (wt.%). This coefficient is dependent on ionic radii difference between the host and guest ions in lead titanate lattice as well as this is dependent on the charges of the guest ions. From these figures it is evident that value of this coefficient increases more in the case of samarium doping and least in the case of other doping. On the other hand value of the coefficient increases with wt. % of the dopants.

RESULT AND DISCUSSION

Incorporation of Sm^{+2} based on the stoicheometric formula. Dielectric constant was found as 2453 at curie temperature of 480°C in the case of 5 wt.% of Sm^{+2} in ceramics. The variation of piezoelectric coefficient with polling field for Sum doped in lead titanate lattice for 1 wt.%, 3 wt.% and 5 wt.% have been presented in Figures The results found were comparatively better than in similar kind of materials reported as so far by various researchers.

ACKNOWLEDGEMENT

I thankfully acknowledge the help rendered by Dr.S.K.S.Parasar **(**KIITS University, Bhubneshwar)for providing facility for HEBM system and Dr.S.K.Sinha BIT, Patna for providing facility for measurement. Also help by Dr.S. K. Swain of Central Instrumentation Facility (CIF), BIT Mesra, for characterization of samples is thankfully acknowledged.

REFERENCES

1. S. K. Sinha, S. Kumari, and R. K. Chaudhary.Jr. of Advance Dielectric (2019)
2. V. Kalem, I. Cam, M. Tim S. Zhang*1*, H. B. Zhang*2*, F. A. Zhao*3*, M. Jiang*1*, H. Y. Xiao*1*, Z. J. Liu*4* & X. T. Zu*3,Nature.com (2017)*
3. ucin, Ceramics International.37, 1265 (2011).
4. T. Ohno, D. Suzuki, K. Ishikawa, H. Suzuki, Adv. Powd. Tech, 18 (2007) 579.
5. B. Tiwari, R. N. P. Choudhary, Sol. Stat. Sci.11 (2009) 219.
6. R. Ranjan, R. Kumar, B. Behera, R. N. P. Choudhary, Mater. Chem. Phys.115, (2009) 473
7. S. K. Pandey, O. P. Thakur, D. K. Bhattacharya, Chandra Prakash, Ratnamala, Chatterjee, J.Alloys and Comp. 468 (2009) 356.
8. B. Tiwari, R. N. P. Choudhary, J. Phys. Chem. Solid. 69 (2008) 2852
9. M. I. Morozov, D. Damjanovic, J. Appl. Phys.104 (2008) M. A. Khan, T. P. Comyn, A. J. Bell, J. Eur. Ceram. Soc. 28, 591 (2008).
10. Z. Zhang, P. Wu, L. Lu, C. Shu, J. Alloys Comp. 449, 362 (2008).
11. R.A. Eichel, P. Erhart, P. Traskelin, K. Albe, H. Kungl, M.J. Hoffmann, Phys.Rev. Lett. 100, 095504 (2008)
12. A. Singh, V. Gupta, K. Sreenivas, R. S. Katiyar; J. Phys. Chem. Sol. 68, 119 (2007)
13. R. A. Eichel, J. Electroceramic. 19 (2007) 11.

Investigation of Charge Transport Properties of RGO-CuSe-Based Schottky Diode by Tuning Graphene Content

Mainak Das[1], Dhananjoy Das[2], Supravat Ghosh[1] and Partha Pratim Ray[1*]

[1] *Department of Physics, Jadavpur University, Kolkata - 700032, West Bengal, India*
[2] *Centre of Nano Science, IIT Kanpur - 208016, Uttar Pradesh, India*
[*] *Corresponding author: parthapray@yahoo.com*

Abstract. Here, we have reported the charge transport properties of reduced graphene oxide-copper selenide (rGO-CuSe) based Schottky diodes by tuning the rGO content over bare CuSe. The diodes showed better performance after incorporation of different weight percentage of rGO, among which the best result was obtained for 5% rGO content. Space charge limited current theory was used to determine charge transport properties like carrier mobility, transit time, and diffusion length. For 5% rGO incorporation, we have achieved a carrier mobility of 8.60×10^{-5} $m^2V^{-1}s^{-1}$ with a 38-fold increase over pure CuSe. The transit time was improved by 22 times and the diffusion length also increased by 30%.

Key Words: Semiconductor, reduced graphene oxide, hydrothermal, Schottky diode, mobility.

INTRODUCTION

The fabrication of Schottky barrier diodes (SBDs) at metal-semiconductor (MS) junctions and the analysis of charge transport have recently received considerable attention in modern electronics [1]. The performance of a SBD depends on some factors, like mobility of charge carriers, recombination rate, and interface quality. CuSe (CS) is a material that has several features such as non-toxicity, tunable microstructure, tunable bandgap in the semiconducting range, and low cost but CS has a high electron-hole recombination rate, which impacts device performance. However, graphene, a carbon-based material has gained attention due to its excellent conductivity, high carrier mobility, electron-hole-suppressing ability and emerged as a promising material for electronic devices [2]. Thus, combining graphene with CS holds promise to enhance charge transport kinetics, specifically by inhibiting recombination in CS. Producing pure graphene is difficult so reduced graphene oxide (rGO) has been synthesized. In this study, we have synthesized rGO-CuSe (RCS) composites with different weight ratios of rGO (0% (CS), 1% (RCS1), 3% (RCS3), 5% (RCS5) and 7% (RCS7)). Subsequently, SBDs were fabricated and the charge transport performances were analyzed by space charge limited current (SCLC) theory. We estimated some charge transport parameters and investigated the effect of rGO on the charge transport of CS.

MATERIALS AND METHODS

Synthesis, Characterization and Device fabrication

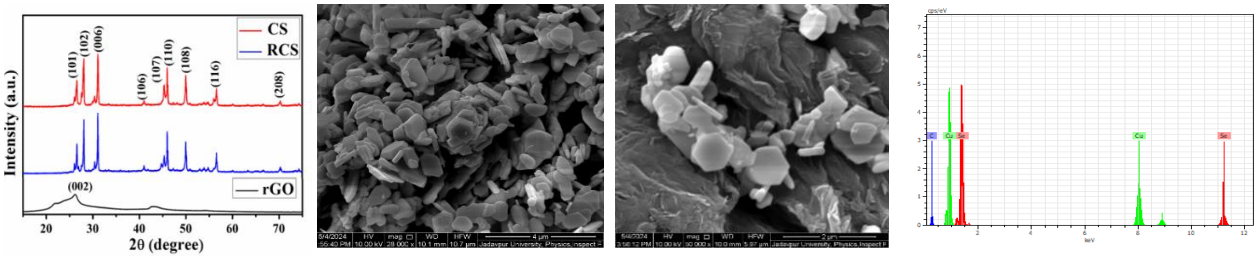
CuSe (CS) was synthesized using hydrothermal method. 0.2 M Copper dichloride dihydrate ($CuCl_2.2H_2O$) and 0.5 g of tartaric acid were dissolved in 25 ml of distilled water while stirring. 3 ml hydrazine hydrate and 3 ml aqueous ammonia were added. A separate aqueous solution of 0.2 M sodium selenite ($Na_2S_2O_3$) was prepared and added to the first mixture. After 15 minutes of stirring, the mixture was transferred to a Teflon-lined stainless-steel autoclave and placed in an oven set at 180 °C for 12 hrs. The collected black material was washed with distilled water and ethanol and dried at 60 °C for 4 hrs. Graphene oxide (GO) was prepared using the Modified Hummers method. Then, hydrazine hydrate was added to the dispersed GO water to obtain reduced graphene oxide (rGO). The resulting black precipitate was sequentially washed with ethanol and distilled water and then heated to collect the desired rGO powder. To produce the rGO-CuSe (RCS) composite, rGO was added to the CS in different weight ratios as rGO weight ratios of 0% (CS), 1% (RCS1), 3% (RCS3), 5% (RCS5), and 7% (RCS7) and stirred for 8 hrs. Then, a similar hydrothermal process was carried out and RCS was obtained by washing several times with distilled water and ethanol and drying at 60 °C for 4 hrs.

The morphology of the sample was assessed using a field emission scanning electron microscope (FESEM), by the FEI Inspect F50 model and the elemental combination was determined using an energy-dispersive X-ray (EDX) analyzer. To analyze the crystalline phase, a powder X-ray diffraction (PXRD) experiment was performed using a Bruker D8 advance X-ray diffractometer, with Cu Ka radiation (λ=1.5418 Å). Current-voltage (I-V) measurements were performed using a Keithley 2635B sourcemeter.

To fabricate SBDs, fluorine-doped tin oxide (FTO) coated glass was cleaned using a sequence of soap solution, acetone, ethanol, and distilled water in an ultrasonic bath. The materials were then spin-coated onto the FTO-coated glass and left to dry, resulting in thin films. The film thickness was approximately 1 μm, as determined by a surface profiler. Metal contacts of aluminium were made to the film by depositing through the thermal evaporation technique. The diode's effective area (A) was maintained at 7.065×10^{-6} m^2 using a shadow mask [3].

RESULTS AND DISCUSSIONS

The PXRD patterns of the samples are shown in Fig. 1(a). The peak (002) of rGO appeared at approximately 2θ=24°-25°. Peaks were observed at 2θ = 26.62°, 28.11°, 31.08°, 41.03°, 45.36°, 46.04°, 50.0°, 56.60° and 70.32° corresponding to the (101), (102), (006), (106), (107), (110), (108), (116) and (208) diffraction planes, respectively. This is confirmed by JCPDS card no. 34-0171 and the phase of CuSe is verified. The spectrum for RCS was similar to that of bare CS. The intensity of the rGO peak was low due to the presence of small amount of rGO in the composite. The FESEM images of the samples are shown below. Figure 1(b) displays hexagonal CS particles, which are approximately 200-250 nm in size. The nice decoration of CS nanoparticles on the rGO sheets is shown in Fig. 1(c). Figure 1(d) represents the EDX spectra of RCS, satisfying the presence of elements (Cu, Se, C) in the composite indicating the successful synthesis of the composite.

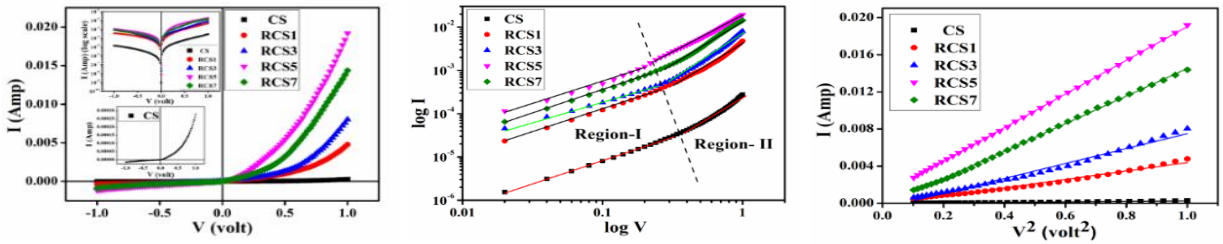


(a) (b) (c) (d)

FIGURE 1. (a) XRD spectra of rGO, CS, and RCS. SEM image of (b) CS and (c) RCS (d) EDX spectra of RCS composite

The I-V characteristics of the devices were measured within a bias voltage range of ±1 V and shown in Fig. 2(a). The devices exhibited excellent rectifying behaviour, indicating Schottky nature. The RCS5-based device demonstrated the highest current. Furthermore, all the RCS7, RCS5, RCS3, and RCS1 devices had higher on/off current ratio, indicating greater rectification compared to CS. The enhanced current in the RCS-based diodes can be attributed to the high conductivity of graphene. The diodes were analyzed by the thermionic emission theory and the I-V dependence can be represented by the equation

$$I = I_0 \exp\left(\frac{qV}{\eta kT}\right)\left[1 - \exp\left(-\frac{qV}{\eta kT}\right)\right] \quad (1)$$



(a) (b) (c)

FIGURE 2. (a) I-V plot of CS and RCS-based SBDs. (b) log I-log V plot and (c) I-V^2 plot for the SCLC region.

To gain a deeper understanding of charge transport, we examined the forward current region using the SCLC theory [4]. In Fig. 2(b), we present the log I vs log V graph, divided into two different regions. The SCLC region (Region-II), where the current follows the relation I α V^2, is depicted in Fig. 2(b). From the I vs V^2 graph Fig. 2(c), we estimated the effective carrier mobility using the Mott-Gurney equation [5].

$$I = \frac{9\mu_{eff}\,\varepsilon_0\varepsilon_r A}{8}\left(\frac{V^2}{d^3}\right) \quad (2)$$

where ε_0 - permittivity of vacuum, ε_r - dielectric const. of material, μ_{eff} - electron mobility, and *d* - thickness of film. The transit time (τ) was determined from the I vs V graph using equation (3), and the diffusion lengths (L_D) of the charge carriers were extracted using equation (4).

$$\tau = \frac{9\varepsilon_0\varepsilon_r A}{8d}\left(\frac{V}{I}\right) \quad (3)$$

$$L_D = \sqrt{2D\tau} \quad (4)$$

where, *D* is the diffusion coefficient, calculated from the Einstein-Smoluchowski equation [6]:

$$\mu_{eff} = \frac{qD}{kT} \quad (5)$$

TABLE 1. Charge transport parameters

Sample	On/Off	μeff ($m^2V^{-1}s^{-1}$)	τ (ns)	L_D (nm)
CS	20	2.26×10^{-6}	329	199
RCS1	26	2.86×10^{-5}	29.9	210
RCS3	38	3.60×10^{-5}	26.0	220
RCS5	52	8.60×10^{-5}	15.2	260
RCS7	44	6.34×10^{-5}	18.5	246

The above tabulated data shows that there is a continuous improvement in charge transport kinetics after incorporating rGO. The mobility of the charge carriers increases with increase in rGO amount and decreases after a certain amount of rGO loading. In comparison to the bare CS, RCS5 showed the best result with highest carrier mobility of 8.60×10^{-5} $m^2V^{-1}s^{-1}$, a huge 38-fold increase in value. The transit time obtained was 15.2 ns that was improved by 22 times and the diffusion length as calculated was 260 nm where it was also increased by 30%. This study shows that, the rGO incorporated CuSe can be beneficial for several device applications.

CONCLUSIONS

In conclusion, CS and RCS nanocomposites with incorporation of different amounts of rGO have been synthesized by hydrothermal method and SBDs have been fabricated with the samples. The I-V characteristics indicated that mobility of the charge carriers greatly depends on the rGO content present in the samples. All rGO-based devices performed better than the CS-based SBDs, where the best performance was observed in Al/RCS5/ITO SBD. This device exhibited a significant 38 times increase in carrier mobility compared to CS. The transit time was improved and diffusion length of the carriers also increased substantially. Therefore, the result suggests a better understanding and further improvement in charge transport of MS devices.

ACKNOWLEDGMENTS

The author would like to thank the University Grants Commission (UGC) for providing the NET-SRF fellowship program and the Department of Physics, Jadavpur University for providing the instrumental facilities.

REFERENCES

1. N.A. Al-Ahmadi, Mater Res Express, Vol. **7**(3), pp. 032001 (2020).
2. Z.-Y. Feng, J.-C. Jiang, and L.-Y. Meng, Dalton Transactions, Vol. 53(27), pp. 11192–11215 (2024).
3. R. Sk, A. Biswas, A. Layek, P. P. Ray, Chemical Physics, Vol. 580**,** pp. 112233 (2024).
4. K.S. Das, M. Das, S. Saha, A. Adhikary, S. Bala, P.P. Ray, R. Mondal, Mater Adv, Vol. 4(23), pp. 6367–6380 (2023).
5. P. Das, M. Das, P.P. Ray, and S.K. Seth, ChemistrySelect, Vol. 9(6), pp. e202303361 (2024).
6. M.A. Islam, Phys Scr., Vol. 70(2–3), pp. 120–125 (2004).

Electron-Phonon Interaction Effects on Electronic Transport in "Bite" Defective Graphene Nanoribbons

Sandeep Kumar*

Department of Physics & Astronomical Science, Central University of Himachal Pradesh, Dharmshala (H.P.) 176215, India.

* Corresponding author: kumar.maxx786@gmail.com

Abstract. In this study, we have numerically calculated the electronic transport through "Bite" defective armchair graphene nanoribbons (AGNRs) when electron-phonon interaction is considered. In the case of "Bite" defective 8-AGNR, we observe a decrease in transmission with an increase in electron-phonon interaction strength but it does not become zero. The overall transmission decreases in the case of "Bite" defective 9-AGNR with an increase in electron-phonon interaction strength, but transmission shifts towards the centre of the band gap and remains zero near zero-energy.

Keywords: bite defects, transmission, AGNR, electron-phonon interaction.

INTRODUCTION

In graphene nanoribbons (GNRs), ribbon width and edge structure determine the controlled band gap through quantum confinement. The properties of GNRs are determined by two fundamental edge structures: zigzag and armchair [1]. Various research studies predict that armchair graphene nanoribbons (AGNRs) display metallic and semiconducting behavior with variation in their width. It has been found that N-AGNRs (N denotes the number of dimer lines in the width) are metallic with N = 3p+2 (p is a non-zero positive integer) and semiconducting otherwise [1]. Generally, the band gap of AGNRs varies inversely with their widths [1]. Experimentally, it is impossible to fabricate defect-free GNRs [2]. The introduction of defects can significantly vary the electronic, magnetic, and transport properties of GNRs [2]. Recently, "Bite" defective GNRs were successfully synthesized [3,4]. Recently, the electronic transport through as-synthesized "Bite" defective AGNRs have been investigated [3, 4]. It has been observed that the presence of "Bite" a defect significantly changes charge transport by restricting transmission in the vicinity of the band edges [3, 4]. In addition to this, the electronic transport behavior of GNRs depends on electron-phonon interactions [5].

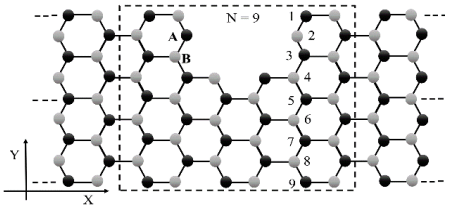


FIGURE 1. Lattice structure of a single "Bite" defective 9-AGNR. The dashed rectangle shows the supercell.

In GNRs, ripple structures lead to symmetric lattice displacements relative to their nearest atoms and are coupled to the electronic densities of the carriers. When electrons move through GNRs, they couple with out-of-plane phonons. This electron-phonon interaction changes the transport properties of GNRs [5]. The symmetric properties of the nearest neighbouring displacement give rise to the interaction of electron density and phonon mode. Within the Holstein model formalism, the out-of-plane vibrations (ZO optical phonons) interact with electrons and are dispersionless [5, 6]. In AGNRs, Rezania et al. investigated the effect of electron-phonon interaction on charge structure factors [5]. In this work, we focus on the impact of electron-phonon interaction on the electronic transport of single "Bite" defective 8- and 9-AGNR (see Fig. 1). We observe a non-zero transmission for metallic 8-AGNR, irrespective of strength of the electron-phonon interaction. However, the transmission of both defective AGNRs (8-AGNR and 9-AGNR) changes dramatically with the electron-phonon interaction parameter.

MATHEMATICAL FORMALISM

By including interaction of electron with phonon, the total system Hamiltonian (*H*) in the Holstein model can be written as [5, 6]:

$$H = H_0 + H_{ph} + H_{el-ph} \tag{1}$$

where $H_0 = \sum_i \epsilon_i c_i^\dagger c_i + t \sum_{\langle ij \rangle} (c_i^\dagger c_j + c_j^\dagger c_i)$, $H_{ph} = \hbar\omega_0 \sum_i b_i^\dagger b_i$, and $H_{el-ph} = g \sum_i (b_i^\dagger + b_i)\, c_i^\dagger c_i$, respectively, represent the unperturbed electron, phonon, and electron-phonon interaction part of *H*. Also, $c_i^\dagger$ (c_j) and $b_i^\dagger$ (b_i) represent the electron and phonon creation (annihilation) operator at site *i*. ϵ_i and g represent the electron-phonon interaction parameter (g = 0 to 0.1 eV) and onsite energy (ϵ_i = 0 eV), respectively. t and $\hbar\omega_0$, respectively, denote the hopping parameter (t = − 2.7 eV) and phonon mode energy ($\hbar\omega_0$ = 0.15 eV) [6].

In order to diagonalize the phononic part of *H*, we employ the Lang-Firsov unitary transformation [6]:

$$U_1 = e^{\frac{g}{\hbar\omega_0}\sum_i (b_i^\dagger + b_i) c_i^\dagger c_i} \tag{2}$$

so that the electronic and phononic annihilation (creation) operators are transformed as $\tilde{b}_i = b_i - \frac{g}{\hbar\omega_0} c_i^\dagger c_i$ $(\tilde{b}_i^\dagger = b_i^\dagger - \frac{g}{\hbar\omega_0} c_i^\dagger c_i)$ and $\tilde{c}_i = c_i exp[-g/\hbar\omega_0 (b_i^\dagger - b_i)]$ $(\tilde{c}_i^\dagger = c_i^\dagger exp[-g/\hbar\omega_0 (b_i - b_i^\dagger)])$. Therefore, the transformed Hamiltonian $(\tilde{H} = U_1^{-1} H U_1)$ can be written as [6]:

$$\tilde{H} = \sum_i (\epsilon_i - \tfrac{g^2}{\hbar\omega_0}) c_i^\dagger c_i + \tilde{t} \sum_{\langle ij \rangle} (c_i^\dagger c_j + c_j^\dagger c_i), \tag{3}$$

where $\tilde{t} = t\, exp\left(-\frac{g^2}{(\hbar\omega_0)^2}\right)$. Also, the presence of electron-phonon interaction affects leads self-energy. The modified self-energy of left (right) lead is defined as [6]:

$$\Sigma_{L(R)} \to \Sigma_{L(R)}\, exp\left(-\tfrac{g^2}{(\hbar\omega_0)^2}\right). \tag{4}$$

Therefore, we get the electron transmission function $(\tilde{T}(E))$ and density of states (DOS) in terms of Green's function as:

$$\tilde{T}(E) = Tr[\Gamma_L G^r(E) \Gamma_R G^a(E)] \tag{5}$$

$$DOS(E) = -\frac{1}{\pi} Im\big(G^r(E)\big), \tag{6}$$

where, $G^r(E) = \left((E + i\eta) + \tilde{H}_c - \Sigma_L - \Sigma_R\right)^{-1}$ is the central part $(\tilde{H}_c)$ retarded Green's function, $\Gamma_{L/R}(E) = -2\, Im\Sigma_{L(R)}(E)$ represents the broadening matrices, and $\Sigma_{L(R)} = \tilde{H}_{cL(R)} g_{L(R)} \tilde{H}_{L(R)c}$ is self-energy in terms of retarded surface Green's function $(g_{L(R)})$ of the left(right) lead. In order to surface Green's function and hence transmission and DOS, we employed the standard non-equilibrium Green's function (NEGF) formalism.

RESULTS AND DISCUSSION

As shown in Fig. 2 (a) and (d), when electron-phonon interaction is not considered, the "Bite" defective 8-AGNR is metallic, while the 9-AGNR is semiconducting. In both AGNRs (8-AGNR and 9-AGNR), the presence of a "Bite" defect results in a flat band at zero-energy in their bandstructures. The increase in electron-phonon interaction strength does not affect the zero-energy flat band and results in a sharp peak at zero-energy in DOS, as shown in Fig. 2 (b) and (e). As shown in Fig. 2 (c), we observe that when electron-phonon interaction is taken into account, the transmission decreases through the "Bite" defective 8-AGNR, but the states present in the zero-energy flat band make transmission non-zero even in the presence of the maximum value of electron-phonon interaction (g = 0.1 eV). In the case of the "Bite" defective 9-AGNR, as shown in Fig. 2 (f), the zero-energy states do not contribute to the transmission through the ribbon. This results in zero transmission around zero-energy as the electron-phonon interaction parameter varies from 0.0 eV to 0.1 eV. However, as previous studies show [5, 6], the enhancement in the electron-phonon interaction parameter reduces the energy width and hence GNR transmission. Moreover, when the electron-phonon interaction is considered, both "Bite" defective AGNRs (8-AGNR and 9-AGNR) exhibit many peaks and asymmetry in the transmission spectrum. The transmission peaks and asymmetry may occur due to the modification in self-energy and effective mass.

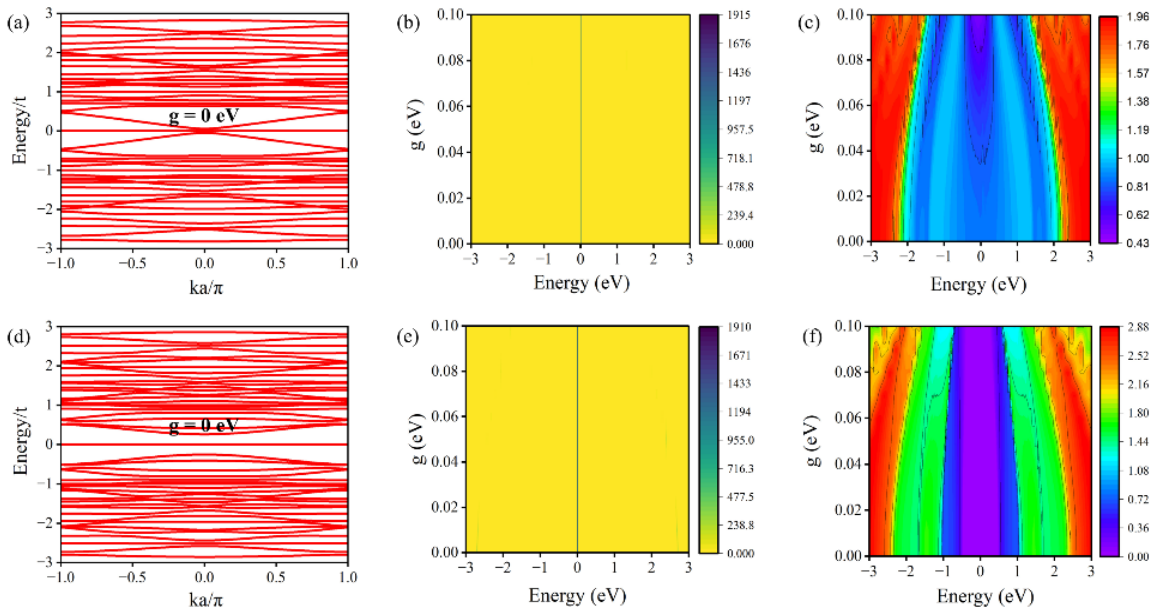


FIGURE 2. The upper panel (a-c) and lower panel (d-f) represent the band structure, DOS, and transmission function for "Bite" defective 8-AGNR and 9-AGNR, respectively.

CONCLUSION

In conclusion, we have investigated the electronic transport through the single "Bite" defective 8-AGNR and 9-AGNR using the Lang-Firsov transformation with NEGF. The metallic "Bite" defective 8-AGNR exhibits non-zero transmission in the electron-phonon interaction. However, overall transmission decreases with an increase in the electron-phonon interaction parameter. In the case of semiconducting "Bite" defective 9-AGNR, irrespective of the electron-phonon interaction, the flat band states do not take part in transmission and result in zero transmission near zero-energy. Moreover, with an increase in electron-phonon interaction strength, the overall transmission decreases and shifts towards zero-energy. Therefore, we expect our findings will be helpful in practical applications based on defective GNRs.

ACKNOWLEDGMENTS

S.K. would like to thank University Grant Commission (UGC)-New Delhi for his research fellowship during the course of this work (Ref. No.: 1256(CSIR-UGC NET DEC.2018)).

REFERENCES

1. A.H. Castro Neto, F. Guinea, N.M. Peres, K.S. Novoselov, and A.K. Geim, Rev. Mod. Phys. **81**, 109-162 (2009).
2. S. Kumar, R. Saklani, S. Pratap, and P. Bhalla, Phys. Scr. **99**, 065944 (2024).
3. M. Pizzochero, K. Čerņevičs, G.B. Barin, S. Wang, P. Ruffieux, R. Fasel, and O.V. Yazyev, 2D Mater. **8**, 035025 (2021).
4. S. Sun, Y. Guan, Z. Hao, Z. Ruan, H. Zhang, J. Lu, L. Gao, X. Zuo, and J. Cai, Nano Res. **15**, 653-658 (2022).
5. H. Rezania and F. Azizi, Chem. Phys. **530**, 110592 (2020).
6. A. Mogulkoc, M. Modarresi, B.S. Kandemir, M.R. Roknabadi, N. Shahtahmasebi, and M. Behdani, Physica B **446**, 85-91 (2014).

Novel TCAD Approach Precisely Simulating Charge Collection Efficiency of 4H-SiC Alpha-particle Detectors

Vivek Jaiswal[1, a)] and P. Vigneshwara Raja[1]

Department of EECE, Indian Institute of Technology Dharwad, Karnataka-580007, India.

[a)]Corresponding author: vj1890671@gmail.com

Abstract. This work reports a precise physics-based TCAD model for simulating charge collection efficiency (CCE) of 4H-silicon carbide (4H-SiC) Schottky barrier diode (SBD) alpha-particle detectors. The simulation results agree well with the state-of-the-art I-V and CCE characteristics of Ni/4H-SiC SBD detectors. Initially, the forward I-V is matched by fine-tuning physical parameters; then the reverse I-V characteristics are validated by employing a trap-assisted tunneling (TAT) model at the deep-level trap at $E_C - 0.73$ eV. To make the simulation more realistic, the 5.486 MeV ^{241}Am alpha-particle-induced electronic energy loss in SiC is computed by SRIM simulation. Subsequently, the linear energy transfer (LET) data calculated from SRIM is incorporated into the TCAD Heavy-Ion (HI) model. The conventional HI model can predict only the drift-induced charge portions of CCE, which is valid at higher detector bias voltages. Hence, a novel approach is adopted to include both drift- and diffusion-induced transient currents in the detector response; thereby the CCE of the detector is accurately simulated over a wide voltage range (0 V to -250 V).

INTRODUCTION

In recent years, 4H-SiC has emerged as an excellent material for alpha-particle detection due to its wide band gap (3.26 eV), low dark current, superior thermal conductivity (4.9 W/cm.K), and room-temperature operation without cooling[1]. We reported[2] that the 4H-SiC SBD detectors can work in challenging nuclear reactor environments up to a neutron fluence of 10^{15} cm^{-2}. Whereas, the commercial Si detector performance degrades severely even at low neutron fluences ($<10^{12}$ cm^{-2})[3], indicating that 4H-SiC-based detectors are more radiation-hard than the Si detectors. K.C. Mandal's group[4] achieved superior energy resolution of 16.2 KeV (0.29%) at 5.486 MeV alpha-particle energy line using the 20 µm thick epitaxial 4H-SiC SBD detectors (with 11.33 mm^2 active area); this energy resolution is very close to that of commercial Si detectors (14 keV and 0.25 % at 5.486 MeV alpha-particles). Thus, Mandal's state-of-the-art results[4] are used for the current simulation validation. Although some simulation studies for 4H-SiC detectors exist in the literature[5,6], transient signal current characteristics were obtained without matching the measured CCE characteristics. Moreover, the drift and diffusion current components are not segregated in the CCE vs. detector bias voltage plot using TCAD simulations. Accounting for the research gap, this work aims to include both drift- and diffusion-induced charge contributions accurately predicting the CCE variation with the bias voltage, using a novel physics-based TCAD heavy-ion (HI) model. Since the current model precisely simulates the 4H-SiC alpha-particle detector characteristics, the simulation studies can be extended in the future to anticipate the detector performance under various operating (at higher temperatures) and intense radiation environments.

SIMULATION MODEL

The 4H-SiC SBD structure is created in the Sentaurus TCAD simulator based on the work by Mandal's group[1,4]. The physics-based TCAD models, such as doping-dependent mobility, velocity saturation effect, SRH recombination, auger recombination, and bandgap narrowing, are chosen. The top Schottky metal work function is adjusted to match the diode turn-on voltage, and an Ohmic contact is employed for the back contact. Before simulating the CCE properties, the forward and reverse I-V characteristics must be validated. First, forward I-V is calibrated by varying the electron mobility and saturation velocity parameters (not shown). Next, the reverse I-V is matched with the experimental data by including the non-local TAT model at the deep-level trap $Z_{1/2}$ at $E_C - 0.73$ eV. Activating the TAT model in other omnipresent traps ($E_C - 0.19$ eV or $E_C - 1.65$ eV) in n-type 4H-SiC either overestimates or underestimates the dark current. Therefore, the TAT model should be specified at a specific trap level to estimate the TAT-induced reverse leakage current perfectly. The novel HI model details are briefly given below:

The TCAD HI model can simulate the alpha-particle produced signal in the detector; specifically how the particle loses energy and generates electron-hole pairs (EHPs) along its line of track. The LET data for 5.486 MeV

alpha-induced signal charge in the SiC is estimated using SRIM simulation. Consequently, LET generation density $G_{LET}(l)$ in the 4H-SiC detector is simulated as per the following expression[7]

$$G_{LET}(l) = a_1 + a_2 l + a_3 e^{a_4 l} + k'[c_1(c_2 + c_3 l)^{c_4} + LET_f(l)] \quad (1)$$

where $LET_f(l)$ is the LET functional dependence of the ion travel length l. The HI model coefficients (a_n, c_n, and k′) of $G_{LET}(l)$ are computed as per the drift-diffusion theoretical model equation of CCE (CCE_{theory})[4]

$$\mathrm{CCE_{theory}} = \frac{1}{\mathrm{E_p}}\int_0^{\mathrm{d}}\left(\frac{\mathrm{dE}}{\mathrm{dx}}\right)\mathrm{dx} + \frac{1}{\mathrm{E_p}}\int_{\mathrm{d}}^{\mathrm{Xr}}\left[\left(\frac{\mathrm{dE}}{\mathrm{dx}}\right)\times \exp\left\{-\left(\frac{\mathrm{x-d}}{\mathrm{Lp}}\right)\right\}\right]\mathrm{dx} \quad (2)$$

where Ep is the alpha-particle energy, dE/dx is the alpha-induced electronic energy loss, d is the depletion thickness, Lp is the carrier diffusion length, and Xr is the alpha-particle projected range in the SiC.

RESULTS & DISCUSSION

SRIM simulation reveals that the projected range of 5.486 MeV alpha-particle in SiC is 17.52 µm. The alpha-particle interaction mechanism with the detector is schematically illustrated in Fig. 1(a). The electronic energy loss in eV/Å is converted to LET in pC/µm using a proper conversion factor[6]. As the alpha particle enters the SBD, it generates EHPs along the track, and more EHPs are created at the end of the track due to the high interaction probability. The HI-induced instant generation rate and total carrier density in the detector are shown in Figs. 1(b) and (c). It is seen that the charge density decreases radially from the center of the track to the outward direction and increases along the track from the location where the heavy ion collides to the projected range of the alpha particle.

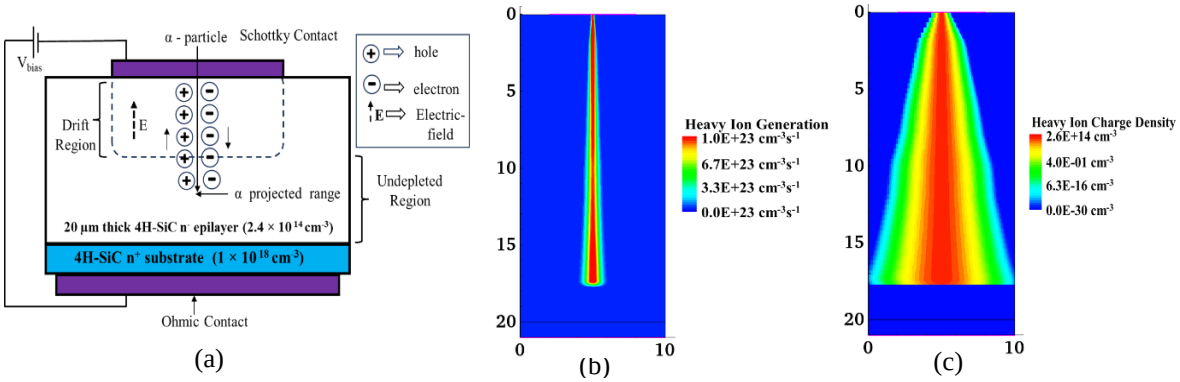


FIGURE 1. (a) Schematic diagram of alpha-particle interaction mechanism with the 4H-SiC SBD detector, (b) Instant generation rate due to the alpha-particles, (c) Total charge density induced in the detector by alpha-particles.

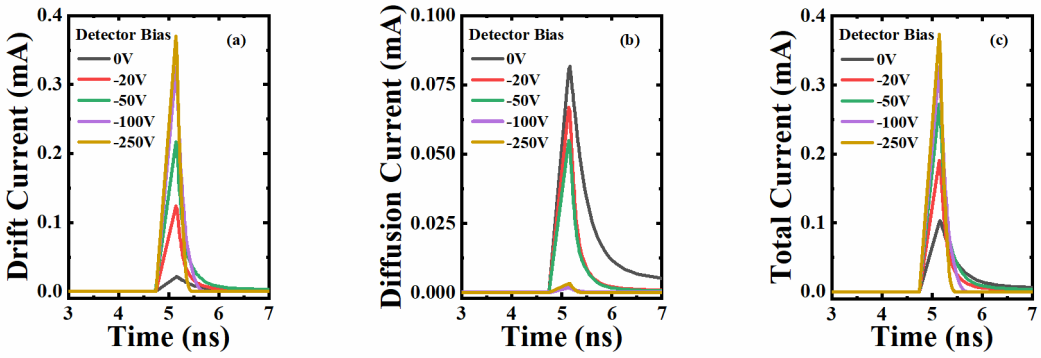


FIGURE 2. (a) Drift-induced transient signal current (b) Diffusion-produced transient signal current, and (c) Total transient signal current induced in the detector, at different bias voltages (0 V to -250 V).

In TCAD model, it is considered that HI strikes the detector at a time of 5 ns and the current transients are simulated in the time range of 0.3 ns to 7 ns. The transient current response for the 4H-SiC detector peaks at t = 5.14 ns, as displayed in Figs. 2(a)-(c). Due to the electric field in the depleted region, the drift current response is more symmetric and less spread over the time range. Whereas, the fall-off time for diffusion transient current is

longer than the rise time as the diffusion-assisted charge collection process is slower in the detector. The transient signal magnitude for the diffusion decreases with the increasing detector bias voltages and the same increases under the drift condition. The combined transient response of drift and diffusion increases with the bias voltage, as perceived in Fig. 2(c). The collected signal charge in the detector is computed by integrating the total transient current. Then, the CCE is estimated by dividing the collected signal charge at the electrodes with the alpha-induced signal charge in the detector.

It is found that the conventional HI model is able to predict only the drift contributed portion of CCE at a high bias voltage. In this work, a new approach is developed to predict the CCE at lower voltages by accounting the diffusion effect. As the voltage increases, the depletion width increases and diffusion-based transport decreases. A linear function is considered for drift component and an exponentially decreasing function is used for the diffusion component, thus the modified LET equation is written

$$G^{m}{}_{\mathrm{LET}}(\mathrm{l}) = \mathrm{k}'[\mathrm{LET}(\mathrm{l})] + \mathrm{k}^{*}[\mathrm{LET}(\mathrm{l}) \times \exp(-\mathrm{d}/\mathrm{L})] \quad (3)$$

where $\mathrm{k}' = 8.53 \times 10^{-4}$,L=18.6 μm for SBD and k^{*} is function of l and L. Beyond full depletion voltage (refer to Fig. 3), 100 % CCE is observed as the drift entirely governs the charge collection. For low voltages (> -80 V), the combination of drift- and diffusion- based eqn. (3) yields a perfect matching with the measured CCE characteristics, as noticed in Figs. 3 (b) and (c).

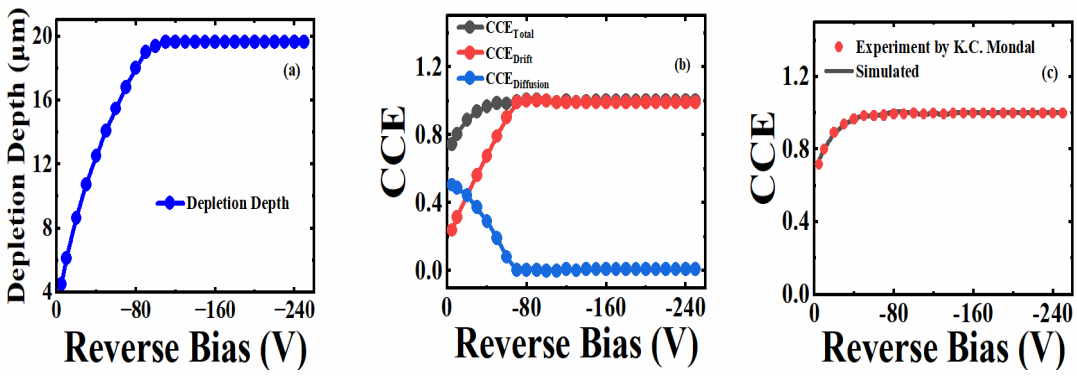


FIGURE 3. (a) Depletion width variation with the bias voltage, (b) Identified drift and diffusion components contributing to the CCE, and (c) simulated CCE is matched with the Mandal's experimental data[4].

CONCLUSION

A physics-based TCAD model for 4H-SiC SBD alpha-particle detector is developed by matching I-V and CCE characteristics. The simulation results show that the conventional HI model for 4H-SiC SBD detector is valid only at higher bias voltages. To overcome this issue, we reported a novel HI model approach to incorporate both drift- and diffusion-produced signal currents in the detector, thus simulated CCE is validated over the entire voltage range.

REFERENCES

1. K. C. Mandal, S. K. Chaudhuri and F. H. Ruddy, IEEE Trans. Nucl. Sci. **70**, 823-830 (2023).
2. P. V. Raja, J. Akhtar, C. V. S. Rao, S. Vala, M. Abhangi and N. V. L. N. Murty, Nucl. Instrum. Methods Phys. Res. A. **869**, 118-127 (2017).
3. P. Raja, N. V. L. N. Murty, C. V. S. Rao and M. Abhangi, IEEE Trans. Nucl. Sci. **62**, 1634-1641 (2015).
4. S.K. Chaudhuri, and K.C. Mandal, Radiation Detection Using n-Type 4H-SiC Epitaxial Layer Surface Barrier Detectors, in *Advanced Materials for Radiation Detection*, (Springer, Switzerland, 2021), pp. 183-209.
5. Y. Sun, Z. Hu, H. Zhang, P. Gong, G. Zhong, L. Hu, G. Gorini, G. Croci and X. Tang, IEEE Sens. J. **24**, 4432-4441 (2024).
6. L. Zhang, Y. Wang, H. Guo, C. Yu, H. Hu, Y. Liu and S. Chen, IEEE Sens. J. **22**, 10620-10629 (2022).
7. Sentaurus TCAD User Guide, Version N-2022.03, Synopsys Inc., San Jose, CA, USA (2022).

Thermal Annealing Induced Enhancement of Electrical Performance in PDMS Assisted Exfoliated multilayer MoS_2 based Field Effect Transistor

Samiksha[1,*], Ramesh Singh Bisht[1] and Pramod Kumar[1]

[1]*Department of Physics, Indian Institute of Technology Bombay, Mumbai 400076, India*

[*]Corresponding author: samikshabhatia@iitb.ac.in

Abstract. This paper investigates the effect of thermal annealing on the electrical properties of exfoliated multilayer MoS_2 based FET. To probe this effect of thermal annealing, the device was annealed at 200 °C for 2 hrs. We observed that off current decreased drastically by three orders of magnitude, increasing the $I_{on/off}$ ratio by three orders. Additionally, mobility increased by 2.5 times, the subthreshold swing reduced by a factor of 8, and hysteresis improved from 13 to 3.7 V. Molybdenum disulphide (MoS_2) was exfoliated onto SiO_2/Si substrate using polydimethylsiloxane (PDMS) stamp. The resulting Exfoliated MoS_2 flake was analysed using an optical microscope and Raman spectroscopy. For measuring electrical response, output (I_d~V_d) and transfer (I_d~V_g) characteristics has been measured.
Keywords: MoS_2 FETs, Multilayer MoS_2, Thermal Annealing, Electrical performance, charge transport.

INTRODUCTION

Two dimensional materials like graphene and transition metal dichalcogenides (TMDs) are getting huge interest for the next generation electronic devices due to their atomic-scale thickness, superior electrical properties, and enhanced mechanical flexibility compared to traditional silicon-based electronics [1]. Graphene exhibits high mobility of 5000 cm^2/Vs, but due to its zero intrinsic band gap, the I_{on}/I_{off} ratio is low which limits its application in switching devices [2]. TMDs are of special interest due to their adjustable band gap and tunable electronic properties [2]. Among TMDs, MoS_2 has been extensively studied for Field effect transistor due to its unique electronic and optical properties [3]. However, MoS_2-based FET face several challenges that limit their electrical performance. These challenges include high contact resistance, trap states at the interface, and charge carrier scattering due to defects and impurities in the MoS_2 channel [4]. Additionally, one of the major reasons behind the observed hysteresis in the transfer characteristics is the quality of the MoS_2/contact interface along with the absorption of water and oxygen molecules on the channel surface [4]. The impact of these effects significantly reduces the electrical performance of the device such as I_{on}/I_{off} ratio, mobility, subthreshold swing (SS), and hysteresis. To enhance the electrical performance of MoS_2-based devices, it is crucial to minimize the impact of the outlined challenges. In this paper, we investigate the effect of thermal annealing on back-gated SiO_2/Si multilayer MoS_2 based FETs. We extracted key electrical parameters from transfer curves before and after annealing the device. Our study demonstrates that annealing is an effective method to enhance device performance, likely due to improved interface quality and reduced trap states. Notably, we observed a threefold increase in the I_{on}/I_{off} ratio. Mobility increased by 2.5 times, the SS decreased by a factor of 8, and hysteresis improved from 13 to 3.7 V. This simple approach marks a significant step toward optimizing the electrical performance for multilayer MoS_2-based FETs for future electronic applications.

FABRICATION AND MEASUREMENT

Molybdenum disulfide (MoS_2) was mechanically exfoliated from a bulk crystal using a polydimethylsiloxane (PDMS) stamp onto a highly doped silicon substrate with a thermally grown 200 nm SiO_2 layer over it [5]. The flake was analyzed with the help of an optical microscope. Photolithography was employed to define the source and drain patterns, followed by the deposition of Ti/Au (30/100 nm) via sputtering. After fabrication, the multilayer MoS_2 channel was characterized by Raman spectroscopy using a setup from Renishaw, Invia Reflex, UK. The device was then thermally annealed at 200 °C for 2 hours on a hot plate. Electrical characteristics were measured at room temperature using the Polaris B1500 Agilent Semiconductor Characterization System before and after annealing. Key parameters such as I_{on}/I_{off} ratio, mobility and SS were extracted from the transfer characteristics.

RESULTS AND DISCUSSION

The morphology of the exfoliated MoS_2 flake was initially analysed using optical microscopy and Raman spectroscopy. As shown in the inset of Figure 1 (a), the optical image reveals a well-defined flake. The Raman spectrum exhibits characteristic peaks at 384.4 cm^{-1} (E_{2g}^1) and 409 cm^{-1} (A_{1g}) and the peak position difference is 24.6 cm^{-1} which, along with optical contrast of the flake, confirms the formation of multilayers [6].

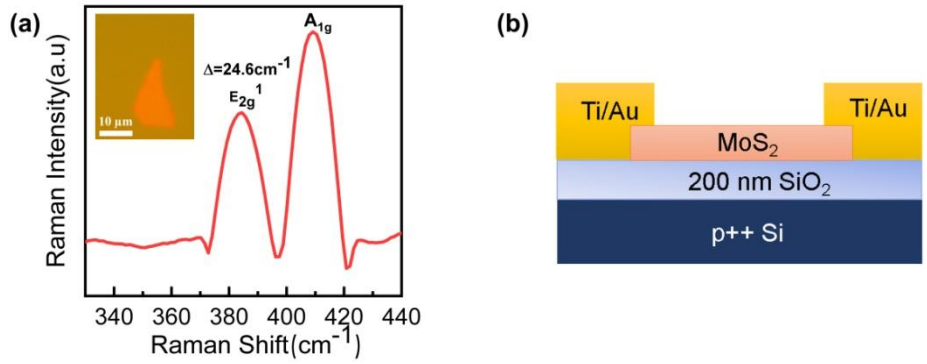


Figure 1. (a) Raman spectra of MoS_2 flake. Inset: optical images of the flake. (b) Schematic of the fabricated device.

The schematic of fabricated device is shown in Figure 1 (b). The electrical performance of the device was evaluated before and after thermal annealing at 200 °C for 2 hours. The transfer curves, both in linear and log scales, are shown in Figure 2. The device demonstrates typical n-type semiconductor behaviour. Mobility was calculated using the equation: $\mu = g_m \frac{L}{WC_{ox}V_d}$; where μ is the mobility, L (4 μm) is the channel length, W (23 μm) is the average channel width, C_{ox} is the gate capacitance per unit area and g_m is the transconductance (dI_d/dV_g), extracted from the linear region of the Figure 2 (a). The electrical performance comparison is shown in Table 1.

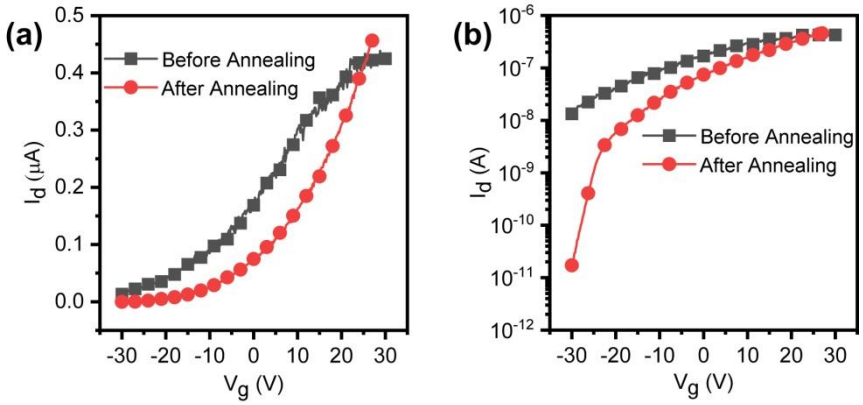


Figure 2. Transfer characteristics before and after annealing at 200 °C for 2 hours at V_d=2 V (a) in linear and (b) log scale.

After thermal annealing, the off current has significantly decreased from 1.3×10^{-8} to 1.7×10^{-11} A while the on current shows a slight decrease. This results in an increased I_{on}/I_{off} ratio from3×10^{1} to 3×10^{4}. These improvements are likely due to annealing-induced structural changes in the MoS_2 channel, which release native point defects at the interface and enhance interface quality, as supported by [7].

TABLE 1. Summary of Electrical Performance of FET.

Condition	I_{on}/I_{off}	Mobility ($cm^2/V{\cdot}s$)	SS (V/decade)	Hysteresis (V)
Before Annealing	3×10^{1}	0.04	22.4	13
After Annealing	3×10^{4}	0.1	2.8	3.7

The mobility is improved from 0.04 to 0.1 cm²/Vs. likely due to reduced scattering centres [8]. The SS is decreased from 22.4 to 2.8 V/decade. This drastic reduction indicates more efficient electrostatic control of the channel by the gate voltage which is a result of the improved interface quality after annealing.

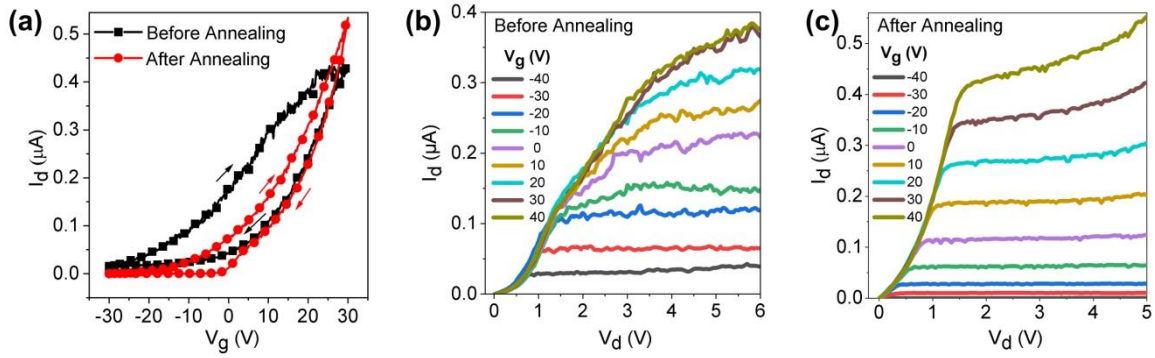


Figure 3: (a) Hysteresis before and after annealing; Output characteristics (b) before annealing, (c) after annealing.

Hysteresis was calculated by the voltage difference at a fixed drain current (I_d) of 0.3×10^{-6} A in forward and backward sweep. Hysteresis was reduced from 13 to 3.7 V as shown in Figure 3 (a). This improvement suggests that annealing mitigates the effects of charge trapping and de-trapping at the MoS_2/contact interface, indicating more stable and reproducible characteristics. The output characteristics are shown in Figures 3 (b) and (c). The post-annealing output curve exhibits a smoother curve and improved linearity in the low-bias region, indicating reduced contact resistance which further supports the enhanced electrical performance. The observed improvements in device characteristics are likely due to a combination of improved channel quality, reduced trap states, and better interface. Further analysis is required to determine the exact mechanism.

CONCLUSIONS

Multilayer MoS_2 based FETs have been successfully fabricated and characterized before and after thermal annealing. Our results indicate significant improvements in the I_{on}/I_{off} ratio from 3×10^1 to 3×10^4, mobility from 0.04 to 0.1 cm^2/Vs, SS from 22.4 to 2.8 V/decade, and hysteresis from 13 to 3.7 V. This study demonstrates the significant impact of thermal annealing on the electrical performance of exfoliated multilayer MoS_2-based FETs.

ACKNOWLEDGEMENT

The authors wish to acknowledge the Indian Institute of Technology Bombay (IITB) for the seed funding and the University Grants Commission (UGC), Government of India for providing the fellowship.

REFERENCES

1. S. Zeng, C. Liu, and P. Zhou, Nat. Rev. Electr. Eng., Vol. 1, pp. 335-348 (2024).
2. G. R. Bhimanapati, Z. Lin, V. Meunier, Y. Jung, J. Cha *et al*., ACS Nano, Vol. 9, pp. 11509-11539 (2015).
3. O. V. Yazyev and A. Kis, Mater. Today, Vol. 18, pp. 20-30 (2015).
4. R. Mathew and J. Ajayan, Mater. Sci. Semicond. Process., Vol. 160, pp. 107397 (2023).
5. K. Choi, Y. T. Lee, S. W. Min, H. S. Lee, T. Nam, H. Kim, and S. Im, J. Mater. Chem. C, Vol. 1, pp. 7803-7807 (2013).
6. G. S. Papanai, I. Sharma, G. Kedawat, and B. K. Gupta, J. Phys. Chem. C, Vol. 123, pp. 27264-27271 (2019).
7. S. D. Namgung, S. Yang, K. Park, A. J. Cho, H. Kim, and J. Y. Kwon, Nanoscale Res. Lett., Vol. 10, pp. 1-6 (2015).
8. Z. Yu, Y. Z. Ong, S. Li, J. B. Xu, G. Zhang, Y. W. Zhang, Y. Shi, and X. Wang, Adv. Funct. Mater., Vol. 27, pp. 1604093 (2017).

Co-existence of Ferro-Antiferromagnetism and Transport Properties in Full Heusler Alloy Fe_2MnAl

Aparna Ashok[1, a)] and Neeru Bhagat[1]

[1]*Department of Applied Science, Symbiosis Institute of Technology, Symbiosis International (Deemed) University, Pune, Maharashtra, 412115, India*

[a)]Corresponding author: aparna007ashok@gmail.com

Abstract. Heusler alloys are widely explored for their potential in various technological applications, including sensors, actuators, energy harvesting systems, and magnetic refrigeration. In the present work, polycrystalline Fe_2MnAl ingots were synthesized by arc melting stoichiometric ratios of high-purity elements under an argon atmosphere, followed by annealing at 800 °C. These samples demonstrated a distinct magnetic transition near 50 K, attributed to antiferromagnetic pinning within an otherwise ferromagnetic matrix. This magnetic phase coexistence is characterized by closely spaced Curie (T_C) and Néel (T_N) temperatures, which were identified through magnetization studies. A notable finding was the emergence of semiconducting behaviour below approximately 120 K (T_C), transitioning to metallic conduction at higher temperatures, as revealed by temperature-dependent resistivity measurements. Additionally, a pronounced negative magnetoresistance, attributed to inhomogeneous magnetic scattering, was observed within this same temperature interval.

INTRODUCTION

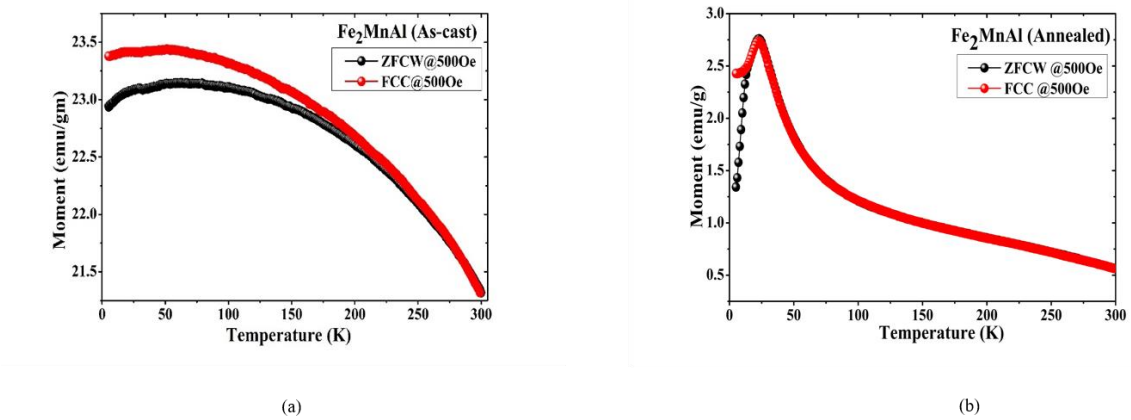
Half-metallic ferromagnets (HMFs) are considered excellent candidates for spintronic applications due to their distinctive spin-polarized characteristics. Their spin-resolved electronic band structure is particularly advantageous for such technologies [1,2]. Among various HMFs, Heusler alloys stand out because they exhibit notable physical properties when compared to conventional metallic ferromagnets and other half-metals. Specifically, Fe_2-based Heusler alloys often display tetragonal distortions, substantial magnetic moments, and elevated Curie temperatures (T_C), which are frequently linked to chemical instabilities. Certain Heusler compounds have been theoretically predicted to demonstrate half-metallicity, characterized by a metallic behaviour in the spin-majority channel and semiconducting features in the spin-minority channel, with a bandgap located near the Fermi energy (E_F) [1–4]. These electronic traits make them promising materials for high-sensitivity magnetic sensors. In addition, many Heusler alloys possess relatively high ferromagnetic Curie temperatures. Structurally, Heusler compounds generally adopt a simple crystal framework; however, their unique electronic and magnetic subsystems give rise to complex kinetic and magnetic responses [3–5]. In ferromagnetic systems, spontaneous magnetization arises due to the lifting of spin degeneracy among conduction electrons, which results in an energy shift between spin-up and spin-down states. In the half-metallic condition, the spin-down channel exhibits a sizeable energy gap (approximately 1 eV) at the Fermi level, whereas the spin-up channel remains gapless at E_F. Factors such as atomic composition, lattice structure, and the presence of antisite disorder significantly influence the electronic band structure of these materials [5–7].

EXPERIMENTAL DETAILS

Polycrystalline ingots of Fe_2MnAl were synthesized by arc melting stoichiometric proportions of high-purity elemental constituents (99.99%) in an inert argon atmosphere. To achieve better chemical homogeneity, the ingots were re-melted three times with flipping between each cycle. Further homogenization was accomplished by annealing the arc-melted ingots at 800 °C for 48 hours in a vacuum furnace. Structural characterization of the alloy was conducted using X-ray diffraction (XRD). Magnetization measurements were carried out under both zero-field-cooled (ZFC) and field-cooled (FC) conditions using a 7 T Vibrating Sample Magnetometer (VSM) integrated with the Magnetic Property Measurement System (MPMS-3, Quantum Design). Temperature-dependent resistivity measurements were performed using a 9 T Physical Property Measurement System (PPMS, Quantum Design), with data collected in both cooling and warming cycles using an in-house developed 8-channel resistance measurement setup.

RESULTS AND DISCUSSIONS

The experimentally prepared as-cast and annealed samples closely matched the disordered *A2*-type structure, with a calculated lattice parameter of a = 5.172 Å. To facilitate comparison, lattice constants for Heusler alloys are generally expressed using the $L2_1$ structure as a reference. Although the primary ordered phase exhibited ferromagnetic behaviour, minor traces of face-centered tetragonal (fct) phases were also detected. These may account for the coexistence of both ferromagnetic and antiferromagnetic characteristics in off-stoichiometric compositions [2,5]. Figures 1(a) and 1(b) illustrate the magnetic behaviour of the alloys, which is significantly influenced by the degree of structural ordering within the system. A gradual transformation from ferromagnetism to antiferromagnetism, passing through a re-entrant magnetic regime, was observed, in line with the structural features discussed. Magnetic studies on Fe_2MnAl-type Heusler alloys indicate that increasing Fe content enhances both the Curie temperature (T_C) and saturation magnetization. At lower magnetic transition temperatures, a separation between field-cooled (FC) and zero-field-cooled (ZFC) susceptibilities is evident in magnetically inhomogeneous systems, where ferromagnetic and antiferromagnetic domains may exist either as distinct long-range phases or as embedded magnetic clusters. This FC-ZFC bifurcation is strongly dependent on the applied magnetic field; when the external field is small, the divergence is pronounced, while stronger fields may shift this divergence point to lower temperatures. As the sample is cooled through T_C or T_N, the inherent antiferromagnetic anisotropy can cause spins to freeze into various configurations, resulting in this ZFC-FC split [1,2]. For the ferromagnetic phase, the Curie temperature is around 300 K, suggesting strong ferromagnetic interactions in Fe-rich compositions. Since Mn atoms contribute to the enhancement of the magnetic moment, their presence may also introduce local disorder. The system experiences competing magnetic interactions — Fe-Fe, Fe-Mn, and Mn-Mn ferromagnetic couplings, as well as Fe-Mn antiferromagnetic coupling — which could promote the development of long-range antiferromagnetic ordering upon isothermal annealing. The observed reduction in magnetization below 50 K is likely due to exchange interactions between two ferromagnetic sublattices associated with Fe and Mn atoms [3].

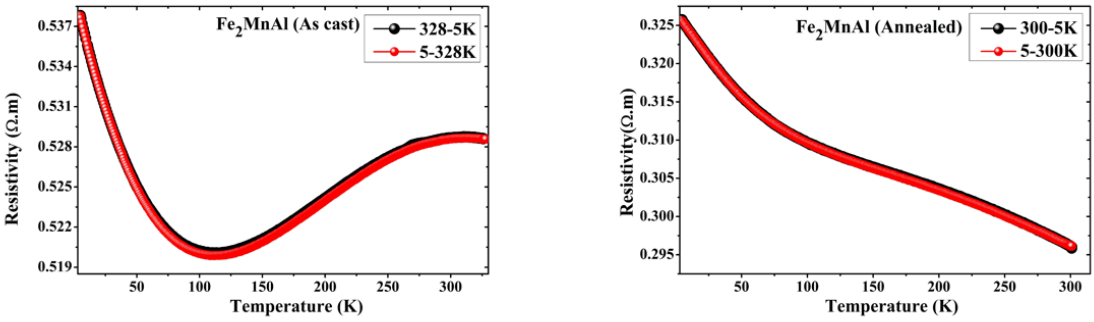


(a) (b)

FIGURE 1. (a) ZFCW and FCC temperature dependent dc magnetization plots at 500Oe for the as-cast and (b) annealed Fe_2MnAl Full Heusler alloy

Figures 2(a) and 2(b) display the temperature-dependent electrical resistance measurements conducted under zero magnetic field conditions over the range of 5–330 K for both as-cast and annealed Fe_2MnAl samples. For the as-cast sample, the resistance exhibits a negative slope below the Curie temperature (T_C), indicating semiconducting behaviour. This shift from metallic to semiconducting conductivity coincides with a magnetic phase transition from ferromagnetic to paramagnetic. The coexistence of antiferromagnetic regions within the ferromagnetic matrix is evident. This transition can be attributed to antiferromagnetic scattering, which stems from a reduction in the effective conduction electron density due to a shrinking Fermi surface—a phenomenon linked to changes in magnetic ordering at T_C [4,5]. In contrast, the annealed samples show semiconducting behaviour across the entire measured temperature range (5–300 K). Alloys such as Fe_2MnAl, which exhibit high resistivity values of ($\rho_0 > 1\ \mu\Omega\cdot m$) over a broad temperature span encompassing both magnetically ordered and disordered states, are known to display a negative temperature coefficient of resistance (TCR) [6]. This elevated resistivity and negative TCR in transition metal-based alloys arise from both scattering mechanisms and the electronic band structure near the Fermi energy (E_F). Scattering is particularly associated with lattice perturbations that reduce the conduction electron mean free path to the order of the lattice constant ($l \sim a$). In Fe_2MnAl, a half-metallic system, the presence of an energy gap at E_F in the spin-down (↓) sub-band further influences transport behaviour [7]. As the material

undergoes a magnetic transition to the paramagnetic state around $T \approx T_C$, the saturation magnetization (M_S) approaches zero, leading to a broad maximum in $\rho(T)$ due to enhanced magnetic scattering [5].



(a) (b)

FIGURE 2. (a) Temperature dependent resistivity measurements at zero field for the as-cast and (b) annealed Fe_2MnAl Full Heusler alloy in the warming and cooling cycle.

CONCLUSION

The interplay between ferromagnetic interactions (Fe–Fe and Mn–Mn) and antiferromagnetic coupling (Fe–Mn) gives rise to a re-entrant spin-glass phase that stabilizes at low temperatures. With increasing Al content, the magnetic ground state of the alloy tends to shift from ferromagnetic to antiferromagnetic, occurring at approximately 23 K and 11 K. The elevated electrical resistivity observed in these alloys indicates the presence of an energy gap at the Fermi level, which is commonly linked to atomic disorder and ferrimagnetic ordering in half-metallic ferromagnetic Heusler systems. Antisite disorder in the structure contributes to the emergence of a negative temperature coefficient of resistance (TCR) for temperatures above T_C. For temperatures below T_C, a similar behaviour in TCR can be attributed to additional resistive contributions from conduction electron scattering caused by imperfections in both the crystal lattice and the magnetic sublattice.

ACKNOWLEDGEMENT

Authors are highly grateful to Dr. Rajeev Rawat, Scientist-H of UGC DAE Consortium for Scientific Research at Indore and his group of research scholars, Suman Karmakar, Rajeev Joshi, Pramod R Nadig and Priyanshi Tiwari for their constant support and guidance to begin and continue this work with all infrastructure and high field-low temperature facilities at the Magneto-transport and Calorimetry laboratory.

REFERENCES

1. M. Acet, E. Duman, E.F. Wassermann, L. Mano˜sa, A. Planes, *J. Appl. Phys*. 92, 3867 (2002).
2. E. Duman, M. Acet, Y. Elerman, A. Elmali, E.F. Wassermann, *J. Magn. Magn. Mater.* 238, 11 (2002).
3. M. Belkhouane, S. Amari, A. Yakoubi, A. Tadjer, S. Méçabih, G. Murtaza, S. Bin Omran, R. Khenata, *J. Magn. Magn. Mater.* 377, 211 (2015).
4. I. Das, E.V. Sampathkumaran, R. Vijayaraghavan, *Phys. Rev. B*. 44, 159 (1999).
5. Liu, Z., Ma, X., Meng, F., Wu, G. *J. All. Comp.* 509(7), 3219-3222 (2011).
6. J. H. Mooij, *Phys. Stat. Solidi A*.17 (2), 521 (1973).
7. Kourov, N. I., Marchenkov, V. V., Belozerova, K. A., Weber, H. W. *J. Expt. Theo. Phys.* 118, 426-431 (2014).

Vertical Schottky Barrier Diodes fabricated from $ZnGa_2O_4$ epilayer grown by MOCVD

Siddharth Rana[1,2,3,*], Fu-Gow Tarntair[2], Ray Hua Horng[2,3] and J.P. Singh[1]

[1]*Physics Department, Indian Institute of Technology Delhi, Hauz Khas, New Delhi 110016, India*
[2]*Institute of Electronics, National Yang Ming Chiao Tung University, Hsinchu 30010, Taiwan, ROC*
[3]*International College of Semiconductor Technology, National Yang Ming Chiao Tung University, Hsinchu 30010, Taiwan,ROC*
[*]*Corresponding author: ranasiddharth444@gmail.com*

Abstract. In this study, we have fabricated vertical Schottky barrier diodes (SBD) based on $ZnGa_2O_4$ epilayer grown by MOCVD on the highly doped bulk $ZnGa_2O_4$ substrate. The electrical properties of the SBD were investigated. The SBD showed an ideality factor of about 1.51 with a forward On voltage of 0.275 V. Additionally, the On/Off ratio was found to be 10^4 with a breakdown voltage of 8.5 V. The highly doped bulk substrate SBD performance was improved by depositing $ZnGa_2O_4$ epilayer. The results present the use of $ZnGa_2O_4$ for the power applications.

KEYWORDS: Metalorganic chemical vapor deposition; Schottky barrier diode; $ZnGa_2O_4$; power electronics; ideality factor.

INTRODUCTION

$ZnGa_2O_4$ stands as a semiconductor, distinguished by its wide bandgap, conductivity, and impressive chemical and thermal stability. In recent times, $ZnGa_2O_4$ has sparked significant attention due to its promising applications across diverse domains: solar-blind ultraviolet photodetectors (PDs)[1], X-ray detectors[2], power devices[3], and phototransistors[4]. Metalorganic chemical vapor deposition (MOCVD) has proven advantageous because of its capacity for rapid deposition and the ability to achieve uniformity across large areas, resulting in the formation of single-crystal structures[5].

Power electronics is the branch that deals with the control and regulation of electrical power via the use of different electronic equipment[6,7]. Power diodes are essential components of power converters and inverters, which are vital in power transmission networks. Herein, we propose a Ni/$ZnGa_2O_4$/Al-based Schottky barrier diode. The $ZnGa_2O_4$ epilayer was grown on the highly doped bulk $ZnGa_2O_4$ substrate. The performance of the SBD was found to be improved with the ideality factor 1.51 and break down voltage around 8.1 V.

EXPERIMENTAL

$ZnGa_2O_4$ epilayer of 100 nm thickness was deposited on highly doped bulk $ZnGa_2O_4$ by MOCVD. Firstly, the Ti/Al (ohmic metal) was deposited on the highly doped side by E-beam deposition. The $ZnGa_2O_4$ epilayer was patterned as circular contacts by coating with photoresist and exposure by the double side mask aligner. Furthermore, Nickel (150 nm) was deposited using E-beam deposition. Then, samples are left in acetone overnight for the lift-off. The detailed process flow is shown in Figure 1.

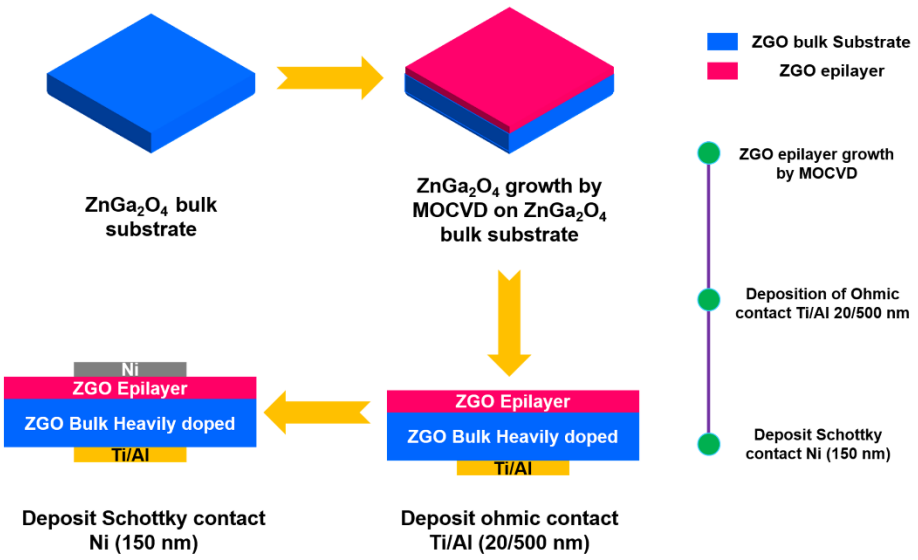


FIGURE 1. Process flow of the fabrication

RESULTS AND DISCUSSIONS

Figures 2(A) and 2(B) depict the I-V curves depicting the ohmic and Schottky nature of the contacts. This verifies the successful development of the Vertical SBD. Additionally, figure 2(C) presents the I-V curve of the different circular contacts ranging from 100 µm to 500 µm. The reverse current increases with an increase in the contact area, suggesting a higher collection of carriers. Moreover, the ideality factor was extracted to be 1.51, and the On/Off ratio was found to be 10^4 from the logarithmic plot of current density with voltage ranging from -2 to 1.5 V

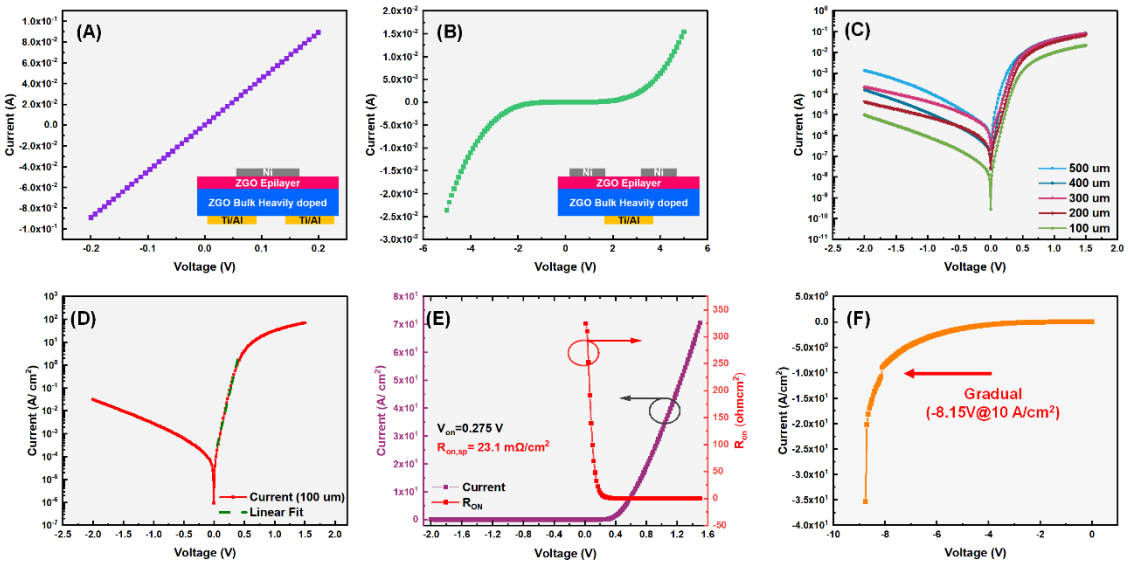


FIGURE 2. I-V curve of the (A)back, (B)front side of SBD, and (C) different circular contacts of SBD. (D) logarithmic current density, (E) on-resistance, and (F) breakdown voltage measurements of the SBD.

. The ideality factor suggests that the overall tunneling effect also exists along with the thermionic conduction mechanism, which is being reduced by the incorporation of the $ZnGa_2O_4$ epilayer. The Specific On resistance was extracted from the linear region and was found to be 23.1 mΩ/cm^2. The turn On voltage was found to be 0.275 V, and the breakdown voltage was 8.5 V, extracted from Figure 2(E-F). The overall results suggest that the deposition of the epilayer can act as a control in modulating the bulk substrate characteristics. Table 1 presents a comparison of the performance of the SBD with the bulk SBD.

TABLE 1 Comparitive analysis of performance with the reported bulk $ZnGa_2O_4$ SBDs.

Type	V_{ON} (V)	R_{ON} (mΩ .cm^2)	Ideality factor	Breakdown Voltage (V)	References
Pt/$ZnGa_2O_4$ (High doping)	0.16	1.13	1.77	5.6	[8]
Pt/ $ZnGa_2O_4$ (Low doping)	0.57	2.83	1.171	43.8	[8]
Ni/$ZnGa_2O_4$ (MOCVD)/$ZnGa_2O_4$ (High doping)	**0.275**	**23.1**	**1.51**	**8.5**	**This work**

CONCLUSION

Vertical SBDs have been fabricated as Ni/$ZnGa_2O_4$ (epilayer)/$ZnGa_2O_4$ (High doping). The results indicate the modulation of the properties of the vertical SBDs of the highly doped bulk $ZnGa_2O_4$ by $ZnGa_2O_4$ epilayer deposition by MOCVD. The fabricated SBD was found to have an ideality factor of 1.51 and an On/Off ratio of 10^4. Additionally, the device possessed lower voltage and Ron values for the turn On voltage. The results present great potential for future use of $ZnGa_2O_4$ for power applications.

ACKNOWLEDGEMENTS

S.R. gratefully acknowledges the Council of Scientific and Industrial Research (CSIR), India, for awarding the research fellowship under grant number 09/086(1472)2020-EMR-I. We extend sincere thanks to the National Science and Technology Council of Taiwan for their financial support under award nos. 112-2218-E-A49-024-MBK, 112-2622-E-A49-011, 112-2622-8-A49-018-SB, and 111-2923-E-A49-003-MY3. We acknowledge the fabrication support provided by the Nano Facility Center, NYCU, and TSRI.

REFERENCES

[1] S. Rana, F.-G. Tarntair, J. P. Singh, R.-H. Horng, in *2023 IEEE Photonics Conf.*, IEEE, **2023**, pp. 1–2.
[2] S. Rana, S. J. Chiu, C. Y. Huang, F. G. Tairtan, Y. G. Lin, D. S. Wuu, J. P. Singh, G. C. Su, P. L. Liu, R. H. Horng, *Mater. Today Adv.* **2023**, *19*, 100411.
[3] S. Rana, F.-G. Tarntair, R.-H. Horng, J. P. Singh, *Mater. Sci. Semicond. Process.* **2024**, *182*, 108712.
[4] S. Rana, F.-G. Tarntair, R.-H. Horng, J. P. Singh, *J. Alloys Compd.* **2024**, *1004*, 175944.
[5] S. Rana, V. Sharma, R. H. Horng, J. P. Singh, *Ceram. Int.* **2025**, DOI: 10.1016/j.ceramint.2025.04.345.
[6] R. H. Horng, A. Sood, S. Rana, N. Tumity, F. G. Tarntair, C. Langpoklakpam, H. C. Kuo, J. P. Singh, *Mater. Today Adv.* **2023**, *18*, 100382.
[7] F. G. Tarntair, C. Y. Huang, S. Rana, K. L. Lin, S. H. Hsu, Y. C. Kao, S. J. Pratap, Y. C. Chen, N. Tumilty, P. L. Liu, R. H. Horng, *Adv. Electron. Mater.* **2024**, *2300679*, 2.
[8] J. Liu, Z. Li, W. Hao, W. Mu, Q. He, X. Zhou, X. Zhao, G. Xu, Z. Jia, X. Tao, S. Long, *IEEE Electron Device Lett.* **2022**, *43*, 2061.

Invar Behavior In Nearly Stoichiometric $TiFe_2$

Myren Azavedo, and K. R. Priolkar, [a)]

School of Physical and Applied Sciences, Goa University, Taleigao Plateau, Goa 403206, India.

[a)] krp@unigoa.ac.in

Abstract. The ability of invar materials to maintain its dimensions under varying temperature conditions have provided a means to control the normal thermal expansion. $TiFe_2$ is one such hexagonal Laves phase intermetallic that displays invar like behavior over a wide temperature range. The crystal structure of $TiFe_2$ displays an complex array of magnetic interactions involving ferromagnetic interactions, arising between the antiferromagnetically coupled Fe-6h planes. The strong competition between the in-plane ferromagnetism and out of plane antiferromagnetism is responsible for the observed invar behavior in the nearly stoichiometric $TiFe_2$.

INTRODUCTION

Zero thermal expansion (ZTE) materials are the need of the hour to control the thermal expansion of materials due to their unusually small thermal expansion so as to ensure the optimal functioning of high-precision devices. Any material whose coefficient of linear thermal expansion is less than 1 ppm/K can be regarded as a ZTE material. Post the discovery of Invar alloys in the late 1890's by Charles Guillaume, a lot of materials have been discovered that exhibit this anomalous expansion behaviour Interestingly, in most of these materials this NTE or invar behavior is driven by magnetism. $TiFe_2$ belongs to the hexagonal Laves phase system, which crystallizes in the $MgZn_2$ (C14) type hexagonal lattice [$P6_3/mmc$]. It is the only stable antiferromagnet with a Néel temperature around room temperature. Ti atoms in the 4f position are non-magnetic while Fe atoms occupy two different atomic positions (6h and 2a) within the unit cell. The Fe atoms at 6h position possess magnetic moment which are ferromagnetically aligned within the plane and the successive 6h planes are aligned antiferromagnetically along the c-axis [1]. The Fe atoms at 2a position do not possess a magnetic moment, as evidenced by neutron diffraction and Mössbauer spectroscopy [2]. These antiferromagnetic and ferromagnetic interactions lead to magnetic frustration which is relieved to some extent via lattice distortion [3]. Therefore, the first order high volume antiferromagnetic to low volume ferromagnetic transition is accompanied by a negative thermal expansion. In this work, we attempt to establish the mechanism of magnetism driven zero thermal expansion in the stoichiometric $TiFe_2$.

EXPERIMENTAL

Polycrystalline $Ti_{33}Fe_{67}$ ($TiFe_2$) were prepared by melting high purity (> 99.99%) Ti and Fe in an inert argon atmosphere via a water cooled arc furnace. The sample was flipped 3-4 times during the melt to ensure homogeneity. The weight loss was less than 1%. The obtained ingot was then cut using low power diamond saw followed by powdering. The sample was then sealed in an evacuated quartz tube and annealed at 1000ºC for 5 hours, then at 800ºC for 96 hours followed by furnace cooling. Powder Xray diffraction was done using a Rigaku Xray diffractometer equipped with Cu K_α radiation. The stoichiometry and compositional homogeneity were verified by SEM-EDS over a 100 μm × 100 μm area of the sample. The EDS composition was estimated to be $Ti_{34}Fe_{66}$ with an error of 2%. The magnetic properties were studied using a Cryogenic S-700X SQUID magnetometer. Low temperature thermal expansion measurements were performed by measuring resistance change of a Kyowa strain gauge in the temperature range 120 K – 380 K.

RESULTS AND DISCUSSION

$TiFe_2$ crystallizes in the C14 type hexagonal structure ($P6_3/mmc$) as shown in Fig 1(a). The lattice parameters were obtained using Le bail method. Low temperature thermal expansion measurements were performed in the temperature range of 120 K to 380 K. $TiFe_2$ exhibits zero thermal expansion in a wide temperature range of 120 K to 340 K and the coefficient of thermal expansion $\alpha_l = {}^{\frac{d\Delta L}{L}}\Big/_{dT}$ is ~ 0.57 ppm/K, as shown in Fig. 1(b). α_l appears to be constant in the range between 120 K to around 340 K beyond which it increases beyond 350 K.

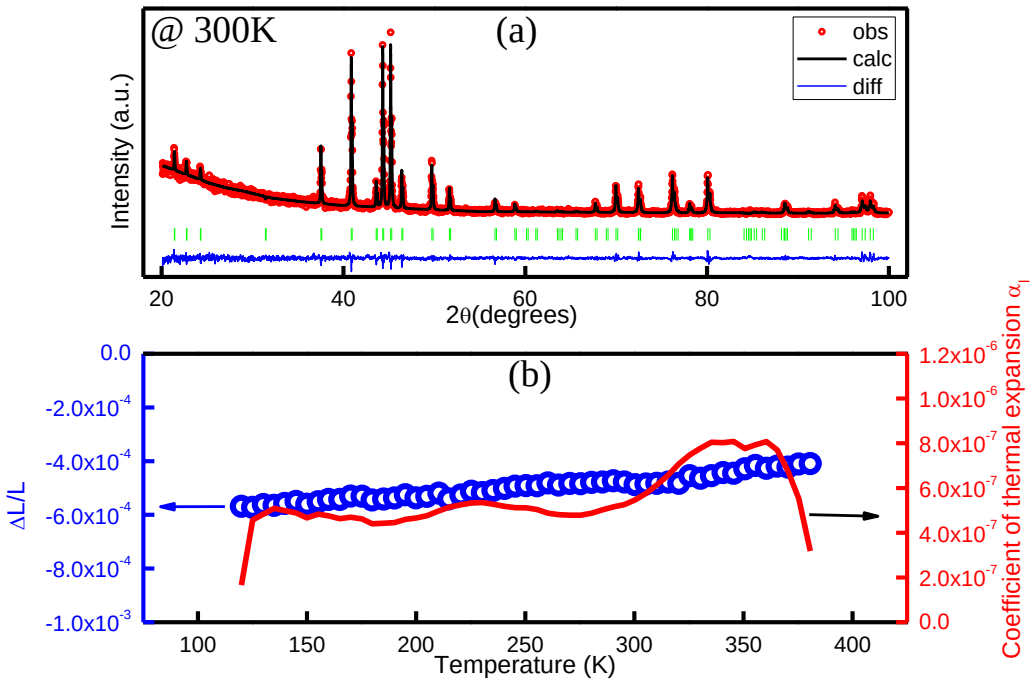


FIGURE 1. (a) Le bail fit XRD pattern for TiFe2 (b) Thermal expansion measurement using strain gauge.

Figure 2 (a) presents the thermomagnetic curve, M(T), for $TiFe_2$ recorded in an applied field of 0.01 T during the zero-field cooled (ZFC), field cooled cooling (FCC) and field cooled warming (FCW) cycles during the temperature interval of 5K to 390K. A subtle increase in magnetization is observed at around 220K signifying a possible magnetic transition. A plot of inverse magnetization vs temperature for T > 200K shown in the inset of Fig. 2(a) denotes two dips in inverse magnetization, one below 350K and the second below 220K indicating weak ferromagnetic transitions. While the second transition agrees with earlier reports [4], the transition at 350K which is much weaker is being reported for the first time. Presence of ferromagnetic correlations is also evidenced by the weak hysteresis in the M-H curve at 350K (Fig. 2(b)). Field-dependent magnetization curves *M(H)*, at several fixed temperatures ranging from 5 to 350 K, are displayed in Fig 2(c). No magnetic saturation is observed till 5T indicating the presence of competing ferro- and antiferromagnetic interactions. All the Arrott plots, shown in Fig. 2(d), are highly concave. Arrott plots are conventionally drawn by adopting the mean field model for which the critical exponent β=0.5. β serves as an important marker in describing the growth of the ordered moment below T_C , with smaller values hinting at a faster growth. A careful Arrott analysis was done from which the value of the critical exponent for this system is found to be around 0.8 indicating a slower growth of the ordered moment owing to the presence of competing interactions [5]. The ferromagnetic phase is associated with a larger volume whereas the antiferromagnetic phase is associated with a smaller volume. The competing ferro- and antiferromagnetic interactions maintains a stable unit cell volume with very negligible changes resulting in zero thermal expansion in this alloy.

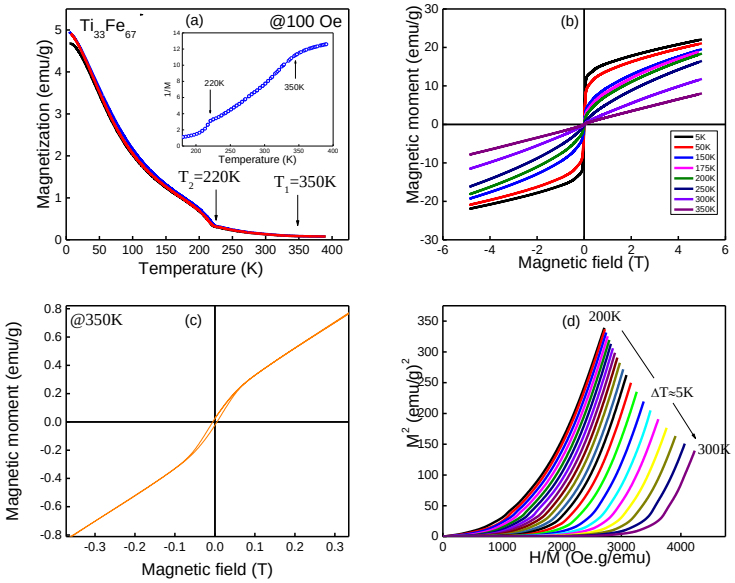


FIGURE 2. (a) Temperature dependence of the magnetization for $TiFe_2$ (b) Magnetization curves of $TiFe_2$ measured between 5 and 350 K. (c) M-H plot at 350K (d) Arrott analysis plots between 200K-300K.

CONCLUSION

In summary, the zero thermal expansion behavior in nearly stoichiometric $TiFe_2$ over a wide temperature range between 120 K to 320 K with α_l = 0.57 ppm/K is due to a strong competition between the ferromagnetic and the antiferromagnetic interactions that is present over the entire temperature range.

ACKNOWLEDGEMENT

Myren Azavedo thanks DST INSPIRE Fellowship (IF190174) and KRP acknowledges financial assistance from Council of Scientific and Industrial Research, New Delhi under 03/1481/2023/EMR-II.

REFERENCES:

1. E.F. Wassermann, M. Acet, B. Rellinghaus, W. Pepperhoff, Journal of Magnetism and Magnetic Materials, 140-144, 241-242 (1995).
2. W. E. Wallace, J. Chern. Phys., **41,**3857 (1964).
3. B. LI *et al.,* Physical Review B, **93**, 224405 (2016).
4. E.F. Wassermann, B. Rellinghaus, Th. Roessel, J. K̈astner, and W. Pepperhoff Eur. Phys. J. B, **5**, 361-365 (1998).
5. N. Assoudi et al, Chemical Physics Letters, **706**, 182-188 (2018)

Exploring 3*d* transition metal substituted $MnCo_{0.7}Fe_{0.3}Ge$

S. Shanmukharao Samatham[1,2], Sateesh Pinninti[3], Akhilesh Kumar Patel[4], Gowrinaidu Babbadi[5,*], Ch. Komala Lakshmi[5], Ramachandra R. K[5], M. Chandra Sekhar[1], Nataraju Gandla[1], Sankararao Yadam[6], K. G. Suresh[7]

[1]Department of Physics, Chaitanya Bharathi Institute of Technology, Gandipet, Hyderabad 500075, India
[2]Department of Physics, SUNY Buffalo State University, Buffalo, NY 14222, USA
[3]Department of Physics, MVGR College of Engineering, Chintalavalasa, Vizianagaram 535005, A. P., India
[4]Research Centre for Magnetic and Spintronic Materials, National Institute for Materials Science, Tsukuba, Ibaraki 305 0047, Japan
[5]Department of Physics, Government College (Autonomous) Rajahmundry, Rajamahendravaram 533 105, Andhra Pradesh, India
[6]Department of Physics, CVR College of Engineering, Ibrahimpatnam, Ranga Reddy, Telangana 501 510, India
[7]Magnetic Materials Laboratory, Department of Physics, Indian Institute of Technology Bombay, Powai, Mumbai 400 076, India

[*]Corresponding author: bgnphy@gcrjy.ac.in

Abstract. In this report, we investigate the magnetic properties of MnCoGe by simultaneously yet partially replacing Mn and Co with 3*d*-transition metals. Fe substitution for Co, i.e., $MnCo_{1-x}Fe_xGe$ resulted in the suppression of high temperature martensitic transition and stabilizes the ferromagnetic state around T_C = 250 K for x = 0.3. Partial replacement of Mn by Ni in $MnCo_{0.7}Fe_{0.3}Ge$ i.e., $Mn_{0.7}Ni_{0.3}Co_{0.7}Fe_{0.3}Ge$ is reported to crystallize in hexagonal structure. The temperature dependent magnetization analysis reveals positive Weiss paramagnetic temperature (indicating ferromagnetic correlations) along with a high temperature paramagnetic to low temperature ferromagnetic transition around 246 K. Decrease of magnetic transition with Ni substitution is attributed to the enhanced antiparallel magnetic interactions of Mn-Ni. Further, the effect of magnetic field on $Mn_{0.7}Ni_{0.3}Co_{0.7}Fe_{0.3}Ge$ will be addressed alongside revelation of universal critical behavior.

Keywords: Magnetic properties; martensitic transition; ferromagnetic state; Weiss paramagnetic temperature; Universal critical behavior.

INTRODUCTION

Discovery of functional materials is an ever-lasting fascinating research field in materials science. A comprehensive understanding of physical properties of magnetic materials provides requisite knowledge about the potential use of these materials in suitable applications. In this regard, intercalation, alloying and substitution/doping are widely practiced methods to fabricate/create new materials. Alloying of metals (transition and rare-earth) has produced numerous magnetic materials with multi-functional properties. Out of many magnetic materials and oxides, Heusler alloys find their unique place in experimental condensed matter physics for being suitable for various technological applications. For example, shape memory alloys, spintronics [1], exchange bias effect, magnetocaloric effect, spin-valve-like behavior [2-4] etc. In particular, 1:1:1 stoichiometric compounds are known for exhibiting coupled magneto-structural phenomenon with magnetic transitions above room temperature. A large temperature window between ferro and antiferromagnetic transitions in these alloys facilitates ample scope to tune the magnetic interactions [5].

MnCoGe crystallizes in orthorhombic (TiNiSi-type) structure and exhibits paramagnetic to ferromagnetic critical temperature of T_C ~ 355 K. A structural transition from hexagonal to orthorhombic occurs at about 420 K. In addition, T_C of hexagonal structure of the compound is 276 K [6-8]. Fe substitution for Co suppresses the structural transition and stabilizes the hexagonal structure at room temperature as reported for $MnCo_{0.7}Fe_{0.3}Ge$ with T_C of about 250 K [9]. Our present work discusses Ni substitution induced changes to the magnetism of $MnCo_{0.7}Fe_{0.3}Ge$.

EXPERIMENTAL METHODS

The polycrystalline specimens used in the present study was arc-melted. High purity elements of Mn, Ni, Co and Ge were taken in stoichiometric ratio and loaded onto a copper-hearth. For adsorption of unwanted gases released during melting process, the Titanium ingot was used as a getter element. The ingots were melted four times by flipping upside down each time, followed by annealing in vacuum sealed quartz tubes. X-ray diffraction pattern was collected at room temperature (RT) using X'Pert Pro x-ray Diffractometer. Magnetization measurements were performed with the help of 2 K/ 90 kOe superconducting quantum interference device-vibrating sample magnetometer. The magnetization characterizations were carried out down to 2 K from room temperature.

RESULTS AND DISCUSSION

Figure 1(a) shows the refined [10] RT x-ray diffraction pattern of $Mn_{0.7}Ni_{0.3}Co_{0.7}Fe_{0.3}Ge$. The refinement complies with Ni_2In-type hexagonal structure. The lattice parameters are $a = b = 4.09$ Å and c =5.25 Å. Figure 1(b) is the conventional unit cell of hexagonal structure drawn using visualization for electronic and structural analysis (VESTA) software [11]. Two Mn/Ni occupies eight corners and four edge-sharing positions. Two Ge atoms and two Co/Fe reside inside the unit cell.

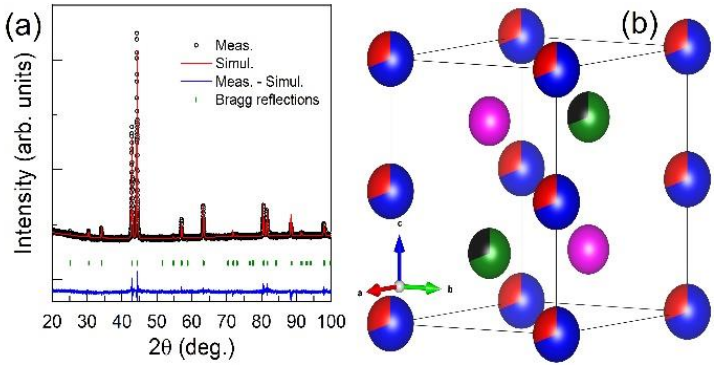


FIGURE 1. (a) $Mn_{0.7}Ni_{0.3}Co_{0.7}Fe_{0.3}Ge$ X-ray diffraction pattern along with the refinement. Half-filled circles represent experimentally collected diffraction pattern while continuous red and blue lines represent the Rietveld simulated and difference patterns respectively. The vertical olive lines represent the Bragg reflections angles. (b) The hexagonal unit cell containing Z = 2 formula units with the color codes for atoms as blue: Mn, red: Ni, pink: Ge, green: Co and black: Fe. Mn and Ni and Co and Fe share the same positions respectively.

Figure 2(a) shows the temperature variation of magnetization $M(T)$ from 2 to 350 K, measured in 100 Oe by applying zero-field cooled (ZFC) and field-cooled warming (FC) protocols. Magnetization increases with the reduction of temperature from 350 K and rises sharply below 250 K. The temperature derivative $dM(T)/dT$ curve (not shown here) exhibits a sharp dip around 246 K which is designated as the critical transition from paramagnetic to ferromagnetic state. In addition, ZFC and FC curves bifurcate below $T_{bifur} \sim 234$ K. The Curie-Weiss law fit of inverse susceptibility (not shown here) using the equation, $\chi^{-1}(T) = (T-\theta_W)/C$, resulted in paramagnetic Weiss temperature $\theta_W \sim 249.6$ K. It is positive and indicates prevailing ferromagnetic interactions. Thus calculated effective magnetic moment is about $\mu_{eff} = 2.59\ \mu_B$/f.u. Shown in figure 2(b) are isothermal magnetization curves as a function of magnetic field $M(H)$, at 4 K and 300 K, measured in five quadrants (0→90→0→-90→0→90 kOe). In the magnetically ordered region, the compound exhibits technical saturation at $H_{sat} = 5.8$ kOe with a saturation moment of about $M_{sat} = 2.38\ \mu_B$. The spontaneous magnetic moment is estimated by extending the high field linear saturation down to zero field, is $M_s = 2.35\ \mu_B$. This is in good agreement with the effective magnetic moment determined from the Curie-Weiss fit. The field dependent magnetization is irreversible with a coercive field of about $H_{coer} \sim 60$ Oe and low remanence magnetic moment of about $M_R = 7.34\times10^{-2}\ \mu_B$. At temperature 300 K, i.e., in the paramagnetic state, $M(H)$ curve does not exhibit magnetic saturation and grows almost linearly. Low saturation magnetic field, negligible coercive field and remanence magnetic moment indicate soft-ferromagnetic behavior of $Mn_{0.7}Ni_{0.3}Co_{0.7}Fe_{0.3}Ge$.

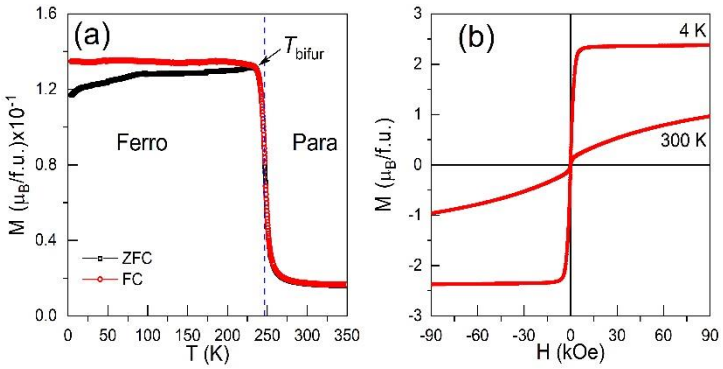


FIGURE 2. (a) Temperature variation of magnetization exhibiting para to ferromagnetic transition around 246 K and a bifurcation temperature around 234 K and (b) Isothermal magnetization curves at 4 and 300 K measured in magnetic field range ± 90 kOe. Soft-ferromagnetic nature is apparent in the magnetically ordered state.

Further, the above results invite a detailed magnetic investigation by measuring $M(T)$ in different magnetic fields in order to construct temperature-magnetic field (T-H) phase diagram. Furthermore, critical exponent study by employing conventional (modified Arrott's plots) and magnetic-entropy methods to unveil the underlying magnetic interactions across the critical temperature.

SUMMARY

Summarizing, the effect of simultaneous substitution of Fe and Ni for Co and Mn respectively in MnCoGe is investigated with the help of structural and magnetic characterizations. $Mn_{0.7}Ni_{0.3}Co_{0.7}Fe_{0.3}Ge$ crystallizes in the hexagonal structure. Thus estimated lattice parameters are $a = b = 4.09$ Å and c =5.25 Å. Magnetization analysis reveals prevailing ferromagnetic interactions in the paramagnetic state and a transition to magnetically ordered state around 246 K. An isothermal magnetization curve at 4 K confirms soft-ferromagnetic nature of the alloy with low saturation magnetic field, negligible coercive field and remanence magnetic moment. Our study emphasizes the need to investigate the magnetic properties of the present alloy and higher substitution of Ni for Mn to disclose the universal magnetic critical behavior and in the quest of exploring magnetocaloric properties.

ACKNOWLEDGMENTS

Gowrinaidu Babbadi acknowledges the financial support through CREATE Fund, Government College (A) Rajahmundry (No: 011/GCRJY/Acad.Cell/CREATE Fund/Research Funding/2023). S. Shanmukharao Samatham and M. Chandra Sekhar acknowledge the financial support from UGC-DAE CSR through Collaborative Research Scheme (CRS) project number CRS/2022-23/01/712. S. Shanmukharao Samatham and Nataraju Gandla acknowledge the Seed Grant (CBIT/PROJ-IH/I031/Physics/D002/2024) by Chaitanya Bharathi Institute of Technology, Hyderabad.

REFERENCES

1. K. Elphick, W. Frost, M. Samiepour, T. Kubota, K. Takanashi, H. Sukegawa, S. Mitani, and A. Hirohata, *Sci. Technol. Adv. Mater.*, Vol. 22, pp. 235–271 (2021).
2. S. Singh, R. Rawat, S. E. Muthu, S. W. D'Souza, E. Suard, A. Senyshyn, S. Banik, P. Rajput, S. Bhardwaj, A. M. Awasthi, and R. Ranjan, *Phys. Rev. Lett.*, Vol. 109, p. 246601 (2012).
3. Y. Venkateswara, J. Nag, S. S. Samatham, A. K. Patel, P. D. Babu, M. R. Varma, J. Nayak, K. G. Suresh, and A. Alam, *Phys. Rev. B*, Vol. 107, p. L100401 (2023).
4. J. Nag, D. Rani, D. Singh, R. Venkatesh, B. Sahni, A. K. Yadav, S. N. Jha, D. Bhattacharyya, P. D. Babu, K. G. Suresh, and A. Alam, *Phys. Rev. B*, Vol. 105, p. 144409 (2022).
5. E. Liu, W. Wang, L. Feng, W. Zhu, G. Li, J. Chen, H. Zhang, G. Wu, C. Jiang, H. Xu, and F. De Boer, *Nat. Commun.*, Vol. 3, p. 873 (2012).
6. A. Szytuła, A. T. Pędziwiatr, Z. Tomkowicz, and W. Bażela, *J. Magn. Magn. Mater.*, Vol. 25, pp. 176–186 (1981).
7. V. Johnson, *Inorg. Chem.*, Vol. 14, pp. 1117–1120 (1975).
8. W. Jeitschko, *Acta Crystallogr. Sect. A*, Vol. 31, pp. 1187–1190 (1975).
9. S. Pinninti and G. N. Raju, *Mater. Res. Express*, Vol. 6, p. 116563 (2019).
10. J. Rodríguez-Carvajal, *Physica B*, Vol. 192, pp. 55–69 (1993).
11. K. Momma and F. Izumi, *J. Appl. Crystallogr.*, Vol. 41, pp. 653–658 (2008).

First-principles study of the electronic structure and magnetism in highly frustrated two-dimensional magnet $CsTbSe_2$

Kuldeep Kargeti,[a)] Shovan Gayen,[b)] and S. K. Panda[c)]

Department of Physics, Bennett University, Greater Noida 201310, Uttar Pradesh, India

[a)] Corresponding author: e20soe802@bennett.edu.in

Abstract. Rare-earth compounds with spins arranged in a frustrated triangular lattice are extremely exotic for unconventional ground state properties. In this context various rare-earth based systems such as $YbMgGaO_4$, $CsNdSe_2$ and $TbInO_3$ have been predicted theoretically as well as experimentally belonging to a class of spin-liquid materials. Motivated by such exotic ground state properties we have theoretically studied the electronic and magnetic properties of less explored Rare-earth based material namely, $CsTbSe_2$, where Tb ions are arranged in a triangular geometry with two dimensional (2D) hexagonal layers. We employed density functional theory + Hubbard U approach including the effects of spin- orbit coupling (SOC) to understand the ground state electronic and magnetic properties in detail. Our electronic structure calculation reveal that $CsTbSe_2$ is a SOC driven insulator with a gap of 1.80 eV. Our results clearly show that antiferromagnetic interactions are dominating in nature with 2D behaviour. Hence, our findings reveal that this material is a frustrated two-dimensional (2D) magnet with insulating ground state and can be a promising candidate for antiferromagnetic spin-liquid or can host incommensurate magnetic structures.

INTRODUCTION

Magnetic frustration arising due to geometry gives rise to many exotic ground states in condensed matter physics[1]. At low temperatures, various underlying interactions lead to highly degenerate ground states that often involve unconventional quantum phenomena. One example of such ground states is attributed to the two-dimensional (2D) triangular lattice with antiferromagnetic (AFM) interactions[2]. One of the frontier research topics in this field is the quantum spin liquid (QSL) state initially proposed by Anderson[3] where a strong quantum fluctuation prevents any long-range order (LRO) down to T = 0 [4,5]. In search of spin-liquid like ground states, systems with large spin orbit coupling like rare-earth ions and having 2D triangular lattice geometry have been the area of interest recently. Recent work on $YbMgGaO_4$ predicts it to be a spin liquid with bond dependent exchange due to presence of large spin-orbit coupling and a prefect triangular lattice like geometry [6,7].

In this work we have theoretically investigated the electronic and magnetic properties of 2D triangular lattice system $CsTbSe_2$ which forms a hexagonal β-$RbScO_2$ type structure with space-group $P6_3/mmc$. This material has been experimentally synthesized earlier with details provided in the given reference[8]. The crystal structure of $CsTbSe_2$ is shown in Fig-1(a) where, 2D layers of Tb ions form a hexagonal network in a-b plane (shown in Fig.1(b)). Tb ions in a-b plane are connected by an edge shared octahedra formed by Se ions. The Tb-Tb distance in the hexagonal network is 4.25 Å and 7.36 Å for 1st and 2nd NN respectively. Tb hexagonal layers along the c-axis are separated by 8.32 Å which also comprises the 3rd NN. This material exhibits no long-range order down to measured 2K with anti-ferromagnetic behavior as reported experimentally. Here we have employed density functional theory + Hubbard U and included spin-orbit coupling (SOC) in our calculations to understand the electronic and magnetic properties in much more detailed manner.

COMPUTATIONAL DETAILS

The calculations reported in this work are carried out using two different approaches namely (a) plane-wave basis as implemented in Vienna ab initio simulation package (VASP)[9,10] (b) full-potential linear muffin-tin orbital (FP-LMTO) method[11,12] as implemented in the RSPt code. To account for exchange and correlation effect, we have employed generalized gradient approximation (GGA)[13] with Hubbard U within the GGA+U framework[14]. The choice of U is made from previous works on Tb based systems given in the following reference[15]. Since rare-earth elements exhibits large spin-orbit coupling (SOC) effects, we have also carried out GGA+U+SOC calculation and compared with GGA+U results. The Brillouin-zone integration was done with a modified tetrahedron method using 9 x 9 x 2 k-mesh in the irreducible part of the Brillouin-zone to achieve self-consistency.

J_1

Cs

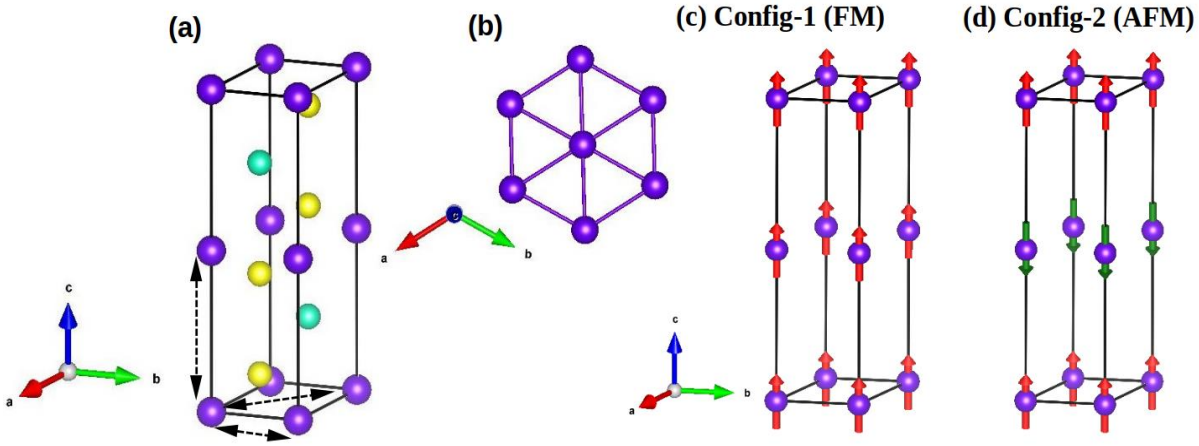


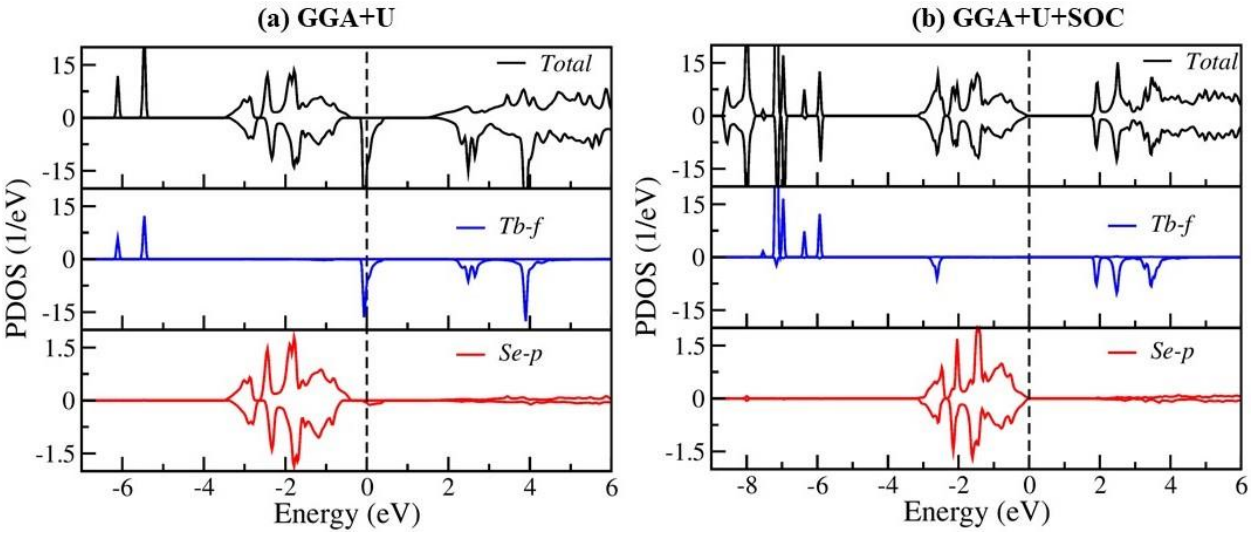
FIGURE 1. (a) Unit cell of $CsTbSe_2$. The 1st, 2nd and 3rd NN Tb-ions are marked with their respective magnetic coupling J_1, J_2 and J_3 (b) The hexagonal network of Tb ions in the *a-b plane.* (c) Ferromagnetic and (d) Antiferromagnetic arrangement of Tb ions for lowest energy magnetic state.

TABLE 1. Energy corresponding to different magnetic configurations obtained from GGA+U and GGA+U+SOC calculations. Spin and orbital moments are also listed.

	GGA+U		GGA+U+SOC	
	Energy (meV)	Spin Moment (μ_B)	Energy (meV)	Spin (orb) Moment (μ_B)
Config-1 (FM)	0.00	5.85	0.00	5.86 (1.28)
Config-2 (AFM)	-0.05	5.85	-0.07	5.86 (1.28)

RESULTS AND DISCUSSION

FIGURE 2. Total and partial density of states obtained from (a) GGA+U and (b) GGA+U+SOC calculation for the lowest energy magnetic configuration.



Electronic structure from GGA+U and GGA+U+SOC calculations

Before delving into the electronic structure of $CsTbSe_2$, we performed GGA+U calculations for two magnetic configurations, depicted in Fig. 1 (c and d). In config-1, Tb ions exhibit ferromagnetic interactions in both the a-b plane and along the c-axis. In config-2, the out-of-plane interaction between Tb ions is antiferromagnetic. The computed energies for these configurations, shown in Table 1, are nearly degenerate in both GGA+U and GGA+U+SOC approaches, suggesting negligible magnetic coupling between Tb layers along the c-axis and classifying the system as a 2D magnetic material. Fig. 2(a) shows the total and partial density of states (TDOS and PDOS) for the lowest energy configuration from

GGA+U calculations. The TDOS indicates a finite spectral weight at the Fermi level, suggesting a metallic nature due to the Tb-*f* orbitals. The spin-up channel for the Tb-*4f* orbital is fully occupied and lies well below the Fermi level, while the minority spin channel is partially occupied, contributing to the spectral weight at the Fermi level. This configuration suggests an f^8 state for the Tb ion and is consistent with a spin moment of 5.85 μ_B. The Se-*p* PDOS shows fully occupied *p* orbitals between 0.5 eV and 3.5 eV below the Fermi level, with no hybridization between the Tb-*f* and Se-*p* orbitals, reflecting the highly localized nature of the Tb-f orbital. Given the heavy size of Tb and the localized nature of *4f* orbitals with large spin moments predicted by GGA+U calculations, it is crucial to consider spin-orbit coupling (SOC) to accurately determine the ground state electronic structure. We performed GGA+U+SOC calculations for both ferromagnetic (FM) and antiferromagnetic (AFM) configurations. Config-2 remains lower in energy, and the small energy difference between configurations confirms weak interlayer interaction. Fig. 2(b) displays the total and partial densities of states (TDOS and PDOS) from GGA+U+SOC calculations, showing an insulating characteristic with a 1.8 eV band gap due to SOC effects on the Tb-*f* orbitals. The PDOS reveals a gap between the minority Tb-*f* states, unlike in GGA+U calculations. The Tb ion has a spin moment of 5.85 μ_B and an orbital moment of 1.28 μ_B. No significant changes are observed in the Se-*p* PDOS with SOC. The TDOS near the Fermi level is dominated by Se-*p* and Tb-*f* states, confirming $CsTbSe_2$ as a SOC-driven insulator.

CONCLUSION

In conclusion, we theoretically studied the electronic and magnetic properties of the rare-earth hexagonal system $CsTbSe_2$. Our GGA+U calculations failed to capture its insulating nature but including SOC revealed a true insulating ground state with a 1.80 eV gap between Se-*p* and Tb-*f* states, classifying it as an SOC-driven insulator. From the difference in energies for FM and AFM configuration, it is evident that $CsTbSe_2$ is 2D system concerning the magnetic behaviour. 2D magnetic behaviour with AFM interactions is one the major reason which causes magnetic frustration preventing long-range ordering, which is also consistent with experimental findings. Large SOC and presence of magnetic frustration suggest a potential spin liquid ground state or incommensurate magnetic structure, motivating further experimental research on $CsTbSe_2$.

REFERENCES

1. Ramirez, A. P. Strongly geometrically frustrated magnets. *Annual Review of Materials Science* **24**, (1994).
2. Collins, M. F. & Petrenko, O. A. Review / Synthèse : Triangular antiferromagnets . *Can J Phys* **75**, (1997).
3. Wannier, G. H. Antiferromagnetism. The triangular Ising net. *Physical Review* **79**, (1950).
4. Husimi, K. & Syozi, I. The Statistics of Honeycomb and Triangular Lattice. I. *Progress of Theoretical Physics* **5**, (1950).
5. Seabra, L., Momoi, T., Sindzingre, P. & Shannon, N. Phase diagram of the classical Heisenberg antiferromagnet on a triangular lattice in an applied magnetic field. *Phys Rev B Condens Matter Mater Phys* **84**, (2011).
6. Li, Y. *et al.* Gapless quantum spin liquid ground state in the two-dimensional spin-1/2 triangular antiferromagnet YbMgGaO4. *Sci Rep* **5**, (2015).
7. Li, Y. *et al.* Rare-Earth Triangular Lattice Spin Liquid: A Single-Crystal Study of YbMgGaO4. *Phys Rev Lett* **115**, (2015).
8. Xing, J. *et al.* Crystal Synthesis and Frustrated Magnetism in Triangular Lattice CsRESe2(RE = La-Lu): Quantum Spin Liquid Candidates CsCeSe2and CsYbSe2. *ACS Mater Lett* **2**, (2020).
9. Kresse, G. & Furthmüller, J. Efficient iterative schemes for ab initio total-energy calculations using a plane-wave basis set. *Phys Rev B Condens Matter Mater Phys* **54**, (1996).
10. Kresse, G. & Hafner, J. Ab initio molecular dynamics for liquid metals. *Phys Rev B* **47**, (1993).
11. Andersen, O. K. Linear methods in band theory. *Phys Rev B* **12**, (1975).
12. Wills, J. M. & Cooper, B. R. Synthesis of band and model Hamiltonian theory for hybridizing cerium systems. *Phys Rev B* **36**, (1987).
13. Langreth, D. C. & Perdew, J. P. Theory of nonuniform electronic systems. I. Analysis of the gradient approximation and a generalization that works. *Phys Rev B* **21**, (1980).
14. Anisimov, V. I., Zaanen, J. & Andersen, O. K. Band theory and Mott insulators: Hubbard U instead of Stoner I. *Phys Rev B* **44**, (1991).
15. Kassimi, F. Z. *et al.* A theoretical study of the electronic, magnetic and magnetocaloric properties of the TbMnO3 multiferroic. *J Magn Magn Mater* **543**, (2022).

Role of Magnetic field on Electronic Specific Heat of Anderson Lattice Model: An Application to Colossal Magnetoresistive Manganites ($Re_{1-x}A_xMnO_3$)

Sunil Panwar *

Department Of Applied Science, Faculty of Engineerinng & Technology, Gurukula Kangari (Deemed to be University), Haridwar, India

* Corresponding author: dr.sunilpanwar66@gmail.com

ABSTRACT: We have studied the role of magnetic field on electronic specific heat (C_v) at different temperatures of rare earth Manganites doped with alkaline earths namely $Re_{1-x}A_xMnO_3$ (where Re = La, Pr, Nd etc., and A= Ca, Sa, Ba etc.) exhibiting colossal magnetoresistance (CMR) phenomena. We have used a two band (l-b) Anderson lattice model Hamiltonian to study these materials in the strong electron- lattice Jahn- teller (JT) coupling regime an approach similar to the two – fluid models. We find the linear coefficient of specific heat C_v / T increases with increasing magnetic field 'h' & 'm' parameters showing the peak at low temperatures & finally decreases at higher values of h, m parameters. We have plotted the curves at temperature 100K & 300K only. We have also observed the role of doping concentration 'x' on specific heat coefficient (C_v / T). It increases with the doping 'x' having the peak near x = 0.3 which shows the optimum value of x and decreases thereafter on higher values of x. Our results are in good agreement with the available experimental data.

KEYWORDS: CMR Manganites; Anderson Lattice Model; Electronic Specific Heat; Variational Method; Magneto-thermal Properties.

1. INTRODUCTION

The complicated behaviours found in doped manganese oxides, particularly those with colossal magnetoresistance (CMR) [1], are not fully described by current theoretical frameworks. Creating an accurate microscopic model remains a major difficulty. Notably, processes like CMR and the metal-insulator transition are intimately related with temperature-driven changes in the electron density of states - commonly referred to as a "pseudogap" [2] or fluctuations in the number of effective charge carriers [3].

Ramakrishnan et al., [4] proposed a theoretical framework to explain the coexistence of localised Jahn-Teller (JT) polarons and delocalised band electrons in doped Rare-Earth Manganites with the general formula $Re_{1-x}A_xMnO_3$. They proposed that this cohabitation occurs naturally when strong JT coupling and orbital degeneracy are present, and that the model can successfully account for a number of manganite properties.

Previously, Panwar et al. [5] created a variational approach based on the Anderson lattice model, which was originally used to analyse the ground-state and thermal characteristics of heavy fermion systems. This approach was then extended to investigate magneto-transport behaviour, such as thermoelectric power and electrical resistivity, in doped Manganites at varied temperatures and magnetic field settings [6-8]. This study investigates how magnetic fields affect the electronic specific heat (C_v) of Rare-Earth Manganites doped with alkaline earth elements at various temperatures.

2. BASIC FORMULATION

The current study utilizes the two-band (ℓ-b) Anderson lattice model Hamiltonian, known as H_{lb}, to characterize Manganites under strong electron-lattice coupling generated by the Jahn-Teller (JT) phenomena. This technique

follows the two-fluid framework, integrating hybridization of the localized (ℓ) and itinerant (b) electron states. The Hamiltonian is represented as follows:

$$Hlb = -\sum_{\langle ij\rangle\sigma} \bar{t}_{ij} \left(b^{+}_{i\sigma}\, b_{j\sigma}\right) - \sum_{i\sigma} E_{jt}\, l^{+}_{i\sigma}\, l_{i\sigma} + \mathrm{U} \sum_{i\sigma} n^{l}_{i\sigma}\; n^{b}_{i\sigma} - J_H \sum_i \boldsymbol{s_i} \cdot \boldsymbol{S_i} - J_F \sum_{\langle ij\rangle} \boldsymbol{S_i} \cdot \boldsymbol{S_j} - \sum_{k\sigma} V_K (l^{+}_{k\sigma}\, b_{k\sigma} + h.c.) - \mu \mathrm{B} \sum_i \boldsymbol{s_i} . \mathbf{h} \quad (1)$$

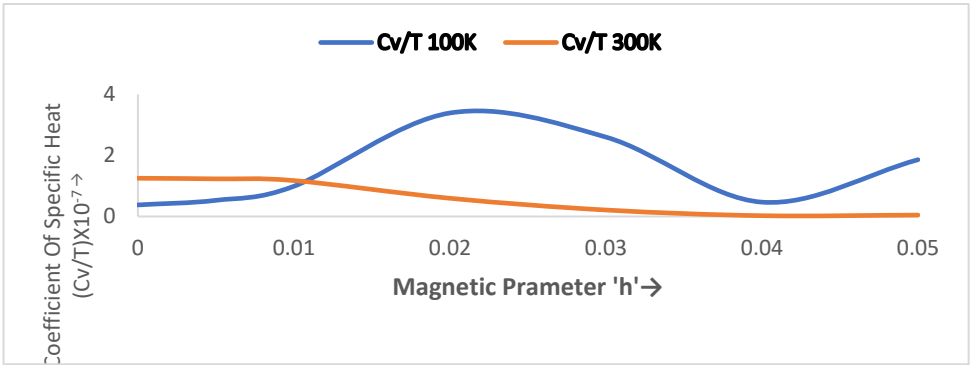
The specifications of the symbols utilised are provided in our prior work, Ref. [6-8]. We follow the electronic specific heat formula that we utilised in previous publications [5].

$$C_V = \frac{\partial \langle E \rangle}{\partial T} = \frac{\partial}{\partial T} \sum_{k\sigma} (E^{-}_{k\sigma} - \mu)\, f^{-}_{k\sigma} \quad (2)$$

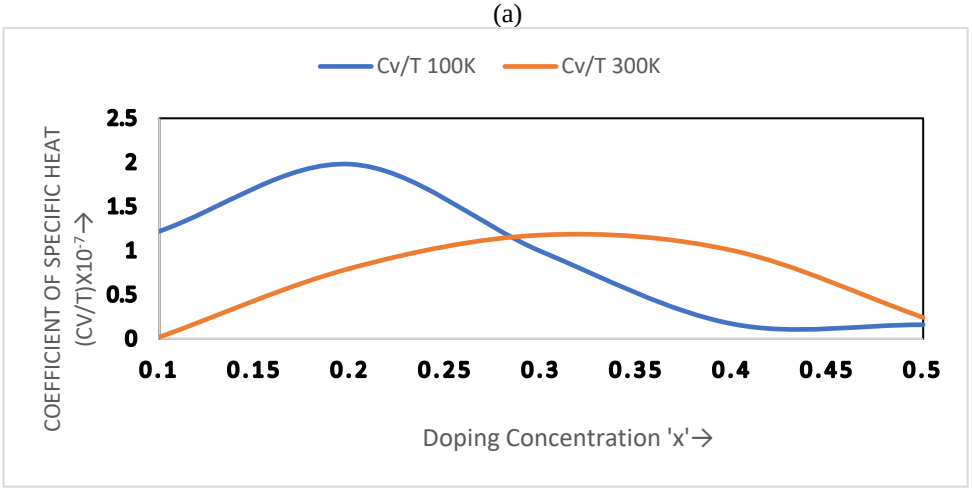
3. RESULT & DISCUSSIONS

In these computations, we have considered the unperturbed conduction band of simple semi-circular density of states $N^{c}{}_{\sigma}(\epsilon_k) = (2/\pi)\sqrt{(1-\epsilon_k^2)}$ (which is centered around zero energy) with band width W=2.0eV, U=5.0, E_{jt} =0.5, V= 0.1 & 0.2 , $\in_F$ = -0.238 eV (for x =0.3) and J_H = 1.0 & 2.0 eV. The Doping concentration 'x' is varied from 0.1 to 0.5. The magnetic parameter h is related to the physical field through $h = g\,\mu_B\, S_c\, H_{phys}/t$. Using g=2, t=0.6 eV & S_c=3/2, we find that parameter h= 0.01 corresponds to H_{phys} =15T whereas the parameter m stands for magnetization per site.

Figures



(a)



(b)

FIGURE 1. Variation of linear coefficient of electronic specific heat (C_v/T) as a function of a) magnetic parameter 'h.' at *x* =0.3; b) doping 'x 'at h= 0.01 & m= 0.1 for a fixed value of V = 0.1 & J_H = 1.0

In Fig. 1, we have shown the linear coefficient of specific heat (C_v/T) values for different values of magnetic field parameters 'h'& 'm' and doping 'x' respectively at fixed values of parameter J_H & V. We have plotted the curves at temperatures 100 K and 300 K only.

In Fig. 1 (a), we find that linear coefficient of specific heat (C_v/T) increases with increasing magnetic field 'h' & 'm' parameters showing the peak at low temperatures & finally decreases at higher values of h, m parameters. The peak disappears at higher temperatures.

We have also observed the role of doping concentration 'x' on specific heat coefficient (C_v/T) in Fig.1 (b). It increases with the doping 'x' having the peak near x=0.3 which shows the optimum value of x and decreases thereafter on higher values of x. Our results are consistent with the current experimental data. The temperature behavior of specific heat agrees qualitatively with the recent experiments in many CMR compounds like $La_{0.815}Sr_{0.185}MnO_3$ **[9]** & $Pr_{0.6-x}Bi_xSr_{0.4}MnO_3$($x$= 0.0-0.15) **[10].** We also find that as temperature increases from 100 K, the maximum in C_v/T is less pronounced & much broader and shifts towards higher doping x- values.

However, doping consistently suppresses conduction and ferromagnetism. It is worth noting that the double exchange (DE) and thus the physical properties of these materials are particularly vulnerable to the lattice effects caused by doping. Much of the research on rare-earth doped CMR materials has been conducted through the doping of RE sites, which causes lattice effects and, eventually, influences double exchange.

4. ACKNOWLEDGMENTS

We would like to acknowledge our great appreciation to U.G.C., New Delhi for the financial support.

5. REFERENCES

1. Y. Tokura, *Colossal Magnetoresistive Oxides* (Gordon and Breach, New York, 2000), and references therein.
2. T. Saitoh et al., Phys. Rev. **B62**,1039 (2000).
3. Y. Okimoto et al., Phys Rev. **B55**,4206 (1997).
4. T.V. Ramakrishnan et al., "Theory of Manganites Exhibiting Colossal Magnetoresistance," in *Colossal Magnetoresistive Manganites* edited by T. Chatterji (Kluwer Academic Publishers, Netherlands, 2004) **Chapter 10**, pp. 417-441.
5. S. Panwar & I. Singh, Solid State Communs. **72**, 711(1989); Phys. Rev. **B50**, 2110 (1994); *J.* Appl. Phys. **76 (10),** 6223(1994); Phys. Stat. Sol. (b) **175** ,487 (1993).
6. S. Panwar et al., Mod. Phys. Lett. **B 28**, No. 24, 1450182(2014).
7. S. Panwar, V. Kumar, A. Chaudhary, R. Kumar & I. Singh., Solid St. Communs.**223** ,32-36 (2015).
8. S. Panwar, V. Kumar, A. Chaudhary, R. Kumar & I. Singh, Solid St. Communs. ,**266**, 50-54 (2017).
9. A. Szewczyk et al., Phys. Rev. **B 71**, 224432(2005).
10. M.D. Daivajna et al., Journal of Alloys & Compounds **588**, 406 (2014).

Structural and Magnetic Properties of the Cluster-Glass Phase of Pseudo-1-D Spin-Chain Compound $Ca_3Co_2O_6$

Amit Maurya[1], D pal[2, *]

[1,2] Department of Physics, Indian Institute of Technology Guwahati, Assam, India.

[*]dpal@iitg.ac.in

Abstract. We investigated the structural and magnetic characteristics of $Ca_3Co_2O_6$ using powder X-ray diffraction (XRD) and magnetization measurements. The quasi-one-dimensional spin chain compound $Ca_3Co_2O_6$ was synthesized via the solid-state reaction method. The sample was characterized using room temperature XRD and magnetic measurements. Rietveld refinement of the XRD data indicates that the sample crystallizes in a rhombohedral phase with space group $R\bar{3}c$. The material undergoes a phase transition from a paramagnetic phase to a disordered antiferromagnetic phase below 25 K (T_{C1}), and a glassy phase appears below 11.20 K (T_{C2}). The magnetization measurements taken with a wait period showed a reduced saturation moment of 0.2 μ_B/f.u. at 9T magnetic field. Additionally, interrupted field cool cooling (IFCC) magnetization measurements demonstrated a magnetic memory effect below the glassy temperature.

INTRODUCTION

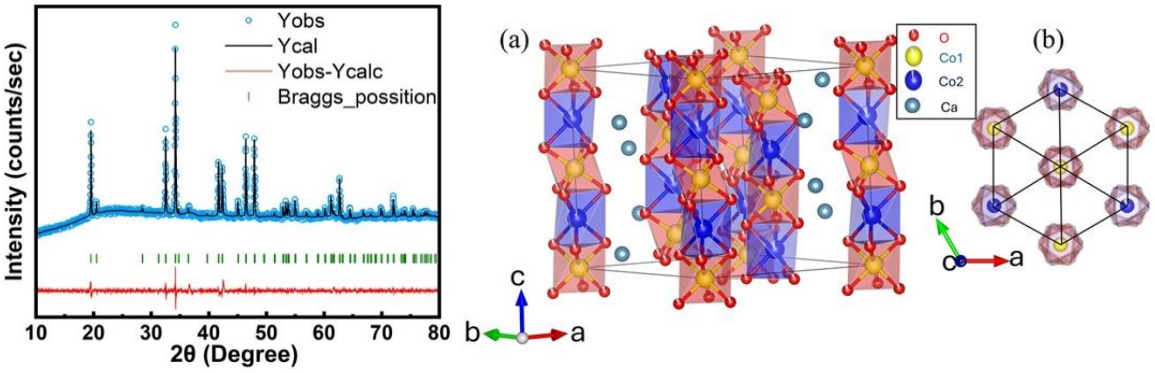
Low-dimensional (pseudo-1D spin-chain) materials have attracted many researchers because of their non-trivial features resulting from strong electron correlation and quantum effects. Among pseudo-1D spin-chain compounds, calcium cobaltite ($Ca_3Co_2O_6$) has received much attention in recent years due to its remarkable thermoelectric properties, magnetic properties, and potential for catalytic applications. $Ca_3Co_2O_6$ is a complex oxide with a unique crystal structure that provides it with excellent thermal and electrical conductivity. $Ca_3Co_2O_6$ belongs to a category of spin chain compounds that have a pseudo-one-dimensional structure with the structural formula $A_3BB'O_6$. Here A represents a nonmagnetic ion while both B' and B belong to the category of transition metals [1–3]. This complex crystallizing in the rhombohedral space group $R\bar{3}c$ [4]. It forms pseudo-one-dimensional spin chains, with Co ions in CoO_6 (Co I) octahedra and CoO_6 (Co II) trigonal prisms, having identical electronic states (charge +3) but different spin states ($S = 0$ and $S = 2$, respectively) [5,6]. The chains are arranged in a triangular pattern in the ab plane, separated by non-magnetic Ca^{2+} cations. A magnetic transition is observed from the paramagnetic state to a disordered antiferromagnetic phase below 25 K (T_{C1}), followed by the emergence of a short-range glassy phase below 10 K (T_{C2}) [1,3]. Its magnetic properties are characterized by ferromagnetic intrachain and antiferromagnetic interchain interactions, leading to magnetic memory effects and magnetization quantum tunneling below T_{C2} [1,3,6].

SAMPLE PREPARATIONS AND EXPERIMENTAL DETAILS

Polycrystalline samples of $Ca_3Co_2O_6$ were synthesized by the solid-state reaction technique. The materials were subjected to powder X-ray diffraction studies at room temperature using a Rigaku X-ray diffractometer (XRD), specifically the TTRAX III model. The microstructural images and particle size were examined using a FESEM Zeiss-made Sigma 300. A Quantum Design Physical Property Measurement System (PPMS) equipped with a VSM probe was used to measure the magnetization data.

RESULTS AND DISCUSSION

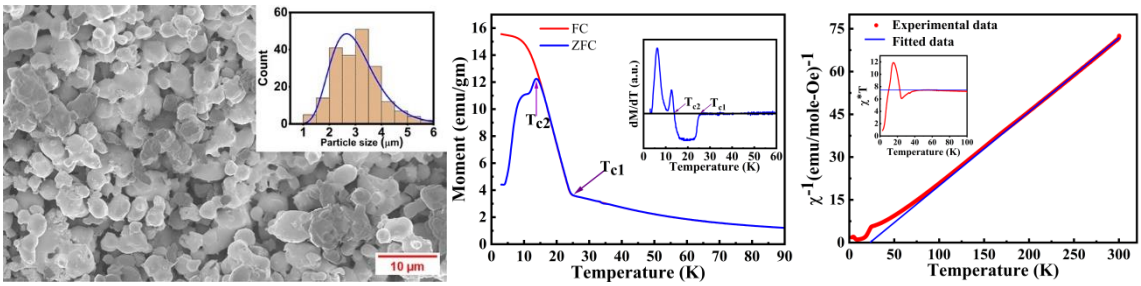
X-ray diffraction (XRD) patterns of the sample were taken at room temperature to confirm the phase formation and phase purity. The Rietveld refinement of the XRD data was performed using the FULLPROF program. As shown in Fig. 1(I), the XRD pattern and its Rietveld refinement confirm that the obtained peaks are consistent with the ICSD data, confirming the absence of impurity phases. The Rietveld analysis validates that the compound is a single-phase material with a rhombohedral crystal structure, belonging to the space group $R\bar{3}c$, and yields a good fit with a χ^2 value of 1.61.



(I) (II)

FIGURE 1. (I) X-ray diffraction patterns with the Rietveld refinement, II(a) Crystal structure of $Ca_3Co_2O_6$ and II (b) Structural projection in the ab plane.

Fig. 1(II) depicts the refined crystal structure of $Ca_3Co_2O_6$ with alternating CoO_6 trigonal prisms and CoO_6 octahedra. From Fig. II(a), it can be seen that the crystal structure is made up of a large number of chains of alternate face-sharing CoO_6 (Co I) octahedral and CoO_6 (Co II) trigonal prisms that run along the c-axis and these chains form a triangle lattice in the ab plane (Fig. II(b)), separated from one another by a nonmagnetic Ca^{2+} cation and surrounded by 6 more chains that are equally spaced apart.

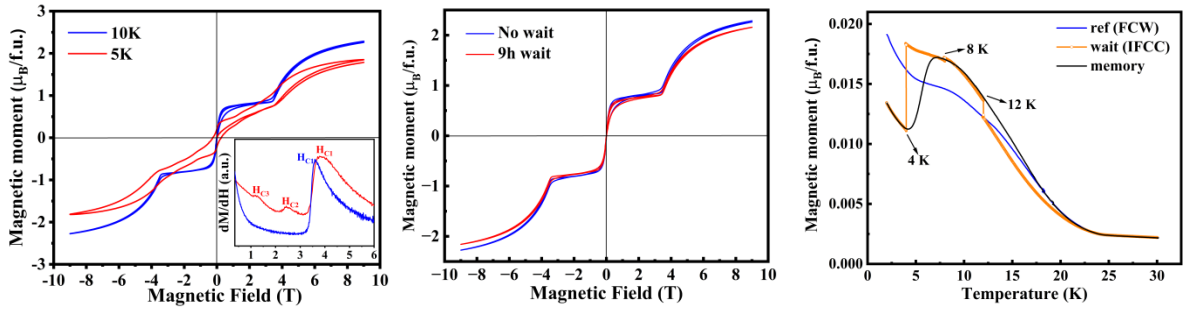


(a) (b) (c)

FIGURE 2. (a) FE-SEM micrograph with grain size distribution (b) DC magnetization (M) vs temperature (T) curve in ZFC and FC (c) the inverse susceptibility (χ^{-1}) vs temperature (T) curves in an applied field of 5 T.

The FE-SEM image of $Ca_3Co_2O_6$ is shown in Fig. 2(a). The bulk $Ca_3Co_2O_6$ samples exhibit well-developed grains with some porosity, and the av. grain size is estimated to be around 2.91 μm. The DC magnetization of $Ca_3Co_2O_6$ was measured under field-cooled (FC) and zero-field-cooled (ZFC) conditions in a 5 T magnetic field. Fig. 2(b) shows the M vs. T curves, indicating an upturn below 25 K in the FC-ZFC magnetization curve. To precisely determine the transition temperatures, derivative analysis (dM/dT) was used on the ZFC data. From the dM/dT vs. T curve (Fig. 2(b) inset), the transition temperatures were obtained 25 K (T_{C1}) which corresponds to the change from a paramagnetic to a disordered antiferromagnetic state and 11.20 K (T_{C2}) below which spin glass behavior started. While the observed T_{C1} matches with previous reports [3], but the observed T_{C2} is slightly higher than the previously reported 10 K. Fig. 2(c) inset plot suggests that the increased T_{C2} value might be due to the presence of ferromagnetic correlations in the paramagnetic region. Additionally, Fig.2(c) illustrates that the inverse magnetic susceptibility of $Ca_3Co_2O_6$ follows the Curie-Weiss behavior. The Curie-Weiss fitting yields an effective magnetic moment (μ_{eff}) of 5.67 μ_B and a Curie temperature (θ) of 22 K.

Fig. 3(a) shows the M-H curves of $Ca_3Co_2O_6$ at 5 K and 10 K, indicating increased magnetic hysteresis with decreasing temperature below the T_{C2}. Additionally, the transition field H_c was determined from the dM/dH vs. H plot, as shown in the inset plot of Fig. 3(a), demonstrating an increase in the no. of magnetic steps (H_{c1}, H_{c2}, and H_{c3}) as the temperature decreases. Fig. 3(b) presents the M-H curves at 10 K with and without a 9-hour wait. Here, wait for the means sample was kept in the zero fields for 9 hours at 10 K before the measurements started, and in case of no wait, measurement was started without leaving the sample in the rest. Due to the glassy nature of $Ca_3Co_2O_6$ below T_{C2}, the sample becomes more stable during the wait, resulting in a lower saturation moment. Up to 3.5 T, both curves are nearly identical, but beyond 3.5 T, a measurable difference of about 0.2(μ_B/f.u.) is observed at 9 T.



(a) (b) (c)

FIGURE 3. (a) M vs. H curves at temperature T = 10 K and 5 K, (b) M vs. H curves at temperature T = 10 K with and without waiting of 9h and (c) Memory effect curves for $Ca_3Co_2O_6$.

The sample was cooled from ambient temperature to 2 K in a 100 Oe field to demonstrate magnetic memory. At 12 K, 8 K, and 4 K, cooling was paused, and the field was turned off for 1.5 hours to allow the sample to settle. After each pause, the field was reapplied, and cooling resumed. The resulting interrupted field-cooled cooling (IFCC) curve, shown in Fig. 3(c), exhibits step-like features at the interruption points. After reaching 2 K, the sample was continuously warmed in the same field, and the memory curve M(T) was recorded up to 30 K. For reference, a field-cooled warming (FCW) curve was measured without interruption. The memory curve follows the IFCC path up to the transition temperature (T_{C2}), indicating the presence of magnetic memory in the system below the T_{C2}.

CONCLUSION

Quasi-1-dimension spin-chain compound $Ca_3Co_2O_6$ is synthesized by the solid-state reaction method and the phase purity (single phase) of the compound has been confirmed by analyzing the XRD refinement. DC magnetization measurements were carried out to demonstrate the system's magnetic properties. Based on the M-T (ZFC-FC) data, the material undergoes a change from being paramagnetic to some degree of disorder antiferromagnetic state at a transition temperature of T_{C1}, then to a glassy state below T_{C2}. We have also investigated magnetization measurements after a waiting period which showed a reduced saturation moment of 0.2 μB/f.u. at 9T magnetic field. Furthermore, the system exhibited memory effects, as evidenced by magnetization measurements using the interrupted field cooling method.

ACKNOWLEDGMENTS

We acknowledge the CIF IIT Guwahati and DST India for the PPMS (SR/FST/PSII–037/2016).

REFERENCES

[1] Hardy V, Lambert S, Lees M R and Paul D M 2003 Specific heat and magnetization study on single crystals of the frustrated quasi-one-dimensional oxide $Ca_3Co_2O_6$ *Phys. Rev. B* **68** 14424

[2] Allodi G et al M R 2011 NMR study of magnetic order, metamagnetic transitions, and low-temperature spin freezing in $Ca_3Co_2O_6$ *Phys. Rev. B—Condensed Matter Mater. Phys.* **83** 104408

[3] Kageyama H, Yoshimura K, Kosuge K, Mitamura H and Goto T 1997 Field-induced magnetic transitions in the one-dimensional compound $Ca_3Co_2O_6$ *J. Phys. Soc. Japan* **66** 1607–10

[4] Fjellvåg H, Gulbrandsen E, Aasland S, Olsen A and Hauback B C 1996 Crystal structure and possible charge ordering in one-dimensional $Ca_3Co_2O_6$ *J. Solid State Chem.* **124** 190–4

[5] Sampathkumaran E V, Fujiwara N, Rayaprol S, Madhu P K and Uwatoko Y 2004 Magnetic behavior of Co ions in the exotic spin-chain compound $Ca_3Co_2O_6$ from Co 59 NMR studies *Phys. Rev. B—Condensed Matter Mater. Phys.* **70** 14437

[6] Aasland S, Fjellvåg H and Hauback B 1997 Magnetic properties of the one-dimensional $Ca_3Co_2O_6$ *Solid State Commun.* **101** 187–92

Edge States for a Ribbon Oriented in the Diagonal Direction in 2D Antiferromagnetically Ordered Semimetals

Garima Goyal[1, a)] and Dheeraj Kumar Singh[1]

[1]Department of Physics and Material Science, Thapar Institute of Engineering and Technology, Patiala-147004, Punjab, India

[a)] Corresponding author: ggarima60_phd20@thapar.edu

Abstract. We explore the nature of edge states in a 2D topological semimetallic state with antiferromagnetic (AFM) ordering in the presence of nearest-neighbor (NN) Rashba spin-orbit coupling (SOC). For this, we adopt a ribbon geometry, different from the conventional arrangement of horizontal or vertical, extended collinearly with the AFM ordering direction (π, π) such that the basis atoms belonging to same sublattice lie on one chain which alternates in between the chains of different sublattices. With this choice of ribbon orientation, we found that the edge state dispersion gaps in the magnetically ordered state, in contrast to the flat bands as obtained with the conventional choice of ribbon geometry. Our findings underscore the influence of ribbon orientation relative to the magnetic ordering direction on the nature of these edge states.

INTRODUCTION

Ever since the breakthrough discovery of topological semimetallic state in graphene, there is a considerable interest in exploring topological phases in diverse systems featuring protected band crossings. Several theoretical and experimental studies in this direction explored symmetry-protected topological phases in various systems, including Fe pnictides with striped magnetic order [1], systems protecting non-symmorphic symmetries [2], AFM ordered non-centrosymmetric systems [3] etc. Further, band crossings in graphene disappear when SOC is taken into account. This created a plethora of interest to investigate systems with protected band crossing in the presence of SOC. One of our recent works shows the existence of topological semimetallic state in the AFM ordered state when in-plane magnetic moments are considered in the presence of nearest-neighbor Rashba SOC λ[4]. For this state, many topological properties such as nature of edge states, single-particle induced QPI patterns, Chern number, have been well investigated.

Edge states play a crucial role in characterizing topological nature of a system. These states are the pairs of states, characterized by spin-momentum locking and propagating in opposite directions, appear as a bridge between conduction and valence bands. These states can be understood as one-dimensional topological insulator with bulk band gap possessing non-zero topological number. Edge states are found in numerous systems such as Dirac and Weyl semimetals or may even appear in the systems lacking magnetic ordering [5].

Dispersion of edge state is typically studied by considering chains of a ribbon extended in one direction while having a finite width in the perpendicular. In the ordered state with two sublattices, chains are conventionally considered to be extended either in (1,0) or (0,1) directions. With this usual consideration of ribbon with AFM order, atoms of different sublattices alternate in every chain and the spin magnetic moments align at an angle of 45° w.r.t. ribbon geometry. The corresponding edge state dispersion is thoroughly explored in our recent calculations [4]. However, a question of general curiosity comes into mind, what happens when the chains are considered to be arranged in the diagonal direction such that the magnetic moments align parallelly with the extended direction of the ribbon and the atoms of a particular sublattice sits on one chain which alternates in between chains of atoms belonging to different sublattices. This configuration presents a novel scenario that warrants further investigation, especially regarding its impact on edge state properties and the overall topological characteristics of the system.

In the present work, we explored the nature of edge states in the magnetically ordered AFM state by considering ribbon oriented at an angle of 45° with respect to (1,0) or (0,1) direction. We performed calculations by constructing a ribbon Hamiltonian when the ribbon is oriented either along $k_x = k_y$ or $k_y = -k_x$. Our observations indicate that for an even number of chains, edge states corresponding to the Weyl points are observed

in the unordered semimetallic state. However, the dispersion gaps when the magnetic ordering is introduced and the system is taken into the semimetallic state. The subsequent section details the model and ribbon Hamiltonians used for this arrangement, followed by a discussion of our results concerning this investigation.

MODEL HAMILTONIAN

We consider a 2D square lattice in which atoms are arranged in an AFM order as shown in figure 1. The lattice is composed to two sublattices A & B such that the atoms of sublattice A have spins oriented in the direction opposite to those of sublattice B. In order to study the AFM state with Rashba SOC, we consider a tight binding Hamiltonian with Hubbard interaction which is given by

$$H = t \sum_{<i,j>,\sigma} (d^{\dagger}_{i\sigma} d_{j\sigma} + h.c.) + \sum_{i} U n_{i\uparrow} n_{i\downarrow} + i\lambda \sum_{i} \sum_{\sigma\sigma'} (\nu_{i,i+\alpha}\, d^{\dagger}_{i,\sigma} d_{i+\alpha,\sigma'} \sigma_{\sigma\sigma'} + h.c.)$$

The first term denotes kinetic energy of an electron with spin σ arising from hopping from site $\boldsymbol{j}$ to the nearest neighbor site $\boldsymbol{i}$ where t is the overlap amplitude of the two wave functions. The second term is onsite Coulomb repulsion which is quartic in electron field operators while the last term represents NN SOC with λ being SOC parameter. Here $\alpha = +\hat{x}$ or $\hat{y}$ and $\nu_{i,i+\alpha} = \nu_{i+\alpha,i} = \pm 1$ depending on the orientation of two NN bonds. The hopping amplitude $t = -1$ is fixed in eV throughout. The onsite Coulomb repulsion term is meanfield decoupled self-consistently into quadratic form and the resulting Hamiltonian in the spin-sublattice basis is written in the following manner.

$$H_{mf} = \sum_{iab} \tau d^{\dagger}_{ia} \, (\boldsymbol{\sigma} \cdot \boldsymbol{\Delta}_i)_{ab} d_{ib}$$

where $\boldsymbol{\Delta}_i = \frac{U}{2}\left(m_{ix}\,\hat{x} + m_{iy}\,\hat{y} + m_{iz}\,\hat{z}\right)$ is the exchange field and $\tau = +1(-1)$ on sublattice A(B).

We examine the edge state dispersion by considering a ribbon geometry as discussed above with original axes as indicated by $X - Y$, the new rotated axes where the ribbon is oriented are denoted by $X' - Y'$ in figure 1. The ribbon oriented along $X' - Y'$, the atoms in one chain belongs to one sublattice while the neighboring chains contains atoms belonging to different sublattice. Note that the atoms in one chain (say, atoms of sublattice B) are placed at the center of two atoms of the neighboring chain (atoms of sublattice A) such that the distance between neighboring chains is $\frac{a}{\sqrt{2}}$, a is the lattice constant is set to be unity and $\lambda = 1$ is fixed throughout.

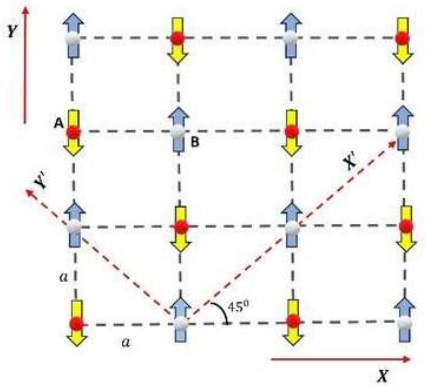


Figure 1: 2D AFM ordered square lattice with original axes shown by $X - Y$ while the rotated axes by $X' - Y'$. The red and grey circles denote basis atoms belonging to sublattice A & B respectively.

Considering the ribbon to be extended along X' but having a finite width along Y', the corresponding ribbon Hamiltonian H_{Rbx} has $2N \times 2N$ dimension with N being the number of chains of a ribbon.

$$H_{Rbx}(\boldsymbol{k}) = \begin{pmatrix} H_0 & H_1 & 0 & 0 & \cdots \\ H_1^{\dagger} & -H_0 & H_1 & 0 & \cdots \\ 0 & H_1^{\dagger} & H_0 & H_1 & \cdots \\ 0 & 0 & H_1^{\dagger} & -H_0 & \cdots \\ \vdots & \vdots & \vdots & \vdots & \ddots \end{pmatrix}$$

where $H_0 = \begin{pmatrix} 0 & -\Delta \\ -\Delta^{*} & 0 \end{pmatrix}$ and $H_1 = \begin{pmatrix} 2tcos(k_{x'}/\sqrt{2}) & -2i\lambda \sin(k_{x'}/\sqrt{2}) \\ 2i\lambda \sin(k_{x'}/\sqrt{2}) & 2tcos(k_{x'}/\sqrt{2}) \end{pmatrix}$

Here, H_0 denotes the coupling within the same chain while H_1 represents coupling between the neighboring chains.

RESULTS AND DISCUSSIONS

Figure 2 illustrates the edge state dispersion for a diagonally oriented ribbon for three different cases.

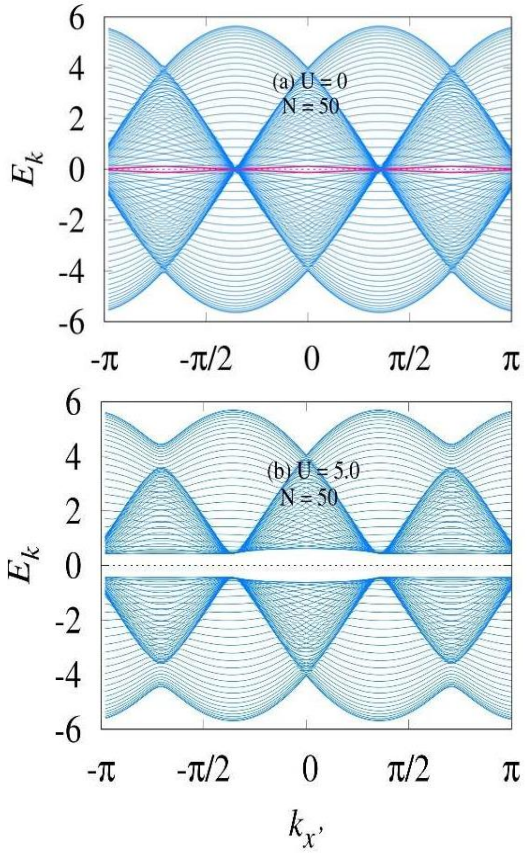


Figure 2: Edge state and bulk band dispersions are plotted for a ribbon extended in X' direction and projected onto 1D BZ having finite width $N = 50$ along Y' direction for (a) the paramagnetic state, $U = 0$ and (b) ordered semimetallic state, $U = 5.0$, keeping $\lambda = 1.0$ fixed.

Case-I: In the paramagnetic state ($U = 0$), for an even number of chains, $N = 50$ (fig. 2(a)), atoms in the first and the last chains belong to different sublattices with opposite spins giving helical nature to edge states. These edge states correspond to Weyl points identified in the energy dispersion of the semimetallic for $U = 0$ (fig.5(a) in reference [4]), highlighted in different colour for clarity. The band crossings are symmetrically located about $k_{x'}$=0, owing to the system's symmetry about $k_{x'} = k_{y'}$ and $k_{x'} = -k_{y'}$. The helical nature of edge states arises due to the system's inversion asymmetry induced by Rashba spin-orbit coupling (SOC).

However, when the number of chains is odd, a flat band is obtained in addition to the edge states corresponding to Weyl points (not shown). Moreover, these crossing points shifts with λ, moving towards high symmetry points for sufficiently large λ. This result has been extensively discussed in reference [6] for zigzag edges, which closely parallels our chosen ribbon configuration.

Case-II: In the AFM ordered semimetallic state, $U = 5.0$ (fig. 2(c)), the dispersion of edge states forms gaps leading to an insulating state. It is important to note that flat bands are obtained as the edge states which are the projections of Weyl points connecting opposite Chern numbers. Further, when the ribbon is extended in Y' direction, the nature of edge states remains the same in all the cases due to system's symmetry about [1,1] and [1, -1].

The above results concretely signify the orientation of the ribbon w.r.t. magnetic ordering direction on the nature of edge state dispersion.

ACKNOWLEDGMENTS

D.K.S. was supported through DST/NSM/R&D_HPC_Applications/2021/14 funded by DST_NSM and start-up research grant SRG/2020/002144 funded by DST-SERB.

REFERENCES

1. G. Goyal and D.K. Singh, *J. Phys.: Condens. Matter* **35** 365501 (2023).
2. S.M. Young and C.L. Kane, *Phys. Rev. Lett.* **115** 126803 (2015).
3. G. Goyal and D.K. Singh, *J. Phys.: Condens. Matter* **36** 265802 (2024).
4. A. Jain, G. Goyal, and D.K. Singh, Phys. Rev. B **110** 075134 (2024).
5. A. Lau and C. Timm, *Phys. Rev. B* **88** 165402 (2013).
6. K. Kubo, *J. Phys. Soc. Jpn.* **93** 024708 (2024).

Structure, Morphology and Magnetic Properties of $TmCrO_3$

Vishesh Sharma[1, a)], Sumit Pokhriyal[1, b)], Darren M. Stohr[2], Awanish Kumar Sharma[3], N. P. Lalla[4], and Shivani Sharma[2, 5]

[1]*Department of Physics, Graphic Era Hill University, Dehradun, India 248002.*
[2]*Kazuo Inamori School of Engineering, Alfred University, Alfred, New York 14802, United States.*

[3]*Department of Physics, Graphic Era Deemed-to-be University, Dehradun, India 248002.*
[4]*UGC-DAE Consortium for Scientific Research, Indore, MP India.*
[5]*National High Magnetic Field Laboratory, Tallahassee, FL 32310, United States.*

[a)]*Corresponding author: phy.vishesh@gmail.com*
[b)]Corresponding author: pl.sumit@gmail.com

Abstract. The structure, morphology, and magnetic behaviour of $TmCrO_3$ are presented here. The crystal structure and phase purity of the sample were confirmed using Rietveld refinement of X-ray and neutron powder diffraction data. Scanning electron microscopy (SEM) equipped with energy dispersive analysis of X-ray (EDX) have been employed to study grain morphology, compositional homogeneity and elemental composition. Temperature dependent DC magnetization measurement revealed an antiferromagnetic transition at 125 K and a spin reorientation transition below 5 K, accompanied by negative magnetization, confirming the anticipated magnetic behavior of $TmCrO_3$.

INTRODUCTION

The rare earth chromates $RECrO_3$ (RE being rare earths), due to their intriguing uses in solid oxide fuel cells, thermoelectric devices, spintronic devices, and multiferroics have sparked considerable curiosity over the past several years [1,2,3,4]. These compounds crystallize in an orthorhombic crystal symmetry, comprising 4 formula units within each unit cell [2]. R^{3+} sublattice orders at very low temperatures, although the Cr^{3+} sublattice typically orders at a higher Néel temperature (T_N = 110–180 K). Temperature induced negative-magnetization (NM) (also called magnetization reversal) is usually observed for most of the members of this family, and it is expected to arise from the AFM interaction between paramagnetic R^{3+} moments and CAFM ordered Cr^{3+} moments below T_N. Magnetization reversal is the process by which the direction of net magnetization in a material changes from positive to negative at a specified temperature known as the compensation temperature in an applied external magnetic field.

Numerous bulk homogeneous systems, including $YbCrO_3$, $SmCrO_3$, $NdMnO_3$, and $Gd_{1-x}Y_xCrO_3$, reveal a signature of magnetization reversal at different temperatures and magnetic fields, indicating involvement of several mechanisms, according to recent investigations [1,2,5,6]. For instance, the exchange coupling between Nd and canted Mn moments induced the sign reversal of magnetization and EB phenomena in $NdMnO_3$, whereas in $YFe_{0.5}Cr_{0.5}O_3$, it was attributed to the rivalry between single-ion magneto-crystalline anisotropy and the Dzyaloshinskii-Moriya interaction. [5,7]. In $Gd_{1-x}Y_xCrO_3$, the magnitude of negative magnetization increases with Y^{3+} substitution, due to enhanced antiparallel alignment of Gd^{3+} moments with Cr^{3+} moments driven by Y-induced structural distortions [6], for $YbCrO_3$ and $SmCrO_3$, the origin of NM has been explained in terms of the competition between the antiparallel coupled rare-earth and transition metal ion's moment [1,2,3]. In the present work, we report the structure, morphology, and magnetic characterization of $TmCrO_3$ using X-ray diffraction (XRD), SEM, EDX, and dc-magnetization studies. Room temperature, crystal structure, and morphology of the sample are confirmed using Rietveld refinement of XRD data, SEM, and EDX analysis. The dc susceptibility behavior has been recorded to determine various magnetic transitions in the studied sample.

EXPERIMENTAL DETAILS

The solid state route has been utilized to synthesize $TmCrO_3$. The stoichiometric amounts of Tm_2O_3 and Cr_2O_3 have been mixed together, and the final sintering has been done at 1250°C. Phase purity of the sample has been checked using XRD equipped with Cu-Kα radiation and neutron powder diffractometer (NPD) at Echidna beam line, Australia. SEM/EDX studies have been performed using a field emission SEM at Alfred University, USA. Magnetic measurements were performed, employing a commercial SQUID magnetometer.

RESULTS AND DISCUSSION

Figure 1 shows the (a) XRD and (b) NPD pattern of the $TmCrO_3$ recorded in ambient conditions. The wavelength of the neutron beam used was 2.43 Å. Both the patterns were Rietveld refined with Fullprof program using orthorhombic symmetry, consistent with literature [4]. All Bragg peaks have been very well fitted with P*nma* space group, and no unaccounted peaks were detected, which indicates the single-phase nature of as prepared $TmCrO_3$. Refined lattice constants using neutron data are a=5.50231(8) Å, b=7.50266(8) Å, and c=5.21107(7) Å, which is consistent with XRD analysis. The value of χ^2 and the Bragg-R factor are mentioned in the respective figures. The occupancies of different atoms have been refined in NPD analysis and found to be fully consistent with the chemical formula. The Tm to Cr ratio is 0.95:1, consistent with EDAX analysis.

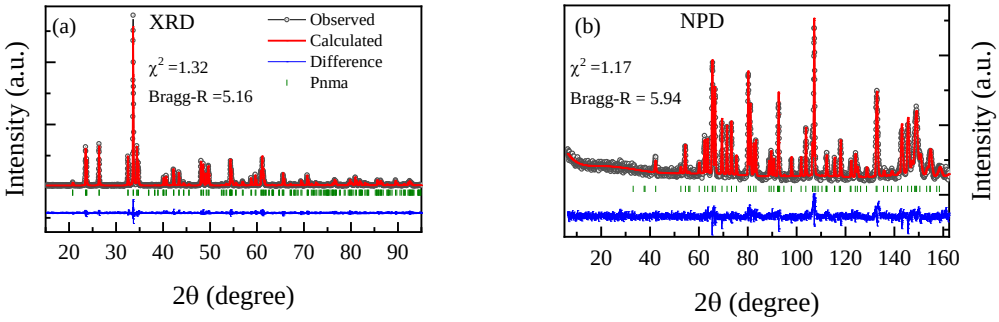


FIGURE 1. *Rietveld fit of (a) XRD and (b) NPD data. The goodness of fit parameters is given in the respective figures.*

Figure 2 (a-c) shows the SEM images in (a) secondary electron mode and (b) backscattered mode, along with (c) EDX spectra of $TmCrO_3$. $TmCrO_3$ powders consist of regular shaped grains, having a non-uniform size distribution. Moreover, the grain size varies from 0.4 to 3 microns. The backscattered image shows a uniform gray contrast of all the grains, confirming the single-phase nature of the sample. Similar images have been recorded at different locations. Additionally, EDX analysis revealed no evidence of impurity peaks, confirming the compounds' purity and uniform composition. The Tm to Cr ratio is 0.85:1, close to the expected value.

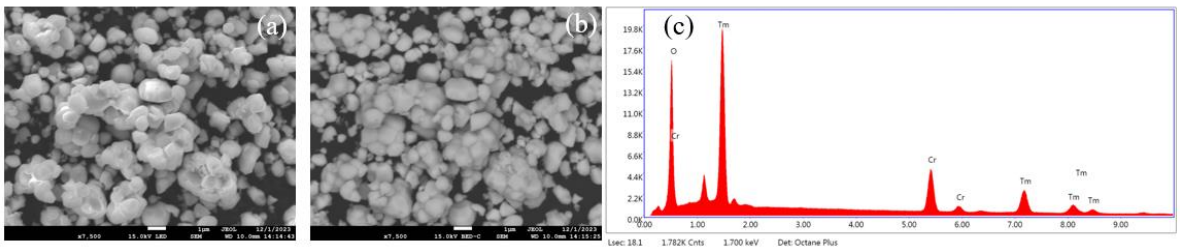


FIGURE 2. *SEM morphology and EDX analysis of $TmCrO_3$.*

Magnetization measurements on polycrystalline materials were conducted up to 7 Tesla throughout a temperature range of 2 to 300 K, with the findings displayed in figure 3(a,b). Figure 3(a) exhibits the ZFC and FC magnetic suceptibility (χ) measured with 0.1 T, exhibiting a canted AFM transition around 125 K. A spin reorientation transition is also observed below 5 K, accompanied by negative magnetization for 0.1 T. The

negative magnetization results from the antiparallel alignment of paramagnetic Tm moments opposite the Cr spins. With decreasing temperature, the magnetization value shows a decreasing trend and approaches zero at the compensation temperature of 18 K. The Curie-Weiss fit of the $1/\chi$ is shown in the inset of figure 3(a) for a temperature range of 150 to 300 K The effective paramagnetic moment is 8.58 μ_B, slightly less than the estimated value using Tm3+ and Cr3+ as magnetic cations. The value of the Weiss constant is -33 K, which indicates antiferromagnetic interaction in TmCrO3, consistent with the literature. [6]. For a range of H values recorded in the FCC mode, the magnetic susceptibility (χ = M/H). The unambiguous S shape curves were observed in M-*vs*-H data for temperatures below 30 K, as expected from a canted AFM system. However, for temperatures above 30 K, typical non saturating linear curves are observed as expected from an AFM phase.

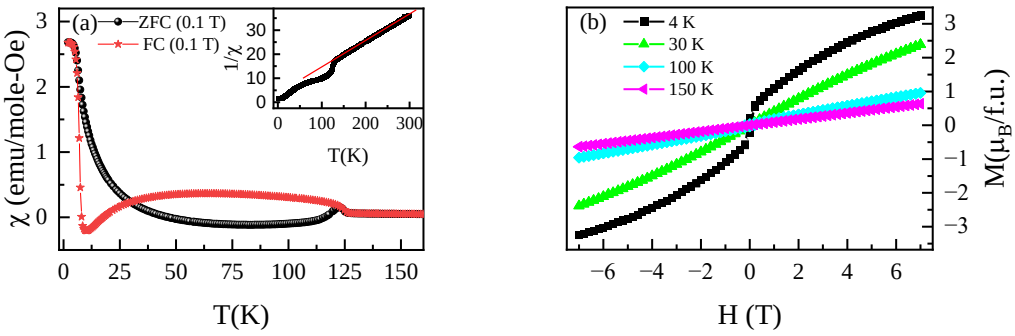


FIGURE 3. *(a) M-vs-T behavior of $TmCrO_3$ measured with 0.1 T in ZFC and FC mode. The inset presents the Curie-Weiss fit of the ZFC data. (b) Isothermal magnetization curves measured at different temperatures.*

CONCLUSIONS

$TmCrO_3$ crystallizes in an orthorhombic structure, confirmed by XRD and NPD results. SEM analysis confirms the homogeneity with uniform grain morphology, and the EDX spectra confirms single-phase nature of the sample. Magnetic tests revealed a canted antiferromagnetic phase transition about 125 K and a spin reorientation transition below 5 K, with negative magnetization detected at a compensation temperature of 18 K.

ACKNOWLEDGMENTS

Magnetic measurements were conducted out at the National High Magnetic Field Laboratory, which is supported by NSF Cooperative Agreement No. DMR-2128556 and the State of Florida.

REFERENCES

1. D. A. Kumar and S. M. Yusuf, Phys. Rev. Mater. 5, 124402 (2021).
2. T. Sau and P. Yadav, S. Sharma, R. Raghunathan, P. Manuel, V. Petricek, U. P. Deshpande, N. P. Lalla Phys. Review B103,144418(2021).
3. T. Sau, S. Sharma, P. Yadav, R. Baumbach, T. Siegrist, A. Banerjee, N. P. Lalla, Phys. Rev. B 106, 064413 (2022).
4. K. Yoshii,Mater. Res. Bull.47, 3243-3248 (2012).
5. A. Kumar, S. M. Yusuf, and C. Ritter,Phys. Rev. B 96, 014427 (2017).
6. P. Jain, S. Sharma, R. Baumbach, A. Kumar Yogi, I. Ishant, M. Majumder, T. Siegrist, M. K. Chattopadhyay, N. P. Lalla, Phys. Rev. B 109, 094410(2024).
7. J. Mao, Y. Sui, X. Zhang, X. Wang, Y. Su, Z. Liu, Y. Wang, R. Zhu, Y. Wang, W. Liu, X. Liu, Sol. Stat. Commun. 151, 1982-1985 (2011).
8. B. B. Dash and S. Ravi, J. Magn. Magn. Mater. 461, 91-99 (2018).

Large Magneto-caloric Effect near Room Temperature in $Ni_{37}Co_{13}Mn_{34}Ti_{16}$ alloy

Sandhya Negi[1,2,*], Anil Chouhan[1], Abhijit Chowdhury[3], Rashmi Singh[3] and Vishnu Kumar Sharma[1,2]

[1]*Magneto-Structural Studies Lab, Accelerator Physics and Synchrotrons Utilization Division, Raja Ramanna Centre for Advanced Technology, Indore, Madhya Pradesh-452013, India.*
[2]*Homi Bhabha National Institute, Training School Complex, Anushakti Nagar, Mumbai 400094, India.*
[3]*Photonic Materials Technology Section, Raja Ramanna Centre for Advanced Technology, Indore, Madhya Pradesh-452013, India.*

[*]Corresponding author*:* sandhyanegi@rrcat.gov.in

Abstract. We report a large magneto-caloric effect in $Ni_{37}Co_{13}Mn_{34}Ti_{16}$ alloy near room temperature across the magnetostructural transition. A maximum entropy change of nearly 8.6 $Jkg^{-1}K^{-1}$ was observed near 307 K for a magnetic field change of 70 kOe. We also observed the effect of heat treatment on the sample.

INTRODUCTION

Greenhouse gas emissions are a major factor driving global climate change. Air conditioning and refrigeration based on the vapour compression cycle are currently responsible for over 10% of greenhouse gas emissions [1]. Therefore, it is necessary to search for technologies alternative to conventional vapour compression based refrigeration. Magnetic refrigeration technology based on magnetocaloric effect (MCE), offers a promising solution as it is more energy efficient and environment friendly [2]. Generally, MCE is defined as the change in temperature (ΔT_{ad}) of a material due to adiabatic variation of applied magnetic field and entropy change (ΔS_m) during an isothermal field excursion. Hence, there is a need to find such materials that exhibit large ΔS_m and ΔT_{ad}. It is observed that materials undergoing a magneto-structural transition show a large entropy change across the transition, as the structural entropy contributes almost half of the total entropy change [3]. Various materials show magneto-structural transition such as $Gd_5(Si,Ge)_4$ family, La-Fe-Si family, MnAs , Fe-Rh and Heusler alloys [4].

Among these materials, Ni-Co-Mn-Ti all d-metal Heusler alloy system (rare-earth free material) is one such family that shows a giant MCE. In 2015, Wei et al. reported ferromagnetic martensite transformation for Ni-Co-Mn-Ti alloy [5]. A ΔS_m of nearly 18 $Jkg^{-1}K^{-1}$ around 265K for a magnetic field excursion of 5T was obtained for $Ni_{35}Co_{15}Mn_{35}Ti_{15}$ alloy [5]. An enhancement in MCE was observed in Ni-Co-Mn-Ti ribbons with ΔS_m of 27 $Jkg^{-1}K^{-1}$ for magnetic field change of 2T [6]. A heat treatment process was optimized for Ni-Co-Mn-Ti alloy leading to sharp phase transitions in bulk alloys with ΔS_m of up to 38 $Jkg^{-1}K^{-1}$ for a magnetic field change of 2T [7].

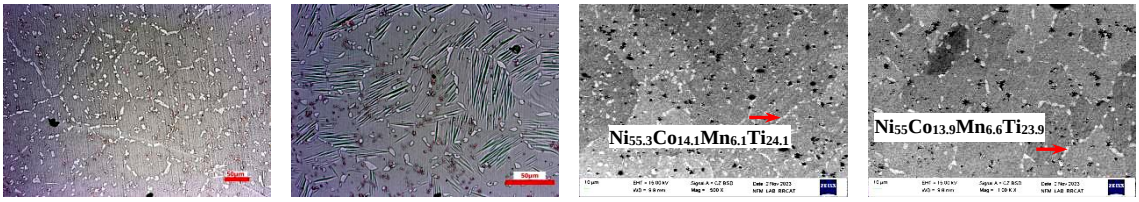
In this study, we examine the magnetocaloric properties of one of the composition of Ni-Co-Mn-Ti alloy.

EXPERIMENTAL DETAILS

$Ni_{37}Co_{13}Mn_{34}Ti_{16}$ alloy was synthesized by arc melting the constituent elements under a high purity argon atmosphere. The resultant sample button was remelted four to six times to ensure the proper mixing of elements. The sample was cut into two pieces for subsequent heat treatment process. Both pieces of the sample were sealed in a quartz tube under argon atmosphere and annealed at 1025^0C for 4 days for homogenization [7]. One of the pieces of alloy was slowly cooled to room temperature (RT) at a rate of 2K/min, while the other one was rapidly quenched in ice water bath. Optical metallography was performed on heat treated samples after polishing and etching the sample surfaces. The field emission scanning electron microscopy (FESEM) and energy dispersive spectroscopy (EDS) measurements (FESEM, Car Zeiss, sigma02, Germany) were carried out to know the microstructure and compositions of the samples. AC-susceptibility measurement as a function of temperature was performed on a home-made single stage CCR based set-up on both samples. Temperature dependent magnetization (M-T) measurements were performed on the slow cooled and quenched samples at various fields using a commercial SQUID magnetometer. The isothermal entropy change (ΔS_m) was calculated using M-T measurements.

RESULTS AND DISCUSSIONS

Figure 1 shows optical metallography results and corresponding FESEM images of the samples at room temperature. The formation of grains and precipitation of second phase (white colour) along the grain boundaries are clearly observed in both samples. EDS measurement confirms that the second phase is Ni rich and Mn deficient. The primary phase (grey colour) composition ($Ni_{36.8}Co_{13.4}Mn_{33.7}Ti_{16}$) closely matches the nominal composition in the quenched (Q) sample, while it is Ni deficient ($Ni_{34.2}Co_{13.4}Mn_{36.5}Ti_{15.4}$) in the slow-cooled (SC) sample. However, the average composition over a large area is quite close to the nominal composition. Martensitic twins are noticed in optical metallography image of quenched sample. Additionally, a third Ti-rich phase, appearing as dark flower-like pattern (black colour) is also present in both samples.



(a) (b) (c) (d)

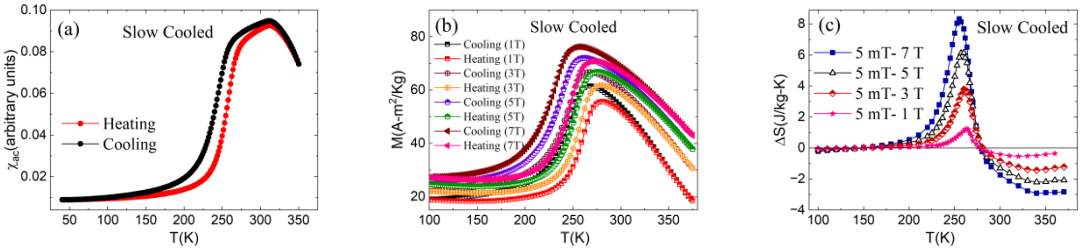
FIGURE 1. Optical metallography images of (a) $Ni_{37}Co_{13}Mn_{34}Ti_{16}$ (SC), (b) $Ni_{37}Co_{13}Mn_{34}Ti_{16}$ (Q) samples. FESEM images of (c) $Ni_{37}Co_{13}Mn_{34}Ti_{16}$ (SC), (d) $Ni_{37}Co_{13}Mn_{34}Ti_{16}$ (Q) samples.

AC susceptibility measurements were performed to know about the existence of magnetic phase transition (Figures 2(a), 2(d)). In both samples, an initial increase in susceptibility during cooling from high temperatures is followed by a subsequent decrease. This behaviour indicates the possibility of two magnetic transitions. The observed thermal hysteresis across the transition at lower temperature indicates a first order phase transition in both samples. The presence of martensitic twins in the microstructure along with hysteresis in AC susceptibility measurement of quenched sample, indicating a combined martensitic and magnetic transition at lower temperatures. In addition, the occurrence of thermal hysteresis across both the transitions in quenched sample suggests the possibility of an overlap between the first order magneto-structural transition and the second order transition. Along with these results it is also observed that the transitions appear broader in the slow-cooled sample and it could be due to the presence of more amount of second phase (disorder).

Temperature dependent magnetization measurements were performed on both samples at various fields. Figures 2(b) and 2(e) show the M-T curves for both samples at a few representative fields. A thermal hysteresis between the field-cooled-cooling (FCC) and the field-cooled-warming (FCW) curves, similar to that seen during AC susceptibility measurements, was observed. ΔS_m is determined by using the following Maxwell's relation [8]:

$$\Delta S_m(T,\Delta H) = \int_{H_1}^{H_2} \left(\frac{\partial M}{\partial T}\right)_{H,P} dH.$$

Figures 2(c) and 2(f) show the isothermal magnetic entropy change as a function of temperature for a few representative field excursions. A maximum entropy change of nearly 8.6 $Jkg^{-1}K^{-1}$ is obtained for magnetic field change of 7T in the case of quenched sample at 307K, which corresponds the region of magneto-structural transition.



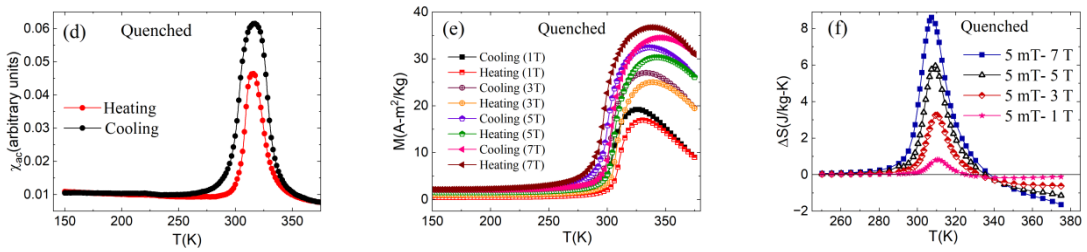


FIGURE 2. Temperature dependent AC-susceptibility, magnetization and entropy change for (a), (b), (c) $Ni_{37}Co_{13}Mn_{34}Ti_{16}$ (SC) and (d), (e), (f) $Ni_{37}Co_{13}Mn_{34}Ti_{16}$ (Q) samples respectively.

CONCLUSION

$Ni_{37}Co_{13}Mn_{34}Ti_{16}$ alloy was synthesized for exploring earth abundant materials which undergo a magneto-structural transition near room temperature. The sample was characterized using optical metallography, scanning electron microscopy and electron dispersive spectroscopy. AC-susceptibility measurement was performed on both samples. Magneto-caloric effect was estimated by temperature dependent magnetization measurement at various fields. The maximum value of entropy change is less than that observed in pure Gd (13.2J/kg-K for the magnetic field excursion of 7T [9]), which is mostly used in prototype proof-of-concept magnetic refrigerators. Our study shows that the working temperature range of the NiCoMnTi alloy system can be tuned by suitable heat treatment process. These results show that Ni-Co-Mn-Ti alloy has a potential to be a good candidate as a magnetic refrigerant.

ACKNOWLEDGMENT

The authors acknowledge Dr. M A Manekar for scientific discussion. The authors also acknowledge the help of SCRF Cavity Characterization and Cryogenics Section, RRCAT for providing liquid helium required for magnetization measurements and HBNI-RRCAT for the financial support.

REFERENCES

1. Y. Dong, M. Coleman, S.A.Miller, Annu. Rev. Environ. Resour. **46**, 83 (2021).
2. V. Franco, J. Blázquez, B. Ingale, A. Conde, The Magnetocaloric Effect and Magnetic Refrigeration Near Room Temperature: Materials and Models, Annu. Rev. Mater. Res. **42**, 42 (2012) .
3. Pecharsky V K, Holm A P, Gschneidner K A Jr and Rink R, Phys. Rev. Lett. **91**, 197204 (2003) .
4. Julia Lyubina, J. Phys. D: Appl. Phys. **50,** 053002 (2017).
5. Z. Y. Wei, E. K. Liu, J. H. Chen, Y. Li, G. D. Liu, H. Z. Luo, X. K. Xi, H. W. Zhang, W. H. Wang, and G. H. Wu, Appl. Phys. Lett. **107**, 022406 (2015).
6. H. Neves Bez, A. K. Pathak, A. Biswas, N. Zarkevich, V. Balema, Y. Mudryk, D. D. Johnson, and V. K. Pecharsky, Acta Mater. **173**, 225 (2019).
7. A.Taubel,B.Beckmann, L. Pfeuffer, N. Fortunato, F. Scheibeel, S. Ener, T. Gottschall, K. P. Skokov, H. Zhang, O. Gutfieisch, Acta. Materialia **201**, 425 (2020).
8. A. M. Tishin and Y. I. Spichkin, *The Magnetocaloric Effect and its Applications* (IOP Publishing Ltd., Bristol, UK, 2003).
9. S. M. Benford and G. V. Brown, J. Appl. Phys. **52,** 2110 (1981).

Beyond ferromagnetic resonance: Effect of inertia tensor on dynamic susceptibility

Subhadip Ghosh[1, a)] and Ritwik Mondal[1]

[1]Department of Physics, Indian Institute of Technology (ISM) Dhanbad, IN-826004, Dhanbad, India

[a)]Corresponding author: *22dr0226@iitism.ac.in*

Abstract. Ultrafast manipulation of magnetic order with magnetic inertia provides an opportunity for advancement of the data storage devices. Several theoretical studies on magnetic inertia have considered inertia as a scalar quantity. Here we investigate the effect of tensorial inertia on the dynamic susceptibility for ferromagnets, as recent works suggest inertia to be a tensor. We found the inertial susceptibility response at THz frequency along with the traditional ferromagnetic resonance at GHz. Their sense of rotation is opposite to each other.

INTRODUCTION

To develop faster and efficient magnetic storage devices, as well as other spintronic devices, an understanding of magnetic spin manipulation in the femtosecond (fs) and picosecond (ps) time scale is rather important [1]. Traditionally, such ultrafast manipulation of the spins can be explained through the spin precessional motion around an effective field governed by the Landau-Lifshitz-Gilbert (LLG) equation. The dynamic susceptibility response of the precessional motion can be observed in the ferromagnetic resonance (FMR) experiments. Such FMR occurs in GHz frequencies in ferromagnets (FMs). However, the recent discovery of spin inertia leading to magnetic inertial dynamics indicates that ferromagnetic spins can be manipulated at higher frequencies, e.g., THz. [4]. Such dynamics can be modelled by using the inertial Landau-Lifshitz-Gilbert (ILLG) equation as in Eq. (1). The origin of the magnetic inertial dynamics has been debated and limited in the literature. However, it has been shown that the magnetic inertia originates from the higher-order spin-orbit coupling. [5]. The magnetic inertial relaxation time has been calculated from first first-principles torque-torque correlation model, and it has a time scale of a few hundred femtoseconds [6]. This fact provides an opportunity in the field of spin manipulation of FM spins at ultrafast time scales, i.e., picoseconds [7]. In several studies, it is anticipated that the inertia parameter η is a tensorial quantity [5]. Here we explore the effect of tensorial inertia on the dynamic susceptibility for FM, considering linear response theory. Our results show that the tensorial magnetic inertia changes the susceptibility response.

MATHEMATICS

We can write the ILLG equation, including the Gilbert damping tensor and the inertia tensor as

$$\frac{\partial \vec{M}}{\partial t} = -\gamma \vec{M} \times \overrightarrow{H_{eff}} + \frac{\vec{M}}{M_0} \times \left(\Gamma \cdot \frac{\partial \vec{M}}{\partial t} \right) + \frac{\vec{M}}{M_0} \times \left(\Lambda \cdot \frac{\partial^2 \vec{M}}{\partial t^2} \right) \qquad (1)$$

Equation (1) contains spin precession around the effective field $\overrightarrow{H_{eff}}$ with γ a gyromagnetic ratio, the Gilbert damping with a damping tensor α , which is a dimensionless quantity, and the inertia tensor □□ which has a dimension of time. We can decompose the inertia tensor (□) into symmetric and antisymmetric parts, which have already been investigated for the Gilbert damping tensor in Ref [8]. The symmetric part can be written as $\Lambda_{ij}^{sym} = \eta\delta_{ij} + I_{ij}$, where $\delta_{ij}$is the Kronecker delta symbol and I_{ij} is a symmetric tensor. Also, the antisymmetric part can be written as $\Lambda_{ij}^{anti-sym} = \epsilon_{ijk}\overrightarrow{D_k}$ with ϵ_{ijk} as Levi-Civita symbol, and $\vec{D}$ is a vector. Using such decomposition in Eq. (1), one can arrive at the form,

$$\frac{\partial \vec{M}}{\partial t} = -\gamma \vec{M} \times \overrightarrow{H_{eff}} + \frac{\alpha}{M_0}\left(\vec{M} \times \frac{\partial \vec{M}}{\partial t}\right) + \frac{\vec{M}}{M_0} \times \left[\eta \frac{\partial^2 \vec{M}}{\partial t^2} + \left(I \cdot \frac{\partial^2 \vec{M}}{\partial t^2}\right) - \left(\vec{D} \times \frac{\partial^2 \vec{M}}{\partial t^2}\right)\right] \quad (2)$$

Note that we have used the scalar Gilbert damping α in this case. The decomposition of the inertial tensor leads to three terms in Eq.(2), where the first term represents the isotropic scalar inertial dynamics with inertial relaxation time η. The second term represents the anisotropic inertial dynamics, and the third term gives the chiral inertial dynamics with the chiral inertia vector $\vec{D}$.

In this study, we consider the effect of anisotropic inertia and chiral inertia on the dynamic susceptibility for ferromagnets (FM). For a single-sublattice FM, we keep the Gilbert damping parameter (α) as a scalar quantity, and consider the ground state is designated by $\vec{M} = M_0\hat{z}$, and it is placed in an external field $\overrightarrow{H_{eff}} = H_0\hat{z}$. Such a model setup is plausible under the equilibrium condition. The free energy of this system is given by $F = -M_0H_0 - \frac{KM_z^2}{M_0^2}$ where K the onsite anisotropy. From this free energy expression, we calculate the effective field as

$$\overrightarrow{H_{eff}} = -\frac{\partial F}{\partial \vec{M}} = \left(H_0 + \frac{2KM_z}{M_0^2}\right)\hat{z} \quad (3)$$

Now, a small in-plane field $h(t)$ will induce a small magnetization $m(t)$ so that the total magnetization will be $\vec{M} = M_0\hat{z} + \overrightarrow{m(t)}$, where $|m| << M_0$ and $\vec{D} = D_0\hat{z}$. In the limit of linear response theory, now we can write the transverse components of Eq. (2) in the following form,

$$h_x = \frac{1}{\gamma M_0}\left[\Omega_0 m_x + \alpha\partial_t m_x + \eta\partial_{tt} m_x + D_0\partial_{tt} m_y + I_{xx}\partial_{tt} m_x + I_{xy}\partial_{tt} m_y - \partial_t m_y\right] \quad (4)$$

$$h_y = \frac{1}{\gamma M_0}\left[\Omega_0 m_y + \alpha\partial_t m_y + \eta\partial_{tt} m_y - D_0\partial_{tt} m_x + I_{yx}\partial_{tt} m_x + I_{yy}\partial_{tt} m_y + \partial_t m_x\right] \quad (5)$$

With $\Omega_0 = \frac{\gamma}{M_0}(H_0M_0 + 2K)$. The matrix of the following equations will be,

$$\begin{pmatrix} h_x \\ h_y \end{pmatrix} = \frac{1}{\gamma M_0}\begin{pmatrix} \Omega_0 + \alpha\partial_t + (\eta + I_{xx})\partial_{tt} & -\partial_t + (D_0 + I_{xy})\partial_{tt} \\ \partial_t + (-D_0 + I_{yx})\partial_{tt} & \Omega_0 + \alpha\partial_t + (\eta + I_{yy})\partial_{tt} \end{pmatrix}\begin{pmatrix} m_x \\ m_y \end{pmatrix} \quad (6)$$

We move to a circularly polarized basis with $m_\pm = m_x \pm im_y = me^{\pm i\omega t}$ and $h_\pm = h_x \pm ih_y = he^{\pm i\omega t}$further we consider the off-diagonal elements on the symmetric tensor I , i.e $I_{xy} = I_{yx} = 0\ and\ \ I_{xx} = I_{yy}$. Putting this into (6), we get a diagonalized matrix,

$$\begin{pmatrix} h_+ \\ h_- \end{pmatrix} = \frac{1}{\gamma M_0}\begin{pmatrix} \Omega_0 - \omega + i(\alpha + D_0\omega)\omega - (\eta + I_{xx})\omega^2 & 0 \\ 0 & \Omega_0 - \omega - i(\alpha + D_0\omega)\omega - (\eta + I_{xx})\omega^2 \end{pmatrix}\begin{pmatrix} m_+ \\ m_- \end{pmatrix} \quad (7)$$

Compared to the equation, $m_\pm = \chi_\pm h_\pm$ we can define the dynamic susceptibility for FM as,

$$\chi_\pm = \frac{\gamma M_0}{\Omega_0 \pm i(\alpha + D_0\omega)\omega - (\eta + I_{xx})\omega^2 - \omega} \quad (8)$$

The real and the imaginary parts of susceptibility are given by,

$$Re(\chi_\pm) = \gamma M_0 \frac{\Omega_0 - \omega - (\eta + I_{xx})\omega^2}{[\Omega_0 - \omega - (\eta + I_{xx})\omega^2]^2 + (\alpha + D_0\omega)^2\omega^2} \quad (9)$$

$$Im(\chi_\pm) = \pm\gamma M_0 \frac{(\alpha + D_0\omega)\omega}{[\Omega_0 - \omega - (\eta + I_{xx})\omega^2]^2 + (\alpha + D_0\omega)^2\omega^2} \quad (10)$$

The real and the imaginary parts of susceptibility are plotted as a function of frequency at FMR in Fig.1(d) without the magnetic inertial effects. However, including isotropic scalar inertia (η), we obtain inertial susceptibility response at THz frequency in Fig.1(a) along with the GHz FMR response, which we don't show here. Further including the anisotropic inertia (I_{xx}) in Fig.1(b), we obtain that the response is shifted in frequency. Including chiral inertia (D_0) in Fig.1(c), we have observed that the curves are wider due to the enhancement in effective

damping. It is important to note that the inertial susceptibility response is opposite to the FMR response. It is because the inertial motion has the opposite sense of rotation to the precessional one. Such behaviour can be observed when we compare the susceptibility responses in Fig. 1(d) with others.

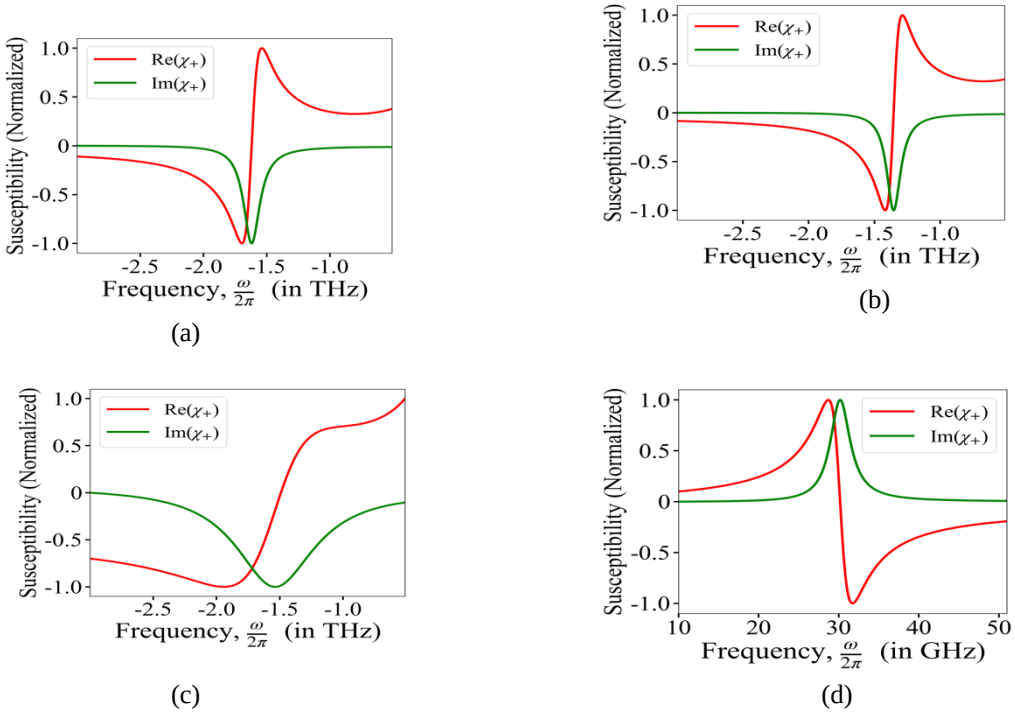


FIGURE 1. Susceptibility as a function of resonance frequency for FM with inertia, i.e., (a) $\eta = 100\ fs, I_{xx} = 0, D_0 = 0$, (b) $\eta = 100fs, I_{xx} = 20fs, D_0 = 0$, (c) $\eta = 100fs, I_{xx} = 0, D_0 = 20fs$. However, (d) shows the susceptibility response without inertia, i.e. $\eta = 0, I_{xx} = 0, D_0 = 0$. The susceptibility response sign changes sign in (d) compared to others because, without inertia, the precession mode has the opposite rotational sense compared to the nutation mode with inertia.

ACKNOWLEDGMENTS

We acknowledge the financial support provided by the Startup Research Grant (SRG) from SERB under Project No. SRG/2023/000612 and the faculty research scheme at IIT(ISM) Dhanbad, India, under Project No. FRS(196)/2023-2024/PHYSICS..

REFERENCES

1. E. Beaurepaire, J.-C. Merle, A. Daunois, and J.-Y. Bigot, "Ultrafast spin dynamics in ferromagnetic nickel", Phys. Rev. Lett. **76**, 4250 (1996).
2. K. Neeraj, N. Awari, S. Kovalev, D. Polley, N. Zhou Hagstr¨om, S. S. P. K. Arekapudi, A. Semisalova, K. Lenz, B. Green, J.-C. Deinert, I. Ilyakov, M. Chen, M. Bawatna, V. Scalera, M. d'Aquino, C. Serpico, O. Hellwig, J.-E. Wegrowe, M. Gensch, and S. Bonetti, "Inertial spin dynamics in ferromagnets", Nat. Phys. **17**, 245 (2021).
3. E. Olive, Y. Lansac, M. Meyer, M. Hayoun, and J.-E. Wegrowe, "Deviation from the Landau-Lifshitz-Gilbert equation in the inertial regime of the magnetization", J. Appl.Phys. **117**, 213904 (2015).
4. T. Kikuchi and G. Tatara, Spin dynamics with inertia in metallic ferromagnets, Phys. Rev. B **92**, 184410 (2015).
5. R. Mondal, M. Berritta, A. K. Nandy, and P. M. Oppeneer, "Relativistic theory of magnetic inertia in ultrafast spin dynamics", Phys. Rev. B **96**, 024425 (2017).
6. S. Bhattacharjee, L. Nordstr¨om, and J. Fransson, "Atomistic spin dynamic method with both damping and moment of inertia effects included from first principles", Phys. Rev. Lett. **108**, 057204 (2012).
7. S. Giordano and P.-M. D´ejardin, "Derivation of magnetic inertial effects from the classical mechanics of a circular current loop", Phys. Rev. B **102**, 214406 (2020).
8. P. Dhali and R. Mondal, "Theory of tensorial gilbert damping in antiferromagnets", J. Phys.: Condens. Matter **36**, 255804 (2024).

Characterization of CeO_2 Nanoparticles with Er^{3+} Doping: Insights from X-ray Diffraction to Magnetic Behavior

R. Niruban Bharathi[1*] and G. Rekha[2]

[1] *Department of Physics, Sri Sai ram Institute of Technology, West Tambaram, Chennai, Tamil Nadu 600044, India.*
[2] *Department of Physics, Science & Humanities, Chennai Institute of Technology, Sarathy Nagar, Kundrathur, Chennai-600069, Tamilnadu, India.*

[1]*Corresponding author: nirubanphd@gmail.com, +91-9790461291*

Abstract. This work reports the synthesis and characterization of Er doped CeO_2 nanoparticles prepared by the combustion method. X-ray diffraction patterns revealed that all the synthesized samples dominate CeO_2 cubic fluorite structure. Absorption spectra analyses report a decrease in bandgap energy for Er-substituted CeO_2 samples from 3.013 to 2.81 eV. The ferromagnetic properties of the samples have been investigated at room temperature by the vibrating sample magnetometer. The origin of magnetism in pure and doped CeO_2 system has been analyzed through F-center mechanism.

Keywords: Cerium Oxide, Dilute Magnetic Semiconductors, Cubic fluorite Structure, Ferromagnetism and F-center mechanism.

INTRODUCTION

Dilute magnetic semiconducting (DMS) produced by replacing non-magnetic cations by transition metals or rare-earth ions have garnered considerable interest among the researchers due to their potential applications in nano-spintronics having a unique feature of displaying semiconducting and ferromagnetic properties at room temperature concurrently [1,2]. The transition metal oxide based DMS such as ZnO, TiO_2, SnO_2 In_2O_3 and NiO_2 has broadly investigated and reported earlier [3]. Recently, rare-earth based DMS especially CeO_2 nanoparticles has evolved with great promise for use in spintronics devices due to its high reversible oxidation state, strong chemical stability and less toxic nature [4]. Considerable research on transition metal doped CeO_2 nanoparticles for spintronics applications have been reported earlier [5]. Based on these reports, creation of oxygen vacancy (V_O) in the lattice is key factor to realize room temperature ferromagnetism (RTFM) in CeO_2 nanoparticles [6]. Nowadays, rare-earth metals ions doped CeO_2 nanoparticles can also result in significant origination of oxygen vacancies in the host lattice as similar to transition metals doping. Particularly, incorporation of Er^{3+} ions into CeO_2 DMS is of particular interest due to the distinctive optical and electrical characteristics introduced by these ions. [7]. Numerous procedures can be followed to synthesize nanocrystalline materials like CeO_2 such as the chemical precipitation method, hydrothermal method, solvothermal method, polymer pyrolysis method, sonochemical method, etc. Of the various methods available, citrate–nitrate auto combustion method is a cost effective and simpler method for the synthesis of homogeneous nanoparticles. In this letter, we study effect of erbium concentration on the structure, optical and magnetic properties of CeO_2 nanoparticles synthesized using citrate–nitrate auto combustion technique.

EXPERIMENTAL PROCEDURES

The typical synthesis process is as follows: Stoichiometric amount of Cerium nitrate hexahydrate ($Ce(NO_3)_3{\cdot}6H_2O$, 99.9%), Erbium (III) nitrate hydrate ($Er(NO_3)_3.xH_2O$, 99.9%) and Citric acid anhydrous ($C_6H_7O_8$, 99.9%) were dissolved in the distilled water under continuous stirring for 2 hours at 60º C to form a viscous gel. The obtained gel is heated on an electric mantle until it burnt to form a fluffy powder. The obtained power was grounded and calcined at 800º C for 4 hours. The crystallographic study was using X- ray powder diffractometer (XRD) (Model: BRUKER D8 ADVANCE) using Cu-Kα radiation (λ = 1.54056 Å). The optical patterns of nanoparticles are carried out by Ultraviolet- Diffuse Reflectance optical spectrometer (UV-DRS) (Model: PERKIN ELMER LAMBDA 25). Magnetic properties are recorded by Vibrating Sample Magnetometer. The magnetic properties were investigated using vibrating sample magnetometer (VSM) (Model: LAKE SHORE 7404).

RESULTS AND DISCUSSION

Structural Analysis

The XRD pattern of pristine and Er doped CeO_2 nanoparticles are shown in Fig. 1 and the peaks from the planes (111), (200), (220), (311), (222), (400) and (331) of all the samples have the cubic fluorite structure in good agreement with the JCPDS card No. 81-0792, without any other impurity peaks present in it, proving thoroughly incorporated Er^{3+} into the CeO_2 host. The estimated value of crystallite size, lattice constant and volume of the samples were listed in Table. 1 suggests that the addition of dopants ions limits crystalline growth and leads to a decrease in crystallite size. The linear increase in lattice constant values may ascribed due to the incorporation of Er^{3+} ions into the host lattice. The difference in the ionic radius plays an important role in variation of volume of the lattice as Er^{3+}, with a larger ionic radius, is replaced by Ce^{4+} host atom, causing an expansion in the volume [8].

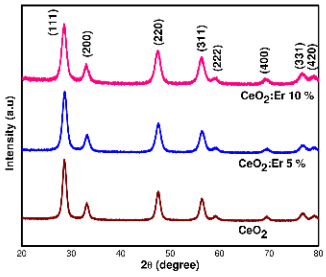


Fig. 1

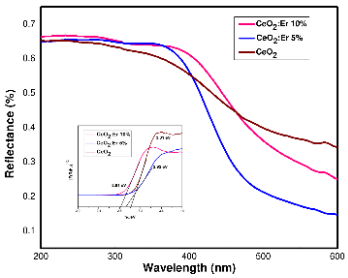


Fig. 2

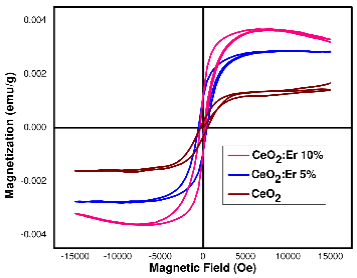


Fig. 3

Figure 1 X-ray diffraction patterns of pure and Er doped CeO_2 nanoparticles, **Figure 2** UV-DRS spectra of pure and Er doped CeO_2 nanoparticles, **(Inset)** Band gap of pure and Er doped CeO_2 nanoparticles and **Figure 3** M–H loops of pure and Er doped CeO_2 nanoparticles

Optical Analysis

Figure 2 shows the diffuse reflectance spectra of pure and Er doped CeO_2 samples. It is seen that the absorption edge of pure CeO_2 sample was at 271 nm in the ultraviolet region which attributes to the charge-transfer transition from 2P valence band of O^{2-} to 4f band of Ce^{4+} [9] and the absorption edges starts to red shift (below 400 nm) with varying Er concentration accredits to interfacial polaron effect emerging from electron–phonon interaction [10]. The band gap of 5% and 10% Er doped CeO_2 decreases to 2.92 eV and 2.81 eV from 3.013 eV of CeO_2 as shown in Fig. 3 (Inset). Addition of Er ions results in the origination of new ground and excited f-energy states in the mid band of CeO_2 and these states starts to traps many excited electrons originating from O^{2-} 2p level resulting in the shrinkage of bandgaps on doping [11].

Magnetic Analysis

Figure 3 shows the M–H curves of undoped and Er-doped CeO_2 nanoparticles measured at room temperature. All samples exhibit ferromagnetic behavior, and the corresponding magnetic parameters like saturation magnetization (M_S), Remanent magnetization (M_R) and coercivity (H_C) have been determined and are listed in Table 1. The room temperature ferromagnetism in pure and doped CeO_2 is often affiliated with F center mechanism involves oxygen vacancies in the host lattice. In pristine CeO_2, a significant concentration of oxygen vacancies and Ce^{3+} ions were present in the CeO_2 nanoparticles. The oxygen vacancies can create local magnetic moments. These vacancies can trap electrons, which in turn interact with the Ce^{3+} ions nearby. The Ce^{3+} ion has an electronic configuration where the 4f orbitals are partially filled, specifically with one unpaired electron. The unpaired electrons in the Ce^{3+} ions and those associated with the oxygen vacancies can engage in an exchange interaction. Thus the exchange interaction results in a net magnetic moment, which can give rise to ferromagnetic behavior in CeO_2 nanoparticles [12]. When Erbium (Er^{3+}) ions are substituted into the CeO_2 lattice, they replace some of the Cerium (Ce^{4+}) ions. Since Er^{3+} has a different oxidation state compared to Ce^{4+}, this substitution induces changes in the local electronic environment of the lattice. This replacement of Ce^{4+} ions with Er^{3+} ions creates charge imbalance in the lattice. To maintain electrical neutrality, oxygen vacancies (V_O) are generated. This is because Er^{3+} has one fewer positive charge than Ce^{4+}, necessitating the creation of vacancies to compensate for the charge difference. With the increase in oxygen vacancies, there is a corresponding rise in the number of Ce^{3+} ions (since

some Ce^{4+} ions are reduced to Ce^{3+} to balance the charge). The presence of these Ce^{3+} ions and oxygen vacancies leads to the formation of Ce^{3+}-V_O-Ce^{3+} complexes. The Ce^{3+}-V_O-Ce^{3+} complexes contribute to the overall magnetic behavior of the material. The exchange interactions between the magnetic moments of Ce^{3+} ions and the electrons associated with the oxygen vacancies enhance the ferromagnetic properties of the nanoparticles. As the number of these complexes increases due to higher vacancy concentrations, the ferromagnetic behavior of the CeO_2 nanoparticles becomes more pronounced [13].

TABLE 1. Physical characteristics of pure and Er doped CeO_2 nanoparticles

Parameters	**Pure CeO_2**	**CeO_2:Er 5 %**	**CeO_2:Er 10 %**
Crystallite Size	8.34	7.69	5.91
Lattice Constant	5.408	5.416	5.422
Volume	158.16	158.86	159.39
M_S	1.6283	2.8432	3.6856
M_R	0.3457	1.0347	1.0804
H_C	364.95	327.57	486.37

CONCLUSION

In summary, $Er_xCe_{1-x}O_2$ nanoparticles were synthesized successfully by a citrate–nitrate auto combustion technique. The XRD pattern reveals a single-phase face-centered cubic (FCC) structure, indicating that Er^{3+} ions successfully substitute Ce^{4+} sites within the CeO_2 lattice. The changes observed in the optical band gap of doped samples confirmed the alteration in electronic structure of CeO_2. Magnetic studies revealed the existence of RTFM with reasonable hysteresis loop for all the samples. The changes in ferromagnetism with doping content were discussed interms of the interaction between oxygen vacancies and Cr^{3+} ions.

REFERENCES

1. W Prellier, A Fouchet and B Mercey,*J.Phys.*: Cond. Matt.,**15,** R1583 (2003)
2. S. A. Wolf, D. D. Awschalom, R. A. Buhrmam, J. M. Daughton, S. Von Molnar, M. L. Roukes, *Science,* **294,** 1488-1493 (2001)
3. H. Ohno, *Science,* **281,** 951 (1998)
4. T. Dietl, H. Ohno, F. Matsukura, J. Cibert and D. Ferrand, *Science,* **287,** 1019-1022 (2000).
5. Lubna R Shah, Bakhtyar Ali, Hao Zhu, W G Wang, Y Q Song, H W Zhang, *J. Phys.: Cond. Matt.,* **21,** 486004-4186013 (2009)
6. Novica Paunovic, Zorana Dohcevic-Mitrovic, Rares Scurtu, Sonja Askrabic, Marija Prekajski, Branko Matovic, *Nanoscale*, **4,** 5469-5478 (2012)
7. R. Niruban Bharathi and S. Sankar, *Sup. and Mic.,* 123, 37-51 (2018)
8. K. C. Anjaneya, G. P. Nayaka, J. Manjanna, G. Govindaraj and K. N. Ganesha, *J .All. Com.,* **578,** 53-59 (2013)
9. R. K. Raji, V. Kurapati, T. Ramachandran, *J. Mater. Sci. Mater. Electron*. **31** 7998–8014 (2020)
10. Ai Zhu Liu, Jian Xin Wang, Chang Rong He, He Miao, Yi Zhang and Wei Guo Wang, *Cer. Inter.,* **39,** 6229-6235 (2013)
11. Fazal Abbas, Tariq Jana, Javed Iqbala, Ishaq Ahmad, M. Sajjad, H. Naqvi, *Appl. Sur. Sci.,* **357,** 931-936 (2015)
12. J. M. D. Coey, A. P. Douvalis, C. B. Fitzgerald, and M. Venkatesan,*Appl. Phys. Lett.,***84,**1332-1334 (2004)
13. Z. V. Popovic, Z. D. Dohcevic-Mitrovic, N. Paunovic, and M. Radovic, *Phys. Rev. B; Con. Matt .Phys.,* **85,** 014302-014309 (2012)

Exploration of Structural and Magnetic Properties of Nd-doped $LaCrO_3$

Kousik Sutradhar[1] and D. Pal[2,*]

[1,2] *Department of Physics, Indian Institute of Technology Guwahati, Guwahati-781039, India.*
[*] d.pal@iitg.ac.in

Abstract. In this paper, we investigate the structural and magnetic properties of polycrystalline $La_{1-x}Nd_xCrO_3$ (x = 0.00, 0.05, 0.15). All the samples were synthesized using the solid-state reaction method. The structural characterization, like phase purity, crystal structure, and surface morphology, was performed through X-ray diffraction (XRD) and field emission scanning electron microscopy (FESEM) techniques. Room-temperature Raman spectroscopy revealed the presence of 11 active modes at 514 nm laser excitation for all the samples. The Neel temperature (T_N) decreases with increasing Nd doping. This indicates that the strength of the Cr^{3+}-Cr^{3+} interaction decreases with Nd substitution. A spin-reorientation transition was observed at low temperatures only for substituted samples. The substitution of Nd introduces an exchange bias within the samples and the maximum exchange bias field (H_{EB}) is found to be -674 Oe for x = 0.15 sample.

1. INTRODUCTION

Perovskite (ABO_3) systems have remained a focal point in condensed matter research for decades due to their intriguing physical behaviors. Among them, rare-earth orthochromites ($RCrO_3$) attract attention for their tunable magnetism and relevance in energy-efficient technologies, including magnetic refrigeration, data storage, magnetoelectric and spintronic applications [1]. These materials consist of a distorted perovskite framework featuring rare-earth ions at the A-sites and Cr^{3+} ions coordinated at the octahedral B-sites. The coexistence of magnetic R^{3+} and Cr^{3+} ions introduces multiple superexchange pathways: Cr^{3+}-O^{2-}- Cr^{3+}, Cr^{3+}-O^{2-}- R^{3+} and R^{3+}-O^{2-}- R^{3+} which are highly sensitive to temperature, resulting in phenomena such as negative magnetization, spin reorientation, exchange bias [2]. The physical properties of $RCrO_3$ compounds can be tuned through ionic substitution and lattice distortion, influencing spin states and magnetic coupling [3]. Studies have shown that factors such as chemical strain, chemical pressure, and other perturbations can be used to tune the lattice structure, magnetic phases, and optical band gap in these orthochromites [4,5]. In this context, $LaCrO_3$ stands out as a promising candidate for investigating magnetic properties in the orthochromites family. It crystallizes in a $GdFeO_3$-type distorted perovskite structure, adopting an orthorhombic symmetry belonging to the Pbnm space group at room temperature, and exhibits an antiferromagnetic ordering around T_N ~ 290 K [6]. Its properties can be significantly modified by substituting the A and B sites, such as substituting the A- site with Gd/ Pr or B- site by Fe/Mn can induce negative magnetization [7,8] M. Aamir et al. demonstrated that replacing Co and Fe at the A and B lattice positions leads to substantial changes in $LaCrO_3$'s magnetism, crystal structure, and its electrical and polarization behaviors [3]. In this work, we have chosen $LaCrO_3$ and substituted its non-magnetic La ions at the A-site with magnetic Nd ions. As the Nd^{3+} ions has a smaller size than La^{3+} hence, the crystal structure is supposed to have a negative chemical pressure. This shrinkage in volume should result in the strengthening of magnetic coupling between the magnetic ions (Cr^{3+} and Nd^{3+}), resulting in the modification of its magnetic properties like exchange bias etc.

2. EXPERIMENTAL DETAILS

Polycrystalline samples of $La_{1-x}Nd_xCrO_3$ (x = 0.0, 0.05, and 0.15) were synthesized via a solid-state technique using stoichiometric amounts of La_2O_3 (99.9%), Nd_2O_3 (99.9%), and Cr_2O_3 (99.6%). The powders were mixed in acetone, ground thoroughly, and sintered at 1300 °C for 24 hours with an intermediate grinding and heating process to ensure phase formation. The crystalline phases were identified using X-ray diffraction data collected on a Rigaku Smart Lab system. A Zeiss Sigma 300 FE-SEM was employed to study the surface features and compositional consistency. Raman Raman measurements were carried out at room temperature using a LabRam HR spectrometer (Horiba Jobin Yvon) with a 514 nm excitation laser. The Quantum Design PPMS platform was utilized to investigate magnetization behavior across temperatures from 3 K to 300 K and magnetic fields up to 9 T.

3. RESULTS AND DISCUSSIONS

3.1 Structural and Microstructure analysis: Figure 1(a) presents the Rietveld refinement of the XRD patterns for $La_{1-x}Nd_xCrO_3$ (x = 0.00 - 0.15), analyzed using the FULLPROF suite. The refinement confirms the formation of a single-phase orthorhombic structure with space group Pbnm (# 62). A gradual reduction in lattice parameters (a, b, c) is observed from (5.5183, 5.4723, 7.7811) for x = 0.0 to (5.5167, 5.4811, 7.7634) for x = 0.15, which is due to the replacement of larger La^{3+} ions (1.16 Å) by the relatively smaller Nd^{3+} ions (1.11 Å).

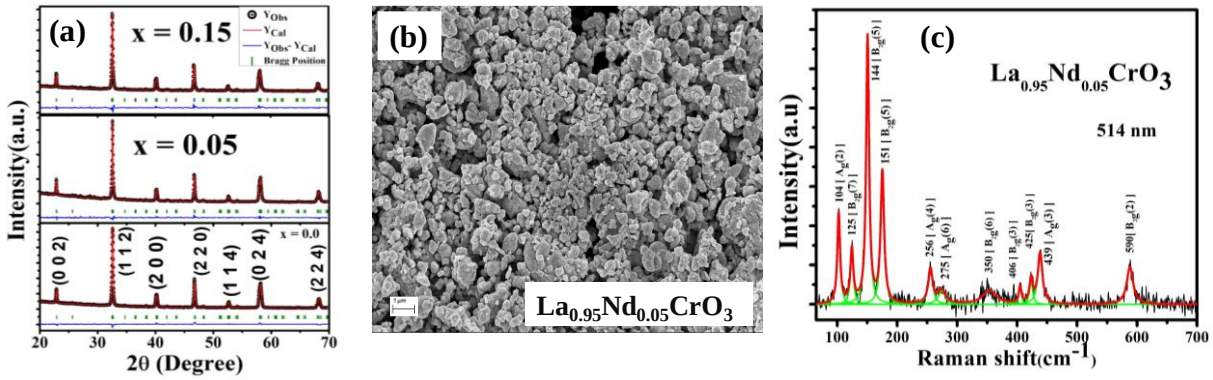


FIGURE 1. (a) Refined XRD patterns of $La_{1-x}Nd_xCrO_3$ (x = 0.0 - 0.15) obtained through Rietveld analysis using FULLPROF. (b) FE-SEM micrograph of $La_{0.95}Nd_{0.05}CrO_3$. (c) Raman spectra of $La_{0.95}Nd_{0.05}CrO_3$ at room temperature.

Figure 1(b) shows the FESEM image of $La_{0.95}Nd_{0.05}CrO_3$, demonstrating the formation of homogeneous and well-formed grains within the micrometre range. Based on group theory, $RCrO_3$ compounds crystallizing in the orthorhombic phase are expected to display 24 Raman-active vibrational modes ($7A_g$, $5B_{1g}$, $7B_{2g}$ and $5B_{3g}$). The Raman spectroscopic analysis of $La_{1-x}Nd_xCrO_3$ identified 11 modes under 514 nm excitation. Figure 1 (c) displays the Raman spectrum of $La_{0.95}Nd_{0.05}CrO_3$, which is consistent with earlier reports on $LaCrO_3$ [9].

3.2 Magnetic properties: - Magnetization as a function of temperature under field-cooled conditions at 500 Oe is presented for $La_{1-x}Nd_xCrO_3$ with x = 0.0 and 0.15, as shown in Figure 2. The magnetic transition observed at T_N = 293 K for the x = 0.0 composition corresponds to the canted antiferromagnetic (AFM) alignment of Cr^{3+} spins, consistent with earlier studies. With the substitution of Nd, the magnetic ordering temperature (/Neel's temperature) T_N decreases to around 242 K (marked by an arrow) for the x = 0.15 sample. A slight increase in magnetization is observed before T_N, marked as T*, possibly pointing to a gradual Cr^{3+} ordering. This behavior may arise due to changes in the canting angle of Cr^{3+} spins, which could evolve continuously from T* to T_N. Below this ordering temperature, the magnetic structure of Cr^{3+} ions, adopting the Γ_2 (F_x,C_y,G_z) configuration, resulting in a weak ferromagnetic component (F_x). As the temperature decreases further, a spin-reorientation phenomenon occurs at approximately (T_{SR}) 30 K, causing a transition of the magnetic structure from Γ_2 (F_x,C_y,G_z) to Γ_1 (A_x,G_y,C_z) configuration, characterized by a decrease in the magnetic moment in the magnetization curve [10]. Below 10 K, the ordering of Nd^{3+} ions occurs, leading to a subsequent increase in the magnetic moment. The field-dependent magnetization (M-H) data of all the samples were recorded at various temperatures within a field range of ±90 kOe. The M-H curve shows a linear behaviour above the spin-reorientation transition temperature (T_{SR}). Figure 3 shows the M–H loop of the $La_{0.85}Nd_{0.15}CrO_3$ at 100 K, and the inset shows a magnified view of the hysteresis loops of the samples x = 0.05 and 0.15 at the cooling field of 5 kOe. The figure clearly shows a slight shift of the M-H loop center away from the origin. Upon reversing the

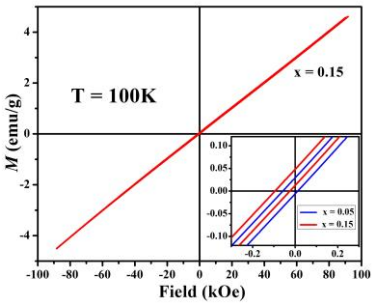


FIGURE 3. Field-dependent M–H loop of x = 0.15 sample. inset shows magnified views of the M–H loops of x = 0.05 and 0.15 samples at the 5kOe cooling field, both at 100K.

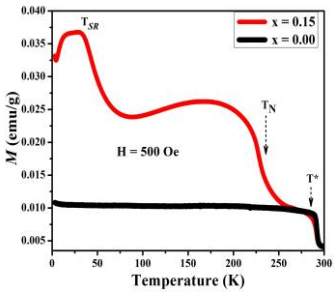


FIGURE 2. Temperature-dependent magnetization (M-T) curve of $La_{1-x}Nd_xCrO_3$(x = 0.0, and 0.15) in FC mode at 500 Oe.

field direction, this shift occurs in the opposite direction, confirming the presence of exchange bias (EB) in the system. The shifting of the loop is found to increase with increasing Nd content in the samples. In order to calculate the exchange bias field (H_{EB}), the relation $H_{EB} = (H_+ + H_-)/2$ is used, which measures the displacement of the field-cooled M-H loop from the origin. Here, H_+ and H_- denote the positive and negative field values at which the magnetization crosses zero. An increase in $|H_{EB}|$ from 293 Oe (x = 0.05) to 674 Oe (x = 0.15) reflects an enhancement in the exchange interaction between Cr^{3+} ions and the A-site cations (La^{3+} and Nd^{3+}) due to Nd substitution.

4. CONCLUSIONS

The polycrystalline $La_{1-x}Nd_xCrO_3$ (x = 0.0-0.15) samples were prepared using the standard high-temperature solid-state route. A slight decrease in lattice parameters was observed with increasing Nd content. Raman spectroscopy at room temperature reveals 11 Raman active phonon modes for all the samples, which is consistent with the orthorhombic Pbnm space group. Nd incorporation leads to a reduction in the magnetic ordering temperature, shifting T_N from 293 K to 242 K. Below T_N, the system exhibited a canted antiferromagnetic structure Γ_2 (F_x, C_y, G_z). Around 30 K, the system's spin structure reconfigures from the Γ_2 (F_x, C_y, G_z) state to the Γ_1 (A_x, G_y, C_z) configuration, indicating a temperature-induced spin reorientation. The EB field ($|H_{EB}|$) increased with increasing doping concentrations, indicating that the exchange interaction between $|La^{3+}+Nd^{3+}|$ with Cr^{3+} was enhanced by the presence of Nd.

ACKNOWLEDGMENTS

We acknowledge the FIST program of DST, India, for the PPMS facility provided at the Department of Physics, IIT Guwahati. We also appreciate the support of the CIF, IIT Guwahati, for providing the necessary characterization facilities for this work.

REFERENCES

[1] Fkhar L, Mahmoud A, Boschini F, Hamedoun M, Benyoussef A, Hlil E-K, Ali M A and Mounkachi O 2020 Structural, Magnetic, and Magnetocaloric Properties in Rare Earth Orthochromite (Sm, Nd, and La)CrO_3 for Cooling Product *J. Supercond. Nov. Magn.* **33** 1023–30

[2] Das H, Rébola A F and Saha-Dasgupta T 2021 Exploring the possible origin of the spin reorientation transition in $NdCrO_3$ *Phys. Rev. Mater.* **5** 124416

[3] Aamir M, Bibi I, Ata S, Jilani K, Majid F, Kamal S, Alwadai N, Raza M A S, Bashir M, Iqbal S, Aadil M and Iqbal M 2021 Ferroelectric, dielectric, magnetic, structural and photocatalytic properties of Co and Fe doped $LaCrO_3$ perovskite synthesized via micro-emulsion route *Ceram. Int.* **47** 16696–707

[4] Kumar A and Yusuf S M 2015 The phenomenon of negative magnetization and its implications *Phys. Rep.* **556** 1–34

[5] Menyuk N, Dwight K and Wickham D G 1960 Magnetization Reversal and Asymmetry in Cobalt Vanadate (IV) *Phys. Rev. Lett.* **4** 119–20

[6] Nithya V D, Jacob Immanuel R, Senthilkumar S T, Sanjeeviraja C, Perelshtein I, Zitoun D and Kalai Selvan R 2012 Studies on the structural, electrical and magnetic properties of $LaCrO_3$, $LaCr_{0.5}Cu_{0.5}O_3$ and $LaCr_{0.5}Fe_{0.5}O_3$ by sol–gel method *Mater. Res. Bull.* **47** 1861–8

[7] Selvadurai A P B, Pazhanivelu V, Jagadeeshwaran C, Murugaraj R, Panneer Muthuselvam I, Chou F C, Md Gazzali P M and Chandrasekaran G 2016 Structural, magnetic and electrical analysis of $La_{1-x}Nd_xCrO_3$ ($0.00 < x < 0.15$): synthesised by sol–gel citrate combustion method *J. Sol-Gel Sci. Technol.* **80** 827–39

[8] Bora T and Ravi S 2014 Negative magnetization and the tunable exchange bias field in $LaCr_{0.8}Mn_{0.2}O_3$ *J. Magn. Magn. Mater.* **358**–**359** 208–11

[9] Iliev M N, Litvinchuk A P, Hadjiev V G, Wang Y-Q, Cmaidalka J, Meng R-L, Sun Y-Y, Kolev N and Abrashev M V. 2006 Raman spectroscopy of low-temperature (Pnma) and high-temperature ($R\bar{3}c$) phases of $LaCrO_3$ *Phys. Rev. B* **74** 214301

[10] Gupta P and Pal D 2021 Spin induced exchange bias and lattice modulation in $Nd_{1-x}Eu_xCrO_3$ *J. Phys. Condens. Matter* **33** 135806

Structural and Magnetic Properties of Sm_2FeCrO_6

Meenakshi[1], Ramovatar[*1,a)], Surendra Kumar[*2,b)]

[1, a)]Department of Physics and Astrophysics, Central University of Haryana, Mahendergarh, Haryana-123031, India

[2,b)]Department of Physics, Shivaji College, University of Delhi, New Delhi-110027, India

Corresponding author(s)[*]: [a)]Ramovatar (ramovatar@cuh.ac.in), and [b)]Surendra Kumar (surendrakumar@shivaji.du.ac.in)

Abstract

This study synthesized the double perovskite Sm_2FeCrO_6 (SMFCO) compound via the sol-gel technique. XRD combined with Rietveld refinement reveals an orthorhombic structure and space group *Pbnm* (No. 62). The lattice parameters were a = 5.2629 Å, b = 5.4203 Å, and c = 7.5037 Å, attributed to a unit volume of 214.055 Å³. FESEM analysis revealed spherical-shaped particles averaging around 330 nm in size, while EDX results validated the existence of Sm, Fe, Cr, and O in the material. Magnetic measurements identified a transition temperature at 260 K, associated with G-type canted antiferromagnetic ordering. An exchange bias (EB) effect was also detected at temperatures below the Néel point. Below the transition temperature, hysteresis suggests weak ferromagnetism, whereas above it, the compound exhibits paramagnetic behavior.

Keywords: Rare-earth double perovskite oxides; sol-gel method; structural and magnetic properties;

1. Introduction

Rare-earth-based perovskite compounds are at the forefront of materials science research owing to their exceptional magnetic, electronic, and optical properties. These compounds, commonly described by the formula $RE_2BB'O_6$, where, composition is described as rare-earth element (RE), two different transition metals are B/B', offer a broad spectrum of functional behaviours. Their versatile properties make them well-suited for applications such as magnetic refrigeration, spintronics, solid-oxide fuel cells, and telecommunication devices [1–5]. Among them, RE_2FeCrO_6 has gained attention because it contains two different 3d transition metals, Cr and Fe, in an equal 1:1 ratio at the B and B' sites. According to the Goodenough-Kanamori rules 180° superexchange pathway between Fe^{3+} and Cr^{3+} ions through oxygen leads to ferromagnetic ordering [5–7], resulting in exotic physical properties [8–11]. In recent studies, Y_2FeCrO_6 and Gd_2FeCrO_6 were prepared and systematically analyzed for their structural framework, optical response, and magnetic behavior. These investigations highlight their promising potential in fields such as spintronics, optoelectronics, and photocatalysis [12,13]. Additionally, the multiferroic properties were also studied in Pr_2FeCrO_6 and Bi_2FeCrO_6 [14,15]. Yao and Xu studied the magnetocaloric effect in the Dy_2FeCrO_6 compound, reporting maximum isothermal magnetic entropy change ($-\Delta S_m$) of 12.64 J kg^{-1} K^{-1} and a relative cooling power (RCP) of 241.1 J kg^{-1} under an applied field change of 0–50 kOe [16]. The significant research interest in exploring other members of the R_2FeCrO_6 perovskite family arises from their diverse magnetic properties. In this paper, we investigated the structural and magnetic properties of Sm_2CrFeO_6 oxide prepared via a sol-gel approach.

2. Experimental details

The sol-gel technique is used to prepare double perovskite Sm_2FeCrO_6 (SMFCO). The molar ratio of 2:1:1 of Precursors $Sm(NO_3)_3.6H_2O$, $Cr(NO_3)_3.9H_2O$, and $Fe(NO_3)_3.9H_2O$ was individually dissolved in the DI water. Subsequently, Citric acid (CA) and ethylene glycol (EG) were added in a molar ratio of 1:1:4 (metals: CA: EG). For proper mixing, continue magnetic stirring and heat at 80 °C for 8 hours until a light brown gel forms. This gel was subsequently dehydrated in an oven at 120 °C for 12 hours. The dried mass was ground into fine powder and calcined at 800 °C for 6 hours. Afterwards, the resulting powder was molded into pellets and finally sintered at 1200 °C in atmospheric air for 24 hours. The structural characteristics of the sample were analyzed using an EcoPro Bruker D8 Advance X-ray diffractometer equipped with Cu-Kα radiation (λ = 1.540 Å). For Data collection, the range of 2θ is 20° to 80° at a 0.02° step size. The surface topography and microstructure were confirmed by a Zeiss Gemini 500 field emission scanning electron microscope (FESEM). Physical Property Measurement System (PPMS, Quantum Design DynaCool), applying magnetic fields up to 7 Tesla, was evaluated for magnetic behaviour.

3. Results and discussions

3.1. Structure analysis

The Rietveld refined XRD pattern of the Sm_2FeCrO_6 (SMFCO) compound was demonstrated in Figure. 1 (a). The absence of any extra peaks confirms the monophasic nature of the compound. The refinement results using FullProf software indicate a good fit with the orthorhombic structure, specifically within the *Pbnm* (62) space group, which is consistent with previously reported compounds [12,17]. The refined lattice parameters are a = 5.2629 Å, b = 5.4203 Å, and c =7.5037 Å, with a unit volume of 214.055 Å^3. The stability of the compound was predicted using the Goldschmidt tolerance factor, which is found to be 0.87, emphasizing the octahedral distortion. The average crystallite size determined using the Scherrer formula, is 56.22 nm.

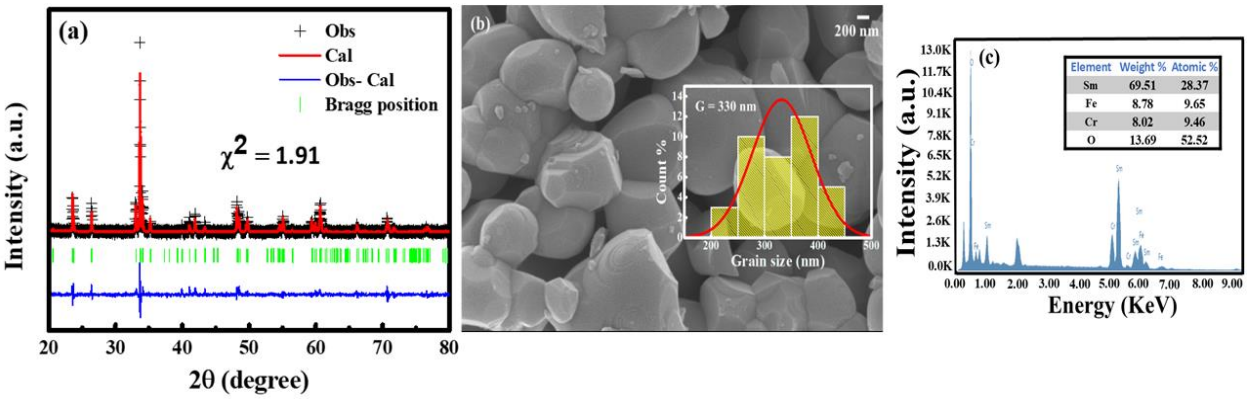


FIGURE 1: (a) Rietveld refined XRD spectra, (b) FESEM micrographs, the inset shows the grain size distribution histograms and (c) EDX spectra of Sm_2FeCrO_6 compound.

3.2. Morphological analysis

The FESEM micrograph of the SMFCO compound is presented in Figure 1 (b), revealing good homogeneity with spherical particles and an average grain size of ~ 330 nm, determined using ImageJ software (as shown in the inset of Figure 1 (b)). EDX spectra confirm the presence of Sm, Fe, Cr, and O elements in their intended proportions Figure 1(c).

3.3. Magnetic analysis

The prepared SMFCO compound magnetic properties were examined through both temperature-dependent magnetization (M(T)) and field-dependent magnetization (M-H). Figure 2 (a) describes the M(T) measurements, which are conducted in both field cooling (FC) and zero field cooling (ZFC) conditions across a temperature range of 3- 300 K at 500 Oe. At high temperatures, the overlap of both curves indicates paramagnetic behavior. As the temperature decreases, the bifurcation between the FC and ZFC curves at around 260 K signifies a transition temperature attributed to G-type antiferromagnetic (AFM) interaction of the Fe^{3+}/Cr^{3+} sublattices, driven by antisymmetric Dzyaloshinskii-Moriya (DM) exchange interactions[11,18]. Further cooling increases magnetization in both curves, indicating an increase in the ferromagnetic contribution. To understand the magnetic behavior of the SMFCO compound, M-H loops were measured at 5 K and 275 K within the range of ±7 T, as depicted in Figure 2 (b). Below the Néel temperature (T_N), the hysteresis loop indicates weak ferromagnetism. Above T_N, the curve exhibits linear behavior, suggesting the paramagnetic nature of the compound. From the M-H loop, several magnetic parameters were extracted, including the coercive field (H_C), and remanent magnetization (M_R). These were determined using the equations: [$M_R = |M_1 + M_2|/2$] and [$H_C = |H_2 + H_1|/2$], where M_1 represents the positive and M_2 is the negative magnetization along the Y-axis, and H_1 is the left and H_2 is the right coercive fields. The values were found to be 0.02 μ_B/f.u. and 6870 Oe. Notably, the SMFCO compound also exhibits an exchange bias effect (H_{EB}), evidenced by the shifting of the hysteresis loop both vertically and horizontally when cooled in the presence of a magnetic field. The H_{EB} is calculated using the following formula[12]: {$H_{EB} = (H_1 + H_2)/2$} and found to be -725 Oe at 5 K. The negative value is due to the positive magnetization of the material [19]. This EB makes it a potential candidate for advanced magnetic storage, switching, and spintronic applications.

4. Conclusion

In this report, the synthesis of Sm_2FeCrO_6 (SMFCO) compound via the sol-gel route resulted in a monophasic orthorhombic perovskite structure associated with the space group of *Pbnm*. notable structural and magnetic properties were studied. The refined lattice parameters and tolerance factor highlight octahedral distortion, while FESEM and EDX analyses validate the uniform morphology and elemental composition of the material. Magnetic studies demonstrate a transition to G-type canted antiferromagnetism at 260 K. Below this temperature, the M-H loops exhibited hysteresis, indicating weak ferromagnetism, while above it, the loops disappeared, reflecting the

paramagnetic behavior. These findings suggest that SMFCO is a promising material for advanced magnetic applications such as spintronics and magnetic refrigeration.

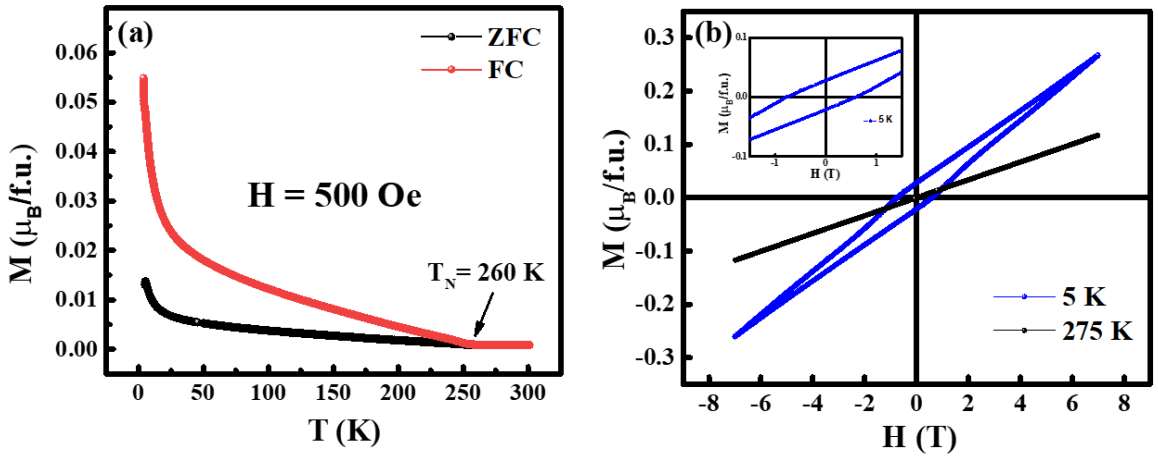


FIGURE 2. (a) Magnetisation curve under both ZFC and FC mode at 500 Oe and, (b) M (H) curves measured at 5 K and 275 K of Sm_2FeCrO_6 compound.

Acknowledgments: The author expresses sincere gratitude to the Bhabha Atomic Research Centre (BARC), Mumbai, for providing the PPMS facility for magnetic measurements. Ms. Meenakshi extends her heartfelt thanks to the CSIR for providing the JRF.

References

1 C. Agarwal, H. Mittal, T. Bano, J. Kumar, M. Gora, and A. Kumar, **10**, 1 (2022).
2 S. Vasala and M. Karppinen, Prog. Solid State Chem. **43**, 1 (2015).
3 L. Li and M. Yan, J. Alloys Compd. **823**, 153810 (2020).
4 L. Li and M. Yan, J. Mater. Sci. Technol. **136**, 1 (2023).
5 Meenakshi, S. Saini, N. Panwar, Ramovatar, and S. Kumar, J. Magn. Magn. Mater. **614**, 172766 (2025).
6 Y. Car, **545**, (1955).
7 J. Kanamori, J. Phys. Chem. Solids **10**, 87 (1959).
8 K. Yao and Y. Xu, J. Supercond. Nov. Magn. **35**, 1307 (2022).
9 K.P. Patra and S. Ravi, J. Appl. Phys. **132**, (2022).
10 S. Ravi, Mater. Lett. **278**, 128448 (2020).
11 S. Kumawat, D.K. Meena, M. Rani, Anuradha, H.S. Mund, and G. Arora, J. Alloys Compd. **978**, 173339 (2024).
12 M.A. Islam, T. Sato, F. Ara, and M.A. Basith, J. Alloys Compd. **944**, 169066 (2023).
13 M.D.I. Bhuyan, S. Das, and M.A. Basith, J. Alloys Compd. **878**, 2 (2021).
14 S. Ravi, J. Rare Earths **36**, 1175 (2018).
15 H. Wu, Z. Pei, W. Xia, Y. Lu, K. Leng, and X. Zhu, J. Alloys Compd. **819**, 153007 (2020).
16 B. Wu, Y. Zhang, D. Guo, J. Wang, and Z. Ren, Ceram. Int. **47**, 6290 (2021).
17 D. Mazumdar and I. Das, Phys. Chem. Chem. Phys. **23**, 5596 (2021).
18 V.M. Gaikwad, M. Brahma, R. Borah, and S. Ravi, J. Solid State Chem. **278**, 120903 (2019).
19 M.P. Sharannia, S. De, R. Singh, A. Das, R. Nirmala, and P.N. Santhosh, J. Magn. Magn. Mater. **430**, 109 (2017).

Inhomogeneous Melting of Vortex Lattice in Superconducting thin Films of MoGe

Rishabh Duhan[1, *], Subhamita Sengupta[1] and Pratap Raychaudhuri[1]

[1]*Tata Institute of Fundamental Research, Department of Condensed Matter Physics and Materials Science, Mumbai, Maharashtra, India.*

[*] Corresponding author: duhan.rishabh@gmail.com

Abstract. Vortex liquid can exist for a large part of phase diagram of thin film superconductors due to higher susceptibility of two-dimensional vortex lattice to thermal and quantum fluctuations. Here we report formation of vortex liquid state at low magnetic field and temperature in superconducting thin films of amorphous MoGe. However, a series of vortex images taken consecutively by scanning tunneling spectroscopy (STS) reveals that the liquid state is inhomogeneous in nature where we observe both static and moving vortices in a mixed landscape.

INTRODUCTION

Vortices in type II superconductors usually forms an ordered hexagonal lattice[1]. Presence of pinning in superconductors can destroy this long-range order and drive the lattice into a vortex glass[2,3]. With increase in temperature or magnetic field this can melt into a vortex liquid[2]. In thin film superconductors, vortex lattice is more susceptible to thermal and quantum fluctuations as it is in two-dimensional limit[4]. This can lead to realization of vortex liquid state at low temperature and field values. Recently, various vortex liquid states have been observed in thin film superconductors[5,6].

Imaging vortices using scanning tunnelling microscope (STM) is an excellent technique that makes it possible to observe structure of the vortex state directly. As STS is a slow measurement, it is difficult to resolve fast moving vortices in a vortex liquid state. However, presence of pinning can slow down these dynamics as attractive force on vortices due to pinning centres can curb this motion. Moreover, the effect of pinning on an existing vortex liquid state is a relatively unexplored area of research as compared to disordering and melting of the vortex lattice.

EXPERIMENTAL

The data analyzed in this work was obtained on a ~ 5 nm thick amorphous MoGe superconducting thin films grown using pulsed laser deposition on SiO_2 substrate[7]. The film exhibits a superconducting transition temperature, T_c = 5 K and upper critical field, H_{c2} ~ 100 kOe. Vortex imaging was performed using low temperature STS. In STS, a voltage modulation $V\ sin(\omega t)$ is applied between between the tip and the sample. As a result, the observed tunnelling current is also modulated, $I(V + dV\ sin(\omega t)) = I(V) + \frac{dI}{dV}|_v . dV\ sin(\omega t)$. Thus, the conductance of the sample can be directly measured using a lock-in amplifier. STS imaging of vortex lattice was performed by taking spatially resolved conductance map $G_N(V,r)$, with the bias voltage fixed near the coherence peak of the superconducting density of states. As the vortex has a normal core surrounded by a superconducting region, vortex manifest itself as dip in the conductance value at its location. STS imaging was carried out at 3 kOe and 450 mK over an area of 1.86 μm x 1.86 μm, with each image acquisition taking approximately 20 minutes[7].

Figure 1(a) shows an individual image, $G_N(V,r)$ map, where intensity is normalised such that highest and lowest value of conductance in the map correspond to 0 and -1 respectively. Local minima in this map correspond to location of vortices. The intensity of minimas in $G_N(V,r)$ map shows a wide variation. The Fast Fourier Transform of the image shows a diffused ring which correspond to destroyed hexagonal order of vortices due to pinning in the superconducting thin film (Fig. 1(b)). To distinguish between amorphous solid and liquid, it is essential to track the temporal evolution of vortex positions. This is achieved by analyzing a series of 10 consecutive conductance maps. Position of minima from all 10 images are plotted together in Fig. 2(a) with different color for each image. We observe that some positions of minima are close to each other and do not vary much across all 10 images. This corresponds to meandering motion of vortices about their mean positions. In contrast, some position of minima occurs at a different position in each image and when plotted together, they form tracks of motion. To look at the network arising out of this motion, we join any two minima position across

all ten images that are separated by distance $d < 0.5a$, where a is the expected bond length between two vortices at 3 kOe. Figure 2(b) shows the vortices connected in this manner forming a network of motion paths.

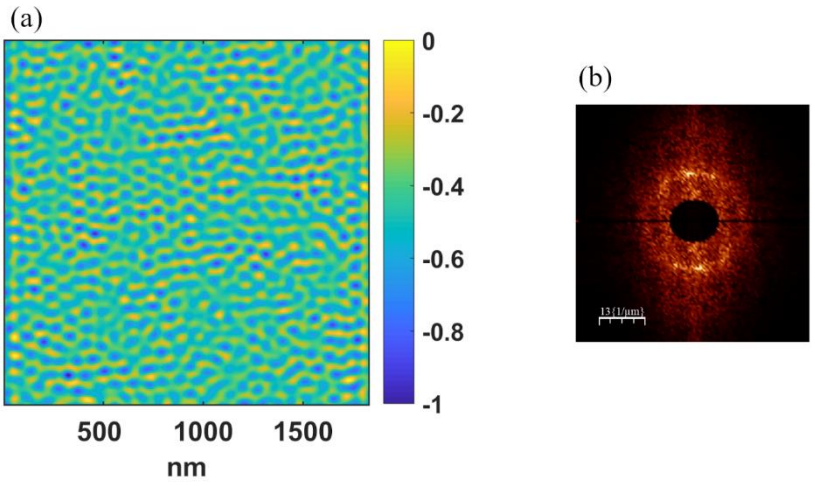


FIGURE 1. Conductance map $G_N(V, r)$ at 3 kOe and 450 mK. (b) Fourier Transform of the image shown in (a).

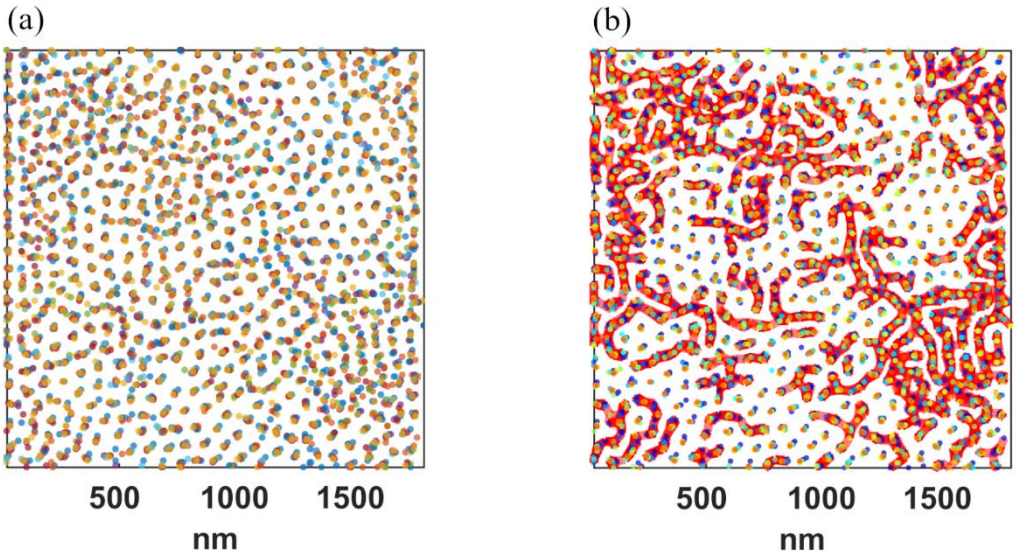


FIGURE 2. Conductance minima positions of 10 consecutive images, overlaid on each other with a different color. (b) Network formed by connecting conductance minima positions as described in the main text.

DISCUSSION

Thermal or quantum fluctuations in the two-dimensional limit of vortex lattice have obscured formation of vortex glass even at low temperature << T_c and magnetic field << H_{c2}. Due to pinning, instead of formation of a homogeneous liquid, we observe an inhomogeneous melting of vortex matter. This results in a large variation in the intensity of minima in the conductance map. The intensity gets smeared due to movement of vortices whereas static vortices give deep minima. Analyzing series of 10 consecutive conductance maps reveal a network of motion paths. Similar network paths were recently seen in superconducting thin films of amorphous Re_6Zr [8]. Hence, this might be a general feature in superconducting thin films.

ACKNOWLEDGMENTS

We acknowledge Department of Atomic Energy (DAE) for funding this project.

REFERENCES

1. A. A. Abrikosov, J. Phys. Chem. Solids, Vol. 2, pp. 199-208 (1957).
2. G. Blatter, M. V. Feigel'man, V. B. Geshkenbein, A. I. Larkin, and V. M. Vinokur, Rev. Mod. Phys., Vol. 66, pp. 1125-1138 (1994).
3. S. C. Ganguli, H. Singh, G. Saraswat, R. Ganguly, V. Bagwe, P. Shirage, A. Thamizhavel, and P. Raychaudhuri, Sci. Rep., Vol. 5, pp. 10613 (2015).
4. D. S. Fisher, M. P. A. Fisher, and D. A. Huse, Phys. Rev. B, Vol.43, pp. 130-159 (1991).
5. I. Roy, S. Dutta, A. N. Roy Choudhury, S. Basistha, I. Maccari, S. Mandal, J. Jesudasan, V. Bagwe, C. Castellani, L. Benfatto, and P. Raychaudhuri, Phys. Rev. Lett., Vol. 122, pp. 047001 (2019).
6. I. Guillamón, H. Suderow, A. Fernández-Pacheco, J. Ses´e, R. Córdoba, J. M. De Teresa, M. R. Ibarra, and S. Vieira, Nat. Phys., Vol. 5, pp. 651-655 (2009).
7. Soumyajit Mandal, Surajit Dutta, Somak Basistha, Indranil Roy, John Jesudasan, Vivas Bagwe, Lara Benfatto, Arumugam Thamizhavel, and Pratap Raychaudhuri, Phys. Rev. B, Vol. 102, pp. 060501 (2020).
8. R. Duhan, S. Sengupta, R. Tomar, S. Basistha, V. Bagwe, C. Dasgupta, and P. Raychaudhuri, Phys. Rev. B, Vol. 108, pp. L180503 (2023).

Low Frequency Electrodynamics of A Pinned Vortex Liquid

Subhamita Sengupta[1, *], Sitakanta Behera[2,] Rishabh Duhan[1] and Pratap Raychaudhuri[1]

[1]*Tata Institute of Fundamental Research, Mumbai, India*
[2]*Indian Institute of Science education and Research, Berhampur, India*

*Corresponding author: sengupta.subhamita@gmail.com

Abstract. Unlike conventional superconductors where the vortex lattice solidifies, the vortex liquid state in a 5nm amorphous Re_6Zr (a-ReZr) thin film persists down to low temperatures and fields without transitioning into a glassy or solid state. This study investigates the compressibility of the vortex liquid under various conditions using a two coil mutual inductance setup. Experimental results show that at higher frequencies, the pinned vortex liquid exhibits shear thickening, similar to non-Newtonian fluids like cornstarch solutions. As frequency increases, vortices have less time to respond, requiring higher magnetic fields to transition into an isotropic liquid state. At 2 K, a clear frequency dependence is observed, while at 0.41 K, the frequency dependence is less pronounced. These findings suggest that the pinned vortex liquid in a-ReZr behaves similarly to a compressible, non-Newtonian fluid.

INTRODUCTION

In the mixed state of a Type II superconductor, vortices form a hexagonal Abrikosov lattice due to repulsive interactions.[1] This order can be disrupted by factors like random pinning, thermal fluctuations, and quantum fluctuations.[2] In conventional superconductors, the vortex lattice generally remains crystalline near the upper critical field or transitions into a disordered state above an order-disorder transition. However, in thin films, the lattice is more susceptible to thermal fluctuations. In a 5 nm thin film of amorphous Re_6Zr (a-ReZr), combined scanning tunnelling microscopy (STM) and magnetotransport studies show that the vortex liquid state persists down to low temperatures and fields, unlike in conventional superconductors where it transitions into a glassy or solid state.[3] In a crystalline solid, weak pinning centers can act collectively to immobilize all vortices, so that dissipation occurs only when the current exceeds a critical threshold. In a vortex liquid, not all vortices are pinned unless individually, leading to inhomogeneous liquid states.[4]
Our previous work revealed that, at low temperature and magnetic field, only a fraction of vortices in 5 nm a-ReZr were mobile, forming a percolative network that expanded as temperature and magnetic field increased, eventually melting the vortex liquid.[3] In this study, we aim to investigate whether the vortex liquid in 5 nm a-ReZr is incompressible, similar to a normal liquid.

EXPERIMENTAL

A 5 nm thin film of a-ReZr ($T_c \sim 4.7$ K) was deposited onto a Si/SiO_2 substrate with an 8 mm circular geometry using pulsed laser deposition (PLD) at room temperature, under a vacuum of 1×10^{-7}torr. A 248 nm KrF excimer laser with 20 ns pulses was used to ablate a Re_6Zr target, utilizing a tightly focused laser spot with a high energy density of approximately 300 mJ/mm² and a repetition rate of 10 Hz. To prevent oxidation of the surface, the as-grown film was capped with a 2 nm Ge layer.

For measurements, the sample was positioned between two coils in a mutual inductance setup (as shown in the schematic in Fig. 1(a)). This setup consists of a quadrupolar primary coil (28 turns) and a dipolar secondary coil (120 turns). When a small AC current is passed through the primary coil, it induces an oscillatory motion in the flux tubes (vortices), which in turn generates a voltage in the secondary coil. The primary coil is designed so that the upper half is wound in one direction and the lower half in the opposite direction, generating a maximum magnetic field of 7 mOe/mA when a small sinusoidal current (less than 5 mA) is applied. The in-phase (V^{in}) and out-of-phase (V^{out}) components of the resulting induced voltage in the secondary coil are measured using a lock-in amplifier.The real (M') and imaginary part (M'') of mutual inductance (M) is defined as $M'^{(\prime\prime)} = \frac{V^{out(in)}}{2\pi I_{acf}}$, corresponding to the inductive and dissipative response of the sample respectively . The two-coil assembly is housed inside a cryostat fitted with an 11 T superconducting magnet.

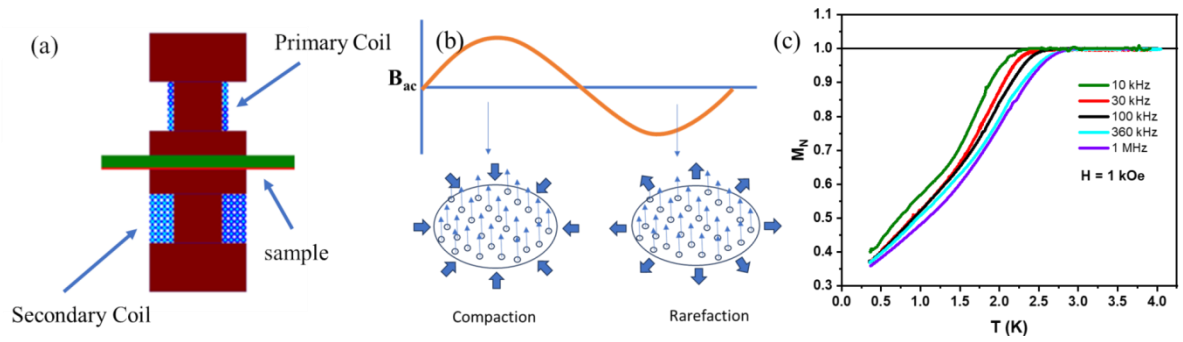


FIGURE 23. (a) Schematic of two coil mutual inductance set up (b) Compaction and rarefaction of pinned vortex liquid on application of ac magnetic field (c) Normalized mutual inductance (real part) as a function of temperature at different frequencies at H= 1 kOe.

RESULTS

We begin with the measurement of M' as a function of temperature (0.35–4.5 K) with an AC current of 0.02 mA passing through the primary coil, varying the frequency from 10 kHz to 480 kHz (Fig. 1), in an externally applied magnetic field of 1 kOe. At a fixed frequency, M' increases with temperature as vortices begin to move, eventually saturating at its highest value when all vortices are mobile, corresponding to the normal state of the sample. Since the normal state value of M'can vary with frequency due to the geometry of the secondary coil, the M'-T curves for different frequencies are normalized by their respective normal state values to enable better comparison. From Fig. 1(c), we observe that the temperature at which M'saturates increases with increasing frequency. This indicates that as the frequency increases, the pinned vortex liquid state takes longer to transition into an isotropic liquid, suggesting that the pinned vortex liquid is compressible, unlike a regular liquid.

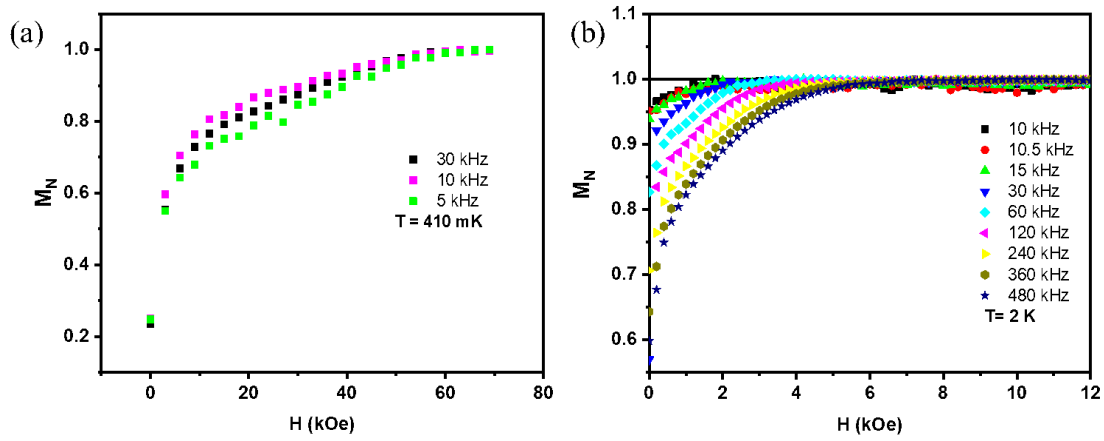


FIGURE 2. Normalized mutual inductance (real part) as a function of magnetic field at different frequencies at (a) T= 410 mK. (b) T = 2 K. The data at 2 K shows clear frequency dependence upto 6 kOe.

In the 5 nm a-ReZr thin film, the pinned vortex liquid spans the H-T plane. At a fixed magnetic field (temperature), more vortices become mobile along the percolative network as the temperature (magnetic field) increases. Therefore, we expect to observe similar frequency dependence when M' is recorded as a function of magnetic field at a given temperature for different frequencies. Figure 2(a) shows the M'-H curves at 410 mK for various frequencies of the driving AC current. At this temperature, no discernible frequency dependence is observed. However, at a higher temperature of 2 K (Fig. 2(b)), a clear frequency dependence is observed up to 6 kOe. Again, the magnetic field at which all vortices start moving increases with increasing frequency, further reinforcing the compressible nature of the pinned vortex liquid.

DISCUSSION

When a small AC current is applied through the primary coil, it generates a time-varying circulating supercurrent in the superconducting film, given by $\boldsymbol{J_S^{ac}}(\mathbf{r},t) = J_S^{ac}(r)\sin(\omega t)\hat{\phi}$. This current exerts a radial oscillatory force on each vortex, described by $\boldsymbol{F_{ac}} = \boldsymbol{J_S^{ac}} \times \hat{z}\Phi_0 = J_S^{ac}(r)\sin(\omega t)\Phi_0\hat{r}$. causing the vortices to oscillate around their equilibrium positions. This causes the vortex lattice (pinned vortex liquid) to undergo oscillatory compression and expansion, while the vortex at the center of the film remains stationary. This motion induces a voltage in the secondary coil, which serves as a measure of the lattice's compressibility.[5]

Normalized *M-H* curves at 410 mK show that as frequency increases, vortices have less time to respond, requiring a higher magnetic field to transition into an isotropic liquid state, indicating shear thickening. At 2 K, a clear frequency dependence is observed, unlike at 0.41 K, where only a small change is seen over the magnetic field range of 0-100 kOe. STM studies performed on an identical sample indicating 60% of vortices are mobile at 10 kOe at 410 mK, while 90% are mobile at 2 K attributes to the frequency dependence.

The normalized *M'-T* curves at H = 1 kOe show that vortex density remains constant while more vortices join the percolating network with increasing temperature. This shear thickening suggests non-Newtonian fluid-like behavior in the pinned vortex liquid, similar to cornstarch solutions. A corn starch solution, when stirred slowly behaves like a liquid but becomes more viscous as stirring increases. In a non-Newtonian fluid, like cornstarch, viscosity increases with increasing rate as well as intensity of shear force. However, in the pinned vortex liquid formed in 5 nm a-ReZr, any discernible dependence on the amplitude of ac excitation is not observed.

CONCLUSION

In this work we investigate the compressibility of pinned vortex liquid in 5 nm a-ReZr. Using a two coil mutual inductance setup, an AC current generates oscillatory supercurrents in the film, causing vortices to oscillate and induce voltage in a secondary coil. This setup measures the compressibility of the vortex system by observing the out-of-phase component of the induced voltage as a function of temperature/magnetic field at different frequencies. The experimental findings show, pinned vortex liquid behaves like a compressible, non-Newtonian fluid.

ACKNOWLEDGMENTS

This work was supported by Department of Atomic Energy, Government of India.

REFERENCES

1. A. A. Abrikosov, J. Phys. Chem. Solids, Vol 2, pp. 199-208 (1957).
2. S. Dutta, I. Roy, J. Jesudasan, S. Sachdev, and P. Raychaudhuri, Phys. Rev. B, Vol 103, pp. 214512 (2021).
3. R. Duhan, S. Sengupta, R. Tomar, S. Basistha, V. Bagwe, C. Dasgupta and P. Raychaudhuri , Phys. Rev. B, Vol 108, pp. L180503 (2023).
4. C. Dasgupta and O. T. Valls, Phys. Rev. B, Vol 72, pp. 094501 (2005).
5. I. Roy, P. Chauhan, H. Singh, S. Kumar, J. Jesudasan, P. Parab, R. Sensarma, S. Bose and P. Raychaudhuri , Phys. Rev. B, Vol 95, pp. 054513 (2017).

Synthesis and Structural Study of Pre-lithiated Silicon Anode in Different Atmospheric Conditions

Ashish Kumar Mishra, Monika, Anjali and Balbir Singh Patial*

Department of Physics, Himachal Pradesh University, Summerhill, Shimla, Himachal Pradesh, 171005, INDIA
**bspatial@gmail.com*

Abstract. Li-ion batteries are regarded as the groundbreaking development in the field of energy storage. Advanced synthesis of material with increased energy density and cycle stability are of significant priorities in meeting the particular and growing demand for energy storage devices. Si is regarded as a good anode material since it has the highest lithiated phase. Its theoretical capacity is around 4199 $mAhg^{-1}$, which is about ten times that of graphite used in conventional batteries. In practical applications, excessive volume expansion during silicon lithiation can lead to lithium loss within the battery unit, reducing its capacity and causing electrode failure or cracking. To address this issue, a pre-lithation procedure was proposed. In this study, a pre-lithiated sample of the most lithiated Li-Si ($Li_{21}Si_5$) phase of Li-Si alloy is primed using the melt solidification method in different atmospheric conditions and structural study is reported and observed.

INTRODUCTION

Now a days, we almost rely on Li-ion batteries for our electrical applications like mobile phones, electric vehicles etc. Existing battery materials consist of lithium cobalt oxide as a cathode and graphite as an anode having limited capacity. In order to meet the green energy target and a preparation for the future of electric vehicles, we must seek out new materials. Traditional battery technology with graphite anode has limitations like capacity fading with time and other disadvantages such as lower energy density and lower theoretical capacity along with volume expansion and Li-loss during battery operation at numerous stages [1]. Some studies have used pre-lithiated anode materials to alleviate the problem of lithium depletion by injecting supplementary lithium into the side that serves as the anode to tackle lithium loss and provide extra lithium inside battery unit [2]. Graphite as anode in conventional batteries has the limited capacity about 376 $mAhg^{-1}$ [3]. Therefore, the research to synthesize the new anode materials is enhancing day by day. Silicon can emerge as anode material with greater energy density (4199 $mAhg^{-1}$) as it forms many stable phases with lithium during lithiation [4]. It is found that $Li_{22}Si_5$ or $Li_{21}Si_5$ being most lithiated phase where one Si atom makes bond with four Li atoms resulting in large amount of lithium stored inside it [5]. There are other means of performing this pre-lithiation of material; (i) forming electrochemical cell or galvanostatic cell unit where lithium metal used as counter electrode, (ii) direct contact with lithium, (iii) melt solidification of synthesized alloy with desired composition etc. [6]. In this paper, the synthesis and structural study of $Li_{21}Si_5$ in open and inert atmosphere is discussed in detail.

EXPERIMENT AND METHOD

$Li_{21}Si_5$ in open environment and $Li_{21}Si_5$ in inert environment are synthesized using the melt solidification technique. Li granular and Si powder were employed in the procedure and weighed according to the molar ratios. The initial experiment involved placing material in an alumina crucible and heating it into a muffle furnace without an inert atmosphere. The furnace's temperature was raised to 750^0C, and the samples were annealed there for an hour. Later, these samples were allowed to cool on their own up to room temperature. A similar procedure was again followed to synthesize this sample in an inert atmosphere. The obtained samples were later ground with a mortar and pestle to yield a powder form of the material. The obtained samples are further characterised for structural study using XRD, SEM, and EDX.

RESULTS AND DISCUSSION

Fig. 1(a) displays the XRD data for $Li_{21}Si_5$ prepared in an open environment designated as $Li_{21}Si_5$ (O). The Scherer equation [7] was used to determine the average crystallite size of the sample, which was approximately 40 nm. Material shows the crystallinity of about 57%. Table 1 gives the values of peak position, FWHM (β), crystallite size (D), dislocation density (δ) and strain (ε). These values shows the production of dislocations and strain inside the synthesized material. XRD data obtained does not match with the ICDD data of the synthesized phase, indicating that the extra peaks in XRD results are attributed to side reactions which occurred during the synthesis inside the muffle furnace. EDX results (Fig. 2(a)) reveal peaks for oxygen, aluminium, and silicon but lithium is not included since typical EDX instruments cannot identify elements lighter than boron when employing a beryllium window. The existence of an oxygen peak in EDX indicates that the material is oxidizing during the process due to lithium's high reactivity in air [8]. The low electronegativity value of 0.98 allowed lithium to easily give up an electron and form bonds or side compounds. Grain size is also estimated and is found equal to 87 nm (Fig. 2(b)). SEM data shows the agglomeration of particles on the surface. SEM data reveals the amorphous morphology of the material which can be observed from the crystallinity percentage of the material. Lithium can react with oxygen in air and may generate lithium oxides, which trap oxygen inside the substance as given in Eq. 1:

$$4\,Li + O_2 \rightarrow 2Li_2O \qquad (1)$$

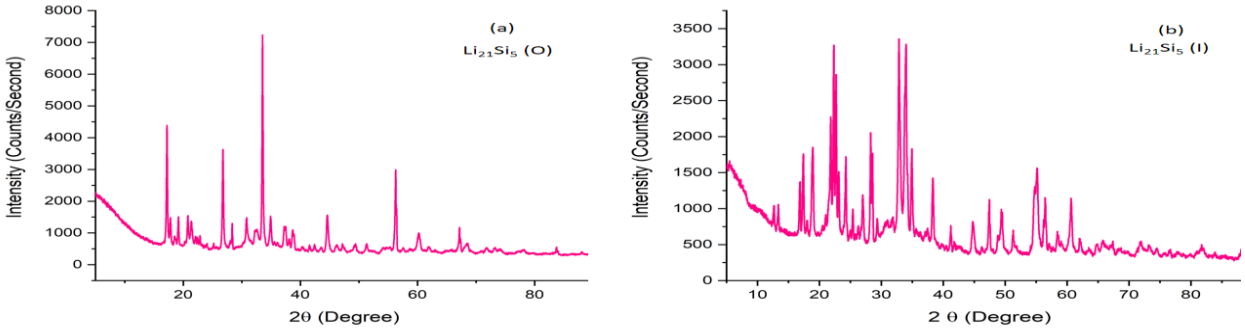


FIGURE 1. (a) XRD obtained for $Li_{21}Si_5$ (O), (b) $Li_{21}Si_5$ (I).

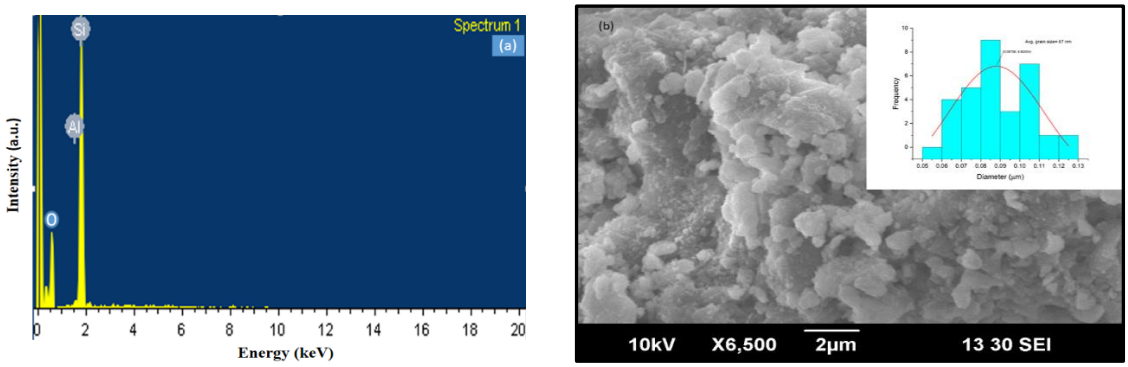


Figure 2. (a) EDX and (b) SEM obtained for $Li_{21}Si_5$ (O).

TABLE 1. Table shows the properties of the materials obtained.

Sample	Peak position	FWHM (β)	Crystallite Size D (nm)	Dislocation Density (δ*10^{15}lines)	Strain (ε *10^{-3})
$Li_{21}Si_5$ (O)	33.54	0.22	37.46	0.71	0.29
$Li_{21}Si_5$ (I)	32.88	0.35	23.09	1.87	0.46

Figure 2 depicts the XRD data acquired for the $Li_{21}Si_5$ synthesized in an inert atmosphere marked as $Li_{21}Si_5$ (I). The XRD result indicates the presence of oxygen within the material, i.e. the formation of lithium oxide throughout the process. Crystallite size using the intense peak calculated and found 23 nm. Increase in the value of dislocation density shows the increase in number of imperfection in the material hence reducing the orderly arrangement of the crystals. These dislocation also causes the increase in micro strain value of the material. Table 1 shows the parameters of the material obtained for intense XRD peak.

CONCLUSION

To realize the potential of green energy and achieve the objective of sustainable development, we must create new battery materials with higher energy density. Pre-lithaition of silicon can assist us to attain this goal and reduce the hurdle of lithium loss inside the battery. However, the volatility of Li-Si phases, as well as problems in their synthesis, can impede this process. Synthesis now necessitates extensive infrastructural and technological developments. Despite being the most lithiated phase $Li_{21}Si_5$, it can react easily in an open atmosphere. Because of their abundance, being able to synthesis these materials would be cost-effective and useful. Even if the sample with phase $Li_{21}Si_5$ gets synthesized inside furnace, it will react with air as soon as it was exposed to open air. Thus a complete inert atmosphere is a must condition to explore pre-lithiated Si anode material.

ACKNOWLEDGMENTS

The first author Ashish Kumar Mishra gratefully acknowledges the Department of Science and Technology, Ministry of Science and Technology, Government of India for DST-INSPIRE fellowship (IF200550).

REFERENCES

1. D. Rehnlund, F. Lindgren, S. Bohme, T. Nordh, Y. Zou, J. Pettersson, U. Bexell, M. Boman, K. Edstrom and L. Nyholm, Energy Environ. Sci., Vol. 10, pp. 1350-1357 (2017).
2. M. N. Obrovac, Curr. Opin. Electrochem., Vol. 9, pp. 8-17 (2018).
3. A. K. Mishra, Monika and B. S. Patial, Material Today Electronics, Vol. 7, 100089 (2004).
4. A. K. Mishra, Monika and B.S. Patial, Anode Materials in Li-ion Batteries, 4th International conference on Condensed and Matter and Applied Physics, October 9-10, 2023, Bikaner, India, AIP Conf. Proc. (2024).
5. Monika, A.K. Mishra and B.S. Patial, Journal of Condensed Matter, Vol. **1**(2), pp. 65-68 (2023).
6. Z. Zhang, H. Wang, M. Cheng, Y. He, X. Han, L. Luo, P. Su, W. Huang, J. Wang and C. Li, Energy Storage Mater., Vol. **42**, pp. 231-239 (2021).
7. Anjali, B. S. Patial and N. Thakur, J. Asian Ceram. Soc., Vol. **8**(3), pp. 777-792 (2020).
8. P. Arora and R. E. White, J. Electrochem. Soc., Vol. **145**(10), pp. 3647-3667 (1998).

Exploring $ZnFe_2O_4$ Hollow Microspheres as Supercapacitor Electrode Material

Moisilee Dutta[1], Priyanka Saha[1], Rituparna Mondal[1*] and Sanjay Kumar[1*]

[1]*Department of Physics, Jadavpur University, Kolkata – 700 032, West Bengal, India*

[*]Corresponding authors: rituparnam.physics@jadavpuruniversity.in, kumar_dsa@yahoo.com

Abstract. Herein, we have reported the structural, microstructural and electrochemical properties of $ZnFe_2O_4$ hollow microspheres synthesized by solvothermal technique. The sample has been characterized by recording the powder x-ray diffraction (PXRD) pattern, electron microscopic images using field emission scanning electron microscopic (FESEM) and high-resolution transmission electron microscopic (HRTEM) techniques. The sample is cubic spinel having $Fd\bar{3}m$ space group and composed of hollow microspheres with average diameter of 326.4 nm and shell thickness of 58 nm. According to N_2 adsorption-desorption study, the pore size and BET surface area are 2.77 nm and 24.54 $m^2\ g^{-1}$, respectively. The sample exhibits pseudocapacitive behaviour with an impressive high specific capacitance value of 993.8 F g^{-1} at 5 mV s^{-1}. Interestingly, the value of the specific capacitance of the sample is found to be increased by 34% after 1000 cycles of galvanostatic charging-discharging.

Keywords: Spinel ferrites, Solvothermal, Hollow microspheres, Supercapacitors, Specific capacitance.

INTRODUCTION

Recently, supercapacitors are evolved as a viable alternative of batteries, especially in automobile and renewable energy sectors. Owing to their rapid charging-discharging property and high energy storage capability, the supercapacitors are emerged as the most promising next-generation energy storage devices. It may be noted that, nano and micro structured spinel ferrites exhibit notably high specific capacitance along with excellent cyclic stability with long-term durability [1]. The size, shape and composition of spinel ferrites play a crucial role to determine their electrochemical properties and on the other hand, these structural and microstructural properties can be easily modified by choosing appropriate synthesis techniques. Though the electrochemical properties of nano structured zinc ferrite are widely investigated [2], for the micro-structured hollow ferrites it is yet to be unfold in many aspects. Thus, study on the electrochemical property of $ZnFe_2O_4$ hollow microspheres and examining how it depends on structural and morphological parameters is appeared to be interesting in the context of their application potential as supercapacitor electrode materials.

MATERIAL SYNTHESIS & CHARACTERIZATION

To prepare zinc ferrite hollow microspheres (ZFHM) by solvothermal method, 5 mmol $FeCl_3.6H_2O$ and 2.5 mmol anhydrous $ZnCl_2$ were dissolved in 50 ml of Ethelene glycol through magnetic stirring for 30 minutes. Then, 2.4 mg of NH_4Ac was added to the mixture and stirred for 6 hours. This solution was poured into a Teflon-lined autoclave and heated at 180°C for 14 hours by placing it inside an oven. Lastly, after washing the black precipitate several times with deionized water (DI) followed by ethanol and drying at 60°C for 6 hours in vacuum, the final product was obtained and identified as ZFHM after characterization.

The working electrode for electrochemical analysis has been fabricated by coating the sample at one cross sectional end of a graphite rod (cross sectional diameter of 3 mm and length 5 cm) following the standard procedure as described in our earlier work [3].

The PXRD data of the material has been recorded by a Bruker D8 advance diffractometer at 25°C using K_α radiation of Cu (λ_{Cu}=1.5406 Å). The morphological study of the sample has been carried out using an FEI INSPECT F50 FESEM. The intricate morphology of ZFHM has been investigated by HRTEM study using an FEI TECNAI TF20 ST D574 instrument. The DRS spectra of the sample has been recorded by a PerkinElmer UV−vis spectrometer (Lambda 35) with a solid-state measurement attachment. The N_2 adsorption-desorption experiment has been performed by using a NOVA 2200E Quantachrome instrument. The electrochemical study of the sample has been conducted by an Autolab, PGSTAT204 electrochemical workstation with an attached software Nova 2.0. All the measurements have been performed using a standard three electrode setup where an Ag/AgCl, platinum wire and the prepared sample coated graphite rod act as reference, counter and working electrodes, respectively. 0.1M of H_2SO_4 solution is used as the electrolyte for cyclic voltammetry (CV) and

galvanostatic charging-discharging (GCD) measurement. From the CV and GCD measurement, the specific capacitance (C_{sp}) has been calculated using the standard formulae [2].

RESULTS AND DISCUSSIONS

The PXRD pattern of the sample matches very well with previously recorded pattern of $ZnFe_2O_4$ (JCPDS card no. 89-1010) and no extra peak due to probable impurity phases has been obtained. For performing quantitative phase analysis, the PXRD pattern (Fig. 1a) of the sample has been fitted using MAUD software. The fitted pattern (red line) matches very well with the experimental profile with GOF value of 2.2. The results clearly indicate the formation of single phase $ZnFe_2O_4$ which crystallized in $Fd\bar{3}m$ space group. The crystallite size as obtained by fitting in MAUD software is ~176.1 nm. The FESEM has been utilized to contemplate the morphological characteristics and particle size distribution of the synthesized sample. The micrograph (Fig. 1b) of ZFHM reveals the spherical structure with homogeneous size and shape where some of the broken spheres confirm the hollowness of the core of the spheres. The average particle size as determined by histogram plot (Fig. 1c) is ~326.4 nm. The HRTEM micrograph reveals a distinct contrast between the outer dark layer and the bright centre of the microspheres (Fig. 1d), confirming the successful formation of a hollow structure with shell thickness ~58 nm. The even outer surface of the microsphere is formed by the cluster of nanoparticles.

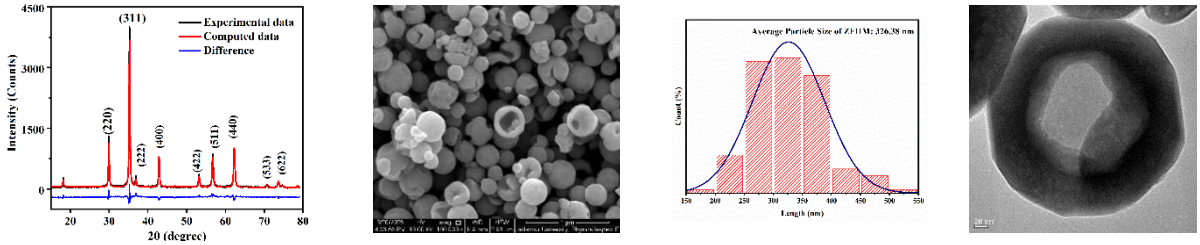


FIGURE 1. (a) PXRD pattern fitted by MAUD (b) FESEM image (c) particle size distribution (d) HRTEM image of ZFHM

To examine the optical property of ZFHM, UV−vis DRS spectra has been recorded in the range of 400 to 800 nm (Fig. 2a). The value of band gap energy (E_g) of the sample is ~1.74 eV determined by Kubelka Munk method indicating E_g is in optical region. It has been found that the ZFHM is a direct band gap semiconductor as E_g is calculated from the plot of $[F(R)h\nu]^2$ vs eV (Fig. 2a inset), where F(R) represents the Kubelka Munk function that is equal to the ratio of molar absorption coefficient and scattering factor, hν being the photon energy. Figures 2b and 2c represent the N_2 adsorption-desorption isotherm and pore size distribution curves of ZFHM, respectively. The isotherm curve suggests that the sample is mesoporous in nature with average pore size and BET surface area of 2.77 nm and 24.54 $m^2\ g^{-1}$, respectively. This porous nature of the sample can elevate the ion diffusion and facilitate easy access of electrolyte ions to the electrode surface [4].

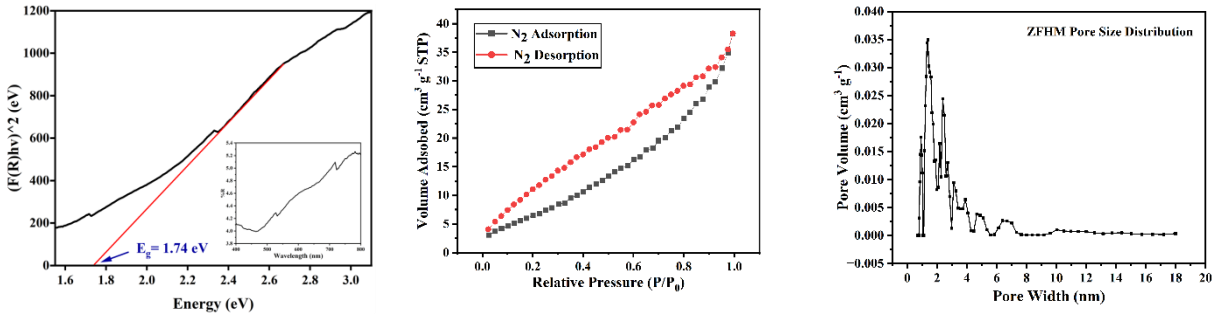
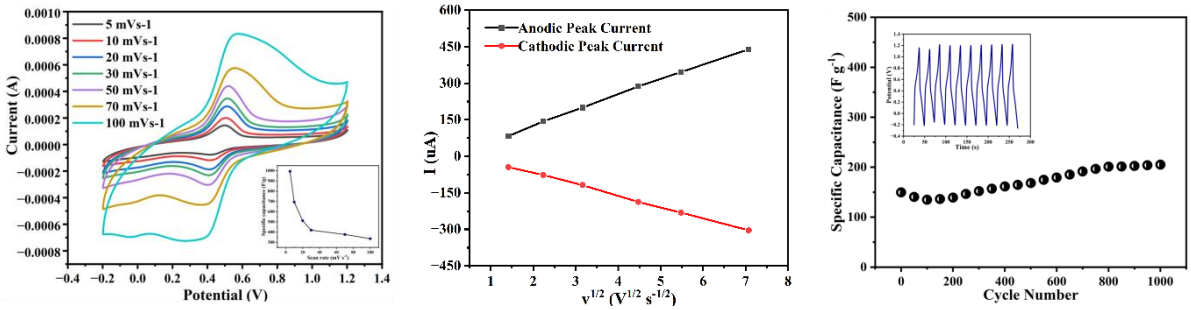


FIGURE 2. (a) Kubelka Munk plot (b) N_2 adsorption-desorption curve (c) Pore size distribution curve

The electrochemical performance of ZFHM has been probed by recording the CV and GCD data. The CV data recorded at different scan rates from 5 to 100 mV s^{-1} between the potential window of -0.2 V and +1.2 V are displayed in fig. 3a. A pair of well-defined redox peaks has been observed in CV curves corresponding to the reversible Faradaic redox reaction (Zn^{+2}/Zn^{+3} or Fe^{+3}/Fe^{+2}).

The values of C_{sp} calculated for different scan rates are listed in table 1 for ZFHM. In 5 mV s^{-1}, the value of C_{sp} is 993.8 F g^{-1} for ZFHM that is superior than the previously reported values of zinc ferrite nano and micro structures [4,5]. It has been observed that C_{sp} decreases while increasing the scan rate as a fewer number of active sites of the electrode material can be accessible in charging/discharging mechanism at higher scan rate (Fig. 3a

inset). Additionally, the plot of anodic and cathodic peak current vs. square root of scan rate (Fig. 3b) shows almost straight-line curves which suggest that reaction on the electrode surface follows diffusion-controlled process [4]. The stability of the sample over a 1000 GCD cycles for the current density 10 A g^{-1} has been recorded where it shows a 34% increase in specific capacitance from its initial value (Fig. 3c) demonstrating that more and more inner electroactive sites get exposed and take part in Faradaic reaction while increasing the GCD cycles [3].



(a) (b) (c)

FIGURE 3. (a) Cyclic voltammetry curve with specific capacitance vs scan rate curve (b) Anodic & cathodic peak current vs square root of scan rate curve (c) stability of specific capacitance in 10 A g^{-1}

TABLE 1: Values of specific capacitance of ZFHM with different scan rates

Scan Rate (mV s^{-1})	5	10	20	30	50	100
Specific capacitance (F g^{-1})	993.8	692.8	511.0	419.2	418.7	376.8

CONCLUSION

$ZnFe_2O_4$ hollow microspheres have been successfully synthesized by a simple solvothermal technique. The study on structural, morphological and optical properties have been performed by PXRD, FESEM, HRTEM, UV-Vis DRS and N_2 adsorption-desorption techniques. It has been shown that the sample is cubic spinel of $Fd\bar{3}m$ symmetry with crystallite size ~176.1 nm. The morphological and N_2 adsorption-desorption studies reveal the porous hollow spherical structure of the sample with average particle size and pore size ~326.4 nm and 2.77 nm, respectively. The sample shows pseudocapacitive behaviour with a high specific capacitance value of 993.8 F g^{-1} at 5 mV s^{-1}. The electrochemical response of the sample is remarkably improved in comparison of its nano and solid micro structured counterparts due to its morphology and porous character.

ACKNOWLEDGMENTS

M. Dutta is grateful to the Department of Physics, Jadavpur University, Kolkata for the instrumental facility and Department of Science and Technology (DST), Govt. of India for providing INSPIRE fellowship.

REFERENCES

1. P. V. Shinde, N. M. Shinde, R. S. Mane, K H Kim, Ferrites for Electrochemical Supercapacitors, Netherlands, Elsevier, 2020, pp. 83–122.
2. A. E. Elkholy, F. E. Heakal and N. K. Allam, RSC Adv., Vol. 7, pp. 51888 (2017).
3. R. Mondal, K. Sarkar, S. Dey, D. Majumdar, S. K. Bhattacharya, P. Sen and S. Kumar, ACS Omega,Vol 4, pp. 12632–12646 (2019).
4. M. Zhu, X. Zhang, Y. Zhou, C. Zhuo, Huang, J., & Li, S. RSC Advances, Vol. 5(49), pp. 39270–39277 (2015).
5. R Roshani and A Tadjarodi, J Mater Sci: Mater Electron,Vol. 31, pp. 23025–23036 (2020).

Effects of different mass loading of La_2NiCrO_6 on the electrodes in supercapacitor performance

I. Ajin and A. Chandra Bose*)

Nanomaterials Laboratory, Department of Physics, National Institute of Technology, Tiruchirappalli 620015, Tamil Nadu, India.
*)Corresponding author: acbose@nitt.edu

Abstract. With the growing demand for portable devices, developing high-performance electrodes for energy storage systems has become a substantial challenge. The critical point for fabricating high-performance equipment is choosing the appropriate electrode materials with optimized electrode parameters. This work proposes lanthanum-based double perovskite material La_2NiCrO_6 (LNC) as a potential electrode material for supercapacitor positive electrode. The proposed LNC material is synthesized using sol-gel followed by a solid-state reaction route. Material confirmation and morphological studies are done using XRD and SEM analysis. A series of electrochemical studies such as galvanostatic charge-discharge (GCD), cyclic voltammetry (CV), and impedance spectroscopy (EIS) are done on the electrodes coated with different mass loading from 0.4 mg to 8 mg (0.4, 0.8, 2, 4, and 8 mg) of active materials. The electrode coated with 0.4 mg of active material exhibits the highest specific capacity of 406 C g^{-1} at the specific current of 1 A g^{-1}, and it displays 90% capacity retention and 99% Coulombic efficiency at the specific current of 10 A g^{-1}.

Keywords: double perovskites, mass loading, supercapacitor, pseudocapacitors, specific capacity.

INTRODUCTION

Nowadays, human society uses vast amounts of energy for their day-to-day activities obtained via the combustion of fossil fuels, which cause global warming. Day by day, the availability of fossil fuels decreases, and global warming causes climate change; because of that, people focus on sustainable and renewable energy sources. Renewable energy sources are intermittent in nature. As a result, electrochemical energy storage (EES) systems are essential to handling the harvested energy in an efficient manner [1-3]. The current energy storage system is heavily dominated by Li-ion batteries (LIBs) owing to their high energy density. This ESS should be needed in various applications ranging from automotive transportation to portable electronics. Despite their widespread adoption, LIBs are limited by their cycle life, potential security risk, and poor power density. The power density of LIBs quickly decreases with its size, restricting the applicability of microbatteries in small-scale wearable electronics. Because of the notable power density supercapacitors are viable candidates for the future generation of energy storage. Properties such as long cycle durability, quick charge/discharge rate, and high-power density make considerable research attention to exploring more [4-6]. The electrode materials play a crucial role in EES systems, and recent studies focus on more electrochemically active low-cost electrodes. Transition metal oxides (TMOs) have an excellent ionic intercalation and are used for supercapacitor applications instead of carbon and conductive polymers. The performance is further boosted through the nanoengineering of electrodes by the combination of TMOs. Perovskite oxides (ABO_3) are a class of materials consisting of a combination of TMOs used as a potential electrode material for supercapacitor energy storage. Perovskites have notable properties such as high thermal stability, excellent ionic conductivity, and exceptional electronic structure. The existence of O_2 vacancies plays an essential role in the intercalation charge storage mechanism. In perovskites, doping of transition metals in A and B sites will alter the oxidation states of the transition metals or else create oxygen vacancies to compensate for the charge. In the literature, 0.8 or 2 mg of active material is coated on the substrate for supercapacitor applications to characterise the electrode performance. However, this low mass loading may not be suitable for practical applications [7, 8]. In this work, a lanthanum-based ABO_3 is prepared by the sol-gel followed by a solid-state reaction method. Lanthanum is at the A site, and two transition metal cations Ni and Cr are at the B site of the ABO_3 structure. This new structure, La_2NiCrO_6 (LNC), is called double perovskite material because of its two metal cations. After the successful synthesis of the material, its electrochemical performance is studied for different mass loadings (0.4, 0.8, 2, 4, and 8 mg) of the material on the Ni-foam.

EXPERIMENTAL SECTION

For synthesis the LNC, 0.2 M of $La(NO_3)_3 \cdot 6H_2O$, 0.1 M of $Ni(NO_3)_2 \cdot 6H_2O$, and 0.1 M of $Cr(NO_3)_3 \cdot 9H_2O$ were dissolved in 100 mL of deionized water. Then, 0.1 M of citric acid was added to this mixture while stirring continuously for 2 h to ensure homogeneity. The mixture was then heated at 80 °C under constant stirring until a viscous gel was formed. This gel was transferred to a crucible and placed in a box furnace at 100 °C for 3 h to remove residual water. Calcination was conducted at 350 °C for 2 h, followed by annealing at 900 °C for 9 h, producing a sample labelled LNC.

Electrochemical studies, were carried out (CV, GCD, and EIS) using a Bio-Logic SP-200 electrochemical workstation configured with a three-electrode system. The pre-cleaned Nickel foam was used to coat the active material. The active material slurry was composed of LNC, polyvinylidene fluoride (PVDF), and carbon black in an 8:1:1 ratio, mixed with a few drops of 1-methyl-2-pyrrolidone (NMP). This mixture was sonicated to achieve uniformity. From the above slurry, 0.4 mg of the active material was then coated onto a 1 cm² area of the Ni-foam, dried at 60 °C for 8 h, denoted as LNC0.4, and used as the working electrode. In the above-mentioned coating procedure, instead of 0.4 mg, the different masses 0.8, 2, 4, and 8 mg were used, and the electrodes are denoted as LNC0.8, LNC2, LNC4, and LNC8, respectively. The reference and counter electrodes were Ag/AgCl and a platinum wire, respectively. CV and GCD tests were conducted within a potential range of 0.0 to 0.6 V and 0.0 to 0.5 V in a 2 M KOH electrolyte solution. EIS measurements were performed across a frequency range from 100 kHz to 100 mHz.

RESULTS AND DISCUSSION

Rigaku Ultima III powder X-ray diffractometer ($CuK_{\alpha 1}$ of wavelength 1.546 Å) was used to analyse the crystal structure of the as-prepared LNC sample. The XRD pattern of LNC is shown in Fig. 1(a); the diffraction peaks at different 2θ values correspond to different miller indices and are matched with the JCPDS number 87-0015. It shows that the primitive cell of LNC has the lattice parameters a = 5.473 Å, b = 7.756 Å, and c = 5.510 Å with an orthorhombic crystal structure. The surface morphology was observed using Carl Zeiss (USA) sigma FE-SEM instrument. LNC has an interconnected spherical granular structure which is shown in Fig. 1(b).

The CV analysis for different mass-loaded electrodes is analysed at the sweep rate of 50 mV s^{-1}, which is shown in Fig. 1(c). Among all the electrodes, the electrode coated with 0.4 mg mass-loaded electrode has the highest CV curve area; the CV analysis for this electrode at different sweep rates is done and shown in Fig. 1(d). As increasing the sweep rate, the CV curve retains its shape, showing the rate capability of the electrode material. The anodic and cathodic peak shift in high sweep rate is due to the polarization effect on electrolyte ions. To find the discharge time, GCD analysis of all electrodes is done at 1 A g^{-1} specific current, which is shown in Fig. 1(e). The specific capacity of the electrodes is calculated using the Eqn. (1)

$$C = \frac{I.\Delta t}{m} \quad (1)$$

where Δt is the discharge time in seconds, I is the current in Ampere, and m is the mass loaded on electrodes in mg. The calculated specific capacity of electrodes are 406, 307, 203, 108, and 42 C g^{-1} for LNC0.4, LNC0.8, LNC2, LNC4, and LNC8, respectively. Among all the electrodes, the electrode loaded with low-mass loading has the highest specific capacity value. As increase the mass-loading on the electrode, there will be a depletion in the charge transfer rate; as a result, specific capacity decreases. The GCD curve for 0.4 mg active material-coated

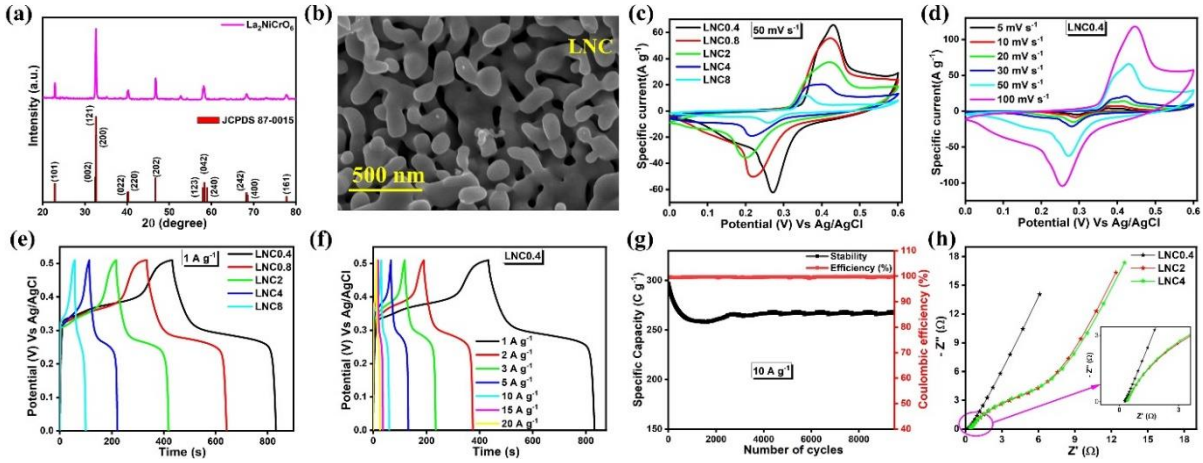


Figure 24: (a) XRD patterns of LNC, (b) FESEM image of LNC, (c) CV curves of electrodes coated with different mass-loading, (d) CV curves of LNC0.4 at different sweep rates, (e) GCD curves of electrodes coated with different mass-loading, (f) GCD curves of LNC0.4 electrode at different specific current, (g) Stability curve of LNC0.4 electrode at 10 A g^{-1}, (h) EIS curves of LNC0.4, LNC0.2, and LNC4 electrodes.

electrodes at different specific currents is shown in Fig. 1(f). As the specific current increases, the ions experience a lack of time to intercalate with the electrodes; as a result, specific capacity decreases with an increase in specific current. The cycle stability and Coulombic efficiency of the LNC0.4 electrode at 10 A g^{-1} are shown in Fig. 1(g), and it shows the stability of 90% and Coulombic efficiency of 99% even after 9,500 cycles. An increase in mass loading will narrow down the ion transport channel leading to increasing the resistance of electrolyte ions. To quantify the resistance experienced by the electrolyte ions, an EIS study is performed and the results are shown in Fig. 1(h). The X-axis intersection in the high-frequency region and radius in the low-frequency region represent the series resistance (R_s) and charge transfer resistance (R_{ct}) experienced by the electrolyte ions. The calculated R_s values are 0.1, 0.27, 0.32 Ω, and R_{ct} values are 0.206, 2.9, 3.2 Ω for LNC0.4, LNC2, and LNC4, respectively. For commercial-level applications, high mass loading is essential; for that case, the electrode fabrication needs to be improved by adding conductive additives like graphene, conductive polymer or carbon nanotube to enhance the electrical conductivity or engineering the surface of the current collector to enhance the adhesion and electrical contact with the active material [9].

CONCLUSIONS

The Lanthanum-based double perovskite (LNC) is synthesized successively through sol-gel followed by solid-state reaction method. After material confirmation, different mass-loading (0.4, 0.8, 2, 4, and 8 mg) of active material is done on the electrode surface and characterized using CV, GCD, and EIS analysis. The electrode with 0.4 mg mass-loading shows a better specific capacity of 406 C g^{-1} at a specific current of 1 A g^{-1}. The same electrode exhibits the stability and Couloumbic efficiency of 90% and 99%, respectively at 10 A g^{-1} specific current. The above results suggest that the perovskite materials show better electrochemical performance in low-mass loading.

ACKNOWLEDGMENTS

Ajin thanks the Ministry of Education for the fellowship support. The authors also thank the Director of the National Institute of Technology, Tiruchirappalli, for providing the instrument facility.

REFERENCES

1. H. Gupta, Y. Dahiya, H. K. Rathore, K. Awasthi, M. Kumar, and D. Sarkar, ACS Appl. Mater. Interfaces **15(36)**, 42685-42696 (2023).
2. W. Li, M. Wu, W. Yang, M. Zhao, X. Lu, Electrochim. Acta. **438**, 141550 (2023).
3. F. Hadji, M. Omari, M. Mebarki, N. Gabouze, A. Layadi, J. Alloys Compd. **942**, 169047 (2023).
4. K. Jiang, M. Gao, Z. Dou, K. Wang, H. Yu, L. Ning, Y. Yang, R. Lv, M. Fu, J. Colloid Interface Sci. **650**, 490-497 (2023).
5. V. V. Mohan, M. Mohan, R. B. Rakhi, Surf. Interfaces. **42**, 103496 (2023).
6. T. Tang, L. Zeng, Y. Liang, S. Jiang, R. Dong, X. Xu, F. Wang, J. Energy Storage. **73**, 109132 (2023).
7. T. C. Doan, B. Muthukutty, H. Yoo, J. Energy Storage. 68, 107648 (2023).
8. A. Yadav, F. N. Mansoorie, A. Saini, M. Bag, ACS Sustain. Chem. Eng. **12(2)**, 1029-37 (2024).
9. S. J. Panchu, K. Raju, P. Singh, D. D. Johnson, H. C. Swart, ACS Appl. Energy Mater. **6(4)**, 2187-2198 (2023).

Impact of Electrolytic Cations in the Pseudocapacitive Performance of $SrFeO_{3-\delta}$

T. Lavaneethan[1], I. Ajin[1], and A. Chandra Bose[1*]

[1]Nanomaterials Laboratory, Department of Physics, National Institute of Technology, Tiruchirappalli 620015, Tamil Nadu, India

[*]Corresponding author: acbose@nitt.edu

Abstract. This work investigates the effect of cations in the electrolyte on the pseudocapacitive performance of $SrFeO_{3-\delta}$. $SrFeO_{3-\delta}$ is synthesized using the sol-gel method, and its structure is analyzed by XRD. Electrochemical studies are conducted in 2 M LiOH, 2 M NaOH, and 2 M KOH using a three-electrode system. $SrFeO_{3-\delta}$ exhibits the highest specific capacity of 338.6 C/g at 1 A/g and retaining 50 % of its capacity after 6000 cycles.

Keywords: Supercapacitor, Energy storage, Electrolytic cations, Perovskite oxide, Redox reaction.

INTRODUCTION

Climate change and global warming have led to government initiatives promoting low-carbon economies and energy efficiency, making renewable energy a crucial alternative source. However, renewable energy systems face intermittent supply and excess energy issues, making energy storage systems practical for managing these challenges [1-2]. Supercapacitors are a viable energy storage option because of their extended cycle life, superior power density, fast charging and discharging, and environmental friendliness. They can complement other energy storage systems like rechargeable batteries [3-4]. Perovskite oxide (ABO_3), with cations A (alkaline earth or rare earth metal) and B (transition metal), exhibits pseudocapacitive behavior, and offers flexible composition for tuning properties like structural stability, electrical conductivity, oxygen vacancies, and cation defects. Its charge storage relies on bulk intercalation/deintercalation, maximizing electroactive area. Anion intercalation with O^{2-} ions enables two-fold charge storage per cycle compared to cation intercalation [5]. $SrFeO_{3-\delta}$ is a perovskite oxide with low toxicity, made from widely available elements without rare-earth elements or precious metals. It accommodates a range of oxygen deficiencies, creating the redox couple Fe^{4+}/Fe^{3+} to maintain neutrality. The electrochemical performance depends on both the electrode material and the electrolyte, where the latter determines the potential window and ionic conduction [6-7]. In this work $SrFeO_{3-\delta}$ is synthesized and studied its electrochemical behavior in three electrolytes: LiOH, NaOH, and KOH.

EXPERIMENTAL SECTION

Synthesis of $SrFeO_{3-\delta}$ and Material Characterization

$SrFeO_{3-\delta}$ was synthesized using the sol-gel method. 0.1 M $Sr(NO_3)_2$, 0.1 M $Fe(NO_3)_3.9H_2O$, and 0.1 M citric acid were dissolved in DD water and stirred for 1 h to form a homogeneous solution. The solution was heated at 90 °C to form a gel, then dried at 100 °C for 8 h to evaporate water content and at 500 °C for 2 h to remove organic compounds present in the gel. The dried gel was ground for 1 h and annealed at 1000 °C for 8 h. The $SrFeO_{3-\delta}$ tested with 2 M LiOH, 2 M NaOH, and 2 M KOH as electrolytes were labeled as SFL, SFN, and SFK, respectively. The crystal structure of the synthesized $SrFeO_{3-\delta}$ were examined by using the PANalytical powder X-ray diffractometer.

Electrochemical measurements

The cyclic voltammetry (CV), galvanostatic charge-discharge (GCD), and electrochemical impedance spectroscopy (EIS) were performed using BioLogic SP-200 electrochemical workstation in three electrode configuration. Active material, carbon black, and Polyvinylidene fluoride (binder) were made as a slurry in a weight ratio of 8:1:1 with NMP (N-Methyl-2-pyrrolidone) as a solvent. 1 mg of the slurry was coated on the precleaned Ni-foam in an area of 1 cm × 1 cm. Thus, 0.8 mg of working material was coated on the nickel foam.

Then it was dried at 60 ºC for 12 h, which acts as a working electrode. Ag/AgCl and platinum electrodes were used as reference and counter electrodes, respectively for the three electrode studies. 2 M LiOH, 2 M NaOH, and 2 M KOH were used as electrolytes. The specific capacity of the material was calculated from the GCD curve using the Eq. (1).

$$C_s = \frac{I\Delta t}{m} \tag{1}$$

Where I is the current applied (in Ampere), Δt is the discharge time (in Seconds), and m is the mass of the active material coated on the Ni-foam (in Grams). The Coulombic efficiency of the electrode was calculated from the GCD curve using Eq. (2).

$$\eta = \frac{t_d}{t_c} \times 100 \tag{2}$$

Where t_d is the discharging time (in Seconds) and t_c is the charging time (in Seconds).

Results and discussion

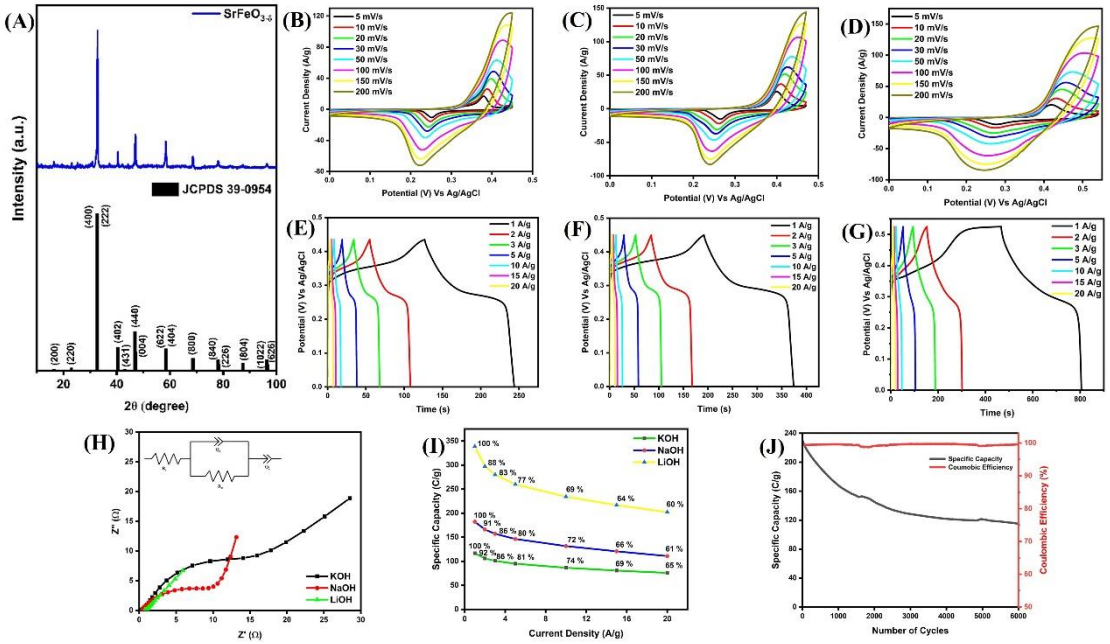


FIGURE 1. (A) XRD pattern of $SrFeO_{3-\delta}$. (B-D) CV curves of $SrFeO_{3-\delta}$ in 2 M KOH, 2 M NaOH, and 2 M LiOH as electrolytes at different scan rates respectively. (E-G) GCD curves of $SrFeO_{3-\delta}$ in different electrolytes at various current densities. (H) Nyquist plots of $SrFeO_{3-\delta}$ in different electrolytes. (I) Effect of current density on specific capacity of $SrFeO_{3-\delta}$. (J) Cyclic stability and Coulombic efficiency for 6000 cycles at a current density of 10 A/g for $SrFeO_{3-\delta}$ in 2 M LiOH.

The crystalline structure of $SrFeO_{3-\delta}$ was identified using the XRD pattern as shown in **Fig 1(a)**. XRD pattern confirms the formation of pure crystalline $SrFeO_{3-\delta}$, which is evident from the absence of any impurity peaks. The peaks at 2θ values 16.4º, 23º, 32.7º, 40.4º, 42.1º, 46.9º, 47.1º, 58.4º, 68.6º, 68.7º, 78.1º, 78.2º, 87.2º, 96.3º, and 96.6º correspond to the Miller indices planes (200), (220), (400), (222), (402), (431), (440), (004), (622), (404), (800), (840), (226), (804), (1022), and (626) respectively. The crystal structure of $SrFeO_{3-\delta}$ is tetragonal with lattice parameters a = b = 10.9340 Å, and c = 7.7050 Å. The peaks match well with the JCPDS data 39-0954.

Figure 1(b-d) shows the CV curve of $SrFeO_{3-\delta}$ in different electrolytes. $SrFeO_{3-\delta}$ exhibits the highest reduction potential in the LiOH electrolyte due to the small cation radius of Li^+. The reduction potential is inversely proportional to cation size. Smaller cation size of Li^+ allows it to intercalate and deintercalate more easily, resulting in maximum charge storage capability in LiOH. The shift in oxidation and reduction peak in different electrolytes are due to polarization. The presence of these redox peaks in the CV curve indicates the pseudocapacitive charge storage behavior of $SrFeO_{3-\delta}$ [8]. The redox reaction in $SrFeO_{3-\delta}$ during electrochemical studies involves the Iron (Fe) atom: Fe^{3+} oxidizes to Fe^{4+} (emitting an electron), and Fe^{4+} reduces to Fe^{3+} (accepting an electron) as shown in the following equation [9].

$$Fe^{3+} \leftrightarrow Fe^{4+} + e^-$$

(3)

The GCD curves of SFK, SFN, and SFL are shown in **Fig 1(e-g).** The specific capacity, calculated using Eq. (1) from the GCD curve, is 116.8 C/g, 182.2 C/g, and 338.6 C/g for SFK, SFN, and SFL respectively at a current density of 1 A/g. The potential window increases in the order of SFK < SFN < SFL. Electrochemical impedance spectroscopy (EIS) was performed for $SrFeO_{3-\delta}$ in the frequency range of 100 to 0.1 kHz in all three electrolytes, with the Nyquist plot and equivalent circuit shown in **Fig 1(h)**. The R_s values of SFK, SFN, and SFL are 0.42 Ω, 0.39 Ω, and 0.01 Ω, and the R_{ct} values are 8.54 Ω, 10.95 Ω, and 0.87 Ω, respectively. **Figure 1(i)** shows that while SFL has the highest specific capacity, its specific capacity retention is the lowest with 60 % at 20 A/g. SFK has the highest specific capacity retention at 65% due to high ionic conductivity, followed by SFN at 61 % [10]. **Figure 1(j)** shows the cyclic stability of SFL, which is 50 % after 6000 cycles at a current density of 10 A/g, with an excellent Coulombic efficiency of ~99.5 %.

CONCLUSION

$SrFeO_{3-\delta}$ is synthesized by sol-gel method at an annealing temperature 1000 ^oC for 8 h. XRD analysis confirms the crystallinity, and it reveals the crystal structure of synthesized $SrFeO_{3-\delta}$ as tetragonal. Due to the smaller size of Li^+ ion, $SrFeO_{3-\delta}$ has exhibited the highest specific capacity of 338.6 C/g at a current density of 1 A/g in 2 M LiOH with a specific capacity retention of 60 %. However, the specific capacity retention is highest in 2 M KOH with 65 % due to its high ionic conductivity. The cyclic stability and Coulombic efficiency of $SrFeO_{3-\delta}$ are measured in 2 M LiOH at a current density of 10 A/g and it is found that $SrFeO_{3-\delta}$ has retained 50 % of its specific capacity at the end of 6000 cycles with exceptional Coulombic efficiency of ~ 99.5%. These results prove that LiOH as a suitable electrolyte for supercapacitor applications.

ACKNOWLEDGMENTS

All authors wish to thank The Director, National Institute of Technology, Tiruchirappalli, Tamil Nadu, for providing instrument facilities.

REFERENCES

1. A. Omri and D. K. Nguyen, Energy **72**, 554-560 (2014).
2. J. Mitali, S. Dhinakaran and A. A. Mohamad, Energy Storage and Saving **1(3)**, 166-216 (2022).
3. A. G. Olabi, Q. Abbas, A. al Makky and M. A. Abdelkareem, Energy **248**, 123617 (2022).
4. J. Libich, J. Máca, J. Vondrák, O. Čech, and M. Sedlaříková, Journal of Energy Storage **17**, 224-227 (2018).
5. A. K. Tomar, A. Joshi, G. Singh, and R. K. Sharma, Coordination Chemistry Reviews **431**, 213680 (2021).
6. M. L. Tummino, Current Research in Green and Sustainable Chemistry **5**, 100339 (2022).
7. I. Goyal, P. Chand, Sunaina, & H. Anand, Energy Nexus **2**, 100013 (2021).
8. A. Mahieddine, L. Adnane-Amara, & N. Gabouze, Journal of Alloys and Compounds **882**, 160754 (2021).
9. P. Soni, S. Singal, A. Yadav, & R. K. Sharma, Journal of Alloys and Compounds, **976**, 173031 (2024).
10. Pal, B., Yang, S., Ramesh, S., Thangadurai, V., & Jose, R., Nanoscale Advances, **1(10)**, 3807–3835 (2019).

Rod-shaped nanostructured Mn-doped CuO Electrocatalyst for oxygen evolution reaction

Afreen A. Chaudhary [1, a)], Dushyant C. Kothari [1, 2] and Pradip B. Sarawade [1, 2, b)]

[1] *National Centre for Nanosciences and Nanotechnology, University of Mumbai (NCNNUM), Vidyanagari, Mumbai 400 098, India.*
[2] *Department of Physics, University of Mumbai, Vidyanagari, Mumbai 400 098, India.*

[a)] Corresponding author: afreen_ps@nano.mu.ac.in
[b)] Corresponding author: pradip.sarawade@physics.mu.ac.in

Abstract. This study explores the synthesis and characterisation of Mn-doped CuO to optimise its electrocatalytic performance in the oxygen evolution reaction for water splitting. A novel rod-shaped nanostructured Mn-doped CuO was prepared using the solvothermal synthesis methodology. Electrochemical evaluations in 1.0 M KOH revealed the fabricated rod-shaped nanostructured CuO doped with 0.23 at. % Mn catalyst exhibits a current density of 10 mA cm^{-2} at an overpotential of 319 mV vs. RHE with a Tafel slope of 120 mV dec^{-1}.

INTRODUCTION

In water electrolysis, the oxygen evolution reaction (OER) constitutes the anodic half-reaction and is limited by a multi-step proton-coupled electron transfer (PCET) mechanism. It requires a high overpotential to overcome its energy barrier. Anodic catalysts are typically employed to reduce this overpotential and enhance current density output. Traditionally, precious metal oxides like RuO_2 and IrO_2 have been highly active for OER in alkaline and acidic media, respectively. However, noble metals are expensive and scarce; there is a growing interest in replacing them with earth-abundant, non-precious metals that maintain catalytic efficiency. Transition metal oxides have attracted growing attention as OER electrocatalysts, with notable advancements reported in recent years. Significantly, Cu-based water oxidation catalysts are increasing because they are abundant, affordable, and have rich redox properties [1], [2]. CuO's structural, optical, and electrical properties can be enhanced by doping it with transition elements [3], [4]. Previous research has shown that electrochemical performance is improved by using Mn-doped CuO oxide for various applications [5], [6]. In the reported study, we successfully synthesised rod-shaped nanostructured Mn-doped CuO using the solvothermal method for oxygen evolution reaction (OER) in a 1.0 M KOH electrolyte. This approach provides precise control over composition and structure, enhancing the material's catalytic activity. The relationships between electrochemical properties and rod-shaped nanostructured morphology were investigated.

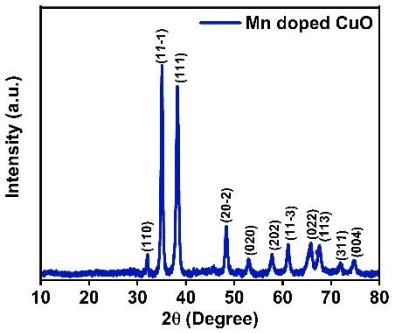
EXPERIMENTAL SECTION

In the solvothermal synthesis, 0.20 M cetyltrimethylammonium bromide (CTAB) and 0.66 M urea (CH_4N_2O) were added to and stirred in 70 mL of cyclohexane (C_6H_{12}). Metal precursors having 0.30 M manganous acetate tetrahydrate ($C_4H_6MnO_4{\cdot}4H_2O$) and 0.30 M copper (II) nitrate trihydrate ($Cu(NO_3)_2{\cdot}3H_2O$) were dissolved in 60 mL of double-distilled water. The two solutions were mixed and stirred at 400 rpm for 30 minutes at ambient temperature, then transferred to a Teflon-lined autoclave and heated for 4 hours at 120 °C. After cooling to ambient temperature, the precipitate was collected by centrifugation, thoroughly washed with distilled water and acetone, and dried for 8 hours in a hot-air oven. The resulting composite was calcined at 450 °C for 4 hours in air to produce the Mn-doped CuO catalyst. The prepared catalyst was then used for further Physicochemical and Electrochemical investigations. The D2 PHASER, Bruker, Germany, was used to collect the powder X-ray diffraction (XRD) patterns, utilising Cu Kα radiation (λ = 0.15418 nm). A Zeiss ULTRA device was used for scanning electron microscopy (SEM) analysis and energy-dispersive X-ray spectroscopy (EDXS). To evaluate the electrocatalytic activity of the solvothermally synthesised Mn-doped CuO, a uniformly dispersed catalyst ink was prepared by adding 5 mg of catalyst, 25 µL of Nafion binder, and 1 mL of isopropyl alcohol (IPA). This mixture was sonicated for 20 minutes. Then, the dispersion (82 µL) was drop-cast onto a 1 cm^2 surface of a nickel foam (NF) with a mass loading of about 0.4 mg cm^{-2}. The drop-cast NF was then dried under a lamp. The electrochemical measurements were performed using a Gamry INTERFACE 1010E workstation. The oxygen evolution reaction (OER) was studied in a 1.0 M KOH electrolyte at ambient temperature using a three-electrode system, comprising a catalyst-deposited nickel foam as the working electrode, a platinum spring as the counter electrode, and a Hg/HgO (1 M

KOH) electrode as the reference electrode. The recorded potentials versus Hg/HgO were converted to the reversible hydrogen electrode (RHE) scale using a standard equation without iR Correction.

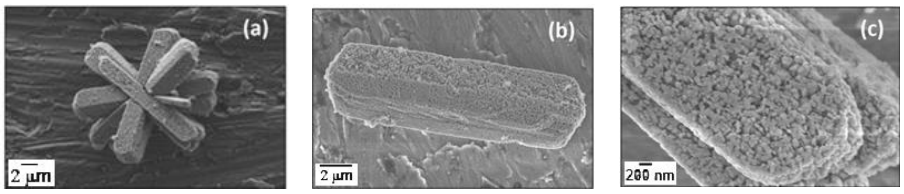
RESULTS AND DISCUSSION

The defined diffraction peaks presented in **FIGURE 1** are indexed to the monoclinic crystal structure of CuO (JCPDS Card No. 48-1548). The positive shift in d values of Mn-doped CuO compared to those of pure CuO is due to the strain induced by Mn^{2+} in the CuO lattice. The surface morphology of the prepared Mn-doped electrode material is revealed through SEM images at various magnifications, as illustrated in **FIGURES 2(a-c)**. The particles are observed to be three-dimensional rod-shaped structures with approximate dimensions of 15.32 µm in length, 3.01 µm in height, and 1.85 µm in width. Closer inspection reveals that the surface of the rod particles is rough, with numerous nanospherical structures present, creating a highly porous texture. This morphology provides more active sites, resulting in improved OER performance. EDX analysis confirmed the elemental composition of Cu, Mn, and O in the sample, with the Mn detected at a concentration of 0.23 at. % (**FIGURE 2 (d)**).



Plane	2□° JCPDS	2□° Observed	d (A°) JCPDS	d (A°) observed
(110)	32.509	32.028	2.752	2.792
(11-1)	35.544	35.053	2.524	2.558
(111)	38.709	38.261	2.324	2.350
(20-2)	48.717	48.363	1.868	1.880
(020)	53.487	53.000	1.711	1.726
(202)	58.265	57.800	1.582	1.593
(11-3)	61.526	61.131	1.505	1.514
(022)	65.813	65.703	1.418	1.420
(113)	67.905	67.596	1.379	1.384
(311)	72.373	71.952	1.305	1.311
(004)	74.978.	74.721	1.266	1.269

FIGURE 1. XRD patterns of rod-shaped nanostructured CuO doped with 0.23 at.% Mn sample and its analysis

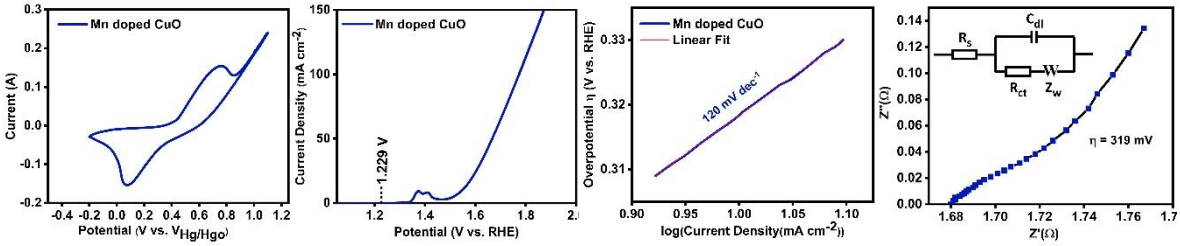


(d)

Element	wt. %	at. %
Cu	74.62	42.59
Mn	00.35	00.23
O	25.03	57.17

FIGURE 2. (a-c) SEM images and **(d)** EDX analysis of rod-shaped nanostructured Mn-doped CuO electrocatalyst

The electrochemical water oxidation performance of a rod-shaped nanostructured Mn-doped CuO catalyst coated on nickel foam was assessed using OER in 1.0 M KOH electrolyte. In **FIGURE 3(a),** the Cyclic voltammetry (CV) performed within the potential window of 1.1 to -0.2 V vs. Hg/HgO revealed distinct redox peaks. **FIGURE 3(b).** Linear sweep voltammetry (LSV) analysis revealed that the catalyst achieved a current density of 10 mA cm^{-2} with an overpotential of 319 mV. The onset potential was 1.47 V vs. RHE, which significantly lowered the energy barrier for the oxygen evolution of the electrocatalyst. The Tafel slope was determined to be 120 mV dec^{-1} in **FIGURE 3(c)**, indicating that the rate-determining step involves efficient electron transfer kinetics and stable intermediate species formation [7]. The Nyquist plot for the synthesised electrode system is shown in **FIGURE 3(d).** The equivalent Randles circuit, including a Warburg impedance element, was used to model the combination of diffusion processes and kinetics. The fitting parameters reveal a low charge transfer resistance (R_{ct}) of 0.246 Ω, which supports the excellent OER activity and efficient electron transport of the prepared catalyst.



(a) (b) (c) (d)

FIGURE 3. (a) Cyclic Voltammogram at 100 mV s^{-1}, **(b)** Linear polarisation curve at a scan rate of 5 mV s^{-1}, **(c)** corresponding Tafel plot, and **(d)** Nyquist plot at an overpotential of 319 mV for synthesised Mn-doped CuO in 1.0 M KOH.

CONCLUSIONS

The successful synthesis of electrocatalyst through the solvothermal route resulted in rod-shaped nanostructured CuO doped with 0.23 at. % Mn. In 1.0 M KOH, the prepared catalyst required an overpotential of 319 mV at a benchmark water oxidation current density of 10 mA cm^{-2} for the oxygen evolution reaction (OER) activity. The promising performance of Mn-doped CuO as an electrocatalyst for OER highlights its potential for practical applications in renewable energy technologies.

ACKNOWLEDGMENTS

Afreen Chaudhary acknowledges the PhD fellowship under the Industry-Academia program from M/s SMT Pvt Ltd. She thanks Ms. Vedangi Shinde for her dedicated assistance in this research.

REFERENCES

[1] T. N. Huan *et al.*, "A Dendritic Nanostructured Copper Oxide Electrocatalyst for the Oxygen Evolution Reaction," *Angewandte Chemie International Edition*, vol. 56, no. 17, pp. 4792–4796, Apr. 2017, doi: 10.1002/anie.201700388.

[2] X. Liu, S. Cui, M. Qian, Z. Sun, and P. Du, "In situ generated highly active copper oxide catalysts for the oxygen evolution reaction at low overpotential in alkaline solutions," *Chemical Communications*, vol. 52, no. 32, pp. 5546–5549, 2016, doi: 10.1039/C6CC00526H.

[3] X. Xiong, C. You, Z. Liu, A. M. Asiri, and X. Sun, "Co-Doped CuO Nanoarray: An Efficient Oxygen Evolution Reaction Electrocatalyst with Enhanced Activity," *ACS Sustain Chem Eng*, vol. 6, no. 3, pp. 2883–2887, Mar. 2018, doi: 10.1021/acssuschemeng.7b03752.

[4] M. Nesa, Md. A. Momin, M. Sharmin, and A. H. Bhuiyan, "Structural, optical and electronic properties of CuO and Zn doped CuO: DFT based First-principles calculations," *Chem Phys*, vol. 528, p. 110536, Jan. 2020, doi: 10.1016/j.chemphys.2019.110536.

[5] P. More *et al.*, "Spray Synthesized Mn-doped CuO Electrodes for High Performance Supercapacitor," *ChemistrySelect*, vol. 7, no. 37, Oct. 2022, doi: 10.1002/slct.202202504.

[6] S. Guţoiu *et al.*, "Enhancement of Dopamine Electrochemical Detection with Manganese Doped Crystalline Copper Oxide," *Coatings*, vol. 13, no. 6, p. 1014, May 2023, doi: 10.3390/coatings13061014.

[7] A. Kapałka, G. Fóti, and C. Comninellis, "Determination of the Tafel slope for oxygen evolution on boron-doped diamond electrodes," *Electrochem commun*, vol. 10, no. 4, pp. 607–610, Apr. 2008, doi: 10.1016/j.elecom.2008.02.003.

Effect of Addition of Pb_3O_4 on the Energy Release of Al/CuO Nanothermite

Rahul [1, *], K. K. Sharma[1] and Vimal Sharma[2]

[1] *Department of Physics and Photonics Science, National Institute of Technology Hamirpur, Hamirpur, 177005, India.*

[2] *Department of Physics, National Institute of Technology Uttarakhand, Srinagar, Uttarakhand, India*

[*] *Corresponding author:* 151999rahul@gmail.com

Abstract. The synthesis of Al/CuO/Pb_3O_4 nanothermites is accomplished using the physical mixing approach with the assistance of ultrasonication. Pb_3O_4 is included as a secondary oxide in these nanothermites. X-ray diffraction (XRD) was performed on these nanothermites to analyze the crystalline phase of their components. The thermite reaction of Al/CuO/Pb_3O_4 nanothermites with varying compositions was investigated using differential scanning calorimetry (DSC). The study revealed that the energy release of Al/CuO nanothermite was enhanced by the addition of Pb_3O_4.

Keywords: X-ray diffraction, differential scanning calorimetry, ultrasonication, nanothermites, energy release

INTRODUCTION

Thermites are binary energetic composites that undergo exothermic reactions when the oxidizer and fuel material interact in redox reactions [1,2]. A thermite reaction is a solid-state diffusion-controlled reaction, the maximum interfacial contact area between the oxidizer and the fuel is desired to achieve higher energy release rates. As the size of constituents of thermite is reduced to nanoscale, their surface area to volume ratio increases, due to which the interfacial contact between fuel and oxide improves. The arrangement of particles at the nanoscale may enhance the rate of reaction and lead to the enhancement in the rate of energy released due to improvement in the interfacial contacts, homogeneity, and diffusivity between the reactants. Thus, at the nanoscale, fuel and metal powder are expected to give better performance [3,4]. In nano-thermite, at least one of the component phases has particle dimensions on the nanometer scale. Nanothermites offer different behavior than traditional thermite, such as enhanced reactivity, high heat release rates, extraordinary combustion efficiency, tailored burning rates, reduced sensitivity, and decreased melting temperatures due to the enhanced intermixing of the fuel and oxidizer constituents along with reduced diffusion lengths between neighboring particles, which allows quicker chemical reactions at the fuel/oxidizer interface [5-7]. The addition of an oxide in nanothermite, makes this ternary nanothermite. In this ternary nanothermite energy, gas release and oxygen quantity for fuel to get oxidized can be tailored and improved by varying the amount of additional oxide [8-10]. In this study, Pb_3O_4 is added as an additional oxide in the Al/CuO nanothermite.

EXPERIMENTAL DETAILS

Three samples of Al/CuO/Pb_3O_4 nanothermites have been synthesized with three different compositions of constituents of nanothermites. In all these samples, the molar ratio of fuel and oxidizer kept 1:1. In the first sample composition ($Al_{(1.2)}/CuO_{(1.0)}/Pb_3O_{4(0.2)}$), Al has 1.2 moles, CuO has 1.0 moles, and Pb_3O_4 has 0.2 moles. In the second sample composition ($Al_{(1.2)}/CuO_{(0.8)}/Pb_3O_{4(0.4)}$), Al has 1.2 moles, CuO has 0.8 moles, and Pb_3O_4 0.4 moles. In the third sample composition ($Al_{(1.2)}/CuO_{(0.6)}/Pb_3O_{4(0.6)}$) Al has 1.2 moles, CuO has 0.6 moles and Pb_3O_4 0.6 moles. In order to make Al-CuO nanothermite, Al nanoparticles, CuO nanoparticles, and Pb_3O_4 nanoparticles were dissolved in ethanol using three different beakers, and then each was subjected to 20 minutes of individual sonication using an ultrasonic probe sonicator. The sonicator produces sound waves that aid in dispersing the agglomerates and ensuring improved mixing of the oxidizer and fuel constituents of the nano-thermite. After that, three of these solutions were combined and sonicated once again for 30 minutes. The mixture is then dried at 70°C while being stirred magnetically to avoid the re-agglomeration of nanoparticles. Finally, the thermite powder that resulted after drying was then ground for 60 minutes to obtain homogeneous samples.

RESULTS AND DISCUSSION

The nanothermites were analyzed using powder XRD to determine their composition. Figure 1 displays the XRD pattern of Al/CuO/Pb_3O_4 nanothermites. The Miller indices of aluminum (Al), copper oxide (CuO), and lead(II,IV) oxide (Pb_3O_4) corresponded to reference numbers 00-001-1180, 01-074-1021, and 00-001-0654, respectively.

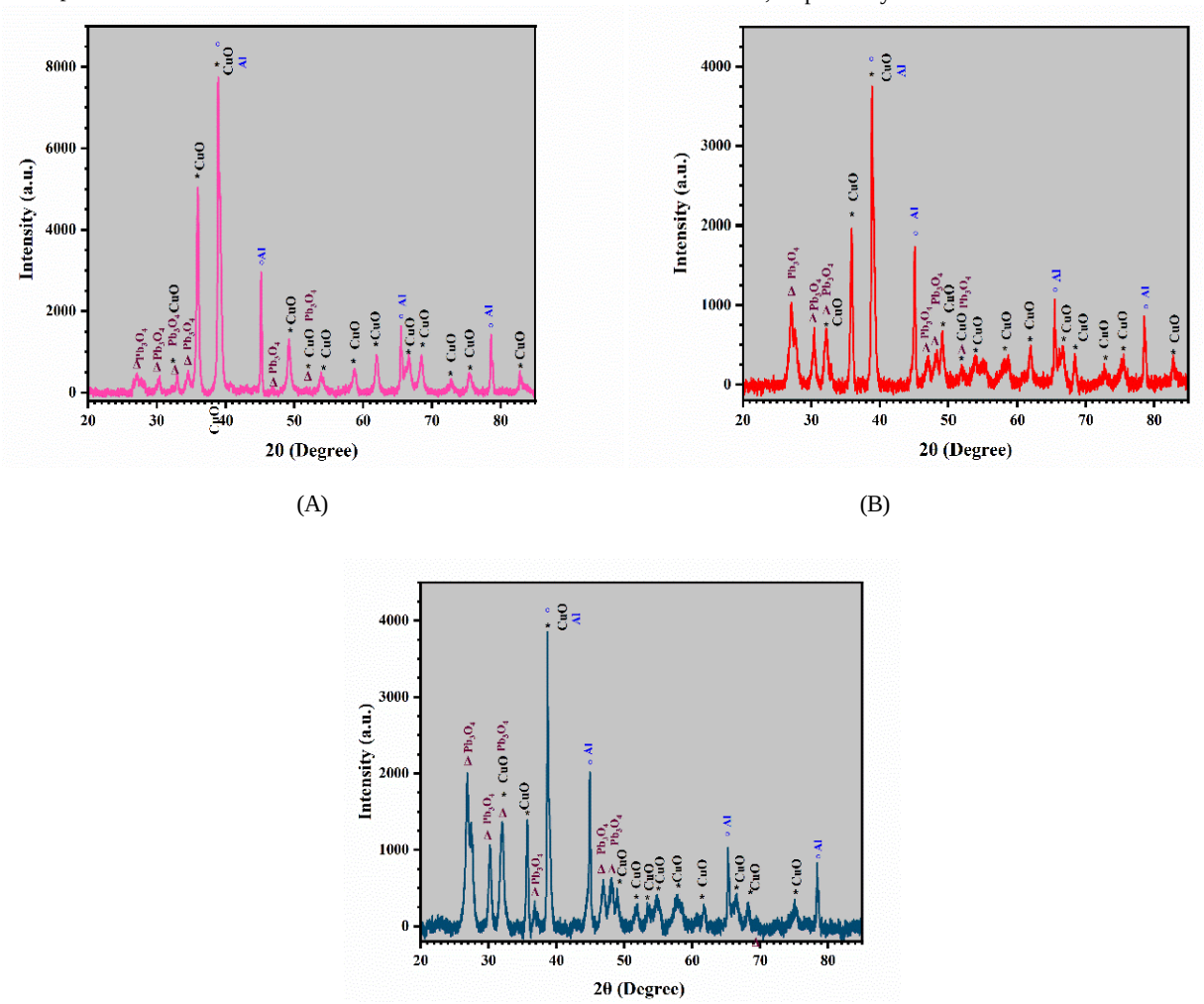
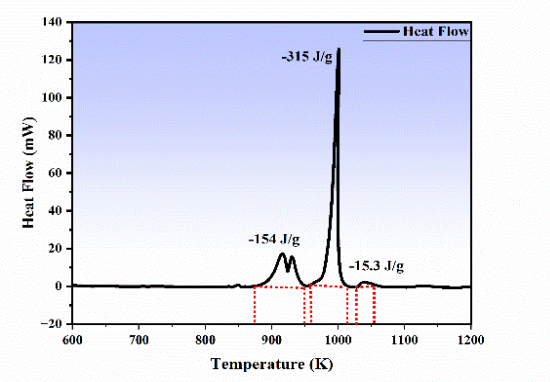
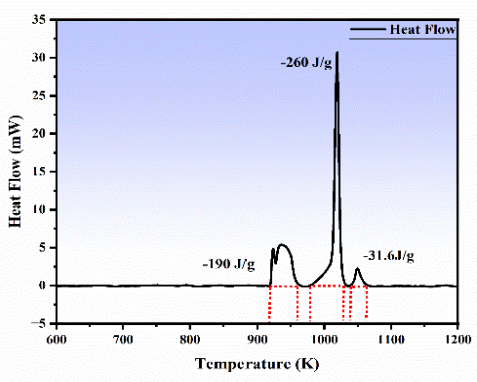


Figure 1. (A) XRD graph of ($Al_{(1.2)}/CuO_{(1.0)}/Pb_3O_{4(0.2)}$), (B) XRD graph of ($Al_{(1.2)}/CuO_{(0.8)}/Pb_3O_{4(0.4)}$) and (C) XRD graph of ($Al_{(1.2)}/CuO_{(0.6)}/Pb_3O_{4(0.6)}$).

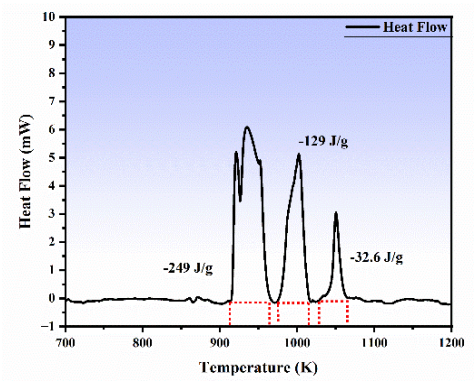
DSC was used to evaluate the thermite reactions of Al/CuO/Pb_3O_4 nanothermites. Figure 2 shows their DSC curves. Total energy release was 484.3 J/g, 481.6 J/g, and 410.6 J/g for $Al_{(1.2)}/CuO_{(1.0)}/Pb_3O_{4(0.2)}$, $Al_{(1.2)}/CuO_{(0.8)}/Pb_3O_{4(0.4)}$ and $Al_{(1.2)}/CuO_{(0.6)}/Pb_3O_{4(0.6)}$ respectively. $Al_{(1.2)}/CuO_{(1.0)}/Pb_3O_{4(0.2)}$, nanothermite has the highest energy release, and this energy release decreases with the increase in the amount of Pb_3O_4 in the considered nanothermites. There are three exothermic peaks observed in these nanothermites. It was observed that the amount of energy released for Al/CuO nanothermite can be varied and improved with the addition of Pb_3O_4 oxide. Onset temperatures for first exothermic peak are 874 K, 919 K, and 914 K, onset temperatures for the second exothermic peak temperature are 959 K, 979 K, and 974 K and onset temperatures for the third exothermic peak are 1026 K, 1039 K, and 1029 K for ($Al_{(1.2)}/CuO_{(1.0)}/Pb_3O_{4(0.2)}$), ($Al_{(1.2)}/CuO_{(0.8)}/Pb_3O_{4(0.4)}$) and ($Al_{(1.2)}/CuO_{(0.6)}/Pb_3O_{4(0.6)}$) respectively.



(A)



(B)



(C)

CONCLUSION

$Al/CuO/Pb_3O_4$ nanothermites of three different compositions were synthesized via a physical mixing method assisted with an ultrasonicator. XRD confirms the presence of all crystalline peaks of constituents of $Al/CuO/Pb_3O_4$ nanothermites. DSC characterization of the considered samples revealed and that energy release value can be varied and improved with the addition of Pb_3O_4 in Al/CuO nanothermite. $(Al_{(1.2)}/CuO_{(1.0)}/Pb_3O_{4(0.2)})$ nanothermite has highest energy release value of 484.3 J/g among the three nanothermites considered.

ACKNOWLEDMENTS

One of the author Rahul would like to thank the financial assistance in the form of fellowship by the Ministry of Education, Govt. of India for completion of this research work.

REFERENCES

1. S. Kabra, S. Gharde, P. M. Gore, S. Jain, V. H. Khire, and B. Kandasubramanian, Nano Express, Vol. 1, pp. 032001 (2020).
2. D. Trache and L. T. DeLuca, Nanomaterials, Vol. 10, pp. 2347 (2020).
3. H. Wang, G. Jian, G. C. Egan and M. R. Zachariah, Combust. Flame., Vol. 161, pp. 2203-2208 (2014).
4. L. Wang, D Luss and K.S. Martirosyan, J. Appl. Phys., Vol. 110, pp. 074311 (2011).
5. K. Sullivan, G. Young and M. R. Zachariah, Combust. Flame., Vol. 156, pp. 302 (2009).
6. J. Shen, Z. Qiao, K. Zhang, J. Wang, R. Li, H. Xu, G. Yang G and F. Nie, Appl. Therm. Eng., Vol. 62, pp. 732 (2014).
7. P. Thakur, V. Sharma and N. Thakur, Physica B: Condens. Matter, Vol. 610, pp. 412803 (2021).
8. S. Li, J. L. Chen, T. Guo, W. Ding, L. Jiang, M. Yao and Y. M. Mao, Def. Technol., Vol 26, pp. 180-190 (2023).
9. J. W. Liu, S. Li, M. Li, Y. Zhou, T. Guo, Z. X. Han and L. Jiang, Propellants Explos. Pyrotech., Vol. 48, pp. e202200290 (2023).
10. J. Chen, T. Guo, W. Ding, J. Song, M. Yao, F. Bei and S. Li, S., Ceram. Int., Vol. 47, pp. 16500-16510 (2021).

Examining potential of $Mn_{0.7}Zn_{0.3}Fe_2O_4$ Solid Microspheres as Supercapacitor Electrode Material: Study on its Electrochemical Performance

S. Gazi[1], P. Saha[1], K. Sarkar[1], R.Mondal[1,a)], S. Kumar[1,a)]

[1]Department of Physics, Jadavpur University, Kolkata-700032, India

[a)]Corresponding author: rituparnam.physics@jadavpuruniversity.in, kumar_dsa@yahoo.com

Abstract. The structural, microstructural characteristics and electrochemical supercapacitive behavior of $Mn_{0.7}Zn_{0.3}Fe_2O_4$ solid microspheres synthesized by template-free solvothermal method have been reported here. The powder x-ray diffraction (PXRD) and Fourier transform infrared (FTIR) spectroscopic study confirms that the sample is well crystallized (~ 43.25 nm), single phase cubic spinel ferrite of $Fd\bar{3}m$ symmetry. The field emission scanning electron microscopic (FESEM) and transmission electron microscopic (TEM) techniques confirm that the individual microspheres having average diameter ~ 248 nm are composed of constituent nanoparticles of size ranging between 10 – 14 nm. The sample exhibits excellent electrochemical behavior with specific capacitance of 2193 F g^{-1} at 2 mV s^{-1} and has long life cycle with 94 % capacitance retention over 1000 cycles. Thus, the sample is promising electrode material for supercapacitor application.

Keywords: MnZn ferrite, supercapacitor, electrochemical performance, solvothermal synthesis, capacitance retention

INTRODUCTION

Owing to their fast charge/discharge rate, high energy capacity, high power density, long life cycle, less temperature sensitivity, electrochemical stability and eco-friendlyness, the supercapacitors have gained significant attention of researchers as energy storage devices to cope up with the need for endlessly rising energy consumption [1, 2]. The performance of supercapacitors impelled by electrochemical reactions depends on mainly electrochemical properties of electrode materials, selection of electrolytes and the potential window of electrodes. However, optimizing specific surface area, rate of electron transfer, interfacial resistance, morphology and structural hierarchy of electrode materials is very crucial for enhancing the capacitance of supercapacitors. Assessment of the performance of microstructured mixed spinel ferrites ($MnZnFe_2O_4$, $CoZnFe_2O_4$, $NiZnFe_2O_4$ etc.) as supercapacitor electrode material carried out in recent past has yielded encouraging results [3]. These microstructured spinel ferrites are composed of nanoparticles, easily dispersible in aqueous media and can accelerate chemical reactions because of their small size, huge number of cations in coordination sites and high surface to volume ratio [3]. Several redox states due to the involvement of two transition metal ions along with multi-valance iron ions (Fe^{2+}/Fe^{3+}) in these ferrites enhances their electrochemical performance [4, 5]. However, $Mn_{0.7}Zn_{0.3}Fe_2O_4$ solid microspheres have not been explored as a potential electrode material for supercapacitors. In this background, the synthesis of $Mn_{0.7}Zn_{0.3}Fe_2O_4$ solid microspheres and the enhancement of their electrochemical performance by tuning their structural, microstructural properties can produce promising results in connection to develop advanced electrode materials for supercapacitor applications.

EXPERIMENTAL

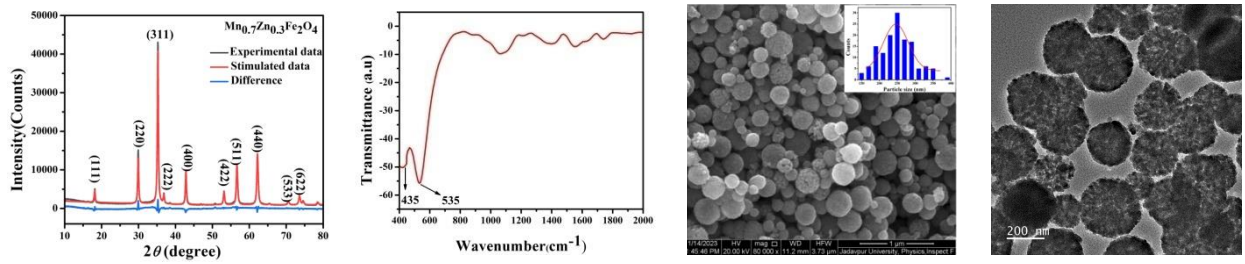
The template free, one-pot solvothermal method has been used to synthesize $Mn_{0.7}Zn_{0.3}Fe_2O_4$ solid microspheres (MZ7030). Stoichiometric amount of metal ferrites ($MnCl_2.6H_2O$, $ZnCl_2.4H_2O$ and $FeCl_3.6H_2O$) are dissolved in 80 ml ethylene glycol (EG) through magnetic stirring. Afterward, 7.2 g of sodium acetate (NaAc) followed by 2 g of PEG 4000 have been added to the solution. After continuous stirring for 3 hours, the mixture has been transferred into a 100 mLTeflon-lined stainless steel autoclave and heated at 180 ºC for 16 h. The precipitate has been then collected, washed and dried at 60 ºC for 6 h in vacuum to obtain the final product.

Bruker D8 Advanced diffractometer, Shimadzu IRAffinity- 1S Fourier transform infrared (FTIR) spectrometer, FEI Inspect F50 field emission scanning electron microscope (FESEM) and Jeol 2100 high resolution transmission electron microscope (TEM) are employed for characterizing the sample thoroughly. All electrochemical measurements i.e., cyclic voltammetry (CV) in the potential range between -0.4 and +0.3 V at the scan rates ranging from 2 to 50 mV s^{-1}, galvanostatic charging discharging (GCD) at the current densities ranging

from 15 to 55 A g^{-1} and cyclic stability over 1000 GCD cycles have been carried out in a three electrode system at 25 °C with 3 M KOH solution as electrolyte by a Autolab PGSTAT204 electrochemical workstation. Platinum wire, saturated Ag/AgCl electrode and prepared sample coated graphite rod (10 µl aqueous solution of the sample was casted drop-wise on one of the circular flat end with surface area ~ 0.13 cm^2 of graphite rod) were used as counter electrode, reference electrode and working electrode, respectively.

RESULTS AND DISCUSSION

All the characteristics peak observed in the PXRD pattern (Fig. 1 (a)) of MZ7030 recorded by using Cu K_α (λ=1.54184 Å) radiation in the 2θ range of 10-80° match well with those of the reported cubic spinel structure (JCPDS ICDD card numbers 04-006-1581). The pattern has been refined by Rietveld based software MAUD2.33 [6] considering $MnFe_2O4/ZnFe_2O_4$ as model system. The experimental pattern matches very well with the fitted one. The values of structural, microstructural and refinement parameter are listed in Table 1. The results of fitting confirm that the sample is single phase cubic spinel with $Fd\bar{3}m$ space group.



(a) (b) (c) (d)

FIGURE 1. (a) PXRD pattern fitted by Maud, (b) FTIR spectrum, (c) FESEM image (inset: histogram drawn from FESEM image) (d) TEM image of $Mn_{0.7}Zn_{0.3}Fe_2O_4$ solid microspheres

TABLE 1. Crystal data and refinement parameters

Parameters	MZ7030
Lattice parameter (a(Å))	8.4327 (4.41x10^{-4})
Density (g cm^{-3})	5.12
Crystallite size (nm)	43.25 (0.32)
Microstrain	4.40 x 10^{-4} (2.72x10^{-5})
Rwp	0.097
Rexp	0.078
GOF	2.46

Two major bands observed at 435 and 535 cm^{-1} in the FTIR spectrum (Fig. 1(b)) appear due to the metal-oxide (M-O) stretching vibrations at the tetrahedral (A) and octahedral [B] sites, respectively, which corroborates with the results of PXRD study. The FESEM and TEM micrographs of MZ7030 depicted in Figs. 1(c) and 1(d) suggest that the particles in the sample is spherical in shape and uniform in size with average diameter is ~ 248 nm. The surface of the microspheres is rough as they are formed by agglomeration of nanoparticles (Fig. 1(d)).

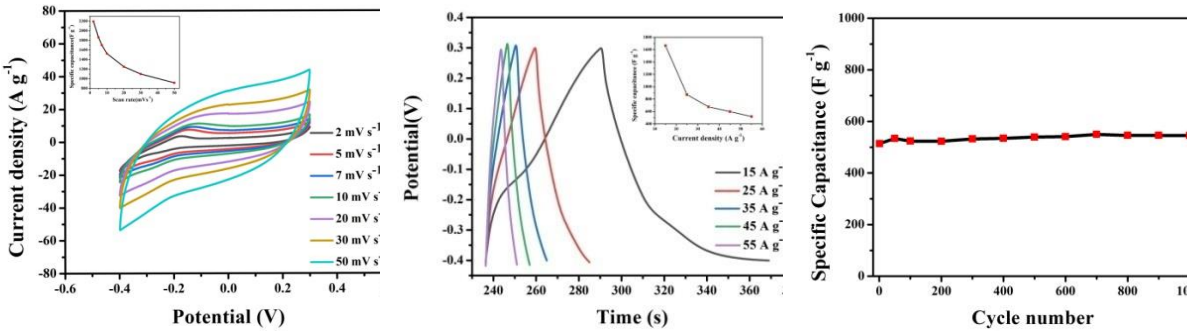
The electrochemical supercapacitive performance of MZ7030 solid microspheres has been investigated through CV and GCD measurements. A prominent oxidation peak at -0.15 V and a feeble reduction peak at -0.35 V are observed in the CV curve (Fig. 2(a)) of the sample. The deviation from linearity in both cycles of GCD curve (Fig. 2(b)) can be attributed to the Faradaic type pseudocapacitive nature of the sample originating due to the charge transfer between electrode and electrolyte through intercalation and electrosorption process [3]. The values of specific capacitance calculated from CV curve at different scan rate and GCD curve at different current density with the help of equations mentioned in our previous work [3] listed in Table 2 and Table 3, respectively.

TABLE 2. Values of specific capacitance (Cs) at different scan rates calculated from CV curve.

Scan rate (mV s^{-1})	2	5	7	10	20	30	50
Specific capacitance (Cs in F g^{-1})	2193	1862	1700	1528	1252	1100	915

TABLE 3. Values of specific capacitance (Cs) at different scan rates calculated from CV curve.

Current density (A g^{-1})	15	25	35	45	55
Specific capacitance (Cs in F g^{-1})	1664	873	676	599	519



(a) (b) (c)

FIGURE 2. (a) CV curve at different scan rates, (b) GCD curve at different current density and (c) cyclic stability over 1000 GCD cycles of $Mn_{0.7}Zn_{0.3}Fe_2O_4$ solid microspheres

The specific capacitance (C_s) decreases with the increase of scan rates in CV measurement (inset of Fig. 2(a)) and current densities in GCD measurement (inset of Fig. 2(b)). At higher scan rate, probability of interaction between the electrode surface and electrolyte reduces and as a result the effective accessible electrochemically active sites taking part in Faradiac reaction reduces, which leads to decrease in the value of C_s with the increase in scan rate. At lower scan rate, electrolyte ions get enough time to access the entire electrode surface, which increases C_s [5]. Longevity of supercapacitor can be probed through cyclic stability measurement as shown in Fig. 2 (c), where GCD is performed over 1000 cycles at current density of 80 A g^{-1}. The capacitance retention of the sample is 94% after 1000 cycles indicating good long term stability of the sample.

CONCLUSION

MZ7030 solid microspheres have been synthesized by one-pot solvothermal method. The PXRD, FESEM, TEM and FTIR study have confirmed that the sample is well crystalline (~ 43.25 nm), single phase cubic spinel ferrite, spherical in shape (average diameter ~ 248 nm) where the size of the nanoparticles forming solid microspheres is in the range of 10 – 14 nm. The sample exhibits excellent electrochemical behavior with high value of specific capacitance of 2193 F g^{-1} at 2 mV s^{-1} and long life cycle with 94 % capacitance retention indicating the sample is appropriate as electrode material for supercapacitor application. From literature survey it appears that the specific capacitance of microstructured ferrite depends on morphology of the sample [2 - 4].

ACKNOWLEDGMENTS

S. Gazi gratefully acknowledges Department of Physics, Jadavpur University for the instrumental facility and UGC Ministry of Minority Affairs for providing Maulana Azad National fellowship.

REFERENCES

1. P. Kumar, M.C. Mathpal, G.K. Inwati, M.-M. Duvenhage, E.L. Meyer, M. Soler and H.C. Swart, Future of Smart Supercapacitors, in *Smart Supercapacitors*, Amsterdam: Elsevier, 2023, pp. 851–866.
2. S. Kumar, F. Ahmed, N.M. Shaalan, N. Arshi, S. Dalela and K.H. Chae, Materials 16, 4328 (2023).
3. R. Mondal, K. Sarkar, S. Dey, D. Majumdar, S. K. Bhattacharya, P. Sen and S. Kumar, ACS Omega Vol. 4 **(7)**, pp. 12632-12646 (2019).
4. M. Saghafi, S.A. Hosseini, Sh. Zangeneh, A. H. Moghanian, V. Salarvand, S. Vahedi and Sh. Mohajerzadeh, SN Appl. Sci. Vol. 1, pp. 1303 (2019).
5. S. A. Al Kiey, R. Ramadan and M. M. El-Masry, Appl. Phys. A Vol.128, pp.473 (2022).
6. L. Lutterotti, MAUDWEB; version 1.9992 (2004)

Relaxor SBT/PVDF-HFP Ferroelectric Flexible Films for Energy Storage and Harvesting Applications

Lalit Kumar Jena[1, a)], Saket Asthana[1]

[1]Advanced Functional Materials Laboratory, Department of Physics, Indian Institute of Technology Hyderabad, Kandi, Sangareddy,502284, Telangana, India

[a)] Corresponding author: ph22resch01006@iith.ac.in

ABSTRACT

The eco-friendly $Sr_{0.7}Bi_{0.2}TiO_3$ (SBT) via the solid-state sintering method was synthesized. The SBT composition was combined with PVDF-HFP polymer via solution casting to fabricate flexible particulate composites. Characteristic peaks of PVDF-HFP polymer with reflections corresponding to the SBT phase were observed from XRD patterns. SEM micrograph shows homogeneous and spherulite structures, which are clearly distinct in the composite film. Enhanced breakdown strength (E_b) of 700 kV/cm was found in 30 wt% SBT/PVDF-HFP. W_{rec} of 64 mJ/cm^3 was estimated, which strengthened its potential in energy storage applications. Moreover, the Piezoelectric Energy harvester (PEH) fabricated using SBT ceramic-infused PVDF-HFP films shows a voltage output of 6V and~13V through different external forces.

Keywords: Relaxor ferroelectrics, Composite film, Piezoelectric Energy Harvester, Solid State Reaction, Solution casting

INTRODUCTION

Flexible and wearable electronics have garnered more attention nowadays. Piezo/ferroelectric materials have been a key asset for the development of sensors, transducers, and energy storage applications owing to their characteristic spontaneous polarization without the application of an external electric field.[1] Lead (Pb) based ferroelectric materials demonstrate great potential in the aforementioned application. However, the European Union has set a limit on the usage of lead in industrial applications, noticing the hazardous effects of Lead-based materials on the environment and human health. Further, Lead-free ferroelectrics are a good substitute for the issues. Compared to normal ferroelectrics, a special class of ferroelectrics called Relaxor Ferroelectrics (RFs) holds great value due to their frequency dispersion nature and broad temperature dependence of dielectric permittivity.[2] Moreover, a slim Polarization (P) versus Electric field (E) behavior with a low remnant polarization (P_r) value in RFs favors their applicability for energy storage applications.[3]

Among the prominent Pb-free ferroelectric ceramics, $Sr_{0.7}Bi_{0.2}TiO_3$ (SBT) possesses good advantages such as relaxor materials with diffused phase transition, better dielectric constant, low remnant polarization, and coercive field.[4] The development of flexible materials is of great importance due to its applicability in flexible Random Access Memory, wearable devices in health monitoring, artificial muscles, e-textiles, electric vehicles, etc. One of the most promising applications of flexible materials is the piezoelectric energy harvester (PEH), which will produce voltage with the application of any external forces. Ceramic-polymer blended composites are now a great approach to be followed to induce mechanical stability and enhance PEH applicability. To enhance the mechanical strength of the ceramic, a non-toxic, biodegradable acid-resistant fluoropolymer, Poly(vinylidenefluoride-hexafluoropropylene) (PVDF-HFP) has been chosen owing to the superior ferroelectric properties, better dielectric constant, and high mechanical strength.[5] In this work, ceramic SBT-added PVDF-HFP polymer-based composites have been synthesized via a solution casting process. Their dielectric and ferroelectric properties have been analyzed for energy-storing and energy-harvesting applications.

METHODS OF PREPARATION

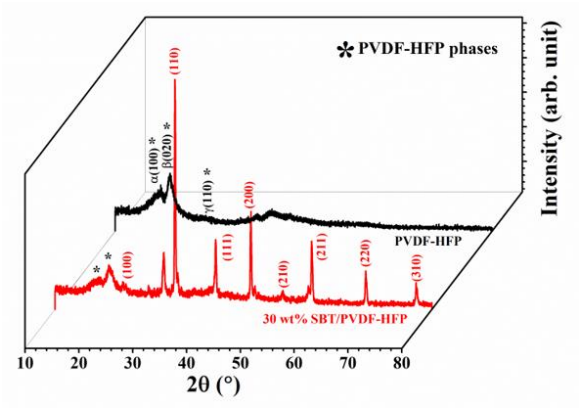
The $Sr_{0.7}Bi_{0.2}TiO_3$ ceramic was synthesized using the conventional solid-state reaction method. $SrCO_3$ ($SrCO_3$, 99%), Bi_2O_3 (Bi_2O_3, 99%), and TiO_2 (TiO_2, 99%) were taken as the precursors for the synthesis. Using Isopropyl Alcohol (IPA) as the medium, the weighed powders were ground for several hours till it was properly mixed. Then the well-mixed powders were kept for calcination at 950 ºC for 3 hours for the phase formation and removal of volatile elements. To fabricate the flexible composite films, the calcined SBT powder was mixed with PVDF-HFP polymer via a solution casting procedure. In this procedure, a polar solvent, N, N-dimethyl formamide, was

used for the dissolution of the PVDF-HFP polymer. First, 20 mL N, N-DMF was taken in a glass beaker, and 1 gm PVDF-HFP pellets were added to it. This solution was magnetically stirred at 60ºC for several hours till the pellets were completely dissolved in the solvent. Then the calcined powder of SBT was added to the solution and kept for several hours, followed by ultrasonication for 1.30 hrs. The solution was cast onto a glass petri dish and heated at a temperature of 80 ºC for 10 hrs for the evaporation of the solvent. This dried SBT/PVDF-HFP film was taken for different characterization to study its various properties. PVDF-based ferroelectric composite films are useful for energy harvesting applications. The PEH was fabricated using copper electrodes on the top and bottom sides of the composite films. To protect the device from external disturbances, the whole device was covered with Kapton tape. The Phase analysis has been done by X-ray diffractometer (Rigaku Smart Lab**,** Japan) with Cu K_α radiation λ= 1.5406Å. Surface morphology, dielectric constant (ε'), and Polarization vs Electric field (P-E) loop have been recorded by scanning electron microscope (Carl Zeiss, Supra40), Novocontrol Alpha A dielectric analyzer, and TF-Analyzer 2000 (aixACCT system, GmbH), respectively.

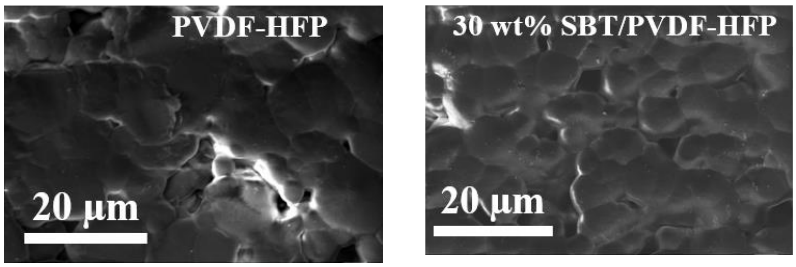
RESULTS AND ANALYSIS

1. Structural and microstructural analysis

X-ray diffraction patterns of pure PVDF-HFP and 30wt% SBT infused PVDF-HFP composites are shown in **Figure 1(a)** in 2θ range of 10º to 80º. Semi-crystalline nature of PVDF-HFP is confirmed by the broadness of the peak in the XRD pattern, which shows prominent peaks around 18.4º, 20.13º, and 26.7º corresponding to the planes (100), (020), and (110) planes respectively. 18º peak corresponds to the non-polar α phase. The 20.13º and 26.7º peaks correspond to the polar β and γ phases.[6] With the addition of SBT ceramic fillers, the intensity of the peaks corresponding to the polymer phase decreases, and the characteristic peaks of SBT appear. The composite shows both the characteristic peaks of both ceramic and polymer phases, which confirms that the ceramic fillers are perfectly incorporated in the polymer matrix. **Figure 1(b) and (c)** demonstrates the SEM micrograph of pure PVDF-HFP and 30 wt% SBT/PVDF-HFP composite films. A smooth surface morphology was observed in pure PVDF-HFP film with spherulite-like structures. However, with the incorporation of SBT ceramic, these homogeneous spherulites are clearly distinct, with fewer voids shown in **Figure 1(c)**.



(a)

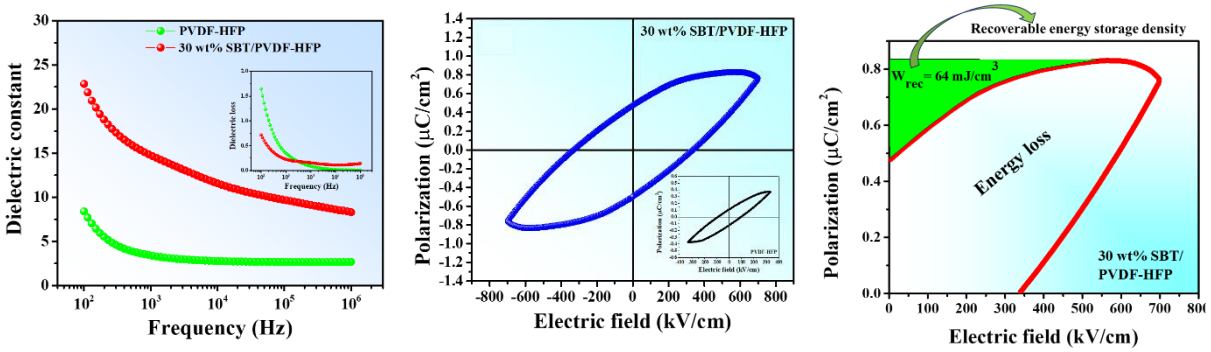


(b) (c)

Figure 1. (a) X-ray diffraction pattern of pure PVDF-HFP and 30 wt% SBT/PVDF-HFP. SEM micrograph of **(b)** PVDF-HFP **(c)** 30 wt% SBT/PVDF-HFP.

2. Dielectric and Ferroelectric Property Analysis

The frequency-dependent dielectric constant curve measured at room temperature in a range of 100 Hz to 1MHz of PVDF-HFP and 30 wt% SBT/PVDF particulate composite films is shown in Figure 2(a). PVDF polymer shows a low dielectric constant because of the electronegativity differences between carbon and fluorine in the CF_2 group. The figure shows that the dielectric decreases rapidly with the increase of frequency, first from 100 Hz to 10^3 Hz, which might be due to the interfacial polarization. Then it decreases slowly as the frequency increases, owing to the larger contribution of dipole polarization.[7] The ceramic-infused PVDF-co-polymer also demonstrates a similar behavior. The pure PVDF-HFP shows a dielectric constant of 8 at 100 Hz. With the addition of SBT filler, the dielectric constant increases to a higher value of 23 due to the accumulation of charge carriers at the interface. The inset of Figure 2(a) shows the dielectric loss behavior of the films with frequency. As the figure demonstrates, the loss decreases with the addition of the ceramic fillers.



(a) (b) (c)

Figure 2. (a) Frequency-dependent dielectric constant and dielectric loss (inset) at room temperature, **(b)**Polarization versus Electric field curve of 30 wt% SBT/PVDF-HFP and PVDF-HFP (inset) at room temperature, **(c)** Recoverable energy storage density calculation for 30 wt% SBT/PVDF-HFP

Figure 2(b). illustrates the polarization versus electric field curve of the synthesized PVDF-HFP and 30 wt% SBT/PVDF-HFP composite films at room temperature and at 1 Hz frequency. The P-E loop of the composite films confirms the presence of the ferroelectric domains. These loops are not saturated as a high poling electric field is required to pole PVDF and PVDF-copolymer. The pure PVDF-HFP shows remnant polarization (P_r) of 0.11 μC/cm^2, a maximum polarization (P_{max}) of 0.37 μC/cm^2, and a coercive field (E_c) of 91 kV/cm as shown in the inset of Figure 2. After the addition of the ceramic fillers, the ferroelectric property of the film is enhanced. P_r, P_{max}, and E_c of SBT/PVDF-HFP composite increase to a value of 0.46 μC/cm^2, 0.8 μC/cm^2, and 332 kV/cm respectively. The higher E_c value indicates the stabilization of the ferroelectric domains. Other than these parameters, the dielectric breakdown strength (E_b) of the materials is defined as the maximum electric field after which the material loses its insulating property. The E_b of 30 wt% SBT/PVDF-HFP is found to be 700 kV/cm, which is higher than the SBT ceramic. This increment may be due to the presence of a polymeric phase between the ceramic grains, which hinders the interaction of these local fields at grain interfaces.[8] Ferroelectrics are of great importance in energy storage applications. The energy storage property can be estimated from the P-E loop using the following equations.[3]

$$W_{rec} = \int_{P_r}^{P_{max}} EdP \quad (1)$$

Where W_{rec} is the recoverable energy storage density. From the equation, it can be established that low P_r and E_c, high P_{max}, and large E_b are the requirements for enhanced recoverable energy storage density value.[9] Using the abovementioned equation, W_{rec} of 30 wt% SBT/PVDF-HFP composite film was calculated to be 64 mJ/cm^3, which shows its applicability in energy storage devices.

3. Piezoelectric Energy Harvester performance

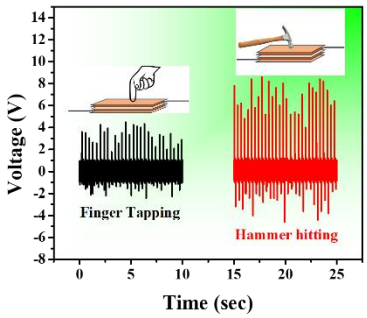


Figure 3. PEH performance of 30 wt% SBT/PVDF-HFP through finger tapping and hammer hitting.

Ceramic-polymer composite films show great potential in flexible piezoelectric energy harvesting applications. When deformation or vibration is applied to the materials, it changes the direction of the dipole moments in the piezoelectric materials, which produces voltages. The dipoles orient in one way when a force is applied, causing the charge to flow through the electrode.[10] A prototype of PEH was fabricated and connected to a digital oscilloscope using the jumper wires to measure the piezoelectric output. The external forces were applied using finger tapping and hammer hitting. A peak-to-peak voltage output of ~ 6V and ~ 13V was obtained by applying finger tapping and hammer hitting, respectively shown in Figure 3. With the increase in the amount of tapping force, the voltage output increases. These results show the potential in various sensing applications such as motion sensing, actuators, electronic devices, etc.

4. Conclusion

The present work includes the synthesis of pure PVDF-HFP and 30 wt% SBT/PVDF-HFP composite films via the solution casting method. XRD patterns of the composites show the presence of peaks corresponding to both polymer phase and ceramic, confirming the perfect incorporation of SBT ceramic filler in the polymer matrix. A high dielectric constant of 23 was obtained in 30 wt% SBT/PVDF-HFP composites compared to the pure PVDF-HFP film. A large dielectric breakdown strength of 30 wt% SBT/PVDF-HFP is found to be 700 kV/cm, suitable for high voltage applications. The recoverable energy storage density of this composite was calculated to be 64 mJ/cm^3. With applied external forces through finger tapping and hammer hitting, a peak-to-peak voltage output of ~ 6V and ~ 13V was obtained, respectively.

ACKNOWLEDGEMENTS

Author SA acknowledges the UGC-DAE (CRS/2021-22/03/553) and L.J. acknowledges DST-INSPIRE, India (Fellowship Code No. IF200296), for financial assistance.

REFERENCES

1. W. Gao, Y. Zhu, Y. Wang, G. Yuan, and J.M. Liu, J. Mater. **6**(1), 1–16 (2020).
2. K. Banerjee, S. Asthana, P.K. Kumari, and M.K. Niranjan, J. Phys. D. Appl. Phys. **51**(11), (2018).
3. V. V. Shvartsman, and D.C. Lupascu, J. Am. Ceram. Soc. **95**(1), 1–26 (2012).
4. P. Zhao, B. Tang, F. Si, C. Yang, H. Li, and S. Zhang, J. Eur. Ceram. Soc. **40**(5), 1938–1946 (2020).
5. K.K. Kishor, and J.T. Kalathi, J. Alloys Compd. **843**, 155889 (2020).
6. S. Panda, and S.K.K. Pasha, Langmuir **39**(37), 13345–13358 (2023).
7. Z. Zhang, Y. Gu, J. Bi, S. Wang, M. Li, and Z. Zhang, Compos. Part A Appl. Sci. Manuf. **85**, 172–180 (2016).
8. A. Dwivedi, V.P. Singh, A. Dwivedi, and A.K. Singh, J. Mater. Sci. Mater. Electron. **34**(28), (2023).
9. S.K. Mev, K. Banerjee, and S. Asthana, J. Alloys Compd. **999**, 174966 (2024).
10. B. Nayak, S. Anwar, A. Kumar, and S. Anwar, ACS Appl. Electron. Mater. **6**(2), 1189–1203 (2024).

Study of Nickel Cobalt Oxide as an Electrocatalyst for Oxygen Evolution Reaction in a Wide Range of Alkaline pH

Manjiree Thakur [a)], Dushyant C. Kothari, Pradip Sarawade [b)]

Department of Physics, University of Mumbai, Vidyanagari, Mumbai 400098, India

[a)] Corresponding author: manjiree.thakur@physics.mu.ac.in
[b)] Corresponding author: pradip.sarawade@physics.mu.ac.in

Abstract. The present study was undertaken to determine the electrocatalytic performance of solvothermally synthesized nickel cobalt oxide for Oxygen Evolution Reaction (OER) in water splitting at different pH. The synthesized electrocatalyst shows spherical flower-like morphology. OER activity increased with increasing pH (pH 8.2 < pH 10.4 < pH 12). The electrocatalyst performs best in extreme alkaline pH. For pH 12, an overpotential of 346 mV vs. RHE at 10 mA cm^{-2}, a Tafel slope of 167 mV $dec^{-1,}$ and an exchange current density of 0.041 mA cm^{-2} are observed.

INTRODUCTION

The water-splitting process consists of two primary reactions: hydrogen evolution reaction (HER) at the cathode and oxygen evolution reaction (OER) at the anode, resulting in the production of hydrogen and oxygen. This overall reaction requires a thermodynamic potential of about 1.23 V. Many transition metal-based electrocatalysts have been studied for HER and OER reactions owing to their cost-effectiveness, earth abundance, high electrochemical stability, and simple synthesis methods [1]. Among them, metal oxides display good catalytic activity towards OER in alkaline media. However, extremely alkaline or acidic conditions cause electrode corrosion and harm the environment; thus, they are not beneficial for long-term use. It is crucial to study catalytic activity for water splitting in a near-neutral medium to overcome this issue. However, splitting neutral or near-neutral media water requires more energy than an extremely acidic or alkaline medium. To increase the efficiency of both HER and OER in these media, it is necessary to understand the reaction mechanism in the different pH ranges. Different reaction kinematics are observed with different pH for oxygen evolution reactions [2]. So far, nickel cobalt oxide catalyst has been widely studied as an OER catalyst in extreme alkaline media, showing overpotential values of around 300 mV [3]. Many have studied nickel cobalt oxide as a catalyst for OER and HER in extreme alkaline medium [4, 5]. Due to high catalytic activity in extreme alkaline conditions, it is necessary to study its performance in a near-neutral medium. Here, we studied the OER activity of nickel cobalt oxide prepared by solvothermal synthesis in a wide alkaline pH range. 0.1 M KOH solution is used for pH 12, and sodium bicarbonate buffer solutions are used to prepare pH 8.2 and 10.4 media. This study is vital in understanding the catalytic activity of nickel cobalt oxide in a wide pH range to develop it further as an efficient near-neutral media OER electrocatalyst.

EXPERIMENTAL

Nickel Cobalt Oxide catalyst was synthesized using a simple solvothermal route. 0.28 M $Ni(NO_3)_2.6H_2O$ and 0.32 M $Co(NO_3)2.6H_2O$ are dissolved in distilled water (35 mL). 1.4 M urea and 0.4 M CTAB are added to 35 mL of cyclohexane and kept under continuous stirring. The metal precursor solution is then added to the mixture of CTAB and urea and stirred for 30 min at 400 rpm to obtain a homogeneous mixture, transferred to a Teflon line autoclave, and maintained in a hot air oven at 120 °C for 4 hrs. The obtained precipitation is then washed thoroughly with acetone and distilled water. After drying at 70 °C, the powder is annealed at 450 °C for 4 hrs in the air to obtain the final metal oxide powder. The electrochemical activity of the prepared catalyst is studied using an Autolab potentiostat/galvanostat workstation. The working electrode was fabricated by drop-casting catalyst ink on the clean nickel foam (NF) surface. For ink preparation, catalyst material (5mg) was added to the mixture of 1 mL isopropyl alcohol (IPA) and 25 µL of 5 % Nafion solution, followed by ultrasonication for 30 min to obtain well-dispersed catalyst ink. The as-prepared ink was deposited on the NF foam (1cm × 1cm) to achieve a loading of~1 mg cm^{-2} and dried under a lamp. Before deposition, NF is cleaned by ultrasonication with

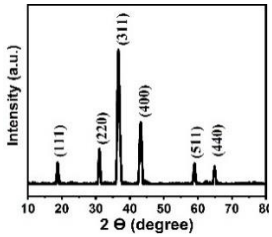
1M HCl, Acetone, and DDW for 5 minutes and dried under a lamp. The powder X-ray diffraction (XRD) pattern was obtained using Cu Kα radiation (λ = 0.15418 nm) on a D2 PHASER instrument from Bruker, Germany. Scanning electron microscopy (SEM) was performed on a Quanta 200F FESEM instrument. All the electrochemical tests were performed using a three-electrode system attached to the Metrohm Autolab potentiostat/galvanostat electrochemical workstation. Catalyst-loaded NF is used as a working electrode, Pt mesh is used as a counter electrode, and Hg/HgO is used as a reference electrode in an electrochemical setup. 0.1 M KOH is used as an electrolyte for pH 12 OER measurements. 0.2 M $NaHCO_3$ and 0.2 M Na_2CO_3 buffer solutions are used for pH 8.2 and 10.4. All the linear sweep voltammetry and cyclic voltammetry curves were performed at a scan rate of 5 mV s^{-1}. The measurements with reference electrode are converted into reversible hydrogen electrode (RHE) using the Nernst Equation as follows,

$$E_{RHE} = E_{Hg/HgO} + 0.581 \text{ for pH 8.2,}$$
$$E_{RHE} = E_{Hg/HgO} + 0.715 \text{ for pH 10.4 and}$$
$$E_{RHE} = E_{Hg/HgO} + 0.833 \text{ for pH 12.}$$

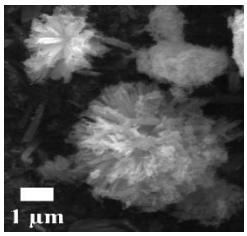
Electrochemical Impedance Spectroscopy (EIS) measurements are used to calculate solution resistance (R_s) and charge transfer resistance (R_{ct}). R_s (19 Ω, 11.8 Ω, and 20.1 Ω for pH 8.2, 10.4, and 12) is measured at the potentials corresponding to the current density 10 mA cm^{-2} in all pHs to calculate iR losses. Tafel slope and exchange current density are calculated by plotting the log of current density (log(j)) vs. overpotential.

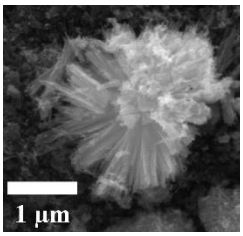
RESULTS AND DISCUSSION

The observed XRD data **(Fig. 1(a,b))** matches with JCPDS file no.00-020-0781, confirming the phase $NiCo_2O_4$ of nickel cobalt oxide. FE-SEM images **(Fig. 2(c,d))** of solvothermally prepared nickel cobalt oxide show a flower-like spherical morphology with small spines growing from the center.



	2 Θ (degree)		d(Å)	
(hkl)	Observed	JCPDS	Observed	JCPDS
111	18.765	18.907	4.725	4.690
220	31.032	31.149	2.880	2.869
311	36.656	38.405	2.450	2.342
400	43.159	44.623	2.094	2.029
511	58.989	59.096	1.564	1.562
440	64.895	64.982	1.436	1.434





(a) **(b)** **(c)** **(d)**

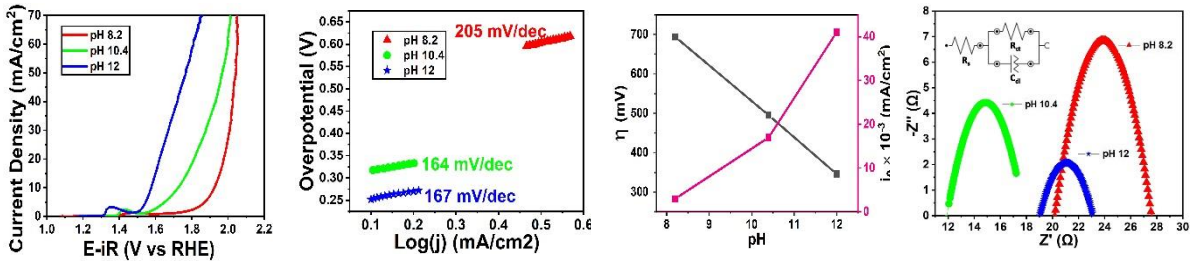
FIGURE 1. (a,b) XRD data of $NiCo_2O_4$ (c,d) SEM Image of the synthesized $NiCo_2O_4$

The OER mechanism in an alkaline medium involves oxidation of the metal active site and metal oxy/hydroxide complexes (M-OH and M-OOH), which are not too weak or strong on the electrode surfaces. On further oxidation of these intermediate sites, oxygen gas is released. This same mechanism is followed in near-neutral alkaline media. In nickel cobalt oxide, the nickel and cobalt sites are activated by electrochemical potential application and catalyze OER through a similar mechanism. The prepared catalyst is tested for OER electrochemical activity in different pH mediums using linear sweep voltammetry (LSV) curves recorded at a scan rate of 5 mVs^{-1}. **Fig. 2 (a)** shows linear polarization curves for nickel cobalt oxide in various pH media with iR corrections. The OER activity improves as the pH increases from near-neutral media (pH 8.2) towards higher alkaline media (pH 12). $NiCo_2O_4$ shows lower overpotential in pH 12 media. For the current density of 10 mA cm^{-2}, the OER overpotentials are 694 mV and 495 mV in pH 8.2 and 10.4, respectively. However, at pH 12, the observed overpotential is 346 mV. Higher current densities of 20 and 50 mA cm^{-2} are achieved at 346 and 535 mV overpotentials. Overpotential values for various pH are listed in **Table 1.**

The Tafel slope is important to determine the rate of the reaction. As shown in **Fig.2(b)**, the Tafel slope for pH 8 is 205 mV dec^{-1}, which is much higher than pH 10.4 (164 mV dec^{-1}) and pH 12 (167 mV dec^{-1}). This suggests that the reaction rate is much slower in the near-neutral medium than in a slightly higher alkaline medium. As obtained from the Tafel plot (Fig.2(b)), exchange current densities increase with the increase in pH. The current density obtained at max pH (pH 12) is 0.041 mA cm^{-2}, much higher than the 0.017 mA cm^{-2} (pH 10.4) and 0.003 mA cm^{-2} (pH 8.2).

TABLE 1 Overpotential (mV) at different Current Densities obtained for the electrolyte having different pH

pH	1 mA cm^{-2}	2 mA cm^{-2}	5 mA cm^{-2}	10 mA cm^{-2}	20 mA cm^{-2}	50 mA cm^{-2}
8.2	**441 mV**	**555 mV**	**642 mV**	**694 mV**	**745 mV**	**814 mV**
10.4	**290 mV**	**350 mV**	**421 mV**	**495 mV**	**583 mV**	**737 mV**
12	**244 mV**	**283 mV**	**316 mV**	**346 mV**	**392 mV**	**535 mV**



(a) **(b)** **(c)** **(d)**

FIGURE 2. (a) LSV curves for nickel cobalt oxide for OER in various pH, (b) Tafel Plots for various pH, (c) Overpotentials (η) and exchange current density(j_0) for different pH, (d) Nyquist plot for different pH electrolytes.

CONCLUSION

The study of $NiCo_2O_4$ as an Electrocatalyst for OER in a broad alkaline pH range shows a decrease in activity with decreasing pH (pH 8.2 < pH 10.4 < pH 12) due to a reduction in the number of ions in the electrolyte required for current conduction. For pH 12, an overpotential of 346 mV vs. RHE at a current density of 10 mA cm^{-2} is observed, along with a Tafel slope of 167 mV dec^{-1} and an exchange current density of 0.041 mA cm^{-2}.

ACKNOWLEDGMENTS

Manjiree Thakur acknowledges the PhD fellowship from M/s SMT Pvt Ltd under the Industry-Academia program. She is grateful to Prof. D. C. Kothari and Dr. Pradip Sarawade for their mentoring and guidance.

REFERENCES

1. Wang, Jiajia, Xiyan Yue, Yanyan Yang, Suchada Sirisomboonchai, Peifen Wang, Xuli Ma, Abuliti Abudula, and Guoqing Guan. "Earth-abundant transition-metal-based bifunctional catalysts for overall electrochemical water splitting: A review." *Journal of Alloys and Compounds* 819 (2020): 153346.
2. Anantharaj, Sengeni, and Vanchiappan Aravindan. "Developments and perspectives in 3D transition-metal-based electrocatalysts for neutral and near-neutral water electrolysis." *Advanced Energy Materials* 10, no. 1 (2020): 1902666.
3. Bodhankar, Pradnya M., Dattatray S. Dhawale, Sarbjit Giddey, Ravi Kumar, and Pradip B. Sarawade. "Well-defined hierarchical teddy bear sunflower-like NiCo 2 O 4 electrocatalyst for superior water oxidation." *Sustainable Energy & Fuels* 6, no. 24 (2022): 5491-5502..
4. Tao, Leiming, Yibing Li, Man Li, Guoying Gao, Xin Xiao, Mingkui Wang, Xingxing Jiang et al. "Nanostructured nickel cobaltite antispinel as bifunctional electrocatalyst for overall water splitting." *The Journal of Physical Chemistry C* 121, no. 46 (2017): 25888-25897.
5. Elakkiya, Rajasekaran, Rajendran Ramkumar, and Govindhan Maduraiveeran. "Flower-like nickel-cobalt oxide nanomaterials as bi-functional catalyst for electrochemical water splitting." *Materials Research Bulletin* 116 (2019): 98-105.

$Li_7La_3Zr_2O_{12}$: A Solid - State Electrolyte For Thin Film Batteries

Anjali[1], Weon Cheol Lim[2,] Aditya Sharma[3], Moditma[1], Sangsul Lee[4,5], Hyun Joon Shin[6], Keun Hwa Chae[2] and Jitendra Pal Singh[1a)]

[1]*Department of Sciences (Physics), Manav Rachna University, Faridabad-121004, India.*
[2] *Advanced Analysis & Data Center, Korea Institute of Science and Technology (KIST), Seoul, Republic of Korea*
[3] *Department of Physics, University of Petroleum and Energy Studies, Dehradun, Uttarakhand 248007, India*
[4]*Pohang Accelerator Laboratory, POSTECH, Pohang-37673, Republic of Korea*
[5]*Department of Semiconductor Engineering, POSTECH, Pohang-37673, Republic of Korea*
[6]*Department of Physics, Chungbuk National University, Cheongju 28644, Republic of Korea*

[a)] Corresponding author: jpsingh@mru.edu.in

Abstract. The growth of $Li_7La_3Zr_2O_{12}$ (LLZO) thin films on glass substrates using radio frequency (RF) sputtering at 50W of RF power is investigated. As-deposited films were annealed at 500ºC. Results from Rutherford Backscattering Spectrometry (RBS) indicate that La, Zr and O are present in as-deposited and annealed films. The thicknesses of both films are 100 nm approximately. The thickness of annealed film estimated from scanning electron microscopic (SEM) measurement is 46 nm. The amorphous character of the film is revealed by X-ray Diffraction (XRD) measurement. Near edge X-ray absorption fine structure (NEXAFS) reflects structure corresponding to the interaction between oxygen ions and metal ions locally.

Keywords. LLZO, NEXAFS, XAS, SEM, TFRB

INTRODUCTION

Solid state electrolytes (SSE's) are the main component for thin film rechargeable batteries (TFRB's) needed for ion movement between anode and cathode. These kinds of batteries provide several benefits over other batteries based on liquid electrolyte's in terms of safety, size, electro-chemical stability and high energy density [1]. Among various SSEs, lithium lanthanum zirconate (LLZO) is a promising material which is considered to be most suitable material for TFRB's which are based on Li^+ [2]. This material possesses moderate ionic conductivity at room temperature. Thus, due to its complex garnet structure, the growth of LLZO thin film is quiet a difficult task with appropriate stoichiometry and thickness. Thus, many efforts are being made in this direction using various deposition techniques such as: Pulsed Laser Deposition (PLD) [3], Chemical Vapor Deposition (CVD) [4] and radio-frequency (RF) sputtering [5].

RF sputtering is a versatile technique which is used to deposit thin films with many advantages such as ability to deposit high quality and uniform thin film by controlling the RF power, substrate temperature and deposition time. This technique is very much effective for the growth of thin films of insulating and dielectric materials because the RF field can reduce the chances of charge build up on target surfaces [6]. Thus, this work aims to deposit LLZO thin film using RF sputtering technique for possible application in thin film batteries.

EXPERIMENTAL SECTION

Procured LLZO sputtering target of 2'' diameter was used for deposition. The target to substrate distance was 4 cm. Base pressure for deposition was 3×10^{-5}Torr and pressure of 3.9 mTorr was maintained during the deposition by flowing the Ar gas in to the chamber. The films were deposited at 50W RF power for about 30 min. Structural characterization was performed using Rigaku Miniflex X- ray diffractometer (XRD) based on Cu K_α radiation of λ = 1.5418 Å. The thickness and compositional analysis of prepared LLZO films was done using Rutherford Backscattering Spectroscopy (RBS) at KIST, Seoul, Republic of Korea and data was analyzed using Rutherford Universal Manipulation Programme (RUMP) software [7]. Energy Dispersive X-ray analysis (EDX) was performed to observe the presence of various elements. Thickness was further investigated using cross section Scanning Electron Microscopy (SEM). To understand the interaction between different ions of LLZO in the film near edge x-ray absorption fine structure spectroscopy (NEXAFS) measurement was done for annealed film in Total Electron Mode (TEY) and Total Fluorescence Mode (TFY).

RESULTS & DISCUSSION

Fig.1(a) shows the RBS spectra of as-deposited and annealed films. The presence of La, Zr and Pt can be observed clearly from RBS data as determined by using RUMP software (Presence of Pt is due to coating to reduce charging during measurements). The thickness was found to be 100 nm and no change in thickness was observed even after annealing. The composition of as – deposited and annealed films was almost same ($Li_7La_{2.2}Zr_2O_{12}$).

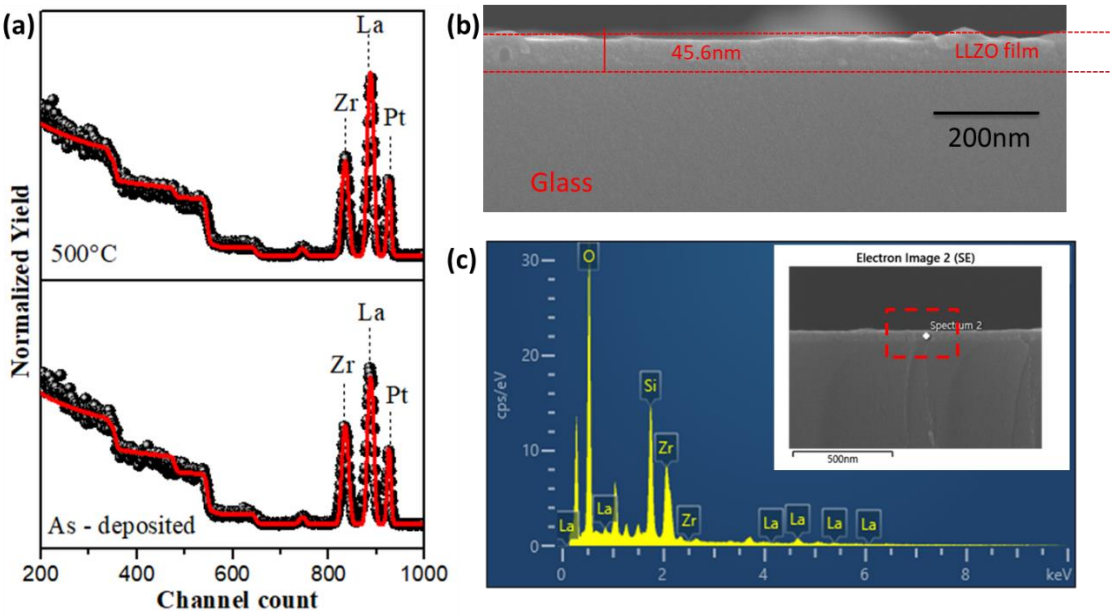


FIGURE1. (a) RBS spectra of as-deposited and annealed LLZO film (b) SEM of annealed film showing film thickness region (c) SEM – EDX spectra of annealed film; inset shows the selected region for collection of EDX data.

Since RBS exhibits no change in thickness and composition of both the films, we further performed SEM measurements on annealed film. Fig.1(b) shows the cross-sectional SEM of the annealed film. Film thickness is determined to be 46 nm, as illustrated in the Fig. The difference in thickness estimated from RBS and SEM is due to different mechanisms of these techniques. EDX spectrum from this film shows presence of O, La and Zr as depicted in Fig.1(c). Peak corresponding to Si comes from the substrate. In both the measurement Li cannot be detected due to its light weight.

Fig. 2(a) shows XRD pattern of the annealed film alongwith standard cubic phase LLZO. Clearly, the film deposited is amorphous in nature as also observed in previous reports [8-9]. Fig. 2(b) shows the oxygen K-edge of LLZO film at 500°C in TEY and TFY mode. The pre-edge feature observed at 533.9 eV in TEY mode corresponds to the formation of LLZO, as reported in previous reports [10]. The broad feature at 540 eV in the bulk sensitivity TFY mode can be attributed to substrate.

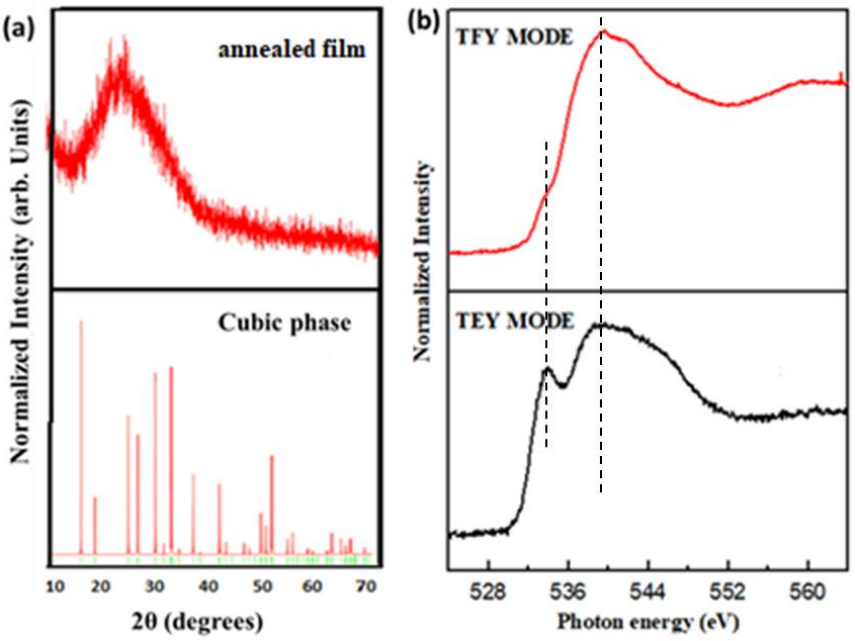


FIGURE 2 (a) XRD of annealed film and standard LLZO in cubic phase drawn using Vesta and (b) O K-edge NEXAFS spectra in TEY and TFY mode for annealed film.

ACKNOWLEDGEMENT

JPS is thankful to SERB, New Delhi for providing financial support for this work via project number RJF2021/000115. KHC acknowledge the support received by grant KIST2V10021.

REFERENCES

1. J. Wan, J. Xie, D.G. Mackanic, W. Burke, Z. Bao and Y. Cui, Materials Today Nano, 4, 1-16 (2018).
2. Lei Zhang, Quanchao Zhuang, Runguo Zheng, Zhiyuan Wang, Hongyu Sun, Hamidreza Arandiyan, Yuan Wang, Yanguo Liu and Zongping Shao, Energy Storage Materials, 49, 299 – 338 (2022).
3. Sangryun Kim, Masaaki Hirayama, Sou Taminato and Ryoji Kanno, Dalton Transactions, 42, 13112 – 13117 (2013).
4. Christoph Loho, Ruzica Djenadic, Michael Bruns, Oliver Clemens and Horst Hahn. Journal of The Electrochemical Society, 164, A6131 (2017).
5. Zongkai Yan,Yu Song,Shuai Wu, Shuai Wu,Yongmin Wu, Shipai Song, Xinyu Wang, Yanlin Zhu ,Junsong Chen, Rui Guo and Yong Xiang, Crystals, 11, 426 (2021).
6. F. Kurdesau, G. Khripunov, A. F. D. Cunha, M. Kaelin, and A. N. Tiwari, Journal of Non-Crystalline Solids, 352, 1466–1470 (2006).
7. E. Andrade, V.M. García, P.K. Nair, M.T.S. Nair, E.P. Zavala, L. Huerta and M.F. Rocha. Nuclear Instruments and Methods in Physics Research Section B: Beam Interactions with Materials and Atoms. 161-163, 635 – 640 (2000).
8. D.J. Kalita, S.H. Lee, K.S. Lee, D.H. Ko and Y.S. Yoon, Solid State Ionics, 229, 14 -19 (2012).
9. Jordi Sastre, Agnieszka Priebe, Max Dobeli, Johann Michler, Ayodhya N. Tiwari and Yaroslav E. Romanyuk, Advanced Materials Interfaces, 7, 2000425 (2020).
10. Younggyu Kim, Dongha Kim, Roland Bliem, Guulin Vardar, Iradwikanari Waluyo, Adrian Hunt, Joshua T. Wright, John P. Katsoudas, and Bilge Yildiz, Chemistry of Materials, 32, 9531- 9541 (2020).

$SrMnO_3$ Perovskite Nanoparticle Embedded in $NiCo_2O_4$ Nanoflower as Electrocatalyst for Oxygen Evolution

Poonam Mor[§], Krishna Kanta Halder[†], Sourabh Barua[§]*

[§]*Department of Physics, Central University of Punjab, Bathinda 151401, India.*

[†]*Department of Chemistry, Central University of Punjab, Bathinda 151401, India.*

*Corresponding author: Sourabh.barua@cup.edu.in

Abstract: Developing electrocatalysts that are efficient, stable, and cost-effective is crucial for advancing the oxygen evolution reaction (OER). In this study, we have synthesized a composite of perovskite $SrMnO_3$ and spinel $NiCo_2O_4$ by a hydrothermal process. The obtained $SrMnO_3/NiCo_2O_4$ exhibits an overpotential of 489 mV at a current density of 10 mA/cm2 and a Tafel slope of 97 mV/dec in alkaline media and an electrochemical surface area of 2.88 cm^2 as calculated from CV.

INTRODUCTION

As a result of the growing environmental concerns and decreasing supply of fossil fuels, significant initiatives have been directed to investigate sustainable energy sources. Electrochemical water splitting has drawn significant interest because of its low energy usage, environmentally friendly nature, and ability to provide extreme results. [1-2] The distinctive properties of perovskite oxide ABO_3 have garnered significant attention. It is well established that approximately 90% of the elements in the periodic table can be stabilized within the perovskite structure [3]. Multicomponent perovskites can be synthesized by partially substituting cations at either the A-site or B-site [3]. This enables the production of novel perovskite compounds to improve desired properties and establish new applications. Electrochemical water splitting involves two half-cell reactions ((HER) and (OER). HER occurs at the cathode, and OER occurs at the anode. According to the Nernest equation, the thermodynamic potentials are E^0_{RHE} =0.00V (HER) and E^0_{RHE} =1.23 V (OER) [4].

METHODOLOGY

$SrMnO_3/NiCo_2O_4$ was synthesized via a hydrothermal method. The starting materials included strontium nitrate ($Sr(NO_3)_2$, 99.995%), cobalt nitrate hexahydrate ($Co(NO_3)_2 \cdot 6H_2O$, 99% AR), and manganese (II) chloride tetrahydrate ($MnCl_2 \cdot 4H_2O$, 99%), all procured from Sigma-Aldrich. Additional reagents such as potassium hydroxide (KOH), anhydrous citric acid (99.5%, Sigma-Aldrich), double-distilled water (H_2O), ethanol (C_2H_5OH, 99.9% AR), and D520 Nafion dispersion solution were obtained from D Tech Solutions. All chemicals were stored in a dry environment and used as received, without further purification.

$SrMnO_3$ was first synthesized by the sol-gel method, following a previously reported procedure [5]. The $SrMnO_3/NiCo_2O_4$ composite was then prepared using a hydrothermal technique [6].

RESULTS AND DISCUSSIONS

XRD Analysis, FESEM, and EDX analysis of $SrMnO_3/NiCo_2O_4$

XRD was employed to investigate the crystallinity of different samples. The diffraction peaks 31.34^0,36.82°, 44.81°,59.27°,69.07° confirm that $SrMnO_3/NiCo_2O_4$ matches with JCPDS card number 01-073-1702. Fig 1(C) EDX data confirm that Sr, Mn, Ni, Co, and O are present in the sample and confirm the composite structure of $SrMnO_3/NiCo_2O_4$. FE-SEM images were used to investigate the synthesized sample's shape, size, and surface morphology. It was observed that $NiCo_2O_4$ exhibits a flower-like morphology. $SrMnO_3/NiCo_2O_4$ exhibits snowflake-like morphology.

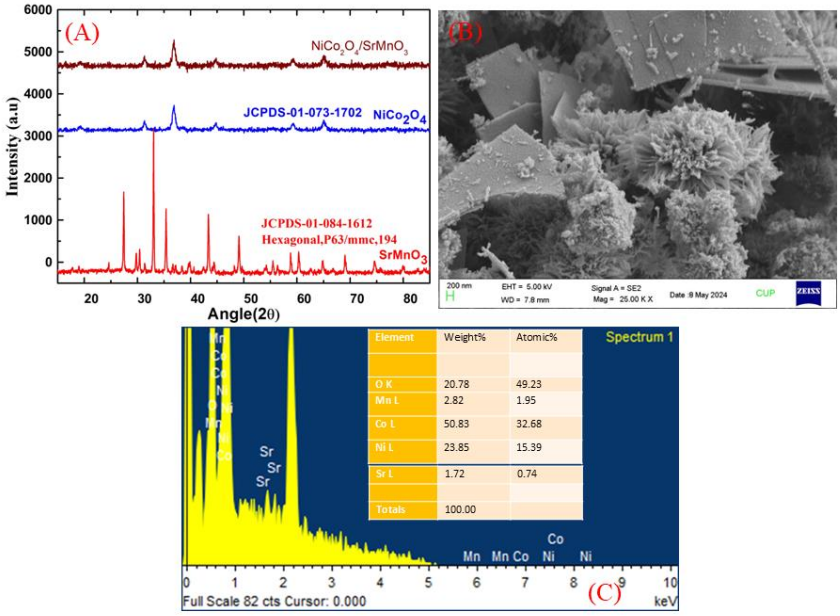


FIGURE 1. (A) XRD pattern of synthesised material $SrMnO_3/NiCo_2O_4$, (B) FE-SEM image of $SrMnO_3/NiCo_2O_4$ at 200 nm (C) EDX spectrum of $SrMnO_3/NiCo_2O_4$ and its atomic composition

Electrochemical Performance (OER in Alkaline Medium)

The electrochemical measurements were conducted using a Metrohm Autolab (Multichannel-204) coupled to a typical three-electrode electrochemical cell controlled by Nova 2.1.4 software. The GC electrode was coated with samples for electrochemical analysis and used as the working electrode. The reference electrode was Ag/AgCl (3 M KCl), and the counter electrode was platinum (Pt). For all experiments, a 1 M KOH electrolyte (pH 13.8) was prepared using double-distilled water. Linear sweep voltammetry (LSV) was conducted by applying a voltage of 0 V to 1 V for OER with respect to Ag/AgCl. The scan rate used was 100 mVs^{-1}. Cyclic voltammetry (CV) studies were performed by applying a potential range of 0.2V to 0.4V vs. Ag/AgCl specifically for OER in alkaline conditions, with a scan rate that ranges from 20 to 100 mVs^{-1}. Electrochemical impedance spectroscopy (EIS) was conducted in a frequency range of 100 kHz to 0.1 Hz at a voltage of 650 mV (vs. Ag/AgCl). All electrocatalysts have a mass content of 0.544 mg/cm^2. According to the Nernst equation (1), all measured potentials were converted to the RHE scale

$$E_{(\mathrm{RHE})} = E_{Ag/Agcl} + 0.059 \times \mathrm{pH} + E_{Ref} \quad (1)$$

After the successful synthesis of $SrMno_3/NiCo_2O_4$ by the hydrothermal method, the (OER) activity was measured in alkaline media. Fig 2 (a) shows the Linear sweep voltammetry (LSV) from which we calculated the overpotential at current density 10 mA/cm^2 defined by equation $\eta = E_{RHE} - 1.23$ V. Fig 2 (b) shows the corresponding Tafel slope calculated from LSV Fig 2 (c) shows the EIS from which we calculated the Rct (charge transfer resistance) 250 Ω . Fig.2(d) shows the cyclic voltammetry (CV) from which we calculated C_{dl} and ECSA (Electrochemical surface area).

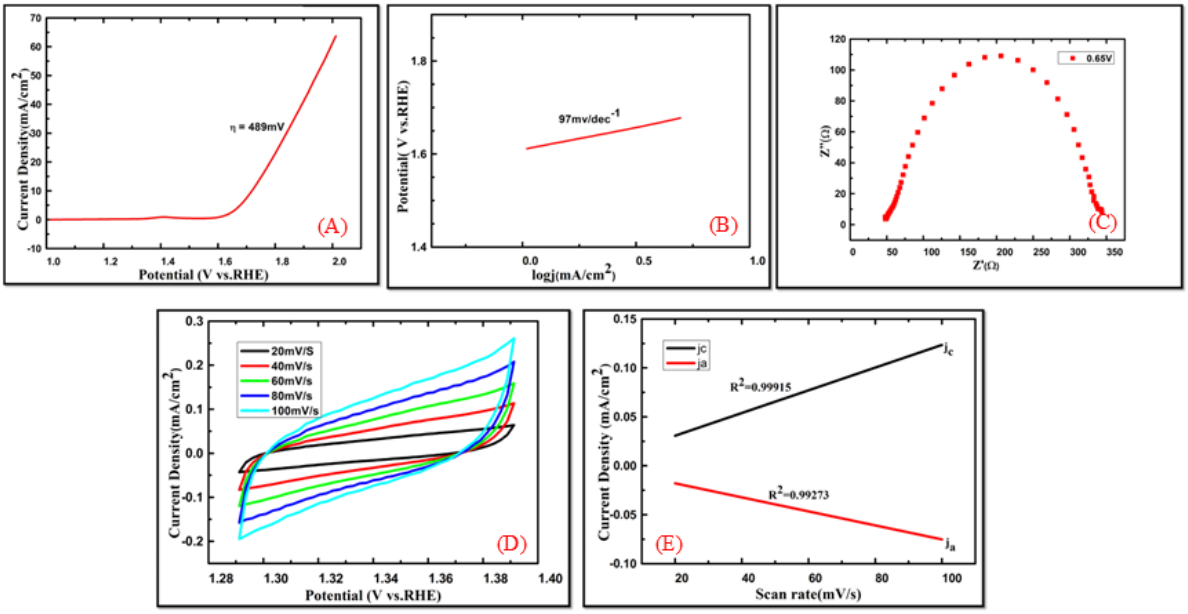


FIGURE 2. (a) Polarization (LSV) plot and (b) the associated Tafel $SrMnO_3/NiCo_2O_4$ (c) Electrochemical Impedance Spectroscopy (EIS) of $SrMnO_3/NiCo_2O_4$ (d) Cyclic Voltammetry (CV) curve of $SrMnO_3/NiCo_2O_4$ (e) ECSA plot of J_a and J_c vs the scan rate for determination of double layer capacitance (C_{dl}).

CONCLUSIONS

We have successfully grown perovskite/spinel oxide ($SrMnO_3$ /$NiCo_2O_4$) composite nanoflowers by the hydrothermal approach. The composite ($SrMnO_3$ /$NiCo_2O_4$) has a low Tafel slope of 97 mV/dec and low overpotential compared to $SrMnO_3$ and $NiCo_2O_4$.Hence, its OER activity is improved.

ACKNOWLEDGEMENTS

PM acknowledges UGC, India, for providing a junior research fellowship. The author also recognizes (CIL), the Central University of Punjab, Bathinda, Punjab, India, for providing various characterization facilities.

REFERENCES

1. Ding, J.T.; Ji, S.; Wang, H.; Linkov, V.; Gai, H.J.; Liu, F.S.; Liu, Q.B.; Wang, R.F. ACS Sustain. Chem. Eng. 7, 3974–3981, 2019.
2. Xiang, W.K.; Yang, N.T.; Li, X.P.; Linnemann, J.L.; Hagemann, U.; Ruediger, O.; Heidelmann, M.; Falk, T.; Aramini, M.; DeBeer, S. Nat.Commun. 2022
3. Zhu, Junjiang, et al," Acs Catalysis 4.9: 2917-2940, 2014
4. A. Li, Y. Sun, T. Yao, H. Han, Chem. Eur. J. 24, 18334, 2018.
5. Doroftei, C., Leontie, L.. J Sol-Gel Sci Technol 97, 146–154 , 2021.
6. Deeksha Kubba, Imtiaz Ahmed, Pawanpreet Kour, Rathindranath Biswas, Harpreet Kaur, Kamlesh Yadav, and Krishna Kanta Haldar ACS Applied Nano Materials, 5 (11), 2022.

Two-Dimensional Be_2P_4/BP Heterostructure as an Anode Material for Sodium-Ion Batteries

Nidhi Verma and Ashok Kumar*

Department of Physics, Central University of Punjab, Bathinda, Punjab, India 151401

*Corresponding author: ashokphy@cup.edu.in

Abstract. To explore the electronic and electrochemical properties of two-dimensional (2D) Be_2P_4/BP heterostructure, density functional theory (DFT) has been employed. The electronical properties of monolayer Be_2P_4 and BP indicate their semiconducting nature having band gaps of 0.5 eV and 0.89 eV, respectively. In addition, we also studied adsorption and storage phenomenon of van der Waals Heterostructure (vdWH) combining Be_2P_4 and experimentally synthesized BP monolayer. The calculated electronic band structure of Be_2P_4/BP heterostructure clearly illustrates semiconducting nature with bandgap of 0.16 eV which changes into metallic during the adsorption of Na atom with high adsorption energy. The computed high specific capacity and low OCV make Be_2P_4/BP heterostructure an appealing choice for energy storage applications.

Key words: 2D heterostructure, anode material, adsorption energy, specific capacity and open-circuit voltage.

INTRODUCTION

Highly efficient rechargeable batteries have garnered significant interest from fundamental research and industrial applications due to the explosive growth of the electronics market. Because of its large reversible capacity and extended cycle life, lithium-ion batteries (LIBs) have found widespread adoption, however, limited energy density of classical graphite anode is no longer sufficient for further use [1]. Hence sodium-ion batteries (SIBs) have generated interest because of their high abundance and low cost. Moreover, with similar physical and chemical characteristics of Li and Na, the existing technologies in LIBs can be directly translated to SIBs. Among other anodes, two-dimensional (2D) materials perform much better electrochemically because of their amazing physical properties, wide surface-to-volume ratio and high electrical conductivity. Combining these 2D materials into a heterostructure is a commonly used technique for modifying characteristics and creating innovative nanoelectronic and energy harvesting applications which can also result in achieving high-performance anode material. In this work, we have also explored the theoretically studied Be_2P_4 and experimentally fabricated BP [2] to make their heterostructure as an anode for SIBs. This heterostructure exhibits semiconducting characteristics with a small band gap of 0.16 eV which turns into metallic during the adsorption of Na-atom. We have primarily investigated the adsorption and storage phenomenon of Na-atoms over Be_2P_4/BP heterostructure which shows that high adsorption energy and specific capacity make heterostructure suitable as an anode for SIBs.

COMPUTATIONAL METHOD

The first-principles simulations are performed using Quantum ESPRESSO software [3]. Electron exchange and correlation are performed using the generalized gradient approximation (GGA) with Perdew-Burke-Ernzerhof (PBE) functionals [4]. Electron-ion interactions are carried out using projector-augmented wave (PAW) pseudopotentials [5]. The structural characteristics and atomic positions are relaxed up to the force convergence of 10^{-5} eV/Å and energy convergence of 10^{-6} eV, respectively. To prevent interaction with analogous images along the z-direction in the 2D material, an interlayer spacing of 30 Å is used. For Brillouin zone integration, 12×12×1 k-point mesh and an 80 Ry plane wave energy cutoff are utilized. In the heterostructure, weak van der Waals interactions are handled using DFT-D3 approach proposed by Grimme [6]. Additionally, the dipole correction has been used for all DFT computations of the heterostructure. To study the adsorption and storage phenomenon, a 2×2×1 supercell of heterostructure was considered.

RESULTS AND DISCUSSIONS

Structural and Electronical Properties

The optimized structures of 2D-Be_2P_4 and BP monolayers are depicted in Fig. 1(A and C). Our calculated lattice parameters of Be_2P_4 (BP) in the hexagonal unit cell are a = 6.19 Å (3.21 Å) having six (two) atoms per unit cell, respectively which is consistent with earlier findings [7]. The obtained electronic band structure using GGA-PBE level of theory shows that the Be_2P_4 and BP monolayer exhibits semiconducting characteristics with direct band gap of 0.5 eV (Fig. 1(B)) and 0.9 eV (Fig. 1(D)), respectively which is also compatible with prior studies. For the Be_2P_4 monolayer, we have also examined the projected density of states (PDOS), which indicates that states above and below the Fermi level are primarily participated by phosphorous atoms. Meanwhile, PDOS of BP reveals that

the states below Fermi level are contributed by mainly phosphorous atoms whereas boron atoms are primarily responsible for the states above the Fermi level.

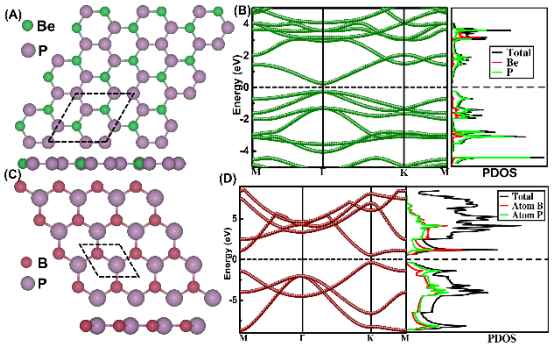


FIGURE 1: (A) Top and side view of Be_2P_4 monolayer (black dashed box shows hexagonal unit cell) **(B)** Electronic band structure and its corresponding PDOS for Be_2P_4 monolayer **(C)** Top and side view of BP monolayer (black dashed box shows hexagonal unit cell) **(D)** Electronic band structure and its corresponding PDOS for BP monolayer.

Be_2P_4/BP heterostructure and its adsorption phenomenon

To pair up the novel Be_2P_4/BP heterostructure efficiently, supercells of both layers are formed following the unit cell of Be_2P_4 monolayer and a 2×2×1 supercell of BP, as illustrated in Fig 2(A). According to these findings, there is a lattice mismatch of 3.71% between both layers. The optimized lattice constants of the Be_2P_4/BP heterostructure are 6.43 Å having an interlayer distance of 3.87 Å indicating that there might be adequate space for a significant number of sodium ions to be accommodated by such a broad interlayer gap. The stability of heterostructure is reported in terms of the binding energy which is calculated using $E_b = \frac{E_{Be_2P_4/BP} - E_{Be_2P_4} - E_{BP}}{n}$, where n is the total number of atoms in the heterostructure. The calculated value of E_b is -29.24 meV/atoms (-5.72 meV/ Å^2) which indicates the weak interlayer interactions in the heterostructure. We also calculated the band structure oh vdWH (Fig. 2(B)), having a minimum band gap of 0.16 eV.

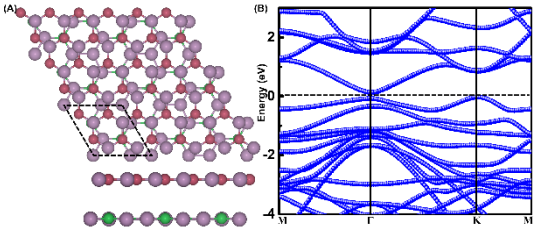


FIGURE 2: (A) Top and side representation of Be_2P_4/BP heterostructure and **(B)** electronic band structure of Be_2P_4/BP heterostructure.

To study adsorption process, we used a 2×2×1 supercell of the heterostructure. For investigating the interaction between the heterostructure and Na atom, the adsorption energy using $E_{ad} = E_{(Be_2P_4/BP)Na} - E_{Be_2P_4BP} - E_{Na}$

Table 1: Adsorption sites, adsorption energies and their respective heights of Na-atoms over Be_2P_4/BP heterostructure. a, b and i in subscript represent adsorption site at above, intermediate and below of heterostructure.

Adsorption sites	**Be_a**	**Be_i**	**Be_b**	**B_a**	**B_i**	**B_b**
Adsorption energy (eV)	-1.21	-2.28	-2.06	-2.01	-2.15	-2.20
Adsorption height (Å)	1.94	2.03	1.89	1.95	1.98	2.00

have been evaluated. We considered two adsorption sites involving hollow site of Be_2P_4 (Be site) as well as hollow site of BP (B site) as represented in Fig. 3(A), for both sites Na-atom adsorbed at the above (a), intermediate (i) and below (b) side of heterostructure. All the obtained adsorption energy and their adsorption height have been listed in Table 1 resulting in the intermediate side of Be-hollow site to be most favourable having adsorption energy of -2.28 eV. During sodiation over heterostructure, band structure also shows transition from semiconducting to metallic characteristics as displayed in Fig. 3(B).

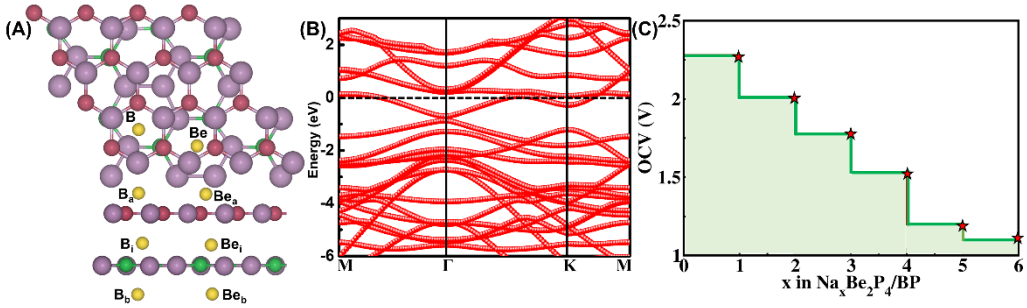


FIGURE 3: (A) Different adsorption sites of Na-atoms over Be_2P_4/BP heterostructure (yellow atom shows Na-atoms) **(B)** Electronic band structure of Be_2P_4/BP heterostructure after adsorption of single Na-atom **(C)** Sodiation OCV plot of Be_2P_4/BP heterostructure.

We also computed the average adsorption energy in order to determine the energetic integrity of the adsorbed heterostructure $(E_{ad})_{ave} = \frac{E_{Be_2P_4/BPNa} - (E_{Be_2P_4/BP} + nE_{Na})}{n}$. This heterostructure can hold up to six Na-atoms. Even after accumulation of six Na-atoms, heterostructure is able to store more Na-atoms as the obtained adsorption is still negative. To get more detailed information of electrochemical phenomenon, we calculated specific capacity of heterostructure using $C = \frac{nzF}{M_{Be_2P_4/BP}}$, where n is maximum number of stored Na-atoms, z is valence electrons of Na-atom, F is the Faradey constant (26.801 Ah/mol) and $M_{Be_2P_4/BP}$ represents the molecular weight of Be_2P_4/BP heterostructure. The calculated specific capacity of heterostructure is 520.32 mAh/g. The open circuit voltage (OCV) is obtained using formula $V = -\frac{(E_{Na})_{Be_2P_4/BPx_2} - (E_{Na})_{Be_2P_4/BPx_1} - (x_2 - x_1)E_{Na}}{x_2 - x_1}$ having a value from 2.27 V to 1.3 V (Fig. 3(C)). All these obtained results make Be_2P_4/BP heterostructure suitable to be employed as an anode material for SIBs.

CONCLUSIONS

In summary, DFT studies are utilized to examine the electrochemical properties of Be_2P_4/BP heterostructure. Both planar Be_2P_4 and BP monolayers exhibit semiconducting properties. We also combine Be_2P_4 and BP having semiconductor properties with band gap of 0.16 eV to study van der Waals heterostructure. This heterostructure shows high adsorption of -2.28 eV and specific capacity (OCV) of 520.32 mAh/g (1.3 V). Our results might encourage the investigation of 2D vdWHs having enough space to accumulate a large number of metal ions for applications in energy storage systems.

ACKNOWLEDGMENTS

NV thanks CSIR for financial support in the form of a Senior Research Fellowship (SRF). The computational resources of the Department of Physics of the Central University of Punjab were used to produce all the results of this work.

REFERENCES

1. J. Zhang, Y. F. Zhang, S. P. Huang, W. Lin and W. K. Chen, The Journal of Physical Chemistry C, Vol. 123, pp. 30809-30818 (2019).
2. O. M. Hernández, J. Guerrero-Sánchez, R. Ponce-Pérez, R. G. Díaz, H. N. Fernandez-Escamilla and G. H. Cocoletz, Applied Surface Science, Vol. *538*, pp. 148163, (2021).
3. P. Giannozzi, S. Baroni, N. Bonini, M. Calandra, R. Car, C. Cavazzoni, D. Ceresoli, G. L. Chiarotti, M. Cococcioni and I. Dabo Journal of Physics: Condensed Matter, Vol. 21, pp. 395502 (2009).
4. J.P. Burke and Y. Wang, Physical Review B, Vol. 54, pp. 16533 (1996).
5. P.E. Physical Review B, Vol. 50, pp. 17953 (1994).
6. S. Grimme, Journal of Computational Chemistry, Vol. 27, pp. 1787-1799 (2006).
7. T. T. Yu, P. F. Gao, Y. Zhang and S. L. Zhang, Applied Surface Science, Vol. 486, pp. 281-286, (2019).

Electrochemical Synthesis Of Nickel Hydroxide, Cobalt Hydroxide And Their Layered Double Hydroxide For Supercapacitor Application

Neha M. Phadte[1, a)], RajeshKumar Shankar Hyam[1, b) *]

[1]*School of Physical and Applied Sciences, Goa University*
[a)] *physics.neha@unigoa.ac.in*
[b)] *rajesh.hyam@unigoa.ac.in*

**Corresponding author: rajesh.hyam@unigoa.ac.in*

Abstract. In the present investigation, Nickel hydroxide ($Ni(OH)_2$), Cobalt hydroxide ($Co(OH)_2$) and ($Ni(OH)_2/Co(OH)_2$) layered hydroxide (LDH) thin films were deposited on stainless steel (SS) substrate potentiostatically. Thin film deposition parameters like concentration of solution and time for deposition were optimized. These thin films were characterized using Raman spectroscopic technique. Electrochemical characterizations i.e. Cyclic Voltammetry and Galvanostatic Charge Discharge of these films were studied.

KEYWORDS

Electrodeposition, Thin film, Metal hydroxide, Layered Hydroxide, Supercapacitor

INTRODUCTION

In light of the continuous depletion of non-renewable energy resources and the rising demand for energy across a wide range of applications, alternative methods for energy harvesting and storage have gained considerable attention. Within this context, the enhancement of storage technologies has become a central focus, with electrochemical energy storage identified as a leading solution. Fuel cells, batteries, and supercapacitors are the primary systems that operate based on the principles of electrochemical energy conversion. Supercapacitors can store extremely large amounts of electrical charge. Compared to batteries, electrochemical supercapacitors are capable of providing a power density of 100-1000 times more, which is very useful in high power burst applications like in accelerating/braking in fast transportation. They can withstand charging and discharging cycles much better than conventional batteries due to their cycle life being more than 100,000 times. A device's capacitance is mostly determined by the properties of the electrode material. The electrode materials' physical and chemical properties determine the required electrode features for application purposes. Electrochemical thin film deposition involves the reduction of cations on the cathode surface from precursor solution. Transition metal oxides or hydroxides as electrode material follow a pseudocapacitive mechanism. This results in higher capacitance values due to its redox reactions and multiple oxidation states. Theoretical capacitance of $Ni(OH)_2$ and $Co(OH)_2$ reported in literature are 2358 Fg^{-1} (voltage window of 0.44V) and 3460 Fg^{-1} (voltage window of 0.6V), respectively [1], indicating that it is possible to improve its capacitance by modifying its chemical and physical properties. Hence, in the present investigation, we are depositing Nickel hydroxide thin film on Cobalt hydroxide thin film electrode and studying their charge storage properties.

EXPERIMENTAL

Electrodeposition was carried out in potentiostatic mode in a three-electrode cell at room temperature. The cell is composed of stainless steel as the working electrode, Ag/AgCl as the reference electrode and platinum foil as the counter electrode. The stainless-steel substrate is roughened using grit papers to give an uneven surface and then ultrasonicated in distilled water, acetone and ethanol for cleaning the surface. Two precursor solutions of different concentrations ($Ni(NO_3)_2.6H_2O$ and $Co(NO_3)_2.6H_2O$) are taken for the electrodeposition. Thin films of these materials of different thickness were grown from (50mM, 100mM, 150mM 300mM and 350mM precursor solutions) to optimize the deposition time parameter. Linear Sweep Voltammetry (LSV) was first performed to determine the reduction potential, followed by Chronoamperometry.

RESULTS AND DISCUSSIONS

Electrodeposition was carried out in potentiostatic mode in a three-electrode cell at room temperature. The cell is composed of stainless steel as the working electrode, Ag/AgCl as the reference electrode and platinum foil as the counter electrode. The stainless-steel substrate is roughened using grit papers to give an uneven surface and then ultrasonicated in distilled water, acetone and ethanol for cleaning the surface. Two precursor solutions of different concentrations ($Ni(NO_3)_2.6H_2O$ and $Co(NO_3)_2.6H_2O$) are taken for the electrodeposition. Thin films of these materials of different thickness were grown from (50mM, 100mM, 150mM 300mM and 350mM precursor solutions) to optimize the deposition time parameter. Linear Sweep Voltammetry (LSV) was first performed to determine the reduction potential, followed by Chronoamperometry.

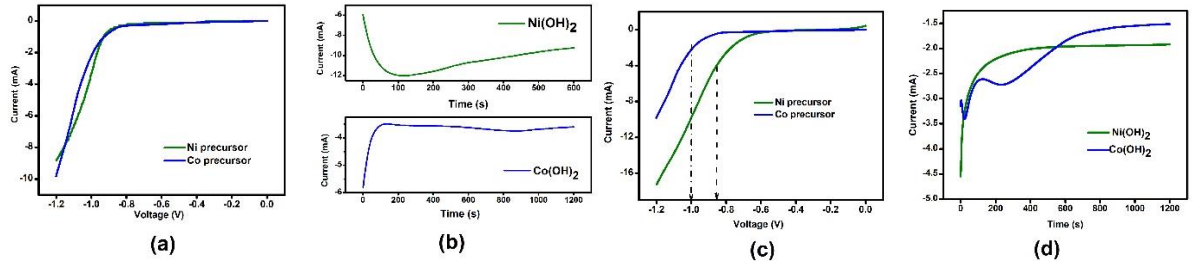


FIGURE 25. (a) LSV of stainless steel working electrode in $Ni(NO_3)_2.6H_2O$ and $Co(NO_3)_2$ precursor solution. (b) (top) Chronoamperometry plot of NH film growth, (bottom) CH film growth. (c) LSV of LDH film deposition. (d) Chronoamperometry of LDH film deposition.

LSV was followed by Chronoamperometry (I vs t) for the film deposition. In the case of $Ni(OH)_2$ film growth, a 10 min time duration and a 20 min for $Co(OH)_2$ film were optimized. In the case of NCH, a 20 min deposition was performed for each layered double hydroxide deposition. The nucleation growth mode was studied using Scharifker-Hills model [2]. Data of current transients was observed to follow instantaneous nucleation growth. The characterizations thus performed were on the three samples, NH, CH and NCH.

The Raman bands obtained matched with the reported literature. It confirmed α-Ni(OH)2 phase. The Raman spectrum for sample NH showed bands of hydroxide stretch at 3662 cm^{-1}, lattice modes at 466cm^{-1}, nitrate stretch at 1055cm^{-1} and 1295cm^{-1} and nitrate bend at 721cm^{-1}. For CH deposit, Raman bands were observed at 522cm^{-1} for CoO symmetric stretching, 455cm^{-1} for OCoO bending and 1046cm^{-1} for OH deformation mode [3][4][5]. For electrochemical characterizations, Cyclic Voltammetry (CV) and Galvanostatic Charge Discharge (GCD) were studied. CV was performed in 1M KOH solution for different scan rates. CV curves showed the pseudocapacitive behaviour of the materials with the oxidation and reduction peaks. With the increase in scan rate, the oxidation and reduction peaks were found to shift to the right and left respectively. This nature is due to the less thickness of the diffuse layer interaction with the increase in scan rate, and also due to the quasi-reversible nature of the redox reactions.

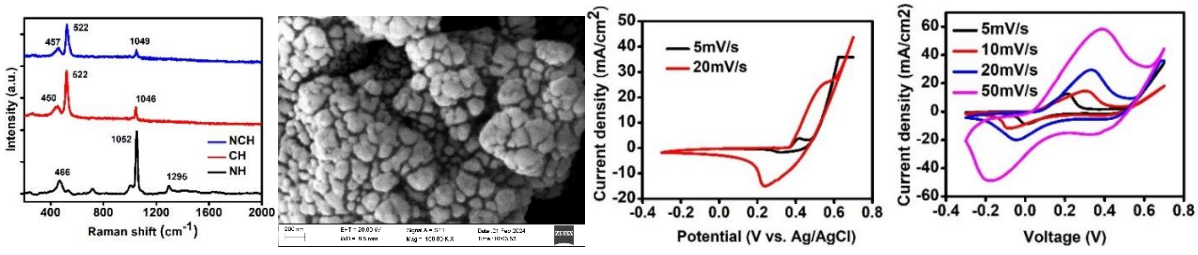
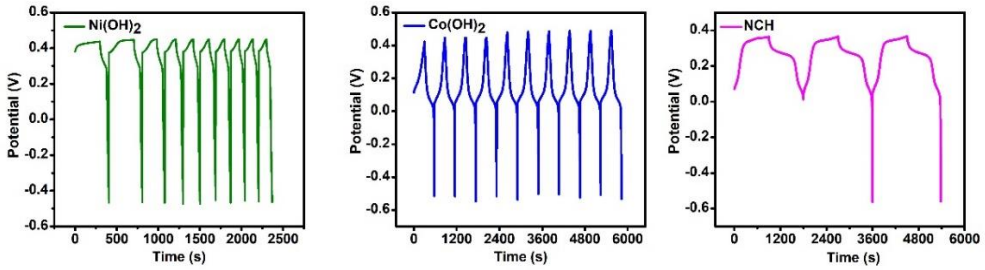


FIGURE 26. (A) Raman Spectroscopy of NH, CH and NCH, (B) SEM of NH, (C) CV of NH, (D) CV of CH.



(A) **(B)** **(C)**

FIGURE 27. Galvanostatic Charge Discharge study of sample (A) NH (B) CH and (C) NCH

Specific capacitance was calculated through GCD using the discharge current and time. NH showed a 43.52 F/g specific capacitance, CH a 309.15 F/g and the NCH deposited sample showed a 461.69 F/g specific capacitance. NCH showed the highest capacitance comparatively, which is due to the combined properties of Nickel hydroxide and Cobalt hydroxide.

CONCLUSIONS

The layered double hydroxide deposition current was observed to be less than the single film deposition. This led to a better film deposition in the case of $Ni(OH)_2/Co(OH)_2$//SS. A specific capacitance of 43.52 Fg^{-1} was achieved for $Ni(OH)_2$//SS film, 309.15 Fg^{-1} for $Co(OH)_2$//SS and 461.69 Fg^{-1} for $Ni(OH)_2/Co(OH)_2$//SS layered hydroxide films, which were calculated from the GCD data.

ACKNOWLEDGMENTS

Miss Neha Phadte acknowledges Goa State Research Foundation (GSRF) for doctoral fellowship and Dr. Rajeshkumar Hyam for UGC-FRP (faculty recharge program).

REFERENCES

1. J. P. Cheng, J. Zhang and F. Liu, RSC Adv., **4**, 38893-38917 (2014)
2. Yuan Yuan , Gong Luo and Ning Li, RSC Adv**.**,**11**, 31526-31532 (2021)
3. Kurt Lawson, Samuel P. Wallbridge, Amy E. Catling, Caroline A. Kirk and Sandra E. Dann, J. Mater. Chem. A, **11**, 789-799 (2023)
4. David S. Hall, David J. Lockwood, Shawn Poirier, Christina Bock and Barry R. MacDougall, J. Phys. Chem. A, 116, **25**, 6771–6784 (2012)
5. Jing Yang, Hongwei Liu, Wayde N. Martens, and Ray L. Frost, J. Phys. Chem. C, 114, **1**, 111–119 (2010)

Exploring Supercapacitive property of MoS_2/g-C_3N_4 composites on Screen-printed Carbon Electrode

[1,2]Ragini Chaturvedi, [2]Amit Garg*

[1]*Department of Electronic Science, University of Delhi, New Delhi 110021, India*

[2]*Acharya Narendra Dev College, University of Delhi, Kalkaji, New Delhi 110019, India*

Corresponding author Email Id: amitgarg@andc.du.ac.in

Abstract. One of the most promising energy storage technologies for future generations is the supercapacitor. In this work, 2D MoS_2 nanosheets are decorated with 2D g-C_3N_4 by cost-effective and eco-friendly method. The structure confirmation was done from XRD. The electrochemical characterization techniques such as cyclic voltammetry (CV) from potential range -1.5 to 0.6 V, and electrochemical impedance spectroscopy (EIS) 1 Hz to 50 KHz were used to explore the supercapacitive properties of MoS_2/g-C_3N_4 composites on screen-printed carbon electrode (SPCE). The areal capacitance calculated is 6.712 mF/cm^2 at 10 mV/s in the potential region -1.5 V to 0.6 V. The result manifests that MoS_2/g-C_3N_4 composites can be promising electrode materials for Supercapacitor applications.

INTRODUCTION

In the modern world, one of the most important essential sectors is the acquisition and storage of energy. Electrochemical energy storage devices (EESs) are crucial for constructing sustainable energy storage systems from the point of generation to the end user as renewable energy sources are sporadic. The supercapacitor is considered as one of the most promising energy storage devices for future generations. Supercapacitors are classified into two groups according to the way they store energy: electric double-layer capacitors (EDLC) [1] and pseudo-capacitors [2]. Supercapacitors are great energy storage devices because they have a lot of benefits like a high-power density, quick charge and discharge rates, great reversibility, long cycle lives, and extended lifespans.

Two-dimensional (2D) nanomaterials with sheet-like structures and high surface-to-volume ratios, such as graphene, metal-organic frameworks, boron nitrides, black phosphorus, transition metal oxides, transition metal dichalcogenides (TMDs), graphitic carbon nitride (g-C_3N_4), layered double hydroxides, and so forth, due to their exceptional physiochemical properties are best candidates for electrode material. TMDs are 2D materials with good electrical properties and a structure similar to graphene. They can be employed as electrode materials by altering their structure or in combination with other nanomaterials. The supercapacitor action depends on the surface area of these nanoparticles. Molybdenum disulfide is widely employed as an electrode material for electrochemical capacitors due to its layered structure resembling graphene, facilitating the accommodation of guest species and electrolyte ions between its layers [3]. The electrochemical properties of MoS_2 stem not only from its ion intercalation capabilities but also from its ability to undergo Faradaic redox reactions, supported by the diverse oxidation states of its molybdenum atoms. Unfortunately, the specific capacitance of MoS_2 remains relatively low due to its insufficient electronic conductivity and limited accessibility to active sites, and thus its further application and development in this sector [3]. Numerous previous studies have utilized highly conductive materials like rGO, GO, pyrrole, polyaniline, etc. to improve the electrical conductivity of MoS_2. While significant progress has been made in modifying carbon-based materials, integrating MoS_2 with g-C_3N_4 in a 2D/2D configuration enhances electrochemical performance due to its high electrical conductivity and chemical stability [2]. Graphitic carbon nitride (g-C_3N_4) is a polymeric material consisting of carbon, nitrogen, and trace amounts of hydrogen, linked together in a tris-triazine pattern. With its high carbon content and electron-rich nature, g-C_3N_4 exhibits superior electrochemical activity, including enhanced wettability, chemical affinity, and the ability to store charge through Faradaic reactions. These characteristics, coupled with its high porosity, make it a widely utilized material in energy storage applications. Its high degree of electron/ion mobility due to its porous nature, g-C_3N_4 can act as nanochannels on the electrode by greatly reducing the diffusion path [4]. Ansari et al. used semiconducting MoS_2-g-C_3N_4 composite as a material for electrodes for electrochemical energy storage and reported a high specific capacitance of 240.85 F/g [5]. According to Nikhitha et al., MoS_2 grown on g-C_3N_4 yields an outstanding specific capacitance value of 515 C/g at 1 A/g and around 66% capacitive retention at 20 A/g,

making it an efficient electrode material [6]. A screen-printed electrode (SPE) serves as a versatile sensor platform in electrochemical analysis and sensing applications due to their precise electrode structures with defined geometries and dimensions and thus provide adaptability, cost-efficiency, portability, and high sensitivity. Typically comprising a working electrode (WE), a counter electrode (CE), and optionally a reference electrode (RE), SPEs function as miniature electrochemical cells. Their performance has been enhanced using pseudocapacitive graphene composites and activated carbon, with techniques like bar-coating, blade-coating, and dispenser printing employed to prepare thick supercapacitor electrodes.

In this study, a simple and eco-friendly approach was employed to fabricate MoS_2/g-C_3N_4 composites. This method is cost-effective and scalable for large-scale production. Electrochemical measurements were conducted on Screen Printed Carbon electrodes (SPCEs) without additional modification. To the best of our knowledge, MoS_2/g-C_3N_4 /SPCE for supercapacitor application has not been reported elsewhere.

EXPERIMENTAL PROCEDURE

The graphitic carbon nitride (g-C_3N_4) was prepared by direct thermal pyrolysis of urea at 500^{o}C [7]. MoS_2 nanosheets were synthesized from bulk MoS_2 powder using a liquid phase exfoliation technique [8]. After that, the synthesis of MoS_2/g-C_3N_4 was done by ultrasonic dispersion method [9]. The capacitive properties of the sample were studied by cyclic voltammetry with a potential window -1.5 V to 0.6 V at various scan speeds from 0.01 V/s to 1 V/s, electrochemical impedance spectroscopy (EIS) from 0.1 Hz to 50 KHz, in the 0.1M KOH electrolyte, using a Sensit Smart Device. SPCEs were connected with the Sensit Smart and then 10µL analyte KOH (0.1M) was drop cast at SPCEs and standardized with suitable applied voltage. Afterwards, a 10µL solution of the prepared sample (1mg/ml) was drop cast within it and all the data were recorded. The areal capacitance (Cs in F /cm^2) of the composites from CV measurements was calculated using the standard equation for different scan rates (inset of Fig.2(c)) with active geometrical area of the working electrode (A = 7.07 mm^2).

RESULT AND DISCUSSION

The XRD pattern of MoS_2, g-C_3N_4, and MoS_2/g-C_3N_4 are shown in Fig. 1. According to the JCPDS card number-(37-1492), the peaks appearing at 14.8°, 33.5°, 40°, 44°, 50.4°, and 60° correspond to (002), (100), (103), (006), (105) and (110) planes respectively indicate the successful formation of MoS_2 nanosheets [8]. For pure g-C_3N_4 the strong peak at 27.5° and weak peak at 13.2° (JCPDS no- 87-1526) confirms its formation [7]. For MoS_2/g-C_3N_4, the main diffraction peaks of MoS_2 and g-C_3N_4 are visible indicating the successful formation of the composites [9]. When g-C_3N_4 is added, the strength of the MoS_2 diffraction peak is reduced and shift towards lower diffraction angle, particularly for the (002) peak. This indicates that the incorporation of g-C_3N_4 effectively suppresses the growth of MoS_2 crystals in composite materials and helps prevent the aggregation of MoS_2 nanosheets [10].

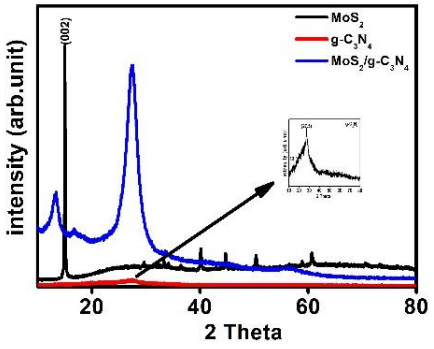


FIGURE 1. XRD of all prepared samples.

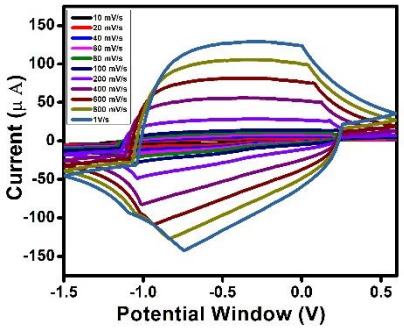


FIGURE 2(a). CV curve at various scan rates.

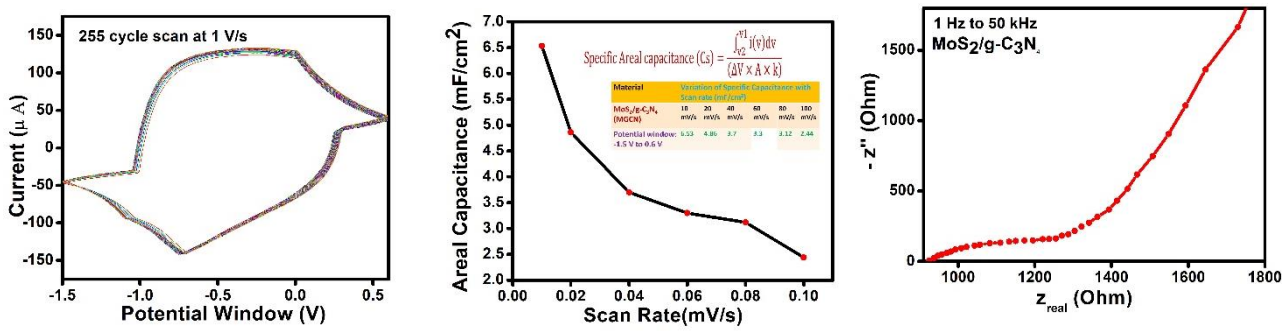


FIGURE 2(b). Represent CV graph up to 255 cycles**. (c)** Variation of Specific capacitance with scan rate. **(d)** Nyquist plot.

Figure 2(a) shows CV curves for MoS_2/g-C_3N_4 analysed in potential range -1.0 to 0.6 V at scan rates 0.01, 0.02, 0.04, 0.06, 0.08, 0.1, 0.2, 0.4, 0.6 ,0.8 and 1V/s. The CV curve exhibits a well-defined redox peak, which is a typical representation of a pseudo-type supercapacitor. Sample showing outstanding electrochemical reversibility and high-rate capability as it maintains a CV shape even at 1 V/s up to 255 cycles(Fig. 2(b)), indicating strong super capacitive behaviour with a large capacitive area. The potential reason for the enhanced performance of MoS_2 with the inclusion of g-C_3N_4 might be attributed to the close contact between g-C_3N_4 and MoS_2, which facilitates the efficient transfer of charge carriers from the edges of MoS_2 layers to g-C_3N_4. The calculated value of the areal capacitance is 6.712 mF/cm^2 at 10 mV/s, which decreases with increase in scan rate (Fig.2(c)). The Nyquist plot from electrochemical impedance spectroscopy (Fig. 2(d)) shows smaller resistance of composites, indicating that the electrode made of a hybrid of MoS_2/g-C_3N_4 has a lower charge transfer resistance and high electrical conductivity.

CONCLUSION

The preliminary findings indicates that MoS_2/g-C_3N_4 composites can act as high-performance electrode materials, that are stable and have a long-life span with reversibility.

ACKNOWLEDGMENTS

The authors would like to express their gratitude to Principal, Acharya Narendra Dev College, University of Delhi for providing infrastructural support and financial support(RC) under the “Anusandhan Kosh scheme of the college.

REFERENCES

1. Liew, Chiam-Wen, S. Ramesh, and A. K. Arof, Energy, Vol. 109, pp. 546-556 (2016).
2. Bhojane, Prateek, Journal of Energy Storage, Vol. 45, pp. 103654 (2022).
3. Ramadoss, Ananthakumar, Taehyun Kim, Gui-Shik Kim, and Sang Jae Kim, New Journal of Chemistry, Vol. 38, pp. 2379-2385 (2014).
4. Yang, Xiaojie, Jian Peng, Lingfei Zhao, Hang Zhang, Jiayang Li, Peng Yu, Yameng Fan, Jiazhao Wang, Huakun Liu, Carbon Energy, Vol. 6, pp. e490 (2024).
5. Ansari, Sajid Ali, and Moo Hwan Cho, Scientific Reports, Vol. 7, pp. 43055 (2017).
6. Joseph, Nikhitha, and A. Chandra Bose, Electrochimica Acta, Vol. 301, pp. 401-410 (2019).
7. Dong, Fan, Liwen Wu, Yanjuan Sun, Min Fu, Zhongbiao Wu, and S. C. Lee, Journal of Materials Chemistry, Vol. 21, pp. 15171-15174(2011).
8. Das, Subrata, Angkita Mistry Tama, Sagar Dutta, Md Shahjahan Ali, and M. A. Basith, Materials Research Express, Vol. 6, pp. 125079 (2019).
9. Wen, M. Q., T. Xiong, Z. G. Zang, W. Wei, X. S. Tang, and F. Dong, Optics Express, Vol. 24, pp. 10205-10212(2016).
10. Kavil, Jithesh, Shabeeba Pilathottathil, Mohamed Shahin Thayyil, and Pradeepan Periyat, Nano-Structures & Nano-Objects, Vol. 18, pp.100317 (2019).

Modulating Perovskite Stability Through Incorporation of 2D Spacer Cations for Solar Cell Application

Km Sakshi [1, a)], Abhimanyu Singh Rana [2, b)] and Soumyendu Roy [1, c)]

[1]*Department of Physics, School of Engineering and Applied Sciences and Centre of Excellence for Nanosensors and Nanomedicine, Bennett University, Greater Noida, UP, 201310, India*

[2]*Centre for Advanced Materials and Devices, BML Munjal university, Gurugram, Haryana, 122413, India*

[a)]Corresponding author: soumyendu.roy@bennett.edu.in,

Abstract. Perovskites, despite having excellent opto-electronic properties and low-cost synthesis method, they are still not suitable choice for commercialization because of their instability in ambient environment. To enhance perovskite stability, a promising strategy involves forming 2D/3D hybrid structures by incorporating spacer cations into the 3D perovskite. This study examines octyl ammonium (OA) as 2D/3D $MAPbI_3$ perovskite, targeting surface and grain boundary defect passivation. Using XRD and SEM, we analyzed OA's impact on thermal stability and film morphology. Results indicate that OA inhibits ion migration, improving thermal stability and potentially leading to more durable and efficient perovskite solar cells.

INTRODUCTION

A distinctive class of compounds known as perovskites gets its name from Lev Perovski, the Russian mineralogist, following its discovery in the Ural Mountains in 1839. These substances possess a characteristic crystal structure and adhere to the general chemical formula ABX_3. Within this formula, the 'A' position is occupied by a monovalent cation (for instance, methylammonium or cesium), the 'B' position by a divalent cation (such as lead or tin), and the 'X' position by a halide anion (like iodide or bromide)(Figure 1(A)).

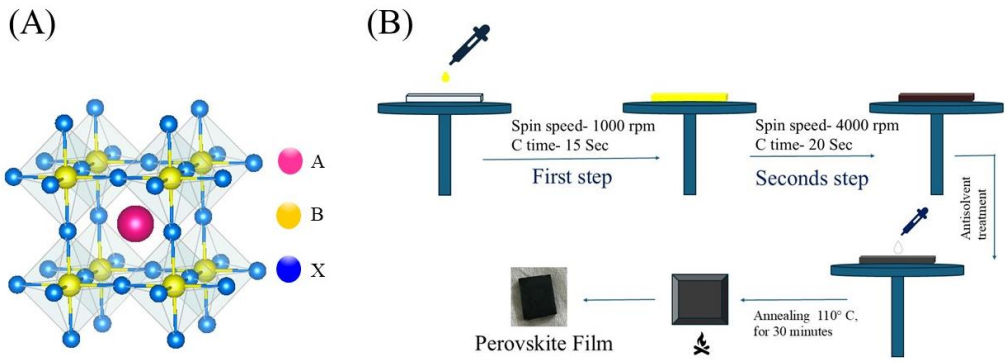


FIGURE 1. (A) ABX_3 crystal structure, (B) Step by step perovskite thin film preparation via solution process method

Perovskites are the potential future of photovoltaic industry because of their desirable optical properties and electrical properties which include wide absorption window from visible to near infrared region of electromagnetic spectrum[2], tuneable bandgap[3], low exciton binding energy[4–6], long charge carrier diffusion length[7] and high-power conversion efficiency[8] (PCE). Despite having achieved high power conversion efficiency, $MAPbI_3$ based solar cell are still not ready for commercialization because of poor stability of $MAPbI_3$ in ambient environmental conditions as MA cation move out from crystal and film degrade into MAI (Methylammonium iodide) and PbI_2 (lead iodide)[9]. An effective technique to improve stability of perovskite includes incorporation of long carbon chain as spacer cations into 3D $MAPbI_3$ structure and make it 2D/ 3D mixed dimensional perovskite[10]. Compared to 3D perovskites, low-dimensional perovskite films, particularly 2D perovskites with both pure 2D and quasi-2D structures, show enhanced durability. This improvement is attributed to the presence of bulky hydrophobic organic spacer molecules within their structure[11]. Introducing bulky organic cations between the inorganic layers in perovskites acts as spacers keeping the inorganic layers apart and making the ion movement difficult within the material. This effectively suppresses ion migration, a primary mechanism responsible for material degradation. Furthermore, the enlarged interlayer spacing induced by these spacers enhances the structural integrity of the crystal lattice, thereby improving resistance to external stresses like temperature.

The general chemical formula for Pseudo 2D perovskite is $(M)_2(A)_{n-1}(B)_n(X)_{3n+1}$, where M is Organic spacer cation, A is monovalent cation, B is divalent cation and X is halide anion. The n value shows the number of

inorganic layers between two spacer cation layers[12]. In this work, the Octylammonium (OA) was incorporated as organic spacer cation to create a 2D/3D perovskite structure. As a result, significant improvement was shown in structural stability of OA incorporated $MAPbI_3$ films in comparison to $MAPbI_3$ film. The results obtained indicate that OA incorporation can significantly delay the degradation mechanism in $MAPbI_3$ film.

EXPERIMENTAL SECTION

FTO substrates 1cm × 1cm were cut and cleaned with solvents in ultrasonicator and ozone cleaner. The substrate was preheated to 80°C before spin coating. 1M $MAPbI_3$ precursor solution was prepared by dissolving Methylamine Hydroiodide (Low water content >99.0%, TCI) and Lead (II) Iodide (99.99%, trace metals basis, TCI) in N,N-Dimethylformamide (99.9%. SRL) and Dimethyl sulfoxide (99%, SRL) and about 50 µL of solution was spread all over substrate and spin coated (SPIN NXGP1 programmable spin coater) the solution in 2 steps: 1000 rpm for 15 seconds in first step and 4000 rpm for 20 seconds in second step. OA-$MAPbI_3$ was deposited by dissolving organic spacer cation Octylammonium iodide (Greatcell Solar®) in proper stoichiometry according to the 2D perovskite formula $(OA)_2(MA)_{n-1}(Pb)_n(I)_{3n+1}$ in $MAPbI_3$ precursor. For antisolvent treatment 150µL of chlorobenzene (extrapure, 99%, SRL) was dropped in last 8 seconds of second step. Immediately after the spin coating program ended, the films were kept on hot plate for annealing at 110°C for 20 minutes as shown in Figure 1(B).

RESULT AND DISCUSSION

Figure 2(A) shows the X-ray diffraction (XRD) patterns of $MAPbI_3$ on FTO substrates. The films were prepared in an open environment with around 60% relative humidity. Strong diffraction peaks of mixed cubic Pm3m (221) and tetragonal 14/mcm phases were observed at 14.01°, 19.89°, 23.42°, 24.11°, 28.28°, 31.70°, 34.81°,40.43° and 42.99° for the 2θ scan in 2D/3D (OA treated $MAPbI_3$) and 3D ($MAPbI_3$). These peaks correspond to the planes (100), (110), (121), (111), (200), (210), (211), (202) and (300) respectively, which is consistent with the earlier results[13] without formation of PbI_2 phase. Generally cubic phase in $MAPbI_3$ is not very stable at room temperature and it converts to tetragonal at temperature lower than 54°C but here cubic phase along with tetragonal phase is maintained at room temperature[14]. Average crystallite size was found to be 224nm which was calculated by Scherrer's equation (1), where K is Scherrer constant (K = 0.9), λ is X-ray source wavelength (λ = 0.15406 nm), β is fullwidth half maxima (FWHM) of peaks and θ is peak position.

$$D = \frac{K\lambda}{\beta cos\theta} \qquad (1)$$

Figure 2(B) shows XRD pattern of degraded sample. After aging the film for one week in ambient environment the PbI_2 peak at 12.6° was very significant and the $MAPbI_3$ peaks intensity decreased to significant amount, which confirms that $MAPbI_3$ is completely degraded into MAI and PbI_2 after a week. Figure 2(C) shows comparison between pristine and aged films with and without treatment with OA. PbI_2 peak was absent in both pristine $MAPbI_3$ and OA-$MAPbI_3$ (OA treated $MAPbI_3$) films. After ageing in ambient environment for 5 hours on 85° C both films were showing PbI_2 peak at 12.6° but PbI_2 content was more in the film without $MAPbI_3$ as comparison to the film OA-$MAPbI_3$ leading to the conclusion that treatment with OA in very small amount (2mg/ml) is reducing ion migration resulting into structural stability. Figure 2(D) shows the surface morphology of $MAPbI_3$ perovskite film on FTO substrate. The film showed a dense pinhole free morphology. Lakka and co-workers confirmed that the rate of degradation of $MAPbI_3$ could be accelerated because of PbI_2 residue present in the perovskite film[15]. As shown in Figure 2(d), there was no residue of PbI_2 in film which is consistent with XRD data. The average grain width of perovskite film is 3 µm.

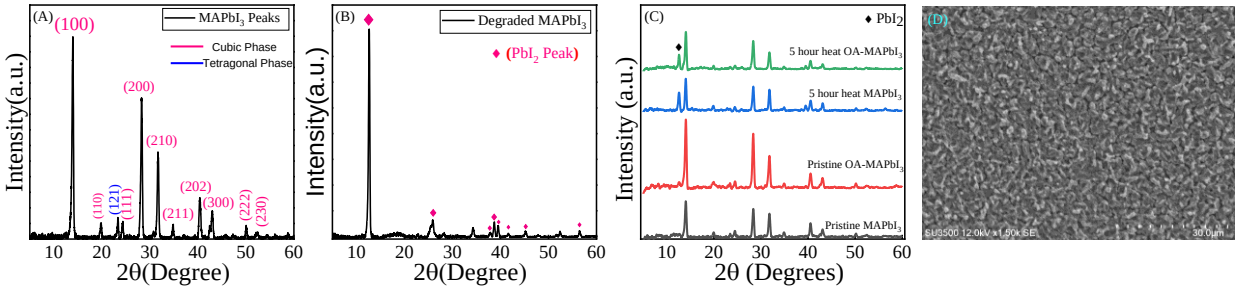


FIGURE 2. (A) XRD pattern for pristine $MAPbI_3$ film (B) XRD pattern for aged $MAPbI_3$ film in ambient environment for one-week (C) XRD peaks of Pristine $MAPbI_3$ and OA-$MAPbI_3$ and aged $MAPbI_3$ and OA-$MAPbI_3$ for 5h in ambient environment at 85°C temperature (D) SEM image for Pristine $MAPbI_3$

CHARACTERIZATION TECHNIQUE

The XRD peaks of perovskite thin films were detected by Bruker AXS Model number -D8 Advance. The morphological characteristic of the thin films was studied using HITACHI Scanning electron microscope (SEM) model number-SU3500. ABX_3 crystal structure in Figure 1 is created using VESTA software.

CONCLUSION

In conclusion, we have experimentally shown that after incorporation of organic long carbon chain spacer cation OA in $MAPbI_3$ making it mixed dimensional (2D/3D) perovskite, greatly improves its thermal stability. Stability towards thermal aging in ambient environment was studied using X-ray crystallography. Reduced ion migration in mixed dimensional perovskite is responsible for this improved stability.

ACKNOWLEDGEMENT

This work was supported by the DST INSPIRE Faculty Fellowship (DST/INSPIRE/04/2015/002287) and the UGC-DAE CSR project (CRS/2022-23/1164) awarded to S. Roy.

REFERENCES

1. Etgar, L. Hole Conductor Free Perovskite-based Solar Cells. (2016).
2. Yin, W. J., Shi, T. & Yan, Y. Unique properties of halide perovskites as possible origins of the superior solar cell performance. *Advanced Materials* **26**, (2014).
3. Hoke, E. T. *et al.* Reversible photo-induced trap formation in mixed-halide hybrid perovskites for photovoltaics. *Chem Sci* **6**, (2015).
4. Hirasawa, M., Ishihara, T., Goto, T., Uchida, K. & Miura, N. Magnetoabsorption of the lowest exciton in perovskite-type compound (CH3NH3)PbI3. *Physica B: Physics of Condensed Matter* **201**, (1994).
5. Tanaka, K. *et al.* Comparative study on the excitons in lead-halide-based perovskite-type crystals CH3NH3PbBr3 CH3NH 3PbI3. *Solid State Commun* **127**, (2003).
6. Ishihara, T. Optical properties of PbI-based perovskite structures. *J Lumin* **60–61**, (1994).
7. Stranks, S. D. *et al.* Electron-hole diffusion lengths exceeding 1 micrometer in an organometal trihalide perovskite absorber. *Science (1979)* **342**, (2013).
8. Kim, D. I., Lee, J. W., Jeong, R. H. & Boo, J. H. A high-efficiency and stable perovskite solar cell fabricated in ambient air using a polyaniline passivation layer. *Sci Rep* **12**, (2022).
9. Ko, H. S., Lee, J. W. & Park, N. G. 15.76% efficiency perovskite solar cells prepared under high relative humidity: Importance of PbI2 morphology in two-step deposition of CH3NH3PbI3. *J Mater Chem A Mater* **3**, (2015).
10. Zou, Y., Gao, Y. & Liu, Y. The role of organic spacers in 2D/3D hybrid perovskite solar cells. *Materials Chemistry Frontiers* vol. 8 82–103 Preprint at https://doi.org/10.1039/d3qm00726j (2023).
11. Gao, Y., Wang, R. & Liu, Y. Progress of Two-dimensional Perovskite Solar Cells Based on Aromatic Organic Spacers. *Faguang Xuebao/Chinese Journal of Luminescence* **44**, (2023).
12. Xu, Y., Wang, M., Lei, Y., Ci, Z. & Jin, Z. Crystallization Kinetics in 2D Perovskite Solar Cells. *Advanced Energy Materials* vol. 10 Preprint at https://doi.org/10.1002/aenm.202002558 (2020).
13. Qiu, J., McDowell, L. L. & Shi, Z. Room-Temperature Cubic Perovskite Thin Films by Three-Step All-Vapor Conversion from PbSe to MAPbI3. *Cryst Growth Des* **19**, 2001–2009 (2019).
14. Poglitsch, A. & Weber, D. Dynamic disorder in methylammoniumtrihalogenoplumbates (II) observed by millimeter-wave spectroscopy. *J Chem Phys* **87**, (1987).
15. Gujar, T. P. *et al.* The role of PbI2 in CH3NH3PbI3 perovskite stability, solar cell parameters and device degradation. *Physical Chemistry Chemical Physics* **20**, (2017).

Bifunctional $NiSe_2$ Nanoclusters for Supercapacitor and Photocatalytic Dye Degradation Applications

Ravi Pratap Singh[1], Prashant S. Alegaonkar[1,*], Kamlesh Yadav [1,2, *]

[1]Department of Physics, School of Basic Sciences, Central University of Punjab, Bathinda-151401, Punjab, India

[2]Department of Physics, University of Allahabad, Prayagraj-211002, Uttar Pradesh, India

*kamleshyadav@allduniv.ac.in (K.Yadav),and prashant.alegaonkar@cup.edu.in (P.S.Alegaonkar)

Abstract. In this study, $NiSe_2$ nanoclusters were prepared using a hydrothermal technique. Structural and morphological characterizations confirmed the formation of the nanocluster architecture. Electrochemical evaluation revealed that the $NiSe_2$-based supercapacitor delivered a specific capacitance of 250 F g^{-1} @ 10 mV s^{-1}, along with a power density of 800 W kg^{-1} and an energy density of 21.7 Wh kg^{-1}. The photocatalytic efficiency of $NiSe_2$ was assessed through the degradation of methyl orange (MO) under sunlight, achieving a degradation rate of 92% within 80 minutes. These results demonstrate the promising capabilities of $NiSe_2$ nanoclusters for both photocatalytic dye removal and advanced energy storage applications.

Keywords: $NiSe_2$, Bifunctional, Supercapacitor, Photocatalytic, Methyl orange

INTRODUCTION

In the 21st century, the ever-growing energy crisis and environmental pollution have become a serious problem, particularly in major developing countries. To find an alternative solution, researchers have made substantial efforts to develop cost-effective and eco-friendly nanomaterials for energy storage and environmental remedial. Ultracapacitors, also known as supercapacitors, exhibit exceptional durability, high energy density, and rapid energy delivery, making them as promising components in the electric vehicle industry [1]. In addition, the release of toxic dyes and chemical reagents from textile, leather, and plastic industries has severely impacted aquatic ecosystems, the environment, and human health. A multifunctional nanomaterial capable of serving as both a supercapacitor electrode and a photocatalyst could offer an effective solution for degrading organic and inorganic pollutants in water, while contributing to sustainable energy systems. The two-dimensional $NiSe_2$ nanomaterials have recently attracted attention within the MX_2 family, where M denotes transition metals and X is a chalcogen. Because of the 2D nanostructure, these materials exhibit a large surface area and a narrow band gap. $NiSe_2$ nanomaterials are gaining attention as a potential material for supercapacitors and photocatalysts, thanks to their optimal electronic arrangement, high density of reactive centers, and ability to access multiple oxidation states [2]. In this work, a facile hydrothermal method is employed to synthesize dual-functional $NiSe_2$ nanomaterials for application in both energy storage and organic pollutant degradation for water treatment.

EXPERIMENTAL DETAILS

SYNTHESIS OF $NiSe_2$ USING HYDROTHERMAL METHOD

To prepare Solution A, approximately 0.96 g of $(Ni(NO_3)_2 \cdot 6H_2O)$ is dissolved in 30 mL of deionized (DI) water. Meanwhile, Solution B was formed by dispersing 0.521 g of selenium powder in 5 mL of $(N_2H_4 \cdot H_2O)$. The two solutions were mixed under constant stirring and then transferred into a 100 mL Teflon-lined autoclave. The sealed autoclave was heated in a vacuum furnace at 200°C for 24 hours to facilitate the hydrothermal reaction. After natural cooling to room temperature, the black precipitate was collected, washed repeatedly with DI water and ethanol, and dried at 70°C for 10 hours.

CHARACTERIZATION

Structural analysis was performed using XRD (PANalytical), while FTIR (Bruker Tensor 27) was used to identify functional groups in the 500–4000 cm^{-1} range. Surface morphology and elemental composition were examined by FESEM (Carl Zeiss Merlin Compact). Electrochemical properties, including CV and GCD, were measured using a CHI 760E workstation [3]. The photocatalytic performance of $NiSe_2$ was tested using methyl orange (MO) dye under both dark and light conditions. About 20 mg of $NiSe_2$ was inserted into 100 mL of MO precursor, stirred for 30 minutes in the dark, then exposed to sunlight for 10 minutes. A 3 mL sample was analyzed using a Shimadzu UV-2450 spectrophotometer.

RESULTS AND DISCUSSION

Figure 1(a) presents the XRD peaks of $NiSe_2$ at around $2\theta \approx 29.90^\circ$, 33.56°, 36.84°, and 50.90°, matching the (200), (210), (211), and (310) planes of the cubic structure (ICDD card: 00-011-0552) [4]. Using the Debye-Scherrer equation, the estimated average crystallite size (*D*) was approximately 20 nm.[3]. FTIR spectra of the $NiSe_2$ display the IR absorption peaks at 729, 1218, 1612, and 3255 $cm^{-1,}$ which are attributed to the Ni-Se, C=O, O-H bending, and O-H stretching bands, respectively, as displayed in **Figure 1(b)** [5]. **Figure 1(c)** represents the FESEM images, revealing the formation of $NiSe_2$ nanoclusters with uniform distribution. The inset image of

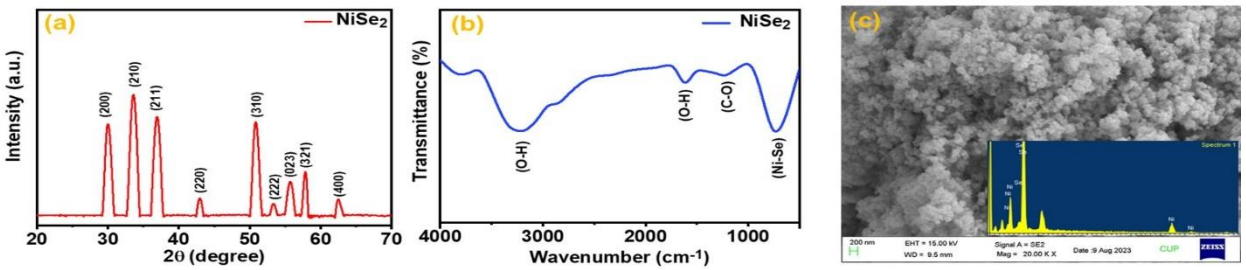


Figure 1(c) displays the EDS spectrum of $NiSe_2$, which confirms the existence of Ni and Se in the stoichiometric ratio of 1:2.

Figure 28. (a) XRD, **(b)** FTIR, **(c)** morphological image, and the inset shows the EDS of $NiSe_2$.

Figure 2(a) shows the CV profile of symmetrical $NiSe_2$-based supercapacitor electrodes recorded at different scan sweeps ranging from 10 to 100 mV s^{-1} with the voltage window of –0.6 to 0.6 V. The appearance of distinct redox peaks indicates the pseudocapacitive nature of $NiSe_2$ nanoclusters. The variation of Csp with scan rate is displayed in **Figure 2(b)**, where $NiSe_2$ nanoclusters exhibit the highest Csp of 250 F g^{-1}, outperforming $NiSe_2$ nanospheres (99 F g^{-1}) and $NiSe_2$/rGO composites (137 F g^{-1}) [6–7]. This superior performance is mainly attributed to the excellent electrical conductivity and reduced dimensions of the $NiSe_2$ nanoclusters, which facilitate improved ion diffusion and offer more electrochemically active sites [8]. Additionally, the charge storage mechanism of $NiSe_2$ follows a power-law relationship described by the equation $i = a \cdot v^b$, where *i* is the peak current, *v* is the scan sweep, and *b* is a constant reflecting the charge storage kinetics [3,4]. The *b* value, approximately 0.5 (inset of **Figure 2(b)**), indicates a diffusion-controlled process. **Figure 2(c)** presents the galvanostatic charge-discharge profile obtained at various current densities between 1 and 3.5 Ag^{-1}. The corresponding Ragone plot (**Figure 2(d)**) illustrates the ED and PD, with the device achieving an ED of 21.7 $Whkg^{-1}$ and a PD of 800 W kg^{-1}.

Figure 2(e) shows the UV-Vis absorption pattern of the MO solution treated with $NiSe_2$ as a photocatalyst. A steady reduction in the absorbance peak at 470 nm indicates the gradual breakdown of the MO dye with increasing exposure time. The photocatalytic performance of $NiSe_2$ towards MO degradation was evaluated using Equation (1):

$$\eta = (C_0 - C_t) \times \frac{100}{C_0} \quad (1)$$

where C_0 denotes the initial concentration of the dye, and C_t represents the dye concentration measured at a specific time t (in seconds). The $NiSe_2$ nanoclusters demonstrate catalytic activity with a 92% MO degradation efficiency after 80 minutes of irradiation. During the degradation process, reactive hydroxyl radicals (•OH) and photogenerated holes interact with the MO dye molecules, breaking them down into non-toxic products. The plot of C/C_0 versus time is illustrated in **Figure 2(f)**, where a continuous decline in absorbance intensity with time is observed. The degradation kinetics of $NiSe_2$ are depicted in the inset of **Figure 2(f)** and are fitted using pseudo-first-order equation **(2)**:

$$-\ln\frac{C_t}{C_0} = kt \quad (2)$$

where the degradation constant is represented by k (min^{-1}) [9]. The linear fit with a correlation coefficient of R = 0.8166 and a k value of 0.0036 min^{-1} indicates that the degradation process follows first-order kinetics.

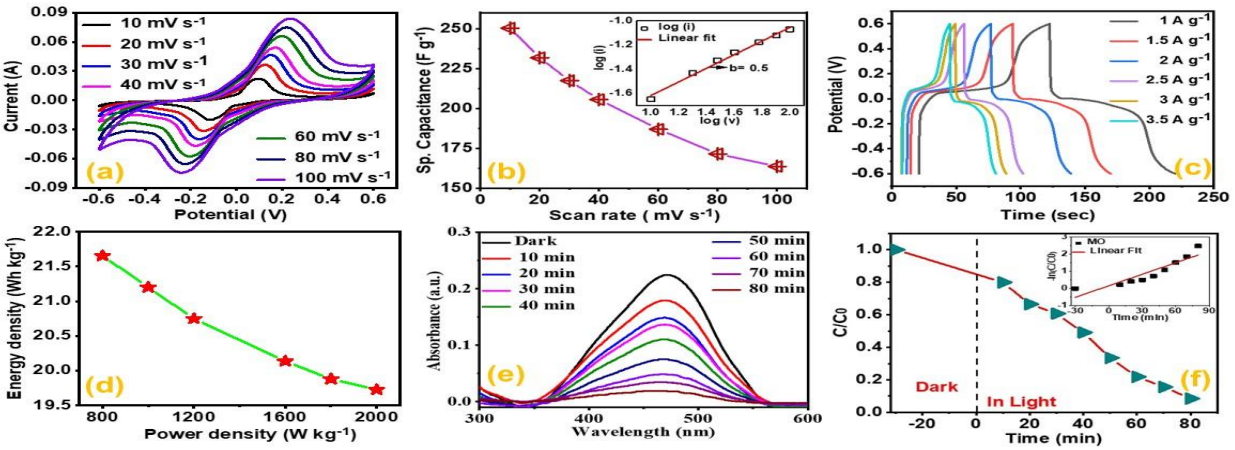


Figure 29. (a) $NiSe_2$ CV profile with various scan step, **(b)** C_{sp} vs. scan sweeps (inset shows log i vs log v), **(c)** GCD curves of $NiSe_2$ with diverse current density, **(d)** Ragone plot, **(e)** UV-vis absorption of $NiSe_2$ for MO dye when exposed to sunlight, and **(f)** Plot of C/C_0 vs time (inset shows photocatalyst kinetic linear fitting curve).

CONCLUSION

In this work, $NiSe_2$ was prepared by using a hydrothermal technique. The electrochemical performance of the symmetric SC demonstrates an E_D of 21.7 Wh kg^{-1} @ P_D of 800 W kg^{-1}. Additionally, $NiSe_2$ shows outstanding catalytic performance, achieving a 92% MO degradation efficiency of MO in 80 minutes of light irradiation. These results suggest that $NiSe_2$ can serve as a dual-functional nanomaterial for both SC applications and dye degradation.

ACKNOWLEDGMENTS

RP acknowledges the financial support provided by CSIR, India, and the laboratory facilities provided by CIL and DoP, CUP, Bathinda.

REFERENCES

1. A. Ramadoss, B. Saravanakumar, S. W. Lee, Y.S. Kim, S. J. Kim, & Z. L. Wang, Piezoelectric-driven self-charging supercapacitor power cell. Acs Nano, 9(4), 4337-4345 (2015).
2. J. Zhou, L. Yuan, J. Wang, L. Song, Y. You, R. Zhou & J. Xu, Combinational modulations of $NiSe_2$ nano dendrites by phase engineering and iron-doping towards an efficient oxygen evolution reaction. Journal of Materials Chemistry A, 8(16), 8113-8120 (2020).
3. R. P. Singh, P. S Alegaonkar, C. Devi, G. K. Yogesh, & K. Yadav, Selenium-enriched $MoSe_2$ as an effective electrode material for supercapacitors and a photocatalyst for dye degradation. Materials Today Communications, 40, 109671 (2024).
4. S. D. Adhikari, A. Roy, P. Kour, K. Kukreti, M. Himanshu, R. P. Singh, & K. Yadav, Bifunctional layered g-C_3N_4 incorporated $NiSe_2$ nanocomposites as a highly efficient photocatalyst and electrode material for supercapacitor applications. Journal of Energy Storage, 92, 112205 (2024).
5. B. A. Khan, R. Hussain, A. Shah, A. Mahmood, M. Z. U. Shah, J. Ismail & M. S. Javed, $NiSe_2$ nanocrystals intercalated rGO sheets as a high-performance asymmetric supercapacitor electrode. Ceramics International, 48(4), 5509-5517(2022).
6. S.R. Sitaaraman, R. Santhosh, P. Kollu, S.K. Jeong, R. Sellappan, V. Raghavan, G. Jacob & A.N. Grace, Role of graphene in $NiSe_2$/graphene composites-Synthesis and testing for electrochemical supercapacitors, Diam. Relat. Mater. 108,107983 (2020).
7. S. Wu, T. Cui, Q. Hu, F. Yin, Q. Feng, S. Zhou, Q. Su, L. Wu & Q. Yang, Mixing solvothermal synthesis nickel selenide on the surface of graphene for high-efficiency asymmetric supercapacitors, Synth. Met. 268, 116490 (2020).
8. T. Kawawaki, Y. Mori, K. Wakamatsu, S. Ozaki, M. Kawachi, S. Hossain, & Y. Negishi, Controlled colloidal metal nanoparticles and nanoclusters: recent applications as cocatalysts for improving photocatalytic water-splitting activity. Journal of Materials Chemistry A, 8(32), 16081-16113 (2020).
9. R. P. Singh, P. Kour, Anu, P. S. Alegaonkar, & K. Yadav. Bifunctional Molybdenum Diselenide ($MoSe_2$) Nanosheets for High-Performance Symmetric Supercapacitor Device and Photocatalytic Dye Degradation Application. In International Conference on Nanotechnology: Opportunities and Challenges, Singapore: Springer Nature Singapore, 27, 423-427 (2022).

Co-precipitation Synthesis of Cobalt Ferrite ($CoFe_2O_4$) Nanoparticles and Their Supercapacitor Applications

Daud Ahmad Ansari[1], Mehraj Ud Din Rather[2], Sharika Afreen[1] and Shahid Husain[1,*]

[1]*Department of Physics, Aligarh Muslim University, Aligarh, 202002, India*

[2]*Department of Electronics and Communication Engineering, SR University, Telangana, 506371, India*

[*]*Corresponding author: s.husaincmp@gmail.com*

Abstract. In the present work, we have synthesized the nanocrystalline cobalt ferrite ($CoFe_2O_4$) through co-precipitation method. Investigations carried out using X-ray diffraction, FTIR and Raman spectroscopy techniques confirm the purity and single phase formation of spinel $CoFe_2O_4$ (CFO) with $Fd\bar{3}m$ space group. Prepared nanoparticles were also tested for its energy storage properties by depositing it on nickel foam, and using it as cathode material in a three-electrode setup. The impressive values of specific capacitance achieved for this material proves its potential candidature for the supercapacitors.

Keywords: *Cobalt ferrite, Co-precipitation, Rietveld, Cyclic Voltammetry, Galvanostatic Charging-Discharging.*

INTRODUCTION

Spinel ferrites commonly represented as MFe_2O_4, where M site is usually occupied by transition metal elements, have long been intriguing topic of research among the material scientists. They are well known to find applicability in diverse fields of science and technology ranging from semiconductor industries to medical sciences [1, 2]. Their distinct structural and physicochemical qualities, as well as the ability to alter them to improve desirable properties, provide them an advantage over other materials with similar properties. $CoFe_2O_4$ (CFO) conforms in inverse spinel cubic structure, with space group $Fd\bar{3}m$. It is one such exemplary material that is widely studied by researchers in distinct disciplines. Researchers are actively trying to synthesize nanoparticles of $CoFe_2O_4$, and its composites with various materials via different improvised techniques to acquire extraordinary results [1,2]. Herein, we are reporting a simple and accurate method for the synthesis of CFO i.e. co-precipitation technique. Furthermore, studying its electrochemical properties clearly highlights the energy storage capability of this material, thus making it a favorable candidate for supercapacitor applications.

EXPERIMENTAL DETAILS

We have implemented co-precipitation method for the synthesis of CFO nanoparticles. Analytical grade cobalt nitrate $Co(NO_3)_2.6H_2O$, and iron nitrate $Fe(NO_3)_3.9H_2O$ procured from CDH chemicals are used to prepare the ferrimagnetic CFO. X-ray diffraction (XRD) study is carried out in the range of 20º-70º on Shimadzu LabX XRD-6100 advanced diffractometer, equipped with Cu K_α radiation source. The FTIR spectrum is acquired in the wavenumber region 400-4000 cm^{-1} using FTIR Spectrum Two, Perkin Elmer instrument. Raman analysis is performed on Renishaw InVia Raman microscope with 785 nm diode laser as the excitation source. ZIVE SP1 potentiostat/galvanostat setup was used to perform the Cyclic Voltammetry (CV) and Galvanostatic Charging-Discharging (GCD) of the CFO nanoparticles.

RESULTS AND DISCUSSION

Structural Studies

X-Ray Diffraction (XRD): The produced powder sample of cobalt ferrite is analysed using XRD technique. The XRD pattern of CFO sample shown in Fig. 1, has been well-matched with standard of JCPDS card number: 22-1086. Absence of any impurity peak confirms the successful phase formation of CFO. The XRD pattern has been

further analysed to evaluate the average size of the crystallites formed, using both Debye-Scherrer and Williamson-Hall (W-H) approaches. Debye-Scherrer method considers only the broadening of peaks due to size of the crystallites, whereas W-H method also takes into account the strain broadening factor while calculating FWHM of the XRD peaks. The crystallite size (D) from Scherrer equation is calculated as: $D= k\lambda/\beta\cos\theta$, λ is the wavelength of X-rays which in this case is 1.54 Å, k is the shape factor (k=0.9), β is the line broadening of the peak, and θ is the Bragg angle. The Williamson-Hall equation is written as: $\beta\cos\theta= k\lambda/D+4\varepsilon\sin\theta$. A plot of $\beta\cos\theta$ vs $4\sin\theta$ results into a straight line as depicted in Fig. 2, whose intercept can be used to evaluate the crystallite size and slope gives the lattice strain (ε). The crystallite sizes found by Debye-Scherrer, and W-H methods are 19 nm and 24 nm respectively.

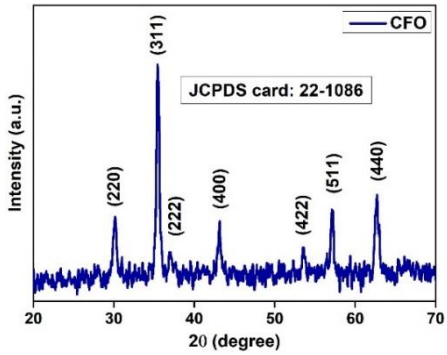


Fig. 1. XRD pattern of pristine CFO

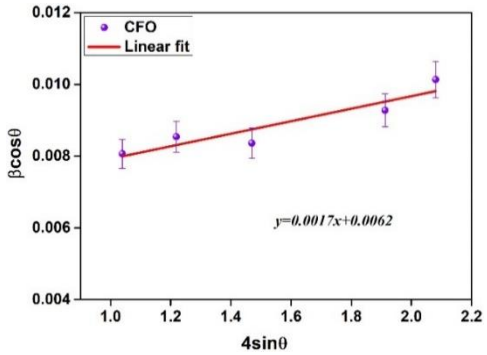


Fig. 2. W-H plot of pristine CFO

FTIR Spectroscopy: The FTIR spectrum of CFO sample has been recorded in the 400-4000 cm^{-1} wavenumber range as shown in Fig. 3. It is found to be consistent with that of $CoFe_2O_4$ reported in the literatures [3]. The presence of strong absorption peaks at around 599 cm^{-1} and 421 cm^{-1} are due to Fe-O and Co-O bonds respectively. Both these vibrational bonds are characteristic of $CoFe_2O_4$, and thus their presence confirms the formation of spinel structure of cobalt ferrite. Few additional peaks have also been observed pertaining to various other bonds such as O-H, C=O, C-H arising due to moisture, and carbonaceous species present unavoidably in the nanoparticles.

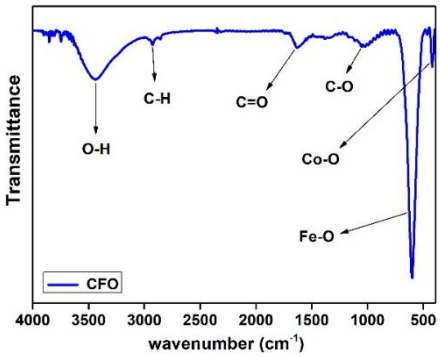


Fig. 3. FTIR spectrum of pristine CFO

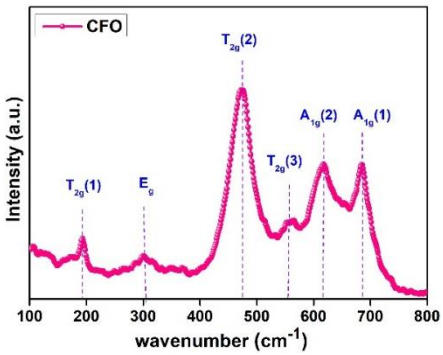


Fig. 4. Raman spectrum of pristine CFO

Raman Analysis: Raman spectrum depicted in Fig. 4, is obtained using 785 nm excitation wavelength in the 100 to 800 cm^{-1} wavenumber regions. Mainly six broad bands are observed at 194, 302, 471, 558, 616, and 684 cm^{-1}, that are consistent with the Raman active modes ($A_{1g}+E_g+3T_{2g}$) predicted by the group theory. The bands at 192 and 302 cm^{-1} represent the T_{2g} and E_g modes respectively. The bands around 471 and 558 cm^{-1} represent T_{2g} modes which correspond to the lattice vibrations of Fe^{3+} and O^{2-} ions at the octahedral site of CFO. The intense vibrational modes observed at 616 and 684 cm^{-1} are attributed to A_{1g} mode, which is associated to the stretching vibrations of Fe^{3+} and O^{2-} ions at the tetrahedral site. The presence of these modes which are trivial to the spinel structure of cobalt ferrite confirms the phase formation of CFO. These findings are consistent with previously reported results in the literature [4].

Electrochemical Studies

Cyclic Voltammetry (CV): The synthesized CFO nanoparticles have been tested for its electrochemical energy storage properties. The CV test has been performed in the voltage range of 0-0.5V vs Ag/AgCl electrode in 6M KOH electrolyte solution. Prior to the testing in the three-electrode setup, the CFO nanoparticles were deposited on Nickel foam, which serves as an excellent substrate, as its meshy structure allows more quantity of material to

be deposited, and significantly enhances the number of available interaction sites of the electrolyte ions with the electrode material. Different CV curves have been obtained at the scan rates of 1, 5, and 10 mV/s respectively, as shown in Fig. 5. Specific capacitance (C_s) through CV curves can be estimated using the formula: $C_s=(\int I \cdot dV)/(m \cdot \nu \cdot \Delta V)$. Here, the numerator part yields the area of the closed curve, m is the mass of our active material, ν is the scanning rate, ΔV is the potential range [5].

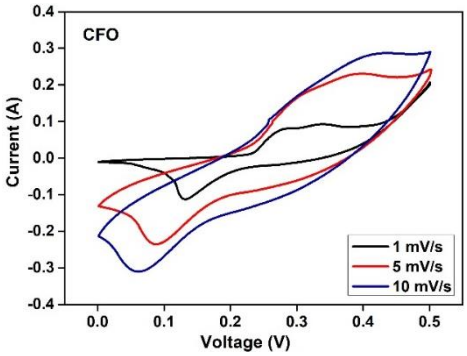


Fig. 5. CV plots of CFO at various scan rates

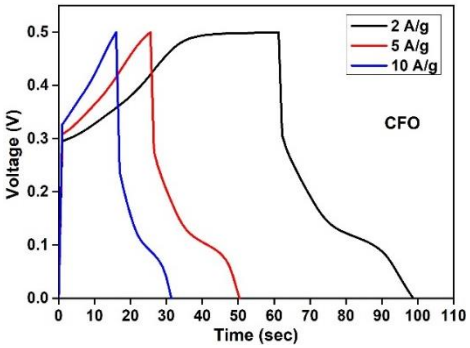


Fig. 6. GCD plots of CFO at various current densities

It is observed that the highest value of specific capacitance attained is 1247 F/g at the lowest scan rate of 1mV/s, followed by 739 and 494 F/g at 5 and 10 mV/s scan rates respectively. It is clearly observable that the value of specific capacitance decreases with the increasing scan rates, which is because of the decrement in the number of accessible sites at faster scan rates [6].

Galvanostatic-Charging Discharging (GCD): GCD study as shown in Fig. 6, has been performed in the 0 - 0.5 V potential range at varying current densities. The non-linear nature of GCD curves ascertains the pseudocapacitive behaviour of the CFO nanoparticles. The specific capacitance (C_s) calculation from GCD data is usually done via the following computational formula: $C_s=(I \cdot \Delta t)/(m \cdot \Delta V)$, where I is the corresponding current density, Δt is the discharging time, ΔV is the potential range, and m is the mass of our active material. At 2 A/g, the CFO nanoparticles deliver impressive specific capacitance of 790 F/g. Noticeably, the C_s decreases with the increasing current density, which is primarily due to the loss of active diffusion sites at higher current density.

CONCLUSIONS

Cobalt ferrite (CFO) nanoparticles have been successfully synthesized via co-precipitation route. The XRD confirm the cubic spinel crystal symmetry with $Fd\bar{3}m$ space group. The values of crystallite size are found to be 19 and 24 nm as evaluated through Debye-Scherrer and Williamson-Hall methods respectively. FTIR spectrum also confirms the spinel structure by giving evidence of Fe-O and Co-O characteristic absorption bands of the CFO. Study of vibrational modes carried out through Raman spectroscopy reflects that the corresponding atomic motions are in agreement with that reported in literature. Energy storage properties of CFO analysed via CV and GCD techniques indicate its pseudocapacitive nature and the excellent values of specific capacitance (C_s) assure that the material is a befitting candidate for fabrication of hybrid supercapacitors.

ACKNOWLEDGEMENTS

Daud Ahmad Ansari is grateful to University Grants Commission (UGC), India for their financial aid by means of CSIR-UGC JRF scheme (Ref. No. 191620223382) to carry out this research work.

REFERENCES

1. M. A. Ansari, et al.; *Nanotechnology Reviews*, Vol. 12, 1, pp. 20230575 (2023).
2. H. D. T. Duong, D. T. Nguyen, K.-S. Kim; *Nanomaterials*, Vol. 11, pp. 3056 (2021).
3. Waldron R. D.; *Phys. Rev.*, Vol. 99, pp. 1727 (1955).
4. Supriya S., Kumar S. and Kar M. *J.*; *Appl. Phys.*, Vol. 120, pp. 215106 (2016).
5. B. Dong, et al.; *ACS App. Mat. & Interfaces*, Vol. 9, pp. 21 (2017).
6. L. Wang, H. Ji, S. Wang, L. Kong, X. Jiang, G. Yang; *Nanoscale*, Vol. 5, pp. 3793-3799 (2013).

Functionalisation of Selenium monolayer with Platinum dichalcogenide for the green Hydrogen production

Anjana E Sudheer[1], Golla Tejaswini[1], D Murali[1*], and Matthias Posselt[2]

[1*]*Department of Sciences, Indian Institute of Information Technology Design and Manufacturing Kurnool Andhra Pradesh, 518007 India*
[2]*Helmholtz-Zentrum Dresden-Rossendorf, Institute of Ion Beam Physics and Materials Research, Dresden, Germany 01328*

[*]dmurali@iiitk.ac.in

Abstract: Here, we introduce the design of highly efficient photocatalyst PtS_2-Se for the water-splitting hydrogen production by first principle methods. The thermal stability of the designed heterostructure at ambient conditions is studied using ab initio molecular dynamics simulations (AIMD). The electronic band structure of the designed structure shows the visible light active bandgap with high band dispersion. The charge density difference and the band alignment indicate the electron transfer from the conduction band minima (CBM) of Se to the PtS_2 monolayer (ML). At the same time holes transfer from valance band maxima (VBM) of PtS_2 to Se monolayer. After the heterostructure construction, the band alignment found type II, which is suitable for ideal photocatalyst. The charge distribution, electronic properties and the obtained band alignment show that the designed heterostructure have promising water splitting capacity.

Key words: photocatalysis, DFT, Hydrogen, TMDs, Heterostructures, Chalcogen layers

INTRODUCTION

Hydrogen is highly accepted as a future fuel as it contain high energy density 120 (MJ/Kg), zero green house gas emission, faster refuelling time compared to other fuels. Among the different hydrogen fuel production techniques, photocatalytic water splitting considered to be highly accepted, as it does not require any additional energy other than solar light and a photocatalyst. The important criteria for the selection of photocatalyst was visible light active bandgap, high carrier mobility as well as suitable band alignment for the water redox reactions.

Recently, chalcogen-based 2D materials have been explored for photocatalytic hydrogen production due to the unique structural properties as well as exceptional carrier mobility. In 2020, Shengcai Li et al performed the first principle-based study on the carbon monochalcogenide materials. Lingling Lv explored group 11 chalcogenides MX (M = Au, Ag, X=S, Se, Te). Their research concluded that these materials also shows good charge mobility as well as suitable bandgap, and can be used as photocatalytic OER agents. But till now, the mono elemental chalcogenide 2D materials are not explored in the field of photocatalytic water splitting. The Se is one of the important candidates in group VI chalcogenides. The bandgap of the Se monolayers are already reported to be suitable for visible light absorption. But, the band alignment of the material need to be improved, for the effective water redox reaction to take place. Functionalisation of selenium with other TMDs, having suitable band alignment may improve the water redox ability of this mono elemental selenium layer. In addition to that, the built in electric field created at the interface also help to decrease the charge recombination as well as increase the e-h separation time in the material. Among the different two dimensional materials, we noticed PtS_2 monolayer having the same atomic arrangement as that of selenium monolayer is suitable for the functionalisation of Se monolayer due to negligible lattice mismatch, high stability, abundant charge carriers for the water redox reaction. So, here we design and explore the electronic, optical and water splitting capacity of PtS_2-Se monolayer.

COMPUTATIONAL METHODS

All DFT calculations are performed using the Vienna Ab initio Simulation package (VASP). The self-iteration scheme is carried out with the Blocked Davidson algorithm. The exchange-correlation functional used for the calculation was Perdew-Burke-Ernzerhof (PBE) within Generalised Gradient Approximation (GGA). For the relaxation of monolayers and heterostructure, kinetic energy cut off for plane-wave basis set selected as 650 eV. The energy and force convergence criteria for the ionic relaxation are chosen to be $1x10^{-6}$ eV/Å and 0.001eV/cell respectively. The k points 16 x 16 x 1 are selected using the Monkhorst- Pack scheme for accurate calculation. A vacuum region of 18 Å was fixed along the c direction to avoid the interaction between adjacent layers due to the periodic images. The interface was constructed using unitcell of both monolayer PtS_2 and Se. The vdW interaction between the monolayers was represented using DFT D2 method of Grimme.

RESULTS AND DISCUSSION

Structural design and stability

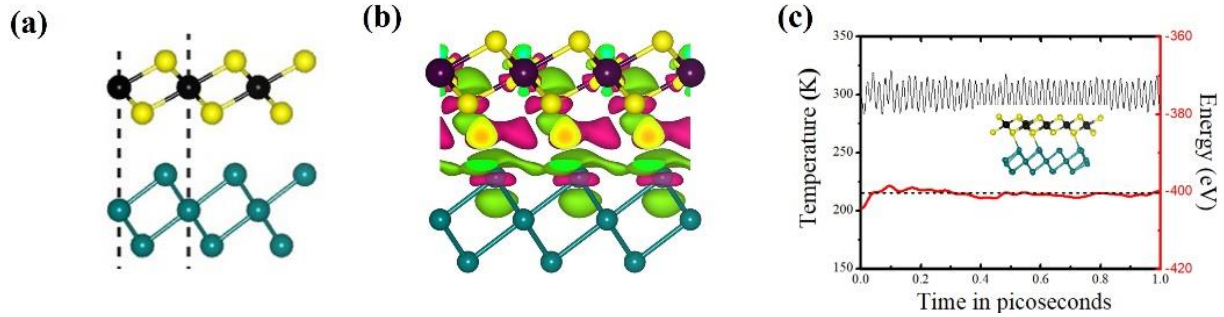
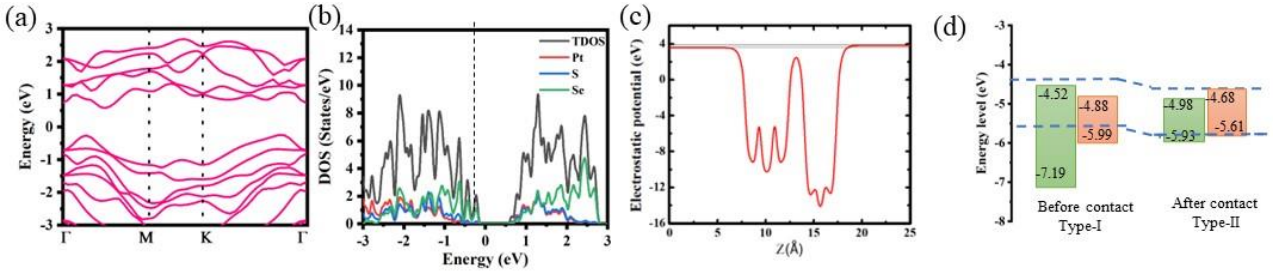


Figure 1. The side view (a), differential charge density plot (b), energy (red) and temperature (black) variation after the AIMD simulation of newly designed PtS_2-Se heterostructure.

Firstly, we have geometrically relaxed the unit cell structures of hexagonal PtS_2 and Se MLs. From the structural analysis, the lattice parameters and the bond length (Pt-S) of the optimised PtS_2 ML are observed to be 3.56 Å and 2.39 Å respectively [1]. In case of selenium ML, the lattice parameter and Se-Se bond length are observed to be 3.74 Å and 2.67 Å respectively, which is in accordance with the previously reported values [2]. To construct the heterostructure, the lattice mismatch between the PtS_2 and Se ML was calculated and found to be less than 6 percent, indicate heterostructure can be constructed with the limited strain on monolayers. The newly constructed heterostructure is in AA stacking arrangement with lattice parameter 3.65 Å and interlayer distance of 3.6 Å. The heterostructure posess a formation energy of -1.16 eV, which indicates the structure is energetically stable. To understand the charge accumulation and depletion regions in the interlayer spacing of the heterostructure, a differential charge density plot was analysed (Fig.1(b)). From the figure, it was found that the negative charge carriers are accumulated near the Se monolayer (green colour in between layers (Fig.1(b)). Also, we observe a charge depletion region near the sulfur atoms of PtS_2 heterostructure (pink colour in between layers (Fig.1(b)). This suggests charge transfer from Se to PtS_2 due to the heterostructure construction. To analyse the stability of this Se-PtS_2 heterostructure, we performed ab initio molecular dynamics (AIMD) calculation at 300 K. The energy and temperature fluctuations of atoms are represented in Fig.1(c). The snapshot after the AIMD simulation is provided in the inset. The fewer fluctuations of energy, temperature, and unbroken bonds after the AIMD simulation indicate the thermal stability of the constructed heterostructure.

Electronic properties and water redox capacity

The electronic properties are explored with the help of band structure and density of states and electrostatic potential energy calculations Fig. 2 (a-c)). First, the band structures of these materials are calculated and plotted along the high symmetry points in the brillouin zone using GGA functional. The bandgap was calculated to be 1.11 eV with indirect in nature (Fig.2(a)). The VBM and CBM are observed in between high symmetry points Γ and M with large dispersion. We have calculated electron effective mass at CBM of band structure. We found that the electrons have effective mass in the range 0.3 m_e to 0.4 m_e, which will be helpful for the fast charge transfer in the material.



F IGURE 2. The band structure (a), density of states (d), electrostatic potential energy diagram and band alignment of newly designed PtS_2-Se heterostructure. In the band alignment diagram, green and orange represent band alignments of PtS_2 and Se MLs.

The density of states of the Janus structures is calculated and found that the VBM and CBM are dominated by the Se and PtS_2 monolayers respectively. The density of states indirectly shows the type II band alignment of the structure (Fig 2(b). Later, planar averaged electrostatic potential was calculated and found that there is a potential drop due to the change in electronegativity of the top and bottom layer of the heterostructure (Fig 2(c)). This is calculated from the difference in vacuum level of top and bottom layer and it is noted to be 0.24 eV in the heterostructure. To analyse the charge transfer during photocatalytic reaction, band alignment diagram of PtS_2 and Se monolayers before contact and after contact was analysed (Fig. 2(d)). The water redox potentials are shifted to more electronegative potential due to the dipole moment formed in the heterostructure construction. The dotted lines represent water reduction and oxidation potential at pH equal to zero. ie water reduction potential shifted from -4.44 to -4.68 eV and water oxidation potential shifted from -5.67 eV to -5.91 eV. Before the heterostructure construction, conduction band and valence band edge positions are calculated with the help of electrostatic potential and band structure calculated for the Se and PtS_2 MLs. It was found that the MLs show type III band alignment before contact. The modification in the band alignment after the heterostructure construction was explored with the help of the vacuum level obtained from the electrostatic potential diagram and the atom-resolved density of analysis. We found that the band alignment changed from type III to type II after the heterostructure construction. When light falls on the MLs, electrons and holes het separated to their respective CBM and VBM respectively. Later, the electrons in the CBM of Se will transfer to the CBM of PtS_2 ML. Similarly, the holes in the VBM of PtS_2 transfer to the VBM of Se ML. Here, charge carriers are separated for a large distance due to the type II band alignment. Finally, the water reduction reaction is carried out in the Se ML and the oxidation reaction carried out in the PtS_2 ML, as these levels are straddling the water redox potential.

CONCLUSION

In summary, we have successfully constructed a novel photocatalyst Se-PtS_2 heterostructure with most suitable stacking arrangement. The designed heterostructure shows thermal stability at ambient conditions. The band structure shows that the designed heterostructure have visible light absorption capacity and high electron mobility. The differential charge density plot shows that the charge transfer is from Se to PtS_2 ML. Later, electrostatic potential energy diagram shows dipole created inside the heterostructure, where potential drop due to the dipole calculated to be 0.24 eV. Finally, the band alignment of MLs compared before and after the heterostructure design. It is clear that the heterostructure shows type II band alignment, after the heterostructure design. The band alignment transition as well as shift in water redox potential helps to decrease the charge recombination by increasing the e-h separation in the heterostructure. In addition to that, this helps CBM and VBM to straddle water redox potentials. The visible light active bandgap, low effective mass, built-in dipole, and suitable band alignment help to improve the water-splitting hydrogen production capacity of designed structure.

REFERENCE

1. Hamza A.H. Mohammed and G. M. Dongho-Nguimdo and Daniel P. Joubert, Structural stability, electronic, optical and lattice thermal conductivity properties of bulk and monolayer PtS_2, Materials Today Communications, 21 (2019)
2. Liu C, Hu T, Wu Y, Gao H, Yang Y, Ren W., 2D Selenium allotropes from first principles and swarm intelligence. Journal of Physics: Condensed Matter.23, 235702 (2019)

Enhanced Photo catalytic Performance of MoS_2/bg-C_3N_4 Hetero-structures for Hydrogen Evolution Reaction: A First-Principles Study

Chet Ram[1, a)], Vaishali Thakur[1], Bharti Thakur[1], Pitamber Kumar[1], Abhishek Chandel[2], Anjna Devi[3], Yogyata Pathania[4], Surjeet Kumar[1], Pushpender Singh[5], Arun Kumar[1]

[1]*Govt. College Bilaspur, Himachal Pradesh, India, 174001*
[2]*Swami Vivekanand Govt. College Ghumarwin, Bilaspur, Himachal Pradesh, India, 174021*
[3]*Govt. College Baroh, Kangra, Himachal Pradesh, India, 176054*
[4]*D. A. V. Post Graduate College Sector-10, Chandigarh, India, 160011*
[5]*R. T. Govt. College Sarkaghat, Mandi, Himachal Pradesh, India, 175024*

[a)]Corresponding author: thakurchetram885@gmail.com

Abstract: This study investigates the potential of a MoS_2/bg-C_3N_4 heterostructure as a promising photocatalyst for hydrogen evolution. Density functional theory calculations were employed to explore the electronic and structural properties of the composite material. The results indicate a significant modification of the electronic structure, with a reduced bandgap and enhanced charge separation due to the formation of the heterojunction. The optimized electronic properties facilitate electron transfer, thereby improving the efficiency of hydrogen production. These findings suggest that the MoS_2/bg-C_3N_4 heterostructure is a promising candidate for developing efficient photocatalysts for sustainable energy conversion.

INTRODUCTION

Photocatalysis offers a promising avenue for sustainable energy conversion and environmental remediation by harnessing solar energy [1]. However, the efficiency of this technology is hindered by rapid charge recombination. To address this, researchers have focused on developing heterojunction photocatalysts, combining different semiconductors to enhance performance. Graphitic carbon nitride (g-C_3N_4) is a visible-light-responsive photocatalyst, but its low light absorption limits its efficiency [2]. Molybdenum disulfide (MoS_2) is a two-dimensional material with a unique structure and suitable bandgap, making it a potential candidate for improving g-C_3N_4 photocatalytic properties [3-6]. This study investigates the potential of a MoS_2/g-C_3N_4 composite as a photocatalyst for hydrogen production. Theoretical calculations suggest that combining these materials can enhance photocatalytic efficiency by modifying their electronic structures.

COMPUTATIONAL DETAILS

DFT calculations within SIESTA [7] utilized Troullier-Martins relativistic pseudopotentials, GGA-PBE exchange-correlation, and HSE06 hybrid functional for accurate band gap prediction. Triple Zeta Double Polarized (TZDP)s basis sets and a 7x7x1 Monkhorst-Pack k-point grid ensured proper Brillouin zone integration. Convergence was achieved with a 300 Ry mesh cutoff and 20 meV confinement energy. A 20 Å vacuum minimized interaction between periodic images. Subsequently, all structures were relaxed until forces on each atom fell below 0.001 eV/Å.

RESULT AND DISCUSSION

A heterostructure was constructed using a 2x2 Molybdenum disulfide monolayer (MoS_2ML) and a 1x1 buckled graphitic carbon nitride (bg-C_3N_4) unit cell, with an interlayer spacing of 3.59 Å. Relaxed structures of all the studied systems are shown in figure 1. Initially, we studied bg-C_3N_4 and MoS_2ML separately to determine their lattice constants and band gaps. Subsequently, we constructed a heterostructure by combining MoS_2ML and bg-C_3N_4 with an inter layer distance of 3.591 Å. The optimized results for MoS_2/bg-C_3N_4 are shown in Table 1.

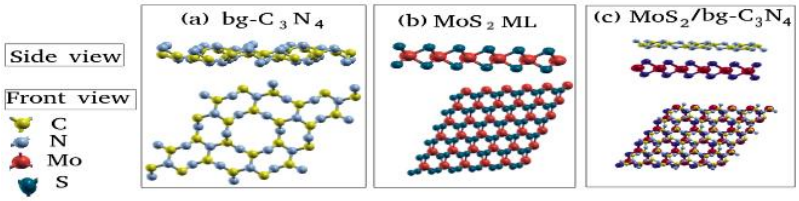
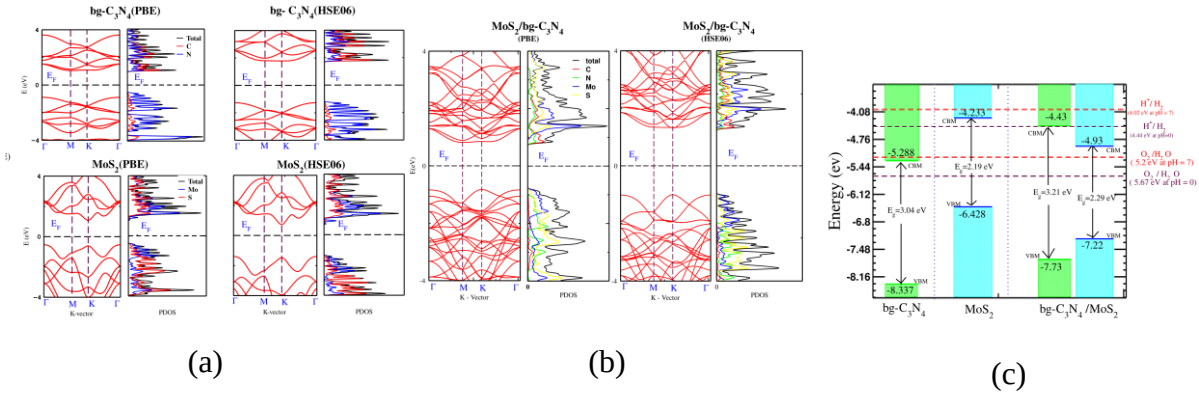


Fig 1: Electronic structure of bg-C_3N_4, MoS_2ML and MoS_2/bg-C_3N_4 hetero-structure.

TABLE 1. Lattice constant (a), inter-layer distance (d), binding energy (E_b) and energy band gap (E_g) of studied systems.

Material	a (Å)	d(Å)	E_b (PBE)eV	E_g (PBE)(eV)	E_g (HSE06)(eV)
bg-C_3N_4	6.390 (7.080 (LDA)) [3]	-	-5.51	1.903	3.04 (4.65(LDA)) [3]
MoS_2ML	3.205 (3.207) [5]	-	-4.90	1.681 (1.626) [5]	2.19
MoS_2/bgC3N4	6.35	3.591	-5.23	1.6417	2.31



(a) (b) (c)

Fig 2: Electronic band and projected DOS of (a) bg-C3N4, MoS_2ML, (b) MoS2/bg-C3N4 hetero-structure and (c) band alignment of bg-C_3N_4, MoS_2ML before and after hetero-structure formation.

The calculated lattice constants are 6.390 Å for bg-C_3N_4, 3.205 Å for MoS_2ML and 6.35 Å for the MoS_2/bg-C_3N_4 heterostructure. To assess structural stability, we have calculated the binding energy for each system using the appropriate formula [8].

$$E_b = \frac{E_{total} - (nE_a + mE_b \ldots)}{n+m+\ldots} \qquad (1)$$

The binding energies obtained are 4.90 eV for MoS_2, 5.51 eV for bg-C_3N_4, and 5.23 eV for MoS_2/bg-C_3N_4, as summarized in Table 1. We have calculated the electronic band gaps using both the Generalized Gradient Approximation (GGA-PBE) and the hybrid functional HSE06 for more accurate results. The band gaps obtained with GGA-PBE are 1.902 eV for bg-C_3N_4, 1.681 eV for MoS_2ML, and 1.641 eV for MoS_2/bg-C_3N_4. With the HSE06 functional, the band gaps increased to 3.04 eV for bg-C_3N_4, 2.19 eV for MoS_2ML, and 2.31 eV for MoS_2/bg-C_3N_4. These HSE06 results align with those reported by Xinyu Zhang *et. al.*[3], suggesting an improvement in photo catalytic performance. Furthermore, we calculated the spin-polarized electronic properties of the studied systems, as shown in Figure 1.

T/PDOS calculations indicate a substantial downshift of both the CBM and VBM of MoS_2 in the MoS_2/bg-C_3N_4 heterostructure. Conversely, the PDOS of bg-C_3N_4 exhibits marked upward shifts in both the VBM and CBM, with a more pronounced shift observed for the VBM. This electronic structure modification results in a considerable reduction of the individual layer bandgaps from 3.04 eV to 2.31 eV within the heterostructure.

Overall, the construction of the MoS_2/bg-C_3N_4 hetero junction efficiently modifies the electronic properties of the MoS_2 phase, facilitating electron transfer and thereby improving Hydrogen Evolution Reaction (HER) activity. Our study demonstrates that the MoS_2/bg-C_3N_4 hetero junction offers enhanced structural stability and electronic properties, making it a promising candidate for photo catalytic applications.

CONCLUSION AND APPLICATIONS

In summary, our findings demonstrate that the MoS_2/bg-C_3N_4 heterostructure exhibits promising potential for photocatalytic applications. The formation of the heterojunction significantly modifies the electronic properties of the constituent materials, leading to a reduced bandgap and enhanced charge separation. This study provides a theoretical foundation for the development of efficient photocatalysts based on the MoS_2/bg-C_3N_4 system, warranting further experimental investigations to validate these findings and optimize the material for practical applications.

ACKNOWLEDGMENTS

Authors would like to thanks to the SIESTA team for providing the code.

REFERENCES

1. Ying Liu [a],Wei Miao [b] Zhong Chen [b] Ducheng Yao [b] Jinguo Wan[g a] Xiaoyan Chen [c] Shun Mao [b], J. Chemical Engineering 496, 153871 (2024)
2. Do Yeon Heo, Mahider Asmare Tekalgne and Soo Young Kim *, EES Catalysis 10.1039/d3ey00229b (2023)
3. Zhe Xue[a], Xinyu Zhang[a], Jiaqian Qin[b], Riping Liu[a], Applied Surface Science 510, 145489 (2020).
4. N. Kumar, H. Bae, H. Lee, T. Hussain, A. Anand, C. Veer Singh, and N. Tit, ACS Appl. Nano Mater. 7, 6873-6884 (2024)
5. A. Devi, A. Kumar, P. K. Ahluwalia, A. Singh, Materials Science and Engineering: B, 271, 115-237 (2021)
6. A. Devi, N. Dhiman, N. Kumar, W. Alfalasi, A Kumar, P. K. Ahluwalia, A. Singh and N. Tit, N*anomaterials 13, 1642 (*2023).
7. J. M. Soler, E. Artacho, J. D Gale, A. García, J. Junquera, P. Ordejón and D. Sánchez-Portal, *J. Phys.: Condens. Matter* 14, 2745 (2022).
8. A. Kumar A. Kumar and P. K. Ahluwalia, Physica E, 62, 136-142 (2014)

A First-Principles Study of Structural and Electronic Properties of 2-Iodoethylammonium Lead Iodide Perovskite

Ritika Negi[1, *], Anjali[1], Nitika Ranpatia[1], Diya Sharma[1], Monika Chandel[1], Yogyata Pathania[2], Anjna Devi[3], Surjeet Kumar[1], Arun Kumar[1]

[1]*Govt. College Bilaspur, Himachal Pradesh, India, 174001*
[2]*D. A. V. Post Graduate College Sector-10, Chandigarh, India, 160011*
[3]*Govt. College Baroh, Kangra, Himachal Pradesh, India, 176054*

[*]Corresponding author: negiritika72@gmail.com

Abstract: The rapid enhancement in efficiency of solid-state solar cells has brought particular focus to hybrid organic–inorganic halide perovskites because of their high photovoltaic efficiency. Our research entailed first-principles calculations to explore the crystal structures, as well as the electronic properties of 3D organic-inorganic hybrid lead iodide pervoskite $[I(CH_2)_2NH_3]_2PbI_4$. The material also exhibits magnetic properties attributed to carbon atoms, offering opportunities for novel device concepts. Our calculations reveal a direct energy band gap of 1.935 eV in the down-spin channel, suggesting potential for solar energy harvesting. The calculated crystal structure parameters are in reasonable agreement to the experimental values. The results approve that these compounds could be promising materials for spintronic and optoelectronic devices.

Keywords: Inorganic-organic hybrid**,** Perovskite, Density Functional Theory, Solar Cells, Spintronics.

INTRODUCTION

Inorganic semiconductors have been the subject of focused research owing to their potential applications in commercial optoelectronic devices [1]. Significant advancements have been achieved in the production of devices utilizing organic electronic materials also over the past few decades [2]. However, the potential for further development in organic materials is currently constrained to areas with relatively low performance.[3]. Exploiting resonant interactions in inorganic-organic hybrid structures is a new step to improve the performance of semiconductor devices. Within the hybrid structure, it is feasible to blend the excellent conductivity of the inorganic semiconductor part with the intense interaction between light and matter of the organic part. The lead iodide based organic-inorganic layered perovskites have potential applications in nonlinear optical devices [4, 5] and novel luminescent devices [6, 7]. The crystal structure of these layered perovskite semiconductors consists of an inorganic framework of lead iodide octahedra connected by organic cation (2-iodoethylammonium) as shown in figure 1 (a). There are two layers of interdigitated 2-iodoethylammonium cations positioned between two successive inorganic $[PbI_4]$ sheets, resulting in an alternating organic–inorganic layered setup. The lead atoms are aligned across layers, producing an eclipsed layout of adjacent layers. In the present work, we have explored crystal and electronic structures of 3D inorganic-organic perovskite namely $[I(CH_2)_2NH_3]_2PbI_4$ for the first time via theoretical DFT calculations using an ab-initio pseudopotential method. Section 2 includes the computational details. While Section 3 describe the result along with their discussions. Section 4 summarizes the conclusion of our study.

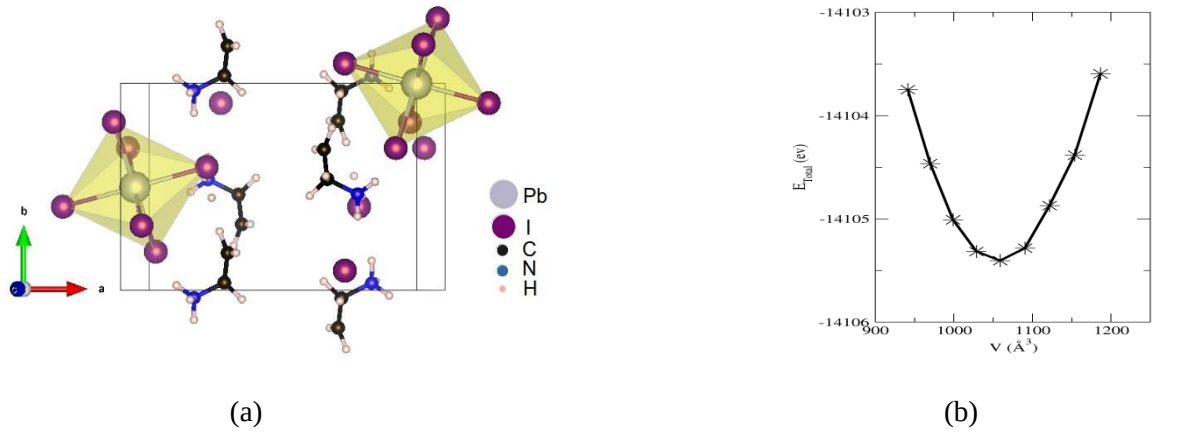


Figure 30: (a) Crystal structure of the 3D inorganic-organic $[I(CH_2)_2NH_3]_2PbI_4$ perovskite Where atoms are represented using different colors: Pb (Grey), I (Purple), C (black), N (blue) and H (pink). **(b)** The structural optimization curve represented the relationship between total energy (E_{Total}) and volume (V).

The structural optimization of $[I(CH_2)_2NH_3]_2PbI_4$ structure is done by using SIESTA, a density functional theory-based code [8], with self-consistent field method. The conjugate gradient method is used for optimization, with the local density approximation and the linear combination of atomic orbitals basis-set. DFT calculations utilized Troullier-Martins relativistic pseudopotentials, GGA-PBE exchange-correlation functional and Double Zeta Polarized basis sets for the electronic structure prediction. A 10x10x10 Monkhorst-Pack k-point grid is used to ensure proper Brillouin zone integration. Convergence is achieved with a 300 Ry mesh cutoff and 20 meV confinement energy. The density of states and charge density are projected on s, p, d orbitals of all atoms.

RESULTS AND DISCUSSION

The lattice parameters of the structure $[I(CH_2)_2NH_3]_2PbI_4$ are determined by the volume optimization approach. Where the total energy (E_{Total}) of the formula unit is optimized at a certain corresponding volume (V) called optimized V, and the minimum E_{Total} that gives an optimized V is called ground state energy. The variations of E_{Total} as with respect to V is shown in Fig. 1 (b). The calculated crystal data is evaluated against the experimental values [9] in Table 1.

The material is found to be magnetic in nature, having a spin magnetic moment of 4 which is primarily due to C atom, as clear from PDOS plots for both up and down spin. The computed spin-resolved band structures are plotted along selected high symmetry paths in the first Brillouin zone, within the energy range of –2.0 to + 3.0 eV. At point Y, the down spin exhibits a direct band gap of 1.935 eV, confirming its semiconducting behavior. In case of up spin case, valence band maxima, VBM and conduction band minima, CBM were pushed apart, resulting in increased direct band gap at Y point to 2.571 eV. Where in the down spin channel, CBM is mainly dominated by C atom with a minor contribution from the Pb atom, whereas VBM in mainly contributed by I atom. But for up spin VBM is mainly dominated by both C and I atoms.

Table 4: *Comparison of obtained crystal data for the studied system with experimental values.*

	Lattice Parameters						**Volume (Å³)**	**Binding Energy (E_b) eV**	**Band Gap (E_g) eV**	
	a(Å)	b(Å)	c(Å)	α (^{0})	β (^{0})	γ (^{0})			Down spin	Up spin
Our results	13.0	9.112	8.989	90.000	97.994	90.000	1058.93	-3.402	1.935	2.571
Exp. Data [9]	12.552	8.761	8.644	90.000	97.994	90.000	941.38	-	-	-

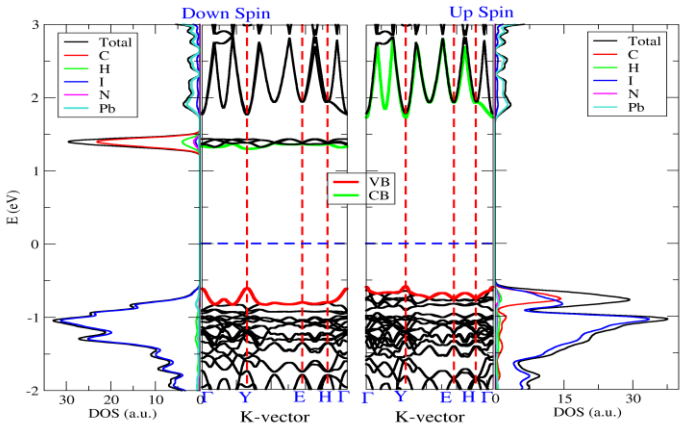


Figure 31: Calculated projected/total density of states and band structure for Down Spin (left) and Up spin (right) of $[I(CH_2)_2NH_3]_2PbI_4$

CONCLUSIONS

Our study demonstrates that $[I(CH_2)_2NH_3]_2PbI_4$ pervoskite **exhibits promising optoelectronic properties.** It demonstrates a direct bandgap of 1.935 eV in the down spin channel, characteristic of a semiconductor. This bandgap falls within the optimal range for efficient solar light absorption. Additionally, the material's magnetic nature, primarily attributed to carbon atoms, offers potential for novel device functionalities. However, a deeper understanding of carrier transport properties like mobility and recombination is essential to assess its suitability for solar cell applications. If these properties prove favorable, this material could be a strong candidate for efficient solar energy conversion.

REFERENCES

1. W. Pisula, *Electron. Mater*. ***4,*** 136-138 (2023).

2. C. Schaack, A. M. Evans, F Ng, M. L. Steigerwald, and C. Nuckolls, *Journal of the American Chemical Society*, ***144*****(1)**, 42–51(2021).

3. V. Agranovich, Y. N. Gartstein, M. Litinskaya. Chemical Reviews **111,** 5179–5214 (2011).

4. K. Ema, J. Ishi, H. Kunugita, T. Ban, T. Kondo. Optical and Quantum Electronics **33**, 1077–1087 (2001).

5. A. Brehier, R. Parashkov, J. S. Lauret and E. Deleporte, Applied Physics Letters **89,** 171110-1 (2006).

6. M. Era, S. Morimoto, T. Tsutsui, S. Saito. Applied Physics Letters **65,** 676–678 (1994).

7. K. Shibuya, M. Koshimizu, Y. Takeoka, K. Asai, Nuclear Instruments and Methods B 194, 207–212(2002).

8. J. M. Soler, E. Artacho, J.D. Gale, A. Garca, J. Junquera, P. Ordejon, D. SanchezPortal, J. Phys. Condens. Matter **14 (11),** 2745–2779 (2002).

9. A. Lemmerer, & D. G. Billing. (2010). *CrystEngComm* ***12*****(4),** 1290–1301.

Impact of Heat Treatment on Phase Formation and the Transport Properties of $AgSbTe_2$ Thermoelectric Materials

S Asha Bhandarkar[1,*], Poojitha G[2], Ashok Rao[2] and Anand Pal[1]

[1]*Department of Physics, Manipal Institute of Technology Bengaluru, Manipal Academy of Higher Education, Manipal 576104, India*

[2]*Centre for Clean Energy, Department of Physics, Manipal Institute of Technology, Manipal Academy of Higher Education, Manipal 576104, Karnataka, India*

[*]*Corresponding author: asha.mitblr2023@learner.manipal.edu*

Keywords: Thermoelectric materials, $AgSbTe_2$, Heat treatment, Phase formation, Secondary phases, Electrical properties

Abstract. In the current study, we have investigated the intrinsic thermodynamic metastable phase of $AgSbTe_2$ and its influence on the electrical and thermal properties. The bulk polycrystalline material of $AgSbTe_2$ was synthesized by the solid-state reaction technique via vacuum encapsulation techniques. The room temperature XRD data show the presence of $AgSbTe_2$, Sb_2Te_3, and Ag_2Te phases in the studied samples, confirming the metastability of $AgSbTe_2$. The temperature dependent electrical resistivity study verified the cationic disorder arrangement in the material. Hall measurement at room temperature showed p-type conductivity. Our study demonstrates importance of thermal treatment in achieving phase stability, a critical property for its enhanced thermoelectric performance.

INTRODUCTION

Silver antimony telluride ($AgSbTe_2$) is a well-known I-V-VI_2 group ternary chalcogenide, forming a cubic rocksalt structure with $Fm\bar{3}m$ space group [1]. $AgSbTe_2$ has recently garnered considerable interest in the renewable energy community due to its excellent thermoelectric performance in the temperature range of 300 to 600 K. The potential of $AgSbTe_2$ to exhibit high thermoelectric performance is attributed to its glass-like intrinsically low thermal conductivity between 0.5 – 0.7 W/mK and a large Seebeck coefficient of approximately 250 μV/K near room temperature [2]. It exhibits p-type conductivity and possesses a narrow energy bandgap with multiple valence bands [1]. The origin of these unique properties is mainly associated with its local crystal structure characterized by the lack of long-range ordering in the arrangement of Ag and Sb atoms in the cationic site, leading to structural disorder in $AgSbTe_2$ [2].

Though $AgSbTe_2$ has shown the potential to be a good thermoelectric material. However, it exhibits an intrinsic thermodynamic metastable phase and generally leads to the formation of Sb_2Te_3 and Ag_2Te secondary phases during synthesis and heat treatment. This is mainly because the formation of $AgSbTe_2$ stable cubic structure occurs in the temperature range of 633 to 847 K and in a slightly off-stoichiometric part of the phase diagram of Sb_2Te_3-Ag_2Te pseudo-binary system. Additionally, cooling below 633 K results in its decomposition into Sb_2Te_3 and Ag_2Te, leading to the secondary phases formation [1], [3]. This affects stability and strongly influences the thermoelectric properties of $AgSbTe_2$. Therefore, it is crucial to investigate the effect of Sb_2Te_3 and Ag_2Te phases on the electrical and thermal properties of $AgSbTe_2$.

In the present work, we have studied the effect of Sb_2Te_3 and Ag_2Te secondary phases on the electrical properties of the stoichiometric composition of $AgSbTe_2$ thermoelectric material. It is found that the presence of Sb_2Te_3-rich phases, with very few $AgSbTe_2$ and Ag_2Te phases, contributes to higher electrical conductivity near room temperature but significantly lowers the Seebeck coefficient (not shown here). This investigation of $AgSbTe_2$ thermoelectric material, in the dominance of secondary phases, highlights the importance of phase stability on its electrical properties.

EXPERIMENTAL DETAILS

The bulk polycrystalline $AgSbTe_2$ compound was synthesised using the solid-state reaction technique. High purity raw materials of Ag (99.9%, LOBA), Sb (99.999%, Goodfellow), and Te (99.999%, Thermofisheries) were mixed in stoichiometric ratio and ground into fine powder using agate-mortar and pestle. The finely ground powder was pelletized under 5 Tons hydraulic press compression and then sealed under a high vacuum of 10^{-5} Torr in a quartz tube. The sealed tube with pellets was slowly heated over 12 hours at 400 °C then raised to 850 °C in 4 hours,

followed by 10 hours annealing later allowing natural cooling to room temperature. After the heat treatment, material was found in ingot form in the quartz tube. Again, the obtained ingots were ground, pelletized, sealed and annealed for 6 hours at 300 °C.

Phase formation and structural analysis of the synthesized material was carried out in the 2θ range of 20° to 80° using Rigaku Miniflex 600 X-ray diffractometer with Cu – K_α source. Room temperature Hall measurement was done in the presence of constant magnetic field of 0.545 T and a continuous supply of 20 mA current using HMS 5500 (Ecopia) instrument employing Van der Pauw method. Temperature dependent electrical resistivity study was conducted in 300 to 600 K temperature range using Linseis LSR3- high temperature thermopower and resistivity system.

RESULTS AND DISCUSSION

Structural analysis

Figures 1(a) and 1(b) depict the room temperature XRD patterns of as-synthesized and the annealed samples, respectively. The observed XRD pattern for the synthesized material shows the presence of $AgSbTe_2$, Sb_2Te_3, and Ag_2Te multiphases. Both patterns exhibit a predominant peak corresponding to the (015) plane of Sb_2Te_3. However, in the annealed sample, there is a notable decrease in the diffraction peak intensity of Sb_2Te_3 peaks and increase in the intensity of $AgSbTe_2$ peaks. Additionally, peak broadening is reduced in the annealed sample compared to the as-synthesized one, making a new peak corresponding to the $AgSbTe_2$ phase clearly visible at 29.28° in Fig. 1(b). The narrowing of the XRD peaks indicates an increase in long-range ordering within the crystal and the reduction of the defects. Despite annealing, the Ag_2Te peak observed at 41.5° remains, although its intensity is reduced. It suggests that the formation of Ag_2Te cannot be eliminated through simple annealing due to the stronger ionic bonding between Ag and Te compared to the covalent bonding of Sb and Te [4]. These structural analysis results highlight the importance of thermal treatment in achieving phase stability of $AgSbTe_2$.

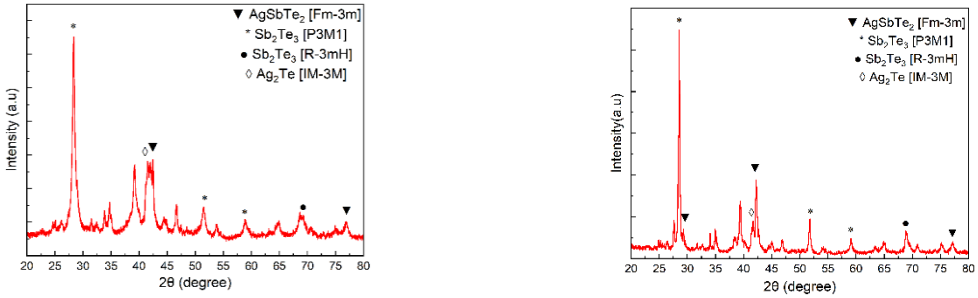


FIGURE 1. XRD pattern of stoichiometric $AgSbTe_2$ (a) as-synthesised (b) after annealing at 300 °C for 6 hours.

Electrical Resistivity and Hall Measurements

Figure 2 displays the electrical resistivity as a function of temperature for the investigated sample. The resistivity increases almost linearly with temperature up to approximately 540 K, after which it decreases with further temperature increase. A maximum resistivity with a small broad hump is observed around 540 K, which can be ascribed to the Ag_2Te phase transition [4]. This small broad hump suggests the presence of very few Ag_2Te phase, corroborating the XRD results.

The increase in resistivity up to 540 K is likely due to a higher scattering due to the multiphase nature of the sample and a broader density of states (DoS) near the Fermi level. The presence of Sb_2Te_3 and Ag_2Te phases in $AgSbTe_2$ is known to cause disorder-induced localization of carriers near the Fermi level [2]. The presence of p-type Sb_2Te_3 in the sample may enhance the effective mass of charge carriers, resulting in a broader DoS near the Fermi level. The subsequent decrease in resistivity above 540 K can be attributed to the coexistence of charge carriers, in line with the narrow band gap and multiple valence bands of $AgSbTe_2$. The Sb_2Te_3-rich phases may influence the electronic properties by causing band convergence, leading to carriers' thermal excitation at higher temperatures [4]. Despite the higher disorder, the observed resistivity is lower than the values reported in the literature [4], [5].

Room temperature Hall measurements showed p-type conductivity with a carrier concentration of $3.80 \times 10^{20}\ cm^{-3}$, electrical conductivity of $5.85 \times 10^{4}\ S/m$, and carrier mobility of $1.39 \times 10^{-3}\ m^2/Vs$. The p-type conductivity observed in the Hall measurements confirms the predominance of the Sb_2Te_3 phase in the sample. The measured carrier concentration and electrical conductivity are slightly higher than those reported in the literature for stoichiometric $AgSbTe_2$ [2], [6], [7]. Sb-Te typically exhibits an electrical conductivity of approximately $10^5\ S/m$ at room temperature with p-type conductivity. The slight deviation in electrical conductivity in the investigated material can be due to the presence of n-type Ag_2Te [8].

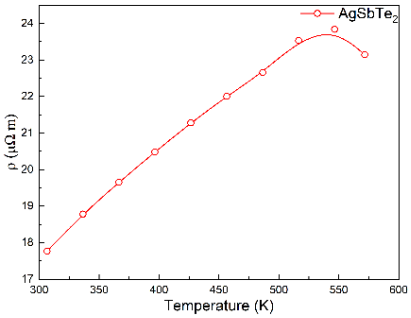


FIGURE 2. Plot of temperature dependent electrical resistivity of studied sample

CONCLUSION

In this work, we investigated the impact of thermal treatment on the phase formation of $AgSbTe_2$ and the influence of secondary phases on its electrical and thermal properties. The annealing process notably increased the intensity of $AgSbTe_2$ peaks while reducing the Sb_2Te_3 peak intensity, indicating enhanced phase stability and long-range ordering. The electrical resistivity measurements demonstrated a nearly linear increase with temperature up to approximately 540 K, followed by a decrease at higher temperatures. The Hall measurements at room temperature confirmed the *p*-type conductivity of the samples studied. Overall, the study underscores the importance of thermal treatment in achieving phase stability and enhancing the properties of $AgSbTe_2$-based materials.

ACKNOWLEDGMENT

SAB would like to thank MAHE Manipal for providing the Dr. TMA Pai Fellowship to conduct this research.

REFERENCES

1. Yi Wu, Pengfei Qiu, Yuan Yu, Yifei Xiong, Tingting Deng, Oana Cojocaru-Miredin, Matthias Wuttig, Xun Shi, Lidong Chen, *Journal of Matreomics*, 1095-1103 (2022).
2. Subhajit Roychowdhury, Tanmoy Ghosh, Raagya Arora, Manisha Samanta, Lin Xie, Niraj Kumar Singh, Ajay Soni, Jiaqing He, Umesh V. Waghmare, Kanishka Biswas, *Science* **371**, 722-727 (2021).
3. Vaishali Taneja, Subarna Das, Kapildeb Dolui, Tanmoy Ghosh, Animesh Bhui, Usha Bhat, Dinesh Kumar Kedia, Koushik Pal, Ranjan Datta, and Kanishka Biswas, *Adv. Mater.*, 2307058 (2024).
4. Jin Hee Kim, Jae Hyun Yun, Seunghun Cha, Seokyeong Byeon, Junyoung Park, Hyungyu Jin, Sujin Kim, Sung-Jin Kim, Jong Ho Park, Jeongin Jang, SuDong Park, and Jong-SooRhyee, *Adv. Funct. Mater.*, 2404886 (2024).
5. Heng Wang, Jing-Feng Li, Minmin Zou, and Tao Sui, *APPLIED PHYSICS LETTERS* **93**, 202106 (2008).
6. Subhajit Roychowdhury, Rajarshi Panigrahi, Suresh Perumal, and Kanishka Biswas, *ACS Energy Lett.*, 349-356 (2017).
7. P.M. Wyzga and K.T. Wojciechowski, *Journal of ELECTRONIC MATERIALS*, 1548-1554 (2016).
8. Paweł Wyzga, Igor Veremchuk, Ulrich Burkhardt, Paul Simon, Yuri Grin, and Krzysztof T. Wojciechowski, *Appl. Sci., 8, 52 (2018).*

Study on Electrochemical Performance of Glass-Ceramics Based Composite Solid Electrolyte for Lithium Battery

Anurup Das[1, 2,*] and Madhumita Goswami[2]

[1]*Glass & Advanced Materials Division, Bhabha Atomic Research Centre, Mumbai 400085, India.*
[2]*Homi Bhabha National Institute, Anushaktinagar, Mumbai 400094, India*

*Corresponding author: anurup@barc.gov.in

Abstract. Commercial liquid electrolyte makes conventional lithium batteries unsafe in terms of flammability. Solid state electrolyte may ensure the improvement over the safety issues. In this study, we report the synthesis of Composite Solid Electrolytes (CSEs) using different weight percent of NASICON-type $Li_{1.25}Al_{0.5}Ge_{1.5}P_{2.75}Mo_{0.25}O_{12}$ (LAGPM) glass ceramics (GC) solid electrolyte along with two suitable polymers. The value of d.c. ionic conductivity of LAGPM is 4.93×10^{-4} Scm^{-1}. TGA analysis shows that the prepared CSEs are thermally stable upto 450ºC. The thickness of the CSEs is ~60µm. Among all the prepared CSEs, the sample containing 60wt% of LAGPM (LAGPM60) possesses the highest quantity of amorphous region. Fabricated solid state cell using LAGPM60 shows a stable specific discharge capacity of 140$mAhg^{-1}$ at the current rate of 1C upto 100cycles.

Key words: Glass, Glass-ceramics, Solid state electrolyte, Lithium ion battery, Polymer battery

INTRODUCTION

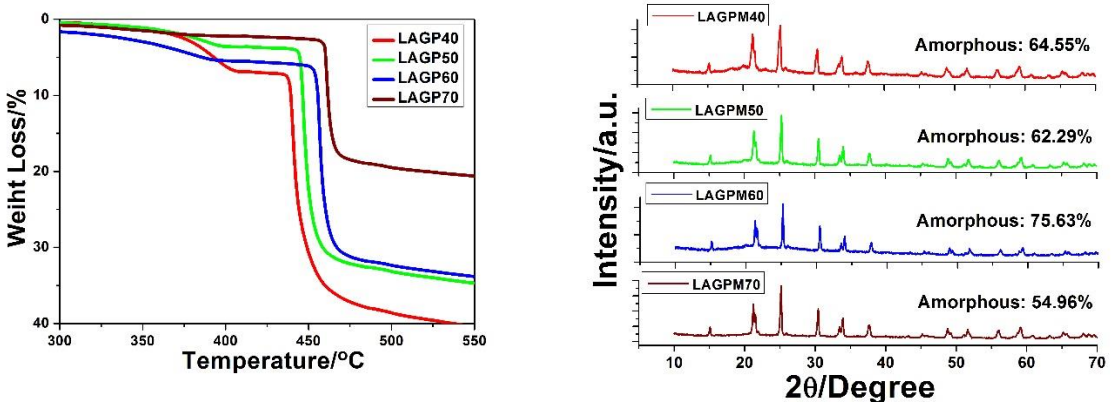
Lithium batteries are extensively used inside various electronic devices for storing energy. High volumetric and gravimetric energy densities of these batteries make superior over other types of energy storage components. Whereas, the commercial lithium batteries are lack of inherent safety because of the liquid electrolytes which are thermally unstable, flammable and reactive in ambient atmosphere [1]. Therefore, to resolve these challenges, it is necessary to substitute the liquid electrolyte with a Solid-State Electrolyte (SSE). Among others, glass-ceramics based **C**omposite **S**olid **E**lectrolytes (CSEs) are becoming quite acceptable because these type of solid electrolytes are thin (~50 to 100µm), flexible and provide minimal interfacial resistance at electrolyte/electrode interface [2, 3]. In this study, we have synthesized the CSE using aluminium and molybdenum doped NASICON-type $LiGe_2(PO_4)_3$ ($Li_{1.25}Al_{0.5}Ge_{1.5}P_{2.75}Mo_{0.25}O_{12}$) glass ceramics (GC) solid electrolyte. P(VDF-HFP) (Poly(vinylidene fluoride-co-hexafluoropropylene)) and PEO (Polyethylene Oxide) are selected as host polymers owing to their favorable properties, including high thermal stability, elevated dielectric constant, and robust electrochemical stability. Thermogravimetric (TG) analysis was carried out to estimate the temperature of the thermal stability. The amorphous content was evaluated through XRD analysis, while the electrochemical performance of the solid-state cell was investigated using galvanostatic charge/discharge testing.

EXPERIEMNTAL

The synthesis and characterization of the $Li_{1.25}Al_{0.5}Ge_{1.5}P_{2.75}Mo_{0.25}O_{12}$ (LAGPM) glass-ceramic material were previously documented in an earlier study [4]. In this work, composite solid electrolytes (CSEs) based on P(VDF-HFP) and PEO were fabricated using the phase inversion technique. To obtain four distinct electrolyte compositions—LAGPM40, LAGPM50, LAGPM60, and LAGPM70—LAGPM was incorporated into the polymer matrix at 40%, 50%, 60%, and 70% by weight, respectively. The resulting membranes were flexible, self-standing, and approximately 60µm thick. All handling and assembly processes were conducted in an argon-filled glove box to maintain an inert environment. The thermal stability of the prepared CSEs was assessed via thermogravimetric analysis (TGA) using a Labsys 1600 instrument (Setaram, France), performed in an argon atmosphere with an alumina crucible at a gas flow rate of 70 $Lmin^{-1}$. X-ray diffraction (XRD) was employed to examine the structural properties of the electrolytes, using a Bruker D8 X-ray diffractometer with Cu Kα radiation, scanned over a 2θ range of 10° to 70°. For electrochemical testing, CR2032-type coin cells were assembled with the CSEs (pre-soaked in a LiTFSI and TEGDME solution) positioned between a $LiFePO_4$ cathode and a lithium metal anode. Charge/discharge cycling and performance analysis were carried out at room temperature using a Neware battery testing system over a voltage window of 2.7–4.0V.

RESULTS AND DISCUSSIONS

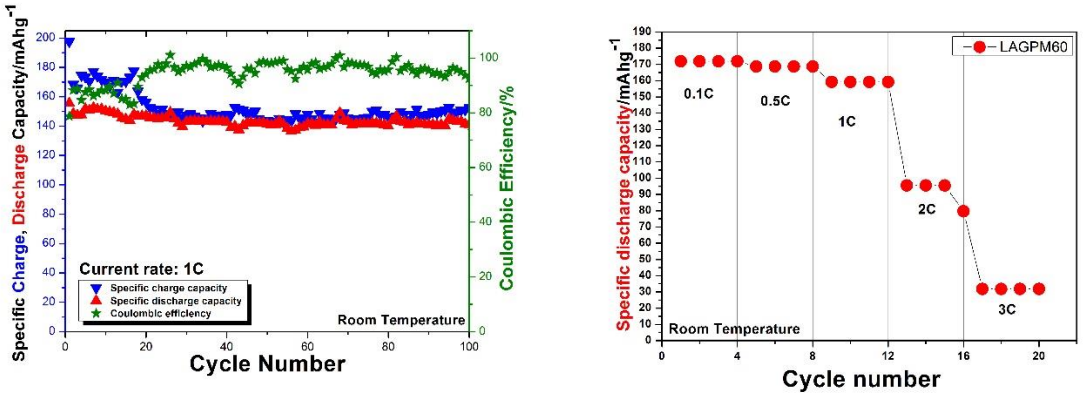
Thermogravimetric plot (Fig. 1(a)) shows the weight changes of the CSEs with increase in temperature. The first dip in the plot in the temperature range of 350 to 375ºC is due to the degradation of PEO polymer. The second sharp decrease in the weight around 450ºC is due to the decomposition of PVDF-HFP polymer. As LAGPM40 has the highest content of polymer (60wt%), the weight loss is more as compared to the other samples. Among the components of the polymeric composite solid electrolyte, LAGPM GC is nonflammable and enhance the thermal stability [5, 6]. Figure 1(b) shows the XRD plots of the CSEs. The instrumental background intensity has been subtracted from the plots. Each plot contains sharp peaks along with broad hump. The sharp peaks arise because of NASICON-type LAGPM crystal which has the space group of R-3c. The peak positions were matched with ICSD database. The area under the broad hump provides the quantification of the amorphous content inside the sample. The incorporated glass ceramics inside the CSEs can transport the lithium ions as it is a solid electrolyte (ionic conductivity: $4.93\times10^{-4}Scm^{-1}$). On the other hand, highest quantity of amorphous content inside the CSE can also improve the migration of Li^+ ions because of weak interaction between the polymer chains [7]. Therefore, LAGPM60 sample can be chosen among other CSEs for further studies as this sample contains 75.63% of amorphous content.



(a) (b)

FIGURE 1. (a) Thermo-gravimetric (b) XRD plots of prepared CSEs samples

Galvanostatic charge/discharge experiment was performed on Li metal/LAGPM60 soaked with LiTFSI+TEGDME/$LiFePO_4$ at the current rate of 1C (=$170mAg^{-1}$). Figure 2(a) shows the specific charge/discharge capacities along with the coulombic efficiency with respect to cycle number. The experiment was carried out at room temperature. Initially, the values of coulombic efficiency were low upto 20th cycle of charge/discharge. After that the values reach almost near to 100% due to the formation of stable Solid Electrolyte Interface (SEI) at the electrolyte/electrode interfaces. The cell exhibits almost stable discharge capacity of ~$140mAhg^{-1}$. Figure 2(b) shows the cell performance at different rates of current. The discharge capacity at 3C is $30mAhg^{-1}$ at room temperature. On the other hand, at 0.1C the cell was providing 100% of its theoretical capacity (~$170mAhg^{-1}$).



(a) (b)

FIGURE 2. (a) Specific charge/discharge capacities up to 100cycles at 1C and Coulombic Efficiency (b) Cell performance at different rates of charge/discharge current

CONCLUSIONS

CSEs were successfully synthesised using phase inversion method. These CSEs can safely be used inside a cell upto 450ºC. XRD data analysis reveals that the presence of LAGPM glass ceramics modifies the overall amorphous content inside the CSEs. LAGPM60sample shows the highest quantity of amorphous region (~75.63%). Amorphous region enhances the lithium migration as compared to crystalline phase inside a polymer electrolyte. The fabricated solid state cell provides 82% of the theoretical specific capacity of $LiFePO_4$ ($170mAhg^{-1}$) at high rate of current (1C) at room temperature. The cell shows almost same values of the specific discharge capacity ($\sim 30mAhg^{-1}$) with respect to each cycle at 3C. This data depicts the fact that this CSE (LAGPM60) can be used inside a solid state cell with good cell performance without compromising the safety issues.

ACKNOWLEDGMENTS

Authors wish to thank Dr. R. Tewari, Group Director, Materials Group, BARC, for encouragement, support and guidance. Authors wish to thank to Mr Pritam Sarkar, TPD, BARC for providing XRD facility. Technical help from Shri Radhakrishnan Nair is gratefully acknowledged.

REFERENCES

1. C. Park, S. Lee, M. Kim, S. Min, G. Kim, S. Park and D. Shin, Electrochim. Acta, Vol. 390, pp. 138808-138816 (2021).
2. A. Murali, M. Sakar, S. Priya, V. Vijayavarman, S. Pandey, R. Sai, Y. Katayama, M.A. Kader and K. Ramanujam, Mater. Lett., Vol. 313, pp. 131764-131767 (2022).
3. A. Das, M. Goswami, K. Illath, T.G. Ajithkumar, A. Arya and M. Krishnan, J. Non-Cryst. Solids, Vol. 558, pp. 120654-120663 (2021).
4. A. Das, M. Goswami, C. Nayak and A. Ananthanarayanan, Mater. Chem. Phys., Vol. 296, pp. 127291-127300 (2023).
5. F. Wu, N. Chen, R. Chen, Q. Zhu, G. Tan and L. Li, Adv. Sci., Vol. 3, pp. 1500306–1500315 (2016).
6. Y.J. Kang, S.J. Chun, S.S. Lee, B.Y. Kim, J.H. Kim, H. Chung, S.Y. Lee and W. Kim, ACS Nano, Vol. 6, pp. 6400–6406 (2012).
7. Q. Guo, Y. Han, H. Wang, S. Xiong, W. Sun, C. Zheng and K. Xie, J. Phys. Chem. C, Vol. 122, pp. 10334–10342 (2018).

Synthesis and Characterization of MnO_2 for High Performance Supercapacitor Electrode Application

Shameela P[1], Fuad Hamdi K[1], Maneesh Chandran[1] and P. Muhammed Shafi [1, *]

[1]*Department of Physics, National Institute of Technology, Calicut, Kerala, 673601, India.*

[*] Corresponding author: muhammedshafi@nitc.ac.in

Abstract. MnO_2 nanomaterials exhibiting high specific capacitance were synthesized via a co-precipitation approach, with the goal of employing them as effective electrode materials in supercapacitor devices. The synthesized δ-MnO_2 was analyzed by X-ray Diffraction (XRD) to verify its phase, Fourier Transform Infrared Spectroscopy (FTIR) to assess its purity, and Scanning Electron Microscopy (SEM) to examine its morphology. Electrochemical evaluations, including Cyclic Voltammetry (CV), Galvanostatic Charge Discharge (GCD), and Electrochemical Impedance Spectroscopy (EIS), were employed to understand its potential for electrochemical energy storage application. The fabricated electrode delivered a specific capacitance of 220 F g^{-1} at a specific current of 1 A g^{-1}. These observations emphasize MnO_2's capability as a high performing electrode material within supercapacitor systems.

Key words: Energy storage, Supercapacitor, MnO_2, Pseudocapacitance, Electrode material, Specific capacitance

INTRODUCTION

Electrochemical capacitors are vital for energy storage in sustainable and renewable energy systems. They operate through two mechanisms: electrochemical double-layer capacitance (EDLC), which involves ion accumulation at the electrode/electrolyte interface, and pseudocapacitance, which involves electron transfer via redox reactions. These mechanisms enable high efficiency in storing and releasing energy [1].

Nanostructured metal oxides are crucial for electrochemical capacitors, with RuO_2 being one of the most optimized materials due to its excellent performance. However, its high cost and toxicity limit its widespread use. Economically viable and safe alternatives like Co_3O_4, NiO, and MnO_2 are explored widely [2,3]. Among them, Manganese dioxide (MnO_2) has become a great choice for supercapacitor applications owing to its natural abundance, non-toxicity, affordability, environmental friendliness, and impressive theoretical capacity (617 mAh g^{-1}). MnO_2 can crystallize into various polymorphs, such as α, β, γ, δ, and λ-MnO_2. Interestingly, δ-MnO_2 is particularly notable for its layered structure, which facilitates fast cationic/anionic intercalations. Additionally, δ-MnO_2 is unique in exhibiting both EDLC and pseudocapacitance-based storage mechanisms[3]. The specific capacitance of MnO_2, particularly in the birnessite and other crystallographic phases, depends on various factors such as morphology, defect concentration, and the Mn(IV)/Mn(III) ratio, which significantly influence the material's capacity to store energy [4]. In this work, MnO_2 is synthesized through a facile co-precipitation method and the electrochemical properties were investigated.

EXPERIMENTAL METHODS

Synthesis of MnO_2

An aqueous redox reaction between stoichiometrically balanced $MnSO_4$ and $KMnO_4$ was employed for the preparation of MnO_2. Analytical grade $MnSO_4 \cdot H_2O$ (0.25353 g) and $KMnO_4$ (0.4741 g) were each separately dispersed in 10 mL of deionized (DI) water. Both precursor solutions were mixed together and maintained under continuous stirring for 6 hours at room temperature. Finally, the dark-brown precipitate was repeatedly washed with DI water by centrifugation until the solution became clear. The obtained sample was heated in an oven at 70 °C for 12 hours to remove moisture.

Characterization Techniques

The crystal structure of MnO_2 was investigated using powder X-ray Diffraction (PXRD), conducted on a Rigaku diffractometer equipped with a X-ray source of Cu Kα radiation (λ = 1.5406 Å). A PerkinElmer Spectrum 2 instrument, covering the spectral range from 4000 to 500 $cm^{-1.}$ Were used to get fourier transform infrared

(FTIR) spectra in transmission mode. The surface morphology of the synthesized MnO_2 was analysed by a FESEM using a Hitachi SU6600 variable pressure system.

Electrochemical investigations were carried out using a Squidstat Plus electrochemical workstation (Admiral Instruments, USA) at ambient temperature. The electrochemical behaviour of the prepared MnO_2 was assessed in a three-electrode system, comprising the MnO_2 as working electrode, a platinum wire as the counter electrode, and an Ag/AgCl reference electrode. For the fabrication of the working electrode, a uniform slurry was prepared by blending 80% MnO_2, 15% acetylene black, and 5% polyvinylidene fluoride (PVDF) with a small amount of N-methyl-2-pyrrolidone (NMP) as the dispersing medium. This mixture was evenly coated onto carbon cloth (0.02545 g, 1 cm^2) by the doctor blade method. The coated electrodes were then dried under vacuum at 60 °C for 12 hours. A 0.1 M Na_2SO_4 aqueous solution was used as the electrolyte. CV was conducted at scan rates of 2, 5, 10, and 20 mV s^{-1} within a potential window of 0 to 1 V. GCD tests were performed at varying specific currents (1, 2, 3, 4, and 5 A g^{-1}) over the same voltage limit. EIS was carried out across a frequency spectrum from 100 kHz down to 100 mHz.

RESULTS AND DISCUSSIONS

The XRD pattern of the synthesized MnO_2 Figure 1a shows broad and low-intensity peaks at $2\theta \approx 12.2°$, 24.8°, 37.0°, and 65.4°, corresponding to the (001), (002), (006), and (119) planes of δ-MnO_2 (JCPDS No. 18-0802), indicating a poorly crystalline nature. Additionally, a few minor peaks marked with asterisks correspond to α-MnO_2, confirming the formation of a mixed-phase material containing both δ- and α-MnO_2.

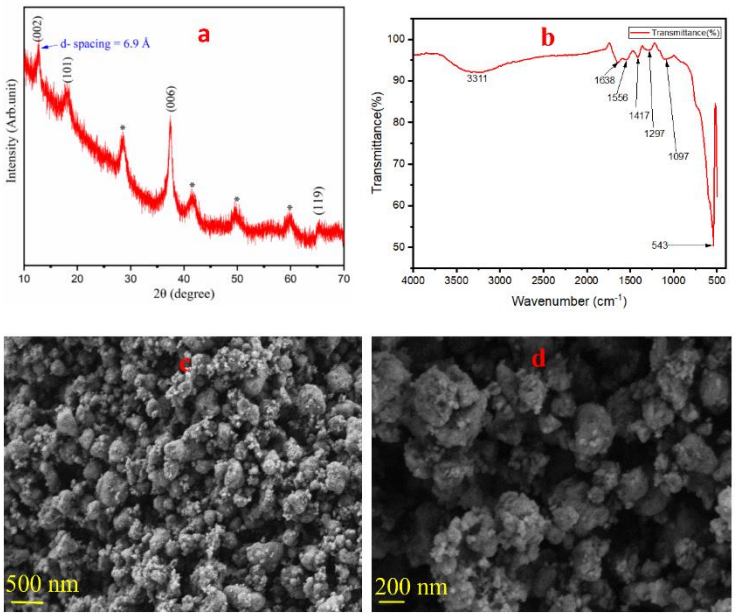


FIGURE 1. (a) XRD Spectrum (b) FTIR Spectrum, (c), (d) SEM images of the MnO_2 sample at magnifications of 20k and 40k.

The FTIR spectrum (Figure 1b) displays significant bands at 543, 1097, 1297, 1417, 1556, 1638, and 3311 cm^{-1}. The peak at 543 cm^{-1} corresponds to Mn-O stretching vibrations, confirming the presence of Mn-O bonds. SEM analysis shows that MnO_2 particles are aggregated into spherical agglomerates (Figure 1c, d).

Cyclic voltammograms (Figure 2 a) of MnO_2 at scan rates from 2 to 20 mVs^{-1} exhibit nearly rectangular shapes, indicating good capacitive behavior and reversibility[5]. As scan rates increase, a distortion in rectangular shape is observed, leading to decreased EDLC contributions at higher scan rates. The GCD curves (Figure 2b, c, d) for MnO_2, recorded at various specific currents (1, 2, 3, 4, and 5 A g^{-1}), display isosceles triangle shapes, reflecting highly reversible redox reactions[6]. The specific capacitance (C_S) decreases from 222 to 115 F g^{-1} as specific current increases from 1 to 5 A g^{-1} (Figure 2e), indicating better utilization of the active material at lower current densities. The Nyquist plot (Figure 2f) shows an ESR of 5.664 **Ω** and a charge transfer resistance (R_{ct}) of 4.227 **Ω**, highlighting good conductivity and enhanced rate capability. The plot at low-frequency region forms a

near-straight line, indicating ion accumulation at the electrode's surface. These findings confirm the superior electrochemical behavior of MnO_2, underscoring its suitability for application in supercapacitors.

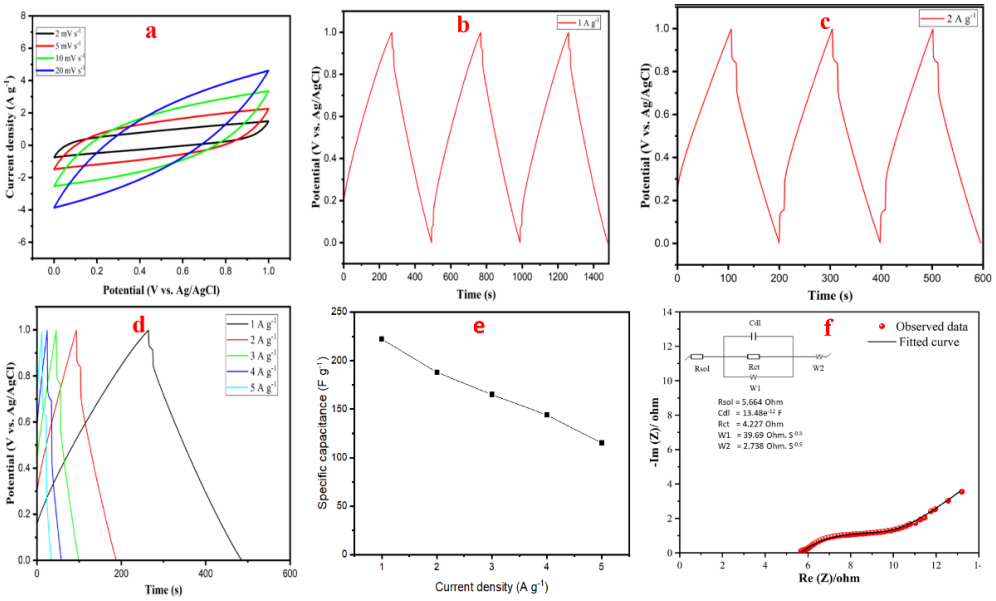


FIGURE 2. (a) Cyclic voltammograms measured at multiple scan rates (b), (c) GCD profile recorded at 1 Ag^{-1} and 2 Ag^{-1} (d) Charge – discharge curves obtained at different specific current (e) Specific capacitance plotted as a function of specific current of charge-discharge cycling (f) Nyquist impedance spectrum (100 kHz-100 mHz).

CONCLUSIONS

Nanostructured MnO_2 displayed promising performance as an electrode material for electrochemical capacitors in a 0.1 M aqueous Na_2SO_4 solution. Electrochemical techniques like CV, GCD, EIS, clearly demonstrated that MnO_2 holds significant potential for supercapacitor electrode applications. The CV analysis indicated that an increase in scan rate resulted in higher specific current accompanied by an increase in specific capacitance. However, this decline was comparatively smaller for the mixed phase MnO_2, suggesting better utilization of the active material. The GCD results revealed that MnO_2 shows outstanding electrochemical characteristics, achieving a specific capacitance of 222 F g^{-1} at 1 A g^{-1} and notable rate performance. Furthermore, the electrode preserved 51.8% of the starting capacitance when the current density was raised from 1 to 5 A g^{-1}. EIS analysis confirmed beneficial electron transfer and good conductivity, with low ESR and R_{ct} values. These results indicate that MnO_2 holds significant potential for use in next-generation supercapacitors. Its combination of high specific capacitance, impressive rate performance, and advantageous impedance properties underscores its suitability for advanced energy storage technologies. Further optimization and study of MnO_2's synthesis and structural properties could enhance its performance and broaden its application potential.

REFERENCES

1. Simon P., Gogotsi Y., Nature Materials, Vol. **7**, pp. 845–854 (2008).
2. Yong-gang W., Xiao-gang Z., Electrochimica Acta, Vol. 49, pp. 1957–1962 (2004).
3. Devaraj S., Munichandraiah N., Journal of Physical Chemistry C, Vol. 112, pp. 4406–4417 (2008).
4. Cremonezzi J. M. D. O., Tiba D. Y., Domingues S. H., SN Applied Science. Vol. 2, pp. 1689 (2020).
5. QianY., Lu S.,Gao F., Journal of Material Science. Vol. 46, pp. 3517–3522 (2011).
6. Munaiah Y., Sundara Raj B. G., Prem Kumar T., Ragupathy P, Journal of Materials Chemistry A. Vol.1, pp. 4300 (2013).

CdSe Quantum Dot Synthesis and Application in Quantum Dot Dye Sensitized Solar Cell

Yugandhara S. Waghode[1], Bhagyashri Bangalkar[1], Syed Habibuddin Syed Abed Ali[1], R N Kamble[1], R R Kalesh[2], Vaishali A Bambole*

[1]*Department of Physics, University of Mumbai, Kalina, Santacruz (E), Mumbai 400 098*

[2]*Department of Physics, Institute of Science, Fort, Mumbai 400 032*

Corresponding Author Email: vaishali.bambole@physics.mu.ac.in

Abstract. Using a safe procedure, Cadmium Selenide (CdSe) quantum dots(QDs) were synthesized by wet chemical method. The synthesized CdSe QDs are characterized by XRD (X-ray diffraction) ranging QDs size from 1.9 nm to 6 nm, SEM (Scanning Electron Microscopy), UV-Visible Spectra (UV-Visible Spectroscopy), and FTIR (Fourier Transform Infrared Spectroscopy). In the application part, to calculate the efficiency of solar cell electrodes, we used the PEC (Photoelectrochemical cell) three-electrode set-up for characterization and Cyclic Voltammetry to check the capacity of the electrode. Using a CdSe material, we have prepared the electrode on ITO with the help of the Drop Cast method, which shows efficiency 1.591 % by PEC test.

Key words: quantum dots (QDs), ITO, efficiency, deposition, wet chemical method, PEC.

1. INTRODUCTION:

In recent years, nanostructured materials have garnered considerable interest owing to their distinct physiochemical characteristics that markedly deviate from those of bulk materials, rendering them highly promising for a wide range of applications in cutting-edge manufacturing and nanotechnological advancement. Quantum Dots (QDs) represent nanoscale semiconductor structures that confine the motion of electrons and holes in x, y, z direction, leading to pronounced quantum confinement effects. The concept of quantum dots was first introduced by Alexei Ekimov through observations in glass matrices, and further developed into colloidal systems by Louis Brus. In 2002, Robert Plass et al. successfully employed QDs as sensitizers in dye-sensitized solar cells (DSSCs), demonstrating their potential in photovoltaic applications. The preparation approach critically influences the composition, structural properties, and functional performance of quantum dots, thereby affecting their optical and electronic characteristics. Among the various renewable energy sources- including wind, hydro, tidal, biomass, biofuels, and geothermal-solar energy remains the most promising due to its abundance and sustainability. Estimates suggest that the solar irradiance received by the Earth in one hour is adequate to sustain the planet's annual energy consumption. Solar cells provide an efficient means of harnessing this energy by converting it into electrical power. Consequently, extensive global research efforts are directed toward improving solar cell technologies for enhanced efficiency and reduced cost. In the present study, Cadmium Selenide (CdSe) QDs were synthesized using a colloidal method with 2-mercaptoethanol as a capping agent to control particle size and stability. Photoelectrodes were constructed in Indium Tin Oxide (ITO) substrate by drop-casting the synthesized quantum dots. These electrodes were tested in a potassium hydroxide (KOH) electrolyte to evaluate their photochemical (PEC) performance. The PEC measurement serves as a fundamental assessment to determine the suitability of the synthesized material for integration into quantum dot-based DSSCs. The overall objective is to develop a low-cost, efficient solar cell device utilizing freely available solar energy.

Quantum dots (QDs) represent nanoscale semiconductor structures that confine the motion of electrons and holes in all spatial directions, leading to pronounced quantum confinement effects.

2. MATERIALS AND METHODS:

2.1 Materials: Cadmium Chloride ($CdCl_2.5H_2O$)(reagent grade, 98%, Sigma-Aldrich), Selenium Metal Powder (Se) (99.99%, Sigma-Aldrich), 2-Mercaptoethanol Pure (HOCH2CH2SH) (99%, SRL) , Sodium Sulphite (Na2SO3) (Sodium sulfite, ≥98%, Sigma-Aldrich).

2.2 Synthesis Of CdSe Quantum Dots: CdSe quantum dots were prepared by first preparing a Sodium Selenosulfate (Na_2SeSO_3) solution from elemental Selenium 0.063 g and Sodium Sulfite 0.304 g in 60ml of water. Separately, Cadmium Chloride 0.1142 g and 2-Mercaptoethanol were dissolved in 500 mL deionized water and degassed with nitrogen for 15minutes. The (Na_2SeSO_3) solution was then rapidly injected into the Cadmium precursor under continuous stirring, followed by heating at 55^0C to facilitate QDs growth. A rapid colour change indicated immediate nucleation, and the reaction was conducted under a nitrogen atmosphere to prevent oxidation.

Wash the QDs with Acetone and Double distilled water three times in a centrifuge for 10minutes. Dry and convert it into powder form.

2.3 Solar Cell Electrode:

2.3.1. Deposition Of Cdse QDs: The ITO conductive glass plate (Indium Tin Oxide) (75 mm×40mm×2 mm) was cleaned with ethanol, and double distilled water for 10mins. After washing, ITO glass was dried in Oven and used to form an electrode. Further, mixed CdSe QDs, binder and linker NMP in equal amount and form viscous slurry deposit it on ITO and form electrode by drop cast method.

3. RESULTS AND DISCUSSIONS:

3.1. XRD Characterization:

XRD analysis was conducted in the 2θ range of 10^0 to 80^0 to investigate the structural properties of CdSe quantum dots (QDs). Prominent XRD peaks indicative of the (100), (002), (101), (102), (110), and (112) planes appeared at 2θ angles of 24.30^0, 26.00^0, 27.05^0, 35.70^0, 43.07^0, and 49.76^0, respectively, as shown in Fig. 1 (1-10). The diffraction pattern confirms that the CdSe QDs synthesized at 50^0C possess a hexagonal wurtzite crystal structure. The averge crystalline size (D) was estimated to be in the range of 3nm-7nm, based on the (002) diffraction plane, using the Scherrer equation (8, 10).

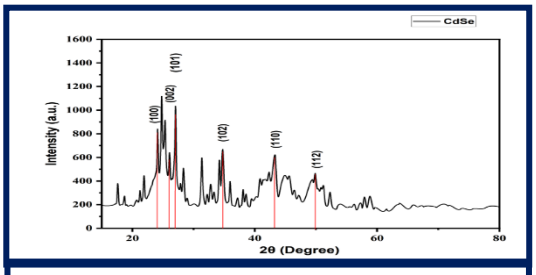


Fig.(1) XRD pattern of CdSe QDs

$D = \frac{0.9\,\lambda}{\beta \cos\theta}$, Where k is 0.9 constant value, λ is XRD machine wavelength, β represents the peak broadening at half of its maximum intensity, θ is Bragg's angel, and D indicate mean grain size of CdSe QDs.

3.2 SEM Characterization:

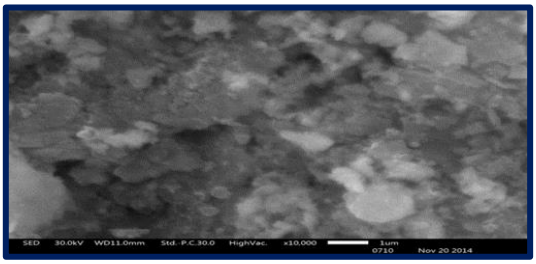


Fig. (2) SEM image of Cdse QDs

Fig.2 presents the surface morphology of the synthesized CdSe quantum dots (QDs), caputured using SEM at magnification of 10000 X. the SEM image reveals a rough and agglomerated surface with irregular grain orientation, indicating a non-uniform morphology. While such surface roughness can enhance charge carrier trapping- potentially beneficial for certain optoelectronic applications- it also contributes to reduced device performance by limiting charge carrier mobility (5). The presence of trapped carriers necessitates additional energy for their mobilization, thereby hindering efficient charge transport within the device.

3.3 UV-Visible Spectroscopy:

Prior to UV-Visible spectroscopic analysis, the colloidal solution was sonicated for 1 hour to ensure uniform dispersion of the CdSe quantum dots (QDs). The combined UV-Vis and Tauc plot Fig. 3 for 2-mercaptoethanol-capped QDs synthesized via 1-hour reflux shows distinct absorption peaks at 240.54nm, 364.75nm, and 619.20nm, with a direct bandgap transition estimated at 2.5 eV. Given that the Bohr exciton radius for bulk CdSe is 5.6nm, the observed optical properties suggest that the synthesized CdSe QDs possess dimensions smaller than the Bohr radius, consistent with quantum confinement effects.

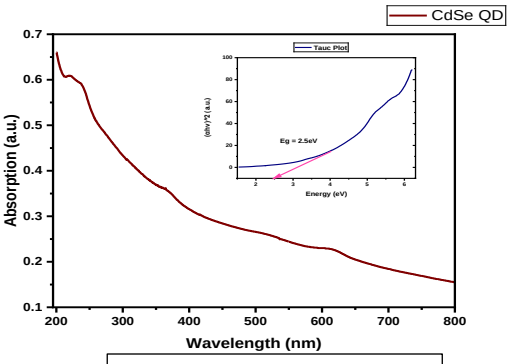


Fig (3) UV & Tauc Graph

3.4. Photo Electrochemical Cell Characterization:

3.4.1. PEC Characterization- IV curve

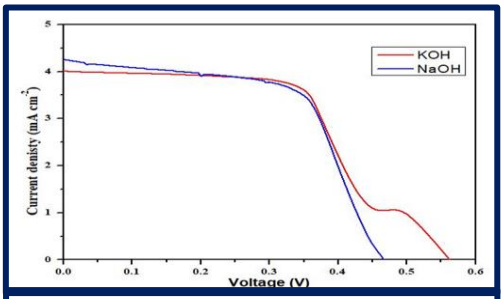


Fig (4) PEC graph of CdSe QDs

For determine the Fill Factor (FF) from the obtain value the formula is (6), $FF = \frac{I_{max} \times V_{max}}{J_{sc} \times V_{oc}}$

Where, the photovoltaic parameters include open-circuit voltage (V_{OC}), short-circuit voltage (I_{SC}), current at the maximum power paoint (I_{MAX}), voltage at the maximum power point (V_{MAX}), and Fill Factor (FF). After we getting FF factor, we have to calculate the efficiency by formula (7), $\eta = \frac{J_{sc} \times V_{oc} \times FF}{P_{in}}$

Where, P_{in} incident light power, η is efficiency. From the above formulas, For NaoH values for $V_{OC} = 0.46\,V$, $J_{SC} = 4.60\,mA/cm^2$, $I_{MAX} = 4.30\,mA/cm^2$ and $V_{MAX} = 0.37\,V$ from this value FF = 75.18 %, and efficiency η = 1.591 %. For KoH Values for $V_{OC} = 0.57\,V$, $J_{SC} = 4.20\,mA/cm^2$, $I_{MAX} = 4.00\,mA/cm^2$ and $V_{MAX} = 0.37\,V$ from this value FF = 61.82%, and efficiency $\eta = 1.479$ % *as per Fig.* 4.The KoH electrolyte is giving high efficiency rate as compare to NaoH electrolyte.

3.4.2. Cyclic Voltammetry- CV Curve

The electrode was investigated using two distinct alkaline electrolytes: Sodium hydroxide (NaOH) and potassium hydroxide (KOH). Among the investigated electrolytes, KOH exhibited relatively superior electrochemical performance. Initial electrochemical characterization conducted in a 1 M KOH solution using Cyclic Voltammetry at a scan rate of 0.05V/s revealed well-defined redox behavior, with a cathodic peak is at 0.30V and an anodic peak is at 0.54V, as shown in Fig. 5.

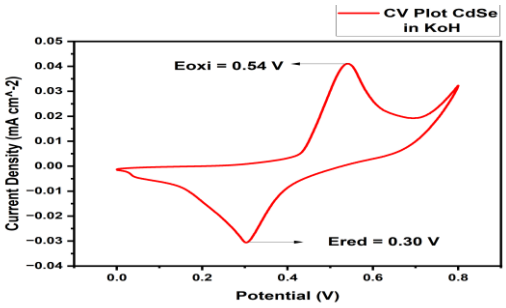


Fig (5) CV Graph

4.CONCLUSION:

Cadmium Selenide QDs were successfully produced by a chemical solution method in the presence of 2-mercaptoethanol as a stabilizing agent at a relatively low temperature of 55^0C. XRD analysis confirmed the formulation of a hexagonal crystal structure with a wurtzite phase. SEM revealed a rough surface morphology, indicative of uneven particle distribution or aggregation. An optical band gap of about 2.5 eV was inferred from the absorption onset observed in the UV-Vis spectrum. FTIR identified characteristic stretching vibrations associated with Cd-Se bonding, confirming the formation of the desired compound along with other molecular groups present. PEC performance of the fabricated CdSe electrodes was evaluated using two different electrolytes NaOH and KOH. The fill factor (FF) values recorded were 61.61 % for NaOH and 55.40% for KOH. The corresponding conversion efficiencies obtained from PEC measurement were 1.204% and 1.240% for NaOH and KOH respectively. Electrochemical analysis via CV in KOH solution demonstrated redox behavior of the electrode, as evidenced by reduction and oxidation peaks at 0.30V and 0.54V respectively. These results conclude synthesized CdSe QDs exhibit promising PEC properties, with improved performance observed in the KOH electrolyte, demonstrating their potential applicability in QD dye-sensitized based photovoltaic devices.

REFERENCES

1. Karan Surana, Pramod K Singh, Hee-Woo Rhee, B. Bhattacharya, "Synthesis, characterization and application of CdSe quantum dots", Journal of Industrial and Engineering Chemistry, Volume 20, Issue 6, Pages 4188-4193, 25 November 2014.
2. Karan Surana, R.M. Mehra, B. Bhattacharya, "Quantum Dot Solar Cells with size tuned CdSe QDs exhibiting 1.51V", Materials Today: Proceedings 5, Volume 5, Issue 3, Part 1, Pages 9108-9113, 2018.
3. Karan Surana , Ibrahim T. Salisu , R.M. Mehra , Bhaskar Bhattacharya, "A simple synthesis route of low temperature CdSe-CdS core-shell quantum dots and its application in solar cell", Optical Materials, Volume 82, Pages 135-140, August 2018.

4. Waleed E. Mahmoud, Amal M. Al-Amri, S.J. Yaghmour, “Low temperature synthesis of CdSe capped 2-mercaptoethanol quantum dots”, Optical Materials, Volume 34, Issue 7, Pages 1082-1086, May 2012.
5. Fida Muhammad,MuhammadTahir, MuhammadZeb, Muttanagoud N. Kalasad , Suhana Mohd Said, Mahidur R. Sarker, Mohd Faizul Mohd Sabri & Sawal Hamid MdAli, “Synergistic enhancement in the microelectronic properties of poly- (dioctylfuorene) based Schottky devices by CdSe quantum dots”, Nature, *Sci Rep* 10, 4828 (2020)
6. Hassan Ghasemi and Mohammad Hazhir Mozaffari, “Synthesis and optoelectronic properties of CdSe quantum dots”, Optics, *18 May 2021*.
7. P Sanjay , K Deepa, J Madhavan and S Senthil, “Synthesis and Spectroscopic Characterization of Cdse Nanoparticles for Photovoltaic Applications”, IOP Conf. Series: Materials Science and Engineering 360,012010,(2018).
8. Soumya R. Deo & Ajaya K. Singh & Lata Deshmukh & Narendra Pratap Singh & Mariya P. Aleksandrova, “Studies on Structural, Morphological and Optical Properties of Chemically Deposited CdS1-xSex Thin Films”, J Fluoresc 26:459–469, (2016).
9. G. Ramalingam, K. Venkata Saravanan, T. Kayal Vizhi, M. Rajkumar and Kathirvelu Baskar, “Synthesis of water-soluble and bio-taggable CdSe@ZnS quantum dots”, RSC Adv., 8, 8516, 2018.
10. He Rong, You Xiaogang, Tian Hongye, Gao Feng, Cui Daxiang, Gu Hongchen, “Synthesis and characterization of monodisperse CdSe quantum dots in different organic solvents”, Front. Chem. China 4: 378−383”, (2006).

Synthesis of MoS_2 Thin Films from Bulk-like to Monolayer and Their Valence Band Offset with SiO_2 Interfaces

U. K. Goutam[1#*], Jagannath[1#], Jyoti Prakash[2#], D. Bhattacharya[3#] and L. M. Pant[1#]

[1]*Technical Physics Division, Bhabha Atomic Research Centre, Mumbai-400085, India*
[2]*Glass and Advance Materials Division, Bhabha Atomic Research Centre, Mumbai-400085, India*
[3]*Atomic and Molecular Physics Division, Bhabha Atomic Research Centre, Mumbai-400085, India*
[#]*Homi Bhabha National Institute, Anushaktinagar, Mumbai-400094, India*

[*]Corresponding author: ukgoutam@rrcat.gov.in

Keywords: Transition metal dichalcogenides, X-ray Photoelectron Spectroscopy, Valence band offset, monolayer, e-beam deposition

Abstract. This study presents the synthesis of MoS_2 thin films ranging from few layers to monolayers and their band offset with SiO_2 interfaces. MoS_2 thin films were synthesized using e-beam deposition followed by sulfurization on SiO_2/Si substrates. Grazing incidence x-ray diffraction (GIXRD) established the 2H phase MoS_2 formation. The valence band offset (VBO) at the MoS_2/SiO_2 interfaces were investigated using x-ray photoelectron spectroscopy (XPS). The VBO were measured and found to be sufficient (>1.0 eV) to suppress gate current, indicating the potential of MoS_2/SiO_2 heterojunctions for high-performance field-effect transistors (FETs) and photodetectors. The findings enhance our understanding of MoS_2-based nano-electronic devices by emphasizing the critical role of accurately controlling film thickness and carefully engineering the interfaces.

INTRODUCTION

Molybdenum disulfide (MoS_2), a layered transition metal dichalcogenide, has garnered considerable interest recently because of its distinctive electronic, optical, and mechanical characteristics [1]. As a direct bandgap semiconductor in its monolayer form, MoS_2 holds immense potential for various applications in nano-electronics, optoelectronics, and flexible devices [2-4]. The ability to synthesize high-quality MoS_2 thin films ranging from few layers to monolayers is crucial for the development of next-generation devices. In particular, understanding the band alignment at the interface between MoS_2 and dielectric materials like silicon dioxide (SiO_2) is essential for optimizing device performance [4-5]. The energy band offset at the MoS_2/SiO_2 interface plays a pivotal role in determining the efficiency and functionality of field-effect transistors (FETs), photodetectors, and other nano-electronic devices. Specifically, achieving sufficient values of Valence Band Offset (VBO) is necessary to suppress gate current and enhance device performance. This study centers on synthesizing MoS_2 thin films ranging from few layers to monolayers through e-beam evaporation followed by sulfurization. The phase and quality of the produced films were evaluated using grazing incidence X-ray diffraction (GIXRD). Additionally, the valence band offset at the MoS_2/SiO_2 interfaces are investigated using x-ray photoelectron spectroscopy (XPS), providing insights into the suitability of these heterojunctions for high-performance FETs and photodetectors. The results of this research enhance the knowledge and advancement of MoS_2-based electronic and optoelectronic devices.

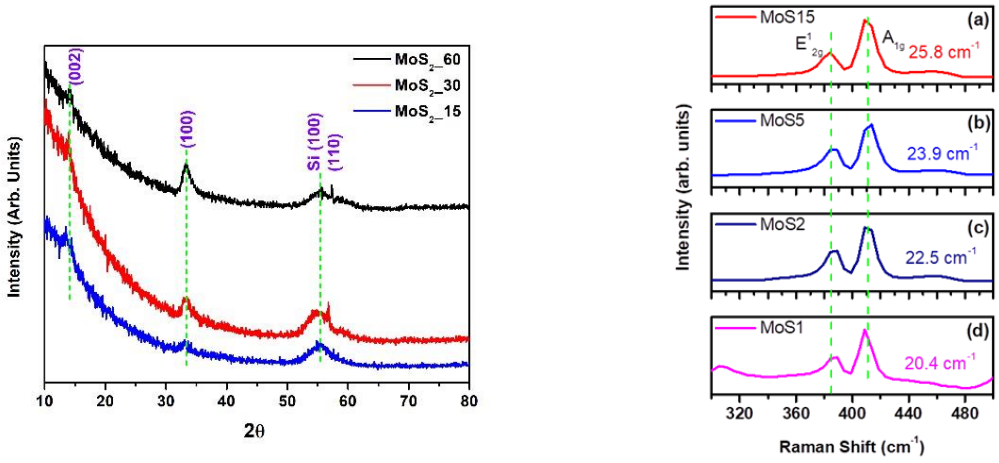
EXPERIMENTAL

Large-area (8 mm dia.) MoS_2 thin films on SiO_2 were synthesized through a two-step process. Initially, Si wafers were cleaned ultrasonically in deionized water followed by isopropyl alcohol, each for 30 minutes. A ~300 nm thick SiO_2 layer was then deposited onto the cleaned wafers using e-beam deposition. Molybdenum thin films were then deposited onto the SiO_2/Si substrates using e-beam deposition for different time intervals of 1, 2, 5, 15, 30, and 60 minutes at ~65 W in an ultra-high vacuum (~2×10^{-8} mbar), using a 2.0 mm Mo rod as the source material. The Mo films, approximately 8.0 mm in diameter, were deposited as circular spots. The films were subsequently sulfurized in a tubular furnace, with the samples positioned at the center and sulfur flakes placed in an alumina boat near the edge of the furnace. Sulfurization was carried out at 780 °C for 1 hour under a 200 SCCM argon flow, resulting in MoS_2/SiO_2 samples, which were collected after cooling. The samples were labeled MoS1, MoS2, MoS5, and MoS15, corresponding to Mo deposition durations of 1, 2, 5, and 15 minutes, respectively.

GIXRD measurements were carried out using a Bruker Discover D8 diffractometer equipped with Cu Kα radiation (λ = 0.154 nm). Room temperature Raman spectroscopy was conducted using a WITec micro-Raman spectrometer with a 514 nm laser. XPS measurements were done at the PES-BL14 HAXPES beamline at the Indus-2 synchrotron using 4.065 keV X-rays.

RESULTS AND DISCUSSION

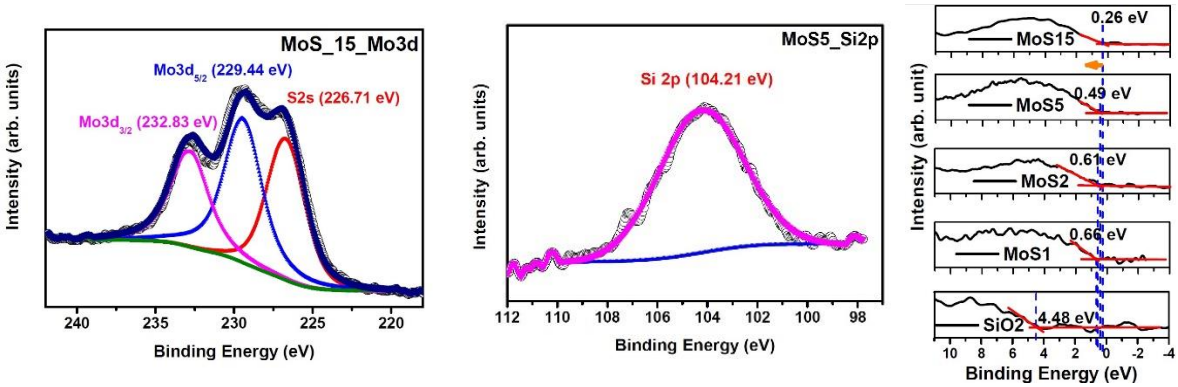
GIXRD measurements were carried out on selected samples deposited on SiO_2/Si substrates within the 2θ range of 10° to 80°, as illustrated in Fig. 1(a). The analysis revealed well-defined diffraction peaks at 2θ angles of 14.2°, 33.3°, and 58.5°, corresponding to the (002), (100), and (110) planes of MoS_2, respectively. These peak positions align with standard reference data for 2H-MoS_2 nanosheets, whose unit cell comprises two S-Mo-S monolayers arranged in a hexagonal structure [6]. This confirms the successful synthesis of few-layer 2H-MoS_2 thin films in all three samples. Raman spectra recorded at room temperature for MoS_2/SiO_2 samples of varying thicknesses, using a 514 nm excitation laser (Fig. 1(b)), exhibited two prominent peaks in the MoS1 sample at 388.33 cm^{-1} and 408.74 cm^{-1}. These are associated with the in-plane (E^1_{2g}) and out-of-plane ($A_{1}g$) vibrational modes of MoS_2, respectively [Fig. 1(d)]. The spacing between these modes (Δω), a key indicator of the number of layers, was found to be 20.4 cm^{-1} for the MoS1 sample, confirming the formation of a monolayer MoS_2 film on the SiO_2 substrate. With increasing film thickness, this Raman shift progressively increased—measured at 22.5 cm^{-1} in MoS2, 23.9 cm^{-1} in MoS5, and 25.8 cm^{-1} in the MoS15 sample—indicating the transition from monolayer to multilayer MoS_2, consistent with the literature [7].



(a) **(b)**

FIGURE 1: (a) GIXRD of MoS_2 thin films synthesized using Mo thin films deposited for 60, 30 and 15 minutes (b) Raman spectra showing the characteristic peaks for in-plane (E^1_{2g}) and out-of-plane ($A_{1}g$) vibrational modes for the samples MoS15, MoS5, MoS2 and MoS1

To examine the band offset at the interfaces, XPS measurements were performed on MoS_2 films deposited on SiO_2/Si substrates, as well as on bare SiO_2/Si. Core level spectra for Mo, S, O, and Si, along with valence band spectra, were collected. For this, five synthesized samples were used; four MoS_2 thin films on SiO_2/Si in which Mo was deposited for 15 min. (MoS15), 5 min. (MoS5), 2 min. (MoS2) and 1 min. (MoS1) and fifth one was bare SiO_2/Si (SiO_2) sample. The valence band XPS spectra were analyzed and valence band maxima (VBM) of the samples were extracted. High-resolution Mo 3d spectra for the four samples (MoS15, MoS5, MoS2, and MoS1) were recorded and fitted using CasaXPS software, employing a Shirley background for baseline correction. Each Mo 3d spectral regions were deconvoluted into three components $Mo3d_{3/2}$, $Mo3d_{5/2}$ and S 2s. Additionally, Si 2p spectra were recorded for four samples (MoS5, MoS2, MoS1, and SiO_2), fitted appropriately, and the Si 2p peak positions were extracted and used for determining the valence band offset (VBO) of the samples. Curve fitted Mo 3d and S 2p for one of the samples is shown in Fig.2. From valence band spectra, it was observed that VBM shifts to higher binding energy side as the MoS_2 film thickness over SiO_2 is reduced or in other words VBM shifts towards Fermi level with increasing MoS_2 film thickness.



(a) **(b)** **(c)**

FIGURE 2: (a) Curve fitted Mo 3d for MoS15 (b) Si 2p for MoS5 and (c) Valence band spectra of all samples

The valence band offset (VBO) (ΔEv) of the MoS_2/SiO_2 structure was calculated utilising Kraut's method [8], based on the VBM and core level values, according to the formula:

$$\Delta Ev = \left(E^{Mo3d5/2} - E_{VBM}\right) - \left(E^{Si\ 2p} - E_{VBM}^{SiO2}\right) - \left(E^{Mo\ 3d5/2} - E^{Si\ 2p}\right) \qquad \text{---- (1)}$$

VBO was evaluated for MoS5, MoS2 and MoS1 samples and were found to be 4.16, 4.04 and 4.00 ±0.05 eV respectively for MoS5, MoS2 and MoS1 samples. The VBO values are large (>1.0 eV) and increases from MoS1 to MoS5 i.e., as the number of layers of MoS_2 increases in the samples. The shifting of Mo $4dz^2$ energy band closer to the Fermi level owing to the interlayer coupling in thicker MoS_2 films [8], causes a shift in the valence band maximum (VBM) and an increase in the conduction band offset (CBO).

In conclusion, large-area MoS_2 thin films with thicknesses varying from bulk-like to monolayer were successfully synthesized on SiO_2/Si substrates using e-beam evaporation and subsequent sulfurization. The resulting films displayed proper stoichiometry consistent with the 2H phase. A Raman mode separation of 20.4 cm^{-1} in the MoS1 sample confirmed monolayer formation on SiO_2, while the progressively larger separations in other samples indicated the presence of few-layer MoS_2 films. The valence band offset for the interfaces of MoS_2/SiO_2 for monolayer and few layers of MoS_2 thin films have been determined using XPS and was found to be ~4.00 ± 0.05 eV. The larger VBO for the samples meet the requirement for CMOS devices.

ACKNOWLEDGEMENTS

Authors thankfully acknowledge Dr. Chandrachur Mukherjee, RRCAT for help in deposition of SiO_2 films on Si wafers. We also acknowledge Dr. P. Gupta, RRCAT for help in GIXRD measurements.

REFERENCES

1. He, Z.; Que, W., Appl. Mater. Today, 3, 23–56 (2016).
2. Xiao Li and Hongwei Zhu, Journal of Materiomics 1 (2015) 33-44
3. Q. H. Wang, K. Kalantar-Zadeh, A. Kis, J. N. Coleman, and M. S. Strano, Nat. Nanotechnol. 7, 699 (2012).
4. S. Manzeli, D. Ovchinnikov, D. Pasquier, O. V. Yazyev, and A. Kis, Nat. Rev. Mater. 2, 17033 (2017).
5. J. Tao, J. W. Chai, Z. Zhang, J. S. Pan, and S. J. Wang, Appl. Phys. Lett. 104, 232110 (2014).
6. Thachnatharen Nagarajan et al.; Scientific Reports; 12, 14108 (2022).
7. M. I. Serna, S. H. Yoo, S. Moreno, Y. Xi, J. P. Oviedo, H. Choi et al., ACS Nano 10, 6054 (2016).
8. Sneha Sinha et al.; J. Appl. Phys. 129, 115303 (2021).

Photocatalytic Degradation of Methyl Orange Using Borophene/TiO_2 Quantum Dots Nanocomposite Under UV Light Irradiation

Akanksha Pandey[1], Tanuja Mohanty[1,*]

[1]*School of Physical Sciences, Jawaharlal Nehru University, New Delhi-110067, India*

[*]*Corresponding author: tanujajnu@gmail.com*

Abstract. This work reports the enhanced photocatalytic activity of titanium dioxide quantum dots (TiO_2 QDs) by forming a nanocomposite with borophene (BP). The successfully synthesis of BP/TiO_2 QDs nanocomposite was done using hydrothermal method followed by its characterization through transmission electron microscopy (TEM) and UV-Vis absorption spectroscopy. The photocatalytic degradation of methyl orange dye was investigated using both pure TiO_2 QDs and the BP/TiO_2 QDs nanocomposite under UV light irradiation. The results demonstrated that the BP/TiO_2 QDs nanocomposite shows higher degradation rate as compared to the pristine TiO_2 QDs. This study highlights an effective way for improving the photocatalytic properties of semiconductor-based materials for the effective removal of organic pollutants.

Keywords: Borophene, TiO_2 quantum dots, Nanocomposite, Photocatalytic degradation, UV light.

INTRODUCTION

Titanium dioxide quantum dots (TiO_2 QDs) have been extensively studied as photocatalysts for degrading environmental pollutants, owing to their large surface area, wide bandgap, and low toxicity. Their photocatalytic activity is based on the generation of photoexcited electron-hole pairs. To improve the efficiency of this process, it is important to enhance the separation and utilization of these charge carriers. However, the rapid recombination of electron-hole pairs and the limited charge transfer ability hinders the overall performance of TiO_2 QDs [1]. An effective approach to address these challenges is to create a nanocomposite by combining TiO_2 QDs with another suitable photocatalyst. Borophene (BP), a two-dimensional sheet of boron atoms, has emerged as a promising material due to its tunable bandgap, excellent electronic properties, and high charge carrier mobility. It has shown potential in catalytic applications particularly for the degradation of organic pollutants [2]. When integrated with TiO_2 QDs, borophene can help reduce charge carrier recombination and improve charge transfer, ultimately enhancing the photocatalytic efficiency of the composite system.

EXPERIMENTAL METHOD

BP/TiO_2 QDs nanocomposite was prepared through the hydrothermal method. 50 mg of as-synthesized TiO_2 QDs nanopowder [3] was mixed with 1mg BP [4] in 25 mL of Milli-Q water and magnetically stirred for 1 hr. This solution was kept at 200^{o}C for 8 hrs using a Teflon-lined autoclave in a muffle furnace. The resulting dispersion was centrifuged and dried to get BP/TiO_2 QDs nanocomposite in powder form.

RESULT AND DISCUSSION

The structural morphology of BP/TiO_2 QDs nanocomposite was done using Transmission electron microscopy (TEM, JOEL 2100F). The UV−Vis absorption spectra have been obtained using an Analytical UV 2080 N spectrophotometer.

TEM Measurement and UV-Vis absorption Spectra

The TEM image of BP/TiO_2 QDs nanocomposite is shown in Fig.1(a). It is visible from the image that TiO_2 QDs are spread over borophene nanosheet which confirms the synthesis of BP/TiO_2 QDs nanocomposite.

The absorption spectra of BP/TiO_2 QDs nanocomposite are shown in Fig.1(b). The optical bandgap is calculated using Tauc formula given in equation (1):

$$\alpha h\vartheta = A(h\vartheta - E_g)^n \quad (1)$$

where $h\vartheta$ is incident photon energy, A is the proportionality constant, α is an absorption coefficient, h is Planck's constant, and $n=2$ for indirect bandgap materials. The inset shows the Tauc plot and the obtained values of indirect bandgap for TiO_2 QDs, and BP/TiO_2 QDs nanocomposite are 4.2 eV and 3.7 eV, respectively.

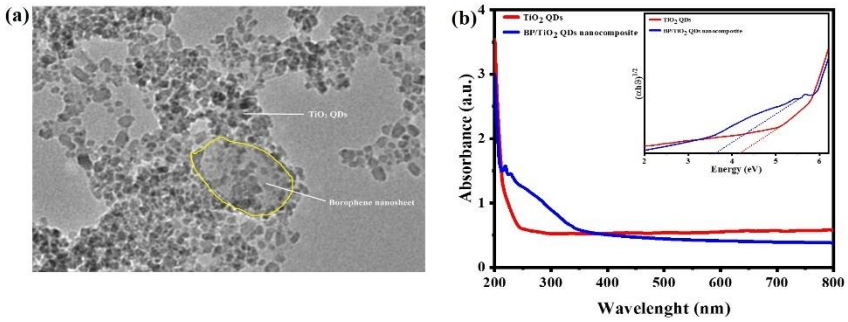


FIGURE.1 (a) TEM image, and (b) UV-Vis absorption spectra.

Photocatalytic Activity

The photocatalytic degradation of 10^{-3} M solution of Methyl orange (MO) was done under UV light irradiation for 100 min. 10mg of TiO_2 QDs and BP/TiO_2 QDs nanocomposite were added separately into the dye solution under constant magnetic stirring for 30 min. 5mL of the resulting solution was taken out and termed as 0 min and the remaining solution was kept under a 250W UV lamp and 5mL solution was taken out at an equal interval of 20 min. After the completion of the process, the photocatalyst was removed by centrifugation, and the supernatant was collected to measure absorption spectra.

The absorption spectra of MO with TiO_2 QDs, and BP/TiO_2 QDs nanocomposite at different time intervals are shown in Fig.2(a&b), respectively. The intensity of MO decreases with increasing time in both photocatalysts. The variation in the concentration of MO at different time with the two photocatalysts is shown in Fig.2(c). It is clear from the graph that the concentration of MO decreases more in BP/TiO_2 QDs nanocomposite photocatalyst than in TiO_2 QDs photocatalyst. The degradation percentage (%) of the organic pollutants was calculated by using equation (2) [5]:

$$\eta = \left[1 - \frac{C}{C_0}\right] \times 100 \tag{2}$$

The degradation rate of MO is higher in BP/TiO_2 QDs nanocomposite photocatalyst than in TiO_2 QDs photocatalyst at every time interval as shown in Fig.2(d). Since the photodegradation of MO in both samples takes place linearly, the catalytic potential was determined by studying the reaction kinetics through the Pseudo first-order model given by equation (3) [6]:

$$-ln\left(\frac{C}{C_0}\right) = kt \tag{3}$$

where C_0 is the initial concentration of MO at t =0 min, C is the concentration at time t min, and k is the rate constant of reaction. The value of k obtained from Fig.3(a &b) for TiO_2 QDs, and BP/TiO_2 QDs nanocomposite photocatalyst are 1.14* 10^{-3} min^{-1} and 2.5*10^{-3} min^{-1}, respectively. The values indicate that BP/TiO_2 QDs nanocomposite acts as a good photocatalyst in comparison to TiO_2 QDs photocatalyst. The large surface area of borophene helps in increasing the adsorption ability and reduces the recombination of photogenerated charge carriers. This enhances the photocatalytic activity of BP/TiO_2 QDs nanocomposite which makes it useful in the elimination of environmental pollutants.

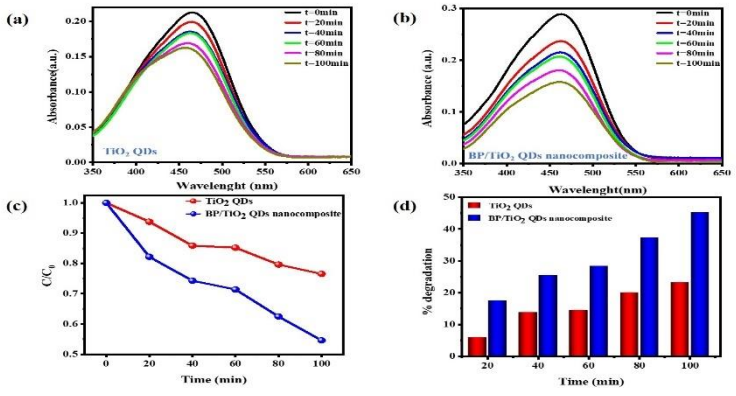


FIGURE.2 UV-Vis absorption spectra of MO with (a) TiO_2 QDs, (b) BP/TiO_2 QDs nanocomposite, (c) Photocatalytic degradation, (d) Degradation percentage of MO with TiO_2 QDs and BP/TiO_2 QDs nanocomposite at different time interval.

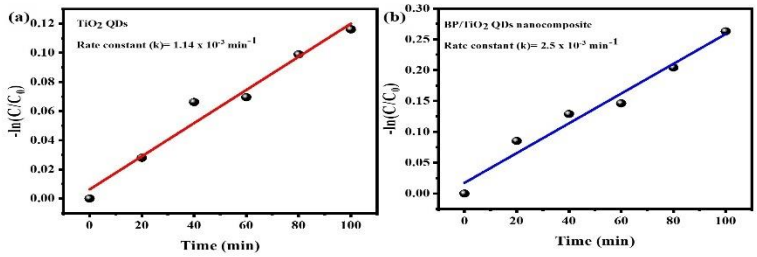


FIGURE.3 Plot of -ln(C/C_0) at different irradiation time for (a) TiO_2 QDs, (b) BP/TiO_2 QDs nanocomposite.

CONCLUSION

BP/TiO_2 QDs nanocomposite is successfully synthesized using the hydrothermal method which was confirmed using TEM measurement and UV-Vis absorption spectroscopy. The photocatalytic degradation of MO using two photocatalysts i.e. TiO_2 QDs, and BP/TiO_2 QDs nanocomposite has been studied. It was found that a small amount of BP/TiO_2 QDs nanocomposite performed better photocatalyst in comparison to the pure TiO_2 QDs. This work shows the potential application of BP/TiO_2 QDs nanocomposite in the removal of organic contaminants in waste water treatment.

ACKNOWLEDGMENTS

The authors are thankful to AIRF, and SCNS, JNU for TEM and UV-Vis absorption measurements. T.M. is grateful to DST-SERB project No. CRG/2022/007270 for consumable support. A.P. acknowledges CSIR, India for a research fellowship.

REFERENCES

1. M. Ge et al. J. Mater. Chem., A 4, 6772-6801 (2016).
2. H. Chand et al. Adv. Mater. Inter., 9, 2200508 (2022).
3. L. Gnanasekaran et al J. Saudi Chem. Soc., 19, 589-594 (2015).
4. H. Li et al. ACS Nano., 12, 1262-1272 (2018).
5. Z. Niazi et al. Photochem. Photobiol. Sci., 20, 87-99 (2021).
6. J. Hua et al. Optik, 171, 95-106 (2018).

Exploration of Hydrogen Decorated Two-dimensional Graphullerene: a First Principle Investigation

Satish Kumar[1, *], Monika Gupta[1], Sanjeev Thakur[1], Reena Kumari[1], Anjna Devi[2], Sheetal Dhiman[1], Monika Chandel[1], Arun Kumar[1]

1. *Department of Physics, Government College Bilaspur, Himachal Pradesh – 174001, India*
2. *Department of Physics, Government College Baroh, Kangra, Himachal Pradesh – 176054, India*

[*]Corresponding author: 97satish02@gmail.com

Abstract: We have systematically studied a two-dimensional (2D) structure of hydrogen decorated graphullerene. We employed an ab initio calculation to examine its structural and electronic properties. Graphullerene is a newly discovered 2D allotrope of carbon which is formed by the use of C_{60} crystal of carbon allotrope. We computed structural and electronic band structure of hydrogen decorated graphullerene, which can be a good replacement for futuristic devices specially for optoelectronic devices due to direct energy band gap (2.74 eV). Which lies in the visible region. It can also be used as hydrogen storage device in the future.

Keywords: DFT, SIESTA, Carbon nanomaterials, Hydrogenated graphullerene, semiconducting properties, hydrogen storage,

INTRODUCTION

In terms of abundance, carbon holds the 15th position in the Earth's crust and stands as the fourth most prevalent element by mass in the universe, coming after hydrogen, helium, and oxygen. Carbon atoms can connect in multiple ways, giving rise to different allotropes characterized by distinct electronic configurations, including sp, sp^2, and sp^3 hybridizations. Carbon exhibits a wide range of allotropes such as graphite, diamond, C_{60} fullerene, amorphous carbon, zigzag single-walled carbon nanotubes [1], carbon nanobuds, and graphene [2] which are structurally distinct forms of the same element. Among these, diamond and graphite are the most well-known, exhibiting remarkably different physical properties. Diamond features a three-dimensional tetrahedral network, where each carbon atom is sp^3 hybridized and bonded to four neighboring atoms, making it one of the hardest naturally occurring materials, widely used in industrial applications. In contrast, graphite consists of stacked layers of carbon atoms with sp^2 hybridization, where each atom forms three bonds in a two-dimensional honeycomb lattice. The discovery that these layers could be separated to create graphene [2], a single atomic layer of graphite, marked a milestone in condensed matter physics**.** Graphite, as an allotrope, is also employed in various applications such as battery electrodes, solar energy devices, and lubricants, due to its ability to withstand high temperatures without chemical degradation**.**

Another interesting carbon form is the C_{60} fullerene, often described as a soccer ball-shaped molecule, consisting of twenty hexagons and twelve pentagons, with each carbon atom sp^2 hybridized and bonded to three adjacent atoms [3]. More recently, Uri Argaman et al**.** identified a novel carbon allotrope called graphullerene, which consists of linear chains of C_{60} units arranged in parallel. Their work focused on the structural and semiconducting properties of graphullerene [4]. Building on this research, we have conducted an investigation into the structural and electronic characteristics of hydrogenated graphullerene

COMPUTATIONAL METHOD

To investigate the properties of both graphullerene and hydrogen-decorated graphullerene, we have utilized density functional theory (DFT) based SIESTA code [5]. We have employed the GGA-PBE functional, A double-zeta polarized (DZP) basis set with a confinement energy of 20 meV was employed. The structure was relaxed using the conjugate gradient (CG) algorithm until the residual forces were below 0.01 eV/Å. A Monkhorst-Pack k-point grid of 10×10×1 was employed for Brillouin zone sampling.. A vacuum layer of 15 Å was added along the z-direction to prevent the interactions among the periodic images. All calculations utilized norm-conserving pseudopotentials for the species which are atomic

RESULT AND DISCUSSION

By building a 2D hexagonal unit cell and inserting a C_{60} molecule within, the crystal structure including the lattice parameters and atomic positions were allowed to relax to a lowest energy configuration in order to determine the structure of graphullerene. The linear, parallel C_{60} chains that make up this two-dimensional structure are joined to one another by two parallel links between individual C-60 units. In pure graphullerene structure, two single bonds originating from every C_{60} unit connect each linear chain to its neighbour. The whole pure graphullerene structure was hydrogenated as shown in figure1. The optimized parameters of pure graphullerene and H-graphullerene listed in table 1.

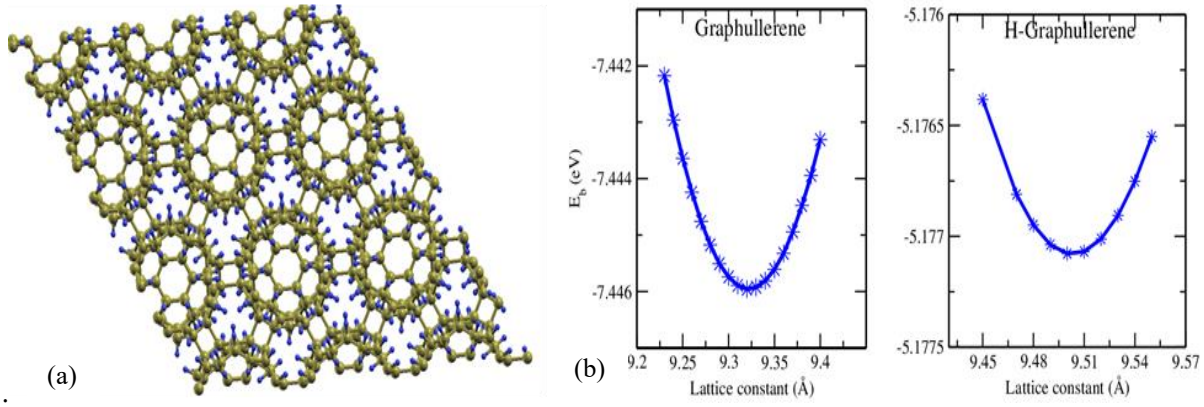


FIGURE 1: (a) Optimized Hydrogenated- Graphullerene structure formed by C60 graphullerene and (b) binding energy of optimized structure of graphullerene & hydrogen decorated graphullerene with lattice constants

TABLE 1: The optimized lattice parameter (a), binding energy (Eb), and band gap (Eg) were evaluated for both pristine and hydrogenated graphullerene

Systems	a (Å)	E_b (eV/atom)	E_g (eV)	b_{C-H} (Å)
Graphullerene	9.32[11]9.169)[4]	-7.44[11] (-8.564)[4]	0.92[11](I) (0.7 (I))[4]	--
H-graphullerene	9.50	-5.1812	2.74	1.11

From the above calculations, we observed that lattice constant of H-graphullerene (9.50Å) is more than graphullerene (9.32Å). Also, graphullerene optimized at higher value than H-graphullerene as shown in binding energy curves in figure 1(b). The average bond length of C-H bond in H-graphullerene is 1.11 Å. Since graphullerene is the first pure carbon two-dimensional semiconductor to be discovered [4], its electrical structure is significant for applications. Inspired from the study of graphullerene, we have utilised the GGA-PBE functional to compute the electronic band structure of H-graphullerene. The pure graphullerene has 0.92 eV indirect band gap (0.7eV reported [4]), which are advantageous for numerous applications. We have observed that the band gap of hydrogen decorated graphullerene increases to 2.74eV which is direct band gap material and lies in the visible region of electromagnetic spectrum. As a result, hydrogenated structures, like graphene, have a number of uses in applications in optoelectronics, energy storage and hydrogen storage devices [6-9].

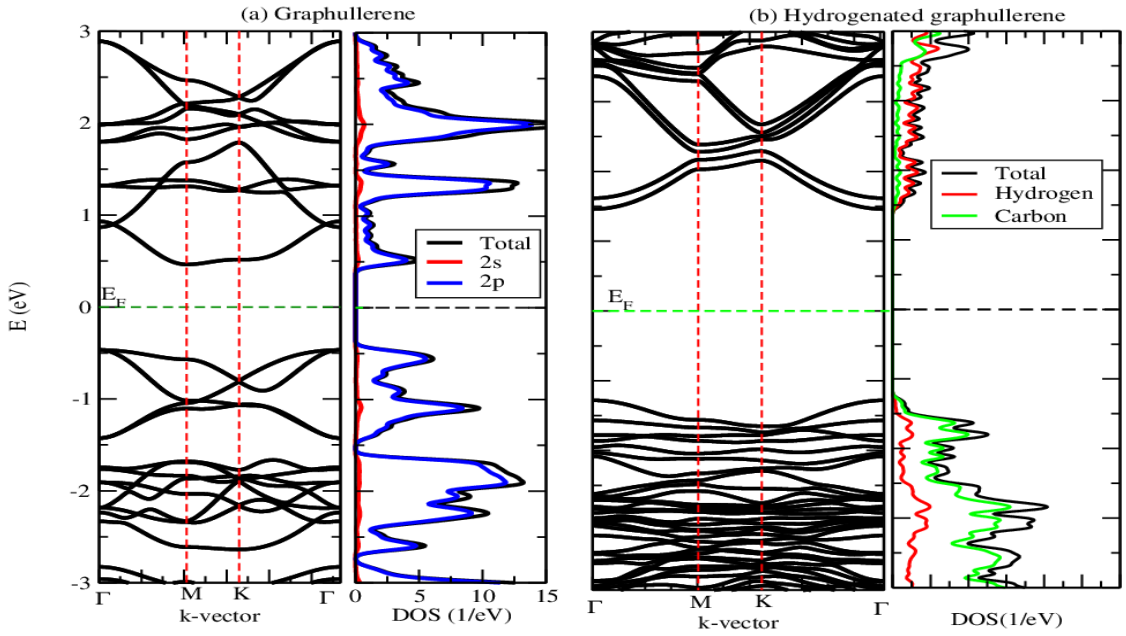


Figure 2: Electronic band structures and projected density of states (PDOS) for (a) pristine graphullerene and (b) hydrogen-functionalized graphullerene. The horizontal green dashed line represents the Fermi level (EF), while the vertical red dashed lines indicate the high-symmetry points in the Brillouin zone.

CONCLUSION

Hydrogen decorated graphullerene has a larger lattice constant and lower binding energy compared to graphullerene. Both graphullerene and its hydrogenated counterpart are a promising semiconducting materials due to their band gap. The band gap of graphullerene is increased significantly upon hydrogenation. Hydrogenated graphullerene (H-graphullerene) exhibits a direct band gap in the visible region. This property makes H-graphullerene a potential candidate for optoelectronic, energy storage and hydrogen storage applications.

REFERENCES

1) Iijima, S. Helical microtubules of graphitic carbon. *Nature*, 354, 56–58. (1991).
2) K. S. Novoselov and A. K. Geim, "The rise of graphene," *Rev. Mod. Phys.*, vol. 81, pp. 109–162, 2009
3) W. I. David, Nature **353**, 147–149 (1991).
4) U. Argaman and G. Makov, "Real-space analysis of charge transfer," *npj Comput. Mater.*, vol. 9, p. 211, 2023.
5) J. M. Soler *et al., J. Phys.: Condens. Matter*, vol. 14, p. 2745, 2022.
6) A. Z. AlZahran and G. P. Srivastava, Applied Surface Science **256**, 19, 2010, 5783-5788.
7) A. Devi, A. Kumar, A. Singh and P. K. Ahluwalia, AIP Conference Proceedings **2115,** 030386 (2019) .
8) S. E. Veras, E. Espada and G. Morell, Carbon Trends **15**, 100360 (2024).
9) A. Devi, A. Kumar, P. K. Ahluwalia A. Singh, Materials Science and Engineering: B **271,** 115237 (2021).
10) L. Yu, J. Xu, B. Peng, G. Qin, and G. Su, J. Phys. Chem. Lett. **13**, 11622–11629 (2022).
11) A. Devi, S. Kumar, A. Kumar J. Journal of Condensed Matter, **3,** 38-40(2025)

Investigation of structural, morphology, thermal, and magnetic properties of $Ni_{0.90}Cu_{0.10}Te_2$ single crystal

Rajkumar Sokkalingam [1] and Arumugam Sonachalam [1, 2, a)]

[1] *Centre for High Pressure Research, Department of Physics, Bharathidasan University, Tiruchirappalli-620 024, India.*
[2]*Tamil Nadu Open University, Chennai-600 015, India.*

[a)]Corresponding author: sarumugam1963@yahoo.com

Abstract. Transition Metal Dichalcogenides (TMDCs) are quasi-two-dimensional materials with notable structural and magnetic properties. Recent research has highlighted intriguing features in the $NiTe_2$ system, especially in TMDCs. In this study synthesized $Ni_{0.90}Cu_{0.10}Te_2$ was synthesized using the self-flex technique to explore the effects of Cu doping on $NiTe_2$'s structural, morphology, thermal, and magnetic properties. X-ray powder diffraction (XRPD) confirmed a trigonal structure with CdI2-type configuration and a *P*3*m*1 space group, validating the crystalline organization. Field emission scanning electron microscope (FESEM) imaging illustrated the layered structure due to Cu doping. Thermal analysis via thermogravimetry differential thermal analysis (TG/DTA) demonstrated stability up to 850 °C, with only a 2% weight loss between 850 and 1000 °C. Magnetization studies in a 1 T field showed paramagnetic behavior across 2 to 200 K temperatures. These findings indicate that Cu doping significantly enhances the magnetic properties of $NiTe_2$, making it suitable for magnetic device applications.

Keywords: Transition Metal Dichalcogenides (TMDCs), Doping, Structural analysis, Magnetic properties,

INTRODUCTION

The investigation into Transition Metal Dichalcogenides (TMDCs) has yielded significant results, identifying them as a novel class with properties that make them valuable for studying emerging physical phenomena [1]. Depending on their chemical compositions and structures, TMDCs can exhibit different types of behaviour like metallic, semi-metallic, semiconducting, insulating, superconducting, charge density wave, and topological phases [2]. TMDCs encompass a broad spectrum of chemical compositions, typically following the formula MX_2 (M = Mo, W, Zr, Pt, Pd, Ni; and X = Te, Se, S), attracting significant interest in condensed-matter physics [3]. The title compound has demonstrated a variety of properties in different applications. Notably, doping has produced unexpected results, such as the induction of superconductivity in single crystals of Re-doped type-II Weyl semimetal $NiTe_2$, with a maximum critical temperature (T_c) of 2.36 K achieved through Re substitution [4]. Additionally, Ti-doped single crystalline samples of $NiTe_2$ have exhibited superconducting properties with a critical temperature close to 4.0 K [5]. This material is highly suitable for electronic and electrical devices, including interconnects, conductive coatings, and electrodes.

EXPERIMENTAL DETAILS

To create the pure, single-crystalline $Ni_{0.90}Cu_{0.10}Te_2$ sample was synthesized by using the self-flux method [3]. XRPD measurements were conducted using a Rigaku X-ray diffractometer. For FESEM and EDS measurements, a Carl Zeiss SIGMA HV Bruker Quantax 200 - Z10 EDS Detector was utilized. Thermal (TG-DTA) characteristics were determined through DTG-60A. Temperature-dependent DC magnetization (M(T)) was measured in a physical property measurement system (PPMS) from Quantum Design, USA.

Results and Discussion

The crystal structural characteristics of $Ni_{0.90}Cu_{0.10}Te_2$ were elucidated using XRPD techniques. Figure 1 displays the crystal structure of $Ni_{0.90}Cu_{0.10}Te_2$. The refinement results of $Ni_{0.90}Cu_{0.10}Te_2$ show crystallizes in a CdI2-type trigonal structure with a *P*-3*m*1 space group. The strong XRPD peaks confirm the high-quality single-crystalline nature of the samples, aligning well with recent reports [3]. Rietveld refinements yield lattice parameters of a = 3.95351 Å, c = 5.42492 Å, and a cell volume V =73.433 Å, consistent with the literature [3].

We reported the investigation of the electrochemical properties of both host and doped compounds [3]. For the combined investigation, here we used the diffraction data as same from the published article [3]. Notably, diffraction planes shift towards higher angles, indicating an enhancement in sample crystallinity and confirming the doping [4]. The XRPD pattern of $Ni_{0.90}Cu_{0.10}Te_2$ indicates that no new peaks appear after the doping process. The shift of diffraction planes towards higher angles during doping is intricately linked to the material's properties. This observation suggests that there were no structural alterations during Cu doping, and the degree of crystalline structure remained unchanged throughout the substitution process. FESEM analysis revealed that $Ni_{0.90}Cu_{0.10}Te_2$ exhibited a layered pattern illustrated in Figure 2 (a), (b). The chemical stoichiometry of the as-grown samples was validated using the EDX spectrum (Figure 2 (c)), allowing the determination of the weight percentages of Ni, Te, and Cu within the $NiTe_2$ crystals. The compositions of all elements present in the grown crystals are outlined in Figure 2 (c) insert. As revealed by the TG-DTA investigation, $Ni_{0.90}Cu_{0.10}Te_2$ exhibited no weight loss up to 850°C, as depicted in Figure 3. This observation underscores the sample's remarkable thermal stability, suggesting its ability to withstand temperatures as high as 850°C without degradation. Notably, the endothermic characteristic observed in the DTA is likely linked to the sample's crystallization process, indicating that the sample undergoes a thermal transformation at temperatures higher than 300°C but below 850°C. A 2.5% weight loss was observed for each component, which may be attributed to the development of oxidation products in $Ni_{0.90}Cu_{0.10}Te_2$ [7]. The M (T) as a function of temperature is depicted in Figure 4. M (T) decreases relatively slowly with increasing temperature, from 1.3 x 10^{-5} at 2 K to 0.8 x 10^{-5} at 200 K, indicating very moderate temperature dependence. As a result, we suppose that, as in the case of $NiTe_2$, band electrons govern the magnetism [3]. The sample is paramagnetic across the full temperature range examined, with no evidence of diamagnetism for $Ni_{0.90}Cu_{0.10}Te_2$. However, below T ~ 15 K, magnetization rapidly increases. Between 200 K and 15 K, the reciprocal magnetization plot exposes the Curie-Weiss law. The obtained negative Curie temperature of -110 K signifies the antiferromagnetic coupling of local moments, which induces the magnetization upturn at low temperatures. However, no magnetic order is observed down to 2 K. The extracted Curie temperature is relatively smaller compared to $NiTe_2$ (-134) [3].

Conclusion

In conclusion, the structural analysis of $Ni_{0.90}Cu_{0.10}Te_2$ was elucidated using X-ray Powder Diffraction (XRPD) techniques, confirming its CdI2-type trigonal structure with a *P*-3*m*1 space group. FESEM confirmed the typical layered patterns in $Ni_{0.90}Cu_{0.10}Te_2$. EDX analysis corroborated the chemical stoichiometry of the samples, with a minimal chemical off-stoichiometry within 1%. Thermal analysis using Tg-DTA revealed the exceptional thermal stability of $Ni_{0.90}Cu_{0.10}Te_2$, which exhibited no weight loss up to 850°C. The magnetization (M) showed a moderate temperature dependence, and the sample exhibited paramagnetic behavior over the entire temperature range, with no evidence of diamagnetism for $Ni_{0.90}Cu_{0.10}Te_2$. These findings provide valuable insights into the structural, thermal, and physical characteristics of $Ni_{0.90}Cu_{0.10}Te_2$, laying the foundation for further exploration of its unique properties and potential applications.

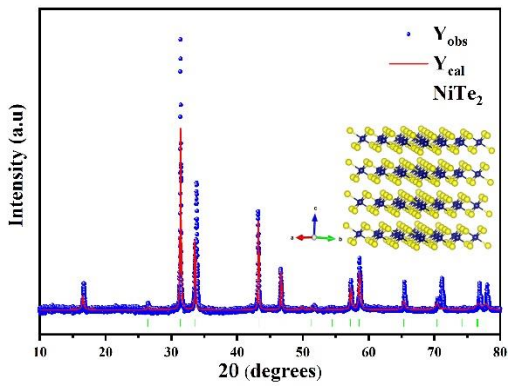


Figure 1. X-ray Powder diffraction pattern together with results of the Rietveld refinement for $Ni_{0.90}Cu_{0.10}Te_2$ and the insert shows the crystal structure of $Ni_{0.90}Cu_{0.10}Te_2$.

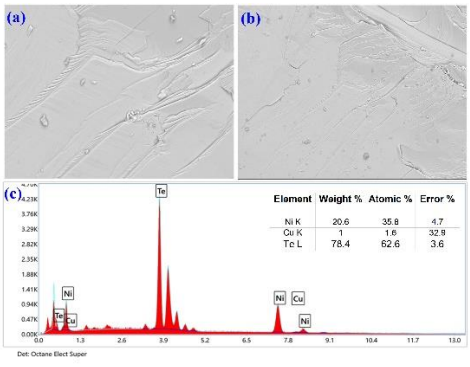


Figure 2. (a), (b) show a FESEM image of $Ni_{0.90}Cu_{0.10}Te_2$, (c) the EDX spectrum of the $Ni_{0.90}Cu_{0.10}Te_2$.

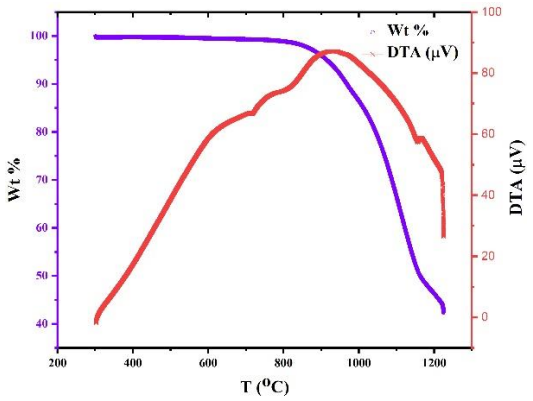


Figure 3. TG-DTA studies of $Ni_{0.90}Cu_{0.10}Te_2$

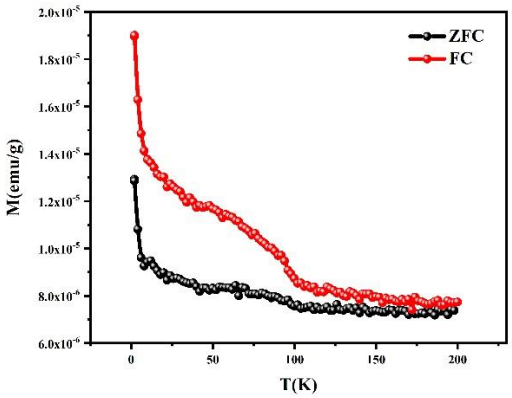


Figure 4. Temperature-dependent magnetization of $Ni_{0.90}Cu_{0.10}Te_2$.

ACKNOWLEDGMENTS

AS wishes to thank DST (MES and SERB), UGC-DAE-CSR (Indore), MHRD-RUSA 2.0, and Indo-Poland for financial support.

REFERENCES

1. Manzeli, S., Ovchinnikov, D., Pasquier, D. *et al*, *Nat Rev Mater* **2**, 17033 (2017).
2. Tomojit Chowdhury, Erick C. Sadler, and Thomas J. Kempa, c*hem. Rev.* 120, 22, 12563–12591 (2020)
3. Sokkalingam, Rajkumar, Manikandan Krishnan, Jesman Sthevan Kovil Pitchai, Sivakumar Periyasamy, Arjun Kumar Bojarajan, Arumugam Sonachalam, and Sambasivam Sangaraju. *Electrochemistry Communications* 171:107872 (2025).
4. Feipeng Zheng , Xi-Bo Li, Peng Tan, Yiping Lin, Lingxiao Xiong, Xiaobo Chen, Ji Feng, *Physical Review B*101, 100505 (R) (2020).
5. Mandal, Manasi, and R. P. Singh, *Journal of Physics: Condensed Matter* 33, no. 13:135602 (2020).
6. B.S.de Lima, R.R.deCassia, F.B.Santos, L.E.Correa, T.W.Grant, A.L.R.Manesco, G.W.Martins, L.T.F.Eleno, M.S.Torikachvili, A.J.S.Machado, *Solid State Communications* 283, 27-31 (2018).
7. Kavirajan, S., J. Archana, S. Harish, M. Navaneethan, S. Ponnusamy, K. Hayakawa, Y. Kubota, M. Shimomura, and Y. Hayakawa, *CrystEngComm* 22, no. 46 :8100-8109 (2020).

First-Principles Study of Optoelectronic and Photocatalytic Properties of Two-Dimensional AlAs/SbI_3 van der Waals Heterostructure

Ramandeep Singh, Poonam Chauhan, and Ashok Kumar*

Department of Physics, Central University of Punjab, Bathinda, Punjab, India 151401
**Corresponding author: ashokphy@cup.edu.in*

Abstract: Using first-principles calculations, we investigated the optoelectronic and photocatalytic properties of a two-dimensional (2D) AlAs/SbI_3 van der Waals (vdW) heterostructure. The thermal stability of AlAs/SbI_3 is characterized in terms of *ab initio* molecular dynamics (AIMD) simulations, which indicates it is highly suitable for practical implementation in experiments. The AlAs/SbI_3 heterostructure possesses an indirect bandgap having a value of 1.63 eV (1.19 eV) at the HSE06 (PBE) level of theory, with optical absorption spectra lying in the visible region. Furthermore, the AlAs/SbI_3 heterostructure properly engulfs the redox potential of water with a type-II scheme. Thus, due to its semiconducting nature, visible region absorption spectra and proper band alignment make AlAs/SbI_3 a promising candidate for futuristic optoelectronic and photocatalytic water splitting fields.

Keywords: First-Principles Study, Thermal stability, Type-II band alignment, Optoelectronic, Photocatalytic activity.

INTRODUCTION

Photocatalytic water splitting is a promising method to overcome the energy crisis and environmental pollution problems by utilizing solar energy. In recent years, the exciting properties of 2D compounds as compared to their bulk counterparts have attracted researchers' attention. 2D materials like graphene, transition metal dichalcogenides (TMDs), and M-Xenes exhibit large surface-to-volume ratios, ultrathin structures, and enhanced carrier mobilities [1]. The high carrier recombination rate and narrow optical absorption limit the use of 2D materials as photocatalysts for water splitting. Whereas the 2D van der Waals (vdW) heterostructures can overcome the limitation of 2D monolayers for water splitting. To evaluate the staggered arrangement of valence band maximum (VBM) and conduction band minimum (CBM) of each monolayer in conjunction with the built-in electric field (EF) in vdW heterostructures, the type-II photocatalytic mechanisms play a significant role. Very recently, the SbI_3 and AlAs monolayers have been experimentally synthesized using the droplet method and molecular beam epitaxy (MBE) [2-3]. SbI_3 belongs to the MX_3 type (e.g, ScI_3, YBr_3, AsI_3, SbI_3) crystal structure, which exhibits intriguing physical properties [4]. On the other hand, AlAs, a notable III-V semiconductor, is known for its high absorption coefficients, electron mobility, and wide bandgap, making it a strong candidate for optoelectronic and photovoltaic applications. The type-II vdW heterostructures enhance photocatalytic performance by modulating band gaps for better light absorption and spatially separating photogenerated carriers to reduce recombination. Motivated by the experimental synthesis of AlAs and SbI_3 monolayers, we have explored the optoelectronic and photocatalytic characteristics of 2D AlAs/SbI_3 vdW heterostructure using first-principles calculations.

COMPUTATIONAL METHOD

The optoelectronic and photocatalytic characteristics of AlAs/SbI_3 vdW heterostructure were carried out using Vienna Ab Initio Simulation Package (VASP), which is based on density functional theory (DFT) [6]. We employed the generalized gradient approximation (GGA) using Perdew-Burke-Ernzerhof (PBE) functional and Heyd-Scuseria-Wrnzerhof (HSE06) parameterization method for the exchange and correlation [7]. We also utilized the DFT-D3 method to address the weak vdW interactions at the heterostructure interface [8]. We employed a plane-wave cutoff energy of 500 eV to ensure simulation accuracy. Geometry optimizations were performed for the vdW heterostructures and their corresponding layers until the forces on each atom were below 0.01 eV/Å. The energy convergence criterion was set at 10^{-5} eV. The thermal stability of the studied heterostructure has been validated by AIMD simulations at room temperature, employing a time step of 5 ps within a 2x2x1 supercell. A vacuum spacing of approximately 25Å was incorporated along the z-direction to

prevent spurious interactions during the heterostructure formation. For optical property calculations, a denser 60x60x1 k-point grid is used.

RESULTS AND DISCUSSION

Geometrical structure and electronic properties

The AlAs and SbI_3 monolayers possess a hexagonal unit cell. Their lattice parameters (a/b= 4.00 Å for AlAs; and a/b = 7.65 Å for SbI_3) are consistent with the literature [8]. The band structure calculations show that both AlAs and SbI_3 monolayers are indirect bandgap semiconductors, having bandgap values of 1.92 eV (1.27 eV) and 2.82 eV (2.22 eV) at the HSE06 (GGA) level of theory, respectively. The AlAs/SbI_3 heterostructure contains 24 atoms with a (4%) lattice mismatch in the hexagonal unit cell. Four different types of stacking patterns (H_1, H_2, H_3, and H_4) are considered, out of which H_1 stacking is more stable to achieve excellent stability, as illustrated in Fig. 1(A-H). The energetic stability of AlAs/SbI_3 heterostructure is characterized in terms of the binding energies (E_b) which is calculated as: $E_b=E_{AlAs/SbI3}-E_{AlAs}-E_{SbI3}$, Where $E_{AlAs/SbI3)}$ represents the total energy of the heterostructure, and E_{AlAs} and E_{SbI3} correspond to the total energies of the freestanding AlAs and SbI_3 layers, respectively. The H_1-stacking exhibited the lowest binding energy of approximately (-0.70eV), comparable to AlSb/ZrS_2 (-0.693eV) vdW heterostructure, which is the most energetically favorable [9].

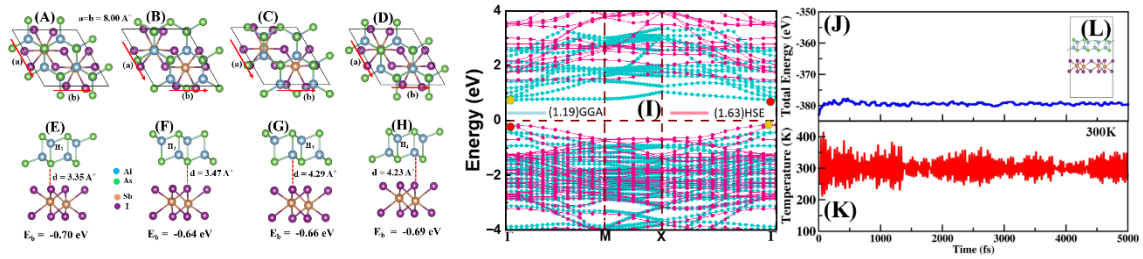


FIGURE 1: (A-D) Top and (E-H) side view of the optimized structures of stacking patterns (H_1, H_2, H_3 and H_4) of the AlAs/SbI_3 vdW heterostructure. (I) The band structure of the AlAs/SbI_3 vdW heterostructure corresponds to the functional GGA and HSE06. (J-K) The fluctuations of energy and temperature during the (AIMD) simulations at room temperature for the H_1 AlAs/SbI_3 vdW heterostructure. (L) The final structure after 5000 fs is shown in the inset.

Further, we analyzed the thermal stability of a 2x2x1 supercell of AlAs/SbI_3 heterostructures (H_1) using (AIMD) simulations at 300K. The results in Fig. 1(J-L) indicate that the atomic structure remained undistorted with minimal fluctuations in total energy and temperature over 5000 fs at 300K. Notably, the AlAs/SbI_3 vdW heterostructure displays an indirect bandgap of 1.19 eV (PBE) and 1.63 eV (HSE06), smaller than the constituent monolayer.

Optical and photocatalytic properties

Next, the optical properties of AlAs/SbI_3 heterostructure is investigated by using the random phase approximation method in terms of optical absorption spectra. The optical absorption A (ω) is calculated by using the imaginary part of the dielectric function, which is given as:

$$A(\omega) = \frac{\omega}{c}\boldsymbol{\varepsilon_i}(\boldsymbol{\omega}) \qquad [1]$$

Where (L) and $\boldsymbol{\varepsilon_i}$ represents the length of the cell in the z-axis and the imaginary part of the dielectric function. The most prominent peak of 2D AlAs and SbI_3 monolayers and the AlAs/SbI_3 vdW heterostructure lies in the visible region Fig. 2(A). The electrostatic potential of the AlAs/SbI_3 heterostructure is depicted in Fig. 2(B).

We explored the photocatalytic properties of the AlAs and SbI_3 monolayer and their corresponding heterostructure. The band alignment of both monolayers, AlAs, SbI_3, and AlAs/SbI_3 vdW heterostructure, are presented in Fig. 2(C). By examining the band edge alignment relative to the reduction potential (H^+/H_2) and the oxidation potential ($E_{H2O/O2}$) of water, which are -4.44 and -5.67 eV, respectively. We found that the highest energy level of AlAs aligns with the lowest energy level of SbI_3. This alignment implies that the energy level of the

heterostructure spans the water oxidation and reduction potential at pH = 0. Thus, the AlAs/SbI_3 vdW heterostructure is an excellent candidate for water decomposition. The heterostructure exhibits significantly higher optical absorption intensities within the visible light spectrum, suggesting a substantial enhancement in sunlight absorption efficiency.

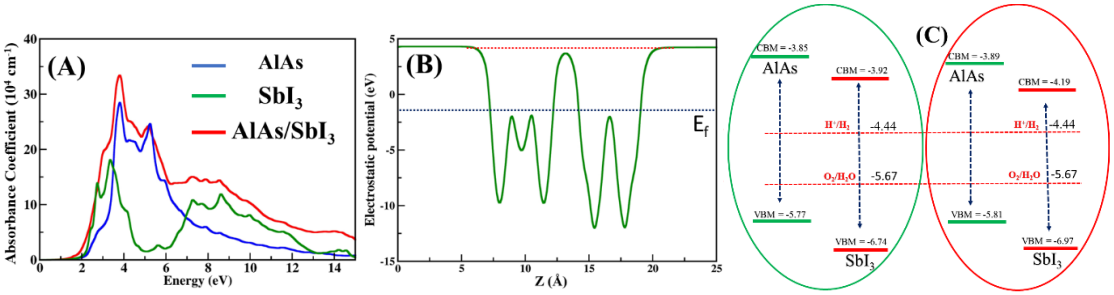


FIGURE 2. (A) Optical absorption spectra of monolayer AlAs, SbI_3 and AlAs/SbI_3 heterostructure. (B) Represents the average electrostatic potential along the z-axis of the AlAs/SbI_3 vdW heterostructure. (C) Band alignment of AlAs/SbI_3 heterostructure corresponding to constituent monolayer before and after contact in the heterostructure.

CONCLUSIONS

In conclusion, we explored the optoelectronic and photocatalytic properties of the AlAs/SbI_3 vdW heterostructure using first-principles calculations. The dynamical stability of the studied heterostructure is explored in terms of AIMD simulation. The AlAs/SbI_3 vdW heterostructure possesses an indirect bandgap semiconductor nature with an optical absorption peak lying in the visible region. The AlAs/SbI_3 vdW heterostructure properly engulfs the redox potential of water, which makes it a potential candidate for optoelectronic and photocatalytic water splitting fields.

ACKNOWLEDGEMENTS

RS and PC acknowledge the financial assistance from the UGC in the form of a junior research fellowship (JRF) and CSIR in the form of a senior research fellowship (SRF), respectively. The computational facility at the Department of Physics at the Central University of Punjab is used to obtain the results presented in this paper. Helpful discussions with Nidhi Verma is highly acknowledged.

REFERENCES

1. Xie, M., Li, Y., Liu, X., & Li, X. A. Applied Surface Science, **591**, 153198 (2022).
2. Tang, J., Ge, F., Chen, J., Zhou, D., Zhan, G., Liu, J., & Wang, L. *Small*, *19*(43), 2301573 (2023).
3. Fleming, R. M., McWhan, D. B., Gossard, A. C., Wiegmann, W., & Logan, R. A., *Journal of Applied Physics*, *51*(1), 357-363 (1980).
4. Liu, P., Lu, F., Wu, M., Luo, X., Cheng, Y., Wang, X. W. & Cho, K. (2017). *Journal of Materials Chemistry C*, *5*(35), 9066-9071 (2017).
5. Kresse, G., & Furthmüller, J. (1996). Physical review B, 54(16), 11169 (1996).
6. Heyd, J., Scuseria, G. E., & Ernzerhof, M. (2003). The Journal of chemical physics, 118(18), 8207-8215 (2003).
7. Faraji, M., Bafekry, A., Fadlallah, M. M., Jappor, H. R., Nguyen, C. V., & Ghergherehchi, M. (2022). *Applied Surface Science*, *590*, 152998 (2022).
8. Grimme, S., Antony, J., Ehrlich, S., & Krieg, H. *The Journal of chemical physics*, *132*(15) (2010).
9. Luan, L., Han, L., Zhang, D., Bai, K., Sun, K., Xu, C. & Duan, L. *International Journal of Hydrogen Energy*, *51*, 1242-1255 (2024).

Tunable Electronic Properties of Dirac Cone Square Tellurene(σ-Te_2)

Ritika Rani[1,3,a)], Ankush Bharti[1, 2] , Narender Paul[4] and Raman Sharma[1]

[1]Department of Physics, Himachal Pradesh University, Shimla, Himachal Pradesh, India, 171005.
[2]Rajiv Gandhi Govt. Polytechnic Banikhet, Chamba, Himachal Pradesh, India, 176303.
[3]Govt. College Daulatpur Chowk, Una, Himachal Pradesh, India, 177204.
[4]Govt. Degree College Ani, Kullu, Himachal Pradesh, India,172026.

[a)]rriti834@gmail.com

Abstract. In this study, we conduct first principles calculations using density functional theory on σ-Tellurene (σ-Te_2). σ-Tellurene is characterized as a Dirac cone material with a Fermi velocity of 9.4×10^5 m/s^{-1}. However, its lack of a band gap limits its utility in conventional electronics. Our work aims to induce a band gap by applying strain and introducing spin-orbit coupling (SOC) effects. Our findings demonstrate that biaxial strain in conjunction with SOC effectively modulates the band gap, resulting in a significant band gap opening (~0.3 eV) at a biaxial strain of 6%. Importantly, the Dirac cone structure remains preserved. A Dirac cone with a narrow band gap holds promising potential for future applications in electronics, electrochemical devices, strain sensors and beyond.

INTRODUCTION

A 2D monolayer of tellurium [1,2] initiates a breakthrough and establishes a new direction for elemental 2D materials in Group VI[3,6]. Our previous research identifies six allotropes of tellurene in both pristine and Janus forms, designated as α-Te, β-Te, γ-Te, δ-Te, η-Te, and σ-Te [4]. Among these σ-Te exhibits a distinctive Dirac cone along the Γ-M_1 path in the Brillouin zone. In this study, we selected the σ-Te allotrope for investigation due to Dirac cone characteristic leading to high conductivity like graphene. Previous studies on two-dimensional (2D) materials have demonstrated various approaches to modulate band gaps, the application of external strain being one of the most effective one. In present study, we investigate the effect of biaxial tensile strain on the electronic properties of a σ-Tellurene monolayer. We successfully demonstrate that the Dirac cone bifurcates along the Γ-M_1 path, yielding a narrow band gap while retaining its fundamental Dirac cone attributes under strain and spin-orbit coupling (SOC) effects. Moreover, the band gap is adjustable through the application of biaxial tensile strain.

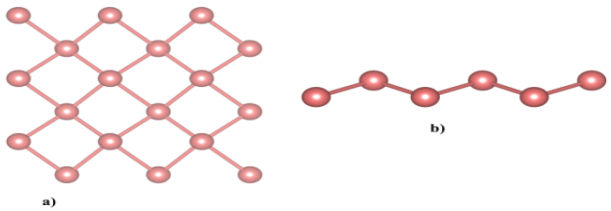


FIGURE 1. a) and b) Top and Side view of optimized σ-Tellurene Phase.

SIMULATION DETAILS

The structural optimization and electronic structure calculations were based on density functional theory (DFT) as implemented in a Vienna ab-initio Simulation Package (VASP). The exchange-correlation energies were treated using GGA-PBE functional. The plane wave cut-off energy of 400 eV has been used. The atomic positions were fully optimized until the forces on all atoms were less than 10^{-6} eV/Å. The energy convergence criteria was

set to 10^{-4} eV/cell. We adopt a 15 × 15 × 1 grid of k-mesh for Brillouin zone integration. To mimic 2D system, we have created a vacuum space of ~20 Å along the z-direction.

Results and Discussions

σ-Tellurene exhibits a chair-like buckled structure akin to X-enes (X=Si, Ge), but with a square lattice rather than hexagonal. We examined the structural and electronic properties of σ-Tellurene with tensile and compressional strain. The strain 'ε' is defined as ($\varepsilon = \frac{l-l_0}{l_0}$), l_0 is unstrained lattice constant. Optimized lattice constant (unstrained) of square-Te is 4.11 Å. The calculated values of Te-Te bond lengths(d) and intralayer X–X vertical distances(h) for unstrained square-Te are shown in Table 1. It is evident that strain influences both bond lengths and vertical distances. Tensile strains elongate the Te-Te bond lengths, while compressive strains shorten them. Vertical X–X distances are decreased by in-plane tensile strains and increased by compressive strains.

Electronic Properties

The structural changes significantly impact the electronic properties of σ-Tellurene. The band gap in the Dirac cone-like structure of σ-Tellurene increases linearly under both tensile and compressive strains. For σ-Tellurene, the spin-orbit coupling (SOC) notably alters the electronic dispersion. Previous studies report band gap opening of magnitude (*Eg*=0.13 eV) along Γ-M_1 path[3]. Our results are consistent (see Table 1) with previous studies and we further demonstrate that the band gap with SOC can be effectively tuned by biaxial strain. Significant band gap opening (*Eg*=0.26 eV) occurs at 6% tensile strain. The sizes of these band gaps are comparable to those of X-enes. The bi-axial strain effectively alters the orbital hybridization and the degree of electron re-distribution. Hence the change in electronic structure of the strained systems.

To gauge the structural stability of equilibrium geometries, formation energy has been calculated as follows:

$$E_f = \frac{1}{2m}\left[E_{\mathrm{Te}_{n-1}X_{n-1}} - \left(E_{\mathrm{Te}_{n-1}} + \mathrm{E}_{X_{n-1}}\right)\right]$$

Here n = 2 and m = 1 for σ-Tellurene. $E_{\mathrm{Te}_{n-1}X_{n-1}}$ = Total energy of the composite system, $E_{\mathrm{Te}_{n-1}}$ and $\mathrm{E}_{X_{n-1}}$ = total energy of first and second Tellurene atom respectively. Negative values of $\mathrm{E_f}$ indicate the exothermic nature of formation (see Table1).

TABLE 1. Structural parameters i.e Intralayer distance (h), Bond length(d) of σ-Tellurene unstrained, under tensile and compressional strain. Values in parentheses are for compressive strain; values outside parentheses are for tensile strain.

System	Strain(%)	h (Å) (PBE)	(d) (Å) (PBE)	E_g(eV) (PBE)	E_g(eV) (PBE+SOC)	E_f (eV)/atom
σ-Tellurene	0	0.90	3.20	0.0[a,b]	0.13[b]	-3.36
	1	0.89(0.92)	3.27 (3.13)	0.01(0.03)	0.14 (0.05)	-3.45 (-3.28)
	2	0.87(0.94)	3.32 (3.10)	0.01(0.04)	0.18 (0.09)	-3.57 (-3.09)
	3	0.85(0.97)	3.36 (3.06)	0.02(0.03)	0.20(0.06)	-3.65(-2.98)
	4	0.83 (1.00)	3.45 (3.03)	0.03(0.05)	0.22 (0.07)	-3.73 (-2.77)
	6	0.82 (1.06)	3.58 (2.97)	0(0.01)	0.26 (0.07)	-3.86 (-2.37)

[a]Ref [4], [b]Ref[3]

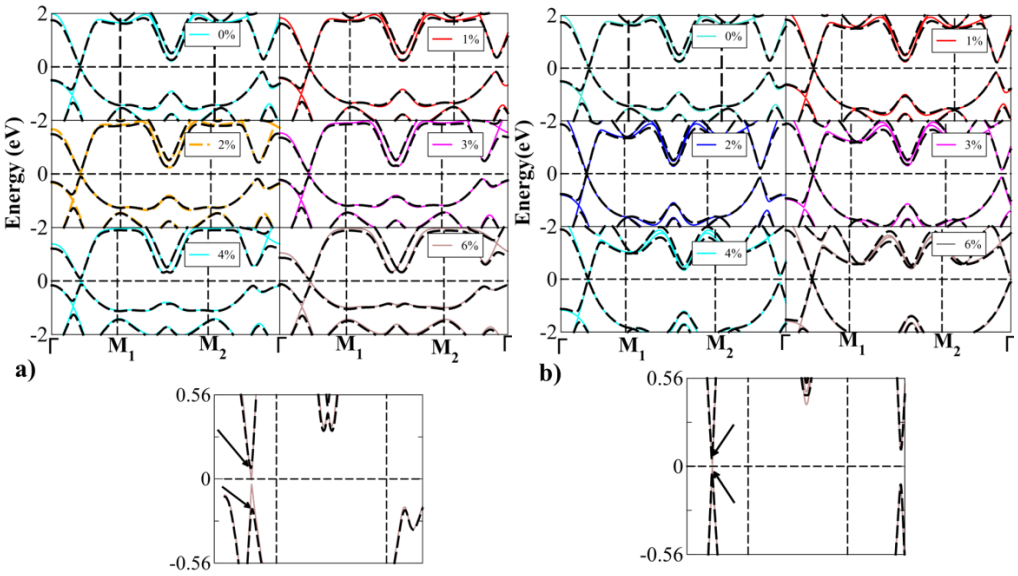


FIGURE 2. Band structure of σ-Tellurene under a) tensile strain and b) compressional strain along with their insets using GGA-PBE functional. Here solid lines show PBE results and dotted one with PBE+SOC functionals.

CONCLUSIONS

Strain-dependent structural and electronic properties have been investigated using density functional theory(DFT). The band gap increases under biaxial strain, transitioning σ-Tellurene from metallic to semiconducting. The Dirac cone-like feature of σ-Tellurene remains preserved with and without strain. However, with PBE+SOC, a band gap opens along Γ-M_1 path. The band gap with PBE+SOC is found to be tunable with strain.This Dirac cone-like material, characterized by a narrow band gap, exhibits promising applications in high-speed electronics, quantum computing, and advanced photovoltaic technologies.

ACKNOWLEDGMENTS

We acknowledge the C V RAMAN and Param Shavak high performance computing facility at Physics Department, Himachal Pradesh University, Shimla, used to obtain the results presented in this work. We also acknowledge National Supercomputing Mission (NSM) for providing computing resources of 'PARAM Siddhi-AI', under National PARAM Supercomputing Facility (NPSF), C-DAC, Pune and supported by the Ministry of Electronics and Information Technology (MeitY) and Department of Science and Technology (DST), Government of India.

REFERENCES

1. Chen, J., et al., *Ultrathin β-tellurium layers grown on highly oriented pyrolytic graphite by molecular-beam epitaxy*. Nanoscale, 2017. **9**(41): p. 15945-15948.
2. Wu, W., et al., *Tellurene: its physical properties, scalable nanomanufacturing, and device applications.* Chemical Society Reviews, 2018. **47**(19): p. 7203-7212.
3. Xian, L., et al., *Square selenene and tellurene: novel group VI elemental 2D materials with nontrivial topological properties.* 2D Materials, 2017. **4**(4): p. 041003.
4. Rani, R., M. Sharma, and R. Sharma, *Optical anisotropy in bare and janus tellurene allotropes from ultraviolet to visible region: A first principle study.* Materials Science and Engineering: B, 2021. **265**: p. 115014.
5. Roldán, R., et al., *Strain engineering in semiconducting two-dimensional crystals.* Journal of Physics: Condensed Matter, 2015. **27**(31): p. 313201.

Two-dimensional van der Waals Electrical Contact of Janus MoSSe with Dirac Semi-Metal FeB_2 Monolayer

Ankush Bharti[1,3, a)], Ritika Rani [1], Jaspreet Singh[2], Ashok Kumar[4], Rakesh Rathore[5] and Raman Sharma [1]

[1]Department of Physics, Himachal Pradesh University (HPU), Shimla, Himachal Pradesh, India.
[2]Department of Applied Science, Guru Nanak Dev Engineering College(GNDEC), Ludhiana, 141006.
[3]Rajiv Gandhi Govt. Polytechnic Banikhet, Chamba, Himachal Pradesh, India, 176303.
[4]Department of Physics, School of Basic Sciences, Central University of Punjab, Bathinda -151401.
[5]Govt. Degree College, Sultanpur, Chamba, Himachal Pradesh, India-176314.

[a)]ankush_bharti@ymail.com

Abstract. In this study, we investigate the structural and electronic properties of a 2D Dirac semi-metal, FeB_2 atop a Janus MoSSe monolayer. The individual characteristics of the layers are well-preserved in the van der Waals (vdW) heterostructure (MoSSe/FeB_2). Notably, a low Schottky Barrier Height (SBH) (~ 0.6 eV) is achieved. Additionally, we demonstrate that an external electric field can tune the band alignment of MoSSe with respect to the Dirac cone of FeB_2. At an electric field of around 1 V/Å, the contact transitions to Ohmic, facilitating control over the SBH. This study identifies the MoSSe/FeB_2 system as a promising candidate for future nano-devices based on vdW materials.

INTRODUCTION

2D van der Waals heterostructure (vdWH) materials show great promise for advanced nano-scale multifunctional future devices. Lack of dangling bonds, interface coupling effects, absence of gap states, stacking sequence, Moiré pattern (twist angle) etc. provide versatile platform to tailor their properties and functionalities. The challenges to realize these properties in devices are: defects due to reaction with air and moisture, technical difficulties in doping, contact resistance (R_c) causing low mobility etc[1]. Present work addresses the issue of contact resistance (R_c) by DFT study of Janus MoSSe monolayer contacted vertically by metal electrode- FeB_2. Significantly low SBH = 0.58 eV is found for MoSSe/FeB_2 Schottky contact. The Schottky contact is n-type and can further be tuned by external electric field(E_f). Transverse E_f = 0.8 and 1.0 V/Ang turns the Schottky contact into Ohmic. Therefore SBH can be controlled by E_f which is essential for excellent device functionalities [3].

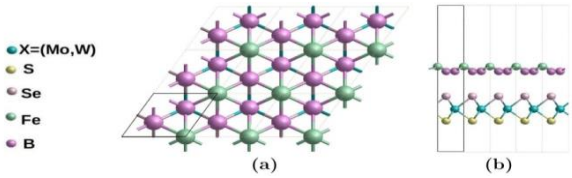


FIGURE 1. (a) Top and (b) side view of Optimized vdW heterostructure MoSSe/FeB_2 .

COMPUTATIONAL DETAILS

A first principle calculations incorporated with Density functional theory (DFT) are performed using SIESTA package. Structural and electronic properties are evaluated using GGA(PBE) exchange-correlation functional while for heterostructure, DRSLL(vdW) functional is used. A double-zeta polarization (DZP) basis set is used for all calculations. Atomic positions were relaxed until forces are less than 10^{-3} eV/Å. The kinetic energy cut-off is taken to be 300 eV. For k-point sampling, Monkhorst-Pack scheme with a k-mesh of 15×15×1 is used. A vacuum of 20 Å is kept to avoid superficial interactions between the neighboring layers.

RESULTS AND DISCUSSIONS

Optimized properties of monolayers/hetero-layer are shown in Table 1. Sum of covalent radii of nearest Se and B atom is 2.02 Å while inter layer distance is 3.42Å confirming the vdW interaction between layers. Binding energy is calculated as $E_B = \left[E_{(MoSSe/FeB_2)} - \left(E_{(MoSSe)} + E_{(FeB_2)}\right)\right]/N$, N is no. of atoms in the cell[4]. The calculated elastic constants (Voigt notation) C_{11}=207.77, C_{22}= 205.74, C_{12}=73.27, C_{66}=67.09 satisfy the Born stability criteria viz. $C_{11}C_{22}$-C_{12}^2>0 and C_{66}> 0. Negative binding energy (E_B), small lattice mismatch (**ε**) coupled with excellent mechanical properties (see Table 1) favors stability and experimental realization of our heterosystem.

TABLE 1. Optimized Geometrical, Mechanical and Electronic parameters of MoSSe, FeB_2 monolayers and MoSSe/FeB_2 vdWH.

Monolayers				**Hetero system**	**a=b(Å)**	**E_B(eV/atom)**	**Young's Modulus(GPa)**	
System	**Method**	**a=b(Å)**	**E_g(eV)**		3.25	-41.75	X	Y
							180.2857	184.6377
MoSSe	PBE	3.22	1.56	**$MoSSe/FeB_2$**	**ε(%)**	**ϕ_n(eV)**	**Poisson Ratios**	
FeB_2	PBE	3.17	0		1.55	0.58	XY	YX
							0.3567	0.3483

Electronic Properties

Electronic properties of monolayers are well preserved in vdW system(Fig2). For in-plane current device(like FET), band bending will happen from MoSSe/FeB_2 (source region) to MoSSe (channel) and is calculated as $\Delta E_f = W - W_M$, where W,W_M= work function of hetero-system and MoSSe layer respectively. ΔE_f= -0.2 (<0) indicates transfer of electrons from MoSSe/FeB_2 to MoSSe making the channel n-type. If FeB_2 is used as metal contact and MoSSe as channel, SBH plays significant role.

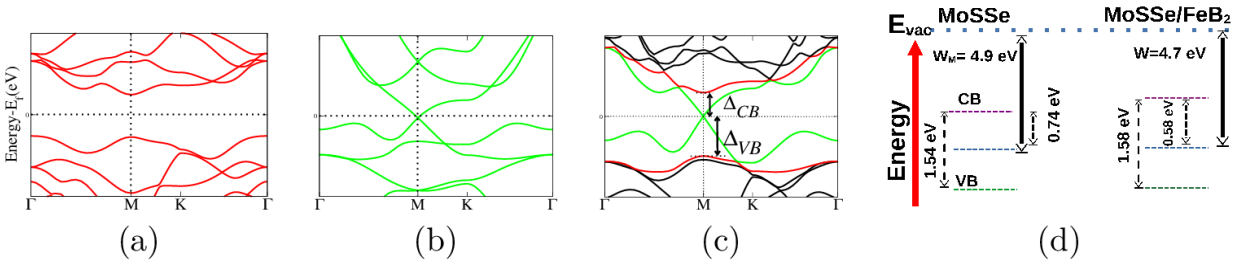


FIGURE 2. Electronic Structure of (a) Janus MoSSe monolayer (b) Dirac-semimetal FeB_2monolayer (c) MoSSe/FeB_2 vdWH (d) band edges of MoSSe and MoSSe/FeB_2. CB and VB are conduction and valence band. W_M is work function of MoSSe and W is work function of MoSSe/FeB_2. All values aligned w.r.t. vacuum level.

We determine SBH by Schottky-Mott rule i.e. $\phi_n = E_{CBM} - E_f$and $\phi_p = E_f - E_{VBM}$[2]. For MoSSe/FeB_2, n-type SBH(ϕ_n)= 0.58 eV and p-type SBH(ϕ_p)= 1eV is found. So, Schottky contact is n-type and conduction will be through electrons. If ϕ_n is reduced to zero, contact will turn to Ohmic. Toward this end, we use transverse electric field to tune the electronic structure. Figure3 shows evolution of band edges ΔCB and ΔVB as function of electric field relative to Dirac cone of FeB_2. At E_f= 0 V/Å, conduction band is close to Fermi-level(FL) leading to n-type Schottky contact.

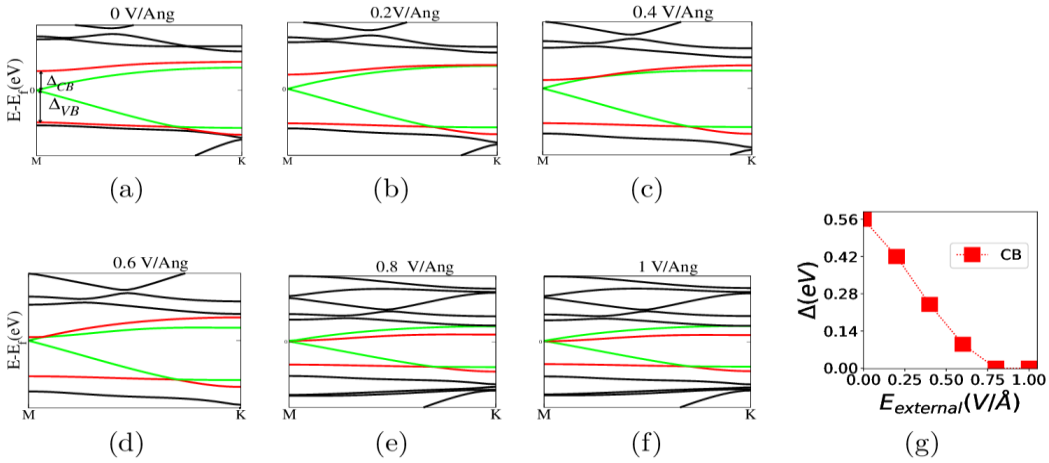


FIGURE 3. (a) to (f) Evolution of band structure as a function of external electric field. (g) Evolution of conduction band edge (CB) of MoSSe (w.r.t Dirac cone of FeB_2)as a function of Electric field . Red (green) colored bands are representing CBM (VBM) of MoSSe and FeB_2.

As the applied positive electric field intensifies, the conduction band offset systematically shifts towards the Fermi level, resulting in a progressive reduction of the Schottky barrier height **(ϕ_n).** This shift continues until the conduction band aligns with the Dirac cone at an electric field strength of 0.8 V/Å and 1 V/Å, thereby transforming the contact into an Ohmic contact. The application of the electric field induces a shift in the Fermi level, which disrupts the system's equilibrium. In the process of re-establishing equilibrium, the band edges undergo reorganization, leading to a modification in the Schottky barrier height (SBH).

CONCLUSIONS

In conclusion, we study the properties of a FeB_2 semi-metal layer atop a Janus MoSSe semiconductor layer. The properties of both layers are preserved in the van der Waals hetero-system. An external electric field tunes the conduction band of MoSSe relative to FeB_2, resulting in a reduction of n-type Schottky barrier. Consequently, we achieve control over the Schottky barrier height, which is essential for designing multifunctional van der Waals devices.

ACKNOWLEDGMENTS

We acknowledge National Supercomputing Mission (NSM) for providing computing resources of 'PARAM Siddhi-AI', under National PARAM Supercomputing Facility (NPSF), C-DAC, Pune and supported by the Ministry of Electronics and Information Technology (MeitY) and Department of Science and Technology (DST), Government of India and Param Shavak HPC facility at Physics Department, HPU, Shimla.

REFERENCES

1. Liu, X., Choi, M. S., Hwang, E., Yoo, W. J., & Sun, J. (2022),*Advanced Materials*, *34*(15), 2108425..
2. Singh, J. and Kumar, A., 2023. First principles study of 2D ring-Te and its electrical contact with a topological Dirac semimetal. *Nanoscale*, *15*(11), pp.5360-5370.
3. Padilha, J. E., Fazzio, A., & da Silva, A. J. (2015). van der Waals heterostructure of phosphorene and graphene: tuning the Schottky barrier and doping by electrostatic gating. *Physical review letters*, *114*(6), 066803..
4. Cao, Liemao, et al. "Two-dimensional van der Waals electrical contact to monolayer MoSi2N4."*Applied Physics Letters* 118.1 (2021).
5. Sachs, B., et al. "Doping mechanisms in graphene-MoS2 hybrids."*Applied Physics Letters* 103.25 (2013).

Electron and Phonon Hydrodynamics in Graphene

Subhalaxmi Nayak *, Cho Win Aung, Thandar Zaw Win,
Ashutosh Dwibedi, Sabyasachi Ghosh, Sesha Vempati

(*Department of Physics, Indian Institute of Technology Bhilai, Kutelabhata, Durg, Chhattisgarh,491002, India.)*

* *Email: subhalaxmin@iitbhilai.ac.in*

Abstract:

Phonons, the quantized modes of lattice vibrations, can be treated as quasiparticles and exhibit hydrodynamic behavior under conditions of low frequency and long wavelength. Phonon hydrodynamics has significant interest due to its crucial role in influencing the electrical and thermal transport properties of crystalline materials such as graphene. In this regime, phonon-phonon scattering dominates over other mechanisms like boundary, impurity, and defect scattering. In this study, we analytically compute and compare key thermodynamic quantities-energy density, number density, pressure, and the specific heat per particle-for both phonons and electrons within the hydrodynamic regime of graphene. We further investigate the temperature dependence of specific heat and benchmark our results against classical models such as the Dulong–Petit law and Einstein's theory. Our findings reveal that, at low temperatures, the contributions from both electrons and phonons to the specific heat deviate from conventional metallic behavior. Additionally, the hydrodynamic nature of electron and phonon transport in graphene may lead to violations of the Wiedemann-Franz law.

Key words: Specific Heat, Kinetic Theory, Electron Hydrodynamics, Phonon Hydrodynamics, Graphene.

INTRODUCTION

Hydrodynamic transport of fundamental particles, electrons, and phonons has attracted a lot of research attention due to their unique characteristics contributing to electrical and thermal properties [1,2]. For instance, electron hydrodynamics are identified experimentally and theoretically in the two-dimensional graphene system [3,4]. Generally, the heat transport is mediated by phonons as well as electrons. The transport of heat through bulk material can be understood by Fourier's law of heat conduction, where the energy carriers simply diffuse. However, in low-dimensional materials such as graphene, the heat conduction is governed by either ballistic or hydrodynamic transport of phonons [5], where the latter notably prevails up to ~300 K [6]. Electron hydrodynamics can be described by an energy-momentum tensor of a continuum system, whose ideal part is described by recent Ref. [7] and dissipative viscous part is described by recent Ref. [8]. One can also build a similar kind of phonon hydrodynamic formalism, mainly aimed by the present proceeding paper.

We first showed the traditional phonon-specific heat in solids from Einstein's theory and the electron-specific heat in solids from free electron theory. Both expressions can be applicable to the non-fluid domain of graphene having high charge carrier density or doping at room temperature. While at low temperatures and towards the charge-neutral point, electron and phonon hydrodynamics are expected [3,4]. The Present article has observed a larger specific heat while transiting from the non-fluid to fluidic domain, which may have a connection in violation of the Wiedemann-Franz law [4,10] near the charge neutrality point.

FORMALISM

Ideal hydrodynamics deals with the macroscopic energy-momentum tensor $T^{\mu\nu}$ and the number flow N^{μ}, whose microscopic expression can be written as (in natural units ħ= $k_B = c = 1$),

$$T^{\mu\nu} = g\int \frac{d^2p}{(2\pi)^2} p^\mu v^\nu f(E) \quad , \tag{1}$$

$$N^\mu = g\int \frac{d^2p}{(2\pi)^2} v^\mu f(E) \ . \tag{2}$$

In the above expressions, the value of μ = (0, i =1,2) is the Lorentz index for time and space in two dimensions. g stands for the degeneracy factor for fluid constituents having energy $p^0 = E$, momentum, and velocity v^i. $f(E)$ is the thermal distribution function for fluid constituents. For phonons, the Bose -Einstein distribution function will be considered i.e., $f(E)=\frac{1}{e^{E/T}-1}$ while for electrons the Fermi Dirac distribution function will be considered i.e., $f(E) = \frac{1}{e^{(E-\mu)/T}+1}$ were μ is the chemical potential or Fermi energy level of electrons in graphene and T is the temperature.

Using the dispersion relation for phonon $E = pv_s$, where v_s is the velocity of sound or phonon in the graphene system, Eq. (1) and (2) will provide the expressions for energy density (ε_{ph}) and number density (n_{ph}) as,

$$\varepsilon_{ph} = T^{00} = g\int \frac{d^2p}{(2\pi)^2} E\, f(E) = \frac{3}{\pi v_s^2}\, \zeta_3 T^3 \ , \tag{3}$$

$$n_{ph} = \ N^0 = g\int \frac{d^2p}{(2\pi)^2}\, f(E) = \frac{3}{2\pi v_s^2}\, \zeta_2 T^2 \ , \tag{4}$$

where $\zeta_n = \frac{1}{\Gamma(n)}\int_0^\infty \frac{x^{n-1}}{e^x-1}\, dx$ is the Riemann − Zeta function.

Using Eqs. (3) and (4), the specific heat (specific heat per particle) for the phonon fluid in the graphene system can be easily found as follows,

$$C_V^{ph} = \frac{1}{n_{ph}}\left(\frac{\partial \varepsilon}{\partial T}\right)_V = 6 \times \frac{\zeta_3}{\zeta_2} = 4.38 \ . \tag{5}$$

Similarly, for the electron hydrodynamic regime, we will use the dispersion relation $E = pv_g$, where v_g is the Fermi velocity of electrons in the graphene system. Eqs. (1) and (2) will provide the expressions for the corresponding energy density (ε_e) and number density (n_e) in terms of the Fermi integral $f_n(A) = \frac{1}{\Gamma(n)}\int_0^\infty \frac{x^{n-1}}{A^{-1}e^x+1}\, dx$ [7]. The specific heat for electron fluid is,

$$C_V^e = 2\left[3\frac{f_3(A)}{f_2(A)} - \frac{\mu}{T}\right]. \tag{6}$$

The above fluid-based expressions of specific heat for phonons and electrons are not considered in traditional solid-state physics. However, in the metal case, where the electrons have a dispersion relation $E = {p^2}/{2m}$, the specific heat due to electrons follows the linear relation with temperature ($C_V^e \propto T$). On the other hand, phonons in metals grossly follow Einstein's theory of specific heat, whose high-temperature limit reaches Dulong Petit law ($C_V^{ph} = 3$) and the low-temperature limit $C_V^{ph} \propto T^3$. For a two-dimensional (2D) graphene system, the Einstein relation of phonon-specific heat per particle can be written as [9],

$$C_V^{ph} = 2\left(\frac{T_E}{T}\right)^2 \frac{exp\left(\frac{T_E}{T}\right)}{\left[exp\left(\frac{T_E}{T}\right)-1\right]^2} \ , \tag{7}$$

where T_E is Einstein's characteristic temperature.

Similarly, the electronic-specific heat in a 2D graphene system can be written as,

$$C_V^e = \frac{4\pi^2}{3}\frac{T}{\mu} \ , \tag{8}$$

which can be obtained from Eq. (6) by considering the limit of $\frac{\mu}{T} \gg 1$ in the Sommerfeld lemma (SL) expansion of Eq. (6). Now connecting with experimental observation fluid aspect in $\frac{\mu}{T} \ll 1$ domain (Dirac fluid) and non-fluid aspect in $\frac{\mu}{T} \gg 1$ domain, we may say that Eqs. (5) and (6) are fluid-based specific heat expressions, whereas Eq. (7) and (8) are non-fluid or solid state-based specific heat expressions.

RESULTS AND REMARKS

In this section, we tried to visualize the non-fluid and fluid-based expressions of electron and phonon-specific heat, and at the end, we also put a remark on the non-fluid to fluid transition of the graphene system.

In Fig.1(A), we have plotted non-fluid based C_V^{ph}(black solid line) and C_V^e(green dashed-dotted line) by using Eq. (7) and (8) respectively. The black solid line represents the conventional Einstein theory of specific heat, which is saturated at 2 (Dulong-Petit law) for the high-temperature region and obeys the T^2 law at the low-temperature domain. The dash-dotted line illustrates the conventional ($C_V^e \propto$ T) relation, which is plotted for Fermi energy μ = 2 eV. We know that the typical ranges of Fermi energy for metals are μ = 2 -10 eV, which can't be tunable much by external means. However, the electron carrier concentration can be tunable via doping techniques, and so μ can be reduced from 2 eV to 0 eV. Now μ = 2 -10 eV and T= 0-300 K range satisfy $\frac{\mu}{T} \gg 1$ domain quite well, so non-fluid base relation $C_V^e \propto$ T works very well. From Fig.1(B), one can see that at μ = 0. 2 -2 eV, SL relation ($C_V^e \propto$ T) works well, but at μ < 0.1eV, the SL relation or Eq. (8) deviates from the general expression of C_V^e given in Eq. (6). As we enter into μ < 0.1eV and T< 100 K range (marked by the dotted blue box), Dirac fluid domain $\frac{\mu}{T} \ll 1$ [3] can be expected and fluid-based expressions - Eq. (5) and (6) provide us enhanced specific heat per particle, with maximum values $C_V^e = 6 \times \frac{\zeta_3}{\zeta_2} = 5.63$ and $C_V^{ph} = 4.38$. An increasing value of specific heat per particle for the electron case in the Dirac fluid domain is linearly related to the thermal conductivity, which may be connected to an increasing value of the Lorenz ratio in the Dirac fluid domain near the charge neutrality point in the graphene system, observed by Ref. [4,10].

We may give a remark on the transition from non-fluid $\left(\frac{\mu}{T} \gg 1\right)$ to fluid $\left(\frac{\mu}{T} \ll 1\right)$ domain by observing the transition from non–fluid-based equations (7) and (8) to fluid-based equations (5) and (6). The higher contribution is attributed to the fluid behavior of electrons, thereby increasing the thermal conductivity of graphene. It may further be noted that the increased contribution may lead to the violation of the Wiedemann- Franz law in the low-temperature domain [4,10].

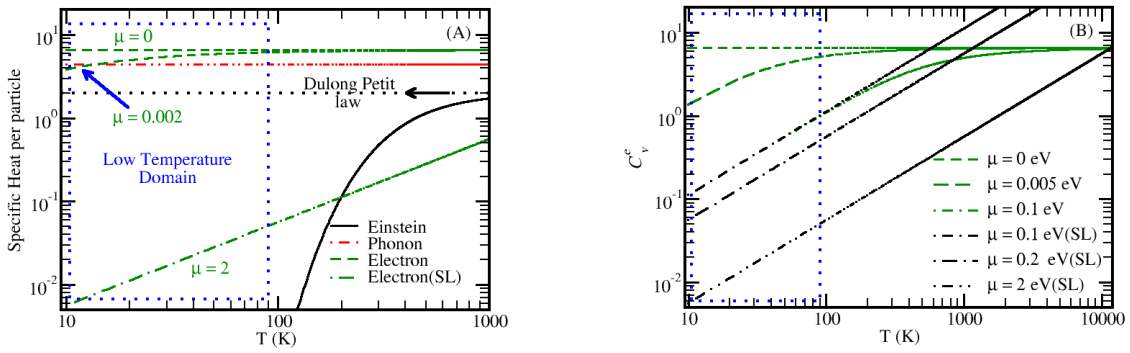


FIGURE .1 (A) Specific heat per particle with reference to temperature (T) for electron, phonon, and Einstein's theory for different values of chemical potential, μ, and Sommerfeld approximation (SL). (B) Specific Heat of electron fluid on graphene with varying chemical potential μ for general and SL expressions, given by Eq. (6) and (8), respectively.

ACKNOWLEDGMENTS

The authors gratefully acknowledge the Ministry of Education (MOE), Govt of India, and thank the other members of the EHD club, Narayan Prasad, Bharat Kukkar, and Gaurav Khandal.

REFERENCES

1. J. A. Sulpizio et al., Nature, Vol. 576, 7785, pp. 75-79 (2019).
2. S. Lee, D. Broido, K. Esfarjani & G. Chen, Nature Communications, Vol. 6, 1, pp. 6290 (2015).
3. A. Lucas & K. C. Fong, Journal of Physics: Condensed Matter, Vol. 30, 5, pp. 053001 (2018).
4. J. Crossno et al. Science, Vol. 351, 6277, pp. 1058-1061 (2016).

5. C. Zhang, S. Chen & Z. Guo, International Journal of Heat and Mass Transfer, Vol. 176, pp. 121282 (2021).
6. Cepellotti, A., Fugallo, G., Paulatto, L., Lazzeri, M., Mauri, F., & Marzari, N., Nature Communications, Vol. 6, 1, pp. 6400 (2015).
7. T. Z. Win, C. W. Aung, G. Khandal & S. Ghosh, Pramana, 99(1), pp. 1-14 (2025).
8. C. W. Aung, T. Z. Win, G. Khandal & S. Ghosh, Physical Review. B, Vol. 108, 23, pp. 23517 (2023).
9. C. Kittel & P. McEuen, Introduction to solid state physics, 8th ed. (John Wiley & Sons, Singapore), pp. 107-129 (2005).
10. T. Z. Win, C. W. Aung, G. Khandal & S. Ghosh, International Journal of Modern Physics B, pp. 2550182 (2025).

Electronic, Mechanical and Electron Transport Properties of 2D Penta-Si_3P_2S Monolayer

Sangeeta Meena, Ramandeep Singh, Nidhi Verma and Ashok Kumar*

Department of Physics, Central University of Punjab, Bathinda, Punjab,151401, India

*Corresponding author: ashokphy@cup.edu.in

Abstract. Two-dimensional (2D) materials with pentagonal structures exhibit unique physical properties and hold significant potential for mechanical and thermal applications. We used density functional theory (DFT) and Boltzmann transport theory to study the electronic, mechanical, and electron transport properties of the 2D Penta-Si_3P_2S monolayer. The Penta-Si_3P_2S monolayer exhibits an indirect bandgap of 1.62 eV (2.30 eV) at the GGA (HSE06) level of theory. It possesses high mechanical stability and a high power factor. These findings suggest that the Penta-Si_3P_2S monolayer to be promising candidate for use in electro-mechanical and thermo-electric devices.

Key-words: 2D material, semiconductor, seebeck coefficient, electronic conductivity and power-factor.

INTRODUCTION

2D monolayers such as h-BN, MoS_2, TMDs, and different carbon allotropes, e.g., graphene and pent-graphene, have garnered significant interest from researchers due to their excellent structural, mechanical, and physical properties [1]. Their exceptional electrical and thermal transport characteristics make them an ideal candidate for thermal energy applications. The successful synthesis of various 2D materials, such as silicene, phosphorene, Penta-$PdSe_2$, and Penta-PdS_2, underscores their potential for future nanoelectronics devices, owing to their unique structural and electronic properties [2]. Inspired by the above experimental synthesized material, we have theoretically explored the stability, mechanical and electronic transport properties of the Penta-Si_3P_2S monolayer. The mechanical properties are explored by subjecting the square unit cell of a 2D Penta-Si_3P_2S monolayer using biaxial strain. Thermoelectric performance parameters of the Penta-Si_3P_2S monolayer, such as electronic conductivity (σ), electronic thermal conductivity (κ_e), power factor (PF), and Seebeck coefficient (S), are obtained in the different temperature ranges of 300K, 500K, and 700 K.

COMPUTATIONAL METHOD

We ran all of the simulations using VASP software [3] utilizing PBE functional. A vacuum separation of 16 Å was incorporated along the z-direction to represent a 2D layer model. The corrected electronic structure was obtained using HSE06 functional. We used a 12×12×1 k-point mesh in reciprocal space. A plane wave cut-off energy of 500 eV is utilized for all the calculations. The energy convergence criterion was set to be 10^{-5} eV. To ensure simulation accuracy, we optimized geometry until each atom's force was below 0.01 eV/Å. Elastic constants are calculated by the VASPKIT tool. We used the BoltzTrap code based on the semi-classical Boltzmann theory to obtain the electronic transport properties of the Penta-Si_3P_2S monolayer[4].

RESULTS AND DISCUSSION

Structural and Electronic Properties

The optimized structure of the Penta-Si_3P_2S is shown in Fig. 1(A). The Si_3P_2S monolayer has a square unit cell consisting of six atoms per unit cell and having lattice parameters of a=b= 4.87Å. To evaluate the energetic stability of a monolayer, we estimated the cohesive energy as -5.03eV/atom, which is higher than silicene (- 3.94 eV/atom)[5] and Germanene (- 3.89 eV/atom)[6], confirming its stability. Note that cohesive energy (E_C) is obtained as:

$$E_C = \frac{E_{Si_3P_2S} - (3E_{Si} + 2E_P + E_S)}{6} \qquad (1)$$

where E_{Si} , E_P and E_S is the energy of isolated Si, P and S atoms, and E_{Si3P2S} is the total energy of the Penta-Si_3P_2S monolayer unit cell. To check the thermal stability of the Penta-Si_3P_2S monolayer, we performed ab initio molecular dynamics (AIMD) simulations at a temperature of 500 K. The total energy and temperature profiles as a function of the time step are shown in Fig. 2(B), which clearly shows that the change in energy and temperature

concerning the time step is very small, indicating the thermal stability of the Penta-Si_3P_2S monolayer. Its dynamical

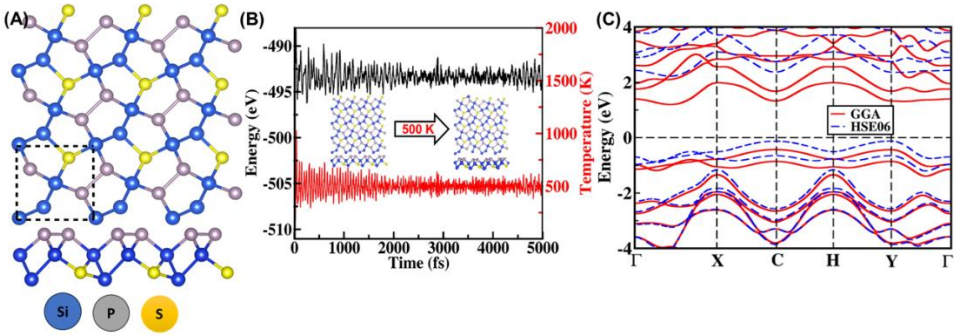


FIGURE 1: (A) Top and Side view **(B)** MD simulation total energy and temperature profiles of Penta-Si_3P_2S monolayer concerning time staps for temperature 500 K. The inset additionally displays the initial and final structure of the monolayer following the 5000 fs. **(C)** The electronic band structure of the Penta-Si_3P_2S monolayer corresponds to the GGA and HSE06 levels of theory, respectively.

stability was established previously in other study [7]. Next, we calculated the electronic band structure of the Penta-Si_3P_2S monolayer, which exhibits an indirect bandgap of 1.62 eV and 2.30 eV, corresponding to the GGA-PBE and HSE06 levels of theory, respectively (Fig. 1(C)).

Mechanical Properties

Further, we investigated the mechanical properties using biaxial strain ($\varepsilon = \frac{(b-b_0)}{b}$, where b is relaxed and b_0 is deformed lattice constants) in the square unit cell of the Penta-Si_3P_2S monolayer using the energy-strain method. The 2D material's elastic strain energy per unit area is expressed as:

$$U(\mathcal{E}) = \frac{1}{2}(C_{11}\mathcal{E}_{xx}^2 + C_{11}\mathcal{E}_{yy}^2) + C_{12}\mathcal{E}_{xx}\,\mathcal{E}_{yy} + 2C_{66}\mathcal{E}_{xy}^2 \qquad (2)$$

Here, C_{11}, C_{22}, C_{12}, and C_{66} are elastic constants. We use quadratic fitting energy curves under biaxial strains to obtain elastic constants. The calculated value of elastic constants are C_{11} = 78.6 N/m, C_{22}=78.0 N/m, C_{12} = 28.3 and C_{66} = 47.608 N/m, which satisfies the mechanical stability criteria of C_{11}>0, $C_{11}*C_{22} > C_{12}*C_{12}$ and det(C_{ij}) > 0 for 2D Penta-Si_3P_2S monolayer. Based on the calculated elastic constants, we further obtained Poisson's ratio (ν), Shear modulus (G) and Young's modulus (Y) having a value of 0.36, 47.46 N/m and 106.2 N/m, respectively. Our results are better than in terms of stability from the previously calculated silicene, germanene, and stanene [8]. These results demonstrate that the Penta-Si_3P_2S monolayer is highly mechanically stable.

Electronic Transport Properties

Semiclassical Boltzmann transport equations were used for electronic transport properties. We calculated the Penta-Si_3P_2S monolayer electronic conductivity (σ), Seebeck coefficient (S), Electronic thermal conductivity (κ_e), and Power factor ($PF=S^2\sigma$) for the temperature range of 300K, 500K, and 700 K as shown in Fig. 2.

$$S_{a,b}(T,\mu) = \frac{1}{evT\sigma_{a,b}} \frac{1}{2} \int \sum(\varepsilon)\,(\varepsilon-\mu)\left[\frac{-\partial f_\mu}{\partial \varepsilon}\right] d\varepsilon \qquad (3)$$

$$\sigma_{a,\ b}(T,\mu) = \frac{1}{V}\int \sum e\left[\frac{-\partial f_\mu}{\partial \varepsilon}\right] d\varepsilon \qquad (4)$$

$$\sum(\varepsilon) = \frac{e^2}{N}\sum \tau\ v_a(j,k)v_a(j,k)\ \frac{\delta(\varepsilon-\varepsilon_{j,k})}{d\varepsilon} \qquad (5)$$

$$k_{a,\ b}(T,\mu) = \frac{1}{\omega}\int \sigma_{a,b}\ \varepsilon\ (\varepsilon-\mu)^2\ \left[\frac{-\partial f_\mu}{\partial \varepsilon}\right] d\varepsilon \qquad (6)$$

here, a and b are cartesian indices in the given equations, f_μ represents Fermi-Dirac distribution function, $\sum(\varepsilon)$ is the transport distribution function, and N is the number of k-points. These properties are plotted against the chemical potential at different temperature ranges. The value of the Seebeck coefficient affects the thermoelectric properties of materials, and a larger value of S indicates a better thermoelectric performance. The Seebeck coefficient of Penta-Si_3P_2S monolayer is calculated at 300K, 500K, and 700 K, is 2552.42 μV/K, 1518.40 μV/K and 1075.85 μV/K, respectively (Fig. 2(A)). The values of the Seebeck coefficient decrease as temperature

increases. The obtained values of the Seebeck coefficient have higher values at temperature 300 K. These results are better than previously obtained 2D Janus HfBrCl (672.69 μV/K), HfBrI (675.06 μV/K) and HfClI monolayer (668.00 μV/K) at mid temperature range.[9]

Using the constant relaxation time approximation (CRPA) method, electric conductivity has a maximum value is 2.505 (10^{-5} /ohm-m) at a temperature of 300 K (Fig. 2(B)). The electronic thermal conductivity (k_e) is obtained to be ~5.3 (W/mK) at a temperature of 700 K (Fig. 2(C)). The power factor defines the efficiency of thermoelectric material, which can be obtained using the Seebeck coefficient and electrical conductivity. The calculated values of the power factor of Penta-Si_3P_2S monolayer are ~0.00093 W/mK^2,0.00148 W/mK^2, and 0.00184 W/mK^2 for p-type at 300 K, 500 K, and 700 K, respectively, while for n-type, 0.0005 W/mK^2,0.001 W/mk^2,0.0015 W/mK^2 at temperatures 300 K, 500 K and 700 K, respectively. These results suggest that the Penta-Si_3P_2S monolayer can be a good candidate for thermoelectric application.

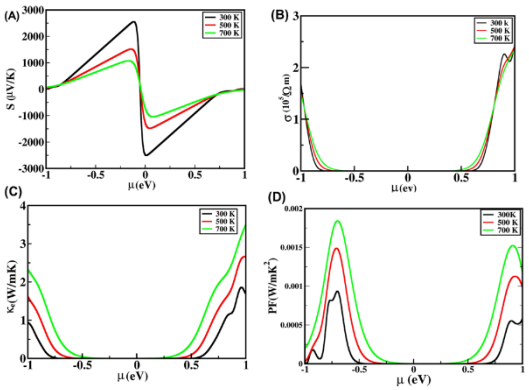


FIGURE 2: (A) Seebeck coefficients, (B) Electrical conductivity (C) Electronic thermal conductivity and (D) Power factor concerning the chemical potential of the Penta-Si_3P_2S monolayer, respectively.

CONCLUSIONS

In summary, utilizing the density functional and Boltzmann transport theory, we investigated the mechanical and electronic transport properties of the Penta-Si_3P_2S monolayer. The monolayer is an indirect band gap semiconductor. Young's and shear modulus value is 106.2 N/m and 47.5 N/m.The calculated values of the Seebeck coefficient and electrical conductivity are 2552.42 μV/K and 2.5052x10^{-5}/ohm-m, respectively, at 700 K. The Si_3P_2S monolayer shows excellent mechanical and thermoelectric performance that can be used for further exploration of energy conversion applications.

ACKNOWLEDGMENTS

SM and RS are grateful to the University Grants Commission (UGC) for financial support in the form of Junior Research Fellowship (JRF), NV acknowledges the senior research fellowship (SRF) from CSIR. For the research work presented in this paper, we utilized computational workstations at the Department of Physics, Central University of Punjab.

REFERENCES

1. Zhang, J. Zhou, Q. Wang, X. Chen, Y. Kawazoe, P. Jena, Proc. Natl. Acad. Sci., Vol. 112, pp. 2372 (2015).
2. V. Shanmugam, R.Mensah, Karthik Babu, Sidique Gawusu, Avishek Chanda, Yongming Tu, R.Esmaeely Neisiany, Michael Försth, Gabriel Sas, Oisik Das, Particle & Particle Systems Characterization, Vol. 39, pp. 2200031(2022).
3. G. Kresese and J. Furthmuller, Physical Review B, Vol. 54, pp. 11169 (1996).
4. Georg K.H. Madsen, David J. Singh b, Computer Physics Communications Vol. 175, pp. 67-71 (2006).
5. N D Drummond, V Zo´lyomi and V I Fal'ko Physical Review B, Vol. 85, pp. 075423 (2012).
6. U Srimathi, V Nagarajan and R Chandiramouli Com Theo. Chem., Vol. 68, pp. 1130 (2018)
7. T Shirnezhad, M Naseri, N Fatahi* and B Arghavaninia, Indian J Phys, Vol. 98(2), pp. 513–523, (2024).
8. Bohayra Mortazavia,Obaidur Rahamana , Meysam Makaremib , Arezoo Dianatc, Gianaurelio Cunibertic, Timon Rabczukd, Physica E, Vol. 87, pp. 228–232 (2017).
9. Shi-Jia Huang a, Tian Zhang b, Zhao-Yi Zeng c, Hua-Yun Geng d, Xiang-Rong Chen a, Vacuum Vol. 224, pp. 11314 (2024).

Effect of Residual Oxygen in Atmospheric Pressure Chemical Vapor Deposition growth of monolayer MoS_2

Shubham Mingwal[1,2,*)], Himanshu Srivastava[1,2], Rahul Aggarwal[3], A.K. Srivastava[1,2] and Pragya Tiwari[1,2]

[1]Accelerator Physics and Synchrotrons Utilization Division, Raja Ramanna Centre for Advanced Technology, Indore - 452013, India
[2]Homi Bhabha National Institute, Training School Complex, Anushakti Nagar, Mumbai 400094, India
[3]Photonics Materials Technology Section, Raja Ramanna Centre for Advanced Technology, Indore - 452013, India
[*)] Corresponding author: smingwal@rrcat.gov.in

Abstract. In this paper, we present the effect of residual oxygen on the growth of monolayer MoS_2 in a two-zone atmospheric CVD system. We demonstrate that inadequate atmospheric oxygen removal from the furnace tube, results in either etched MoS_2 flakes or irregular flakes on the substrate, whereas effective removal of atmospheric oxygen from the tube by purging with high flow of Ar gas, yields monolayer MoS_2 triangular flakes. The as-grown samples were studied with fluorescence optical microscope and Raman spectroscopy.

INTRODUCTION

The various applications of monolayer MoS_2 in the fields of photonics, nano-electronics, opto-electronics etc., have been demonstrated due to its excellent electronic and optical properties. This has led to the research towards growing better quality of monolayer MoS_2 [1,2]. Among the numerous techniques for depositing monolayers of MoS_2, Atmospheric Pressure Chemical Vapor Deposition (APCVD) is the most economical approach for scaling to industrial level production. Additionally, APCVD eliminates the need for a vacuum apparatus, making the growth simpler [3]. But, the problem in an APCVD system is that the residual atmospheric oxygen (RAO) adversely affects the growth of these MoS_2 films. Though, the problem of RAO is known, but to the best of our knowledge, a systematic study for the effect of RAO on the growth of monolayer MoS_2 and its solution in APCVD has not yet been done. In this paper, we have investigated the effect of RAO inside the furnace tube on the growth of the monolayer MoS_2 in a two-zone APCVD system, before and after the CVD reaction. An effective way to overcome this problem has also been presented. When RAO is present in the system, we obtain either the irregular grown flakes of intermediate Moly Oxysulphide phase or oxygen etched flakes of MoS_2, but when oxygen is purged out of the system with Ar gas, we obtain the flakes of monolayer MoS_2 with size up to 70 µm. The quality of MoS_2 flakes was observed by Raman spectroscopy and optical florescence microscopy.

EXPERIMENTAL METHOD

The fig.1 shows the schematic diagram of APCVD system used for the growth of MoS_2 films. It is a two-zone furnace system. Sulfur is evaporated in zone-1 at 180°C and carried by Ar gas to zone-2, where it reacts with the vapor of MoO_3 at 830°C. The reaction is carried out for 3 min. The MoS_2 layers get deposited on SiO_2/Si substrate, kept 5 cm away from MoO_3 precursor. The temperature profile for the two zones is given in fig. 2.

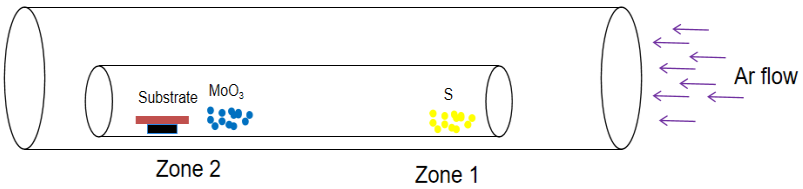


FIGURE 1. Schematic diagram of the CVD system

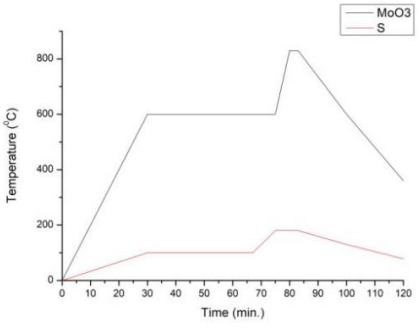


FIGURE 2. Temperature profile for the S and MoO_3

To see the effect of RAO, three sets of experiments were done. In set #1, the chamber was not purged and RAO was present in the system and the sample was extracted at growth temperature. In set #2, the tube was purged with 1000 sccm flow to carry the sulphur to reaction zone as well as to purge out the byproducts and the excess precursors in order to avoid excess deposition. The sample was extracted at growth temperature. In set #3, the procedure was same as of set #2 but the furnace was allowed to cool down naturally in a flow of 1000 sccm of Ar gas, till the sample was extracted at room temperature. It helped in isolating the environment around the substrate from the RAO at high temperature.

RESULT AND DISCUSSION

Fig. 3 shows the result of set #1. No flakes having the characteristic triangular shape of MoS_2 were formed, suggesting the absence of MoS_2 phase and possibility of the formation of intermediate Moly Oxysulfide phase only [3]. Fig. 4 presents the oxygen etched flakes of MoS_2 that are formed in the set #2. An enlarged view of etched flake is shown in the inset of fig. 4. The flakes, though show an outline of triangular shapes suggesting initial formation of MoS_2, but only reminiscent of the material in the form of dots can be seen finally due to the oxygen etching.

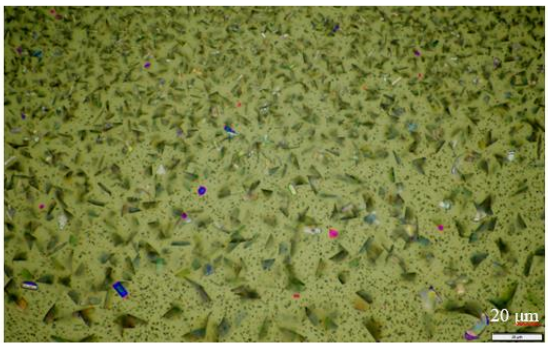


FIGURE 3. Optical image of sample without purging the oxygen.

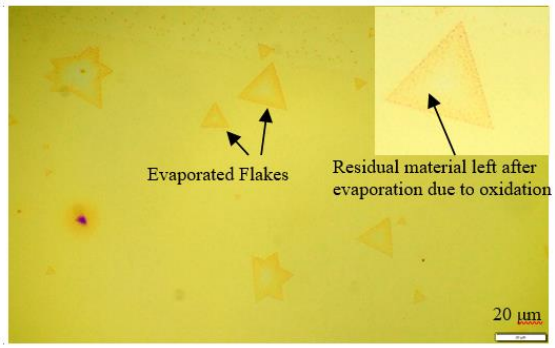


FIGURE 4. Optical image of oxygen etched sample extracted at high temperature. (Enlarged view of the flake in inset)

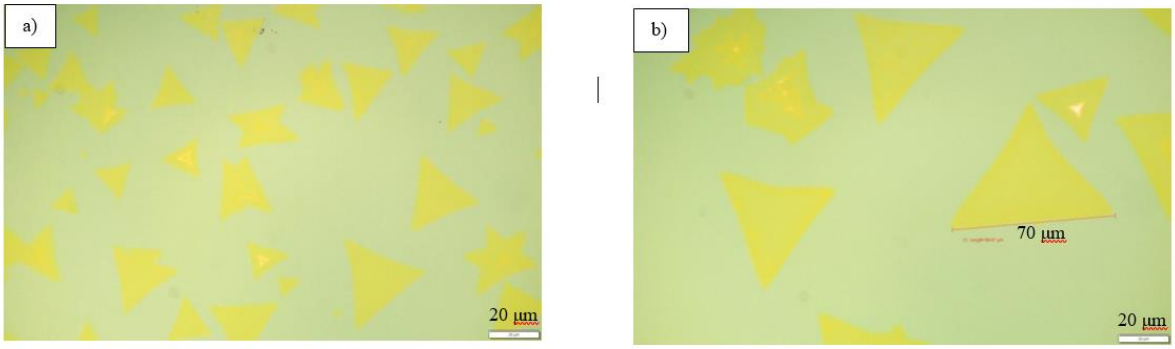


FIGURE 5. a) and b) Optical images of MoS_2 flakes at two different sites after extraction at room temperature.

Fig. 5a, b shows the optical images of the sample set #3. The triangular flakes of the sizes up to 70 µm were grown over a large area. Fluorescence Microscopy and Raman spectroscopy were used to confirm the formation of monolayer MoS_2. Fig.6 presents the fluorescence image of MoS_2 monolayer flakes, which shows that the fluorescence is emitted from the entire flakes. This suggests the formation of MoS_2 monolayer [4]. Similar measurements on set #1 and #2 did not show any fluorescence from the deposited structures, which implied the absence of monolayer MoS_2. Raman spectrum in Fig.7 shows the two peaks corresponding to in-plane $E_{2g}{}^1$vibration mode at ~386 cm^{-1} and out-of-plane A_{1g} vibration mode at ~404 cm^{-1} of MoS_2. The difference between these peaks is equal to ~18 cm^{-1}, which is consistent with the peak difference of monolayer MoS_2 as reported in literature [4].

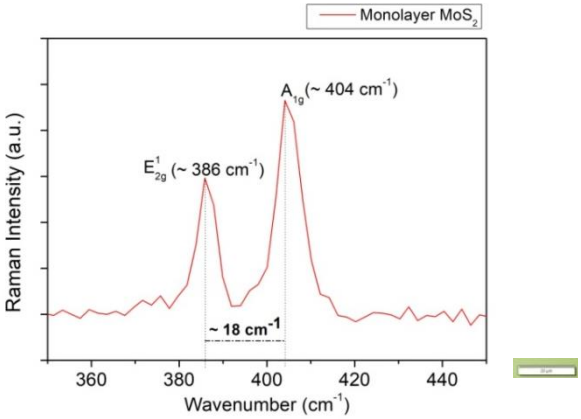




FIGURE 6. Florescence image of MoS_2 monolayer flakes (c) **FIGURE7.** Raman spectra of 2D MoS_2 monolayers.

Comparing the samples of set #2 and #3, the role of atmospheric oxygen is evident. Extraction of the deposited layers at high temperature, results in the etching of MoS_2 flakes by the oxygen and its evaporation, whereas extraction at room temperature doesn't etch the flakes due to low temperature of the sample. The triangular flakes, which is a preliminary confirmation of MoS_2 formation, is present in set #2 and #3 but not set #1, implying the detrimental role of RAO during CVD reaction also. The presence of oxygen doesn't let the MoS_2 phase to form and instead intermediate Moly Oxysulphide phases were formed. Thus, it is necessary to ensure the absence of atmospheric oxygen during the formation of MoS_2 by APCVD and one of the ways has been demonstrated here.

CONCLUSION

In this paper, it is shown that APCVD is an efficient way to approach for the low-cost production of monolayer MoS_2. It was found that RAO is detrimental to the formation monolayer MoS_2 and should be avoided in the CVD chamber during entire growth. An effective method to isolate the CVD chamber form RAO has been suggested; it led to the formation of large size (~70 µm) monolayer MoS_2 as confirmed by fluorescence optical microscopy and Raman spectroscopy.

ACKNOWLEDGEMENT

The authors acknowledge the help of Dr. Chandrachur Mukherjee for the coating of SiO_2 on Si substrate. They are thankful to Dr. Tapas Ganguli and Doctoral Committee (DC-4) for their valuable comments and suggestions and also thank RRCAT and HBNI Mumbai for financial support.

REFERENCES

1. R.K. Prasad, and D.K. Singh, ACS Omega, Vol. 8, pp. 10930-10940 (2023).
2. B. Ding, C. Zhu, T. Wang, L. Li, and Z. Li, SIA WILEY Vol. 56, pp. 22-31 (2023).
3. T. Tsafack, S.F. Bartolucci, and J.A. Maurer, J. Phys. Chem. Vol. 122, pp. 7320-7327 (2018).
4. S. Sharma, P. Chauhan, S. Rane, U. Raj, S. Srivastava, Z.A. Ansari, D.R. Chowdhury, and B.K. Gupta, Scientific Reports Vol. 13, pp. 4146 (2023).

MoS_2 Nanostructures for Selective Detection of 2,5-Dimethylfuran: A Potential Breath Test Marker for Lung Cancer

Saransh Chanouria[1,*], Nikhil Kumar[1], Deeksha Kumari[1], Ritika[1], Radhika Sharma[1], Samiksha Chauhan[1], Sheetal Dhiman[1], Yogyata Pathania[2], Arun Kumar[1]

[1] *Govt. College Bilaspur, Himachal Pradesh, 174001, India.*
[2] *D.A.V. Post Graduate College, Sector-10, UT. Chandigarh, 160011, India.*

[*] Corresponding author: *saransh8003@gmail.com*

Abstract. This investigation examines the potential of MoS_2 nanoribbon and nanoflake as gas sensors for detecting volatile organic compounds (VOCs) associated with lung cancer, such as 2,5-Dimethylfuran (C_6H_8O), using Density functional theory calculations (DFT). Upon adsorption of VOCs, a significant decrease in band gap or HUMO-LUMO is observed, indicating enhanced conductivity suitable for gas sensing applications. The MoS_2 nanoribbon and nanoflake displays particularly strong adsorption energy and a promising sensor response, emphasizing its potential in developing sensitive and selective gas sensors for early lung cancer detection.

INTRODUCTION

The exploration of breath analysis as a non-invasive means of detecting lung cancer is currently underway by scientists. Lung cancer is a major global health threat associated with smoking and chemical exposure, with a grim prognosis of 86% of patients succumbing within five years of diagnosis [1]. Early detection is crucial, and breath analysis focuses on identifying VOCs presents in exhaled breath, which include 2,5-Dimethylfuran, which are unique to lung cancer patients [2]. These VOC profiles act as "breathprints," offering a promising screening tool due to the simple and speed of breath collection [3]. In this paper, molybdenum disulfide (MoS_2) nanoribbons and nanoflakes are being investigated as sensors to effectively detect these cancer-related molecules.

COMPUTATIONAL DETAILS

All calculations based on DFT were carried out using the SIESTA-software package [4]. The exchange-correlation interactions among electrons modeled using the Perdew-Burke-Ernzerhof (PBE) [5] functional of generalized gradient approximation (GGA). We have used relativistic pseudopotentials. A double zeta polarization (DZP) basis set was used for calculations with a confinement energy of 20 meV. A mesh cutoff energy (300 Ry) was employed for calculations. A Monkhorst pack [6] of (1x10x1) and (1x1x1) was used for the one-dimensional (1D) nanoribbon [7] and zero-dimensional (0D) nanoflake of MoS_2 respectively.

RESULTS AND DISCUSSION

Structural Properties: Firstly, we optimized the MoS_2 nanoribbon (with 84 atoms) and MoS_2 triangular nanoflake (with 70 atoms). Thereafter, 2,5-Dimethylfuran was kept on both the structures and optimized to ensure the stability and accuracy of our simulations (fig.1). The optimized distances were found to be 3.25 Å and 2.82 Å respectively. The adsorption energies of -0.160 eV and -0.133eV were observed for nanoribbon and triangular nanoflake respectively. These negative values suggest stronger interactions between the adsorbate and substrates, leading to more stable adsorption configurations

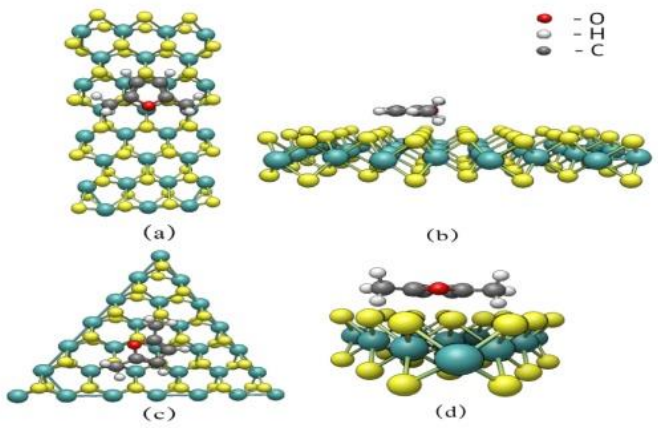


FIGURE 32: (a) Top & (b) Side view of $MoS_2NR@C_6H_8O$, (c) Top & (d) side view of $MoS_2TR@C_6H_8O$.

Electronic Properties: To evaluate the sensing capabilities, we analyzed the electronic properties associated with the adsorption of 2,5-Dimethylfuran on MoS_2 nanoribbon and nanoflake. Specifically, we calculated the adsorption energies, which provide insights into the stability of adsorbate on the substrates.

$$E_{ads} = E^{tot}_{subs/ads} - E^{tot}_{subs} - E^{tot}_{ads}$$

Where $E^{tot}_{subs/ads}$ and E^{tot}_{subs} are total energies of substrate with and without the adsorbate respectively and E^{tot}_{ads} is the total energy of adsorbate. Also, we examined the change in electronic band structure and HUMO-LUMO energy gap ($E_{H\text{-}L}$) on adsorption.

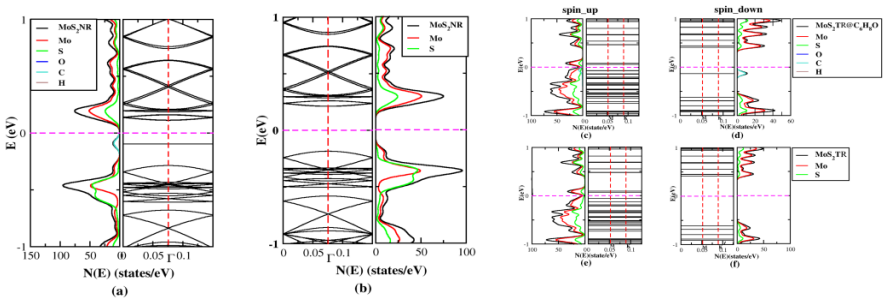


FIGURE 33: PDOS and Electronic Band structure and HUMO-LUMO of (a) $MoS_2NR@C_6H_8O$, (b) MoS_2NR (c), (d) $MoS_2TR@C_6H_8O$ and (e), (f) MoS_2TR for both spin up and spin down.

Fig. 2 indicates that the band gap of MoS_2 nanoribbon is 0.396 eV but on adsorption of C_6H_8O, band gap is decreased to 0.207 eV. On the other hand, the HUMO-LUMO gap of triangular nanoflake is 0.1266 eV and 1.033eV for spin up and spin down respectively (fig. 2 (e), (f)), while on adsorption of molecule it changed to 0.1264 eV and 0.544 eV respectively as shown in fig 2(c), (d). The decreased E_g and $E_{H\text{-}L}$ for nanoribbon and nanoflake respectively suggest a modification in the material's conductivity and optical properties, which can be exploited for gas sensing applications. Additionally, the Polarized Density of States (PDOS) corresponding to $MoS_2NR@C_6H_8O$ and $MoS_2TR@C_6H_8O$ are shown in Fig. 3 (b), (c), respectively.

Table 1: Distance of Molecules from the substrate (d), spin moment (s), energy band gap (E_g), adsorption energy (E_{ads}) and sensor response (S) for the studied systems.

Substrate	d(Å)	μ (μ_B)	E_g/E_{H-L}(eV)	E_{ads}(eV)	S%
MoS_2NR	-	-	0.396	-	-
$MoS_2NR@C_6H_8O$	3.24	-	0.207	-0.160	7.1
MoS_2 TR	-	14.00	0.126(□), 1.033(□)	-0.133	7.59(□), 9.83(□)
$MoS_2TR@C_6H_8O$	2.82	54.02	0.126(□), 0.544(□)	-0.133	7.59(□), 9.83(□)

Sensor Response: To quantify the sensor response, the density of states (DOS) before & after the adsorption process at the fermi level is calculated using the Drude formula.:

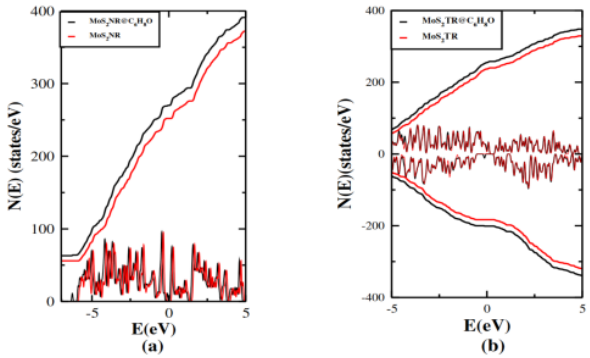


FIGURE 34: Total DOS and DOS for (a) $MoS_2NR@C_6H_8O$, (b) $MoS_2TR@C_6H_8O$ along with DOS of MoS_2 nanoribbon and nanoflake.

The sensor response (in terms of DOS) (S) is then estimated using the formula [8]:

$$S = \frac{|N_F^{(aft.ads)} - N_F^{(bef.ads)}|}{|N_F^{(bef.ads)}|} \times 100 \quad (2)$$

where $N_F^{(bef.ads)}$, $N_F^{(aft.ads)}$ are the DOS at E_F before and after adsorption, respectively. The gas sensor response of $MoS_2NR@C_6H_8O$ is 7.1% while for triangular nanoflake ($MoS_2TR@C_6H_8O$) sensor response is 7.59% for spin up and 9.83% for spin down respectively.

CONCLUSION

Our research investigated the adsorption of C_6H_8O on MoS_2 nanoribbons and nanoflakes using GGA functionals, demonstrating a significant decrease in band gap size for MoS_2 Nanoribbon while in case of nanoflake the HUMO-LUMO is decreased for spin up or increased in case of spin down MoS_2 Nanoribbon. This indicates potential improvements in conductivity and optical properties, positioning MoS_2 nanoribbon or nanoflake as a promising choice for gas sensing applications. The calculated adsorption energies consistently showed negative values, suggesting stable adsorption of C_6H_8O on MoS_2, with MoS_2 nanoribbons exhibiting the strongest interaction. This further supports their suitability for gas sensing. Sensor response calculations based on density of states revealed positive responses across all MoS_2 structures, emphasizing their effectiveness in gas sensing applications. In conclusion, our findings highlight the potential of MoS_2, particularly nanoribbons or spin down nanoflake, in altering electronic properties through C_6H_8O adsorption to enhance gas sensing capabilities.

REFERENCES

1. I. Horvath, Z. Lazar, N. Gyulai, M. Kollai, and G. Losonczy, "European Respiratory Journal" **34**, 261-275 (2009).

2. A. Ulanowska, T. Kowalkowski, E. Trawińska, and B. Buszewski, “Journal of breath research**”, 5**(4), 046008 (2011).
3. H. J. O'neill, S. M. Gordon, M. H. O'neill, R. D. Gibbons, and J. P. Szidon, “Clinical chemistry” **34**, 1613-1618 (1988).
4. JM. Soler, E. Artacho, JD. Gale, A. García, J. Junquera, P. Ordejón, and D. Sánchez-Portal, “Journal of Physics: Condensed Matter” **14**, 2745 (2002).
5. J.P. Perdew, K. Burke, and M. Ernzerhof, Physical review letters **77**, 3865 (1996).
6. Y. Wang, P. Wisesa, A. Balasubramanian, S. Dwaraknath, and T. Mueller, “Computational Materials Science” **187**: 110100 (2021).
7. A. Devi, A. Kumar, P.K. Ahluwalia and A. Singh, Materials Science and Engineering*: B, **271***, 115-237 (2021)
8. N. Kumar, H. Bae, H. Lee, T. Hussain, A. Anand, C. Veer Singh, and N. Tit, CS Appl. Nano Mater. ***, 7***, 6873-6884 (2024)

XPS and Structural Characterization of Layered MoS_2 Formed by Thermal Evaporation

Megha Mishra[1] and Teny Theresa John[1, *]

[1] *Department of Physics, Birla Institute of Technology and Science, Pilani, K K Birla Goa Campus, Zuarinagar, Sancoale, Goa 403726, India.*

[*] *Corresponding author: teny@goa.bits-pilani.ac.in*

Abstract. This study presents the synthesis and characterization of MoS_2 thin films prepared by thermal evaporation. XRD patterns confirm the formation of molybdenum disulfide (MoS_2) in the β-2H phase with high crystallinity, while FESEM images illustrate well-stacked layers. X-ray Photoelectron Spectroscopy (XPS) analysis reveals uniform stoichiometry throughout the surface of the film.

Keywords: Thermal Evaporation, Layered MoS_2, X-ray Photoelectron Spectroscopy, Depth analysis.

INTRODUCTION

Since the isolation of a single layer of graphene in 2004, which led to the Nobel Prize in Physics in 2010 there has been a surge of interest in two-dimensional (2D) materials within the research community. MoS_2 is an anisotropic 2D material composed of vertically stacked layers held together by van der Waals forces, belonging to the transition metal dichalcogenides family which is currently being explored for its electronic, optical, catalytic, and sensing properties due to its unique structure [1,2]. Naturally, MoS_2 is found in the 2H phase [2], but other metastable phases like 3R, 1T, and 1T' also exist, differing in layer stacking and Mo coordination. Many methods have been applied to form various structures and morphologies of MoS_2 [3] to be applied in various application including Chemical Vapor Deposition (CVD), Molecular Beam Epitaxy, Chemical Bath Deposition. Thermal evaporation offers a better alternative for depositing high-quality films, widely used in nanoscale fabrications due to its low cost, ease of implementation, high deposition rates, and minimal contamination. The morphology of the produced film can be controlled by optimization of the current, voltage used in the deposition. However, to produce monolayer or layered nanosheets, various exfoliation methods have been used on bulk MoS_2 [4]. In this work, we prepare MoS_2 with morphology of layered nanosheets using thermal evaporation under high vacuum conditions. We then analyze its XPS spectra to gain a deeper understanding of the composition which can further help in understanding the underlying mechanism involved in various application such as gas sensing.

MATERIALS AND METHODS

A thermal evaporation unit by High Vacuum Products and Instruments was used for the deposition. The thin films were deposited on Si/SiO_2 substrates on an area of 6mm x 6mm. Before deposition, the substrates were thoroughly cleaned using ultrasonication in a solution of acetone, ethanol, and distilled water. For the film deposition, 60 mg of MoS_2 powder (≥ 99.99% purity) obtained from Sigma-Aldrich was used. This powder was placed in a molybdenum boat. The boat was heated applying current of 6 A under a vacuum of 5×10^{-6} mbar. The films were then annealed in a vacuum at 200°C for 1 hour which were then characterized. To find out the crystallinity of the prepared films, D8 ENDEAVOR Bruker diffractometer was used, with a Cu Kα source ($\lambda = 0.154$ nm) was utilized, in a range of $2\theta = 10°$ to 60°. FESEM and Energy Dispersive Analysis (EDAX) were conducted using Quanta FEI-450 FEG. XPS measurements were done using a Thermo Scientific K-Alpha X-ray Photoelectron Spectrometer system. Depth analysis was conducted by etching the surface in cycles of 2 nm thickness, with a total of 20 etching cycles.

RESULTS AND DISCUSSIONS

Figure 1 shows the XRD pattern of the thin film annealed in vacuum at 200 °C. A prominent (100) peak confirms the formation of β-2H MoS_2 (ICCD 00-037-1492). A peak at 2θ = 33.04° corresponds to the Si/SiO_2 substrate. The inset highlights a weak but characteristic (002) peak at 14.4°, along with the (004) reflection. Figure. 2 illustrates the formation of layered MoS_2 sheets with well-stacked layers of the synthesized MoS_2. The EDAX analysis, as shown in the Figure. 3, reveals peaks for Mo and S, indicating the successful formation of Mo and S on the substrate.

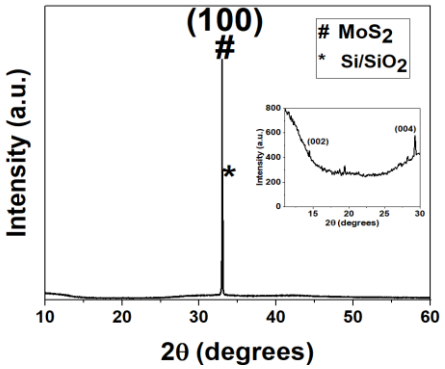


FIGURE 1. XRD pattern of synthesized MoS_2

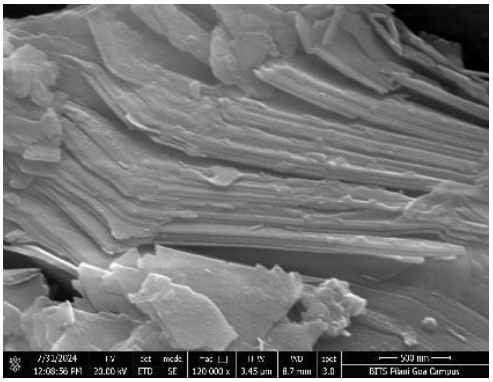


FIGURE 2. FESEM image of layered sheet of MoS_2.

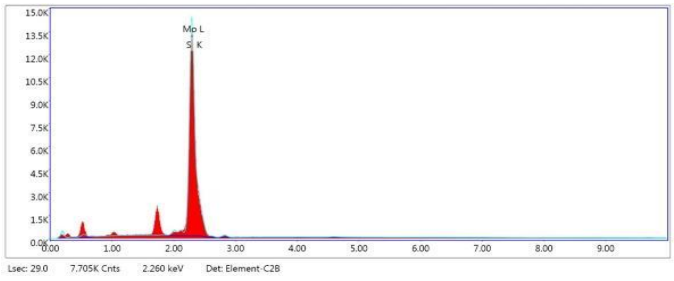


FIGURE 3. EDAX pattern of MoS_2.

The XPS survey scan spectra shown in Figure. 4(a) have been calibrated against the C1s peak at 284.8 eV. The Si2p peaks observed in the survey spectrum are attributed to the Si/SiO_2 substrate. The high-resolution spectra of the Mo3d peak, as illustrated in Figure. 4(b), exhibit the Mo3d doublet with $Mo3d_{5/2}$ and $Mo3d_{3/2}$, indicating the characteristic +4 oxidation state [5,6]. Additionally, the peak at 235.60 eV corresponds to Mo in the +6 oxidation state, suggesting the incorporation of oxygen into the grown MoS_2 film. This oxygen incorporation could occur as substitutional atoms at sulfur sites, as adsorbed oxygen, or as an interfacial Mo-oxide layer due to Mo-oxygen bonding at the MoS_2 - SiO_2 interface, as evident from the O1s spectrum and the presence of unreacted sulfur in the S2p spectrum. Furthermore, a S2s is observed at 226.21 eV [7]. In the core level spectra of S2p, shown in Figure. 4(c), two prominent peaks ($S2p_{1/2}$ and $S2p_{3/2}$) are observed at 162.04 and 163.68 eV, respectively, which match well with the binding energy of S^{2-} ions [5,7]. A smaller peak at 165 eV is attributed to S-S bonding, possibly due to unreacted sulfur, while the peak at 168.71 eV and 170.07 eV indicates the formation of sulfate groups through the oxidation of sulfur [8]. For the O1s spectra, as illustrated in Figure. 4(d), the peak at 532.75 eV corresponds to SiO_2 [7], and the peak at 531.02 eV is associated with surface-adsorbed oxygen contributions of lattice oxygen O^{2-} (in the Mo–O bond) [6]. The line scan as seen in Figure. 4(e) confirms the uniform distribution of Mo and S across the surface of the film, suggesting a uniform film. The atomic percentages of Mo and S are 31% and 69%, indicating that the stoichiometry is preserved in these films. Depth analysis of Mo (Figure. 4(f)) reveals that with etching, there is a shift of the binding energy. This shift is attributed to change in chemical state of Mo from the surface of the film to the inner layers [7]. The presence of Mo and S is observed throughout the sample, with adsorbed oxygen groups on the surface resulting in a lower concentration of Mo and S at the surface. As we move towards the interior, the concentrations of Mo and S increase before decreasing again near the substrate. After 15 levels of etching, the peaks related to S^{2-} of sulfur reduce significantly and

broaden (Figure. 4(g)), although Mo still exists in lower content. This could be due to Mo combining with oxygen atoms or Si atoms in SiO_2, forming a molybdenum oxide (MoO_x) or molybdenum silicon oxide layer [7].

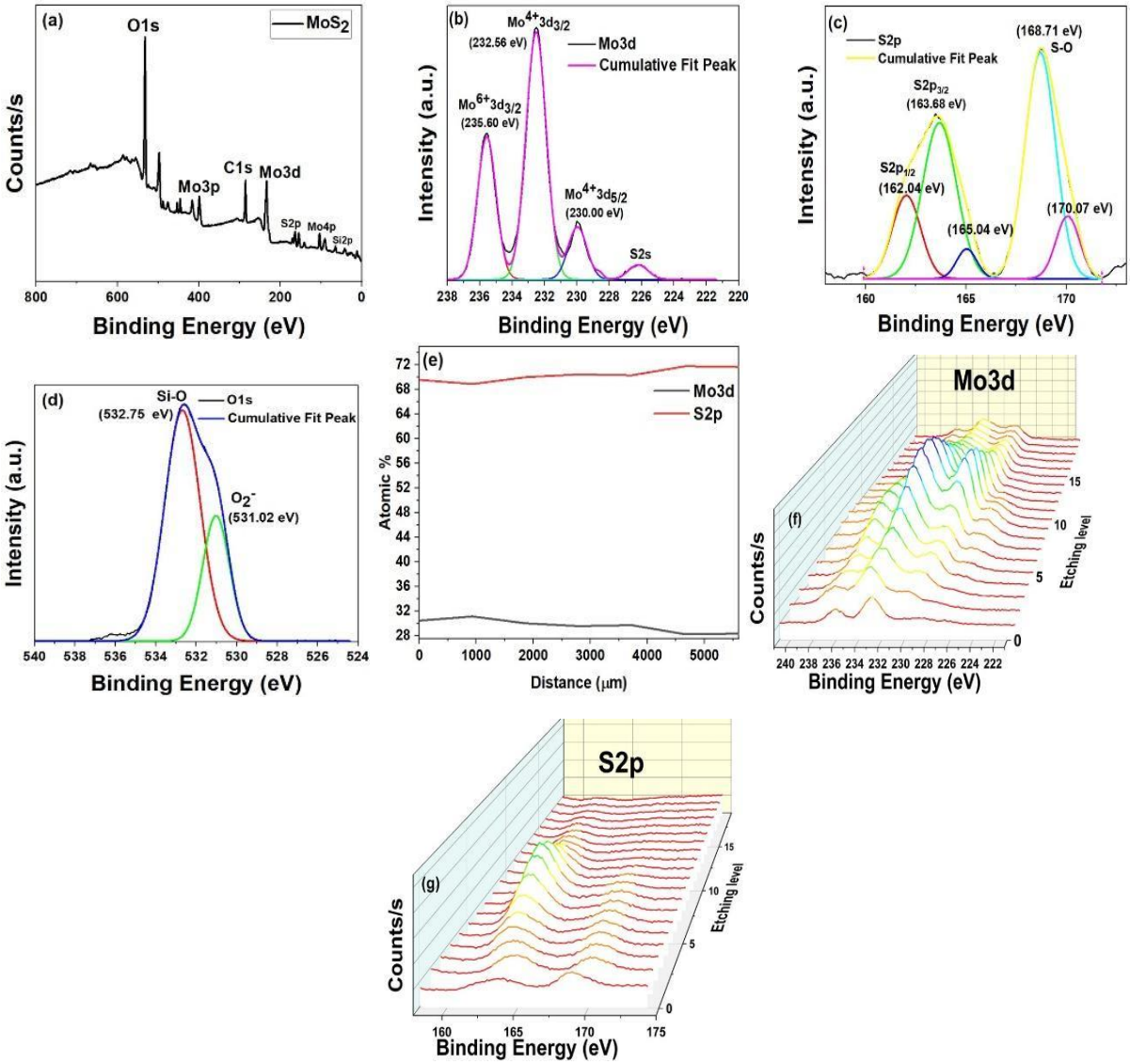


FIGURE 4. XPS results: (a) Survey scan; narrow scans of (b) Mo3d (c) S2p (d) O1s (e) line scan; depth analysis of (f) Mo3d and (g) S2p.

CONCLUSION

In summary, we successfully synthesized MoS_2 thin films with well-stacked layers, as confirmed by XRD patterns and FESEM images. XPS analysis revealed a uniform distribution of Mo and S throughout both the surface and depth of the film, with the stoichiometric ratio of Mo and S. These MoS_2 layered thin films can be directly utilized for various applications. Additionally, this is a potential straightforward method for integrating these films into heterojunctions for future device applications. They can also be easily exfoliated for further use.

ACKNOWLEDGMENTS

The authors thank BITS Pilani KK Birla Goa Campus for the financial support for carrying out the work. The Central Sophisticated Instrumental Facility (CSIF), BITS, Goa for XRD, SEM and EDAX measurements. XPS measurements were supported by the DBT-Builder project (BT/INF/22/SP42543/2021).

REFERENCES

[1] V. Shokhen, Y. Miroshnikov, G. Gershinsky, N. Gotlib, C. Stern, D. Naveh, D. Zitoun, On the impact of Vertical Alignment of MoS_2 for Efficient Lithium Storage, Sci Rep 7 (2017) 3280.

[2] X. Tian, S. Wang, H. Li, M. Li, T. Chen, X. Xiao, Y. Wang, Recent advances in MoS_2-based nanomaterial sensors for room-temperature gas detection: a review, Sensors & Diagnostics 2 (2023) 361–381.

[3] S. Dam, A. Thakur, A. G., S. Hussain, Synthesis and characterisation of MoS_2 thin films by electron beam evaporation, Thin Solid Films 681 (2019) 78–85.

[4] S. Ghayeb Zamharir, R. Karimzadeh, S.H. Aboutalebi, Laser-assisted tunable optical nonlinearity in liquid-phase exfoliated MoS_2 dispersion, Applied Physics A 124 (2018) 692.

[5] S. Huang, Z. You, Y. Jiang, F. Zhang, K. Liu, Y. Liu, X. Chen, Y. Lv, Fabrication of Ultrathin MoS_2 Nanosheets and Application on Adsorption of Organic Pollutants and Heavy Metals, Processes 8 (2020) 504.

[6] X.-Q. Qiao, F.-C. Hu, F.-Y. Tian, D.-F. Hou, D.-S. Li, Equilibrium and kinetic studies on MB adsorption by ultrathin 2D MoS_2 nanosheets, RSC Adv 6 (2016) 11631–11636.

[7] S. Hussain, J. Singh, D. Vikraman, A.K. Singh, M.Z. Iqbal, M.F. Khan, P. Kumar, D.-C. Choi, W. Song, K.-S. An, J. Eom, W.-G. Lee, J. Jung, Large-area, continuous and high electrical performances of bilayer to few layers MoS_2 fabricated by RF sputtering via post-deposition annealing method, Sci Rep 6 (2016) 30791.

[8] X.-J. Lv, G.-W. She, S.-X. Zhou, Y.-M. Li, Highly efficient electrocatalytic hydrogen production by nickel promoted molybdenum sulfide microspheres catalysts, RSC Adv 3 (2013) 21231.

Effect of Solvents in Optical Tuning of WS_2 Quantum Dots

Naresh Mandhan[1], Vidyotma Yadav[1], Tanuja Mohanty[1, a)]

[1]*School of Physical Sciences, Jawaharlal Nehru University, New Delhi – 110067,*

INDIA. [a)]Corresponding Author: tanujajnu@gmail.com, tmohanty@mail.jnu.ac.in

Abstract: Tungsten disulfide (WS_2) is a transition metal di-chalcogenide (TMD) exhibiting luminescent properties when reduced to zero-dimensional size, i.e. quantum dots (QDs). In this work, the solvent effect impacts the optical and structural properties of WS_2 quantum dots (QDs).The QDs have been synthesized in three different solvents using a liquid-phase exfoliation method. The optical properties have been studied using UV-vis absorption and photoluminescence (PL) spectroscopy. The confirmation and size estimation of synthesized WS_2 QDs in various solvents have been done using XRD measurement. The impact of an effective solvent has been observed as an enhancement in optical properties, such as increment in optical band gapand enhanced luminescence effect.The WS_2 QDs in DMSO solvent has the highest band gap as evaluated from UV-Vis absorption spectra and the particle size for the same is smallest. Thus, the UV-Vis study agrees with the XRD study, implying that DMSO is a better solvent for synthesizing WS_2 QDs. DMSO has become an effective solvent that exfoliates the QDs in an efficient manner. The bandgap values estimated from PL emission spectra agreed with the UV-Vis absorption evaluated values. Thus, this research helps understand the role of various solvents in tuning the optical properties of WS_2 QDs.

INTRODUCTION

The strong luminescence effect observed in WS_2 monolayer sheets and quantum dots makes them a potential candidate in quantum information technology, semiconductor-based spintronics and optoelectronic devices. WS_2 is a transition metal di-chalcogenide (TMD) arranged in a layered form where each layer is connected via Van der Waals force. The TMDs atoms are covalently bound to each other within the layer, forming an X-M-X arrangement, where M represents the metal and X represents the chalcogen. WS_2, among other TMDs, possess unique optical and electrical properties [1].WS_2 QDs possess high thermal stability, good water solubility, and good photostability [2]. Quantum confinement plays a key role in dealing with quantum dots, as charge confinement in all lateral dimensions leads to the formation of QDs.WS_2 QDs are anticipated to possess a higher PL quantum yield than WS_2 2D sheets, potentially due to the quantum confinement effect and increased exciton binding energy. These QDs exhibit a direct bandgap that may be modifiedup to ~5.0eV, whereas WS_2 monolayer sheets have a direct bandgap of ~1.9eV. Here, a liquid phase exfoliation method was used to synthesize WS_2 QDs in different solvents and their effect is observed on its optical and structural properties.This work has demonstrated the role of solvents in the optical tuning of WS_2 QDs. Tuning the size of QDs is a key parameter to enhance their performance in device fabrication.

MATERIAL AND METHODS

The bulk WS_2 powder of particle size ~2µm (99%), ethanol, dimethyl sulfoxide (DMSO), dimethyl formaldehyde (DMF), and deionized water (DI) were used in their original form as purchased from Sigma Aldrich and SRL. A simple top-down approach, liquid phase exfoliation was employed to synthesize WS_2 QDs in three different solvents (DMSO, DMF and a 35:65 mixture of ethanol and DI).Initially, a 25mg/ml solution was taken and ground with a mortar and pestle before being transferred to a bottleand more solvent was added to obtain a 1mg/ml solution. A 30- minute bath sonication was performed on the solution maintaining room temperature. Consequently, the solution was treated with a probe sonicator of Sonics Vibra cell with a 12mm diameter, 450W power, and an amplitude of 43.A 4 hours probe sonication was followed with a pulse on/off ratio of 3/2 sec respectively, keeping the solution in an ice bath to avoid heating.The collected sample was centrifuged using REMI R-24 centrifugation equipment at

12000 rpm. The supernatant was collected from the centrifuge tubes and stored in transparent glass bottles for various characterization. The samples were deposited on clean Si substrate for further studies.

RESULTS AND DISCUSSION

In this article, the synthesized WS_2 QDs in different solvents were subjected to characterization techniques to evaluate the changes in optical and structural properties. UV-Vis absorption spectroscopy and XRD measurement confirmed the synthesis of WS_2 QDs in DMSO, DMF and ethanol:DI. PL spectroscopy has been performed using Cary Eclipse setup and its effect has been observed in WS_2 QDs.

UV-Visible Absorption Studies

UV-Vis absorption spectroscopy is a potent tool to identify the sample and study its linear optical properties. UV-Vis absorption spectroscopy has been performed utilizing a SHIMADZU UV-Vis 2600 spectrometer. Figure 2 (a) has presented the UV-Vis absorption spectra for WS_2 QDs in all three solvents (DMSO, DMF and 35:65 mixture of ethanol:DI).The absorption spectra of the aqueous dispersion of QDs were recorded against incident wavelength (nm).The characteristic peak corresponding to WS_2 QDs in DMSO, DMF and ethanol:DI solvents were observed at ~ 291 nm, 338 nm and ~312 nm, respectively [3]. The absorption peak in this region confirms the existence of WS_2 QDs. It is believed that the presence of these peaks can be described to the excitonic transitions from deep valance band states to the conduction band states.To extend the UV-Vis absorption studies, the Tauc's relation has been employed on the spectra presented in Fig. 1(b). Considering WS_2 QDs as direct bandgap material, Tauc's plot has provided insight into the optical properties such as bandgap.The band gap value (E_g) has been obtained by the photon energy axis intersecting with the linear extended portion of the Tauc curve. The estimated bandgap values from Tauc's plot are ~3.70 eV, 3.97eV and 4.30eV for WS_2 QDs in DMF, ethanol:DI and DMSO solvents, respectively.The UV-Vis study infers that QDs have been exfoliated to give the highest bandgap in the DMSO solvent.

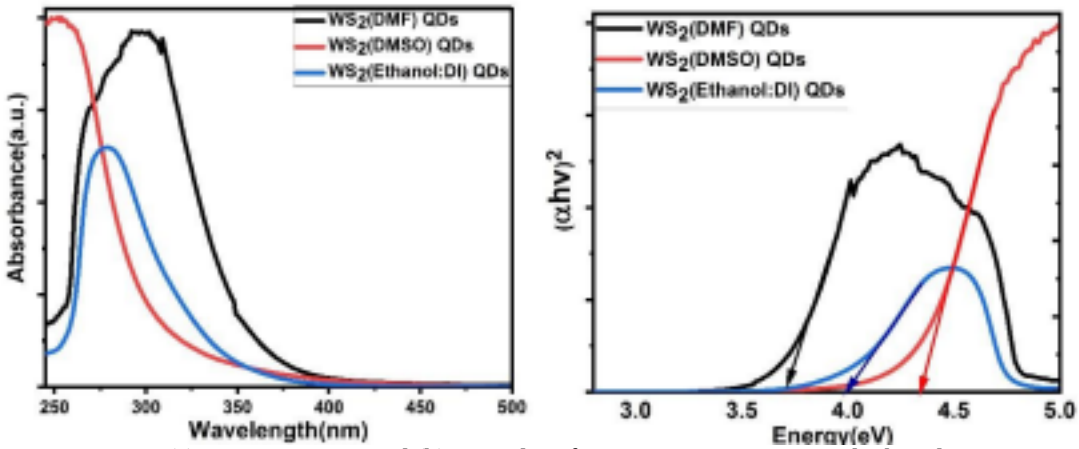


FIGURE 1. (a) UV-vis spectra and (b)Tauc plot of WS_2 in DMSO, DMF and ethanol:DI.

The effectiveness of these different solvents might be explained by a few characteristic parameters of the solvents, such as relative permittivity, surface tension etc [4]. These parameters play a significant role in determining the efficacy of a solvent used as a dispersive media.These parameters might be responsible for the bandgap modulation in WS_2 QDs when exfoliated with different solvents. A noticeable rise in bandgap will lead to the subsequent modulation of optical properties.

XRD Analysis

XRD measurement has been carried out (using Miniflex Rigaku CuK_α)for confirmation of quantum dots. XRD is a non-destructive method conducted for ascertaining materials' crystal structure and phase composition.The effectiveness of the solvent has also been observed in the crystalline nature of the WS2 QDs. Figure 2 depicts the XRD pattern for QDs in all three solvents.

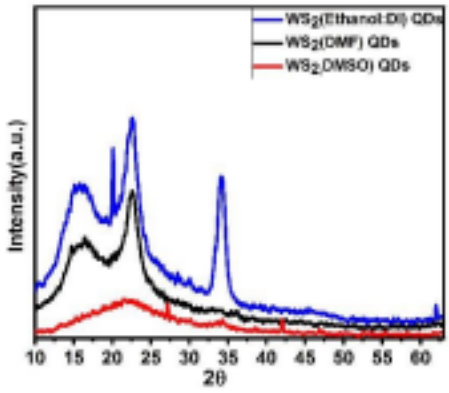


FIGURE 2. (a) XRD pattern of WS_2 in DMSO, DMF and ethanol:DI.

The XRD pattern of WS_2 QDs synthesized in different solvents has revealed the crystalline nature via various diffraction peaks corresponding to the characteristic peak positions of WS2 QDs. The peak present in the range ~12°-14° represents the (002) plane and a broad band present at ~34° confirms the presence of the (101) plane as well as the (008) plane is also visible in the QDs. Out of all the samples, The XRD pattern for QDs with DMSO solvent agrees more with the crystalline nature of WS_2 QDs. In addition to the peaks mentioned above, the intense peak at ~26° confirms the presence of the (006) plane and an intense peak at ~43° confirms the presence of the (104) plane corresponding to the characteristic planes of WS_2 QDs [4]. Studying the crystallinity of the synthesized WS_2 QDs, the one synthesized in DMSO solvent exhibits the most crystalline nature.

PL Studies

Figure 3 shows the PL spectra of WS_2 QDs in different solvents. The WS_2 quantum dots in each solvent has been excited at various wavelengths (350nm, 360nm, 370nm,380nm and 390nm) to record the modifications in their PL emission. The recorded emission spectra in a single solvent has not shown much variation at various excitation wavelengths. Here, in this work, an excitation wavelength-independent PL emission is reported for the same solvent implying the homogenous size of the QDs [5].However, a significant variation on the emission spectra for QDs in different solvents is observed for a particular excitation. The change in the photoluminescence spectra indicates the size-dependent photoluminescence emission for WS_2 QDs.

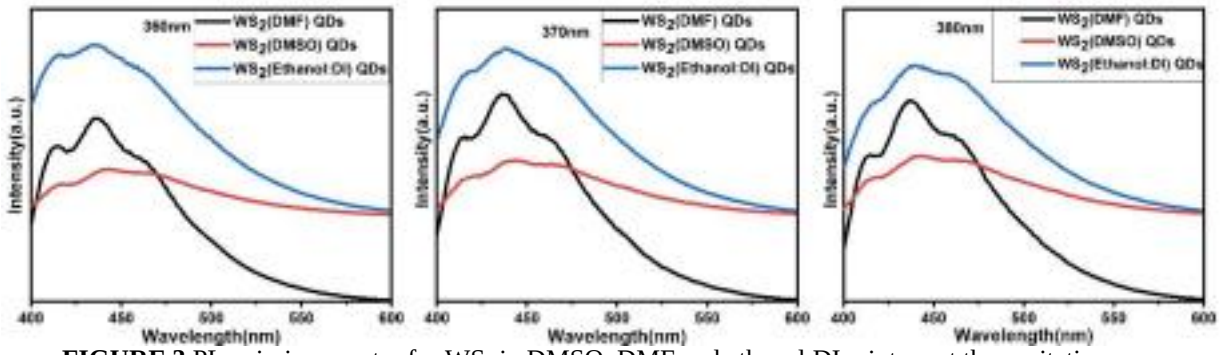


FIGURE 3.PLemission spectra for WS_2 in DMSO, DMF and ethanol:DI mixture at the excitation wavelength (a) 360nm, (b) 370 nm and (c) 380nm

The PL emission spectra for WS_2 QDs in DMSO, DMF and ethanol:DI was observed at three excitation wavelengths (360nm, 370nm and 380nm), as shown in Fig. 3(a)-(c). Interestingly, the QDs synthesized in DMSO, display a broad emission as compared to other solvent at each excitation wavelength leads to the enhancement in the PL emission of WS_2 QDs.The PL spectra exhibits the maximum emission at ~ 444.5nm, 436.25nm and 437.16nm for WS_2 QDs in DMSO, DMF and ethanol:DI, respectively. A solvent-dependent significant shift was observed for the QDs for each excitation.The PL emission spectra can be deconvoluted into three peaks. The first

two components of these three peaks, present in the range ~390-410nm and ~430-445nm, are named a neutral exciton A and excitonB, respectively. The next component, present in the range ~480-500nm, is named defect bound exciton X [3]. The first two components can be used to estimate the bandgap values for the QDs, as it indicates the direct bandgap transition from the split valence band at the k point to the conduction band.The high spin-orbit coupling in the d orbital of the Tungsten (W) atom causes the valence band edge to split near the k valley [3].The bound excitonic peak X is supposed to be originated from surface defects. The bandgap values of WS_2 QDs were also estimated using PL emission spectra in all three solvents. As the bandgap is

highest for WS_2 QDs in DMSO solvent thus, the quantum confinement effect implies the smallest size quantum dots for DMSO solvent.

CONCLUSION

In this article, the impact of three distinct organic solvents (DMSO, DMF and a mixture of ethanol:DI) was observed on the optical and structural properties of WS_2 quantum dots. The optical properties of the synthesized QDs have been studied utilizing UV-Vis absorption and photoluminescence spectroscopy. XRD measurement has been performed on the QDs to conduct structural analysis. UV-Vis absorption spectra show that the QDs synthesized in DMSO solvent have the largest bandgap (4.3 eV). The presence of crystalline planes of WS_2 QDs in the XRD pattern confirms the successful exfoliation of the quantum dots. The XRD measurements have also confirmed that the WS_2 QDs show higher crystallinity in DMSO solvent with the smallest particle size.PL spectroscopy confirms the presence of WS_2 QDs of homogeneous size generating good emission spectra in the blue to green region.The maximum emission peak intensity of the QDs was observed at ~444.9nm in DMSO, ~436.25nm in DMF and ~437.16nm in a mixture of ethanol:DI. The A and B excitonic peaks of PL spectra help determine the bandgap of QDs. PL spectra indicates that the smallest QDs were obtained in the DMSO solvent.The bandgap values estimated from PL spectra agreed with the evaluated bandgap values from UV-Vis absorption. Thus, this research helps understand the role of various solvents in tuning the optical properties of WS_2 QDs.

ACKNOWLEDGMENTS

The authors are thankful to CIF, M.Sc Chemistry Lab, JNU for XRD and PL measurement and SBT, JNU (CIF) for UV-Vis measurement. NM and VYare grateful to CSIR for providing financial support throughfellowship. Tanuja Mohanty is grateful to DST-SERB, project no- CRG/2022/007270.

REFERENCES

1. Parth Kasana, Tanmay Mahanta and Tanuja Mohanty, AIP Conference Proceedings **2265**, 030184 (2020). 2. N. P. Mani and J Cyriac, New J. Chem. **44**, 10840 (2020).

3. Bora, Larionette P.L. Mawlong et al., Journal of Colloid and Interface Science **561**, 519-532 (2020). 4. S. Sharma, S. Bhagat et al., J Mater Sci. **52**,11326–11336(2017).

5. Wenjing Miao, Xinwen Gai et.al., Mater. Adv. **3**, 1772 (2022).

Engineering Zinc Oxide Electron Transport Layers for $MAPbI_3$ Perovskite Solar Cells

Anand Pandey
Physics Department, University of Allahabad, Prayagraj, 211002, India.
Centre for Nanotechnology, Indian Institute of Technology Guwahati 781039, Assam, India

Corresponding author: anandpandeyau@gmail.com

Abstract. Electron transport layers (ETLs) in perovskite solar cells (PSCs) are essential in deciding their efficiency, charge collection, and photovoltaic device parameters. Inorganic ETLs like SnO_2, TiO_2, and ZnO are currently employed to fabricate PSCs. Despite its superior optoelectronic properties, ZnO is often overlooked in PSCs due to its chemical instability with metal halide perovskites, requiring modifications like chemical doping and surface passivation. This study focuses on engineering ZnO ETLs by incorporating different concentrations of fullerene (C_{60}) to examine the structural, optical, and device performance of C_{60}-modified ZnO ETLs in $MAPbI_3$ PSCs. The $MAPbI_3$ photoactive layers have been fabricated onto pristine and modified ZnO ETLs using a spin coating technique. Incorporating C_{60} into ZnO reduces microstructural and optical defects, such as micro-strain, Urbach energy, and trap levels, while enhancing the optoelectronic properties of $MAPbI_3$. This leads to better optical properties and improved structural stability, ultimately boosting the performance of photovoltaic devices.

INTRODUCTION

Perovskite solar cells (PSCs) have attained a power conversion efficiency (PCE) of 26 % due to their easy-to-scale synthesis, low cost, and suitable optoelectronic properties such as considerable carrier diffusion length, ambipolar charge transport, low exciton binding energy, high absorption coefficients, and tunable optical band gap [1]. A typical perovskite solar cell (PSC) consists of halide perovskite as a photoactive absorber layer, which is inserted between an electron transport layer (ETL) and a hole transport layer (HTL) [2]. Generally, hole-blocking materials such as SnO_2, TiO_2, ZnO, fullerene (C_{60}), and their derivative are utilized as ETLs. Electron-blocking materials such as PEDOT: PSS, NiO_x, P3HT, Spiro-OMeTAD, PTAA, *etc*, are commonly used as HTLs. When light shines from the transparent conducting oxide (TCO) side and is absorbed into the perovskite photoactive layer, electron-hole pairs are generated, which are further collected from the ETL or HTL side with the help of a suitable electrode [3]. Thus, selecting TCO, ETLs, and photoactive layers is necessary for better photovoltaic device performance. Inorganic ETLs like SnO_2, TiO_2, and ZnO have recently been utilized to fabricate PSCs. Despite ZnO's superior optoelectronic properties, such as better optical transmittance, higher electrical conductivity, and energy band alignment with methylammonium lead iodide ($MAPbI_3$) perovskite compared to other ETLs, it is often overlooked. This is due to its chemical instability when in contact with $MAPbI_3$, which leads to the decomposition of $MAPbI_3$ into its components [4]. To avoid this, ZnO layers must be modified using chemical doping, surface passivation, *etc*. In this work, ZnO ETLs were modified by incorporating another ETL, i.e., C_{60}, and the effects of this incorporation on ZnO were systematically investigated through structural, morphological, optical, and electrical analyses. Additionally, C_{60}-modified ZnO ETLs were used to fabricate $MAPbI_3$ perovskite films and solar cells to understand their charge transport properties and optical and microstructural defects.

EXPERIMENTAL METHODS

Materials Synthesis & Characterization

As per previous reports, zinc oxide (ZnO) or C_{60}-modified ZnO and $MAPbI_3$ perovskite layers have been synthesized [2,5]. To prepare C_{60}-modified ZnO solutions at varying ratios, C_{60} was added to the 0.35 M ZnO solution in different amounts of 0.25 mg/ml, 0.50 mg/ml, and 1.00 mg/ml, followed by thorough stirring. The resulting solutions were designated as ZnO (0 mg/ml C_{60}), ZnC1 (0.25 mg/ml C_{60}), ZnC2 (0.50 mg/ml C_{60}), and ZnC3 (1.00 mg/ml C_{60}). The fabricated thin films have been characterized using an X-ray diffractometer (PROTO-AXRD) for their structural properties using a copper-K_α radiation source, and a UV-Vis spectrophotometer (Unicam 5625) for their optical properties. Electrical characterizations of solar cells were carried out using the electric source meter (Keithley-2400) integrated with the solar simulator (AAA, PET).

Device Fabrication

The detailed schematic steps of the fabrication of PSCs are given in Fig. 1. In short, ETL layers like ZnO or fullerene (C_{60}) modified ZnO precursor were spin-coated on pre-cleaned and patterned fluorine doped tin oxide (FTO) substrates (2000 rpm, 40 s) and subsequentially annealed at 200 ºC for one h in hotplate. The photoactive layer precursor solution was prepared by mixing equal molar amounts of lead iodide (PbI_2) and methyl ammonium lead iodide (MAI) in anhydrous N, N-dimethylformamide (DMF) solution [2]. The precursor solution was stirred for 10-12 h at 60 ºC. The perovskite precursor solution was deposited on the top of pristine and modified ZnO substrates at 4000 rpm for 30 s and annealed for 10 min at 100 °C. Furthermore, 16 mg/ml poly(3-octylthiophene) (P3OT) dissolved in chlorobenzene was deposited on the top of the $MAPbI_3$ layer at 2000 rpm for 60 seconds. Finally, the Ag electrode (80 nm) was thermally deposited under the base pressure of 1×10^{-6} torr using shadow masks of active device area 0.04 cm^2 to complete the solar cell.

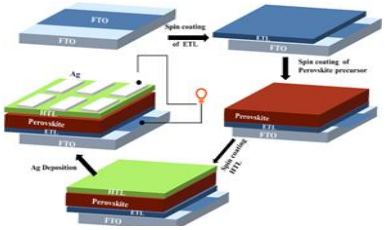


FIGURE 1. Fabrication steps of perovskite solar cells

RESULTS AND DISCUSSIONS

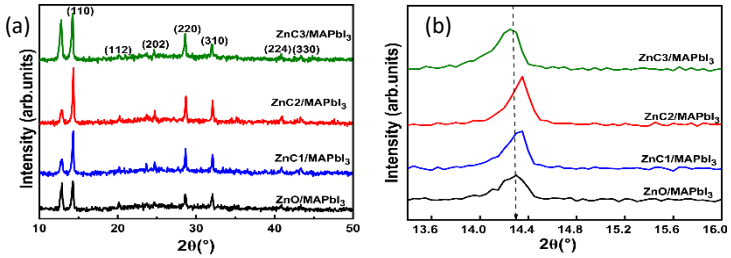


TABLE 1. Summary of structural parameters

Sample	D (nm)	δ (nm^{-2})	ε ($\times10^{-3}$)
ZnO	57	3.0	1.62
ZnC1	95	1.1	1.19
ZnC2	66	2.3	0.17
ZnC3	25	16	-2.94

FIGURE 2. (a) XRD pattern and (b) Zoom-in (110) diffraction plane around 14°of $MAPbI_3$ perovskite films fabricated onto pristine and C_{60}-modified ZnO ETLs

Figure 2 (a) shows the XRD pattern of $MAPbI_3$ perovskite films deposited onto pristine ZnO and C_{60}-modified ZnO ETLs. Peak positions at 14°, 20°, 24.7°, 28.6°, 32°, 40°, and 43° are assigned to the (110), (112), (202),(220), (310), (224), and (330) diffraction plane of the tetragonal of $MAPbI_3$ perovskite crystal structure, respectively [9]. Further, it was observed that peak positions near 12° are correspond to PbI_2. The intensity of the PbI_2 peak decreases at a specific concentration of C_{60}-modified ZnO layers, indicating the better structural stability of $MAPbI_3$ films. Further, we have found a slight shift in the $MAPbI_3$ films fabricated into different C_{60}-modified ZnO layers, as shown in Fig. 2 (b). This shift may be due to structural or optical defects [10]. To determine the structural defects, the micro-strain (ε), dislocation density (δ), and crystallite size (D) have been evaluated using the Williamson-Hall method, reported elsewhere [11], and the value of structural parameters has been summarized in Table 1.

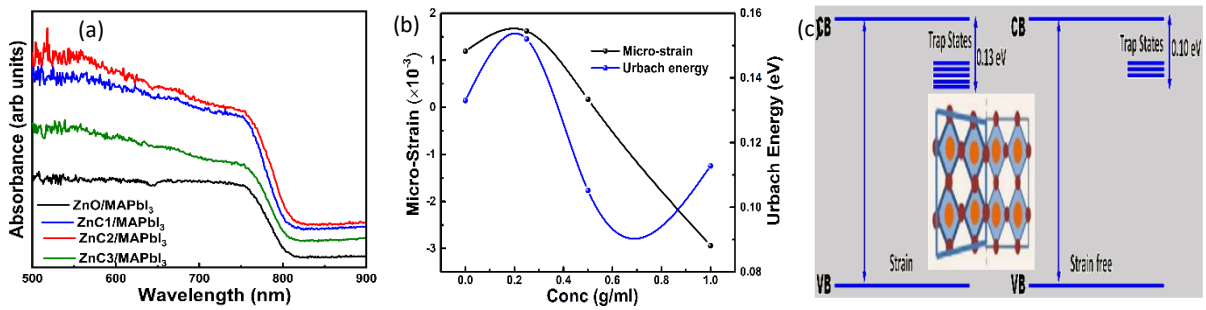


FIGURE 3. (a) UV-Vis absorbance spectra, (b) dependence of micro-strain and Urbach energy on C_{60} concentration, and (c) representation of trap states of $MAPbI_3$ films fabricated onto pristine and C_{60}-modified ZnO ETLs

The micro-strain has been observed to be minimized for $MAPbI_3$ perovskite films fabricated onto C_{60}-modified ZnO ETLs, indicating reduced micro-structural defects and lattice strain [12,13]. The UV-Vis absorbance spectra of $MAPbI_3$ films fabricated onto various ZnO ETLs have been given in Fig. 3 (a). All the $MAPbI_3$ films were fabricated onto modified ZnO layers, resulting in better optical absorption than the pristine one with a band gap of 1.52 eV. Further, the optical defects have been determined using the Urbach energy method [13], reported elsewhere, and similar trends between the optical and structural defects have been found, as displayed in Fig. 3(b-c). The trap levels were also significantly reduced from 0.13 eV to 0.10 eV, indicating the superior optoelectronic properties of $MAPbI_3$ films fabricated onto modified ZnO ETLs [14].

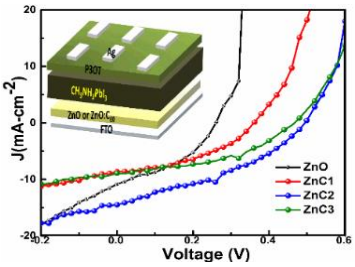


FIGURE 4. *J-V* characteristics of PSCs under illumination

Figure 4 depicts the current-voltage (*J-V*) characteristics under illumination of PSCs fabricated on pristine and modified ZnO ETLs. C_{60}-modified ZnO-based PSCs have enhanced PCE compared to pristine ZnO. The improvements in PSCs' efficiency primarily stem from the improved interface between C_{60}-modified ZnO layers and $MAPbI_3$ layers, which reduces microstructural and optical defects and facilitates faster charge extraction, thereby enhancing photovoltaic device parameters [15].

CONCLUSION

Herein, ZnO ETLs have been engineered by incorporating C_{60} in different amounts, and the influence of C_{60}-modulated ZnO ETLs on the structural, surface morphological, and optical properties has been examined. Structural results of the fabricated ETLs depict ZnO's hexagonal wurtzite crystal structure. Morphological results display the granular film morphology, which changes with C_{60} concentration. $MAPbI_3$ films fabricated onto modified ZnO ETLs depict better structural stability and enhanced optical absorbance with reduced trap levels. Additionally, localized optical and micro-structural defects in $MAPbI_3$ films fabricated onto modified ZnO ETLs have been significantly diminished. These improvements result in better photovoltaic device parameters of C_{60}-modified ZnO-based perovskite solar cells. Further research in this direction is essential to explore the potential of modified ZnO ETLs in various optoelectronic devices.

ACKNOWLEDGMENTS

Author Anand Pandey thanks the Department of Science & Technology, New Delhi, India, for the financial assistance through the INSPIRE program vide DST/INSPIRE Fellowship/2017/IF170763 under the AORC Scheme.

REFERENCES

1. NREL, *Best Research-Cell Efficiencies* (USA, 2024).
2. A. Pandey, Studies On Organometal Halide Perovskite Materials And Their Applications To Photovoltaic Devices, University of Allahabad, 2023.
3. S. J. Fonash, *Solar Cell Device Physics*, Second (Elsevier Academic Press, USA, 2010).
4. E. Moustafa, L. F. Marsal, and J. Pallarès, ACS Appl. Energy Mater. **5**, 4390 (2022).
5. A. Pandey, A. Garg, and L. Kumar, ECS J. Solid State Sci. Technol. **11**, 104002 (2022).
6. P. K. Samanta, N. K. Rana, and B. S. Kar, Phys. Scr. (2022).
7. E. Nowak, M. Szybowicz, A. Stachowiak, W. Koczorowski, D. Schulz, K. Paprocki, K. Fabisiak, and S. Los, Appl. Phys. A Mater. Sci. Process. **126**, 1 (2020).
8. A. Macková, P. Malinský, A. Jagerová, R. Mikšová, O. Lalik, P. Nekvindová, J. Mistrík, P. Marvan, Z. Sofer, V. Holý, J. D. Schutter, U. Kentsch, A. Azarov, and A. Galeckas, J. Phys. D. Appl. Phys. **55**, 215101 (2022).
9. V. Kumar, V. Nagal, R. Kumar, S. Srivastava, B. K. Gupta, M. Kumar, A. K. Hafiz, and K. Singh, RSC Adv. **10**, 34651 (2020).
10. G. Yuan, W. Xie, Q. Song, S. Ma, Y. Ma, C. Shi, M. Xiao, F. Pei, X. Niu, Y. Zhang, J. Dou, C. Zhu, Y. Bai, Y. Wu, H. Wang, Q. Fan, and Q. Chen, Adv. Mater. **35**, 2211257 (2023).
11. A. Pandey and L. Kumar, Phys. B Condens. Matter **628**, 413566 (2022).
12. W. Kong, C. Zhao, T. Huang, X. Li, J. Xing, Z. Yu, P. Yang, W. Li, and W. Yu, ACS Appl. Mater. Interfaces **14**, 28154 (2022).
13. Y. Liu, J. Banon, K. Frohna, Y. Chiang, and G. Tumen-ulzii, ACS Energy Lett. **8**, 250 (2023).
14. G. Kim, H. Min, K. S. Lee, D. Y. Lee, S. M. Yoon, and S. Il Seok, Science (80-.). **370**, 108 (2020).
15. H. Zhu, S. Teale, M. N. Lintangpradipto, S. Mahesh, B. Chen, M. D. McGehee, E. H. Sargent, and O. M. Bakr, Nat. Rev. Mater. **8**, 569 (2023).

Carbon Nanotube Based Composite Thin Film Coatings for Stray Light Control Space Applications

Sonia Saini[1,2], Kuntala Bhattacharjee[1,*] and Girish M. Gouda[2]

[1]*Indian Institute of Space Science and Technology (IIST), Thiruvananthapuram, 695 547, India*

[2]*Laboratory for Electro-Optics Systems (LEOS), ISRO, Bengaluru, 560 058, India*

[a)]Corresponding author: kbhattacharjee@iopb.res.in ; kuntala.iopb@gmail.com
[b)]first author: sonia.discover2342@gmail.com

Abstract. The research focuses on demonstrating low dimensional carbon derivative-based black thin film coatings with low light reflectance, essential for high absorber coatings to control stray light. The study details a successful process for producing stable thin films of carbon nanotubes (CNTs) and nanoscrolls (CNS) on aluminum (Al) substrate, achieving 2-3% reflectance in the visible (VIS) and near-infrared (NIR) spectrum. We report the first experimental evidence of direct manifestation of CNS formation from single-walled nanotube (SWNT) bundles via oxidative purification, significantly reducing contaminants and revealing scrolling of graphitic sheets (GS). Transmission electron microscopy (TEM) showed CNS and multi-walled carbon nanotubes (MWCNTs) emergence due to sequential chemical processing of SWNTs, revealing radial merging and catalyst particle-induced axial tearing. Scanning electron microscopy (SEM) displayed curled and folded graphene sheets, contributing to CNS formation. Microstructural studies via SEM and atomic force microscopy (AFM) identified microcavities and pores on the CNS composite films' surface, crucial for the low reflectance observed. These films maintained low reflectance in the VIS-NIR spectrum, proving durable under extreme space conditions. The thesis covers the preparation, characterizations, and testing of the CNT-CNS composite thin film coatings for low-light scattering applications, with space environmental simulation tests (SEST) indicating promising space usage potential.

Keywords: carbon nanotubes, carbon nanoscroll, composites, thin films, space applications.

Introduction

Carbon nanotubes (CNTs), with their 1D structure and excitonic optical transitions, show great promise as black absorber coatings due to their superior light-trapping ability and intrinsic properties [1]. Discovered by Sumio Iijima in 1991 [2], CNTs have become technologically significant due to their unique physico-chemical properties [1]. CNTs are categorized as single-walled (SW) CNTs that consist of a single layer of sp^2 hybridized carbon atoms in cylindrical symmetry and multi walled (MW) CNTs are nested structures of graphene layers, whereas carbon nanoscrolls (CNS) are spiral structures of rolled graphene sheets. CNS offers distinct advantages such as open-ended morphology, tunable diameter, and high carrier mobility. CNT forests have achieved high absorption such as 0.9997 [3]. Despite significant research on CNT thin films and forests, the light absorption properties of CNS are less understood. Theoretical and experimental studies suggest CNS's potential as absorber coatings [3].

We present a novel and straightforward spray coating method for creating CNT-CNS blended composite thin films on flexible aluminium (Al) substrates, achieving exceptional low reflectance levels of 2-3% in the visible and near-infrared (VIS-NIR) spectrum. Furthermore, we provide empirical evidence of CNS formation through the transformation of scrolling graphite sheets. These coatings are uniform and space environmentally stable. Characterization methods such as Raman spectroscopy, fourier transform infrared spectroscopy (FTIR), X-ray photoelectron spectroscopy (XPS), X-ray diffractometer (XRD), high-resolution transmission electron microscopy (HRTEM), field emission scanning electron microscopy (FESEM), and atomic force microscope (AFM) reveal the films' microstructural properties. Preliminary space environmental simulation tests (SEST) indicate the coatings' stability and potential for stray light control applications in spaceborne devices.

EXPERIMENTAL

The high-pressure carbon monoxide (HIPCO) SWCNTs having diameter 0.6 to 1.1 nm, and length 400-1000 nm obtained as a dry black powder in form of 96% SWCNTs along with Fe metallic impurities. Therefore, post-synthesis purification is necessary to remove these contaminants. In this study [Fig.1(a)], purification was achieved through wet oxidation at 300°C, followed by concentrated (conc.) HCl acid wash and annealing at 900°C in an inert environment. Functionalization of CNTs involved mixing conc. H_2SO_4 and HNO_3 in a 3:1 volume ratio with the purified powder. This mixture was stirred at 70°C for 8 hours, neutralized with deionized water. The

functionalized CNT powder was filtered and dried under vacuum at room temperature (RT). The dried powder was mixed with a polyurethane binder and a solvent, ultrasonicated for 60 minutes to achieve a well-dispersed solution. This solution was spray-coated onto preheated Al substrate using a hand airbrush in a glove box under a controlled nitrogen atmosphere [Fig.1(b)]. After coating, the samples were allowed to cool to RT.

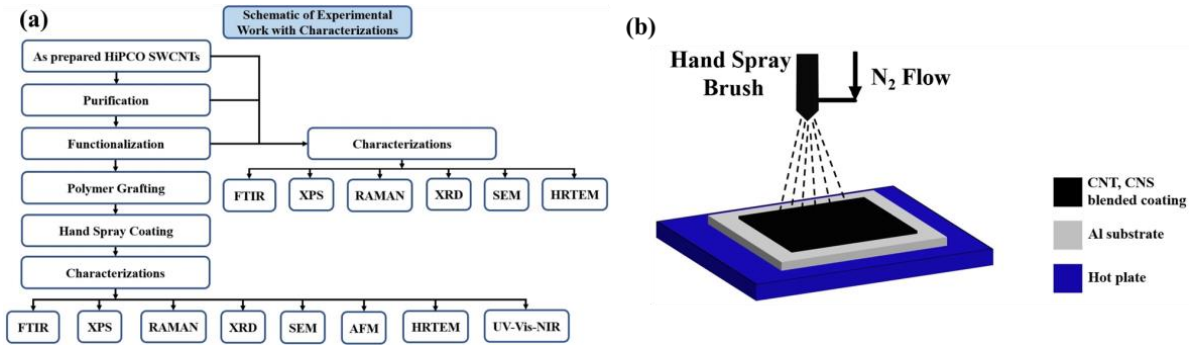


FIGURE 1. (a) flow char of Schematic of the experimental work. (b) depiction of the spray process.

FTIR absorption spectra of the KBr-powdered CNT pellets were measured using a PerkinElmer Spectrum GX spectrometer in the range of 4000 to 500 cm^{-1}. XPS measurements were performed by an AXIS Ultra DLD spectrometer to study chemical composition of the purified sample. Measurements were carried out using monochromatic Al Kα (1486.3eV) X-ray source operating at 117 W power. Survey spectra were acquired with a pass energy of 160 eV, whereas, for high-resolution O1s and C1s spectra, a pass energy of 20 eV with a step size of 0.1 eV was used. Data was analyzed using Shirley background correction and Gaussian/Lorentzian function with GL line shapes of varying full width half maxima (FWHM) for component peaks. Raman spectroscopy analysis was carried out with the Lab Ram HR 800 instrument. The surface morphology of the samples was examined by the Zeiss SEM Ultra55. AFM measurements were performed using a Bruker Dimension ICON instrument in tapping mode. HRTEM measurements were carried out using a FEI-Titam themis instrument operated at 300 kV, by drop casting on Cu grids. XRD measurements were performed using a Smartlab X-ray diffractometer by Rigaku cooperation, with data collected using monochromatic Cu Kα radiation (1.54 Å) at 40 kV and 30 mA. The spectral properties of the coated films were analyzed using the PerkinElmer Lambda 950, UV-VIS-NIR spectrometer in the range of 400 to 2500 nm. SESTs were conducted on the spray-coated samples using environmental test facilities available at LEOS, Bengaluru.

RESULTS AND DISCUSSION

XRD Study

Normalized FTIR spectra of purified and functionalized CNTs are shown in [Fig.2(a)]. Chemical incorporation of various functional components on the sidewalls of the CNTs indicates a successful functionalization of the CNTs. The absorption feature obtained at 3393 cm^{-1} [Fig.2(a)] is assigned to ─OH stretching, C═O stretching around 1734 cm^{-1} [Fig.2(a)] and at 1626 cm^{-1} is assigned to stretching of C═C graphitic group [4]. Absorption peak seen at 1375 cm^{-1} is attributed to ─C—O stretching. The most intense peak at 1067 cm^{-1} is associated with the C─O alkoxy group [Fig.2(a)] [5]. XPS measurements carried out on the purified sample, Fig.2(b) and (c) correspond to C1s and O1s lines respectively. C1s spectrum after deconvolution [Fig.2(b)] exhibits 5 peak features at around 284.6, 285, 286, 287, 289 eV which we assign to C=C sp^2, C-C sp^3, C-O alkoxy group, C=O carbonyl or epoxy -C-O-C- and O-C=O carboxyl group [6,7] respectively. The fitted O1s spectrum [Fig.2(c)] exhibit 3 spectral lines at 531.6, 532.8 and at 534 eV. The peak corresponding to 531.6 eV is attributed to -C=O, at 532.8 eV is assigned to -C-O- of COOH [8] and at 534 eV can be associated to C-OH bonds [83].

Normalized Raman spectra of samples are shown in Fig. 2(d-f). Radial breathing modes (RBMs) of SWCNTs, [Fig. 2(d)] occur between 150 and 350 cm^{-1} due to A_g symmetry of carbon[10]. D band intensity and FWHM increase from purified to the coated film [Fig. 2(e, f)], with peak positions shifting up (1343.66 to 1363.52 cm^{-1}), indicating an increase in the diameter. The intensity ratio of G to D band (I_G/I_D) decreases post-functionalization due to increased sp^3 hybridization [Fig. 2(d-f)] [10]. The G band position, influenced by elastic strain, shifts downward. Additionally, the 2D band is broader in the coated sample. XRD of the purified, functionalized and coated samples are shown in Fig.2(g-i). Peaks at ~26° and 44°, corresponding to the (002) and (101) graphitic planes (JCPDS card no. 01-075-1621) [Fig.2(g-i)]. In Fig.2(g), peaks with higher intensity and narrower FWHM, indicating better crystallinity. Fig.2(g, h) show peaks at ~42° for the (100) planes of graphitic carbon. A broad

onset at 18° is attributed to the CNS component in coated sample [Fig.2(i)] due to the solvent trapped in between the CNS layers [Fig.2(i)] [11].

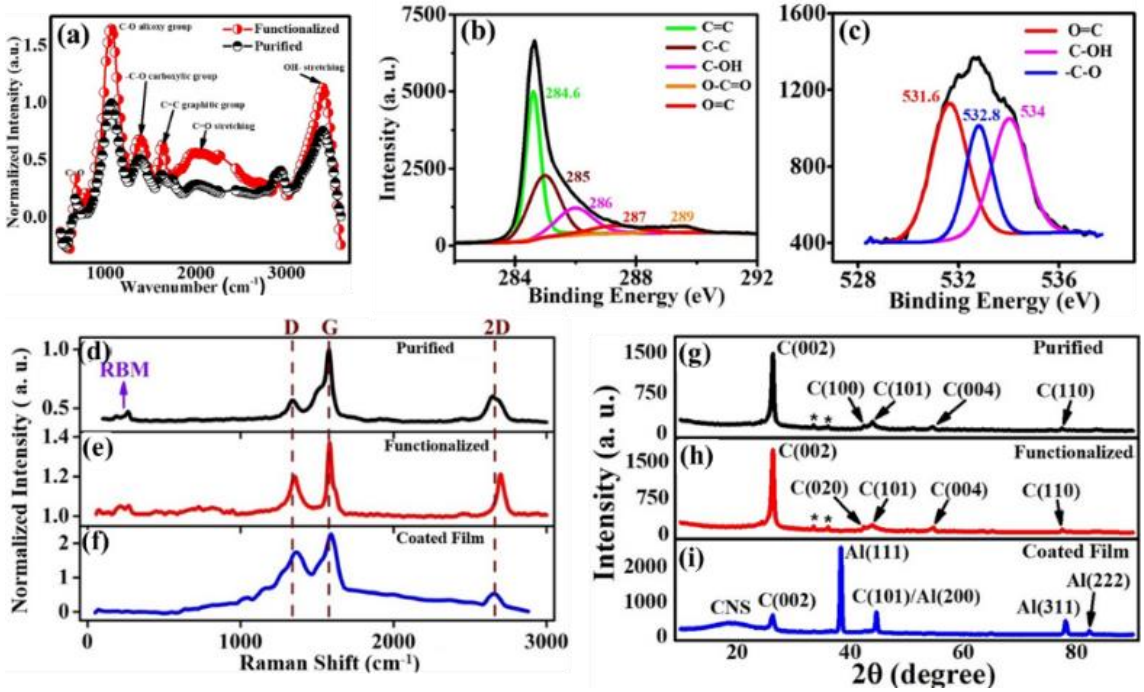


FIGURE 2. FTIR of purified and functionalized samples in (a), XPS of purified sample for C1s and O1s in (b) and (c), Raman analysis for purified (d), functionalized (e) and coated film (f), XRD of purified (g), functionalized (h) and coated film (i).

tem Studies

TEM investigations carried out on purified [Fig.3(a-f)], functionalized [Fig.3(g-l)] and coated [Fig.3(m-p)] samples. SWCNTs bundles along with Fe impurity particles [Fig.3(a-c)] (seen as dark spots), MWCNTs with graphitic spacing Fig.3(d-e) and CNS [Fig.3(f)] are evident. Attachment of functional groups onto the sidewalls of CNTs is evident in Fig.3(g). Signature of SWCNT networks with periodicity can be seen in Fig.3(h-j). Amorphous walls of functionalized MWCNTs are evident in Fig.3(k) and CNS scrolling in [Fig.3(l)]. For coated film, SWCNT bundle [Fig.3(m)], MWCNT with graphitic spacing [Fig.3(n)], entangled MWCNTs [Fig.3(o)] and GS curling into CNS [Fig.3(p)] are prominent.

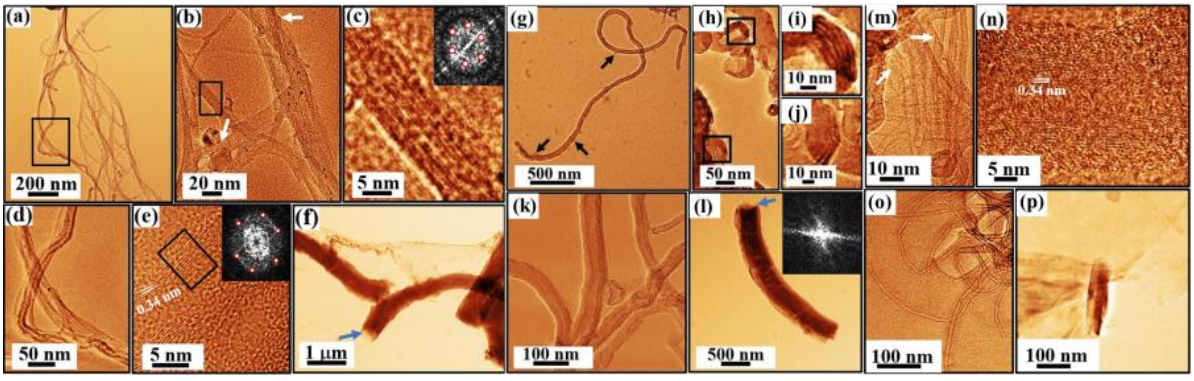


FIGURE 3. TEM of the purified sample, (a) network of SW and MW CNTs with impurity particles. (b, c) Evidence of SWCNTs marked by arrows. Inset of (c) shows the hexagonal symmetry from the SWCNT bundle. (d) MWCNTs from the marked area in (a). (e) MWCNT with graphitic (002) plane spacing of ~0.34 nm. Inset of (e) is the FFT from the selected area [rectangle]. (f) Folding of GS to form CNS. The open-end of CNS is marked with an arrow. For the functionalized sample, (g) attachment of functional groups [marked with arrows]. (h) Evidence of SWCNT bundles. Two regions in (h) [marked with squares], show the periodic alignment of SWCNTs as (i) and (j). Amorphous walls of the MWCNTs in (k). CNS with an open-end [marked with arrow] in (l) with inset: FFT of the CNS. For coated film, (m) SWCNTs (marked with arrows), (n) the graphitic plane stacking in MWCNTs, (o) the entwined MWCNT structures and (p) depicts the formation of CNS from GS.

For the purified sample, evidence of CNT nesting [Fig. 4(a)] and CNS with unfused [Fig. 4(b)] and open [Fig. 4(c)] ends is shown (marked by arrows). Nesting occurs due to σ and π bonds of the carbon atoms, with σ bonds forming a strong hexagonal carbon network and π bonds, perpendicular to the tube surfaces, resulting in weak vdW interactions [12]. After functionalization, there is even dispersion of CNTs [Fig. 4(d, f)], folding of GS to form CNS [Fig. 4(e)]. For the coated films [Fig. 4(g-i)], the cross-sectional view [Fig. 4(g)] reveals a film thickness of approximately 200 - 250 μm with interlinked forests [Fig. 4(h, i)] with cavities [Fig. 4(i)] on the surface (marked by circles).

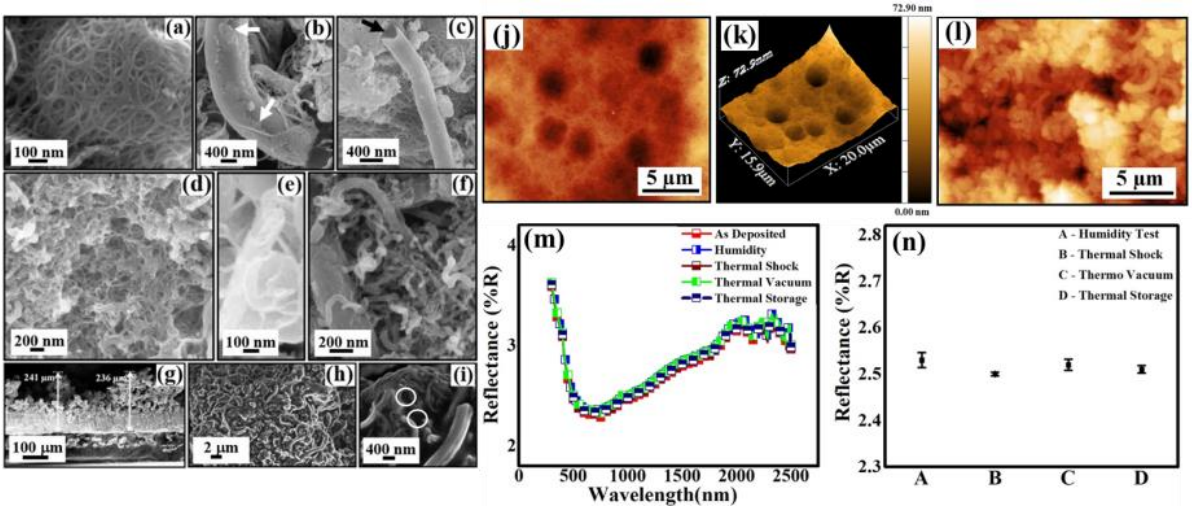


FIGURE 4. SEM of purified (a-c), functionalized (d-f) and coated (g-i) samples. The unfused edges of the CNS are marked by arrows in (b) and (c) respectively. A cross-sectional view of the coated film on the Al substrate is shown in (g) with the thickness marked. The cavities formed on the coated film are shown by circles in (i). AFM micrographs of the coated film surface (j-l). (j, l) show the surface morphology with microcavities/holes. (l) 3D projection of surface. (m) Optical reflectance studies on the coated film as well as after subjecting to SEST. (n) The standard deviation of the mean reflectance values after performing SEST w.r.t. the film.

AFM investigations on the coated films [Fig. 4(j-l)] show crosslinked forests of CNTs[12] and surface microcavities [Fig. 4(j, k)]. These pores are crucial for trapping light through multiple reflections [109].
The hemispherical reflectance for the coated film, both before and after subjecting it to SEST, are shown in Fig. 4(m). Across the spectral band of 500 - 1500 nm, a uniform reflectance variation is observed, with a minimum value of 2.3%. This behavior remains consistent after performing SEST, which includes humidity, thermal shock, thermal vacuum, and thermal storage tests, demonstrating the film's stability. Fig. 4(n) presents the standard deviation of the mean reflectance values post-SEST relative to pre-SEST values. The variation in mean reflectance is falling within the error limit, with percentage deviations ranging from 0.4 to 1.6. The thermal shock test yields the smallest variation, while the humidity test shows the highest.

CONCLUSION

Research on carbon-based black coatings is evolving, with optical properties tailored for specific applications like unwanted light control in thermal detectors, sensors and, spacecraft components. We developed stable CNT-CNS thin films via spray coating, achieving unprecedented low reflectance (2.3-2.8%) in the 500-1500 nm range. Our investigations reveal microstructural changes in SWCNTs, with MWCNTs and CNS emerging as processing-induced modifications. While MWCNTs are known for excellent optical absorption, CNS shows even greater potential. Analysis indicates that surface cavities and pores enhance light trapping capabilities. SEST results confirm these coatings as promising for space-related stray light control applications.

REFERENCES

[1] J. Lehman, C. Yung, N. Tomlin, D. Conklin, and M. Stephens, Applied Physics Reviews **5**, 011103 (2018).

[2] A. Gromov, S. Dittmer, J. Svensson, O.A. Nerushev, S.A. Perez-García, L. Licea-Jiménez, R.

Rychwalski, and E.E.B. Campbell, Journal of Materials Chemistry **15**, 3334 (2005).
[3] Z.-P. Yang, L. Ci, J.A. Bur, S.-Y. Lin, and P.M. Ajayan, Nano Letters **8**, 446 (2008).
[4] A. Misra, P.K. Tyagi, M.K. Singh, and D.S. Misra, Diamond and Related Materials **15**, 385 (2006).
[5] M.M. Stylianakis, J.A. Mikroyannidis, and E. Kymakis, Solar Energy Materials and Solar Cells **94**, 267 (2010).
[6] Y. Xing, L. Li, C.C. Chusuei, and R. V. Hull, Langmuir **21**, 4185 (2005).
[7] W. Sun, Z. Liu, C. Jiang, Y. Xue, W. Chu, and X. Zhao, Catalysis Today **212**, 206 (2013).
[8] Z. Yang, H. Peng, W. Wang, and T. Liu, Journal of Applied Polymer Science **116**, 2658 (2010).
[9] E. Desimoni, G.I. Casella, A. Morone, and A.M. Salvi, Surface and Interface Analysis **15**, 627 (1990).
[10] Q.M. Li and M.X. Shi, Proceedings of the Royal Society A: Mathematical, Physical and Engineering Sciences **464**, 1941 (2008).
[11] C.M. White, R. Banks, I. Hamerton, and J.F. Watts, Progress in Organic Coatings **90**, 44 (2016).
[12] S. Iijima, Nature **354**, 56 (1991).

The Future of Wearable Sensors: Ultrasensitive PDMS-PEDOT: PSS-AgF Nano-composites for Stretch and Motion Sensing

Debashish Nayak[1, a)], Tusharkanta Nayak[1, b)], Deviprasad Sahoo[1, c)] and Smita Mohanty[1, d)], Ram Bilash Choudhary[2,e)]

[1] *School for Advanced Research in Petrochemicals (SARP), Laboratory for Advanced Research in Polymeric Materials (LARPM), Central Institute of Petrochemicals Engineering & Technology (CIPET), Patia, Bhubaneswar, Odisha, India- 751024.*
[2]*NCML, Department of Physics, IIT (ISM) Dhanbad, Jharakhand*

[a)] Corresponding author: debashishiitism@gmail.com

Abstract. Flexible and wearable e-skin sensors have garnered considerable interest due to their potential in future smart sensing applications. However, sensitivity, biosignal detection, and implantability remain significant concerns in the advancement of embedded devices. Specifically, electrode compatibility and durability issues arise from the fragility of metal electrodes. This study presents an innovative skin-interactive polymer-based patch sensor developed using PDMS-PEDOT:PSS-Ag flex nanocomposites. The sensor, along with its encapsulation, has a remarkably slim profile of 0.30 mm. The compatibility of the PU encapsulation with the human body was assessed by measuring the contact angle and surface roughness, which were 57.65° and 0.151 nm, respectively. The results suggest excellent biocompatibility and ideal surface smoothness for wearable technology. The sensor exhibited impressive performance, showing relative resistance changes of around 580% for finger movements and 630% for neck stretching. These findings indicate that the patch sensor is highly effective in monitoring various aspects of human physiology, including movement, breathing, pulse, and pulmonary function, holding great potential for future biomedical applications and wearable sensors.

INTRODUCTION

Flexible and wearable electronics have been the subject of rapid advancement in recent years, garnering considerable interest for their potential applications in artificial e-skins, displays, robotics, sensors, IoT, battery-free technologies, and defense[1]. Within the realm of biomedical research, artificial sensor systems show great promise for various applications. Our current research is primarily centered around the development of ultrasensitive wearable and skin-mountable sensors. These sensors have the potential to revolutionize healthcare by enabling the monitoring of health conditions, tracking physiological activities, and assisting diagnostic systems. The sensors demonstrate exceptional performance in detecting human gestures, delivering precise feedback even under conditions of bending, stretching, or twisting[2].

Researchers are currently investigating polymeric nanocomposites with high electrical conductivity because of their potential to revolutionize various fields, such as wearable bioelectronics, modern devices, and human-machine interfaces[3]. The materials under investigation have demonstrated outstanding performance, indicating their potential for future research and technological progress. Among these, PDMS-PEDOT:PSS-Ag flex nanocomposites have emerged as a particularly promising alternative to traditional rigid electronics. The flexibility of these devices enables their seamless integration onto curved skin surfaces, a critical factor in ensuring accurate and high-quality collection of physiological data[4]. In this study, we present our findings on the fabrication process of a polyurethane (PU) encapsulation and its corresponding properties. Additionally, we discuss the synthesis of the polydimethylsiloxane(PDMS)-poly(3,4-ethylenedioxythiophene): poly (styrenesulfonate) (PEDOT:PSS)-silver (Ag) flexible sensing layer. Furthermore, the application of this material in sensor device fabrication is examined and its performance in monitoring finger movements and neck stretching is evaluated. The objective of these investigations is to evaluate the sensor's appropriateness for advanced biomedical applications, such as monitoring human motion, pulse, respiration, and other physiological functions in real-time.

MATERIALS DEVELOPMENT AND SENSING DEVICE FABRICATION

Materials: Polyurethane granules, Tetrahydrofuran (THF), PEDOT: PSS, Ag flex, PDMS, Ethanol, and DI water.
Development of Polyurethane film for encapsulation: Firstly, a beaker was used to hold a solution of 30 ml of THF. After preparing the solution, 5wt% of PLA based PU granules were incorporated and left to mix for 24

hours at room temperature. The resulting well-dissolved PU solution was then used to cast a film using a film casting instrument. The casting liquid is left to sit for 24 hours in order to eliminate the solvent and create a clear film as shown in Figure 1(a).

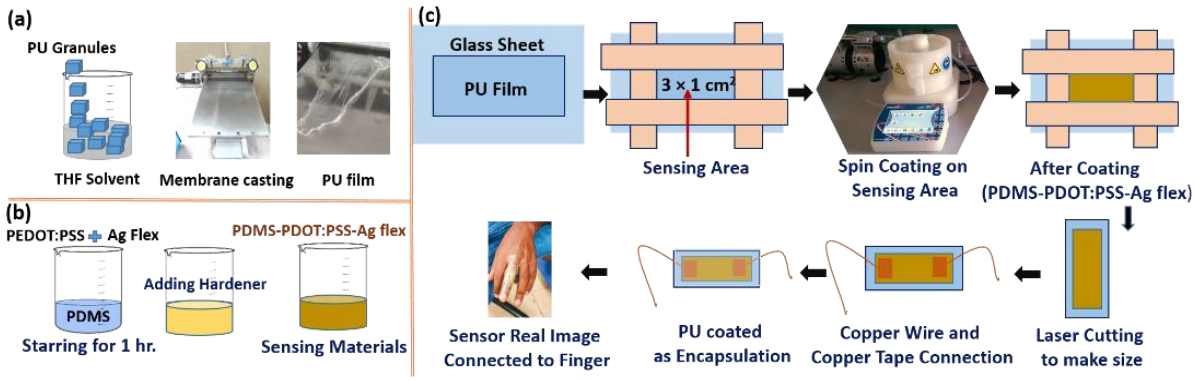


Figure 1: (a) Development of PU film; **(b)** synthesis of sensing Materials; **(c)** Fabrication of patch sensors.

Sensing layer Development: A PU film was carefully positioned on a glass slide, with a specific sensing area of 3x1 cm² being covered by Kapton tape. The sensing layer material PDMS-PEDOT:PSS-Ag flex (see Figure 1(b)) was applied onto the PU by spin-coating it at a speed of 500 rpm for 30 seconds. Afterwards, the curing process involved placing the material in an oven set at a temperature of 60°C for a duration of 12 hours. Afterward, the sensors were sized using a laser cutter. Wires were connected to the sensors using tape to ensure electrical connectivity. At last, the PU was applied to the surface of the sensing layer to provide protection. Figure 1(c) showed the fabrication process of sensor. The sensors were prepared for practical applications, such as monitoring human body movements, finger motions, and pulse sensing.

RESULT AND DISCUSSION

The structural morphology of the PU film is depicted in Figure 2(a), revealing a uniform film without any cracks. This characteristic makes it suitable for the coating of the sensing layer. Figure 2(b) shows the evenly distributed material that can be used to develop a conductive surface for efficient charge transfer. The contact angle of 57.65° observed for the PU film, as shown in Figure 2(c) of the sensors that come into contact with the human body, suggests a moderate level of wettability. This level of wettability is considered ideal as it strikes a balance between comfort and functionality. The angle of the film is important for its interaction with bodily fluids such as sweat. It needs to be just right so that it doesn't become too saturated or repel the fluids. This is crucial for accurate sensor readings and to ensure that the film maintains its structural integrity. Furthermore, the moderate contact angle of the sensor enhances its adhesion to the skin, reduces the potential for irritation, and guarantees long-term reliability and comfort during prolonged use. The roughness of the PU film was measured at 0.151 nm using AFM, as shown in Figure 2(d), suggesting a highly smooth surface. The low roughness of the surface is of great importance for researchers studying sensors in contact with the human body, as it helps to minimize skin irritation and improve overall comfort, especially during extended periods of use. The smooth surface of the sensor also aids in maintaining consistent and reliable performance by minimizing signal noise that could potentially arise from surface irregularities. Furthermore, the low roughness of the surface contributes to improved adhesion of the film to the skin, resulting in more stable and precise measurements. Therefore, the 0.151 nm roughness of the PU film presents a favorable characteristic for wearable sensor applications, as it effectively balances comfort, performance, and reliability.

Human Motion Detection: The fabricated PDMS-PEDOT:PSS-Ag flex nanocomposites-based strain sensor possesses desirable characteristics, including compact size, high sensitivity, broad sensing range, and skin-mimicking properties, making it ideal for wearable motion detection. Evaluations on different body parts, such as the finger and neck, showed excellent adhesion and precise movement detection, as illustrated in Figure 3 (e and f). Consistent relative resistance changes were observed when the sensor was bent at a constant angle, with significant variations occurring with changes in the bending angle. These resistance changes are attributed to the deformation of the conductive network within the nanocomposites material, which affects electron pathways and alters resistance. During finger exercises, the sensor exhibited a rapid response with an average relative resistance change of around 580%. This change results from the strain applied to the nanocomposites material, causing stretching and compressing, which modifies its electrical properties. In neck stretching, the sensor showed a consistent response at certain angles, with notable variations observed when the angle was adjusted, leading to an average relative resistance change of approximately 630%. These results suggest that the sensor is highly effective

for monitoring human movement and has potential applications in biomedical monitoring, such as breathing, pulse, and pulmonary function.

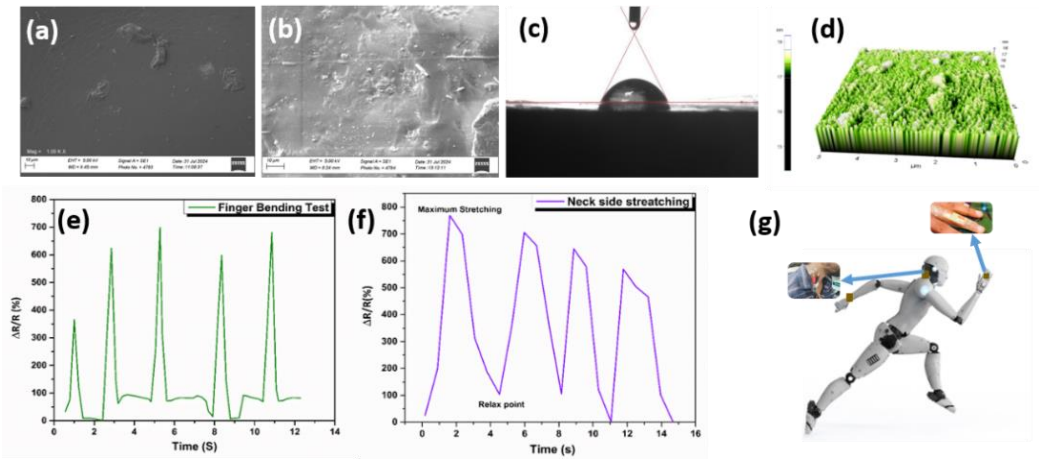


Figure 2: SEM image for (a) PU film, (b) PDMS-PEDOT:PSS-Ag; (c) Contact Angle of PU; (d) AFM of PU film; human motion detection (e) finger bending, (f) neck movement, (g) an overview of patching site location

CONCLUSIONS

In conclusion, we have effectively created a state-of-the-art wearable patch-type strain sensor, measuring just 0.30 mm in total thickness. This sensor has a sensing layer made of PU-encapsulated PDMS-PEDOT:PSS-Ag flex nanocomposites for best performance. With a contact angle of 57.65° and outstanding surface roughness of 0.151 nm, the PU film provides comfortable and efficient adherence to the human body. The performance of our sensor was verified by large resistance variations: 580% for finger motions between 0° and 90° and 630% for neck stretching. These astounding findings demonstrate the sensor's potential for cutting-edge biological uses, such as the real-time monitoring of a person's breathing, heart rate, movement, and pulmonary function.

ACKNOWLEDGMENTS

D. Nayak including all authors would like to acknowledge the Centre of Excellence (CoE) on ‘Manufacturing of Next Generation Bio-Medical Devices’ from DCPC Govt. of India (F.No:25012/01/2020-PC-II (FTS:16020) for the financial support to perform this research.

REFERENCES

1. A. Manikkavel, V. Kumar and S.S. Park, *Colloids Surfaces A Physicochem. Eng. Asp.* **688**, 133536 (2024).
2. M.U. Zaheer, and S.H. Chang.. *Adv. Compos. Mater.* **33**, 456–477 (2024).
3. T. Truong and J. Kim. *Polymers (Basel).* **16**, 373 (2024).
4. I. Elizabeth, C. Athira, S. J. Paul, and B. P. Singh. *Carbon Lett.* **34**, 1187–1195 (2024).

Energy Harvesting by Cellulose-PEDOT: PSS Aerogel-Based Triboelectric Nanogenerator

Deviprasad Sahoo[1, a)], Debashish Nayak[1], Sashwata Sahoo[1], Tusharkant Nayak[1], and Smita Mohanty[1]

[1] CIPET: School for Advanced Research in Petrochemicals (SARP) - Laboratory for Advanced Research in Polymeric Material (LARPM), Bhubaneswar, Odisha, India, 751024.

[a)] Corresponding author: deviprasad.sahoo9696@gmail.com

Abstract. This study presents a novel Triboelectric Nanogenerator (TENG) based on cellulose-PEDOT: PSS aerogel and PDMS for sustainable energy harvesting. The TENG, simulated using COMSOL Multiphysics, and experimentally operated in contact separation mode leverages the unique properties of cellulose aerogels for high electrical output yielding efficient output (60 V Voc, 100 nA Isc, 50 nC Qsc). This promising technology opens up new possibilities for mechanical energy harvesting and health monitoring applications.

INTRODUCTION

With recent advancements in flexible electronics and sensing technologies, it is now feasible to fabricate flexible and lightweight health monitoring devices. To facilitate this functionality, there is a need for a compact energy supply unit that possesses high energy density and self-charging capability. Energy harvesting devices that have recently emerged have shown promise in harnessing ambient and human-based energy sources to power sensor systems. TENG has emerged as a promising nanotechnology for sustainable energy harvesting based on the coupling effect of triboelectrification and electrostatic induction [1]. When subjected to mechanical stimuli, the electric charges transfer between two different media upon contact, converting mechanical-to-electric energy. It generally consists of tribopositive and tribonegative layers operating across different energy harvest modes (vertical contact separation, lateral sliding, single electrode, and freestanding). The performance of TENG can be optimized by using a wide variety of tribo-materials and by selecting a suitable mode of operation, which can be measured by the output parameters like open circuit voltage (Voc), short-circuit current (Isc), and short-circuit charge transferred (Qsc). In recent years cost-effective advanced polymeric and biomaterials have shown significant results across energy harvesting technology. However, studies related to TENG based on cellulose aerogel materials is very limited [2]. The unique interconnected 3D networks and air-filled pores of these cellulose aerogels have the potential to facilitate high-electrical output performance due to the synergistic effect of solid−solid contact electrification between the two electrification layers, and the gas−solid contact electrifications between the inner surface [3]. In this work, we have simulated a TENG device by COMSOL Multiphysics to obtain the electric potential distribution across different separation distances of tribopostive, and tribonegative layers. Understanding the fundamental operating principle and how different parameters impact the overall performance of the device can provide valuable insights for designing the device structure to achieve the best results in specific applications [4]. Based on the simulated model, we have fabricated a cellulose-PEDOT: PSS aerogel and PDMS-based TENG and analyzed its potential for health monitoring applications. The cellulose is extracted from sugarcane bagasse by using the TEMPO oxidation method and interacted with PEDOT: PSS followed by the freeze-drying method to form a porous aerogel structure. The synthesized material is characterized using FTIR, and SEM and their electrical output is measured by operating the TENG in contact separation mode. The efficient output of the device (Voc upto 60 V, Isc upto 100 nA, and Qsc upto 50 nC) can power smaller electronic circuits like LEDs and can charge capacitors. The performed study promises effective applicability in mechanical energy harvesting and further possibilities in health monitoring devices [5].

MATERIALS & METHODS

The developed energy harvesting device is based on the TENG mechanism. First, the TENG design is simulated using COMSOL Multiphysics (Version 6.2.0.415) to obtain the electric potential distribution across different separation distances of tribopostive and tribonegative layers. Two-dimensional finite element modeling was developed to simplify the numerical computation without sacrificing its fundamental physics significance. The parameters used in this simulation are listed in **TABLE 1**. Based on the simulated design TENG device is assembled experimentally. Cellulose-PEDOT: PSS-based aerogel composite and PDMS films were deposited as

tribopositive and tribonegative layers of the TENG device respectively. The cellulose nano-fibers were extracted from sugarcane bagasse using TEMPO oxidation technique to incorporate PEDOT: PSS composites, followed by aerogel preparation using the freeze-drying method. Fourier-transform infrared spectroscopy (FTIR) analysis was carried out by using FTIR NICOLET I S 50, for cellulose, TEMPO-oxidized cellulose, and aerogel samples. The morphological appearance of cellulose and cellulose- PEDOT: PSS aerogel is analyzed by Scanning electron microscopy (SEM: EVO MA 15, Carl Zeiss SMT). By adding 4 ml of PDMS base and 0.04 ml of curing agent to a petri dish, 0.5 mm thick PDMS films were synthesized. After that, both the tribo-positive and negative layers were assembled to fabricate a TENG device (4 cm x 2cm) operatable by contact separation mode. The copper electrode was utilized as a contact to both layers. The electrical output of the device such as open circuit voltage (Voc), short circuit current (Isc), and short circuit charge transferred (Qsc) is measured by using Keithley electrometer 6517b.

TABLE 1. Utilized parameters in the calculation of TENG's output characteristics.

	Parameter values
Dielectric 1	ε_{r1} – 2, L = 5mm, H – 0.1 mm
Dielectric 2	ε_{r1} – 3, L – 5 mm, H – 0.1 mm
Copper Contact	ε_{r1} – 1, L – 5 mm, H – 0.001 mm
Surface charge density	8 μC
Maximum separation	0.005 m
Max velocity	1 m/s

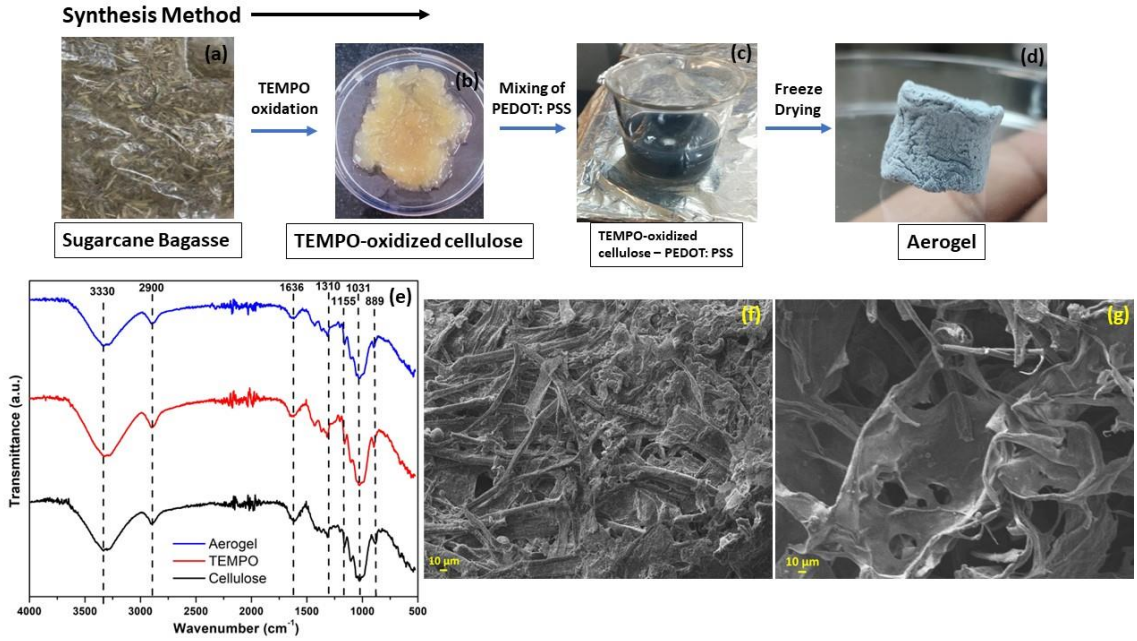


FIGURE 1. (a-d) Synthesis method of cellulose - PEDOT: PSS. (e) FTIR spectra of the synthesized sample. (f) SEM images of cellulose and cellulose-PEDOT: PSS aerogel.

RESULTS & DISCUSSION

The unique interconnected 3D networks and air-filled pores of aerogels facilitate high-electrical output performance due to the synergistic effect of solid−solid contact electrification between the two electrification layers, and the gas−solid contact electrifications between the inner surface. Based on this concept the fabricated TENG device made up of cellulose-PEDOT: PSS aerogel and PDMS have shown optimum electrical output. In

FTIR spectra, (Fig 1e) the interaction between cellulose nano-fibrils and PEDOT: PSS is observed from the diminishing peak at 1636 cm $^{-1}$ due to the protonation of CNF. Fig. 1f and 1g show the morphological appearance of CNF and CNF-PEDOT: PSS aerogel. The increase in 3D networks and air-filled pores of aerogels may have facilitated the high-electrical output performance. From the 2D TENG finite elemental modeling, it is observed that the electric potential in open circuit conditions increased up to 18 V at a maximum separation of y = 0.005 m, as shown in Fig. 2a and 2b. The simulated model has provided information about fundamental operating principles and the impact of structural parameters on the overall performance of the device. This information has provided valuable insights for designing the device structure to achieve the best results. The experimentally fabricated device was tapped continuously over a period of 40 s to record the obtained electrical output by using an electrometer. It has provided optimal output performance, with Voc up to 60 V (Fig. 2d), Isc up to 100 nA (Fig. 2f), and Qsc (Fig. 2g) up to 50 nC. Such output performance can be utilized to power smaller electronic circuits like LEDs, watches, etc., and power capacitors to work as a self-powered sensor.

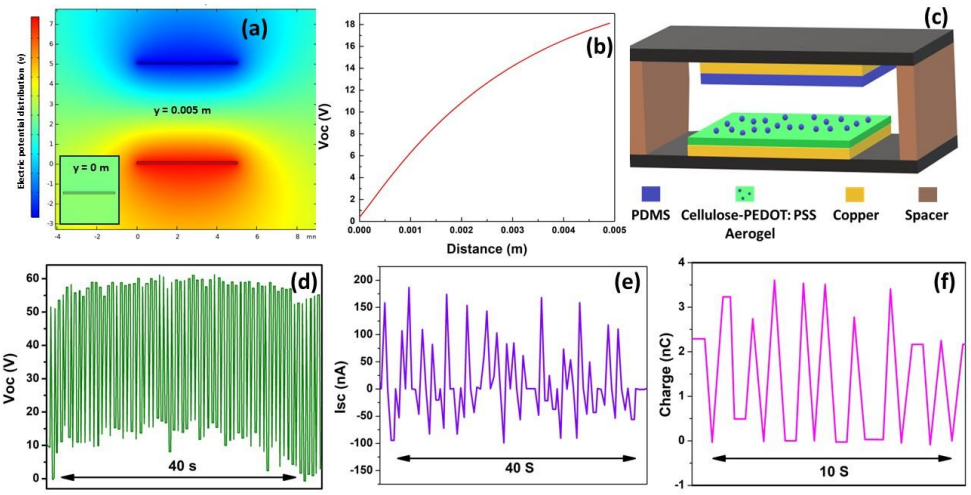


FIGURE 2. (a-d) Synthesis method of cellulose - PEDOT: PSS. (e) FTIR spectra of the synthesized sample. (f) SEM images of cellulose and cellulose-PEDOT: PSS aerogel.

CONCLUSIONS

The fabricated TENG device has shown excellent electrical outputs comparable to some recent works based on TENG, suggesting the effective performance of cellulose/PEDOT: PSS-based aerogel and PDMS tribo-layers Moreover, The CNF aerogel-based TENG is also capable of sensing physiological movements and charging micro-electronic devices. The proposed device also has the potential to harvest energy from cardiovascular activity while simultaneously monitoring its behavior for early detection of cardiovascular abnormalities. This technology would revolutionize the health monitoring device sector and other cutting-edge applications based on energy harvesting from aerogel-based electronic devices and the management of renewable energy resources.

ACKNOWLEDGMENTS

D. Sahoo, including all authors would like to acknowledge the Center of Excellence (CoE) on ‘Manufacturing of Next Generation Bio-Medical Devices’ from DCPC Govt. of India (F. No: 25012/01/2020-PC-II (FTS: 16020) for the financial support to perform research.

REFERENCES

1. T. Cheng, et al., Adv. Mater Technol 2019, 4 (3), 1800588.
2. J. Zhou, et al., ACS Appl. Mater Interfaces 2018, 10 (33), 27902–27910.
3. N. Meng, et al., Adv. Funct. Mater 2024, 34 (23), 2313534.
4. S. Niu, et al., Adv. Funct. Mater 2014, 24 (22), 3332–3340.
5. F. Yi, et al., Adv. Funct. Mater 2019, 29 (41), 1808849.


ANTON PAAR INDIA PVT. LTD.
LASER SCIENCE SERVICES
Registration Desk